Talanta

Aims & Scope

Talanta provides a forum for the publication of original research papers, preliminary communications, and critical reviews in all branches of pure and applied analytical chemistry. Papers are evaluated based on established guidelines, including the fundamental nature of the study, scientific novelty, substantial improvement or advantage over existing technology or methods, and demonstrated analytical applicability. Original research papers on fundamental studies, and novel sensor and instrumentation development, are especially encouraged. Novel or improved applications in areas such as clinical and biological chemistry, environmental analysis, geochemistry, and materials science and engineering are welcome.

Analytical performance of methods should be determined, including interference and matrix effects, and methods should be validated by comparison with a standard method, or analysis of a certified reference material. The developed method should especially comprise information on selectivity, sensitivity, detection limits, accuracy, and reliability. However, applying official validation or robustness studies to a routine method or technique does not necessarily constitute novelty. Proper statistical treatment of the data should be provided. Relevant literature should be cited, including related publications by the authors, and authors should discuss how their proposed methodology compares with previously reported methods.

Since classical spectrophotometric measurements and applications (including derivative spectrophometry), fluorimetry, solvent extraction, titrimetry, chemometrics, etc. are well established and are considered routine analytical methods, studies in such areas should demonstrate a unique and substantial advantage over presently known systems. New reagents or systems should demonstrate clear advantage, and their presentation should be comprehensive rather than generating a series of similar papers for several analytes or similar reagents. Modifications of reagents should demonstrate significant improvements. Obvious application of known chemistries or methods to established instrumental techniques are discouraged.

Application of established analytical approaches to relatively simple matrices having no major interferences, such as pharmaceutical preparations, are discouraged unless considerable improvements over other methods in the literature are demonstrated. Papers dealing with analytical data such as stability constants, pK_a values, etc. should be submitted to more specific journals, unless novel analytical methodology is demonstrated, or important analytical data are provided which could be useful in the development of analytical procedures.

Development of an automatic solid phase extraction and liquid chromatography mass spectrometry method by using a monolithic column for the analysis of Cyclosporin A in human plasma

Covadonga Alvarez [a], Irving W. Wainer [b],*

[a] *Department of Pharmaceutical Technology, Faculty of Pharmacy, Complutense University of Madrid, 28040 Madrid, Spain*
[b] *Laboratory of Bioanalytical Chemistry, Gerontology Research Center, National Institutes of Health, 5600 Nathan Shock Drive, Baltimore, MD 21224-6825, USA*

ABSTRACT

A sensitive and specific and automated liquid chromatography–electrospray mass spectrometric (LC–ESI-MS) assay for the quantification of Cyclosporin A in human plasma was developed. Following a simple protein precipitation step, the supernatant was extracted on-line and directly injected into the system LC–ESI-MS. A relatively new type of monolithic column consisting of a silica rod with bimodal pore structure was used to achieve a retention time of 2.4 min with a very low backpressure at a flow rate of 1 ml/min. The assay was linear from 0.050 to 1.000 μg/ml. The mean recovery was 91%. The mean inter-day and intra-day precisions were 1.85% and 2.83%, respectively. The combination of the automated solid phase extraction and the low retention time achieved with this columns increase the throughput and decrease the time of analysis of each sample. This technology is useful in order to improve the efficiency of the bioanalytical studies.

Published by Elsevier B.V.

1. Introduction

Monolithic materials for the use in HPLC are one of the tools for bioanalysis [1,2]. Different monolithic-type HPLC columns based on silica for fast separation have developed achieving speed, sensitivity and selectivity with low backpressure.

The use of the Merck Chromolith columns is described in this paper. These columns are prepared according to a sol–gel process, which is based on the hydrolysis and polycondensation of alkoxysilanes in the presence of water-soluble polymers [3,4].

The method leads to rods made of one piece of porous silica with a defined porous structure. The main feature of silica rods columns is a higher total porosity, about 15% higher than for conventional particulate HPLC columns. The column pressure drop is therefore much lower, allowing to operate at higher flow rates including flow gradients. Consequently, the high speed and good separation can be achieved at the same time using this type of monolithic column. The important feature of this is its relevance in high-throughput bioanalysis [5]. The method described has been used to screen over 4000 compounds thus far and has met the sensitivity and reproducibility criteria on over 97% of the compounds tested. The advantage of this method is that development time is no longer needed to investigate new drug candidates, and little, if any, sample preparation time is required. The result is increased productivity through higher sample throughput.

As a direct result of the short analysis times offered by these monolithic columns, sample preparation has become the rate-limiting step. Much effort has also been devoted in order to automate the sample preparation step [6]. Another possible approach to overcome the problem of high pressure associated with small particles is to fabricate a column made of one piece of a porous solid with small-sized skeletons and relatively large through-pores which could provide both low pressure drop and high column efficiency. The skeletons can be meso-porous or microporous to have double-pore structures, or even nonporous. The most important features are high mechanical stability of beds and the freedom in the ratio of through-pore size to skeleton size. Several examples of such monolithic columns made of an organic polymer have been reported recently.

The Cyclosporin A (CsA) (Fig. 1) has been used widely as an autoimmune drug in organ transplantation, treatment of autoimmune disorders and psoriasis [7]. The analysis of CsA in biological samples by high-performance liquid chromatography has been reported before [8–10]. The most sensitive method was achieved by coupling liquid chromatography to mass spectrometry (LC-MS) [11] or tandem mass spectrometry (LC-MS-MS) [12].

A first side-by-side comparison of the two main types of commercially available monolithic nano-LC column used in reversed-phase liquid chromatography by using them to analyze a real-life proteomics sample (*A. thaliana* chloroplast) has been

* Corresponding author. Tel.: +1 410 558 8498; fax: +1 410 558 8409.
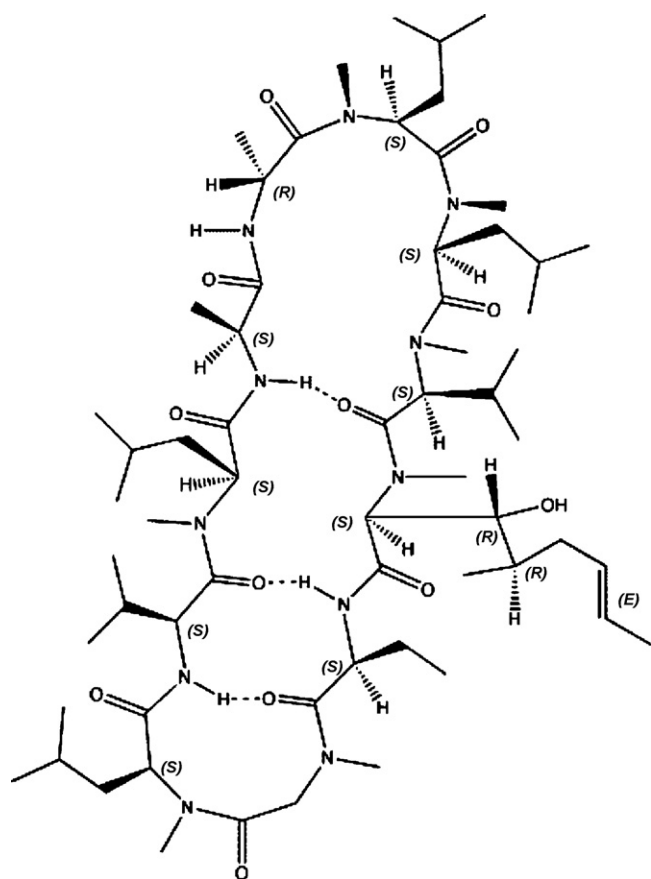*E-mail address:* wainerir@grc.nia.nih.gov (I.W. Wainer).

Fig. 1. Chemical structure of Cyclosporin A.

studied [14]. Superior separations were difficult to achieve on PS-DVB when strict MS-targeted conditions were adhered to (i.e. no additional ion-pairing agents were permitted in the mobile phase). In such cases, the conclusion was that nano-LC columns made from monolithic silica outperform those made from polystyrene in terms of separation efficiency and number of peptides collected. In addition, the higher permeability of the monolith allowed higher flow rates to be used, which enabled an increase in the information throughput. This should be of particular interest to those who wish to couple RP–HPLC with separation methods without sacrificing analytical throughput.

The aim of this work was to develop a new LC-MS method for CsA determination in human plasma by using the monolithic-type columns (Chromolith Performance) in combination with an automatic solid phase extraction (SPE) system in order to approach for optimizing its extraction and quantitation, after oral administration, achieving fast separation and high throughput.

2. Experimental

2.1. Chemicals

HPLC grade acetonitrile was purchased from Fisher Scientific (Fairlawn, NJ, USA). Ultra-pure water was obtained from Mili-Q water purification system (Millipore, Milford, MA, USA). Analytical grade ammonium acetate was obtained from J.T. Baker (Phillipsburg, NJ, USA). CsA was purchased from Sigma–Aldrich (St. Louis, MO, USA). Blank human plasma (Sodium heparin as anticoagulant) was used to prepare calibration and quality control samples (Valley Biomedical).

2.2. Instrument

The HPLC equipment consisted of an HP 1100 Series with a ChemStation (Hewlett Packard, Waldbronn, Germany) with electrospray, positive mode (API–ES). The separation column was Chromolith Performance RP-18e (10 mm × 4.6 mm) from Merck (Merck KgaA, Darmstadt, Germany) was eluted by 90% acetonitrile/10% ammonium acetate buffer pH 5.1 with a flow rate of 1 ml/min. The injection volume was 50 μl and the column temperature was maintained at 43 °C.

The LC–API–ES-MS conditions were set as follows: the fragmentor voltage was 250 V, the nitrogen gas flow was maintained at 11 l/min, the nebulizer pressure was set up at 40 psig, the positive capillary voltage was 3500 V and the drying gas temperature was 350 °C. The quantification is based on the total peak area of the CsA in SIM chromatogram.

2.3. Automatic sample preparation

The extractions were performed in an automatic Gilson ASPEC XL (West Beltline, Hwy, USA). The system is designed for the automation and optimization of SPE in order to provide a more efficient sample preparation. In addition the system is fitted with an injection valve for performing SPE with on-line injection onto the system.

Plasma samples (500 μl) were loaded onto the extraction cartridges (Oasis HLB, Waters Corporation, Milford, MA, USA), which had been preconditioned sequentially using 500 μl of methanol and 500 μl of water. The cartridge was then washed using 500 μl of water followed by elution with 500 μl of methanol with 2% of HCl. The eluted samples were directly injected into the LC–API–ES-MS system.

2.4. Methods

2.4.1. Optimization of LC–API–ES-MS experimental conditions
In order to set up the optimized conditions, the following parameters were tuned: the fragmentor voltage (50–250 V), the capillary voltage (1000–4000 V), the nebulizer pressure (40–60 psig) and the drying temperature (200–350 °C).

2.4.2. Calibration curve
The determination of CsA was based on the external standard method. Five point calibration curves (triplicate injections) were created at 0.05, 0.125, 0.250, 0.500 and 1.000 μg/ml.

2.4.3. Recovery, precision and accuracy
The recoveries were determined by comparing the peak areas of plasma premixed with a known amount of CsA with that of an equivalent amount of standard CsA dissolved in pure methanol. For intra-day precision, spiked plasma samples with three different concentrations (0.050, 0.250 and 1.000 μg/ml) were analyzed. For the inter-day precision, the above samples were analyzed on three subsequent days.

Accuracy was measured using CsA standard samples (0.050, 0.125, 0.250, 0.500 and 1.000 μg/ml) and calculated as the deviation from the theoretical values.

3. Results and discussion

3.1. Optimization of the LC–API–ES-MS conditions

In order to measure the concentration of CsA in plasma with high sensitivity the API–ES interface parameters including the fragmentor voltage, the positive capillary voltage and the drying gas temperature were tested.
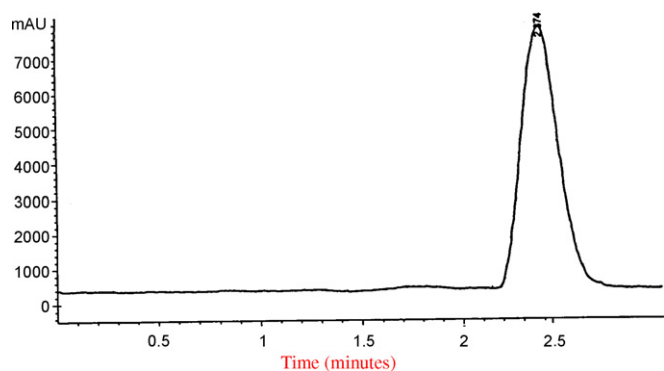
Fig. 2. Chromatographic profile of Cyclosporin A (CsA) after optimization of the chromatographic system.

The fragmentor was set up at 250 V. The positive capillary voltage was raised at 3500 V, and the optimal conditions for the drying gas temperature was approached at 350 °C.

With the optimal conditions the peak quality is shown in Fig. 2. As can be seen in Fig. 2 the retention time obtained is ≈2.4 min, due to the high porosity of the monolithic silica rod columns which posses a higher total porosity, allowing the use of a high flow rate achieving a low backpressure. The decrease on retention time is evident in comparison with previous studies. Salm et al. [13] obtained a retention time of 17 min for CsA by using a 10 μm Bondepak C_{18} column (3.9 mm × 300 mm I.D., 10 μm particle sizes, Waters, Milford, USA). The mobile phase was a mixture of acetonitrile–methanol–deionized water (55:15:30) (v/v/v). The use of other type of particulate column (phenyl type) is also described in the bibliography for CsA samples [10] achieving a retention time of 8 min.

3.2. Linearity, accuracy and recovery of the LC–API–ES–MS method

The LOD, defined as the minimum analyte concentration that produced an instrumental signal significantly different from that of the blank, was calculated in accordance with the IUPAC's criterion, i.e. as the analyte concentration giving a signal exceeding that of the blank (y_B) by 3 times its standard deviation (S_B). The LOQ, defined as the minimum analyte concentration needed to ensure precise quantitative measurements, was determined similarly, using 10 times the standard deviation for the blank instead. Thus, LOD and LOQ were calculated from the following expression:

$$LOD(LOQ) = \frac{y_B + 3(10)S_B}{b}$$

where b is the slope of the calibration curve. The limit of detection (LOD) and the limit of quantification (LOQ) for the CsA in plasma were 0.0004 and 0.015 μg/ml, respectively.

The standard curve was created between 0.050 and 1.000 μg/ml with a typical correlation coefficient of 0.9989

Table 1
Accuracy of the LC–ESI–MS method ($n = 3$).

Theoretical concentration (μg/ml)	Measured concentration (μg/ml)	C.V. (%)	Accuracy (%)	Deviation (%)
0.050	0.046	4.70	91.86	−8.14
0.125	0.124	2.07	99.88	−0.12
0.250	0.259	1.92	103.86	+3.86
0.500	0.497	3.60	99.43	−0.57
1.000	1.092	4.30	109.18	+9.18

($A = -5399.16 + 6511.32 \times C$), where A achieves the absorbance obtained and C de-concentration achieved expressed in μg/ml. The peak area increased also linearly over the range from 0.015 to 5.000 μg/ml (correlation coefficient 0.99). Detailed accuracy data obtained by the analysis of a set of spiked plasma samples are listed in Table 1. The coefficient of variance (C.V.) was less than 3% over the whole analytical range and the deviations were less than 10%. Detailed precision data obtained by the analysis of a set of spiked plasma samples are listed in Table 2. The coefficients of variance for both, intra-day and inter-day data were less than 3% over the whole analytical range.

When CsA was added to blank plasma, over 90% was recovered with the 2% HCl methanol extraction in the automatized ASPEC XL system and analyzed by the optimized procedure (Table 2).

Table 2 shows the inter-day and intra-day precisions which were less than 3% for 0.050, 0.125 and 1.000 μg/ml samples.

The previous results show that the developed method has a good accuracy, recovery and precision, than other existing methods described before [15], but with the main advantage of the increased throughput due to the monolithic column which allows the decrease on the retention time (2.4 min) in comparison with other methods described before [10,11] and the automated SPE system in a sequential input. This input consists in a total extraction time of 6 min, while the LC-MS system is analyzing the previous sample. This total and real time of 6 min/sample allows the system to analyze 10 samples/h. At this point the blood samples under this study were analyzed following this possibility.

Other methods have been described in literature with the similar purpose [16]. It has been shown that the use of short monolithic silica columns coupled to mass spectrometry provides reduced analytical run times for the purpose of metabolite identification from different samples compared to conventional analytical chromatography, with no loss in chromatographic performance.

3.3. Application of the new method

Previous studies have shown that the absorption of oral CsA was shown to be slow and incomplete [17]. Peak blood CsA concentrations occurred between 1 and 8 h after dosing. The peak blood concentration ranged from 0.165 to 3.431 μg/ml. Therefore our method is perfectly up to be used in pharmacokinetic studies after oral administration of CsA. This is the beginning for further studies that will be developed in the future.

Table 2
Recovery (%) of CsA ($n = 3$) from human plasma and precision of the LC–ESI–MS method.

Concentration (μg/ml)	Recovery (% ± SD)	Precision (C.V. %)	
		Intra-day (average)	Inter-day (average)
0.050	94.58 ± 2.48	(1.68, 1.69, 1.73) 1.70	(2.62, 2.59, 2.64) 2.62
0.125	92.37 ± 6.46	(2.06, 2.10, 2.06) 2.07	(3.10, 2.97, 3.21) 3.09
1.000	92.39 ± 4.73	(1.93, 1.79, 1.80) 1.80	(2.86, 2.97, 2,60) 2.80
		Mean average (C.V. %)	
		1.84	2.81

4. Conclusions

The results shown in this report describe a simple and sensible analytical method for the CsA in biological samples after oral administration. The monolithic-type column Chromolith decreased the retention time of the CsA from 12 min with phenyl columns [10] into 2.4 min, and in combination with the highly automated nature of the method significantly improved the sample analysis throughput (6 min/sample). The LC–API–ES-MS method can detect samples in the range of 0.015–5.000 μg/ml with linear response.

Added in proof

Salm et al. [18] have recently reported an lc-ms assay for CsA with a run time of 1.5 min per sample.

Acknowledgements

References

[1] S. Hjerten, J.L. Liao, R. Zhang, J. Chromatogr. 473 (1989) 273.
[2] S. Hjerten, Y.M. Li, J.L. Liao, J. Mohammad, K. Nakazato, G. Petterson, Nature 356 (1992) 810.
[3] H. Minakuchi, K. Nakanishi, N. Soga, N. Ishizuka, N. Tanaka, Anal. Chem. 68 (1996) 3498.
[4] H. Minakuchi, K. Nakanishi, N. Soga, N. Ishizuka, N. Tanaka, J. Chromatogr. 762 (1997) 135.
[5] R. Plumb, G. Dear, D. Mallet, J. Ayrton, Rapid Commun. Mass Spectrom. 15 (2001) 986.
[6] J.P. Allanson, R.A. Biddlecombe, A.E. Jones, S. Pleasance, Rapid Commun. Mass Spectrom. 10 (1996) 811.
[7] D. Faulds, K.L. Goa, P. Benfield, Drugs 45 (1993) 953.
[8] J. Tuominen, T. Suortti, K. Ishikawa, J. Lundell, Y. Koga, Rapid Commun. Mass Spectrom. 12 (1998) 1085.
[9] D.W. Holt, A. Johnston, B.D. Kahan, R.G. Morris, M. Oellerich, L.M. Shaw, Clin. Chem. 46 (2000) 872.
[10] O. Van Tellingen, M. Kemper, F. Tijssen, J. Van Asperen, W.J. Nooijen, J.H. Beijnen, J. Chromatogr. B: Biomed. Sci. Appl. 719 (1998) 251.
[11] L. Zhou, D. Tan, J. Theng, L. Lim, Y.P. Liu, K.W. Lam, J. Chromatogr. B: Biomed. Sci. Appl. 754 (2001) 201.
[12] J. Simpson, Q. Zhang, P. Ozaeta, H. Aboleneen, Ther. Drug Monit. 20 (1998) 294.
[13] P. Salm, R.L. Norrisd, P.J. Taylor, D.E. Davis, P.J. Ravenscroft, Ther. Drug Monit. 15 (1993) 65.
[14] V. Guryča, S. Kieffer-Jaquinod, J. Garin, C. Masselon, Anal. Bioanal. Chem. 392 (2008) 1291.
[15] J.R. Ptachcinski, R. Venkataramanan, J.T. Rosenthal, G.U. Buckart, R.J. Taylor, T.R. Hakala, Clin. Pharmacol. Ther. 38 (1985) 296.
[16] G. Dear, R. Plumb, D. Maliert, Rapid Commun. Mass Spectrom. 15 (2001) 152.
[17] Y.J. Lee, S.J. Chung, C.K. Shim, J. Pharm. Biomed. Anal. 22 (1) (2000) 183.
[18] P. Salm, P.J. Taylor, F. Rooney, Ther. Drug Monit. 30 (2008) 292.

Strategies for the identification of urinary calculus by laser induced breakdown spectroscopy

Jesús Anzano *, Roberto-Jesús Lasheras

Laser Laboratory and Environment, Department of Analytical Chemistry, Faculty of Sciences, University of Zaragoza, Pedro Cerbuna #12, 50009 Zaragoza, Spain

ARTICLE INFO

ABSTRACT

The present work studies two different strategies to identify urinary calculus. On one hand, (linear or parametric and rank or non-parametric) correlation methods using a μ-LIBS system are studied. On the other hand, elemental ratios of reference materials are determined by using a higher-energy laser and an Echelle spectrograph with an ICCD camera, although without microscope. A data-treatment method was applied for each system and real samples of kidney stones – previously analyzed by IR spectroscopy – were used for reliable evaluation of two identification strategies.

© 2009 Elsevier B.V. All rights reserved.

1. Introduction

Stone formation in urinary tracts or kidney is known as urolithiasis. About 4% of Spanish women and men develop a kidney stone at some time in their life—an increasing prevalence in both sexes. Its incidence rate is 0.27% in Spain; therefore, there are 1.7 millions of inhabitants suffering from kidney-stone disease and 100,000 new cases appear every year [1].

Approximately 75% of these stones are usually composed of calcium sales (50% of these stones are calcium oxalate, CaOx) and 10–20% are composed of uric acid (UA). In Zaragoza (Spain), an epidemiology study showed that 40% of stones are composed of calcium oxalate (CaOx), 30.6% of calcium oxalate and calcium phosphate (CaP) mix, 21.7% of uric acid, 0.9% of magnesium ammonium phosphate (MgP), 0.9% of cystine and 5.9% of others (sodium urate, calcium carbonate, etc.)

Therapy to prevent calculi recurrence requires estimating the composition of urinary calculi. Traditional wet chemistry techniques, X-ray diffraction and infrared (IR) spectroscopy are the current analytical methods [2]. These techniques include some disadvantages; for instance, wet chemical analysis requires large sample amounts, while X-ray diffraction cannot detect amorphous samples. IR spectroscopy has been applied within clinical chemistry but often provides complex spectra with contributions from a sizeable number of unknown interfering substances [2]. IR spectroscopy has often been combined with complex software such as

multivariate calibration methods. Thus, Fourier transform infrared spectroscopy (FT-IR) has been used to perform a computerized search in several libraries and partial least-squares (PLS) regression has been tested for the most frequent urinary compositions. However, these techniques require several steps of data preprocessing [3]. To minimize data treatment, artificial neural network models for detecting the most frequent stone compositions have been studied [4] and a single reflection accessory for FT-IR and neural network algorithm interpretation has been developed; however, visual inspection of spectra is still necessary [2].

Laser induced breakdown spectroscopy (LIBS) or Laser induced plasma spectrometry (LIPS) has been used for clinical analysis [5–8]. LIBS' advantages for clinical analysis are: sample treatment is not necessary and little amount of sample is used; this technique is not destructive and, therefore, the sample may be re-analyzed by means of other techniques; and it is very fast and the sample can be studied by using microscope when the μ-LIBS system is used.

LIBS has been used to identify organic compounds by means of different strategies: (i) correlating the LIBS spectrum of unknown compounds with library spectra [9,10], (ii) determining the ratios of different emission lines and molecular bands [11–16], and (iii) using artificial neural networks [17]. The parametric and non-parametric correlation method involves studying multiple emission lines and molecular bands. However, methods working with determining ratios almost exclusively consist of a few lines and bands.

Although limitations for identification exist – due to the loss of molecular information in plasma – the technique achieves excellent potential for online, real-time analysis. Nd:YAG laser has been used for other applications due to its simplicity, easy operation, high efficiency, low cost and suitability. Previous papers [9,10] have

* Corresponding author. Tel.: +34 976762684; fax: +34 976761292.
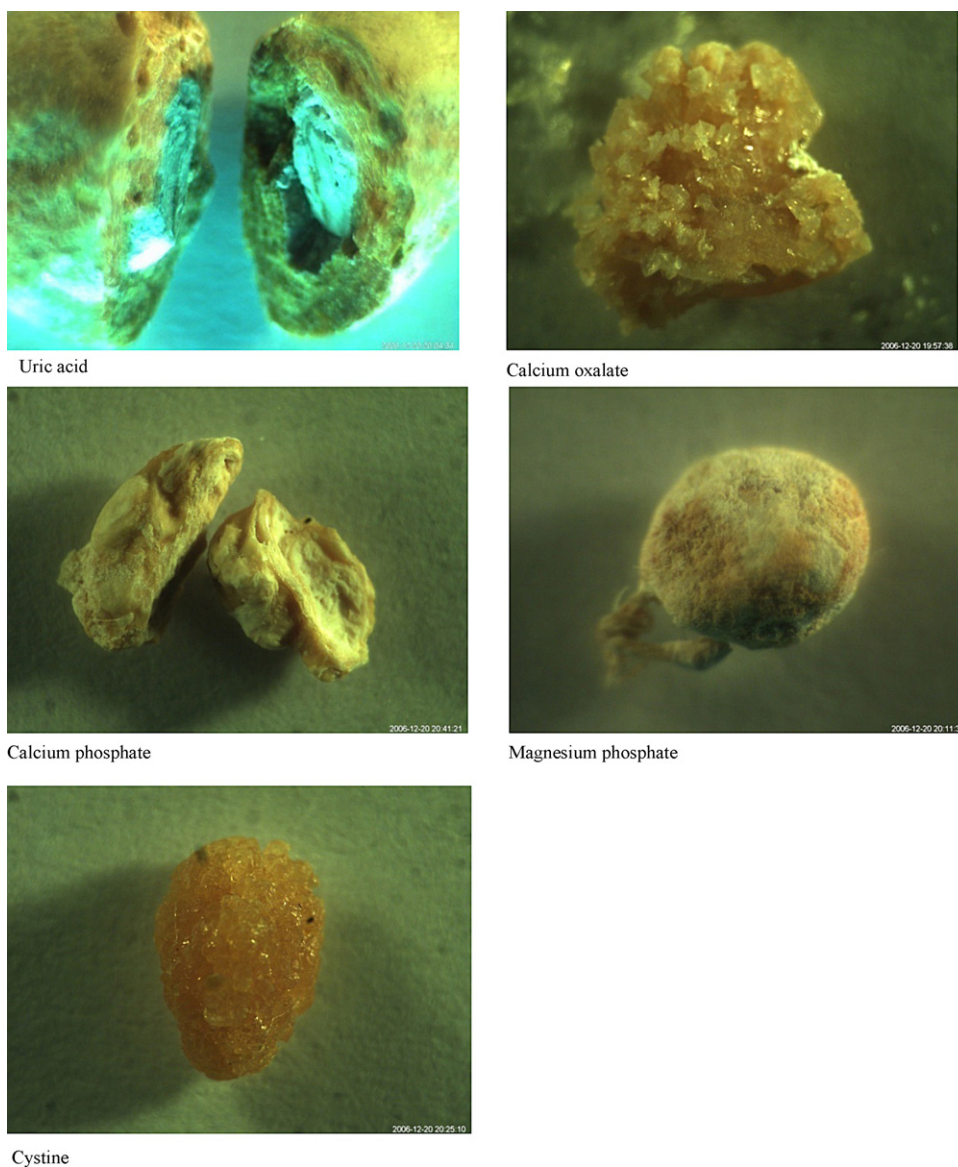*E-mail address:* janzano@unizar.es (J. Anzano).

Fig. 1. Kidney stones analyzed.

shown that simple statistical correlation methods – such as linear and rank correlations – can be successfully applied for the identification of solid and particulate materials. Other papers prove the application of the LIBS technique for elemental analysis of renal calculus with concentrations of majority elements both in percentages (Ca and Mg) and ppm (Na, K, Sr, etc.) [19], and for analysis of the spatial distribution of these elements [20] in renal calculus. However, results on the different elements are only at quantitative level and these works do not clearly study the application of LIBS for renal-calculus identification. These papers reveal that LIBS offers a suitable method to obtain quantitative information [19,20] on spatial distribution [20] of elements in the different kinds of stones found in the human body, without destroying the stones.

Two different strategies and instruments are studied in the present work. On one hand, (linear or parametric and rank or non-parametric) correlation methods using a μ-LIBS system are studied. On the other hand, elemental ratios of reference materials are determined by using a higher-energy laser and an Echelle spectrograph with an ICCD camera, although without microscope.

The aim of the first strategy is identifying urinary calculus by means of a μ-LIBS by using a spectrum library, and linear and rank correlation. This method involves studying all emission lines and molecular bands appearing in spectra from 200 to 850 nm. The objective in the second strategy is to identify kidney stones by determining intensity ratios from elemental lines and measuring ratios of several elements such as C, Ca, H, Mg, N, O and P.

2. Experimental

2.1. Reactives and samples

The library was prepared from the most frequent composition of urinary calculi by using calcium oxalate, calcium phosphate, cystine (Scharlau, extra pure), uric acid (Panreac, PRS) and mixes (calcium phosphate and magnesium phosphate 1:1, calcium oxalate and calcium phosphate 1:1) as reference materials. A pellet of each compound and mix was prepared. Standards (0.50–0.75 g) were mixed with a mortar and pressed at 10^5 N for 5 min.

Real samples of kidney stones provided by the University Hospital of Zaragoza were analyzed. Some samples were broken open to analyze their interior part, since stone core may differ from stone exterior; stone core is the reason for the occurrence of urinary calculus. Photographs of the most frequent stones are shown in Fig. 1.
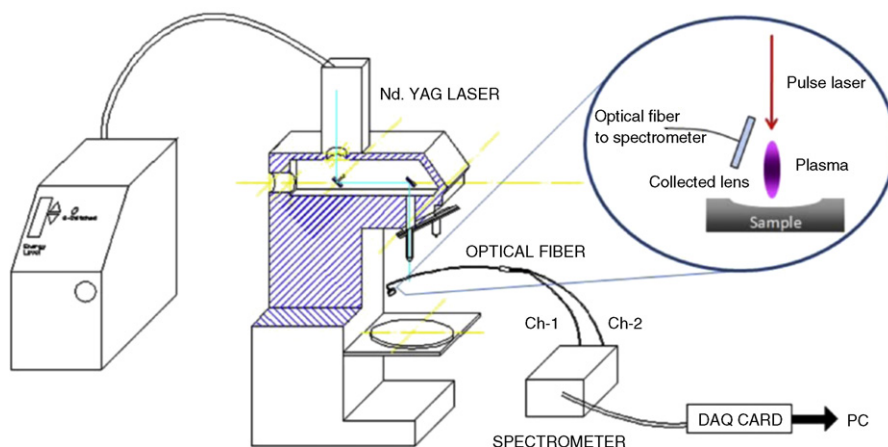
Fig. 2. μ-LIBS system.

All real samples of kidney stones were previously analyzed by IR spectroscopy.

2.2. Instrumental setup

2.2.1. Strategy A: correlation methods

The equipment consisted of a Nd:YAG laser (Quantel, model Ultra CFR) coupled to a microscope; a 30× focalization lens was used. Pulse energy was approximately 9 mJ. Both laser and spectrometer are synchronized by a trigger pulse from a home-made compact pulse generator. Radiation from the laser spark is collected with a bifurcated optical fiber connected to a dual-channel Ocean-Optics mini spectrometer (SD2000, Ocean Optics Inc., Dunedin, FL, USA). Plasma was collected in non-collinear mode. The μ-LIBS system used is shown in Fig. 2. The position of the collimating lens (74-UV Ocean Optics, it has an f/2 fused silica lens for 200–2000 nm, 5-mm diameter, 10-mm focal length) was adjusted for maximum light collection. The spectrometer has the following characteristics: channel one (slave), 230–310 nm spectral range, 3600 mm^{-1} holographic grating, 25 mm slit, 0.3 nm spectral resolution, 2048 pixel linear CCD array; and channel two (master), 200–850 nm spectral range, 600 mm^{-1} grating blazed at 400 nm, 25 mm slit, 1.3 nm spectral resolution, 2048 pixel linear CCD array.

Spectrometer is driven from a laptop computer (hp invent, Omnibook XE3) via a DAQCard−700 interface (National Instruments, USA).

2.2.2. Strategy B: ratios method

The remainder instrumentation used consisted of a Nd:YAG laser, an xyz stage carrying the sample (Standa 011957), a spectrograph and an intensified charged coupled device (ICCD) detector. A Nd:YAG laser (Brilliant Quantel, Q-Switched) with a 115 mJ laser pulse energy at the second harmonic of 532 nm, a 4.4 ns pulse duration and 0.7 Hz repetition frequency was used with a 90-mm focal length lens. Plasma light was collected and transported to spectrograph by lens and optical fiber (fused silica, 50-μm core diameter). An external collector/collimator was used as collected lens; its position was adjusted at 200 mm by a diode laser (Andor, HE-OPI-0009). An Echelle spectrograph (Andor Mechelle ME5000, 195-mm focal length, F/7, λ/Δλ 5000, spectral range from 200 to 975 nm) was coupled to an ICCD detector (Andor iStar DH734, 1024 × 1024-pixels, 13.6 × 13.6-μm^2/pixel, 18-mm intensifying diameter and exposure time was 0.011 s). This system was calibrated by a Hg:Ar lamp (Ocean Optics, HG-1, Hg–Ar lines 253–922 nm). MCP gain was fixed at 180. A 1-μs measurement gate delay time and a 1-μs integration time were used.
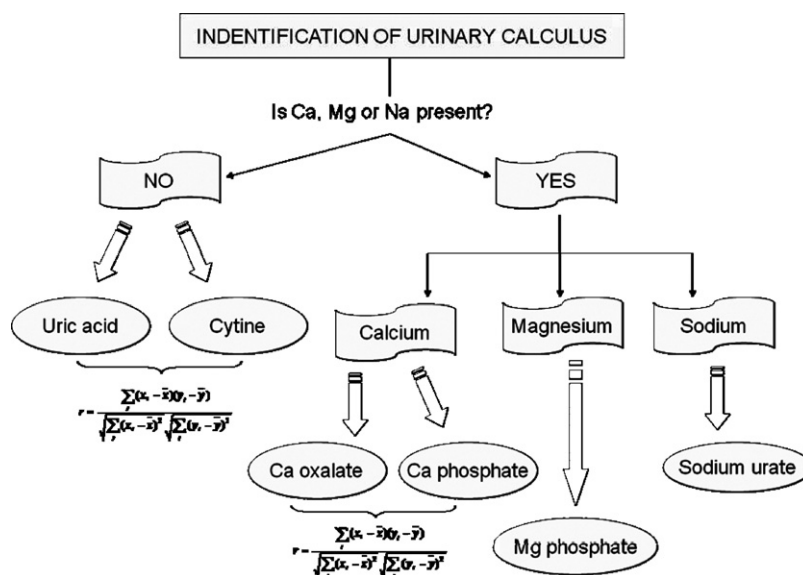
Fig. 3. Methodological scheme using correlation methods.
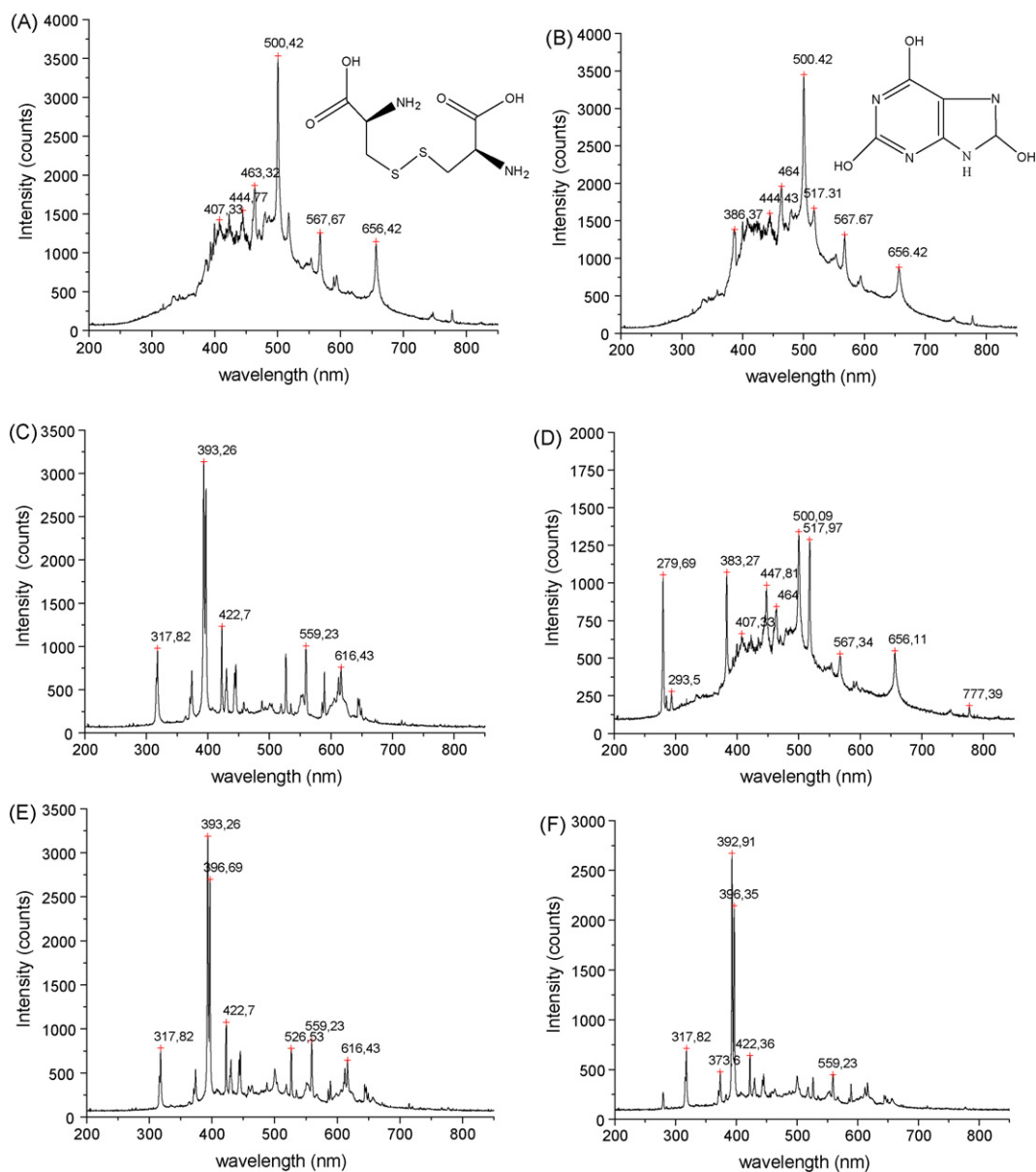
Fig. 4. LIBS spectra of reference materials used for the library: (A) CY, (B) UA, (C) CaP, (D) MgP, (E) CaOx and (F) CaP and MgP mix.

2.2.3. Methodology with strategy A

Optimization was carried out by means of collector-lens adjustment by using a diode laser and microscope diaphragm width maximizing the signal value. Delay time could not be modified due to the home trigger used; therefore, delay time was fixed.

The spectra library was prepared with pure compounds and mixes (CaOx, CaP, MgP, UA, CY and CaP MgP mix). Five replicates were analyzed for each compound and spectra average was introduced as reference spectrum. Samples were analyzed at five different points. A methodology scheme for this strategy is shown in Fig. 3. If a metal (Ca, Mg or Na) is not present in the LIBS spectra, the sample may be UA or CY and is identified by its correlation coefficient. If a metal (Ca, Mg or Na) is present and its emission lines predominate in the spectrum (weak emission lines are not indicative), there are three possibilities, if this metal is (a) calcium (its emission lines are: 317.82, 393.26, 370.83, 373.6, 393.26, 396.69, 430.18, 443.41, 445.45, 526.52 and 559.91 nm), then the sample may be CaOx or CaP and correlation methods must be applied; (b) magnesium (its emission lines are: 279.69, 285.36, 293.50, 382.93 and

518.30 nm), the sample may be MgP; and (c) sodium (its emission lines are: 589 and 820.36 nm), the sample may be sodium urate. Linear (parametric) and non-parametric (rank) correlation methods were applied in this LIBS system for correct compound identification, independently from the previously explained methodology, which is only used as a first indicator. Besides, two spectral windows (200–400 and 200–850 nm) with the same resolution were studied due to interferences (atmospheric nitrogen and oxygen) appearing at high wavelengths.

Simple application software was designed for data treatment. It calculates average spectrum, stores the spectra library and calculates both linear and rank correlation coefficients.

2.2.4. Methodology with strategy B

Delay time was optimized. In this optimization carbon (247.9 nm) and hydrogen (656.2 nm) lines were studied depending on signal/noise value.

The second strategy consists on calculating C:Ca:H:Mg:N:O:P ratios in reference samples and thus the critical values of these

Table 1
Emission lines and bands using μ-LIBS.

	Wavelength (nm)
Calcium	316.06 (w,II); 317.82 (m,II); 370.83 (w,II); 373.6 (w,II); 393.26 (s,II); 396.69 (s,II); 430.18 (w,I); 443.41 (w,I); 445.45 (w,II); 526.52 (w,I); 559.91 (w,I)
Carbon	247 (w,I)
Swan band (C2)	467 (m,II), 517 (s,II); 550 (m,II)
CN band	388 (s)
Hydrogen	656.4 (s,alpha-hydrogen)
Magnesium	279.69 (m,I,II); 285.36 (w,I); 293.50 (w,I,II); 382.93 (s,I); 518.30 (s,I)
Nitrogen	500 (s,II); 746.8 (w,I)
Oxygen	777 (w,triplet)
Sodium	588–589 (s,doublet)

w: weak; m: medium; s: strong.
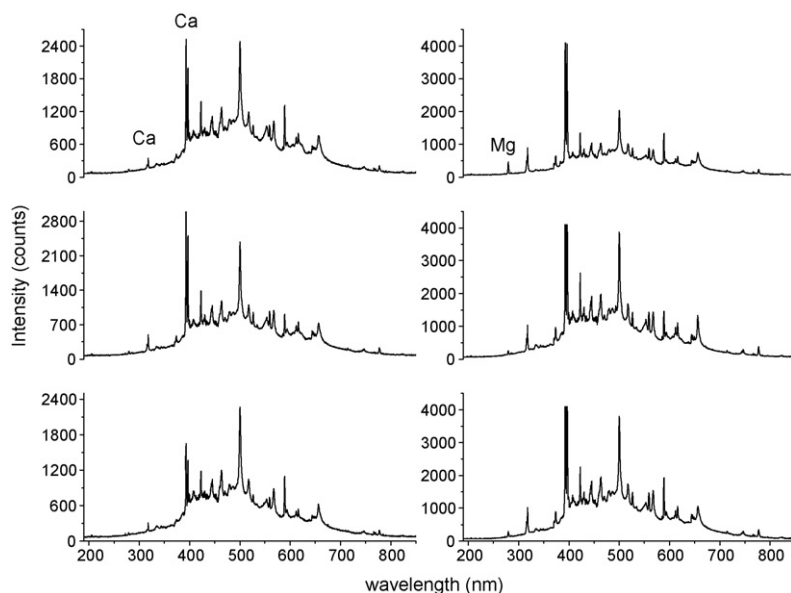
Fig. 5. Sample #1 spectra.

ratios may be assigned to identify the composition of kidney stones. Thirty determinations were carried out for each reference and real sample, each determination being the average of thirty shots and discrepancy values are evaluated by the simple Grubbs' test

($p = 0.05$). A simple application was designed for data treatment; this software application allows getting to know the intensity value in both emission lines and molecular bands. In addition, it automatically calculates all ratios, their average in 10 shots, standard
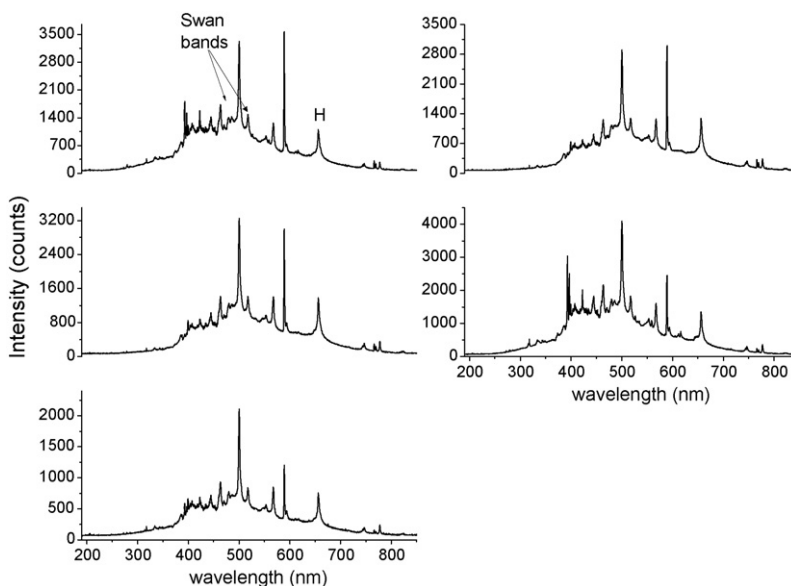
Fig. 6. Sample #2 spectra.
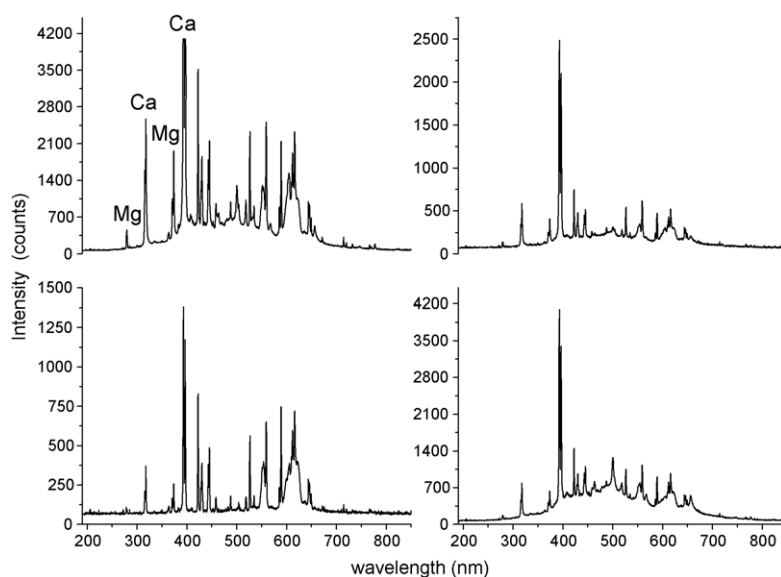
Fig. 7. Sample #3 spectra.

deviation and %RSD, while all ratios are checked by means of the simple Grubbs' test. Selected emission lines were under the following experimental conditions: calcium at 318.0 nm, carbon at 247.9 nm, hydrogen at 656.2 nm, magnesium at 383.8 nm, nitrogen at 744.4 nm, oxygen at 777.4 nm and phosphor at 253.6 nm; these lines are free from spectral interference. Echelle spectrograph allowed us getting a signal-ratio-free sample matrix, laser and detector fluctuations, since this spectrograph is able to show high spectral windows (from 200 to 975 nm) with very high resolution

(0.1 Å), detecting all elements and bands simultaneously without overlapping.

Calculated ratios were: (i) H/C ratio is the most important ratio since it allows identifying [11] and differentiating [15] organic compounds; both uric acid and cystine are identified by this ratio, and it also may be used to identify calcium oxalate; (ii) O/N ratio under atmospheric conditions: not very useful in this study; (iii) Ca/C ratio indicates calcium sales, differentiating between calcium oxalate and calcium phosphate, since CaP values must be higher than CaOx
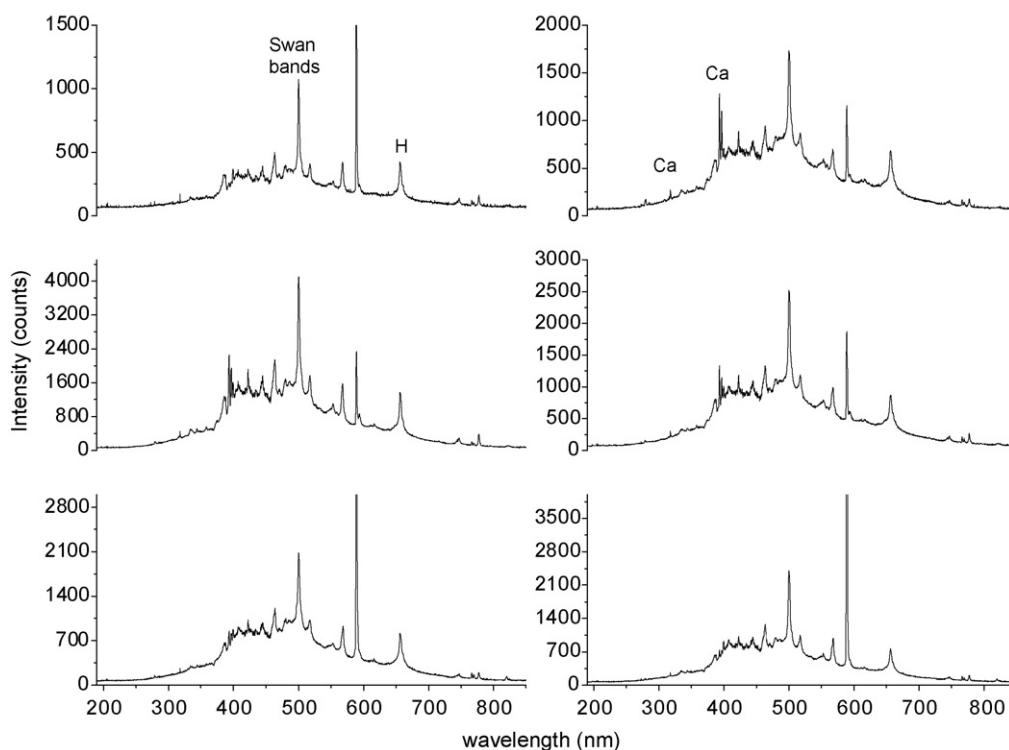
Fig. 8. Sample #4 spectra.

values; (iv) Mg/C ratio indicates magnesium sales, whenever this value is high; (v) Ca/H ratio identifies calcium sales and differentiates between them; (vi) Mg/H ratio identifies magnesium sales; and (vi) P/(P + C) ratio indicates the presence of phosphates, thus, being possible to differentiate between calcium oxalates and calcium phosphate.

3. Results and discussion

3.1. Strategy A: μ-LIBS system with compact detector (CCD) and correlation method

The crater diameter used by μ-LIBS was approximately 0.18 mm and irradiance was $7.1 \times 10^9\,W\,cm^{-2}$. In spite of the low laser energy pulse used, high irradiance was obtained in this system due to focalization by means of a microscope.

The LIBS spectra used as reference to prepare the library are shown in Fig. 4. Cystine and uric acid spectra (Fig 4A and B, respectively) are very similar. The most important emission lines for both compounds are: one strong line appears approximately at 500 nm (maybe atmospheric nitrogen N II [10,18]); alpha-hydrogen (H_α) at 656 nm and oxygen (O I) at 777 nm. The molecular bands found are: carbon Swan bands from carbon dimmer (C2) at 517 and 550 nm and CN bands at 388 nm. Average spectra of cystine and uric acid were introduced as reference in the LIBS library. The spectrum of CaOx (Fig. 4C) shows the main emission lines of calcium at 317.82; 373.6; 393.26 and 396.69 nm; and some other weak lines at 430.18, 443.41, 445.45, 526.53 and 559.23 nm. Emission lines of N II (500 nm), O I (777 nm) and H_α (656.3 nm) are also shown. Magnesium lines from MgP (Fig. 4D) were found at 279.69, 285.36, 293.50, 383.27 and 517.97 nm. The CaP spectrum (Fig. 4E) looks like CaOx, although Swan bands appear at 517 and 550 nm in the CaOx spectrum. In Table 1 the emission lines and bands are indicated.

All average spectra were introduced in the spectra library and, subsequently, real samples were analyzed. The previously explained methodology was applied and its linear and rank correlation coefficients were calculated by using two spectral windows: (a) from 200 to 400 nm, and (b) from 200 to 800 nm. Atmospheric interferences (N II and O II) may be eliminated by using a width window.

Samples were analyzed by IR spectroscopy. The first real sample spectra (M1) show the presence of calcium as majority element and a weak presence of magnesium (Fig. 5). This sample may then be CaOx and/or CaP, although this stone may be composed of a little amount of MgP. Linear correlation coefficients calculated for the narrowest spectral window indicate that sample composition is CaOx (r = 0.9632, 0.9929, 0.9858, 0.9703, 0.9100 and 0.9732). The rank correlation coefficient is not as accurate as the linear correlation one.

The second real sample spectra (M2) show the absence of calcium and magnesium and the sodium line is weak (Fig. 6); only calcium and sodium traces were present in some spectrum. Therefore, this sample may be UA or CY. The linear correlation coefficient points to CY (0.977, 0.9273, 0.9937 and 0.9718) using the width spectral window. Worse results were again obtained by using all spectral data and rank correlation.

In the third sample spectra (M3) calcium and magnesium lines appear (Fig. 7). Then, correlation coefficients must be calculated. These coefficients point to a CaP and MgP mix. Finally, the last sample spectra (M4) do not present calcium and magnesium lines (Fig. 8), although calcium is detected on external surface, due to precipitation of calcium sales on the original stone. In this case, it is important to identify the composition of stone internal-core because kidney-stone formation is due to this compound. Then, this core may be UA or CY, the linear coefficient (200–400 nm) pointing to UA (r = 0.9925).

3.2. Strategy B: Echelle spectrograph and ratio method

The crater diameter used in this second experimental design was 0.4 mm; thus, irradiance was $5.2 \times 10^9\,W\,cm^{-2}$. It was lower than the μ-LIBS system, despite laser energy was thirteen times higher and pulse duration was reduced to a half in this second system. This was due to the focalization system of the microscope in the μ-LIBS system.

Signal/noise (S/N) value was studied for delay-time optimization, and carbon and hydrogen emission lines were analyzed. Delay time was optimized between 100 and 2000 ns by using the carbon and hydrogen lines at 247 and 656 nm, respectively. S/N variations depending on delay time are shown in Fig. 9A and B for carbon and hydrogen line, respectively. A high intensity value for carbon can be observed at 247.9 nm (Fig. 9A) at low delay times (<500 ns). However, S/N ratios were very low at these times, even below detection limit (S/N < 3), due to high noise (background). Optimal delay-time for carbon was 1000 ns. The behaviour of intensity and S/N values for hydrogen (Fig. 9B) were similar and optimal delay time was 500 ns; this may happen since lifetime of hydrogen emission is shorter. On the other land, hydrogen S/N values were higher than carbon's values. Therefore, the delay time used as optimal was 1000 ns. Integration time was also optimized, being optimal at 1000 ns.

Now C:Ca:H:Mg:N:O:P ratios of reference samples are calculated by using chemical standards. These values are used for calculating the critical values of these ratios, which shall in turn be used
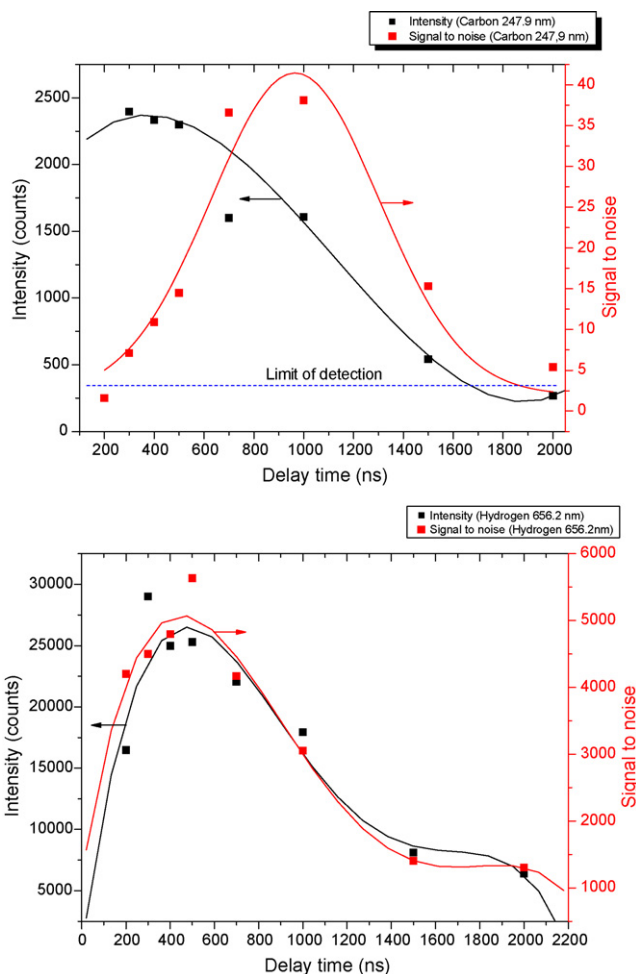

Fig. 9. Variation of S/N depends on delay time.

Table 2
C:Ca:H:Mg:N:O:P ratios calculated using chemical standards.

	UA	CY	CaOx	CaP	MgP
H/C_1	5.86 ± 0.57	11.4 ± 1.3	6.9 ± 0.9	23.9 ± 3.4	33.3 ± 6.6
O/N	3.3 ± 0.2	3.2 ± 0.2	2.6 ± 0.3	3.5 ± 0.2	3.4 ± 0.2
Ca/C_1	0.47 ± 0.06	0.88 ± 0.25	42.0 ± 12.0	376 ± 52	4.4 ± 0.6
Mg/C_1	1.45 ± 0.19	1.4 ± 0.3	3.6 ± 0.5	11.5 ± 1.7	70.5 ± 8.8
Ca/H	0.084 ± 0.015	0.050 ± 0.003	5.8 ± 1.2	16.2 ± 1.2	0.17 ± 0.03
Mg/H	0.23 ± 0.03	0.11 ± 0.02	0.51 ± 0.05	0.51 ± 0.06	2.6 ± 0.4
$P/(P+C_1)$	0.11 ± 0.01	0.16 ± 0.04	0.46 ± 0.04	0.88 ± 0.02	0.85 ± 0.02

$n = 30$, $p = 0.05$.

to identify kidney composition. The emission lines chosen under these experimental conditions for C, Ca, H, Mg, N, O and P are 247.9, 318.0, 656.2, 383.8, 744.4, 777.4 and 253.6 nm, respectively. These lines are free from spectral interference. Due to the high resolution provided by Echelle spectrograph, all selected lines are free from interferences from studied elements.

C:Ca:H:Mg:N:O:P ratios calculated by using chemical standards (UA, CY, CaOx, CaP and MgP) are shown in Table 2 ($n = 30$ and $p = 0.05$) and their spectra in Fig. 10. The phosphorus emission line showed the lowest sensitivity at 253.6 nm in studied elements. Detection limit was calculated as the amount with a signal/noise ratio ≥ 3; thus, phosphorus detection limit was 2.3% under these experimental conditions. This limit was enough for the identification of urinary calculus; only majority compounds were the aim of the present study. Compounds without either carbon or hydrogen or nitrogen in their chemical formulas (e.g., CaP and MgP) or only one of these elements would produce ratios of H/C, O/N, etc. These ratios shall be produced since emission at the corresponding wavelengths comes from atmospheric sources of C, H, N (CO_2, H_2O and N_2) and the most important source may be impurities from reference materials and samples. Something similar occurs with the

presence of Ca and Mg in UA and CY patterns, Ca in magnesium phosphate and Mg in calcium salts, whose presence are impurities in patterns. These impurities do not affect analysis results, since only majority elements are indicators of the composition of renal calculus, which may also contain remains of other compounds different than the majority one or that which originates calculus formation (once calculus has been formed, other compounds may settle on this nucleus).

UA and CY ratios are similar, only the H/C1 ratio can be used to differentiate between them. These compounds can differ of calcium and magnesium sales due to higher Ca and Mg ratios. CaOx differs from CaP since the Ca/C_1 ratio of CaOx is lower than that of CaP due to the presence of carbon in CaOx; besides, $P/(P+C_1)$ ratio of CaP is higher. All ratios are used to assign the critical values which shall be used to analyze real samples. These critical values are shown in Table 3.

Some kidney stones were analyzed by using these ratios and obtained values are shown in Table 4. Sample #1 could not be calcium and magnesium sales since Ca/C_1 and Mg/C_1 ratios are below 2 (1.6 and 1.9, respectively) and Ca/H and Mg/H are also below 0.5. Then, it may be CY or UA: the H/C1 ratio (6.5) points to CY. Sample #2
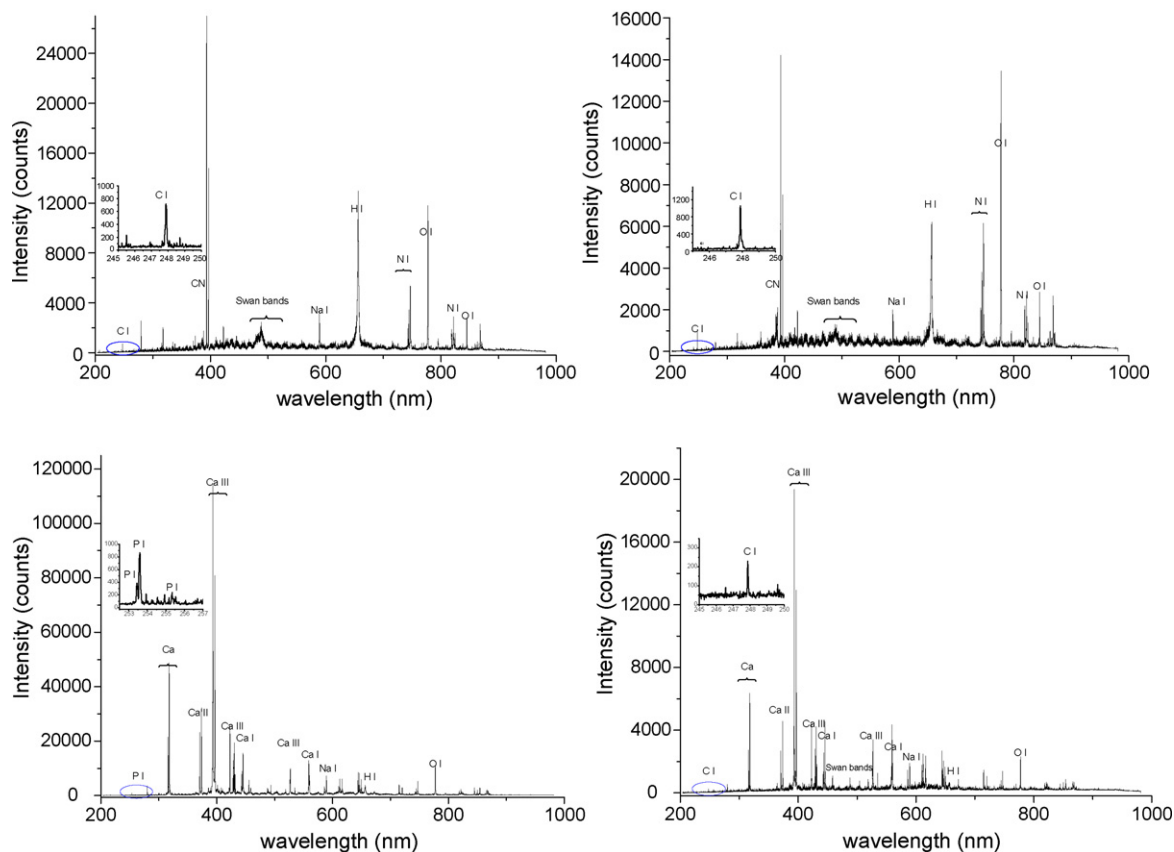

Fig. 10. Spectra obtained from chemical standards.

Table 3
Critical values used for the identification of kidney stones.

	Uric acid	Cystine	Calcium oxalate	Calcium phosphate	Magnesium phosphate
H/C_1	<6	>6	>6	>6	>6
Ca/C_1	<2	<2	60 > r > 10	>60	
Mg/C_1	<2	<2			>20
Ca/H	<0.5	<0.5	8 > r > 4	>8	
Mg/H	<0.5	<0.5			>1
$P/(P+C_1)$	<0.5	<0.5	<0.6	>0.6	>0.6

Italicized text: the most important values for its identification.

Table 4
Results of analyzed samples.

	Sample #1	Sample #2	Sample #3
H/C_1	6.5	3.4	8.5
Ca/C_1	1.6	1.5	80
Mg/C_1	1.9	2.0	4.6
Ca/H	0.26	0.47	9.5
Mg/H	0.30	0.60	0.55
$P/(P+C_1)$	0.36	0.40	0.70

is similar to Sample #1; again it may be CY or UA. As H/C1 is below 6 (3.4), then this sample is UA. Calcium ratios in Sample #3 point to calcium sales; therefore, it may be CaOx or CaP. The P/(P + C1) ratio confirms the presence of phosphates as majority salt in the sample; therefore, it is CaP. H/C1 and Ca/H ratios also confirm this composition. All LIBS identifications of kidney stones were confirmed by IR spectroscopy.

4. Conclusions

In this work two LIBS instrument designs have been developed for identification of urinary calculi: (a) a micro-LIBS system with a compact detector, CCD camera, (μ-LIBS); and (b) a conventional LIBS system with an Echelle spectrograph and an ICCD camera. One data-treatment method was studied for each system and real samples of kidney stones – previously analyzed by IR spectroscopy – were used for reliable evaluation of two identification strategies. In both instrumentations, visual examination of the spectra was enough to distinguish between organic (UA, for instance) and non-organic compounds (CaP, for instance). Statistical correlation analysis using linear (parametric) and non-parametric (rank) correlation was applied in the LIBS system. Besides, two spectral windows (200–400 and 200–850 nm) were studied due to intense interferences – atmospheric nitrogen and oxygen – appearing at high wavelengths. The best results were obtained by using linear correlation and spectral windows between 200 and 400 nm. Another identification system was carried out by using different instrumentation and a method based in intensity-peak ratios. This method reached successful results in all analyzed samples. Both methods and instrumentations have been proven as reliable strategies for urinary-calculi identification, although the method based

on intensity-peak ratios may provide better analytical information about the analyzed sample.

References

[1] M.A. Aibar, A.P. Gutierrez, M.P. Rodrigo, K. Laborda, A.B. Hernández, G. Blaso, Acta Urol. Esp. 28 (2004) 661–665.
[2] M. Volmer, J.C.M. De Vries, H.M.J. Goldschmidt, Clin. Chem. 47 (2001) 1287–1296.
[3] M. Volmer, A. Block, B.G. Wolthers, A.J. de Ruiter, D.A. Doornbos, W. van der Slik, Clin. Chem. 39 (1993) 948–954.
[4] M. Volmer, B.G. Wolthers, H.J. Meting, T.H.Y. de Haan, P.M. Coenegracht, W. van der Slik, Clin. Chem. 40 (1994) 1692–1697.
[5] L. St-Onge, E. Kwong, M. Sabsabi, E.H.B. Vadas, J. Pharm. Biomed. Anal. 36 (2004) 277–284.
[6] C. Samuels, F.C. DeLucia, K.L. McNesby, A.W. Miziolek, Appl. Opt. 42 (2003) 6205–6209.
[7] P.B. Dixon, D.W. Hahn, Anal. Chem. 77 (2005) 631–638.
[8] O. Samek, H.H. Telle, D.C.S. Beddows, BMC Oral Health 1 (2001) 1–9.
[9] B. Gornushkin, A. Ruiz-Medina, J.M. Anzano, B.W. Smith, J.D. Winefordner, J. Anal. Atom. Spectrom. 15 (2000) 581–586.
[10] J. Anzano, M. Casanova, M.S. Bermúdez, R.J. Lasheras, Polym. Test 25 (2006) 623–627.
[11] M. Tran, Q. Sun, B.W. Smith, J.D. Winefordner, J. Anal. Atom. Spectrom. 16 (2001) 628–632.
[12] F. Ferioli, P. Puzinauskas, V. Paulius, S.G. Buckley, Appl. Spectrosc. 57 (2003) 1183–1189.
[13] S. Kaski, H. Häkkänen, J. Korppi-Tommola, J. Anal. Atom. Spectrom. 19 (2004) 474–478.
[14] L. St-Onge, E. Kwong, M. Sabsabi, E.B. Vadas, Spectrochim. Acta Part B: Atom. Spectrom. 57 (2002) 1131–1140.
[15] C. López-Moreno, S. Palanco, J.J. Laserna, F. DeLucia, A.W. Miziolek, J. Rose, R.A. Walters, A.I. Whitehouse, J. Anal. Atom. Spectrom. 21 (2006) 55–60.
[16] G. Asimellis, A. Giannoudakos, M. Kompitsas, Spectrochim. Acta Part B: Atom. Spectrom. 61 (2006) 1253–1259.
[17] R. Sattmann, I. Monch, H. Krause, R. Noll, S. Couris, A. Hatziapostolou, C. Mavromanolakis, E. Fotakis, R. Larrauri, Miguel, Appl. Spectrosc. 52 (1998) 456–461.
[18] J.M. Anzano, I.B. Gornushkin, B.W. Smith, J.D. Winefordner, Polym. Eng. Sci. 40 (2000) 2423–2429.
[19] X. Fang, S.R. Ahmad, M. Mayo, S. Iqbal, Lasers Med. Sci. 20 (2005) 132–137.
[20] V.K. Singh, A.K. Rai, P.K. Rai, P.K. Jindal, Lasers Med. Sci. (2008), doi:10.1007/s10103-008-0635-2.

Electrochemical hydride generation of thallium

M.H. Arbab-Zavar [a,*], M. Chamsaz [a], A. Yousefi [b], N. Ashraf [a]

[a] *Department of Chemistry, Faculty of Science, Ferdowsi University of Mashhad, Mashhad, Iran*
[b] *Pare-Taavous Research Institute, Mashhad, Iran*

A B S T R A C T

An electrochemical hydride generation (ECHG) technique was developed to improve the determination of thallium by atomic spectrometry. The technique is based on the catholyte variation system for production of thallium hydride. Using Pb–Sn alloy as cathode, a transient peak shaped signal was achieved and its height, the maximum absorbance value, was taken as an analytical parameter. Parameters that might affect the hydride generation efficiency were investigated and the analytical performance of the method under the optimized experimental conditions was assessed. The linear range was 1–250 ng mL^{-1} for thallium and the relative standard deviation of the method was 4.2% (RSD, $n = 7$). The LOD for thallium was found to be 0.8 ng mL^{-1}, showing a significant improvement relative to conventional chemical hydride generation techniques. The proposed method was applied to the determination of thallium in unalloyed zinc standard reference material. This method offers high sensitivity, simplicity, rapidness, freeness from reagent and low acid consumption.

© 2009 Elsevier B.V. All rights reserved.

1. Introduction

Thallium has been found to be an environmentally hazardous element because of its toxic effects. This metal is introduced into the environment mainly as the waste product of zinc, cadmium, and lead industries and also results from the combustion of coal. It is regarded as one of the most toxic heavy metals causing both chronic and acute poisoning [1]. It is, therefore, important to detect and determine thallium in a wide range of matrices, i.e. environmental, biological, clinical, geological, and metallurgical samples. Since the total concentration of thallium is generally very low, an analytical technique with high sensitivity and low detection limit is required. There are several analytical techniques available for determination of thallium, i.e. spectrophotometry and fluorimetry, atomic absorption and fluorescence spectrometry, inductively coupled plasma and isotope dilution mass spectrometry, potentiometry and voltammetry, and nuclear techniques [2,3]. Among these, stripping voltammetry has received the most attention owing to its high sensitivity and ability to detect the redox species of metals. However, analysis of thallium by this method suffers from interferences by other metals especially cadmium [4]. Although flame atomic absorption spectrometry (FAAS) is a simple and easily available technique, its application is restricted due to lack of sensitivity for trace determinations of thallium.

Vapour generation techniques in combination with atomic absorption spectrometric determination (AAS) are sensitive analytical methods. These techniques offer several advantages relative to conventional nebulization methods, which include improved selectivity, elimination of nebulizer, analyte preconcentration, and more efficient analyte atomization [5–8]. However, reports on thallium vapour generation are few [9–14]. Thallium vapour generation, presumably as hydride, was first reported by Yan et al. [9]. The method was less sensitive than conventional FAAS, as well as being subjected to large positive interferences from the presence of other hydride-forming elements. Ever since, many attempts have been made to improve its sensitivity. These include applying continuous flow methodologies [10], in situ trapping of hydrides in a graphite tube along with electrothermal AAS determination [11], using palladium and rhodamine B as enhancement reagent in flow injection hydride generation AAS [12], and employing an integrated atom trap atomizer in hydride generation AAS [13]. Although the application of trapping techniques somewhat improves the limit of detection, the efficiency of hydride generation is still low.

Electrochemical hydride generation (ECHG) proved to be a suitable alternative to conventional chemical hydride generation due to several advantages. The most significant advantages include elimination of NaBH$_4$ (an expensive unstable substance, and also a source of contamination), similar reaction media for all hydride-forming elements, better tolerance of interferences, better reproducibility, higher sensitivity, and independence from analyte oxidation state when using cathode materials with high hydrogen overvoltage [15]. As far as our review shows, there is no report on electrochemical hydride generation of thallium. In the present research, effort

---

* Corresponding author. Tel.: +98 511 8797022; fax: +98 511 8796416.
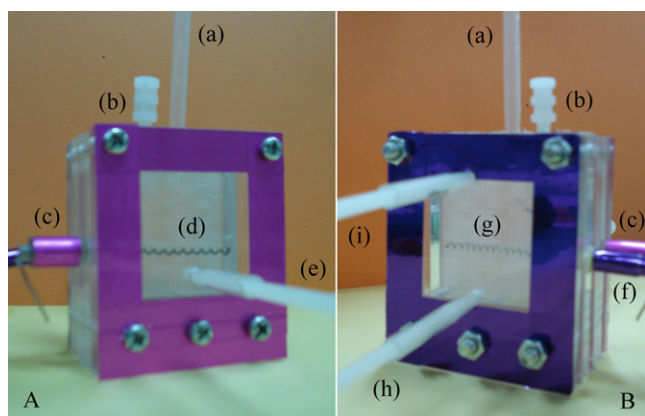 *E-mail address:* arbab@um.ac.ir (M.H. Arbab-Zavar).

Fig. 1. Electrochemical hydride generation cell. Cathodic (A) and anodic (B) compartments: connection to quartz tube atomizer (a); sample inlet (b); cathode holder (c); helix shaped Pb–Sn cathode (d); carrier gas entry (e); anode holder (f); helix shaped Pt anode (g); anolyte inlet (h); anolyte outlet (i).

has been made to develop a technique for electrochemical hydride generation of thallium. Using catholyte variation system [16,17], a transient peak shaped signal was obtained and its height, the maximum absorbance value, was measured as an analytical parameter. Accordingly, this technique resulted in improvement on thallium hydride generation. A mechanism for electrochemical generation of thallium hydride is proposed. Effective and operative parameters on the obtained signal were optimized. Analytical performance of the method was compared to the previously reported chemical hydride generations of thallium.

2. Experimental

2.1. Instrumentation

A Shimadzu 680 atomic spectrometer (Shimadzu, Japan) equipped with an electrically heated quartz tube atomizer (150 mm length, 4.2 mm inner diameter) operated at 1000 °C was used for atomic absorption measurements. Thallium hollow cathode lamp (Hamatsu Photonics, Japan) operated at 3 mA was employed as radiation source. The spectral bandwidth was set at 0.5 nm and absorbance was measured at 276.8 nm.

2.2. Electrochemical hydride generation system

Various views of the batch electrolytic hydride generator are shown in Fig. 1. Electrochemical hydride generator consists of two compartments; batch cathodic (Fig. 1A and continuous anodic (Fig. 1B) chambers separated by a nafion membrane (Dupont, USA) and has been described in details in the previous publications [16,17].

A programmable power supply (Promax FA-851, Spain, maximum current of 2 A and maximum voltage of 32 V) operating at constant current and voltage modes is connected to the electrochemical cell.

2.2.1. Cathodic compartment

Carrier gas (Argon, 99.999% pure) entry is placed at the bottom of the cathodic compartment. This design facilitates the separation of gaseous products from the cathode surface and aqueous solution. The gaseous reaction products; hydrides and hydrogen formed at the cathode, are separated from aqueous solution, and directed to the electrically heated quartz tube by the carrier gas stream via a connecting tube (PVC, length of 20 cm, 3 mm i.d.) and determined under the operating conditions by AAS. As the cathodic materials,

lead, tin, lead–tin (Pb–Sn 37:67, Asahi solder, Singapore, 0.8 mm diameter), graphite, tungsten wire (99.98% pure, AESAR, Johnson Matthey Inc., 0.5 mm diameter), dental amalgam (32% Ag, 14.7% Sn, 6.7% Cu and 46.7% Hg amalgam, coltèn whaledent®, USA), platinum (Merck), and silver wire have been investigated. After the termination of a run process, a peristaltic pump drains off the contents of the cathodic compartment.

2.2.2. Anodic compartment

A platinum coil (surface area of 1 cm^2) serves as the anode. The anolyte is circulated by a multiple channel peristaltic pump (Gilson, Minipuls 3, ANACHEM) to remove oxygen from the anodic compartment. The circulated anolyte needs only to be changed after 40 h of operation.

2.3. Data acquisition and transformation

The transient signals were recorded using a graphical printer (PR-5) equipped with a monitor and transformed to digital data using an in-house software (Graph-7).

2.4. Procedure

Initially, the electrochemical hydride generation cell was connected to quartz tube atomizer via PVC tubing. Then, the circulation of the anolyte (0.5 mol L^{-1} Na$_2$CO$_3$) was started and the flow rate of the carrier gas adjusted. In each regular measuring cycle, the electrode (cathode) was placed into its position and connected to power supply. The acidified thallium solution (catholyte solution containing analyte) was then introduced and measurement performed by applying an appropriate voltage to the cell (between the cathode and the anode). The gaseous electroreaction products were transported to the quartz tube atomizer by the carrier gas stream and the transient signal was measured. The transient signal was peak shaped and its maximum absorbance value was measured as an analytical parameter.

2.5. Reagents and materials

All chemicals were of analytical grade except cited otherwise. Standard solution (1000 µg mL^{-1}) of Tl(I) was prepared by dissolving the proper amounts of thallium(I) nitrate (Prolab) in dilute nitric acid solution. Solutions of 1 mol L^{-1} of HCl, HNO$_3$ and H$_2$SO$_4$ were prepared by diluting analytical grade concentrated acids. Working solutions were prepared by mixing the proper amounts of Tl standard solutions and 1 mol L^{-1} sulfuric acid solution and diluting to desired volume.

2.6. Reference material

Validation of the method described in this work was carried out using certified unalloyed zinc reference material. The European Reference Material ERM®-EB325 was purchased from the Institute for reference materials and measurement (IRMM).

2.7. Sample preparation

Exactly, 1 g of the solid reference material was weighted, transferred to a 50 mL Erlenmeyer flask, and 5 mL of concentrated nitric acid was then added. After complete dissolution of the solid sample, the remaining solution was evaporated at the temperature of 80 °C to approximately 0.5 mL final volume. Then, 50 mL of deionized water and 3.3 g of ammonium carbonate were added, respectively. After 30 min, the mixture was filtered through a glass filter, transferred to a 200 mL calibrated flask, and diluted to volume with
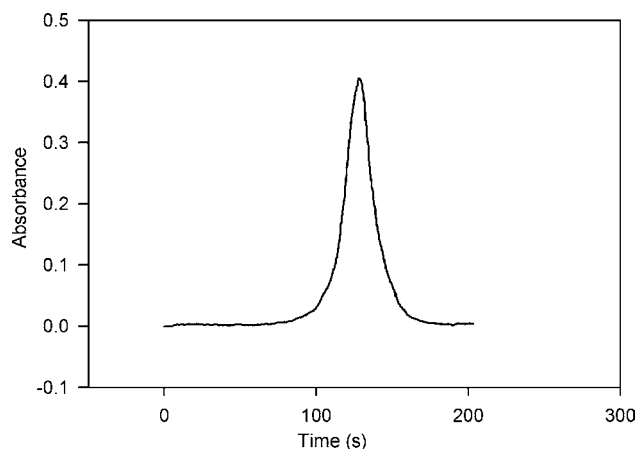
Fig. 2. Transient peak shaped signal resulted from electrochemical hydride generation of thallium (200 ng mL^{-1}) under optimized condition.

deionized water. Prior to the analysis, appropriate dilutions were performed depending on the concentration level of the thallium.

3. Results and discussion

3.1. Generation of thallium hydride species

Catholyte variation electrochemical system was applied to generate thallium hydride species. The method has been described in details in previous publications [16,17]. During electrolysis, the hydronium ions and water are gradually reduced to hydrogen molecules. Meanwhile, sodium ions are diffused from anodic chamber through the nafion membrane and the pH is increased during the electrolysis due to low concentration of hydronium ions. The peak shaped transient signal (Fig. 2) produced during electrolysis process is observable at neutral to moderately basic pH values.

To account for the mechanism of thallium hydride generation, the initial reaction is considered to be the electrodeposition of Tl ions at the surface of Pb–Sn cathode [1,2]. By considering the values of standard potential: $Tl^{3+} + 2e^- \rightarrow Tl^+$; $+1.25$ V, $Tl^{3+} + 3e^- \rightarrow Tl$; $+0.92$ V and $Tl^+ + e^- \rightarrow Tl$; -0.34 V, deposition of both Tl^+ and Tl^{3+} would occur at the electrode surface, at highly negative working potentials employed. High hydrogen overvoltage, negative working potentials, and high electrolytic currents facilitate this process:

$$Tl^+ \rightarrow Tl(Pb–Sn) \tag{1}$$

$$Tl^{3+} \rightarrow Tl(Pb–Sn) \tag{2}$$

Pb–Sn alloy used as the cathode material involves sp-metals with filled d-orbital, so low hydrogen adsorbing power and high hydrogen overvoltage is expected [24]. This hypothesis is supported by our previous experiments showing high hydrogen overvoltage for Pb–Sn alloy relative to Pt, graphite, Sn and Pb [17]. Therefore, the following electrochemical mechanism is proposed for thallium hydride formation [24]:

$$Tl(Pb–Sn) + e^- + H_3O^+ \rightarrow TlH + H_2O + Pb–Sn$$

$$Tl(Pb–Sn) + 3e^- + 3H_3O^+ \rightarrow TlH_3 + 3H_2O + Pb–Sn$$
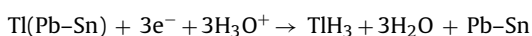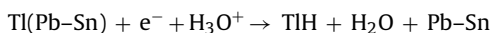
The real identity of the generated species is unknown. When quartz tube atomizer was in the room temperature, no signal was observed. By raising the temperature, the signal was gradually increased. This observation ensures that the generated vapours are in the molecular form.

There have been many studies considering the stability of thallium hydride species, i.e., TlH, TlH$_2$, TlH$_3$, Tl$_2$H$_2$, TlTlH$_2$ and Tl$^+$(H$_2$)$_n$

Table 1
Optimized operating condition.

Operating parameter	Optimized value
Anolyte concentration (mol L^{-1})	0.5
Anolyte flow rate (mL min^{-1})	6
Sample volume (mL)	13
Catholyte concentration (mol L^{-1})	0.003
Carrier gas flow rate (mL min^{-1})	100
Atomizer temperature (°C)	1000
Cathode surface area (cm^2)	1.75
Applied voltage (V)	20

[18–23]. The monovalent Group 13 hydrides have been all detected in the gas phase and their spectroscopic properties are currently known [21].

3.2. Optimization of operating parameters

The influence of fundamental operating parameters, primarily the cathode material, catholyte and anolyte types, electrolytic current and potential, cathode surface area, atomizing temperature, and concentration of the anolyte and catholyte was thoroughly studied and will be discussed later. The optimized values for operating conditions have been shown in Table 1.

3.2.1. Cathode material

Lead, tin, Pb–Sn alloy, tungsten, platinum, silver, dental amalgam, and graphite rod were examined as the cathodic materials. With sulfuric acid (0.003 mol L^{-1}) as the catholyte solution, the signals generated using all cathodic materials were negligible except those from tin and Pb–Sn. Tungsten, platinum, silver, and graphite rod were not able to produce any detectable thallium hydride signal, probably because of their low hydrogen overvoltages. In the case of dental amalgam, thallium was deposited at the surface of the electrode as amalgam and no detectable signal was produced. Despite of high hydrogen overvoltage values reported for lead [17,24], no signal was produced and by applying higher voltages, complete deterioration of the electrode was observed. Tin and Pb–Sn alloy generated transient peak shaped signals with greater sensitivity for Pb–Sn alloy. High hydrogen overvoltage [17] and microcrystalline structure of Pb–Sn alloy were supposed to be responsible for the higher efficiency. Based on these observations, Pb–Sn alloy was preferred as the cathodic material and used for the rest of the experiments.

3.2.2. Catholyte and anolyte electrolyte solutions

Supporting electrolyte is necessary to provide electric conductivity. So, dilute solutions (0.01 mol L^{-1}) of HCl, H$_2$SO$_4$ and HNO$_3$ were examined as catholyte solutions. Generation of hydrides took place in all acidic media. The signals attained with nitric and hydrochloric acids were not considerably different; where in the case of sulfuric acid, the generated signal was of higher intensity. Therefore, sulfuric acid was selected as catholyte supporting solution for further experiments. Precipitation and complex formation between Tl$^+$ and chloride ions in hydrochloric acid [25] and oxidizing properties of NO$_3^-$ in nitric acid decrease the tendency of thallium ions for reduction and deposition at the electrode surface. Based on the proposed mechanism, this results in the reduction of hydride generation efficiency.

As anolyte solutions, equimolar solutions of Na$_2$CO$_3$, Na$_2$SO$_4$, NaCl, KNO$_3$ and H$_2$SO$_4$ were tested. Except for H$_2$SO$_4$, all electrolytes produced similar signals. When H$_2$SO$_4$ was used, the system was not able to produce any detectable signal. This is in accordance with the proposed mechanism. Based on the catholyte variation mechanism, pH plays an essential role in the generation of hydrides. The pH of the solution would be adjusted from acidic to
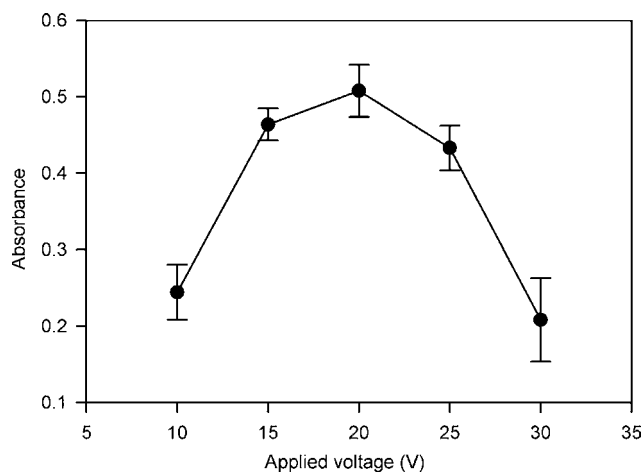
Fig. 3. Effect of the applied voltage on thallium hydride signal.

Fig. 4. Comparison between constant current and constant voltage working modes.

basic by two major phenomena: first, consumption of hydronium ions during electrolysis and second, their transport through the nafion membrane. In the case of Na_2CO_3, Na_2SO_4, NaCl, and KNO_3, hydronium ions diffuse from cathodic chamber through nafion membrane while Na^+ ions enter from the anodic chamber. This process decreases the concentration of hydronium ions and thus increases the pH of the solution. In the case of H_2SO_4 as anolyte solution, although the hydronium ions are consumed during electrolysis process, more hydronium ions diffuse from anodic chamber due to much higher concentration of sulfuric acid (about 150 times). This process will prevent any pH variation; therefore, the suitable pHs for evolution of hydrides would never be reached. Na_2CO_3 solution was selected because of its inertness and higher conductance for pH dependent membrane.

3.2.3. Designating electrolysis working mode

Most of the electrochemical hydride generation systems utilize high catholyte concentrations ($1–3\,mol\,L^{-1}$). In such systems, constant current and constant voltage modes are not distinguishable. In fact, constant currents lead to constant voltages during electrolysis process and vice versa. The main difference of the present system (catholyte variation) lies in this point. In the present system, the concentration of catholyte is lowered to approximately 1%. Therefore, the composition of the catholyte as well as the concentration of the ions and the ionic conductance in the cathodic chamber vary during electrolysis process. At these conditions, two working modes are possible: constant current and constant voltage modes. Both systems were examined to find the most suitable and sensitive working mode.

3.2.3.1. Constant voltage mode.
Working voltage is limited by the power supply operation. The maximum voltage attainable by the power supply is 32 V. Generation of hydrides was studied in the range of 0–32 V. As shown in Fig. 3, the most intense signal was attained at 20 V.

3.2.3.2. Constant current mode.
High working electrolysis currents are needed to efficiently produce thallium hydride. For each catholyte concentration, the maximum practical current was applied and the signal was recorded. Considering peak height as the analytical parameter, in all cases the intensities were much lower than constant voltage mode. Fig. 4 shows the signals obtained by exerting 125 mA constant current and 20 V constant voltage to a solution of thallium in $0.003\,mol\,L^{-1}$ of sulfuric acid. As the results show, although the peak area of the signal obtained in the constant current mode is somewhat higher than that obtained by apply-

ing constant voltage, this peak is broad and noisy while presenting low reproducibility. By contrast, the signal obtained in the constant voltage mode is sharp, symmetrical and reproducible. Moreover, the evolution time in the constant voltage mode is about one-third in comparison to the constant current mode. Thereupon, constant voltage mode (with 20 V) was selected as a suitable working mode. Working in constant current mode is suggested where trapping techniques are used.
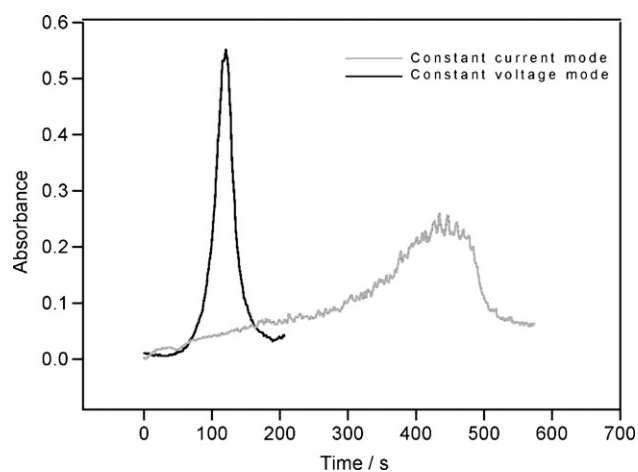
3.2.4. Influence of aging of the cathode

Replicate experiments were performed without replacing the old electrode. Results (Fig. 5) show that using the electrode for the second and third consecutive runs will produce only 80% of signal attainable for the first run. By using the electrode in more replicates, the signal gradually declines to 30% in the 12th replicate. This proves that the active sites of the electrode are deteriorated during the electrolysis process, resulting in a change of surface composition. Based on such observations, the Pb–Sn electrode was replaced at the beginning of each experiment to obtain a reproducible signal.

3.2.5. Influence of the cathodic surface area

Enlarging the cathode surface will result in increasing the electrolytic current and the active sites for generation of hydrides; both phenomena elevate the efficiency of hydride generation. Influence of the cathodic surface area on the hydride generation efficiency was investigated over the range of $0.6–2.0\,cm^2$ as shown in Fig. 6.
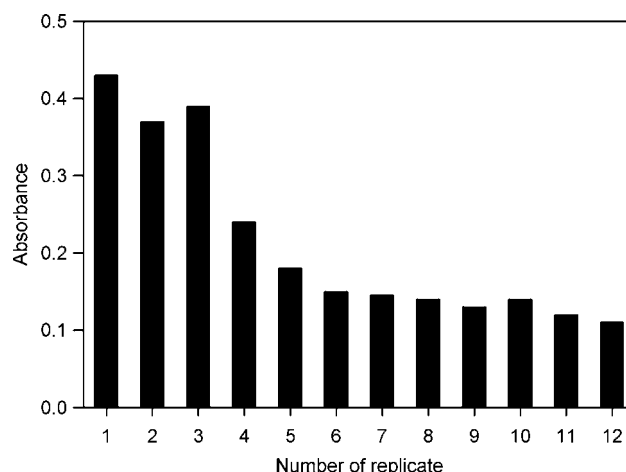
Fig. 5. Influence of the electrode aging on the signal intensity.
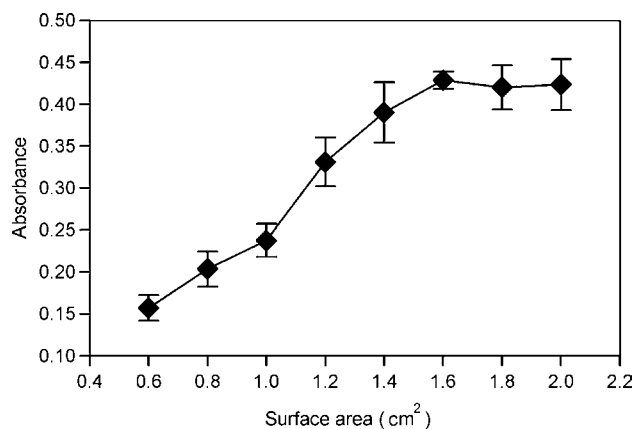
Fig. 6. Optimization of cathode surface area.

Extension of the cathodic surface to $1.5\,cm^2$ resulted in a sharp increase in the signal, followed by a distinctive decrease of the slope. In practice, a helix shaped cathode with the surface area of $1.75\,cm^2$ was used.

3.2.6. Influence of the anolyte flow rate

The effect of the anolyte flow rate was investigated within $0–7.5\,mL\,min^{-1}$ interval. Circulation of the anolyte prevents consuming extra amounts of the anolyte and hence maintaining a constant concentration of the anolyte during the experiment. Also, by circulating the anolyte in the system, the sensitivity and reproducibility would increase. As shown in Fig. 7, the maximum signal intensity was achieved in the range of $3–6\,mL\,min^{-1}$ and the sensitivity decreased at higher flow rates. Therefore, the flow rate of $6\,mL\,min^{-1}$ was chosen as the optimized parameter.

3.2.7. Influence of sample volume

Increasing the volume of the sample resulted in higher signal intensity. The maximum capacity of the cathodic chamber was 18 mL. However, due to upward flowing of the carrier gas, it was impossible to utilize the entire volume. In practice, sample volumes more than 13 mL would be resulted in liquid blocking of the connecting tube, thus spoiling the sensitivity and reproducibility. Therefore, 13 mL was selected as the optimized practical sample volume.

3.2.8. Influence of the carrier gas flow rate

Carrier gas would be necessary to immediately transfer the generated hydrides at the electrode surface to the quartz tube atomizer.
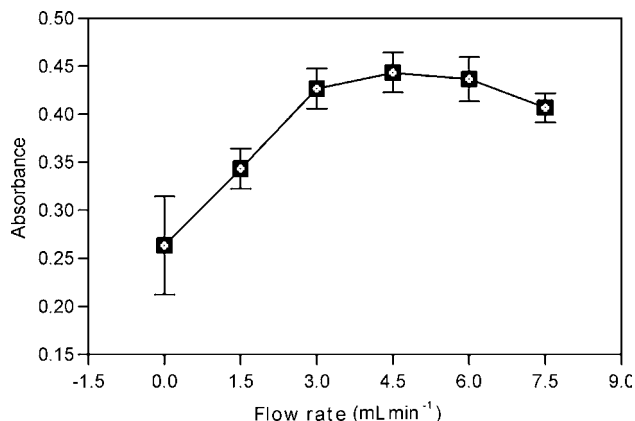

Fig. 7. Optimization of anolyte (Na_2CO_3, $0.5\,mol\,L^{-1}$) flow rate.
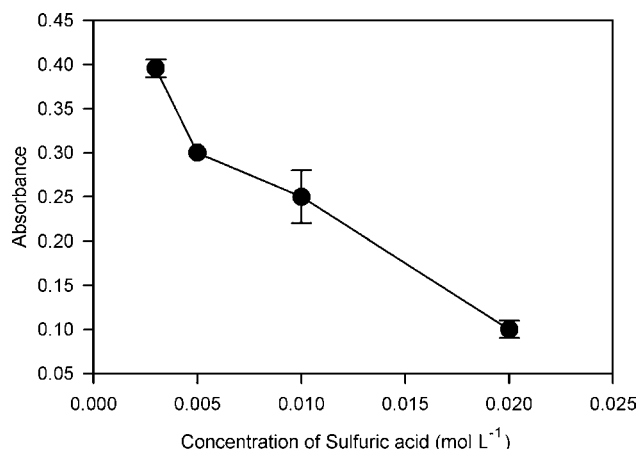
Fig. 8. Optimization of catholyte (sulfuric acid) concentration.

Increasing the flow rate of the carrier gas led to higher sensitivity and lower evolution time for the signal. The flow rate of $100\,mL\,min^{-1}$ was selected as an optimized flow rate, since the higher flow rates may result in liquid blocking of the connecting tube and low reproducibility.

3.2.9. Concentration of catholyte

Concentration of hydronium ion varies during the electrolysis process. When the acidic catholyte solution is neutralized, the signal starts to rise. Therefore, it is expected that higher concentrations of catholyte lead to longer evolution times of the signal. However, this would be true if the system was working at constant current mode. In constant voltage mode, employed in this work, concentration of catholyte is also a determining factor on electrolytic current. Increasing the catholyte concentration would lead to higher electrolytic currents and therefore, shorter peak evolution times. In fact, the catholyte concentration affects two compromising factors on the evolution time. Moreover, concentration of catholyte has a significant impact on the sensitivity. With respect to the generation efficiency of the volatile hydrides and the amount of H_2 co-produced in the reaction, the concentration of acid is very critical for the performance of the ECHG. The influence of sulfuric acid concentration as the catholyte was studied within the range of $0.003–0.02\,mol\,L^{-1}$. The results show that the lower acidic concentrations produce more sensitive signals, since the peak area and the peak height (Fig. 8) both increased by lowering the acid concentration. The use of the concentrations lower than $0.003\,mol\,L^{-1}$ was avoided because of considerable loss of reproducibility and destructive effects on nafion membrane.

3.3. Analytical performance

3.3.1. Analytical figures of merit

The calibration curve was constructed under the optimized conditions (Table 1) within the $1–1000\,ng\,mL^{-1}$ concentration interval of thallium and found to be linear in the range of $1–250\,ng\,mL^{-1}$. The results of this calibration are listed in Table 2. The sensitivity of

Table 2
Analytical figures of merit for EcHG of Tl.

Parameter	Value
Calibration sensitivity ($ng\,mL^{-1}$)	1.68×10^{-3}
Dynamic range ($ng\,mL^{-1}$)	1–250
Characteristic concentration ($ng\,mL^{-1}$)	1.0
Detection limit ($ng\,mL^{-1}$)	0.8
RSD (%)	4.2

Table 3
Effect of co-existing ion (concentration of $10\,\mu g\,mL^{-1}$) for determination of $100\,ng\,mL^{-1}$ Tl.

Species	Recovery (%)
NO_3^-	93
NO_2^-	87
Cl^-	102
$C_2O_4^{2-}$	78
PO_4^{3-}	89
Al^{3+}	99
Cu^{2+}	130
Cd^{2+}	78
Zn^{2+}	100
Mn^{2+}	10
Mg^{2+}	0
Co^{2+}	5
Ni^{2+}	0
Pb^{2+}	59
Sn^{2+}	55
Cr^{3+}	0
Hg^{2+}	102

Table 4
Analytical results of thallium for certified reference material.

Sample	Found (mg kg^{-1})	Certified (mg kg^{-1})	Recovery (%)
ERM®-EB325	37.0 ± 2.7	36.8 ± 1.2	100.5

the method, as determined from the slope of the calibration graph, is 1.68×10^{-3} absorbance ng^{-1} mL. Calculated absolute detection limit based on the variability of the blank ($3\,s_b$ criterion) for seven measurements is $0.8\,ng\,mL^{-1}$. The reproducibility (RSD) for seven replicate measurements at $120\,ng\,mL^{-1}$ of thallium, was obtained to be 4.2%. A simple comparison of the detection limit with those calculated in the previously existing HG-AAS methods shows a remarkable improvement relative to simple batch chemical hydride generation ($0.6\,\mu g\,mL^{-1}$) [9], continuous flow methodologies ($4\,ng\,mL^{-1}$) [10] and flow injection hydride generation-AAS ($3.4\,ng\,mL^{-1}$) [12]. Also, it is comparable with hydride generation-in situ trapping-AAS ($0.4\,ng\,mL^{-1}$) [13].

3.3.2. Interferences from metal ions and hydride-forming elements

A wide variety of transition metal ions and other hydride-forming elements are known to interfere with the hydride generation by releasing the volatile hydrides in CHG as well as in ECHG, and thus limit the analytical applicability of both techniques [5,15]. In the present study, the influence of concomitant ions was evaluated by analysis of $100\,ng\,mL^{-1}$ of thallium in $0.003\,mol\,L^{-1}$ H_2SO_4 in the presence of $10\,\mu g\,mL^{-1}$ of foreign ions. The results are shown in Table 3. There are several mechanisms responsible for the interfering effects in electrochemical hydride generation. Interferences of the transition metals such as Ni^{2+}, Co^{2+}, Cr^{3+}, Fe^{3+} and Mn^{2+} have been shown to be a result of modification of the cathode surface by the reduced interferents. Transition metals are deposited on the cathode surface and dispersed over the surface, so that the cathode and thus the hydrogen overvoltage will be altered [26–29]. Since the Pb–Sn alloy is a cathode with high hydrogen overvoltage value, deposition of most of the metal ions will reduce the hydrogen overvoltage, lowering the efficiency of hydride genera-

tion. Although this phenomenon may interpret the results, further investigations are required to provide better understanding of the individual interfering effects. Since there are significant interferences from major constituents of real matrices, standard addition method is recommended for real sample analysis.

3.4. Accuracy of the method

To establish the accuracy of the method, certified unalloyed zinc (ERM®-EB325) was analyzed. Using the standard addition technique, a recovery of 100.5% was achieved (Table 4). The concentration of Tl found (37.0 ± 2.7) well agreed with the certified value (36.8 ± 1.2).

4. Conclusion

Catholyte variation electrochemical hydride generation was successfully employed to produce thallium hydride species which are supposed to be thallium(I) hydride. The proposed method overcomes the problems of CHG method for production of thallium hydride. The main advantages of the proposed method over the conventional chemical hydride generation method would be its high sensitivity, simplicity, rapidness, freedom of reagent, cost-effectiveness, low acid consumption and environmental cleanness. Efforts are currently being made to overcome its drawbacks by improving the electrochemical hydride generation technique.

References

[1] I. Bodek, W. Lyman, W.F. Reehl, D.H. Resebatt, Environmental Inorganic Chemistry, Permagon Press, New York, 1988.
[2] A.K. Das, M.L. Milli Dutta, M. Cervera, M. de la Guardia, Microchem. J. 86 (2007) 2.
[3] A.K. Das, R. Chakraborty, M.L. Cervera, M. de la Guardia, Anal. Bioanal. Chem. 385 (2006) 665.
[4] J. Zen, J. Wu, Electroanalysis 9 (1997) 302.
[5] P. Pohl, Trends Anal. Chem. 23 (2004) 21.
[6] A. Ramesh, P. Riyazuddin, Anal. Sci. 21 (2005) 1401.
[7] A. D'Ulivio, Spectrochim. Acta: Part B 59 (2004) 793.
[8] T. Nakahara, Anal. Sci. 21 (2005) 477.
[9] D. Yan, Z. Yan, G. Cheng, A. Li, Talanta 31 (1984) 133.
[10] L. Ebdon, P. Goodal, S. Hill, J. Anal. Atom. Spectrom. 10 (1995) 317.
[11] Y. Liao, G. Chen, D. Yan, A. Li, Z. Ni, Anal. Chim. Acta 360 (1998) 209.
[12] Z. Daan, X. Shukun, Atom. Spectrom. 21 (2000) 136.
[13] H. Matusiewicz, M. Krawczyk, J. Braz. Chem. Soc. 18 (2007) 304.
[14] M. Wei, S. Jiang, J. Anal. Atom. Spectrom. 14 (1999) 1177.
[15] F. Laborda, E. Bolea, J.R. Castillo, Anal. Bioanal. Chem. 388 (2007) 743.
[16] M.H. Arbab-Zavar, M. Chamsaz, A. Youssefi, M. Aliakbari, Anal. Chim. Acta 546 (2005) 126.
[17] M.H. Arbab-Zavar, M. Chamsaz, A. Youssefi, M. Aliakbari, Anal. Chim. Acta 576 (2006) 215.
[18] E.M. Bulewicz, T.M. Sugden, Trans. Faraday Soc. 54 (1958) 830.
[19] P. Hunt, P. Schwerdtfeger, Inorg. Chem. 35 (1996) 2085.
[20] X. Wang, L. Andrews, J. Phys. Chem. A 108 (2004) 3396.
[21] S. Aldridge, Chem. Rev. 101 (2001) 3305.
[22] K. Balasubamanian, J.X. Tao, J. Chem. Phys. 94 (1991) 3000.
[23] P. Scwerdtfeger, P.D.W. Boyd, G.A. Bowmaker, H.G. Mack, H. Oberhammer, J. Am. Chem. Soc. 111 (1989) 15.
[24] E. Denkhaus, F. Beck, P. Buechler, R. Gerhard, A. Golloch, Fresenius J. Anal. Chem. 370 (2001) 735.
[25] A.A. Ensafi, B. Rezaei, Microchem. J. 60 (1998) 75.
[26] W.W. Ding, R.E. Sturgeon, J. Anal. Atom. Spectrom. 11 (1996) 421.
[27] E. Bolea, F. Laborda, M.A. Belarra, J.R. Castillo, Spectrochim. Acta: Part B 56 (2001) 2347.
[28] E. Denkhaus, A. Golloch, X.M. Guo, B. Huang, J. Anal. Atom. Spectrom. 16 (2001) 870.
[29] E. Bolea, D. Arroyo, G. Cepria, F. Laborda, J.R. Castillo, Spectrochim. Acta: Part B 61 (2006) 96.

Analysis of parabens in cosmetics by low pressure liquid chromatography with monolithic column and chemiluminescent detection

J. Ballesta Claver, M.C. Valencia, L.F. Capitán-Vallvey *

Solid Phase Spectrometry Research Group, Department of Analytical Chemistry, Campus Fuentenueva, Faculty of Sciences, University of Granada, E-18071 Granada, Spain

ARTICLE INFO

ABSTRACT

This paper presents an application of chromatographic separation based on an ultra-short monolithic column and chemiluminescent detection in an FIA type instrument manifold for the determination of four paraben mixtures: methylparaben (MP), ethylparaben (EP), propylparaben (PP) and butylparaben (BP). The separation is achieved in 150 s using two consecutive carriers: first 12% ACN:water that changes 75 s after injection to 27% ACN:water. The detection is based on the oxidation of the hydrolysis product of parabens, p-hydroxybenzoic acid, with Ce(IV) in the presence of Rhodamine 6G which evokes chemiluminescence of sufficient intensity to enable a sensitive determination of these species. After optimization of the variables involved, the analytical method is characterized, displaying the following values for concentration ranges, detection limits and precision, as relative standard deviation at low concentration (0.15 mg l^{-1})—MP: from 9.9×10^{-7} to 3.3×10^{-4} M; 1.9×10^{-8}; 5.6%; EP: from 9.0×10^{-7} to 3.3×10^{-4} M; 2.8×10^{-8}; 3.5%; PP: from 8.3×10^{-7} to 9.9×10^{-5} M; 2.3×10^{-8}; 4.2%; and BP: from 7.7×10^{-7} to 9.9×10^{-5} M; 4.2×10^{-8} M; 6.2%. The method was applied and validated satisfactorily for the determination of these parabens in cosmetic samples, comparing the results against a liquid chromatography reference method.

© 2009 Elsevier B.V. All rights reserved.

1. Introduction

The combination of chromatography with flow techniques offers some interesting characteristics. Flow methods present advantages in simplicity, low cost, versatility, speed, and, usually, good analytical figures, but typically do not allow the separation of analyte mixtures. Liquid chromatography is a well-established technique with high selectivity and performance, but it requires much more expensive instrumentation than flow techniques. This justifies the combination of flow techniques, such as flow injection analysis (FIA) [1], sequential injection analysis (SIA) [2] and multisyringe flow injection analysis (MSFIA) [3] with low pressure chromatographic separations to achieve selective low-cost methodology with respect to traditional liquid chromatography (LC).

The key of this merging of techniques is monolithic columns, a high cross-linked porous monolithic polymer, with well-defined, bimodal pore-size distribution, mesopores for retention and larger macropores for through-flow that provide good separation power and high chemical stability and flow characteristics (up to 15 ml min^{-1}) [4,5].

Different combinations of flow techniques and monolithic materials have been used for separations of drug mixture [1–3,6,7], pollutants such as polyaromatic hydrocarbons [8] and inorganic cations and anions mixtures [5,9–11]. In all these methods, the detector used is DAD or conductivity.

Chemiluminescence (CL), observed when the vibronically excited product of an exoergonic reaction relaxes to its ground state with the emission of photons, has been widely used as a detection method in different techniques such as LC, capillary electrophoresis, thin layer chromatography and FIA [12]. In this paper we are interested in the use of chemiluminescence detection in low pressure chromatographic separations using a FIA system that includes a monolithic column, due to the good detection limits and versatility, in order to improve the characteristics of these methods.

There are different types of chemistries used for CL generation, but one of the most useful is the combination of Ce(IV) and Rhodamine 6G. This reaction was applied with FIA to determine different compounds such as chlorpromazine [13], phentolamine [14], hydrochlorothiazide [15], ferulic acid [16] and parabens [17]. All these FIA determinations were performed without any separation steps.

CL detection has rarely been used in low pressure chromatographic systems with a monolithic column using FIA manifolds. Thus, Adcock et al. [1] propose a hybrid FIA/LC system for the separation of six alkaloids and four biogenic amines using a 25 mm length

---

* Corresponding author.
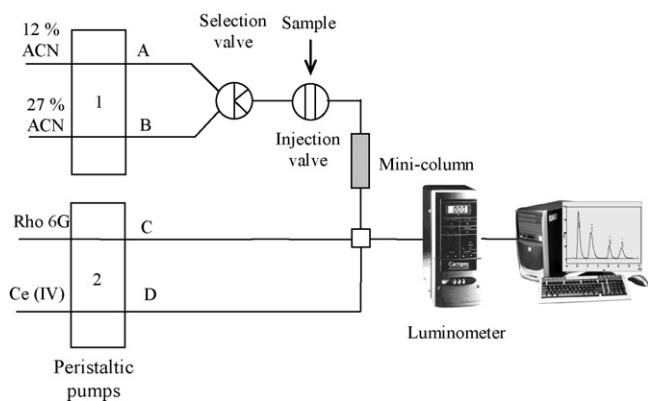 *E-mail address:* lcapitan@ugr.es (L.F. Capitán-Vallvey).

Fig. 1. FIA manifold for the separation of parabens with a mini-column and CL detection.

monolithic column with tris(2,2′-bipyridyl)ruthenium(III) and permanganate CL detection. Paull et al. [18] use a 3 mm long chelating monolithic disk for the selective retention and CL determination of Cu(II) based on 1,10-phenanthroline and hydrogen peroxide chemistry.

Parabens are a homologous series of hydroxybenzoic acid esterified at the C-4 position, including methyl, ethyl, propyl and butyl, used as an antimicrobial in foods, beverages, pharmaceuticals and cosmetics [19,20]. Their presence in cosmetics, especially for consumers that use them in a daily basis and in large quantities, could induce allergic contact dermatitis [21]. Their uses are regulated by Cosmetic Directive 76/768/EEC in amounts up to a maximum concentration of 0.4% in the finished product for one ester and up to 0.8% for mixtures of esters [22].

We have previously studied the separation of parabens alone [23] or in mixtures with other additives [24] using a low pressure chromatographic system with a monolithic column and spectrophotometric detection. The aim of this paper is to use chemiluminescence as a detection system for parabens determination to increase the sensitivity of the method and its application to cosmetics analysis.

2. Experimental

2.1. Reagents and chemicals

Methylparaben (MP) (Sigma–Aldrich Química S.A., Madrid, Spain, 99%), ethylparaben (EP), propylparaben (PP), and butyl-

paraben (BP) (last three from Fluka, Madrid, Spain, 99%) 1.6×10^{-2} M stock solutions were prepared by exact weighing of each compound and dissolution in acetonitrile (ACN) (Panreac Química S.A., Barcelona, Spain, 99.9% (v/v) HPLC grade). These solutions were spectrophotometrically stable when protected from light and kept in the refrigerator at $4\,^\circ$C at least for two months. Working solutions were prepared by appropriate dilution with water while maintaining 12% (v/v) ACN. A working standard solution containing the four parabens at 6.5×10^{-4} M each were prepared and kept in the refrigerator at $4\,^\circ$C.

The CL reagents used were 10^{-2} M ammonium cerium(IV) sulfate dihydrate (99%) and 1 M of sulfuric acid, both by Merck (Madrid, Spain) and 10^{-3} M of Rhodamine 6G chloride (Rho 6G) 95% by Sigma. All chemicals used were of analytical-reagent grade. Aqueous solutions were prepared using reverse-osmosis type quality water produced by a Milli-RO 12 plus Milli-Q purification system (Millipore, Bedford, MA, USA).

2.2. Apparatus and software

The flow analysis setup consisted of two Gilson Minipuls-2 (Gilson, Inc., Middleton, USA) four channel peristaltic pumps working at a constant flow rate and two variable volume Rheodyne 5041 teflon rotary valves (one as injection valve and another as selection valve). PTFE tubing (Omnifit, Cambridge, England) (0.8 mm i.d. and 1.6 mm o.d.) and various end-fittings and connectors of different diameters were used. As the separation element in the flow system we used a C_{18} monolithic mini-column (Chromolith Guard Cartdrige RP-18 endcapped) (5 mm × 4.6 mm i.d.) from Merck (Darmstadt, Germany). Chemiluminescence measurements were performed with a CL-1 Camspec luminometer (Camspec Ltd., Cambridge, UK) interfaced to a personal computer via an INT7 - 24 bit A/D integration board.

Other instruments used were a Hewlett Packard HP-8453 diode array spectrophotometer (Nortwalk, CT, USA) interfaced to a PC and equipped with a Hellma 138-QS flow cell with 1 mm light path, an Agilent 1100 series liquid chromatograph with DAD detector provided with a C_8 Zorbax column used to validate the proposed method and a Crison digital pH-meter with combined glass-saturated calomel electrode (Crison Instruments, Barcelona, Spain). Software programs used to treat the data were CSW32 software package supplied by DataApex Ltd. v 1.2.5 (2001) (Prague, Czech Republic) used for the acquisition and manipulation of the luminescence data; Statgraphics software package (Manugistics Inc. and Statistical Graphics Corporation, USA, 1992), ver.4.0 (1993) and Microsoft Office 2003.
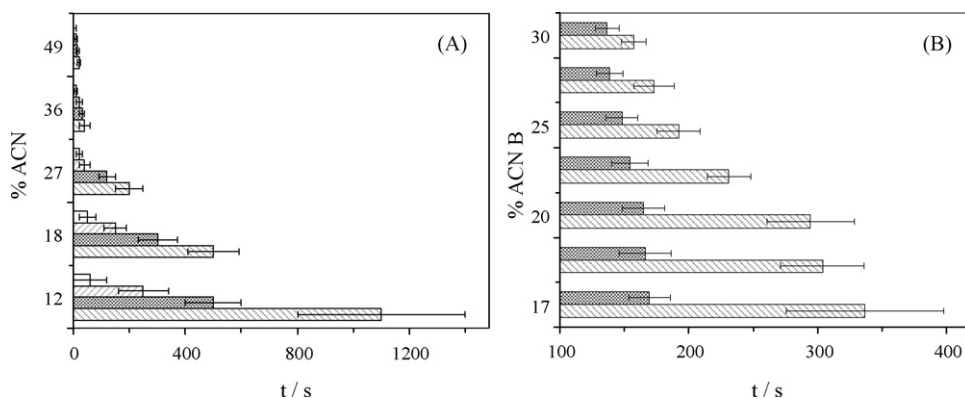
Fig. 2. (A) Retention time dependence on ACN percentage for different parabens. Each point is the average of three measurements. Conditions—carrier: ACN/water. Standards: diluted with the same carrier, 12.5 mg l^{-1}. Flow rate: 1.4 ml min^{-1}. Loop volume: 150 μl. (B) Dependence of retention time on carrier B composition. Conditions—carrier A: 12% ACN/water and carrier B: ACN/water. Flow rate: 2.6 ml min^{-1}. Standards: diluted with the same carrier, 12.5 mg l^{-1}. Loop volume: 150 μl. Bars represent the retention time of parabens and horizontal lines represent the peak broadness. Legend: (□) MP, (▨) EP, (▦) PP, and (▧) BP.
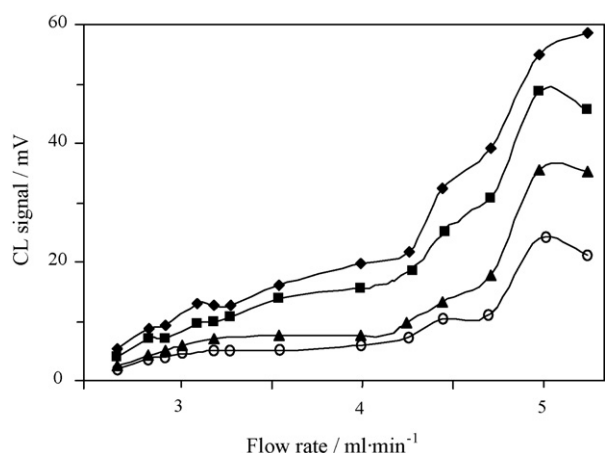
Fig. 3. Variation of the CL emission signal with flow rate. Conditions: 10^{-2} M Ce(IV); 10^{-4} M Rho 6G; standards 2 mg l^{-1} (($\blacklozenge$) MP, ($\blacksquare$) EP, ($\blacktriangle$) PP, and ($\bigcirc$)BP). The x-axis shows the total flow composed for the two pumps in the system.

2.3. Procedure

2.3.1. Standards and samples

A standard or sample solution containing between 10^{-6} and 10^{-4} M each in MP, EP, PP and BP was inserted into the flow analysis system through a loop valve injector of 75 μl of capacity with the same composition as the carrier A. The carrier A stream (12% ACN:H$_2$O, v/v) at a flow rate of 2.6 ml min^{-1} was changed to carrier B (27% ACN:H$_2$O, v/v) 75 s after the injection valve was opened, through the selection valve (see Fig. 1). After the sample plug reached the monolithic mini-column, the carrier containing the already separated analytes was mixed using a 4-way connector with two solutions for CL generation at a flow rate of 2.5 ml min^{-1} using a second peristaltic pump. The first solution was 2×10^{-2} M of Ce(IV), dissolved in 2 M H$_2$SO$_4$, and the second 4×10^{-4} M Rho 6G. The CL analytical signal used for paraben determination corresponds to the difference between the maximum CL intensity ($I_{standard}$) and CL background ($I_{background}$). The relationship between the concentration and peak height was established by conventional calibration with external standards.

2.3.2. Reference

As reference method, an adaptation of the LC–DAD method proposed by Borremans et al. [25] was used. A 5 μm C$_8$ silica in a 150 mm × 4.6 mm column along with water/acetonitrile/methanol/tetrahydrofuran (60/25/10/5) isocratic mobile phase at a constant flow rate of 1.0 ml min^{-1} was used. The chromatograms were obtained at a wavelength of 254 nm. To obtain the calibration function, five different concentrations and three replicates each of the different parabens with peak height as analytical parameter were used.

2.3.3. Maintenance

For correct maintenance of the flow system, especially the mini-column, before the analysis carrier A had to be passed at a flow rate of 2.6 ml min^{-1} for 5 min to condition the mini-column. After the analysis and when the last peak arrived at the baseline, 150 s after injection valve was opened, the flow system was conditioned again with carrier A for 30 s. In order to improve the lifetime of the mini-column, after use it was washed for 5 min with carrier A and then with water for another 5 min.

2.4. Sample preparation

For the analysis of the cleaning mousse, an adequate amount (typically 1 g) was weighed, and mixed with 5 ml of MeOH. The
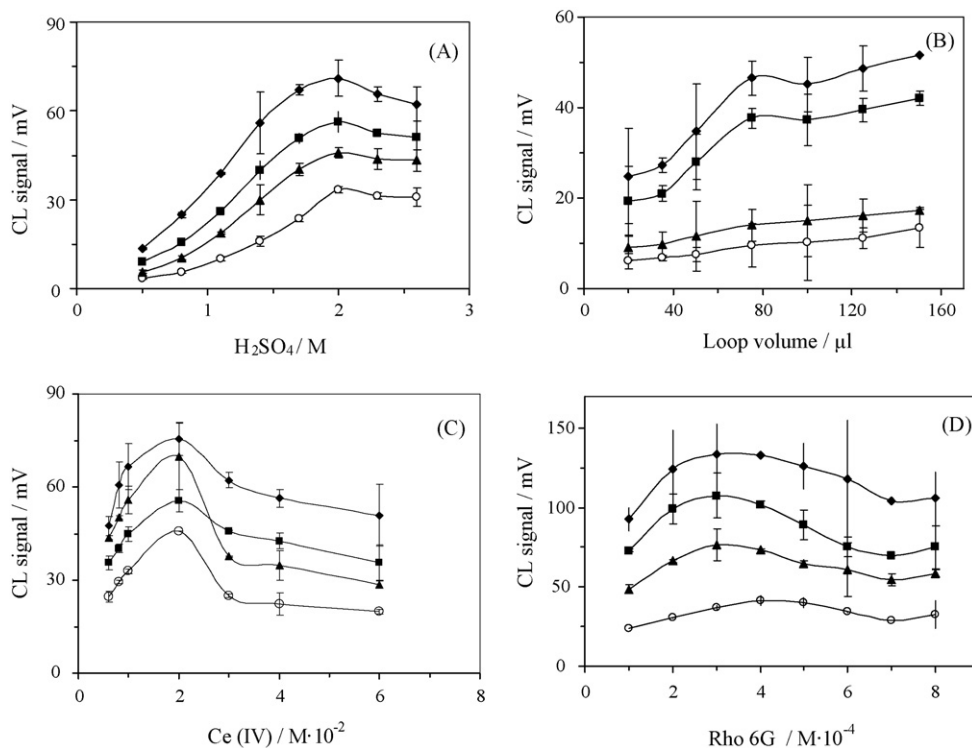
Fig. 4. Optimization of CL reagent concentration. (A) H$_2$SO$_4$ concentration—conditions: Ce(IV) 10^{-2} M; Rho 6G 10^{-4} M; loop volume 75 μl. (B) Loop volume—conditions: Ce(IV) 10^{-2} M; Rho 6G 10^{-4} M; H$_2$SO$_4$ 0.5 M. (C) Ce(IV) concentration—conditions: Rho 6G 10^{-4} M; H$_2$SO$_4$ 2 M; loop volume 75 μl. (D) Rho 6G concentration—conditions: Ce(IV) 2×10^{-2} M; H$_2$SO$_4$ 2 M; loop volume 75 μl. In all cases we used a mixture of 2 mg l^{-1} for each paraben (($\blacklozenge$) MP, ($\blacksquare$) EP, ($\blacktriangle$) PP, and ($\bigcirc$) BP). Bars represent the repeatability of CL signals (three replicates per point).

solution was sonicated for 10 min, and filtered through 0.45 μm filters [26]. An adequate amount of this filtrate was diluted to 10 ml.

For the analysis of cleaning towels, an adaptation of the procedure proposed by Saad et al. [27] was applied. An adequate amount (typically 3 g) was weighed and cut into strips to improve contact with the solvent. 25 ml of ACN were added and placed in an ultrasonic bath for 30 min at 50 °C and then the mixture was filtered through a 0.45 μm filter. Finally, the solution was evaporated to dryness and dissolved with 10 ml of ACN.

In both cases the basic procedure was applied to the samples. Samples were measured in triplicate and the mean peak height values were used for data acquisition.

3. Results and discussion

The widely used alkyl hydroxybenzoates (as preservatives) are a mixture of the first four homologues and their resolution requires a separation step. In a previous paper [23] we studied the feasibility of that separation using a monolithic mini-column included in a flow system with UV detection. Here we combined the separation ability of monolithic mini-columns with the advantages of chemiluminescent detection for paraben analysis. The typical advantages in terms of selectivity, by choosing the suitable chemiluminescent chemistry, and sensitivity, as is usual with an emissive technique, were observed. Next we studied first the chromatographic separation of parabens with an FIA system using simple spectrophotometric detection, and second, their post-column CL

detection, considering the influence of separation conditions on this CL detection.

3.1. Separation procedure

As a separative element, a monolithic mini-column, the Chromolith commercial guard cartridges, C_{18} reverse phase silica 5 mm in length and 4.6 mm diameter was selected. The system back pressure was reduced using tubing with 0.8 mm i.d. being the maximum flow rate attained 2.6 ml min^{-1}.

The main variable that influenced separation is the carrier composition used, typically made up of a buffer and an organic solvent. As the four parabens have very similar pK_a (MP 8.87; EP 8.90; PP 8.87; BP 8.79) [28], pH is not very relevant for paraben separations for which reason we did not use any buffer. Additionally, we did not adjust the acidity conditions required for CL reaction (H_2SO_4 2 M) to prevent the hydrolysis of parabens during separation.

Of the several carriers tested, the best results were obtained with ACN/water and MeOH/water mixtures. After comparing both carriers, we selected the ACN/water solution because it needed a lower percentage of ACN to obtain the same results than the MeOH/water carrier. The retention behaviour of parabens is according to their polarity: MP < EP < PP < BP (the more methylene groups the molecule has, the greater the retention time; log P: 1.91 MP; 2.34 EP; 2.94 PP; 3.50 BP [28]), as expected (Fig. 2). Additionally, if we consider the effect of both solvents in CL detection, we observe a decrease in CL emission. Thus, 20% MeOH means a decrease in
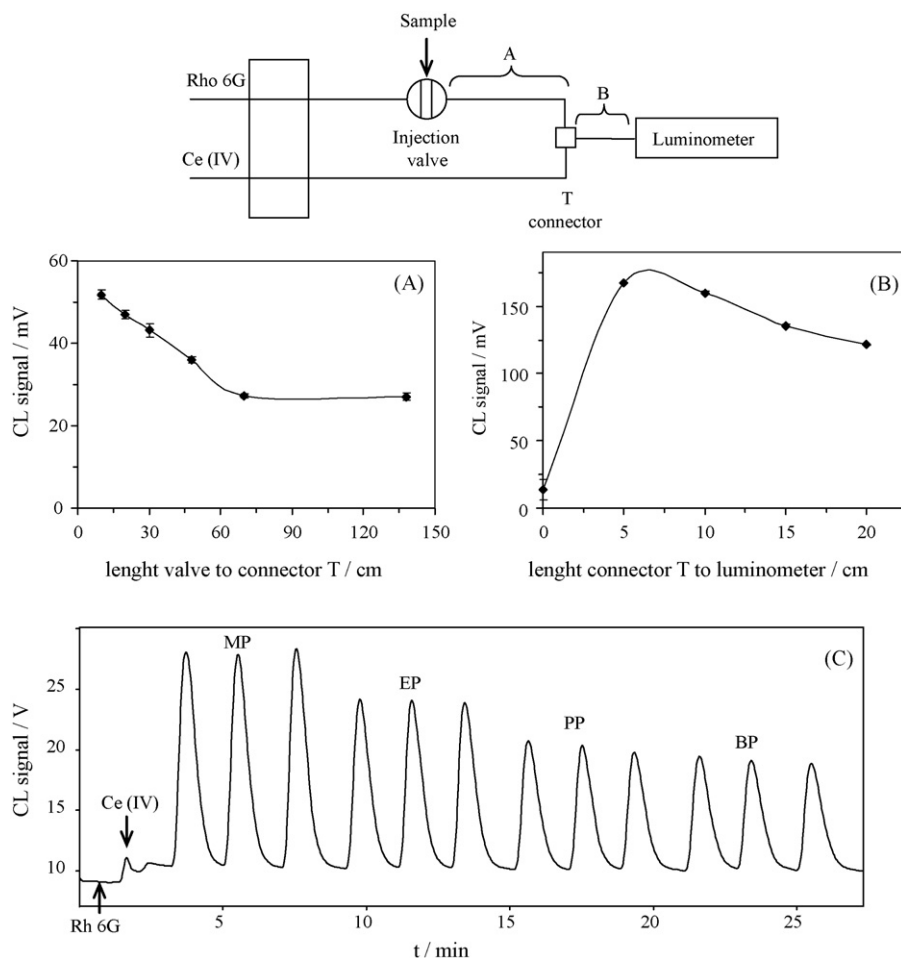
Fig. 5. Manifold used to discuss the CL mechanism: (A) dependence of CL signal with distance from injection valve to T-connector; (B) dependence of CL signal distance from T-connector to luminometer; (C) CL record from solutions containing 1 mg l^{-1} in each parabens injected separately. Conditions: Ce(IV) 2×10^{-2} M, Rho 6G 4×10^{-4} M, 2 M of sulfuric acid and 75 μl of loop volume at a flow rate of 2.5 ml min^{-1}.

Table 1
Analytical parameters for the MP–EP–PP–BP mixture.

Parameter	MP		EP		PP		BP	
	Height	Area	Height	Area	Height	Area	Height	Area
b	76.6	479.2	49.0	473.7	8.0	443.8	11.5	68.0
S_b	25.8	129.6	17.5	135.6	6.0	199.8	3.7	39.3
a (M^{-1})	9.3×10^6	1.0×10^8	6.3×10^6	1.0×10^8	7.6×10^6	6.2×10^7	4.2×10^6	7.2×10^7
S_a (M^{-1})	1.8×10^5	9.2×10^5	1.2×10^5	9.6×10^5	1.3×10^5	1.4×10^6	8.0×10^4	8.4×10^5
R^2 (%)	99.3	99.9	99.3	99.9	99.6	99.2	99.5	99.8
LDR (M)	9.9×10^{-7} to 3.3×10^{-4}	9.9×10^{-7} to 3.3×10^{-4}	9.0×10^{-7} to 3.3×10^{-4}	9.0×10^{-7} to 3.3×10^{-4}	8.3×10^{-7} to 9.9×10^{-5}	8.3×10^{-7} to 9.9×10^{-5}	7.7×10^{-7} to 9.9×10^{-5}	7.7×10^{-7} to $9. \times 10^{-5}$
LOD (M)	1.9×10^{-8}	9.2×10^{-9}	2.8×10^{-8}	9.6×10^{-9}	2.3×10^{-8}	1.6×10^{-8}	4.2×10^{-8}	1.3×10^{-8}
LOQ (M)	6.4×10^{-8}	3.1×10^{-8}	9.4×10^{-8}	3.2×10^{-8}	7.8×10^{-8}	5.2×10^{-8}	1.4×10^{-7}	4.4×10^{-8}
RSD[a] (%)	5.6	4.2	3.5	5.4	4.2	8.7	6.2	9.3
RSD[b] (%)	2.9	3.8	4.3	2.3	5.2	5.4	3.7	5.3

b, intercept; S_b, standard deviation of intercept; a, slope; S_a, standard deviation of slope; R, correlation coefficient; LDR, linear dynamic range; LOD, limit of detection (ten replicates); LOQ, limit of quantification.

[a] Relative standard deviation (five replicates) for 0.15 mg l^{-1} (low concentration) of parabens.

[b] Relative standard deviation for 15 mg l^{-1} of parabens (high concentration).

CL of 34.7% and 15% ACN means a reduction in CL of 5.3%, a similar effect to that described by Santiago Valverde et al. [29]. This fact also supports the selection of ACN:water as a carrier.

As Fig. 2A shows, the resolution of four parabens in the mini-column is possible working in isocratic mode. 18% ACN/H_2O can be chosen, obtaining an analysis time of 600 s. However, the selection of 12% ACN/H_2O produces better CL sensibility, but with an analysis time of 23.3 min. The increase in the flow rate decreases the analysis time (500 s at 12% of ACN/H_2O) but it is too high, due to the high retention time for the two last parabens, PP and BP. Consequently, we selected the maximum flow rate of 2.6 ml min^{-1} and studied the minimization of the analysis time by decreasing the polarity of the carrier, switching after MP and EP were eluted (75 s after injection). To this end, we introduced a new carrier B composed of ACN/H_2O. In this way, PP and BP are sped up as seen in Fig. 2B, obtaining the best retention time at 27%.

The consecutive use of these two carriers makes it possible to obtain a good resolution between all peaks (Rs > 1.2) and a reasonable analysis time (150 s). With carrier A, ACN/water 12%, we separated MP and EP and with carrier B, ACN/water 27%, PP and BP. In those conditions, the retention times for the four parabens are 29 s MP, 65 s EP, 104 s PP and 125 s BP.

3.2. Optimization of CL detection

The optimization of the CL conditions was studied independently and univariantly for a mixture of the four parabens and compromise values were selected. In this case, the configuration of the FIA manifold is different from other cases previously described for CL detection [17,30] in order to prevent the saturation of the mini-column with Rho 6G which decreases performance. For this reason we used different flow lines for Rho 6G and the parabens.

3.2.1. Total flow rate

As seen in Fig. 1, we used two peristaltic pumps for the two stages of the setup: separation and detection. Since the flow rate of the pump used for the separation was set at 2.6 ml min^{-1}, we studied the dependence of CL emission with respect to the total flow rate achieved, by adjusting the flow rate of the pump used for CL detection. Fig. 3 shows that CL emission increases with the flow rate up to 5.1 ml min^{-1}, and then decreases. This means that the maximum CL emission increases as the flow rate does when the reaction is produced closer to the flow cell, but at higher rates, the CL emission maxima moves away from the flow cell and the signal decreases. Thus, we worked at 2.5 ml min^{-1} for the flow rate of the pump used for CL detection.

3.2.2. H_2SO_4 concentration

Detection, which involves Ce(IV) and different fluorophores such as Rho 6G, requires strong acidic conditions, coming in this case from the H_2SO_4 used for the Ce(IV) solution. Fig. 4A shows a maximum emission at 2 M H_2SO_4 for all parabens. This behaviour is due to the fact that the higher the H_2SO_4 concentration, the higher the hydrolysis of parabens, increasing the signal according to the CL mechanism [17]. The explanation for this is shown in the following mechanism section.

3.2.3. Loop volume

We studied loops of different lengths, and consequently different volumes, from 20 to 150 µl. As is usual with chromatography, the width of the peak increased and the resolution decreased at higher volumes. Additionally, Fig. 4B shows a small increase in the CL signal with the loop volume. When the loop volume increased from 20 to 150 µl, the chromatographic parameters increased; thus

Table 2
Comparison of determination of paraben mixtures in cosmetics samples with different analytical techniques.

Method	Compounds	Range (μM)	LOD (μM)	Precision (%)	Application	Reference
DAD detection						
Electrophoresis	MP	3.0–49	2.1	2	Cosmetics	[36]
	EP	3.5–57	1.8	1		
	PP	3.3–54	1.4	1		
	BP	3.6–58	2.9	1		
LC	MP	6.6–26	0.1	2	Cosmetics	[37]
	EP	6.0–240	0.2	3		
	PP	5.5–221	0.2	3		
	BP	5.1–205	0.2	2		
FIA mini-column	MP	32–823	31.7	1	Cosmetics	[23]
	EP	38–658	11.5	3		
	PP	57–1070	17.3	3		
	BP	112–1970	33.7	4		
CL detection						
FIA (no separation)	MP	0.003–0.9	0.002	1	Food	[17]
	EP	0.02–3	0.01	1		
	PP	0.03–5	0.01	2		
	BP	0.04–4	0.03	2		
LC	MP	0.03–46	0.01	3	Cosmetics	[26]
	EP	0.03–54	0.02	2		
	PP	0.03–55	0.02	2		
	BP	0.03–51	0.03	2		
FIA (mini-column)	MP	1–330	0.02	6	Cosmetics	This paper
	EP	0.9–330	0.03	4		
	PP	0.8–100	0.02	4		
	BP	0.8–100	0.04	6		

the retention time (13.7%); height (101.7%); area (116.3%); bandwidth (16.2%); resolution (3.3); analysis time (14.3%). Volumes greater than 150 μl give strongly overlapping results (Rs < 0.5). We selected 75 μl as the optimum loop volume as a compromise between the analytical the analytical signal, analysis time and bandwidth.

3.2.4. Cerium(IV) concentration

The effect of Ce(IV) concentration on the CL intensities of parabens was examined. Different concentrations between 6×10^{-3} and 6×10^{-2} M were used obtaining the best CL signal for the parabens at 2×10^{-2} M (Fig. 4C). The decrease of the signal at higher Ce(IV) concentrations has been described in the literature and ascribed either: (1) to an absorption of radiation by the excess of yellow Ce(IV) solution [17] or (2) to the fact that the maximum of the reaction occurs before the solution reaches the luminometer because the reaction rate increases with Ce(IV) concentration [14]. In order to study the reason of this influence, we performed an indirect experiment using a new FIA manifold (Fig. 5). We observed that an increase in distance B (>5 cm) decreased the CL signal (Fig. 5B), due to the fact that the maximum CL emission occurred inside the tubing, before reaching the flow cell, when we increased its length at a constant Ce(IV) concentration, which agrees with the hypothesis of Liu and Huang [14].

3.2.5. Rhodamine 6G concentration

The concentration of aqueous Rho 6G, studied from 10^{-4} to 8×10^{-4} M, also affected the CL signal (Fig. 4D). As the working concentration, we selected 4×10^{-4} M because of its better repeatability. When the concentration of Rho 6G increases, the CL emission decreases slowly because of the formation of nonfluorescent dimers of Rho 6G which act as an efficient quencher of the monomer [31].

3.2.6. Ionic strength

Ionic strength was studied by adding different amounts of NaCl to the carrier (up to 0.25 M), having, as could be expected for these analytes, no influence on the retention times, although a small influence in peak height was observed (for MP, PP and BP increases 2.1%, 7.6% and 7.6%, respectively, and for EP a 5.1% decrease). Consequently, no salt was added to the carrier.

3.3. Chemiluminescence mechanism

The mechanism of the Ce(IV)–Rho 6G reaction has been studied extensively in the literature [13,14,30,32] and its reaction mechanism with parabens has been discussed by Zhang et al. [26] and Cui et al. [17]. Here we discuss the mechanism and offer some additional data to confirm it.

When Ce(IV) reacts with Rho 6G a small chemiluminescent emission occurs, as can be observed by the small peak at the beginning of the CL record in Fig. 5C. This emission is due to the redox reaction:

$$Ce(IV) + Rho\,6G \rightarrow Ce(III)^* + Rho\,6G_{ox} \tag{1}$$
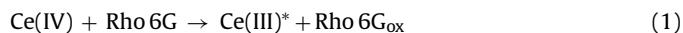
The Rho $6G_{ox}$ is nonfluorescent [33] and the Ce(III) is in excited state. This Ce(III)* can return to this fundamental state with a small CL emission, but in the presence of fluorophore Rho 6G transfers its energy, emitting more fluorescence [30]:

$$Ce(III)^* + Rho\,6G \rightarrow Ce(III) + Rho\,6G^* \rightarrow Rho\,6G + h\nu \tag{2}$$

The addition of a phenolic compound, as is the case with parabens, to this redox reaction strongly increases the CL emission. For parabens, it has been suggested that the reaction is due to the p-hydroxybenzoic acid (PHBA) generated by acidic hydrolysis:

$$paraben + H_2SO_4 \rightarrow PHBA + RH \tag{3}$$

where RH is the corresponding alcohol.

Produced PHBA is easily oxidized by Ce(IV) producing Ce(III)* [17] giving the corresponding oxidation products that consists of 3,4-dihydroxybenzoic acid, 1,4-hydroquinone and 1,4-benzoquinone [34], indicated as $PHBA_{ox}$ in the following equation:

$$Ce(IV) + PHBA \rightarrow Ce(III)^* + PHBA_{ox} \tag{4}$$

Table 3
Recovery results obtained for the paraben mixtures in cosmetics.

Compounds	Samples			
	Cleaning mousse		Cleaning towels	
	Spiked level (mg g^{-1})	Recovery[a] (%)	Spiked level (mg g^{-1})	Recovery[a] (%)
MP	0.22	111.4 ± 7.6	1.56	107.2 ± 2.8
EP	0.34	92.1 ± 8.5	0.48	83.3 ± 2.9
PP	0.20	104.5 ± 6.5	0.45	100.3 ± 3.8
BP	0.18	99.2 ± 4.3	–	–

[a] Values are means for three determinations ± standard deviation.

This Ce(III)* in the presence of Rho 6G gives rise to a more intense emission because of the higher Ce(III)* production from PHBA [13] (Eq. (2)).

Indeed, we observed that PHBA produced the CL emission, but we checked that different parabens working at the same concentration (see Fig. 5C) produced a different CL intensity. This apparently contradictory result could be ascribed to the different hydrolysis rate of each paraben. An increase in the alkyl chain length of parabens increases their resistance to hydrolysis [19], which decreases when the carbon chain does, lowering the CL signal, data that agrees with the enzymatic hydrolysis study of parabens by Valkova et al. [35]. Thus, each peak in Fig. 5C corresponds to the PHBA coming from a different hydrolyzed paraben.

To support the above mechanism, it is assumed that those Eqs. (1) and (4) occur at the same time, but in a different extension, and thus we used different FIA manifolds, shown in Fig. 5, to test this assertion. If Ce(IV) is mixed first with parabens, a higher hydrolysis and more CL emission occur. We observed this behaviour when we used a short tube from the injection valve to the T-connector (Fig. 5A), because at this length (15 cm) there is no time to complete the mixing of the Rho 6G with the paraben in the flow line. When all the reagents are mixed together (Fig. 5A, length tube >60 cm) the CL emission is lower due to lower Ce(III)* production because Eqs. (1)–(4) occur at the same time.

3.4. Analytical parameters

The calibration functions for each paraben were obtained using eight standards and three replicates each and all responded to a linear function with the form: $I = aX + b$.

Table 1 presents the analytical parameters for the proposed paraben determination. The limit of detection (LOD) ($K = 3$) and the limit of quantification (LOQ) ($K = 10$) of the method were established according to IUPAC. The sampling frequency was approx. 20 h^{-1}. From Table 1 it is apparent that the use of the peak area as the

Fig. 6. CL record for standards and samples (cleaning mousse and cleaning towels).

Table 4
Results obtained for the paraben mixtures by reference and proposed methods.

Sample	MP (mg g^{-1})			EP (mg g^{-1})			PP (mg g^{-1})			BP (mg g^{-1})		
	Proposed method[a]	Reference method[a]	P_v[b] (%)	Proposed method[a]	Reference method[a]	P_v[b] (%)	Proposed method[a]	Reference method[a]	P_v[b] (%)	Proposed method[a]	Reference method[a]	P_v[b] (%)
Cleaning mousse	0.64 ± 0.01	0.670 ± 0.001	5.0	0.14 ± 0.01	0.153 ± 0.001	15.5	0.21 ± 0.01	0.210 ± 0.001	68.9	0.194 ± 0.004	0.203 ± 0.001	6.7
Cleaning towels	0.73 ± 0.01	0.73 ± 0.01	97.4	0.210 ± 0.002	0.208 ± 0.001	71.9	0.20 ± 0.01	0.201 ± 0.001	5.0	–	–	–

[a] Mean of three determinations ± SD. The data are expressed in mg of paraben per gram of product (three replicates per point).

[b] P_v: P-value.

analytical parameter presents more sensitivity but lower repeatability than using the peak height. For that reason, we chose the peak height, as is usual with chemiluminescent methods, for the analytical applications.

Comparing the analytical characteristics of the different methods for paraben analysis found in the literature (Table 2), we observed that the LC shows the highest lineal range when compared to low pressure flow techniques and capillary electrophoresis. Moreover, the use of CL detection decreases the LOD in general (tenfold lower) as well as the repeatability, and increases the lineal range (one range). The coupling of chemiluminescence for detection in separation techniques improves the analytical determination of parabens.

3.5. Analytical applications

The proposed method was applied to cosmetics samples (cleaning towels and cleaning mousse). One of them contained only three parabens (cleaning towels) and the other contained the four (cleaning mousse) (Fig. 6).

For the extraction of parabens in the cosmetics products studied, we used an adaptation of the procedure based on ACN proposed by Saad et al. [27] for the cleaning towels and on the use of MeOH for the cleaning mousse [26]. The quantitativeness of the extraction procedures was tested through the addition of known amounts of each paraben. Recoveries of the different parabens (Table 3) ranged between 92.0 and 111.4%.

Table 4 shows that the proposed CL method is validated by comparison with an LC reference method [25].

The proposed method has several advantages over the usual LC method: it uses very simple, fast instrumentation that is cheaper and has better detection limits. The drawbacks of this methodology concern its lower precision and limited capacity for separation due to the column length, although it is sufficient for the determination of these parabens.

4. Conclusions

We succeeded in separating the mixture of four parabens MP, EP, PP and BP using a low pressure chromatographic system with an ultra-short monolithic column (5 mm) with chemiluminescent detection. The use of chemiluminescent detection based on the Ce(IV)–Rhodamine 6G chemistry improves the lineal range and lowers the detection limit some two orders of magnitude with respect to spectrophotometric detection while maintaining the precision. CL detection increases the sensitivity of the method for its application to cosmetics analysis. The results were chemometrically validated and compared with an LC reference method. The described method is practical, simple, rapid and inexpensive and can determine the parabens at $\mu g\,l^{-1}$ with a precision between 2 and 6%. This method shows a short analysis time (150 s) and is easy to maintain.

References

[1] J.L. Adcock, P.S. Francis, K.M. Agg, G.D. Marshall, N.W. Barnett, Anal. Chim. Acta 600 (2007) 136.
[2] P. Chocholous, D. Satinsky, P. Solich, Talanta 70 (2006) 408.
[3] H.M. Gonzalez-San Miguel, J.M. Alpizar-Lorenzo, V. Cerda-Martin, Talanta 72 (2007) 296.
[4] K. Cabrera, J. Sep. Sci. 27 (2004) 843.
[5] S. Pelletier, C.A. Lucy, J. Chromatogr. A 1118 (2006) 12.
[6] D. Satinsky, J. Huclova, R.L.C. Ferreira, M.C. Montenegro, P. Solich, J. Pharm. Biomed. Anal. 40 (2006) 287.
[7] J. Klimundova, D. Satinsky, H. Sklenarova, P. Solich, Talanta 69 (2006) 730.
[8] P.N. Nesterenko, M.A. Rybalko, Dokl. Chem. 404 (2005) 178.
[9] B. Paull, C.O. Riordain, P.N. Nesterenko, Chem. Commun. (2005) 215.
[10] D. Connolly, D. Victory, B. Paull, J. Sep. Sci. 27 (2004) 912.
[11] D. Victory, P. Nesterenko, B. Paull, Analyst 129 (2004) 700.
[12] C. Dodeigne, L. Thunus, R. Lejeune, Talanta 51 (2000) 415.
[13] Y. Huang, Z. Chen, Talanta 57 (2002) 953.
[14] W. Liu, Y. Huang, Anal. Chim. Acta 506 (2004) 183.
[15] J.A. Murillo Pulgarin, A. Alanon Molina, G. Perez-Olivares Nieto, Anal. Chim. Acta 518 (2004) 37.
[16] J.P. Wang, N.B. Li, H.Q. Luo, Spectrochim. Acta A 71 (2008) 204.
[17] A. Myint, Q. Zhang, L. Liu, H. Cui, Anal. Chim. Acta 517 (2004) 119.
[18] E. Tyrrell, P.N. Nesterenko, B. Paull, J. Liquid Chromatogr. Relat. Technol. 29 (2006) 2201.
[19] M.G. Soni, I.G. Carabin, G.A. Burdock, Food Chem. Toxicol. 43 (2005) 985.
[20] S.H. Kang, H. Kim, J. Pharm. Biomed. Anal. 15 (1997) 1359.
[21] E. Nettis, M. Marcandrea, M.C. Colanardi, M.T. Paradiso, A. Ferrannini, A. Tursi, Allergy 58 (2003) 1304.
[22] Scientific Committee on Consumer Products, European Commission Extended Opinion on the Safety Evaluation of Parabens, 2005, SCCP/0873/05, 1-11.
[23] J.F. Garcia-Jimenez, M.C. Valencia-Miron, L.F. Capitan-Vallvey, J. Anal. Chem., in press.
[24] J.F. Garcia-Jimenez, M.C. Valencia, L.F. Capitan-Vallvey, Anal. Chim. Acta 594 (2007) 226.
[25] M. Borremans, J. van Loco, P. Roos, L. Goeyens, Chromatographia 59 (2004) 47.
[26] Q. Zhang, M. Lian, L. Liu, H. Cui, Anal. Chim. Acta 537 (2005) 31.
[27] B. Saad, M. Bari, M.I. Saleh, K. Ahmad, M. Talib, J. Chromatogr. A 1073 (2005) 393.
[28] T. Angelov, A. Vlasenko, W. Tashkov, J. Liquid Chromatogr. Relat. Technol. 31 (2008) 188.
[29] R. Santiago Valverde, I. Sanchez Perez, F. Franceschelli, M. Martinez Galera, M.D. Gil Garcia, J. Chromatogr. A 1167 (2007) 85.
[30] H. Cui, Q. Zhang, A. Myint, X. Ge, L. Liu, J. Photochem. Photobiol. A 181 (2006) 238.
[31] T. Taguchi, S. Hirayama, M. Okamoto, Chem. Phys. Lett. 231 (1994) 561.
[32] Y. Ma, X. Jin, M. Zhou, Z. Zhang, X. Teng, H. Chen, Anal. Chim. Acta 489 (2003) 173.
[33] S. Feng, X. Chen, G. Zhang, J. Fan, L. Jianyan, Huaxue Fence 39 (2003) 221.
[34] C.K. Duesterberg, T.D. Waite, Environ. Sci. Technol. 41 (2007) 4103.
[35] N. Valkova, F. Lepine, L. Labrie, M. Dupont, R. Beaudet, J. Biol. Chem. 278 (2003) 12779.
[36] U. Uysal, T. Guray, J. Anal. Chem. 63 (2008) 982.
[37] L. Labat, E. Kummer, P. Dallet, J.P. Dubost, J. Pharm. Biomed. Anal. 23 (2000) 763.

Determination of cadmium and lead species and phytochelatins in pea (*Pisum sativum*) by HPLC–ICP-MS and HPLC–ESI-MSn

Danuta Barałkiewicz [a],[*], Małgorzata Kózka [a], Aneta Piechalak [b], Barbara Tomaszewska [b], Paweł Sobczak [a]

[a] Department of Trace Elements Analysis by Spectroscopy Method, Faculty of Chemistry, Adam Mickiewicz University, Grunwaldzka 6, 60-780 Poznań, Poland
[b] Department of Biochemistry, Faculty of Biology, Adam Mickiewicz University, Umultowska 89, 61-614 Poznań, Poland

ABSTRACT

An analytical approach based on hyphenated techniques was used for studying the speciation of cadmium and lead in *Pisum sativum*. Proper preservation conditions were employed to avoid the oxidation of –SH groups and corresponding decomposition of metal-binding complexes. SEC column was washed with 5 mM beta-mercaptoethanol and then samples were analysed using ICP-MS as a detector. Results showed that cadmium is the inhibitor of lead uptake. HPLC–ESI-MSn assays revealed fragmentation pathways of phytochelatins.

© 2009 Elsevier B.V. All rights reserved.

1. Introduction

Trace elements play an important role in the functioning of life on our planet. Some of them can be highly toxic, whereas others can be essential. These effects are very often related to particular form in which the element is present [1]. Often these different chemical forms of a particular element or its compounds are referred to as "species".

Cadmium and lead are widespread heavy-metal pollutants released into the environment by human activities. The presence of Pb^{2+} and Cd^{2+} in the environment leads to numerous disturbances in many metabolic processes in plants. Inhibition of growth is a major symptom.

Higher plants, algae and some fungi respond to potentially toxic levels of metal ions mainly by the chelation and sequestration of the excess of the element into harmless compounds. When exposed to heavy-metal ions, plants induce thiol peptides to protect cell structures against toxicity [2]. Phytochelatins (PCs) (III class metallothioneins) prevail over other thiols and are the most important among such peptides. PCs are short non-protein heavy-metal-binding peptides, the synthesis of phytochelatins takes place under the influence of heavy metals in most plants. Its general structure is $(\gamma Glu\text{-}Cys)_n\text{-}Gly$ ($n = 2$–11) [3]. PCs are synthesized through the action of the enzyme PC synthase [EC 2.3.2.15] in which glutathione and its homologs are the substrates, this enzyme is constitutively

present in the cytoplasm of plant cells [4]. The presence of heavy metals is essential for the biosynthesis of PCs to proceed. The cadmium ions are the most efficient activator of PC synthase between the metals belonging to groups 11–15 in the fourth, fifth and sixth period in the periodic table. Phytochelatins and glutathione chelate metal ions and, then, as low-molecular complexes LMW-HM, they are transported into the vacuole. There, they are released and form solid complexes with, for instance, organic acids or long-chained PCs or S^{2-}, thus forming high-molecular complexes HMW [15]. Apart from the main PCs family one can find other groups of phytochelatins in different plant species like homo-phytochelatins $(\gamma Glu\text{-}Cys)_n\text{-}\beta Ala$ or iso-phytochelatins $(\gamma Glu\text{-}Cys)_n\text{-}Glx$.

Hyphenated techniques, such as HPLC–ICP-MS and HPLC–ESI-MSn seem to be the best analytical instruments to study metal speciation in plants. They were applied in phytoremediation research as well as in the understanding of metal accumulation mechanism [5–9].

ICP-MS is the best detector for the determination of not only total metal at the trace level but also type or size of compounds engaged in metal binding [7,10,12,13]. It can be connected with various HPLC separation techniques, from which SEC is considered to be the most suitable [10–12]. Recently, Navaza et al. presented SEC–ICP-MS results on the speciation of cadmium and arsenic in plant [14]. However, they tested these two metals separately. Very few studies under cadmium binding deal with possible interactions with other heavy metals. Plants have developed complex mechanisms to control the uptake and metabolic pathways of different metals [15]. It is natural that metabolic links between these metals exist and some of them are well documented [15,16]. Cd^{2+} ions can inter-

fere with some Zn-dependent processes [15] due to their chemical similarity, for example. Such interactions can be pinpointed using detection techniques such as ICP-MS or AAS. Protective effect of selenium against mercury toxicity [12], reduced Zn uptake in Cu presence [16] or enhanced Pb uptake in Cu presence [17] are just few examples.

The HPLC–ESI-MS[n] technique may be successfully used for the identification of metal-binding compounds. Recently, Xuan et al. applied this hyphenated technique to the separation and identification of metal–phytosiderophores complexes. Identification of compounds was made on the basis of observed and calculated m/z values [18]. It is, however, possible to provide undoubtful identification using sequential MS[n] experiments in conjunction with ion trap (IT). Such assay may reveal complex fragmentation patterns of the studied compounds. Such information is invaluable in speciation analysis. Speciation analysis is the analytical activity of identifying and/or measuring the quantities of one or more individual chemical species in a sample [19]. Depending on possibilities and purposes it is possible to perform both qualitative and quantitative observations. Qualitative test are primarily used when particular species is unknown or accurate result is not important (for example, only confirmation of the presence is needed).

In this study, we used hyphenated techniques to identify compounds engaged in Cd and Pb metabolism and to perform analysis of metal complexes induced in *Pisum sativum* exposed to cadmium and lead. These identified compounds might be the valuable source of information to study metal accumulation mechanism for bioremediation processes.

2. Experimental

Analytical grade reagents and deionised, ultrafiltered water were used throughout. For RPLC separation method gradient-grade-pure acetonitrile (JT Baker) was used. For sample preparation suprapur HNO_3 (Merck) was used. The Branson Model 1210 ultrasonic bath (USA) was used for metal species extraction from plant tissues. The Heraeus Instruments (Germany) Model Biofuge fresco refrigerated ultracentrifuge was used for the separation of the supernatant from plant tissues.

2.1. ICP-MS and SEC conditions

For peptide separation the size-exclusion Superdex Peptide 75 HR 10/30 (Pharmacia Biotech, Sweden) column was used. Its exclusion limit is 100 kDa (an optimum separation range is 3–70 kDa). The column was calibrated with cysteine ($M_r = 121$ Da), glutathione ($M_r = 307$ Da), metallothionein ($M_r \approx 7000$ Da) and human albumin–Fe complex ($M_r = 66,000$ Da). The column was washed for 30 min with 30 mM Tris buffer (pH 7.4) with 5 mM BMSH before each separation to remove metal ions adsorbed on the stationary phase. 30 mM Tris buffer with 10 mM NaCl (pH 7.4) was an eluate.

The ICP-MS instrument was an Agilent 7500ce ICP mass spectrometer (Agilent Technologies, Tokyo, Japan), which was used as an element specific detector for scanning metal content in plant sample. SEC eluate was introduced into ICP-MS system through Babington nebuliser fitted in Scott's spray chamber. ICP-MS measurement conditions are listed in Table 1. Isotopes monitored were [111]Cd, [112]Cd, [114]Cd and [206]Pb, [207]Pb, [208]Pb. The calibration graphs were obtained for metal concentration within range $0.1–100.0$ µL^{-1}.

2.2. HPLC–ESI-MS conditions

Chromatographic separations were performed using a Model HP 1100 gradient HPLC pump (Agilent Technologies, Germany) as the delivery system. Injections were made using a Model 7725 injection valve with injection loop 100 µL (Rheodyne, Cotati, USA) for SEC analysis. LC analysis of plant extracts in connection to ESI-MS was performed using a 20-µL loop. RPLC separation was carried out on C_{18} column, 150 mm × 2.1 mm (Alltech-Ultima) in gradient mode.

The ESI-MS experiments were performed using ion trap mass spectrometer Esquire 3000 (Bruker Daltonics, Germany) equipped with an electrospray ion source. Conditions and parameters are presented in Table 2.

2.3. Sample material

Plants of pea (*P. sativum*) var. 'Kwestor' were soaked in water for 4 h and then germinated in the dark at 24 °C for 3 days. After that seedlings were grown hydroponically in Hoagland solution. Seven-day-old seedlings were exposed to Pb (0.5 mmol L^{-1}), Cd (0.1 mmol L^{-1}) and Pb + Cd (both 0.1 mmol L^{-1}) ions. The ions were added as a Pb(NO$_3$)$_2$ and CdCl$_2$. Plant material was sampled after 96 h of incubation with metals, roots were separated, washed and immediately frozen.

2.4. Sample preparation for SEC–ICP-MS analysis

Weighted sample (1 g of root material) was frozen in liquid nitrogen and stored in temperature −80 °C. Then root sample was ground

Table 1
SEC and ICP-MS parameters.

SEC conditions	
Column	Superdex Peptide 75 HR 10/30
Calibration	Cysteine ($M_r = 121$ Da)
	Glutathione ($M_r = 307$ Da)
	Metallothionein ($M_r \approx 7000$ Da)
	Human albumin–Fe complex ($M_r = 66,000$ Da)
Mobile phase	30 mM Tris buffer with 10 mM NaCl (pH 7.4)
ICP-MS parameters	
Spectrometer	Agilent 7500 ce with Octopole Reaction System
Sampler and skimmer	Nickel
Forward power	1320 W
Plasma gas flow rate	14.85 L min^{-1}
Dwell time	1 s
Number of replicate	4
Scanning mode	Pulse
Isotopes monitored	[111]Cd, [112]Cd, [114]Cd, [206]Pb, [207]Pb, [208]Pb
Internal standards	[45]Sc, [115]In, [133]Cs
Nebulizer	Micromist

Table 2
HPLC and ESI-MS parameters.

HPLC conditions	
Column	Alltech-Ultima, C_{18} column, 150 mm × 2.1 mm × 5 µm
Mobile phase	A: 0.5% formic acid in water
	B: 95% acetonitrile with 0.5% formic acid
Flow rate	0.2 mL min^{-1}
Injection volume	20 µL
Gradient program	
Time [min]	% of B
0	0.2
25	17
32	55
40	55
ESI-MS parameters	
ESI source voltage	4 kV
Nebulisation pressure	30 psi
Dry gas flow	9.0 L min^{-1}
Temperature	310 °C
m/z range for data acquiring	50–1200

Table 3
Microwave oven program.

Time [min]	Power [W]
0	0
2	100
4	100
6	250
10	250
13	450
20	450
~60	Cooling

with mortar and pestle with the addition of 30 mM Tris–HCl (pH 7.4) dedicated to water-soluble metal complexes. The pH of used solution should be neutral to avoid breaking up of metal–peptide complex. The extracts were sonificated and centrifuged twice (15 min at 15,000 rpm). The separated supernatant was filtered with 0.45 μm syringe filter and injected on size-exclusion column immediately.

2.5. Sample preparation for total metal concentration analysis

Roots were left to dry on air, weighted and ground with mortar and pestle. Samples were mineralized with 1 mL of HNO_3 and 4 mL of water in microwave oven. Mineralization program is presented in Table 3. Mineralized samples were diluted to 10 mL with water and analysed with ICP-MS.

2.6. Sample preparation for HPLC–ESI-MS^n analysis

Weighted sample (0.5 g of frozen root material) was ground with mortar and pestle with the addition of 5% sulfosalicylic acid. The homogenate was centrifuged twice (10 min at 10,000 rpm) at 4 °C. The separated supernatant was filtered with 0.45 μm syringe filter.

3. Results and discussion

3.1. Effect of exposure to Cd and Pb to the metal speciation in pea roots

The comparison (Fig. 1) between the SEC–ICP-MS chromatograms showed differences in elution times and the intensities of Cd and Pb signals in examined root extracts. While the mobile phase was buffer at pH 7.4 to stabilize metal–peptide complexes, still very little of Pb (0.2–1%) and Cd (3–8%) was extracted from the root samples. Total amount of Pb in root samples was between 2.7 and 30 mg g^{-1} and Cd concentration was around 0.9–2.7 mg g^{-1} (Table 4). The most of the heavy-metal ions were bonded among others to the cell wall compounds as lignin, pectin or mugenic acid, and only about 1% of total accumulated by plant metal penetrate through cell wall and membrane to cytosol [20]. Recovery of cadmium for SEC was established as 70% and 62% for Pb. In plants exposed to Cd and Cd + Pb, cadmium eluted mainly in two peaks. The metal complex stability depended on the few main factors such

Table 4
Cadmium and lead concentration in pea roots and plant extracts.

Cadmium and lead dose [mM]	Total Cd concentration [mg g^{-1}]	Total Pb concentration [mg g^{-1}]
0.1 Cd	2.67	–
0.5 Pb	–	30.31
0.1 Cd + 0.1 Pb	0.89	2.68
Concentration of Cd and Pb in root extracts (% of total metal amount)		
10 mM Tris–HCl, pH 7.4	0.07–0.10 (3–8%)	0.03–0.08 (0.2–1%)
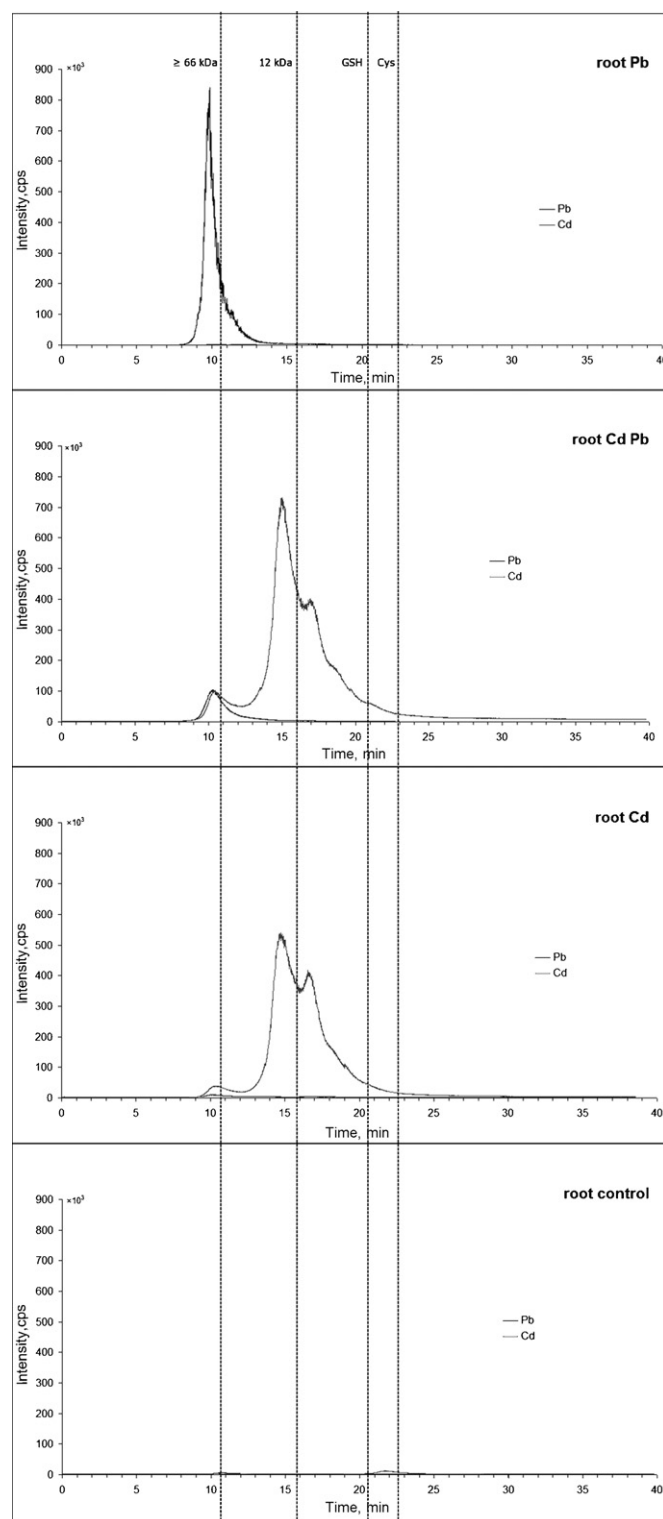
Fig. 1. Size-exclusion HPLC chromatograms with ICP-MS selective detection of Cd and Pb of pea root extracts.

as pH, temperature and total analysis time. The conditions of extraction and separation were determined in previous experiments (data not included). The similar research was done for Cd-PCs [21,22] or As-PCs [23].

Former is related to cadmium complex with bioligand of molecular mass higher than 12 kDa and can be observed both in Cd and Cd + Pb extracts. This finding corresponds with the results of other
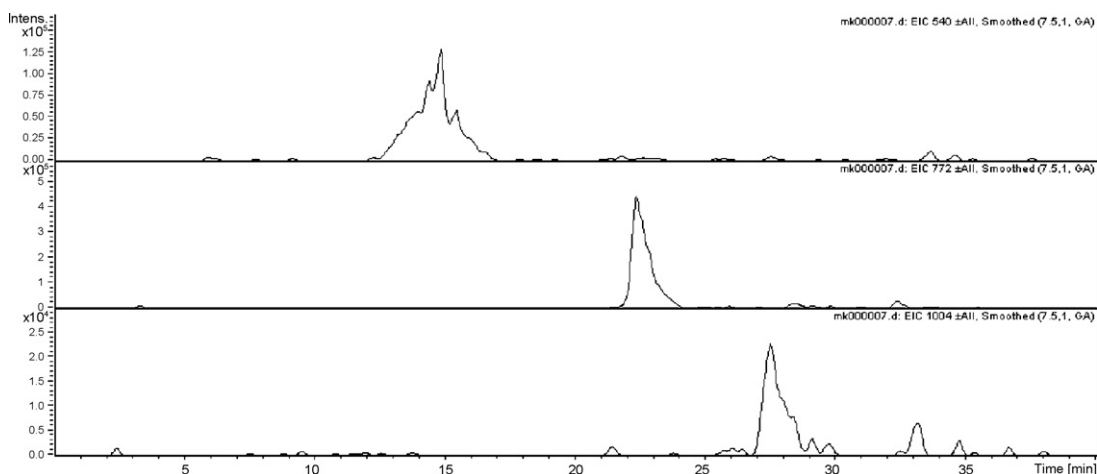
Fig. 2. HPLC–ESI-MS^n chromatogram of pea root with Cd and Pb extract as the EIC.

researchers [5–7,24]. The latter was better divided in Cd extract and is related with metal complex of molecular mass between 10 and 12 kDa.

As for Cd, there were no larger differences in SEC–ICP-MS chromatograms between plants cultivated with one or two metals. Peak which eluted first – molecular mass 66 kDa – appeared in samples with Cd and Pb but, as for Pb, it was nine times higher than cadmium bioligand. Pb was eluted in one peak from size-exclusion column and was six times higher in plant extract exposed to Pb than to Cd/Pb. It affirmed our previous studies [25] that pea roots accumulated strongly higher lead concentration when there was no cadmium in solution. In studied plants cadmium was rather an inhibitor of Pb uptake. In pea roots cultivated with both Cd + Pb cadmium level was 67% lower than Cd amount in roots of plants treated

with 0.1 mM Cd. However the lead amount was over 90% lower than in roots of plants exposed only to 0.5 mM Pb. The antagonistic interaction between cadmium and lead were reported also for other plants for example mustard [26] but Kadukova et al. [27] observed positive effect of Cd presence on Pb accumulation in roots of *Nerium oleander*. These results suggest that the character of interaction between metals depends also on the plant species. Recently Youn-Joo et al. showed that the toxicity of cadmium and lead together does not differ significantly from their standalone presence [28].

3.2. Separation and identification of phytochelatins in P. sativum

Identification of target compounds in extracts was done with HPLC–ESI-MS^n analyses in positive and negative ion mode. HPLC
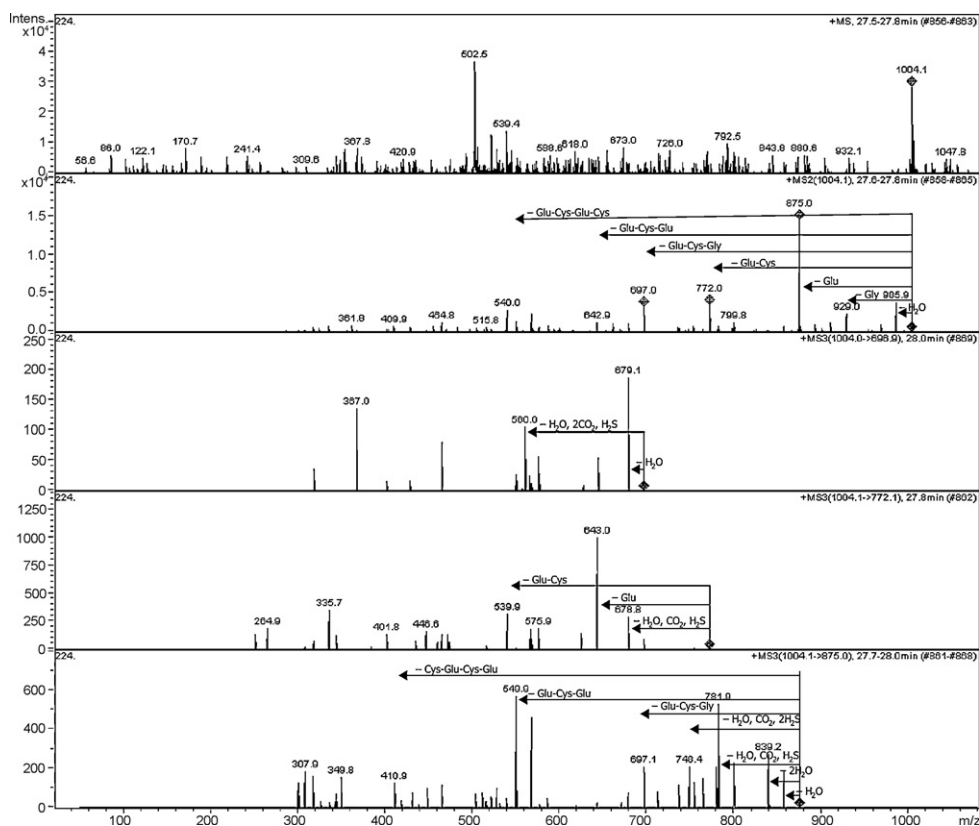
Fig. 3. Fragmentation of PC4 from chromatographic peak observed at EIC 1004.

chromatograms were observed as extracted ion current (EIC) for the following values: 540, 772 and 1004 m/z ratios which correspond with PC$_2$, PC$_3$ and PC$_4$, respectively (Fig. 2). Each peak was analysed with ESI-MS with ion trap (IT). Protonated molecules [M+H]$^+$ outweighed the others. It was possible to use the ion trap for deeper scan of phytochelatins' ions and perform multiple CIS MS/MS experiment, either. The most intense daughter ions in the MS spectra were chosen for further fragmentation. As a result we obtained MS^n spectra (Fig. 3) which definitely confirmed the presence of phytochelatins. One can notice that m/z ratios of signals from daughter ions correspond with the structure of phytochelatins.

Identification of phytochelatins was also carried out with ESI-MS spectra obtained for the whole sample instead single chromatographic peaks (Fig. 4). Based on the m/z ratio following phytochelatins were identified: PC$_2$ (m/z 540), PC$_3$ (m/z 772) and PC$_4$ (m/z 1004). Moreover, ESI-MS mass spectra confirmed that hPC$_2$ (m/z 554), hPC$_3$ (m/z 786), PC$_2$-γGlu (m/z 411) and PC$_3$-γGlu (m/z 786) are present in samples (Fig. 4). In plants cultivated with cadmium we observed the most intensive signals for PC$_3$ and PC$_4$, while in plants treated with lead for PC$_2$.
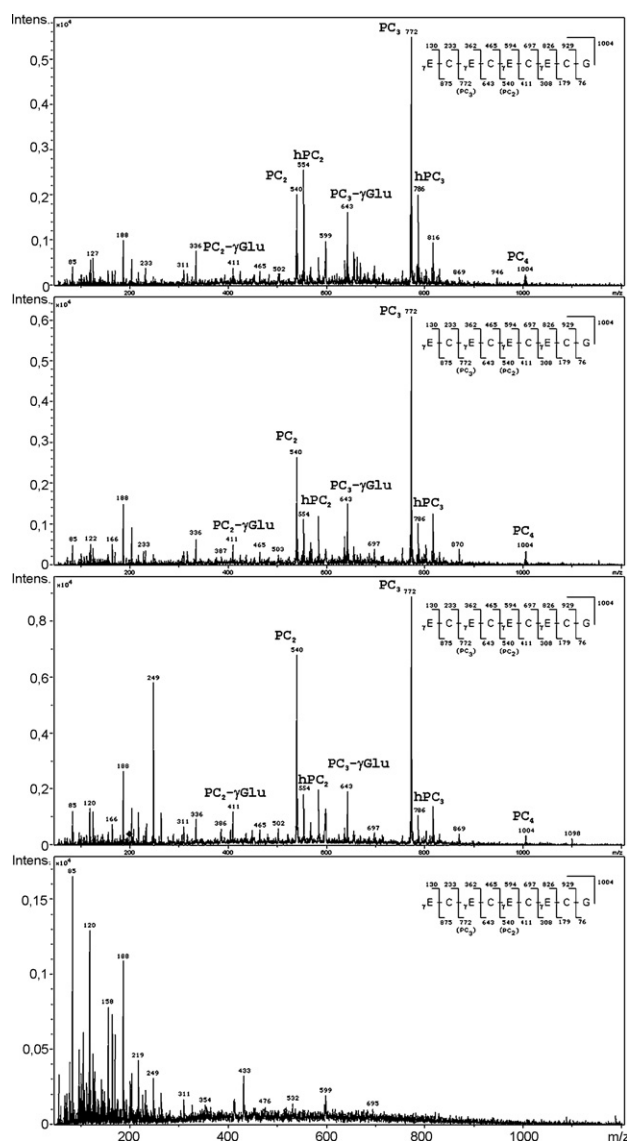
These agree with the results of Srivastava et al. who studied the synthesis of phytochelatins in response to cadmium stress in *Cuscuta reflexa* [29]. The presence of phytochelatin in plants exposed to cadmium was strictly connected with metal detoxification and sequestration. In plants cultivated with lead were not observed as Pb-PCs complexions. This suggests another role of phytochelatin, in plants cultivated with lead we observe and also identify using HPLC ESI IT MS oxidised form of PCs (data not included). Probably phytochelatins play role as antioxidants in lead treated plants [30]. In pea root extracts phytochelatins and homo-phytochelatins were determined. This analytical procedure allowed for the identification of phytochelatins and PC homologs.

4. Conclusions

Size-exclusion chromatography coupled to ICP-MS detection is the proper technique for screening metal complexes in plants.

Electrospray mass spectrometry allows the identification of phytochelatins in extracts from roots of pea plants. Ion trap enables the determination of the amino acid sequence of PCs and unambiguous identification of thiol compounds. In our previous studies [20,25] total concentration of phytochelatins in pea samples was determined by HPLC with their post-column derivatization. Identification of respective PCs and hPCs was not possible due to the lack of standards.

Presented results provide new information about cadmium and lead complexes and their interactions in *P. sativum*. These knowledge might be very usuful for use pea plant in bioremediation in its climate zone.

Acknowledgement

References

[1] I. Pais, J.B. Jones, The Handbook of Trace Elements, St. Lucie Press, 1997, p. 32.
[2] H. Kubota, K. Sato, T. Yamada, T. Maitani, Phytochemistry 53 (2000) 239.
[3] E. Grill, E.L. Winnacker, M.H. Zenk, Science 230 (1985) 674.
[4] S. Clemens, E.J. Kim, D. Neumann, J.I. Schroeder, EMBO J. 18 (1999) 3325.
[5] I. Leopold, D. Gunther, Fresen. J. Anal. Chem. 359 (1997) 364.
[6] I. Leopold, D. Gunther, J. Schmidt, D. Neumann, Phytochemistry 50 (1999) 1323.
[7] Z. Wei, J.W. Wong, D. Chen, Microchem. J. 74 (2003) 207.
[8] J. Szpunar, S. McShheehy, K. Połeć, V. Vacchina, S. Mounicou, I. Rodriguez, R. Łobiński, Spectrochim. Acta B 55 (2000) 779.
[9] V. Vacchina, S. Mari, P. Czernic, L. Marques, K. Piaelli, D. Schaumloffel, M. Lebrun, R. Łobiński, Anal. Chem. 75 (2003) 2740.
[10] J. Szpunar, Analyst 125 (2000) 963.
[11] R.N. Collins, J. Chromatogr. A 1059 (2004) 1.
[12] J. Meija, M. Montes-Bayón, J.A. Caruso, A. Sanz-Medel, Trends Anal. Chem. 25 (1) (2006) 44.
[13] A. Sanz-Medel, M. Montes-Bayón, M.L. Fernandez-Sánchez, Anal. Bioanal. Chem. 377 (2003) 236.
[14] A.P. Navaza, M. Montes-Bayón, D.K. LeDuc, N. Terry, A. Sanz-Medel, J. Mass Spectrom. 41 (2006) 3.
[15] S. Clemens, Biochimie 88 (2006) 1707.
[16] S. Puig, N. Andrés-Colás, A. García-Molina, L. Feñarrubia, Plant, Cell Environ. 30 (2007) 271.
[17] J.S. Weis, T. Glover, P. Weis, Environ. Pollut. 131 (2004) 409.
[18] Y. Xuan, E.B. Scheuermann, A.R. Meda, H. Hayen, N. von Wirén, G. Weber, J. Chromatogr. A 1136 (2006) 73.
[19] D.M. Templeton, F. Ariese, R. Cornelis, L.-G. Danielsson, H. Muntau, H.P. van Leeuwen, R. Lobinski, Pure Appl. Chem. 72 (2000) 1453.
[20] A. Piechalak, B. Tomaszewska, D. Baralkiewicz, A. Malecka, Phytochemistry 60 (2002) 153.
[21] V. Vacchina, K. Połec, J. Szpunar, J. Anal. Atom. Spectrom. 14 (1999) 1557–1566.
[22] B.B.M. Sadi, A.P. Vonderheide, J.-M. Gong, J.I. Schroeder, J.R. Shann, J.A. Caruso, J. Chromatogr. B 861 (2008) 123–129.
[23] K. Bluemlein, A. Raab, J. Feldmann, Anal. Bioanal. Chem. 393 (2009) 357–366.
[24] K. Połeć-Pawlak, R. Ruzik, K. Abramski, M. Ciurzyńska, H. Gawrońska, Anal. Chim. Acta 540 (2005) 61.

Fig. 4. Electrospray mass spectra of plant tissue (exposed to Cd and Pb) extracts.

[25] M. Kózka, D. Barałkiewicz, A. Piechalak, B. Tomaszewska, Chem. Anal. 51 (2006) 427.
[26] Z.-X. Niu, L.-N. Sun, T.-H. Sun, Y.-S. Li, H. Wang, J. Environ. Sci. 19 (2007) 961–967.
[27] J. Kadukova, E. Manousaki, N. Kalogerakis, Acta Metall. Slovaca 12 (2006) 181–187.
[28] A. Youn-Joo, K. Young-Mi, K. Tae-Im, J. Seung-Woo, Sci. Total Environ. 326 (2004) 85.
[29] S. Srivastava, R.D. Tripathi, U.N. Dwivedi, J. Plant Physiol. 161 (2004) 665.
[30] D. Baralkiewicz, M. Kozka, P. Kachlicki, A. Piechalak, B. Tomaszewska, Int. J. Environ. Anal. Chem. 88 (2008) 979–988.

Enzyme class identification in cleaning products by hydrolysis followed by derivatization with *o*-phthaldialdehyde, HPLC and linear discriminant analysis

M. Beneito-Cambra, V. Bernabé-Zafón, J.M. Herrero-Martínez, E.F. Simó-Alfonso, G. Ramis-Ramos*

Department of Analytical Chemistry, Faculty of Chemistry, University of Valencia, Doctor Moliner 50, 46100 Burjassot, Valencia, Spain

A R T I C L E   I N F O

A B S T R A C T

The enzymes present in raw materials of the cleaning industry (enzyme industrial concentrates) and in household cleaners were isolated by precipitation with acetone and hydrolyzed with HCl. The resulting amino acids were derivatized with *o*-phthaldialdehyde, and the derivatives were separated by HPLC. The peaks of 14 amino acids were observed using a C18 column and a multi-segmented gradient of acetonitrile-water in the presence of a 5 mM citric/citrate buffer of pH 6.5. Using either normalized peak areas (divided by the sum of the peak areas of the chromatogram) or ratios of pairs of peak areas as predictor variables, linear discriminant analysis models, capable of predicting the enzyme class, including proteases, lipases, amylases and cellulases, were constructed. For this purpose, both enzyme industrial concentrates and detergent bases spiked with them were included in the training set. In all cases, the enzymes of the evaluation set, including industrial concentrates, spiked detergent bases and commercial cleaners were correctly classified with assignment probabilities higher than 99%.

© 2009 Elsevier B.V. All rights reserved.

1. Introduction

Today, enzymes are important components of most laundry and dishwasher cleaners, spot removers and other household products [1]. In fact, enzymes for cleaning products constitute the largest division of the world market for industrial enzymes [2]. Using enzymes, substantial reductions of washing times and temperatures, with the subsequent savings of water and energy are achieved. Further, the concentrations of surfactants and harsh chemicals as alkalis and strong oxidants are reduced [1], with the additional benefit of a better care of fabrics during washing. Mainly proteases, amylases, lypases and cellulases are used in the formulations. Proteases are used to remove protein-rich soil stains (as blood and grass), amylases are addressed to solubilise starch-containing stains, also preventing starch from adhering to fabrics and dishes, lypases help in removing fat and edible oil stains, and cellulases are used to remove fuzz and little balls of fibers from the surface of cotton fabrics. In spite of their interest in the detergent industry, and in environmental and toxicological studies [3], identification and quantification methods for enzymes in cleaning products have been scarcely investigated. Enzymes are commonly detected and quantified by monitoring the hydrolysis of a substrate, or by precipitation with an antiserum [1,2,4–6].

Enzymes of different classes largely differ in molecular structure, also having rather dissimilar amino acid profiles, which can be useful for enzyme class identification. After hydrolysis, the amino acid concentration profile of the enzyme can be established by a variety of analytical techniques, including gas chromatography previous derivatization with ethyl chloroformate [7,8], or with a silylating reagent [9], automated ion exchange chromatography previous hydrolysis [10], and a variety of HPLC methods [11–19]. Among these, RP-HPLC with pre-column derivatization using either phenylisothiocyanate or *o*-phthaldialdehyde (OPA), in the presence of a reagent containing an –SH group, is most frequently used [11]. Using OPA, isoindoles, which can be detected by either UV–vis spectrophotometry [16], fluorimetry [12,14,19] or electrochemical techniques [13], are quickly and easily obtained. Among the SH-group-containing additives, 3-mercaptopropionic acid, *N*-acetylcysteine (NAC) [12,16,20] and ethanethiol [17], which yield rather stable isoindoles, have been recommended. Amino acid concentration profiles of protein hydrolyzates have been used to classify protein-binding media used in works of art [21,22], vegetable oils [23], and rice cultivars [24]. The contents of free amino acids have been also used to classify tea varieties [25] and to authenticate high quality beer [26]. Multivariate data treatment techniques, including artificial neural networks [21] and linear discriminant analysis (LDA) [22,23], have been used to construct the models for class prediction.

In this work, we describe a method for the identification of the enzyme class in raw materials of the cleaning industry and household cleaners. The enzymes are first precipitated with acetone and hydrolyzed with HCl, the resulting amino acids are derivatized with OPA in the presence of NAC, and their concentration profiles are established by RP-HPLC with UV–vis detection. Then, either the

* Corresponding author. Tel.: +34 963 543 003; fax: +34 963 544 436.
E-mail address: ramis@uv.es (G. Ramis-Ramos).

Table 1
Class, commercial name and manufacturer of the enzymes used in this work.

Class	Commercial name	Manufacturer	Set
Protease	Alcalase 2.5L	Novozymes	Training[b]
	Savinase 16L, Type EX	Novozymes	Evaluation
	Everlase 16L, Type EX	Novozymes	Evaluation
	Esperase 8.0L	Novozymes	Evaluation
	Polarzyme 12T[a]	Novozymes	Evaluation
	Bioproteasa L 450	Biocon	Training
	Bioproteasa L 800	Biocon	Training
	Enziprot 450L	ChemWorld	Evaluation
	Deterzyme L 660	Enmex	Evaluation
	Deterzyme Apy L 560	Enmex	Evaluation
	Properase 1600L	Genencor	Evaluation
	Purafect Prime HA	Genencor	Evaluation
	Properase 4000D[a]	Genencor	Evaluation
	Excellase 2250D[a]	Genencor	Evaluation
	Purafect OX 8000D[a]	Genencor	Evaluation
Amylase	Termamyl Ultra 300L	Novozymes	Training[b]
	Duramyl 300L, Type DX	Novozymes	Evaluation
	Stainzyme 12L	Novozymes	Training
	Enziamilasa	ChemWorld	Training
	Purastar ST 15000L	Genencor	Evaluation
	Purastar ST 6000D[a]	Genencor	Evaluation
Cellulase	Endolase 5000L	Novozymes	Evaluation
	Carezyme 4500L	Novozymes	Training[b]
	Celluzyme 0,7T[a]	Novozymes	Evaluation
	Deterzyme CL-5	Enmex	Training
	Puradax HA 400E[a]	Genencor	Evaluation
	Puradax EG 7000L	Genencor	Training
Lipase	Lipolase 100L, Type EX	Novozymes	Training
	Lipex 100L	Novozymes	Training[b]
	Lipolase 100T[a]	Novozymes	Training
	Lipex 100T[a]	Novozymes	Evaluation

[a] Samples supplied as granular solids, the other samples were liquid concentrates.
[b] Used both as supplied and to spike the detergent bases of Table 2.

normalized peak areas (divided by the sum of the peak areas of the chromatogram), or ratios of pairs of peak areas, are used as predictors in the construction of LDA models for enzyme class prediction.

2. Experimental

2.1. Reagents and samples

Reagent grade acetone, absolute ethanol, sodium hydroxide, acetonitrile (MeCN) (HPLC grade, Scharlau, Barcelona, Spain) and hydrochloric acid (37%, Panreac, Barcelona) were employed. Other reagents were o-phthaldialdeyde (OPA), N-acetylcysteine (NAC) (Fluka, Buchs, Switzerland), boric acid (Panreac, Barcelona) and citric acid (anhydrous, Sigma, St. Louis, MO, USA). Glycine (Gly) and the following levo-amino acids were used as standards: Alanine (Ala), arginine (Arg), aspartic acid (Asp), glutamic acid (Glu), histidine (His), isoleucine (Ile), leucine (Leu), lysine (Lys), methionine (Met), phenylalanine (Phe), serine (Ser), threonine (Thr), tyrosine (Tyr), valine (Val) and cysteine (Cys) (Sigma). Tryptophan, which is completely destroyed during acid hydrolysis, and asparagine and glutamine, which are converted into Asp and Glu [27], were not included in this study.

The enzyme industrial concentrates of Table 1 were kindly donated by Novozymes (Bagsvaerd, Denmark), Biocon (Bangalore, India), ChemWorld (Barcelona), Enmex (Tlalnepantla, Mexico) and Genencor (Rochester, NY, USA). Polyethoxylated fatty alcohols (Dehydol LT-7, Cognis, Düsseldorf, Germany), sodium lauryl sulfate, oleine and sodium cumene sulfonate (kindly donated by Químicas Oro, San Antonio de Benegéber, Spain), were used to prepare two detergent bases with the composition given in Table 2. Two commercial laundry cleaners containing protease (composi-

Table 2
Composition of the two detergent bases used in this work (wt%).

Component	I	II
Sodium lauryl sulfate	5	10
Oleine	10	5
Polyethoxylated fatty alcohols	10	15
Sodium cumene sulfonate	5	5
Water	70	65

tion declared by the manufacturers) were purchased at the local market.

2.2. Instrumentation and working conditions

A chromatograph (HP 1100, Agilent, Waldbronn, Germany) composed by the following modules: quaternary pump, degasser, thermostated column compartment, automatic sampler and UV–vis variable multiwavelength detector, was used. A Kromasil C18 column (250 mm × 4 mm I.D., 5 μm particle size, Análisis Vínicos, Tomelloso, Spain) was used. Elution gradients, including the optimized multi-segmented gradient of Table 3, were accomplished by mixing 5% and 50% MeCN solutions (mixtures A and B, respectively), both buffered with 5 mM citric acid/sodium citrate at pH 6.5. Flow rate was 1 mL min^{-1}, and 5 μL aliquots were injected. Detection was performed at 335 nm. Peak areas were measured with the ChemStation-LC v.10.02 software (Agilent). Excel (Microsoft) was used to normalize the variables, and to transfer them to the SPSS software (v. 12.0.1, Statistical Package for the Social Sciences, Chicago, IL, USA) for LDA model construction.

2.3. Procedures

The enzymes were hydrolyzed according to a procedure adapted from literature [7,22]. Enzyme liquid concentrates were processed as follows: About 1 g was weighed, 4 mL acetone was added, and the precipitate was isolated by centrifugation. The supernatant was discarded, 200 μL 12 M HCl was added and the tube was vortex shaken, well closed with a PTFE patch screw-cap (vacuum was not used), and kept at 110 °C in an oven with forced air circulation for 24 h. For granular solid concentrates, about 1 g was weighed, 5 mL water was added, and the suspension was sonicated for 15 min. After centrifugation, 1 mL of the supernatant was taken, and enzyme precipitation and hydrolysis was accomplished as described above for liquid concentrates. About 5 g of the detergent bases of Table 2 and the commercial cleaners were weighed. Previous precipitation, the detergent bases were spiked with either 50 μL or 50 mg of liquid or granular industrial concentrates of enzymes, respectively. Then, the enzymes were precipitated by shaking with 20 mL acetone. The precipitate, isolated by centrifugation, was dissolved in 1 mL water, reprecipitated with 4 mL acetone, and treated as indicated above. In all cases, after hydrolysis, the residue was shaken with 5 mL of a 1:1 ethanol/aqueous 0.1 M HCl mixture. The suspension was passed through a 0.45 μm Nylon filter and derivatized, or stored at −20 °C until use. Two aliquots of each enzyme indus-

Table 3
Optimal multi-segmented gradient accomplished by mixing 5% (A) and 50% (B) MeCN/water solutions, both buffered at pH 6.5 with 5 mM sodium citrate/citric acid.

Time (min)	A (%)	B (%)
0	100	0
28	72.5	27.5
36	70	30
42	44.4	55.6
50	42.4	57.6
55	0	100

trial concentrate, spiked detergent base and commercial sample were hydrolyzed, the two hydrolyzates were diluted as indicated and derivatized, and an aliquot of each one was injected.

The derivatization reagent, containing 1.25×10^{-2} M OPA and 2.5×10^{-2} M NAC, was buffered with 1 M boric acid/sodium borate at pH 9.5. This mixture, protected from light with aluminium foil, was stored at 4 °C and renewed weekly. Aliquots of 100 μL of the hydrolyzates were mixed with 1 mL OPA–NAC solution. To identify amino acid peaks along the chromatograms, stock solutions containing an amino acid or mixtures of two or three amino acids (1000 μg mL^{-1} each) were prepared, and aliquots were derivatized as indicated. After derivatization, these solutions were both directly injected or used to spike the hydrolyzates when required.

2.4. LDA modelling and stepwise algorithm for selection of predictors

LDA, a supervised technique for class prediction, is widely recognized as an excellent tool to obtain vectors showing the maximal resolution between classes or categories. In LDA, vectors minimizing the Wilks' lambda, λ_{w}, are obtained [28]. This parameter is the sum of squares of the Euclidean distances between points belonging to the same category, divided by the total sum of squares, all the distances being calculated along the vectors which constitute the model. Values of λ_w approaching zero are obtained with well-resolved categories, whereas the presence of at least a pair of partially overlapped categories made λ_w to approach one. Up to $N - 1$ discriminant vectors are constructed by LDA, being N the lowest value of either the number of predictors or the number of categories.

To select the predictors to be included in the models, the SPSS stepwise algorithm was used. The inclusion of a predictor significantly contributing to increase the discriminating capability of the model makes λ_w to decrease. According to the stepwise algorithm, a predictor is selected when the reduction of λ_w produced after its inclusion in the model exceeds an entrance threshold, F_{in}. However, the entrance of a new predictor modifies the significance of all the predictors which are already present in the model. For this reason, after the inclusion of a new predictor, a rejection threshold, F_{out}, is used to decide if a predictor should be removed from the model. The process terminates when there are no predictors entering or being eliminated from the model. The default values of F_{in} and F_{out} provided by SPSS, 3.84 and 2.71, respectively, were initially adopted.

3. Results and discussion

3.1. Optimization of OPA–NAC derivatization and chromatographic conditions

The conditions for OPA–NAC derivatization, initially taken from literature [29], were further optimized using hydrolyzates of Alcalase 2.5L. First, the OPA concentration was increased, while both an OPA/NAC molar ratio of 1:2 and an OPA–NAC/hydrolyzate ratio (v/v) of 10:1 were maintained at fixed values. The peak areas increased when the OPA–NAC concentration increased from 2.5×10^{-4} M [29] to 1.25×10^{-2} M. Then, 1.25×10^{-2} M, close to the OPA solubility in water [30], was selected. Owing to the increase of the dilution factor, the peak areas were reduced to ca. 50% when the OPA–NAC volume was increased from 1 to 2 mL, while maintaining an hydrolyzate volume of 100 μL. The amino acid peak areas also decreased when the hydrolyzate volume was increased to 0.5 mL, which could be due to a reduction of the reaction yield at the decreasing pH of the mixture. Thus, further studies were performed with an OPA–NAC/hydrolyzate ratio of 10:1 (v/v). Under these con-
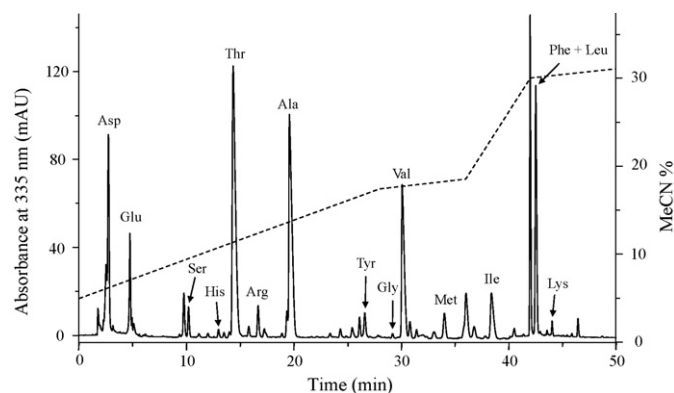

Fig. 1. Chromatogram of a hydrolyzate of Alcalase 2.5L showing the peaks of the isoindoles of the amino acids and the optimal multi-segmented gradient (dashed line). Other conditions as indicated in Section 3.1.

ditions, the other enzymes of Table 1 also provided satisfactory peak intensities.

To optimize the chromatographic separation of the amino acids, the multi-segmented gradient of Concha-Herrera et al. [29] was initially used. This consisted of three linear steps where the MeCN concentration was increased as follows: 5–18.5% (30 min), 18.5–22% (40 min) and 22–27.5% (10 min). However, with this gradient a few peaks overlapped at long retention times. Then, careful trial-and-error optimization of the multi-segmented gradient was carried out in order to improve resolution between the critical peak pairs. With the gradient described in Table 3, and as illustrated in Fig. 1, all the amino acid peak pairs, except the Phe/Leu pair, were baseline resolved. Also, the Ser peak, which was well resolved in the chromatogram of Fig. 1, was only partially resolved from an unidentified peak (see Fig. 1) in the chromatograms of a few other enzymes. Thus, to construct LDA models, the Ser peak was not used, and the Phe/Leu peak pair was jointly measured, 13 peak areas corresponding to 14 amino acids being then selected.

3.2. Data matrices and construction and evaluation of the LDA models

In order to reduce the variability associated to the total amount of protein recovered from the samples and to their hydrolysis, normalized rather than absolute values of the peak areas were used. For this purpose, two normalization procedures were tried. In procedure A, the area of each amino acid peak was divided by the sum of the areas of all the amino acid peaks of the chromatogram. In procedure B, the area of each amino acid peak was divided by each one of the areas of the other 12 amino acid peaks; in this way, and taking into account that a pair of peaks should be considered only once, $(13 \times 12)/2 = 78$ non-redundant ratios of peak areas were obtained.

To construct LDA models for enzyme class prediction, the training set was first constituted by the enzyme industrial concentrates indicated in Table 1. Three enzymes from each one of the four enzyme classes were selected. As indicated in Section 2.3, two aliquots of each enzyme were hydrolyzed and injected; however, only the average of the peak areas of the two injections was included in the training matrix. In this way, the internal variance of the categories was reduced, which was important to also reduce the number of variables selected by the stepwise algorithm during model construction. Therefore, the training matrices were initially constituted by 12 objects each (3 enzymes × 4 enzyme classes × 1 average of two hydrolyzates) and either 13 or 78 variables obtained according to normalization procedures A and B, respectively.

The resulting LDA models were used to predict the enzyme class in the two detergent bases spiked with the four enzymes indi-

cated in Table 1. Data obtained from a total of 16 chromatograms were evaluated (4 enzyme industrial concentrates × 2 detergent bases × 2 hydrolyzed aliquots of each mixture). However, the two models showed a poor prediction capability (25–30% of correct assignments for a 95% probability level) which was attributed to the matrix effect produced by the anionic surfactants and other components present in large concentrations in the detergent bases. Thus, in order to increase the prediction capability of the models, data obtained with the spiked detergent bases were also included in the training set. Thus, the expanded training matrices had 20 objects (3 enzyme industrial concentrates plus 2 spiked detergent bases × 4 enzyme classes × 1 average of two hydrolyzates), and either 13 or 78 predictors as indicated. Then, the duplicate hydrolyzates of the enzyme industrial concentrates of Table 1 which were not included in the training set, plus the duplicated hydrolyzates of the spiked detergent bases and the two commercial cleaners, were used to construct the evaluation matrices. Thus, the two evaluation matrices had 58 objects each (19 industrial concentrates of enzymes plus 8 spiked detergent bases and 2 cleaning products × 2 hydrolyzates each).

Using normalization procedure A, an LDA model with 9 variables, showing an excellent resolution between all the possible pairs of categories ($\lambda_w = 0.032$), was obtained. However, only a 30% of the samples of the evaluation set were correctly classified by this model. On the other hand, using normalization procedure B, an LDA model with 8 variables, showing a slightly better value of λ_w (0.019) than the previous model (0.032) was obtained. Further, all the 58 samples of the evaluation set were correctly classified, with assignment probabilities higher than 99%. The predictors and respective standardized coefficients of the three discriminant functions of this model are shown in Table 4. The use of ratios of areas of peak

Table 4
Predictors and their corresponding standardized coefficients of the optimal LDA model.

Selected variables	f_1	f_2	f_3
Asp/Val	0.92	0.56	−0.55
Glu/His	0.63	−0.76	1.76
Glu/Ala	0.07	1.04	0.82
His/Thr	0.20	−3.77	2.29
Thr/(Leu + Phe)	1.09	0.25	1.46
Ala/Tyr	−0.45	2.35	−1.70
Ala/(Leu + Phe)	−1.26	0.15	0.15
Gly/Ile	0.97	1.47	0.81

pairs as predictors, rather than individual peak areas, prevented from reliably assigning any particular relevance to the discriminant capability of individual amino acids.

As observed in Fig. 2A, the variance gathered by discriminant function f_1 was mainly associated to the resolution between the protease class and the rest of the classes (amylase + lipase + cellulase), whereas discriminant function f_2 explained variance associated to the resolution of the amylase class with respect to the rest of the classes (protease + cellulase + lipase). Finally, according to Fig. 2B, the lipase class was resolved with respect to the other classes (protease + cellulase + amylase) mainly along discriminant function f_3. As illustrated in Fig. 2C by using a plane oblique to the three discriminant functions, all the possible pairs of classes were very well resolved.

Then, the peak areas of the most stable amino acids (Ala, Arg, Asp, Glu, Gly, His, Leu, Lys and Phe) were exclusively used as predictors to construct an LDA model. In this case, the following four peak area ratios were selected by the stepwise algorithm: Glu/His,
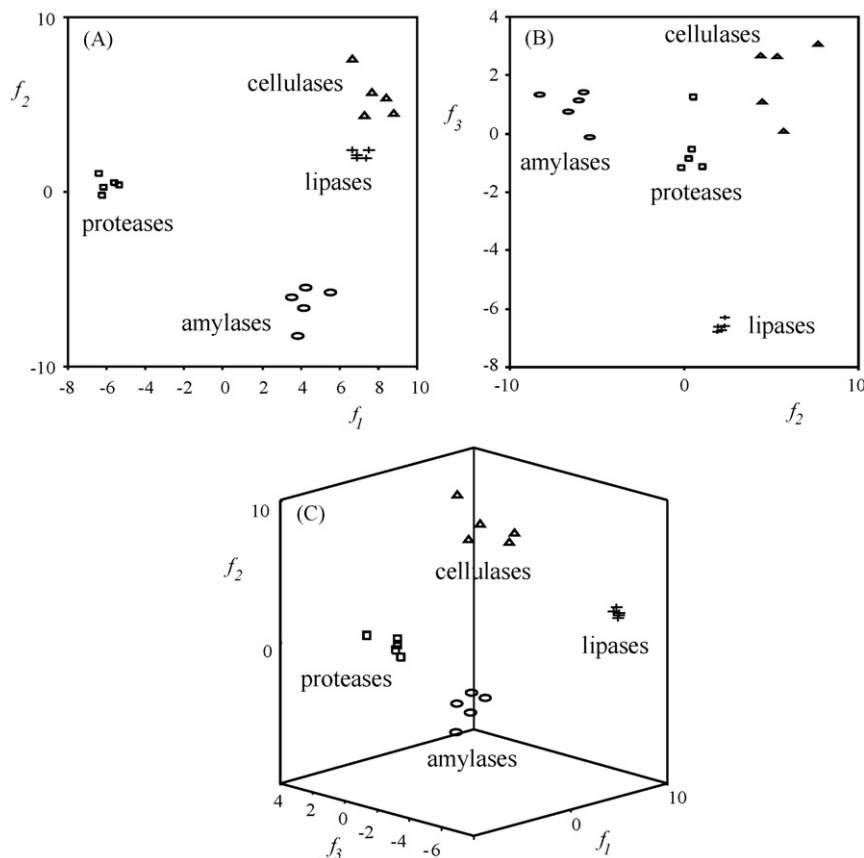

Fig. 2. Score plots on the planes of the first and second (A), and second and third discriminant functions (B), and on an oblique plane of the 3D space defined by the three discriminant functions (C) of the LDA model of Table 4.

Glu/Ala, His/Ala, Ala/(Leu + Phe). This model gave $\lambda_W = 0.387$, and the score plots along the discriminant functions showed well-resolved classes. The resolution between classes was only slightly lower than that observed in Fig. 2 for the model obtained with the eight predictors of Table 4.

4. Conclusions

An HPLC–UV–vis method for class identification of the enzymes found in cleaning products according to the protease, amylase, lypase and cellulase classes, has been developed. For this purpose, after precipitation and hydrolysis, the amino acids were derivatized with OPA–NAC and aliquots were chromatographed. A C18 column and multi-segmented gradient elution with MeCN/water were used to separate the isoindoles of the amino acids. An LDA model with an excellent prediction capability was obtained by using ratios of the areas of the peaks taken by pairs as predictors, and by including both enzyme industrial concentrates and spiked detergent bases in the training set. All the objects of the evaluation set, including enzyme industrial concentrates, spiked detergent bases and commercial cleaners, were correctly assigned with a 99% probability.

Acknowledgements

References

[1] H.S. Olsen, P. Falholt, J. Surfact. Deterg. 1 (1998) 555.
[2] Novozymes, Enzyme Handbook, Publication no. 2002-18372, Bagsvaerd, 2002.
[3] Human Health and Environmental Risk Assessment on ingredients of cleaning products, http://www.heraproject.com.
[4] E. Dunn, R. Brotherton, Analyst 96 (1971) 159.
[5] N. Kulkarni, R.V. Gadre, Biotechnol. Lett. 21 (1999) 897.
[6] K. Lorentz, Clin. Chem. 46 (2000) 644.
[7] J.V. Gimeno-Adelantado, R. Mateo-Castro, M.T. Doménech-Carbó, F. Bosch-Reig, A. Doménech-Carbó, J. De la Cruz-Cañizares, M.J. Casas-Catalán, Talanta 56 (2002) 71.
[8] J. De la Cruz-Cañizares, M.T. Doménech-Carbó, J.V. Gimeno-Adelantado, R. Mateo-Castro, F. Bosch-Reig, J. Chromatogr. A 1025 (2004) 277.
[9] L. Rampazzi, F. Cariati, G. Tanda, M.P. Colombini, J. Cult. Herit. 3 (2002) 237.
[10] R.D. Phillips, J. Food Sci. 48 (1983) 284.
[11] I. Molnár-Perl, J. Chromatogr. A 891 (2000) 1.
[12] I. Molnár-Perl, J. Chromatogr. A 913 (2001) 283.
[13] Y.V. Tcherkas, L.A. Kartsova, I.N. Krasnova, J. Chromatogr. A 913 (2001) 303.
[14] Y.V. Tcherkas, A.D. Denisenko, J. Chromatogr. A 913 (2001) 309.
[15] M.C. García-Álvarez-Coque, M.J. Medina-Hernández, R.M. Villanueva-Camañas, C. Mongay-Fernández, Anal. Biochem. 180 (1989) 172.
[16] V. Concha-Herrera, J.R. Torres-Lapasió, G. Vivó-Truyols, M.C. García-Álvarez-Coque, Anal. Chim. Acta 582 (2007) 250.
[17] R. Hanczkó, A. Jámbor, A. Perl, I. Molnár-Perl, J. Chromatogr. A 1163 (2007) 25.
[18] M.G. Chernobrovkin, E.N. Shapovalova, D.T. Guranda, P.A. Kudryavtsev, V.K. Švedas, O.A. Shpigun, J. Chromatogr. A 1175 (2007) 89.
[19] V. Pereira, M. Pontes, J.S. Câmara, J.C. Marques, J. Chromatogr. A 1189 (2008) 435.
[20] V. Concha-Herrera, G. Vivó-Truyols, J.R. Torres-Lapasió, M.C. García-Álvarez-Coque, Anal. Chim. Acta 518 (2004) 191.
[21] R. Lletí, L.A. Sarabia, M.C. Ortiz, R. Todeschini, M.P. Colombini, Analyst 128 (2003) 281.
[22] J. Peris-Vicente, E. Simó-Alfonso, J.V. Gimeno-Adelantado, M.T. Doménech-Carbó, Rapid Commun. Mass Spectrom. 19 (2005) 3463.
[23] M.J. Lerma-García, G. Ramis-Ramos, J.M. Herrero-Martínez, E.F. Simó-Alfonso, Rapid Commun. Mass Spectrom. 21 (2007) 3751.
[24] G.Y. Wang, T. Abe, T. Sasahara, Breeding Sci. 48 (1998) 129.
[25] A. Alcázar, O. Ballesteros, J.M. Jurado, F. Pablos, M.J. Martín, J.L. Vilchez, A. Navalón, J. Agric. Food Chem. 55 (2007) 5960.
[26] T. Erbe, H. Brückner, J. Chromatogr. A 881 (2000) 81.
[27] W.J. Hurst, Methods of Analysis for Functional Foods and Nutraceuticals, CRC Press, Boca Raton, FL, USA, 2002.
[28] B.G.M. Vandeginste, D.L. Massart, L.M.C. Buydens, S. De Jong, P.J. Lewi, J. Smeyers-Verbeke, Data Handling in Science and Technology, Part B, Elsevier Science, Amsterdam, 1998.
[29] V. Concha-Herrera, J.R. Torres-Lapasió, G. Vivó-Truyols, M.C. García-Álvarez-Coque, J. Liq. Chromatogr. R.T. 29 (2006) 2521.
[30] Advanced Chemistry Development (ACDLabs) software v9.04 in SciFinder, Chemical Abstracts Service, http://www.cas.org/SCIFINDER.

Letter to the Editor

Reply to comments of Tsikas on "Determination of S-nitrosoglutathione and other nitrosothiols by p-hydroxymercurybenzoate derivatization and reverse phase chromatography coupled with chemical vapor generation atomic fluorescence detection" by Bramanti et al.

Dear Editor,

We are glad to comment on letter by Tsikas [1] on our recent paper [2] and further discuss the analytical merits of RSNO determination in biological samples.

The letter raises primarily two questions which we intend to address: the level of nitrosothiols (RSNOs) and their precursors detected, and the accuracy of methods for RSNO determination in human plasma.

1. About the level of RSNOs

The letter has questioned the "high" levels of RSNOs found in plasma of healthy humans by *p*-hydroxymercurybenzoate derivatization method [2].

A similar criticism was expressed by Tsikas on papers reporting either "too high" [3–11] or "too low" [12,13] RSNO content in plasma samples.

The main objection of the author to our results is that μM levels of RSNOs would be "incompatible with human life". Unfortunately, this claim is not supported by any reference.

Both *in vitro* and *in vivo* studies have reported that the EC50 of RSNOs for vasorelaxation and inhibition of platelet aggregation are >200 nmol/l [14,15], and that the bronchodilator action of RSNOs was shown to occur at micromolar concentrations [16]. On the other hand, recent findings suggest that an increase of 50 nmol/l in the plasmatic levels of RSNOs (due to S-nitrosoglutathione or NO infusion as a bolus) leads to a change in the diameter of conduit and resistance vessels [17]. Furthermore, Tsikas himself determined 60 μM GSNO in rat plasma after 20 min [18] infusion, and Hogg et al. observed cardioprotective effects of S-nitrosocysteine (SNOC) after heart 30 min perfusion with 10 μM SNOC [19].

It is clear that RSNO concentration in plasma and its role is still subject to active research and far from being conclusive. Thus, the claim of incompatibility of "high" (0.2–3 μM) GSNO concentrations with human life, we believe, is a major departure from the current scientific knowledge.

2. About the concentration level of precursors of RSNOs

The other issue raised is related to the "high" plasmatic levels of S-nitrosohomocysteine (SNOhC) and other RSNOs.

Concerning the argument of Tsikas, that the levels of 1000 nM of SNOhC are too high because they are about one order of magnitude higher than its precursor (L-homocysteine) levels (100 nM), Tsikas made the assumption that (L-homocysteine + SNOhC) ≤ 200 nM. This assumption also implies that SNOhC belongs to reduced pool of thiols and behaves as a reduced thiol. This is highly questionable because all RSNOs must be reduced before the determination of RS fragment both in our methods [2] and in the method of Tsikas [18]. In healthy individuals, plasma total concentration of species containing the RS-moiety of homocysteines (L-homocysteine + homocystine + SNOhC) ranges from 5 to 12 μM, 1.5–5% is reduced (100–600 nM) [20] and over 97% is in its oxidized form (70% protein-bound, 30% free disulfide form). This means that 30% oxidized form comprises homocystine + SNOhC, i.e. about 1.5–4 μM total oxidized form.

It is clear that any assumption on the thiol/RSNO ratio could only be made when a consolidated methods for RSNOs determination is available.

3. About the accuracy and validation of analytical method

Tsikas claims that "improper method validation and lacking method specificity" hinders our method [1].

In the absence of certified reference materials, samples tested in an interlaboratory exercise, or consolidated analytical methods/protocols for RSNOs, spike recovery measurement is clearly a useful tool of method evaluation. It is worth to point out that this approach has been used by many, including Tsikas in his work on the determination of GSNO in human and rat plasma [18], which represents together with ours [2] the only two reports published in the literature that base GSNO determination on the determination of RS-fragment. The specificity of the method is rested on the retention time and on the highly selective elemental detection of the mercury tag associated with the thiols. The thiol–mercury

complexes were also characterized by mass spectrometry as described in the paper.

In our published method we also evaluated the possible sources of inaccuracy, which could affect the derivatization reaction (paragraph 3.4.2 Ref. [2]). In brief, NEM is used during sampling step both to avoid RSH interference and to eliminate RSH reducing power toward Cu(II) [21]. GSSG and other RSSR do not react with PHMB in the presence of ascorbate or in its absence. Thus, both S–S bond and C–S bond are not broken by PHMB/ascorbate reaction in buffer or plasma ultrafiltrate, and RSNOs are selectively determined. The working principle of the method, i.e. the simultaneous decomposition and derivatization of the thiolic part of RSNOs, which is the basis of our method, is unique. Moreover, since PHMB/AA-mediated derivatization of RSNO does not passes through the free thiols, excess NEM does not interfere with the analysis.

The additional criterion proposed by Tsikas to test the reliability of analytical procedures in biological systems, i.e. "*the concentration of relevant representatives of the system in the basal state*", is absolutely valid. However, the expected/basal values for RSNOs are largely unknown/controversial (see discussion above) and we believe that an open-mind attitude should be maintained waiting for future analytical developments. One should never put the carriage before the horse.

References

[1] D. Tsikas, Talanta (2009), doi:10.1016/j.talanta.2009.03.030.
[2] E. Bramanti, K. Jacovozzi, L. D'Ulivo, C. Vecoli, R. Zamboni, Z. Mester, A. D'Ulivo, Talanta 77 (2008) 684.
[3] V.A. Tyurin, S.X. Liu, Y. Tyurin, N.B. Sussman, C.A. Hubel, J.M. Roberts, R.N. Taylor, V.E. Kagan, Circ. Res. 88 (2001) 1210.
[4] P. Moriel, I.R.O. Pereira, M.C. Bertolami, D.S.P. Abdalla, Free Radic. Biol. Med. 30 (2001) 318.
[5] D. Tsikas, J. Frolich, Circ. Res. 90 (2002) e39.
[6] M. Marzinzig, A.K. Nussler, J. Stadler, E. Marzinzig, W. Barthlen, N.C. Nussler, H.G. Beger, S.M. Morris, U.B. Bruckner, Nitric Oxide 1 (1997) 177.
[7] Z.A. Massy, D. Borderie, T. Nguyen-Khoa, T.M. Drueke, O.G. Ekindjian, B. Lacour, Nephrol. Dial. Transpl. 18 (2003) 153.
[8] P.J. Wlodek, J. Kucharczyk, M.M. Sokolovska, A. Milkowski, A. Markiewicz, O.B. Smolenski, L.B. Wlodek, Clin. Chim. Acta 327 (2003) 87.
[9] D. Tsikas, Nitric Oxide 9 (2003) 53.
[10] D. Tsikas, J. Frolich, Nephrol. Dial. Transpl. 18 (2003) 2199.
[11] D. Tsikas, J. Frolich, Clin. Chim. Acta 339 (2004) 195.
[12] D. Taubert, R. Roesen, C. Lehmann, N. Jung, E. Schomig, J. Am. Med. Assoc. 298 (2007) 49.
[13] D. Tsikas, R. Rossi, J. Am. Med. Assoc. 298 (2007) 1862.
[14] W.R. Mathews, S.W. Kerr, J. Pharmacol. Exp. Ther. 267 (1993) 1529.
[15] J.M. Tullett, D.D. Rees, D.E. Shuker, A. Gescher, Biochem. Pharmacol. 62 (2001) 1239.
[16] B. Gaston, J. Reilly, J.M. Drazen, J. Fackler, P. Ramdev, D. Arnelle, M.E. Mullins, D.J. Sugarbaker, C. Chee, D.J. Singel, J. Loscalzo, J.S. Stamler, Proc. Natl. Acad. Sci. U.S.A. 90 (1993) 10957.
[17] T. Rassaf, P. Kleinbongard, M. Preik, A. Dejam, P. Gharini, T. Lauer, C. Heiss, B.-E. Strauer, M. Feelisch, M. Kelm, Circ. Res. 91 (2002) 470.
[18] D. Tsikas, J. Sandmann, S. Rossa, F.-M. Gutzki, J.C. Frohlich, Anal. Biochem. 273 (1999) 32.
[19] N. Hogg, K.A. Broniowska, J. Novalija, N.J. Kettenhofen, E. Novalija, Free Radic. Biol. Med. 43 (2007) 1086.
[20] M.A. Mansoor, A.M. Svardal, P.M. Ueland, Anal. Biochem. 200 (1992) 218.
[21] D.R. Noble, D.L.H. Williams, Nitric Oxide 4 (2000) 392.

Emilia Bramanti [a,*], Valeria Angeli [a,1],
Zoltan Mester [b], Alessandro D'Ulivo [a,1]
[a] *Italian National Research Council-Istituto per i Processi Chimico-Fisici, Laboratory of Instrumental Analytical Chemistry, Via G. Moruzzi 1, 56124 Pisa, Italy*
[b] *Institute for National Measurement Standards, National Research Council Canada, 1200 Montreal Rd., Ottawa, ON K1A 0R6, Canada*

[*] Corresponding author. Tel.: +39 050 315 2293; fax: +39 050 315 2555.
E-mail address: emilia@ipcf.cnr.it (E. Bramanti)

[1] Tel.: +39 050 315 2293; fax: +39 050 315 2555.

Modified cupric reducing antioxidant capacity (CUPRAC) assay for measuring the antioxidant capacities of thiol-containing proteins in admixture with polyphenols

Sema Demirci Çekiç, Kevser Sözgen Başkan, Esma Tütem, Reşat Apak*

Istanbul University, Faculty of Engineering, Department of Chemistry, Avcilar 34320 Istanbul, Turkey

A B S T R A C T

Proteins are not considered as true antioxidants but are known to protect antioxidants from oxidation in various antioxidant activity assays. This study aims to investigate the contribution of proteins, especially thiol-containing proteins, to the observed overall antioxidant capacity measured by known methods. To determine the antioxidant properties of thiol-containing proteins, the CUPRAC method of antioxidant assay using the oxidizing reagent Cu(II)-neocuproine previously used for simultaneous analysis of cystine and cysteine was adopted. While the CUPRAC method is capable of determining all antioxidant compounds including thiols in complex sample matrices, the Ellman method of thiol quantitation basically does not respond to other antioxidants. The antioxidant quantities in the selected samples were assayed with the ABTS and FRAP methods as well as with the CUPRAC method. In all applied methods, the dilutions were made with a standard pH 8 buffer used in the Ellman method by substituting the Na_2EDTA component of the buffer with sodium citrate. On the other hand, the standard CUPRAC protocol was modified by substituting the pH 7 ammonium acetate buffer (at 1 M concentration) with 8 M urea buffer adjusted to pH 7 by neutralizing with 6 M HCl. Urea helps to partly solubilize and denature proteins so that their buried thiols be oxidized more easily. All methods used in the estimation of antioxidant properties of proteins (*i.e.*, CUPRAC, Ellman, ABTS, and FRAP) were first standardized with a simple thiol compound, cysteine, by constructing the calibration curves. The molar absorptivities of these methods for cysteine were: $\varepsilon_{CUPRAC} = 7.71 \times 10^3$, $\varepsilon_{Ellman} = 1.37 \times 10^4$, $\varepsilon_{ABTS} = 2.06 \times 10^4$, and $\varepsilon_{FRAP} = 2.98 \times 10^3 \, L \, mol^{-1} cm^{-1}$. Then these methods were applied to various samples containing thiols, such as glutathione (reduced form:GSH), egg white, whey proteins, and gelatin. Additionally, known quantities of selected antioxidants were added to these samples to show the additivity of responses.

© 2009 Elsevier B.V. All rights reserved.

1. Introduction

Dairy products can be beneficial for the protection of consumers against oxidative stress by several mechanisms. Milk antioxidants can play a major role in inhibiting lipid peroxidation and maintaining continued food quality of such products. Many dairy products (such as milk, skimmed milk, whey, casein, lactoferrin, etc.) as well as fractions prepared from them show antioxidative effect [1].

Whey or milk plasma is the liquid remaining after milk has been curdled and strained; it is a protein-rich by-product of the manufacture of cheese or casein. The proteins obtained from whey may act as thickener and gelling agent, emulsifier, and water retainer. The whey proteins constitute about 20% of total milk proteins. The most important milk proteins are β-lactoglobulin, α-lactalbumin, serum albumin, and immunoglobulins. α-Lactalbumin is an important whey protein present in human and cow's milk, and β-lactoglobulin

exists in cow's milk; these two proteins constitute nearly a half of whey proteins. These proteins exist in soluble form in the whey fraction obtained from milk, and bear disulfide (R–S–S–R′) groups [2]. A main structural difference between these two proteins is that α-lactalbumin does not have free thiol groups that can serve as the starting point for a covalent aggregation reaction, meaning that it will not form gels upon denaturation and acidification. The possible mechanisms of antioxidant action of whey are believed to comprise chelation of transition metal ions by lactoferrin, and free radical scavenging of tyrosine, cysteine and similar amino acid moieties in these proteins. The sulfhydryl (or thiol: –SH) groups are known to be free radical scavengers, and β-lactoglobulin bears one such thiol functionality [3]. The free thiol group in β-lactoglobulin may act as a chain-breaking antioxidant by conversion into the more stable thiyl-radicals as a result of its reaction with lipid peroxyl radicals:

$$ROO^\bullet + R–SH \rightarrow ROOH + R–S^\bullet$$
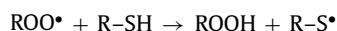
Thus, since the thiyl reactivity for hydrogen (H) atom abstraction is low, lipid autooxidation is halted by thiols. Due to the reactivity of thiols for reactive oxygen species (ROS) and lipid peroxyl radicals by

---

donation of a H-atom, whey proteins may exhibit antioxidant activity. The reactivity of this thiol group may be markedly increased by heat-denaturation possibly as a result of thiol/disulfide interchange reactions stemming from the exposure of the thiol group [4].

Glutathione (GSH) is the major low molecular weight tripeptide thiol in mammalian cells where it is essentially responsible for antioxidant defense. Its action is usually favoured by enzymes like glutathione peroxidase and glutathione S-transferase. GSH has the capability of regenerating other important defense resources such as vitamins C and E from their $1-e$ oxidized radicals, and of directly participating in the destruction of ROS [5].

Gelatin is a protein produced by partial hydrolysis of collagen extracted from the bones, connective tissues, organs, and intestines of animals such as domesticated cattle and horses. On the average, gelatin contains 86% collagen, 11% water, and 3% mineral matter. Gelatin may be used as a stabilizer, thickener, gelling agent, or texturizer in foods such as ice cream, jams, yogurt, cream cheese, and margarine. Nagatsuka et al. have observed with the aid of chemiluminescence measurements strong peroxyl radical scavenging properties of gelatin obtained from collagen [6].

The most abundant proteins present in egg white are albumins that belong to the class of water-soluble proteins. About 63% of all proteins in egg white is constituted by the main protein, ovalbumin, that can chelate transition metal ions *via* its sulfhydryl groups. The other concerned proteins are ovoglobulin, ovomucin, conalbumin, ovomucoid, and avidin. Dávalos et al. investigated the antioxidant activity of peptides derived from egg white proteins by enzymatic hydrolysis, and reached the conclusion that free radical scavenging antioxidant peptides and amino acids not only act individually, but also cooperatively and synergistically [7].

Almajano et al. investigated the antioxidant activity (AOA) of green tea catechins in oil-in-water emulsions in the absence and presence of bovine serum albumin (BSA) using antioxidant assay methods comprising ferric thiocyanate peroxide value, FRAP, and ABTS, and found out that although BSA had very little AOA in the absence of catechins, samples containing a combination of BSA with each of the catechins showed good stability and the increase in AOA was synergistic for all four catechins tested. However, these authors ascribed the observed synergistic increase in AOA by BSA to physical mechanisms such as facilitated transport of antioxidant catechins to the oil-water interface *via* albumin binding, resulting in reduced rate of oxidation at the interface [8]. Taguchi et al. investigated the antioxidant effects of various food proteins such as gluten, casein, gelatin, gliadin, and egg white, and concluded that especially wheat gliadin and hen's egg white were effective in protecting edible oils (such as safflower and sardine oils) against oxidation. Again it was the approach of these authors to ascribe the observed AOA to physical factors, such as the penetration of edible oils deep into the recesses of gliadin particles at low to moderate humidity, thereby giving rise to delayed oxidation [9]. The common point noticeable in all these explanations is that proteins are not antioxidants by virtue of their chemical nature, but they can act in a way as antioxidants by enhancing the AOA of true antioxidant compounds by physical means.

Although some data exists about the content of individual antioxidants in milk, methods have to be devised for measuring the total antioxidant capacity (TAC) of milk and whey without distinguishing the contributions from individual compounds, as most antioxidants act in cooperation. Since each TAC assay has its own unique redox potential, mechanism, rate, and responsiveness to lipophilic antioxidants, the TAC or AOA of antioxidants may vary in different biological systems depending on the method employed and the conditions of the assay. Chen et al. [1] have investigated the TAC of bovine milk by using spectrophotometric (ABTS and FRAP) and amperometric methods, though with some problems. For example, the TAC of whey as measured by the ABTS method

increased with pH, and there occurred protein precipitation at the low pH of the FRAP method. Moreover, most of the ferric-reducing power of whey was found in the low molecular weight (LMW) fraction, again stressing the limitations of the FRAP method in assessing the TAC of peptides and proteins as high molecular weight (HMW) fractions [1]. The FRAP assay was previously suggested to be unsuitable for serum proteins and for LMW thiol (–SH) compounds such as glutathione and lipoic acid [10].

In this communication, it has been aimed to measure the TAC of certain proteins present in various edible products, especially of thiol-containing proteins, and to determine the contribution of –SH proteins to the measured overall antioxidant capacity of mixtures, with a modified cupric reducing antioxidant capacity (CUPRAC) assay method. The chromogenic oxidizing reagent of the CUPRAC assay, bis(neocuproine: 2,9-dimethyl-1,10-phenanthroline)copper(II), was previously used for the assay of biologically important reductants [11], cysteine [12], vitamin E [13], vitamin C [14]. The CUPRAC method, capable of measuring all types of antioxidants including thiols, was initially developed for food antioxidants [15], then for human serum [16]. The method was extensively compared in performance to other TAC assays [17,18], and have recently been adapted to measure the hydroxyl radical scavenging ability of antioxidants [19]. The CUPRAC findings of the thiol components of antioxidant mixtures were also compared to the measurements made with the Ellman method that specifically responds to thiols, but gives weak or no response to other antioxidants [20]. The tested samples were also measured for TAC with ABTS [21], specifically with the ABTS radical cation generated by hydrogen peroxide + horseradish peroxidase (HRP) [22,23]; and with FRAP [24] methods. It is noteworthy that only two TAC assay methods, namely CUPRAC and ABTS, are capable to simultaneously measure lipophilic and hydrophilic antioxidants with the same precision due to the solubility of their single-charged chromophores in both aqueous and organic solvent media [25] (the higher-charged chromophores may only be soluble in aqueous medium due to increased ion–dipole interaction with water). It is known that among the electron transfer (ET)-based total antioxidant capacity (TAC) assays, Folin and FRAP (ferric reducing antioxidant power) methods are more appropriate for measuring hydrophilic antioxidants (in aqueous or aqueous-alcoholic solutions) due to the high charge of their chromophores, while DPPH is more suitable for lipophilic antioxidants in organic solvent media [17]. Thus it is expected to measure the TAC of high molecular weight (HMW) fractions as well as of LMW antioxidants with CUPRAC and ABTS methods, and to compare the results. All the selected methods were calibrated with a simple and complex thiol compound, *i.e.*, cysteine and reduced glutathione (GSH), respectively, and additivity of TAC values were tested in each complex sample, namely egg white, whey, and gelatin, by making standard additions of antioxidants to these protein samples. To the best of our knowledge, this is the first study reporting the measurement of the TAC of thiol-containing proteins in admixture with phenolic antioxidants after taking up the protein fractions with a suitable buffer (*e.g.*, for the egg white sample) that neither causes the precipitation of proteins nor interferes with the selected antioxidant assay (specifically CUPRAC assay).

2. Materials and methods

2.1. Chemicals and solutions

Analytical reagent grade neocuproine (2,9-dimethyl-1,10-phenanthroline) hydrochloride was supplied from Sigma Chemical Co., catechin, quercetin, 2,4,6-tris-(2-pyridyl)-1,3,5-triazine (TPTZ), and $FeCl_3 \cdot 6H_2O$ from Fluka Chemicals, 6-hydroxy-2,5,7,8-

tetramethylchroman-2-carboxylic acid (trolox), and caffeic acid from Aldrich Chemical Co., CuCl$_2$·2H$_2$O, tris(hydroxymethyl) aminomethane (Tris), glycine, tri-sodium citrate 5,5-hydrate, urea, sodium dodecyl sulfate (SDS), L(+)-cysteine, reduced glutathione (GSH), 5,5′-dithio-bis(2-nitrobenzoic acid) (DTNB) (Ellman's reagent), acetic acid, sodium acetate, 2,2′-azinobis(3-ethylbenzothiazoline-6-sulfonic acid) diammonium salt (ABTS), horseradish peroxidase (HRP), H$_2$O$_2$ (30%, by wt.), ethanol (EtOH), trichloroacetic acid (TCA), hydrochloric acid (36.5%, by wt.), and all other chemicals from E. Merck. The standard solutions were prepared as follows:

2.1.1. Standard tris-buffer at pH 8
The standard tris-buffer described in the literature [20] was prepared by replacing disodium-EDTA with citrate. The buffer contained 0.086 M tris(hydroxymethyl) aminomethane, 0.09 M glycine, and 4 mM citrate; the final pH was adjusted to 8.0 with the addition of 2 M HCl. This buffer was used as diluent in all experiments.

2.1.2. TCA solution
5% (w/v), to precipitate the proteins.

2.1.3. Protein dissolution buffer (pH 6.8)
The buffer contained 50 mM Tris, 2% SDS, and 8 M urea (the final pH of solution was adjusted to 6.8 with 2 M HCl) [26]. This buffer was used for dissolving TCA-precipitated egg white proteins in the experiments.

2.1.4. Antioxidant standard solutions
Standard solutions at 1 mM concentration of antioxidants, namely trolox (TR), quercetin (QR), caffeic acid (CFA), and catechin (CAT) were prepared from pure solids by dissolving with EtOH. These solutions were subsequently diluted to their final concentrations using standard tris-buffer as diluent.

2.1.5. Cysteine (CYS) solution
A suitable weight was dissolved with 0.5 mL of 1 M HCl solution, and diluted to volume with distilled water to yield a cysteine solution at 10 mM.

2.1.6. Glutathione (GSH) solution
Dissolved with distilled water to yield 10 mM solution.

2.1.7. CUPRAC reagent solutions
CuCl$_2$·2H$_2$O (1.0×10^{-2} M, in distilled water), neocuproine (7.5×10^{-3} M, in EtOH), and pH 7.0 urea buffer (a suitable amount of urea was dissolved in standard tris-buffer, 6 M HCl was added to adjust the pH to 7.0, and diluted with distilled water so as to yield a final total urea molarity of 8 M) were prepared. The original pH 7.0 buffer (NH$_4$Ac solution) of the CUPRAC method [15] was replaced with urea containing standard tris-buffer at pH 7.0 in this work.

2.1.8. Ellman reagent solutions
DTNB solution at 4 mg/mL of standard tris-buffer was prepared. pH 8.0 buffer (the standard tris-buffer containing sufficient urea was adjusted to pH 8.0 with the addition of 6 M HCl, and diluted with distilled water so as to yield a final total urea molarity of 8 M).

2.1.9. FRAP reagent solutions
The pH 3.6 buffer (0.3 M acetic acid buffer), TPTZ (1.0×10^{-2} M, in EtOH), and FeCl$_3$·6H$_2$O (2.0×10^{-2} M ferric chloride, in 0.02 M aqueous HCl) were mixed at a volume ratio of 10:1:1 to obtain the freshly used FRAP reagent.

2.1.10. ABTS reagent solutions
ABTS (4.0×10^{-3} M, in distilled water), H$_2$O$_2$ (1.2×10^{-4} M, in EtOH), and HRP (2.4×10^{-5} M, in EtOH-distilled water mixture) solutions were prepared.

2.2. Instruments

The spectra and absorption measurements were recorded in matched quartz cuvettes using a Varian CARY 1E UV–vis spectrophotometer (Australia). Other related apparatus and accessories were a Clifton water bath, E521 Metrohm Herisau pH-meter equipped with glass electrodes (Switzerland), Ultra-Turrax CAT X-620 model homogenizer apparatus (Staufen, Germany), and Elektromag vortex stirrer (Istanbul, Turkey). Centrifugations were carried out with an Elektromag (M 4812 P) laboratory centrifuge apparatus (Istanbul, Turkey).

2.3. Procedures

2.3.1. Antioxidant capacity and thiol assays
2.3.1.1. *Modified CUPRAC method of TAC assay applicable to protein fractions.* One milliliter of 1.0×10^{-2} M CuCl$_2$·H$_2$O, 1 mL of 7.5×10^{-3} M Nc, and 2 mL of pH 7.0 urea buffer were mixed. To this mixture were added $(1.0 - x)$ mL of pH 8 standard buffer and (x) mL sample or standard antioxidant solution or a mixture of both. The final mixture at 5.0 mL total volume was let to stand at room temperature for exactly 30 min, and the absorbance at 450 nm was recorded against a reagent blank.

It should be noted that the users of the original CUPRAC method [15] should revert to the pH 7.0 buffer defined in this work, and should not use the ammonium acetate buffer therein, which would otherwise cause the precipitation of proteins. The pH 7.0 buffer used here is the one pertaining to Ellman's method [20] of thiol determination, but adjusted to pH 7.0 instead of pH 8.0.

2.3.1.2. *Ellman's method.* A volume of (x) mL sample + $(1 - x)$ mL standard tris-buffer at pH 8 + 2 mL pH 8.0 urea buffer + 30 μL Ellman's reagent were added in this order to obtain a mixture of 3.03 mL final volume. The absorbance at 412 nm was recorded after 2 min of mixing the sample with reagents [20].

2.3.1.3. *FRAP method.* A volume of 3 mL FRAP reagent + 0.3 mL distilled water + 0.1 mL sample were mixed into a final volume of 3.4 mL. The absorbance at 595 nm was read after 6 min.

2.3.1.4. *ABTS method.* A volume of 0.5 mL ABTS + 0.5 mL H$_2$O$_2$ + 0.5 mL HRP were mixed. At the end of the 5th minute, (x) mL sample + $(0.5 - x)$ mL standard tris-buffer were added (the final volume was 2.0 mL), and the absorbance at 730 nm was read at the 10th minute. The sample and reference (blank) absorbances were best recorded against ethanol, and the sample absorbance subtracted from that of the blank to correlate the absorbance difference (ΔA_{730nm}) with antioxidant concentration.

During application of all the described methods, it should be noted that proteins may denature with alcohol and precipitate out in ethanolic solutions. Therefore all dilutions must be made with standard tris-buffer at pH 8.0. As the tested antioxidants and cysteine may show reduced stability at pH 8.0, all dilutions should be made just prior to assays, and antioxidants should not be let to stand in pH 8.0 buffer solutions for an uncontrolled time period.

2.3.2. Preparation of real samples for analysis
2.3.2.1. *Egg white (EW).* The egg white was completely separated from the yolk, weighed (36.9199 g), and suspended in distilled water to make a 250 mL final solution. A 5 mL aliquot was withdrawn, and 5 mL of 5% TCA was added into it. The mixture was

centrifuged for 10 min, the upper liquid phase was decanted, and the precipitate was washed twice with distilled water. The isolated protein fraction was dissolved in 10 mL of protein dissolution buffer.

2.3.2.2. Whey proteins (WP). The whey liquids separated from the curd was passed through a glass fibre (GF)/polyethyleneterephtalate (PET) 1.0/0.45 μm filter, and diluted as required with the standard tris-buffer prior to analysis.

2.3.2.3. Gelatin (GL). Appropriate weight (1.4700 g) of bovine gelatin supplied from the herbalist was dissolved in distilled water, and diluted to 20 mL with the standard tris-buffer prior to analysis.

3. Results and Discussion

3.1. CUPRAC assay results

3.1.1. CUPRAC calibration curves of antioxidants alone and in protein solutions

The CUPRAC method is based on Cu(II)–Cu(I) reduction by antioxidants in the presence of neocuproine, but EDTA preferentially stabilizes the higher oxidation state of copper resulting in a decrease in the redox potential of the reagent which may subsequently cause incomplete oxidation of certain antioxidants. Therefore, the standard tris-buffer described in the literature [20] was prepared in this work by replacing disodium-EDTA with citrate. The standard solutions of cysteine (CYS) and reduced glutathione (GSH) were prepared by dilution of appropriate volumes of stock solutions with the standard buffer to $(1–9) \times 10^{-5}$ M (CYS) or $(2–10) \times 10^{-5}$ M (GSH) in final solution of color development. The corresponding calibration equations with the modified CUPRAC procedure were:

$$A = 7.71 \times 10^3 c - 0.008 \quad (r^2 = 0.997) \text{ for CYS, and}$$
$$A = 8.19 \times 10^3 c - 0.0085 \quad (r^2 = 0.999) \text{ for GSH}$$

where A is the CUPRAC absorbance at 450 nm, and c is the molar concentration of the compound tested. Thus the slope of the calibration line is also the molar absorptivity (in the units of $L\,mol^{-1}\,cm^{-1}$) for the given compound with the modified CUPRAC method. The slope-intercept forms of calibration equations of the modified CUPRAC method of TAC assay applied to various antioxidants alone and in complex matrices such as the solutions of GSH, egg white, whey, and gelatin are tabulated in Table 1. For the experiments, suitable aliquots of 1 mM ethanolic standard solutions of the antioxidants (trolox: TR, quercetin: QR, catechin: CAT, and caffeic acid: CFA) were diluted with the standard buffer to the desired concentration range (such that the CUPRAC absorbance at 450 nm would lie within 0.2–1.2 absorbance units).

Regression analysis of the results shown in Table 1 revealed that absorbance *vs* concentration relationships with the modified CUPRAC procedure were perfectly linear (r^2 ranged between 0.995 and 0.999) for the antioxidants tested. Two-way ANOVA (ANalysis Of VAriance) analysis showed that the calibration lines of antioxidants in the standard buffer alone and in complex (peptide or protein) matrices were essentially parallel, and there was
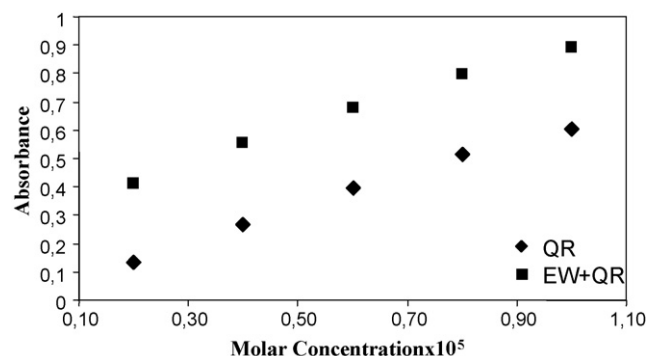

Fig. 1. Calibration curves (lines) of quercetin alone and in egg white solution.
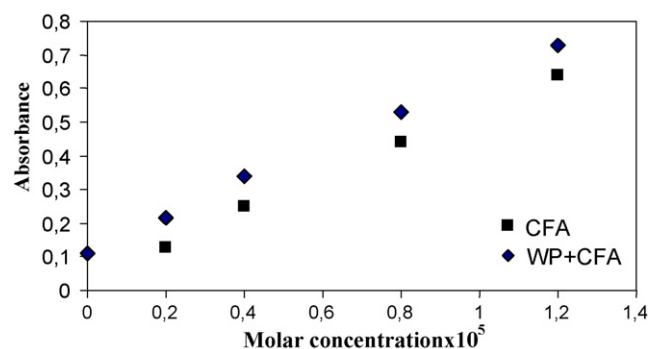

Fig. 2. Calibration curves (lines) of caffeic acid alone and in whey proteins solution.

no difference at 95% confidence level between the slopes of these lines (see Figs. 1 and 2 as examples). This means there was no interaction of interferent nature between the tested antioxidants and the antioxidant constituents of complex matrices (*i.e.*, peptide or protein fractions) that would otherwise cause chemical deviations from Beer's law. The additivity of TAC values of antioxidants obtained with the proposed CUPRAC method is thus secured in protein or peptide matrices. The only exception was that there was a slight enhancement of molar absorptivity of trolox in GSH solution, pointing out to a possible synergistic interaction between these two antioxidants in the selected buffer medium. Also the molar absorptivity of QR and CAT in the proposed method were roughly at the same level (Table 1), contrary to the fact that in the original CUPRAC method [15] the trolox equivalent antioxidant capacities (TEAC values) of CAT (3.1) and QR (4.4) were different. This might show that the antioxidant power of CAT as measured with the modified CUPRAC method was enhanced in the urea buffer of this work compared to that in ammonium acetate buffer, the mechanism of which needs further investigation. One possible reason is the demonstrated ability of urea to alter the nature of intermolecular hydrophobic interactions in solutions of self-aggregation, *e.g.*, of methylene blue [27]. As for flavonoid-type antioxidants, it is known [28] that flavonoid-derived quinones and quinonoid compounds could be produced in significant concentrations in media

Table 1
Slope-intercept forms of calibration equations of the modified CUPRAC method of TAC assay applied to various antioxidants alone and in complex matrices such as the solutions of GSH, egg white, whey, and gelatin.

Antioxidant	Matrix:Alone[a]	GSH solution	Egg white	Whey	Gelatin
Trolox	$1.69 \times 10^4 c - 0.007$	$1.74 \times 10^4 c + 0.329$	$1.60 \times 10^4 c + 0.103$	$1.60 \times 10^4 c + 0.102$	$1.60 \times 10^4 c + 0.116$
Quercetin	$5.93 \times 10^4 c + 0.027$	$5.92 \times 10^4 c + 0.328$	$6.00 \times 10^4 c + 0.306$	$5.82 \times 10^4 c + 0.158$	$6.05 \times 10^4 c + 0.142$
Catechin	$6.26 \times 10^4 c + 0.021$	$6.50 \times 10^4 c + 0.365$	$6.13 \times 10^4 c + 0.274$	$6.29 \times 10^4 c + 0.157$	$6.40 \times 10^4 c + 0.189$
Caffeic acid	$5.04 \times 10^4 c + 0.036$	$5.00 \times 10^4 c + 0.343$	$5.25 \times 10^4 c + 0.133$	$5.14 \times 10^4 c + 0.118$	$4.97 \times 10^4 c + 0.126$

[a] Equations in the column represent calibration lines for mentioned antioxidant alone.

Table 2
The CUPRAC absorbances of egg white (EW) protein solutions in admixture with standard antioxidants (TR, QR, and CAT); to suitable aliquots of EW stock solution were added varying volumes of standard antioxidant solutions at 0.1 mM concentration.

Sample composition	$A_{observed}$	$A_{expected}$	Relative error, (%)
0.4 mL EW	0.2027		
0.4 mL EW + 0.6 mL TR	0.3702	0.3791	−2.3
0.4 mL EW + 0.2 mL QR	0.4264	0.4490	−5.0
0.4 mL EW + 0.2 mL CAT	0.4149	0.4313	−3.8
0.5 mL EW	0.2415		
0.5 mL EW + 0.5 mL TR + 0.2 mL QR	0.5948	0.6464	−8.0
0.3 mL EW	0.1408		
0.3 mL EW + 0.3 mL TR + 0.3 mL QR + 0.3 mL CAT	0.5053	0.5278	−4.3

of low water content, *e.g.*, in hydrophobic protein cavities and at the surface of biological membranes. Here, reduced water activity may be a key parameter in the enhancement of protein oxidizability. Investigators on streptococcal NADH peroxidase have proposed that low-to-moderate concentrations of urea stabilize the intermediate state between native and denatured forms, which is held responsible for the observed changes in both active-site thiol reactivity and redox properties of the protein [29]. Urea – in combination with SDS – significantly increase the reactivity of thiols and disulfides that may be buried within the protein matrix [30]. In this work, presence of 8 M urea is thought to partly denature proteins and to lower the reduction potential of disulfide/thiol couples in peptides/proteins enhancing thiol oxidizability [29].

3.1.2. CUPRAC absorbances of antioxidants in admixture with proteins

To suitable aliquots of egg white stock solution were added varying volumes of standard antioxidant solutions (at 0.1 mM concentration) to form binary, ternary, and quaternary mixtures. These final solutions were subjected to modified CUPRAC analysis, and the theoretically expected and experimentally observed absorbances at 450 nm were compared (Table 2) to confirm the hypothesis regarding the additivity of absorbances (or TAC values). The theoretically expected absorbance can be found by multiplying the absorptivity of each mixture constituent with its concentration, and then summing up the products. Similar experiments were repeated using whey (Table 3) and gelatin proteins (Table 4), and GSH (Table 5). The accordance of expected and observed absorbances (see Tables 2–5, relative errors were within 0.4–8.0%, mean 4.1 ± 1.8%) confirms the additivity of TAC values of antioxidant constituents of the mixtures comprising standard antioxidants and protein fractions. The possible reason for the additivity of the CUPRAC absorbances for (protein + polyphenols) mixtures under the optimized reaction conditions (Figs. 1 and 2; Tables 2–4) is that any plausible 1:1 flavonol-protein complexes (*e.g.*, quercetin-bovine serum albu-

Table 4
The CUPRAC absorbances of gelatin (GL) solution in admixture with standard antioxidants (TR, QR, CFA, and CAT); to suitable aliquots of GL stock solution were added varying volumes of standard antioxidant solutions at 0.1 mM concentration.

Sample composition	$A_{observed}$	$A_{expected}$	Relative error, (%)
1 mL GL	0.3062		
1 mL GL + 0.2 mL QR	0.4765	0.5058	−5.7
1 mL GL + 0.2 mL CA	0.5107	0.5282	−3.3
1 mL GL + 0.2 mL CFA	0.5037	0.5222	−3.5
1 mL GL + 0.4 mL TR	0.4385	0.4178	+5.0
1 mL GL + 0.2 mL QR + 0.2 mL CAT	0.6663	0.7107	−6.2
1 mL GL + 0.2 mL QR + 0.2 mL CAT + 0.4 mL TR	0.9624	1.0117	−4.9

min: QR-BSA) have complexation constants (K_f) at the order of 10^4 [28] whereas 2–3 quercetin glycoside molecules exhibit a looser binding to each molecule of BSA. On the other hand, it has been shown that a 2−e reductant like ascorbic acid having a standard potential difference of 0.4 V with the CUPRAC redox couple (*i.e.*, Cu(II)/Cu(I)-neocuproine) may show a CUPRAC oxidation equilibrium constant at the order of $K_f \approx 10^{13}$ [25]. Thus, the thermodynamically more favourable CUPRAC redox equilibrium is expected to be predominant over any protein-flavonol complexation which would not hinder additivity of the CUPRAC absorbances for (protein + polyphenols) mixtures.

3.2. Ellman assay results

Ellman synthesized in 1959 a water-soluble (at pH 8) aromatic disulfide [DTNB: 5,5′-dithiobis(2-nitrobenzoic acid)] and showed this reagent to be useful for determination of sulfhydryl groups [31]. This thiol-specific reagent (DTNB) reacts with a thiol group to release 5-thio-2-nitrobenzoate (TNB⁻), which ionizes to the TNB^{2-} dianion (yellow chromophore) in water at neutral and alkaline pH. Ellman assay responds well to thiol compounds, but not to conventional phenolic antioxidants (with the exception of its very weak response to QR). Thus, CYS or GSH can be selectively determined among other phenolic antioxidants with the DTNB reagent (Ellman assay). CYS working solution at 2.5×10^{-4} M was freshly prepared from the stock solution using the standard buffer as diluent, and aliquots between 0.25 and 1.0 mL were taken for analysis. Ellmann assay was calibrated with cysteine to yield the calibration line equation:

$$A = 1.37 \times 10^4 c + 0.0017 \quad (r^2 = 0.9992)$$

where A is the 412 nm absorbance obtained with DTNB reagent, and c is the molar concentration of CYS. The Ellman calibration equation for GSH was:

$$A = 1.40 \times 10^4 c + 0.0619 \quad (r^2 = 0.9998)$$

Table 3
The CUPRAC absorbances of whey protein (WP) solution in admixture with standard antioxidants (TR, QR, CFA, and CAT); to suitable aliquots of 1:1 (v/v) diluted WP stock solution were added varying volumes of standard antioxidant solutions at 0.1 mM concentration.

Sample composition	$A_{observed}$	$A_{expected}$	Relative error, (%)
0.5 mL WP	0.3062		
0.5 mL WP + 0.2 mL QR	0.5369	0.5541	−3.1
0.5 mL WP + 0.2 mL CAT	0.5554	0.5957	−6.8
0.5 mL WP + 0.2 mL CFA	0.4813	0.4963	−3.0
0.5 mL WP + 0.4 mL TR	0.4276	0.4392	−2.6
0.5 mL WP + 0.2 mL QR + 0.2 mL CAT	0.7872	0.8362	−5.8
0.5 mL WP + 0.2 mL QR + 0.2 mL CAT + 0.4 mL TR	0.8659	0.9273	−6.6
0.5 mL WP + 0.2 mL QR + 0.2 mL CAT +0.4 mL TR + 0.2 mL CFA	1.1641	1.1806	−1.4

Table 5
The CUPRAC absorbances of glutathione (GSH) working solution in admixture with standard antioxidants (TR, QR, CFA, and CAT); to suitable aliquots of GSH stock solution were added varying volumes of standard antioxidant solutions at 0.1 mM concentration.

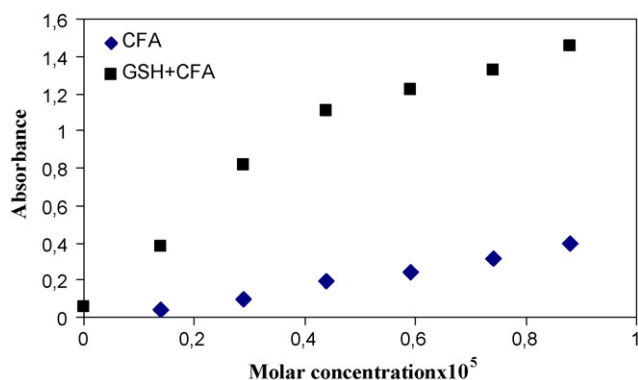| Sample composition	$A_{observed}$	$A_{expected}$	Relative error, (%)
0.25 mL GSH	0.3967		
0.25 mL GSH + 0.2 mL QR	0.6931	0.7057	−1.8
0.25 mL GSH + 0.2 mL CAT	0.7799	0.7564	+3.1
0.25 mL GSH + 0.2 mL CFA	0.5923	0.5899	+0.4
0.25 mL GSH + 0.4 mL TR	0.5605	0.5335	+4.7
0.25 mL GSH + 0.4 mL TR + 0.2 mL QR	0.8187	0.8445	−3.0
0.25 mL GSH + 0.4 mL TR + 0.2 mL QR + 0.2 mL CAT	1.0775	1.1338	−5.0
0.25 mL GSH + 0.4 mL TR + 0.2 mL QR + 0.1 mL CAT	1.2259	1.2539	−2.2

Fig. 3. FRAP calibration curves of CFA alone and in a fixed amount of GSH.

3.3. FRAP assay results

FRAP assay was calibrated against both thiol and phenolic antioxidants to yield the following calibration curve equations:

$$A = 2.98 \times 10^3 c - 0.0341 \quad (r^2 = 0.9973) \text{ for CYS}$$
$$A = 2.13 \times 10^3 c - 0.0586 \quad (r^2 = 0.9945) \text{ for GSH}$$
$$A = 4.98 \times 10^4 c - 0.0295 \quad (r^2 = 0.9993) \text{ for TR}$$
$$A = 3.94 \times 10^4 c + 0.0299 \quad (r^2 = 0.9993) \text{ for CAT}$$
$$A = 5.00 \times 10^4 c - 0.0468 \quad (r^2 = 0.9977) \text{ for CFA}$$
$$A = 1.08 \times 10^5 c - 0.0515 \quad (r^2 = 0.9972) \text{ for QR}$$

As can be seen from these calibration curves, the absorbance *vs* concentration relationships were not linear (low r^2 values), and the curves did not pass through the origin (high absolute values for intercepts). The response to thiol compounds (CYS and GSH) was very low. When increasing amounts of phenolic antioxidants (CFA, QR, and CAT) were added to a fixed amount of GSH, the FRAP absorbance *vs* concentration curves were not parallel to the original calibration lines of antioxidants alone (in standard buffer). An example of this situation can be seen in Fig. 3 where the calibration line of CFA alone was not parallel to that of CFA in a fixed amount of GSH, showing that the TAC values are not additive in the FRAP assay using the selected buffer medium. As can be seen in Table 6, there were great differences between the expected and observed TAC values of thiol-containing antioxidant mixtures assayed by FRAP. This means FRAP cannot be useful in precisely determining the TAC of thiol-containing mixtures, and of protein fractions in the selected medium. It has been previously established that the CUPRAC reagent is fast enough to oxidize thiol-type antioxidants, whereas the FRAP method does not totally react with thiol-type antioxidants like glutathione [16,17]. The reason for this may be the half-filled d-orbitals of high-spin Fe(III) attributing it a chemical inertness, while the electronic structure of Cu(II) enables fast kinetics.

Table 7
The ABTS absorbances of GSH (at 5 mM concentration) in admixture with 0.05 mM TR and CFA, 0.02 mM CAT, and 0.03 mM QR.

Mixture	$\Delta A_{observed}$	$\Delta A_{expected}$	Relative error, (%)
0.2 mL GSH	0.2564		
0.2 mL GSH + 0.2 mL QR	0.6309	0.6933	−9.0
0.2 mL GSH + 0.2 mL TR	0.3739	0.3588	+4.2
0.2 mL GSH + 0.2 mL CAT	0.5454	0.5254	+3.8
0.2 mL GSH + 0.2 mL CFA	0.5301	0.5479	−3.2
0.1 mL GSH + 0.1 mL TR + 0.1 mL CAT	0.2869	0.2972	−3.5
0.1 mL GSH + 0.1 mL QR + 0.1 mL CFA	0.4210	0.4178	+0.8
0.1 mL GSH + 0.1 mL TR + 0.1 mL QR+ 0.1 mL CAT	0.5601	0.5249	+6.7
0.1 mL GSH + 0.1 mL TR + 0.1 mL QR + 0.1 mL CAT + 0.1 mL CFA	0.7007	0.6573	+6.6

The FRAP reagent (*i.e.*, ferric tripyridyltriazine) gives incomplete oxidation for thiols and for hydroxycinnamic acids within the reaction protocol time of the assay [17]. Thus mixtures of either cysteine or GSH with polyphenolic antioxidants, especially with hydroxycinnamic acids and CAT, gave erratic results of absorbance additivity (Table 6) where the observed total absorbances of mixtures by far exceeded that of expected values from individual constituents. Though not proven at this stage, this may also result from the increased vulnerability of such antioxidants in mixtures in regard to FRAP oxidation.

3.4. ABTS assay results

ABTS assay was calibrated against both thiol and phenolic antioxidants to yield the following calibration curve equations:

$$A = 2.06 \times 10^4 c - 0.060 \quad (r^2 = 0.9991) \text{ for CYS}$$
$$A = 3.98 \times 10^4 c + 0.021 \quad (r^2 = 0.9981) \text{ for GSH}$$
$$A = 3.80 \times 10^4 c - 0.0224 \quad (r^2 = 0.9947) \text{ for TR}$$
$$A = 1.74 \times 10^5 c - 0.1102 \quad (r^2 = 0.9996) \text{ for CAT}$$
$$A = 6.74 \times 10^4 c - 0.0406 \quad (r^2 = 0.9998) \text{ for CFA}$$
$$A = 1.28 \times 10^5 c + 0.0286 \quad (r^2 = 0.9992) \text{ for QR}$$

ABTS method was shown to give linear responses to both thiol-type and phenolic antioxidants tested. The molar absorptivity of CAT was higher than that of QR in the selected buffer medium, possibly due to the contribution of urea to intermolecular interactions in solutions containing aggregates. Similar to the observation in original CUPRAC assay [15] the original ABTS/TEAC method gave a lower response to CAT, and this finding needs to be further explored. Table 7 shows that ABTS assay is capable of relatively precisely predicting the TAC of thiols in admixture with phenolic antioxidants, confirming that it may be useful to assay protein fractions. One of the problems associated with ABTS assay is its enhanced response to pH elevation. However, the compatible form of ABTS assay with

Table 6
The FRAP absorbances of CYS or GSH (at 5 mM concentration) in admixture with standard antioxidants (TR, QR, CFA, and CAT); to suitable aliquots of CYS or GSH stock solutions were added varying volumes of standard antioxidant solutions at 0.5 mM concentration.

Mixture	$A_{observed}$	$A_{expected}$	Relative error, (%)
0.1 mL CYS + 0.02 mL CAT	1.4247	0.6876	>100
0.1 mL CYS + 0.02 mL QR	1.0749	0.8248	+30
0.1 mL CYS + 0.02 mL CFA	1.4258	0.6848	>100
0.08 mL GSH + 0.02 mL TR	0.3312	0.3355	−1.3
0.01 mL GSH + 0.02 mL QR	0.7724	0.3232	>100
0.01 mL GSH + 0.02 mL CAT	0.8822	0.1845	>100
0.01 mL GSH + 0.02 mL CFA	0.8153	0.1826	>100
0.01 mL GSH + 0.01 mL TR + 0.01 mL CAT	0.7332	0.2145	>100
0.01 mL GSH + 0.01 mL QR + 0.01 mL CFA	1.0196	0.2724	>100
0.01 mL GSH + 0.01 mL TR + 0.01 mL CAT + 0.01 mL QR	0.964	0.3388	>100
0.01 mL GSH + 0.01 mL TR + 0.01 mL CAT + 0.01 mL QR + 0.01 mL CFA	1.163	0.3655	>100

Table 8
TAC measurements of solutions containing proteins and GSH tripeptide (results reported as cysteine-equivalents, in the units of mol/L CYS).

Sample	Ellman	CUPRAC	FRAP	ABTS
Egg white (EW)	3.0×10^{-4}	5.0×10^{-4}	4.5×10^{-4a}	7.5×10^{-4}
Whey proteins (WP)	1.6×10^{-4}	6.7×10^{-4}	5.0×10^{-4}	9.6×10^{-4}
Gelatin (GL)	0.3×10^{-4}	4.2×10^{-4}	10.0×10^{-4}	22.0×10^{-4}
GSH solution (5.0×10^{-4} M)	5.3×10^{-4}	5.2×10^{-4}	3.6×10^{-4}	10.5×10^{-4}

^{a} Measured in the filtrate due to precipitation observed at the end of 6 min.

protein fractions is the one involving the generation of ABTS cation radical with H_2O_2 + HRP rather than that generated with persulfate, as the latter would cause precipitation reactions in protein solutions. Another problem is the high TEAC coefficient of ABTS for GSH (1.05 in this assay), which is not compatible with its regular antioxidant action, i.e., GSSG/GSH ratios increase from 0.01 to 0.1 during combat against oxidative stress [32]. This means GSH and certain protein thiols may undergo reversible 1−e oxidation to the corresponding disulfides under normal conditions of protein stabilization and thiol protection [33] (with an expected TEAC coefficient of 0.5, as found with CUPRAC), and are not irreversibly oxidized to sulfenic, sulfinic, and sulfonic acids corresponding to two or more electron oxidations [16]. Oxidation reactions of protein thiols as a part of antioxidant action involving two or more electrons are less likely in vivo [34]. The ABTS/persulfate antioxidant assay method was shown to treat GSH as a reductant capable of giving ≈2 electrons (TEAC of ABTS/persulfate method for GSH varied between 1.3 and 1.5 [16]). Since the molar absorptivity of ABTS for thiols closely depends on the manner how the ABTS$^{•+}$ radical cation is produced, the ABTS/HRP/H_2O_2 method used in the current study yields a distinctly higher molar absorptivity for GSH than for CYS, depending on the extent of thiol oxidation. On the other hand, the CUPRAC method gives a close molar absorptivity for both cysteine and GSH, corresponding to a clear 1−e oxidation, in accordance with the extent of physiological reversible oxidation reactions of these thiols during antioxidant action in the human metabolism.

3.5. Application of the TAC assays to real solutions

Real samples (solutions of protein fractions and GSH tripeptide) were first diluted with pH 8.0 standard buffer at a volume ratio of 1:1 (for ABTS assay, this diluted sample was rediluted at 1:3). Each final sample was assayed twice with the TAC measurement methods (by taking 0.5–1.0 mL sample aliquots for CUPRAC, Ellman, and FRAP, and 0.3 mL aliquots for ABTS), and the corresponding TAC values were reported as CYS equivalents with the aid of a calibration curve drawn for each assay with CYS standards. The results shown in Table 8 reveal that CUPRAC can estimate the correct amount of GSH, because both CYS and GSH act as 1−e reductants toward the CUPRAC reagent, Cu(Nc)$_2^{2+}$. Furthermore, the same data (in Table 8) show that CUPRAC neither underestimates nor overestimates the true TAC value of protein solutions, which is probably comprised of not only thiols but certain amino acid moieties on these proteins [35]. In buffers of reduced water activity (like guanidium hydrochloride), it has been reported that the ABTS$^{•+}$ radical scavenging activities of both proteins; α-lactalbumin and β-lactoglobulin, increase most likely as a result of solvent exposure of amino acids previously buried in the interior of proteins [36]. Fig. 4 depicts the curvilinear range of responses of the applied TAC assays with respect to dilution of egg white (EW) protein extracts. The highest linear correlation coefficient of absorbance vs dilution ratio was obtained with CUPRAC ($r^2_{(CUPRAC)}$ = 0.9067, $r^2_{(Ellman)}$ = 0.8849, $r^2_{(ABTS)}$ = 0.8194). The dilution sensitivity is considered to be important for certain protein-bearing matrices such as human serum. For
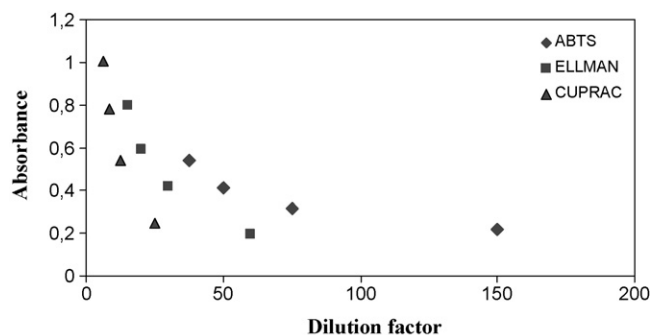

Fig. 4. The curvilinear range of responses of the applied TAC assays (Ellman, CUPRAC, and ABTS) with respect to dilution of EW protein extracts.

example, when the found antioxidant capacities (as micromolar trolox equivalents) of serum extracts using the CUPRAC method were recorded against expected capacities at varying dilutions, excellent linear curves passing through the origin were reported [16] as a distinct advantage over the Randox-TEAC (i.e., the commercialized version of ABTS-TEAC) assay in which dilution of serum might produce up to a 15% increase in the TEAC values [10].

4. Conclusions

In general, proteins are not considered as true antioxidants but are accepted to protect antioxidants from oxidation in various antioxidant activity assays. In most assays measuring total antioxidant capacity (TAC), proteins are not taken into account (e.g., in assays carried out in the hydrophilic fraction of human serum) and remain in the precipitate (obtained by using perchloric acid, trichloroacetic acid, ammonium sulfate, etc.). This study has verified that the contribution of proteins, especially thiol-containing proteins, to the observed TAC is by no means negligible, and can be measured by known methods. Various protein fractions (EW, WP, and GL) and peptides (like GSH) may either respond to these TAC assays directly via their free –SH groups, or indirectly after protein denaturation through their exposed (originally buried) thiol groups. The employed urea buffer also aids to expose these thiols to TAC assays. Urea – in combination with SDS – maximize the reactivity of thiols and disulfides that may be buried within the protein matrix [30]. Presence of 8 M urea partly denaturates proteins and significantly lowers the reduction potential of disulfide/thiol couples in peptides facilitating thiol oxidizability [29]. Ellman reagent can only respond to these thiols (but not to other phenolic antioxidants), whereas the other tested methods may also exhibit sensitivity toward certain amino acid moieties on these proteins. In order that a selected TAC assay be applicable to protein fractions, its response to complex mixtures should be equal to the sum of the responses recorded for individual mixture constituents. Additivity of TAC is a prerequisite for comparing the TAC values of complex samples. Among the tested TAC assays, only CUPRAC and ABTS/H_2O_2/HRP possess this property of additivity, though the latter method may give a high response at elevated pH.

Only CUPRAC and ABTS methods have reagents (or chromophores) that are soluble in both aqueous and organic solvents, and may therefore serve the need to simultaneously measure hydrophilic and lipophilic antioxidants. However, the results obtained with the ABTS assay is quite dependent on the manner how the colored radical reagent of ABTS$^{•+}$ is generated. Although FRAP assay may have a limited use for low molecular weight antioxidants (e.g., in whey) [1], experiments in urea buffer have shown that FRAP is neither sensitive to thiol-type antioxidants nor gives an additive TAC response to complex mixtures. This study reports for the first time the measurement of the TAC of thiol-containing pro-

teins in admixture with phenolic antioxidants after taking up the protein fractions with a suitable buffer (*e.g.*, for the egg white sample) that neither causes the precipitation of proteins nor interferes with the selected antioxidant assay (specifically CUPRAC assay), and is expected to be useful in estimating the TAC values and hence food qualities of dairy products and other protein-containing food varieties in further studies.

Acknowledgements

References

[1] J. Chen, H. Lindmark-Månsson, L. Gorton, B. Åkesson, Int. Dairy J. 13 (2003) 927.
[2] A.E. Özen, M. Kılıç, Gıda Teknolojileri Elektronik Dergisi 3 (2007) 45.
[3] L.M. Tong, S. Sasaki, D.J. McClements, E.A. Decker, J. Agric. Food Chem. 48 (2000) 1473.
[4] R.E. Møller, H. Stapelfeldt, L.H. Skibsted, J. Agric. Food Chem. 46 (1998) 425.
[5] R. Rossi, A. Milzani, I. Dalle-Donne, F. Giannerini, D. Giustarini, L. Lusini, R. Colombo, P. Di Simplicio, J. Biol. Chem. 276 (10) (2001) 7004.
[6] N. Nagatsuka, K. Harada, M. Ando, K. Nagao, Int. J. Mol. Med. 16 (2005) 427–430.
[7] A. Dávalos, M. Miguel, B. Bartolomé, R. López-Fandiño, J. Food Prot. 67 (9) (2004) 1939.
[8] M.P. Almajano, M.E. Delgado, M.H. Gordon, Food Chem. 102 (2007) 1375.
[9] K. Taguchi, K. Iwami, M. Kawabata, F. Ibuki, Agric. Biol. Chem. 52 (2) (1988) 539.
[10] G. Cao, R.L. Prior, Clin. Chem. 44 (6) (1998) 1309.
[11] E. Tütem, R. Apak, F. Baykut, Analyst 116 (1991) 89.
[12] E. Tütem, R. Apak, Anal. Chim. Acta 255 (1991) 121.
[13] E. Tütem, R. Apak, E. Günaydı, K. Sözgen, Talanta 44 (1997) 249.
[14] K. Güçlü, K. Sözgen, E. Tütem, M. Özyürek, R. Apak, Talanta 65 (2005) 1226.
[15] R. Apak, K. Güçlü, M. Özyürek, S.E. Karademir, J. Agric. Food Chem. 52 (2004) 7970.
[16] R. Apak, K. Güçlü, M. Özyürek, S.E. Karademir, M. Altun, Free Radic. Res. 39 (2005) 949.
[17] R. Apak, K. Güçlü, B. Demirata, M. Özyürek, S.E. Çelik, B. Bektaşoğlu, K.I. Berker, D. Özyurt, Molecules 12 (2007) 1496.
[18] R. Apak, K. Güçlü, M. Özyürek, S.E. Çelik, Microchim. Acta 160 (2008) 413.
[19] M. Özyürek, B. Bektaşoğlu, K. Güçlü, R. Apak, Anal. Chim. Acta 616 (2008) 196.
[20] N. Sava, I. Van der Plancken, W. Claeys, M. Hendrickx, J. Dairy Sci. 88 (2005) 1646.
[21] N.J. Miller, C. Rice-Evans, M.J. Davies, V. Gopinathan, A. Milner, Clin. Sci. 84 (1993) 407.
[22] A. Cano, J. Hernández-Ruiz, F. Garcia-Cánovas, M. Acosta, M.B. Arnao, Phytochem. Anal. 9 (1998) 196.
[23] M.B. Arnao, A. Cano, M. Acosta, Food Chem. 73 (2001) 239.
[24] I.F.F. Benzie, J.J. Strain, Anal. Biochem. 239 (1996) 70.
[25] M. Özyürek, B. Bektaşoğlu, K. Güçlü, N. Güngör, R. Apak, Anal. Chim. Acta 630 (2008) 28.
[26] E. Papp, P. Száras, T. Korcsmáros, P. Csermely, FASEB J. 20 (2006) E235.
[27] K. Patil, R. Pawar, P. Talap, Phys. Chem. Chem. Phys. 2 (2000) 4313.
[28] O. Dangles, C. Dufour, S. Bret, J. Chem. Soc., Perkin Trans. 2 (1999) 737.
[29] L.B. Poole, A. Claiborne, J. Biol. Chem. 264 (1989) 12322.
[30] K.-Y. Chan, B.P. Wasserman, Cereal Chem. 70 (1993) 22.
[31] G.L. Ellman, Arch. Biochem. Biophys. 82 (1959) 70.
[32] I.A. Cotgrave, R.G. Gerdes, Biochem. Biophys. Res. Commun. 242 (1998) 1.
[33] C. Johansson. Biochemical Properties of Human Glutaredoxins, PhD Thesis, The Medical Nobel Institute for Biochemistry, Karolinska Institutet, Stockholm, Sweden, 2004.
[34] D.A. Dickinson, H.J. Forman, Biochem. Pharmacol. 64 (2002) 1019.
[35] K. Sozgen, S. Demirci Çekiç, E. Tütem, R. Apak, Talanta 68 (2006) 1601.
[36] M.R. Clausen, L.H. Skibsted, J. Stagsted, J. Agric. Food Chem. 57 (2009) 2912–2929.

Determination of perchlorate in river by ion-pair hollow-fiber liquid-phase microextraction coupled with electrospray ionization tandem mass spectrometry

Hsin-Chang Chen, Wen-Tsen Chen, Wang-Hsien Ding*

Department of Chemistry, National Central University, Chung-Li 320, Taiwan

ABSTRACT

This paper describes the analysis of perchlorate (ClO_4^-) in surface water samples by a rapid and reliable ion-pair hollow-fiber liquid-phase microextraction (HF-LPME) method coupled with flow-injection electrospray ionization tandem mass spectrometry (ESI-MS–MS) technique. The effects of the type and concentration of ion-pairing reagents, extraction time, temperature and pH value on the quantitative extraction of perchlorate by ion-pair HF-LPME were investigated and optimized. Di-*n*-hexyl ammonium acetate (DHAA) was employed to form an extractable ion-pair complex with aqueous perchlorate. The characteristic ions $[ClO_4\text{-}ClO_4\text{-}DHA]^-$ at *m/z* 384.6 and 386.7 were observed in the ESI negative-ionization mode. The predominant product ions $[ClO_4]^-$ at *m/z* 99 and 101 were used for quantitation and to maximize the detection selectivity and sensitivity. The limit of detection (LOD) was 0.5 µg/L. The reliability and precision of the standard addition method of ion-pair HF-LPME for the determination of trace levels of perchlorate in surface water were demonstrated.

© 2009 Elsevier B.V. All rights reserved.

1. Introduction

Perchlorate (ClO_4^-) gained a great amount of attention as an environmental contaminant after it was detected in abnormally high concentrations in drinking water supplies in the western United States in 1997. Nowadays, detection of perchlorate contamination in the environment and in foodstuffs continues to increase, especially in groundwater, drinking water, milk, vegetables and even in bottled water [1–10]. The presence of perchlorate in drinking water, agricultural irrigation sources, and food supplies is of great concern because it can have an adverse impact on human health through interfering with iodide uptake by the thyroid [11]. A relationship exists between fireworks display and the environmental occurrence of perchlorate, for example, the concentration of perchlorate in a municipal lake was found to have increased dramatically within 14 h after a fireworks display [8]. This relationship stimulated our interest to investigate the content and distribution of perchlorate in Taiwan, where fireworks use is widespread in festivals, wedding celebrations and religion activities. Furthermore, many unlicensed fireworks factories exist in suburban or rural areas in Taiwan may threaten not only the environment but also the safety of the residents of those areas.

The determination of perchlorate in environmental water samples is most often performed using (i) suppressed ion chromatography (IC) coupled with conductivity detection (CD) [1–3], and (ii) electrospray ionization mass spectrometry (ESI-MS) or ESI-tandem mass spectrometry (ESI-MS–MS) with IC, liquid chromatography (LC) [4–8], or flow-injection analysis (FIA) [9,10]. ESI-MS and ESI-MS–MS techniques have been applied widely to the analysis of perchlorate in environmental samples because of their high sensitivity and specificity. Several sample preparation techniques have been applied for perchlorate analysis in various water samples, including standard addition [9], ion-pair liquid–liquid extraction (ion-pair LLE) [10], or sample pretreatment with ion-exchange cartridges [1,4,6,7]. Currently, liquid-phase microextraction (LPME), a simple and cost-efficient technique, has emerged as an attractive alternative for sample preparation (see Refs. [12–14] and reference therein). Hollow-fiber-protected LPME (HF-LPME) coupled with GC–MS or LC–MS has been applied successfully to the determination of various organic contaminants in environmental, biological and food samples (see Refs. [12–16] and reference therein). However, combination of HF-LPME with tandem mass spectrometry to analyze anionic analytes (e.g., perchlorate) in complex environmental samples has not been reported.

In this study, the effects of various operating parameters on the extraction of perchlorate from aqueous samples by ion-pair HF-LPME were evaluated. Di-*n*-hexylammonium acetate (DHAA) was applied in this ion-pair HF-LPME coupled with ESI-MS–MS analysis because of its volatility, its weak signal suppressing effect, and the relatively low abundances of its Na+, K+ adducts, which simplify the mass spectra interpretation [17]. Moreover, this developed method

---

* Corresponding author. Tel.: +886 3 4227151x65905; fax: +886 3 4227664.
E-mail address: wanghsiending@gmail.com (W.-H. Ding).

was applied for the first time to extract perchlorate directly from complex environmental samples at a trace-level.

2. Experimental

2.1. Reagents and materials

HPLC-grade methanol was purchased from Merck (Darmstadt, Germany). Reagent-grade 1-octanol was used as received from Fluka (Buchs, Switzerland). The reagent-grade ion-pair reagents: di-*n*-propylammonium acetate (DPAA), di-*n*-butyl ammonium acetate (DBAA), di-*n*-amylammonium acetate (DAAA), di-*n*-hexylammonium acetate (DHAA) and decyltrimethylammonium bromide (DeTMA-Br) were purchased from TCI (Tokyo, Japan). Sodium perchlorate (used as the standard) was obtained from Sigma–Aldrich (St. Louis, USA). All other chemicals were of analytical grade and used as received. Deionized water was further purified using a Millipore water purification device (Millipore, Bedford, USA). A stock solution of perchlorate standard (1000 μg/mL) was prepared in deionized water. The Accurel Q3/2 polypropylene hollow fiber membrane (600-μm I.D., 200-μm wall thickness, 0.2-μm pore size) for HF-LPME was obtained from Membrana (Wuppertal, Germany). The hollow fiber (30-cm in length) was cleaned ultrasonically in acetone for 20 min and air-dried prior to use. A 100-μL syringe equipped with a conical needle tip (SGE, Sydney, Australia) was used for LPME experiments.

2.2. Sample collection

Water samples were collected on November 7, 2007, 6 days after an explosion at a firework factory in Miao-Li County, Taiwan. Sample-A (specific conductance 370 μS/cm) was collected in a ditch, 20 m from the point of explosion. Sample-B (specific conductance 500 μS/cm) was collected from Ho-Long River at the location of the ditch exit. The third water sample (Sample-C, specific conductance 390 μS/cm) was also collected from Ho-Long River, but 20 km downstream from the site of the explosion. The pH of each sample was ca. 7.1. Upon arrival at laboratory, the samples were immediately passed through a 0.45-μm membrane filter, and then subjected to the ion-pair HF-LPME procedures using the standard addition method for quantitation.

2.3. Ion-pair HF-LPME

The LPME device and the basic principle of Hollow-fiber-protected LPME involving ion-pair formation have been described elsewhere [15]. The hollow fiber (30-cm in length) was firstly dipped for 8 min in 1-octanol. Subsequently, 100 μL of 1-octanol was injected into the lumen of the hollow fiber, and then the fiber was placed in a 40-mL sample-vial with 40 mL of sample solution containing 4 mM DHAA. For optimal extraction (see Section 3.2), a water bath's temperature was controlled at 30 °C using a remote probe, and the sample was stirred at 300 rpm (100 rpm = 10.47 rad/s) for 40 min. After extraction, the 1-octanol was retracted into a 100-μL micro-vial, and then an aliquot of 60-μL was injected by flow-injection into ESI-MS–MS system. Each piece of fiber was employed only once to avoid any possibility carryover.

2.4. Flow-injection ESI-MS–MS

A mixture of methanol and dichloromethane (70:30, v/v) was used as the carrier liquid of the flow-injection system and the flow-rate was 0.1 mL/min. No LC column was required for this analysis. Perchlorate was detected using an Agilent LC-MSD Trap SL mass spectrometer (Palo Alto, USA) equipped with an ESI in negative-ionization mode. The detection parameters were optimized by

Table 1
Experimental optimized conditions.

Ion-pair LPME	
Fiber length	30 cm
Ion-pairing reagent	4 mM DHAA
Extraction solvent	1-octanol
Stirring rate	300 rpm
Extraction time	40 min
Extraction temperature	30 °C
pH	7.0
Flow injection	
Carrier liquid	MeOH: CH_2Cl_2 (70:30, v/v)
Injection volume	60 μL
Flow-rate	0.1 mL/min
Negative ESI-MS–MS	
Capillary voltage	4000 V
Drying gas temperature	325 °C
Drying gas flow-rate	3.5 L/min
Nebulizing gas pressure	22 psi
Fragmentation amplitude	0.25 V
Precursor ions	m/z 384.6 and 386.7 $[ClO_4\text{-}ClO_4\text{-}DHA]^-$
Product ions	m/z 99 $[^{35}ClO_4]^-$ and m/z 101 $[^{37}ClO_4]^-$

estimating the signal intensity through a series of continuous-infusion experiments. Mass spectra were collected in the scan range m/z 80–450. The optimized ESI parameters (see Section 3.1 and Table 1) were applied. The helium background gas was maintained at a pressure of 6×10^{-6} Torr during the MS–MS measurements. Quantitation of perchlorate was performed through product ion scans recording two transitions.

3. Results and discussion

3.1. Optimization of ESI-MS–MS

A mixture of methanol and dichloromethane (70:30, v/v) as the carrier liquid to transport the ion-paired perchlorate complex into ESI-MS–MS system was applied to obtain the highest ionization signal, which has been described by Magnuson et al. [10]. The effect of several parameters were evaluated to optimize the ESI ionization efficiency and thereby obtain the highest and most stable signal-to-noise (S/N) ratio for the intensity of the flow-injection peak under MS–MS conditions. Fig. 1 displays that the capillary voltage was optimized at 4000 V (tested between 1000 and 6000 V); the drying gas temperature and drying gas flow-rate were optimized at 325 °C (tested between 300 and 400 °C) and 3.5 L/min (tested between 2 and 8 L/min), respectively; and the nebulizing gas pressure was optimized at 22 psi (tested between 10 and 50 psi) (Table 1). Under ESI-MS conditions, a stable and predominant complex featuring one DHA cation and two perchlorate anions ($[ClO_4\text{-}ClO_4\text{-}DHA]^-$) at m/z 384.6 and 386.7 were detected. Similar complexes formed through ion pairing between a cation and perchlorate ions have been reported previously [10]. Under the optimized MS–MS conditions, the predominant product ions $[ClO_4]^-$ at m/z 99.1 and 101.2 were observed as a result of the loss of the DHA cation and one perchlorate anion. These predominant product ions as quantitation ions were used to maximize the detection selectivity and sensitivity.

3.2. Ion-pair HF-LPME

Table 1 also lists the optimized conditions of the ion-pair HF-LPME technique. The extraction solvent in HF-LPME should be compatible with the fiber and have low volatility. According to previously reports [12–16,18], 1-octanol has been employed in the extraction of various organic compounds with satisfied extraction efficiency. Therefore, 1-octanol was selected as the extraction solvent for the study.
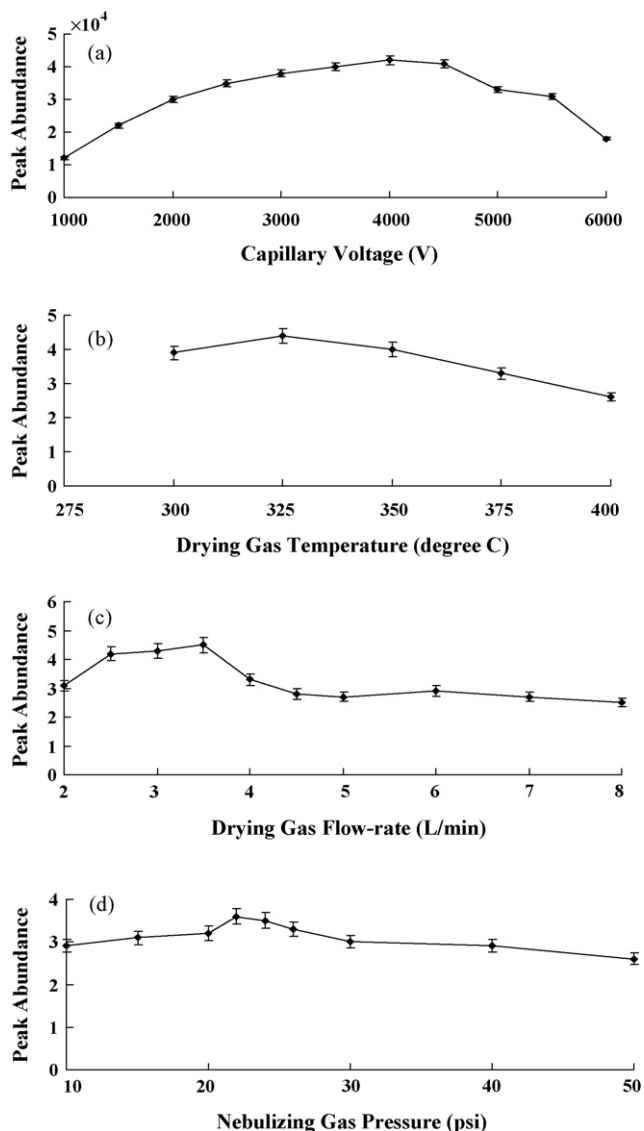
Fig. 1. Effects of the (a) capillary voltage, (b) drying gas temperature, (c) drying gas flow-rate and (d) nebulizing gas pressure on the peak abundance of negative ESI-MS–MS detection. Three replicate experiments were performed; the error bars represent the standard deviations.

The ion-pairing reagent plays two roles in this extraction method: (i) it neutralizes the perchlorate ion so that its ion-pair complex may be readily extracted by 1-octanol, and (ii) it increases of m/z signal of the perchlorate complex to avoid interference from ions of lower masses. The performance of four ion-pairing reagents, DPAA, DBAA, DAAA, and DHAA, which were commonly used for the LC–ESI-MS analyses of acidic organic compounds, was evaluated. In addition, the ion-pairing reagent DeTMA-Br, which has been applied previously for perchlorate ion-pair LLE analysis [10], was also tested. After extraction for 40-min at a stirring rate of 300 rpm at 30 °C, a strong and stable signal was observed when DHAA was employed as the ion-pairing reagent because of its weak signal suppressing effect and simple mass spectrum. No or weak signals were detected when employing the other four reagents (data not shown). Although DeTMA-Br has been applied successfully in an ion-pair LLE study [10], it appears to be inappropriate to use in ion-pair HF-LPME studies, presumably due to its long alkyl chain. Therefore, DHAA was used as the ion-pairing reagent to extract perchlorate from water samples.
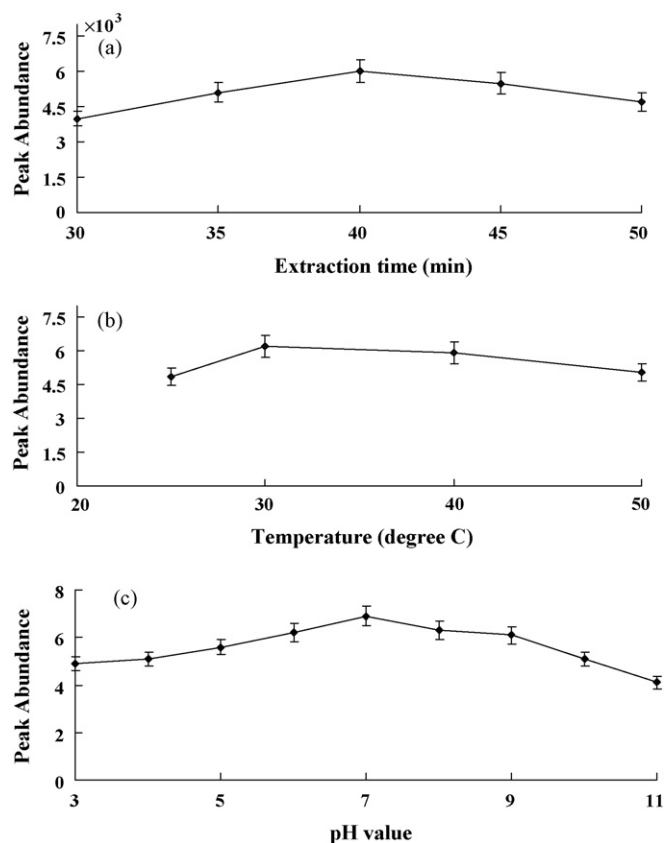
Fig. 2. Effects of the (a) extraction time, (b) extraction temperature and (c) pH value on the peak abundance of ion-pair HF-LPME. The spiked concentration of perchlorate was 5 μg/L. Three replicate experiments were performed; the error bars represent the standard deviations.

The extraction time must be sufficiently long to allow equilibrium to be reached for the partitioning of the ion-paired perchlorate complex between the aqueous and extraction solvent. However, the extraction solvent might transfer into the aqueous phase at too longer extraction times, causing the extraction efficiency to decrease through a solvent depletion effect [18]. Fig. 2(a) shows that the peak abundances increased upon increasing the extraction time from 30 to 40 min. After 45 min, the peak abundance decreased; in this case, some 1-octanol was observed on the surface of the aqueous samples. Hence, an extraction time 40 min was used for our subsequent experiments. The effects of the concentration of DHAA and stirring speed were also evaluated. However, the average peak abundance ($65 \pm 5 \times 10^2$) was not significantly different at the concentrations of DHAA varies from 4 to 7 mM, and stirring speed varies from 100 to 300 rpm (data not shown).

In most cases, the extraction temperature for LPME experiments has not been evaluated; i.e., they have always been performed at room temperature (see Refs. [12–14] and reference therein). A non-uniform extraction temperature might affect the reproducibility of the results because a fluctuation temperature influences the kinetic energy of the ion-paired analytes and, therefore, affect mass transfer through the fiber. Thus, for the first time, the effect of the temperature was studied on the extraction efficiency of HF-LPME. Fig. 2(b) shows that the peak abundance increased upon increasing the extraction temperature from 25 to 30 °C, presumably because the kinetic energy of the ion-paired complexes and their mass-transfer process from the sample solution to the extraction solvent both increased in response to higher temperatures. However, the peak abundance decreased upon increasing the temperature from 30 to 50 °C, presumably the rising temperature increasing the

Table 2
Quantitation of perchlorate in environmental samples using the standard addition method.

Sample	Equation	r^2	R.S.D. (%)	Detected concentration
A	$y = 19109x + 623448$	0.994	4.8	130 µg/L
B	$y = 1952.5x + 12252$	0.999	7.2	6.3 µg/L

possibility of solvent immersion and depletion and also affects the equilibrium constant of extraction process, which can led to loss of the analyte from the lumen of the fiber. Therefore, the extraction temperature was maintained at 30 °C. The pH value is an important factor affecting the extraction of ionic compounds through ion-pair HF-LPME [18]. Fig. 2(c) shows that the peak abundance of ion-pair complex of perchlorate increased slowly when the pH value of sample solution was increased from 3.0 to 7.0 and then decreased upon increasing the pH value from 7.0 to 11.0. This observation may be attributed to the pH value of sample solution influencing the existing form of ion-pair reagent, DHAA, and affecting the extraction efficiency of perchlorate. Therefore, the pH value of sample solution was maintained at 7.0 for subsequent experiments. This result is consistent with that normally applicable to ion-pair HF-LPME in the extraction of acidic herbicides [18].

3.3. Method performance and applications

The analytical characteristics of the developed method in terms of its linear response range, reproducibility and limit of detection (LOD) were investigated to estimate the efficiency and the feasibility of applying it to the environmental samples. The linearity was calculated from five-level calibration curve in the range from 1 to 100 µg/L. The precisions of the curve, as indicated by the relative standard deviation (R.S.D.) was 12.6%, with a correlation coefficient (r^2) of 0.995. The limit of detection (LOD) was determined through HF-LPME of spiked blank river samples, the value was 0.5 µg/L for a 40-mL water sample, defined at an S/N ratio of 3, which is similar to previous reports [1,9].

The developed method in conjunction with the standard addition method was employed to quantitate perchlorate ion in three surface water samples obtained near the site of an explosion at an illegal fireworks factory. Five series vials each containing 40-mL of a water sample were spiked with standard perchlorate solution to obtain final concentrations of 5, 10, 20, 40, and 50 µg/L, respectively. Table 2 displays the quantitation results and the reproducibilities of the standard addition curves. The correlation coefficients (r^2) of the curves in environmental samples were greater than 0.994. The

R.S.D.s for Samples-A and -B were 4.8% and 7.2%, respectively. Relatively high level of perchlorate (130 µg/L) was detected in Sample-A even through 6 days had elapsed after the accident at the fireworks factory. This high concentration of perchlorate in Sample-A arose primarily from the explosion. Perchlorate was not detected in Sample-C, possibly because of dilution.

4. Conclusions

A rapid and reliable ion-pair HF-LPME coupled with ESI-MS–MS technique were developed and optimized to determine perchlorate in environmental water samples. The DHAA ion-pairing reagent provided excellent extraction efficiency for perchlorate through HF-LPME, and it was also sufficiently volatile for use in the ESI-MS–MS system. The low cost and single use of fibers eliminate the possibility of the carry-over problems. Overall, our results suggest that ion-pair HF-LPME is a good alternative extraction method for the determination of perchlorate in environmental samples; it is a simple, effective, and environmental friendly analytical method.

Acknowledgement

References

[1] H.P. Wagner, B.V. Pepich, C. Pohl, D. Later, R. Joyce, K. Srinivasan, D. Thomas, A. Woodruff, B. DeBorba, D.J. Munch, J. Chromatogr. A 1118 (2006) 85.
[2] A.B. Kirk, P.K. Martinelango, K. Tian, A. Dutta, E.E. Smith, P.K. Dasgupta, Environ. Sci. Technol. 39 (2005) 2011.
[3] J.V. Dyke, K. Ito, T. Obitsu, Y. Hisamatsu, P.K.P.K. Dasgupta, B.C. Blount, Environ. Sci. Technol. 41 (2007) 88.
[4] Y. Li, E.J. George, Anal. Chem. 77 (2005) 4453.
[5] S.C. Wendelken, L.E. Vanatta, D.E. Coleman, D.J. Munch, J. Chromatogr. A 1118 (2006) 94.
[6] S.A. Snyder, B.J. Vanderford, D.J. Rexing, Environ. Sci. Technol. 39 (2005) 4586.
[7] Y. Shi, P. Zhang, Y. Wang, J. Shi, Y. Cai, S. Mou, G. Jiang, Environ. Int. 33 (2007) 955.
[8] R.T. Wilkin, D.D. Fine, N.G. Burnett, Environ. Sci. Technol. 41 (2007) 3966.
[9] C.J. Koester, H.R. Beller, R.U. Halden, Environ. Sci. Technol. 34 (2000) 1862.
[10] M.L. Magnuson, E.T. Urbansky, C.A. Kelty, Anal. Chem. 72 (2000) 25.
[11] M.A. Greer, G. Goodman, R.C. Pleus, S.E. Greer, Environ. Health Perspect. 110 (2002) 927.
[12] E. Psillakis, N. Kalogerakis, Trends Anal. Chem. 22 (2003) 565.
[13] S. Pedersen-Bjergaard, K.E. Rasmussen, J. Chromatogr. A 1184 (2008) 132.
[14] T. Barri, J.-Å. Jönsson, J. Chromatogr. A 1186 (2008) 16.
[15] K.E. Rasmussen, S. Pedersen-Bjergaard, M. Krogh, H.G. Ugland, T. Gronhaug, J. Chromatogr. A 873 (2000) 3.
[16] L. Zhao, H.K. Lee, Anal. Chem. 74 (2002) 2486.
[17] H.C. Chen, S.P. Wang, W.H. Ding, J. Chromatogr. A 1102 (2006) 135.
[18] J. Wu, H.K. Lee, Anal. Chem. 78 (2006) 7292.

High-sensitivity detection of polysaccharide using phosphodiesters quaternary ammonium salt as probe by decreased resonance light scattering

Zhanguang Chen [a,*], Guoliang Liu [a,b], Maohuai Chen [c], Mingyao Wu [c]

[a] Department of Chemistry, Shantou University, Shantou 515063, China
[b] Department of Biology, Shantou University, Shantou 515063, China
[c] Medical College, Shantou University, Shantou 515041, China

ABSTRACT

Phosphodiesters quaternary ammonium salt (PQAS) displayed quite intense light scattering in aqueous solution under the optimum condition. In addition, the resonance light scattering (RLS) signal of PQAS was remarkably decreased after adding trace amount polysaccharide with the maximum peak located at 391 nm. It was found that the decreased RLS intensity of the PQAS − PPGL system (ΔI_{RLS}) was in proportion to PPGL concentration in the range of 0.1–30 ng mL^{-1}, with a lower detection limit of 0.05 ng mL^{-1}. Based on this rare decreased RLS phenomenon, the novel method of the determination of purified polysaccharide of Gracilaria Lemaneiformis (PPGL) at nanogram level was proposed in this contribution. The proposed approach was used to determine purified polysaccharide extracted from Gracilaria Lemaneiformis with satisfactory results. Compared with the reported polysaccharide assays, this proposed method has good selectivity, high sensitivity and is especially simple and convenient. Moreover, the mechanism of the reaction between PQAS and polysaccharide was investigated by RLS, fluorescence, and fluorescence lifetime spectra.

© 2009 Elsevier B.V. All rights reserved.

1. Introduction

Carbohydrates, the third kind of important biomacromolecules in biology, have taken part in almost all of the life processes such as biosynthesis, cellular recognition, viral and bacterial infection, and tumor cell metastases [1]. Although the determination of polysaccharide is important, the published paper on this area is rare. Sulfated purified polysaccharide of Gracilaria Lemaneiformis (sulfated PPGL), a class of polysaccharides, has become an attractive material in the field of pharmaceutics because it has many pharmacological effects such as anti-cancer, anti-cardiovascular disease, anti-virus, anti-oxidation, immune enhancement, and so on [2]. Therefore, the quantitative determination of sulfated PPGL is quite significant. Several methods including the colorimetric method [3], the prelabeling method [4,5], the bioassay method [6,7], and the high-performance liquid chromatography (HPLC) [8] have been used to determine the polysaccharide. However, the colorimetric method which is a classical method encounters the low selectivity. The prelabeling method suffers from complicated operation and is time-consuming. The bioassay method is concerned with the sensitive biochemical reaction, such as clotting, which limits its applications. In addition, the HPLC is limited by the complex operation and expensive apparatus.

Thus, it is extremely essential to develop a simple, sensitive and accurate method for polysaccharide determination.

Resonance light scattering (RLS) is a sensitive and selective technique for monitoring molecular aggregation. Since Pasternack et al. first established the RLS technique to study the biological macromolecules with a common fluorescence spectrometer [9,10], RLS studies have attracted great interest among researchers. In the decade years, RLS technique has been used to determine various biological macromolecules such as nucleic acid [11–14], protein [15–18] and medicine [19–21]. Besides, there are only few papers about the determination of polysaccharide [22–24]. However, the study and determination of the sulfated PPGL using PQAS as probe by RLS technique have not yet been reported.

In this contribution, phosphodiesters quaternary ammonium salt (PQAS, Fig. 1) self-aggregated into the micelle that induced a very intense RLS intensity under optimum conditions. The intense RLS intensity of PQAS remarkably decreased after adding a trace amount of PPGL. Moreover, the change of RLS intensity of the PQAS–PPGL system (ΔI_{RLS}) was directly proportional to the PPGL concentration in a certain range. Based on the infrequent decreased RLS phenomenon, a high-sensitivity detection of polysaccharide at nanogram level was developed in this paper. PQAS is one of gemini amphiphiles. Gemini surfactants have structures that are unique to the world of surfactants for possessing two long hydrophobic hydrocarbon chains and two polar headgroups covalently attached through a spacer group and were first synthesized by Menger and

* Corresponding author. Fax: +86 754 8290 2767.
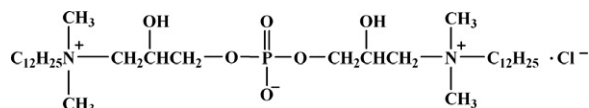E-mail address: kqlu@stu.edu.cn (Z. Chen).

Fig. 1. The structure of phosphodiesters quaternary ammonium salt (PQAS).

Littau [25]. Furthermore, PQAS has shown interesting properties in different areas such as skin care, antibacterial regimens, construction of high porosity materials, analytical separations, drug carriers, and solubilization processes [26,27]. The direct determination of polysaccharide using PQAS as probe has not yet been reported. Our experimental results showed that this proposed approach had the advantages of simplicity, high sensitivity and relative absence of interferences. The polysaccharides in synthetic and real extracted samples were determined with satisfactory results. In this contribution, spectral characteristics, the optimum conditions, and the mechanism of the reaction between PQAS and sulfated PPGL were investigated. In addition, understanding and predicting possible interactions that occur between polysaccharide and gemini zwitterionic surfactant will be useful in both academic and commercial applications [28].

2. Materials and methods

2.1. Apparatus

The RLS spectra and intensity were measured with an LS-55 spectrofluorometer (PerkinElmer, USA) using a quartz cuvette (1.0 cm × 1.0 cm). The scan electron microscopy (SEM) images were obtained by means of a Hitachi-600 scan electron microscopy (Tokyo, Japan). The steady-state fluorescence and the fluorescence lifetime were measured with an FLS-920 picosecond fluorescence lifetime spectrometer (Edinburgh Instruments, UK). All pH measurements were made with a DELTA 320-S acidity meter (Mettler-Toledo Instruments Co. Ltd., Shanghai, China).

2.2. Reagents

The sulfated purified polysaccharide of *Gracilaria lemaneiformis* (PPGL), purchased from China Pharmaceutical Biological Products Analysis Institute, was directly dissolved in doubly distilled water without further purification and stored at 1–4 °C.

The Britton-Robinson (BR) buffer solution (pH 7.0–9.5) was used to control the acidity of the solution, which was made up of $0.04 \, \text{mol L}^{-1}$ phosphoric acid, $0.04 \, \text{mol L}^{-1}$ acetic acid, $0.04 \, \text{mol L}^{-1}$ boric acid, and $0.2 \, \text{mol L}^{-1}$ sodium hydroxide.

All the reagents used were of analytical grade without further purification or the best grade commercially available. Water used throughout was doubly distilled.

2.3. Preparation of PQAS

Phosphodiesters quaternary ammonium salt (PQAS) was synthesized and characterized by the infrared (IR) spectrum according to the literature [26]. The structure of PQAS obtained was illustrated in Fig. 1. The $4.0 \times 10^{-3} \, \text{mol L}^{-1}$ working solution was prepared by directly dissolving 0.262 g precisely weighed PQAS product in 100 mL freshly obtained doubly distilled water.

2.4. Extraction of PPGL [29]

The artificial culture *Gracilaria Lemaneiformis* (KF981 strain, supplied by nan'ao marine research station of Shantou University, Shantou, China) was thoroughly washed with distilled water to remove the impurities such as sand and salt. Then it was dried

at 60 °C and ground up. The powder was passed through a 60-mesh sieve and was stored in a sealed brown container. Before each weighing, the powder was dried to constant at 105 °C and cooled to the room temperature.

Precisely weighed powder was dissolved and extracted by the conventional hot water extraction method. The extracted solution was centrifugalized at 2500 rpm for 15 min. The suspension was transferred to a virginal centrifuge tube. Subsequently, three times amount of ethanol was added and mixed completely. Equally important, the mixture was placed at 4 °C overnight and then centrifugalized. After the precipitate was freeze-dried, it got the crude polysaccharide of *Gracilaria Lemaneiformis*. Extracted polysaccharide was further purified by dissolving the crude sample and adding appropriate 70% (w/v) trichloroacetic acid solution. Especially, the mixture was placed at 4 °C overnight and centrifugalized. Besides, the suspension was neutralized by 5% sodium hydroxide. In addition, the solution was further extracted by the dialysis assay for more than 3 days. Finally, after the extracted solution was carried out freeze-drying, it got the purified polysaccharide of *Gracilaria Lemaneiformis*. Meanwhile, protein and other impurities were removed with the operation above.

2.5. Sample preparation

One milliliter Britton-Robinson buffer, 1.50 mL PQAS solution and appropriate standard polysaccharide or sample solution were successively added to a 10-mL calibrated flask, and then the mixture was diluted to the mark with doubly distilled water and stirred thoroughly. The sample was removed from the calibrated flask and placed in a cuvette for RLS, steady-state fluorescence or fluorescence lifetime measurements. Normally, lifetime measurements were carried out immediately after preparing the sample and then were repeated after several hours of incubation.

2.6. Experimental procedures

The resonance light scattering (RLS) spectrum was obtained by scanning simultaneously the excitation and emission monochromators ($\Delta\lambda = 0.0 \, \text{nm}$) from 250 nm to 700 nm. The extent of light scattering was measured at the maximum wavelength with slit width at 5.0 nm for the excitation and emission. Based on the spectrum, the RLS intensity was measured at 391.0 nm. The change of RLS intensity of PQAS that decreased by the addition of polysaccharide was represented as $\Delta I_{\text{RLS}} = I_{\text{RLS}}^0 - I_{\text{RLS}}$, where I_{RLS}^0 and I_{RLS} were the RLS intensities of PQAS without and with the polysaccharide.

Steady-state fluorescence spectrum was measured using an FLS-920 picosecond fluorescence lifetime spectrometer. PPGL fluorescence was monitored using excitation at 247.0 nm and emission at 304.0 nm.

Fluorescence lifetime was obtained by time-correlated single-photon counting with a Picoquant picosecond pulsed diode laser (50 ps pulsewidth) for excitation. The sample was excited at 247.0 nm by a sub-nanosecond pulsed diode laser with a repetition rate of 10 MHz. The 304.0 nm emission was used for sample excitation. The decay curve was recovered by tail fitting with the instrument-specific software (Edinburgh Instruments). Data normally were collected to a constant peak value of a 1000 counts. The measurements were repeated three times to obtain the best dataset. The fluorescence lifetime was performed at room temperature (21–23 °C).

3. Results and discussion

3.1. Spectral characteristics

The RLS spectra of PPGL, PQAS and the PQAS–PPGL system at pH 9.0 were exhibited in Fig. 2. As Fig. 2 illustrates that the RLS signal
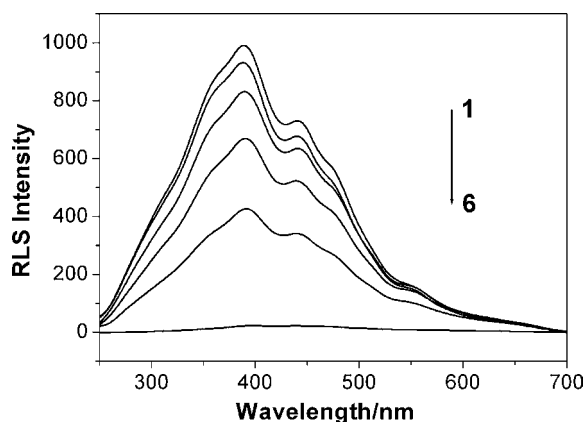
Fig. 2. Resonance light scattering spectra of the PQAS–PPGL system. Conditions: $C_{PQAS} = 6.0 \times 10^{-4}$ mol L^{-1}; C_{PPGL} (µg mL^{-1}): 1, 0; 2, 0.002; 3, 0.005; 4, 0.01; 5, 0.02; 6, 1.0 (without PQAS); pH 9.0.
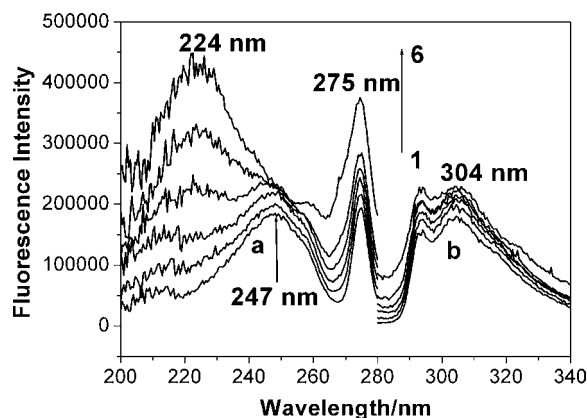

Fig. 4. The fluorescence excitation (a) and emission (b) spectra of PPGL in the absence and presence of PQAS. Conditions: $C_{PPGL} = 10.0$ µg mL^{-1}; C_{PQAS} (mol L^{-1}): 1, 0; 2, 4×10^{-5}; 3, 8×10^{-5}; 4, 1.6×10^{-4}; 5, 4.0×10^{-4}; 6, 8.0×10^{-4}; pH 9.0.

of PQAS was quite intense, that of PPGL was very small in aqueous solution over the scanning wavelength range of 250–700 nm. The intense RLS intensity of PQAS can be clearly denoted with a maximum peak located at 391.0 nm. In addition, there was a RLS shoulder peak at 443.0 nm. However, the intense RLS signal of PQAS was remarkably decreased when a trace amount of PPGL was added. Moreover, the change of RLS intensity (ΔI_{RLS}) was found to increase with the increasing PPGL concentration with a maximum peak located at 391.0 nm. Therefore, 391.0 nm was selected as the analytical wavelength for the further study. In general, this rare decreased RLS phenomenon indicated that the interaction between PPGL and PQAS had occurred, which disaggregated PQAS aggregation, resulting in the remarkable decrease of intense RLS intensity of PQAS. The results from scanning electron microscopy (Fig. 3) confirmed the inference. Fig. 3 illustrated that the micelles of PQAS molecules were disaggregated after adding PPGL, which induced the decrescent size of the RLS particles. According to the Rayleigh formula [9,10], the larger the size of the particles, the stronger the signal of the scattering light. Thus, the intense RLS signal of PQAS was decreased after interacting with PPGL.

To study the interaction between zwitterionic gemini surfactant and polysaccharide, the fluorescence property of PPGL in the absence and presence of PQAS was investigated. The excitation (a) and emission (b) spectra of PPGL were demonstrated in Fig. 4. It can be seen that two excitation peaks were located at 247.0 nm and 275.0 nm, and one emission peak was located at 304.0 nm. The fluorescence intensity of the PPGL–PQAS system was enhanced after adding PQAS. In addition, the blue shift of the maximal exci-

tation peak from 247.0 nm to 224.0 nm was observed when PQAS combined with sulfated PPGL (Fig. 4), manifesting that the PPGL environment became more hydrophobic after the formation of the PPGL–PQAS complex [30].
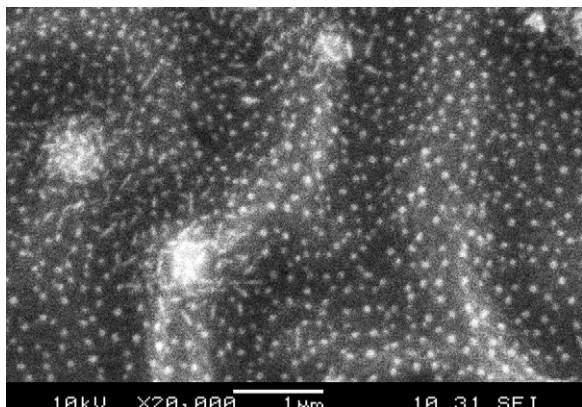
In order to obtain more information, the study on fluorescence lifetime of PPGL (10.0 µg mL^{-1}) in the absence and presence of PQAS was implemented in BR buffer solution (pH 9.0). It was found that the fluorescence decay curve was more satisfactory when the excitation wavelength was set at 247.0 nm and the emission was monitored at 304.0 nm. Therefore, all fluorescence lifetime assays were monitored using excitation at 247.0 nm and emission at 304.0 nm. Fig. 5 illustrated that the fluorescence decay curve of PPGL was remarkably affected by adding PQAS. That was ascribed to the fact that the new complex formed between PQAS and PPGL had different fluorescence lifetime, which inhibited self-aggregation of PQAS, resulting in the remarkable decrease of RLS signal of the experimental system. Moreover, the fluorescence decay curves of PPGL after adding varying concentrations of PQAS were nearly overlapped (see the curves 2–4 in Fig. 5). It was concluded that the increasing PQAS concentration did not affect the fluorescence lifetime of the PPGL–PQAS complex, which pointed out that the interaction force between them was quite stable.

3.2. Effect of pH

PQAS is one of zwitterionic gemini surfactants with two hydrophilic headgroups and two hydrophobic hydrocarbon chains.
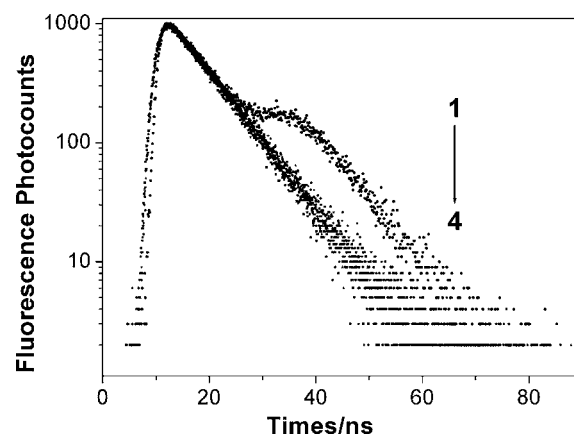

Fig. 3. Scanning electron micrograph of PQAS particles in the presence of PPGL. Conditions: $C_{PQAS} = 6.0 \times 10^{-4}$ mol L^{-1}; $C_{PPGL} = 0.02$ µg mL^{-1}; pH 9.0.

Fig. 5. Fluorescence decay curves of PPGL (10.0 µg mL^{-1}) in the absence and presence of PQAS in BR buffer solution (pH 9.0). Conditions: $C_{PPGL} = 10.0$ µg mL^{-1}; C_{PQAS} (mol L^{-1}): 1, 0; 2, 8×10^{-5}; 3, 2.0×10^{-4}; 4, 4.0×10^{-4}.
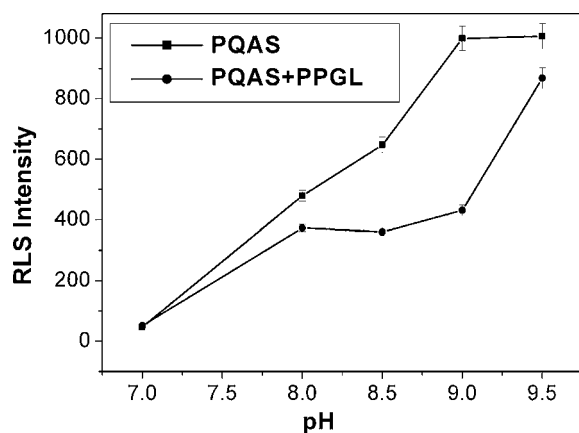
Fig. 6. Effect of pH on the resonance light scattering (RLS) intensity. Conditions: $C_{PQAS} = 6.0 \times 10^{-4}$ mol L^{-1}; $C_{PPGL} = 0.02\ \mu g\ mL^{-1}$. The measurement was repeated in quintuplicate and values were averaged. The curves represent the averages and standard deviations; $^*P < 0.05$. Some error bars are obstructed by the symbols of the points.

Therefore, the pH value of the solution has a significant influence on the acid–base equilibrium of PQAS molecule.

The effect of pH value on RLS signal of the assay system was studied over the pH range 7.0–9.5. As shown in Fig. 6, RLS intensities of both PQAS and the PQAS–PPGL systems were greatly affected by different pH values. The RLS signal increased with the increasing pH value. However, the RLS intensity of PQAS reached the maximum and began to keep constant when pH value was 9.0. The change of RLS intensity (ΔI_{RLS}) reached the maximum with pH 9.0. Therefore, pH 9.0 was chosen for the further assay determination in this research and the optimum volume of BR buffer was 1.0 mL.

3.3. Effect of PQAS concentration

Fig. 7 presented the effect of PQAS concentration on RLS intensity. It can be seen that PQAS concentration had great influence on RLS intensity of the assay system. The RLS intensities, including I_{RLS}^0 and I_{RLS}, increased significantly with the increase of PQAS concentration in the range of 2.0–6.0×10^{-4} mol L^{-1}. However, the RLS signal of PQAS began to go beyond the detection limit of the instrument when its concentration was more than 6.0×10^{-4} mol L^{-1}. Moreover, the intrinsic RLS intensity of PQAS nearly reached the
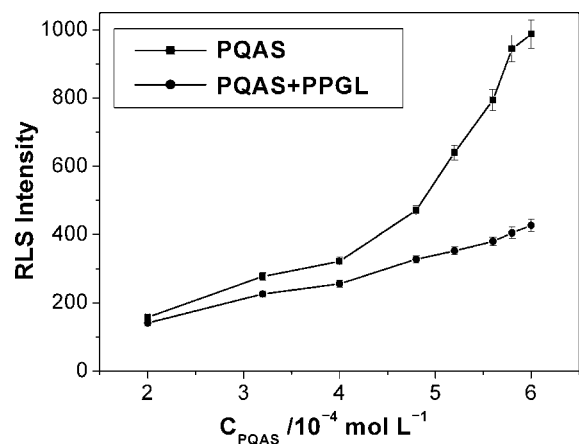
Fig. 7. Effect of phosphodiesters quaternary ammonium salt (PQAS) concentration on the resonance light scattering (RLS) intensity. Conditions: $C_{PPGL} = 0.02\ \mu g\ mL^{-1}$; pH 9.0. The measurement was repeated in quintuplicate and values were averaged. The curves represent the averages and standard deviations; $^*P < 0.05$. Some error bars are obstructed by the symbols of the points.
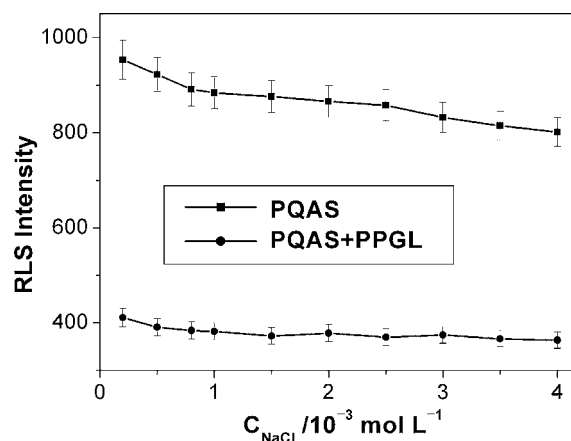
Fig. 8. Effect of ionic strength on the resonance light scattering (RLS) intensity. Conditions: $C_{PQAS} = 6.0 \times 10^{-4}$ mol L^{-1}; $C_{PPGL} = 0.02\ \mu g\ mL^{-1}$; pH 9.0. The measurement was repeated in quintuplicate and values were averaged. The curves represent the averages and standard deviations; $^*P < 0.05$.

maximum value when its concentration was 6.0×10^{-4} mol L^{-1} and a maximum change of RLS intensity (ΔI_{RLS}) was observed at the same condition. Therefore, 6.0×10^{-4} mol L^{-1} PQAS was selected in this study.

3.4. Effect of ionic strength

As displayed in Fig. 8, the effect of ionic strength influenced significantly on the RLS intensity of PQAS, whereas it influenced slightly on the RLS intensity of the PQAS–PPGL system. It was possible that the high-shielding effect of NaCl concentration, counteracting the positive and negative charge of PQAS molecule, weakened self-aggregation, which induced the decrease of RLS intensity of PQAS. RLS signals of PQAS and the PQAS–PPGL system were remarkably decreased after adding low concentration of NaCl solution, which indicated that the electrostatic interaction was also one of the main driving forces governing their combination. RLS signal of the PQAS–PPGL system began to decrease slightly when NaCl concentration reached 5.0×10^{-4} mol L^{-1}. Moreover, the change of RLS intensity (ΔI_{RLS}) decreased with the increasing ionic strength.

3.5. Incubation time and stability

The assay incubation time and stability of PQAS and the PQAS–PPGL system were carried out by determining RLS intensity every 2 min for 2 h immediately after mixing throughly. The results demonstrated that the reaction between PQAS and PPGL occurred rapidly at room temperature (<4 min) and the change of RLS intensity of the experimental system (ΔI_{RLS}) reached the maximum. Besides, RLS intensity remained nearly stable for at least 80 min. Accordingly, this assay is rapid with good stability and can be a useful tool in the determination of PPGL.

3.6. Tolerance of foreign substances

The selectivity and effect of the foreign substances on the determination was tested by analyzing a standard solution of PPGL ($0.02\ \mu g\ mL^{-1}$) to which increased amounts of interfering species were added. The tolerance levels of the tested foreign substances were listed in Table 1. As shown in Table 1, most of the monosaccharides, disaccharides, metal ions at high concentration hardly affected the determination. In addition, the surfactants including anion, cationic and other zwitterionic surfactants were also tolerated at high concentration, which demonstrated that there was specific binding between PQAS and PPGL. Starch was the main inter-

Table 1
Effects of the potential interfering substances on the determination of polysaccharide (0.02 μg mL^{-1}) under the optimum conditions.

Interfering substances	Concentration	Change in I_{RLS} ($n = 3$, %)
Glucose	400.0 μg mL^{-1}	−3.8
Fructose	400.0 μg mL^{-1}	−2.9
Sucrose	400.0 μg mL^{-1}	+4.3
Lactose	400.0 μg mL^{-1}	+4.6
Malic acid	50.0 μg mL^{-1}	+1.8
Starch	50.0 ng mL^{-1}	+6.8
BSA[a]	50.0 ng mL^{-1}	+4.3
HSA[b]	50.0 ng mL^{-1}	+4.1
K$^+$, Cl$^-$	500.0 μmol L^{-1}	+2.1
Ca^{2+}, Cl$^-$	50.0 μmol L^{-1}	−3.6
Cd^{2+}, Cl$^-$	10.0 μmol L^{-1}	−1.4
Zn^{2+}, Cl$^-$	10.0 μmol L^{-1}	+2.5
Co^{2+}, Cl$^-$	10.0 μmol L^{-1}	+1.8
Pb^{2+}, NO$_3^-$	25.0 μmol L^{-1}	−2.3
Hg^{2+}, SO$_4^{2-}$	25.0 μmol L^{-1}	+4.7
Mg^{2+}, SO$_4^{2-}$	10.0 μmol L^{-1}	−1.2
Mn^{2+}, SO$_4^{2-}$	10.0 μmol L^{-1}	+1.3
Al^{3+}, SO$_4^{2-}$	5.0 μmol L^{-1}	+3.3
Ni^{2+}, NO$_3^-$	10.0 μmol L^{-1}	+2.5
Cr^{3+}, NO$_3^-$	5.0 μmol L^{-1}	+3.6
SLS[c]	2.0 μg mL^{-1}	+3.8
SDBS[d]	2.0 μg mL^{-1}	+4.2
SDS[e]	2.0 μg mL^{-1}	+4.6
CTMAB[f]	5.0 μg mL^{-1}	+4.9
CTAB[g]	3.0 μg mL^{-1}	+4.0
HSB[h]	0.5 μg mL^{-1}	+2.5
BS-12[i]	1.0 μg mL^{-1}	+5.0

[a] BSA, Bovine serum albumin.
[b] HAS, Human serum albumin.
[c] SLS, Sodium lauryl sulfate.
[d] SDBS, Sodium dodecyl benzene sulfonate.
[e] SDS, Sodium dodecyl sulfate.
[f] CTMAB, Cetyltrimethylammonium bromide.
[g] CTAB, Hexadecyl trimethyl ammonium bromide.
[h] HSB, Cocamidopropyl hydroysultaine.
[i] BS-12, Lauryl betaine.

fering material because it was due to the fact that a strong RLS signal was denoted from the starch solution system. In addition, BSA and HAS can be only tolerated at very low concentration. Thus, the protein in the biochemical sample must be removed before the determination of polysaccharide by the proposed method. However, all the interferences in the analysis can be minimized by dilution with water, which offers this method with the possibility of the quantitative analysis of polysaccharide in biological samples.

3.7. Calibration curve and detection limit

Under the optimum conditions, it was found that the decrement of RLS intensity of the PQAS–PPGL system (ΔI_{RLS}) was linearly with the concentration of PPGL in the range of $0.1-30$ ng mL^{-1}. The linear regression equation was $\Delta I_{RLS} = 4.52 + 28841C$ (μg mL^{-1}) with a correlation coefficient of 0.9978 ($n = 8$). The detection limit was 0.05 ng mL^{-1}. The limit of detection (LOD) is given by $3S_0/S$, where 3 is the factor at the 99% confidence level, S_0 is the standard deviation of the blank measurements ($n = 11$), and S is the slope of the calibration curve. The comparison of this method with other RLS method is presented in Table 2. It can be pointed out that this proposed approach has the lower detection limit because the slope of the linear regression equation of this method is larger than that of other enhanced RLS methods.

3.8. Analysis of samples

To test the accuracy of this assay, recoveries of polysaccharide from artificial samples were analyzed and the results were indi-

Table 2
Comparison with other RLS methods of determination of polysaccharide.

Polysaccharide	Linear regression equation (C, μg mL^{-1})	Detection limit (ng mL^{-1})	References
RL gly[a]	$\log I = 0.42 + 0.98 \log C$		[21]
O gly[b]	$\log I = 0.19 + 1.01 \log C$		[21]
C gly[c]	$\log I = 0.38 + 0.94 \log C$		[21]
RL gly	$\log(LSI) = 1.04 + 0.531 \log C$		[22]
O gly	$\log(LSI) = 1.04 + 0.501 \log C$		[22]
C gly	$\log(LSI) = 1.03 + 0.511 \log C$		[22]
Glycogen		2	[23]
PPGL[d]	$\Delta IRLS = 4.52 + 28841C$	0.05	This work

[a] RL gly, rabbit liver glycogen.
[b] O gly, oyster glycogen.
[c] C gly, clam glycogen.
[d] PPGL, purified polysaccharide of *Gracilaria Lemaneiformis*.

cated in Table 3. The samples tested, being made up of different foreign tolerated ions including several kinds of metal ions and saccharine substances were determined by the proposed approach. Recovery values obtained were in the range 98.5–102.7%, which demonstrated the high selectivity and sensitivity of this method and indicated that the proposed method was applicable to determine PPGL in complex mixtures. Moreover, the proposed method was performed to determine purified polysaccharide extracted from *Gracilaria Lemaneiformis* with satisfactory results, which suggested that the assay of determining polysaccharide was practical (Table 4).

3.9. The mechanism

PQAS, one of the gemini surfactants, is a group of amphiphiles possessing two polar headgroups, a spacer group and two long hydrophobic hydrocarbon chains. Additionally, the two oppositely charged headgroups are covalently attached through a spacer group. Many works have shown that the spacer plays a major role in the aggregation properties of these surfactants. For PQAS, the oxygen atom of the hydrophilic spacer can form hydrogen bonds with water and reduce the unfavorable hydrocarbon–water contacts, making it easier for the spacer to be located at the micelle–water interface [31]. Furthermore, additional hydration at the level of the spacer chain should mitigate the Coulombic repulsion between the headgroups. These characteristics facilitate self-aggregation of gemini amphiphiles [31,32]. Further, PQAS can self-aggregate, possibly along with spherical aggregates called micelle, into tubules and vesicle-sized structures [27], producing the larger size particles which induces intense RLS signal with resonance Rayleigh scattering theory [33,34]. The deduction is verified by the results from scanning electron microscopy (Fig. 3).

Table 3
Determination of polysaccharide in synthetic samples.

Sample (ng mL^{-1})	Non-protein substances[a]	Found[b] (ng mL^{-1})	Recovery ($n = 6$, %)
PPGL 1.0	BSA, Ca^{2+}, Cd^{2+}, Mg^{2+}, Na$^+$, Glucose, fructose, sucrose, lactose, starch	0.985 ± 0.051	98.5
PPGL 5.0	BSA, Al^{3+}, Zn^{2+}, Hg^{2+}, Co^{2+}, Glucose, fructose, sucrose, lactose, starch	5.135 ± 0.082	102.7
PPGL 10.0	HSA, K$^+$, Ni^{2+}, Mn^{2+}, Pb^{2+}, Glucose, fructose, sucrose, lactose, starch	10.126 ± 0.105	101.3

[a] 5.0 ng mL^{-1}: BSA, HSA; 80.0 μg mL^{-1}: glucose, fructose, sucrose, and lactose; 2.0 ng mL^{-1} starch; 1.0×10^{-6} mol L^{-1} metal ions; 6.0×10^{-4} mol L^{-1} PQAS.
[b] Data shown are averages ±standard deviations from six independent experiments.

Table 4
The results of the determination of purified polysaccharide of *Gracilaria Lemaneiformis*.

Samples	Found value (ng mL^{-1})	Standard added (ng mL^{-1})	Recovery value[a] (ng mL^{-1})	Recovery ($n = 6$, %)
1	4.5	5	9.3 ± 0.08	97.9
2	6.2	5	10.9 ± 0.10	97.3
3	8.5	5	13.3 ± 0.09	98.5
4	12.3	5	17.1 ± 0.14	98.8

[a] Data shown are averages ±standard deviations from six independent experiments.

The interactions between sulfated PPGL, a hydrophilic anionic polysaccharide, and gemini amphiphiles were investigated using RLS, fluorescence and fluorescence lifetime techniques. The main initial interaction between sulfated PPGL and gemini amphiphiles had electrostatic character, and probably proceeded between the charged centers on the macromolecular chain and the charged heads of the surfactant. The dependence of RLS intensity of the PQAS–PPGL system on the pH and the ionic strength is fully compatible with this interpretation.

As evidenced from the blue shift of the maximal excitation peak when PQAS bound to sulfated PPGL (Fig. 4), it was concluded that the PPGL environment became more hydrophobic after binding to PQAS. In addition, the fluorescence lifetime assays demonstrated that the new complex between PQAS and PPGL had different fluorescence lifetime from PPGL. When sulfated PPGL was added, the self-aggregation of PQAS molecule was disaggregated, inducing the decrescent size of the RLS particles, which then induced decreased RLS intensity (Fig. 3).

4. Conclusion

PQAS denoted a very intense light scattering in aqueous solution at pH 9.0. In addition, the intense RLS signal of PQAS displayed the dominated decreased RLS phenomenon after the addition of sulfated PPGL. Based on the rare decreased RLS phenomena, the novel method for the determination of polysaccharide at nanogram levels was developed in this contribution. Compared with the reported polysaccharide assays, this proposed method had good selectivity, high sensitivity and was especially simple and convenient. The method was applied to analyze the polysaccharide in extracted samples from *Gracilaria Lemaneiformis* with satisfactory results. Moreover, this proposed method can be an automatic process for the quantitative analysis of polysaccharide only combined with other techniques such as flow injection analysis system [35–37].

Acknowledgements

References

[1] T.K. Lindhorst, Essentials of Carbohydrate Chemistry and Biochemistry, 3rd ed., Wiley-VCH, Weinheim, Germany, 2007.
[2] X.Y. Huang, Y.L. Hu, X.N. Zhao, Y. Lu, J.M. Wang, F. Zhang, J.L. Sun, Carbohyd. Polym. 73 (2008) 303–308.
[3] L.H. Koehler, Anal. Chem. 24 (1952) 1576–1579.
[4] J. Dawes, B.A. Hodson, D.S. Pepper, Thromb. Haemost. 62 (1989) 945–949.
[5] A.N. De Belder, K. Granath, Carbohydr. Res. 30 (1973) 375–378.
[6] J. Dawes, B.A. Hodson, I.R. MacGregor, D.S. Pepper, C.V. Prowse, Ann. N. Y. Acad. Sci. 556 (1989) 292–303.
[7] U. Cornelli, J. Fareed, Semin. Thromb. Hemost. 25 (1999) 57–61.
[8] Y. Lv, X.B. Yang, Y. Zhao, Y. Ruan, Y. Yang, Z.Z. Wang, Food Chem. 112 (2009) 742–746.
[9] R.F. Pasternack, C. Bustamante, P.J. Collings, A. Giannetto, E.J. Gibbs, J. Am. Chem. Soc. 115 (1993) 5393–5399.
[10] R.F. Pasternack, P.J. Collings, Science 269 (1995) 935–939.
[11] L. Zhang, C.Z. Huang, Y.F. Li, S.J. Xiao, J.P. Xie, J. Phys. Chem. B 112 (2008) 7120–7122.
[12] Y.F. Long, C.Z. Huang, Talanta 71 (2007) 1939–1943.
[13] Y.Q. Cheng, Z.P. Li, Y.Q. Su, Y.S. Fan, Talanta 71 (2007) 1757–1761.
[14] Z.G. Chen, W.F. Ding, F.L. Ren, J.B. Liu, Y.Z. Liang, Anal. Chim. Acta 550 (2005) 204–209.
[15] Y.F. Li, X.W. Shen, C.Z. Huang, Talanta 75 (2008) 1041–1045.
[16] Z.G. Chen, J.B. Liu, Y.L. Han, Talanta 71 (2007) 1246–1251.
[17] L.J. Dong, X.G. Chen, Z.D. Hu, Talanta 71 (2007) 555–560.
[18] Z.G. Chen, T.Y. Zhang, F.L. Ren, W.F. Ding, Microchim. Acta 153 (2006) 65–71.
[19] Z.G. Chen, G.L. Liu, M.Z. Chen, B.J. Xu, Y.R. Peng, M.H. Chen, M.Y. Wu, Talanta 77 (2009) 1365–1369.
[20] Z.L. Jiang, S.M. Wang, A.H. Liang, F.X. Zhong, Talanta 77 (2009) 1191–1196.
[21] Z.G. Chen, Y.R. Peng, J.H. Chen, L. Zhu, J. Pharmaceut. Biomed. 48 (2008) 946–950.
[22] S.Z. Zhang, F.L. Zhao, K.A. Li, S.Y. Tong, Anal. Chim. Acta 431 (2001) 133–139.
[23] S.Z. Zhang, F.L. Zhao, K.A. Li, S.Y. Tong, Talanta 54 (2001) 333–342.
[24] M.H. Xiang, X. Xu, D.X. Li, F. Liu, N. Li, K.A. Li, Talanta 76 (2008) 1207–1211.
[25] F.M. Menger, C.A. Littau, J. Am. Chem. Soc. 113 (1991) 1451–1452.
[26] C.G. Ricci, M.I. Cabrera, J.A. Luna, R.J. Grau, Synlett 11 (2002) 1811–1814.
[27] A.V. Peresypkin, F.M. Menger, Org. Lett. 1 (1999) 1347–1350.
[28] D.S. Yin, W.Y. Yang, Z.Q. Ge, Y.J. Yuan, Carbohydr. Res. 340 (2005) 1201–1206.
[29] M. Zhang, S.W. Cui, P.C.K. Cheung, Q. Wang, Trends Food Sci. Tech. 18 (2007) 4–19.
[30] Y.W. Wang, N.B. Li, H.Q. Luo, Luminescence 23 (2008) 126–131.
[31] X.Y. Wang, J.B. Wang, Y.L. Wang, H.K. Yan, Langmuir 20 (2004) 53–56.
[32] F.M. Menger, J.S. Keiper, Angew. Chem. Int. Ed. 39 (2000) 1906–1920.
[33] Q.G. Liao, Y.F. Li, C.Z. Huang, Talanta 71 (2007) 567–572.
[34] W. Lu, B.S.F. Band, Y. Yu, Q.G. Li, J.C. Shang, C. Wang, Y. Fang, R. Tian, L.P. Zhou, L.L. Sun, Y. Tang, S.H. Jing, W. Huang, J.P. Zhang, Microchim. Acta 158 (2007) 29–58.
[35] Y. Li, L.J. Dong, Y.H. Zhang, Z.D. Hu, X.G. Chen, Talanta 71 (2007) 109–114.
[36] L. Qi, Z.Q. Han, Y. Chen, J. Chromatogr. A 1110 (2006) 235–239.
[37] E. Vidal, M.E. Palomeque, A.G. Lista, B.S. Fernández Band, Anal. Bioanal. Chem. 376 (2003) 38–41.

Novel prediction of interactive mode between antibiotics and their DNA/protein targets based on the antibiotic structure parameters

Jing Chen, Xiaoquan Lu *

College of Chemistry & Chemical Engineering, Northwest Normal University, Lanzhou, 730070, China

ARTICLE INFO

ABSTRACT

This paper focuses on investigating the structure parameters of antibiotics which have decisive influence on the interactive mode between antibiotics and DNAs. The analytical results of Best Prediction Set Support Vector Machine Method (BPSSVM) show that the number of N atoms, the number of double bonds, the number of lone-pair electrons, the molar refractivity and the molecular radius are the main structure parameters which functionally decide their reactive modes. It is clear that the BPSSVM is potent in predicting the interactive modes between antibiotics and DNAs.

1. Introduction

Many research results about the interaction mechanisms between antitumor drugs and DNAs have been reported [1–4]. DNA carries the heritage information and instructs biological synthesis of proteins and enzymes through processing the replication and transcription of genetic information in the life process. Developing novel reagents which can recognize sites and probe the structure and function of nucleic acid is a potent approach for recognizing and determining duplex DNAs. Antibiotics exert their primary biological functions by interfering with the normal cellular functions of bacteria and fungi so as to prevent further infection in the host. The intercalation and groove binding are their principal reactive modes. Those regular functions include cell wall biosynthesis, membrane function, DNA replication, DNA transcription, and RNA translation or protein synthesis and activity.

To understand how molecules bind to DNA is helpful in the area of drug design and genetic diseases therapy [5]. The ultraviolet–visible spectroscopy [6,7], the fluorescence spectroscopy [8,9] and the atomic force microscopy (AFM) [10] have been applied to identify their reactions. A great progress has been made to research the interactions between DNAs and drug moleculars [11,12]. Piezoelectric quartz crystal impedance (PQCI) analysis is a very powerful method to study the kinetic interactive process of antitumor drugs and DNAs [13]. The π–π stacking interactions stabilize integrates of DNA and the intercalating drugs which insert between two adjacent base pairs in a DNA helix with their flat heteroaromatic ring systems. Multiaromatic ring drugs form minor groove bonds with a characteristic curved shape that is isohelical with the target groove, such as pyrrole, furan, or benzene that is connected by the bond possessing torsional freedom [14]. Some noncovalent interactions such as van der Waals interactions, hydrophobic forces and hydrogen bonds stabilize DNA–drug complexes. Obviously, the structure information of drug moleculars is crucial for investigating their interactive modes with DNAs.

The analytical methods of Chemometrics and Bioinformatics have exhibited strong abilities in extracting both chemical and biological information [15–17]. It has been reported that SVM is one of the most successful classification algorithms in the data mining area and provides good performance for anomaly network intrusion detection [18–20]. Viewing the input data as two sets of vectors in an N-dimensional space, an SVM will construct two parallel hyperplanes, each of which would "push up against" one data set so as to maximize the "margin" between the two sets. In this way, the empirical classification error can be minimized [18–20].

In this paper, the Best Prediction Set Support Vector Machine Method (BPSSVM) method based on SVM focuses on determining the interactive modes between various drugs and DNAs. Thirty antibiotics are investigated to either construct or train the determining model. Docking simulation is also applied to understand it.

2. Methods

2.1. The Best Prediction Set Support Vector Machine Method (BPSSVM)

SVM maps the input vectors $\mathbf{x} \in \mathbf{R}^d$ into a high dimensional feature space $\Phi(\mathbf{x}) \in \mathbf{H}$ and constructs an Optimal Separating Hyper-

* Corresponding author. Tel.: +86 931 7971276; fax: +86 931 7971276.
E-mail address: luxq@nwnu.edu.cn (X. Lu).

Table 1
Twenty-four structure parameters of antibiotics.

Twenty-four parameters of molecular structure		
Number of N atom	Length of O–O bond	Electronic energy
Double bond	Sum of rings (the atom C >5)	Principal Moment of Inertia-X
Lone-pair electrons	Balaban index	Principal Moment of Inertia-Y
Molar refractivity	Wiener index	Principal Moment of Inertia-Z
Radius	Molecular Topological Index	Partition coefficient (octanol/water)
Length of N–N bond	Connolly solvent-excluded volume	HOMOEnergy
Number of O atom	Connolly accessible area	LUMOEnergy
Length of N–O bond	Connolly molecular area	Sum of atom

plane (OSH), which maximizes the margin, the distance between the hyperplane and the nearest data points of each class in the space H. The kernel function $K(\mathbf{x}_i, \mathbf{x}_j)$ defines an inner product in the space H and performs the mapping Φ. Furthermore, different mappings construct different SVMs. SVM implements the following decision function:

$$f(x) = \text{sgn}\left(\sum_{i=1}^{N} y_i \alpha_i k(x, x_i) + b\right) \tag{1}$$

where the coefficients α_i are obtained by solving the following convex Quadratic Programming (QP) problem:

$$\sum_{i=1}^{N} \alpha_i - \frac{1}{2}\sum_{i=1}^{N}\sum_{i=1}^{N} \alpha_i \alpha_j \cdot y_i y_j \cdot K(x_i, x_j), \quad 0 \leq \alpha_i \leq C$$

$$\sum_{i=1}^{N} \alpha_i y_i = 0, \quad i = 1, 2, \ldots, N. \tag{2}$$

Here, $C > 0$ is the penalty parameter of the error term, which controls the trade off between margin and misclassification error. $\mathbf{x}_j \ (\alpha_i > 0)$ are *Support Vectors*. The *Radial Basic Function* (RBF) kernel nonlinearly maps samples into a higher dimensional space, so it, unlike the linear kernel, can handle the case when the relation between class labels and attributes is nonlinear. It can be written as:

$$K(x_i, x_j) = \exp(-\gamma ||x_i - x_j||^2) \tag{3}$$

The kernel function and the penalty parameter C are simultaneously selected to specify one SVM for a given dataset. SVM can globally optimize the solution of the QP problem, handle large feature spaces, effectively avoid overfitting by controlling the margin and automatically identify a small subset made up of informative points, etc.

The reactive mode prediction of antibiotic and DNA is a multi-class classification problem. A simple strategy to handle the multi-class classification is to reduce the multi-classification to a series of binary classifications. For a k-class classification, k SVMs are constructed. The ith SVM will be trained with all of the samples in the ith class with positive labels and all other samples with negative labels. Unknown sample is classified into the class that corresponds to the pre-trained SVM with the highest output value. The software used to implement SVM is LibSVM [21] which can be freely downloaded from http://www.csie.ntu.edu.tw/~cjlin/libsvm for academic use. Therefore, the BPSSVM can be obtained by the following program:

```
Random one parameter from one to the parameter number
+ one parameter from one to the parameter number-1
SVM training
+ one parameter from one to the parameter number-2
SVM training
. . .
Next, until the error is the lowest.
```

2.2. Docking simulations

DOCK6.0 program using the crystal structures to generate atomic grids. All ligand and water molecules are removed. Chimera Tools package (http://www.cgl.ucsf.edu/mailman/confirm/chimera-users/ea0691d4f6e694173207320e56f5779d8edbf5e1) are used to prepare the ligand for docking performance, to assign the hydrogen atoms addition and Gasteiger charges [22] to the ligand and to produce final docked conformations within a fixed protein structure. AMBER score implements MM GB/SA simulations with traditional all-atom AMBER force field [23] (http://amber.scripps.edu) for protein atoms, and general AMBER force field [24] for ligand molecules. The interaction between the ligand and the protein is represented by electrostatic and van der Waals energy terms, and the solvation energy is calculated using Generalized Born (GB) solvation model. The surface area term is derived using a fast LCPO algorithm [25]. The AMBER score is calculated as:

$$E(\text{Complex}) - [E(\text{Receptor}) + E(\text{Ligand})] \tag{4}$$

where $E(\text{Complex})$, $E(\text{Receptor})$ and $E(\text{Ligand})$ represent the energy of the complex, receptor and ligand, respectively. During AMBER score calculation, the input coordinates and parameters of the complex, ligand and receptor are read into the system. After reading the input coordinates, minimization using conjugate gradient method is performed to remove the bad contacts. This is followed by MD simulation (Langevin dynamics at constant temperature), and a short minimization to get the final energy of the system. The particular arrangement of the ligand and the protein can be defined by a set of values in dock_in file describing the translation, orientation, and conformation of the ligand with respect to the protein having a fixed conformation. Each set of ligand value corresponded to a gene, whereas the atomic coordinates correspond to a phenotype. The docking fitness is based on the total interaction energy of the ligand with protein. This paper proposes Dock6.0 (https://dock.compbio.ucsf.edu/retrieve_dock_distribution.html) to investigate the reactive model of antibiotics and its protein targets and their reaction mechanisms.

3. Results and discussion

3.1. BPSSVM prediction

The reactive modes of thirty antibiotics and DNAs, which include minor groove [14,26–29], intercalation [30,31,4,32–35] and electrostatic [4,36], have been reported and collected here for investigating their structure parameters which have important functions to decide their reactive modes. The twenty-four collected parameters which can obviously reflect their structure characteristics (such as, the double bond can reflect molecular electron cloud density) are listed in Table 1. Among them, the octanol (o)/water (w) partition coefficient (p) which is useful for example in estimating distribution of drugs within the body is defined as the ratio of a chemical's con-

Table 2
The BPSSVM predicting results and docking results between antibiotics and DNAs/protein targets (I: intercalation. M: minor groove. E: electrostatic).

	N atoms	Double bonds	Lone-pair electrons	Molar refractivity	Radius	Interactive mode		PDB ID	Energy score (kJ/mol)	H-bond length (Å)
						Reported	Predicted			
Netropsin [16]	10	7	5	11.7535	10	M				
Hoechst33258 [14]	6	11	4	12.0034	9	M		1PPK	−43.7944	Gln238 N–/O: 3.031; Gly35 O/N–: 3.102
AMAC [20]	1	7	1	−99.9	4	I				
DB244 [17]	4	10	3	14.4971	10	M	M/I$_{LVQ}$	1RTD	−45.5669	Lys66 O/N–: 3.462; Gln151 O/N–: 3.149
WP776 [21]	1	12	15	16.1471	9	I				
DADM [22]	1	9	17	13.789	7	I		1RTD	−36.9471	Glu53 O/O–: 2.748; Lys49 O/O–: 3.081
NOM [22]	1	7	27	19.6832	10	I/E		1NNC	−35.6926	Asp412 O/N–: 2.969; Arg419 N–/O: 3.090
CGP40215A [18]	9	11	5	10.9743	8	M	M/I$_{LVQ}$			
DB293 [14]	6	11	4	11.1203	8	M				
MHE [23]	2	8	3	8.5155	5	I				
DNR [21]	1	9	15	13.1721	7	I	I/I$_{LVQ}$	1ENT	−43.4540	Tyr222 O–/O: 2.967; Asp30 O/O–: 3.306
DB351 [14]	4	10	2	10.8091	7	M		1RTD	−20.3336	Trp71 O/N– 3.254
NMHE [23]	2	8	2	8.3449	5	I				
WP756 [21]	2	12	15	16.7586	10	I	I/I$_{LVQ}$			
APTQ [23]	4	8	3	7.2971	5	I		1RTD	−20.3336	Trp71 O/N–: 3.254
DB75 [19]	4	10	3	10.2139	7	M				
ADM [22]	1	9	17	13.3252	7	I				
DB818 [19]	6	11	3	11.7155	8	M	M/I$_{LVQ}$			
2,7-DAM [27]	4	5	3	7.4356	5	I/E				
Berenil [14]	7	9	4	8.8709	7	M/I		1JQE	−36.9243	Glu86 O/N–: 2.862; Cys217 O/N–: 2.997
Ethidum bromide [24]	3	10	0	−99.9	5	I				
MDPTQ [23]	5	8	4	11.3762	8	I				
DB226 [17]	4	10	3	14.8519	10	M		1STC	−56.8237	Glu127 O/N–s: 3.400
Proflavine [27]	3	7	0	7.0187	4	I	I/I$_{LVQ}$	1CI7	−25.9567	Glu65 O/N–: 3.436
DAM [22]	1	9	15	13.1721	7	I	I/I$_{LVQ}$	1EED	−47.4440	Asp32 O/N: 2.923; Tyr222 O/O–: 3.238
Mitoxantrone [25]	4	8	10	11.819	9	I		1APT	−51.5010	Asp213 O/O–: 2.649; Asp115 O/N–: 2.793
Distamycin [16]	9	10	2	12.9925	11	M		1PPK	−45.3953	Asp33 O/N–: 2.842; Asp213 O/N–: 2.884
Propidium [27]	4	10	0	−99.9	5	I	I/I$_{LVQ}$			
MMQ1 [26]	4	11	4	13.4662	10	I				
WP758 [21]	2	12	15	16.5158	10	I		1APT	−48.2776	Glu15 O/O–: 2.602; Thr217 N–/O: 3.486

centration in the octanol phase to its concentration in the aqueous phase of a two-phase o/w system (C_o/C_w). Hydrophobic drugs with high p-values are preferentially distributed to hydrophobic compartments such as lipid bilayers of cells while hydrophilic drugs with low p-values preferentially are found in hydrophilic compartments such as blood serum [37]. Balaban index ($N\sum_{ij}\sqrt{R_iR_j}$, N is the number of tree graph border, R_i and R_j are the sum of the row i and j in distance matrix of the tree graph.) measures the ramification and tends to increase with molecular ramification. Wiener index (($1/2)\sum_i\sum_j N_{ij}$, N_{ij} is the number of bond between two atoms) is a topological index of a molecule, defined as the sum of the numbers of edges in the shortest paths in a chemical graph between all pairs of non-hydrogen atoms in a molecule. Molecular area, accessible area and solvent-excluded volume which are calculated by Chem3D follow the Connolly routine [38].

The reactive modes between these compounds and DNAs which are predicted by the BPSSVM method are listed in Table 2. The structure parameters of twenty-two antibiotics are selected at random to construct the training model and the structure parameters of eight remained antibiotics are applied to train this model. The input parameters form 22×24 matrix. To enhance the accuracy of predicted model, the regularization parameter selects a bigger value 1 and the loss function selects a lower value 0.07. All of their predicted reactive modes are identical with the experimental results. The results shown in Table 2 are clear that the number of N atoms, the number of double bonds, the number of lone-pair electrons, the molar refractivity and the molecular radius are the main structure

parameters which functionally decide their reactive modes. From experimental results, the increase of N atom number forces the interaction between antibiotics and DNAs to minor groove (Table 2). Lone-pair bonding pair repulsion is greater than lone-pair bonding pair repulsion, and lone-pair bonding pair repulsion is greater than bonding pair–bonding pair repulsion. This repulsion directly affects the interaction between antibiotics and DNAs. From Table 2, higher lone-pair electron number force their interaction to intercalation. The molar refractivity is a measure of the total polarizability of a mole of a substance and is dependent on the temperature, the index of refraction and the pressure. The temperature is a vital factor which can affect the molecular motions when antibiotics react with DNAs. The molecular radius directly decides whether it can enter into the DNA groove or not. Their reactive modes are intercalations when these parameter values are lower. The increase of these parameters forces their reactive modes to tend to the minor groove.

3.2. Artificial neural network (ANN) prediction

The artificial neural network solves very complex problems with the help of interconnected computing elements [39]. LVQ [40] is probably one of the most widely used neural network learning algorithms for pattern recognition problems. A LVQ network has a first competitive layer and a second linear layer. The competitive layer learns to classify input vectors in much the same way as the competitive layers of self-organizing [39] and the linear layer transforms the competitive layer's classes into target classifications.
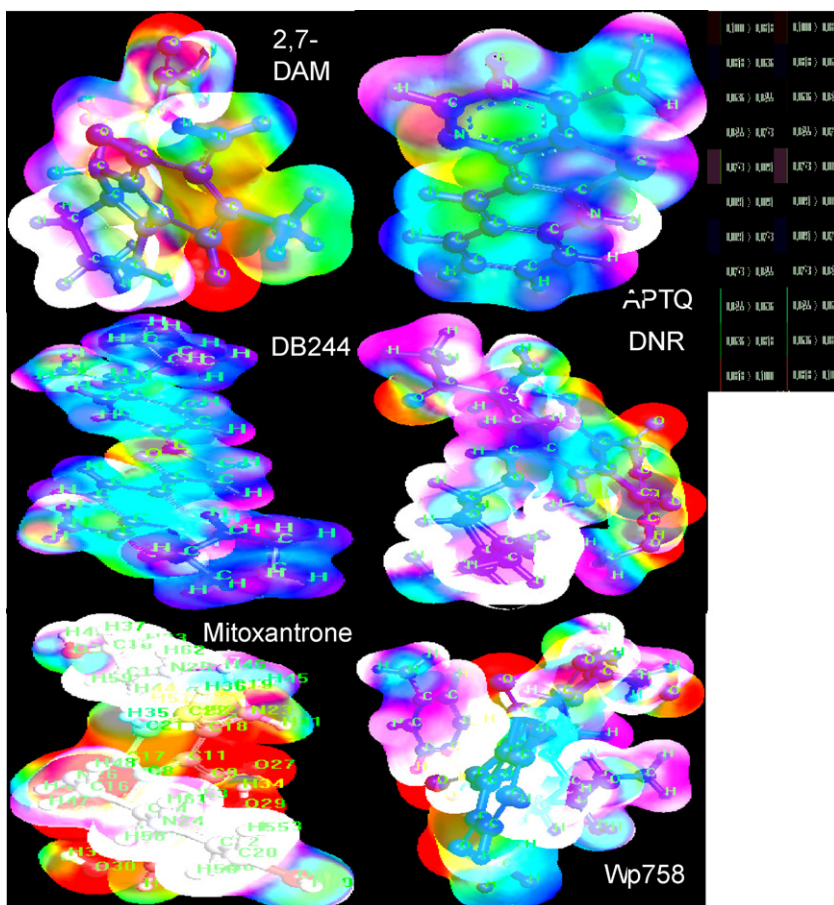
Fig. 1. The ESP-mapped density surfaces of six randomly selected antibiotics from original thirty antibiotics.

Here, the structure parameters of antibiotics are applied to construct the training model of LVQ. The predicted results are listed in Table 2. From the results, it is clear that the predicting ability of LVQ is lower than BPSSVM. Its several predicted reactive modes do not accord with the reports.

3.3. Electrostatic potential (ESP) analysis

The electrostatic potential (ESP) depicts the potential energy felt by a positive "test" charge at a particular point in space. Negative ESP region is stable for the positive test charge and positive ESP region is instable for it. Thus, an ESP-mapped density surface (Arguslab4.0.1. Mark A. Thompson Planaria Software LLC, Seattle, WA. http://www.arguslab.com) shows regions of a molecule that might be more favorable to nucleophilic or electrophilic attack, making these types of surfaces useful for qualitative interpretations of chemical reactivity. The ESP-mapped density surfaces can also be thought that they show where the frontier electron density for the molecule is greatest (or least) relative to the nuclei. Fig. 1 shows the ESP-mapped density surfaces of six randomly selected antibiotics in all of the thirty moleculars. It is easy to find out their nucleophilic or electrophilic attacking regions according to the different figure colors. Their main electron-donating groups are nitrogen and oxygen which can be more active than others while reacting with other active species.

3.4. Docking analysis

To further investigate the reactions between the electron-donating groups of these antibiotics and vital species, random fourteen antibiotics are submitted to Target Fishing Dock [41] following their calculating rules to extract their protein targets. Dock shows an unexpectedly better screening performance in the enrichment rates while each docking program has some merits over the other docking programs in some aspects [42]. Here, the more refined docking energy scores of them are obtained by the Dock6.0 program and the detailed H-bonds between them are listed in Table 2. It is clear that the strongest H-bonds are formed between N–N, N–O and O–O. These proteins listed in Table 2 have the best energy scores. However, not all of the target proteins of these antibiotics obtain these good energy scores, some of which are inferior. Many of these antibiotics obtain good energy scores with 1EED and 1RTD proteins. Their detailed H-bonds are listed in Table 3 and 1EED obtain relatively stronger energy scores than 1RTD. The crystal structures of endothiapepsin (PDB ID: 1EED) [43], a fungal aspartic proteinase (EC 3.4.23.6), cocrystallized with two oligopeptide renin inhibitors, PD125967 and PD125754, have been determined at 2.0-A resolution and refined to R-factors of 0.143 and 0.153, respectively. According to its report, the structures reveal that the S3 pocket accommodates one naphthyl ring with conformational changes of the Asp 77 and Asp 114 side chains, the other naphthyl group residing in the S4 region. The P3–P2 hydroxyethylene analogue of PD125754 [43] forms a hydrogen bond with the NH of Thr 219, thereby making the same interaction with the enzyme as the equivalent peptide groups of all inhibitors studied so far. Many of thirty antibiotics form strong H-bonds with one oxygen atom of Asp 77, Asp 114 (Fig. 2, red structure) and Thr 219 (Fig. 2, orange structure) side chains (Table 3). Fig. 2 depicts the detailed interactive modes between these antibiotics and 1EED. A few of them can be its good inhibitors.

Table 3
The detailed docking results between 1EED, 1RTD and their antibiotics targets.

PDB ID	Antibiotics	Energy score	H-bond length (Å)
1EED (Endothiapepsin)	DAM	−53.62	Gly217 O/O−: 3.123; Tyr222 O−/O: 2.830
	DNR	−42.84	
	DADM	−54.04	Asp12 O/N−: 2.926; Thr219 O/O−: 2.962
	Distamycin	−63.3	Gly217 O/N−: 3.069; Asp215 O/N−: 3.149; Thr218 O/N−: 3.293
	Hoechst33258	−46.52	
	WP758	−46.57	
	Mitoxantrone	−58.79	Tyr222 O−/O: 2.978; Thr219 O/N−: 3.092; Asp114 O/O−: 3.535
	DB226	−38.24	Asp77 O/N−: 3.143
1RTD (DNA polymerase/reverse transcriptase; HIV-1 reverse transcriptase)	DAM	−45.15	Lys65 N−/O: 2.848
	DNR	−42.05	
	DB244	−42.97	
	Proflavine	−33.3	
	DADM	−54.45	Ala114 N−/O: 2.953; Lys219 N−/O: 3.111
	WP758	−43.13	Lys219 N−/O: 3.264; Ala114 N−/O: 3.277 Lys65 N−/O: 3.408
	APTQ	−39.29	
	DB226	−42.03	
	DB351	−45.64	
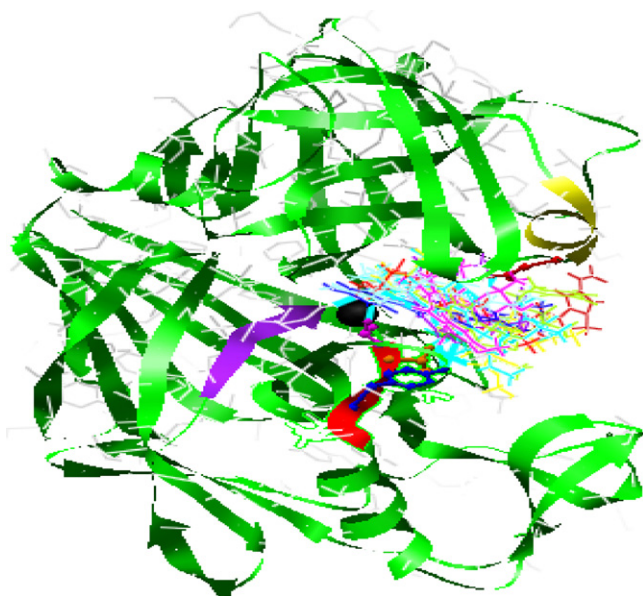
Fig. 2. The docking results between 1EED protein and its antibiotic targets.

4. Conclusions

In this paper, the structure parameters of antibiotics which have a decisive influence on the interactive modes between antibiotics and DNAs are investigated by the BPSSVM method. The analytical results show that the number of N atoms, the number of double bonds, the number of lone-pair electrons, the molar refractivity and the molecular radius are the main structure parameters which functionally decide their reactive modes. The ESP-mapped density surfaces of antibiotics and their docking results with their protein target obtain the further evidence. It is clear that the BPSSVM is potent in predicting the interactive modes between them.

Acknowledgements

References

[1] A. Erdem, M. Ozsoz, Turk. J. Chem. 25 (2001) 469.
[2] H.B. Su, P. Wiliams, M. Thompson, Anal. Chem. 67 (1995) 1010.
[3] X. Chu, G.L. Shen, J.H. Jiang, T.F. Kang, B. Xiong, R.Q. Yu, Anal. Chim. Acta 373 (1998) 29.
[4] M.S. Ibrahim, Anal. Chim. Acta 443 (2001) 63.
[5] Z.Q. Frank Qiu, M. Lu, Appl. Soft. Comput. 3 (2003) 177.
[6] D.P. Arya, R.L. Coffee Jr., B. Willis, A.I. Abramovitch, J. Am. Chem. Soc. 123 (2001) 5385.
[7] D.P. Arya, R.L. Coffee Jr., I. Charles, J. Am. Chem. Soc. 123 (2001) 11093.
[8] E. Feinstein, E. Canaani, L.M. Weiner, Biochemistry 32 (1993) 13156.
[9] L.M. Guo, W.J. Dong, X.F. Tong, C. Dong, S.M. Shuang, Talanta 70 (2006) 630.
[10] T. Banerjee, R. Mukhopadhyay, Biochem. Biophys. Res. Commun. 374 (2008) 264.
[11] D.S. Pilch, M.T. Martin, C.H. Nguyen, J.S. Sun, E. Bisagni, J. Am. Chem. Soc. 115 (1993) 9942.
[12] L.L. Shen, L.A. Mitscher, P.N. Sharma, T.J. O'Donnell, D.W.T. Chu, C.S. Cooper, T. Rosen, A.G. Pernet, Biochemistry 28 (1989) 3886.
[13] L. Tian, W.Z. Wei, Y. Mao, Clin. Biochem. 37 (2004) 120.
[14] K.X. Wan, T. Shibue, M.L. Gross, J. Am. Chem. Soc. 122 (2000) 300.
[15] Y.N. Ni, D.Q. Lin, S. Kokot, Talanta 65 (2005) 1295.
[16] X.Q. Lu, J. Chen, R. Wang, L. Wang, H.D. Liu, J. Chem. 19 (2006) 648.
[17] A. Sadana, Biosens. Bioelectron. 18 (2003) 985.
[18] H. Lee, J. Song, D. Park, Proceedings of the RSFDGrC, LNAI, 3642, 2005, p. 511.
[19] J. Zheng, M. Hu, Proceedings of the WAIM, LNCS, 3739, 2005, p. 333.
[20] T. Ambwani, Proceedings of the International Joint Conference on Neural Networks, 3, 2003, p. 2300.
[21] C.C. Chang, C.J. Lin, LIBSVM: a library for support vector machines. 2001. Software available at http://www.csie.ntu.edu.tw/~cjlin/libsvm.
[22] J. Gasteiger, M. Marsili, Tetrahedron 36 (1980) 3219.
[23] J. Wang, W. Wang, P.A. Kollman, D.A. Case, J. Mol. Graph. Model. 25 (2006) 247.
[24] J. Wang, R.M. Wolf, J.W. Caldwell, P.A. Kollman, D.A. Case, J. Comput. Chem. 25 (2004) 1157.
[25] J. Weiser, P.S. Shenkin, W.C. Still, J. Comput. Chem. 20 (1999) 217.
[26] I. Haq, Arch. Biochem. Biophys. 403 (2002) 1.
[27] S. Mazur, F.A. Tanious, D.Y. Ding, A.K.D.W. Boykin, L.J. Simpson, S. Neidle, W.D. Wilson, J. Mol. Biol. 300 (2000) 321.
[28] B. Nguyen, M.P.H. Lee, D. Hamelberg, A. Joubert, C. Bailly, R. Brun, S. Neidle, W.D. Wilson, J. Am. Chem. Soc. 124 (2002) 13680.
[29] S. Mallena, M.P.H. Lee, C. Bailly, S. Neidle, A. Kumar, D.W. Boykin, W.D. Wilson, J. Am. Chem. Soc. 126 (2004) 13659.
[30] C.V. Kumar, E.H. Asuncion, J. Am. Chem. Soc. 115 (1993) 8547.
[31] H.T.-B. Haj, M. Salerno, W. Priebe, H. Kozlowski, A. Garnier-Suillerot, Chem. Biol. Interact. 145 (2003) 349.
[32] M. Gopal, S. Shenoy, L.S. Doddamani, J. Photochem. Photobiol. B 72 (2003) 69.
[33] X.G. Qu, J.B. Chaires, J. Am. Chem. Soc. 123 (2001) 1.
[34] S.F. Wang, T.Z. Peng, C.F. Yang, J. Biochem. Biophys. Methods 55 (2003) 191.
[35] M.-P. Teulade-Fichou, C. Carrasco, L. Guittat, C. Bailly, P. Alberti, J.-L. Mergny, A. David, J.-M. Lehn, W.D. Wilson, J. Am. Chem. Soc. 125 (2003) 4732.
[36] G.S. Kumar, Q.Y. He, D. Behr-Ventrua, M. Tomasz, Biochemistry 34 (1995) 2662.
[37] A. Leo, C. Hansch, D. Elkins, Chem. Rev. 71 (1971) 525.
[38] M.L. Connolly, J. Appl. Crystallogr. 16 (1983) 548.
[39] P.B. de Harrington, Anal. Chem. 66 (1993) 2167.
[40] T. Kohonen, Proceedings of the IEEE (Special Issue on Neural Networks), 78, 1990, p. 1464.
[41] H.L. Li, Zh.T. Gao, L. Kang, H.L. Zhang, K. Yang, K.Q. Yu, X.M. Luo, W.L. Zhu, K.X. Chen, J.H. Shen, X.Ch. Wang, H.L. Jiang, Nucleic Acids Res. 34 (2006) 219.
[42] K. Onodera, K. Satou, H. Hirota, J. Chem. Inf. Model. 47 (2007) 1609.
[43] J. Cooper, W. Quail, C. Frazao, S.I. Foundling, T.L. Blundell, C. Humblet, E.A. Lunney, W.T. Lowther, B.M. Dunn, Biochemistry 31 (1992) 8142.

Determination of thiosulfate in human urine by high performance liquid chromatography

Grażyna Chwatko, Edward Bald *

Department of Environmental Chemistry University of Lodz, 163 Pomorska Street, 90-236 Lodz, Poland

ABSTRACT

Thiosulfate is a sulfate analogue with a thiosulfur substituent and is found in human samples. Its concentration in urine is increased in some diseases and after exposure to hydrogen sulfide gas. We have developed a sensitive, simple and cheap method for thiosulfate determination in urine. The method is based on precolumn derivatization with 2-chloro-1-methylquinolinium tetrafluoroborate followed by reversed-phase liquid chromatography separation and ultraviolet detection of 1-methyl-2-thioquinolone at 375 nm. The calibration curve for thiosulfate was linear in the tested range 0.5–50 μmol L^{-1} with correlation coefficient better than 0.999. The analytical recovery and relative standard deviation values for precision within the calibration range were from 90.1% to 104.2% and from 2.39% to 5.59%, respectively. The lower limit of detection and quantitation were 0.3 and 0.5 μmol L^{-1}, respectively. The mean (range) concentration of thiosulfate normalized against creatinine for apparently healthy seven women and six men was 2.21 (1.45–2.77) and 2.51 (1.36–4.89) mmol mol^{-1} creatinine, respectively. We monitored thiosulfate in urine samples from one volunteer for 24 h. The urinary excretion of thiosulfate was 21.4 μmol per 24 h. This method can be used for routine clinical monitoring thiosulfate in urine. Cysteine and cysteinylglycine can be measured concurrently, if needed.

© 2009 Elsevier B.V. All rights reserved.

1. Introduction

Thiosulfate, sulfate analogue with a thiosulfur substituent, is a naturally occurring product of sulfur metabolism, and is found in human samples. Thiosulfate is a biological indicator, especially in urine, of exposure to hydrogen sulfide gas, because its concentration increases in consequence of exposure to H$_2$S [1,2]. Moreover thiosulfate concentrations in urine increase in sulfite oxidase deficiency [3], Down's syndrome [4] and in allergic patients after consuming food containing sulfites [5]. Sodium thiosulfate has been approved for use for many years for treating cyanide poisoning as a chelator of cations, dermatologic topical treatment of acne and versicolor, and recently as chemoprotectant against the auditory neuronal toxicity and loss of hearing associated with carboplatin and cisplatin chemotherapy for head and neck cancer therapy and proposed for treatment of calciphylaxic-calcific uremic arteriopathy [6].

For many years, urinary determination of thiosulfate has been based on cyanolysis of thiosulfate and colorimetric determination of ferric thiocyanate complex [7,8]. Only few chromatographic methods for the assay of thiosulfate in human urine have been described in the literature. Techniques used were gas chromatography–mass spectrometry (GC–MS) [1,9], gas chromatography–electron capture detector (GC–ECD) [2], suppressed ion chromatography with conductimetric detection [10], ion-exclusion chromatography with electrochemical detection [11] or reverse-phase ion-pair liquid chromatography with fluorescence detection [12]. Some methods were described in review [13]. In this paper, the application of standard liquid chromatography equipment with ultraviolet detector for determination of thiosulfate in urine with sensitivity 0.3 μmol L^{-1} is described. The method requires neither extraction, nor preconcentration and uses simple sample preparation in the form of a single derivatization with 2-chloro-1-methylquinolinium tetrafluoroborate.

2. Experimental

2.1. Chemicals and reagents

2-Chloro-1-methylquinolinium tetrafluoroborate (CMQT) – a derivatization reagent – was synthesized in our laboratory as described earlier [14]. Perchloric acid (PCA), hydrochloric acid (HCl), sodium hydrogen phosphate heptahydrate (Na$_2$HPO$_4$·7H$_2$O) and sodium dihydrogen phosphate dihydrate (NaH$_2$PO$_4$·2H$_2$O) were from J.T. Baker (Deventer, Netherlands). Trichloroacetic acid (TCA) and lithium hydroxide monohydrate (LiOH·H$_2$O) were from Merck (Darmstadt, Germany). L-Cysteine (CSH) was from Reanal

(Budapest, Hungary), HPLC-grade acetonitrile was from Labscan (Dublin, Ireland). Cysteinylglycine (CGSH), cysteamine (IS – internal standard) and creatinine (Crn) were from Sigma (St. Louis, USA). 2-Mercaptopropionic acid (2MPA) and 3-mercaptopropionic acid (3MPA) were purchased from Fluka (Buchs, Switzerandland). Sodium thiosulfate and sodium thiocyanate were received from POCH (Gliwice, Poland). Sodium hydrosulfide was from Aldrich (Steinheim, Germany). Stock standard solutions were prepared by dissolving an appropriate amount of thiosulfate, thiocyanate (final concentration $0.1\,mol\,L^{-1}$) in water, sulfide (final concentration $0.1\,mol\,L^{-1}$) in $0.1\,mol\,L^{-1}$ NaOH and thiols (final concentration $0.01\,mol\,L^{-1}$) in $0.01\,mol\,L^{-1}$ HCl. The working solutions were prepared by dilution with water as needed. For derivatization a $0.1\,mol\,L^{-1}$ water solution of CMQT was used. To prepare phosphate buffer ($0.1\,mol\,L^{-1}$) appropriate quantities of sodium hydrogen phosphate heptahydrate and sodium dihydrogen phosphate dihydrate solutions were mixed. TCA buffer was prepared using $0.05\,mol\,L^{-1}$ trichloroacetic acid and adjusted to the desired pH (2.5) with lithium hydroxide ($0.05\,mol\,L^{-1}$). The pH of the buffers was adjusted by potentiometric titrations. The titration system was calibrated with standard pH solutions. All reagents were tested and found to be stable for unattended analysis.

2.2. Instrumentation

HPLC analyses were performed with a Hewlett-Packard (Waldbronn, Germany) HP 1100 Series system equipped with quaternary pump, an autosampler, thermostated column compartment, vacuum degasser and diode-array detector and controlled by HP ChemStation software. The separations were accomplished with a GraceSmart RP18 (5 μm, 150 mm × 4.6 mm) analytical column (GRACE, Lokeren, Belgium). Water was purified using a Millipore Milli-QRG system (Vien, Austria). For pH measurement, an HI 221 (Hanna Instruments, Woonsocket, RI, USA) pH meter was used.

2.3. Sample collection and pretreatment

Urine was collected from apparently healthy, ethnically homogenous, volunteers. Urine samples were processed as soon as possible, but not later than 4 h after collection.

For the measurement of thiosulfate to 500 μL of urine were added 250 μL of pH 2 or 7.4 ($0.1\,mol\,L^{-1}$) phosphate buffer, 10 μL of IS – internal standard solution ($0.25\,mmol\,L^{-1}$ of cysteamine) and 10 μL of $0.1\,mol\,L^{-1}$ CMQT. The mixture was vortex-mixed, put aside for 5 min and acidified with 50 μL of $3\,mol\,L^{-1}$ PCA followed by centrifugation (5 min, 12,000 g). A 20 μL aliquot of solution was transferred into the HPLC system.

For analysis of creatinine, 20 μL of urine was diluted 1:500 and then injected into the chromatographic system [15].

2.4. Chromatographic conditions

Final analytical solution (20 μL) was injected using an autosampler into a GraceSmart column. For separation of the derivatives of thiosulfate, cysteine, cysteinylglycine and internal standard gradient elution was used: 0–2 min, 10% B; 2–5 min, 10–35% B; 5–8 min, 35–70% B; 8–9 min, 70–10% B; 9–11 min, 10% B, where *A* is $0.05\,mol\,L^{-1}$ pH 2.5 TCA buffer, and B is acetonitryle. The flow-rate used was $1.2\,mL\,min^{-1}$ and the column was kept at a temperature of 25 °C. The analytical wavelengths were 375 and 355 nm for thiosulfate and thiols derivatives, respectively. For separation of only thiosulfate derivative isocratic elution, with a mobile phase consisting of a mixture of acetonitryle and water in the ratio of 60:40 (v/v), was used. The flow-rate and the column temperature were $1\,mL\,min^{-1}$ and 25 °C, respectively.

Creatinine was chromatographed isocratically; the mobile phase was a 98:2 (v/v) mixture of $15\,mmol\,L^{-1}$ phosphate buffer, pH 7.4, and acetonitrile at a flow-rate of $1\,mL\,min^{-1}$. The temperature was 25 °C and the detector wavelength 234 nm [15].

Peaks identification was based on comparison of retention times and diode-array spectra, taken at real time of analysis, with corresponding set of data obtained for authentic compounds.

2.5. Calibration

To prepare the calibration standards used to determine thiosulfate, reduced cysteine and cysteinylglycine in human urine, portions of 500 μL of phosphate buffered saline (PBS) or urine were each placed in a sample tube and spiked with the growing amount of the working standard solution of analytes to give concentrations of thiosulfate 0.5, 1.0, 2.5, 5.0, 10.0, 20.0, 30.0, 50.0, cysteine 0.2, 0.5, 1.0, 2.0, 5.0, 10.0, 20.0, 30.0 and cysteinylglycine 0.2, 0.5, 1.0, 2.0, 3.0, 5.0, 10.0, $15.0\,\mu mol\,L^{-1}$, respectively. Calibration standards in triplicate were processed according to recommended analytical procedure (Section 2.3 and Section 2.4). The calibration curves were obtained by least-squares linear regression analysis of the thiosulfate/IS or cysteine/IS or cysteinylglycine/IS derivative peak height ratios versus analyte concentration. The slopes of the calibration curves were used to calculate the analytes concentrations. Lower limits of detection (LLD) and quantitation (LLQ) were experimentally estimated by analysis of PBS samples spiked with decreasing concentration of the standard analytes until the signal-to-noise ratio reached 3:1 and 6:1, respectively.

2.6. Search for internal standard

Standard water mixture of 2-mercaptopropionic acid, 3-mercaptopropionic acid and cysteamine were tested as candidate internal standards for the analytical procedure leading to determination of thiosulfate and urinary thiols. Each of these compounds was added to the water standard solution mixture of thiosulfate, cysteine and cysteinylglycine to achieve a final concentration of $10\,\mu mol\,L^{-1}$ and the resultant solution was subjected to all steps of the analytical procedure. The performance of the chosen compound was checked with human urine as well.

2.7. Stability of thiosulfate in urine

To assess stability of thiosulfate in urine, freshly collected urine was split into two parts, and then kept at ambient temperature and 4 °C. A 500 μL of urine samples were processed, without delay and after 0.5, 1, 2, 3, 4, 5, 6, 7, 8 and 24 h, respectively as described in Section 2.3 and Section 2.4.

2.8. Selectivity

In order to prove the ability of the method to differentiate and quantify thiosulfate in the presence of other urine components, water standard solutions of sulfide and thiocyanate, each at concentration of $10\,\mu mol\,L^{-1}$, were processed according to the recommended procedure (Section 2.3 and Section 2.4). The same treatment have undergone urine samples obtained from six apparently healthy donors each spiked with sulfide solution to give final concentration of $25\,\mu mol\,L^{-1}$.

3. Results and discussion

Thiosulfate is one of the major metabolites of sulfide and is formed by its oxidation. Thiosulfate concentration in urine is increased after exposure to H_2S gas and in some diseases. To the best of our knowledge, however, only three gas chromatography
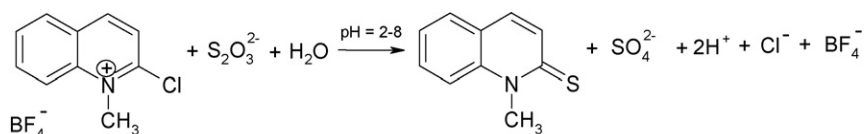
Fig. 1. Chemical derivatization reaction equation of thiosulfate with CMQT.

[1,2,9] and three liquid chromatography [10–12] methods for thio-sulfate determination have been described in literature. Most of available methods suffer from problem such as additional remove of interfering compounds during sample preparation [7,8] or during separation by "column-switching" chromatography [10], double converting reaction to finale analytical product [1,2,9] and high limit of detection [12]. Our new HPLC method for determination of thiosulfate in urine has not required extraction or preconcentration. It is based on single derivatization with CMQT followed by ion-pairing reversed-phase liquid chromatography separation and ultraviolet detection of 1-methyl-2-thioquinolone (MTQ). If necessary, this approach might be complemented for determination of urinary cysteine and cysteinylglycine.

3.1. Derivatization

2-Chloro-1-methylquinolinium tetrafluoroborate (CMQT) has been used as the derivatization reagent for thiols since 2001 [14] but not for thiosulfate. The CMQT reagent and its reaction with hydrophilic thiols have been described in details elsewhere [14–17]. Briefly, the CMQT derivatization reaction leads to the rapid formation of 2-S-quinolinium derivatives in slightly alkaline aqueous solution. The derivatization reaction of thiosulfate with CMQT is shown in Fig. 1. Thiosulfate reacts with CMQT, in a fully water environment to form 1-methyl-2-thioquinolone, in the stoichiometric ratio of 1:1 as was proven by continuous variation method (Fig. 2). The reaction of CMQT with thiol or thiolulfate is accompanied by an analytically advantageous bathochromic shift of the absorption maximum from 328 nm for the reagent to 350 or 375 nm for the maximum of the 2-S-quinolinium derivative of thiol or 1-methyl-2-thioquinolone, respectively (Fig. 3). The derivatization
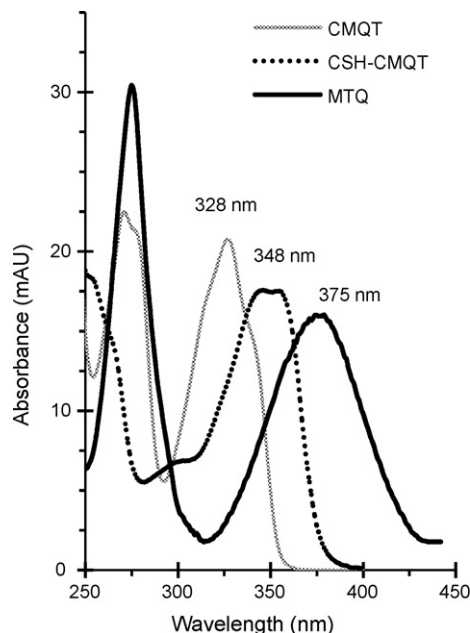
Fig. 3. Comparison of the absorption spectra of derivatization reagent (CMQT) with 1-methyl-2-thioquinolone (MTQ) and cysteine derivative (CSH-CMQT).

reaction yield was optimized in terms of pH, reagent excess and time. Optimal reaction pH for derivatization of thiosulfate with CMQT occurred in the range 2.0–8.0 (Fig. 4), and the reaction was completed after 2 min with 10-fold reagent excess at room temperature. However, for the concurrent determination of thiosulfate and main urinary thiols cysteine and cysteinylglycine pH 7.4 is recommended.
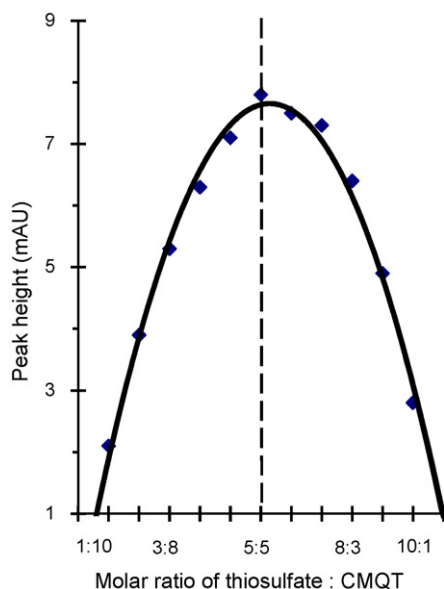
Fig. 2. Estimation of stoichiometric molar ratio by continuous variation method for the reaction of CMQT with thiosulfate.
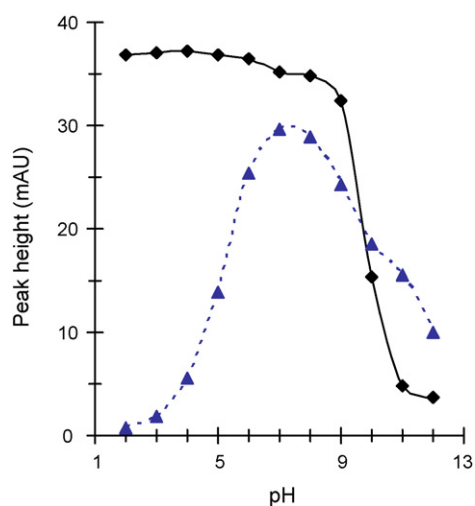
Fig. 4. Derivatization reaction yield for thiosulfate (-♦-) and sulfide (- -▲- -) as a function of the pH. Conditions: ten-fold CMQT, derivatization reagent excess, time 5 min, concentration of each analyte 10 μmol L^{-1}. Analysis was done by HPLC as described in Section 2.4

3.2. Chromatography

Two different chromatographic conditions were established for the separation of thiosulfate derivative from those of urinary thiols. In the procedure with gradient elution, MTQ reached the detector after 8.7 min and CSH-CMQT, CGSH-CMQT and IS-CMQT eluted earlier in the form of baseline-separated peaks at 6.8, 7.0 and 7.3 min, respectively (Fig. 5a and b). In the case where urine thiols are not of interest, isocratic elution can be applied in order to shorten the analysis time. The second advantage of the isocratic elution is a simple eluent, water and acetonitrile, the buffer is not necessary. Under this condition CMQT derivatives of plasma thiols elute with the solvent front but MTQ after 2.9 min (Fig. 5c).

3.3. Internal standard approach

In order to minimize the contributions of sample preparation, injection variations and column deterioration to the final results, the internal standard were used. We tested three thiols, that not appear in normal human urine, as candidate internal standard. As can be seen from the chromatogram depicted in Fig. 5a, the CMQT derivatives of 2-mercaptopropionic acid, 3-mercaptopropionic acid and cysteamine were baseline separated from derivatives of thiosulfate, cysteine and cysteinylglycine in standard water sample. The derivatives of 2MPA and 3MPA eluted too far from thiosulfate derivative and coeluted with urinary matrix components. Therefore, cysteamine was used as internal standard for the analysis.

3.4. Validation study

The method validation procedure encompassed linearity, precision, recovery, selectivity, limit of detection and quantitation, and stability.

The relationship between detector response and thiosulfate concentration was continuous and repeatable and was demonstrated using a seven-point calibration curve. We prepared two different sets of calibration samples by adding thiosulfate to urine or PBS. At each concentration, three replicates were assayed as described in Section 2.5. The calibration curve was linear in the tested range from 0.5 to 50 μmol L^{-1} PBS or urine. This calibration range can be easily extended up if required. The equations for the linear regression line were $y = 0.0384(\pm0.0034)x + 1.2475(\pm0.0725)$ for the urine and $y = 0.0387(\pm0.0008)x + 0.0005(\pm0.0001)$ for the PBS matrix; outliers were not excluded. The coefficient of correlation for the calibration regression was 0.999 in both cases. The differences between calibration slopes in the urine and PBS matrices were not statistically significant. Thus, the matrix of calibration sample did not significantly affect quantification.

In order to judge the quality of the elaborated method precision and recovery were determined. The intra- and inter-day precision and recovery were measured in urine or PBS samples spiked with thiosulfate in three replicates. The inter-day precision and recovery were evaluated on three consecutive days in a week. As shown in Table 1, with no outliers excluded, the intra-day and inter-day imprecision (R.S.D.) were within 2.79–5.33% and 4.64–9.92% for PBS samples, and within 1.40–7.32% and 4.70–7.89% for urine samples, respectively. Recovery values were from 91.2% to 108.2%.

The interference of thiocyanate and sulfide in analysis of urine for thiosulfate was studied. Thiocyanate does not react with CMQT derivatization reagent and consequently no detector response to this compound was observed under recommended experimental conditions.

It is unlikely that sulfide will be present in urine. Only one work [2] reports the presence of sulfide in the blood of victim of fatal poisoning, but not in urine. Provided that sulfide is present for different reasons, the urine sample should be treated with
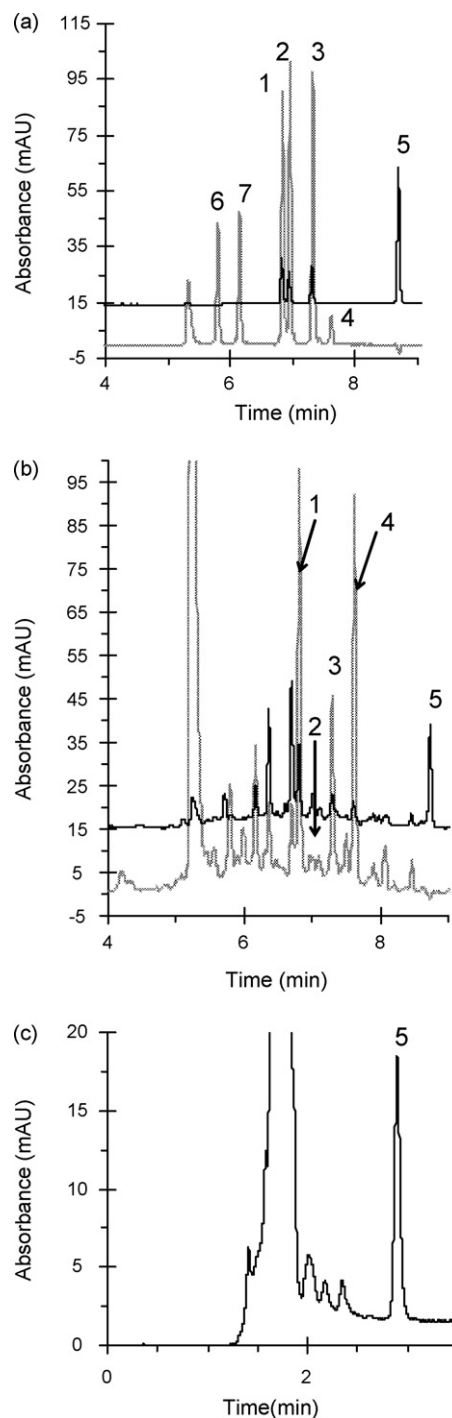

Fig. 5. Typical HPLC chromatograms of water standard solution and urine sample: (a) standard water solution, concentration of each analyte 10 μmol L^{-1}; (b) urine sample gradient profile of cysteine, cysteinylglycine and thiosulfate, concentration 20.26 μmol L^{-1} (2.26 mmol mol^{-1} Crn), 1.39 μmol L^{-1} (0.16 mmol mol^{-1} Crn) and 18.70 μmol L^{-1} (2.08 mmol mol^{-1} Crn), respectively; (c) urine sample isocratic profile of thiosulfate, concentration 18.70 μmol L^{-1} (2.08 mmol mol^{-1} Crn). Peak 1, CSH-CMQT; Peak 2, CGSH-CMQT; Peak 3, IS-CMQT; Peak 4, CMQT excess; Peak 5, MTQ; Peak 6, 2MPA; Peak 7, 3MPA. Solid line – chromatograms obtained at analytical wavelength 375 nm and dot line at 355 nm. Chromatographic condition described in Section 2.4

CMQT at pH 2. In this acidic environment thiosulfate forms easily 1-methyl-2-thioquinolone derivative whereas sulfide practically does not react with CMQT (Fig. 4 and Fig. 6a and b). When derivatization takes place at pH 7.4 the detector response corresponds to the sum of thiosulfate and sulfide (Fig. 6a and b). For simultaneous

Table 1
Results from the study of precision and recovery for thiosulfate in PBS and human urine ($n = 3$).

Sample	Amount added (μmol L^{-1})	Amount found ± S.D. (μmol L^{-1})	R.S.D. (%)	Recovery (%)
Intra-day				
PBS	0.5	0.46 ± 0.01	3.27	91.2
	5	5.05 ± 0.27	5.33	101.6
	50	50.16 ± 1.40	2.79	100.3
Urine	0	34.52 ± 2.53[a]	7.32	–
	0.5	35.06 ± 2.19	6.26	107.4
	5	39.46 ± 1.87	4.73	98.7
	50	87.37 ± 1.22	1.40	105.7
Inter-day				
PBS	0.5	0.53 ± 0.05	9.92	105.8
	5	4.87 ± 0.33	6.67	97.5
	50	51.74 ± 2.45	4.64	105.5
Urine[b]	0.5	0.54 ± 0.04	7.89	108.2
	5	5.16 ± 0.33	6.41	103.2
	50	49.34 ± 2.32	4.70	98.7

[a] Endogenous concentration.
[b] Concentration after subtraction of endogenous amount of thiosulfate.

determination of thiosulfate and main urinary thiols derivatization has to be performed at pH 7.4.

The lower limits of detection and quantitation for thiosulfate were estimated by analysis of PBS samples containing derivatization reagent spiked with decreasing amounts of thiosulfate. They were established to be 0.3 and 0.5 μmol L^{-1}, respectively. At these concentrations the signals-to-noise ratios were 3 and 6, respectively.

Because the collection of urine samples from a large patients group at the same time is very difficult, a suitable manner for sample storage is essential. The stability of endogenous thiosulfate in urine ex vivo at different temperatures was tested. Thiosulfate in urine was found to be stable at room temperature for 8 h and at 4 °C for at least 24 h. After 24 h the recovery for thiosulfate at 25 and 4 °C was 67.9% and 95.8%, respectively. But the stability of endogenous thiols was less. Cysteine and cysteinylglycine are fairly stable during 4 h after urine collection [16]. Therefore, the urine samples were processed as soon as possible, but not later than 4 h after collection, when cysteine and cysteinylglycine were estimated together with thiosulfate.

3.5. Application of the method

The method was applied to determination of thiosulfate urinary excretion in man. Urine was received from 13 volunteers, 8–66 years old (seven women and six men). Results from analysis are shown in Table 2. The mean (S.D.) concentrations of urinary thiosulfate were 15.88 (8.80) μmol L^{-1} for women and 30.58 (22.07) μmol L^{-1} for men, and varied from 6.22 to 30.35 and 8.02 to 60.93 μmol L^{-1}, respectively. Endogenous cysteine and cysteinylglycine were also estimated (Table 3). To facilitate comparison for different individuals the analytical results for urinary thiosulfate and thiols were normalized against creatinine. The mean (S.D.) concentration of
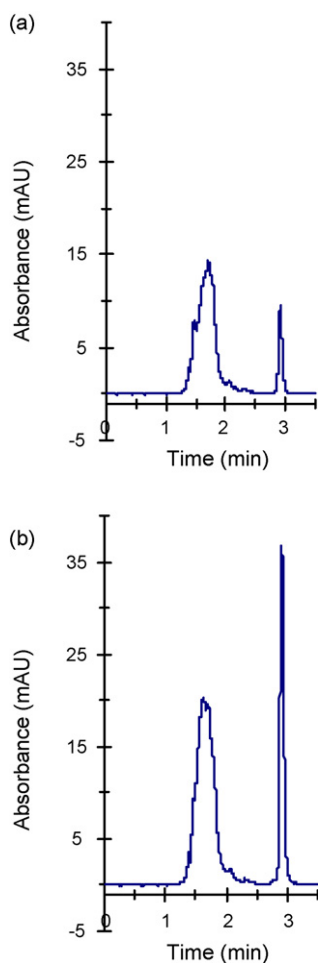
Fig. 6. Chromatograms of urine sample spiked with sulfide to give final concentration of 25 μmol L^{-1}; (a) derivatization at pH 2 and (b) derivatization at pH 7.4. Endogenous concentration of thiosulfate 7.5 μmol L^{-1}. Isocratic elution as described in Section 2.4.

Table 2
Concentrations of thiosulfate in human urine.

Gender (F, M)	Age (year)	Concentration	
		(μmol L^{-1})	(mmol mol^{-1} Crn)
F	22	20.05	2.34
F	23	30.35	1.97
F	25	15.63	2.77
F	38	6.22	1.45
F	39	11.15	1.99
F	56	21.43	2.54
F	63	6.31	2.39
M	8	60.93	4.89
M	36	55.73	3.31
M	37	18.84	1.42
M	38	8.02	1.36
M	54	22.21	1.96
M	66	17.73	2.16

Table 3
Urinary reference values for thiosulfate, reduced cysteine and cysteinylglycine.

	Mean ± S.D.	Range
Females, n = 7		
Age (year)	38.0 ± 16.3	22–63
Thiosulfate[a]	2.21 ± 0.40	1.45–2.77
Cysteine[a]	2.33 ± 1.24	0.65–3.74
Cysteinylglycine[a]	0.25 ± 0.12	0.08–0.32
Males, n = 6		
Age (year)	39.8 ± 19.6	8–66
Thiosulfate[a]	2.51 ± 1.36	1.36–4.89
Cysteine[a]	0.92 ± 0.40	0.24–1.22
Cysteinylglycine[a]	0.58 ± 1.07	0.06–2.76

[a] Values are expressed in mmol mol^{-1} creatinine
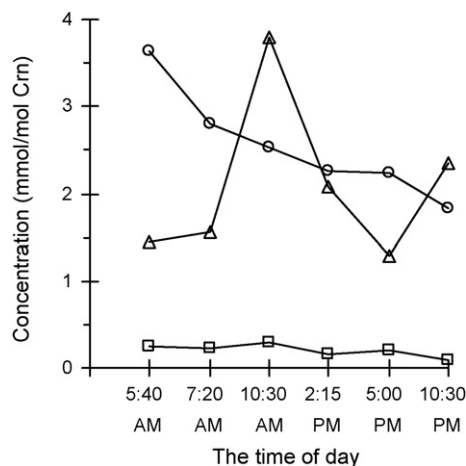
Fig. 7. Dependence of urinary excretion of thiosulfate (△), cysteine (○) and cysteinylglycine (□) on the time of day. First two samples (5:40 AM and 7:20 AM) were taken under the fasting state.

urinary thiosulfate recalculated against creatinine in tested group was 2.35 (0.94) mmol mol^{-1} Crn, that is similar to results reported by Belardinelli et al. [4] for control group (2.59 (0.47) mmol mol^{-1} Crn), but much higher (around 300-fold) than reported by Durand and Weinstein (7.2 μmol mol^{-1} Crn) for volunteers before exposure to H_2S [1]. Our study showed no difference between normalized urine thiosulfate in men and women ($P > 0.05$). To determine daily flux, we monitored thiosulfate, cysteine and cysteinylglycine in urine samples from one volunteer for 24 h. The amount of urinary thiosulfate, cysteine and cysteinylglycine varied from 1.29 to 3.80, from 1.82 to 3.63 and from 0.10 to 0.29 mmol mol^{-1} Crn, respectively, depending on the time of the day (Fig. 7). The daily excretion was 21.4 μmol for thiosulfate, 27.8 μmol for cysteine and 2.1 μmol for cysteinylglycine. In the earlier reports the daily excretion of thiosulfate was 18.9–44.5 [7] and 4.0–72.0 μmol [8]. Fig. 5 clearly shows how important is fasting or non fasting state for the urine collection in a study on usefulness of thiosulfate as an indicator of hydrogen sulfide poisoning or diagnoses of some diseases.

4. Conclusion

The analytical method described in this paper is sufficiently simple, sensitive and rapid for the routine determination of thiosulfate in human urine. Moreover, the urinary thiols (cysteine and cysteinylglycine) can also be measured during the same analytical run. If thiosulfate is the only analyte of interest, samples can be injected every 3.5 min because the MTQ elutes after 2.9 min. The limit of detection (LLD, 0.3 μmol L^{-1}) is similar to or better than those of HPLC methods for thiosulfate determination in urine described earlier. Xu et al. [11] reported LLD equal to 0.67 μmol L^{-1}, and Shea and Howell [12] reported 3.2 μmol L^{-1}. Our method can be used for routine clinical monitoring and in pharmacokinetic studies. The implementation of this liquid chromatographic method would be facilitated because it uses an ultraviolet detector, which is standard instrumentation in hospital laboratories and known for its stability and low demands in terms of maintenance.

Acknowledgment

References

[1] M. Durand, P. Weinstein, Forensic Toxicol. 25 (2007) 92–95.
[2] S. Kage, K. Takekawa, K. Kurosaki, T. Imamura, Int. J. Legal Med. 110 (1997) 220–222.
[3] D.E.C. Cole, J. Evrovski, Clin. Chem. 42 (1996) 654–655.
[4] M.C. Belardinelli, A. Chabli, B. Chadefaux-Vekemans, P. Kamoun, Clin. Chem. 47 (2001) 1500–1501.
[5] M. Torun, A. Bayhan, G. Yentur, Clin. Chem. 35 (1989) 1792–1793.
[6] M.R. Hayden, D. Goldsmith, J.R. Sowers, R. Khanna, Int. Urol. Nephrol. 40 (2008) 443–451.
[7] B. Sorbo, S. Ohman, Scand. J. Clin. Lab. Invest. 38 (1978) 521–527.
[8] V. Voroteliak, D.M. Cowley, T.H.J. Florin, Clin. Chem. 39 (1993) 2533–2534.
[9] S. Kage, T. Nagata, K. Kudo, J. Anal. Toxicol. 15 (1991) 148–150.
[10] D.E.C. Cole, J. Evrovski, R. Pirone, J. Chromatogr. B 672 (1995) 149–154.
[11] J. Xu, Y. Wang, Y. Xian, H. Li, L. Jin, K. Tanaka, H. Haraguchi, A. Itoh, Chromatographia 56 (2002) 449–453.
[12] M. Shea, S. Howell, Anal. Biochem. 140 (1984) 589–594.
[13] D.E.C. Cole, J. Evrovski, J. Chromatogr. A 789 (1997) 221–232.
[14] E. Bald, R. Glowacki, J. Liq. Chromatogr. Rel. Technol. 24 (2001) 1323–1339.
[15] K. Kusmierek, R. Glowacki, E. Bald, Anal. Bioanal. Chem. 385 (2006) 855–860.
[16] K. Kusmierek, G. Chwatko, E. Bald, Chromatographia 68 (2008) S91–S95.
[17] P. Kubalczyk, E. Bald, Anal. Bioanal. Chem. 384 (2006) 1181–1185.

Electrochemical characterization of a superoxide biosensor based on the co-immobilization of cytochrome *c* and XOD on SAM-modified gold electrodes and application to garlic samples

Montserrat Cortina-Puig*, Xavier Muñoz-Berbel, Carole Calas-Blanchard, Jean-Louis Marty

IMAGES EA 4218, Université de Perpignan Via Domitia, 52 avenue Paul Alduy, 66860 Perpignan Cedex, France

ABSTRACT

This paper describes the characterization and optimization of an amperometric cytochrome *c* (cyt *c*)-based sensor for the determination of the antioxidant capacity of pure substances and natural samples. The cyt *c* and the xanthine oxidase (XOD) enzyme were co-immobilized on the electrode using the combination of several long-chain thiols. The self-assembled monolayer (SAM) was optimized in terms of composition and ratio between thiols. The immobilization protocol for both cyt *c* and XOD and the SAM formation time were evaluated through electrochemical methods, such as cyclic voltammetry (CV), square wave voltammetry (SWV), chronoamperometry (CA) and impedance spectroscopy (IS). Finally, the biosensor was applied to the determination of the antioxidant capacity of pure alliin and two compounds extracted from garlic bulbs.

© 2009 Elsevier B.V. All rights reserved.

1. Introduction

Reactive oxygen species (ROS) represent the most important free radicals generated in living systems, especially the superoxide ($O_2^{\bullet-}$), the peroxyl ($ROO^{\bullet}$), the alkoxyl ($RO^{\bullet}$) or the hydroxyl ($OH^{\bullet}$) radicals. ROS, naturally generated during the metabolism, can damage biological structures such as proteins, lipids or DNA [1]. This oxidative damage is thought to play a causative role in aging [2,3] and several degenerative diseases associated with it, such as heart disease [4,5], cataracts [6,7], cognitive dysfunction [8,9] and cancer [10,11]. Antioxidants, which quench reactive free radicals, can prevent the oxidation of other molecules and thus they can have health-promoting effects in the prevention of degenerative diseases [12]. The interest in antioxidants is increasing because of their high capacity in scavenging free radicals related to various diseases [13].

Traditionally, antioxidants have been detected using chromatographic, spectrophotometric or fluorescence approaches [14]. Lately, electrochemical biosensors have become promising tools since they provide the advantage of rapid and real-time analysis, which increase the assay speed, flexibility, low cost and favour the development of automated and multi-target systems [15]. Electrochemical methods based on biosensors are particularly suitable for the sensitive determination of the $O_2^{\bullet-}$ radical at real-time. These methods have been classically based on either superoxide dismutase (SOD) or cytochrome *c* (cyt *c*).

The first one is based on the specific dismutation of the $O_2^{\bullet-}$ radical by SOD to produce hydrogen peroxide (H_2O_2), followed by the detection of electrooxidation of H_2O_2 at the electrode surface [16,17]. However, the oxidation potential of H_2O_2 is very high (>0.5 V vs. Ag/AgCl), hence resulting in interference problems that limit their practical application.

The second group is based on the reduction of cyt *c* immobilized on gold electrodes by the $O_2^{\bullet-}$ radical and the following reoxidation of the protein at the electrode surface. Commonly, the $O_2^{\bullet-}$ radical is enzymatically produced in solution using the xanthine oxidase (XOD)/hypoxanthine (HX) system. Thus, the obtained oxidation current is proportional to the $O_2^{\bullet-}$ concentration [18]. Usually, the electron transfer between the electrode and the redox protein is extremely slow. Consequently, traditional electrochemical methods cannot detect it [19]. An elegant way to modify gold electrodes, the most commonly used in this area, is the formation of self-assembled monolayers (SAMs). Long-chain alkanethiols show a high efficiency of communication between cyt *c* and the electrode [20–22]. However, these sensors usually show very small signal responses due to spontaneous dismutation of the $O_2^{\bullet-}$ radical in the way from the bulk, where it is generated as previously detailed, to the electrode surface where reacts with the cyt *c*.

This paper describes the characterization and application of a superoxide biosensor based on the co-immobilization of cyt *c* and

XOD on SAM-modified gold electrodes. The composition of the SAM, the time formation and the process of immobilization of the cyt *c* and XOD on the SAM-modified electrodes were optimized according to the intensity of the cyt *c* oxidation peak and the activity of the XOD enzyme. The developed biosensor was then applied to the determination of the antioxidant capacity of pure alliin and two compounds extracted from garlic bulbs.

2. Materials and methods

2.1. Reagents and chemicals

XOD from buttermilk (EC 1.17.3.2), catalase from bovine liver (EC 1.11.1.6), cyt *c* from horse heart and HX, 1-ethyl-3-(3-dimethylaminopropyl)carbodiimide (EDC), 11-mercapto-1-undecanol (MU), 11-mercaptoundecanoic acid (MUA), 3,3′-dithiodipropionic acid (DTDPA), potassium hexacyanoferrate (III), potassium hexacyanoferrate (II) trihydrate, uric acid and 30% H_2O_2 were purchased from Sigma (St. Quentin Fallavier, France). N-hydroxysuccinimide (NHS) and pure alliin were provided by Fluka (France). All reagents were of analytical grade and were used without further purification. All solutions were prepared using Milli-Q water.

Both alliin and allicin extracted from garlic bulbs were kindly provided by Dr. E. Touloupakis from the University of Crete. Alliin solutions were prepared in 50 mM sodium phosphate buffer (Na-PBS) pH 6.5 while allicin was diluted in 96% ethanol (Carlo Erba, Italy).

2.2. Electrochemical measurements

Electrochemical measurements were carried out using an AUTO-LAB PGSTAT12 Potentiostat (Eco Chemie, BV, The Netherlands) containing a FRA-2 module. Cyclic voltammetry (CV) and square wave voltammetry (SWV) measurements were recorded between −0.15 and 0.25 V at a scan rate of 100 mV s^{-1}. Chronoamperometric (CA) data were obtained by applying 150 mV for 15 s. Impedance spectroscopy (IS) spectra were recorded at the open circuit potential (0.25 ± 0.05 vs. Ag/AgCl) over a frequency range from 50 kHz to 0.1 Hz, using a sinusoidal AC potential perturbation of 5 mV. The measurement time was around 8 min after registering 18 points per frequency decade. All measurements given in this work are in relation to the Ag/AgCl reference electrode.

Amperometric measurements for the determination of the scavenging capacity of several antioxidants were made using a 641VA potentiostat (Metrohm, Switzerland), connected to a BD40 (Kipp & Zonen, The Netherlands) *X–t* recorder at 150 mV. Assays were performed in triplicate with three different electrodes.

2.3. Electrode pre-treatment and preparation

Gold screen-printed electrodes (DropSens, Spain) of 12.6 mm^2 were used as working electrodes. A platinum wire and a double-junction Ag/AgCl electrode (Thermo Orion 900200) were used as counter and reference electrodes.

Electrodes were electrochemically cleaned by cycling the potential between 0 and +1.4 V at the scan rate of 100 mV s^{-1} in 0.1 M H_2SO_4 until the characteristic cyclic voltammogram for a clean gold electrode was obtained. After this, electrodes were rinsed with water and ethanol and incubated in the ethanolic solution containing the thiols. The modified gold surface was then rinsed thoroughly with absolute ethanol and with water to remove any unattached thiol molecules. Cyt *c* and XOD were then immobilized on the modified electrode surface. Regarding the literature, four different procedures for their immobilization were tested, based on direct adsorption or on covalent attachment.

Protocol 1: Electrodes were incubated in a 50 μM cyt *c* + 50 mU mL^{-1} XOD solution, prepared in 5 mM K-PBS pH 7.0, for 2 h [23].

Protocol 2: Electrodes were first incubated in a 50 μM cyt *c* + 50 mU mL^{-1} XOD solution in buffer for 2 h. After washing with the buffer solution, electrodes were incubated in an aqueous solution of 5 mM EDC for 30 min [24].

Protocol 3: Electrodes were also incubated in a 50 μM cyt *c* + 50 mU mL^{-1} XOD solution in buffer. After 2 h, and without a cleaning step, EDC was added to obtain a concentration of 5 mM, and electrodes were incubated with the solution for 30 min [25].

Protocol 4: Electrodes were first incubated in an aqueous solution of 200 mM EDC and 50 mM NHS for 30 min. The excess of EDC and NHS was eliminated by cleaning with buffer. Finally, electrodes were incubated in a 50 μM cyt *c* + 50 mU mL^{-1} XOD solution in buffer for 30 min [20].

Lastly, the cyt *c*/XOD-modified electrodes were rinsed again with the same buffer solution to remove non-attached substances.

Fresh electrodes were prepared before each experiment.

2.4. Measurement of the superoxide scavenging capacity

The detection principle was based on the redox reaction between the cyt *c* and the $O_2^{\bullet-}$ radical generated by the HX/XOD system. The immobilized cyt *c* was reduced by $O_2^{\bullet-}$ and immediately regenerated at the electrode surface polarized at its oxidation potential (150 mV vs. Ag/AgCl). The generated oxidation current was proportional to the superoxide concentration in solution. The addition of antioxidants reduced the radical concentration and thus the oxidation current, allowing the quantification of the antioxidant capacity.

All amperometric experiments were carried out under constant stirring in 0.1 M Na-PBS with 100 μM EDTA pH 7.5. Before measurements, a catalase solution (final concentration in the cell = 10 U mL^{-1}) was added to avoid interferences from the H_2O_2, generated as a final product of the enzymatic reaction or by the spontaneous dismutation of $O_2^{\bullet-}$. Once the stable baseline was established, the HX solution was added into the cell (final concentration = 80 μM) and a steady-state superoxide level was recorded corresponding to the maximum response. Stock solutions of HX were prepared in 50 mM K-PBS pH 7.5 with 0.01 M KCl and 0.5 mM EDTA.

In the investigation of the role of superoxide scavengers, aliquots of the antioxidant samples were added and the current decrease was recorded after the addition of 80 μM HX. The decrease of the signal was normalized regarding the initial ROS signal, which minimized the sensitivity variation between sensors. This initial ROS signal was recorded before each addition of antioxidant in order to obtain more precise differential measurements. The antioxidant capacity was calculated by considering the sample concentration necessary for 50% signal inhibition (IC$_{50}$). This value was used for comparison between antioxidants: low IC$_{50}$ corresponded to a high antioxidant capacity.

The direct influence of all tested samples on the CV of cyt *c* was investigated before the determination of their antioxidant capacity.

3. Results and discussion

3.1. Optimization of the SAM composition

Electrodes were prepared as detailed in Section 2.3 (*protocol* 4) using several compositions and ratios of thiols selected from the literature. In terms of composition, 10 mM MUA (10-MUA) [24], 5 mM MU and 5 mM MUA (5-MU/5-MUA) [20], 3.75 mM MU and 1.25 mM MUA (3.75-MU/1.25-MUA) [26] and 5 mM MU, 5 mM MUA and 5 mM DTDPA (5-MU/5-MUA/5-DTDPA) [27] were chosen. Table 1

Table 1
Magnitude of the oxidation peak current for the cyt *c* when using different compositions and ratios of thiols samples. CV was performed in 5 mM K-PBS pH 7.0. Standard deviations are given from three electrodes.

SAM composition	I (μA)
10-MUA	0.048 ± 0.006
5-MU/5-MUA	0.102 ± 0.006
3.75-MU/1.25-MUA	0.125 ± 0.005
5-MU/5-MUA/5-DTDPA	0.107 ± 0.007

shows the magnitude of the oxidation peak for the cyt *c* when using the thiols samples previously described.

The 3.75-MU/1.25-MUA mixture was found to give the highest peak intensity and thus, this composition was used in the following assays.

3.2. Optimization of the cyt c and XOD immobilization process

As detailed in Section 2.3, four different procedures for the immobilization of the cyt *c* and the XOD were tested, based on direct adsorption or on covalent attachment. Table 2 shows the current response of the anodic peak of the cyt *c* depending on the protocol of immobilization.

The highest current response was obtained when using the *protocol* 1. However, this sensor showed low stability and a huge reduction of the signal was recorded after 10 min. On the other hand, sensors prepared following the *protocol* 4 showed high signal responses and long stability with time. Further, by co-immobilizing cyt *c* and XOD through this protocol, amperometric signal responses were found to be almost 15 times bigger than those reported in the bibliography [21,22]. As cyt *c* and XOD were very close, generated $O_2^{\bullet-}$ radicals could quickly react with cyt *c*, avoiding its spontaneous dismutation. From this point, all the electrodes of this work were prepared by following the *protocol* 4.

3.3. Optimization of the SAM formation time

Biosensors preparation was made as detailed in Section 2.3. The SAM formation process was monitored using IS as described in Section 2.2 by following the isolating properties of the SAM. Fig. 1a shows the impedance spectra of bare and SAM-modified electrodes in $Fe(CN)_6^{3-/4-}$ after different exposure times to the thiols solution (from 1 to 168 h of exposure). IS spectra were fitted to the equivalent circuit shown inset and the magnitude of the charge transfer resistance, R_{CT}, obtained from the fitting was plotted in Fig. 1b.

The R_{CT} value was found to increase with the exposition time to the thiols solution until 96 h, when a relative constant value was obtained. This suggested that the adsorption and rearrangement of thiols on the electrode surface to build a SAM impeded ferrocyanide molecules to flow and exchange electrons with the gold. 96 h may be the time required for the thiols to completely cover the electrode surface.

SWV and CA data were respectively used to determine the amount of cyt *c* and the activity of the XOD immobilized on the electrode surface with the exposition time. These measurements

Table 2
Variation of the oxidation peak current for the cyt *c* with time, depending on the protocol of immobilization. CV was performed in 5 mM K-PBS pH 7.0.

Protocol of immobilization	I (μA) ($t = 0$ min)	I (μA) ($t = 10$ min)	% Signal decrease
Protocol 1	0.250	0.124	50.3
Protocol 2	0.091	0.078	13.9
Protocol 3	0.063	0.053	15.5
Protocol 4	0.126	0.125	0.1
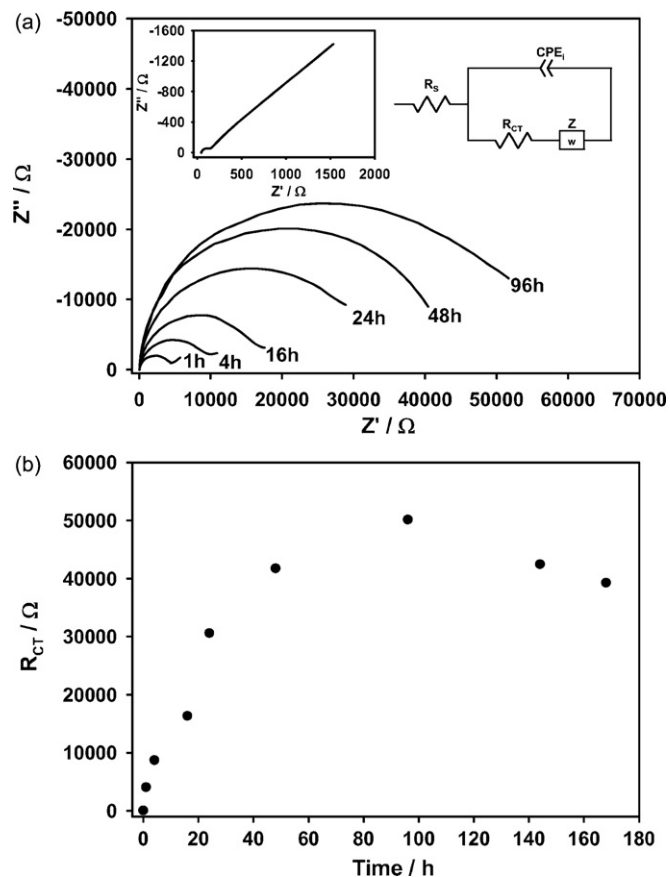
Fig. 1. (a) Complex plane plot of the gold screen-printed electrodes in 1 mM $Fe(CN)_6^{3-/4-}$ with the incubation time. The impedance plot of a bare gold electrode and the equivalent circuit used in the fitting of the data are shown in the inset. The circuit contains the solution resistance (R_S), the charge-transfer resistance (R_{CT}), the Warburg's impedance (Z_W) and the interface constant phase element (CPE_i). (b) Representation of the variation of the R_{CT} magnitude (after fitting with the equivalent circuit here exposed) with the incubation time.

were made by following the protocols detailed in Section 2.2. Fig. 2a shows the SWV response peak of cyt *c* covalently immobilized on the electrode after different times of incubation. The intensity of the cyt *c* peak with the incubation time is represented inset.

The cyt *c* peak current increased with the exposition time until 96 h, when it reached a plateau. Thus, the maximum amount of cyt *c* immobilized was obtained after at least 96 h of exposition. No redox wave was observed at the bare electrode (data not shown).

On the other hand, Fig. 2b shows the current response of the XOD enzyme after several incubation times. In this case, the maximum response of the enzyme was also found after 96 h of incubation of the sensor in the thiols solution. Thus, all the sensors used in this work were incubated at least 96 h in the thiols solution.

3.4. Electrochemical characterization of immobilized cyt c

The electrochemical properties of the immobilized cyt *c* were evaluated using CV as described in Section 2.2 but modifying the scan rate from 20 to 100 mV s^{-1}. Characteristic cyclic voltammograms for cyt *c* immobilized on a mixed SAM are shown in Fig. 3a. A pair of well-defined redox peaks were observed with a formal potential, $E^{o\prime}$ taken as $(E_p^c + E_p^a)/2$, of 62 mV and with a peak-to-peak separation value, ΔE_p, of 41 mV, at a scan rate of 100 mV s^{-1}. As can be seen, the peak-to-peak separation remained constant with the increase of the scan rate, and both the anodic and cathodic peak currents were linear with the scan rates (the inset of Fig. 3a), indicating a typical adsorption-controlled electrode.
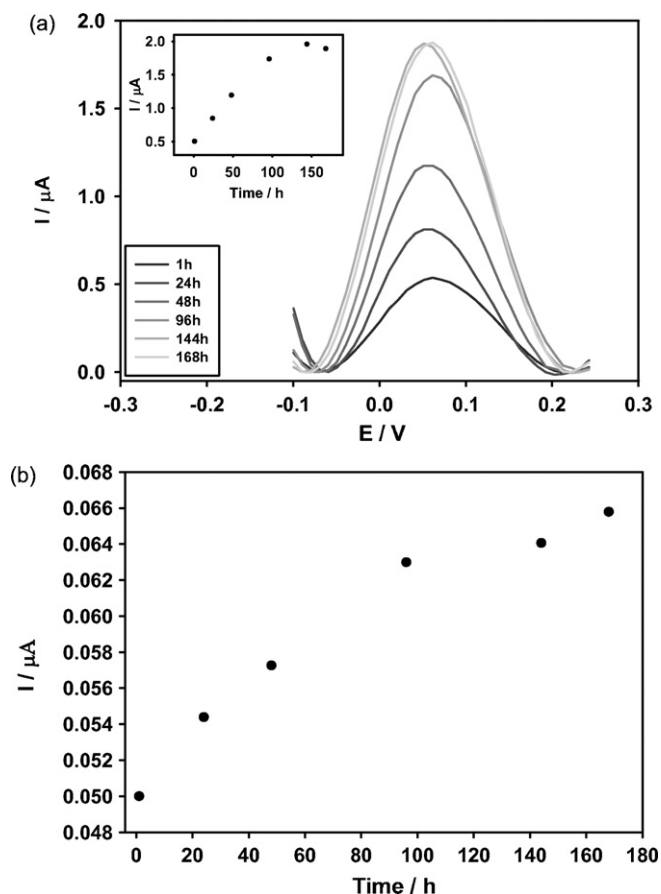
Fig. 2. (a) Representation of the current response of the cyt *c* covalently immobilized on electrodes modified after different times of incubation in the thiols solution. Measurements were performed in 5 mM K-PBS pH 7.0. The dependence of the peak current on the incubation time is shown inset. (b) Representation of the current response corresponding to the XOD activity with the incubation time in the thiols solution. Current values were obtained from CA in 5 mM K-PBS pH 7.0 containing 80 μM HX.

Fig. 3. (a) Cyclic voltammograms of the cyt *c* immobilized on the electrode at different scan rates (from inner to outer): 20, 30, 40, 50, 60, 70, 80, 90 and 100 mV s^{-1} in 5 mM K-PBS pH 7.0 at room temperature. Inset: the cathodic and anodic peak currents are plotted versus the scan rate (ν). (b) Representation of the dependence of the steady-state cathodic peak current on the pH. Cyclic voltammetry was performed in 5 mM K-PBS.

According to Laviron's equation [28]:

$$I_p = \frac{n^2 F^2 A \Gamma \nu}{4RT} = \frac{nFQ\nu}{4RT} \tag{1}$$

where I_p is the peak current of the anodic or cathodic peaks, Γ is the surface coverage of the electroactive substance (mol cm^{-2}), A is the electrode area (cm^2), Q is the quantity of charge (C), calculated from the peak area of the voltammograms, n is the number of electrons transferred. F, R, T and ν have their usual meanings. From the slope of the I_p–ν curve, n was calculated to be 1.1. Therefore, the redox of cyt *c* on a SAM-modified gold electrode is a single electron transfer reaction. The average surface coverage (Γ) of the immobilized cyt *c* was calculated to be 14.5 pmol cm^{-2}. This value was very close to the theoretical monolayer coverage, 14.3 pmol cm^{-2}, which was estimated using the crystallographic dimensions of cyt *c* (3.0 mm × 3.4 mm × 3.4 mm), and assuming one molecule with the long axis parallel to the electrode surface (3.4 mm × 3.4 mm) [29].

The small peak-to-peak separation value illustrates a fast electron transfer rate. The electron transfer rate constant, k_S, was estimated to be 42.8 s^{-1} using the following equation:

$$m = \frac{RTk_S}{Fn\nu} \tag{2}$$

when $n\Delta E_p < 200$ mV [28], where m is a parameter related to the peak-to-peak separation. F, R, T, n and ν have their usual meanings.

On the other hand, the effect of pH was investigated from 5.0 to 8.5. Fig. 3b shows the change of cathodic peak intensity with pH. As can be seen, the maximum response appeared at pH 7.5. Thus, to obtain the maximum sensitivity and bioactivity, a buffer of pH 7.5 was used throughout the research.

3.5. Optimization of the HX concentration

In the optimization of the HX concentration, CA measurements were carried out as described in Section 2.2 using eight solutions, ranging from 0 to 140 μM HX. The current response of the sensor with the concentration of HX was plotted (Fig. 4). As can be seen, the current response increased from 0 to 80 μM, when it stabilized and thus, 80 μM HX was chosen as the optimal concentration for the development of the scavenging biosensor.

3.6. Response of the biosensor to potential interferences

The influence of H_2O_2 and uric acid, the final products of the enzymatic $O_2^{\bullet-}$ generation system, was also investigated. An externally added H_2O_2 concentration of 480 μM (six times HX concentration) showed an influence on the $O_2^{\bullet-}$ signal of about 4%. Furthermore, the sensor gave no response to the same externally added uric acid concentration.
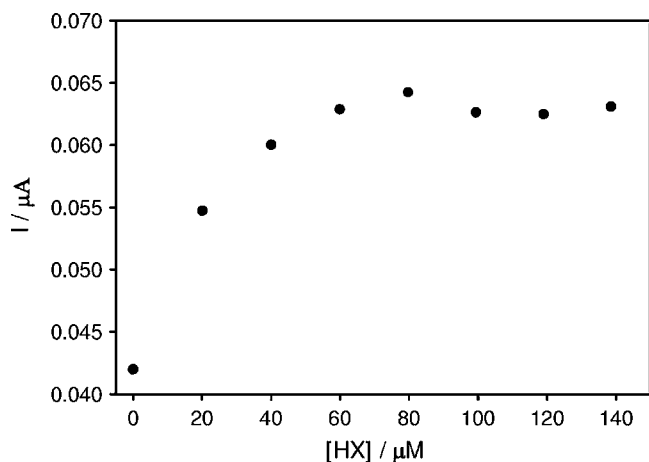
Fig. 4. Dependence of the CA oxidation current on the HX concentration using the cyt *c*/XOD-modified electrodes. Current values were obtained in 0.1 M Na-PBS with 100 μM EDTA pH 7.5.

3.7. Application of the superoxide radical sensor to the detection of the antioxidant capacity of pure substances and real samples of garlic

The developed biosensor was then applied to the determination of the antioxidant capacity of *Allium* species, particularly pure alliin and both natural alliin and allicin extracted from garlic bulbs. It has been previously reported that organosulfur compounds from garlic inhibit the peroxidation of lipids and possess antioxidant and radical scavenging activity [30].

In this case, amperometric measurements were made by following the protocols detailed in Sections 2.2 and 2.4. In Fig. 5 the current decrease versus the alliin concentration is shown.

The hyperbolic fit of alliin extracted from garlic bulbs allowed the determination of IC$_{50}$. Such behaviour corresponds to the empirical Hill equation, which can describe a variety of sensor responses [31]:

$$y = \frac{Bx}{C + x} \tag{3}$$

where *y* and *x* respectively correspond to the percentage of signal inhibition and the antioxidant concentration in solution, and *B* and *C* are constant values. Thus, the IC$_{50}$ of the alliin extracted from garlic bulbs was calculated to be $100 \pm 8\ \mu g\,mL^{-1}$.
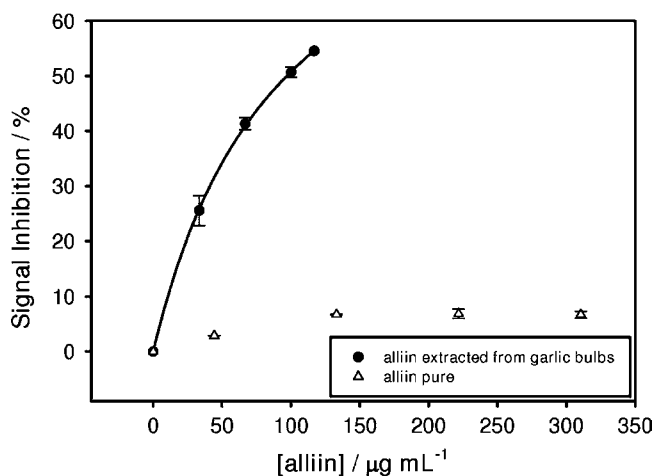
Fig. 5. Representation of the signal inhibition with the concentration of pure alliin and alliin extracted from garlic bulbs. Superoxide generated with 80 μM HX. Error bars are deduced from three repeated measurements.

However, pure alliin showed a poor antioxidant capacity. This fact agrees with other studies showing its weak antioxidative activity [32]. Therefore, the antioxidant capacity of the alliin extracted from garlic bulbs may be attributed to the presence of other antioxidant substances generated during the extraction process.

On the other hand, allicin extracted from garlic bulbs was found to have prooxidant properties (data not shown). Although allicin is thought to be the principal bioactive compound present in garlic extracts, some of its properties make it difficult to be used in practice: it is chemically unstable at room temperature and readily decomposes to other species, which may reduce its antioxidant activity or even enhance prooxidant activity [33].

The direct influence of the alliin extracted from garlic bulbs on the CV of cyt *c* was investigated. CV and SWV measurements were performed in buffer and in a 161 μg mL^{-1} alliin solution. The influence of this antioxidant on cyt *c* peak currents was less than 1%. Furthermore, the mixed SAM showed effective blocking for the tested antioxidants and no faradaic responses were observed.

4. Conclusions

In this paper, an enzymatic biosensor based on the co-immobilization of cyt *c* and XOD was developed for the detection of the antioxidant capacity of pure substances and garlic extracts. The composition and ratio between thiols and the protocol to co-immobilize the cyt *c* and the XOD were optimized to supply high current signals. The 3.75-MU/1.25-MUA mixture and the *protocol* 4, where the cyt *c* and the XOD were immobilized on the previously activated mixed SAM, were found to be the optimal conditions. In terms of incubation time, after 96 h of incubation the amount of cyt *c* and the XOD activity reached a maximum and thus, this time was chosen as the minimum time necessary for the correct reorganization of the thiols. This biosensor was applied to the detection of the antioxidant capacity of pure alliin and alliin and allicin extracted from garlic bulbs. Alliin extracted from garlic bulbs showed better antioxidant capacity than the pure one, probably for the presence of other antioxidants in the sample which enhanced their effect.

Acknowledgment

References

[1] H.E. Seifried, D.E. Anderson, E.I. Fisher, J.A. Milner, J. Nutr. Biochem. 18 (2007) 567.
[2] K.B. Choksi, J. Papaconstantinou, Free Radic. Biol. Med. 44 (2008) 1795.
[3] M.Y.B. Çimen, Clin. Chim. Acta 390 (2008) 1.
[4] S.K. Wattanapitayakul, J.A. Bauer, Pharmacol. Ther. 89 (2001) 187.
[5] B.Z. Simkhovich, M.T. Kleinman, R.A. Kloner, J. Am. Coll. Cardiol. 52 (2008) 719.
[6] V.N. Reddy, E. Kasahara, M. Hiraoka, L.R. Lin, Y.S. Ho, Exp. Eye Res. 79 (2004) 859.
[7] M.A. Marchetti, W. Lee, T.L. Cowell, T.M. Wells, H. Weissbach, M. Kantorow, Exp. Eye Res. 83 (2006) 1281.
[8] V. Valcour, B. Shiramizu, Mitochondrion 4 (2004) 119.
[9] X. Zhu, M.A. Smith, K. Honda, G. Aliev, P.I. Moreira, A. Nunomura, G. Casadesus, P.L.R. Harris, S.L. Siedlak, G. Perry, J. Neurol. Sci. 257 (2007) 240.
[10] W. Yan, W. Chen, L. Huang, J. Contr. Release 130 (2008) 22.
[11] A. Roessner, D. Kuester, P. Malfertheiner, R. Schneider-Stock, Pathol. Res. Pract. 204 (2008) 511.
[12] H. Basu, A. Vecchio, F. Flider, F. Orthoeter, J. Am. Oil Chem. Soc. 78 (2001) 665.
[13] E.M. Silva, J.N.S. Souza, H. Rogez, J.F. Rees, Y. Larondelle, Food Chem. 101 (2007) 1012.
[14] L.M. Magalhães, M.A. Segundo, S. Reis, J.L.F.C. Lima, Anal. Chim. Acta 613 (2008) 1.
[15] B. Prieto-Simón, M. Cortina, M. Campàs, C. Calas-Blanchard, Sens. Actuators B 129 (2008) 459.
[16] L. Campanella, G. Favero, L. Persi, M. Tomassetti, J. Pharm. Biomed. Anal. 23 (2000) 69.
[17] Y. Tian, L. Mao, T. Okajima, T. Ohsaka, Anal. Chem. 74 (2002) 2428.

[18] K. Tammeveski, T.T. Tenno, A.A. Mashirin, E.W. Hillhouse, P. Manning, C.J. McNeil, Free Radic. Biol. Med. 25 (1998) 973.
[19] H.A.O. Hill, G.A. Lawrance, J. Electroanal. Chem. 270 (1989) 309.
[20] B. Ge, F. Lisdat, Anal. Chim. Acta 454 (2002) 53.
[21] S. Ignatov, D. Shishniashvili, B. Ge, F.W. Scheller, F. Lisdat, Biosens. Bioelectron. 17 (2002) 191.
[22] F. Lisdat, B. Ge, E. Ehrentreich-Forster, R. Reszka, F.W. Scheller, Anal. Chem. 71 (1999) 1359.
[23] R.A. Clark, E.F. Bowden, Langmuir 13 (1997) 559.
[24] K.B. Holt, Langmuir 22 (2006) 4298.
[25] M.K. Beissenhirtz, R.C.H. Kwan, K.M. Ko, R. Renneberg, F.W. Scheller, F. Lisdat, Phytother. Res. 18 (2004) 149.
[26] A.V. Krylov, M. Beissenhirtz, H. Adamzig, F.W. Scheller, F. Lisdat, Anal. Bioanal. Chem. 378 (2004) 1327.
[27] L. Codognoto, E. Winter, J.A.R. Paschoal, H.B. Suffredini, M.F. Cabral, S.A.S. Machado, S. Rath, Talanta 72 (2007) 427.
[28] E. Laviron, J. Electroanal. Chem. 100 (1979) 263.
[29] R.E. Dickerson, T. Takano, D. Eisenberg, O.B. Kallai, L. Samson, A. Cooper, E. Margoliash, J. Biol. Chem. 246 (1971) 1511.
[30] K. Prasad, V.A. Laxdal, M. Yu, B.L. Raney, Mol. Cell. Biochem. 154 (1996) 55.
[31] I. Borisov, A. Lobanov, A. Reshetilov, B. Kurganov, Appl. Biochem. Microbiol. 36 (2000) 215.
[32] R. Hirata, S. Matsushita, Biosci. Biotechnol. Biochem. 60 (1996) 484.
[33] M. Yin, W. Cheng, J. Agric. Food Chem. 46 (1998) 4097.

Electrochemical determination of arsenite in neutral media on reusable gold nanostructured films

Ying Du, Wei Zhao, Jing-Juan Xu, Hong-Yuan Chen*

Key Laboratory of Analytical Chemistry for Life Science, Ministry of Education of China, School of Chemistry and Chemical Engineering, Nanjing University, Nanjing 210093, China

ARTICLE INFO

ABSTRACT

We report a simple and novel method of stirring-only-driven accumulation and electrochemical determination of arsenite (As(III)) with both of the oxidation and reduction peaks associated with As(0)/As(III) using a gold nanofilm electrode in neutral solution. Under stirring, a large amount of As(III) was deposited on the modified electrode and the electrochemical response was greatly amplified. The accumulated As(III) on the electrode showed well-defined redox couple in 0.1 M blank phosphate buffer solution (pH 7.0), which could be used for the measurement of As(III). Under optimal conditions, As(III) could be detected in the range from 0.20 to 375 ppb with a detection limit of 0.04 ppb. In particular, with the use of the reduction peak of As(III) the modified electrode exhibits excellent performance for As(III) determination even in the presence of abundant Cu(II). The regeneration of the electrodes is facile with good reproducibility. The electrochemical system was applied to analyze As(III) in lake water, As(III) spiked tap water and drinking water.

1. Introduction

Arsenic is a poisonous chemical and widely distributed throughout the earth's crust. Due to the mobile characteristic of arsenic and its compounds, those substances exist naturally in rocks, soil and minerals, and can easily contaminate the water for people's daily usage [1,2]. Although various chemical forms of arsenic can be found in natural environment, arsenic in water are mainly presented as trivalent arsenite (As(III)) and pentavalent arsenate (As(V)), while As(III) is more toxic [1]. As(III) is associated with cancers of the skin, lung, bladder and kidney, and it is hazardous to animals and human beings even at a low level in drinking water [3]. As(III) contamination of ground water has been reported in Argentina, Bangladesh, China, India, Mexico, the United States and many other countries in the world [4]. According to the last edition of the WHO Guidelines for Drinking-Water Quality (1993), the guideline value for arsenic in drinking water is 10 ppb [5]. So sensitive and reliable As(III) detection methods are urgently required to guard us from polluted water. To this end, many laboratory-based analytical methods, such as atomic absorption spectrometry, inductively coupled plasma with mass spectrometry and atomic fluorescence spectrometry, have been used for the accurate analysis of arsenic [6–8]. However, these methods are hindered by the requirement of expensive and large-scale instruments, the need of highly trained technicians, and the relatively high general running costs for each sample. Furthermore, acidic media used in some methods is not a mild condition [9]. Compared with techniques above, electrochemical methods, with high sensitivity, simple operation and low-cost instrument, show paramount importance for As(III) detection [10–13]. At one time, hanging mercury drop electrode with regenerated surface had been utilized for the detection of As(III) [14]. However, the toxicity of mercury limits its application. Later the alternatives of mercury like novel metals [15] (such as Ag, Pt, and Au,) and boron-doped diamond electrode [16], have been proved as suitable modified materials and electrode substrates for the electroanalysis of As(III) and some people have done excellent work on it [17–19]. Generally speaking, electrochemical methods to detect arsenite in water using modified electrodes (such as gold or platinum nanoparticles modified glass carbon electrode or boron-doped diamond electrodes) can be summarized to two categories: anodic stripping voltammetry (ASV) and directly catalytic oxidation of As(III), both of them have their own benefits and shortcomings. In virtue of the electrochemical predeposition step (during which As(III) is reduced to As(0) and deposited on the electrode surface), the former one can realize the successful determination of As(III) with a low detection limit, but it suffers from the interference by various metals like Cu(II), especially when it presents in a large amount in water systems. It is because that Cu(II) can be easily codeposited with As(III) at a certain potential. And due to the little separation of the stripping potentials

* Corresponding author. Tel.: +86 25 8354862; fax: +86 25 8354862.
E-mail address: hychen@nju.edu.cn (H.-Y. Chen).

of As(III) and Cu(II), if the concentration of Cu(II) is sufficiently high, the stripping peak of Cu(II) will partly, or even totally mask the As(III) signal (as shown in Fig. 7A) [12]. The latter one, which depended on Pt nanoparticles (or other materials) to catalyze the oxidation of As(III) to As(V) without the enrichment process, made narrower linear range and worse detection limit of As(III) detection [18].

In this study, a simple, rapid, and reliable approach has been developed for sensitive determination of low level As(III) in various water samples, featuring the stirring-only-driven accumulation of target on a porous gold nanofilm modified gold disk electrode. The gold nanofilm was obtained by applying a high potential such as 10 V vs. SCE to the gold electrode, following a reduction step by glucose, in which the gold atoms on the gold electrode surface were reconstructed, forming a porous and granular nano-gold film with a mass of active adatom-state Au*. It has been reported that the adatom-state Au* with a porous microstructure is highly desirable for trapping OH^- anions and forming Au^*OH_{ads} [20–22]. Owing to the unique property of the nano-gold film, As(III) could be easily accumulated on the gold nanofilm only under stirring in neutral solution due to the strong interaction between Au^*OH_{ads} and As(III). After the predeposition, As(III) was determined in blank PBS (pH 7.0) via linear sweeping voltammetry (LSV). At the initial potential of −0.7 V, the deposited As(III) on the gold nanofilm was reduced to As(0) immediately. Subsequently, As(0) could be oxidized to As(III) in anodic process, which would remain on the electrode surface and was reduced in the reverse scan. It made both the two peaks could be used for quantitative assay of As(III) concentration. And in particular, due to the well separation of the reduction peaks of deposited Cu(II) and As(III) (the potential difference between the reduction peaks of As(III) and Cu(II) is about 670 mV), the reduction peak was demonstrated to exhibit superior performance when a mass of interferences existed. The proposed method has been further verified by real sample assay. It is the first report on the mechanically enrichment of As(III) in neutral solution for the electrochemical detection of aqueous As(III). And it solved the problems of enrichment and anti-interference simultaneously. Compared with previous works, this method offers obvious advantages that it not only avoids the utilization of high concentration acidic media, but also provides a new approach for As(III) detection based on its reduction current, which can avoid the influence of many other ions coexisting in natural water system (such as Cu^{2+}, K^+, and NO_3^-). Moreover the gold nanofilm can be in situ prepared by a green, simple and fast way, which can be easily regenerated.

2. Experiments

2.1. Reagents

Arsenic trioxide, β-D-glucose, copper nitrate, disodium hydrogen phosphate ($Na_2HPO_4 \cdot 12H_2O$), sodium dihydrogen phosphate ($NaH_2PO_4 \cdot 2H_2O$), sodium hydroxide and hydrochloric acid were purchased from Shanghai Chemical Reagent Co. (Shanghai, China). All the chemicals were of analytical grade. 18 MΩ ultrapure water was used throughout the experiment. The application in real sample analysis was performed using Nanjing tap water from Nanjing Tap Water General Company, China, drinking water of Sensation from Coca Cola Company and drinking water of NongFu Spring from NongFu Spring incorporated company. The real lake water was obtained from Xuan Wu lake in Nanjing, China. The tap water and drinking water were spiked with 0.1 μM As(III). The lake water was spiked with 0.05, 0.1, and 0.15 μM As(III) before it was filtered. Blank lake water sample was prepared as described above without adding As(III). The pH values of all the water samples were adjusted to 7.0 before detection.

2.2. Preparation of gold nanofilm modified electrodes

A bulk gold disk electrode (diameter 2.0 mm) was abraded with fine SiC paper, polished carefully with 0.3 and 0.05 μm alumina slurry, and then sonicated in water and absolute ethanol, respectively. The procedure for the preparation of the modified electrodes was described in our previous work [21]. The cleaned gold electrode was first anodized under a high potential of 10 V in 0.1 M phosphate buffer (pH 7.0) for 5 min. The color of the oxidized electrode surface turned salmon pink. Then, the electrode was dipped in β-D-glucose aqueous solution with different concentrations for 10 min. The color of the gold electrode surface turned black after a while and a porous gold nanofilm was obtained on the top of the gold electrode. Both the anodized potential and the time of polarization and reduction were optimized.

2.3. Deposition of As(III) and Cu(II) on the gold nanofilm

Gold nanofilm modified electrodes were dipped into phosphate buffer (pH 7.0) containing different concentrations of As(III) for 15 min under stirring. After being rinsed carefully, it was immersed into an As(III) free PBS (pH 7.0) for electrochemical detection of As(III). Both deposition time and pH were optimized. The residual As(III) on the gold nanofilm could be removed by oxidation at 0.6 V for 60 s. Interference metal such as Cu(II) was deposited on the nanofilm together with As(III) using the same procedure. The regeneration of electrode after deposition of Cu(II) was carried out by immersing the electrodes in 0.1 M nitric acid solution, followed by a cyclic scan in a potential range of −0.6 to 0.6 V at 0.1 V s^{-1} for 10 cycles.

2.4. SEM characterization

Morphologies of gold slides after in situ preparation of gold nanofilm and deposition of As(III) on the gold nanofilm were studied on a JEOL JSM-6700F field emission scanning electron microscope (Japan).

2.5. XPS characterization

Valence of arsenic deposited on the surface of gold nanofilm was studied by an Escalab MKII X-ray photoelectron spectrometer (England), using nanomonochromatized Mg Kα X-ray as the excitation source and choosing C 1s (284.7 eV) as the reference line.

2.6. Electrochemical experiments

All electrochemical experiments were performed on a CHI 660 electrochemical workstation (CH Instruments Inc., USA) employing a conventional three-electrode system with a gold disk electrode (2.0 mm diameter) as working electrode, a platinum disk electrode (2.0 mm diameter) as auxiliary electrode, and a saturated calomel electrode (SCE) as reference electrode. All the detection measurements were carried out under a gentle nitrogen stream.

3. Results and discussion

3.1. Characterization of As(III) deposition on the gold nanofilm

Gold has been found to be a superior substrate for the voltammetric determination of As(III) via electrochemical predeposition, however, to date there has been no report on stirring-only-driven deposition of As(III) on gold or gold nanoparticles modified electrodes in aqueous solutions. In order to confirm the deposition process, SEM was used to investigate the morphology and distribution of the As(III) deposited on the surface. After the oxidation under
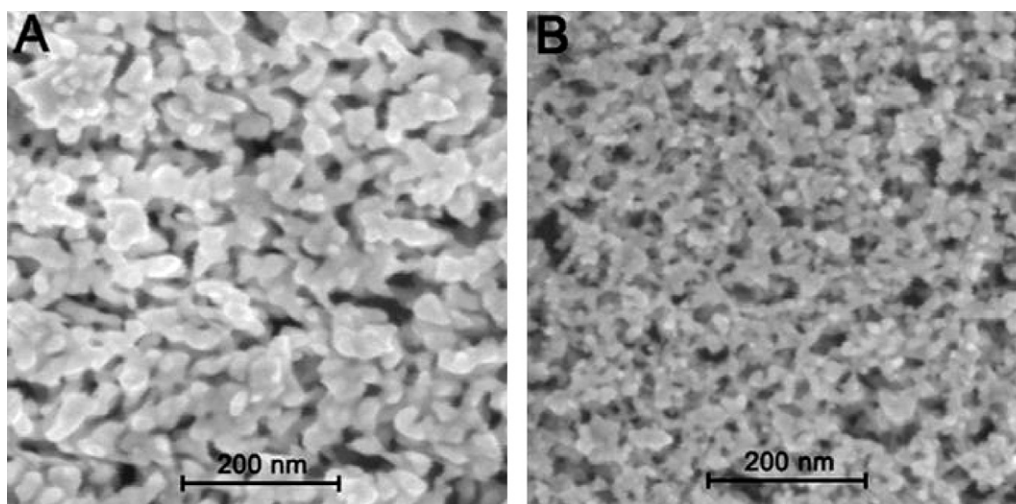
Fig. 1. SEM images of the gold nanofilm modified gold slides (A) prior to and (B) after deposition of As(III) in 0.1 M PBS (pH 7.0) containing 1.0 mM As(III) under stirring for 30 min.

high potential and reduction by glucose, the Au atoms on the surface were reconstructed to small gold nanocrystal seeds which is shown in Fig. 1A. The resulting film had a porous configuration, indicating a larger gold surface area and more highly active gold atoms exposed on the surface. After being dipped into phosphate buffer solution (pH 7.0) containing 1.0 mM As(III) for 30 min together with stirring, an obvious change of the morphology was observed (Fig. 1B). Many smaller nanoparticles were found on the whole surface of the film, showing that As(III) had been deposited on the gold nanofilm successfully. This is completely different from the morphology of As(0) deposited on the gold nanofilm by electrochemical reduction as well as that of As(0) being codeposited with Au on the surface of diamond electrode [23].

The valence of As deposited on the gold nanofilm surface was investigated using XPS with binding energy was calculated on the basis of that of carbon (284.7 eV). Fig. 2 is the As 3d X-ray photo-electron spectra with peak located at 44.4 eV (this binding energy had been calculated by correcting the shift of the spectra caused by charging effect during the XPS analysis process), approaching the binding energy of As(III) but much higher than that of As(0). This result indicated that the deposited As exists as As(III) and no electron transfer process occurred in the enrichment procedure. It is well known that the nanoscaled gold holds many different proper-

ties compared with its bulk form. The high surface energy of the gold nanoparticles makes it incline to adsorb other molecules [24,25]. In previous studies, the gold nanofilm was found to have abundant adatom-state Au* which could easily form Au*OH$_{ads}$ through chemisorption in neutral solutions [20–22]. Once the gold nanofilm electrode was dipped in 0.1 M PBS containing As(III), it would adsorb As(III) through surface complexation between Au*OH$_{ads}$ and As(III). It may be similar to the interaction between the adsorbate (such as Cu(II), As(III)) and goethite [26,27]. As a result, the accumulation of As(III) can be achieved in a mild condition.

To get more information about the stirring-only-driven deposition of As(III), cyclic voltammograms at the gold nanofilm modified electrode after deposition in 5.0 μM As(III) solution were recorded in 0.1 M pH 7.0 PBS under different potential ranges. The relevant curves are shown in Fig. 3. The initial potential was set at −0.3 V. When it was scanned to positive direction, no redox peak was observed. While in the following scans from 0.3 to −0.7 V, a pair of well-defined peaks appeared at −0.577 and −0.137 V and both of the redox peak currents were nearly 400 times higher than those obtained on the bare gold electrode. The peak located at −0.577 V
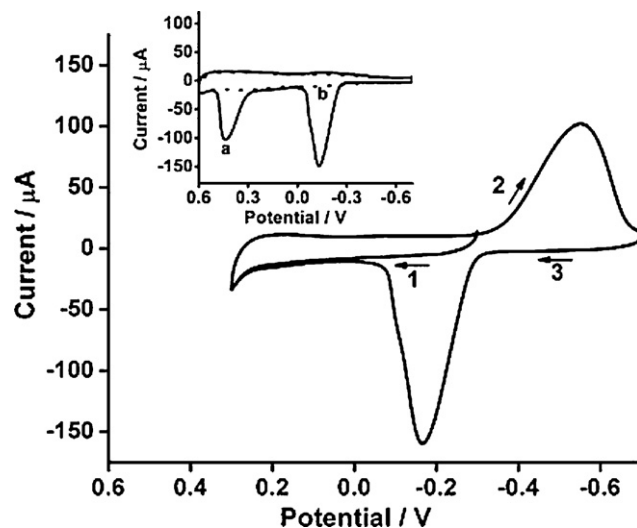

Fig. 2. XPS of As 3d spectrum after deposition in 0.1 M PBS (pH 7.0) containing 1.0 mM As(III) under stirring for 30 min.

Fig. 3. Cyclic voltammograms of gold nanofilm modified electrode in 0.1 M PBS (pH 7.0) after deposition in 0.1 M PBS (pH 7.0) containing 5.0 μM As(III) under stirring for 15 min with different scan ranges: −0.7 to 0.3 V (initial potential: −0.3 V); inset: −0.7 to 0.6 V (a and b); potential scan rate: 100 mV s^{-1}.
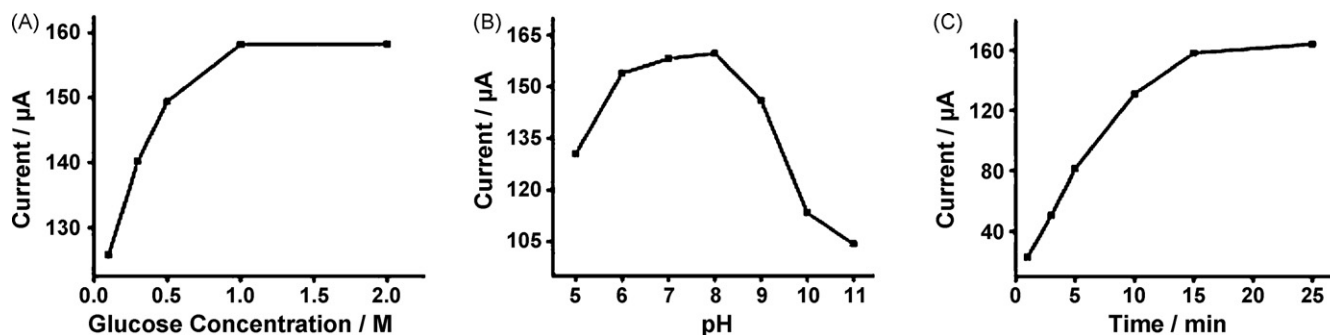
Fig. 4. Dependences of oxidation peak currents of As on the glucose concentration for the fabrication of gold nanofilm modified electrodes (A), deposition solution pH (B), and deposition time (C), when one parameter changes while the others are under their optimal conditions. The oxidation peak currents of As are obtained in 0.1 M As(III) free PBS (pH 7.0) in the scan ranges of −0.7 to 0.3 V after As(III) was accumulated on the gold nanofilm modified electrodes in 0.1 M PBS (pH 7.0) containing 5.0 μM As(III) under stirring for 15 min, potential scan rate: 100 mV s^{-1}.

was the result of the reduction of As(III) to As(0) and the other at −0.137 V was due to the oxidation of As(0) to As(III) [17]. This could be explained by the fact that after being deposited on the modified electrode, As(III) maintained the state when the scanning potential was from −0.3 to 0.3 V. In the following cycle from 0.3 to −0.7 V, As(III) was reduced to As(0) at the potential of −0.577 V and then oxidized to As(III) at −0.137 V, resulting in the appearance of As(III)/As(0) redox peaks. Compared with that in acidic condition (the stripping potential of As(0) is at about 0.150 V), the oxidation potential of As(0) (−0.137 V) in neutral PBS is more negative, in accordance with the theory that increasing pH makes the standard reduction potential of As(III)/As(0) shift negatively [23]. Different from the electrochemical deposition and detection of As(III) by anodic stripping voltammetry in acidic media, in which only As(0) can exist on the electrode surface, here, both of As(III) and As(0) can exist stably on the surface of modified electrode, and the electroreduction of As(III) to As(0) is performed completely in the scan range without the competitive generation of H_2 or AsH_3. Thus both the redox peak currents of As(III)/As(0) can be used to indicate the concentration of As(III) in samples (shown in Figs. 5 and 8).

Interestingly, when the scanning range was up to −0.7 to 0.6 V, a new peak at 0.440 V appeared, while in the reversal cathodal scan, no obvious reduction peak was present (Fig. 3 inset a). The new peak at 0.440 V was attributed to the oxidation of As(III) to As(V) [16], while As(V) was generally considered electrochemically irreducible, which resulted in no peak observed during the reversal scan [28]. After several cycles, in the range of −0.7 to 0.6 V, all redox peaks of As (As(0) ↔ As(III), As(III) → As(V)) disappeared completely (Fig. 3 inset b), indicating that As(III) could be oxidized to As(V) entirely. XPS experiment shows that no As left on the gold nanofilm surface, meaning that As(V) desorbed from the surface of gold nanofilm. It is probably due to the repulsion between $HAsO_4^{2-}$ and Au^*OH_{ads} and makes As(V) easily desorb from the electrode surface (the dominant species of As(V) in pH 7.0 solution is $HAsO_4^{2-}$ (pK_2 = 7.0)). This provides an easy way to regenerate the gold nanofilm modified electrode after each detection.

3.2. Optimization

The effective deposition of As(III) on the gold nanofilm surface depends on the fabrication conditions of the gold nanofilm and the deposition conditions of As(III). Therefore, a series of measurements were performed to investigate the most suitable conditions for As(III) detection. It was found that the reduction process of gold oxide was responsible for the properties of gold nanofilm modified electrode. Glucose as a nontoxic, gentle reducing agent is proved suitable for the fabrication of gold nanofilms [21]. Furthermore, the concentration of glucose was optimized for the detection of As(III).

Linear sweep voltammetry was applied to detect the deposition quantity of As(III) on the electrode surface. By comparison of the oxidation peak current of As (Fig. 4A), we found that when the glucose concentration was 0.1 M, the peak current of deposited As (at −0.137 V) was only about 60% of the maximum with the glucose concentration of 1.0 M. The peak current increased nonlinearly with the increase of glucose concentration and reached a plateau stage when the concentration of glucose was up to 1.0 M. This result can also be predicted from the color of gold film. When we use 0.1 M glucose as reducing medium, the color of the gold electrode surface changed to grey black, even the reduction time was prolonged up to 30 min. When 1.0 M glucose was used as reducing medium, the color of the gold electrode surface turned to black within 10 min (here, "black" means gold nanofilm is completely reduced). Therefore, we chose 1.0 M as the optimal concentration of glucose.

The characteristic of the gold nanofilm and As(III) species in 0.1 M PBS under different pH conditions may determine the interaction between them and subsequently have great influence on the accumulation efficiency of As(III). Therefore, the influence of pH for deposition solution was investigated (Fig. 4B). In the pH range of 6–9, the oxidation peak currents of As maintained 90% of the maximum response. However, it decreased obviously at pH lower than 6 or higher than 9. It is assumed that in weak acidic solution, the adsorptive interaction between Au^* and OH_{ads} weakens, resulting in the decrease of the adsorption of As(III). In addition, when the pH is higher than 9, the dominant species of As(III) in the solution is $H_2AsO_3^-$ (pK_1 = 9.2) and there may be a repulsive interaction between Au^*OH_{ads} and $H_2AsO_3^-$, which also affect the deposition of As(III). As a result, an optimal deposition pH of 7.0 (neutral condition) was selected. Fig. 4C shows the relationship between the oxidation peak currents (at −0.137 V) and the deposition time of the 5.0 μM As(III) deposited on the gold nanofilm modified electrode in 0.1 M pH 7.0 PBS. In the first 15 min, the peak current increased linearly with time. After that, longer deposition time did not enhance the response significantly. Therefore, 15 min was chosen as the optimal parameter based on a balance between the maximum response signal and excessive deposition time.

3.3. Detection of As(III)

As(III) detection experiments with LSV were carried out under the optimal deposition conditions. Fig. 5 shows the LSV currents corresponding to different As(III) concentrations. Calibration curve in Fig. 5 held a linear relationship between the oxidation peak current and concentration of As(III) in the range of 0.20–375 ppb (R = 0.997), with detection limit of 0.04 ppb. After each measurement, the potential was kept at 0.6 V for 1 min to remove residual As, and the renewed electrode could be used in the next detec-
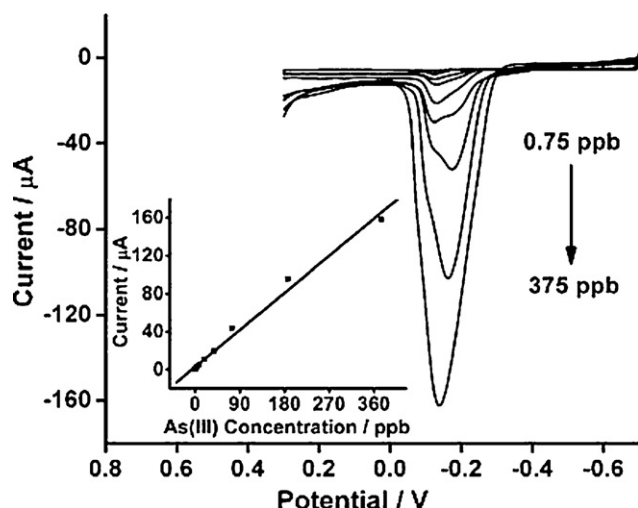
Fig. 5. LSV of gold nanofilm modified electrode in 0.1 M PBS (pH 7.0) after deposition in 0.1 M PBS (pH 7.0) with different concentrations of As(III) under stirring for 15 min, potential scan rate: $100\,mV\,s^{-1}$. Inset: calibration curves of the oxidation peak currents associated with the deposition of different concentrations of As(III).
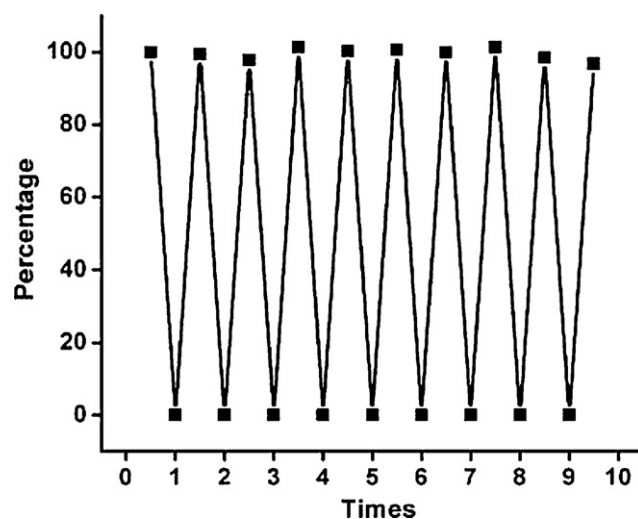

Fig. 6. Continuous measurements of 7.5 ppb As(III) for 10 times. After each measurement, the potential was kept at 0.6 V for 1 min, in order to make As(III) deposited on the gold nanofilm be completely cleared from the surface.

tion. The response reproducibility for the gold nanofilm modified electrode is shown in Fig. 6, and the result is acceptable with the relative standard deviation of 4.7% for 10 consecutive measurements of $0.10\,\mu M$ As(III) in neutral condition.

3.4. Interference studies

In conventional anodic stripping voltammetry, the main cause of interference in the determination of As(III) is the co-electrochemical reduction of other metal cations (especially Cu(II)). For instance, Cu(II) can be reduced together with As(III) at a certain potential (the standard electrode potential (φ vs. SHE) of Cu(II)/Cu(0) is 0.337 V and that of As(III)/As(0) is 0.248 V) and the competition for deposition between As(III) and Cu (II) on the electrode surface reduces the stripping peak current of As(III). Furthermore, if the concentration of the interference is high enough, the As(III) peak can be overlapped completely. Herein, interference studies in As(III) detection were performed to examine the influence of Cu(II) that commonly existed in many water systems. Fig. 7A shows the effect of Cu(II) contamination on the detection of As(III) in 1.0 M HCl with electrodeposition at −0.1 V for 300 s. In the acidic

medium, a sharp Gaussian stripping peak for As(III) at 0.095 V was obtained (curve a). However, when $50\,\mu M$ Cu(II) was added into the $5.0\,\mu M$ As(III) solution in 1.0 M HCl, after electrodeposition only a broad stripping peak appeared at 0.423 V (curve b) and the oxidation peaks of Cu and As are totally overlapped. This result confirms the shortcoming of electrochemical deposition in the detection of As(III) with interference.

When As(III) and Cu(II) were accumulated by the way of stirring and detected in neutral medium, interesting result was obtained (shown in Fig. 7B). After deposition, two pairs of redox peaks appeared in 0.1 M pH 7.0 PBS in the potential range of −0.75 to 0.35 V. The redox peaks with potentials of −0.101 and −0.601 V were assigned to the redox of As(III)/As(0), and the peak potentials of 0.248 and 0.068 V were due to the redox of Cu(II)/Cu(0). Compared with the analysis of As(III) and Cu(II) in acidic condition by electrodeposition, though the redox peak currents of As(III)/As(0) slightly decreased after the codeposition of Cu(II) on the surface of gold nanofilm, they were separated well from the peaks of Cu. Moreover, the reduction peak can hardly be influenced by the deposition of Cu(II) because of the potential separation of approximate 670 mV between the reduction peaks of Cu(II) and As(III). Therefore, the reduction peak current was applied in the determination of As(III)
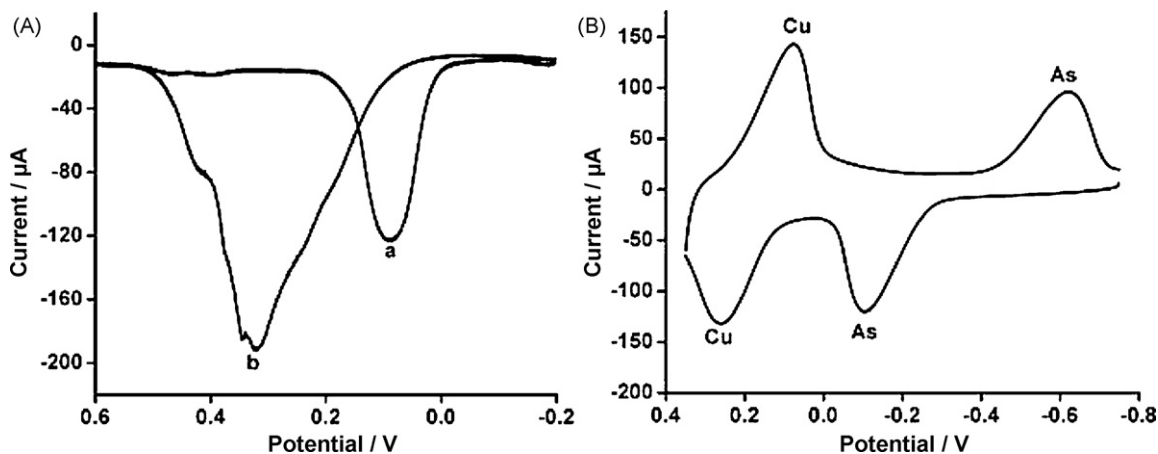

Fig. 7. Interference of $50.0\,\mu M$ Cu (II) on the detection of $5.0\,\mu M$ As(III) in different conditions: (A) LSV of gold nanofilm modified electrode after deposition in 1 M HCl with $5.0\,\mu M$ As(III) (a) and $5.0\,\mu M$ As(III) together with $50.0\,\mu M$ Cu (II) (b), predeposition condition: −0.1 V vs. SEC for 300 s and potential scan rate: $100\,mV\,s^{-1}$. (B) Cyclic voltammogram of gold nanofilm modified electrode in 0.1 M PBS (pH 7.0) after deposition in 0.1 M PBS (pH 7.0) containing $5.0\,\mu M$ As(III) together with $50.0\,\mu M$ Cu (II) under stirring for 15 min, potential scan rate: $100\,mV\,s^{-1}$.

Table 1
Recovery of As(III) in real samples.

Sample	Concentration added (μM)	Concentration found (μM)	Recovery (%)
Tap water	0.10	0.0991 ± 0.0037	99.1 ± 3.7
Sensation	0.10	0.0982 ± 0.0040	98.2 ± 4.0
NongFu Spring	0.10	0.103 ± 0.0047	103 ± 4.7
	0.05	0.0498 ± 0.0042	99.6 ± 8.4
Xuan Wu lake water	0.10	0.0982 ± 0.0050	98.2 ± 5.0
	0.15	0.148 ± 0.0028	98.7 ± 1.9
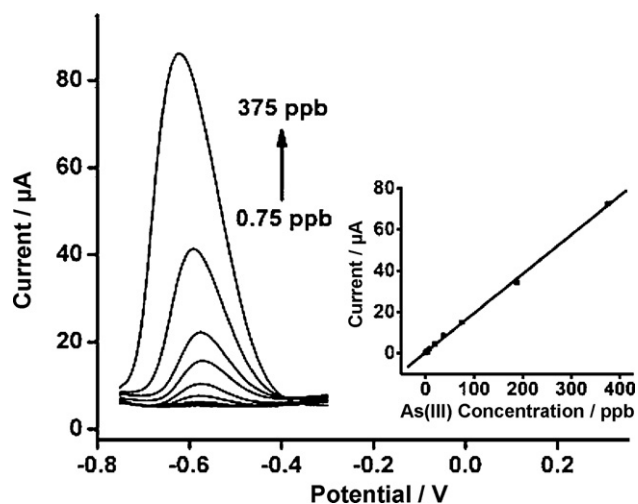
Fig. 8. The reduction peaks of LSV of gold nanofilm modified electrode in 0.1 M PBS (pH 7.0) after deposition in 0.1 M PBS (pH 7.0) with different concentrations of As(III) under stirring for 15 min in the presence of 50.0 μM Cu(II), potential scan rate: 100 mV s^{-1}. Inset: calibration curves of the reduction peak currents associated with the deposition of different concentrations of As(III).

when it coexisted with Cu(II). Increasing the ratio of Cu(II)/As(III) in the deposition solution (even the value of Cu(II)/As(III) is up to 5000) scarcely affects the linear relationship between the concentrations and reduction peak currents of As(III). This is attributed to the special enrichment method and the strong interaction between As(III) and the gold nanofilm. The dependence of the reduction peak currents on different concentrations of As(III) in the presence of 50 μM Cu(II) is shown in Fig. 8. It could be seen that the linear range of As(III) was 0.75–375 ppb, and the LOD value increased slightly to 0.12 ppb.

3.5. Analysis of As(III) in water samples

To evaluate and prove the possibility for applying the gold nanofilm electrode for water sample assay, the accumulation and detection of As (III) were performed using the modified electrode in 0.10 μM As(III)-spiked tap water and drinking water (present in Table 1), and satisfactory results were obtained. Using the proposed strategy, the concentration of As(III) in real water sample such as Xuan Wu lake water was determined as 0.04 μM. In order to prove the accuracy of the obtained data, recovery experiments were performed by spiking to Xuan Wu lake water samples with different concentrations (Table 1), and acceptable data of recoveries were obtained.

4. Conclusions

We have established a unique stirring-only-driven enrichment and electrochemical detection method for As(III) in practical water

samples based on the gold nanofilm modified electrode, which are simple and rapid without using high concentration acid or other special materials. The gold nanofilm with a nanoporous configuration and abundant highly active Au* makes it suitable for the effective deposition of As(III), which in turn makes the modified electrode available for the analysis of As(III) in neutral solution using both of the As(0) oxidation peak and As(III) reduction peak. The gold nanofilm is stable under continuous detections and regenerations and a range of five orders of magnitude with LOD of 0.04 ppb has been achieved for As(III) detection. It can be used to detect As(III) in real water samples. Further studies will be focused on utilization of this electrode for simultaneous detection of other hazardous materials together with As(III) in water samples.

References

[1] C. Su, R.W. Puls, Environ. Sci. Technol. 35 (2001) 1487.
[2] B.K. Mandal, K.T. Suzuki, Talanta 58 (2002) 201.
[3] G.F. Nordberg, B.A. Fowler, M. Nordberg, L. Friberg, Handbook on the Toxicology of Metals, Elsevier Press, 2007.
[4] World Health Organization, website: www.who.int/entity/water_sanitation_health/dwq/arsenicun8.pdf.
[5] World Health Organization, website: www.who.int/mediacentre/factsheets/fs210/en/.
[6] C.J. Wei, J.X. Liu, Talanta 73 (2007) 540.
[7] World Health Organization, website: www.who.int/entity/water_sanitation_health/dwq/arsenicun2.pdf.
[8] N. Campillo, R. Penalver, P. Vinas, I. Lopez-Garia, M. Hernandez-Cordoba, Talanta 77 (2008) 793.
[9] P. Salaun, B. Planer-Friedrich, C.M.G. Van Den Berg, Anal. Chim. Acta 585 (2007) 312.
[10] X. Dai, O. Nekrassova, M.E. Hyde, R.G. Compton, Anal. Chem. 76 (2004) 5924.
[11] E. Majid, S. Hrapovic, Y.L. Liu, K.B. Male, J.H. Luong, Anal. Chem. 78 (2006) 762.
[12] X. Dai, R.G. Compton, Analyst 131 (2006) 516.
[13] L. Xiao, G.G. Wildgoose, R.G. Compton, Anal. Chim. Acta 620 (2008) 44.
[14] W. Holak, Anal. Chem. 52 (1980) 2189.
[15] D.Q. Hung, O. Nekrassova, R.G. Compton, Talanta 64 (2004) 269.
[16] T.A. Ivandini, R. Sato, Y. Makide, A. Fujishima, Y. Einaga, Anal. Chem. 78 (2006) 6291.
[17] L. Rassaei, M. Sillanpää, R.W. French, R.G. Compton, F. Marken, Electroanalysis 20 (2008) 1286.
[18] S. Hrapovic, Y.L. Liu, J.H.T. Luong, Anal. Chem. 79 (2007) 500.
[19] B. Kumar Jena, C. Retna Raj, Anal. Chem. 80 (2008) 4836.
[20] K.A. Assiongbon, D. Roy, Surf. Sci. 594 (2005) 99.
[21] W. Zhao, J.J. Xu, C.G. Shi, H.Y. Chen, Electrochem. Commun. 8 (2006) 773.
[22] J.T. Zhang, H.Y. Ma, D.J. Zhang, P.P. Liu, T. Fang, Y. Ding, Phys. Chem. Chem. Phys. 10 (2008) 3250.
[23] Y. Song, G.M. Swain, Anal. Chem. 79 (2007) 2412.
[24] L.D. Burke, W.A. O'Leary, J. Appl. Electrochem. 19 (1989) 758.
[25] C.M. Ruan, W. Wang, B.H. Gu, J. Raman Spectrosc. 38 (2007) 568.
[26] T. Saito, L.K. Koopal, S. Nagasaki, S. Tanaka, Environ. Sci. Technol. 39 (2005) 4886.
[27] S.R. Kanel, B. Manning, L. Charlet, H. Choi, Environ. Sci. Technol. 39 (2005) 1291.
[28] R. Prakash, R.C. Srivastava, P.K. Seth, Electroanalysis 15 (2003) 1410.

Trace iodine quantitation in biological samples by mass spectrometric methods
The optimum internal standard

Jason V. Dyke [a], Purnendu K. Dasgupta [b,*], Andrea B. Kirk [b]

[a] *Department of Chemistry and Biochemistry, Texas Tech University, Lubbock, TX 79409-1061, United States*
[b] *Department of Chemistry and Biochemistry, The University of Texas at Arlington, Arlington, TX 76019-0065, United States*

ABSTRACT

Accurate quantitation of iodine in biological samples is essential for studies of nutrition and medicine, as well as for epidemiological studies for monitoring intake of this essential nutrient. Despite the importance of accurate measurement, a standardized method for iodine analysis of biological samples is yet to be established. We have evaluated the effectiveness of ^{72}Ge, ^{115}In, and ^{129}I as internal standards for measurement of iodine in milk and urine samples by induction coupled plasma mass spectrometry (ICP-MS) and of ^{35}Cl^{18}O$_4^-$, ^{129}I$^-$, and 2-chlorobenzenesulfonate (2-CBS) as internal standards for ion chromatography-tandem mass spectrometry (IC-MS/MS). We found recovery of iodine to be markedly low when IC-MS/MS was used without an internal standard. Percent recovery was similarly low using ^{35}Cl^{18}O$_4$ as an internal standard for milk and unpredictable when used for urine. 2-Chlorobenzebenzenesulfonate provided accurate recovery of iodine from milk, but overestimated iodine in urine samples by as much as a factor of 2. Percent recovery of iodine from milk and urine using ICP-MS without an internal standard was ∼120%. Use of ^{115}In predicted approximately 60% of known values for both milk and urine samples. ^{72}Ge provided reasonable and consistent percent recovery for iodine in milk samples (∼108%) but resulted in ∼80% recovery of iodine from urine. Use of ^{129}I as an internal standard resulted in excellent recovery of iodine from both milk and urine samples using either IC-MS/MS and ICP-MS.

1. Introduction

During the present decade there has been great interest on perchlorate in the environment [1,2]. Although unreactive at physiological pH, perchlorate is a powerful competitive inhibitor for the transport of the essential iodide ion via the sodium-iodide symporter [3,4] and excessive intake of perchlorate may result in iodine deficiency. Obviously, this is of greater concern in a population that is already iodine deficient or in a borderline status [5,6]. Iodine nutrition status is generally judged by urinary output [5,7,8]. In addition, iodine content of food for infants, notably milk, is of great importance as iodine nutrition affects the neurodevelopment of the young [9–11]. There is thus great interest in trace determination of iodine, particularly in biological fluids such as milk and urine [12,13].

In milk and urine, iodine dominantly exists as iodide. The classical approach to iodine estimation is the kinetically based Sandell–Kolthoff reaction [14] which exploits the catalysis of the oxidation of As(III) with Ce(IV) by iodide. In idealized standards, the reaction can be followed either colorimetrically (Ce(IV) is yel-

low) or fluorometrically (Ce(III) is fluorescent). However, many other compounds commonly present in biological samples can interfere. Such interferences are typically removed by digesting the sample with chloric acid at 105–115 °C for 30–60 min, however, it is difficult to insure that all interfering species are removed [15]. More recently, digestion with less hazardous ammonium persulfate has replaced chloric acid; it is also easier to use, however, the samples must still be heated to 91–95 °C for 30 min during digestion [16]. Substantial care must be exercised during digestion to prevent the loss of volatile iodine as iodide could potentially be oxidized into iodine by the persulfate. On the positive side, the Sandell–Kolthoff approach is one of the few inexpensively accessible spectrometric approaches that can provide the requisite sensitivity for measuring iodine at low levels in these samples.

Mass spectrometry has long been a formidable tool for qualitative identification; it is also extraordinarily sensitive. Iodine determination by induction coupled mass spectrometry and iodide determination by chromatography–electrospray ionization mass spectrometry have both been widely used. When it comes to quantitative analysis, mass spectrometry is plagued by a number of problems. For accurate quantitation, one must be wary of isobaric interferences and matrix effects [17]. As a general issue in ICP-MS, polyatomic interferences and oxide formation must also

be avoided. Some of these negative effects can be overcome by specific knowledge of the behavior of the analyte of interest. In ICP-MS, oxide formation can be overcome, for example, by properly choosing operating parameters, such as plasma gas composition, nebulizer flow rate, and radio frequency power [17,18]. Isobaric and polyatomic interferences can be overcome by either monitoring a different isotope of the same element or correcting for the interferant by quantitating it as well [17,19]. In ESI-MS isobaric interferences are typically overcome by preceding the MS with a liquid/ion chromatographic separation technique, which temporally separates the analytes that lead to mass fragments of identical mass to charge ratios (m/z, hereinafter the unit Thomson (Th) is used, see Ref. [20]). Non-isomeric isobaric interferences that persist in co-eluting after chromatography can be resolved in ESI-MS by tandem mass spectrometry (MS/MS) techniques.

However, the one problem that cannot be solved is effects that arise from variations in the matrix components or as a result of the matrix itself. Matrix effects in MS constitute a more serious problem in two different ways. First, changing levels of electrolytes in the samples cause dramatic fluctuations in the ionization efficiency [21]. This change in ionization efficiency leads to changing signal intensities recorded by the MS. Second, matrix components can deposit in the MS, such as the entrance cones, and cause residue build up. These deposits can block the entrance to the mass analyzer and cause a reduction in signal over time [22,23]. Together or alone, ionization suppression and residue build up can lead to substantial errors. Unless compensated, such errors can amount to an order of magnitude.

Effects from matrix variations and system stability can be corrected by using internal standards (IS) [24]. ISs are purposefully added to all samples and standards at equal concentrations. The IS is a component that is not indigenously present in any sample or is present at negligible concentrations compared to the amount that is added [25]. The IS should also not significantly affect the concentration of the AI present in the sample. The IS is typically added in equal amounts to all standards and samples. For an IS to function correctly, as system or matrix conditions change, any change in the signal attributed to the constant IS concentration must be reflected in a proportionate change in the analyte of interest (AI). The amount of the IS added should not markedly alter the overall sample composition/ionic strength and the IS should be of similar, but not identical, molecular/atomic weight as the analyte of interest [25,26]. The sensitivity of many mass spectrometers varies with the m/z ratio. Often low m/z ions are not as easily transferred from the ionization source to the mass analyzer compared to higher m/z ions [27,28]. In addition, the sensitivity of the instrument for the AI and IS should be similar for the IS to provide correct matrix compensation; this is especially true in ICP-MS. Finally, the IS should behave in a similar way to the AI. In ICP-MS the IS should have a similar first ionization potential to the AI [25,26]. In chromatography–ESI-MS/MS the IS should have an elution time close to that of the AI (ideally co-elute), so it elutes in a similar matrix as the AI. For this same reason, gradient elution should not be used in nonsuppressed ion chromatography (IC) or liquid chromatography (LC) when using an IS that does not fully co-elute with the AI.

Isotope dilution mass spectrometry (IDMS) [29,30] is a special type of internal standardization in MS quantitation. IDMS uses an isotopically modified version of the AI as the IS. Using an isotopically modified version of the AI is the best way to meet all of the requirements of an IS. In perchlorate analysis, using quadruply ^{18}O-labeled perchlorate ($^{35}Cl^{18}O_4$, 107 Th) as an IS has proven, for example, to be the method of choice for quantitation [31,32]. An isotopically labeled IS must, nevertheless, meet the other requirements outlined earlier; in addition, within the experimental duration, the isotopic labeling must be stable [25].

We compare here the performance of several different species used as ISs for iodide/iodine analysis. For IC-MS/MS we compare the performance of $^{35}Cl^{18}O_4$, ^{129}I, and 2-chlorobenzene sulfonate (2-CBS) as internal standards for iodide quantitation. For ICP-MS we compare the performance of ^{72}Ge, ^{115}In, and ^{129}I as ISs for iodine quantitation. In all cases the iodide quantitation data compensated by the appropriate IS are compared to uncorrected values and to each other.

2. Experimental

2.1. Standards and reagents

All solutions were prepared using 18.2 MΩ cm deionized water (Milli-Q Element A10 ultrapure water system, Millipore). Stock standard solutions (1000 mg/L each) of iodine, germanium, and indium were prepared by dissolving 0.1308 g of KI (www.vwrsp.com), 0.1927 g of InCl$_3$ (www.sial.com) and 0.1441 g of GeO$_2$ (www.Strem.com) in 100 mL of water, 2% HNO$_3$, and 40 mM NaOH, respectively. A 1.0 mg/L quadruply ^{18}O-labeled perchlorate solution (www.iconisotopes.com) and a 100 nCi carrier-free ^{129}I solution as KI (www.ipl.isotopeproducts.com) were purchased. Based on the certified value of the activity, and the known half-life of ^{129}I (1.57×10^7 years), the 100 nCi K^{129}I solution contained ∼56.6 mg/L ^{129}I. Working solutions of 1.0 mg/L of germanium, indium, and $^{129}I^-$ were prepared by diluting 0.1 mL, 0.1 mL, and 1.765 mL, respectively, to a final volume of 100 mL with water. The 2-CBS solution was prepared in the laboratory from alkaline hydrolysis of the corresponding commercially available sulfonyl chloride (www.sial.com).

2.2. Ion chromatography and ESI-MS/MS

All chromatography was preformed on a Dionex DX-600 ion chromatograph with an IS25 isocratic pump, EG40 eluent generator, an ASRS-Ultra 2-mm suppressor and a CD25 conductivity detector. Chromeleon 6.0 chromatography software was used for system control. Separation was performed on a Dionex IonPac AG-16 (2 mm × 50 mm) guard column and IonPac AS-16 (2 mm × 250 mm) anion separation column. The injection loop volume was 25 μL. The eluent used was 60 mM KOH at a flow rate of 0.25 mL/min. The IC effluent was sent to the ESI-MS/MS.

A ThermoElectron TSQ Quantum Discovery Max MS was used in the negative electrospray ionization mode with a heated electrospray ionization probe (HESI) to increase sensitivity. The MS data was acquired using Xcalibur version 2.0 software package. The HESI probe temperature of the ESI-MS was set at 325 °C, the ion transfer capillary was set at 275 °C and the ionization potential was set at 4.5 kV. The MS operated in the selected reaction monitoring mode (SRM). The monitored ions had SRM m/z transitions of: $107.0 \rightarrow 89.0$ ($^{35}Cl^{18}O_4{}^-$), $127.0 \rightarrow 127.0$ ($^{127}I^-$), $129.0 \rightarrow 129.0$ ($^{129}I^-$), and $191.0 \rightarrow 80.0$ (2-CBS, $^{12}C_6H_4{}^{32}S^{16}O_3{}^{35}Cl^-$). Iodide was quantified using the area ratio of iodide to the internal isotopic standard chosen for the correction and compared to a calibration curve composed of AI/IS ratios measured in the prepared standards.

2.3. ICP-MS

An X Series II ICP-MS (www.thermo.com) was used in the direct infusion mode.

The peristaltic pump built into the ICP-MS was used to prime the sample into the Peltier-cooled (3 °C) nebulizer at 1.6 mL/min for 45 s and then continuously aspirate the sample into the nebulizer at 0.8 mL/min. Each measurement cycle consisted of a 20-s qualitative mass survey scan followed by three 32-s long quantitative mass

scans. Once the sampling was complete, the auto sampler probe was washed in DI water for 1 min before storage and reuse.

2.4. Sample preparation and addition of internal standard

Most biological samples must be digested, extracted or otherwise processed before they can be analyzed. Ideally, spiking with an IS should be conducted as the very first step; this is especially true of IDMS. Addition of such an IS as the first step can compensate for any analyte loss during processing. However, for ISs that are not simple isotopically substituted analogs, if analyte loss does occur during sample processing, differential loss behavior of the IS and the AI can render accurate quantitation problematic. Fortunately, initial experiments in the present case for either the milk or urine samples showed that statistically the results did not differ whether the IS was spiked as a first step or just before analysis, suggesting that there was no (differential) loss of the analyte (or the IS) during processing. For the purposes of the present paper, the following reasons led us to chose to generate detailed data where the IS was added just before analysis: (1) the primary motivation was to identify the best (as well as acceptable) IS markers for IC–ESI-MS/MS and ICP-MS determination of iodide/iodine and not to be confounded by recovery issues of specific sample processing methods, (2) much more sample is processed than is analyzed. Often, the processed/extracted samples are diluted further prior to analysis. Adding IS at the first stage and having a reasonable concentration of the IS in the final analyzed sample requires IS amounts that can increase the analytical cost/sample, especially when the IS is expensive, as is often true for an isotopically labeled IS. However, as a general analytical practice we do recommend that the IS be added to the sample prior to any manipulations.

Human milk samples were processed by a streamlined procedure that has been described in detail elsewhere [33]. Briefly, 20 mL aliquots of the milk sample were put in 50-mL capacity centrifuge tubes and centrifuged at 16,000 rpm at 15 °C for 25 min (Sorvall RC-6+, www.thermo.com; Fiberlite F-13-14X50CY rotor, www.piramoon.com). The liquid portion of the resulting sample was decanted to the top of a prewashed PL-10 Centricon Plus-20 centrifugal filter device (UFC2 LGC 24, www.millipore.com). The Centricon devices were centrifuged at 5000 rpm at 15 °C for 90 min. A 0.5 g aliquot of prewashed Amberlyst 15 macroreticular cation-exchange resin (www.sial.com) was added to the dialyzate; the sample was vortexed for 5 min and allowed to stand for 10 min. The sample was then taken into a prewashed 10-mL disposable syringe and passed through a prewashed 25 mm, 0.45 μm pore size nylon membrane syringe filter prior to analysis. Extracted milk samples were spiked with varying levels of iodide for standard recovery experiments. Milk samples were diluted $4\times$ and $10\times$ with water for IC-MS/MS and ICP-MS analysis, respectively. Samples for IC–ESI-MS/MS analysis were spiked to a concentration of 10 μg/L of $^{129}I^-$, 5 μg/L of $^{35}Cl^{18}O_4^-$, and 25 μg/L of 2-CBS prior to being loaded into the auto sampler (Finnigan Surveyor Auto sampler Plus, www.thermo.com). Samples for ICP-MS analysis were spiked to a concentration of 10 μg/L of $^{129}I^-$, ^{72}Ge, and ^{115}In prior to analysis. The milk samples used in this study had been analyzed before in a previous study [6]. The samples were selected such that one sample in each experiment had moderate to low levels of iodide present and the other had high levels of iodide present.

Urine samples were filtered with a 0.45 μm nylon syringe filter and spiked with varying levels of iodide for standard recovery experiments. The samples were then diluted $5\times$ and $10\times$ with water for IC-MS/MS and ICP-MS analysis, respectively. Samples for IC-MS/MS analysis were spiked to a concentration of 10 μg/L of $^{129}I^-$, 5 μg/L of $^{35}Cl^{18}O_4^-$, and 25 μg/L of 2-CBS prior to analysis. Samples for ICP-MS analysis were spiked to a concentration of 10 μg/L of $^{129}I^-$, ^{72}Ge, and ^{115}In prior to analysis. The urine samples used in this study had been collected for a previous study [6] and analyzed before. The samples were selected such that one sample in each experiment had moderate to low levels of iodide present and the other had high levels of iodide present.

2.5. Standard addition and recovery

Stock urine and milk extract samples were split into several equal aliquots and spiked with a high concentration ^{127}I standard to have final spiked iodide concentrations ranging between 0 μg/L and 150 μg/L I. The samples were then spiked with an individual IS whose efficacy was being tested.

2.6. Temporal reproducibility

We conducted a study where various processed milk and urine samples (a total of 25), spiked with the appropriate IS, were each analyzed twice by IC-MS/MS and one particular additional milk sample was additionally inserted randomly in this sequence 10 times, each time being analyzed twice like all the other samples. The results for these 10 repeated probe samples ($n = 2$ ea) are discussed.

3. Results and discussion

3.1. Internal standard selection

The choice of an appropriate IS for mass spectrometric iodine quantitation has not been obvious. Leading researchers in the field had used isotopically labeled perchlorate as an IS for both perchlorate and iodide quantitation [13]. Although this may provide some correction, it may not fully correct for matrix effects due to the different retention times and ionization behavior of the analytes.

A more appropriate selection for an iodide IS might be a compound that co-elutes with iodide. It is known that 4-chlorobenzene sulfonate (4-CBS) co-elutes with perchlorate on certain IC columns [34]. Although iodide and perchlorate do not co-elute, they are both highly polarizable spherical monoanions (the reason why perchlorate physiologically competes with iodide) and elute close to each other. It is reasonable that a different chlorobenzenesulfonate isomer may co-elute with iodide on certain IC columns. We found that of the three isomers (2-, 3-, 4-), 2-CBS elutes the closest (retention time, t_R, 7.3 min) to iodide (t_R, 6.7 min) on an AS-16 (Dionex) IC column under our standard isocratic elution conditions (Fig. 1) and could even be made to co-elute at higher eluent strengths.

The other alternative for an iodine IS is an iodine isotope. Iodine-127 is the only naturally occurring stable isotope of iodine. There are several radioactive iodine isotopes that originate from the nuclear fission of uranium and plutonium [35] or from the cosmic ray spallation of atmospheric xenon [36]. Many of these isotopes, especially ^{131}I, are used in medicine as tracers for nuclear imaging, and for treating various thyroid-related conditions. The major problem with using a radiotracer in mass spectrometry is contamination of the equipment as well as vacuum and vent systems with radioactive material. This will be a particular problem with radioiodine because it is so easily taken up by the mammalian thyroid. Of the 14 major radioactive isotopes of iodine, only ^{129}I has a half-life ($t_{1/2}$) > 60 d. ^{129}I has a $t_{1/2}$ = 15.7 million years [37,38]. ^{129}I is the only isotope of iodine that would not lead to an unacceptable extent of radioactive contamination when used at measurable concentrations. This is because the half-life of ^{129}I is so long that an appreciable concentration represents very little radioactivity; for example, a 5 mL sample aliquot that has been spiked with 10 μg/L level of ^{129}I contains 387 pmol ^{129}I, amounting to <16 pCi in radioactivity. Relative to this, the Nuclear Regulatory commission considers the handling and purchase of up to 100 nCi of ^{129}I exempt from
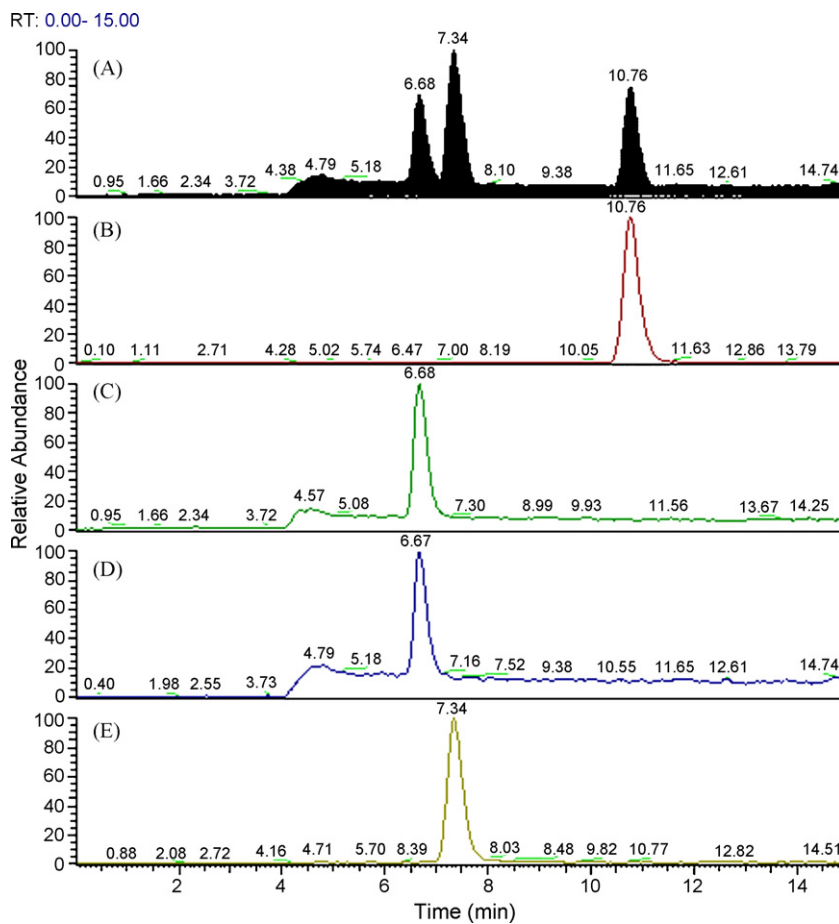
Fig. 1. IC-MS/MS chromatogram of (A) the total ion current, (B) 5 μg/L $^{35}Cl^{18}O_4^-$, (C) 5 μg/L $^{127}I^-$, (D) 10 μg/L $^{129}I^-$, and (E) 25 μg/L 2-chlorobenzene sulfonate.

regulations [39]. ^{129}I decays by weak β- and γ-emissions (64 keV and 25 keV, respectively, [38]), compared to this, on an average the human body contains 0.12 μCi worth of ^{40}K, which also primarily emits β- and γ-emissions (520 keV and 160 keV, respectively) [40,41]. The naturally occurring ratio of ^{129}I to ^{127}I is estimated at 1.5×10^{-12} [42]; it is found in higher ratios only around regions that have experienced nuclear fallout [43,44]. Since iodide derived from ^{127}I and ^{129}I are chemically equivalent, ^{129}I should be an ideal choice as an IS for iodide/iodine quantitation in any type of mass spectrometry; there are, however, no reports of its use thus far in chromatography–MS/MS analysis.

In the case of ICP-MS, germanium, as germanium dioxide, has been claimed to be an appropriate IS for iodide analysis [45,46]. Germanium is an attractive element to use as an IS because it is not abundant in the earth's crust (1.5 mg/kg) [47] and is not likely to be abundant in biological samples. Importantly, it also has a first ionization potential (IP) of 7.9 eV that is not far from that of iodine's (10.45 eV) [48]. Excluding astatine, radon and xenon (which cannot be incorporated into a sample as a tracer for obvious reasons) the 10 elements closest in first IP (spanning 9.4–13.6 V) to iodine are Zn, Se, As, S, Hg, P, C, Br, Cl, and H. These are all likely to be present in biological samples, in varying and possibly significant levels. One drawback for ^{72}Ge is that its m/z ratio (72 Th) is much different from that of iodine (127 Th); this may put iodine and germanium into different intrinsic gain regions of the ICP-MS.

Indium (^{115}In) is a very common IS used in ICP-MS analysis, widely chosen because of its low natural abundance and an intermediate value of 115 Th that falls nearly in the middle of the m/z values for the elements across the periodic table; it is considered a

good IS for many of the mid mass range elements. However, while indium has a close m/z value to that of iodine, at 5.79 eV its first IP is much lower [48].

As with IC–ESI-MS/MS, ^{129}I should be the best IS for iodine analysis as well. Being the same element, they of course have the same IP. The very small difference between the m/z value of the two isotopes puts them into the same sensitivity range of the ICP-MS. The analytical problem of measuring iodine in foods and other biological material has been a challenging one and it has been so acknowledged for some time [49]. The advent of the ICP-MS did not necessarily mean that this was accepted as the best and most accurate solution. The use of ^{129}I as an IS for iodine determination by ICP-MS was simultaneously introduced by three different groups [50–52]. Haldimann et al., one of these pioneers, have continued to use ^{129}I as IS [53–55] and although they initially reported significant iodide memory effects in the nebulizer and some isobaric interference from ^{129}Xe present in the argon gas. Others have used ^{129}I as an IS with solid samples with the further addition of Pd, this iodophilic element prevents iodine loss during ashing and removal of organics [56]. Recently Bruchert et al. have used ^{129}I enriched iodide and iodate in gel electrophoresis coupled to an ICP-MS to measure these species in aerosol samples [57]. However, overall, not many have adopted ^{129}I as the IS of choice in iodine determination. Beginning with NHANES 2000, the Centers for Disease Control had adopted ICP-MS as the preferred method of iodine analysis in urine but utilized ^{130}Te as the IS [58]. The difference plots vs. the Sandell–Kolthoff method suggested that significant differences may exist for individual samples. Similarly, recent work by others continues to use other ISs, e.g., ^{103}Rh [59].
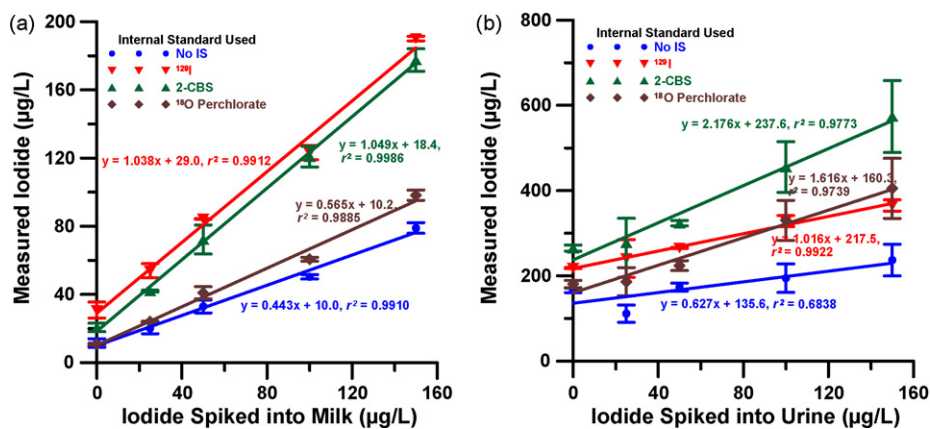
Fig. 2. Iodide recoveries (a) for a milk sample (Milk-1, Table 1) and (b) for a urine sample (Urine-2, Table 1). Different ISs were used to correct the iodide data obtained on an IC-MS/MS. The error bars indicate ±1 standard deviation.

3.2. Standard addition and recovery

A good way to measure the effectiveness of an IS is to perform a standard addition experiment. Data from spiked samples (see Section 2) were collected and processed using the respective IS response for correction. These corrected data were compared among themselves as well as to results obtained without any correction. The correspondence of the slope of the standard addition plot (vide infra) to unity indicates the efficacy of a particular IS for the intended correction.

3.3. Spike recovery for added iodide IC-MS/MS

Fig. 2a and b shows the standard addition results of a milk and urine sample, respectively. When no ISs were used, poor recoveries (slope of the standard addition curve 0.323 ± 0.090 to 0.854 ± 0.251) were observed for both milk and urine. These data are summarized in Table 1. Obviously, the quantitation of iodide/iodine is quite poor without an IS.

The use of ^{18}O enriched perchlorate as an IS for iodide turns out to be a poor choice as well: the recoveries ranged from $38.0 \pm 7.4\%$ to $161.6 \pm 15.3\%$. Three of the four samples analyzed showed recoveries below 78.1%, while one gave a significantly superquantitative recovery. This is likely due to the significantly different retention times of the two analytes in the chromatographic system resulting in varying amounts of other ion precursors eluting in the different temporal windows from one sample to another. The matrix composition thus changes dramatically in the windows that iodide and perchlorate elute and the two analytes are thus detected in very different matrices in different samples, regardless of any similarity between the analytes themselves. If in fact the two analytes also differ in their ionization behavior, further inaccuracies in quantitation will occur. It is to be noted that perchlorate was analyzed using the MS/MS mode and was fragmented in the second quadrupole of the triple quadrupole system during the analysis, while iodide, a monoatomic species, was not fragmented. Rather in the latter case

we sought to fragment most everything else that may be present with iodide in the second quadrupole such that the only 127 Th species to enter the third quadrupole should be iodine. However, even if the latter strategy is successful, it cannot compensate if differing extents of ^{127}I$^-$ are formed in the ionization process and are selected by the first quadrupole.

Using 2-CBS as an IS has the advantage of more accurately reflecting the background matrix of the iodide peak as it elutes very close to iodide. In milk samples, 2-CBS indeed appears to be a good IS for iodide. It shows recoveries that range from $102.1 \pm 14.6\%$ to $104.9 \pm 2.3\%$ for the two test milk samples. However, the recovery of iodide using 2-CBS as an IS in urine samples is very different. In urine the iodide spike recovery was found to be between $206.2 \pm 6.7\%$ and $217.6 \pm 19.1\%$. Since the IS correction is calculated as an area ratio of the iodide signal to the IS signal a recovery of 200% indicates that the 2-CBS signal has been reduced by ~50% relative to iodide. It appears that some other species present in the Urine matrix may be selectively suppressing the ionization and detection of 2-CBS. Even though 2-CBS elutes near iodide and works well for milk samples, it is clear that it cannot be applied to all samples.

The best results were obtained with ^{129}I-iodide as the IS. For the two initial test samples, the recoveries were $101.4 \pm 6.2\%$ and $98.9 \pm 6.2\%$, respectively, for milk and urine (Table 1). These were by far the best recoveries for iodide in both milk and urine samples taken together. The isotopic IS has the advantage that it not only co-elutes with iodide but it behaves identically to the analyte in the ionization process and has a very similar mass. The disadvantage to using the ^{129}I isotope is that trace amounts of ^{127}I are present within the stock solution. This results in a small amount of ^{127}I being added to the sample. However, since the same amount is added to all samples and standards, the minute amount is corrected by running a blank sample in the calibration curve. The cost of ^{129}I is not insignificant; 10 mL of a 5 mg/L stock solution costs over US$500 whereas 2-CBS can be readily made from 2-chlorobenzenesulfonyl chloride at a negligible cost.

Table 1
Iodide recoveries in milk and urine samples using different internal standards for signal correction on an IC-MS/MS. Slopes and correlation coefficients resulting from duplicate analysis of matrix spiked at five levels with ^{127}I and quantified using four different IS approaches.

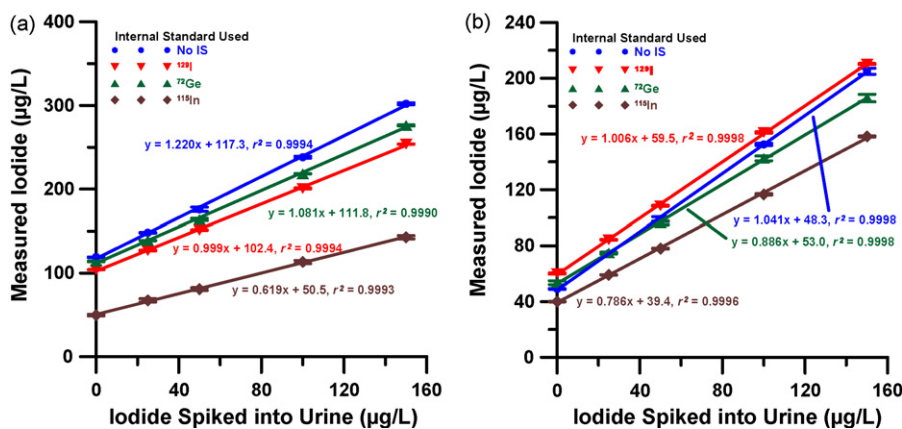|	% Recovery, IC-MS/MS			
	No IS	^{129}I	2-CBS	^{18}O perchlorate
Milk #1	44.3 ± 2.4 ($r^2 = 0.9910$)	103.8 ± 5.7 ($r^2 = 0.9912$)	104.9 ± 2.3 ($r^2 = 0.9986$)	56.5 ± 3.5 ($r^2 = 0.9885$)
Milk #2	32.3 ± 9.0 ($r^2 = 0.8101$)	98.9 ± 2.7 ($r^2 = 0.9977$)	102.1 ± 14.6 ($r^2 = 0.9422$)	38.0 ± 7.4 ($r^2 = 0.8984$)
Urine #1	85.4 ± 25.1 ($r^2 = 0.7937$)	96.2 ± 3.2 ($r^2 = 0.9966$)	206.2 ± 6.7 ($r^2 = 0.9969$)	78.1 ± 2.4 ($r^2 = 0.9971$)
Urine #2	62.7 ± 24.6 ($r^2 = 0.6838$)	101.6 ± 5.2 ($r^2 = 0.9922$)	217.6 ± 19.1 ($r^2 = 0.9773$)	161.6 ± 15.3 ($r^2 = 0.9739$)

Fig. 3. Iodide recoveries from (a) milk and (b) urine sample. Different ISs were used to correct the iodide data obtained on an ICP-MS. The error bars indicate ±1 standard deviation.

3.4. Spike recovery for added iodide ICP-MS

Iodide spike recoveries were greater than 100% when no IS was used to correct the raw ICP-MS data, as seen in Fig. 3a and b and Table 2. Iodine recovery was acceptable in only one of the urine samples ($104.1 \pm 0.8\%$). The other three samples exhibited a recovery averaging 120%.

While ^{115}In may be a widely used IS for ICP-MS analysis, it performed poorly for iodine determination for both milk and urine, showing the lowest recoveries ($61.9 \pm 0.9\%$ and $53.0 \pm 7.1\%$, respectively) of the three evaluated ISs. The lower IP of indium (5.8 eV vs. 10.5 eV for I) allows it to be more easily ionized by the argon plasma than iodine which results in underestimation of the latter.

Germanium has been reported as an appropriate IS for iodide analysis [45] and we have ourselves shown its suitability as an IS for iodine in iodized table salt samples [46]. However, diluted table salt solutions at a more or less constant concentration represent a more or less invariant matrix compared to biological samples such as milk and urine. With ^{72}Ge is used as an IS for iodine analysis in milk it shows recoveries are only slightly high ($108 \pm 1\%$). However, the recoveries were much lower (80.5–88.7%) for urine samples. The presence of Ge in urine is not the likely reason as Ge urinary concentrations in populations not subjected to occupational exposure to Ge are usually below the typical ICP-MS LOD for Ge ($0.25\,\mu g/L$) [60]. Compared to In, the first ionization potential of Ge (7.9 eV) is closer to that of iodine but the m/z value is much less which may affect the correction. In any case, ^{72}Ge obviously would not appear to be a generally applicable choice as an IS for iodine analysis in all biological matrices.

As with IC-MS/MS, ^{129}I was the best choice as an IS for iodide analysis by ICP-MS as well. Iodide spike recoveries were $99.1 \pm 2.2\%$ for milk and $102.6 \pm 5.7\%$ for urine. No other IS provided recoveries in both matrices that were as good.

3.5. Temporal reproducibility

Measurement reproducibility is an important consideration – in theory, even if an IS indicates low recovery, it can be successfully used if the recovery is consistently reproducible across samples. With many real samples, especially biological samples, traces of salt and organic matter can be deposited on various system components, especially the sample/skimmer cones between the atmospheric pressure region and the high vacuum region. In ICP-MS, material is also deposited in the torch. In IC-MS/MS, the ion transfer tube and electrospray needles are other susceptible regions. All can affect the eventual signal.

To an extent, a good IS may be able to correct for such changing conditions within the MS. If it is unable to do so, a consistent change in the quantitative results will be seen as the same sample is run repeatedly. As described in the experimental section, the IC-MS/MS results for a total of 25 samples, each spiked with the appropriate IS, were each analyzed twice with one particular additional milk sample additionally inserted randomly in this sequence 10 times, each time being analyzed twice like all the other samples. The results for these 10 repeated probe samples ($n = 2$ ea) are shown in Fig. 4, as other samples are run. All results are reported with the first measurement of the test probe (Sample #3) normalized as 100; (based on the average of the measurements based on the ^{129}I IS, this sample contained $78.4 \pm 4.9\,\mu g/L$ I). Note that #1–15 are milk samples while #16–34 (with the exception of the repeated probe milk samples # at 23, 26, 29, 32, (and 35)) are urine samples.

It will be observed that without any IS, even before the urine samples are run, the variability within individual measurements are very high, reaching to >50% in relative standard deviation. After beginning to run the urine samples, the situation only gets worse: The results range from ~45% to ~127% of the original value. Using the ^{35}Cl^{18}O$_4$ as IS provided somewhat better reproducibility and

Table 2
Iodide recoveries in milk and urine samples using different internal standards for signal correction on an ICP-MS. Slopes and correlation coefficients resulting from duplicate analysis of matrix spiked at five levels with ^{127}I and quantified using four different IS approaches.

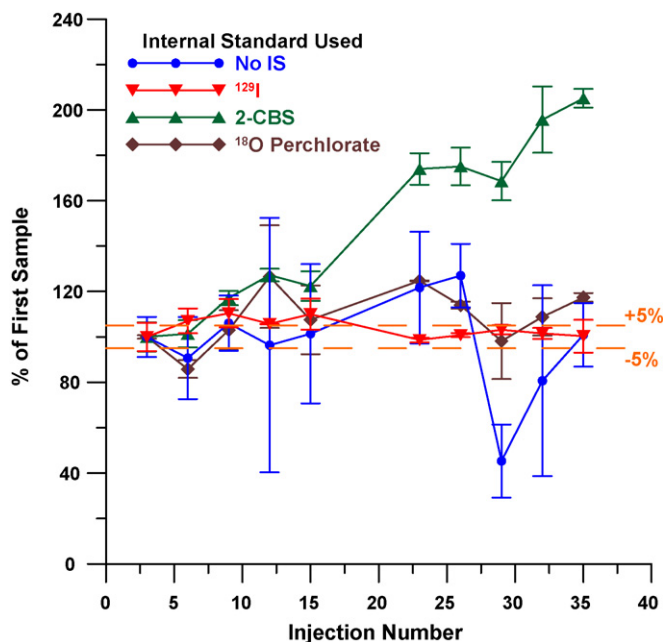|	% Recovery, ICP-MS			
	No IS	^{129}I	^{72}Ge	^{115}In
Milk #1	118.0 ± 1.9 ($r^2 = 0.9993$)	98.3 ± 1.7 ($r^2 = 0.9991$)	108.0 ± 1.4 ($r^2 = 0.9995$)	64.7 ± 1.5 ($r^2 = 0.9985$)
Milk #2	122.0 ± 1.8 ($r^2 = 0.9994$)	99.9 ± 1.4 ($r^2 = 0.9994$)	108.1 ± 2.0 ($r^2 = 0.9990$)	61.9 ± 0.9 ($r^2 = 0.9993$)
Urine #1	119.5 ± 3.8 ($r^2 = 0.997$)	104.6 ± 5.8 ($r^2 = 0.9910$)	80.5 ± 5.0 ($r^2 = 0.9886$)	53.0 ± 7.1 ($r^2 = 0.9486$)
Urine #2	104.1 ± 0.8 ($r^2 = 0.9998$)	100.6 ± 0.9 ($r^2 = 0.9998$)	88.6 ± 0.7 ($r^2 = 0.9998$)	78.6 ± 0.9 ($r^2 = 0.9996$)

Fig. 4. Reproducibility of iodide measurement in a milk sample using different internal standards for signal correction. Data were collected using an IC-MS/MS. The error bars indicate ±1 standard deviation.

Fig. 5. Reproducibility of iodide measurement in a milk sample using different internal standards for signal correction. Data were collected using an ICP-MS. The error bars indicate ±1 standard deviation.

there was no consistent trend with time. However, the results varied from 86% to 126% relative to the initial measurement. Using 2-CBS on the other hand, one sees a continuous and consistent increase in the IS-corrected signal with time, indicating that the detection of the 2-CBS derived ion was being increasingly affected by the changing conditions of the MS; by the end of the experiment, the same sample was being measured at twice its original value.

Using ^{129}I as the IS was much better in comparison to the above – the average of all 10 runs was $103.8 \pm 4.3\%$ of the first run. To be fair, even ^{129}I was not a panacea; while significant underestimation was rare, up to 10% overestimation was observed on two occasions. This should be regarded as the ultimate performance limits in absolute accuracy with these types of samples.

A similar experiment was conducted with 21 milk and urine samples on an ICP-MS, in between which the same probe milk sample as above was interspersed 10 times. In this case, each sample was measured three times. The results are shown in Fig. 5. Using no IS here actually provides good reproducibility ($99.4 \pm 0.7\%$ of first run) until the urine samples are run (beginning with run 17). From that point, the signal consistently increases with time. Exactly the opposite is observed when the results are corrected with ^{72}Ge as an IS. With only milk samples run, the results showed excellent reproducibility ($100.6 \pm 0.4\%$) but soon as urine samples were analyzed, the recovery started decreasing consistently. This is mirror image behavior in comparison with the raw signal (no IS) and suggests that the ^{72}Ge IS signal probably remains invariant – the observed results are largely, if not wholly, due to the ^{127}I signal actually increasing with time.

Overall this behavior was understandable. Considerable care was taken to remove fats, proteins, and all material with MW > 10,000 from the from the milk matrix. The resulting sample is very clean as compared to the raw milk. On the other hand, the urine samples were merely diluted 10-fold. The urine matrix consists primarily of water, salts, urea/ammonia, and several small organic molecules. Urine samples contained significantly more dissolved solids than the processed milk samples. In the case of IC-MS/MS, the chromatography itself provides for significant sample cleanup
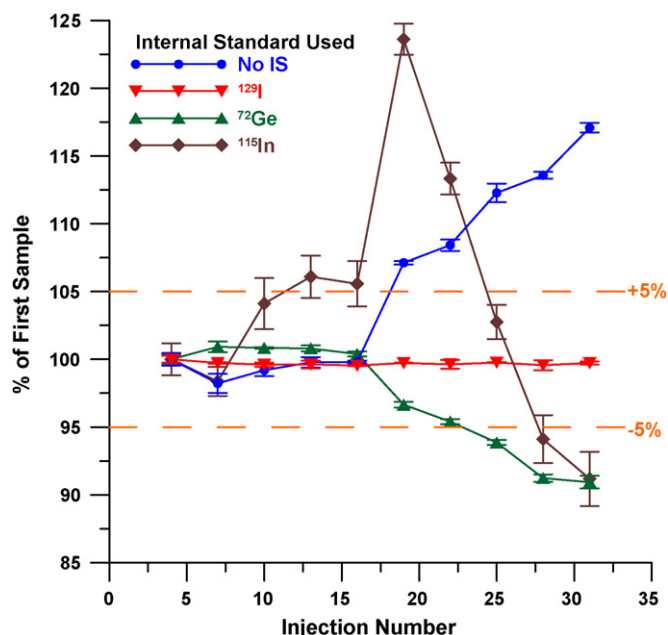
(very little of the original accompanying material elutes in the window where the column effluent is directed to the MS to monitor the peak(s) of interest), whereas in the absence of a chromatography step preceding it, direct determination by ICP-MS is affected much more significantly. The use of ^{115}In as IS results in unpredictable behavior. Prior to running urine samples, the signal of the probe milk sample was more or less reproducible ($102.8 \pm 3.4\%$), it increased abruptly to 123.6% of the first run after the first urine sample and decreased slowly thereafter as more urine samples were run.

Again, ^{129}I showed the greatest stability of all ISs used; the performance in this case was nearly flawless. All data ranged between 99.5% and 100% of the first run and the worst relative standard deviation was 0.4%. The average of all 10 runs was $99.7 \pm 0.1\%$ of the first sample. This suggests that under normal circumstances iodine measurements will be largely unaffected by the cleanliness of the sample and the mass spectrometer with the use of this IS.

4. Conclusions

For almost any real sample analysis by mass spectrometry, reliable quantitative results cannot be obtained without the use of an appropriately chosen IS. Some ISs, such as 2-CBS or ^{72}Ge, may be useful for iodide/iodine analysis for certain types of samples, but it is clear that neither are appropriate for all types of biological samples. Other ISs, such as ^{18}O enriched perchlorate and ^{115}In do not appear to be very reliable for iodide/iodine measurements. By far the best IS to use for iodide analysis is the isotope ^{129}I. Although it is radioactive, the 16 million year half-life of ^{129}I leads to very little cause for concern from its radioactivity. A long half-life also means that the concentration of a standard solution does not change appreciably. It is an excellent choice as an IS for iodide/iodine analysis by MS; its low natural abundance helps the cause. It is versatile in its ability to provide matrix corrections for both milk and urine and also in compensating for changing conditions in the mass spectrometer itself.

Acknowledgments

References

[1] P.K. Dasgupta, K. Martinelango, W.A. Jackson, T.A. Anderson, K. Tian, R.W. Tock, S. Rajagopalan, Environ. Sci. Technol. 39 (2005) 1569–1575.
[2] A.B. Kirk, P.K. Martinelango, K. Tian, A. Dutta, E.E. Smith, P.K. Dasgupta, Environ. Sci. Technol. 39 (2005) 2011–2017.
[3] O. Dohan, C. Portulano, C. Basquin, A. Reyna-Neyra, L.M. Amzel, N. Carrasco, Proc. Natl. Acad. Sci. U.S.A. 104 (2007) 20250–20255.
[4] N. Tran, L. Valentin-Blasini, B.C. Blount, C.G. McCuistion, M.S. Fenton, E. Gin, A. Salem, J.M. Hershman, Am. J. Physiol. Endocrinol. Metab. 294 (2008) E802–E806.
[5] E.N. Pearce, H.R. Bazrafshan, X. He, S. Pino, L.E. Braverman, Thyroid 14 (2004) 327–328.
[6] P.K. Dasgupta, A.B. Kirk, J.V. Dyke, S.-I. Ohira, Environ. Sci. Technol. 42 (2008) 8115–8121.
[7] J.G. Hollowell, N.W. Staehling, W.H. Hannon, D.W. Flanders, E.W. Gunter, G.F. Maberly, L.E. Braverman, S. Pino, D.T. Miller, P.L. Garbe, D.M. DeLozier, R.J. Jackson, J. Clin. Endocrinol. Metab. 10 (1998) 3401–3408.
[8] S.-I. Ohira, A.B. Kirk, J.V. Dyke, P.K. Dasgupta, Environ. Sci. Technol. 42 (2008) 9419–9423.
[9] B.S. Hetzel, Lancet 2 (1983) 1126–1127.
[10] P. Laurberg, S.B. Nohr, K.M. Pedersen, A.B. Hreidarsson, S. Andersen, I.B. Pedersen, N. Kudsen, H. Perrild, T. Jorgensen, L. Ovesen, Thyroid 10 (2000) 951–963.
[11] J.B. Stanbury, A.E. Ermans, P. Bourdoux, C. Todd, E. Oken, R. Tonglet, G. Vidor, L.E. Braverman, G. Medeiros-Neto, Thyroid 8 (1998) 83–100.
[12] A.B. Kirk, J.V. Dyke, C.F. Martin, P.K. Dasgupta, Environ. Health Perspect. 115 (2007) 182–186.
[13] B.C. Blount, L. Valentin-Blasini, Anal. Chim. Acta 567 (2006) 87–93.
[14] E.B. Sandell, I.M. Kolthoff, Mikrochim. Acta 1 (1937) 9–25.
[15] J. Benotti, N. Benotti, S. Pino, H. Gardyna, Clin. Chem. 11 (1965) 932–936.
[16] S. Pino, S.L. Fang, L.E. Braverman, Clin. Chem. 42 (1996) 239–243.
[17] D.A. Skoog, F.J. Holler, T.A. Nieman, Principles of Instrumental Analysis, 5th ed., Harcourt Brace, New York, 1998, pp. 262–269.
[18] P. Dulski, Fresenius J. Anal. Chem. 350 (1994) 194–203.
[19] K.J.R. Rosman, P.D.P. Taylor, Pure Appl. Chem. 70 (1998) 217–235.
[20] R.G. Cooks, A.L. Rockwood, Rapid Commun. Mass Spectrom. 5 (1991) 93.
[21] S. Tan, G. Horlick, J. Anal. At. Spectrom. 2 (1987) 745–763.
[22] T. Akagi, T. Hirata, A. Masuda, Anal. Sci. 6 (1990) 397–400.
[23] D.T. Heitkemper, J.A. Caruso, Appl. Spectrosc. 44 (1990) 228.
[24] E.H. Evans, J.J. Giglio, J. Anal. At. Spectrom. 8 (1993) 1–18.
[25] S.M. Nelms, ICP Mass Spectrometry Handbook, Blackwell, Boston, 2005, pp. 150–175.
[26] J.J. Thompson, R.S. Houk, Appl. Spectrosc. 41 (1987) 801–806.
[27] E.C. Kempen, J.S. Brodbelt, Anal. Chem. 72 (2000) 5411–5416.
[28] J.C. Schwartz, M.W. Senko, J.E.P. Syka, J. Am. Soc. Mass Spectrom. 13 (2002) 659–669.
[29] J.D. Fassett, P.J. Paulsen, Anal. Chem. 61 (1989) 643A–649A.
[30] A. Lasztity, M. Viczian, X. Wang, R.M. Barnes, J. Anal. At. Spectrom. 4 (1989) 761–766.
[31] United States Environmental Protection Agency, Determination of Perchlorate in Drinking Water by Liquid Chromatography Electrospray Ionization Mass Spectrometry http://www.epa.gov/safewater/methods/pdfs/methods/met331_0.pdf Accessed January 6, 2009.
[32] P.K. Martinelango, J.L. Anderson, P.K. Dasgupta, D.W. Armstrong, R.S. Al-Horr, R.W. Slingsby, Anal. Chem. 77 (2005) 4829–4835.
[33] J.V. Dyke, A.B. Kirk, P.K. Martinelango, P.K. Dasgupta, Anal. Chim. Acta 567 (2006) 73–78.
[34] L. Yu, Q. Cheng, J. Canas, L. Valentin-Blasini, B.C. Blount, T. Anderson, Anal. Chim. Acta 567 (2006) 66–72.
[35] B.C. Purkayastha, G.R. Martin, Can. J. Chem. 34 (1956) 293–300.
[36] D.R. Schink, P.H. Santschi, O. Corapcioglu, P. Sharma, U. Fehn, Earth Planet. Sci. Lett. 135 (1995) 131–138.
[37] J.F. Emery, S.A. Reynolds, E.I. Wyatt, G. Gleason, Nucl. Sci. Eng. 48 (1972) 319–323.
[38] Argonne National Laboratory, Human Health Fact Sheet, Iodine, http://www.ead.anl.gov/pub/doc/iodine.pdf Accessed January 14, 2008.
[39] United States Nuclear Regulatory Commission, October 1, 2007, 10 CFR 30.71 Schedule B, http://www.nrc.gov/reading-rm/doc-collections/cfr/part030/part030-0071.html.
[40] G. Kramer, Environmental and Background Radiation — Food and the Human Body, http://www.hps.org/publicinformation/ate/q322.html.
[41] Argonne National Laboratory, Potassium-40, http://www.ead.anl.gov/pub/doc/potassium.pdf.
[42] J.E. Moran, U. Fehn, R.T.D. Teng, Chem. Geol. 152 (1998) 193–203.
[43] U. Rao, U. Fehn, Y. Muramatsu, H. McNeil, P. Sharma, D. Elmore, Environ. Sci. Technol. 36 (2002) 1271–1275.
[44] G. Krupp, D.C. Aumann, J. Environ. Radioact. 46 (1999) 287–299.
[45] T. Eickhorst, A. Seubert, J. Chromatogr. A 1050 (2004) 103–109.
[46] P.K. Dasgupta, Y. Liu, J.V. Dyke, Environ. Sci. Technol. 42 (2008) 1315.
[47] D.R. Lide, CRC Handbook of Chemistry and Physics, 74th ed., CRC Press, Boca Raton, FL, 1993, p. 14-9.
[48] Environmental, Chemistry & Hazardous Materials News, Careers & Resources, Periodic Table of Elements Sorted by 1st Ionization Potential (eV), http://environmentalchemistry.com/yogi/periodic/1stionization.html Accessed January 14, 2009.
[49] J.A. Pennington, S.A. Schoen, G.D. Salmon, B. Young, R.D. Johnson, R.W. Marts, J. Food Compos. Anal. 8 (1995) 171–217.
[50] G. Radlinger, K.G. Heumann, Anal. Chem. 70 (11) (1998) 2221–2224.
[51] M. Haldimann, B. Zimmerli, C. Als, H. Gerber, Clin. Chem. 44 (1998) 817–824.
[52] Y. Gelinas, G.V. Iyengar, R.M. Barnes, Fresenius J. Anal. Chem. 5 (1998) 483–488.
[53] M. Haldimann, A. Eastgate, B. Zimmerli, Analyst 125 (2000) 1977–1982.
[54] M. Haldimann, A. Alt, A. Blanc, K. Blondeau, J. Food Compos. Anal. 18 (2005) 461–471.
[55] M. Haldimann, R. Wegmuller, M. Zimmermann, Eur. Food Res. Technol. 218 (2003) 96–98.
[56] M. Resano, E. Garcia-Ruiz, L. Moens, F. Vanhaecke, J. Anal. At. Spectrom. 20 (2005) 81–87.
[57] W. Bruchert, A. Helfrich, N. Zinn, T. Klimach, M. Breckheimer, H.W. Chen, S.C. Lai, T. Hoffmann, J. Bettmer, Anal. Chem. 79 (2007) 1714–1719.
[58] K.L. Caldwell, C.B. Maxwell, A. Makhmudov, S. Pino, L.E. Braverman, R.L. Jones, J.G. Hollowell, Clin. Chem. 49 (2003) 1019–1021.
[59] P. Macours, J.C. Aubry, B. Hauquier, J.M. Boeynaems, S. Goldmanc, R. Moreno-Reyes, J. Trace Elem. Med. Biol. 22 (2008) 162–165.
[60] H.A. Roels, J.P. Buchet, J. Environ. Monit. 3 (2001) 67–73.

Simultaneous chemiluminescence determination of promazine and fluphenazine using support vector regression

Ali A. Ensafi[*], F. Hasanpour, T. Khayamian

Department of Chemistry, Isfahan University of Technology, Isfahan 84156-83111, Iran

ABSTRACT

In this work, chemiluminescence (CL) behaviors of two selected phenothiazines, namely promazine and fluphenazine hydrochloride, were investigated for their simultaneous determination using oxidation of $Ru(bipy)_3^{2+}$ by Ce^{4+} ions in acidic media. This method is based on the kinetic distinction of the CL reactions of fluphenazine and promazine with $Ru(bipy)_3^{2+}$ and Ce^{4+} system in a sulfuric acid medium. Least square support vector regression models were constructed for relating concentrations of both compounds to their CL profiles. The parameters of the model consisting of σ^2 and γ were optimized using all possible combinations of σ^2 and γ to select the model with the minimum root mean square cross validation. Under optimized conditions, the univariate calibration curve was linear over the concentration ranges of 0.4–30.0 $\mu g\,mL^{-1}$ and 0.07–5.0 $\mu g\,mL^{-1}$ with detection limits of 0.1 $\mu g\,mL^{-1}$ and 0.04 $\mu g\,mL^{-1}$ for promazine and fluphenazine, respectively. The influence of potential interfering substances on the determination of promazine and fluphenazine were studied. The proposed method was used for simultaneous determination of both compounds in synthetic mixtures and in spiked human plasma.

© 2009 Elsevier B.V. All rights reserved.

1. Introduction

Phenothiazines, referred to as major tranquilizers, produce a specific improvement in the behavior of psychotic patients without causing addiction [1,2]. Monitoring of such compounds in human fluid is important for toxicological indicators. However, it is difficult to detect these trialkylamine compounds as they do not absorb very well in the UV–vis region since they have low molar absorptivities. Phenothiazines have a phenothiazine ring with different substituents attached at the 2- and 10-position. Piperazine and aliphatic derivatives are two main classes of phenothiazines those differ with respect to the substituent on nitrogen atom. Fluphenazine, 2-[4-[3-[2-(trifluoromethyl)-10H-phenothiazin-10-yl] propyl]-piperazin-1-yl] ethanol, belongs to the piperazine class of phenothiazines. Due to its neuroleptic and antidepressive effects, fluphenazine has been widely used in the treatment of psychotic patients [3].

Promazine hydrochloride (PMH), chemically known as 3-(10H-phenothiazin-10-yl)-N,N-dimethylpropan-1-amine hydrochloride, is an aliphatic phenothiazine. It is mainly used as an antipsychotic and antiemetic agent and, additionally, as an adjunct agent in the management of severe pain [4]. Selected phenothiazines (promazine and fluphenazine) are frequently used with psychotic patients in psychiatric practice. The toxic thresholds of promazine

and fluphenazine in plasma were reported to be 1 $\mu g\,mL^{-1}$ and 0.1 $\mu g\,mL^{-1}$, respectively [5].

Several analytical techniques have been applied for the determination of those drugs including electrophoresis [6,7], spectrophotometry [8,9], and electrochemistry [10,11]. For the determination of similar multi-component mixtures (such as phenothiazines), most detection systems are combined with HPLC [12,13] and GC [14]. These separation techniques usually require time-consuming sample preparations and, in some cases, derivatization as well.

Chemiluminescence is known as a powerful analytical technique with high sensitivity, wide linear range and simple instrumentation. However, CL faces the challenge of selectivity in the case of similar structure compounds. In recent years, a combination of powerful multivariate calibration methods and some analytical techniques has been used to allow for simultaneous determination of multi-component compounds without previous separation. Support vector machine is an algorithm based on statistical learning theory introduced by Cortes and Vapnik [15]. Support vector models (SVMs) were originally developed to solve the classification problem, but they have been extended to solve regression problems, as well [16].

In this work, the CL detection system in conjugation with the least square support vector regression model (LS-SVM) was used to synchronously determine fluphenazine and promazine. This method is based on different reduction rates of Ru^{3+} produced in the reaction between $Ru(bipy)_3^{2+}$ and acidic Ce^{4+} by promazine and fluphenazine. LS-SVM models were constructed to relate CL profiles

* Corresponding author. Tel.: +98 311 3913268; fax: +98 311 3912350.
E-mail address: Ensafi@cc.iut.ac.ir (A.A. Ensafi).

Table 1
Analytical parameters of the previous CL methods for the determination of promazine and fluphenazine ($\mu g\,mL^{-1}$).

Species	CL reaction	Linear ranges	Detection limits	References
Fluphenazine	Ce^{4+} reaction sensitized by Rhodamine B	0.5–90	0.01	[17]
Fluphenazine	Luminol–$KMnO_4$ reaction	0.0020–5.0	0.002	[18]
Promazine	Electrogenerated tris(2,2-bipyridyl)Ru^{3+}	1.6–320	0.17	[19]
Promazine	Electrogenerated tris(2,2-bipyridyl)Ru^{3+}	0.32–128	0.16	[20]
Promazine	Luminol-ferricyanide	0.145–2.00	0.080	[4]
Promazine*	$Ru(bipy)_3{}^{2+}$-Ce^{4+}	0.4–30.0	0.1	Proposed method
Fluphenazine*	$Ru(bipy)_3{}^{2+}$-Ce^{4+}	0.07–5.0	0.04	Proposed method

* Simultaneous determination of promazine and fluphenazine.

of promazine and fluphenazine to their concentrations. The model predicts promazine and fluphenazine concentrations in synthetic mixtures and spiked plasma. Table 1 summarizes the analytical parameters in the previously reported CL methods and in our proposed method for the determination of the two drugs under study.

2. Theory

2.1. Theory of least square support vector regression

Least square support vector machines (LS-SVMs) are an alternate formulation of SVM described by Suykens et al. [21]. The LS-SVM can resolve linear and non-linear multivariate calibration problems in a relatively fast manner. A detailed description of the application of LS-SVM to quantification is reported in [22,23]. Here, we will only briefly describe the theory of LS-SVM. Linear least square models fit a linear relation between the spectrum x_i and the reference value y_i, where y_i and x_i denote the i-th column of Y and X, respectively; and X represents a $[n \times p]$ matrix containing p spectral responses of n samples. Y is computed from Eq. (1):

$$(Y = \omega X + b_0) \tag{1}$$

The best relation is attained when the cost function (Q) containing a penalized regression (e_i) error term is minimized:

$$Q = \frac{1}{2}\omega^T\omega + \frac{1}{2}\gamma\sum_{i=1}^{N}e_i^2 \tag{2}$$

subject to:

$$y_i = \omega^T\phi(x_i) + b_0 + e_i \qquad i = 1, \ldots, n \tag{3}$$

where φ denotes the feature map, ω is a weight decay which is used to regularize weight sizes and penalize large weights and b_0 is the model offset. The second part of the cost function is used to minimize the error of training data. SVMs regression is based on kernel substitution where X is replaced by a $[n \times n]$ kernel matrix (K). K is defined as:

$$\kappa = \begin{pmatrix} k_{1,1} & \cdots & k_{1,n} \\ \vdots & \ddots & \vdots \\ k_{n,1} & \cdots & k_{n,n} \end{pmatrix} \tag{4}$$

where k_{ij} is defined by the kernel function:

$$k_{i,j} = \langle \phi(x_i).\phi(x_j) \rangle \tag{5}$$

Kernel functions are defined as any function in the input space corresponding to an inner product in some feature space. There are a number of kernels that can be used in support of vector machines. These include linear, polynomial, radial basis function (RBF) and sigmoid. The RBF, $\exp(-||x_i - x_j||^2/2\sigma^2)$, is by far the most popular choice of kernel types because of their localized and finite responses across the entire range of the real x-axis. In order to achieve a good generalization model, it is important to do careful tuning of the RBF kernel constant, σ, and regularization constant, γ, for training data.

3. Experimental

3.1. Instrumentation and software

CL analysis was applied using a 0.50 cm light path length quartz cell. The chemiluminescence signal was measured by a Hammamatso PMT (mode R_{212}) using a low pass filter whose output was connected to a data processing system.

Spectrometric measurements were performed using a UV–vis spectrophotometer, JASCO V-570 (PMT). The free LS-SVM toolbox (LS-SVM v1.5, Suykens, Leuven, Belgium) was used with MATLAB to derive all the LS-SVM models.

3.2. Reagents

All the solutions were prepared using reagent grade chemicals and doubly distilled water.

Promazine and fluphenazine standard solutions ($0.30\,mg\,mL^{-1}$) were daily prepared by dissolving 30.0 mg of each compound (Sigma–Aldrich, Germany) in 100 mL of water, stored in a refrigerator and protected from light. The working solutions were prepared by appropriately diluting the stock solution. $Ru(bipy)_3{}^{2+}$ stock solution ($1.0 \times 10^{-2}\,mol\,L^{-1}$) was prepared by dissolving 0.3740 g of tris(2,2′-bipyridyl) dichlororuthenium(II) hexahydrate (Sigma–Aldrich) in 50 mL of water.

Ce^{4+} solution ($1.0 \times 10^{-2}\,mol\,L^{-1}$) was prepared by dissolving 0.548 g of ceric ammonium nitrate (Riedel-de Haën, Germany) in proper volumes of $1.0\,mol\,L^{-1}$ of H_2SO_4 and diluting to the mark with distilled water in 100 mL volumetric flasks.

3.3. General procedure

Based on our experiments, the relationship between CL intensity and the promazine and fluphenazine concentrations was linear in the range of 0.4–30.0 $\mu g\,mL^{-1}$ and 0.07–5.0 $\mu g\,mL^{-1}$ for promazine and fluphenazine, respectively. In this range, a 5-level full factorial experimental design was used for preparing standard solutions to maximize the statistical information content in the chemiluminescence profile. Aliquot (200 μL) of $3.0 \times 10^{-3}\,mol\,L^{-1}$ of $Ru(bipy)_3{}^{2+}$ was mixed with different mixtures of promazine and fluphenazine. Then, $5.5 \times 10^{-3}\,mol\,L^{-1}$ of Ce^{4+} in $0.090\,mol\,L^{-1}$ H_2SO_4 were transferred in a microsyringe into the 0.50 cm path light length quartz cell and the chemiluminescence intensity was measured against time.

3.4. Procedure for spiked serum

Plasma samples were deproteinated using acetonitrile, no extraction procedure was necessary [24]. An aliquot of standard solution of promazine and fluphenazine was added to 1.0 mL of plasma. The mixture of the standard solutions of promazine and fluphenazine plus plasma was centrifuged for 2 min. Then, 2.0 mL of acetonitrile was added to plasma and centrifuged for 10 min at
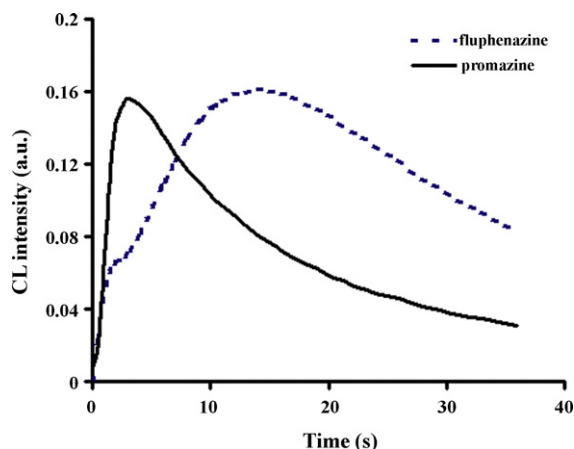
Fig. 1. Typical CL signals of $1.0\,\mu g\,mL^{-1}$ of promazine and fluphenazine in batch system using $0.090\,mol\,L^{-1}$ H_2SO_4, $3.0\times10^{-3}\,mol\,L^{-1}$ $Ru(bipy)_3^{2+}$ and $5.5\times10^{-3}\,mol\,L^{-1}$ Ce^{4+}.

Fig. 2. Influence of H_2SO_4 concentration on the sensitivity. Conditions: $1.0\,\mu g\,mL^{-1}$ promazine and fluphenazine with $3.0\times10^{-3}\,mol\,L^{-1}$ $Ru(bipy)_3^{2+}$ and $5.5\times10^{-3}\,mol\,L^{-1}$ Ce^{4+}.

3000 rpm. The supernatant was transferred to a small conical flask and evaporated to dryness under the stream of nitrogen. The dry residue was diluted appropriately so that the concentrations of fluphenazine and promazine were in the dynamic range of their calibration curves. A blank solution was prepared by treating the drug-free plasma in the same way. The absolute recovery was determined by comparing the representative CL profile of the plasma sample and the standard drug at identical concentrations. The final solutions were divided into two parts: one for HPLC-UV determination as an official method and the other for the proposed CL method.

4. Results and discussion

In order to investigate the CL behaviors of aliphatic and piperazine classes of phenothiazines, four phenothiazine compounds including promazine, chlorpromazine, fluphenazine and perphenazine were selected as models. We found that light emission-time profile for promazine and chlorpromazine (the aliphatic class) were narrow with a high CL intensity at about 3 s after mixing of the reactants, whereas the CL intensity of fluphenazine and perphenazine (the piperazine class) were broad with the highest intensity at 13 s after mixing of the reactants. This observation indicates that the kinetic characteristics of the piperazine class are significantly different from those of the aliphatic class of phenothiazines.

This investigation was focused on obtaining the CL signal with the highest sensitivity, in the first stage and the most resolved CL profiles for promazine and fluphenazine, in the second. Traditionally, batch and continuous flow methods are two basic sample-injection modes commonly used for CL analysis. The batch mode has such advantages as high sensitivity and minimized reagent consumption while it also yields a highly efficient time-resolved CL [25,26]. However, the CL intensity may be subject to poor precision due to variation in mixing. We chose the batch system to achieve the best condition for resolving the mixture. Typical CL profiles of promazine and fluphenazine are shown in Fig. 1. As can be seen, fluphenazine gives a broad peak with the highest CL intensity at 13.5 s whereas the maximum CL intensity of promazine appears at approximately about 3.2 s. Chemiluminescence based on the oxidation of $Ru(bipy)_3^{2+}$ has proven to be a sensitive detection system for ternary and secondary amines. The mechanism involves oxidation of $Ru(bipy)_3^{2+}$ and amines by Ce^{4+}. The oxidation of amines produces radicals. These radicals reduce $Ru(bipy)_3^{3+}$ to the excited state which subsequently emits

light [27] as follows:
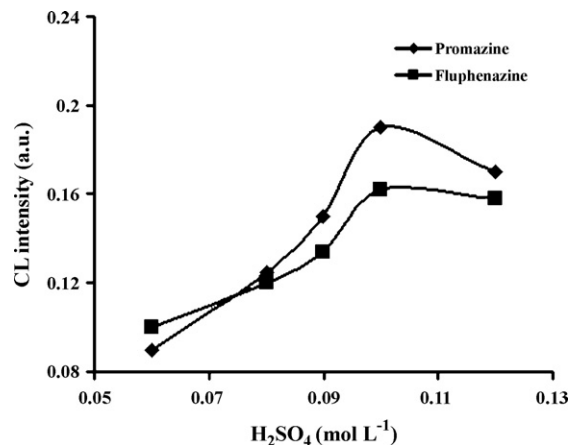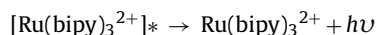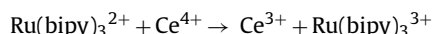
$$Ru(bipy)_3^{2+} + Ce^{4+} \rightarrow Ce^{3+} + Ru(bipy)_3^{3+}$$

$$Ru(bipy)_3^{3+} + analyte \rightarrow [Ru(bipy)_3^{2+}]* + (analyte)OX$$

$$[Ru(bipy)_3^{2+}]* \rightarrow Ru(bipy)_3^{2+} + h\upsilon$$

The light intensity is proportional to the analyte concentration.

4.1. Effect of experimental variables

In this work, the chemical and instrumental factors needed to be optimized were Ce^{4+}, $Ru(bipy)_3^{2+}$ and sulfuric acid concentrations. Optimization was conducted based on the method of Murillo Pulgarin et al. [28]. According to this method, CL responses of both compounds are initially plotted against each factor at different levels. Then, based on the CL profiles of both compounds, a compromised condition is selected.

The influence of H_2SO_4 concentration for promazine and fluphenazine determination was evaluated using different sulfuric acid concentrations over the range of 0.06–0.12 mol L^{-1} (Fig. 2). The results show that at a constant concentration of Ce^{4+}, the CL peak of fluphenazine came to be narrow with increasing H_2SO_4 concentration. This led to the overlapping of the CL profiles of both compounds. In this regard, a H_2SO_4 concentration of 0.090 mol L^{-1} was selected for the compromised condition of resolution and sensitivity.

The influence of Ce^{4+} concentration over the range of 3.0×10^{-3}–6.0×10^{-3} mol L^{-1} was investigated for both drugs (Fig. 3). The results show that the CL intensities of promazine and fluphenazine increased when Ce^{4+} concentration was rising. The highest intensity was achieved at 5.5×10^{-3} mol L^{-1}; therefore, this concentration of Ce^{4+} was selected for further experiments.

The variation of the CL intensity with $Ru(bipy)_3^{2+}$ concentration in the range of 1.0×10^{-3}–4.0×10^{-3} mol L^{-1} was investigated for CL intensity of promazine and fluphenazine. The results showed that the CL signal for promazine and fluphenazine increased with increasing $Ru(bipy)_3^{2+}$ concentration up to 3.0×10^{-3} mol L^{-1} and slightly decreased afterwards. So, we selected 3.0×10^{-3} mol L^{-1} of $Ru(bipy)_3^{2+}$ concentration for further experiments.

4.2. Univariate calibration graph

Under the optimized conditions, the CL signal was found to be linear in the concentration ranges of 0.07–5.0 µg mL^{-1} for
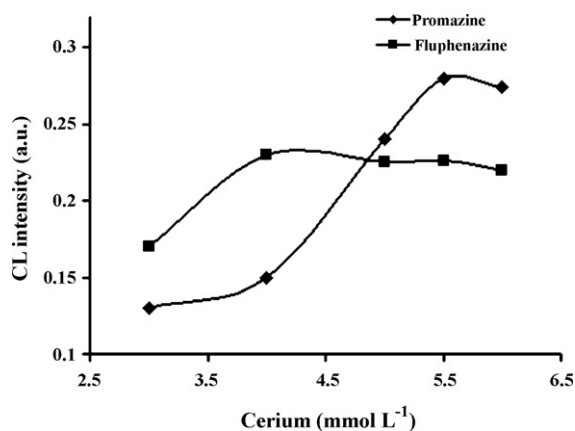
Fig. 3. Influence of Ce^{4+} concentration on the sensitivity. Conditions: $1.0\,\mu g\,mL^{-1}$ promazine and fluphenazine with $3.0 \times 10^{-3}\,mol\,L^{-1}$ $Ru(bipy)_3^{2+}$ and $0.090\,mol\,L^{-1}$ H_2SO_4.

fluphenazine and 0.4–$30.0\,\mu g\,mL^{-1}$ for promazine with the linear equations of $I_{CL} = 0.042C_{Fluphenazine} + 0.053$, ($r^2 = 0.9900$) and $I_{CL} = 0.013C_{Promazine} + 0.037$, ($r^2 = 0.9950$), where I_{CL} is CL intensity and C is the concentration of the drugs in $\mu g\,mL^{-1}$.

The relative standard deviations for ten replicates determinations were calculated as 4.3% and 3.2% for $1.0\,\mu g\,mL^{-1}$ promazine and fluphenazine concentrations, respectively.

4.3. Multivariate calibration graph

Optimizing parameters γ and δ^2 is the first step in obtaining the optimal LS-SVM models. The LS-SVM was performed with radial basis function (RBF) as a kernel function. A training set of 25 samples was taken. Then, the root mean square error of cross validation (RMSECV) was calculated for each combination of γ and δ^2. Finally, the gamma and sigma values were selected that yielded a minimum in RMSECV. These parameters were optimized generating a model in the range of 1–1000. The optimum pairs of (δ^2, γ) obtained for promazine and fluphenazine were (95, 290) and (129, 120), respectively. The prediction ability of the constructed models was evaluated using the validation set (the synthetic mixture) and the relative standard errors of the predictions (RSEP) were calculated as follows:

$$RSEP(\%) = 100 \times \sqrt{\frac{\sum_{i=1}^{n}(Y_i - \hat{Y}_i)^2}{\sum (\hat{Y}_i)^2}}$$

where, Y_i is the predicted concentration, $\hat{Y}_i$ is the observed value of concentration and n is the number of samples in the validation set. Table 2 shows the RMSEP and RSEP for each phenothiazine drugs in the synthetic mixture.

Detection limit was defined as $3\sigma_0$ [29], where σ_0 is the standard deviation in the predicted concentration of promazine and fluphenazine in a blank sample. The values for the detection limit were $0.1\,\mu g\,mL^{-1}$ and $0.04\,\mu g\,mL^{-1}$ for promazine and fluphenazine determination by LS-SVM, respectively.

5. Interfering study

In order to the selectivity of the proposed method, interference effects of some organic and inorganic compounds commonly present in human serum and also some redox active compounds were studied by recovering $2.0\,\mu g\,mL^{-1}$ of promazine and/or fluphenazine in the presence of potential interfering substances. The tolerance of each substance was taken as the largest amount yielding an error of less than 3σ in the analytical signal of $2.0\,\mu g\,mL^{-1}$ promazine (σ is the standard deviation in 10 times determination of $2.0\,\mu g\,mL^{-1}$ of promazine). The results are given in Table 3 confirmed that many common substances did not affect their determination.

Table 2
Composition of synthetic mixtures and predicted values for promazine and/or fluphenazine ($\mu g\,mL^{-1}$).

Synthetic mixture		Predicted concentration	
Promazine	Fluphenazine	Promazine	Fluphenazine
7.0	0.08	6.6	0.08
9.0	1.50	9.2	1.46
1.50	3.00	1.52	2.90
0.40	4.00	0.35	3.85
15.0	2.50	14.4	2.63
20.0	0.15	19.0	0.14
RMSEP		0.52	0.092
RSEP (%)		4.6	3.90

Table 3
Effect of foreign substances on the determination of $2.0\,\mu g\,mL^{-1}$ promazine and/or fluphenazine under the optimized conditions.

Substance	Concentration ratio of the substance to promazine (mol/mol)
Sucrose, Glucose, Fructose, Starch, Serine, Valine, Threonine, Cl^-, Urea, K^+, Na^+, NO_3^-	1000[*]
Lactose, Leucine	500
Alanine, Glycine, Proline, HCO_3^-, CO_3^{2-}, PO_4^{3-}, Cu^{2+}, Cd^{2+}, Ca^{2+}, Uric acid, Aspartic acid,	
Tyrosine, Fe^{2+}, Mg^{2+}, Citrate, Stearic acid	100
Paracetamol	50
Dopamine, Ciprofloxacin	10
Tryptophane, Cysteine, Ascorbic acid	1

[*] Maximum concentration of the substances was tested.

Table 4
Comparison of the results of CL and UV for determination of promazine and fluphenazine in spiked human plasma.

Synthethic mixture		CL method[a]		Reference method[a] [12]		F_{exp}[b]		t_{exp}[c]	
PMH	Fluphenazine	PMH	Fluphenazine	PMH	Fluphenazine	PMH	Fluphenazine	PMH	Fluphenazine
0.70	0.075	0.76 ± 0.06	0.081 ± 0.030	0.72 ± 0.02	0.077 ± 0.010	9.0	9.0	1.84	0.18
1.40	0.32	1.37 ± 0.08	0.34 ± 0.06	1.38 ± 0.03	0.29 ± 0.04	7.1	2.25	0.20	0.73
7.00	1.70	6.73 ± 0.11	1.63 ± 0.10	6.86 ± 0.06	1.60 ± 0.06	3.36	2.77	1.77	0.45
11.00	3.00	11.20 ± 0.05	2.76 ± 0.09	11.00 ± 0.08	2.90 ± 0.03	2.56	9.0	3.32	2.45
16.00	4.00	15.57 ± 0.09	3.90 ± 0.11	15.70 ± 0.08	4.10 ± 0.06	1.12	3.36	1.77	2.72
27.00	5.00	26.80 ± 0.12	5.10 ± 0.10	26.90 ± 0.08	4.80 ± 0.09	2.25	1.23	1.22	3.87

[a] (Mean value ($\mu g\,mL^{-1}$) $\pm$ S.D.($n = 3$)).
[b] F-test calculated, theoretical value = 39.0 ($P = 0.05$).
[c] Student t-test calculated, theoretical value = 4.3 ($P = 0.05$).

6. Application

In order to evaluate the applicability of the proposed method, spiked human serum was analyzed for the simultaneous determination of promazine and fluphenazine. At these concentrations of spiked drugs, the possibility for the dilution of the supernatant decreases because increasing dilution leading to ultimate concentrations would not fit in the dynamic range of the calibration graphs. The results are given in Table 4. The results were also confirmed by HPLC method [12] (with UV detection at 254 nm). These results show that the performance of the models was slightly unsatisfactory at lower concentrations of the calibration curve. Statistical analysis of the results using student *t*-test and the variance ratio *F*-test were used to compare the two methods for their accuracy and precision, which revealed the potential applicability of the proposed method.

7. Conclusion

A new CL method was introduced for simultaneous determination of promazine and fluphenazine. Chemiluminescence method combined with LS-SVM as a multivariate calibration method was found suitable for simultaneous determination of these two phenothiazines compounds. The advantages of the proposed method are sensitivity, speed and simplicity of instrument. The system shows good reproducibility and accuracy for determination of these drugs in spiked plasma.

Acknowledgements

References

[1] A.G. Goodman, L.S. Gilman, The Pharmacological Basis of Therapeutics, Pergammon Press, New York, 1996.
[2] S.C. Sweetman, The Complete Drug Reference, 34th Ed., Pharmaceutical Press, London, 2005, pp.675, 699, 703, 717.
[3] H.J. Moeller, Nervenarzt 71 (2000) 329.
[4] F.J. Lara, A.M. Garcia-Campana, L.G. Amiz-Gracia, J.M. Bosque-Sendra, F. Ales-Barrero, Electrophoresis 27 (2006) 2348.
[5] R. Regenthal, M. Krueger, C. Koeppel, R. Preiss, J. Clin. Monit. 15 (1999) 529.
[6] K. Madej, M. Kala, M. Wozniakiewicz, Chromatographia 62 (2005) 533.
[7] D.C. Le, C.J. Morin, M. Beljean, A.M. Siouffia, P.L. Desbene, J. Chromatogr. A 1063 (2005) 235.
[8] J. Karpinska, H.P. Tarasiewicz, B. Branch, Anal. Lett. 30 (1997) 2365.
[9] M.A. Koupparis, A. Barcuchova, Analyst 111 (1986) 313.
[10] F. Belal, S.M. El-Ashry, I.M. Shehata, M.A. El-Sherbeny, D.T. El-Sherbeny, Mikrochim. Acta 135 (2000) 147.
[11] B. Zeng, F. Huang, Talanta 64 (2004) 380.
[12] M.A. Saracino, M. Amore, E. Baioni, C. Petio, M.A. Raggi, Anal. Chim. Acta 624 (2008) 308.
[13] C. Pistos, J.T. Stewart, Biomed. Chromatogr. 17 (2003) 465.
[14] M. Franklin, D.H. Wiles, D.J. Harvey, Clin. Chem. 24 (1978) 41.
[15] C. Cortes, V. Vapnik, Mach. Learn 20 (1995) 273.
[16] V. Vapnik, Statistical Learning Theory, John Wiley, New York, 1998.
[17] F.A. Aly, A.A. Alwarthan, N.A. Alarfaj, Anal. Chim. Acta 358 (1998) 255.
[18] Y. Li, W. Niu, J. Lu, Talanta 71 (2007) 1124.
[19] H.N. Choi, S.H. Cho, Y.J. Park, D.W. Lee, W.Y. Lee, Anal. Chim. Acta 541 (2005) 47.
[20] G.M. Greenway, S.J.L. Dolman, Analyst 124 (1999) 759.
[21] J.A.K. Suykens, T. Van Gestel, J. De Brabanter, B. De Moor, J. Vandewalle, Least-Squares Support Vector Machines, World Scientifics, Singapore, 2002.
[22] A. Niazi, J. Zolgharnein, S. Afiunizadeh, Anal. Sci. 23 (2007) 1311.
[23] A. Borin, M.F. Ferrao, C. Mello, D.A. Maretto, R.J. Poppi, Anal. Chim. Acta 579 (2006) 25.
[24] F.A. Aly, S.A. Al-Tamimi, A. Alwarthan, Talanta 53 (2001) 885.
[25] T.P. Ruiz, C.M. Lozano, V. Tomas, J. Fenoll, Anal. Chim. Acta 485 (2003) 63.
[26] Z. He, H. Gao, L. Yuan, Y. Zeng, Analyst 122 (1997) 1343.
[27] A.W. Knight, G.M. Greenway, E.D. Chesmore, Anal. Proc. 32 (1995) 125.
[28] J.A. Murillo Pulgarin, L.F. Garcia Bermejo, M.N. Sanchez Garcia, Anal. Chim. Acta 602 (2007) 66.
[29] R. Boque, J. Ferre, N.M. Faber, F.X. Rius, Anal. Chim. Acta 451 (2002) 313.

Biosensor for chlorogenic acid based on an ionic liquid containing iridium nanoparticles and polyphenol oxidase

Suellen C. Fernandes[a], Sally K. Moccelini[a], Carla W. Scheeren[b], Pedro Migowski[b], Jairton Dupont[b], Melina Heller[a], Gustavo A. Micke[a], Iolanda C. Vieira[a,*]

[a] *Department of Chemistry, Universidade Federal de Santa Catarina, 88040-900 Florianópolis, SC, Brazil*
[b] *Institute of Chemistry, Universidade Federal do Rio Grande do Sul, 91501-970 Porto Alegre, RS, Brazil*

ARTICLE INFO

ABSTRACT

A biosensor based on the ionic liquid, 1-*n*-butyl-3-methylimidazolium hexafluorophosphate containing dispersed iridium nanoparticles (Ir-BMI.PF$_6$) and polyphenol oxidase was constructed. This enzyme was obtained from the sugar apple (*Annona squamosa*), immobilized in chitosan ionically crosslinked with oxalate. The biosensor was used for determination of chlorogenic acid by square wave voltammetry. The polyphenol oxidase catalyzes the oxidation of chlorogenic acid to the corresponding *o*-quinone, which is electrochemically reduced back to this substance at +0.25 V *vs.* Ag/AgCl. Under optimized operational conditions the chlorogenic acid concentration was linear in the range of 3.48×10^{-6} to 4.95×10^{-5} mol L^{-1} with a detection limit of 9.15×10^{-7} mol L^{-1}. The biosensor was applied in the determination of chlorogenic acid in organic and decaffeinated coffee and the results compared with those obtained using the capillary electrophoresis method. The recovery study for chlorogenic acid in these samples gave values of 93.2–105.7%.

1. Introduction

Ionic liquids (ILs) derived mainly from the association of the 1,3-dialkylimdiazolium cation with various non-coordinating anions are compounds with various interesting physico-chemical properties. Most of these fluids are non-volatile, do not have measurable vapor pressure, possess good electrochemical and thermal stability, high density, excellent ionic conductivity, and good solubility of inorganic and organic substances, and they are non-flammable [1–3]. In particular the hydrophobic 1-*n*-butyl-3-methylimidazolium hexafluorophosphate (BMI.PF$_6$) is one of the most popular and most used ILs [4]. The imidazolium-based ILs are used in several areas, such as electrolytes for battery, solvents for organic synthesis and catalysis, electrolytes for conducting polymer actuator systems and supports for the immobilization of enzymes [1–5].

Catalysis can be considered as one of the most popular applications of transition metals, especially noble metals, because of their high catalytic activity in many chemical reactions. The incorporation of metal (e.g., gold, iridium, platinum, palladium and silver) nanoparticles into carbon, and even in metal electrodes, has received considerable interest. The catalytic effect of these nanoparticles has been shown to increase the sensitivity of the electrode

because electron transfer is better promoted [6–17]. The relation between transition metal nanoparticles and ILs offers considerable potential and has been used in the construction of sensors [8–13]. The high performance of biosensors based on metal nanoparticles has been reported in the literature [8–17], verifying the advantages of effective mass transport, stability, high effective surface area and control over the electrode microenviroment.

Enzymes are generally active in ILs [2]. The existence of hydrogen-bonded nanostructures with polar and non-polar regions in ILs may be responsible for the stabilization of the supported enzyme, which can sustain their functionality under strongly denaturing conditions. The application of ILs in the determination of the direct electrochemistry of enzymes has been investigated since they are considered appropriate media for supporting biocatalytic processes with high polarity, selectivity, fast rate and enzyme stability [1–3].

Immobilized enzymes are used mainly in biosensors for analytical applications because, compared with free enzymes, they generally have lower activity and a better Michaelis constant [18]. Immobilization of an enzyme under conditions close to those of its natural environment usually results in a more stable and efficient enzyme, due to interactions with the support. Chitosan has been widely used for the immobilization of enzymes and other biomolecules owing to its biocompatibility with this biomaterial [18,19]. As with other polymer gels, such as gelatin, xanthan and agarose, it is used as a matrix to immobilize enzymes for its application in biosensor development [19]. Chitosan is a polysaccharide

* Corresponding author. Tel.: +55 48 3721 6844; fax: +55 48 3721 6850.
E-mail address: iolanda@qmc.ufsc.br (I.C. Vieira).

composed mainly of 1,4-linked 2-amino-2-deoxy-b-ᴅ-glucan and it has been widely crosslinked with many covalent or ionic crosslinking agents and modified physically to change its properties [18–22]. It is a polycationic polymer and, consequently, reactions with negatively charged components, either molecules or ions, can lead to the formation of a network through ionic bridges between the polymeric chains. Ionic interactions between the negative charges of the crosslinker and positively charged groups of chitosan are the main interactions inside the network [19,23].

Polyphenol oxidase is a copper-containing enzyme, extensively distributed in nature. This enzyme is responsible for the catalytic oxidation of *o*-diphenols to their corresponding *o*-quinones. These *o*-quinones take part in a series of chemical reactions and react non-enzymatically with a diversity of substances in the presence of oxygen to form pigments. Therefore, they are responsible for the quality deterioration of many fruits and vegetables during post-harvest processing. Moderately unstable, this enzyme is susceptible to inactivation at elevated temperatures and under extreme pH conditions [24,25].

Phenolic compounds are extensive secondary plant metabolites, derived from benzoic and cinnamic acids and they are known to play an important role in plant resistance and growth regulation. Moreover, they have been shown to have potential beneficial effects on human health and are considered to be an important contributor to diverse biological activities acting as anti-oxidant, anti-carcinogenic, and anti-inflammatory agents. Chlorogenic acid is a phenolic compound present in plants such as artichoke leaves, burdock root, dandelion root, echinacea root and in the popular coffee bean, the major source of this acid in the human diet [26–28].

Studies have revealed the particular effects of habitual coffee drinking on various aspects of health such as neurological conditions, metabolic disorders, psychoactive responses and liver function. Roasting degrades approximately 32–52% of the chlorogenic acid in coffee beans and it is easily hydrolyzed into caffeic acid and quinic acid, compounds responsible for the astringent and bitter flavors of the coffee aroma. Therefore, the determination of chlorogenic acid in coffee is an important aspect of the quality control of the final product, since its aroma characteristics determine the commercial value [27,28]. In view of this, it is very important to develop analytical methods of reduced cost but with good sensitivity and selectivity, as well as short response times. Several analytical methods have been used to determine chlorogenic acid (Table 1) including chemiluminescence, high performance liquid chromatography, capillary electrophoresis and electroanalytical methods [29–37].

In this study, we propose a novel biosensor for determination of chlorogenic acid in organic and decaffeinated coffee. Polyphenol oxidase from the sugar (or custard) apple (*Annona squamosa*) was immobilized in chitosan ionically crosslinked with oxalate. These biomaterials, along with the IL 1-*n*-butyl-3-methylimidazolium hexafluorophosphate containing dispersed iridium nanoparticles (Ir-BMI.PF$_6$), were used to build the biosensor. Furthermore, a novel biosensor for the determination of chlorogenic acid with simplicity,

high sensitivity, fast response and good stability characteristics was developed.

2. Experimental

2.1. Reagents and solutions

All reagents were of analytical grade and all solutions were prepared with water from a Millipore (Bedford, MA, USA) Milli-Q system (Model UV Plus Ultra-Low Organic Water). Chlorogenic acid, catechol, caffeine, caffeic acid, citric acid, fructose, glucose, glutamic acid, sucrose and tartaric acid were purchased from Aldrich. Chitosan (deacetylation degree of 85%), sodium oxalate and Tween 80 were obtained from Sigma. Graphite powder (Acherson #38) and Nujol were obtained from Fisher Scientific and Aldrich, respectively. The sugar (or custard) apples (*A. squamosa*) were purchased from a local market in Florianópolis (Santa Catarina, Brazil).

2.2. Synthesis of ionic liquids BMI.PF$_6$ and Ir-BMI.PF$_6$

The ionic liquid 1-*n*-butyl-3-methylimidazolium hexafluorophosphate (BMI.PF$_6$) was prepared according to a known procedure and dried under reduced pressure (1.0×10^{-3} bar) at 65 °C for 24 h. The purity (>99.4%) of this ionic liquid can be determined through its ^{1}H NMR spectrum using the intensity of the ^{13}C satellites of the imidazolium M-methyl group as an internal standard. NMR analysis was performed on a Varian Inova 300 spectrometer. Infrared spectra were obtained using a Bomem B-102 spectrometer [38].

The ionic liquid BMI.PF$_6$ containing dispersed iridium nanoparticles (Ir-BMI.PF$_6$) was prepared in a Fischer–Porter bottle containing an orange solution of the organometallic precursor iridium. Bis(1,5-cyclooctadiene) tetrafluoroborate {[Ir(cod)$_2$]BF$_4$} (5 mg, 0.01 mmol) was added to 1 mL of the BMI.PF$_6$ ionic liquid and the mixture was stirred at room temperature for 15 min. The system was then maintained for 2 h at 75 °C and 4 bar of H$_2$ pressure. After stirring for 2 h a black 'solution' was obtained containing the Ir-BMI.PF$_6$ (0.36% of Ir) [39] and a sample was analyzed by transmission electron microscopy (TEM).

2.3. Ionic liquid Ir-BMI.PF$_6$ characterization instrumentation

The morphology and the size distribution of the Ir-BMI.PF$_6$ were obtained through TEM analysis. The morphology and the electron diffraction (ED) of the obtained particles were investigated using a JEOL JEM – 2010 equipped with an energy dispersive X-ray spectroscopy (EDS) system and JEOL JEM – 1200 EXII electron microscope operating at accelerating voltages of 200 and 120 kV, respectively.

The sample for TEM analysis was prepared by dispersion of the iridium nanoparticles in the ionic liquid (Ir-BMI.PF$_6$) in acetone at room temperature. The suspension was collected on a carbon-coated copper grid. The histogram of the nanoparticle size

Table 1
Analytical methods for determination of chlorogenic acid.

Methods	Accuracy	Linear range	Detection limit	Reference
HPLC	90%	0.8–3 mg L^{-1}	0.2 mg L^{-1}	[31]
HPLC	85.56–94.92%	0.16–2.5 µg mL^{-1} and 2.5–40.0 µg mL^{-1}	0.04 µg mL^{-1}	[32]
CZE	95%	1–20 µg mL^{-1}	0.25 mg L^{-1}	[33]
HPLC	96%	0.2–4 µg mL^{-1}	0.02 mg L^{-1}	
Chemiluminescence	94.0–105.2%	5.0×10^{-8} to 5.0×10^{-5} g mL^{-1}	5.7×10^{-9} g mL^{-1}	[34]
Biosensor	93.2–106.1%	5.0×10^{-6} to 1.45×10^{-4} mol L^{-1}	8.0×10^{-7} mol L^{-1}	[35]
Biosensor	96.5–102.6% and 91.3–115.5%	4.89×10^{-6} to 3.20×10^{-4} mol L^{-1} and 4.89×10^{-6} to 4.85×10^{-5} mol L^{-1}	8.02×10^{-7} and 8.52×10^{-7} mol L^{-1}	[36]
Biosensor	92–119%	1.0×10^{-6} to 5.0×10^{-5} mol L^{-1}	7.0×10^{-7} mol L^{-1}	[37]
Biosensor	93.2–105.7%	3.48×10^{-6} to 4.95×10^{-5} mol L^{-1}	9.15×10^{-7} mol L^{-1}	This work

distribution was obtained from measurement of around 300 particles, and was reproduced in different regions of the Cu grid, assuming spherical shape, found in an arbitrary chosen area of enlarged micrographs.

2.4. Instrumentation and electrodes

Electrochemical measurements were performed at room temperature using an Autolab PGSTAT12 potentiostat/galvanostat (Eco Chemie, The Netherlands) operating with data processing software (GPES, software version 4.9.006, Eco Chemie). The three-electrode system was composed of the biosensor as the working electrode, an Ag/AgCl electrode (3.0 mol L^{-1} KCl) as the reference and a platinum wire as the auxiliary electrode. A Hitachi centrifuge, model Himac CR 20B2, was used in the preparation of the sugar apple homogenate. A B572 (Micronal) spectrophotometer was used with an optical path of 1.0 cm (quartz cell) for the determination of polyphenol oxidase activity. A scanning electron microscope (SEM - Philips, model XL30 microscope) at an accelerating voltage of 15 kV was used in the analyzed of the carbon pastes modified with the Ir-BMI.PF$_6$ and PPO used for the construction of the biosensor. Electropherograms were obtained with an Agilent Technologies automated HP^{3D}CE capillary electrophoresis apparatus (Palo Alto, CA, USA), equipped with a diode array detector.

2.5. Obtainment of the polyphenol oxidase and determination of the activity

The polyphenol oxidase (PPO) enzyme was obtained from the sugar apple (*A. squamosa*) tissue. Twenty-five grams of this plant material were homogenized in a mixer with 100 mL of phosphate buffer solution (0.1 mol L^{-1}; pH 7.0) for 1 min. The homogenate was rapidly filtered and centrifuged at 18,000 rpm for 2 min at 4 °C. The resulting supernatant was stored at 4 °C in a refrigerator and utilized as a source of polyphenol oxidase after determination of the activity. One unit of activity was defined as an increase in the amount of enzyme that causes a change in absorbance of 0.001 min^{-1} at 420 nm for *o*-quinone produced by the reaction between 2.8 mL of catechol solution (5.0×10^{-2} mol L^{-1}) in 0.1 mol L^{-1} phosphate buffer (pH 7.0) and 0.2 mL of the enzymatic extract.

2.6. Chitosan crosslinking, polyphenol oxidase immobilization and biosensor construction

The chitosan used as the support for immobilization of polyphenol oxidase was prepared according to the following procedure: chitosan (1.0%, m/v) was dissolved in an aqueous solution of acetic acid (3.0%, v/v) containing three drops of the surfactant Tween 80 (2.0%, v/v) at room temperature. Ionic crosslinked chitosan was formed spontaneously on adding 50.0 mL of sodium oxalate (5.0%, w/v) to the chitosan solution under stirring. The solid was separated by centrifugation (10 min; 3000 rpm), filtered, and washed twice with water and phosphate buffer solution (pH 6.0) to remove the excess of reagents. The crosslinked chitosan powder was collected, dried and stored in a desiccator at room temperature until use.

Aliquots of the homogenate containing 300–1500 unit of PPO mL^{-1} were added to 30.0 mg of the ionic crosslinked chitosan powder. These mixtures were dried at room temperature and investigated together, in different Ir-BMI.PF$_6$:Nujol proportions (0:100; 25:75; 50:50; 75:25; 100:0% (w/w)), for the building of the biosensors.

The construction procedure for the biosensor involved hand-mixing 70.0 mg of graphite powder and 30.0 mg of support containing 1200 unit mL^{-1} of PPO for 20 min in a mortar. The Ir-BMI.PF$_6$ (60.0 mg) was then added to this mixture which was mixed for at least 20 min to guarantee uniform dispersion and produce the final paste. This uniform paste was tightly packed into the cavity of a syringe (1.0 mm internal diameter) and a copper wire was inserted to establish the external electrical contact. The carbon paste electrode without PPO was prepared following the same steps.

2.7. Electrochemical measurement and coffee sample preparation

Square wave and cyclic voltammetry measurements were carried out in 0.1 mol L^{-1} phosphate buffer (pH 6.0) and the required volume of chlorogenic acid or sample solutions with the following parameters: potential range between +0.40 and +0.10 V; frequency of 30.0 Hz; scan increment of 3.0 mV; pulse amplitude of 100.0 mV. All measurements were reported *vs.* Ag/AgCl (3.0 mol L^{-1} KCl) after a suitable initial stirring time of 60 s in order to homogenize the solution.

Two samples of organic coffee (A and B) and two of decaffeinated coffee (C and D) were acquired from a local supermarket in Flori-
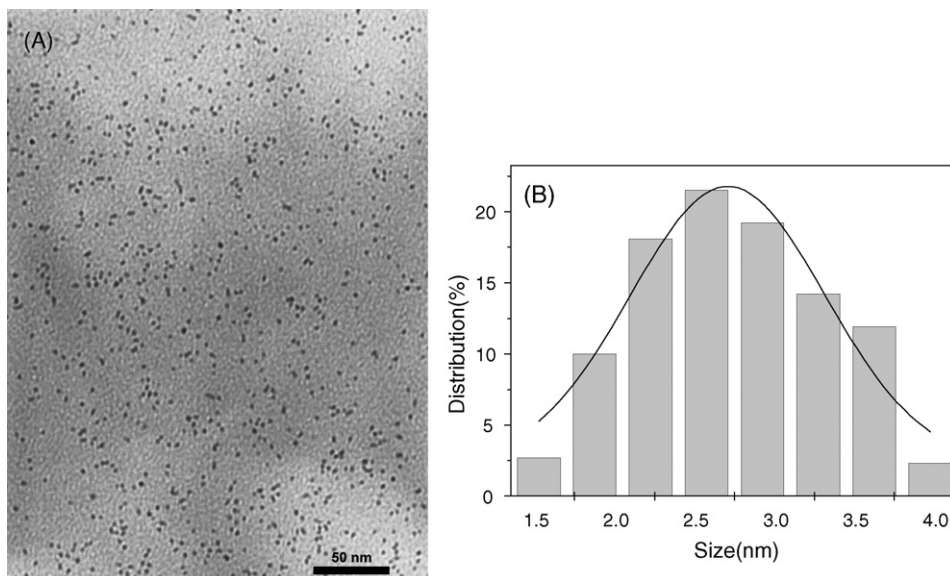

Fig. 1. (A) TEM micrograph of iridium nanoparticles in BMI.PF$_6$ and (B) histogram of the particle size distribution.

anópolis (Santa Catarina, Brazil). For the determinations, 1.5 g of soluble coffee (A and C) and 3.0 g instant coffee (B and D) were prepared in triplicate in 50 mL of hot water. For the electrochemical measurements using the proposed biosensor, 30 μl of these coffee samples were transferred to the cell containing 10 mL of phosphate buffer solution (0.1 mol L^{-1}; pH 6.0).

3. Results and discussion

3.1. Morphology and size of the iridium nanoparticles

Fig. 1A shows the morphology, investigated by transmission electron microscopy, of the iridium nanoparticles dispersed in the ionic liquid BMI.PF$_6$ and Fig. 1B gives the histogram of the particle size distribution. As can be seen, the mean diameter of the iridium particles was around 2.5 nm. The nanoparticle patterns are similar to those obtained by Fonseca [39] from the H$_2$ reduction of [Ir(cod)Cl]$_2$ in BMI.PF$_6$. Subsequently, this Ir-BMI.PF$_6$ was used as a binder in the construction of the biosensor containing polyphenol oxidase immobilized in chitosan ionically crosslinked with oxalate.

3.2. Immobilization of polyphenol oxidase and enzymatic reaction

Chitosan, a natural biopolysaccharide, has attracted significant interest due to its well-documented properties, such as biocompatibility, low toxicity and biodegradability. It is widely used in the
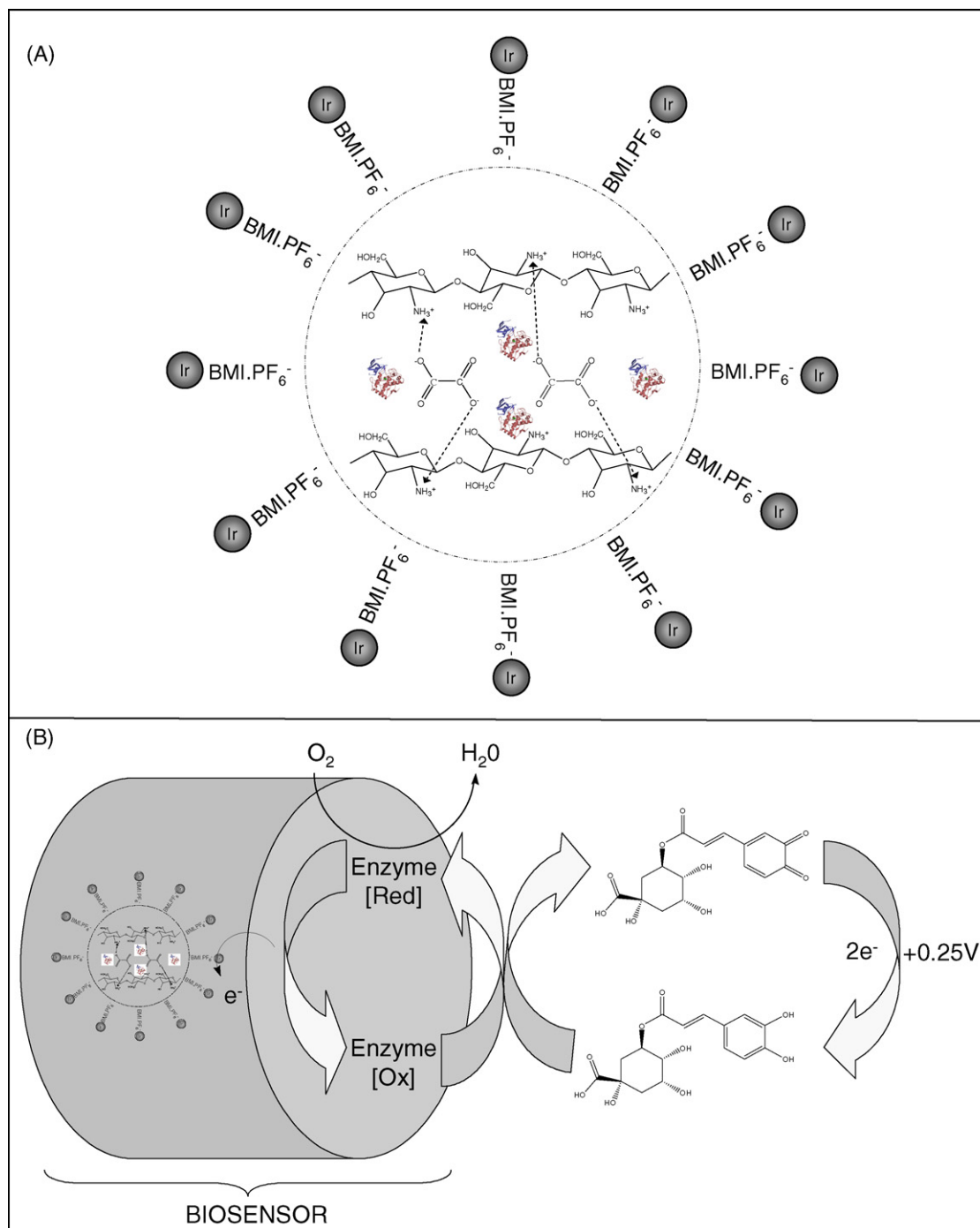
Fig. 2. Schematic representation of (A) immobilization of PPO on chitosan crosslinked with oxalate and (B) reaction involving chlorogenic acid on the surface of the biosensor.

pharmaceutical, food and biotechnological industries. Crosslinked chitosan is commonly used in controlled drug delivery [21,22,40]. Oxalate is an anion which interacts with chitosan via electrostatic forces to form ionic crosslinking. The positively charged amino groups of chitosan can react with the negatively charged oxalate via electrostatic attraction to form ionically crosslinked networks. Fig. 2A shows a schematic representation of the immobilization of the PPO from the sugar apple plant material in ionically crosslinked chitosan which leads to the proposed biosensor having a high stability and long lifetime.

Polyphenol oxidase catalyzes the oxidation of a variety of phenolic compounds, with the simultaneous reduction of the oxygen of the water molecule. Chlorogenic acid is oxidized in the presence of this enzyme to its respective o-quinone, which is electrochemically reduced back to chlorogenic acid on the biosensor surface at a potential of +0.25 V, as shown in Fig. 2B.

3.3. Morphology of the plain CPE and biosensor

The morphological characteristics of the sensors were studied using scanning electron microscopy. Fig. 3A and B shows the plain carbon paste electrode (CPE) and the biosensor, respectively. Considerable differences in the surface of the Ir-BMI.PF$_6$-PPO and the plain carbon paste can be observed. The CPE is characterized by a surface formed of isolated and irregular carbon flakes of graphite and each layer could be clearly distinguished. On the other hand, the surface of the carbon paste modified with Ir-BMI.PF$_6$ and the immobilized PPO enzyme appeared to be smoother and more uniform, and no separated carbon layers could be observed due to the high viscosity of the ionic liquid, which was packed homogeneously into

Fig. 3. Scanning electron micrograph of (A) plain CPE and (B) biosensor containing ionic liquid Ir-BMI.PF$_6$ and immobilized PPO.

the empty spaces between the graphite powder particles. Because of the higher ionic conductivity, the IL is not limited to serving as a binder for graphite, but may also work as a charge-transfer bridge facilitating the electron transfer [41].

3.4. Ir-BMI.PF$_6$–PPO contribution

To evaluate the contribution of the ionic liquid BMI.PF$_6$ containing iridium nanoparticles and PPO different sensors were constructed and compared. The electrochemical behavior of chlorogenic acid using these sensors was investigated by square wave voltammetry in the potential range of +0.5 to 0.0 V vs. Ag/AgCl. Fig. 4 shows the voltammograms obtained using the (a) plain CPE, (b) BMI.PF$_6$–CPE, (c) Ir-BMI.PF$_6$–CPE and (d) Ir-BMI.PF$_6$–PPO electrodes, in a 1.46×10^{-5} mol L^{-1} chlorogenic acid solution in phosphate buffer (0.1 mol L^{-1}; pH 6.0). As can be seen, a greater response to the chlorogenic acid solution was obtained using the biosensor containing Ir-BMI.PF$_6$ and immobilized PPO enzyme, when compared with the other sensors. Based on these results it is assumed that Ir-BMI.PF$_6$ offers a favorable microenvironment for PPO, which facilitates the electron transfer on the biosensor surface. This study confirms the catalytic contribution of the Ir-BMI.PF$_6$ and the efficiency of the immobilized PPO enzyme.

3.5. Optimization of the biosensor

The parameters of ionic liquid:Nujol ratio, pH and enzyme concentration, along with the frequency, pulse amplitude and scan increment used in the square wave voltammetry, were investigated to obtain the optimum response conditions for operation of the proposed biosensor.

The initial experiments were conducted to investigate the optimum ionic liquid content in the composition. Ratios of 100:0; 75:25; 50:50; 25:75 and 0:100% Nujol: IL were studied by square wave voltammetry. The analytical signals (resultant peak currents) for a 2.83×10^{-5} mol L^{-1} chlorogenic acid solution increased until only ionic liquid was present in biosensor. Since 100% of Ir-BMI.PF$_6$ was found to give the best sensitivity of the responses this was used for construction of the subsequent biosensors.

The solution pH is important to the electrochemical reaction and was investigated by detection of chlorogenic acid in phosphate or acetate buffer solution (0.1 mol L^{-1}) ranging from 5.0 to 9.0. The
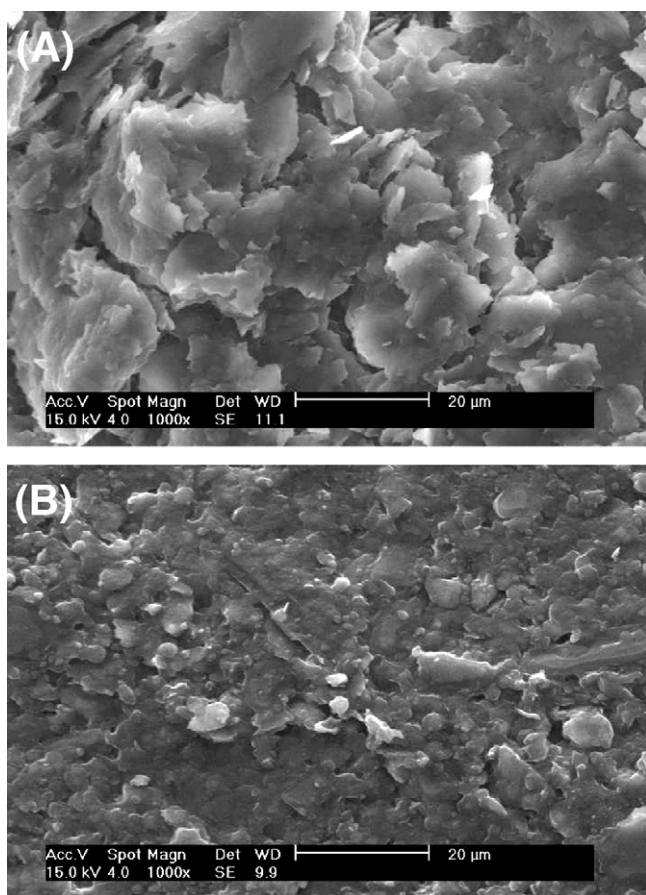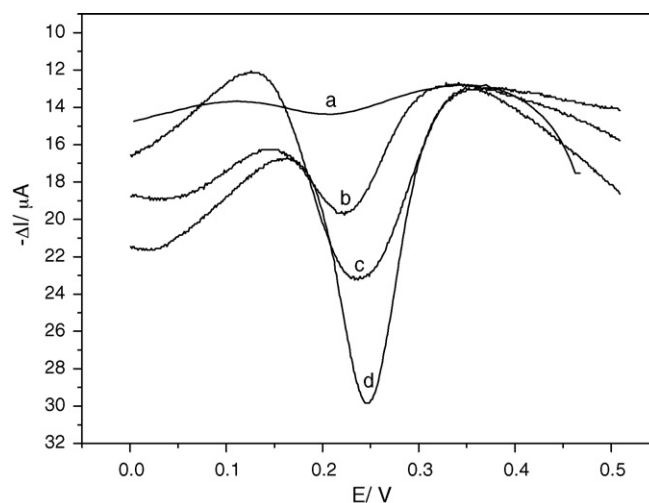

Fig. 4. Square wave voltammograms obtained using (a) plain CPE, (b) BMI.PF$_6$–CPE, (c) Ir-BMI.PF$_6$–CPE and (d) Ir-BMI.PF$_6$–PPO in a 1.46×10^{-5} mol L^{-1} chlorogenic acid solution in phosphate buffer (0.1 mol L^{-1}; pH 6.0) at pulse amplitude 100 mV, frequency 30 Hz and scan increment 1.0 mV.

Table 2
Optimization of experimental variables.

Parameters investigated	Range studied	Optimal value
IL composition (% w/w)	0–100	100
PPO (unit mL^{-1})	300–1500	1200
pH	5.0–9.0	6.0
Frequency (Hz)	10–100	30
Pulse amplitude (mV)	10–100	100
Scan increment (mV)	1.0–10.0	1.0

resulting peak-shaped pH profile showed a maximum sensitivity response at pH 6.0, the peak current of chlorogenic acid decreasing at higher values. Thus, pH 6.0 was adopted for further studies.

The amount of PPO enzyme in the paste preparation was optimized from 300 to 1500 unit mL^{-1} and the biosensor response increased until 1200 unit mL^{-1} and decreased with higher values of PPO in the paste. Based on this result, pastes containing 1200 unit mL^{-1} of PPO were prepared to perform further experiments.

Finally, the parameters of square wave voltammetry were optimized for the best performance of the biosensor under the same conditions cited above. Frequency (10–100 Hz), pulse amplitude (10–100 mV) and scan increment (1.0–10.0 mV) were evaluated. Overall, the optimized parameters can be summarized as follows: frequency 30 Hz; amplitude 100 mV and scan increment 1.0 mV. Table 2 summarizes the relevant analytical information and gives the best value found in the optimization of the biosensors.

3.6. Reproducibility, repeatability and stability of the biosensor

The reproducibility was investigated using three biosensors constructed independently, and indicated an acceptable reproducibility with a relative standard deviation of 1.81% for the response to 2.83×10^{-5} mol L^{-1} chlorogenic acid solution (pH 6.0). The repeatability of the biosensor performance also was studied by successive measurements of seven replicates of chlorogenic acid and the relative standard deviation was 4.30%. This indicates that the biosensor has good reproducibility due to the high sensitivity and efficiency of the immobilization of the PPO enzyme on the electrode.

The stability of the biosensor was investigated by measuring the electrochemical response (cathodic peak currents) to a 2.83×10^{-5} mol L^{-1} chlorogenic acid solution (pH 6.0) over a 150-day period without surface renewal. When the biosensor was stored at room temperature and measurements taken every 1–8 days, no notable change was observed.

3.7. Analytical performance of biosensor

Fig. 5 displays the square wave voltammetry response and the analytical curve of the cathodic peak current *vs.* chlorogenic acid concentration using the proposed biosensor under the selected conditions mentioned above. It was found that the resultant peak current was linear for chlorogenic acid concentrations in the range of 3.48×10^{-6} to 4.95×10^{-5} mol L^{-1}, with a detection limit (S/N = 3) of 9.15×10^{-7} mol L^{-1}. The linear regression equation was expressed as $-\Delta I$ (μA) = 0.4879 + 5.1621 $\times 10^{7}$ [chlorogenic acid] with a correlation coefficient of r = 0.9996.

The good analytical performance and stability of the proposed biosensor can be attributed to the excellent immobilization of polyphenol oxidase from the sugar apple (*A. squamosa*) in chitosan ionically crosslinked with oxalate and the high conductivity of the ionic liquid containing dispersed Ir nanoparticles. The contribution of the iridium nanoparticles was compared with reports in the literature [16,17] and other biosensors based on gold, palladium and platinum nanoparticles [8–15].
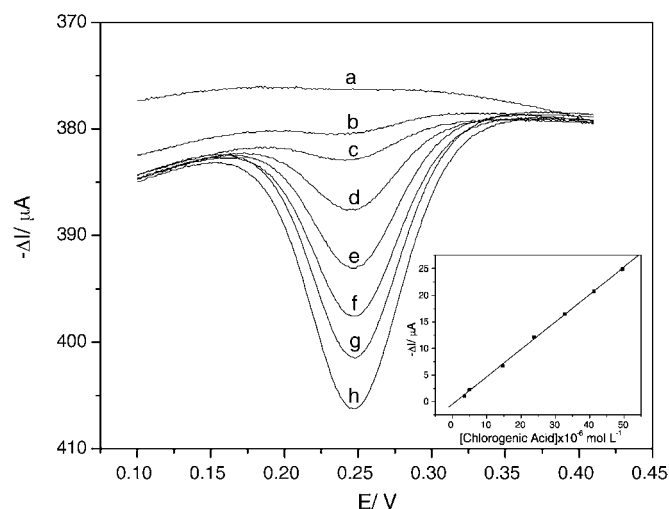

Fig. 5. Square wave voltammograms obtained using the proposed Ir-BMI.PF$_6$–PPO biosensor in (a) 0.1 mol L^{-1} phosphate buffer solution (pH 6.0) and chlorogenic acid solutions at the following concentrations: (b) 3.48×10^{-6} mol L^{-1}, (c) 4.95×10^{-6} mol L^{-1}, (d) 1.46×10^{-5} mol L^{-1}, (e) 2.38×10^{-5} mol L^{-1}, (f) 3.27×10^{-5} mol L^{-1}, (g) 4.13×10^{-5} mol L^{-1} and (h) 4.95×10^{-5} mol L^{-1} at pulse amplitude 100 mV, frequency 30 Hz and scan increment 1.0 mV. Inset: the analytical curve of chlorogenic acid.

The analytical features of the biosensor in terms of chlorogenic acid determination, and those for other analytical methods, are given in Table 1. The accuracy, stability (not shown in Table 1), linear range and limit of detection of the proposed biosensor were compared with others reported previously in the literature [31–37].

3.8. Recovery, interference and analytical application

Recovery experiments were carried out in order to evaluate the interference from matrix effects of coffee samples. This study was performed by adding known amounts of standard solutions to the samples (1.80, 8.65 and 15.0 mg L^{-1}) followed by analysis using the proposed biosensor. Satisfactory values between 93.2 and 105.7% for chlorogenic acid were obtained for the recovery, thus indicating that there is no interference from the sample matrix in the proposed method and also that the proposed method is suitable for use in these samples.

The effect of possible interferents, such as caffeine, caffeic acid, citric acid, fructose, glucose, glutamic acid, sucrose and tartaric acid, on the determination the chlorogenic acid in coffee was also investigated. The ratio of the concentration of chlorogenic acid to that of each substance was fixed at 1:1. Only caffeic acid caused a positive interference (12.0%) when present at the same concentration as the analyte. The observed interference was not critical, however, since caffeic acid is present at lower concentration levels than those investigated. The data were in agreement with those obtained employing other biosensors [35]. None of the other substances interfered in the performance of the proposed biosensors.

This biosensor was used to determine chlorogenic acid in different organic and decaffeinated samples using the standard addition method. Table 3 presents the chlorogenic acid concentrations determined in coffee samples employing the proposed biosensor and the capillary electrophoresis method. The results determined by the biosensor were in satisfactory agreement with those given by the capillary electrophoresis method, indicating that it is viable to apply the proposed biosensor to determine chlorogenic acid in coffee samples.

Table 3
Chlorogenic acid determination $(g\,L^{-1})$ in organic (A and B) and decaffeinated (C and D) coffee samples.

Sample	Chlorogenic acid $(g\,L^{-1})$		Relative error (Re%)
	Capillary electrophoresis	Biosensor[a]	
A	0.71 ± 0.01	0.71 ± 0.02	0.0
B	0.60 ± 0.02	0.58 ± 0.02	−3.33
C	0.97 ± 0.02	0.99 ± 0.01	+2.06
D	1.01 ± 0.02	0.96 ± 0.01	−4.95

Re = biosensor *vs.* capillary electrophoresis.

[a] *n* = 4; confidence level of 95%.

4. Conclusions

In this paper, the construction of a biosensor containing Ir-BMI.PF$_6$ and PPO immobilized in crosslinked chitosan was described. This biosensor offers advantages such as good sensitivity and linearity with a low detection limit and ease of preparation and renewal compared with the conventional carbon paste electrode. Immobilization of the enzyme in biocompatible chitosan together with Ir-BMI.PF$_6$ applied in the determination of chlorogenic acid in organic and decaffeinated coffee samples was showed to be a simple and efficient analytical method.

Acknowledgments

References

[1] J. Dupont, P.A.Z. Suarez, Phys. Chem. Chem. Phys. 8 (2006) 2441.
[2] Z. Yang, W. Pan, Enzyme Microb. Technol. 37 (2005) 19.
[3] D. Wei, A. Ivaska, Anal. Chim. Acta 607 (2008) 126.
[4] P.A.Z. Suarez, J.E.L. Dullius, S. Einloft, R.F. De Souza, J. Dupont, Polyhedron 15 (1996) 1217.
[5] S.F. Wang, H.Y. Xiong, Q.X. Zeng, Electrochem. Commun. 9 (2007) 807.
[6] C.M. Welch, R.G. Compton, Anal. Bioanal. Chem. 384 (2006) 601.
[7] J.M. Pingarrón, P. Yáñez-Sedeño, A. González-Cortés, Electrochim. Acta 53 (2008) 5848.
[8] A.I. Gopalan, K.-P. Lee, D. Ragupathy, Biosens. Bioelectron. 24 (2009) 2211.
[9] R. Gao, J. Zheng, Electrochem. Commun. 11 (2009) 608.
[10] C. Xiang, Y. Zou, L.-X. Sun, F. Xu, Electrochem. Commun. 10 (2008) 38.
[11] F. Li, Z. Wang, C. Shana, J. Song, D. Han, L. Niu, Biosens. Bioelectron. 24 (2009) 1765.
[12] P. Santhosh, K.M. Manesh, S. Uthayakumar, S. Komathi, A.I. Gopalan, K.-P. Lee, Bioelectrochemistry 75 (2009) 61.
[13] A. Safavi, N. Maleki, F. Tajabadi, E. Farjami, Electrochem. Commun. 9 (2007) 1963.
[14] S. Hrapovic, Y. Liu, K.B. Male, J.H.T. Luong, Anal. Chem. 76 (2004) 1083.
[15] J. Yu, D. Yu, T. Zhao, B. Zeng, Talanta 74 (2008) 1586.
[16] W.-Y. Liao, C.-C. Liu, T.-C. Chou, Analyst 133 (2008) 1757.
[17] J. Shen, L. Dudik, C.-C. Liu, Sens. Actuators B 125 (2007), 106.C.
[18] I.R.W.Z. Oliveira, S.C. Fernandes, I.C. Vieira, J. Pharm. Biomed. Anal. 41 (2006) 366.
[19] S.C. Fernandes, I.R.W.Z. Oliveira, O. Fatibello-Filho, A. Spinelli, I.C. Vieira, Sens. Actuators B 133 (2008) 202.
[20] G. Demirel, G. Ozçetin, F. Sahin, H. Tümtürk, S. Aksoy, N. Hasirci, React. Funct. Polym. 66 (2006) 389.
[21] H.M. Fahmy, M.M.G. Fouda, Carbohydr. Polym. 73 (2008) 606.
[22] A. Bernkop-Schnürch, A. Heinrich, A. Greimel, Eur. J. Pharm. Biopharm. 63 (2006) 166.
[23] W. Chen, H. Tang, Z. Ou, H. Wang, Y. Yang, Electrochim. Acta 53 (2007) 2065.
[24] V.B.A. Kumar, T.C.K. Mohan, K. Murugan, Food Chem. 110 (2008) 328.
[25] J.-P. Zamorano, O. Martínez-Álvarez, P. Montero, M.C. Gómez-Guillén, Food Chem. 112 (2009) 104.
[26] J.S. Bonita, M. Mandarano, D. Shuta, J. Vinson, Pharm. Res. 55 (2007) 187.
[27] K. Fujioka, T. Shibamoto, Food Chem. 106 (2008) 217.
[28] J.G. Dorea, H.M. da Costa, Br. J. Nutr. 93 (2005) 773.
[29] M. Krizman, D. Baricevic, M. Prosek, J. Pharm. Biomed. Anal. 43 (2007) 481.
[30] M. Vaher, M. Koel, J. Chromatogr. A 990 (2003) 225.
[31] Q. Liu, W. Cai, X. Shao, Talanta 77 (2008) 679.
[32] Q. Chang, M. Zhu, Z. Zuo, M. Chow, W.K.K. Ho, J. Chromatogr. B 760 (2001) 227.
[33] F. Kvasnička, J. Čopíková, R. Ševčík, J. Krátká, A. Syntytsia, M. Voldřich, Cent. Eur. J. Chem. 6 (2008) 410.
[34] X. Wang, J. Wang, N. Yang, Food Chem. 102 (2007) 422.
[35] M.L. Carvalho, M. Santhiago, R.A. Peralta, A. Neves, G.A. Micke, I.C. Vieira, Talanta 77 (2008) 394.
[36] S.K. Moccelini, A. Spinelli, I.C. Vieira, Enzyme Microb. Technol. 43 (2008) 381.
[37] L.D. Mello, M.D.P.T. Sotomayor, L.T. Kubota, Sens. Actuators B 96 (2003) 636.
[38] C.C. Casssol, G. Ebeling, B. Ferrera, J. Dupont, Adv. Synth. Catal. 348 (2006) 243.
[39] G.S. Fonseca, G. Machado, S.R. Teixeira, G.H. Fecher, J. Morais, M.C.M. Alves, J. Dupont, J. Colloid Interf. Sci. 301 (2006) 193.
[40] L. Zhang, S.L. Kosaraju, Eur. Polym. J. 43 (2007) 2956.
[41] N. Maleki, A. Safavi, F. Tajabadi, Anal. Chem. 78 (2006) 3820.

Arsenic speciation in marine product samples: Comparison of extraction–HPLC method and digestion–cryogenic trap method

Wenhua Geng, Rieko Komine, Toshiharu Ohta, Tsunenori Nakajima, Hirokazu Takanashi, Akira Ohki *

Department of Bioengineering, Faculty of Engineering, Kagoshima University, 1-21-40 Korimoto, Kagoshima 890-0065, Japan

ARTICLE INFO

ABSTRACT

For the arsenic speciation in marine product samples, two types of pretreatment-analysis combination were compared. One is the combination of solvent extraction and high performance liquid chromatography (HPLC) followed by a highly sensitive arsenic detection, while the other is the combination of alkaline digestion and cryogenic trap (CT) method followed by a highly sensitive arsenic detection. For six certified reference materials (CRMs) of marine animal samples, the concentrations of arsenobetaine (AsB) obtained from the extraction–HPLC method were very consistent with those of trimethylated arsenic species measured by the digestion–CT method. For four seaweed samples, the determination of three arsenosugars (Sugar-1, Sugar-2, and Sugar-3) was favorably carried out by the extraction–HPLC method. Those seaweed samples were also subjected to the digestion–CT method, and the amounts of dimethylated arsenic species measured by the method were approximately equal to the sum of the amounts of dimethylarsinic acid (DMAA) and three arsenosugars (Sugar-1 + Sugar-2 + Sugar-3) obtained from the extraction–HPLC method.

1. Introduction

Arsenic is a well-known toxic element, and it is also known that the toxicity is varied with the degree of methylation; thus, the toxicity tends to decrease in the order, arsenous acid $(As(III)) >$ arsenic acid or arsenate $(As(V)) \gg$ monomethylarsonic acid $(MMAA) \approx$ dimethylarsinic acid $(DMAA) >$ trimethylated species (arsenobetaine (AsB) etc.), and their structures are shown in Fig. 1. Therefore, it is very important to conduct the speciation of arsenic species. There have been many reports about the speciation of arsenic species, and Gong et al. [1] and Francesconi and Kuehnnelt [2] reviewed the various analytical methods for arsenic speciation. For the separation of arsenic species, high performance liquid chromatography (HPLC) is the most frequently used, and this method is followed by an efficient detection of trace arsenic species, such as inductively coupled plasma mass spectrometry (ICPMS) and hydride generation atomic fluorescence spectrometry (HGAFS). The combination of HPLC and these detection methods (ICPMS and HGAFS) is called HPLC–ICPMS and HPLC–HGAFS, respectively.

Another separation procedure, which has been used, is the cryogenic trap (CT) method. In this method, NaBH$_4$-reduction of arsenic species is carried out to produce arsine gases, and the gases are cryogenically trapped, which is followed by the volatilization of arsine

gases. By the reduction, inorganic (As(III) and As(V)), monomethylated, dimethylated, and trimethylated species will turn into AsH$_3$, CH_3AsH_2, $(CH_3)_2AsH$, and $(CH_3)_3As$, respectively; the boiling points of these arsine derivatives are -55, 2, 36, and $52\,^\circ$C, respectively. Thus, the volatilization of each arsine gas can be successively carried out, so that the separation of these gases is favorably attained.

The CT method is the first arsenic speciation method which was applied to environmental and biological samples [3]. The HPLC method has taken over the CT method, because the latter provides not the whole information of each arsenic species but only the information of the number of methyl group which directly attaches to arsenic atom.

However, there have been still several studies using the CT method [4–12], and an automatic arsenic speciation instrument based on the CT method is now commercially available [9]. Compared to the HPLC method, the CT method has some advantages: (i) the instrumental cost is not so high; (ii) the measuring time is very short; (iii) the information of methyl group number is easily obtained. For the HPLC method, the most frequently used column is an anion-exchange type, for which the separation of arsenobetaine (AsB, a typical trimethylated arsenic species) and other neutral species, such as As(III), is usually difficult.

Another advantage of the CT method is that it can be favorably coupled with a simple pretreatment method for biological samples, alkaline digestion, in which the sample is heated in an alkaline solution [8]. The alkaline digestion can provide not only the decomposition of proteins but also the transformation of hydride

---

* Corresponding author. Tel.: +81 99 285 8335; fax: +81 99 285 8339.
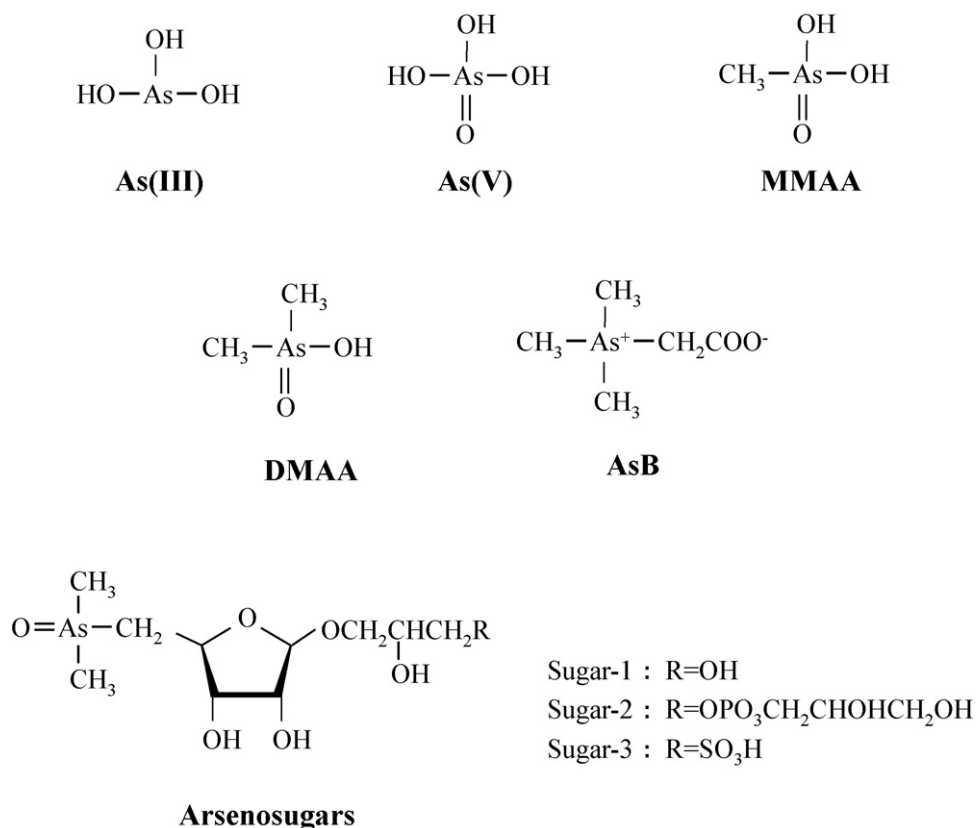*E-mail address:* ohki@be.kagoshima-u.ac.jp (A. Ohki).

Fig. 1. Structures of arsenic species.

generation-inactive species, such as AsB, into active species, such as trimethylarsine oxide. On the other hand, the extraction by a proper solvent has been usually used for the pretreatment of biological samples when the HPLC method is performed. However, this method is time-consuming compared to the alkaline digestion method.

So far, only a few studies have been done about the comparison of the two methods (HPLC and CT methods) by use of same samples. Guerin et al. [7] reported the comparative study of the two methods when the same water and inorganic samples were analyzed. However, there have been no such studies for biological samples. It is well known that methylated arsenic species are often present in marine organisms [1,2]. For the arsenic speciation in biological samples, it is necessary to conduct a proper pretreatment method before the analysis. However, there have been no studies about the comparison of the two methods focusing on the combination of pretreatment and analysis.

In this study, the arsenic speciation in biological samples, various marine product samples including not only certified reference materials (CRMs) but also real seafood samples, was carried out by the two types of pretreatment-analysis combination, the extraction–HPLC method and the digestion–CT method. The comparison between the two methods was done, especially in terms of the analysis of AsB and arsenosugars.

2. Experimental

2.1. Reagents and solutions

Sodium arsenate (Na$_2$HAsO$_4$·7H$_2$O), sodium arsenite (NaAsO$_2$), and DMAA were purchased from Wako Pure Chemical Industries Ltd., while MMAA and AsB were obtained from Tri Chemical Laboratories Inc. (Yamanashi, Japan). Distilled water was further purified by a Milli-Q system and used throughout the experiments. Analytical-grade reagents were used for the preparation of all solutions. All arsenic standard solutions were freshly prepared by serial dilution from a stock solution (1000 mg-As l^{-1}).

2.2. Samples

Six CRMs from National Research Council, Canada (DORM-2, dogfish muscle; DOLT-2, dogfish liver; and TORT-2, lobster hepatopancreas), National Institute of Standard and Technology, USA (NIST-1566b, oyster tissue), Community Bureau of Reference, EC (BCR-422, cod muscle tissue), and National Institute of Advanced Industrial Science and Technology, Japan (NMIJ-7402a, cod muscle tissue), were used. These CRMs have the certified values of total arsenic, while a few of them possess the speciation data (AsB for DORM-2 and NMIJ-7402a). Thus, the arsenic speciation data, which have been reported in the literatures for the CRMs, are listed in Table 1. Also, four eating seaweed samples, which include *Laminaria* sp., *Undaria pinnatifida*, *Hizikia fusiformis*, and *Monostroma nitidum wittrock* purchased at a local supermarket, were tested.

2.3. HPLC–HGAFS

The HPLC system was fitted with a JASCO PU-2080 pump with a Rheodyne injector and a 200 μl loop injector. The separation of the arsenic species occurred in a 250 mm × 4.1 mm Hamilton PRP-X100 column (Hamilton, Reno, NV, USA), and the flow rate of the mobile phase was adjusted to 1.1 ml min^{-1}. The photooxidation of the arsenic compounds was performed in a PSA 10.570 ultraviolet (UV) oxidation system using a K$_2$S$_2$O$_8$ solution (2%, w/v) at a flow rate of 0.36 ml min^{-1}. Hydride generation of volatile arsines prior to the detection was performed using on-line solutions of NaBH$_4$ and HCl at a flow rate of 1.8 ml min^{-1}, and atomic fluores-

Table 1
Certified and literature values of the concentrations of arsenic species in CRMs.

CRM	Total arsenic (certified) (μg-As g^{-1}, dry weight)	Arsenic species (μg-As g^{-1}, dry weight)					Ref.
		As(III)	As(V)	MMAA	DMAA	AsB	
DORM-2	18.0 ± 1.1	–	–	–	–	16.4	Certified
		n.d.	n.d.	<0.03	0.28	16.0	[13]
		n.d.	n.d.	<0.003	0. 30	15.9	[14]
		n.d.	n.d.	n.d.	0.66	15.8	[15]
DOLT-2	16.6 ± 1.2	n.d.	0.007	0.042	1.24	6.09	[16]
TORT-2	21.6 ± 1.8	n.d.	0.68	0.15	1.33	13.6	[17]
		n.d.	0.41	0.20	1.03	13.1	[18]
		n.d.	n.d.	0.03	0.97	13.8	[14]
BCR-422	21.1 ± 0.5	n.d.	n.d.	n.d.	n.d.	20.6	[19]
NMIJ-7402a	36.7 ± 1.8	–	–	–	–	33.1	Certified
NIST-1566b	7.65 ± 0.65	n.d.	0.07	0.04	1.69	1.24	[20]

n.d.: not detected.

cence spectrometry (AFS) detection was obtained with a PSA 10.055 Millennium Excalibur (PS Analytical, Orpington, UK). Detailed conditions are listed in Table 2, while the schematic representation of HPLC–HGAFS is shown in Fig. 2a.

2.4. CT–HGAAS

An appropriate volume of a standard or sample solution (0.1–2.0 ml) and 40 ml of HCl (1%, w/v) solution were introduced into a Pyrex glass reaction vessel, to which 5 ml of NaBH$_4$ (10%, w/v) solution was progressively injected using an injector within 30 s under continuous stirring for hydride generation. After the water vapor and CO$_2$ were removed by using ice/water plus ice/NaCl baths and a glass tube containing solid NaOH, respectively, the arsines generated were cryogenically trapped in a 430 mm × 5.0 mm Pyrex grass U-tube packed with quartz wool for 3 min, which had been immersed in liquid nitrogen. When the U-tube was warmed, the arsines trapped were volatilized in the sequence of their boiling points, and were introduced into a quartz-tube atomizer and determined with an atomic absorption spectrometer (AAS) (Nippon Jarrel Ash AA-890). Detailed conditions are listed in Table 3, and the CT–HGAAS system is illustrated in Fig. 2b.

Table 2
Instrumental and analytical conditions for HPLC–HGAFS.

HPLC	
Anionic column	Hamilton PRP-X100 (10 μm, 250 mm × 4.1 mm)
Guard column	Hamilton PRP-X100 (10 μm, 4.6 mm × 4.1 mm)
Mobile phase	25 mmol l^{-1} KH$_2$PO$_4$, pH 5.8
Flow rate of mobile phase	1.1 ml min^{-1}
Injection volume	200 μl
On-line photooxidation	
UV system	PSA 10.570 UV system
K$_2$S$_2$O$_8$	2% (w/v) in 0.5% (w/v) NaOH
Flow rate of K$_2$S$_2$O$_8$	0.36 ml min^{-1}
Hydride generation	
NaBH$_4$	1.4% (w/v) in 0.1% (w/v) NaOH
Flow rate of NaBH$_4$	1.8 ml min^{-1}
HCl	1.5 mol l^{-1} (UV lamp off) or 8 mol l^{-1} (UV lamp on)
Flow rate of HCl	1.8 ml min^{-1}
Detection (atomic fluorescence spectrometry)	
Detector	Excalibur (PS Analytical, Kent, UK)
Lamp	Hollow cathode arsenic lamp, 197.3 nm
Primary current	27.5 mA
Boost current	35.0 mA
Carrier gas	Argon, 300 ml min^{-1}

2.5. Pretreatment of samples

When HPLC–HGAFS was performed, the extraction of arsenic species from the sample was conducted. A 0.25 M H$_3$PO$_4$ solution (10 ml) containing 0.5 g of powdery sample was shaken in a stoppered centrifuge tube for 12 h. After centrifugation, the solution was analyzed by HPLC–HGAFS. For CT–HGAAS, the samples were subjected to an alkaline digestion. A 2 M NaOH solution (5 ml) was mixed with 0.05 g sample, and heated at 90–95 °C for 3 h. After cooling, the solution was analyzed by CT–HGAAS. These two types of pretreatment-analysis combination, extraction–HPLC method and digestion–CT method, are schematically presented in Fig. 2.

When the four seaweed samples were analyzed, the samples were vacuum-dried at 60 °C for 3–4 days and ground in an agate-mortar to make a powder, and then the resulting powdery sample was subjected to the extraction–HPLC method and the digestion–CT method.

For each run, the pretreatment of a sample was prepared by the extraction or alkaline digestion at least in duplicate, and the HPLC–HGAFS or CT–HGAAS analysis of each corresponding sample was carried out twice. From these more than four measurements, the mean value and standard deviation for the concentration of arsenic species in the sample were obtained.

3. Results and discussion

3.1. Arsenic speciation in CRMs (marine animal products) by the extraction–HPLC method

Based on the optimized conditions for HPLC–HGAFS described in Table 2, the separation of arsenic species (As(III), As(V), MMAA, and DMAA) was attained, when a mixed solution of standard com-

Table 3
Instrumental and analytical conditions for CT–HGAAS.

| Hydride generation	
HCl	1% (v/v), 40 ml
NaBH$_4$	10% (w/v) in 0.1% (w/v) NaOH, 5 ml
Trapping	
Column	Quartz wool in quartz glass U-tube (430 mm × 5.0 mm)
Trapping time	3 min
Room temperature time	1 min
Flow rate of helium	500 ml min^{-1}
Detection (atomic absorption spectrometry)	
Detector	AA-890 (Nippon Jarrell Ash)
Lamp	Hollow cathode arsenic lamp, 197.3 nm
Lamp current	12 mA
Quartz cell temperature	1050 °C
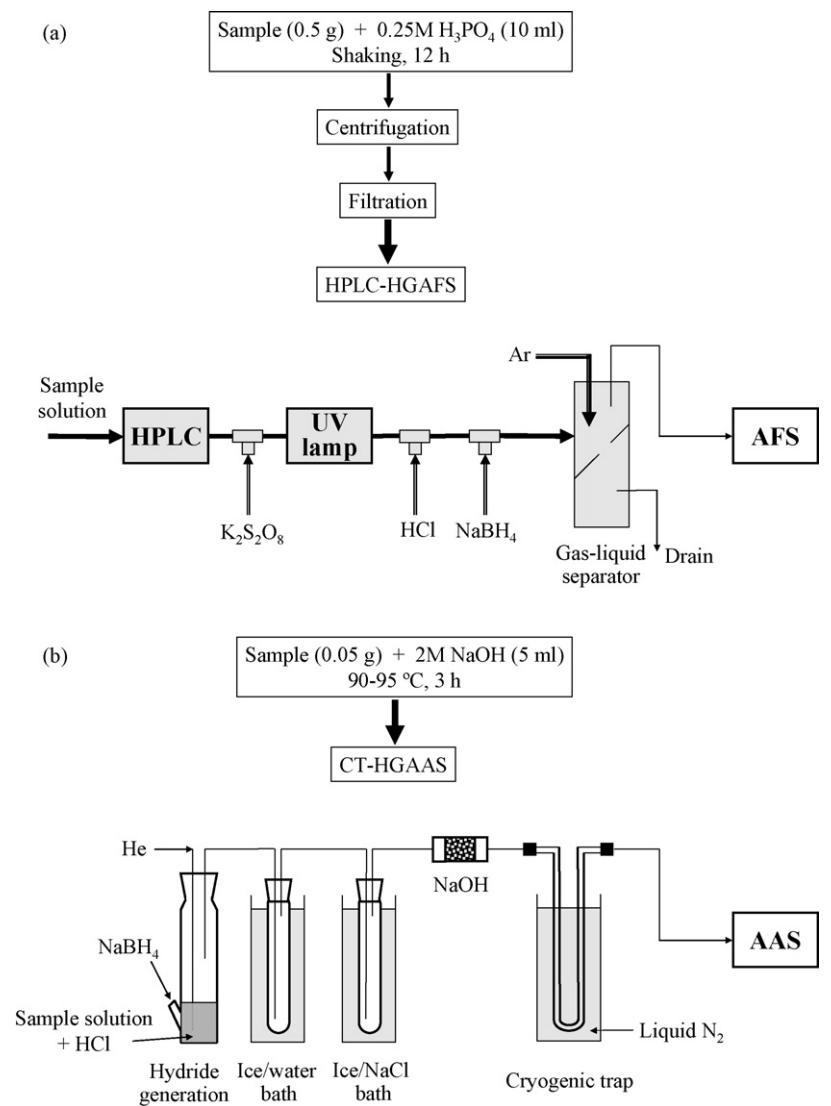
Fig. 2. Schematic diagrams of extraction–HPLC method (a) and digestion–CT method (b).

pounds was measured. The chromatogram is presented in Fig. 3a. For the detection of AsB, the sample was on-line photooxidized by using a UV oxidation system and an oxidizing agent ($K_2S_2O_8$) before the hydride generation procedure. As shown in Fig. 3b, the AsB peak was overlapped with the As(III) peak. Therefore, the quantification

of AsB was done by using the difference between with and without the photooxidation procedure. Compared to the result in a previous paper [7] in which the same HPLC column had been used, the separation between As(III) and DMAA in this study (Fig. 3a) was a little worse, probably due to column conditions. For the separation
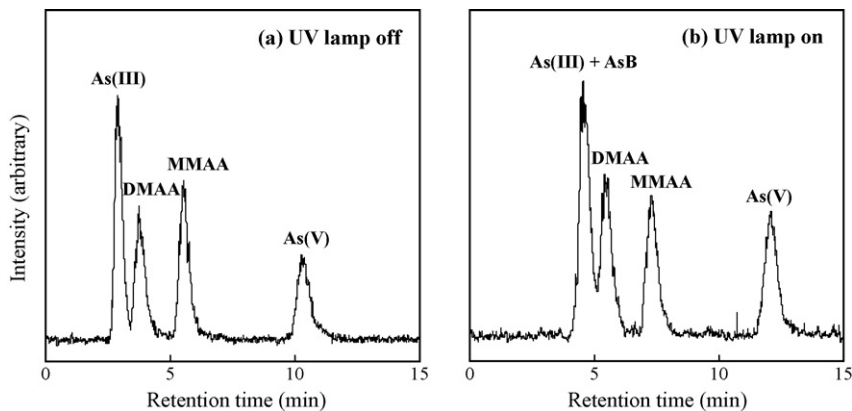
Fig. 3. Chromatograms of HPLC–HGAFS for a mixed solution of As(III), As(V), MMAA, DMAA, and AsB (25 μg-As l^{-1} each).

Table 4
Arsenic speciation in CRMs by the extraction–HPLC method.

CRM	Arsenic species (μg-As g^{-1}, dry weight)				
	As(III)	As(V)	MMAA	DMAA	AsB
DORM-2	n.d.	n.d.	n.d.	0.39 ± 0.12	16.5 ± 0.4
DOLT-2	n.d.	n.d.	n.d.	1.45 ± 0.08	6.47 ± 0.09
TORT-2	n.d.	0.45	n.d.	1.39 ± 0.08	14.6 ± 0.6
BCR-422	n.d.	n.d.	n.d.	n.d.	19.8 ± 0.1
NMIJ-7402a	n.d.	n.d.	n.d.	n.d.	31.6 ± 1.1
NIST-1566b	n.d.	n.d.	n.d.	0.70 ± 0.01	1.61 ± 0.02

n.d.: not detected.

Table 5
Arsenic speciation in CRMs by the digestion–CT method.

CRM	Arsenic species (μg-As g^{-1}, dry weight)			
	Inorganic	Monomethylated	Dimethylated	Trimethylated
DORM-2	n.d.	n.d.	n.d.	15.6 ± 0.2
DOLT-2	n.d.	n.d.	2.15 ± 0.12	6.08 ± 0.10
TORT-2	n.d.	n.d.	2.97 ± 0.21	13.5 ± 0.2
BCR-422	n.d.	n.d.	n.d.	19.8 ± 0.2
NMIJ-7402a	n.d.	n.d.	n.d.	30.0 ± 1.0
NIST-1566b	n.d.	n.d.	2.24 ± 0.33	1.48 ± 0.19

n.d.: not detected.

between AsB and DMAA (Fig. 3b), baseline separation is difficult, which had been described in previous papers [21,22].

When the arsenic speciation in biological samples is carried out by HPLC–HGAFS or HPLC–ICPMS, the solvent extraction by use of a methanol/water mixture has been frequently used for the recovery of arsenic species from the samples [20,23,24]. Recently, it is reported that a H_3PO_4 solution is also effective not only for soil samples but also for biological samples [15,25,26]. In this study, the solvent extraction with a 0.25 M H_3PO_4 solution was attempted for the six CRMs. The results of arsenic speciation by the extraction–HPLC method are indicated in Table 4, which are quite similar to those in the literatures (Table 1). It is proposed that the H_3PO_4 solution favorably works for the recovery of each arsenic species in marine product samples.

3.2. Arsenic speciation in CRMs (marine animal products) by the digestion–CT method

A mixed solution of As(III), As(V), MMAA, DMAA, and AsB was subjected to the alkaline digestion, and the resulting solution was analyzed by CT–HGAAS under the optimal conditions shown in Table 3. The chromatogram obtained is presented in Fig. 4. It is reported that inorganic arsenic (As(III) and As(V)), MMAA, DMAA, and AsB produce arsine, monomethylarsine, dimethylarsine, and trimethylarsine, respectively, by the alkaline digestion followed by the hydride generation procedure in CT–HGAAS [8]. As shown in Fig. 4, the chromatogram gives four peaks, which are assigned to As(III) + As(V) (inorganic arsenic), MMAA (monomethylated arsenic), DMAA (dimethylated arsenic), and AsB (trimethylated arsenic). For the six CRMs, the digestion–CT method was carried out, and the results are indicated in Table 5.

When only MMAA was subjected to the alkaline digestion followed by CT–HGAAS, major monomethylated arsenic peak and small inorganic arsenic peak (2–3%) were detected. This result suggests that the cleavage of As–CH$_3$ bond slightly occurs during the digestion. For other methylated arsenic species, DMAA and AsB, such a cleavage was scarcely observed. Thus, it is concluded that the digestion–CT method can be used for the approximate determination of MMAA, DMAA, and AsB.

3.3. Comparison between the extraction–HPLC method and the digestion–CT method for the arsenic speciation in CRMs

As shown in Fig. 5, the amounts of trimethylated arsenic obtained from the digestion–CT method are very consistent with those of AsB from the extraction–HPLC method. It is evident that almost all of the trimethylated arsenic species present in the CRMs is AsB, and also that the AsB in the samples is exclusively transformed into a hydride generation-active species, such as trimethylarsine oxide.

As shown in Fig. 6, the amounts of dimethylated arsenic species obtained from the digestion–CT method are considerably higher than those of DMAA from the extraction–HPLC method, when the three CRMs were analyzed. It is anticipated that the dimethylated species in the samples involve other species, such as arsenosugars. Inorganic arsenic species (As(III) and As(V)) and monomethylated species (MMAA) were not detected in the CRMs.

Actually, there were some other small peaks observed in the HPLC chromatograms of the CRMs, when the photooxidation was carried out; those peaks may be assigned to arsenosugars. However,

Fig. 4. A chromatogram of CT–HGAAS for a mixed solution of As(III), As(V) (25 μg-As l^{-1} each), MMAA, DMAA, and AsB (50 μg-As l^{-1} each).
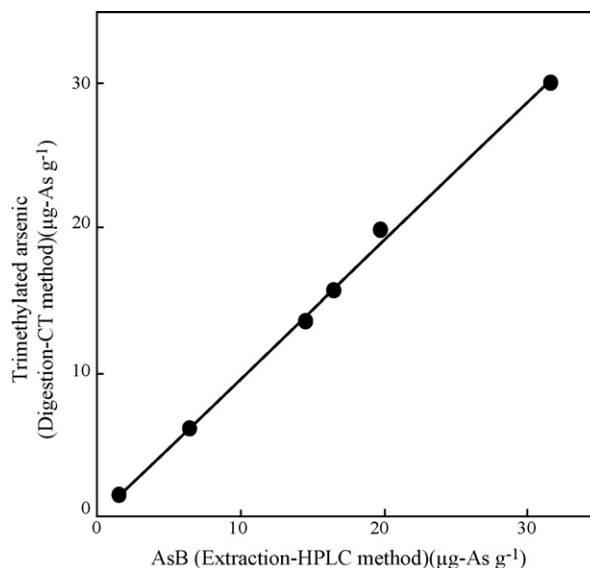
Fig. 5. Plot of the concentrations of AsB obtained from the extraction–HPLC method against those of trimethylated arsenic species from the digestion–CT method (six CRMs).
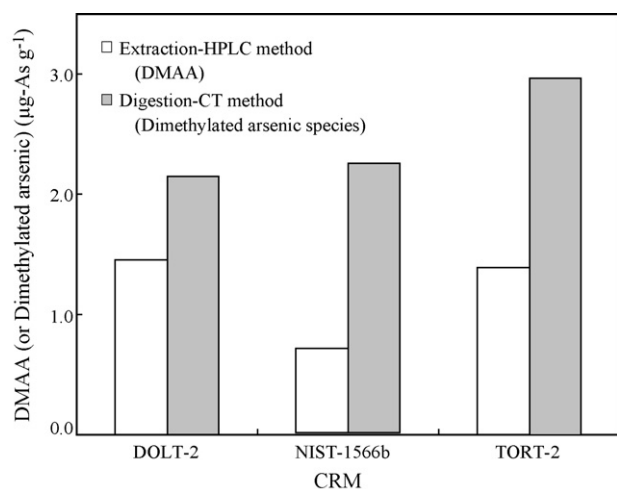
Fig. 6. Comparison of the extraction–HPLC method (DMAA) and the digestion–CT method (dimethylated arsenic species).

Fig. 7. A chromatogram of arsenosugers in *Laminaria* sp. by the extraction–HPLC method.

the concentrations of arsenosugars in the CRMs (marine animal samples) are very low, and an arsenosugar peak (Sugar-1) is overlapped by the peaks of As(III) and AsB in the HPLC chromatogram. This will be explained later.

3.4. Arsenic speciation in seaweed samples by the extraction–HPLC method

As mentioned above, the comparison between the extraction–HPLC method and the digestion–CT method cannot be favorably performed when the CRM samples are used. It is well known that seaweeds contain a notably high concentration of arsenosugars [27–29]. Therefore, seaweed samples are used for the comparison between the extraction–HPLC method and the digestion–CT method in terms of the analysis of dimethylated species. Because proper CRM samples for seaweed cannot be available, four eating seaweeds, *Laminaria* sp., *U. pinnatifida*, *H. fusiformis*, and *M. nitidum wittrock*, were purchased at a local supermarket, and tested for the arsenic speciation.

A dried powdery sample of *Laminaria* sp. was subjected to the extraction–HPLC method. When the photooxidation procedure was not applied, several peaks, some of which may be assigned to arsenosugars, were observed in the chromatogram; however, only As(III) and DMAA peaks were accurately determined. On the other

hand, the peaks of arsenosugars were clearly obtained with the photooxidation procedure as shown in Fig. 7. Three peaks appeared, and these were assigned to Sugar-1, Sugar-2, and Sugar-3 according to the literatures [27–29] (see Fig. 1). The extraction–HPLC method was also carried out for the other seaweed samples, and the concentrations of arsenic species were obtained. The results are listed in Table 6.

The Sugar-1 peak was overlapped with the As(III) peak. Therefore, the quantification of Sugar-1 was conducted by using the difference between with and without the photooxidation procedure. As mentioned before, the AsB peak may appear at the same position. When the digestion–CT method was carried out for the four seaweed samples, trimethylated arsenic species was not detected (see Table 7). Therefore, the presence of AsB peak in the chromatogram was ignored. Because pure compounds of arsenosugars were not available, the concentrations of arsenosugars were calculated using the calibration curve of DMAA.

Seaweeds, *Laminaria* sp. and *U. pinnatifida*, contained fairly high concentrations of the three arsenosugars, while *M. nitidum wittrock* had a low concentration of Sugar-1. On the other hand, majority of arsenic species in *H. fusiformis* was As(V), which has been reported in the literatures [30,31].

3.5. Arsenic speciation in seaweed samples by the digestion–CT method

For the same seaweed samples, the digestion–CT method was performed. The results are listed in Table 7. As described above,

Table 6
Arsenic speciation in four seaweed samples by the extraction–HPLC method.

Sample	Arsenic species (μg-As g^{-1}, dry weight)							
	As(III)	As(V)	MMAA	DMAA	AsB	Sugar-1	Sugar-2	Sugar-3
Laminaria sp.	0.64 ± 0.05	n.d.	n.d.	1.03 ± 0.02	n.d.	7.65 ± 0.36	9.81 ± 0.52	27.4 ± 1.6
Undaria pinnatifida	0.78 ± 0.03	n.d.	0.27 ± 0.07	0.91 ± 0.02	n.d.	9.97 ± 0.50	5.45 ± 0.14	8.43 ± 0.34
Hizikia fusiformis	n.d.	78.2 ± 0.4	n.d.	n.d.	n.d.	10.6 ± 0.1	n.d.	n.d.
Monostroma nitidum wittrock	n.d.	n.d.	n.d.	n.d.	n.d.	2.22 ± 0.08	n.d.	n.d.

n.d.: not detected.

Table 7
Arsenic speciation in four seaweed samples by the digestion–CT method.

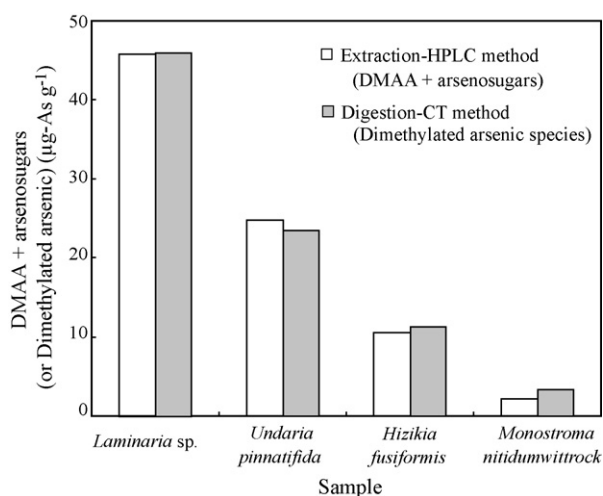| Sample	Arsenic species (μg-As g^{-1}, dry weight)			
	Inorganic	Monomethylated	Dimethylated	Trimethylated
Laminaria sp.	0.36 ± 0.05	n.d.	45.9 ± 0.4	n.d.
Undaria pinnatifida	0.21 ± 0.03	n.d.	23.5 ± 0.4	n.d.
Hizikia fusiformis	79.9 ± 0.3	n.d.	11.3 ± 0.5	n.d.
Monostroma nitidum wittrock	0.66 ± 0.04	n.d.	3.32 ± 0.18	n.d.

n.d.: not detected.

Fig. 8. Comparison of the extraction–HPLC method (DMAA + arsenosugars) and the digestion–CT method (dimethylated arsenic species).

almost no trimethylated arsenic species were detected for the four seaweed samples. It has been reported that seaweeds do not contain trimethylated arsenic species, such as AsB [29]. Comparing the data from the extraction–HPLC method and those from the digestion–CT method, it is assumed that arsenosugars are decomposed into hydrogenation-susceptible DMAA during the alkaline digestion.

Actually, for each seaweed sample, the sum of the amounts of DMAA and three arsenosugars (Sugar-1 + Sugar-2 + Sugar-3) obtained from the extraction–HPLC method is approximately equal to the amount of dimethylated species from the digestion–CT method, as indicated in Fig. 8. It is proposed that the three arsenosugars can be exclusively transformed into DMAA, which is favorably detected as dimethylated arsenic in the CT method. Further, the seaweeds contain small amounts of As(III), which is detected as inorganic arsenic by the digestion–CT method.

For *H. fusiformis*, inorganic arsenic was detected in a considerable amount, which is comparable to the amount of As(V) obtained by the extraction–HPLC method (Table 6). Also, dimethylated arsenic was observed, and the amount was similar to that of Sugar-1.

Consequently, it is found that the arsenosugars in seaweed samples can be favorably measured as dimethylated arsenic by use of the digestion–CT method, while As(III) and As(V) present in the samples are detected as inorganic arsenic.

4. Conclusion

The comparison of the extraction–HPLC method and the digestion–CT method in terms of arsenic speciation in various marine product samples was carried out. For six CRMs, the amounts of trimethylated arsenic species obtained from the digestion–CT method were very consistent with those of AsB from the extraction–HPLC method. It is found that almost all of the trimethylated arsenic species present in the CRMs is AsB, and also that the AsB in the sample is exclusively transformed into

a hydrogenation-active species (probably trimethylarsine oxide) in the alkaline digestion procedure. However, the concentrations of dimethylated arsenic species obtained from the digestion–CT method are considerably higher than those of DMAA from the extraction–HPLC method. For four seaweed samples, the sum of the amounts of DMAA and three arsenosugars (Sugar-1 + Sugar-2 + Sugar-3) from the extraction–HPLC method was proved to be approximately equal to the amount of dimethylated arsenic species from the digestion–CT method, suggesting that the arsenosugars are favorably transformed into hydrogenation-active species (DMAA) in the digestion procedure. It is concluded that, by use of the digestion–CT method, the concentration of AsB in marine animal samples and that of arsenosugars in seaweed samples can be approximately assessed.

References

[1] Z. Gong, X. Lu, M. Ma, C. Watt, X.C. Le, Talanta 58 (2002) 77.
[2] K.A. Francesconi, D. Kuehnnelt, Analyst 129 (2004) 373.
[3] R.S. Braman, C.C. Foreback, Science 182 (1973) 1247.
[4] J.L. Burguera, M. Burguera, C. Rivas, P. Carrero, Talanta 45 (1998) 531.
[5] J.C. Ng, D. Johnson, P. Imray, B. Chiswell, M.R. Moore, Analyst 123 (1998) 929.
[6] A.G. Howard, C. Salou, J. Anal. At. Spectrom. 13 (1998) 683.
[7] T. Guerin, N. Molenat, A. Astruc, R. Pinel, Appl. Organometal. Chem. 14 (2000) 401.
[8] Suhendrayatna, A. Ohki, T. Nakajima, S. Maeda, Chemosphere 46 (2002) 325.
[9] R. Zhao, M. Zhao, H. Wang, Y. Taneike, X. Zhang, Sci. Total Environ. 371 (2006) 293.
[10] R. Regmi, B.F. Milne, J. Feldmann, Anal. Bioanal. Chem. 388 (2007) 775.
[11] S. Musil, T. Matousek, Spectrochim. Acta B 63 (2008) 685.
[12] T. Matousek, A. Hernandez-Zavala, M. Svoboda, L. Langrova, B.M. Adair, Z. Drobna, D.J. Thomas, M. Styblo, J. Dedina, Spectrochim. Acta B 63 (2008) 396.
[13] W. Goessler, D. Kuehnelt, C. Schlagenhaufen, Z. Slejkovec, K.J. Irgolic, J. Anal. At. Spectrom. 13 (1998) 183.
[14] M.A. Suner, V. Devesa, O. Munoz, D. Velez, R. Montoro, J. Anal. At. Spectrom. 16 (2001) 390.
[15] I. Pizarro, M. Gomez, C. Camara, M.A. Palacios, Anal. Chim. Acta 495 (2003) 85.
[16] R. Wahlen, S. McSheehy, C. Scriver, Z. Mester, Anal. At. Spectrom. 19 (2004) 876.
[17] J.A. Brisbin, C. B'Hymer, J.A. Caruso, Talanta 58 (2002) 133.
[18] J. Kirby, W. Maher, J. Anal. At. Spectrom. 17 (2002) 838.
[19] J. Alberti, R. Rubio, G. Rauret, Fresenius J. Anal. Chem. 351 (1995) 415.
[20] Z. Slejkovec, J.T. van Elteren, A.R. Byrne, Talanta 49 (1999) 619.
[21] R.E. Paproski, X.C. Le, Anal. Chim. Acta 526 (2004) 69.
[22] S. Rattanachongkiat, G.E. Millward, M.E. Foulkes, J. Environ. Monit. 6 (2004) 254.
[23] J.L. Gomez-Ariza, D. Sanchez-Rodas, I. Giraldez, E. Morales, Analyst 125 (2000) 401.
[24] J.L. Gomez-Ariza, D. Sanchez-Rodas, I. Giraldez, E. Morales, Talanta 51 (2000) 257.
[25] M.J. Ellwood, W.A. Maher, Anal. Chim. Acta 477 (2003) 279.
[26] S.G. Salgado, M.A.Q. Nieto, M.M.B. Simon, Talanta 68 (2006) 1522.
[27] A.D. Madsen, W. Goessler, S.N. Pedersen, K.A. Francesconi, J. Anal. At. Spectrom. 15 (2000) 657.
[28] Z. Slejkovec, E. Kapolna, I. Ipolyi, J.T.V. Elteren, Chemosphere 63 (2006) 1098.
[29] V.W.M. Lai, W.R. Cullen, C.F. Harrington, K.J. Reimer, Appl. Organomet. Chem. 11 (1997) 797.
[30] S. Hirata, H. Toshimitsu, Appl. Organomet. Chem. 21 (2007) 447.
[31] S. Ichikawa, M. Kamoshida, K. Hanaoka, M. Hamano, T. Maitani, T. Kaise, Appl. Organomet. Chem. 20 (2006) 585.

Review

Sample treatment and determination of pesticide residues in fatty vegetable matrices: A review

Bienvenida Gilbert-López, Juan F. García-Reyes, Antonio Molina-Díaz*

Analytical Chemistry Research Group, Department of Physical and Analytical Chemistry, University of Jaén, 23071 Jaén, Spain

ABSTRACT

A demanding task in pesticide residue analysis is yet the development of multi-residue methods for the determination of pesticides in vegetables with relatively high fat content (i.e. edible oils and fatty vegetables). The separation of pesticides and other chemical contaminants from high-fat food samples prior to subsequent steps in the analytical process is yet a challenging issue to which much effort in method development has being applied. This review addresses the main sample treatment methodologies for pesticide residue analysis in fatty vegetable matrices. Even with the advent of advanced hyphenated techniques based on mass spectrometry these complex fatty matrices usually require extensive sample extraction and purification. Current methods involve the use of one or the combination of some of the following techniques for both the sample extraction and clean-up steps: liquid–liquid partitioning, solid-phase extraction (SPE), gel-permeation chromatography (GPC), matrix solid-phase dispersion (MSPD), etc. An overview of methods developed for these contaminants in fatty vegetables matrices is presented. Sample extraction and purification techniques are discussed and their most recent applications are highlighted. This review emphasizes that sample preparation is a critical step, but also the determination method is, and cannot be treated separately from sample treatment. In recent years, the appearance and use of new, more polar pesticides has fostered the development of liquid chromatography/mass spectrometry (LC–MS) besides gas chromatography. The main features of LC–MS for the analysis of multi-class pesticides in fatty vegetable samples will be also underlined, with an emphasis on the multi-class, multi-residue strategy and the difficulties associated.

Contents

* Corresponding author. Tel.: +34 953 212147; fax: +34 953 212940.
  E-mail address: amolina@ujaen.es (A. Molina-Díaz).

1. Introduction

Pesticide testing in foodstuffs is a challenging application involving the simultaneous trace analysis of a wide range of agrochemicals. Over 800 compounds are applied to agricultural crops in order to control undesirable moulds, insects or weeds [1]. Considering that the presence of trace amounts of both pesticide residues and their degradation products could be potential health hazards, they have to be controlled. Monitoring pesticide residues in food is therefore of great interest to ensure "food safety" in terms of pesticide residue levels. For this reason, numerous regulations such as the European Union directives have set maximum residue limits (MRLs) for pesticides in food [2–4].

In pesticide testing, the development of multi-residue methods, which allows proper control of a large number of pesticides in a unique analysis, is basically the main applied strategy [4]. However, the different classes and physico-chemical properties make difficult the development of methodologies which cover all the analytes under study. Sometimes, different sample treatment methodologies are necessary. The selection of sample preparation methodology is highly dependent on both analyte and sample nature. In relation to the later, sample preparation methods are developed taking into consideration the fat content, being the limit between "fatty" and "non-fatty" food matrices usually set at 2–5% [5].

Non-fatty foods of plant origin represent the most frequently analyzed samples for pesticide residues. Among this group, special attention is paid to fruits and vegetables that are mostly consumed raw or after minimum postharvest processing. In addition, fruits and vegetables represent the main ingredients in products intended for infants and small children ("babyfood") in which pesticide residues are specially strictly regulated and monitored [6]. For these matrices (i.e.: tomato, lettuce, apples, etc.), we can found comprehensive, straightforward and reliable methods in the literature (based on acetonitrile or ethyl acetate partitioning) [4,5].

In contrast, the analysis of pesticide residues in fatty vegetable matrices is yet a challenging issue, because of the inherent complexity of the matrix. This fosters the development of strategies to isolate/extract the pesticide fraction from the whole fatty matrix. In fact, it is very difficult to avoid the co-extraction of fatty material, even more, taking into account that some of the pesticides which are usually targeted are fat-soluble non-polar compounds (viz. organochlorine), and tends to concentrate and remain in the fat. Since, high recoveries of most multi-class pesticides must be obtained in a ideally fat-free extract, an additional clean-up step is usually included prior to subsequent steps in the analytical process [7,8].

Many multi-residue procedures employing different clean-up techniques and a variety of detection methods have been reported for the determination of pesticide residues in fatty vegetable matrices. A relatively recent review described the chromatographic methods available for the determination of pesticide residues in olive oil and olives [8]. This review addresses the main sample treatment methodologies for pesticide residue analysis in fatty vegetable matrices, including all kinds of fatty vegetables matrices (such as soybean or avocado) together with all kind of vegetable oils (Table 1). Even with the advent of advanced hyphenated techniques based on mass spectrometry these complex fatty matrices usually require extensive sample extraction and purification. Current methods involve the use of one or the combination of some of the following techniques for both the sample extraction and clean-up steps: liquid–liquid partitioning, adsorption chromatography, gel-permeation chromatography (GPC), solid-phase extraction (SPE), matrix solid-phase dispersion (MSPD), etc. From all these techniques, the more commonly applied approach for pesticide extraction in fatty vegetable matrices so far is liquid par-

Table 1
Summary of the main vegetables with high-fat content[a] [14].

Commodity	Fat content (%)	Features/composition
Vegetable oils		
Olive oil	100	13.8% saturated, 72.9% monounsaturated fatty acids
Soybean oil	100	15.6% saturated, 22.8% monounsaturated fatty acids
Sunflower oil	100	9% saturated, 57% monounsaturated
Corn oil	100	12.9% saturated, 27.6% monounsaturated
Sesame oil	100	14.2% saturated, 39.7% monounsaturated fatty acids
Peanut oil	100	16.9% saturated, 46.2% monounsaturated fatty acids
Mustard oil	100	59% monounsaturated fatty acids
Fatty vegetables		
Olives	18–25	–
Avocado	14.66	73.2% water
Oat	6.9	8.2% water, 66% carbohydrates
Nuts, acorns, raw	23.86	27.9% water, 40.7% carbohydrates
Nuts, almonds unroasted	49.4	4.7% water, 21.7% carbohydrates
Nuts, coconut meat	33.49	46.9% water, 15.2% carbohydrates
Nuts, hazelnuts or filberts	60.7	5.3% water, 16.7% carbohydrates
Nuts, walnuts english	65	4.07% water, 13.7% carbohydrates
Soybean green, raw	6.8	67% water, 11.0% carbohydrates
Sesame	49.7	23.4% carbohydrates

[a] USDA National Nutrient Database for Standard Reference, Release 20 (2007). (http://www.nal.usda.gov/fnic/foodcomp/search/).

titioning with organic solvents followed by a clean-up with SPE or GPC. Over 70% of the methods are based on this scheme, being the separation, identification and quantitation of the pesticides undertaken by chromatographic techniques coupled to mass spectrometric detectors. An overview of methods developed for these contaminants in fatty vegetables matrices is presented. Sample extraction and purification techniques are discussed and their most recent applications are outlined. This review emphasizes that sample preparation is a critical step, but also determination is, and cannot be treated separately from sample treatment but all as one. In recent years, the appearance and use of new, more polar pesticides has prompted the use of liquid chromatography/mass spectrometry instead of gas chromatography. Its advantaging features for the analysis of multi-class pesticides in fatty vegetable samples will be also highlighted.

2. Sample treatment techniques for pesticide residue analysis in fatty vegetable matrices

2.1. General considerations

Despite advances in the sensitivity of analytical instrumentation for the end-point determination of analytes in food samples, a pre-treatment is usually required to extract and isolate the target analytes from the food matrix, thus facilitating their determination [9,10]. In most cases, although the analytes of interest are isolated from the bulk matrix, several contaminants may also be co-extracted, as well as part of the matrix, which could interfere in the determination step of the analysis. Consequently, further purification of the extract is required before the analytes determination. This step is called the clean-up step and aims at the isolation of the target analytes from potential interfering co-extractives as well as discarding the extraction solvent and preparing the target analytes in an appropriate chemical form for its characterization and quantification.

Therefore, pesticide residue analysis protocols involve two main stages: the isolation of the pesticides from the matrix (sample treatment) and the analytical method for the determination. Sample

treatment, which involves both the extraction of the pesticides and the purification of the sample extract obtained, still remains as the bottleneck of the entire procedure, despite much progress on automation has been accomplished [11].

The choice of sample treatment is also related to the detection method. The more sensitive and specific detection method is used, the less stages of sample treatment will be required. If non-selective detectors (such as NPD or FID in gas chromatography (GC) or UV in liquid chromatography (LC)) are used, then the number of stages of the sample treatment will be higher and a more detailed clean-up will be required. In contrast, if state-of-the-art mass spectrometric techniques (i.e. tandem mass spectrometry using triple quadrupole instruments) are used in combination with GC or LC, then there is no need to perform a dedicated clean-up of the sample extract. Alternatively, appropriate dilutions can be carried out if the sensitivity of the method is enough to meet the concentration levels targeted. In contrast, the use of non-dedicated cleanup stages can foster the occurrence of matrix-effects during the detection step in both GC and LC methods. A matrix-effect is considered to be a suppression or enhancement of the analyte response due to the presence of co-eluting matrix constituents during the course of the (chromatographic) run [12]. Matrix-effects can be estimated by comparing the response obtained from a standard solution and that from a spiked sample extracted. The matrix-effects are generally due to the influence of co-eluting compounds on the actual ionization process, that is well before the analyte ion enter the mass analyzer. Therefore matrix-effects must be solved prior to analyte ionization, for instance by eliminating the sample constituents responsible of the matrix-effects, which would involve improvements on sample treatment and/or the chromatographic separation. As an alternative, lowering the injected sample volume or performing dilutions of the sample extract might help to overcome this problem, although this decreases the overall method performance in terms of limits of detection [12].

The sample treatment applied depends heavily on the complexity of the matrix. In general in pesticide analysis in crops, we distinguish between four types of matrices when developing or validating a method: high water content (e.g. tomato), high acidic content (e.g. citrus), high sugar content (i.e. raisins) and high-fat content (olives or avocado). In all cases, it is often necessary clean-up stages to remove non-desirable components of the matrix such as pigments (chlorophyll, carotenoids), triacylglicerides, lecitine, etc. There are several accepted methods for pesticide multi-residue analysis in fruits and vegetables samples with high water, acidic or sugar content. Probably the most complex matrices are those with high-fat content, basically because of it is quite complex to extract the pesticides without co-extraction of lipids, which usually are difficult to remove from the extract and may harm the detection system [7,8].

Another issue is the nature and number of analytes targeted in the method. There is a wide range of analytes with different physico-chemical properties. For this reason, more generic (less specific) treatment should be applied when developing multi-residue methods. On the contrary, when dealing with a family of compounds, more specific or selective methods can be applied (i.e.: the use of molecularly imprinted polymers). Finally, it should be noted that it is desirable that the method involves low solvent consumption, to be environmentally friendly and also safer to apply by the analyst [13].

A clear distinction should be made when developing methodologies for the sample treatment of fatty vegetables matrices with relatively high-fat content (i.e. up to 25% fat) and edible vegetable oils (*ca.* 100% fat composition), the latter being generally more complex. Table 1 shows the composition and main features of main fatty vegetable matrices [14]. An overview of selected methods classified according to the sample treatment techniques used

for the determination of pesticides in fatty vegetable matrices is included in Table 2 [15–80].

2.2. Techniques

Typically, most protocols for the extraction of pesticides in food exploit the partitioning of analytes between the matrix (solid or semisolid) phase and either a water-immiscible solvent (solvent-based methodologies) or a sorbent material (sorbent-based procedures).

2.2.1. Solvent-based extraction and clean-up methodologies

To date, liquid partitioning is probably the main strategy used for the sample treatment of pesticides in fatty matrices. Although manually shaking a finely dispersed solid or semisolid sample with a suitable solvent can be effective, blending the sample in the presence of the solvent in a high-speed homogenizer often ensures sample disruption and a better analyte extraction. This technique so called liquid-phase extraction (LPE) or liquid–solid extraction (LSE), is the most popular for extracting contaminants in food samples such as eggs, fruits and vegetables [5,81]. Nowadays there are various well known and efficient general extraction procedures based on acetonitrile [82,36], ethyl acetate [83–86] or acetone [86,87]. These extraction methodologies, effective for extracting both polar and non-polar compounds, are typically straightforward, and cost-effective, allowing a throughput of *ca.* 30–50 extractions per day in a medium size laboratory [88]. The main advantages are simplicity and effectiveness depending on the solvent used. The large volume of (toxic) solvents and the lack of automation are amongst the main pitfalls of this methodology.

Liquid partitioning between the fatty matrix dissolved in hexane and acetonitrile was one of the earliest methods reported for the isolation of pesticides in food matrices with high-fat content (i.e. edible oils) [8,89]. Using an appropriate ratio of acetonitrile to hexane, the insecticides were preferentially partitioned into the polar acetonitrile layer. The bulk of the lipids remained solubilized in the non-polar hexane because of their relatively high hydrocarbon content. This approach is far from adequate for the clean-up of samples for pesticide analysis at the levels required by today's standards using GC or LC instrumentation. However, it did provide a basis for further developments.

When liquid partitioning is used, it is just a part of the method and usually acts with different roles in combination with other methodologies. For instance:

1. It can be used combined with SPE purification using cartridges or a dispersive solid-phase clean-up [82].
2. It can be used for preliminary partitioning/fractionation before GPC, MSPD or other methodologies.
3. It can be used as a single purification stage (using appropriate solvent combinations)
4. Only as a single liquid–liquid extraction procedure (dirty for vegetable oils).

2.2.1.1. Procedures based on liquid partitioning (combined with SPE).
The QuEChERS method (stands for quick, easy, cheap, effective, rugged and safe) widely extended for fruit and vegetables [82], have been also applied to fatty vegetable matrices such as avocado, olives and even olive oil (diluting the matrix with water) [38,39]. This basic procedure is based on a liquid partitioning with acetonitrile followed by a dispersive SPE clean-up with primary secondary amine (PSA) [36,37,82] (Fig. 1). The main advantage of this protocol is the relatively low solvent consumption, at least as compared to previous liquid partitioning based methods. In the case of fatty matrices, the clean-up was performed using a combination of PSA, graphitized carbon black (GCB) and C_{18}. Recently, an alternative

Table 2
Summary of recent methodologies described for the sample treatment and chromatographic determination of pesticide residues in fatty vegetables matrices [15–80].

	Matrix	Sample treatment and clean-up step	Determination	Recovery rates (%)	Anal. features	Ref.
Solvent-based (extraction and clean-up) techniques						
Liquid partitioning						
Amitrole, dimethoate and diuron	Olive oil	Liquid partitioning of olive oil dissolved in n-hexane with acetonitrile/H$_2$O (HCOOH 1%) 80:20 (v/v). Direct injection of aqueous extract by LC–MS	LC–MS/MS ESI-QQQ-(+)	70–95% RSD range: 1–8%	LOD $\leq$ 0.01 mg kg^{-1}	[15]
15 organophosphorus pesticides	Olive oil	Liquid partitioning (twice) of olive oil (dissolved in n-hexane) with acetonitrile saturated with n-hexane	GC-NPD GC-FID	73–166% RSD range: 2–18%	LOD range 0.0001–0.001 mg kg^{-1}	[16]
Dimethoate, parathion-methyl, fention, methidathion, parathion-ethyl	Olive oil	Liquid partitioning with acetonitrile and centrifugation. No clean-up	GC-FID	78–97% RSD range: 2–11%	LOQ $\leq$ 0.05 mg kg^{-1}	[17]
Rotenone	Olives	Liquid partitioning with acetonitrile	HPLC	75–104% RSD: 8%	LOD: 0.02 mg kg^{-1}	[18]
Deltamethrin	Olives	Partitioning with acetone/petroleum ether dichloromethane using a high-speed blender, clean-up by partitioning with n-hexane	LC–MS/MS	73–96% RSD range: 1.3–9.6%	LOQ: 0.01 mg kg^{-1}	[19]
13 organophosphorus insecticides	Olive oil	Liquid–liquid partition (twice) (2 g of olive oil dissolved in 2 mL hexane) with 10 mL of acetonitrile	GC-NPD	74–118% RSD range: 1–16%	LOD range 0.001–0.02 mg kg^{-1}	[20]
Multi-residue of 19 multi-class pesticides	Avocado	Extraction by ultrasonication using a methanolic ammonium acetate–acetic acid buffer followed by centrifugation. 1:5 dilution (0.2 g commodity mL^{-1})	LC–MS/MS MRM mode	70–120% RSD range: non-available	LOQ < 0.02 mg kg^{-1}	[21]
169 multi-class pesticides	Soya	Extraction with acetone/CH$_2$Cl$_2$ liquid petroleum. "Dilute and shot strategy" (1:20 dilution)	LC–MS/MS ESI-QQQ-(+ and −)	70–120%, RSD < 20% (>70% pesticides)	LOD range: 0.0001–0.002 µg kg^{-1} LOQ range: 0.01–0.1 mg kg^{-1}	[22]
Diquat and paraquat	Olive oil	Liquid partitioning (twice): 2 g olive oil dissolved in 2 mL of n-hexane with 2 mL and H$_2$O 5 mM HFBA	LC-Electrospray-(+)-QQQ-MS/MS; ion pairing formation with HFBA	>92% RSD < 7%	LOD: 0.004 mg kg^{-1}	[23]
108 multi-class pesticides	Avocado	Extraction with methanol–water and partition into dichloromethane	LC-Electrospray-QQQ-MS/MS (+ and −)	70–120% RSD range $\leq$25%	LOQ <0.01 mg kg^{-1}	[24]
Liquid partitioning + SPE/MSPD						
35 multi-class pesticides	Olive oil	Olive oil dissolved in n-hexane. Liquid partitioning with acetonitrile. Clean with Envicarb SPE cartridge (graphitized non-porous carbon)	GC-ECD GC-NPD	71–107% RSD range: 2.4–12%	LOQ range: 0.002–0.05 mg kg^{-1}	[25]
28 multi-class pesticides	Soybean oil	Low-temperature fat precipitation, followed by a clean-up process based on dispersive solid-phase extraction with PSA and C$_{18}$ as sorbents and magnesium sulfate for the removal of residual water	GC–MS SIM 3 ions	70–110% RSD < 20%	LOQ range: 0.02–0.25 mg kg^{-1}	[26]
Dimethoate and fenthion	Olive oil	Liquid partitioning with acetonitrile saturated with hexane, followed by clean-up using a C$_{18}$ cartridge (C$_{18}$)	GC-Q-MS (SIM) GC-NPD	78–84% RSD range: non-available	N/A	[27]
Multi-residue of 30 insecticides (organophosphorus, organochlorine, pyrethroids) and 5 triazine herbicides	Olive oil	Liquid partitioning with acetonitrile (olive oil dissolved in hexane), clean-up first with an SPE Envicarb cartridge and final step with a normal phase Diol SPE cartridge	GC-ECD GC-NPD	71–107% RSD range: 0.3–5.8%	N/A	[28]
Multi-residue of organochlorine, organophosphorus and PCBs	Olive oil	Liquid partitioning with acetonitrile: dichloromethane 95:5, followed by clean-up by SPE using C$_{18}$ (500 mg) and Florisil	GC-ECD GC-NPD	88–105% RSD < 5%	N/A	[29]

Analytes	Matrix	Extraction/clean-up	Instrument	Recovery/RSD	LOD/LOQ	Ref.
Simazine, atrazine, propazine, terbuthylazine, diuron, oxyfluorfen, diflufenican and norflurazone	Olive oil	Liquid partitioning with acetonitrile/hexane and clean-up with Florisil column	GC–MS/MS	90–102% with RSD range: 8–11%	LOQ range 0.04–0.05 mg kg^{-1}	[30]
Azimsulfuron, isoproturon, pencycuron, pyrazosulfuron-ehtyl, chlortoluron, diuron, chloroxuron, cyclosulfamuron, ethoxysulfuron	Soybean	Liquid partitioning with acetonitrile, followed by a clean-up with 2 liquid–liquid extraction with n-hexane and SPE using C$_{18}$ cartridges and acetonitrile as eluting solvent	LC-TOFMS ESI (+)	70–114% RSD range: 2–11%	LOD average: 0.0003–0.01 mg kg^{-1}	[31]
52 multi-class pesticides (non GC amenable): 43 pesticides and 9 pesticide metabolites	Avocado	Liquid partitioning with MeOH:water followed by a clean-up step using SPE HLB	LC–MS/MS ESI-QQQ-(+) MRM mode	70–110%; RSD < 15%	LOQ average <0.01 mg kg^{-1}	[32]
186 multi-class pesticides	Soybean; sesame	Liquid partitioning with acetonitrile/ethyl acetate. Clean-up using a PSA/SAX cartridge. Eluent solvent: acetone-n-hexane (30:70, v/v)	GC–MS SIM; 3 ions	Recoveries > 50% for 128 compounds; RSD 4–21%	N/A	[33]
Multi-residue of 53 multi-class pesticides	Olives	Liquid partitioning with acetonitrile, followed by clean-up using a Florisil cartridge	LC–MS/MS ESI-QQQ-(+) MRM mode	70–109% RSD < 20%	LOQ range 0.0005–0.01 mg kg^{-1}	[34]
Multi-residue of 18 herbicides and insecticides	Olives	Liquid partitioning with acetonitrile. SPE with graphitized carbon black (GCB) cartridges	GC-ECD GC-NPD	69–88% RSD range: 1–15%	N/A	[35]
341 multi-class pesticides	Avocado, coconut	Ethyl acetate partitioning followed by dispersive solid-phase extraction clean-up (using PSA and graphitized carbon black) (clean-up only for the GC–MS large volume injection method. LC–MS/MS without clean-up)	LC–MS/MS (140) ESI-QQQ-(+) GC–MS (201)	74–114% (>92% pesticides) RSD range: 11–22%	LOQ average: 0.01 mg kg^{-1}	[7]
QuEChERS						
229 multi-class pesticides	Avocado	QuEChERS (liquid partitioning with acetonitrile followed by a clean-up step based on dispersive solid-phase extraction with PSA).	GC–MS/MS and LC–MS/MS	70–120% (90–110% for 206 pesticides)	LOQ <0.01 mg kg^{-1}	[36]
32 multi-class pesticides	Fatty food with relatively low fat content (i.e. avocado)	QuEChERS (liquid partitioning with acetonitrile followed by a clean-up step based on dispersive solid-phase extraction with PSA)	GC–MS/MS and LC–MS/MS	70–120% RSD ≤15%	LOQ <0.01 mg kg^{-1}	[37]
16 multi-class pesticides	Olive oil	QuEChERS method modified for high-fat content matrices: liquid partitioning with acetonitrile followed by clean-up with PSA-GCB-C$_{18}$	GC–MS and LC–MS/MS	70–109% and RSD < 20% (GC–MS) 88–130% (LC–MS/MS); RSD < 10%	N/A	[38]
100 multi-class pesticides	Olive oil	QuEChERS: liquid partitioning with acetonitrile followed by clean-up with PSA-GCB-C$_{18}$	ESI-QQ-LIT (QTRAP)-(+)	Non-available	LOQ range: 0.0002–0.02 mg kg^{-1}	[39]
Liquid partitioning + MSPD						
Multi-residue of triazines, organophosphorus, organochlorine and pyrethroids	Olive oil	Preliminary liquid partitioning with acetonitrile saturated with petroleum ether followed by MSPD extraction with aminopropyl and clean-up with Florisil	GC-Q-MS (modo SIM) LC-Electrospray-MS/MS	80–120% RSD < 10%	LOD range (LC–MS): 0.0002-0.03 mg kg^{-1}; (GC–MS): 0.003–0.06 mg kg^{-1}	[40]
Herbicides simazine, atrazine, diuron and terbuthylazine	Olive oil	Preliminary liquid partitioning with acetonitrile saturated with petroleum ether followed by MSPD extraction with aminopropyl and clean-up with Florisil	LC-Electrospray TOF/MS	80–120% RSD <10%	LOD range 0.001–0.005 mg kg^{-1}	[41]
Liquid partitioning + low-temperature precipitation						
Multi-residue of 17 pesticides (3 triazines and 14 organophosphorus insecticides)	Olive oil	Liquid partitioning with acetonitrile followed by low-temperature fat precipitation and removal at −20 °C. Clean-up with Sep-Pak alumina N column	GC-NPD	77–104% RSD range: 7–16%	LOD range 0.005–0.04 mg kg^{-1}	[42]

Table 2 (*Continued*)

	Matrix	Sample treatment and clean-up step	Determination	Recovery rates (%)	Anal. features	Ref.
Endosulfan and 5 pyrethroid insecticides	Olive oil	Two extraction methods: (a) liquid partitioning with acetonitrile (olive oil dissolved in hexane); (b) mix olive oil with acetonitrile and low-temperature fat removal at −20 °C. Final clean-up with Sep-Pak alumina N column	GC-ECD	71–91% RSD range: 6–17%	LOD range 0.02–0.05 mg kg^{-1}	[43]
Acephate, methamidophos and monocrotophos	Crude palm oil	Extraction with acetonitrile, followed by low-temperature clean-up process (10 °C), followed by a discoloring process using a SPE cartridge with GCB.	GC	85–109% RSD <15%	LOD: 0.01 mg kg^{-1}	[44]
14 organophosphorus pesticides	Soybean oil; sesame oil; peanut oil	Extraction with acetonitrile and low-temperature clean-up	GC-FPD GC–MS	Recoveries >50% RSD <15%	LOD range: 0.002–0.005 mg kg^{-1}	[45]
Azinphos-methyl, chlorpyrifos, λ-cyhalothrin, deltamethrin, diazinon, dimethoate, endosulfan and fention	Olives	Liquid partitioning with acetonitrile. Low-temperature fat precipitation clean-up, and final clean-up with SepPak cartridge (alumina)	GC-ECD GC-NPD	Non-available	Non-available	[46]
19 insecticides and triazine herbicides	Olives	Liquid partitioning with acetonitrile. Low-temperature fat precipitation clean-up, and final clean-up with SepPak cartridge (alumina)	GC-ECD GC-NPD	71–99% RSD range: 5–15%	Non-available	[47]
Liquid partitioning + GPC						
100 multi-class pesticides	Olive oil	Liquid partitioning with *n*-hexane/acetonitrile mixture followed by a GPC clean-up	GC–MS/MS QQQ (MRM mode)	70–110% RSD range: 3–18%	LOQ < 0.004 mg kg^{-1}	[48]
Multi-residue of 32 pesticides (organochlorine, triazines and organophosphorus	Olive oil	Liquid partitioning with acetonitrile saturated with hexane followed by GPC clean-up	GC–MS/MS	89–105% RSD range: 4–14%	LOQ range 0.0005–0.02 mg kg^{-1}	[49]
Multi-residue of 26 pesticides and polyciclic aromatic hydrocarbons	Olive oil	Liquid partitioning with acetonitrile saturated with hexane followed by GPC clean-up	GC–MS/MS (Chemical Ionization (CI) and Electron impact (EI) ionization)	84–110% RSD range: 3–7%	LOQ range 0.0003–0.03 mg kg^{-1}	[50,51]
65 multi-class pesticides	Avocado	Liquid partitioning with ethyl acetate:cyclohexane assisted by high-speed blender; clean-up by GPC; pressurized liquid extraction also tested	GC–MS/MS	70–110% RSD < 19%	LOQ range: 0.00004–0.008 mg kg^{-1}	[52]
Endosulfan sulfate, diuron and terbuthylazine	Olives	Preliminary liquid partitioning (twice) with petroleum ether, using a high-speed blender (ultraturrax). Liquid–liquid partition with acetonitrile saturated with *n*-hexane. Final clean-up step with GPC	GC–MS/MS	82–136% RSD range: 5–11%	LOQ range 0.0002–0.005 mg kg^{-1}	[53]
32 multi-class pesticides	Olives	Preliminary liquid partitioning with petroleum ether, using a high-speed blender (ultraturrax). Liquid partitioning with acetonitrile saturated with *n*-hexane. Final clean-up step with GPC	GC-ECD GC-NPD GC–MS/MS	82–134% RSD < 16%	LOQ range: 0.0001-0.005 mg kg^{-1}	[54]
Liquid partitioning + MAE or PLE						
9 organophosphorus pesticides (dimethoate, diazinon, pirimiphos methyl, parathion methyl, malathion, fenthion, chlorpyriphos, methidathion and azinphos methyl)	Olive oil	Microwave-assisted liquid–liquid extraction with partition of organophosphorus pesticides between an acetonitrile–dichloromethane mixture and oil. Clean-up of extracts was performed with ENVICarb solid-phase extraction cartridge using dichloromethane as the elution solvent	GC-NPD and GC–MS/MS (QQQ) for confirmative purposes	62–99% RSD < 11%	LOQ range 0.007–0.02 mg kg^{-1}	[55]
Abamectin	Avocado	Microwave-assisted extraction (MAE) followed by solid-phase extraction (SPE) using a C18 cartridge, and elution with acetonitrile	LC-fluorescence detection with derivatization	90–100% RSD < 12%	LOD: 0.001 mg kg^{-1}	[56]

65 multi-class pesticides	Avocado	Pressurized liquid extraction (PLE) with acetate:cyclohexane (1:1) as solvent, followed by clean-up by GPC	GC–MS/MS	72–110% RSD < 19%	LOQ range: 0.00004–0.008 mg kg^{-1}	[52]

Sorbent-based (extraction and clean-up) techniques
SPE-based

18 organochlorine insecticides	Olive oil	Solid-phase extraction with Extrelut-3 (Kieselghur); Florisil column clean-up and final clean-up with Extrelut-1	GC-ECD	72–104% RSD range: 8–11%	LOD ≤0.01 mg kg^{-1}	[57]
Multi-residue of pyrethroids	Soya oil	SPE and clean-up with 2 cartridges "on-line": Extrelut-3 and a second cartridge mixture of Extrelut 1 + C$_{18}$	GC-ECD	80–111% RSD range: 6–33%	N/A	[58]
7 pyrethroid insecticides (cypermethrin, deltamethrin, fenvalerate, cyfluthrin, allethrin, cyhalothrin and permethrin)	Vegetable oils	SPE with graphitized carbon black (GCB) cartridges	GC-ECD	94–105% RSD range: 1.4–5.2%	LOD ≤0.002 mg L^{-1}	[59]
18 organophosphorus insecticides	Olive oil	SPE extraction with 2 cartridges "on-line": Extrelut-3 and C$_{18}$	GC-NPD	82–110% RSD range: 2–16%	LOD range 0.001–0.02 mg kg^{-1}	[60]
15 organochlorine pesticides	Soya oil; corn oil; olive oil	SPE extraction with 2 cartridges "on-line": Extrelut-3 and C$_{18}$. Clean-up in a Florisil column	GC-ECD	70–103% RSD range: 3–18%	LOQ average <0.020 mg kg^{-1}	[61]
Pyrethroid insecticides (tetramethrin, bifenthrin, phenothrin, cyhalothrin, permethrin, cyfluthrin, cypermethrin, flucythrinate, esfenvalerate, fluvalinate and deltamethrin)	Olive oil; sunflower oil; corn oil; soybean oil	Solid-phase extraction (SPE) with combined solid supports phases: treated alumina and C$_{18}$	GC–MS/MS	91–104% RSD range: 1–10%	LOD range 0.0003–0.001 mg kg^{-1}	[62]
Organochlorine, organophosphorus (and PCBs)	Olive oil	Olive oil dissolved with hexane. Extraction on Extrelut-QE column; followed by SPE clean-up with two cartridges (C$_{18}$ and alumina) SPE	GC-NPD GC-ECD GC–MS/MS	66–105% RSD range: 5–21%	LOQ range 0.001–0.025 mg kg^{-1}	[63]

MSPD

Multi-residue of triazines, organophosphorus organochlorine and pyrethroids	Olives	Extraction by MSPD using aminopropyl followed by clean-up with Florisil column	GC-Q-MS (SIM) LC–MS/MS	80–120% RSD <10%	LOD range 0.0004–0.004 mg kg^{-1} LC–MS/MS and; 0.008–0.08 mg kg^{-1} (GC-MS)	[40]
Phosmet residues and its metabolites (phosmet-oxon, phthalimide, N-hydroxymethyl-phthalimide, and phthalic acid)	Olives	Extraction of olives by MSPD using as sorbent C$_{18}$ and acetonitrile as eluent	GC–MS SIM mode with derivatization	65–98% RSD < 12%	LOD < 0.06 mg kg^{-1}	[64]
Imazethapyr, imazaquin, metsulfuron-methyl, carboxin, chlorimuron-ethyl, and tebuconazole	Soybean	MSPD as the extraction technique followed by a clean-up step, using a C$_8$ co-column	HPLC diode array UV detection	60–120% RSD range: 3–27%	LOQ range 0.04–0.08 mg kg^{-1}	[65]
Dimethoate, malathion, lufenuron, carbofuran, 3-hydroxycarbofuran, thiabendazole, difenoconazole and trichlorfon	Coconut	Matrix solid-phase dispersion using C$_{18}$ as sorbent material	GC–MS SIM; 3 ions	70–99% RSD < 15%	LOD range 0.02–0.17 mg kg^{-1}	[66]

Table 2 (*Continued* **)**

	Matrix	Sample treatment and clean-up step	Determination	Recovery rates (%)	Anal. features	Ref.
HS-SPME						
7 organophosphorus insecticides	Olive oil	Headspace Solid Phase Micro-extraction (with PDMS fibres)	GC-FID	Non available	LOD range 5–10 μg L^{-1}	[67]
Multi-residue 13 organophosphorus (dimethoate, diazinon, fenitrothion, malathion, fenthion, parathion ethyl, methyl bromophos, methidathion, ethion) and metabolites (omethoate, malaoxon, fenthion sulfoxide and fenthion sulfone)	Olive oil	Headspace Solid Phase Micro-extraction (with PDMS fibres)	GC-FID	80–106% RSD < 10%	LOD average <0.01 mg kg^{-1}	[68]
Miscelaneous techniques						
GPC						
Multi-residue of 28 organophosphorus	Edible oils	On-line extraction and clean-up by GPC-GC. 0.25 g of oil is dissolved in cyclohexane and 20 μL injected in GPC-GC set-up	GPC-GC-FID	Non-available	LOD average: 0.002 mg kg^{-1}	[69]
Multi-residue of 17 organophosphorus pesticides	Olive oil	On-line extraction, clean-up and determination by GPC-GC. 1 g of oil is dissolved in ethyl acetate/cyclohexane and 30 μL injected in GPC-GC set-up	GPC-GC-NPD	83–103% RSD range: 4–22%	LOD range 0.005–0.01 mg kg^{-1}	[70]
Multi-residue of 30 Pesticides (organochlorine, organophosphorus, triazines, pyrethroids, etc.)	Olive oil	0.5 g olive oil dissolved in 5 mL THF. Direct extraction and clean-up by GPC	GC-Q-MS (SIM) LC-Electrospray-Q-MS (SIM)	3–99% with RSD range: 1.6–30% (GC); 28–91% with RSD range: 0.5–5% (LC)	Non-available	[71]
19 organochlorine pesticides	Edible vegetable oils	1.25 g olive oil dissolved in 10 mL ethyl acetate:cyclohexane (1:1). Direct extraction/clean-up by GPC.	GC-QQQ-MS/MS	63–111% RSD range: 1–18%	LOD range 0.0001–0.002 mg kg^{-1}	[72]
LC–GC coupling						
Carbaryl, simazine, atrazine, lindane, diazinon, fenitrothion, terbutryn, parathion	Olive oil	Extraction and clean-up by on-line coupling (TOTAD interface) of (reversed phase liquid chromatography (RPLC) and GC (RPLC–GC)	RPLC-GC-FID	19–92% RSD range: 4–9%	LOD: 0.1–0.3 mg L^{-1}	[73]
Chlorpyrifos, diazinon, fenitrothion, phenthoate, parathion, ethion, and fenthion (organophosphorus), and atrazine and simazine (triazines)	Olive oil	Extraction and clean-up by on-line coupling (TOTAD interface) of RPLC and GC (RPLC-GC)	RPLC-GC-FID	Non-available	Non-available	[74,75]

Fenitrothion, parathion, diazinon, chlorpyrifos, methylchlorpyrifos, malathion, phenthoate, ethion (organophosphorus), simazine (triazine), α-endosulfan, β-endosulfan, endosulfan sulphate, lindane (organochlorine)	Olive oil	Extraction and clean-up by on-line coupling (TOTAD interface) of RPLC and GC (RPLC–GC)	RPLC-GC-NPD RPLC-GC-ECD	Non-available	LOD range: 0.001–0.09 mg L^{-1} (NPD detector) and 0.001–0.09 mg L^{-1} (ECD detector)	[76]
Chlorpyrifos, fenitrothion, methidathion, parathion, lindane, carbaryl, atrazine, terbutryn	Olive oil	Extraction and clean-up by on-line coupling (TOTAD interface) of RPLC and GC (RPLC–GC)	RPLC-GC-NPD	Non-available	LOD: 0.18–0.44 mg L^{-1}	[77]
Diazinon, methylchlorpyrifos, malathion, fenitrothion, chlorpyrifos, parathion, phenthoate, chlorfenvinphos, methidathion, ethion, captan, oxyfluorfen, α-endosulfan, β-endosulfan, and lindane	Pistachio nut, peanut, walnut, hazelnut, sunflower seed	On-line coupling of RP-HPLC and GC	GC	Non-available	LOD range: 0.0001–0.06 mg kg^{-1}	[78]
Supercritical fluid extraction						
Multi-residue of organochlorine and organophosphorus pesticides	Edible oils	Supercritical fluid extraction. Clean-up using a Florisil cartridge	GC-ECD GC-NPD	0–171% RSD (%) non-available	Non-available	[79]
303 multi-class pesticides	Soybeans	Supercritical fluid extraction with carbon dioxide followed by column purification using an Envicarb/NH$_2$ cartridge	GC–MS	70–120% for more than 80% of the pesticides. RSD < 10%	LOQ <0.05 mg kg^{-1}	[80]
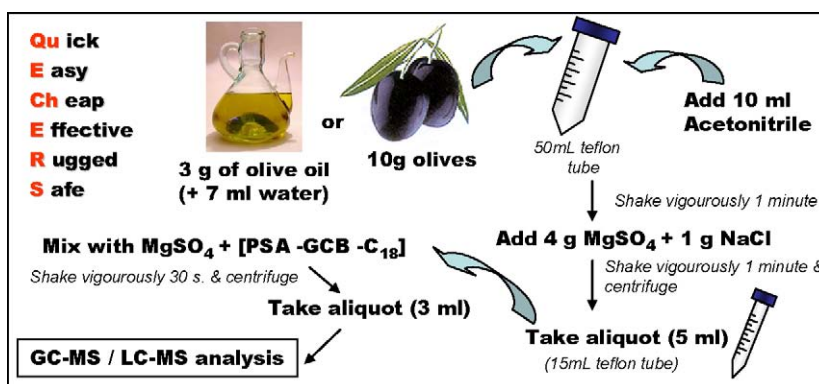
Fig. 1. Schematic procedure of QuEChERS modified for high-fat content vegetable matrices. For details, see [38].

procedure similar to QuEChERS, but performed the clean-up step using SPE in cartridges (so that it can be easily automated) has been reported [11]. It offers advantages in terms of solvent consumption and increased automation of the procedure.

A similar approach was proposed by Garrido-Frenich et al. [34], using QuEChERS-based liquid partitioning (acetonitrile), but the clean-up is performed with a Florisil cartridge instead of PSA, prior to liquid chromatography tandem mass spectrometry (LC–MS/MS). They analyzed low-fat vegetables using the QuEChERS procedure without clean-up, but when dealing with high-fat content samples such as olives, it was necessary to add a clean-up step after the acetonitrile extraction despite lipids are not supposed to be very soluble in this solvent. The authors proposed the use of Florisil clean-up, obtaining clean extracts after passing the raw acetonitrile extract through the cartridge. The same clean-up strategy was proposed by Aramendia et al. for olive oil samples, but using hexane to dissolve the matrix prior to partitioning with acetonitrile [30].

Klein and Alder proposed a simple multi-residue method for the LC–MS/MS determination of 108 pesticides based on partitioning with methanol and water, centrifugation and final clean-up using a ChemElut cartridge with dichloromethane as eluting solvent [24]. Hernández et al. proposed a similar extraction procedure for the multi-residue determination of 52 pesticides in avocado using a partitioning with methanol:water (80:20, v/v) with 0.1% formic acid followed by a clean-up step using hydrophilic–lipophilic balanced polymer-based reverse phase cartridges (Oasis HLB). In this study, several of the less polar compounds – the late eluting analytes – showed low recoveries (<60%) in avocado samples, this related probably with the high-fat content, which somehow did not fit well with the chosen solvent. This example illustrates the difficulties on the development of a unique procedure for the extraction of a wide range of pesticides with different physical properties (i.e.: polarity and/or lipid solubility).

Hirahara et al. proposed a method for 186 pesticides in crops by gas chromatography/mass spectrometry using acetonitrile as solvent [33]. After a preliminary clean-up based on partitioning with *n*-hexane, a clean-up was performed using a minicolumn with an strong anion exchanger (SAX) and PSA minicolumn. Sometimes, the best strategy to avoid or minimize clean-up stages and also matrix-effects is simply diluting the sample extract, to avoid these problems but keeping enough sensitivity in order to meet the targeted regulatory requirements. This can be undertaken when using sophisticated instrumentation. An example of this strategy was described by Pizzuti et al. for the determination of 169 pesticides in soya grain by LC–MS/MS [22]. A 1:20 dilution of the extracts was proposed. Samples were mixed and extracted with a mixture of acetone, dichloromethane and light petroleum with anhydrous sodium sulfate using a Polytron high-speed blender. The final extracts, with a corresponding concentration of 0.05 g soya mL^{-1}, were directly

analyzed by LC–MS/MS, without further clean-up step. This is a reliable solution only if sensitivity is not an issue, because of the use of sensitive sophisticated tandem mass spectrometry instruments.

A straightforward approach was proposed by Granby et al. [21]. The authors proposed a multi-residue method (based on LC–MS) of 19 multi-class pesticides in avocado using a simply liquid–liquid extraction by ultrasonication using methanolic ammonium acetate/acetic acid buffer, and final centrifugation. No further clean-up was required. Recoveries between 70% and 120% were obtained. Results from participation in three intercomparisons proved the accuracy of the method. As the analytical procedure does not include any concentration or clean-up steps, it is easy, and fast to perform, making it applicable for routine analysis in pesticide monitoring programs. The key of the procedure was the negligible matrix-effect due to the partial dilution of the sample (just 0.2 g commodity per mL of extract).

These later straightforward procedures are more complex to implement in the case of edible oils, which often requires various clean-up stages, owing to the inherent complexity of the sample due to the high-fat content.

Amvrazi et al. reported a comprehensive study on different extraction procedures based on liquid partitioning for the multi-class determination of 35 pesticides in olive oil [25]. For the development of the final extraction method, three different extraction procedures (a) partition of pesticides between acetonitrile–hexane solution of the oil; (b) partition between saturated acetonitrile with hexane–hexane saturated with acetonitrile solution of the oil; and (c) partition between acetonitrile–oil) were tested for the optimization of the highest recoveries with the lowest oil residue and a series of experiments for the estimation of the efficiency of different clean-up procedures were performed. Liquid–liquid extraction of the oil solution in hexane with acetonitrile followed by a solid-phase extraction clean-up of the extract using Envicarb (GCB) gave the best results for the target organophosphorus and triazine compounds (see Fig. 2). For the determination of pyrethroids, and organochlorine compounds, the acetonitrile extract (from the Envicarb) was additionally cleaned through a Diol-SPE cartridge.

2.2.1.2. Liquid partitioning combined with low-temperature fat precipitation. Liquid–liquid partitioning combined with low-temperature fat precipitation is a simple combination that has been proposed for pesticide residue analysis in fatty vegetable matrices. This procedure was proposed for the determination of endosulfan and pyrethroid insecticides in olive oil [42,43]. Another sample treatment method for pesticide analysis in fatty matrices (soybean oil, peanut oil and sesame oil) was proposed for the determination of 16 organophosphorus pesticides using partitioning with acetonitrile and low-temperature clean-up (using tubes stored overnight
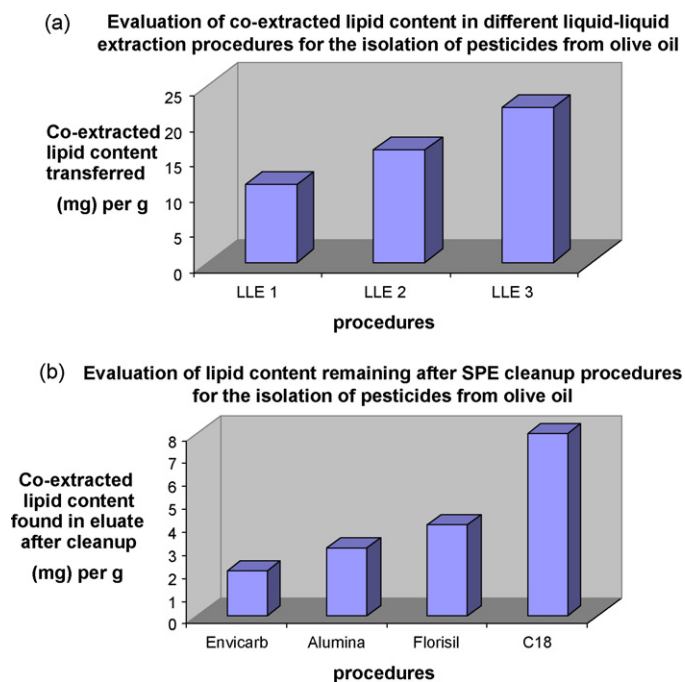
Fig. 2. Study of different liquid–liquid extraction and clean-up procedures for the determination of pesticides in olive oil. Evaluation of co-extracted lipid content. For details, see [25]. (a) Co-extraction of lipids in liqud–liquid extraction procedures for the isolation of pesticides from olive oil. Comparison between different liquid–liquid extraction procedures: (1) partition of pesticides between acetonitrile–hexane solution of the oil (LLE1); (2) partition between saturated acetonitrile with hexane–hexane saturated with acetonitrile solution of the oil (LLE2); and (3) partition between acetonitrile–oil (LLE 3); (b) remaining lipid content after SPE clean-up. Comparison of different SPE-based clean-up procedures for the isolation of pesticides from olive oil: 4 SPE cartridges were tested to optimize the clean-up procedure following selected LLE1: Envicarb, Alumina, Florisil and C_{18}. For details, see text.

at −20 °C) [45]. The same authors proposed the same approach for 28 multi-class pesticides by gas chromatography–mass spectrometry (GC–MS), but using an additional clean-up based on dispersive solid-phase extraction with PSA and C_{18} as sorbents and magnesium sulfate for the removal of residual water (these steps similar to QuEChERS) [26]. Yeoh et al. proposed a method for determining pesticide residues in crude palm oil using acetonitrile and a clean-up with low-temperature precipitation and a SPE step with carbograph (GCB) [44].

2.2.1.3. Microwave-assisted extraction.

All the solvent-based methods are based on liquid–liquid extraction performed by a mechanical or manual shaking, which hampers the throughput of the developed methods. Microwave-assisted extraction (MAE) is well suited for routine analysis and offer a considerable reduction in time and solvent consumption, and high-throughput of samples. MAE has been successfully applied to extraction of organic compounds from solid or semisolid matrices [90,91]. That early development has resulted in specialized microwave instruments provide temperature-controlled, closed-system operation, permitting the processing of many samples simultaneously. Recently, MAE has been proposed for the extraction of pesticide residues in avocado, avocado oil and olive oil [55,56]. Fuentes et al. proposed a method using MAE to assist the liquid–liquid extraction of pesticides in avocado oil and olive oil [55]. An additional clean-up step using an Envi-carb SPE cartridge was proposed. The method is relatively simple, low solvent-consuming and has a good throughput of samples (10 samples can be analyzed in 4 h). Hernández-Borges et al. proposed a MAE of abamectin residues in avocado [56]. Homogenized avocado samples were extracted once with 20 mL

acetonitrile:water 4:1 (v/v) in a microwave oven for 26 min at 700 W with a maximum temperature of 80 °C. An additional clean-up step was performed using a C_{18} SPE cartridge.

2.2.1.4. Pressurized liquid extraction.

A relatively new automated extraction method is pressurized liquid extraction (PLE), also called accelerated solvent extraction (ASE) which is based on a extraction under elevated temperature (50–200 °C) and pressure (500–3000 psi) conditions for short time periods (5–10 min) [92]. This technique has been used for pesticide extraction in complex matrices as foods, vegetables, fruits, fish, and tissues [93–97]. In PLE (Fig. 3), a solid sample is packed into the extraction cell and analytes are extracted from the matrix with conventional low-boiling solvents or solvent mixtures at elevated temperatures up to 200 °C and pressure (30–200 atm) to maintain the solvent in the liquid state.

A very interesting feature of this technique is the possibility of full automation and many samples can be extracted sequentially. However, the extraction efficiency of ASE is dramatically influenced by extraction pressure and temperature conditions. In addition, sample matrix-effects also affect the extraction efficiency. Therefore, the extraction behavior of ASE is not plain and the optimization of operating conditions is laborious. Another weakness of ASE is that, when using hydrophobic organic solvents, the presence of relatively high water percentages in the sample strongly decreases analyte extraction efficiency, as water hinders contact between the solvent and the analyte. Fernandez-Moreno et al. evaluated the use of ASE extraction for the determination of pesticides in avocado using gas chromatography tandem mass spectrometry (GC–MS/MS) [52]. They found satisfactory results on the extraction of avocado samples, with recovery rates similar to those obtained with conventional liquid partitioning with a high-speed blender (polytron). The main problem was the need to perform a desiccation step in order to increase the penetration of the solvent in the matrix. The procedure involving conditioning the hydromatrix material overnight was found to be less convenient that liquid partitioning with polytron, in terms of cost, simplicity and reduced sample pre-treatment, even taking into account the advantaging automation capabilities of PLE instruments.

2.2.2. Sorbent-based (extraction and clean-up) techniques

With the exception of headspace solid-phase microextraction (HS-SPME) and MSPD, the primarily role of SPE-based methodologies in sample treatment protocols for fatty vegetables is as
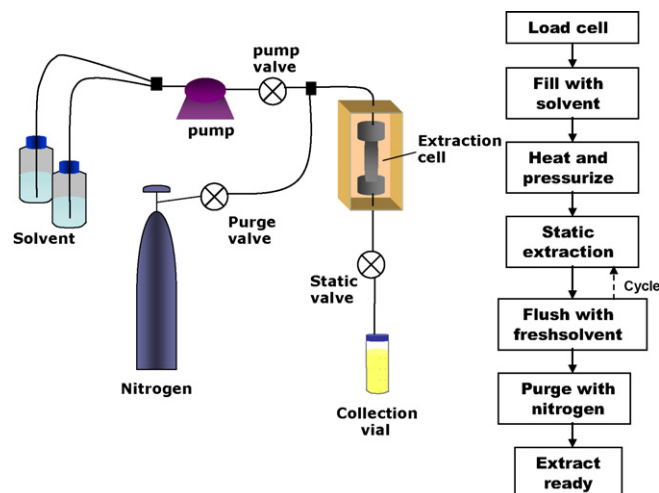
Fig. 3. Schematic experimental set-up of a pressurized liquid extraction system.

clean-up tool. SPE is usually performed in a column/cartridge in order to remove interfering species.

2.2.2.1. Solid-phase extraction. Solid-phase extraction is one of the most popular techniques in sample preparation [98]. In the case of fatty vegetable matrices, it has been used mainly for clean-up purposes. Amongst the advantages of SPE over liquid partitioning procedures are higher precision and throughput, and lower solvent consumption, avoiding also the formation of emulsions, which are often time-consuming. Additionally, SPE can be easily incorporated into automated analytical procedures with relatively simple and inexpensive equipment, which can lead to greater accuracy and precision and higher laboratory throughput [98]. The main issue in method development in SPE stages is the choice of sorbent material and the elution protocol. Typical sorbents for SPE are shown in Table 3.

A plethora of methods have been developed so far for fatty vegetable matrices using SPE (Table 2). Most of the methods reported usually combine a preliminary small-scale liquid–liquid partitioning of sample (removing 80–90% of fat content of the matrix) with a subsequent SPE cartridge clean-up. The combination of these techniques reduce the lipid content of the final extract to a level permitting reliable quantification by GC or LC with selective detection. Although several types of adsorbents were available, early method development was centered on the use of Florisil (magnesium silicate) columns [89]. Other materials commonly applied to lipid sample clean-up include alumina and silica gel. All of these materials function as polar sorbents which strongly retain the polar lipids when eluted with organic solvents of relatively low polarity. Fat extracts are typically placed on these columns in non-polar solvents and the analytes are eluted with solvents of increasing polarity. As the solvent polarity is increased, lipids begin to co-elute. Hence, the effectiveness of clean-up for a particular analyte is dependent upon the solvent strength required for its elution. These adsorption methods are therefore most useful for analytes of relatively low polarity, e.g., many organochlorine pesticides and polychlorinated byphenyls (PCBs). For more recent polar pesticides different sorbents and combinations of them have been proposed by several authors. Some of the procedures are performed in the same step of the liquid partitioning (i.e. dispersive solid-phase extraction (QuEChERS) [82]) or can be performed passing the extract from liquid partitioning through a cartridge containing a sorbent, which ideally only retain potential interfering species [11]. In this step, the use of an appropriate eluting solvent is also an important aspect in the method development.

Florisil, alumina, silica, C_{18}, vinylbenzene polymers, and carbon, although useful for particular classes of pesticides, were found to be inadequate for clean-up of matrices and the recovery of a diverse list of pesticides [99,100]. Recent sample treatment protocols focus on the use of either a unique sorbent or the combination of two or more commercially available SPE sorbents for clean-up [101]. These approaches include the use of PSA alone [82], PSA and C_{18} adsorbents for dispersive SPE [37], GCB alone [102], the combination of GCB and PSA columns as the dual layer SPE cartridges [103–105], the combination of GCB and aminopropyl as the dual-layer SPE cartridges [106] [107], the combination of SAX and PSA as the dual-layer SPE cartridges [108], the combination of GCB, PSA and SAX columns as the tri-layer SPE cartridges [109,110] and the combination of C_{18} and ENVI-Carb (GCB)/NH$_2$ [111]. Other SPE clean-up approaches include the sole use of PSA [102], combinations of GCB and PSA [103–105,109], GCB and aminopropyl [106,107], GCB, PSA and SAX [103,110], and polystyrene divinylbenzene (PDB) and diethylaminopropyl (DEA) [110].
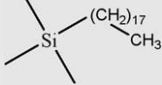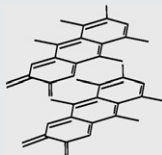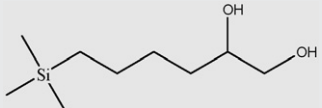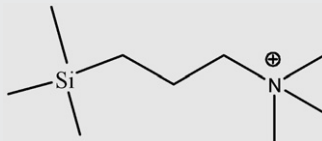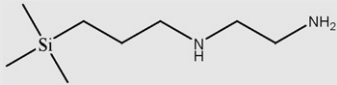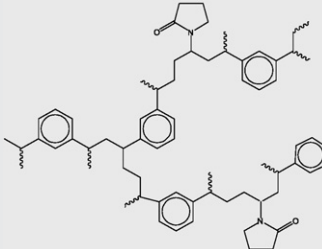
In a recent report, Shimelis et al. [101] evaluated the performance of different sorbent for clean-up of fatty vegetable matrices. The authors highlighted the use of dual-layer SPE, using a combination of PSA with GCB for sample clean-up during multi-residue pesticide screening of agricultural and food products. The retention of fatty acids by the PSA sorbent was quantified and the effect of the elution solvent on the retention of fatty acid on the SPE cartridge was evaluated. The use of stronger elution solvents to elute certain pesticides from graphitized carbon was shown to interfere with the capacity of PSA to bind fatty acids. The ability of the PSA to retain fatty acids was found to be highly dependent on the conditioning and elution protocols. A necessity to use a stronger solvent in order to elute planar pesticides from dual-layer GCB/PSA SPE weakens the capacity of the PSA for removal of fatty acids from samples. Therefore, practical applications of dual-layer GCB/PSA cartridges should be limited to food samples with lower levels of fatty acids. A suitable protocol was tested using GCB/PSA dual-layer SPE to clean-up several food matrices and to simultaneously screen multiple fortified pesticides with a wide range of physico-chemical properties. With a few exceptions, pesticide recoveries were between 85% and 110%, and sample-to-sample differences of less than 5% were achieved, demonstrating the versatile suitability of the dual-layer SPE to sample clean-up. Another study reported by He and Liu [112] investigated the influence of elution protocols on the capacity of PSA for removal of fatty acids. The authors reported that the use of toluene, hexane and/or acetone in the elution severely reduces the capacity of PSA for removal of fatty acids. They suggested that the applications of GCB/PSA dual layer should be limited to non-fatty foods and/or food with a low amount of fat because fatty acids make severe interference with GC–MS determination of some pesticides.

2.2.2.2. Matrix solid-phase dispersion. As shown in Fig. 4, matrix solid-phase dispersion is a SPE based strategy in which a fine dispersion of the matrix is mixed with a sorbent material (C_{18}, alumina, silica, etc.) with a mortar and a pestle [113–116]. Usually, solid samples are prepared for subsequent extraction and/or clean-up by a stepwise process that begins with the disruption of the sample. After blending, the sorbent material is often packed into a minicolumn, where the analytes are eluted by a relatively small volume of a suitable eluting solvent. Many MSPD procedures also employ "co-columns" to obtain further fractionation and to achieve a better removal of matrix interferences. The co-column material (Florisil or silica, in example) is packed into the bottom of the same column of the sorbent, cleaning the sample as it elutes from the MSPD sorbent–matrix mixture. Addition of eluting solvent to the column may be preceded by use of some or all of the solvent to backwash the mortar and pestle. Most applications have utilized 5–10 mL of solvent to perform analyte extraction. Evidence from some studies indicates that most target analytes are eluted in the first 4 mL of extractant, provided that 0.5 g of the sample is mixed with 2 g of the solid support. The main advantages of MSPD procedure compared to other extraction techniques are as follows:(1) the analytical protocol is simplified and shortened; (2) the possibility of emulsion formation is eliminated; (3) solvent consumption is substantially reduced; and (4) the extraction efficiency of the analytes is enhanced as the entire sample is exposed to the extractant. An interesting feature of the MSPD technique is that it can be used for extracting analytes from both solid and liquid foods. The main disadvantage is the lack of automation of the procedure.

Ferrer et al. proposed a simple sample preparation strategy for the multi-residue determination of pesticides in olives based on MSPD using aminopropyl as sorbent material and acetonitrile as eluting solvent followed by identification and quantitation by GC–MS and LC–MS/MS [40]. A similar approach was also proposed for the same determination on olive oil samples, using an additional preliminary partitioning with acetonitrile saturated with petroleum ether. Due to the complexity of the sample, the clean-up step prior to analysis was mandatory, particularly in olive samples. The developed protocol included a clean-up step using a

Table 3
Main characteristics of sorbents used for pesticides in fatty matrices.

Sorbent (raw or SPE cartridge)	Structure/formula	Sorbent material	Retention mechanism
Alumina-N (N-alumina)	Al_2O_3	Crystalline chromatographic alumina for neutral pH (6.5)	Adsorption
LC-Florisil	$MgSiO_2$	Magnesium silicate	Adsorption
LC-C$_{18}$		Polymerically bonded octadecyl endcapped (10% C) silica	Reversed phase
Envi-Carb™, Carbograph Extract-Clean™ (graphitized carbon black – GCB)		Graphitized non-porous carbon. Carbon surface comprised of hexagonal ring structures interconnected and layered into graphic sheets	Adsorption/reversed phase
Diol bonded silica (Diol)		Polymerically bonded 2,3-di-hydroxypropoxy-propyl (7% C) silica	Normal phase
Strong anion exchange (SAX)		A polymerically bonded quarternary amine that remains positively charged at all pH levels. Selectivity can be modified by changing the counter ion with the appropriate buffer during conditioning.	Anion exchange. Improved retention of weaker anions (e.g., carboxylic acids)
Extrelut™	$SiO_2 \cdot nH_2O$	Inert diatomaceous earth: specially processed wide-pore kieselguhr with a high pore volume; chemically inert; naturally occurring product.	Absorption. For lipophilic compounds in aqueous samples.
Primary secondary amine (PSA)		Polymerically bonded PSA phase (5% C) silica	Normal phase or weak anion exchange
Oasis HLB		Hydrophilic–lipophilic balanced copolymer (HLB) of N-vinylpyrrolidone and divinylbenzene	Adsorption/reversed phase. Wide range of analytes with different polarities

co-column packed with an appropriate sorbent material. Three different materials were evaluated for clean-up: Florisil, silica and alumina. Alumina was discarded, because of the low effectiveness on removing matrix interferences. Both silica and Florisil yielded similar cleanliness of the extracts, but the recoveries using Florisil were found to be higher for the studied pesticides (triazines and endosulfan).

Cunha et al. proposed a similar approach for the determination of phosmet and its metabolites in olives using C$_{18}$ and MgSO$_4$ as sorbent and acetonitile as eluting solvent [64]. They found that C$_{18}$ and MgSO$_4$ as matrix sorbents have advantageous effects on extraction yields compared with polar sorbents such as silica, alumina, Florisil or aminopropyl. No additional clean-up step was proposed. Maldaner et al. proposed a method for the determination of six pesticides in soybeans using MSPD with silica and a clean-up step with C$_8$ co-column using ethyl acetate and methanol as eluting solvent. The additional clean-up step was proposed because the extracts obtained contained relatively large quantities of co-extracted fat and proteins [65]. Silva et. al proposed a simple and effective extraction method based on MSPD to determine dimethoate, malathion, lufenuron, carbofuran, 3-hydroxycarbofuran, thiabendazole, difenoconazole and trichlorfon in coconut pulp using gas chromatography–mass spectrometry. Different parameters of the method were evaluated, such as type of sorbent (C$_{18}$, alumina, silica-gel and Florisil), the amount of sorbent and eluent (dichloromethane, acetone, ethyl acetate, acetonitrile, *n*-hexane and *n*-hexane:ethyl acetate (1:1, v/v)). The best results were obtained using 0.5 g of coconut pulp, 1.0 g of C$_{18}$ as dispersant sorbent, 1.0 g of Florisil as clean-up sorbent and acetonitrile saturated with *n*-hexane as eluting solvent.

2.2.2.3. Head-space solid-phase microextraction (HS-SPME). Solid-phase microextraction (SPME) is an extraction technique introduced by Pawlyszyn [117–120] as an alternative to other extraction
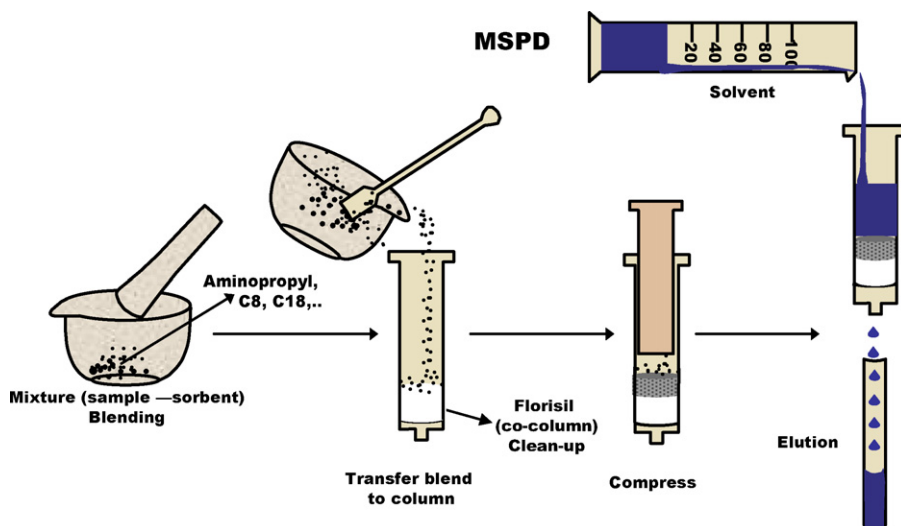
Fig. 4. Schematic procedure of matrix solid-phase dispersion (MSPD).

methods, because it integrates sampling, extraction, concentration and sample introduction into a single step without the use of a solvent. In SPME, the extraction of the target analytes from the sample matrix to the fibre happens either directly (with the coated fibre immersed in the liquid sample (direct SPME) or in the headspace (this technique known as HS-SPME [121]). In HS-SPME, the coated fibre is suspended above the sample in a vial. After equilibrium is reached (a good exposure time takes 15–25 min), the fiber is introduced into the injection port of a GC instrument, where analytes are thermally desorbed and analyzed. Factors influencing the extraction step include fiber type, extraction time, ionic strength, sample pH, extraction temperature and sample agitation. Variables affecting the desorption step include temperature, desorption time, focusing oven temperature. In contrast, complex matrices like edible oils do not allow a direct extraction being only HS-SPME an appropriate alternative. This methodology has been proposed for the analysis of organophosphorus pesticide residues in olive oil [67,68].

Tsoutsi et al. [67] proposed HS-SPME for the determination of 7 organophosphorus insecticides in olive oil samples. In this work the extraction capacity of four fiber coatings were evaluated: polyacrylate (PA 85 μm), carbowax-divinylbenzene (CW-DVB 65 μm), polydimethylsiloxane (PDMS, 65 μm) and polydimethylsiloxane (PDMS, 100 μm), which was found that provided the better recovery rates for the studied pesticides. The parameters affecting the HS-SPME process such as temperature, extraction time, addition of salts and stirring rate were optimized. The same authors reported another study with 13 organophosphorus insecticides (including four metabolites) [68]. Six different sorbents were evaluated for the fiber coating: carboxen/polydimethylsiloxane 75 μm (CAR/PDMS, 75 μm), carboxen/polydimethylsiloxane 85 μm (CAR/PDMS, 85 μm), polydimethylsiloxane divinylbenzene 65 μm (PDMS-DVB, 65 μm), polydimethylsiloxane 7 μm (PDMS, 7 μm), polydimethylsiloxane 30 μm (PDMS, 30 μm) and polydimethylsiloxane 100 μm (PDMS, 100 μm) (selected). After the extraction, the thermal desorption of the analytes was achieved by inserting the fibre into the injection port and held at 250 °C for 7 min. No carry over effect was detected after that time. The HS-SPME method was proven to be a suitable tool for quantitative/qualitative analysis of organophosphorus insecticides in olive oil. However, in this later study, they reported the occurrence of matrix-effects (even using HS-mode), which might affect the accuracy of these methods for quantitation purposes, being necessary the use of matrix-matched standards.

Amongst the advantages it should be mentioned the higher automation degree compared to other more laborious protocols. The procedure can be completely automated using an autosampler with HS-SPME equipment. Other advantages of HS-SPME are the inherent high sensitivity and the absence of solvents and sample pre-treatment required, thus minimizing of sample manipulation and contamination. Main disadvantages include poor fibre-to-fibre reproducibility, and poor precision and ruggedness on the determinations. The technique is limited to relatively volatile compounds, and matrix-effects showed up in complex matrices. Finally, relatively expensive consumables and a dedicated and careful optimization of different experimental conditions and parameters are required, making HS-SPME not straightforward for multi-residue methods.

2.2.3. Gel-permeation chromatography

GPC is an established method for the fractionation and/or clean-up of fatty matrices of both plant and animal origin [89]. It is generally recommended for purifying extracts obtained from complex samples. GPC is one of the more widely extended technique in routine laboratories for the analysis of pesticides residues in vegetable oil, generally after a preliminary liquid–liquid partition with acetonitrile, using GC analysis with different detectors (ECD, NPD and MS) [8] (see Table 2). There are methods based on the direct extraction and clean-up of pesticides from olive oil without liquid–liquid partition step, only by means of GPC. However, in order to enlarge the life of the columns and chromatographic systems – in both the extraction and determination steps – and to obtain cleaner extracts it is highly recommendable to perform the partitioning step prior to GPC. The experimental set up required for a GPC method is represented in Fig. 5a. An aliquot of a vegetable oil, dissolved in an apolar solvent or an aliquot form the extract obtained in a preliminary partitioning step (i.e. with acetonitrile saturated with hexane) is injected in the GPC system. The selected fraction containing the pesticides is collected and after solvent exchange step, the sample analyzed by chromatographic techniques. These GPC systems comprises a LC pump a fraction collector and a detector (optional). The columns are made from polymeric porous microspheres, which enables the separation of compounds according to their molecular weights. Using this principle, pesticide fraction is separated from the high molecular weight triglycerides fractions.

GPC-based methods provide good recovery rates for a large number of pesticides and can be easily implemented – at least the
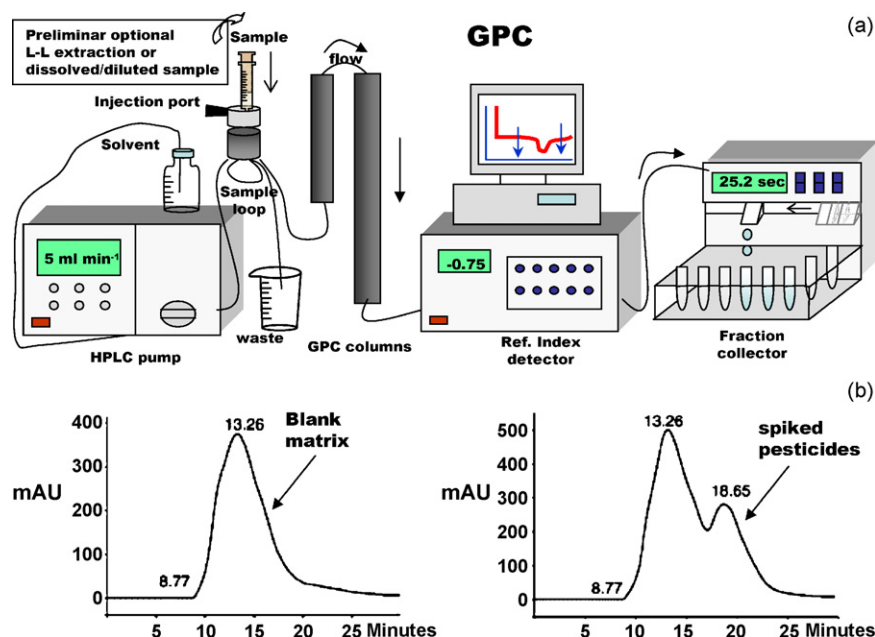
Fig. 5. (a) GPC set up; (b) GPC chromatograms at 254 nm of: (a) a blank avocado sample and (b) a blank avocado sample spiked with a standard mixture of the target pesticides at 50 μg kg^{-1}. Adapted from [52] with permission.

GPC step – in an automated fashion, using appropriate software and a fraction collector. Therefore, the high degree of automation is the key advantaging feature of this method, particularly compared with other manual methods (e.g. liquid–liquid extraction). In contrast, the main drawback is the partial overlapping between the pesticide fraction and the components from the matrix (mainly triglycerides). It is difficult to setup optimized conditions to fully resolve the pesticide fraction from the matrix, even using high-performance GPC columns. For this reason, an additional clean-up on Florisil is usually included after GPC step. GPC has been used for a wide range of fatty vegetable matrices such as vegetable oils [48–51,69–72], avocado [52] or olives [54].

As an example, the GPC separation of pesticides from avocado is shown in Fig. 5b [52]. Matrix interferences eluted about 9 and 20 min, and the pesticides eluted between 15 and 22 min. From 15 to 22 min eluted about the third part of the matrix components overlapping with the pesticide signal. A more efficient GPC separation of the fat and target pesticides was not achieved, even changing the mobile phase composition (studied in the range 25/75–75/25 (v/v) ethyl acetate:cyclohexane) and flow (varied between 1 and 5 mL/min). The starting of the fraction collected was set at 15 min because later times did not recover all the target pesticides. An additional carbofrit-guard column system was proposed to enable the analysis of large number of samples and to protect the chromatographic system [52]. Normally, the fractionation time interval is selected in order to yield a clean extract despite some of the pesticides under study will not be fully recovered. In addition, the acquisition and maintenance costs of the instrumental and the large amount of toxic solvents consumed per analysis are important drawbacks of this methodology.

In order to increase the throughput and automation of extraction methods, on-line GPC–GC coupling was proposed [69,70,122]. The pesticide-containing fraction (monitored by a UV detector) from the GPC fractionation step was transferred on-line to the gas chromatograph using a loop-type interface. After solvent evaporation through the solvent vapor exit, subsequent GC separation and detection was performed. Another similar approach based on the coupling of GC with semi-preparative chromatographic techniques is on-line coupling of reverse phase liquid chromatography

and gas chromatography (LC–GC) using a TOTAD (total oven transfer adsorption–desorption) interface. In coupled LC–GC, the specific components of a complex matrix are prefractionated by LC and then transferred on-line to the GC system for analytical separation and detection. In this way, the LC step replaces the sample preparation steps, including extraction, clean-up, and concentration, which are time-consuming, use a large amount of toxic organic solvent, and frequently involve errors and analyte loss.

Automated coupled on-line LC–GC systems have as main advantage the higher degree of automation as compared to other methodologies. This is particularly important when a large number of samples require analysis. This LC–GC methodology has been extensively described for the analysis of pesticide residues in olive oil and other fatty vegetable matrices (nuts, pistachio nut, hazelnut peanut, etc.) [73–78,123]. However, the solvent consumption is still higher than desirable and the instrumentation is expensive with a complex assembly.

2.2.4. Supercritical fluid extraction (SFE)

Carbon dioxide has been by far the most used supercritical fluid for extracting a variety of pesticides from solid matrices, such as soil, sediments, vegetables, animal tissues and foodstuffs [124]. The main advantages are the use of non-toxic, non-flammable, inexpensive fluid (such as CO_2), the automation due to the instruments available for that purpose and also the ability of being coupled to chromatographic systems. Finally, relatively selective and fast extraction procedures can be performed by modifying the density of the supercritical fluid. Increasing the density of the fluid increases the extraction yield of high molecular weight compounds. The density of the fluid can be varied by varying its temperature and pressure. However, nowadays the use of SFE has decreased dramatically during the last years, due to the high cost of the instrumentation and the difficulties in method development concerning the optimization of the extraction conditions on the sample.

SFE is conceptually not difficult to perform. The extraction vessel is filled with a sample and placed in a heated extraction chamber. A pump is used to supply a known pressure of the supercritical fluid to an extraction vessel which is thermostated at a temperature above
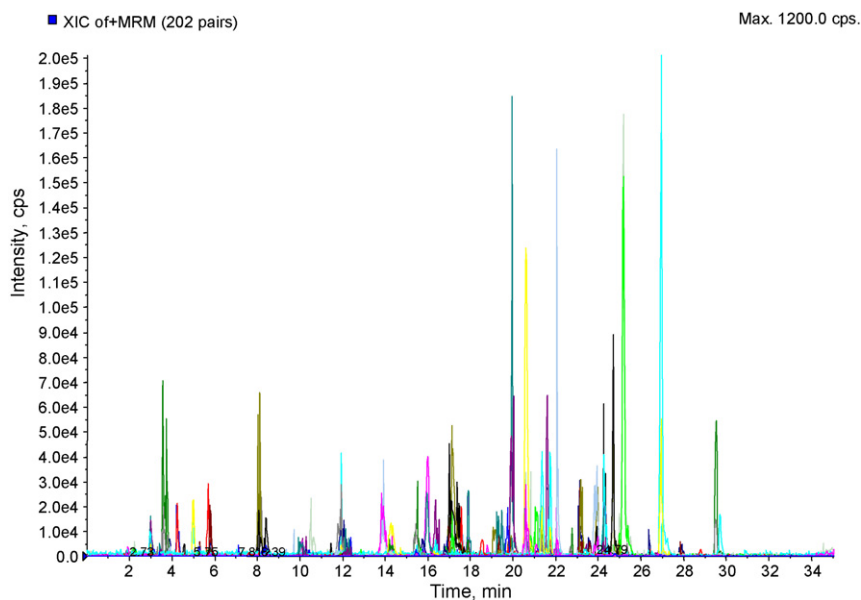
Fig. 6. Example of a large-scale multi-residue method for the analysis of 100 multi-class pesticides in olive oil by LC–MS/MS using a QTRAP analyzer in MRM mode and electrospray ionization in positive ion mode. Extracted ion chromatogram corresponding to 202 MRM transitions at a $10\,ng\,g^{-1}$ concentration for an extract of olive oil. Reproduced from [39] with permission.

the critical temperature of the supercritical fluid. During the extraction, the analytes are removed from the bulk sample matrix into the fluid and swept into a decompressing region. Here, the supercritical fluid becomes a gas and is vented, while analytes abandoning the gas are collected in a vial containing a small volume of a suitable solvent such as methanol (so-called solvent mode). A variation of this scheme is that of substituting the collecting liquid at the outlet of the extractor with a sorbent cartridge such as C_{18} (so-called sorbent mode).

The extraction of hydrophobic compounds from complex matrices containing sugar, proteins, and fat can be achieved almost quantitatively, but polar molecules give poor recovery rates [79]. The recovery of these compounds can be improved significantly by adding of a modifying solvent, such as methanol or acetonitrile [81]. Scarcely any recent literature is available on the use of SFE for determining pesticides in fatty vegetable matrices. Ono et al. developed a multi-residue method for the determination of over 300 pesticides in soybeans using SFE and GC–MS, obtaining recoveries between 70% and 120% for 245 out of the 303 compounds tested [80]. Carbon dioxide was used as a supercritical fluid and acetone as collection solvent. An additional clean-up step was required for soybean samples using a C_{18} cartridge and after that an Envicarb-NH_2 cartridge column. Despite its selectivity and automation capabilities, the interest in SFE has decreased dramatically, mainly due to the high cost of the instrumentation and the critical dependence of the extraction conditions on the sample, leading to time-consuming and complex optimization procedures and difficulty in using this technique routinely.

3. Identification and quantitation of pesticides in fatty vegetables

The identification of pesticides in vegetable samples with high-fat content is a difficult task, which requires selective techniques, because interfering species from the matrix often mask the signal of the target compounds [8]. For these reasons, the use of chromatographic techniques coupled with mass spectrometric detection is usually the choice. Along with chromatographic methods we should mention that the development of screening methods for the same purposes but using immunoanalytical techniques is a valu-

able approach. Interesting ongoing research on the development of fast methodologies for the screening of pesticide residues in fatty matrices using immunoalytical techniques has been accomplished [125–127] although they are not covered in detail in the present review.

Separation techniques such as LC and GC are well suited for the analysis of complex multi-component samples such as food. However, the analysis of food matrices requires well-designed sample preparation procedures. The raw extract that is obtained after the initial extraction of pesticides is often unsuited for direct instrumental analysis, especially when this extract has been concentrated in order to bring the mass of analyte in the detectable range of the final determination system. Despite this progress, chromatographic systems yet can handle only limited amount of extracted material because otherwise deterioration of quantitative performance can occur. Therefore, a clean-up stage of the raw extract is often needed depending on the selectivity of the determination method. Primarily, because the matrix components can have a negative effect on both the life-time and analytical performance (i.e. matrix-effects) of the (chromatographic) separation/detection system, and also in order to remove potential co-eluting or interfering species present in the raw extract.

This remarks the need to consider both sample treatment and determination steps together, since both stages are clearly connected. In general, the more complex the matrix, lower the level of pesticides targeted and the lower the selectivity of the final separation/detection system, the more clean up will be required. Less specific detection methods must be accompanied by dedicated sample treatment including clean-up stages. However, if high specific detection methods (i.e. MS/MS with a triple quadrupole) are used, the need for extensive clean-up procedure during sample preparation is substantially reduced. The selectivity and sensitivity of state-of-the-art instruments is so high that most of the potential adverse effects of bulk matrix on the system performance (ion suppression, partial contamination of the column, etc.) can be often circumvented by dilution instead of a thorough clean-up stage, keeping enough sensitivity for the selected application. Although this seems to be a very simple approach, it cannot always be applied because it inevitably increases the detection limits of the compounds of interest.

Up to date, the most widely used approach for the analyses of pesticide residues in fatty vegetables is yet gas chromatography/mass spectrometry (GC–MS). Mass spectrometric detection systems have replaced formerly used non-selective detection systems (i.e. NPD, ECD, etc.) [8]. Some authors have reported that even electron capture detectors detection in gas chromatography often failed to give reliable identification of targeted compounds [30]. In fact, according to the guidelines proposed by DG SANCO [12], these non-selective detectors do not provide selectivity enough to confirm the presence of a substance. The use of mass spectrometric techniques is mandatory to obtain unambiguous identification. In this sense, the EU has established an identification criterion for contaminants in animal feed), which involves the use of mass spectrometric techniques in order to meet the confirmation criteria, based on the use of identification points (a different number of points is assigned according to the type of mass spectrometric detection used (viz. MS/MS, high resolution, SIM mode, etc) [128]. This criterion is however rejected by other authors to be applied in food contaminants though [129]. What is actually accepted without a question is that mass spectrometry is currently the most powerful tool commonly available to analytical chemists for identification of organic compounds in a variety of matrices.

During recent years, a number of papers have been published on multi-residue analysis of pesticides in food by GC–MS and LC–MS as reviewed by Pico et al. [130] and Alder et al. [131]. The use GC–MS is particularly suited to the analysis of volatile and non-polar compounds. Mass spectrometric detectors provide selectivity enough to detect pesticide residues in both olives and olive oil samples at low concentration levels. There are various techniques in GC–MS. Probably the most widely extended technique in routine laboratories is gas chromatography/mass spectrometry using a single quadrupole analyzer in selected ion monitoring mode. It enables appropriate limits of detection, in compliance with the regulations established for a wide range of pesticides and commodities, including olives and olive oil [8].

However, the results in terms of selectivity, sensitivity and confirmation degree improve remarkably when tandem mass spectrometry is applied. GC–MS/MS using either triple quadrupole in selected reaction monitoring or ion trap instruments, enable the unambiguous identification and quantitation of a large number of compounds in complex fatty matrixes [48]. The additional MS stage of MS/MS instruments provide enhanced selectivity, reducing the noise from the matrix and thus improving selectivity and signal-to-noise ratios of analytes [8].

The tendency towards the use of these new polar (and less volatile) agrochemicals have prompted the use of liquid chromatography/mass spectrometry (LC–MS), which has been accepted as a routine technique for regulatory monitoring purposes in pesticide residue analysis. For instance, in a recent study from Alder et al. [131], for a total of 500 pesticides, LC–MS gave overall better results than GC–MS regarding the number of compounds that can be tested by each technique. They found that 453 out of the 500 tested compounds were amenable by LC–MS, while only 365 could be analyzed by GC–MS. Only, for the organochlorines, the use of GC–MS is advantageous with regards to LC–MS, due to the low polarity and lack of ionizable moieties of these apolar compounds by LC-electrospray-MS. Therefore, there are several reasons to apply LC–MS for the analyses of pesticides residues in fatty vegetable matrices. First, the number of pesticides used is increasing everyday, and these compounds are more polar and thus, less amenable their analysis by GC–MS.

The main drawback associated with LC–MS for pesticide residue analysis in food is analyte signal suppression or enhancement due to matrix-effects [12,132]. Ion suppression or enhancement is the result of components (matrix co-extractives) that suppress or enhance the ionization of, or compete in the ionization process with the component of interest. It is a phenomenon difficult to control since even components of the sample that do not appear in the chromatogram can cause ion suppression. This can also occur in GC–MS, in which matrix also introduces a bias during the detection and quantitation steps [133]. The matrix-effects take place in the injection port, in the separative system (retention gap and/or analytical column) and in the ionization process (matrix might cause ionization potential modification of the analytes). The main consequence of matrix-effect is an increasing or decreasing analyte signal in the presence of the matrix compared to that obtained with neat (solvent) standards. The possible strategies leading to elimination or reduction of matrix-effects might include [10,12,132,133]: (a) reduction of the amount of matrix components in injected sample by employing a more selective extraction procedure or a more extensive sample clean-up; (b) decrease the amount of injected sample; (c) improvement of chromatographic separation (optimization of mobile phase composition and/or change of stationary phase. If matrix suppression/enhancement phenomena cannot be circumvented, appropriate calibration technique (external matrix-matched standards, or isotopic labelled internal standard) might be used to compensate for matrix-effects.

To achieve better sensitivity and selectivity of target analytes detection, tandem mass spectrometry (MS/MS) is a generally the preferred option for quantitation purposes. The use of LC–MS/MS with triple quadrupole (QQQ) instruments in multiple reaction monitoring (MRM) mode is so far the more appropriate technique for target analysis. It provides excellent sensitivity and selectivity. In LC–QQQ–MS/MS, target ion isolation, fragmentation and mass analysis of fragments are performed *quasi* in parallel with overall (dwell) times as low as 2–5 ms per transition. These values can result in the analysis of over 200 transitions in each time window with acceptable (10-point peak) chromatographic peak shape. Fig. 6 shows an example of large-scale multi-residue method for the analysis of 100 multi-class pesticides in olive oil using LC–MS/MS [39] with a hybrid triple quadruple linear ion trap instrument. The extracted ion chromatograms corresponding to 202 MRM transitions at a $10\,\mu g\,kg^{-1}$ for an extract of olive oil are shown overlapped. The 100 compounds are included in a unique time segment. Satisfactory performance for quantitative analysis was still achieved when reduced dwell times (5 ms) were used, even though this affects the S/N ratio and peak area. The maximum number of MRM transitions that could be acquired per segment with these conditions was 240, which evidences the potential for developing methods for a large number of compounds although it must be taken into consideration that the analysis is associated with the sample preparation and an extraction procedure as comprehensive as the MS-based multi-residue method is required.

Liquid chromatography time-of-flight mass spectrometry (LC-TOFMS) offers attractive features for the analysis of pesticides in complex matrixes. TOF analyzers are capable of 10,000 or more full-width at half maximum (FWHM) resolving power [134]. LC-TOFMS benefits from the high resolving power of signals on the m/z axis, enabling the measurement of accurate masses of ions with mass accuracy better than 3 ppm [134]. Accurate mass analysis of ions usually yield the elemental composition of parent and fragment ions, which can be used for unambiguous identification and/or confirmation of a target species [134] or to identify unknown or unexpected compounds ("non-target analysis") [135].

Fig. 7 shows an example of the selectivity provided by LC-TOFMS analysis due to the relative high mass resolution of TOF analyzers (i.e. 10,000–15,000 FWHM), which enable the removal of potential isobaric matrix interferences. The example shows the analysis of $10\,\mu g\,kg^{-1}$ of diuron in olive oil [41]. When a wide m/z window (i.e.: 0.2 Da) is selected in the extracted ion chromatogram for m/z 233 (diuron), other interferences might be present in the sample matrix as it is observed from the peak at 20.9 min (Fig. 7b.1). When
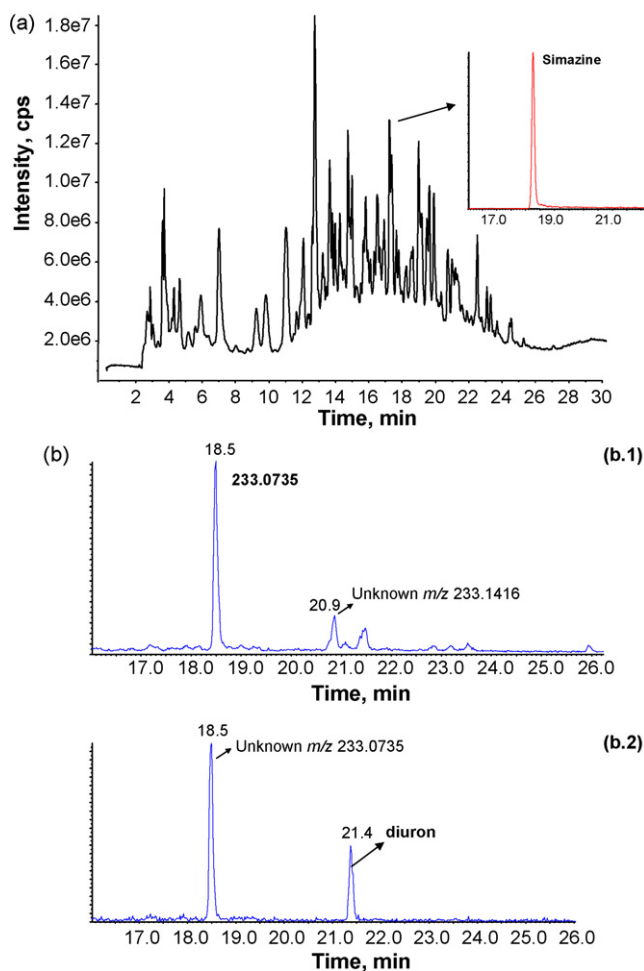
Fig. 7. (a) Total ion chromatogram corresponding to the LC-TOFMS analysis of a olive sample spiked with $100 \, \mu g \, kg^{-1}$ of herbicide simazine. The extracted ion chromatogram (XIC) for the corresponding protonated molecule of simazine (XIC, $m/z \, 202.05 \pm 0.05 \, Da$) is also shown as an inset; (b) extracted ion chromatogram for diuron at $m/z \, 233$ in an spiked olive oil extract ($10 \, \mu g \, kg^{-1}$ diuron) using two different accurate mass windows: (a) 0.2 Da and (b) 0.05 Da. For details, see text. Adapted from [41] with permission.

the same window is narrowed down to 0.05 Da (Fig. 7b.2), the main interference disappears leading to a more selective identification for the target compound. Furthermore, this selectivity improves the signal-to-noise ratio leading to better method detection limits overall.

LC-TOFMS has been successfully applied to the identification and determination of several classes of pesticides in vegetables samples [134,135], including analyses of herbicides residues in olive oil [41]. The main advantage of this methodology is the potential for developing of automated methods for the large-scale screening of pesticides (for instance 300 pesticides [136]) based on the use of accurate mass databases [88,136,137]. Another interesting feature of LC-TOFMS is the ability to identify and characterize degradation products of pesticides in food together with unknown or "non-target" unexpected pesticides without the use of primary standards, owe to the use of accurate mass measurements of ions providing elemental compositions of unknown ions [134,138].

4. Conclusions

Despite the advances in separation and detection of the chromatographic systems, clean-up remains important for obtaining reliable data. There is still a need for effective, environmen-

tally friendly and fast methodologies for sample treatment and determination of pesticide residues in fatty vegetable matrices. The development of such procedures combined with modern chromatographic-mass spectrometric techniques will enable analysis at the low levels now required by legislation for many pesticides, but more importantly, result in methods which produce more reliable data to support food safety monitoring programs.

For pesticide multi-residue analysis, the use of low-solvent consumption sorbent-based protocols which involve minor cost, based only on the use of disposable chemicals or sorbents (such as QuEChERS or alternative liquid partitioning-SPE based methods) have replaced older methods which were based or expensive instrumental set-up (e.g. SFE) and/or those consuming large amounts of toxic solvents (e.g. GPC). This is the trend although it is impossible to develop a unique protocol covering such a wide range of compounds. Therefore, selected sorbents that provide effective cleanup might involve losses of key analytes or classes. Automation of both extraction and clean-up stages is also an advantageous feature that can considerably increase sample throughput and reduce costs of analysis.

The degree of selectivity provided by the detection technique is critical on the extension to which clean-up is required. This also depends on the matrix, and the concentration of the targeted species. When a more selective detection system is used instead, a thorough sample clean-up may not be necessary since the interfering compounds are simply not detected or can be discriminated by using either MS/MS or high resolution mass spectrometry, both achieving the efficient and mass selective separation of the characteristic analyte(s) ions, ignoring those from the matrix or from other components. However, some sample preparation may still be needed, otherwise interferences and signal suppression for LC–MS can occur, even where there is no obvious sample signal.

Finally, "multi-class" large-scale multi-residue methods targeting large number of pesticides are highly desirable, although the different nature, classes and physico-chemical properties of pesticides hamper the development of such methodologies. Different versatile sample preparation procedures discussed throughout the text are capable to circumvent the main problems associated with this kind of matrices and permit the development of multi-residue methods when combined with selective and sensitive methodologies based on GC–MS(/MS) and/or LC–MS(/MS).

References

[1] C. Tomlin, The Pesticide Manual—A World Compendium, 13th ed., British Crop Protection Council (BCPC), Hampshire, 2003.

[2] Regulation (EC) No 396/2005 of the European Parliament and of the council of 23 February 2005 on maximum residue levels of pesticides in or on food and feed of plant and animal origin and amending Council Directive 91/414/EC (2003); Regulation (EC) 299/2008 amending regulation 396/2005 on maximum residue level of pesticides in or on food and feed of plant and animal origin, as regards the implementing powers conferred on the commission.

[3] Council Directive of 15 July 1991 (91/414/EEC) concerning the placing of plant protection products on the market (OJL 230 19.8.1991, p. 1) (1991).

[4] L. Martín-Plaza, in: A.R. Fernández-Alba (Ed.), Chromatographic-Mass Spectrometric Food Analysis for Trace determination of Pesticide Residues, Comprehensive Analytical Chemistry, vol. XLIII, Elsevier, The Netherlands, 2005 (Chapter 2).

[5] K. Mastovska, P. Worsfold, A. Townshend, C. Poole (Eds.), Encyclopedia of Analytical Science, 2nd ed., Elsevier, 2005, pp. 251-261.

[6] Commission directive 2006/125/EC of 5 December 2006 on processed cereal-based foods and babyfoods for infants and young children. Official Journal of

European Union L339/16 (December 6, 2006) and subsequent updates (Council decision of 9 October 2007).

[7] S.M. Walters, Anal. Chim. Acta 236 (1990) 77–82.
[8] J.F. Garcia-Reyes, C. Ferrer, M.J. Gomez-Ramos, A. Molina-Díaz, A.R. Fernández-Alba, Trends Anal. Chem. 26 (2007) 239.
[9] H.G.J. Mol, in: Y. Picó (Ed.), Food Toxicants Analysis, Elsevier, B.V, Amsterdam, 2007.
[10] D.J. Fletouris, in: Y. Picó (Ed.), Food Toxicants Analysis, Elsevier B.V, Amsterdam, 2007.
[11] F.J. Schenck, A.N. Brown, L.V. Podhorniak, A. Parker, M. Reliford, J.W. Wong, J. AOAC Int. 91 (2008) 422.
[12] W.M.A. Niessen, P. Manini, R. Andreoli, Mass Spectrom. Rev. 25 (2006) 881.
[13] S. Armenta, S. Garrigues, M. De la Guardia, Trends Anal. Chem. 27 (2008) 497.
[14] USDA, USDA Nacional Nutrient Database for Standard Reference, Release 20 (2007); http://www.nal.usda.gov/fnic/foodcomp/search/ (2007).
[15] M.A. Aramendía, M. De Juan, F. Lafont, A. Marinas, J.M. Marinas, J.M. Moreno, J.M. Porras, O.M. Sobrino, F.J. Urbano, R. Vílches, Symposium Científico-Técnico EXPOLIVA 2005 (Foro de la tecnología oleícola y la calidad (TEC-8)), 2005.
[16] A.E. Hiskia, M.E. Atmajidou, D.F. Tsipi, J. Agric. Food Chem. 46 (1998) 570.
[17] G. Dugo, G. Di Bella, L. La Torre, M. Saitta, Food Control 16 (2005) 435.
[18] P. Cabras, P. Caboni, M. Cabras, A. Angioni, M.T. Russo, J. Agric. Food Chem 50 (2002) 2576.
[19] D. Zimmer, C. Philipowski, B. Posner, A. Gnielka, E. Dirr, M. Dorff, J. AOAC Int. 89 (2006) 786.
[20] P. Cabras, A. Angioni, M. Melis, E.V. Minelli, F.M. Pirisi, J. Chromatogr. A 761 (1997) 327.
[21] K. Granby, J.H. Andersen, H.B. Christensen, Anal. Chim. Acta 520 (2004) 165.
[22] I.R. Pizzutti, A. De Kok, R. Zanella, M.A. Adaimea, M. Hiemstra, C. Wickert, O.D. Prestes, J. Chromatogr. A 1142 (2007) 123.
[23] M.A. Aramendia, V. Borau, F. Lafont, A. Marinas, J.M. Marinas, J.M. Porras, F.J. Urbano, Food Chem. 97 (2006) 181.
[24] J. Klein, L. Alder, J. AOAC Int. 86 (2003) 1015.
[25] E.G. Amvrazi, T.A. Albanis, J. Agric. Food Chem. 54 (2006) 9642.
[26] L. Li, Y. Xu, C. Pan, Z. Zhou, S. Jiang, F. Liu, J. AOAC Int. 90 (2007) 1387.
[27] A.M. Tsatsakis, I.N. Tsakiris, M.N. Tzatzarakis, Z.B. Agourakis, M. Tutudaki, A.K. Alegakis, Food Addit. Contam. 20 (2003) 553.
[28] E.G. Amvrazi, T.A. Albanis, Proceedings of the 9th International Conference on Environmental Science and Technology Greece, 2005.
[29] R. Raoux, J.L. Coustille, S. Rambaud, Oleagineux, Corps Gras Lipides 4 (1997) 71.
[30] M.A. Aramendía, V. Borau, F. Lafont, A. Marinas, A. Marinas, J.M. Moreno, F.J. Urbano, Food Chem. 105 (2007) 855.
[31] X. Cui, X. Gao, X. Chu, W. Yong, Y. Ling, M. Yang, X. Li, D. Wang, Y. Fang, J.A. Zweigenbaum, Anal. Lett. 40 (2007) 1117.
[32] F. Hernandez, O.J. Pozo, J.V. Sancho, M. Bijlsma, M. Barreda, E. Pitarch, J. Chromatogr. A 1109 (2006) 242.
[33] Y. Hirahara, M. Kimura, T. Inoue, S. Uchikawa, S. Otani, A. Haganuma, N. Matsumoto, A. Hirata, S. Maruyama, T. Iuzuka, M. Ukyo, M. Ota, H. Hirose, S. Suzuki, Y. Uchido, J. Health Sci. 51 (2005) 617.
[34] A. Garrido Frenich, J.L. Martinez Vidal, E. Pastor-Montoro, R. Romero-Gonzalez, Anal. Bioanal. Chem. 390 (2008) 947.
[35] E.J. Avramides, EPRW 2006, 2006.
[36] S.J. Lehotay, A. De Kok, M. Hiemstra, P. Van Bodegraven, J. AOAC Int. 88 (2005) 595.
[37] S.J. Lehotay, K. Matovska, S.J. Yun, J. AOAC Int. 88 (2005) 630.
[38] S.C. Cunha, S.J. Lehotay, K. Mastovska, J.O. Fernandes, M.B.P.P. Oliveira, J. Sep. Sci. 30 (2007) 620.
[39] M.D. Hernando, C. Ferrer, M. Ulaszewska, J.F. García-Reyes, A. Molina-Díaz, A.R. Fernández-Alba, Anal. Bioanal. Chem. 389 (2007) 1815.
[40] C. Ferrer, M.J. Gómez, J.F. García-Reyes, I. Ferrer, E.M. Thurman, A.R. Fernández-Alba, J. Chromatogr. A 1069 (2005) 183.
[41] J.F. García-Reyes, C. Ferrer, E.M. Thurman, A.R. Fernández-Alba, I. Ferrer, J. Agric. Food Chem. 54 (2006) 6493.
[42] C. Lentza-Rizos, E.J. Avramides, F. Cherasco, J. Chromatogr. A 912 (2001) 135.
[43] C. Lentza-Rizos, E.J. Avramides, E. Visi, J. Chromatogr. A 921 (2001) 297.
[44] C.B. Yeoh, A. Kuntom, S. Dorasamy, M.R. Omar, M.Y.M. Nor, M.R.R. Noh, Eur. J. Lipid Sci. Technol. 108 (2006) 960.
[45] L. Li, Z. Zhou, C. Pan, C. Qian, S. Jiang, F. Liu, Chromatographia 66 (2007) 625.
[46] E.G. Amvrazi, T.A. Albanis, J. Agric. Food Chem. 56 (2008) 5700.
[47] E.J. Avramides, S. Gkatsos, J. Agric. Food Chem. 55 (2007) 561.
[48] A. Garrido-Frenich, J.L. Fernández-Moreno, J.L. Martínez-Vidal, F.J. Arrebola Liébanas, J. Agric. Food Chem. 55 (2007) 8346.
[49] M. Guardia-Rubio, M.L. Fernández de Córdova, M.J. Ayora-Cañada, A. Ruiz-Medina, J. Chromatogr. A 1108 (2006) 231.
[50] A. García-Sánchez, N. Ramos-Martos, E. Ballesteros, Anal. Chim. Acta 558 (2006) 53.
[51] E. Ballesteros, A. García-Sánchez, N. Ramos-Martos, J. Chromatogr. A 111 (2006) 89.
[52] J.L. Fernandez-Moreno, F.J. Arrebola-Liébanas, A. Garrido-Frenich, J.L. Martínez-Vidal, J. Chromatogr. A 1111 (2006) 97.
[53] M. Guardia-Rubio, A. Ruiz-Medina, A. Molina-Díaz, M.J. Ayora-Cañada, J. Agric. Food Chem. 54 (2006) 8538.
[54] M. Guardia-Rubio, R.M. Marchal-López, M.J. Ayora-Cañada, A. Ruiz-Medina, J. Chromatogr. A 1145 (2007) 195.
[55] E. Fuentes, M.E. Báez, A. Quiñones, J. Chromatogr. A 1207 (2008) 38.

[56] J. Hernández-Borges, L.M. Ravelo-Pérez, E.M. Hernández-Suárez, A. Carnero, M.A. Rodríguez-Delgado, Chromatographia 67 (2008) 69.
[57] A. Di Muccio, R. Dommarco, D.A. Barbini, A. Santilio, F. Vergori, G. De Merulis, L. Sernicola, J. Chromatogr. A 552 (1991) 241.
[58] A. Di Muccio, P. Pelosi, D.A. Barbini, T. Generali, S. Girolimetti, P. Stefanelli, A. Leonelli, G. Amándola, L. Vergori, E.V. Fresquet, J. Chromatogr. A 833 (1999) 19.
[59] A. Ramesh, M. Balasubramanian, Analyst 123 (1998) 1799.
[60] L. Rastrelli, K. Totaro, F. De Simone, Food Chem. 79 (2002) 303.
[61] A. Di Muccio, T. Generali, D.A. Barbini, P. Pelosi, A. Ausili, F. Vergori, S. Girolometti, J. Chromatogr. A 765 (1997) 61.
[62] F.A. Esteve-Turrillas, A. Pastor, M. De la Guardia, Anal. Chim. Acta 553 (2005) 50.
[63] C. Yagüe, S. Bayarri, P. Conchillo, R. Lázaro, C. Pérez-Arquillé, A. Herrera, A. Ariño, J. Agric. Food Chem. 53 (2005) 5105.
[64] S.C. Cunha, J.O. Fernandes, M.B.P.P. Oliveira, Talanta 73 (2007) 514.
[65] L. Maldaner, C.C. Santana, I.C.S.F. Jardim, J. Liquid Chromatogr. Related Technol. 31 (2008) 972.
[66] M.G.D. Silva, A. Aquino, H.S. Dórea, S. Navickiene, Talanta 76 (2008) 680.
[67] C. Tsoutsi, T.A. Albanis, Int. J. Environ. Anal. Chem. 84 (2004) 3.
[68] C. Tsoutsi, K.I.D. Hela, T.A. Albanis, Anal. Chim. Acta 573–574 (2006) 216.
[69] G.A. Jongenotter, M.A.T. Kerkhoff, H.C.M. van der Knaap, B.G.M. Vandeginste, J. High Resol. Chromatogr. 22 (1999) 17.
[70] J.J. Vreuls, R.J.J. Swen, V.P. Goudriaan, M.A.T. Kerkhoff, G.A. Jongenotter, U.A.T. Brinkman, J. Chromatogr. A 750 (1996) 275.
[71] S. Barrek, O. Paisse, M.-F. Grenier-Loustalot, Anal. Bioanal. Chem. 376 (2003) 355.
[72] K. Patel, R.J. Fussell, M. Hetmanski, D.M. Goodall, J. Chromatogr. A 1068 (2005) 289.
[73] R. Sánchez, A. Vazquez, J.C. Andini, J. Villén, J. Chromatogr. A 1029 (2004) 167.
[74] R. Sánchez, J.M. Cortes, J. Villén, A. Vázquez, J. AOAC Int. 88 (2005) 1255.
[75] R. Sánchez, A. Vazquez, J. Villen-Altamirano, J. Villen, J. Sci. Food Agric. 86 (2006) 129.
[76] E. Diaz-Plaza, J.M. Cortes, A. Vazquez, J. Villen, J. Chromatogr. A 1174 (2007) 145.
[77] R. Sánchez, A. Vázquez, D. Riquelme, J. Villén, J. Agric. Food Chem. 51 (2003) 6098.
[78] J.M. Cortes, R.M. Toledano, J. Villén, A. Vazquez, J. Agric. Food Chem. 56 (2008) 5544.
[79] M.L. Hopper, J. Chromatogr. A 840 (1999) 93.
[80] Y. Ono, T. Yamagami, T. Nishina, T. Tobino, Anal. Sci. 22 (2006) 1473.
[81] S. Bogialli, A. Di Corcia, M. Nazzari, in: Y. Picó (Ed.), Food Toxicants Analysis, 2007, pp. 269.
[82] M. Anastassiades, S.J. Lehotay, D. Stajnbaher, F.J. Schenck, J. AOAC Int. 86 (2003) 412.
[83] A. Andersson, H. Palsheden, Fresenius. J. Anal. Chem. (1991) 339.
[84] H.G.J. Mol, R. Van Dam, O.M. Steijger, J. Chromatogr. A 1015 (2003) 119.
[85] A. Agüera, S. Lopez, A.R. Fernandez-Alba, M. Contreras, J. Crespo, L. Piedra, J. Chromatogr. A 1045 (2004) 125.
[86] K. Barnes, R.J. Fussell, J. Startin, M.K. Pegg, S.A. Thorpe, S.L. Reynolds, Rapid Commun. Mass Spectrom. 11 (1997) 159.
[87] M.A. Luke, J.E. Froberg, H.T. Masumoto, J. AOAC. Int. 56 (1975) 1020.
[88] A.R. Fernandez-Alba, J.F. García-Reyes, Trends Anal. Chem. 27 (2008) 973.
[89] A.K.D. Liem, R.A. Baumann, A.P.J.M. de Jong, E.G. van der Velde, P. Van Zoonen, J. Chromatogr. A 624 (1992) 317.
[90] R.M. Smith, J. Chromatogr. A 1000 (2003) 3.
[91] D.E. Raynie, Anal. Chem. 78 (2006) 3997.
[92] B.E. Richter, B.A. Jones, J.L. Ezzell, N.L. Porter, Anal. Chem. 68 (1996) 1033.
[93] K. Adou, W.R. Bontoyan, P.J. Sweeney, J. Agric. Food Chem. 49 (2001) 4153.
[94] P. Suchan, J. Pulkrabova, J. Hakslova, V. Kocourek, Anal. Chim. Acta 520 (2004) 193.
[95] M. Mezcua, M.R. Repetti, A. Agüera, C. Ferrer, J.F. García-Reyes, A.R. Fernández-Alba, Anal. Bioanal. Chem. 389 (2007) 1833.
[96] T. Pihlström, G. Isaac, M. Waldebäck, B.G. Österdahl, K.E. Markides, Analyst 127 (2002) 554.
[97] C. Blasco, G. Font, Y. Pico, J. Chromatogr. A 1098 (2005) 37.
[98] M.C. Hennion, J. Chromatogr. A 856 (1999) 3.
[99] S.J. Lehotay, M.A. Ibrahim, J. AOAC Int. 78 (1995) 445.
[100] T. Cairns, M.A. Luke, K.S. Chiu, D. Navarro, E.G. Siegmund, Rapid Commun. Mass Spectrom. 7 (1993) 1070.
[101] O. Shimelis, Y. Yang, K. Stenerson, T. Kaneko, M. Ye, J. Chromatogr. A 1165 (2007) 18.
[102] M. Syhre, G. Hanschmann, R. Heber, J. AOAC Int. 81 (1998) 513.
[103] Y. Saito, S. Kodama, A. Matsunaga, A. Yamamoto, J. AOAC Int. 87 (2004) 1356.
[104] F.J. Schenck, S.J. Lehotay, V. Vega, J. Sep. Sci. 25 (2002) 883.
[105] L.V. Podhorniak, J.F. Negron, F.D. Griffith, J. AOAC Int. 84 (2001) 873.
[106] F.J. Schenck, D.J. Donoghue, J. Agric. Food Chem. 48 (2000) 6412.
[107] J. Fillion, F. Sauve, J. Selwyn, J. AOAC Int. 83 (2000) 698.
[108] Y. Yamazaki, T. Ninomiya, J. AOAC Int. 82 (1999) 1474.
[109] F.J. Schenck, S.J. Lehotay, J. Chromatogr. A 868 (2000) 51.
[110] R.S. Sheridan, J.R. Meola, J. AOAC Int. 82 (1999) 982.
[111] H. Kondo, E. Amakawa, H. Sato, Y. Aoyagi, K.J. Yasuda, Food Hyg. Soc. Jpn. 44 (2003) 161.
[112] Y. He, Y.-H. Liu, Chromatographia 65 (2007) 581.
[113] S.A. Barker, J. Chromatogr. A 880 (2000) 63.
[114] S.A. Barker, J. Chromatogr. A 885 (2000) 115.

[115] S.A. Barker, J. Biochem. Biophys. Methods 70 (2007) 151.
[116] M. García-López, P. Canosa, I. Rodríguez, Anal. Bioanal. Chem. 391 (2008) 963.
[117] C.L. Arthur, J. Pawliszyn, Anal. Chem. 63 (1991) 2145.
[118] J. Pawliszyn, Solid Phase Microextraction: theory and practice, Wiley-VCH, 1997.
[119] J. Pawlisyzn, Applications of Solid Phase Microextraction, Royal Society of Chemistry, 1999.
[120] Z. Zhang, M.J. Yang, J. Pawliszyn, Anal. Chem. 66 (1994) 847A.
[121] D.A. Lambropoulou, I.K. Konstantinou, T.A. Albanis, J. Chromatogr. A 1152 (2007) 70.
[122] B. Jongenotter, H.G. Janssen, LC-GC Europe 15 (2002) 338.
[123] G. Flores, E.M. Díaz-Plaza, J.M. Cortés, J. Villén, M. Herraiz, J. Chromatogr. A 1211 (2008) 99.
[124] S.J. Lehotay, J. Chromatogr. A 785 (1997) 289.
[125] M. Garces-Garcia, E.M. Brun, R. Puchades, A. Maquieira, Anal. Chim. Acta 556 (2006) 347.
[126] M. Garcés-García, S. Morais, M.A. González-Martínez, R. Puchades, A. Maquieira, Anal. Bioanal. Chem. 378 (2004) 484.
[127] E.M. Brun, M. Garces-Garcia, R. Puchades, A. Maquieira, J. Agric. Food Chem. 53 (2005) 9352.
[128] F. André, K.K.G. De Wasch, H.F. De Brabander, S.R. Impens, L.A.M. Stolker, L. van Ginkel, R.W. Stephany, R. Schilt, R. Schilt, D. Courtheyn, P. Bonnaire, P. Fürst, P. Gowik, G. Kennedy, T. Kuhn, J.-P. Moretain, Trends Anal. Chem. 20 (2001) 435.
[129] S.J. Lehotay, K. Mastovska, A. Amirav, A.B. Fialkov, T. Alon, P.A. Martos, A. De Kok, A.R. Fernandez-Alba, Trends Anal. Chem. 27 (2008) 1070.
[130] Y. Picó, C. Blasco, G. Font, Mass Spectrom. Rev. 23 (2004) 45.
[131] L. Alder, G.K.G. Kempe, V. Vieth, Mass Spectrom. Rev. 25 (2006) 838.
[132] J. Hajslova, J. Zrostlikova, J. Chromatogr. A 1000 (2003) 181–197.
[133] C. Przybylski, F. Hommet, J. Chromatogr. A 1201 (2008) 78–90.
[134] I. Ferrer, J.F. García-Reyes, A.R. Fernández-Alba, Trends Anal. Chem. 24 (2005) 671.
[135] J.F. García-Reyes, M.D. Hernando, A. Molina-Diaz, A.R. Fernández-Alba, Trends Anal. Chem. 26 (2007) 828.
[136] M. Mezcua, O. Malato, J.F. García Reyes, A. Molina-Diaz, A.R. Fernández-Alba, Anal. Chem. 81 (2009) 913.
[137] J.F. García Reyes, M.D. Hernando, C. Ferrer, A. Molina-Diaz, A.R. Fernández-Alba, Anal. Chem. 79 (2007) 7308.
[138] J.F. García-Reyes, I. Ferrer, E.M. Thurman, A. Molina-Díaz, A.R. Fernández-Alba, Rapid Commun. Mass Spectrom. 19 (2005) 2780.

Glossary

ASE: accelerated solvent extraction
CAR/PDMS: carboxen/polydimethylsiloxane
CI: chemical ionization
CW-DVB: carbowax-divinylbenzene
DEA: diethylaminopropyl
ECD: electron-capture detector
EI: electron ionization

ENVI-Carb[TM]*:* graphitized carbon black (GCB)-based sorbent (Supelco)
ESI: electrospray ionization
FID: flame ionization detector
Florisil: magnesium silicate-based sorbent
FWHM: full-width at half maximum of a chromatographic peak
GC: gas chromatography
GCB: graphitized carbon black
GC–MS: gas chromatography/mass spectrometry
GC–MS/MS: gas chromatography/tandem mass spectrometry
GPC: gel-permeation chromatography
HLB: hydrophilic–lipophilic balanced polymer-based sorbent (Oasis[TM], Waters)
HS-SPME: head-space solid-phase microextraction
HPLC: high-performance liquid chromatography
LC: liquid chromatography
LC-ESI-MS/MS: liquid chromatography/tandem mass spectrometry, using electrospray ionization
LC–GC: liquid chromatography–gas chromatography
LC–MS: liquid chromatography/mass spectrometry
LC/MS/MS: liquid chromatography/tandem mass spectrometry
LC-TOFMS: liquid chromatography time-of-flight mass spectrometry
LPE: liquid-phase extraction
LSE: liquid-solid extraction
MAE: microwave-assisted extraction
MSPD: matrix solid-phase dispersion
NPD: nitrogen–phosphorus detector
PA: polyacrylate
PCBs: polychlorinated biphenyls
PDB: polystyrene divinylbenzene
PDMS: polydimethylsiloxane
PDMS-DVB: polydimethylsiloxane–divinylbenzene
PLE: pressurized liquid extraction
PSA: primary secondary amine
QQQ: triple quadrupole analyser
QTRAP: quadrupole linear ion trap
QuEChERS: "Quick, Easy, Cheap, Effective, Rugged and Safe" extraction method based on liquid partitioning with acetonitrile
RPLC: reversed phase liquid chromatography
SAX: strong anion exchanger sorbent
SFE: supercritical fluid extraction
SIM: selected ion monitoring
SPE: solid-phase extraction
SPME: solid-phase microextraction
SRM: selected reaction monitoring
TOF: time-of-flight analyser
TOTAD: "through oven transfer adsorption–desorption" interface
UPLC: ultra-performance liquid chromatography
UV: ultraviolet

Microwave-assisted digestion procedures for biological samples with diluted nitric acid: Identification of reaction products

Mário H. Gonzalez [a,b], Gilberto B. Souza [a], Regina V. Oliveira [c], Lucimara A. Forato [d], Joaquim A. Nóbrega [c], Ana Rita A. Nogueira [a,*]

[a] Grupo de Análise Instrumental Aplicada, Embrapa Pecuária Sudeste, P.O. Box 339, 13560-970 São Carlos, SP, Brazil
[b] Instituto de Química de São Carlos, Universidade de São Paulo, São Carlos, SP, Brazil
[c] Departamento de Química, Universidade Federal de São Carlos, São Carlos, SP, Brazil
[d] Embrapa Instrumentação Agropecuária, São Carlos, SP, Brazil

ARTICLE INFO

ABSTRACT

Microwave-assisted sample preparation using diluted nitric acid solutions is an alternative procedure for digesting organic samples. The efficiency of this procedure depends on the chemical properties of the samples and in this work it was evaluated by the determination of crude protein amount, fat and original carbon. Soybeans grains, bovine blood, bovine muscle and bovine viscera were digested in a cavity-microwave oven using oxidant mixtures in different acid concentrations. The digestion efficiency was evaluated based on the determination of residual carbon content and element recoveries using inductively coupled plasma optical emission spectrometry (ICP OES). In order to determine the main residual organic compounds, the digests were characterized by nuclear magnetic resonance (^{1}H NMR). Subsequently, studies concerning separation of nitrobenzoic acid isomers were performed by ion pair reversed phase liquid chromatography using a C18 stationary phase, water:acetonitrile:methanol (75:20:5, v/v/v) + 0.05% (v/v) TFA as mobile phase and ultraviolet detection at 254 nm. Sample preparation based on diluted acids proved to be feasible and a recommendable alternative for organic sample digestion, reducing both the reagent volumes and the variability of the residues as a result of the process of decomposition. It was shown that biological matrices containing amino acids, proteins and lipids in their composition produced nitrobenzoic acid isomers and other organic compounds after cleavage of chemical bonds.

© 2009 Elsevier B.V. All rights reserved.

1. Introduction

Sample preparation is one of the most time-consuming steps and also one of the main sources of contamination in an analytical procedure. This step must become easier, cheaper and faster according to green chemistry trends. Spectrochemical instrumental techniques for elemental analysis generally require complete sample decomposition. The destruction of organic matter in biological samples is the main parameter when decomposition efficiency is evaluated [1]. However, this efficiency depends on the original chemical composition of the sample and the temperature used during the digestion process. For instance, when concentrated nitric acid is employed carbohydrates matrices are rapidly decomposed at 140 °C, while protein molecules are decomposed at 150 °C, and lipid molecules require approximately 160 °C [2]. No correlation was observed between residual carbon content (RCC) and protein content when fat and protein contents of biological samples were correlated with RCC after microwave-assisted digestion. However, it was shown that protein-rich samples are easily decomposed than fat rich materials [3].

Nitric acid is frequently used in sample decomposition processes due to its simple manipulation, easy purification and efficiency in oxidation of organic compounds present in biological samples [4,5]. Concentrated nitric acid suffers thermal decomposition producing different water soluble oxides, such as NO, NO_2, NO_3^-, N_2O, N_2O_3, N_2O_4, N_2O_5, N_2O_6, HNO and HNO_2, with oxidant characteristics [6]. The formation of these gaseous decomposition products caused a sharp increase in pressure with barely no temperature change.

Closed-vessel microwave-assisted digestion with diluted acid solutions is an efficient alternative for sample preparation of organic samples for inorganic analysis using spectrochemical techniques [7–10]. Compared to concentrated nitric acid, diluted nitric acid solutions generate less residues, led to lower standard deviations and do not require high dilution factors before analyte measurements. Additionally, it is also necessary to take into account the involved chemical processes. Gaseous NO is generated during the oxidation of the organic constituents by HNO_3 action. Nitrous oxide is volatilized from the heated solution and reacts with O_2

* Corresponding author. Tel.: +55 16 34115616; fax: +55 16 34115600.
E-mail address: anarita@cppse.embrapa.br (A.R.A. Nogueira).

present in the gas phase of the reaction vessel. Consequently, NO_2 is generated and this gas is reabsorbed in the solution. Then, a disproportionate reaction occurs leading to the formation of NO_3^- and NO and the reaction cycle repeats itself up to the point that there is no O_2 in the gas phase of the closed vessel [11].

Previous studies were developed to identify organic residues generated during acid digestion. Mörner carried out systematic studies involving decomposition of protein samples by conventional heating with HNO_3 [12]. Benzoic, oxalic, picric, terephthalic acids and *m*- and *p*-nitrobenzoic acids (NBAs) were the products identified after decomposition. Species of *p*-nitrophenylalanine were described by Takayama and Tsubuku as mild nitration products in protein samples [13].

Pratt et al. identified organic residues of decomposition of bovine liver (National Institute of Science and Technology, standard reference material 1577a) using high performance liquid chromatography (HPLC) and voltammetric techniques. The main decomposition products formed were isomers of *m*- and *p*-nitrobenzoic acids when applying microwave-assisted nitric acid digestion [14].

Reaction products formed during the digestion of biological samples were also investigated by other authors [15–18]. Results have shown the need of employing different sample digestion methods according to the sample matrix and the technique being used [16]. The main digestion products were isomeric mixtures of nitrobenzoic acids and aromatic compounds [15,17,18].

Residual carbon contents were employed in order to evaluate the efficiency of microwave-assisted acid digestion of plant materials by using different concentrations of nitric acid with hydrogen peroxide. It was demonstrated by characterization of products formed by ^1H NMR that diluted acid nitric solutions led to less complex mixtures of residues when compared to concentrated nitric acid [19].

In the work here described the efficiency of microwave-assisted acid digested procedures for animal and plant samples were evaluated by identifying the reaction products using spectroscopic and chromatographic techniques.

2. Experimental

2.1. Instrumentation and instrument parameters

A model 6750 Freezer/Mill Spex Certiprep (Metuchen, USA) with a self-contained liquid nitrogen bath was used with model 6751 grinding vials.

Total carbon content was determined by elemental analyzer CHNS EA 1108, Fisons Instruments (Italy). Kjeltec Auto Sampler System 10035, Tecator (Vancouver, Canada) was used for crude protein determination. The fat content was determined using an accelerated solvent extractor—ASE, Ankom, model XT 2016 (Macedon, USA).

A microwave oven system equipped with perfluoalcoxi (PFA) vessels and temperature sensor Multiwave, Anton-Paar (Graz, Austria) was employed for sample digestion.

Residual carbon and mineral contents were determined by inductively coupled plasma optical emission spectrometry ICP OES Vista RL, Varian, Mulgrave (Australia).

The ^1H NMR spectra were acquired using a Varian Inova 400 spectrometer. The ^1H NMR spectra were recorded in deuterated methanol at 30 °C and tetramethylsilane (TMS) was added as an internal standard, using 32 transients, a $\pi/2$ pulse of 10 μs and a delay of 2 s and an acquisition time of 3.7 s.

The high performance liquid chromatographic system (HPLC) consisted of a Shimadzu LC-10ATVP pump (Kyoto, Japan), with the pump containing a valve FCV-10AL for selecting solvent, an autoinjector model SIL 10AVP, a degasser model DGU-14A, a SCL 10AVP

interface and a SPD-6AV UV-visible detector operated at 254 nm. Data were acquired by Shimadzu Class-VP software.

Separation of *o*-, *m*- and *p*-nitrobenzoic isomers was achieved using a C18 column (250 mm × 4.6 mm I.D., 5 μm particle size), purchased from Thermo Electron Corporation (Waltham, USA). Chromatographic experiments were carried out using an isocratic elution mode with a mobile phase consisting of water:acetonitrile:methanol (75:20:5, v/v/v) + 0.05% (v/v) trifluoracetic acid (TFA) at a flow rate of 1.0 mL min^{-1}. The column was kept at room temperature and the volume of injection was 10 μL. *o*-, *m*- and *p*-nitrobenzoic acids were identified based on the retention time of standard solutions for each compound.

2.2. Reagents, standards and samples

Deionized water with a Milli-Q® System Millipore (Bedford, MA, USA) was used to prepare all solutions. All glassware was immersed in 10% (v/v) HNO_3 for 36 h and rinsed with water.

Reagent grade concentrated nitric acid (Carlo Erba, Italy) and 30% (w/v) hydrogen peroxide (Mallinckrodt, Mexico) were employed.

Multielement reference solutions were prepared from 1000 mg L^{-1} stock solutions Titrisol® Merck (Darmstadt, Germany). Carbon reference solutions were prepared from 1000 mg L^{-1} urea sock solution Synth (São Paulo, Brazil).

HPLC grade methanol, acetonitrile and chloroform were purchased from J.T. Baker (Phillipsburg, NJ, USA). Analytical grade ethyl ether was also provided by J.T. Baker.

Bovine blood, bovine viscera and soybeans grains samples were all provided by Embrapa Pecuária Sudeste (São Carlos, SP, Brazil). Certified bovine muscle NIST SRM 8414 was used for checking accuracy and method validation (Gaithersburg, MD, USA).

The standard stock solutions for *o*-, *m*- and *p*-nitrobenzoic acid isomers were purchased from Across Organics (Geel, Belgium).

2.3. Procedure

2.3.1. Sample preparation for ICP OES determination

All samples were ground in a freezer mill operated at liquid nitrogen temperature (−195 °C). Before grinding, these samples were lyophilized in glass flasks connected to the vacuum system of a freeze-drier operated at −195 °C for 80 h, and further stored at −10 °C [20].

The crude protein content was obtained from total nitrogen determination by Kjeldahl method based on that most proteins of the studied samples are composed by 16% of nitrogen. The fat content was determined by accelerated solvent extraction (ASE) by solubilization of the ether soluble compounds. These procedures are based on AOAC International [21].

Sample masses of 200 mg were microwave-assisted digested using 2 mL HNO_3 solution in different concentrations (14, 7 and 2 mol L^{-1}) plus 1 mL of H_2O_2 of 30% (w/v) in a closed vessel. After decomposition, digested solutions were transferred to volumetric flasks and diluted with water to 15.0 mL. The microwave oven heating program was performed in five steps: (1) 2 min at 250 W; (2) 2 min at 0 W; (3) 4 min at 650 W; (4) 5 min at 850 W; and (5) 5 min at 1000 W.

Elemental and residual carbon contents were determined by ICP OES with radial view configuration. In order to remove volatile carbon compounds, digests were heated for 20 min at 120 °C [1] and afterwards purged with N_2 to remove dissolved CO_2 and minimize interferences. The instrumental parameters adopted were: 40 MHz generator frequency; 1.3 kW RF power; 15 L min^{-1} plasma gas-flow rate; 1.5 L min^{-1} auxiliary gas-flow rate; 0.9 L min^{-1} nebulizer gas-flow rate; cyclonic nebulization chamber; concentric nebulizer; 0.8 mL min^{-1} sample flow rate; and emission wavelengths (nm):

Table 1
Original contents of carbon, hydrogen, nitrogen, sulfur, crude protein (CP) and ether extract (EE) for the evaluated samples (mean ± standard deviation, $n = 3$).

Sample	N (%)	C (%)	H (%)	S (%)	Crude protein (%)	Ethereal extract (%)
Bovine blood	13.6 ± 0.2	47.2 ± 0.6	7.2 ± 0.8	0.75 ± 0.1	80.5 ± 0.4	1.6 ± 0.29
Bovine muscle	13.2 ± 0.1	50.1 ± 0.8	7.6 ± 0.4	0.81 ± 0.1	80.1 ± 0.43	10.8 ± 0.14
Soybean	7.1 ± 0.3	50.9 ± 0.5	7.8 ± 0.3	0.42 ± 0.1	41.4 ± 0.01	20.4 ± 0.74
Bovine viscera	3.2 ± 0.8	65.6 ± 0.9	10.2 ± 0.7	–	18.9 ± 0.67	63.7 ± 0.31

C(I) 193.025; Ca(II) 396.847; Fe(II) 279.553; K(I) 766.491; Mg(II) 280.275; Na(II) 588.995; P(I) 213.628; and Zn(I) 202.549.

2.3.2. Sample preparation for ^{1}H NMR analysis

After performing microwave-assisted digestions, the organic remaining compounds were extracted using ethyl ether (2.0 mL). Then, the organic phase was evaporated at 30 °C and the residues were reconstituted in deuterated methanol (0.8 mL) and tetramethylsilane (TMS) for ^{1}H NMR analysis.

2.3.3. Sample preparation for HPLC analysis

After performing microwave-assisted digestions, the organic remaining compounds were extracted using a liquid–liquid procedure. A volume of 3.0 mL of the digested solution was mixed by vortex action for 1 min with ethyl ether (2.0 mL). Then, the organic phase was rotary evaporated at 30 °C and the residue was reconstituted in 1.0 mL of methanol. Solutions were mixed by vortex action for 15 s and aliquots of 200 μL were transferred to auto-sampler vials and finally 10 μL volumes were injected into the HPLC system.

3. Results and discussion

3.1. Elemental analysis (C, H, N and S), crude protein (CP) and ether extract (EE)

The contents of C, H, N and S, crude protein and ether extract for the original samples, bovine blood and viscera, soybeans grains and the SRM muscle (NIST 8414), are presented in Table 1.

The initial carbon content varied from 47% to 65%, and the greatest concentration was found in bovine viscera sample. Nitrogen amounts were greater in bovine blood and bovine muscle samples, both around 13%. Bovine viscera samples presented the greatest content of ether extract, followed by soybeans grains, which also presented intermediate value of protein, around 42%. Blood and bovine muscle presented the greatest contents of crude protein, around 81%.

3.2. Residual carbon content and element recoveries

The RCC values obtained for each investigated sample are presented in Fig. 1.
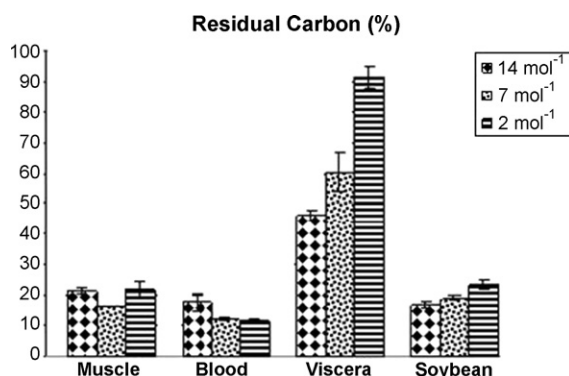
Fig. 1. Residual carbon content (%) in digested samples with different oxidant mixtures.

It can be seen for viscera sample containing around 64% of EE that a decrease in acid concentration led to an increase in RCC values. The use of a solution containing 2 mol L^{-1} HNO$_3$ was not effective for promoting complete digestion of viscera samples, resulting in RCC of 90%. Solid residues and a yellowish color were observed during for viscera digest due to its incomplete decomposition. The same effect was observed for soybeans grains, containing around 21% of EE. However, this effect was less pronounced when compared to bovine viscera. Differences of structural lipids between animal and vegetable samples would be a possible explanation. Samples digested with concentrated nitric acid solutions presented greater standard deviations. On the other hand, for samples containing greater amounts of crude protein an opposite effect was observed. A decrease of acid concentration led to a decrease in RCC from 22% to 15%. The SRM bovine muscle presented RCC of 23% when decomposed using a 14 mol L^{-1} of HNO$_3$ solution. On the other hand, solutions containing 2 mol L^{-1} HNO$_3$ resulted in similar RCC, around 22%

Temperature is the principal factor for evaluating sample digestion procedures. In this study the temperatures reached in all samples were: 160–170 °C for 14 mol L^{-1}; 170–180 °C for 7 mol L^{-1} and 180–200 °C for 2 mol L^{-1} nitric acid concentrations. The hypothesis to explain the decrease in RCC when diluted nitric acid solution was employed is related to the observed increment in temperature values when the concentration of water molecules increased in the solution. However, diluted acid solutions were inefficient for digesting viscera samples containing the greatest amount of fats in their composition.

A certified reference material was employed for evaluating accuracy. Determined and certified concentrations are shown in Table 2. For calcium and magnesium amounts in SRM bovine muscle, it was verified that suitable recoveries occurred when a 2 mol L^{-1} HNO$_3$ solution was employed. It was observed that for Fe and Zn, digestions with diluted acid solutions presented results closer to the certified values. Accuracy was improved when using a 2 mol L^{-1} HNO$_3$ solution for digestions. The use of 7 mol L^{-1} of HNO$_3$ solution presented RCC of 16% and proper mineral recoveries with low RCC and smaller deviations when compared to digestions using concentrated HNO$_3$.

The use of diluted solutions can prevent the formation of insoluble salts, and improve the solubility of some minerals [11].

3.3. Identification of reaction products by ^{1}H NMR

Considering ^{1}H NMR spectra obtained for digests after decomposition using 14 and 7 mol L^{-1} HNO$_3$ for blood and bovine muscle samples, the presence of organic residues in the aliphatic region (δ 0.5–3.0 ppm) was confirmed, as well as intense and abundant signal in the typical region of nitro-aromatics compounds (δ 7.0–10.5 ppm; Fig. 2). Different amounts and lower variety of organic compounds were verified when oxidant mixtures were compared. At high concentration, high pressure and high temperature, it was observed an increase in the oxidant power of the reaction mixtures, which oxidizes a greater amount of compounds, generating a wider variety of organic residues.

Digests of bovine viscera obtained using 7 mol L^{-1} of HNO$_3$ were analyzed by ^{1}H NMR, and it was observed peaks in the δ

Table 2
Mineral concentration in samples digested with 2 mL of HNO_3 in different concentration plus 1 mL of H_2O_2 (30% w/v; mean ± standard deviation, $n = 3$).

		Mineral concentration ($mg\,kg^{-1}$)						
		Ca	Fe	K	Mg	Na	P	Zn
Bovine muscle ($mol\,L^{-1}$)								
Certified		145 ± 20	71.2 ± 9.2	10517 ± 37	960 ± 95	2100 ± 80	8360 ± 450	142 ± 12
Found	14	131 ± 14	50 ± 8	10609 ± 838	1089 ± 34	1491 ± 42	9640 ± 204	174 ± 12
	7	155 ± 10	75 ± 7	11587 ± 570	1113 ± 27	1957 ± 30	8703 ± 192	149 ± 10
	2	143 ± 11	69 ± 6	10145 ± 410	1031 ± 17	2031 ± 17	10655 ± 162	138 ± 11
Bovine blood	14	174 ± 4	1692 ± 57	745 ± 22	56 ± 2	5899 ± 222	860 ± 93	198 ± 3
	7	196 ± 4	1867 ± 19	683 ± 11	64 ± 2	6414 ± 127	896 ± 73	236 ± 8
	2	199 ± 8	1942 ± 14	693 ± 20	66 ± 3	6624 ± 110	907 ± 77	249 ± 4
Soybean	14	1874 ± 44	113 ± 10	10870 ± 389	2629 ± 37	116 ± 24	6207 ± 231	19 ± 4
	7	1960 ± 40	133 ± 15	11286 ± 136	2847 ± 55	78 ± 10	6351 ± 103	46 ± 4
	2	2005 ± 44	129 ± 14	11694 ± 196	2981 ± 43	100 ± 12	6889 ± 254	53 ± 5
Bovine viscera	14	2510 ± 281	99 ± 2	1810 ± 76	134 ± 10	1021 ± 30	3646 ± 185	11 ± 3
	7	2382 ± 762	117 ± 2	1644 ± 72	133 ± 17	1030 ± 34	3638 ± 377	18 ± 2
	2	2437 ± 189	–	1508 ± 97	140 ± 14	868 ± 96	3689 ± 377	21 ± 4

8.4 ppm region, evidencing the presence of nitro-compounds. A signal at δ 5.2 ppm in digests obtained using 2 mol L^{-1} HNO$_3$ could be attributed to the presence of water in the sample (δ 4.7 ppm), overlapping with other peaks as, for example, free fatty acid, which present a typical signal at δ 5.3 ppm [22]. It may be inferred that

diluted nitric acid solution did not have sufficient strong oxidative action for bovine viscera sample digestion.

For soybeans grains samples, differences can be observed in the nitro-derivative aromatic compound region (δ 7.0–10.5 ppm; Fig. 2). The signal at δ 5.2 ppm was not observed for this sample. In all
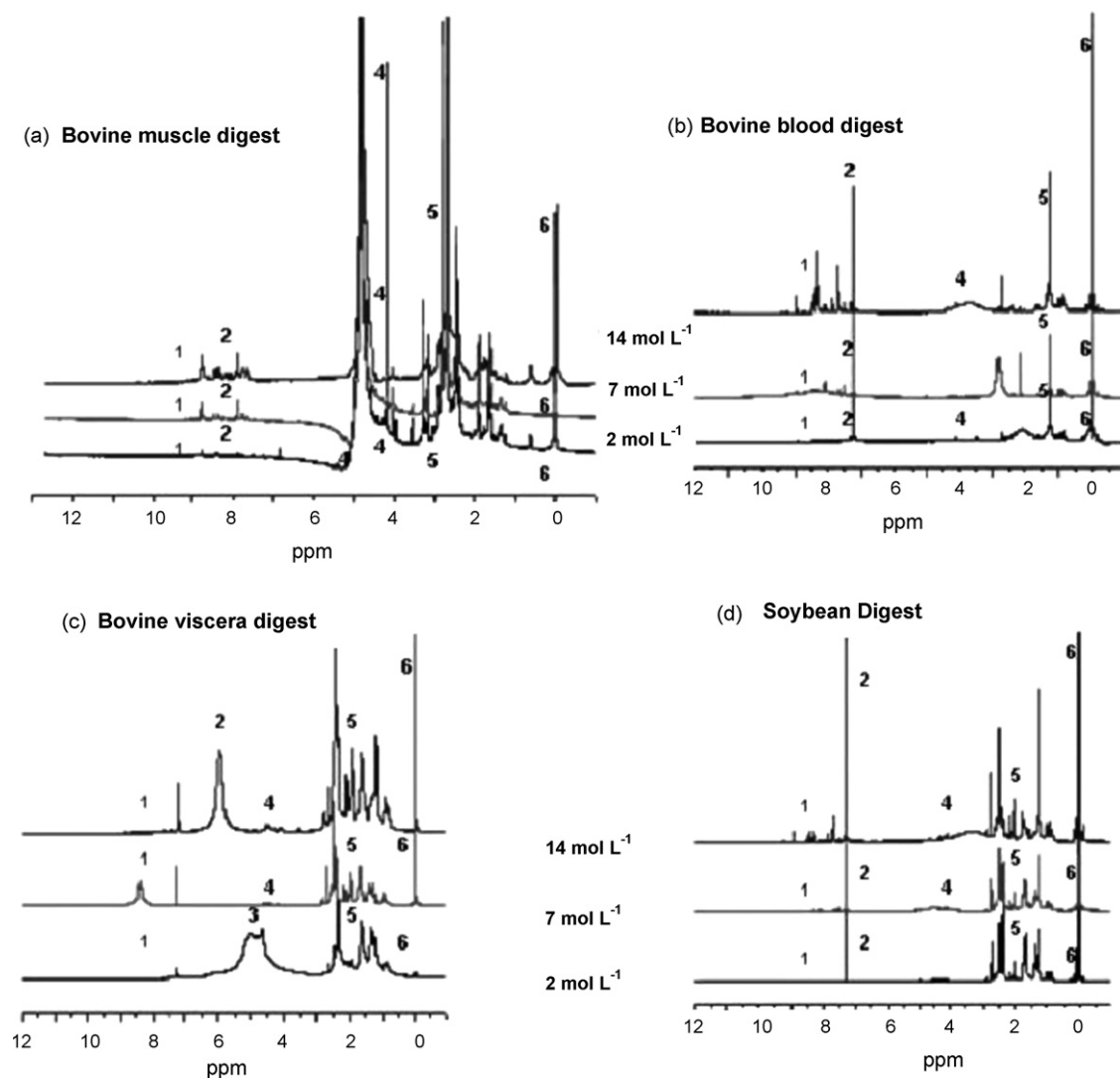
Fig. 2. ^{1}H NMR spectra of the organic residue of digested samples: (1) aromatic; (2) aliphatic nitro-compounds; (3) hydrogens on doubly bonded from unsaturated fatty acids; (4) carbinolic hydrogens; (5) aliphatic; (6) TSS signal.
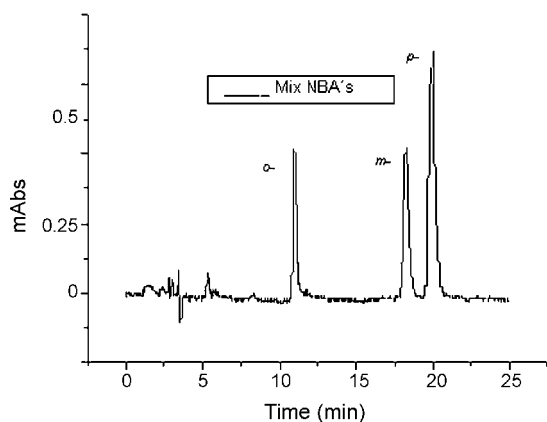
Fig. 3. Chromatograms for standard mixture of o-, m- and p-nitrobenzoic acid. Chromatographic conditions: C$_{18}$ column with water:acetonitrile:methanol (75:20:5, v/v/v) + 0.05% TFA as mobile phase, 1.0 mL min^{-1} of flow-rate, 10 μL of volume injection and 254 nm of detection wavelength.

cases, small peaks, probably carbinolic hydrogen, were observed at δ 4.0–4.7 ppm region [19].

3.4. Separation of reaction products by HPLC-UV

Preliminary experiments were based on the use of different mixtures of water:acetonitrile; water:methanol and water:acetonitrile:methanol as mobile phase for retention of all three nitrobenzoic acid isomers. However, these compounds were not enough retained under any evaluated conditions. In order to elucidate the influence of ion pair additives in the mobile phase and according to a previous work by Chen and Zhang [22], a modified mobile phase employing trifluoracetic acid (TFA) as ion pair was evaluated to simultaneously separate all target isomers of nitrobenzoic acid. Two different proportions of eluent were used to achieve efficient separation of the compounds under isocratic mode, water:acetonitrile:methanol (70:20:10, v/v/v) + 0.05% (v/v) TFA and water:acetonitrile:methanol (75:20:5, v/v/v) + 0.05% (v/v) TFA. This later mobile phase led to effective separation and appropriate retention times for o-, m- and p-nitrobenzoic acids within 25 min analysis time.
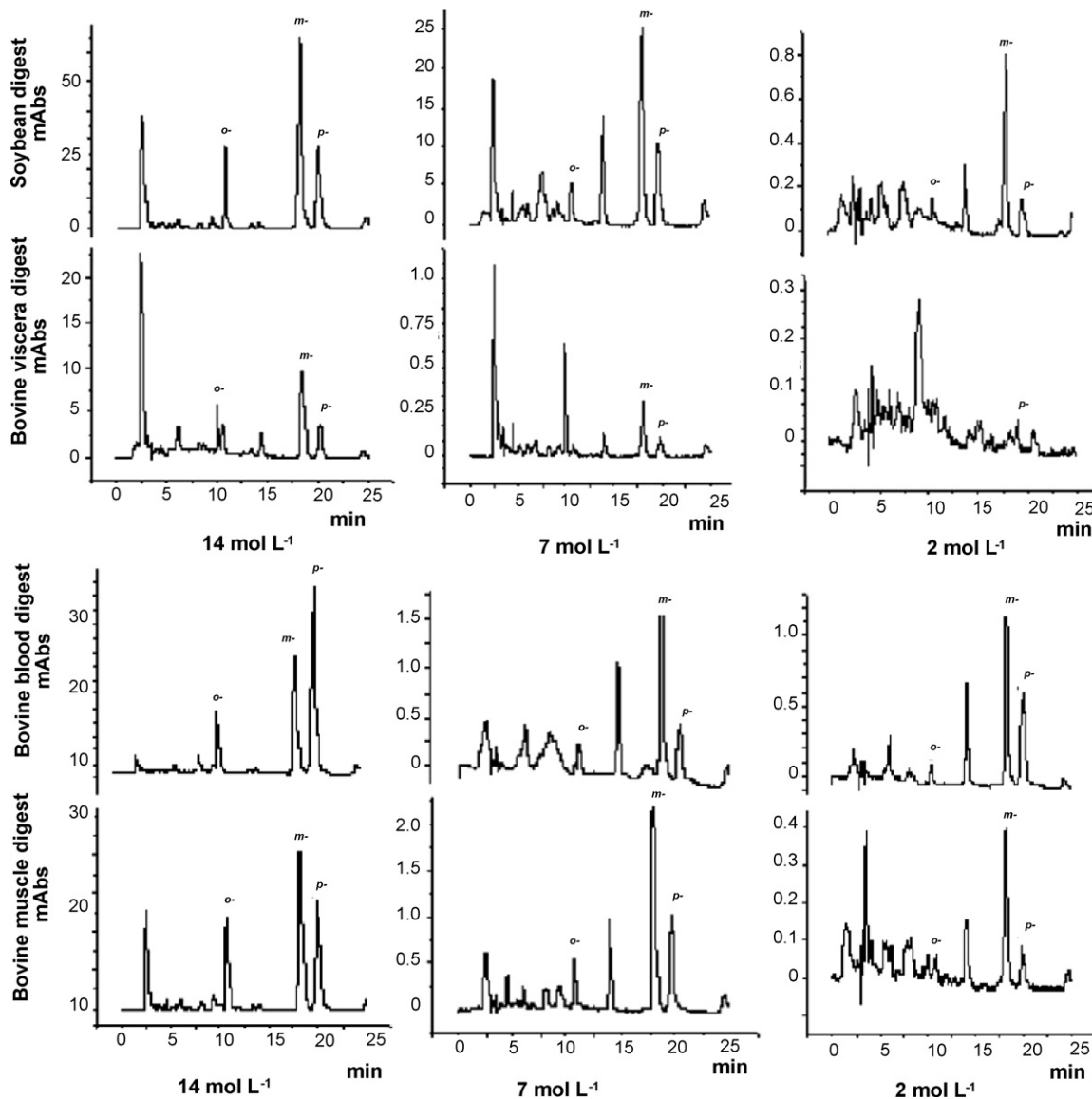
Fig. 4. Chromatograms for bovine muscle, blood, viscera and soybean grains. Chromatographic conditions: C$_{18}$ column, water:acetonitrile:metanol (75:20:5, v/v/v) + 0.05% TFA as mobile phase, 1.0 mL min^{-1} of flow-rate, 10 μL of volume injection and 254 nm of detection wavelength.

The improvement of the separation of the three isomers by adding an ion pair additive into the mobile phase improved the separation of all compounds, and this effect might be explained considering the ionization suppression of the acid group and a possible ion pair formation between the cationic portion of the molecules and the anionic portion of the TFA. The chromatogram obtained for the three isomers at 5 μg mL^{-1} concentration is shown in Fig. 3. The retention times of *o*-NBA, *m*-NBA and *p*-NBA were 10.9, 18.2 and 19.9 min, respectively.

The chromatograms of bovine muscle and blood digested using three different nitric acid concentrations for digestions are shown in Fig. 4. It may be seen that lower contents of NBA isomers were formed when employing diluted acid solutions. The isomers species were identified by matching the retention time of the chromatographic peaks with those of the standards.

Similar characteristics were observed for bovine viscera and soybeans grains (Fig. 4). The *o*-NBA is absent in viscera digested using 2 and 7 mol L^{-1} of nitric acid solutions, and only *p*-NBA appears in the viscera decomposed with 2 mol L^{-1}.

Comparing the digested solutions with the original sample compositions, biological matrices with structural amino acids, proteins and lipids produced nitrobenzoic acid isomers and other organic compounds owing to the cleavage of chemical bonds. The *m*-nitrobenzoic acid was formed in most digestion conditions.

Results obtained in this study are in agreement with the literature. The mechanism of decomposition is similar in almost all cases, generating a mixture of NBA's. These results extend the previous study published by Pratt et al. [14], since these authors concluded that the formation of the three isomers indicates that the dominant mechanism in microwave-assisted digestion is the nitration of the aromatic ring followed by oxidation of the amino acid side chain for bovine liver samples. Daniel et al. have shown that for vegetable samples (NIST SRM peach leaves), the isomers of nitrobenzoic acid are the major products at temperatures around 180 °C [17]. Würfels et al. described that there is a quantitative degradation of saturated and monounsaturated chains of C–H and, in contrast, there is not a complete mineralization of polyunsaturated fat in HNO$_3$ medium [15]. Aliphatic and aromatic acids, nitro-compounds, oxalates and inorganic nitrates and phosphates were found as a decomposition product in different samples analyzed by Reid et al. [16].

Based on green chemistry principles, the use of diluted acids for digestions led to relevant advantages, such as cost reduction, minimization of residues, reduction of blank values, and prevention of damages to components of the equipment [11,19].

4. Conclusions

The use of diluted acids was proven to be a feasible and recommendable alternative, reducing the volume of the reagents and the amount and variety of digestion residues.

The ^{1}H NMR spectra obtained for digests in diluted nitric acid medium are simpler than those obtained when using 14 mol L^{-1} HNO$_3$. Concentrated solutions presented a broader variety of organic compounds, such as nitro-derivative aromatic compounds, and a higher amount of aromatic aliphatic compounds.

The separation of isomers *o*-, *m*- and *p*-nitrobenzoic acid was possible employing ion pair reversed phase HPLC-UV. The qualitative method developed allowed to evaluate different digests. Taking into account the effectiveness of digestions of complex samples with diluted nitric acid solutions one may wonder why this approach has not been used before. Probably this can be explained by the relatively recent availability of closed reaction vessels that can withstand high pressure and high temperature. Additionally, these vessels have enough volume to contain oxygen gas in sufficient amount to promote the regeneration of nitric acid according to the mechanism proposed. Last but not least, these vessels also present an intense temperature gradient in the first step of the heating program which favors condensation of gas products formed by oxidation reactions.

References

[1] A. Krushevska, R.M. Barnes, C.J. Amarasiriwaradena, H. Foner, L. Martines, J. Anal. Atom. Spectrom. 7 (1992) 851–858.
[2] H.M. Kingston, L.B. Jassie, J. Res. Natl. Bur. Stand. (US) 93 (1988) 269–274.
[3] E.N.V.M. Carrilho, A.R.A. Nogueira, J.A. Nóbrega, G.B. Souza, G.M. Cruz, Fresen. J. Anal. Chem. 371 (2001) 536–540.
[4] M. Würfels, E. Jackwerth, Fresen. J. Anal. Chem. 44 (1985) 322–345.
[5] M. Würfels, E. Jackwerth, M. Stoeppler, Anal. Chim. Acta 226 (1989) 1–16.
[6] F.A. Cotton, G. Wilkinson, Advanced Inorganic Chemistry, 6th ed., Wiley-Interscience, New York, 1999.
[7] S. Dugenest, M. Ollé, A. Ribes, M.F. Grenier-Loustalot, Analysis 26 (1998) 256–260.
[8] P.Y.T. Chow, T.H. Chua, K.F. Tang, B.Y. Ow, Analyst 120 (1995) 1221–1223.
[9] Y.Z. Chao, M.K. Wong, L.L. Koh, Y.C. Wee, J. Anal. Atom. Spectrom. 11 (1996) 585–590.
[10] M. Miyazawa, M.A. Pavan, M.F. Block, Commun. Soil Sci. Plant Anal. 15 (1984) 141–147.
[11] L.C. Trevizan, G.L. Donati, A.R.A. Nogueira, J.A. Nóbrega, in: M.A.Z. Arruda (Ed.), Trends in Sample Preparation, Nova Science Publishers, New York, 2007.
[12] C.T. Mörner, Hoppe-Seyleïr, Z. Physiol. Chem. 95 (1915) 263–266.
[13] Y. Takayama, Y. Tsubuku, Bull. Chem. Soc. Jpn. 17 (1942) 109–112.
[14] K.W. Pratt, H.M. Kingston, W.A. MacCrehan, W.F. Koch, Anal. Chem. 60 (1988) 2024–2027.
[15] M. Würfels, E. Jackwerth, M. Stoeppler, Anal. Chim. Acta 226 (1989) 17–30.
[16] H.J. Reid, S. Greenfield, T.E. Edmonds, Analyst 120 (1995) 1543–1548.
[17] M.M. Daniel, J.D. Batchelor, C.B. Rhoades, B.T. Jones, Atom. Spectrosc. 19 (1998) 198–203.
[18] I.V. Kubrakova, A.A. Formanovskii, T.F. Kudinova, N.M. Kuz'min, J. Anal. Chim. Acta 54 (1999) 460–465.
[19] G.C.L. Araújo, M.H. Gonzalez, A.G. Ferreira, A.R.A. Nogueira, J.A. Nóbrega, Spectrochim. Acta B 57 (2002) 2121–2132.
[20] AOAC Official Methods of Analysis of AOAC International, 16th ed., 1995.
[21] L.A. Forato, L.A. Colnago, R.C. Garratt, M.A. Lopes, Biochim. Biophys. Acta 106 (2000) 106–114.
[22] P. Chen, M. Zhang, J. Chromatogr. A 773 (1997) 365–367.

Detection of deletion mutations in DNA using water-soluble cationic fluorescent thiophene copolymer

Hongliang Guan, Peng Zhou, Shang Zeng, Xianglei Zhou, Yun Wang, Zhike He*

Key Laboratory of Analytical Chemistry for Biology and Medicine, College of Chemistry and Molecular Sciences, Wuhan University, Wuhan 430072, PR China

ARTICLE INFO

ABSTRACT

In this contribution, we designed a fluorescent thiophene copolymer to detect insertion/deletion mutation in DNA by doping aldehyde group in the main chain. The fluorescence of the copolymer could be dramatically quenched on the addition of single-stranded DNA (ssDNA) via strong electrostatic interactions and electronic/energy transfer. Although the complementary ssDNA made the fluorescence recover, the hydrogen bonds and chemical coupling also played a significant role between the unpaired bases and aldehyde group, which could differentiate the subtle differences in such mutant DNA. The influence of buffer pH, concentration of NaCl, heating time and the temperature was systemically investigated and the proposed method was then successfully applied to detect real sample. With the respect to the linearity, limit of detection precision, specificity, this procedure could provide sensitive methodologies for the rapid detection and identification of nucleic acids.

1. Introduction

Since the three dimensional structure of DNA was elucidated and human genomes sequences were decoded [1], the linkage between encoded chemical information and genetic inheritance has become an area under intense investigation for better understanding and treating the complex diseases of humans. For example, the A → T point mutation in human β-globin gene caused a single amino acid change from Glu to Val, leading to sickle cell anemia [2]. Whereas, the high-throughput screening and accurate detection of deficiency in genome is meaningful and important in molecular biology research area and DNA chemical structure [3–5]. To achieve these goals, Nucleic acid-based hybridization has emerged as a reliable approach for direct and specific identification of numerous biological analytes [6–8]. Among them, automated DNA sequencers and polymerase chain reaction indeed provide invaluable tools for genotyping studies. However, these methods are often time-consuming and need complicated protocols. Other more conventional methods are nearly highlightened on detecting one or more bases mismatch in double-stranded DNA [9–11]. Insertion and deletion of extra nucleotides on a single chain are referred as insertion mispairs which is manifested as extra nucleotides in one strand. Extra bases in one strand of DNA or RNA may result from a variety of natural mechanisms. Usually they can arise as intermediates during recombination or result from DNA polymerase

slippage during replication [12–13]. Up to date, there are only a few methods used for analyzing such special sequences. In these cases, the detection relies on a modification of the electrical and/or optical properties of an oligonucleotide functionalized fluorophore [14–16]. Although some other standard methods, such as gel electrophoresis, work well to detect insertion/deletion mutation, but the number of deleted bases should be more than tens of bp [17]. Therefore, it is a challenge to find new approaches that are simpler and faster for insertion/deletion recognition and detection [18]. Herein, for the first time, we report an investigation using a water-soluble cationic fluorescent conjugated copolymer as a signal transducer to detect insertion/deletion in dsDNA with high selectivity and sensitivity.

Water-soluble fluorescent conjugated polymers (conjugated polyelectrolytes, CPE), which are characterized by a π-delocalized electronic structure, have gained enormous attention as novel functional materials. The transfer of exciton along the whole backbone of the CPE to an energy/electron acceptor can result in an amplification of the fluorescence signals [19–21]. Therefore, CPEs offer an excellent platform for detecting a wide range of chemical and biological agents, such as physiological ion, nucleic acids and proteins [22–25]. In addition, careful incorporation of a functional group into CPEs will yield complex with some unique properties, e.g. sensitive to relatively small perturbations, including changes in temperature, solvent, or chemical environment [26–27]. For the purpose, there is a growing interest in the design and development of chemical and biosensors. Undoubtedly the functionalized polythiophene have been one of the subjects of many investigations. On one hand, they are easy to prepare and modify, and thiophene polymers can be

---

* Corresponding author. Tel.: +86 27 87162672; fax: +86 27 68754067.
E-mail address: zhkhe@whu.edu.cn (Z. He).
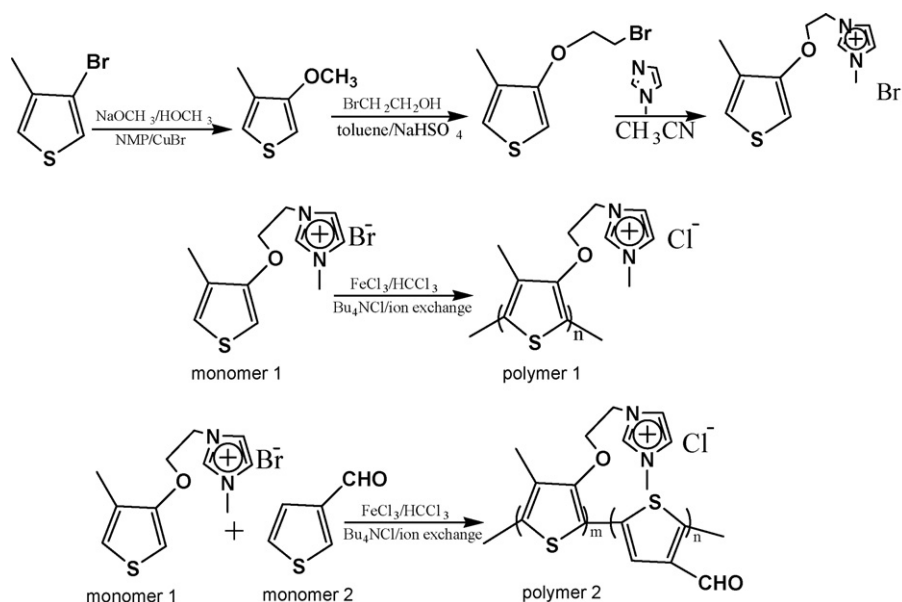
Scheme 1. The synthetic route of thiophene copolymer and polymer.

obtained via direct polymerization of the corresponding monomers from oxidation by FeCl$_3$ or other coupling reagents. On the other hand, polythiophene bear chromic, optical and electrochemical activities. The interactions between the side chains (ligands) and different analytes (targets) can be detected from the change in both side-chain and backbone conformations without any labeling process [28–29]. In this work, we improved the qualities of poly-thiophene derivative according to previously published methods [30–31]. 3-Thiophenecarboxaldehyde was incorporated into the main chain during polymerization (Scheme 1) and expected to have interaction with unpaired bases. Although the obtained copolythio-phene (polymer 2, CPT) exhibits chromic and optical properties similar to that of poly (3-alkoxy-4-methylthiophene) (polymer 1, PT), it still maintains its own advantages.

2. Experimental

2.1. Materials

All reagents were purchased from Sigma–Aldrich (St. Louis, USA) and used without further purification, all the solvents were from Sinopharm Company (Shanghai, China) and dried following standard procedure prior to experiment. All oligonucleotides were purchased from Shanghai Sangon Biological Engineering Technology & Services Co., Ltd. The concentration of DNA was determined by measuring the absorbance at 260 nm in a 3 mL quartz cuvette.

2.2. Apparatus

^{1}H and ^{13}C NMR were measured on a Varian Mercury-VX300 spectrometer and reported in δ (ppm) values with TMS as an internal standard (unless otherwise noted). Mass spectra were obtained on a Shimadzu GCMS QP2010 plus mass spectrometer in low-resolution electron-impact. UV–vis absorption spectra were taken on a TU-1900 Spectrophotometer (Beijing Purkinje General Instrument Co., Ltd.). Fluorescence measurements were obtained in a 3 mL quartz with optical pathlength of 1.0 cm at room temperature by using a LS-55 Luminescence Spectrometer (PerkinElmer, USA), scan speed was at 1200 nm/min. All the spectra were recorded in 10 mM Tris–HCl buffer solution (containing 0.1 M NaCl, pH 8.0). The water was purified on a Millipore filtration system ($\geq$18.2 MΩ cm).

2.3. Synthesis of polymer 1 and polymer 2

2.3.1. Preparation of 3-methoxy-4-methylthiophene

3-Bromo-4-methylthiophene (10 g, 56.5 mmol) and CuBr (5.0 g, 34.8 mmol) were added to a mixture of 50 mL of sodium methoxide (28% in methanol) and 30 mL NMP and refluxed for 3 days under argon atmosphere. After cooling, the solid was filtrated. The filtrate was washed with water and extracted several times with diethyl ether. The organic phase was dried with MgSO$_4$ and the evaporated. The resulting oil was purified by chromatography on a silica gel column with hexanes as eluent, yield 84%. ^{1}H NMR (CDCl$_3$, 300 MHz) δ = 2.09 (s, 3H); 3.81 (s, 3H); 6.16 (d, J = 3.0 Hz, 1H), 6.82 (s, 1H). 13C NMR (CDCl$_3$, 300 MHz) δ = 12.89, 57.50, 95.86, 120.28, 129.16, 157.26. MS (m/z, %): 128 (M$^+$, 100), 113(90), 85(40), 45(55).

2.3.2. Preparation of 3-(2-Bromo)ethoxy-4-methylthiophene

3-Methoxy-4-methylthiophene (3.0 g, 23.4 mmol) was added to a mixture of 30 mL of toluene, 2-bromo-1-ethanol (6.5 g, 52.0 mmol) and of NaHSO$_4$ (300 mg, 2.5 mmol) under argon atmosphere and heated at 100 °C until the produced methanol was distilled off. The reaction mixture was allowed to cool to room temperature and washed several times with water, and then extracted with diethyl ether. The organic phase was combined and dried with MgSO$_4$, filtered and evaporated to dryness. The crude product was submitted to column chromatography using silica gel and hexanes, yield 60%. ^{1}H NMR (CDCl$_3$, 300 MHz) δ = 2.17 (s, 3H); 3.67 (t, J = 5.4 Hz, 2H); 4.26 (t, J = 6.6 Hz, 2H), 6.20 (d, J = 2.7 Hz, 1H), 6.87 (t, J = 1.5 Hz, 1H). 13C NMR (CDCl$_3$, 300 MHz) δ = 13.05, 29.51, 69.88, 97.41, 120.62, 129.48, 155.34. MS (m/z, %): 222/220 (M$^+$, 40), 114(100), 85(38), 45(55).

2.3.3. Preparation of monomer 1

1-Methyl-imidazole (1.5 mL, 18.4) was added into a solution of 3-(2-bromoethoxy)-4-methylthiophene (0.80 g, 3.6 mmol) in CH$_3$CN (35 mL). The resulting reaction mixture was stirred at 70 °C under argon atmosphere for 2 days. After evaporation of the solvent, the crude product was washed twice with warm ethyl acetate and twice with diethyl ether at room temperature to provide monomer 1 as a white solid, yield 88%. ^{1}H NMR (CDCl$_3$, 300 MHz) δ = 2.00 (s, 3H); 4.00 (s, 3H); 4.32 (t, J = 4.2 Hz, 2H); 4.90 (t, J = 4.5 Hz, 2H), 6.20 (d, J = 0.3 Hz, 1H), 6.78 (t, J = 2.1 Hz, 1H), 7.26 (s, 1H), 7.46 (s, 1H), 10.55 (s,

Table 1
The oligonucleotide used in this study.

Probe Y	5′-CCA TGC GAA CAA TTC AAC CG-3′
Target X_1	5′-CGG TTG AAT TGT TCG CAT GG-3′
X_2	5′-CGG TTG AAT TGT TCG CAT GP-3′
X_3	5′-CGG TTG AAT TGT TCG CATPP-3′
X_4	5′-CGG TTG AAT TGT TCG CAPPP-3′
X_5	5′-CGG TTG AAT TGT TCG CPPPP-3′

P represented here allele gene with its base deleted.

1H). ^{13}C NMR (CDCl$_3$, 300 MHz) δ = 11.74, 36.51, 49.18, 68.94, 98.55, 112.93, 121.46, 122.79, 123.09, 128.52, 137.44, 154.78.

2.3.4. Preparation of two polymers

A solution of monomer 1(0.5 g, 1.9 mmol) in chloroform (20 mL), was added dropwise to a solution of anhydrous FeCl$_3$ (1.0 g, 6.2 mmol) in chloroform (30 mL) under argon atmosphere. The mixture was stirred at room temperature for 2 days. After evaporation of the solvent, the compound was washed quickly with methanol and dissolved in an excess of acetone, precipitated by addition of an excess of tetrabutylammonium chloride. The black-red polymer was dissolved in methanol by adding a few drops of anhydrous hydrazine. After the solution was evaporated again, the resulting polymer was washed again several times with a saturated solution of tetrabutylammonium chloride in acetone and by Soxhlet extraction with acetone over a period of 10 h, and then dried under reduced pressure to give polymer 1 (PT), yield 62%. The preparation of polymer 2 (CPT) was the same to that of polymer 1, monomer 1(0.45 g, 1.74 mmol) and 3-thiophenecarboxaldehyde (monomer 2, 0.04 g, 0.35 mmol) were added in molar proportion of 5:1, thus the CPT can be sufficiently precipitated by adding tetrabutylammonium chloride. During final treatment of CPT, anhydrous hydrazine was not used to keep aldehyde group intact in CPT. The obtained CPT are bright red with its maximum excitation and emission wave length are 397 nm and 520 nm in pure water, yield 59%

2.4. Measurements

2.4.1. Assay for fluorescence

The stock solutions of PT and CPT (2×10^{-4} M, per repeat unit) were dissolved in pure water and used by appropriate dilution, all the oligonucleotides solutions (1×10^{-5} M, Table 1) were prepared in 10 mM Tris–HCl buffer prior to use. For fluorescence assay, in 5 mL Eppendorf tube, a 20 μL of CPT or PT solution was added to 4 mL Tris–HCl aqueous solution, followed by the addition of 10 μL the capture oligonucleotide (Y), respectively. The target oligonucleotide X_1–X_5 was then added in proportion to perform hybridization. The final concentration of CPT or PT was 5.0×10^{-7} M, probe Y was 2.5×10^{-8} M. The mixture were incubated in water at 45 °C for 10 min and cooled to room temperature to obtain dsDNA-CPT or PT complex (also called triplex, its maximum UV–vis spectra was at 420 nm).

2.4.2. The lifetime of two polymer-dsDNA triplex

CPT-Y-X_3 and PT-Y-X_3 were selected for measurement and prepared in 10 times than that for fluorescence measurements. The excitation source was a mode-locked Ti:sapphire laser (Mira 900, Coherent) with a pulse width of ~3 ps at a repetition rate of 76 MHz. The lifetime of two triplexes was determined in a 3 mL quartz with optical pathlength of 1.0 cm at room temperature. The samples were excited at 400 nm and signal was collected in reflective mode equipped with GG455and 700FL filter slide, and the photoluminescence spectra were recorded by a monochromator (Spectrapro 2500i, Acton) with a liquid-nitrogen-cooled CCD detector (SPEC-10, Princeton). The time-resolved PL decay traces were recorded by a time-correlated single photon counting system (PicoQuant GmbH).
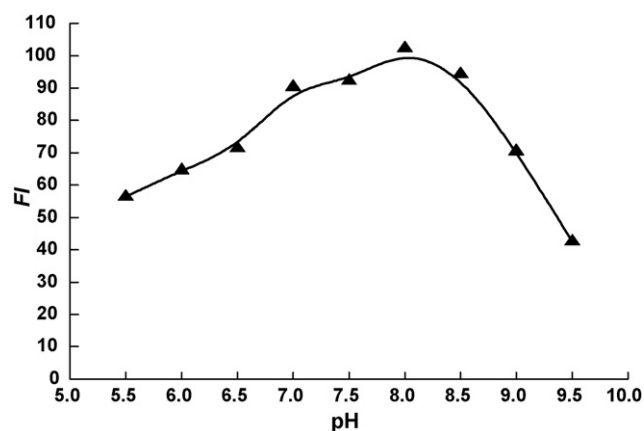
Fig. 1. The influence of pH on the fluorescence of the solution, [CPT] = 5.0×10^{-7} M in 0.01 M Tris–HCl buffer(containing 0.1 M NaCl).

3. Results and discussion

3.1. The optimization of pH and NaCl concentration

During DNA hybridization process, the pH value of solution and the concentration of NaCl were vital to the sensitivity of the system. Suitable pH value and NaCl of the media are helpful for conformation transfer and stabilization of double strand construction, also the hybridization time can be shortened. Leclerc's group have optimized the media for PT to obtain desired results [29,31], but CPT is different from PT. In order to achieve the good peak of CPT, improved sensitivity and shortened analysis time in this contribution. It was still necessary to optimize situation for efficient detection. Firstly, hybridization buffer was 0.01 M Tris–HCl, the pH value of solution ranging from 5.5 to 9.5 was set to monitor the fluorescence change of copolymer-dsDNA triplex. It could be seen in Fig. 1, when pH was at 8.0, the fluorescence intensity of CPT was at its maximum; then operation at optimum pH, the concentration of NaCl was tested, it was found in Fig. 2 that 0.08–0.3 M NaCl could provide the best result, and 0.1 M NaCl was selected for the system.

3.2. Recognition of base-deleted DNA

A serial of experiments were performed in order to determine whether CPT could effectively recognize the base deletion in dsDNA. As shown in Fig. 3, at room temperature, the emission of CPT at 520 nm in the optimized buffer (0.01 M Tris–HCl/0.1 M NaCl, pH
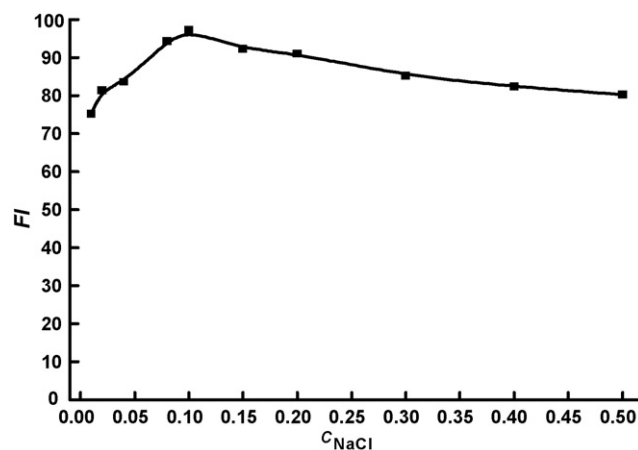
Fig. 2. The influence of NaCl on the fluorescence of the solution, [CPT] = 5.0×10^{-7} M in 0.01 M Tris–HCl buffer, pH 8.0.
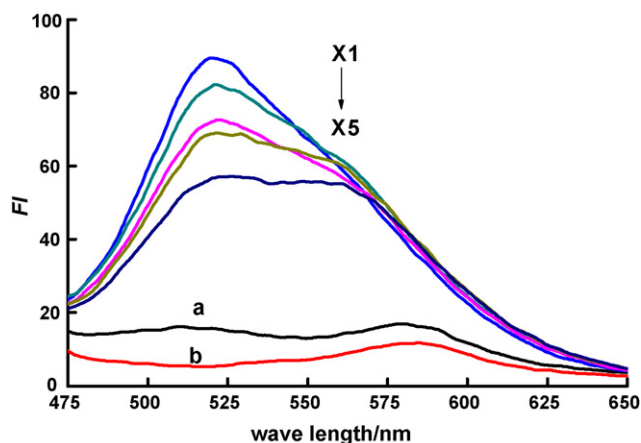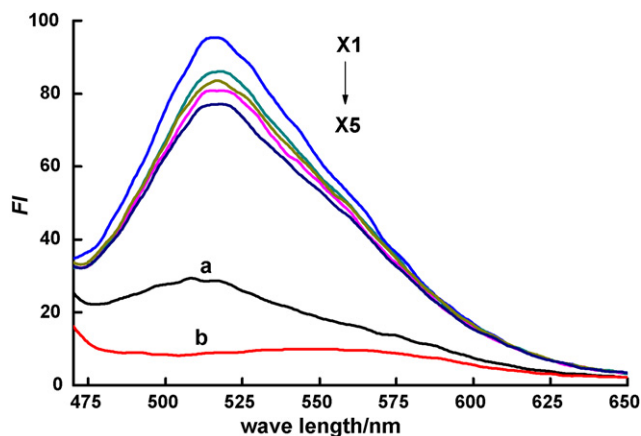
Fig. 3. The fluorescence spectra of (a) CPT in 0.01 M Tris–HCl buffer (pH 8.0, containing 0.1 M NaCl) and (b) PT + probe Y; $X_1 - X_5$ were copolymer + Y + $X_1 - X_5$, respectively. [CPT] = 5.0×10^{-7} M, [Y] = [$X_1 - X_5$] = 2.5×10^{-8} M. Excitation wave length is at 420 nm.

8.0) was weak (Fig. 3, a). The stoichiometrical addition of probe Y to CPT solution could quench the emission intensity (Fig. 3b), but the quenching constant K_{SV} = 3.2×10^4 M^{-1} was far less than that in pure water, which was 5.6×10^8 M^{-1}. Once the equivalent of perfect matched target X_1 was added, after incubation in water at 45 °C for 10 min, the fluorescence was greatly enhanced (Fig. 3, X_1), and no further increase was observed in the presence of excessive target X_1. Other targets (X_2–X_5) with one or more bases deletion in the 3′ end (shown in Table 1) also increased the emission intensity to some extent, but less than the completely complementary strand (Fig. 3, X_2–X_5). Interestingly, apart from the quenched fluorescence intensity, with more bases deleted, the curves were broadening gradually. To verify the differentiating ability of PT, controlled experiments were carried out in the same condition. As shown in Fig. 4, no other pronounced changes were observed except for the slightly decreased fluorescence (Fig. 3, X_1–X_5).

It is well documented that the cationic CPEs could bind with negatively charged DNA phosphate through electrostatic interaction and other effects [32–34], which leads to the fluorescence quenching of the polymer. Addition of completely complementary DNA would recover the fluorescence of the CPEs. Imperfect complementary DNA, such as one or more mismatched base sequence, could only make partial recovery of the fluorescence. Thus special
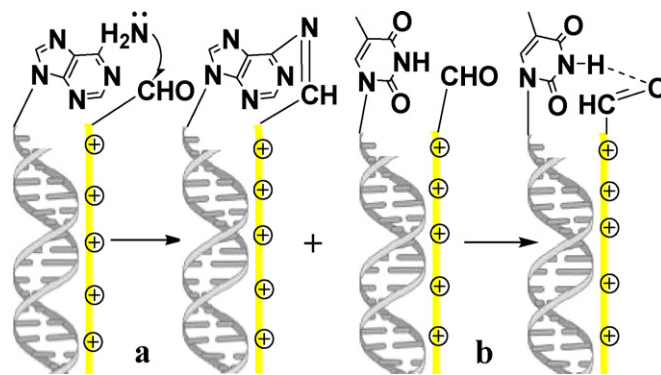
Scheme 2. The schematic formation of covalent bond (a) and hydrogen bond (b) between unpaired bases and aldehyde group.

DNA sequences were identified according to the recovered strength of fluorescence. As for the copolymer, positive charged backbone brought ssDNA to close proximity to form duplex, therefore the fluorescence was quenched via strong electrostatic interaction and electronic/energy transfer. Upon addition of complementary strand and after incubation at 45 °C for about 10 min, a triplex complex was formed, which led to great enhancement of the fluorescence. In marked contrast to the case of PT in Fig. 4, the curves of CPT showed different behaviors (Fig. 3). There might be two factors accounting for such phenomena. Firstly, due to the existence of aldehyde residues as side groups, oxygen and hydrogen atoms in the backbone might form hydrogen bonds with those unpaired bases in triplex. When the hydrogen bonds form among complementary bases, they were exceptionally stable and comparatively unreactive with electrophiles, nucleophiles, and light in the aqueous environment. Secondly, carbonyl such as aldehydes, can react with amines to form Schiff base intermediates that are in equilibrium with their free forms. The unpaired bases contain amino groups, which attacked active aldehyde group to form covalent bonds, and further stabilization of the covalent bond by a reversible dehydration reaction leads to Schiff base. Moreover, the π electrons in C=N bond could also disturb the π–π conjugated chain. The two factors together might induce a significant change in conformation of triplex, which generated a different emission state of the copolymer (Scheme 2). As shown in Fig. 4, without aldehyde group doped in the main chain of PT, no distinct behavior could be observed except for slightly decreased emission compared with

Fig. 4. The fluorescence spectra of (a) PT in 0.01 M Tris–HCl buffer (pH 8.0, containing 0.1 M NaCl) and (b) PT + probe Y; $X_1 - X_5$ were polymer + Y + $X_1 - X_5$, respectively. [PT] = 5.0×10^{-7} M, [Y] = [$X_1 - X_5$] = 2.5×10^{-8} M. Excitation wave length is at 420 nm.
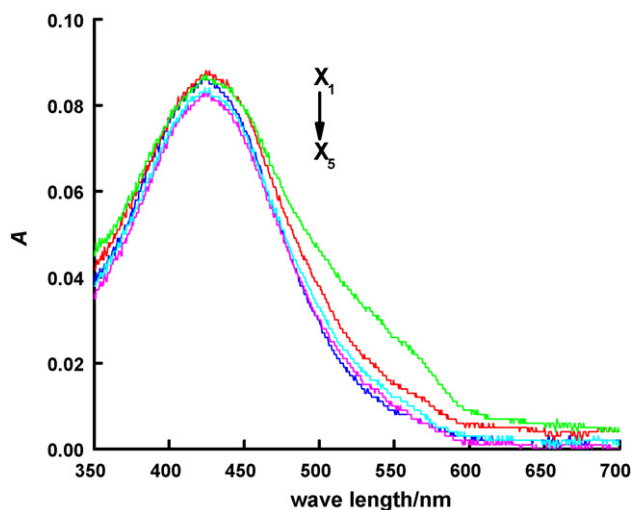
Fig. 5. The absorption of PT-dsDNA triplex in 0.01 M Tris–HCl buffer (pH 8.0, containing 0.1 M NaCl), [X_{1-5}] = 1.0×10^{-6} M, [PT] = 2×10^{-5} M, on per repeat unit.
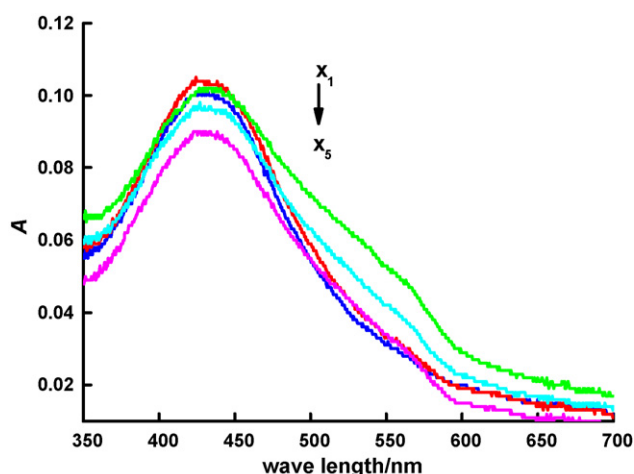
Fig. 6. The absorption of CPT-dsDNA triplex, in 0.01 M Tris–HCl buffer (pH 8.0, containing 0.1 M NaCl), $[X_{1-5}] = 1.0 \times 10^{-6}$ M, $[CPT] = 2 \times 10^{-5}$ M, on per repeat unit.
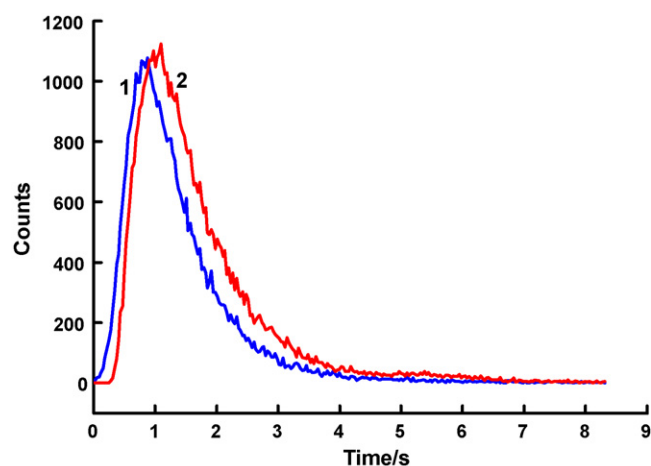

Fig. 7. The lifetime measurement of two triplexes, 1, PT-Y-X_3; 2, CPT-Y-X_3, $c_{PT} = c_{CPT} = 5 \times 10^{-6}$ M, $X_3 = 2.5 \times 10^{-7}$ M, in 0.01 M Tris–HCl buffer (pH 8.0, containing 0.1 M NaCl) at room temperature.

perfect matched strands. Although the two polymers had practically the same repeating thiophene units in the polymer backbone, the UV–vis absorption spectra of triplex also demonstrated subtle differences due to the presence of aldehyde in the chain. After triplex was formed, a new absorption feature appeared at 420 nm, but the peak width at half height of CPT-dsDNA was broader than that of PT (Figs. 5 and 6).

3.3. The fluorescence lifetime of two triplexes

Now that the interaction mechanism of two triplexes was varied from each other, the fluorescence lifetime of the two should be different. CPT-Y-X_3 and PT-Y-X_3 were selected for evaluation. As our anticipation, measured in the same experimental conditions, the lifetime of CPT-Y-X_3 was 1.00 ns, longer than that of PT-Y-X_3, which was 0.86 ns. The lifetime of a fluorophore represented its inherent quality, but would change when a new exciplex was formed with external stimuli [35]. The main difference of two triplexes originated from the main chain that doped with aldehyde, and it was the aldehyde that associated with unpaired bases led to the diversity of triplexes lifetime (Fig. 7).

4. The determination of perfect matched ssDNA and base-deleted DNA

4.1. Linearity range

Since the resulting copolymer could effectively recognize the specific sequence dsDNA, we then expected it can be used to quantitatively detect ssDNA, and three target ssDNA(X_{1-3}) were chose for assay. Under the optimized condition, the experiments showed that the increase of fluorescence intensity at 520 nm could quantitatively reflect the added amount of target ssDNA in the concentration range of $0.5–25 \times 10^{-9}$ M. Calibration curves were constructed with a series of target ssDNA concentrations. Each point of the calibration graph corresponded to the mean value obtained from 5 independent measurements. The linearity curves were defined by

the fluorescence intensity (y) vs. concentrations (x, expressed in nM) of each ssDNA, and all the equations, together with the correlation coefficient, were listed in Table 2.

4.2. Sensitivity and specificity

A signal-to-noise ratio (S/N) of approximately 3:1 was generally considered to be acceptable for estimating the limit of detection (LOD). The measured LOD value of each ssDNA (X_{1-3}) and the relative standard deviation (R.S.D.) were also shown in Table 2. The LOQ was the lowest concentration of each ssDNA that could be quantified with acceptable precision and accuracy, which was defined as S/N = 10. The measured LOQ value was 0.10, 0.17 and 0.23 nM, respectively, for the proposed method. The specificity of the system depended on the complementary bases, whereas non-complementary ssDNA or other nucleotides could not make the fluorescence recovery.

4.3. Precision

The precision was studied with respect to repeatability and intermediate precision. In order to measure the repeatability of the system, five consecutive solutions containing 10.0 nM of each target ssDNA were added to copolymer/Y duplex under the same condition. The amount of X_{1-3} was found to be 9.97 ± 0.04, 10.01 ± 0.03 and 9.97 ± 0.05 nM with their R.S.D. were 0.87%, 1.29% and 1.57%, respectively. These values indicated that the proposed method had high repeatability and precision for ssDNA detection.

4.4. The determination of real samples

Special oligonucleotide pair for bird flu type H1N1 similar to probe Y and target X_{1-3} was designed for detection. After asymmetrical PCR amplification and purification, the concentrations of each sequence were determined by recording the absorbance at 260 nm, and then treated as described in the procedure for measurement. Each of the samples was repeated for three times and

Table 2
The equation of target ssDNA, LOD, LOQ and the correlation coefficient (x, nM, $n = 5$).

Target ssDNA	Equation	LOD (nM)	LOQ (nM)	R.S.D (%)	Correlation coefficient
X_1	$y = 3.35x - 1.87$	0.10	0.24	0.76	0.9978
X_2	$y = 2.47x - 1.42$	0.17	0.29	0.83	0.9932
X_3	$y = 2.25x + 0.21$	0.23	0.37	0.89	0.9917

Table 3
Recovery test for real samples ($n = 3$).

Target ssDNA	Original[a] (nM)	Added[b] (nM)	Found (nM)	Mean recovery (%)	R.S.D. (%)
X_1	10.00	5.00	14.88 ± 0.08	97.20	1.07
X_2	10.00	5.00	14.86 ± 0.10	96.91	1.25
X_3	10.00	5.00	14.75 ± 0.11	95.37	1.33

[a] Original: Concentration of standard solution.
[b] Added: Concentration of sample solution determined by UV–vis spectrum at 260 nm.

the acceptable recovery was set as between 95% and 105% for the system. The obtained results in Table 3 were in agreement with the concentrations calculated by the absorption spectra.

5. Conclusion

In summary, a simple, rapid and sensitive method for recognition of bases deletion in dsDNA was established based on an improved polythiophene copolymer. The recognition process relies on strong electrostatic and hydrophobic interactions, hydrogen bonds and chemical coupling also play a significant role in distinguishing the subtle differences in dsDNA. The method also can be applied for detection ssDNA with very low LOD. With respect to some reported methods for detecting such mutant, the proposed method is quite rapid, feasible, and without any complicated labeling or modification. Thus the novel copolythiophene allows a versatile procedure for fast recognition and detection of oligonucleotides.

Acknowledgements

Appendix A. Supplementary data

Supplementary data associated with this article can be found, in the online version, at doi:10.1016/j.talanta.2009.03.034.

References

[1] H. Echols, M.F. Goodman, Mutat. Res. 236 (1990) 301–311.
[2] D.Y. Wu, L. Ugozzoli, B.K. Pal, R.B. Wallace, Proc. Natl. Acad. Sci. 86 (1989) 2757–2760.
[3] A. H-, J. Al Attar, S. Norden, A.P. O'Brien, Monkman, Biosens. Bioelectron. 23 (2008) 1466–1472.
[4] X. Lin, P. Wu, W. Chen, Y. Zhang, X. Xia, Talanta 72 (2007) 468–471.
[5] M.B. Coulter-Mackie, D.A. Applegarth, J.R. Toone, L. Gagnier, Clin. Biochem. 31 (1998) 627–632.
[6] J. Choi, J.H. Lima, S. Rhob, D. Jahng, J. Lee, K.J. Kim, Talanta 74 (2008) 1056–1059.
[7] S. Reisberg, L.A. Dang, Q.A. Nguyen, B. Piro, V. Noel, P.E. Nielsen, L.A. Leb, M.C. Pham, Talanta 76 (2008) 206–210.
[8] Z. Zhang, M. Gerstein, Nucleic Acids Res. 31 (2003) 5338–5348.
[9] U. Asseline, M. Chassignol, Y. Aubert, V. Roig, Org. Biomol. Chem. 10 (2006) 1949–1957.
[10] I. Willner, F. Patolsky, Y. Weizmann, B. Willner, Talanta 56 (2002) 847–856.
[11] M. Endo, T. Majima, Chem. Commun. 22 (2006) 2329–2331.
[12] C.-H. Hsieh, J.D. Griffith, Proc. Natl. Acad. Sci. 86 (1998) 4833–4837.
[13] J.J. Miret, B.O. Parker, R.S. Lahue, Nucleic Acids Res. 24 (1996) 721–729.
[14] H. Kashida, H. Asanuma, M. Komiyama, Chem. Commun. (2006) 2768–2770.
[15] D. York, K. Welch, I.Y. Goryshin, W.S. Reznikoff, Nucleic Acids Res. 26 (1998) 1927–1933.
[16] R. Yui, E.T. Matsuura, Mutat. Res. 594 (2006) 155–161.
[17] L. Glover, S. Alsford, C. Beattie, D. Horn, Nucleic Acids Res. 35 (2007) 872–880.
[18] D. Tian, Q. Wang, P. Zhang, H. Araki, S. Yang, M. Kreitman, T. Nagylaki, R. Hudson, J. Bergelson, J. Chen, Nature 455 (2008) 105–108.
[19] L. Chen, D.W. McBranch, H.L. Wang, R. Helgeson, F. Wudl, D.G. Whitten, Proc. Natl. Acad. Sci. 96 (1999) 12287–12292.
[20] P.S. Heeger, A.J. Heeger, Proc. Natl. Acad. Sci. 96 (1999) 12219–12221.
[21] X. Yang, X. Zhao, X. Zuo, K. Wang, J. Wen, H. Zhang, Talanta 77 (2009) 1027–1031.
[22] H. Sun, F. Feng, M. Yu, S. Wang, Macromol. Rapid Commun. 28 (2007) 1905–1911.
[23] S. Wang, G.C. Bazan, Adv. Mater. 15 (2003) 1425–1428.
[24] X. Duan, S. Wang, Z. Li, Chem. Commun. (2008) 1302–1304.
[25] A. H-, M. Ho, Leclerc, J. Am. Chem. Soc. 125 (2003) 4412–4413.
[26] H. Huang, K. Wang, W. Tan, D. An, X. Yang, S. Huang, Q. Zhai, L. Zhou, Y. Jin, Angew. Chem. Int. Ed. 43 (2004) 5635–5638.
[27] S.J. Dwight, B.S. Gaylord, J.W. Hong, G.C. Bazan, J. Am. Chem. Soc. 126 (2004) 16850–16859.
[28] H.-A. Ho, M. Leclerc, J. Am. Chem. Soc. 125 (2003) 4412–4413.
[29] K.F. Karlsson, P. Åsberg, K.P.R. Nilsson, O. Inganäs, Chem. Mater. 17 (2005) 4204–4211.
[30] H.-A. Ho, M. Boissinot, M.G. Bergeron, G. Corbeil, K. Doré, D. Boudreau, M. Leclerc, Angew. Chem. Int. Ed. 41 (2002) 1548–1551.
[31] K. Faïd, M. Leclerc, Chem. Commun. 24 (1996) 2761–2762.
[32] Ho-A. Ho, K. Dore, M. Boissinot, M.G. Bergeron, R.M. Tanguay, D. Boudreau, M. Leclerc, J. Am. Chem. Soc. 127 (2005) 12673–12676.
[33] S.W. Thomas III, G.D. Joly, T.M. Swager, Chem. Rev. 107 (2007) 1339–1386.
[34] K.P.R. Nilsson, O. Inganäs, Nat. Mater. 2 (2003) 419–424.
[35] E. Vuorimaa, A. Urtti, R. Seppänen, H. Lemmetyinen, M. Yliperttula, J. Am. Chem. Soc. 130 (2008) 11695–11700.

Comparative evaluation of Dy(III) selective poly(vinyl) chloride based membrane electrodes of macrocyclic tetraimine Schiff's bases

V.K. Gupta *, Manoj K. Pal, Ashok K. Singh

Department of Chemistry, Indian Institute of Technology Roorkee, Roorkee 247667, India[1]

ARTICLE INFO

ABSTRACT

Three different derivatives of macrocyclic tetraimine Schiff's base have been synthesized and explored as a neutral ionophores for preparing poly(vinyl chloride) based membrane sensors selective to Dy^{3+}. The addition of sodium tetraphenyl borate and various plasticizers, viz., o-NPOE, DBP, DBBP, DOP and CN has been found to substantially improve the performance of the sensors. The best performance was obtained with the sensor no. 1 having membrane of Schiff's base (SL-1) with composition (w/w) SL-1 (4.5%): PVC (30.5%): o-NPOE (59.5%): NaTPB (5.5%). This sensor exhibits Nernstian response with slope 19.4 mV/decade of activity in the concentration range of 10^{-8} to 1.0×10^{-2} M Dy^{3+}, performs satisfactorily over wide pH range of (2.8–7.2) with a fast response time (10 s). The sensor was also found to work satisfactorily in partially non-aqueous media up to 20% (v/v) content of acetonitrile, methanol or ethanol. The proposed sensor can be used over a period of 1.5 months without significant drift in potentials. The sensor has been also utilized for the determination of Dy^{3+} level in different soil samples.

© 2009 Elsevier B.V. All rights reserved.

1. Introduction

Although the dysprosium has negligible toxic effect on human beings, only mild toxicity can be produced by ingestion of soluble salts of dysprosium. It was calculated that a dose of 500 g or more would be needed to put a person's life at risk. Dysprosium has number of applications that make its analysis more advantageous. Dysprosium is used, in conjunction with vanadium and other elements, for making laser materials [1]. It is used for nuclear control rods; dysprosium oxide (also known as dysprosia) with nickel cement compounds which absorb neutrons readily without swelling or contracting under prolonged neutron bombardment, is being used for cooling rods in nuclear reactors [2]. Dysprosium also used in semiconductor device [3,4] and can be used in some metal alloys to provide strength [5]. Therefore its determination in mineral and salt solutions is very important

There are lots of techniques for the determination of dysprosium such as A.A.S [6], ICP-MS [7] and ICP-AES [8]. These methods either are time-consuming, involve multiple sample manipulations, or are too expensive for most analytical laboratories; ion-selective electrodes (ISE) provide analytical procedures for such situations as they are fast, convenient, having minimum sample pre-treatment requirement and may also be suitable for online analysis. In view of such advantages, a number of lanthanide ion selective sensors based on poly(vinyl) chloride have been developed such as La^{3+} [9,10], Yb^{3+} [11], Gd^{3+} [12], Sm^{3+} [13], Er^{3+} [14], Tb^{3+} [15] and also on Dy^{3+} [2,16,17–19]. Although lot of work has been done on Dy^{3+} selective membrane electrodes with good selective ranges, no one did comparative evaluation of Dy^{3+} selective membrane electrodes; therefore authors have been synthesized three different derivatives of macrocyclic tetraimine Schiff's base for comparative evaluation of Dy^{3+} selective membrane electrodes and improved the detection limit compared to reported work.

2. Experimental

2.1. Reagents and materials

1,2-ethanediamine, high molecular weight polyvinyl chloride (PVC), potassium tetra fluoroborate (KBF_4) and 1,4-butadiamine Aldrich (Wisconsin, USA), tri-n-butylphosphate (TBP) BDH (Poole, England), chloronapthalene (CN), dibutylphthalate (DBP) and dibutyl(butyl) phosphonate (DBBP) Mobile (Alabama, USA), o-nitrophenyl octyl ether (o-NPOE), Oleic acid (OA) Sisco research Lab (Mumbai, Maharashtra, India), dioctylphthalate (DOP) renkem (Gurgaon, India) and potassium tetrakis(4-chlorophenyl borate) (KTpClPB) fluka (Ronkonkoma, NY) were purchased and used as

* Corresponding author. Tel.: +91 1332285801; fax: +91 1332273560.
E-mail addresses: vinodfcy@iitr.ernet.in, vinodfcy@gmail.com (V.K. Gupta).
[1] May be working from September 2009 at King Fahd University of Petroleum and Minerals, Dhahran, Saudi Arbia.

received. 0.1 M stock solutions were prepared by dissolving AR grade metal nitrates in double distilled water and standardized wherever necessary. The working solutions of different concentration were prepared by diluting the stock solutions.

2.2. Synthesis of ligands

2.2.1. Synthesis of bis(5-formyl-2-thienyl)methane, S_A [20]

A solution of bis(5-bromo-2-thienyl)methane [21] (6.3 g, 19.0 mmol) in dry ether (40 ml) was added over a period of 10 min to 15% buthyllithium–hexane solution (19.0 g) in dry diethyl ether (30 ml) at −40 to −50 °C under N_2 atmosphere. Then, N,N-dimethyl formamide (DMF) (2.8 g, 38 mmol) in dry diethyl ether (20 ml) was added over a period of 5 min; the mixture was stirred for 1 h at room temperature. After this, the solution was added to crushed ice (100 g); the ether layer was washed successively by a 5% HCl aqueous solution, a saturated $NaHCO_3$. After removing the solvent, the crude product was crystallized with ethanol to give colorless product.

Color: colorless; mp: 95 °C; I.R (KBr): 1645 cm^{-1} (CHO); ^{1}H NMR (CDCl$_3$): δ = 4.43 (2H, s), 7.00 (2H, d, J = 3.6 Hz), 7.62 (2H, d, J = 3.6 Hz) and 9.83 (2H, s, CHO); MS m/z 236 (M$^+$, 100%)

2.2.1.1. Synthesis of 31,32,33,34-tetrathia-3,6,18,21-tetraazapentacyclo[26.2.1.1^{8,11}.1^{13,16}.1^{23,26}] tetratriaconta-1(30), 2,6,8,10,13,15,17, 21,23,25,28-dodecaene, SL-1.
A solution of S_A (0.25 g, 1.0 mmol) in CHCl$_3$ (20 ml) and a solution of 1,2-ethanediamine (0.06 g, 1.0 mmol) in CHCl$_3$ (20 ml) were added simultaneously to the CHCl$_3$ (20 ml) over a period of 1.5 h with stirring at room temperature. After stirring for 30 min, the reaction mixture was filtered in order to remove any insoluble precipitate; the filtrate was then dried over Na$_2$SO$_4$ and concentrated. The yellow powder, thus obtained, was washed with ethanol (20 ml × 2) giving SL-1 (2.2 g, 83%). Color: colorless; mp: 158 °C; I.R (KBr) 2820, 1620, and 840 cm^{-1}; ^{1}H NMR (CDCl$_3$) δ = 3.83 (8H, s), 4.20 (4H, s), 6.73 (4H, d, J = 3.6 Hz), 7.03 (4H, d, J = 3.6 Hz.) and 8.15 (4H, s); MS m/z 520 (M$^+$, 10%). Elemental analysis was corresponding to the structure as given in Fig. 1.

2.2.2. Synthesis of 12,12,27,27-tetramethyl-31,32,33,34-tetrathia-3,6,18,21-tetraazapentacyclo [26.2.1.1^{8,11}.1^{13,16}.1^{23,26}] tetratriaconta-1 (30), 2,6,8,10,13,15,17,21,23,25,28-dodecanene, SL-2

The solution of 2,2-bis(5-formyl-2-thienyl) propane, synthesized by the same procedure as given above [22] (2.6 g, 10 mmol) in CHCl$_3$ (50 ml) and 1,2-ethanediamine (0.6 g, 10 mmol) in CHCl$_3$ (100 ml) were added simultaneously to 50 ml of CHCl$_3$ over a period of 15 h with stirring at room temperature; the mixture was stirred for an additional 30 h. After usual work-up, the crude product was obtained as yellow powder, which was recrystalized with CHCl$_3$–hexane to give SL-2 (2.4 g, 84%). Color: pale-yellow; mp: 233 °C; I.R (KBr): 2970, 2930, 2830, 1630 and 800 cm^{-1}; ^{1}H NMR (CDCl$_3$) δ = 1.80 (12H, s), 3.79 (8H, s), 6.74 (4H, d, J = 3.6 Hz), 6.99 (4H, d, J = 3.6 Hz); ^{13}C NMR (CDCl$_3$): δ = 32.41, 40.92, 61.07, 123.61, 130.04, 155.83 and MS m/z 576 (M$^+$, 26%). Elemental analysis corresponds to the structure given in Fig. 1.

2.2.3. Synthesis of 13,13,29,29,-tetramethyl-33,34,35,36-tetrathia-3,7,19,23-tetraazapentacyclo [28.2.1.1^{9,12}.1^{14,17}.1^{25,28}] hexatriaconta-1(32), 2,7,9,11,14,16,18,23,25,27,30-dodecaene, SL-3

The solution of 2,2-bis(5-formyl-2-thienyl) propane, synthesized by same procedure as given above (2.6 g, 10 mmol) in CHCl$_3$ (50 ml) and 1,3-propanediamine (0.6 g, 10 mmol) in CHCl$_3$ (100 ml) were added simultaneously to 50 ml of CHCl$_3$ over a period of 15 h with stirring at room temperature; the mixture was stirred
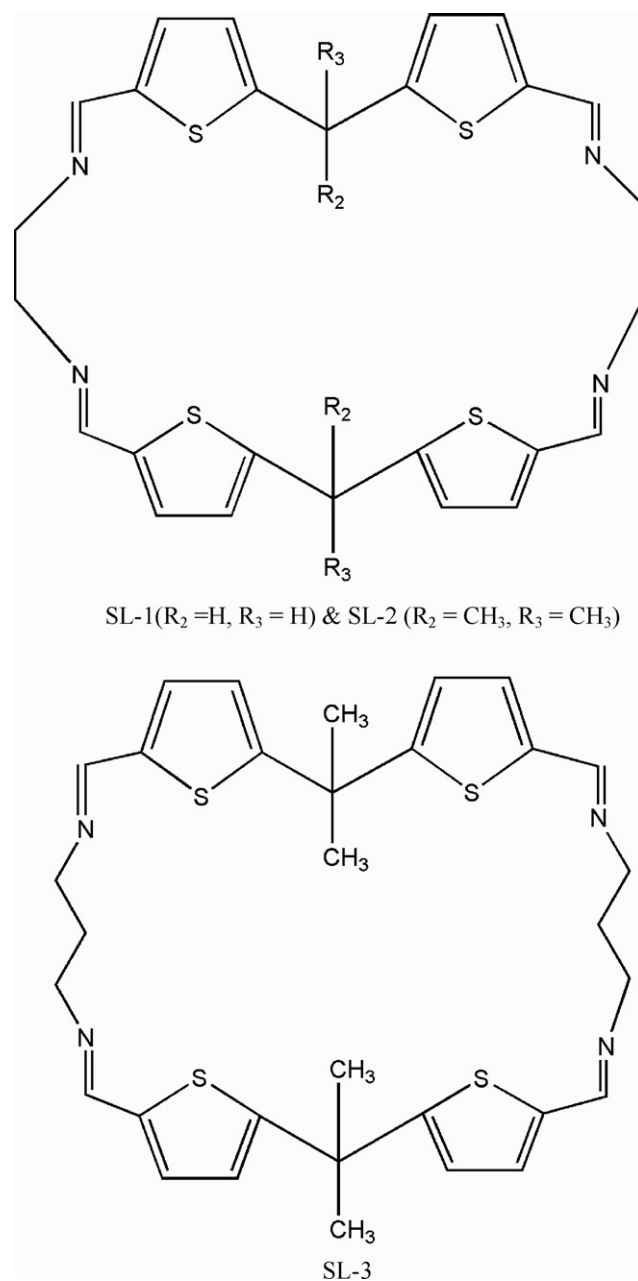
Fig. 1. Structures of macrocycli Schiff's bases SL-1, SL-2 and SL-3.

for an additional 30 h. After usual work-up, the crude product was obtained as colorless powder, which was recrystalized with CHCl$_3$–hexane to give SL-3 (14%). Color: colorless; mp: 270 °C; I.R (KBr): 2975, 2840 and 1630 cm^{-1}; ^{1}H NMR (CDCl$_3$) δ = 1.40–2.40 (16H, m), 3.53 (8H, t, J = 7.2 Hz), 6.76 (4H, d, J = 3.6 Hz), 7.00 (4H, d, J = 3.6 Hz) and 8.20 (4H, s); ^{13}C NMR (CDCl$_3$): δ = 31.74, 32.38, 40.89, 58.60, 123.54, 129.64, 140.56, 154.46 and 157.94 cm^{-1} MS m/z 604 (M$^+$, 1%). Elemental analysis corresponds to the structure given in Fig. 1.

2.3. Fabrication of electrodes

The membranes have been fabricated as suggested by Craggs et al. [23]. The PVC-based membranes have been prepared by dissolving appropriate amounts of Schiff's bases (SL-1 and SL-2), different anionic additives NaTPB, OA, KTpClPB, KBF4 and plasticizers DBP, o-NPOE, CN, DOP and PVC in THF (5 ml). The components were

Table 1
The composition (%, w/w) of best optimized membranes of different ligands.

Electrode type	Ionophore	PVC	Additives	Plasticizer	Working concentration range (M)	Detection limit (M)	Slope (±0.2 mV/ decade of activity)	Response time (s)
1	SL-1(4.5)	30.5	NaTPB(5.5)	o-NPOE(59.5)	5.4×10^{-8} to 1.0×10^{-2}	4.1×10^{-8}	19.4	10
2	SL-2(4.5)	30.5	NaTPB(5.5)	o-NPOE(59.5)	3.2×10^{-7} to 1.0×10^{-2}	2.1×10^{-7}	18.5	10
3	SL-3(4.5)	30.5	NaTPB(5.5)	o-NPOE(59.5)	2.1×10^{-6} to 1.0×10^{-2}	1.7×10^{-6}	17.8	11

added in terms of weight percentages. The homogeneous mixture was obtained after complete dissolution of all the components, concentrated by evaporating THF and it has been poured into poly-acrylate rings placed on a smooth glass plate. The viscosity of the solution and solvent evaporation was carefully controlled to obtain membranes with reproducible characteristics and uniform thickness otherwise the response of the membrane sensors have shown a significant variation. The membranes of 0.4 mm thickness were removed carefully from the glass plate and glued to one end of a "Pyrex" glass tube. It is known that the sensitivity, linearity and selectivity obtained for a given ionophore depends significantly on the membrane composition and nature of plasticizer used [24]. Thus, the ratio of membrane ingredients, time of contact, concentration of equilibrating solution, etc. were optimized after a good deal of experimentation to provide membranes, which generate reproducible and stable potentials. The membranes having only PVC as membrane ingredient (dummy membranes) have also been prepared to observe whether any background potentials were being produced due to binding material or not. The potentials were not generated without the electroactive material in the membrane.

2.4. Conditioning of membranes and potential measurements

The membranes were equilibrated for 2 days in 0.01 M DyCl$_3$ solution. The potentials have been measured by varying the concentration of DyCl$_3$ in test solution in the range of 1.0×10^{-8} to 1.0×10^{-1} M. The standard DyCl$_3$ solutions of metal salt have been obtained by gradual dilution of 0.1 M DyCl$_3$ solution and pH adjusted (pH 5.2) using Tris–HCl buffer. The potential measurements were carried out at $25 \pm 1\,^\circ$C using saturated calomel electrodes (SCE) as reference electrodes with the following cell assembly:

Hg/Hg$_2$Cl$_2$|KCl (satd.)|1.0 M DyCl$_3$||PVC membrane||test solution|Hg/Hg$_2$Cl$_2$|KCl (satd.)

3. Result and discussion

3.1. Effect of internal solution

The proposed electrodes were also examined at different concentrations of inner reference solution (1.0×10^{-1} to 1.0×10^{-4} M) and potential response of the electrodes based on SL-1, SL-2 and SL-3 membranes have been observed. It was found that the best results in terms of slope and working concentration range has been obtained with internal solution of activity 1.0×10^{-1} M. Thus, 1.0×10^{-1} M concentration of the reference solution was quite appropriate for the smooth functioning of the proposed electrodes.

3.2. Optimization of membrane electrodes

Once the membrane electrodes based on different ligands (SL-1, SL-2 and SL-3) have been synthesized and as their responses were checked against different concentration of Dy^{3+}, further to get the best results, membrane compositions have been optimized using different concentration of anionic additives: NaTPB, OA, KTpClPB,

KBF4 and plasticizers: TEHP, DBP, o-NPOE, CN, DOP, PVC and it was observed that the best response in terms of detection limit, working range, response time and slope observed with electrode no. 1 having composition (%, w/w); (SL-1) (4.5%): PVC (30.5%): o-NPOE (59.5%): NaTPB (5.5%) (Table 1). Although the response time and slopes are almost similar, working range and detection limit are different. This effect can be explained on the basis of cavity effect (size of cavity) of different ligands as SL-2 has –CH$_3$ in place of –H of SL-1 that makes SL-1 more selective for Dy^{3+} compared to SL-2 and SL-3, as it can easily fit into the cavity. SL-3 has some larger cavity compared to both SL-1 and SL-2 that makes it less selective compared to both of them.

3.3. Determination of formation constant

Formation constant of the ion–ionophore complex within the membrane phase is a very important parameter that dictates the practical selectivity of the sensor. In this method, two membrane segments are fused together, with only one containing the ionophore, to give a concentration-polarized sandwich membrane. A membrane potential measurement of this transient condition reveals the ion activity ratio at both interfaces, which translates into the apparent binding constants of the ion–ionophore complex [25]. In this method, complex formation constants are obtained by neglecting ion pairing. As reported, the membrane potential E_M is determined by subtracting the cell potential for a membrane without ionophore from that for the sandwich membrane. The formation constant is then calculated from the following equation.

$$\beta_{ILn} = \left(L_T - \frac{nR_T}{Z_I}\right)^{-n} \exp\left(\frac{E_M z_I F}{RT}\right) \tag{1}$$

where L_T is the total concentration of ionophore in the membrane segment, R_T is the concentration of lipophilic ionic site additives, n

Table 2
The formation constants of macrocyclic ligands–metal complexes.

Cations	SL-1 Formation constant (log β_{ILn})[a] $\pm$ S.D.	SL-2 Formation constant (log β_{ILn})[a] $\pm$ S.D.	SL-3 Formation constant (log β_{ILn})[a] $\pm$ S.D.
Na$^+$	0.42 ± 0.03	0.37 ± 0.02	0.34 ± 0.03
K$^+$	0.38 ± 0.04	0.32 ± 0.04	0.30 ± 0.04
Ag$^+$	1.46 ± 0.06	1.05 ± 0.05	1.04 ± 0.03
Cu^{2+}	3.21 ± 0.10	3.10 ± 0.23	3.09 ± 0.22
Pb^{2+}	3.58 ± 0.34	3.44 ± 0.03	3.41 ± 0.01
Cd^{2+}	3.52 ± 0.23	3.41 ± 0.21	3.39 ± 0.06
Zn^{2+}	3.40 ± 0.06	3.38 ± 0.23	3.35 ± 0.21
Co^{2+}	3.15 ± 0.22	3.10 ± 0.11	3.09 ± 0.12
Cr^{3+}	4.52 ± 0.40	4.48 ± 0.07	4.45 ± 0.21
Ce^{3+}	5.15 ± 0.21	5.10 ± 0.16	5.07 ± 0.08
Nd^{3+}	5.21 ± 0.32	5.18 ± 0.30	5.13 ± 0.04
Sm^{3+}	5.33 ± 0.23	5.29 ± 0.23	5.25 ± 0.19
Eu^{3+}	5.34 ± 0.21	5.33 ± 0.19	5.31 ± 0.23
Gd^{3+}	5.40 ± 0.23	5.38 ± 0.21	5.36 ± 0.18
Tb^{3+}	5.45 ± 0.33	5.43 ± 0.05	5.40 ± 0.12
Dy^{3+}	8.86 ± 0.01	7.83 ± 0.04	6.86 ± 0.08
Ho^{3+}	5.43 ± 0.15	5.40 ± 0.05	5.36 ± 0.13
Er^{3+}	5.51 ± 0.31	5.49 ± 0.12	5.47 ± 0.21

[a] Mean value $\pm$ standard deviation (four measurements).

Table 3
Selectivity coefficient (log $_{\text{Dy}^{3+},\text{B}}^{\text{pot}}$) values observed for best Dy(III) selective electrodes as calculated by fixed interference method.

Interfering ion (B)	Selectivity coefficient (log $_{\text{Dy}^{3+},\text{B}}^{\text{pot}}$) by FIM[a]		
	Sensor no. 1	Sensor no. 2	Sensor no. 3
Na^+	−4.24	−4.39	−4.73
K^+	−4.34	−4.53	−4.82
Ag^{3+}	−4.22	−4.34	−4.68
Co^{2+}	−3.91	−3.95	−3.97
Zn^{2+}	−3.88	−3.89	−3.90
Cd^{2+}	−3.64	−3.68	−3.75
Pb^{2+}	−3.54	−3.61	−3.63
Cr^{3+}	−3.44	−3.47	−3.50
Ce^{3+}	−3.34	−3.38	−3.41
Nd^{3+}	−3.21	−3.28	−3.31
Sm^{3+}	−3.10	−3.16	−3.21
Eu^{3+}	−3.05	−3.11	−3.18
Gd^{3+}	−2.93	−2.96	−2.98
Ho^{3+}	−2.91	−2.93	−2.95
Tb^{3+}	−2.85	−2.87	−2.89
Er^{3+}	−2.79	−2.84	−2.87

[a] Fixed interference method.

is the ion–ionophore complex stoichiometry, and R, T and F are the gas constant, the absolute temperature, and the Faraday constant, respectively. The ion I carries a charge of z_I. The determined formation constants (log $\beta_{\text{IL}n}$) for the examined different complexes were recorded in Table 2. The elapsed time between sandwich fusion and exposure to electrolyte was typically <1 min. The potential was recorded as the mean of the last minute of a 5 min measurement period in the appropriate salt solution. The potential of such sandwich membranes remains free of diffusion-induced potential drifts for about 20 min. Standard deviations were obtained based on the measurements of sets of at least three replicate membrane disks that were made from the same parent membrane. A careful analysis of the data in Table 2, reveals that Dy^{3+} ion has significant cation-binding characteristics.

3.4. Potentiometric selectivity

To investigate the selectivity of the proposed membrane electrodes, a fixed interfering ion method (FIM) was used [26–31]. The emf of a cell comprising an ion-selective electrode and a reference electrode (SCE cell) was measured for solutions of constant activity of the interfering ion (0.01 M), aB, and varying activity of the primary ion, aA. The emf values obtained are plotted versus the logarithm of the activity of the interfering ion. The intersection of the extrapolated linear portions of this plot indicates the value of aA that is used to calculate $K_{\text{Dy}^{3+},\text{B}}^{\text{pot}}$

$$K_{\text{Dy}^{3+},\text{B}}^{\text{pot}} = \frac{a\text{Dy}^{3+}}{(a\text{B})^{z_A/z_B}} \qquad (2)$$

where aDy3+ is the activity of the primary ion (Dy^{3+}) at the lower detection limit in the presence of interfering ion B with activity of aB, having zA and zB their respective charges. The values of selectivity coefficient so determined for best responsive membrane electrodes of SL-1, Sl-2 and SL-3, obtained results were compiled in Table 3. It was observed that the selectivity of electrode no. 1, towards Dy^{3+} is higher over most of the reported membrane electrodes (Table 4) in terms of detection limit, working range and response time. Next all studies were carried out with best responsive membrane electrode no. 1.

3.5. Response study of sensor no. 1 with different metal ions

In this study various PVC-membrane ion-selective electrodes with the synthesized Schiff's base were prepared, having identi-

cal composition (SL-1) (4.5%): PVC (30.5%): o-NPOE (59.5%): NaTPB (5.5%) and tested for different cations. The potential response of the electrodes based on SL-1 for different cations are shown in Fig. 2.
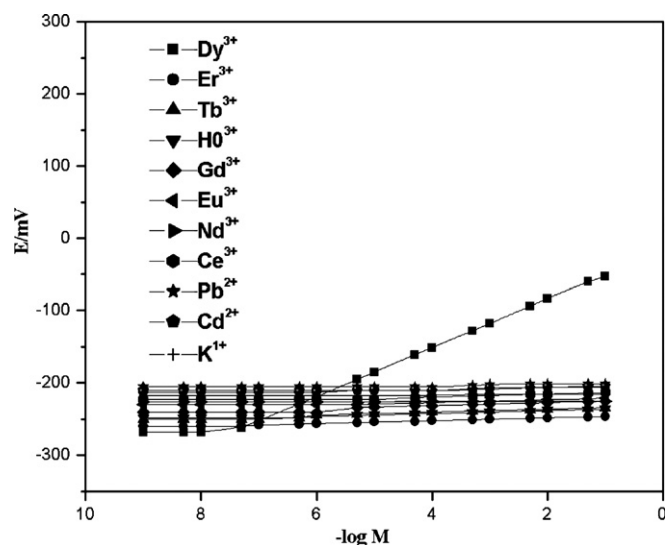
Fig. 2. The response study of best responsive sensor no. 1 with different metal ions.

3.6. pH and non-aqueous effect

The pH dependence response of the sensor no. 1 has been tested in the range of 1.5–8.0 at two Dy^{3+} concentrations of 1.0×10^{-3} and 1.0×10^{-4} M. The pH was adjusted with dilute nitric acid or sodium hydroxide solutions. The potential of the sensor was determined as a function of pH and the results are shown in Fig. 3. The potential remains constant over the pH range of 2.8–7.2, which may be taken as the working pH range of the sensor assembly. The performance of the sensor no. 1 was further assessed in partial non-aqueous media, i.e. methanol–water, ethanol–water and acetonitrile–water mixture. The results obtained are compiled in Table 5 and show that up to 20% non-aqueous content no significant change occurs in the slope and working concentration of the
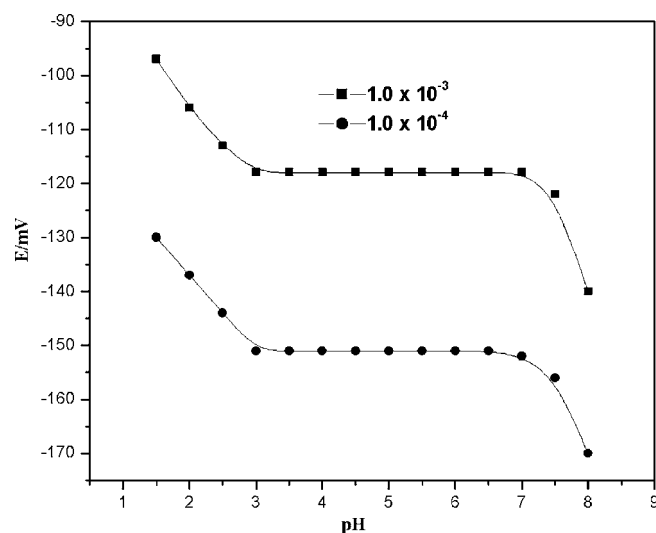
Fig. 3. pH response of sensor no. 1 at two concentrations (1.0×10^{-3} and 1.0×10^{-4} M).

Table 4
Comparative study of best responsive membrane electrode no. 1, with reported literature.

Reference	Inophore	Working range (M)	Dectection limit (M)	Slope (mV/decade of activity)	Response time (s)
[16]	N,N-bis(pyrrolidene)benzne-1,2-diamine	1.0×10^{-5} to 1.0×10^{-1}	6.0×10^{-6}	20.6 ± 0.2	<20
[2]	[(E)-N-(2 hydroxybenzyli-dene)benzohydraide]	1.0×10^{-6} to 1.0×10^{-2}	8.0×10^{-7}	20.1 ± 0.8	<20
[17]	Procaine	1.0×10^{-6} to 1.0×10^{-1}	7.9×10^{-7}	20.1 ± 0.1	<10
[18]	6-Hydrazino-1,5-diphenyl-6,7-dihydropyrazolo[3,4-d]pyrimidine-4(5H)-imine	8.0×10^{-7} to 1.0×10^{-1}	4.2×10^{-7}	19.6 ± 0.3	<10
[19]	Benzoxazoleguanidine (BG)	1.0×10^{-6} to 1.0×10^{-1}	4.7×10^{-7}	19.5 ± 0.4	<10
[This work]	Derivative of bis(5-bromo-2-thienyl)methane, SL-1	5.4×10^{-8} to 1.0×10^{-2}	4.1×10^{-8}	19.4 ± 0.2	10

sensor. However, above 20% non-aqueous content, the working concentration of the sensor is significantly reduced, and thus the sensor can only be utilized in mixtures containing up to 20% non-aqueous content.

3.7. Dynamic response time and life time

The critical response characteristics of the proposed Dy^{3+} selective electrode were investigated according to IUPAC recommendations [27–29], and the result thus obtained was 10 s (for reaching >95% of its equilibrium potential). This is most probably due to the fast exchange kinetics of complexation–decomplexation of Dy^{3+} ions with SL-1 at the test solution–membrane interface. The corresponding emf versus time plot was finally used for the evaluation of the practical response time of the electrode. The practical reversibility required for the Dy^{3+} sensor, to reach a potential within ± 1 mV of the final equilibrium value, after successive immersion of a series of nickel ion solutions, each having a 10-fold difference in concentration, was measured (Fig. 4). The sensing behavior of the membrane remained unchanged when the potentials were recorded either from low to high concentrations or vice versa. The life time of best responsive sensor no. 1 was found to be 1.5 months after which ingredients start leaching out of the membrane and finally result in the destruction of membrane.

Table 5
The performance of sensor no. 1 in partially non-aqueous media.

Non-aqueous content (%, v/v)	Working concentration range (M)	Slope (± 0.2 mV/decade of activity)
0	5.4×10^{-8} to 1.0×10^{-2}	19.4
Methanol		
10	5.4×10^{-8} to 1.0×10^{-2}	19.4
15	5.5×10^{-8} to 1.0×10^{-2}	19.4
20	5.5×10^{-8} to 1.0×10^{-2}	19.4
25	7.6×10^{-7} to 1.0×10^{-2}	18.5
30	4.4×10^{-6} to 1.0×10^{-2}	17.5
Ethanol		
10	5.4×10^{-8} to 1.0×10^{-2}	19.4
15	5.4×10^{-8} to 1.0×10^{-2}	19.4
20	5.5×10^{-8} to 1.0×10^{-2}	19.4
25	6.8×10^{-7} to 1.0×10^{-2}	18.4
30	4.2×10^{-6} to 1.0×10^{-2}	17.8
Acetonitrile		
10	5.4×10^{-8} to 1.0×10^{-2}	19.4
15	5.5×10^{-8} to 1.0×10^{-2}	19.4
20	5.5×10^{-8} to 1.0×10^{-2}	19.4
25	5.6×10^{-7} to 1.0×10^{-2}	19.1
30	7.1×10^{-6} to 1.0×10^{-2}	17.6
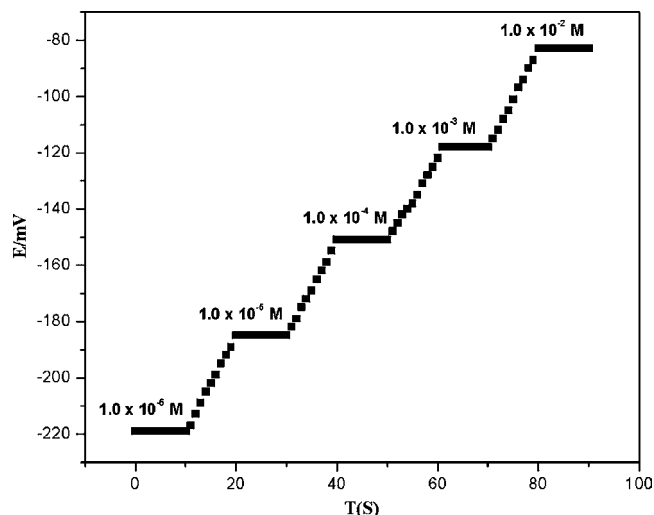
Fig. 4. Dynamic response study of sensor no. 1 at concentration range of 1.0×10^{-2} to 1.0×10^{-6} M.

Table 6
Determination of dysprosium in soil samples.

Sample no.	Proposed sensor (ppm ± S.D.)[a]	Arsenazo method (ppm ± S.D.)[a]
1	68.3 ± 0.3	64.7 ± 0.4
2	54.3 ± 0.5	53.2 ± 0.3
3	34.8 ± 0.3	31.6 ± 0.4
4	23.4 ± 0.4	21.4 ± 0.3
5	31.5 ± 0.3	29.5 ± 0.4

[a] Triplicate measurement.

4. Analytical application

4.1. Determination of Dy^{3+} in soil samples

The analytical application of proposed sensor was utilized to assess the Dy^{3+} concentration in soil samples as determined by reported method [17]. 1.0 g sample was weighed into a PTFE beaker, and 5 ml of 70% $HClO_4$ and 10 ml of 48% HF were added. The sample was heated in sand bath to incipient dryness. The acid attack with $HClO_4$ and HF (1 + 2) was repeated three times to complete digestion of the silicate matrix. Then the samples were transferred into flasks and diluted with 5 ml of NaOH 5% and distilled water to 50 ml (pH ~5.4) and the Dy^{3+} ion concentration in the samples was determined. The result, derived from triplicate measurements with the same sensor, was found to be in satisfactory agreement with that determined by Arsenazo method (Marczenko 1986), as it can be seen from Table 6.

5. Conclusion

Three different derivatives of macrocyclic tetraimine Schiff's base have been synthesized and explored for comparative analysis of best Dy^{3+} selective response and it was observed that sensor no. 1 is good selective compare to sensor no. 2 and 3. In this way author explain the cavity effect of all the proposed sensors and proved that sensor no. 1 has best suited cavity effect for selective response against Dy^{3+}.

Acknowledgement

References

[1] R. Jing, C. Dan-Ping, Y. Guang, X. Yin-Shing, Z. Huai-Dan, C.G. Rong, Chin. Phys. Lett. 24 (2007) 1958.
[2] M.R. Ganjali, M. Dodangeh, H. Ghorbani, P. Norouzi, M. Adib, Anal. Lett. 39 (2006) 495.
[3] R. Thomas, J.J. Saavedra-Arias, N.K. Karan, N.M. Murari, R.S. Katiyar, P. Ehrhart, R. Waser, Solid state commun. 147 (2008) 332.
[4] B.J. Mohan Reddy, G.P. Jyothi, M.V. Ramana Reddy, M.N. Chary, N.N. Reddy, Phys. Status Solidi 137 (2006) 241.
[5] L.L. Rokhlin, N.I. Nikitina, Met. Sci. Heat Treat. 41 (1999) 271.
[6] J.C. Vanloon, J.H. Galbraith, H.M. Aarden, Analyst 96 (1971) 47.
[7] M. Ridd, Advanced analytical centre James Cook University of North Queens Townville QLD Report on determination of trace of rare earth elements in basalt by ICP-MS.
[8] J.J. Lai, G.C. Jamieson, J. Pharm. Biomed. Anal. 11 (1993) 1129.
[9] M.R. Ganjali, A. Daftari, M. Rezapour, Talanta 59 (2003) 613.
[10] M.R. Ganjali, M.R. Pourjavid, M. Rezapour, S. Haghgoo, Sens. Actuators B 89 (2003) 21.
[11] M.R. Ganjali, L. Naji, T. Poursaberi, M. Shamsipur, S. Haghgoo, Anal. Chim. Acta 475 (2003) 59.
[12] M.R. Ganjali, M. Tahami, M. Shamsipur, T. Poursaberi, S. Haghgoo, M. Hosseini, Electroanalysis 15 (2003) 1038.
[13] M. Shamsipur, M. Hosseini, K. Alizadeh, M.F. Mousavi, M.R. Ganjali, M. Arca, V. Lippolis, Anal. Chem. 75 (2003) 5680.
[14] M.R. Ganjali, M. Rahimi, B. Maddah, A.B. Moghimi, Anal. Sci. 20 (2004) 1427.
[15] M.R. Ganjali, A. Ghesmi, M. Hosseini, M.R. Pourjavid, M. Rezapour, M. Shamsipur, M.N. Salavati, Sens. Actuators B 105 (2005) 334.
[16] M.R. Ganjali, J. Ravanshad, M. Hosseini, M. Salavati-Niasari, M.R. Pourjavid, M.R. Baezzate, Electroanalysis 16 (2004) 1771.
[17] M.R. Ganjali, P. Norouzi, F. Faridbod, N. Hajiabdollah, B. Larijani, Y. Hanifehpour, Anal. Lett. 40 (2007) 2544.
[18] H.A. Zamani, M.R. Ganjali, N. Seifi, Collect. Czech. Chem. C 72 (2007) 1189.
[19] Hassan Ali Zamani, M. Mohaddeszadeh, Anal. Lett. 41 (2008) 2710.
[20] T. Sone, Y. Ohba, R. Watanabe, Bull. Chem. Soc. Jpn. 62 (1989) 1346.
[21] Y.L. Goldfarb, M.L. Kirmalova, Zh. Obshch. Khim. 26 (1956) 3409.
[22] M. Sy, M. Maillet, Bull. Soc. Chim. Fr. (1965) 1495.
[23] A. Craggs, G.J. Moody, J.D.R. Thomas, J. Chem. Educ. 51 (1974) 541.
[24] T. Katsu, K. Ido, K. Takaishi, H. Yokosu, Sens. Actuators B 87 (2002) 331.
[25] Y. Qin, Y. Mi, E. Bakker, Anal. Chim. Acta 421 (2000) 207.
[26] P.M. Gehrig, W.E. Morf, M. Welti, W. Simon, Helv. Chim. Acta 73 (1990) 203.
[27] G. Guilbault, R. Durst, H. Freiser, J. Thomas, Pure Appl. Chem. 48 (1976) 127.
[28] R.P. Buck, E. Lindner, Pure Appl. Chem. 66 (1994) 2527.
[29] C. Macca, Anal. Chim. Acta 512 (2004) 183.
[30] E. Pretsch, E. Bakker, P. Buhlmann, Anal. Chem. 72 (2000) 1127.
[31] Y. Umezawa, Handbook of Ion-Selective Electrodes: Selectivity Coefficients, CRC Press, Boca Raton, FL, 1990.

Electro-oxidation and determination of trazodone at multi-walled carbon nanotube-modified glassy carbon electrode

Rajesh N. Hegde, Nagaraj P. Shetti, Sharanappa T. Nandibewoor *

P.G. Department of Studies in Chemistry, Karnatak University, Dharwad 580003, India

ABSTRACT

A simple and rapid electrochemical method was developed for the determination of trace-level trazodone, based on the excellent properties of multi-walled carbon nanotubes (MWCNTs). The MWCNT-modified glassy carbon electrode was constructed and the electrochemical behavior of trazodone was investigated in detail. The cyclic voltammetric results indicate that MWCNT-modified glassy carbon electrode can remarkably enhance electrocatalytic activity towards the oxidation of trazodone in neutral solutions. It leads to a considerable improvement of the anodic peak current for trazodone, and allows the development of a highly sensitive voltammetric sensor for the determination of trazodone. Trazodone could effectively accumulate at this electrode and produce two anodic peaks at about 0.73 V and 1.00 V. The electrocatalytic behavior was further exploited as a sensitive detection scheme for the trazodone determination by differential-pulse voltammetry. Under optimized conditions, the concentration range and detection limit are 0.2–10 μM and 24 nM, respectively for trazodone. The proposed method was successfully applied to trazodone determination in pharmaceutical samples. The analytical performance of this sensor has been evaluated for detection of analyte in urine as a real sample.

© 2009 Elsevier B.V. All rights reserved.

1. Introduction

Trazodone,(2-{3-[4-(3-chlorophenyl)-1-piperazinyl}propyl]-1,2,4-triazole[4,3-a]pyridine-3(2H)-one hydrochloride, TRZ (Fig. 1) is a weak inhibitor of monoamine reuptake and its major mechanism of action seems to be the antagonism at serotonin 5-HT$_2$/5-HT$_{10}$ receptors [1]. TRZ is used for the treatment of major depression, sometimes in conjunction with selective serotonin reuptake inhibitors, like fluoxetine [2]. Unlike the tricyclic antidepressants, TRZ does not inhibit the peripheral reuptake of noradrenaline, although it may indirectly facilitate neuronal release. TRZ blocks central α_1-adrenoceptors and appears to have no effect on the central reuptake of dopamine [3]. Also TRZ is used to control sleep disturbance symptoms when using serotonin and norepinephrine reuptake inhibitors [4]. TRZ is mainly metabolized in the liver by the cytochrome isoform CYP3A4. The most important metabolite thus formed is 3-(1-clorophenyl)piperazine [5], which was a serotonergic agonist with a long half-life [6]. The main side effects associated with TRZ administration are: nausea, insomnia, agitation, dry mouth, constipation, headache, hypotension, blurred vision and confusion [7]. For these reasons, it was important to analyze TRZ in real samples.

Some methods have been reported for the determination of TRZ in pharmaceutical formulations or biological samples including spectrophotometry [8], gas chromatography [9] and high performance liquid chromatography (HPLC) [10,11]. Certain electrochemical studies have also been performed by polarography [12], cyclic voltammetric, coulometric and exhaustive electrolysis on the carbon paste electrode [13], voltammetry by comparison with chromatography [14], voltammetry using platinum electrode in rotating condition [15] and by using direct current, differential-pulse and alternating current polarography [16]. Although HPLC has been widely applied because of its high sensitivity and selectivity and the ability to minimize interferences, it is time consuming, solvent-usage intensive and requires expensive devices and maintenance. Electrochemical detection of analyte is a very elegant method in analytical chemistry [17].

Carbon nanotubes (CNTs) continue to receive remarkable attention in electrochemistry [18,19]. Since their discovery by Iijima [20] in 1991 using transmission electron microscopy, CNTs have been the subject of numerous investigations in chemical, physical and material areas due to their novel structural, mechanical, electronic and chemical properties [21]. The subtle electronic properties suggest that CNTs have the ability to promote charge transfer reactions when used as an electrode [22]. The modification of electrode substrates with multi-walled carbon nanotubes (MWCNTs) for use in analytical sensing has been documented to result in low detection limits, high sensitivities, reduction of over potentials and resistance to surface fouling. MWCNTs have been introduced as electrocat-

* Corresponding author. Tel.: +91 836 2770524; fax: +91 836 2747884.
E-mail address: stnandibewoor@yahoo.com (S.T. Nandibewoor).
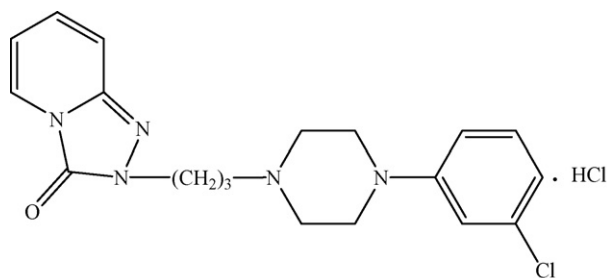
Fig. 1. Chemical structure of trazodone.

alysts [23–25] and CNTs-modified electrodes have been reported to give super performance in the study of a number of biological species [26].

To our knowledge, voltammetric determination of TRZ using a MWCNTs-modified glassy carbon electrode (GCE) has not been reported yet. The objective of the present work is to develop a convenient and sensitive method for the determination of TRZ based on the unusual properties of MWCNTs-modified electrode. Here we report the electrochemical oxidation of TRZ on MWCNTs-modified glassy carbon electrode. The ability of the modified electrode for voltammetric response of selected compound was evaluated. Finally, this modified electrode was used for the analysis of TRZ in pharmaceutical and urine samples. The resulted biosensor exhibits high sensitivity, rapid response, good reproducibility and freedom of other potentially interfering species.

2. Experimental

2.1. Reagents

TRZ was purchased from Sigma–Aldrich and used without further purification. A 10 mM stock solution was made in doubly distilled water. Multi-walled carbon nanotubes were from Sigma–Aldrich (>90%, O.D.: 10–15 nm, I.D.: 2–6 nm, length: 0.1–10 μm). The phosphate buffers from pH 3–11.2 were prepared in doubly distilled water as described by Christian and Purdy [27]. Other reagents used were of analytical or chemical grade, and their solutions were prepared with doubly distilled water.

2.2. Apparatus

Electrochemical measurements were carried out on a CHI1110A electrochemical analyzer (CH Instrument Company, USA) coupled with a conventional three-electrode cell. A three-electrode cell was used with a Ag/AgCl as reference electrode, a Pt wire as counter electrode and a bare glassy carbon electrode with a diameter of 2 mm (modified and unmodified) were used as working electrodes, respectively. All of the used electrodes were from CHI Co. and all the potentials in this paper are given against the Ag/AgCl (3 M KCl). Solution pH was measured with an Elico LI120 pH meter (Elico Ltd., India).

2.3. Preparation of MWCNTs and modified electrode

Multi-walled carbon nanotubes was refluxed in the mixture of concentrated H_2SO_4 and HNO_3 for 4–5 h, then washed with doubly distilled water and dried in vacuum at room temperature. The MWCNTs suspension was prepared by dispersing 2 mg MWCNTs in 10 ml acetonitrile using ultrasonic agitation to obtain a relative stable suspension. The GCE was carefully polished with 0.30 and 0.05 μm α-alumina slurry on a polishing cloth, and then washed in an ultrasonic bath of methanol and water, respectively. The cleaned GCE was coated by casting 15 μl of the black suspension of MWCNTs

and dried in air. The electroactive areas of the MWCNT-modified GCE and the bare GCE were obtained by cyclic voltammetry (CV) using 1.0 mM $K_3Fe(CN)_6$ as a probe at different scan rates. For a reversible process, the Randles–Sevcik formula has been used [28]:

$$i_{pa} = (2.69 \times 10^5)n^{3/2}AD_R^{1/2}Co\,\nu^{1/2} \tag{1}$$

where i_{pa} refers to the anodic peak current, n is the number of electrons transferred, A is the surface area of the electrode, D_R is diffusion coefficient, ν is the scan rate and Co is the concentration of $K_3Fe(CN)_6$. For 1.0 mM $K_3Fe(CN)_6$ in 0.1 M KCl electrolyte, $n = 1$, $D_R = 7.6 \times 10^{-6}\,cm^2\,s^{-1}$, then from the slope of the plot of i_{pa} versus $\nu^{1/2}$, relation, the electroactive areas were calculated. In bare GCE, the electrode surface was found to be 0.04638 cm^2 and for MWCNT-modified GCE, the surface was nearly 4–4.5 times greater.

2.4. Analytical procedure

The MWCNT-modified GCE was first activated in phosphate buffer (0.2 M, pH 7.0) by cyclic voltammetric sweeps between 0 and 1.4 V until stable cyclic voltammograms were obtained. Then electrodes were transferred into another 10 ml of phosphate buffer (0.2 M, pH 7.0) containing proper amount of TRZ. After accumulating for 180 s at open circuit under stirring and following quiet for 10 s, potential scan was initiated and cyclic voltammograms were recorded between +0.2 and +1.3, with a scan rate of 50 mV s^{-1}. All measurements were carried out at room temperature of $25 \pm 0.1\,^\circ$C.

2.5. Sample preparation

Ten pieces of TRZ tablets were powdered in a mortar. A portion equivalent to a stock solution of a concentration of about 1.0 mM was accurately weighed and transferred into a 100 ml calibrated flask and completed to the volume with double distilled water. The contents of the flask were sonicated for 10 min to affect complete dissolution. Appropriate solutions were prepared by taking suitable aliquots of the clear supernatant liquid and diluting them with the phosphate buffer solutions. Each solution was transferred to the voltammetric cell and analyzed by standard addition method. The differential-pulse voltammograms were recorded between 0.40 and 0.90 V after open-circuit accumulation for 180 s with stirring. The oxidation peak current of TRZ was measured. The parameters for differential-pulse voltammetry (DPV) were pulse width of 0.06 s, pulse increment of 4 mV, pulse period of 0.2 s, pulse amplitude of 50 mV and scan rate of 20 mV s^{-1}. To study the accuracy of the proposed method and to check the interferences from excipients used in the dosage form, recovery experiments were carried out. The concentration of TRZ was calculated using standard addition method.

3. Results and discussion

3.1. Cyclic voltammetric behavior of TRZ

The cyclic voltammograms of TRZ at a bare GCE and at MWCNT-modified GCE were shown in Fig. 2. It can be seen that the TRZ oxidation peaks at the bare GCE was weak and broad due to slow electron transfer, while the response was considerably improved at the MWCNT-modified GCE. At the bare GCE, the peaks were at about 0.79 V (peak A) and 1.10 V (peak B), but on the MWCNT-modified GCE, the peaks appeared at 0.73 and 1.00 V with considerable enhancement in the peak current. This was attributed to the electrocatalytic effect caused by MWCNTs.

It also showed that no reduction peak was observed in the reverse scan, suggesting that the electrochemical reaction was a totally irreversible process. Nevertheless, it was found that the oxi-
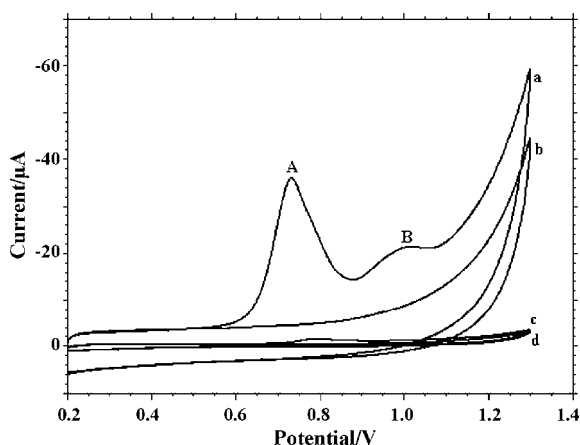
Fig. 2. Cyclic voltammograms of 10 μM TRZ on MWCNT-modified GCE (a) and bare GCE (c). Blank CVs of MWCNT-modified GCE (b) and bare GCE (d). Scan rate: 50 mV s^{-1}; supporting electrolyte: 0.2 M phosphate buffer with pH 7.0; accumulation time: 180 s (at open circuit); volume of MWCNTs suspension: 15 μl.
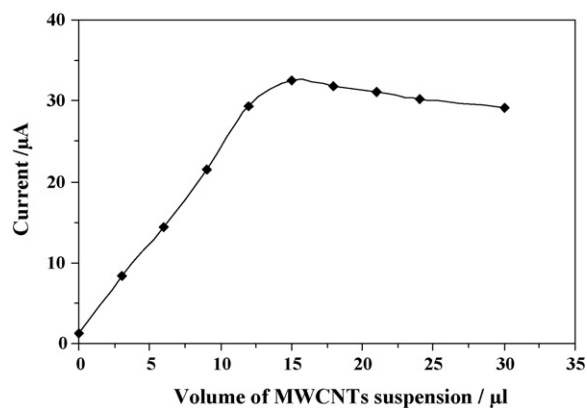

Fig. 4. Influence of MWCNTs suspension (0.2 mg ml^{-1}) volume used on the anodic peak current. Other conditions are as in Fig. 2.

dation peak current of TRZ showed a remarkable decrease during the successive cyclic voltammetric sweeps (Fig. 3). After the second sweep, the peak current decreased greatly and finally remained unchanged. This phenomenon may be due to the fact that the adsorption of TRZ or its oxidative product occurs at the film electrode surface. Therefore, the voltammograms corresponding to the first cycle and peak A were generally recorded, since peak A was intense than B.

3.2. Influence of amount of MWCNTs

Fig. 4 shows that the amount of MWCNTs has influence on the peak current. When the amount is from 12 to 18 μl, the peak current is more stable and higher. After that amount, it decreases. This is related to the thickness of the film. If the film was too thin, the TRZ amount adsorbed was small, resulting in the small peak current. When it was too thick, the film conductivity reduced and the film became not so stable as MWCNTs could leave off the electrode surface. Thus it blocks the electrode surface and hence the peak current decreases. At 15 μl of MWCNTs, the peak current was highest. Therefore, 15 μl MWCNTs suspension solution was used in the remaining studies.

3.3. Influence of accumulation potential and time

It was important to fix the accumulation potential and time when adsorption studies were undertaken. Both conditions could affect the amount of adsorption of TRZ at the electrode. Bearing this in mind, the effect of accumulation potential and time on peak current response was studied by CV. The concentration of TRZ used was 10 μM.

When accumulation potential was varied from +0.4 to −0.4 V, the peak current changed a little. Hence, accumulation at open circuit was adopted. The peak current increased very rapidly with increasing accumulation time, which induced rapid adsorption of TRZ on the surface of the modified electrode. The peak current reached the maximum after 180 s and then being unchanged (Fig. 5). This indicates the saturation accumulation. As too long accumulation time might reduce the stability of MWCNTs film, 180 s was generally chosen as accumulation time.

3.4. Influence of pH

Within the range of pH 3.0–11.2, the peak potential shifted to less positive values for both the peaks with increasing the pH of the buffer solution (Fig. 6). However, by increasing the pH, the potential of the peak A is shifted to less positive values till pH 7.0, then becomes almost pH independent (Fig. 7). Basically, two linear regions are obtained, one between pH 3.0 and 7.0 with a slope of 53 mV/pH and another between pH 7.0 and 11.2 with a slope of

Fig. 3. Successive cyclic voltammograms of 10 μM TRZ on MWCNT-modified GCE. Other conditions are as in Fig. 2.
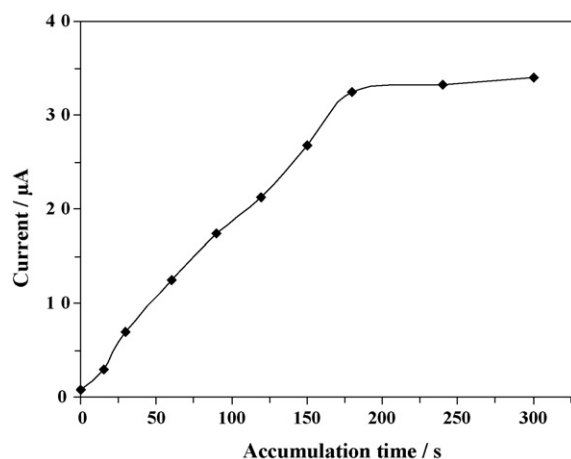
Fig. 5. Variation of the anodic peak current with accumulation time. Other conditions are as in Fig. 2.
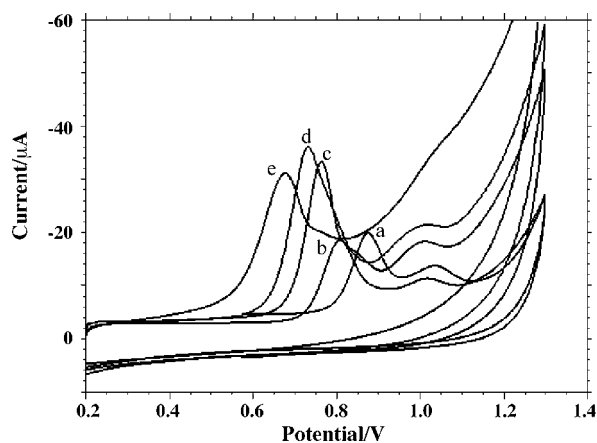
Fig. 6. Influence of pH on the shape of anodic peak. pH: 3.0 (a), 5.0 (b), 6.0 (c), 7.0 (d) and 10.0 (e). Other conditions are as in Fig. 2.

Fig. 9. Cyclic voltammograms of 10 μM TRZ on MWCNT-modified GCE with different scan rates. (a)–(f) were 10, 50, 100, 150, 200 and 300 mV s^{-1}, respectively. Other conditions are as in Fig. 2.

3.5. Influence of scan rate

Useful information involving electrochemical mechanism usually can be acquired from the relationship between peak current and scan rate. Therefore, the electrochemical behavior of TRZ at different scan rates from 10 to 300 mV s^{-1} (Fig. 9) was also studied. There is a good linear relationship between peak current and scan rate. The equations are $I_p = 556.43\nu + 4.46$; $r = 0.9943$ and $I_p = 71.43\nu - 0.408$; $r = 0.996$, for peaks A and B, respectively as shown in Fig. 10. This indicates that the electrode process was controlled by adsorption rather than diffusion. In addition, there was a linear relation between $\log I_p$ and $\log \nu$, corresponding to the following equation: $\log I_p = 0.968 \log \nu + 2.75$; $r = 0.9985$ and $\log I_p = 0.9827 \log \nu + 1.933$; $r = 0.9962$, for peaks A and B, respectively (Fig. 11). The slopes of 0.968 and 0.9827 are close to the theoretically expected value of 1.0 for an adsorption controlled process [29].

The peak potential shifted to more positive values with increasing the scan rates. The linear relation between peak potential and logarithm of scan rate can be expressed as $E_p = 0.8588 + 0.0817 \log \nu$; $r = 0.991$ and $E_p = 1.0979 + 0.0729 \log \nu$; $r = 0.986$, for the peaks A and B, respectively (Fig. 12).

As for an irreversible electrode process, according to Laviron [30], E_p is defined by the following equation:

$$E_p = E^{0\prime} + \left(\frac{2.303RT}{\alpha nF}\right) \log \left(\frac{RTk^0}{\alpha nF}\right) + \left(\frac{2.303RT}{\alpha nF}\right) \log \nu \qquad (2)$$

Fig. 7. Influence of pH on the peak potential of TRZ for peaks A and B. Other conditions are as in Fig. 2.

14 mV/pH. The intersection of the curves is located around pH 7.5, which was close to the pK_a of the piperazine moiety [13]. The first trend corresponds to the conditions where the molecule is oxidized in its mono-protonated form. The intensity was increased to a high value at pH 7.0 (Fig. 8), then the peak intensity decreases continuously. By increasing the pH of the solution, the potential of the peak B changes very little and is almost pH independent. The highest intensity for the peak B was obtained around pH 6.0. Above pH 8.0, the peak B was no longer present. As compared to peak A, peak B was less intense and moreover it can be observed within pH 8.0.

Fig. 8. Variation of peak currents of peaks A and B with pH. Other conditions are as in Fig. 2.

Fig. 10. Dependence of the oxidation peak current of peaks A and B on the scan rate.
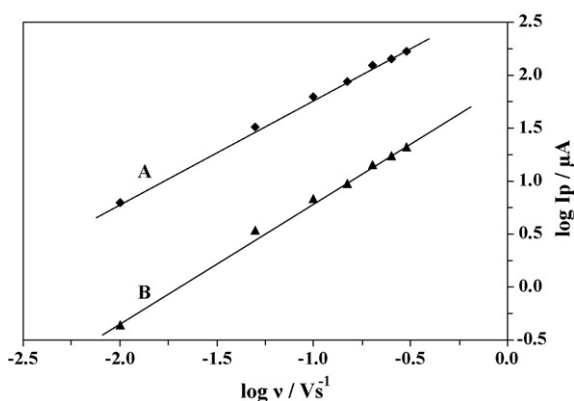
Fig. 11. Dependence of the logarithm of peak current on logarithm of scan rate for peaks A and B.

where α (alpha) is the transfer coefficient, k^0 the standard heterogeneous rate constant of the reaction, n the number of electrons transferred, ν (nu) the scan rate and $E^{0'}$ is the formal redox potential. Other symbols have their usual meanings. Thus the value of αn can be easily calculated from the slope of E_p versus log ν. In this system, for peak A, the slope was 0.0817, taking $T = 298$, $R = 8.314$ and $F = 96480$, αn was calculated to be 0.7238. According to Bard and Faulkner [31], α can be given as

$$\alpha = \frac{47.7}{E_p - E_{p/2}} \text{mV} \tag{3}$$

where $E_{p/2}$ is the potential where the current is at half the peak value. So, from this we got the value of α to be 0.8378. Further, the number of electron (n) transferred in the electro-oxidation of TRZ was calculated to be 0.864–1.0. The value of k^0 can be determined from the intercept of the above plot if the value of $E^{0'}$ is known. The value of $E^{0'}$ in Eq. (2) can be obtained from the intercept of E_p versus ν curve by extrapolating to the vertical axis at $\nu = 0$ [32]. For peak A, the intercept for E_p versus log ν plot was 0.8588 and $E^{0'}$ was obtained to be 0.7207, the k^0 was calculated to be $1.3828 \times 10^3 \text{ s}^{-1}$. Similarly for the peak B, n was found to be 0.894–1.0 and k^0 was $1.5659 \times 10^3 \text{ s}^{-1}$.

So, we may assume that oxidation steps of TRZ were located on the piperazine moiety, which represents a typical redox system with two electron oxidation processes in acidic and basic media. The mechanism of oxidation of TRZ for the peak A follows as given below. We may postulate that when the aliphatic nitrogen of the piperazine moiety, distal to the benzene ring of the molecule is protonated, oxidation occurs with the removal of a proton (Fig. 13A). Above pH 8.0, oxidation exclusively occurs at the most

basic piperazine nitrogen (distal) following the well-established aliphatic tertiary amine oxidation pathway [33]. TRZ looses an electron to form a cation radical, which on loosing a proton and an electron in subsequent steps to form a quaternary Schiff base. Thus resulted quaternary Schiff base was rapidly hydrolysed to the secondary amine, 1-(3-chloro-phenyl)-piperazine and an aldehyde, 3-(3-oxo-[1,2,4]triazolo[4,3-a]pyridin-2-yl)-propionaldehyde. Such a mechanism of oxidation for peak A is shown in Fig. 13A.

The oxidation mechanism for peak B is entirely different, as it was present up to pH 8.0 only. This oxidation step of TRZ occurs at the triazolopyridine moiety of the molecule. The mechanism for peak B is shown in Fig. 13B, in which TRZ loses an electron from nitrogen attached to the aliphatic chain to form a cation radical. This cation radical on rapid hydrolysis gives 2-({3-[4-(3-Chloro-phenyl)-piperazin-1-yl]-propyl}-hydrazono)-2H-pyridine-1-carboxylic acid, which on decarboxylation gives rise to N-{3-[4-(3-chloro-phenyl)-piperazin-1-yl]-propyl}-N-(1H-pyridin-2-ylidene)-hydrazine. Such proposed mechanisms and all the results obtained are in agreement with the report of Kauffmann et al. [13].

3.6. Calibration curve

In order to develop a voltammetric method for determining the drug, we selected the differential-pulse voltammetric mode, because the peaks are sharper and better defined at lower concentration of TRZ than those obtained by cyclic voltammetry, with a lower background current, resulting in improved resolution. According to the obtained results, it was possible to apply this technique to the quantitative analysis of TRZ. The phosphate buffer solution of pH 7.0 was selected as the supporting electrolyte for the quantification of TRZ as it gave maximum peak current at pH 7.0. The peak at about 0.68 V was considered for the analysis. Differential-pulse voltammograms obtained with increasing amounts of TRZ showed that the peak current increased linearly with increasing concentration, as shown in Fig. 14. Using the optimum conditions described above, linear calibration curves were obtained for TRZ in the range of 0.2–10 μM. The linear equation was I_p (μA) = 1.8714 + 0.4931C ($r = 0.9984$, C is in μM). Deviation from linearity was observed for more concentrated solutions, due to the adsorption of TRZ or its oxidation product on the electrode surface. Related statistical data of the calibration curves were obtained from five different calibration curves. The limit of detection (LOD) and quantification (LOQ) were 24 and 81 nM, respectively. The LOD and LOQ were calculated using the following equations:

$$\text{LOD} = 3s/m; \quad \text{LOQ} = 10s/m.$$

where s is the standard deviation of the peak currents of the blank (five runs), and m is the slope of the calibration curve. The detection limits reported at different electrodes are tabulated in Table 1. This method was better as compared with other reported electrochemical methods [13,15,16].

In order to study the reproducibility of the electrode preparation procedure, a 1.0 μM TRZ solution was measured with the same electrode (renewed every time) for every several hours within day, the R.S.D. of the peak current was 3.26% (number of measurements = 6). As to the between day reproducibility, it was similar to that of within day if the temperature was kept almost unchanged. Owing to the adsorption of TRZ or its oxidative products on to the electrode surface, the current response of the modified electrode would decrease after successive use. In this case, the electrode should be modified again.
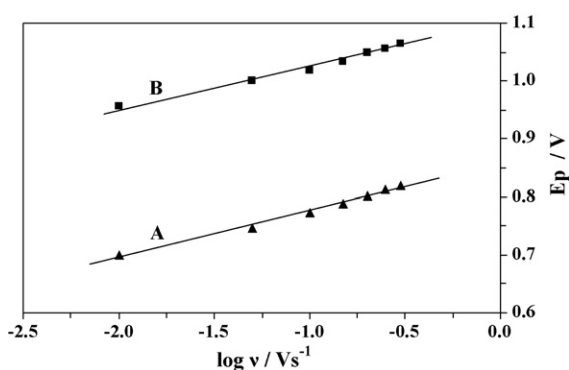

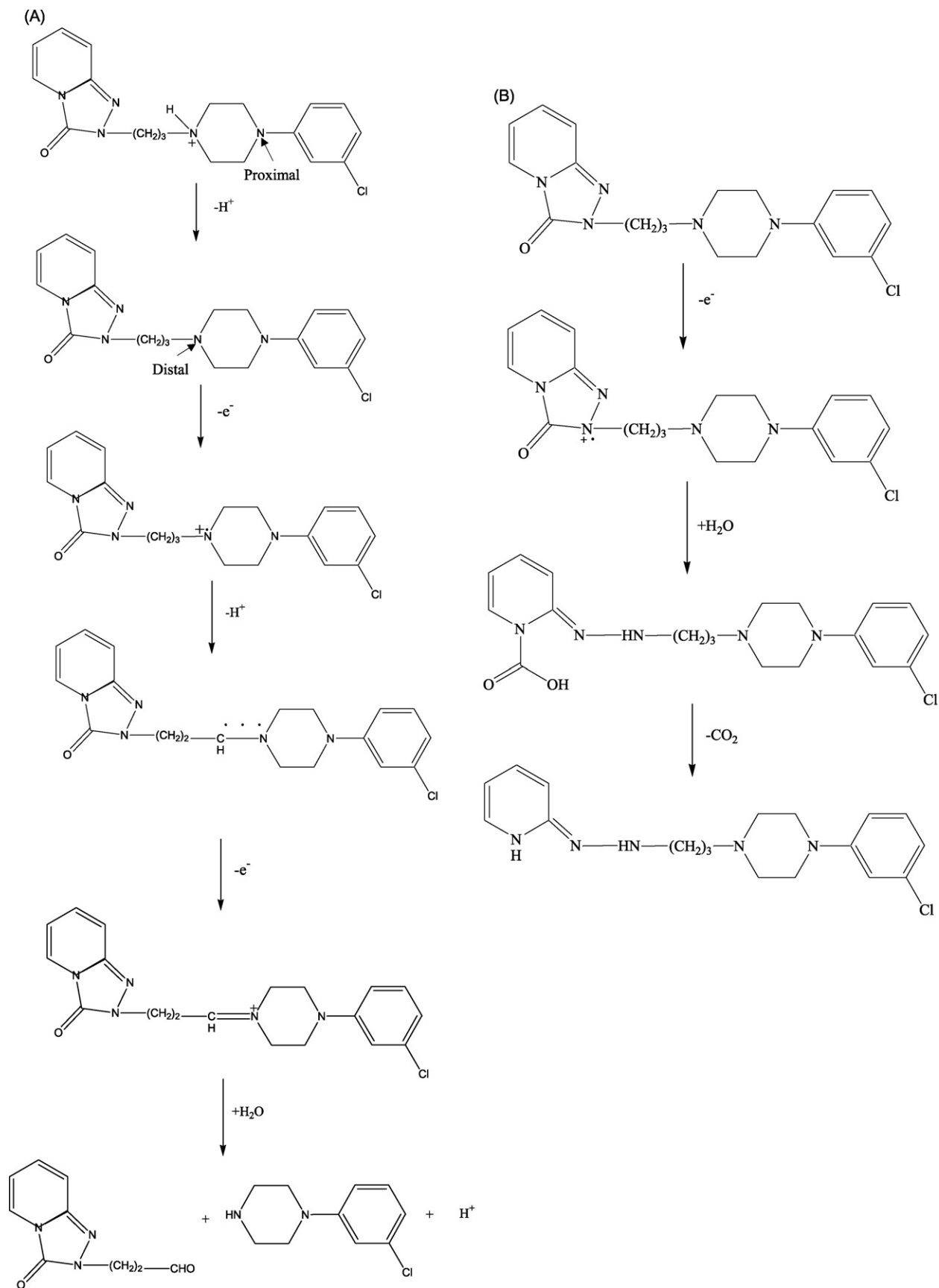**Fig. 12.** Relationship between peak potential and logarithm of scan rates for the peaks A and B.

Fig. 13. (A) Probable mechanism for the oxidation of TRZ for peak A. (B) Probable mechanism for the oxidation of TRZ for peak B.

Table 1
Comparison of detection limits for TRZ at different electrodes.

Electrodes	Detection limits	Refs.
Carbon paste electrode	100 nM	[13]
Platinum electrode (stationary)	2500 nM	[15]
Platinum electrode (rotating)	1700 nM	[15]
Dropping mercury electrode	7397 nM	[16]
MWCNT-modified GCE	24 nM	Present work

Table 2
Comparative studies for TRZ in Depryl and Tazodac tablets by proposed and literature methods and mean recoveries in spiked tablets.

	DPP [16]	Depryl[a]	Tazodac[a]
Labelled claim (mg)	100.0	25.0	25.0
Amount found (mg)[b]	101.0	24.94	24.86
R.S.D. (%)	–	0.29	1.09
Added (mg)	–	10.0	10.0
Found (mg)	–	9.97	9.65
Recovered (%)[c]	–	99.7	96.5
% Of recovery in R.S.D.	–	0.32	1.04

[a] Names of the tablets.
[b] Each value is the mean of five experiments.
[c] Recovery value is the mean of five experiments.

3.7. Tablet analysis

In order to evaluate the applicability of the proposed method in the pharmaceutical sample analysis, two commercial medicinal samples containing TRZ viz. Depryl (Cipla Co. India) and Tazodac (Zy-Alidac Co. India) were studied. The procedures for the tablet analysis were followed as described in Section 2.5. The results are in good agreement with the content marked in the label (Table 2).

The recovery test of TRZ ranging from 0.5 to 5.0 μM was performed using differential-pulse voltammetry. Recovery studies were carried out after the addition of known amounts of the drug to various pre-analyzed formulations of TRZ. The recoveries in different samples were found to lie in the range from 98.7% to 102.2%, with R.S.D. of 2.94%.

3.8. Interference

Under the optimum experimental conditions, the effects of potential interferents on the voltammetric response of 1.0 μM TRZ were evaluated. The experimental results (Table 3) show that thousand-fold of glucose, starch, sucrose, dextrose, talk, gum acacia, lactic acid and tartaric acid, and 100-fold of citric acid and oxalic acid did not interfere with the voltammetric signal of TRZ. However, 10-fold of ascorbic acid had apparent influence on the voltammetric signal of TRZ.

Table 3
Influence of potential interferents on the voltammetric response of 1.0 μM TRZ.

Interferent	Concentration (mM)	Signal change (%)
Glucose	1.0	−1.21
Starch	1.0	−3.13
Sucrose	1.0	−0.89
Dextrose	1.0	−1.32
Citric acid	1.0	−7.23
Magnesium stearate	1.0	+1.61
Talc	1.0	+0.92
Gum acacia	1.0	+2.25
Ascorbic acid	1.0	+180.65
Lactic acid	1.0	+2.52
Tartaric acid	1.0	−2.65
Oxalic acid	1.0	+10.24
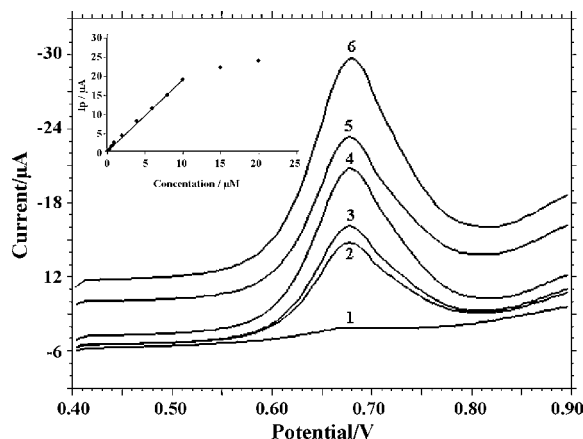
Fig. 14. Differential-pulse voltammograms of MWCNT-modified GCE in TRZ solution at different concentrations: 0.2 (1), 1.0 (2), 2.0 (3), 4.0 (4), 6.0 (5) and 8.0 (6) μM. Inset: plot of the peak current against the concentration of TRZ.

Table 4
Determination of TRZ in urine samples.

Urine	Spiked (μM)	Detected (μM)	Recovery (%)
Sample 1	0.3	0.3015	100.50
Sample 2	0.7	0.7009	100.13
Sample 3	3.0	3.096	103.20
Sample 4	7.0	6.941	99.15

3.9. Detection of TRZ in urine samples

The developed differential-pulse voltammetric method for the TRZ determination was applied to urine samples. The recoveries from urine were measured by spiking drug free urine with known amounts of TRZ. The urine samples were diluted 100 times with the phosphate buffer solution before analysis without further pre-treatments. A quantitative analysis can be carried out by adding the standard solution of TRZ into the detect system of urine sample. The calibration graph was used for the determination of spiked TRZ in urine samples. The detection results of four urine samples obtained are listed in Table 4. The recovery determined was in the range from 99.15% to 103.2% and the R.S.D. was 1.72%.

4. Conclusions

In this work, a multi-walled carbon nanotube-modified glassy carbon electrode has been successfully developed for electrocatalytic oxidation of TRZ in phosphate buffer solution. When the potential was made to move, TRZ produced two anodic peaks at about 0.73 and 1.00 V in 0.2 M pH 7.0 phosphate buffer. MWCNTs showed electrocatalytic action for the oxidation of TRZ, characterizing by the enhancement of the peak current, which was probably due to the larger surface area of MWCNTs. A suitable oxidation mechanism was proposed. The peak at about 0.68 V was suitable for analysis and the peak current was linear to TRZ concentrations over a certain range under the selected conditions. This sensor can be used for voltammetric determination of selected analyte as low as 24 nM with good reproducibility. The modified electrode has been used to determine TRZ in pharmaceutical samples. The proposed method offered the advantages of accuracy and time saving as well as simplicity of reagents and apparatus. In addition, the results obtained in the analysis of TRZ in spiked urine samples demonstrated the applicability of the method for real sample analysis.

References

[1] G.J. Marek, C.J. McDougle, L.H. Price, L.S. Seiden, Psychopharmacology 109 (1992) 2.
[2] M. Maes, E. Vandoolaeghe, R. Desnyder, J. Affect Disorders 41 (1996) 201.
[3] K. Partill (Ed.), Martindale, The Complete Drug Reference, 32nd ed., The Pharmaceutical Press, Massachusetts, 1999, p. 309.
[4] G. Bertschy, E. Ragama-Pardos, M. Muscinico, A. Ait-Ameur, L. Roth, C. Osiek, F. Ferrero, Pharm. Res. 51 (2005) 79.
[5] S. Rotzinger, J. Fang, G.B. Baker, Drug Metab. Dispos. 26 (1998) 572.
[6] N. Samad, M.A. Haleem, D.J. Haleem, J. Chem. Soc. Pakistan 28 (2006) 605.
[7] S.C. Sweetman (Ed.), Martindale, The Complete Drug Reference, 34th ed., Pharmaceutical Press, London, 2004, p. 319.
[8] S.N. Dhumal, P.M. Dikshit, I.I. Ubharay, B.M. Mascarenhas, C.D. Gaitonde, Indian Drugs 28 (1991) 565.
[9] A.J.H. Louter, R.A.C.A. Vander Wagt, U.A.T. Brinkman, Chromatographia 40 (1995) 500.
[10] X. Kang, C. Pan, Q. Xu, Y. Yao, Y. Wang, D. Qi, Z. Gu, Anal. Chim. Acta 587 (2007) 75.
[11] A. de Castro, M.M.R. Fernadez, M. Laloup, N. Samyn, G. De Boeck, M. Wood, V. Maes, M. lopez-RIvadulla, J. Chromatogr. A 1160 (2007) 3.
[12] J.C. Vire, A. Squella, J.M. Kauffmann, L.J. Nunez-Vergara, G.J. Patriarche, Anal. Lett. 20 (1987) 1467.
[13] J.M. Kauffmann, J.C. Vire, G.J. Patriarche, L.J. Nunez-Vergara, J.A. Squella, Electrochim. Acta 32 (1987) 1159.
[14] L.J. Nunez-Vergara, J.A. Squella, K.L. Barnafi, J.C. Vire, J.M. Kauffmann, G.J. Patriarche, Anal. Lett. 19 (1986) 2307.
[15] D. Dogrukol-Ak, V. Zaimoglu, M. Tuncel, Eur. J. Pharm. Sci. 7 (1999) 215.
[16] N. El-Enany, F. Belal, M.S. Rizk, J. Pharm. Biomed. Anal. 30 (2002) 219.
[17] R.N. Hegde, S.T. Nandibewoor, Anal. Lett. 41 (2008) 977.
[18] A. Markoci, Electroanalysis 19 (2007) 739.
[19] M. Trojanowicz, Trend Anal. Chem. 25 (2006) 480.
[20] S. Iijima, Nature 354 (1991) 56.
[21] P.M. Ajayan, Chem. Rev. 99 (1999) 1787.
[22] J.M. Nugent, K.S.V. Santhanam, A. Rubio, P.M. Ajayan, Nano Lett. 1 (2001) 87.
[23] A. Merkoci, Microchim. Acta 152 (2006) 157.
[24] J.J. Gooding, Electrochim. Acta 50 (2005) 3049.
[25] C.E. Banks, R.G. Compton, Analyst 131 (2006) 15.
[26] G. Zhao, Z. Yin, L. Zhang, X. Xian, Electrochem. Commun. 7 (2005) 256.
[27] G.D. Christian, W.C. Purdy, J. Electroanal. Chem. 3 (1962) 363.
[28] B. Rezaei, S. Damiri, Sens. Actuators B Chem. 134 (2008) 324.
[29] D.K. Gosser, Cyclic Voltammetry: Simulation and Analysis of Reaction Mechanisms, VCH, New York, 1993, p. 43.
[30] E. Laviron, J. Electroanal. Chem. 101 (1979) 19.
[31] A.J. Bard, L.R. Faulkner, Electrochemical Methods Fundamentals and Application, 2nd ed., Wiley, 2004, p. 236.
[32] W. Yunhua, J. Xiaobo, H. Shengshui, Bioelectrochemistry 64 (2004) 91.
[33] M. Masui, H. Sayo, Y. Tsuda, J. Chem. Soc. (B) (1968) 973.

Lead determination in whole blood by laser ablation coupled with inductively coupled plasma mass spectrometry

Hui-Fang Hsieh, Wei-Shan Chang, Yi-Kong Hsieh, Chu-Fang Wang*

Department of Biomedical Engineering and Environmental Sciences, National Tsing Hua University, Hsinchu 30013, Taiwan

ARTICLE INFO

ABSTRACT

This work describes a simple procedure for blood lead level determination. The proposed method requires little sample pretreatment and subsequent direct analysis of a dried blood spot on a filter membrane using laser ablation coupled with inductively coupled plasma mass spectrometry (LA-ICP-MS). In general, LA-ICP-MS studies are somewhat limited by the lack of matrix-matched standards for calibration purposes. Here we describe aqueous standard calibration and matrix-matched calibration methods. This method was validated by analysis of the reference materials. With the matrix-matched calibration method, the recovery ranged from 97.8% to 112.8%, while the aqueous standard calibration method ranged 90.4% to 122.4%. The lower detection limit was estimated as 0.1 ng mL^{-1}. The determination precision, expressed as the relative standard deviation (RSD), was not worse than 10% for all results. A sample throughput of approximately 5 min per sample made it possible to rapidly screen a large number of samples.

1. Introduction

Lead (Pb) is a toxic metal that occurs naturally in the environment. However, most of the high levels found throughout the environment come from human activities such as leaded gasoline combustion, lead-based paint, batteries, pipes, pesticides, solder, plastic stabilizers, shot and sinkers [1]. The Pb determination in human blood is important in assessing the present internal exposure of an individual. It is well known that children are more sensitive to the health effects of lead than adults [1,2]. A greater proportion of systemically circulating lead reaches the brain of children, especially those 5 years of age or younger. The developing nervous system is especially vulnerable to this neural damage [2]. The World Health Organization (WHO) has defined whole blood lead concentrations >30 μg dL^{-1} in adults as indicative of significant exposure and recommends chelation therapy when the whole blood lead concentration exceeds 60 μg dL^{-1} [3]. Children's immature organs are especially sensitive and their developing nervous system will be destroyed when the blood lead level is higher than 10 μg dL^{-1}. Children with blood lead levels (BLLs) >10 μg dL^{-1} (1 μg dL^{-1} = 0.0483 μmol L^{-1}) are at an increased risk for learning and behavioral problems [1]. The Centers for Disease Control and Prevention (CDC) of the United States action level for children ≤7 years of age is 10 μg dL^{-1}. The CDC recommends that medical evaluations be performed for all children with blood lead levels equal to or greater than 20 μg dL^{-1}. Medical treatment (i.e., chelation ther-

apy) is indicated when the whole blood lead concentration is higher than 45 μg dL^{-1} [4].

Several analytical methods are available for analyzing the lead concentration in liquid blood including electrothermal atomic absorption spectrometry (ETAAS) [5–10], hydride generation atomic fluorescence spectrometry (HG-AFS) [11,12], anodic stripping voltammetry techniques [13–15] and inductively coupled plasma spectrometry [8,9,16–21]. ICP-MS is one of the most sensitive trace element techniques available. Whole blood samples are analyzed by ICP-MS directly after simple dilution or decomposition of the organic matrix. However, the determination of ng mL^{-1} range Pb in blood is often limited due to contaminations and impurities during sample pretreatment processes such as an extraction, dilution or microwave-assisted digestion. Since the amount of collected blood must be at least several milliliters, it is difficult to acquire blood samples from children through invasive pediatric venipuncture. In addition, liquid blood sample must be fixed with appropriate conserving mixtures immediately after sampling and storage at low temperature [7–9,19,21]. Owing to these, the preparation of dried blood spots on filter paper has been investigated as an alternative to liquid blood for Pb measurement [22–27]. Use of dried filter blood spot samples for blood lead concentration measurement in pediatric subjects is also a desirable screening option due to the relative ease of collection, storage and transport [3,26,27]. The analysis of dried filter blood spots for Pb typically involves some type of sample pretreatment, such as extraction or blood spot punch ashing, followed by analysis using atomic absorption spectrometry [22–26] or inductively coupled plasma mass spectrometry [27]. During these pretreatment procedures some problems such as incomplete

---

* Corresponding author. Tel.: +886 3 571 5131 34222; fax: +886 3 572 7298.
E-mail address: cfwang@mx.nthu.edu.tw (C.-F. Wang).

recovery or contamination can be an issue for Pb determination [3,25].

Laser ablation (LA) systems can ablate solid samples directly while connected to ICP-MS for trace and ultrace element determination. This technique has been successfully applied to the determination of geological, environmental and biological samples [28–30]. The conventional method for introducing a sample into the plasma is the nebulization of a solution, therefore prior to analysis the sample must be dissolved. One of the advantages of laser ablation over solution nebulization, as a means of sample introduction, is that laser ablation creates dry plasma. This may reduce the amount of oxygen introduced into the plasma and should therefore minimize the occurrence of interfering oxide species [31]. However, oxide interferences for lead isotopes can be negligible due to the extremely low content of Os, Ir and Pt in blood. Other advantages of laser ablation chemical analysis include no chemical procedures for dissolution, reduced risk of contamination or sample loss, analysis of very small samples not separable for solution analysis, and determination of spatial distributions of elemental composition [28,29]. One work has demonstrated that laser ablation can be used as a direct sample introduction method for dried blood spot Pb determination using LA-ICP-time-of-flight (TOF)-MS. However, this method requires additional study [32]. Although LA-ICP-MS is very attractive, the main problem with this method is quantification if no suitable standard reference materials with a similar matrix composition are available [28,30,33]. Using matrix-matched standards for calibration is advantageous, but this approach is limited by the lack of suitable materials. Some certified reference materials are commercially available, but they are costly and the range of matrices available does not cover every type of sample.

This study presents a method to detect and quantify $ng\,mL^{-1}$ Pb levels in blood samples using LA-ICP-MS. The analysis requires only micro droplets of blood sample (0.5 μL), which can be obtained through a finger or heel stick or venipuncture. This method is generally considered handy and less traumatic to children. Little sample pretreatment is needed, so that the risk of contamination through sample pretreatment can be reduced.

2. Experimental

2.1. Instrumentation

An UP-213 laser ablation system (New Wave Research Inc., Fremont, CA) was coupled to an Agilent 7500a ICP-MS (Agilent Technologies, Santa Clara, CA). The sample surface is irradiated with deep-UV (213 nm) output from a frequency-quintupled Nd:YAG (neodymium doped yttrium aluminum garnet crystal) laser. Experiments were carried out at 20 Hz using the grid spot scanning mode with 100% applied laser energy (1.9 mJ). The laser was operated using the largest spot size (110 μm) and a defocused beam to maximize the laser beam area and produce a relative large signal. The total acquisition time per sample was 285 s, this include the 20-s equilibration and stabilization time between the different blood spot ablations. Peak areas were used for the final quantitation of analyte concentrations. The operating parameters for LA-ICP-MS are provided in Table 1. Optimization of the plasma and mass spectrometer was accomplished using solution nebulization, prior to switching to LA sample introduction. A 1 $ng\,mL^{-1}$ Tl standard solution was used to obtain a maximum and stable signal at m/z 205. PTFE filter membrane (Pall Corporation, Ann Arbor, MI) was used as substrates on which all sample aliquots were deposited and dried.

2.2. Reagents and solutions

All chemicals were of analytical reagent grade and were used without further purification. The 65% (v/v) nitric acid (Merck,

Table 1
LA-ICP-MS operating conditions.

Instrument	Parameter	Value
ICP-MS		
	RF power	1.5 kW
	Plasma argon gas flow	15 $L\,min^{-1}$
	Auxiliary argon gas flow	1.0 $L\,min^{-1}$
	Make up argon gas flow	0.15 $L\,min^{-1}$
	Carrier argon gas	1.0 $L\,min^{-1}$
	Sampler/skimmer cone	Nickel
	Acquisition mode	Time-resolved analysis
	Acquisition time	285 s
Laser ablation		
	Wavelength	213 nm
	Output energy	100%
	Laser energy	20 $J\,cm^{-2}$ (1.9 mJ)
	Defocus setting	2 mm
	Carrier argon gas	1.0 $L\,min^{-1}$
	Laser scanning mode	Grid of spots
	Repetition rate	20 Hz
	Dwell time	8 s
	Intersite pause	5 s
	Spot size	110 μm
	Raster spacing	150 μm
	Grid spacing	200 μm

Darmstadt, Germany) was of Suprapur grade. Deionized water was produced by reverse osmosis of tap water followed by deionization (Millipore, Molsheim, France) to yield 18.2 $M\Omega\,cm^{-1}$ resistivity reagent.

A 1000 $\mu g\,mL^{-1}$ standard Pb solution (Merck, Darmstadt, Germany) was used as the aqueous standard stock solution. Certified reference materials (CRM) were used to check the proposed method performance. BCR 635 bovine blood was available from IRMM (Institute for Reference Materials and Measurement), Geel, Belgium. It was provided as a lyophilized material which, once reconstituted with 5 mL of deionized water, contained $210 \pm 24\,ng\,mL^{-1}$ Pb. SRM (Standard Reference Material) 966 bovine blood was from NIST (National Institute of Standards and Technology), MD, USA. SRM 966 contains two concentration levels: a level 1 contains $15.6 \pm 0.5\,ng\,mL^{-1}$ Pb and a level 2 contains $252.7 \pm 2.2\,ng\,mL^{-1}$ Pb. The CRM Seronorm trace elements whole blood level-3 (SERO AS, Billingstad, Norway) was reconstituted with 5 mL of deionized water. The reconstituted blood contained $503 \pm 19\,ng\,mL^{-1}$ Pb.

2.3. Establishment of trial calibration curves for LA-ICP-MS

Calibrations were carried out against aqueous and Seronorm matrix-matched standard solutions. Aqueous Pb standard solution was prepared from 1000 $\mu g\,mL^{-1}$ stock solution. All calibrants were prepared from stock solution after subsequent appropriate dilution with 2% nitric acid. Methylene blue was added to 100 $\mu g\,mL^{-1}$ as an indicator as well as improving the ablation yield. The aqueous standard calibration curve was linear over the concentration range of 0–588 $ng\,mL^{-1}$ for the Pb. The Seronorm whole blood CRM was used as matrix-matched calibrants. All calibrants were prepared by serial dilution with deionized water, and ranged from 0 to 503 $ng\,mL^{-1}$. Both a blank filter and a blank standard filter were also ablated to investigate the signal-to-noise ratio of this method.

2.4. Sample introduction by LA

For the LA-ICP-MS analysis, 0.5 μL of each solution was pipetted onto the surface of a hydrophobic filter membrane in the form of small droplets. With the distinct of water repel tendency of hydrophobic surface, the aqueous droplet placed on a filter membrane form a drop to minimize its contact area. After drying,
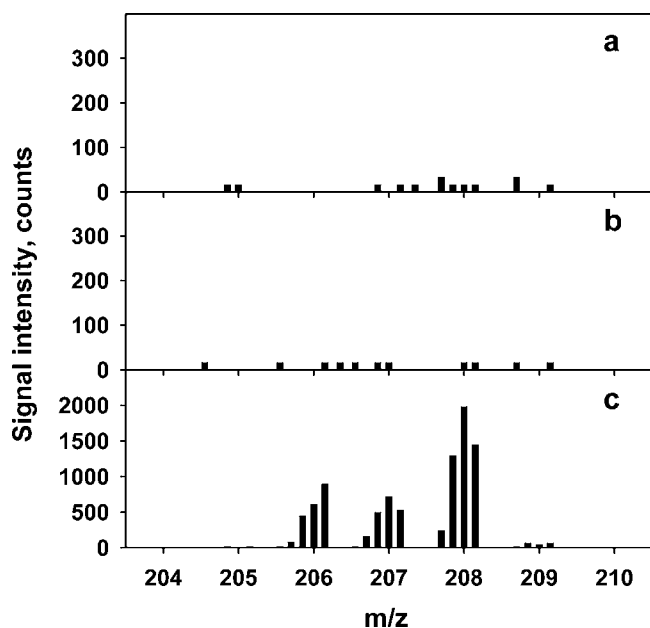
Fig. 1. Mass spectra of (a) gas blank, (b) PTFE filter membrane and (c) blood droplet samples. The droplet volume was 0.5 μL and the concentration of Pb was 252 ng mL^{-1}.

the aqueous droplets were deposited onto the surface of a filter membrane in the form of small and thick spots. The dried filter membranes were placed into the LA sampling chamber for ICP-MS analysis.

3. Results and discussion

3.1. Feasibility of LA-ICP-MS

To determine the blood sample Pb concentration using LA-ICP-MS, the system was optimized as listed in Table 1.

As the laser beam moved across the filter surface, both the sample and filter matrix were rapidly heated and ablated to form an aerosol that was then transported into the ICP-MS with argon carrier gas. Ablation products were converted into ions in the plasma, which subsequently orthogonally accelerated into the MS for analytes mass spectral analysis.

Fig. 1 shows the mass spectra of the gas blank, filter membrane blank and blood droplet samples for Pb isotopes, respectively. The gas blank represents the signal collected only with argon gas and the laser off. The blood sample Pb concentration was 252 ng mL^{-1} (Fig. 1c). The figure indicates that no significant background was
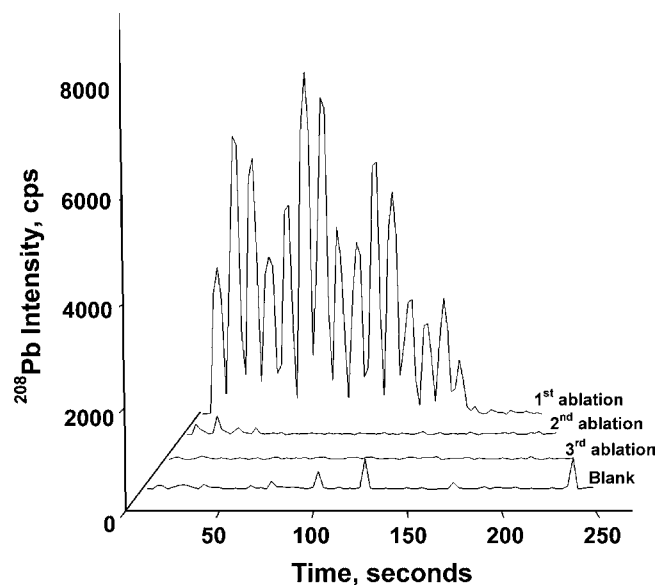
Fig. 3. Total ion chromatogram of ^{208}Pb obtained by LA-ICP-MS. The volume of the droplet was 0.5 μL and the concentration of Pb was 503 ng mL^{-1}.

detected for the Pb from PTFE filter membrane, confirming that no significant contamination was contributed from this substrate.

As shown in Fig. 2a, the blood droplets dried on the filter membrane surface formed a roughly rounded thick layer that can hardly be ablated with a single laser shot. The blood spot diameters were about 700–900 μm. The LA system scanning mode can be single or multi-spot analysis, straight-line scans and rastering. In the preliminary experiments, various scan modes provided by UP-213 were tested for the best ablation results. After evaluation, a 4 × 5 spot grid scanning method was used in this study. Fig. 2a illustrates the grid mode arrangement. Twenty laser ablation spots were applied to ablate each blood droplet. It was found that complete desorption from the filter surface can be achieved using this arrangement with the other optimized operational conditions including 2 mm defocus distance, 100% laser energy, 8 s dwell time, 5 s intersite pause, and 20 Hz repetition rate. It was observed from Fig. 2b that no residual remains on the filter and the filter membrane still maintains its integrality after the ablation process.

Further evidence of complete ablation is also shown in Fig. 3. Four data sets are exhibited in the graph. The BK line is the ablation signal for a blank filter membrane. The others are three consecutive ablation data from the same blood droplet. The signal intensity of the first ablation was quite obvious, however, signals for the second and third ablations were less than that for the background. The results illustrate that the dried blood spot was completely
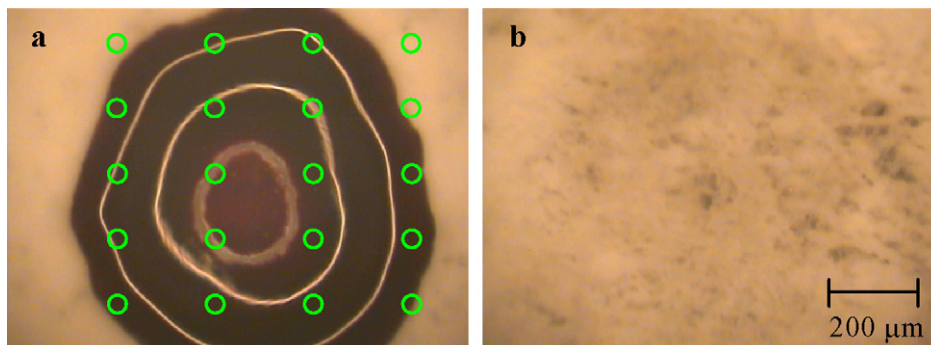
Fig. 2. Images of dried blood droplet on the PTFE filter membrane. (a) Before ablation and (b) after ablation.

Table 2
Comparison of the measured and target concentrations from three blood samples.

Reference sample	Analyte	Concentration (average ± S.D.) (ng mL^{-1})		
		Certified values	Measured values[a,b]	Measured values[a,c]
NIST SRM966 Level 1	^{206}Pb	15.6 ± 0.5	14.1 ± 0.8	15.3 ± 0.6
	^{207}Pb		15.0 ± 0.2	17.6 ± 0.2
	^{208}Pb		14.5 ± 0.8	16.9 ± 0.7
NIST SRM966 Level 2	^{206}Pb	252. 7 ± 2.2	309 ± 6.0	253 ± 20
	^{207}Pb		270 ± 8.5	275 ± 23
	^{208}Pb		273 ± 2.0	269 ± 21
IRMM BCR635	^{206}Pb	210 ± 24	253 ± 8	206 ± 6
	^{207}Pb		226 ± 8	230 ± 7
	^{208}Pb		232 ± 8	230 ± 7
Seronorm L-3	^{206}Pb	503 ± 19	614 ± 10	–
	^{207}Pb		488 ± 9	–
	^{208}Pb		506 ± 9	–

S.D.: standard deviation.

[a] $n = 3$.

[b] Determined with liquid standard solution calibration curve.

[c] Determined with Seronorm calibration curve.

ablated by the first ablation. This data was in accordance with our expectation that the blood would be ablated completely without perforating the PTFE filter membrane.

3.2. Calibration curves by LA-ICP-MS

Four different ^{208}Pb calibration curves, including an aqueous standard solution and three blood standard reference materials (SRMs) were established in this study. The aqueous standard solution matrices were 2% nitric acid and 100 mg L^{-1} methylene blue. Numerous proteins and fats are included in the blood sample as well as SRMs. As shown in Fig. 4a, the linearities of all ^{208}Pb calibration curves were excellent and their slopes were close to each other. The correlation coefficients of these calibration curves are in the range of 0.9965–0.9988. This illustrates that, with the proposed method,

Fig. 4. Calibration curves of ^{208}Pb built from Seronorm matrix-matched and aqueous standard solution. The error bars indicate ± 3 standard deviations.

the matrix effect can be negligible and a universal Pb calibration curve can be established. The data with different matrices fit well with the universal calibration curve as shown in Fig. 4b. As a result, the self-prepared aqueous standard solution can be employed to replace the expensive difficult-to-prepare blood standard reference materials. Similar results were obtained for ^{206}Pb and ^{207}Pb as well.

3.3. Real sample analysis validation

To evaluate the accuracy of proposed method in determining Pb in blood samples, reference materials including Seronorm trace element human whole blood, NIST SRM 966 bovine blood and BCR-635 human blood were used as real samples in this study. As shown in Table 2, the Seronorm and the aqueous standard solution were used as calibration standards, respectively, to examine the Pb recoveries for different reference materials. All reported data in the Table 2 are the mean values from replicate ($n \geq 3$) sample ablations. Using a matrix-matched standard (Seronorm), recoveries of ^{206}Pb, ^{207}Pb and ^{208}Pb were 97.8%, 112.8%, and 108.4% in SRM 966 Level 1, 100.3%, 108.7% and 106.6% in SRM 966 Level 2, and 98.3%, 109.6% and 109.3% in BCR 966, respectively. A universal calibration method using the aqueous standard solution also proved to be valid for different reference materials with recoveries of Pb isotopes ranging from 90.4% to 122.4%, respectively. There is a notable systematical discrepancy between the result of ^{206}Pb and other Pb isotopes while determination with liquid standard solution calibration was done. For standard of low Pb concentration (SRM 966 Level 1), a significantly lower recovery of ^{206}Pb was observed if comparing with other high Pb concentration standards (SRM 966 Level 2, BCR635, Seronorm L-3). The reason of this can be attributed to the interference of matrix effect. While the matrix-matched standard solution calibration was applied, a good agreement between Pb isotopes was obtained. It is suggested that a signal of ^{207}Pb or ^{208}Pb should be selected for quantification purpose with the aqueous standard calibration method.

Several sub-samples of various reference materials in a number of analytical runs for blood samples were also performed to evaluate the precision of the proposed method. The precision of the determinations, expressed as the relative standard deviation (RSD), were not worse than 10% for all results.

The analytical figures of merit obtained using Seronorm matrix-matched and aqueous standard solution calibration methods are summarized in Table 3. The correlation coefficient (R), resulted from linear fittings to the calibration points ($n = 3$), was ranged from 0.9897 to 0.9988. With the Seronorm matrix-matched calibration
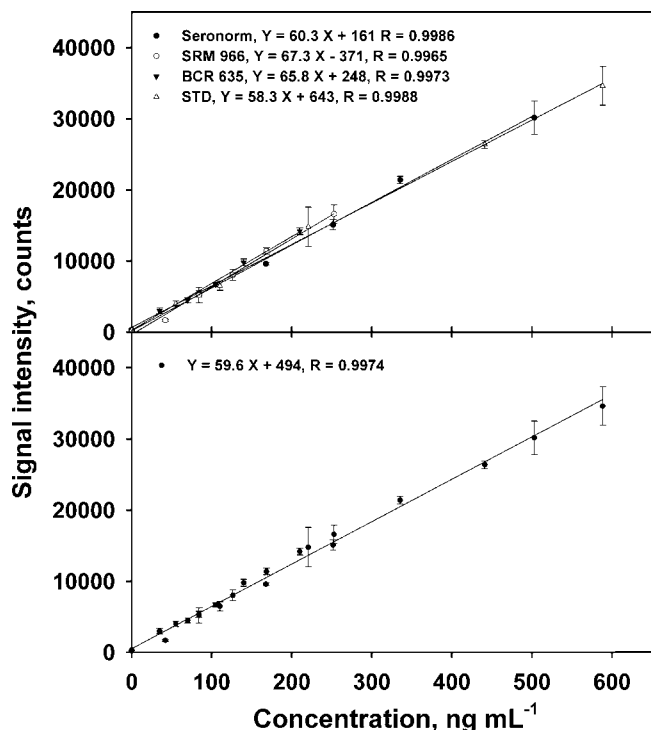
Table 3
Figures of merit.

	^{206}Pb	^{207}Pb	^{208}Pb
Seronorm			
R	0.9985	0.9983	0.9986
LOD (ng mL^{-1})	2.0	1.9	1.4
RSD (%)	5	9	8
Aqueous standards			
R	0.9897	0.9956	0.9988
LOD (ng mL^{-1})	0.14	0.23	0.1
RSD (%)	6	6	9

R, correlation coefficient; LOD, limit of detection; the RSD was assessed from repeated runs of one of the calibration standards, 84 ng mL^{-1} for Seronorm and 55 ng mL^{-1} for aqueous standard.

Table 4
Comparison of characteristics between conventional ICP-MS and LA-ICP-MS.

	Conventional ICP-MS [8,9,17–21]	The proposed method
Sample preparation	Laborious	Simple
Quantification possibility	Excellent	Excellent
Detection limits	0.008–4.82 ng mL^{-1}	0.1–2.0 ng mL^{-1}
Amount of analyte/sample	100–1000 µL	0.5 µL
Precision	<10%	<10%
Analysis time	Longer	Shorter
Contamination risk	High	Low

method, the calibration curve was linear from 0 to 503 ng mL^{-1}, while with the aqueous standard calibration method, it was linear from 0 to 588 ng mL^{-1}. Limit of detection calculated as three times the standard deviation of the blank PTFE filter was presented in Table 3. Chronic whole blood lead concentrations <10 µg dL^{-1} (100 ng mL^{-1}) are considered acceptable in children from CDC. The ^{208}Pb detection limit in this method was only 0.1 ng mL^{-1}, which is suitable for blood lead level determination in children.

3.4. Comparison with conventional method

Unlike other direct solid sample analysis methods such as X-ray fluorescence (XRF), the proposed method has excellent perfor-mance in Pb blood sample determination that can be rapidly analyzed quantitatively with an error less than 10%. In comparison to the conventional ICP-MS, time-consuming sample preparation steps can be avoided and the risk of contamination significantly reduced. This is of great importance for the blood sample analysis. A comparison between the conventional ICP-MS and proposed LA-ICP-MS for Pb blood sample determination is listed in Table 4. A major advantage of the proposed method is the sample amount minimization to only 0.5 µL which is easy to sample from a finger or heel stick in children.

A comparison of the proposed analytical procedure with other blood lead determination techniques is summarized in Table 5. The sensitivity of this procedure has been significantly improved comparing with those of the blood filter sampling techniques [22,23,26,32]. The proposed method provides data which is comparable in detection limit to other analytical techniques but with

Table 5
Comparison of different analytical techniques for determination of blood lead.

Methods/sample pretreatments	Sample amount	LOD, ng mL^{-1}	RSD (%)/ng mL^{-1}	Ref.
ETAAS				
Microwave digestion	2 mL	1.2		5
High-pressure bomb digestion	5 mL	25–116[a]	7.0–11.8[b]	6
Proteins precipitation and dilution	200 µL	0.65	1.5–13.0[b]	7
Dilution		15	6.0–14.0 (50)[c]	10
Sequential injection HG-AFS				
Wet digestion	50 µL	0.014	0.7 (2.0)[c]	11
Flow injection HG-AFS				
Wet digestion and then on-line resin column preconcentration	50 µL	0.004	1.6 (0.4)[c]	12
ICP-MS				
Wet digestion	1 mL	0.1	1.1	8
Dilution	200 µL	0.5	1.35 (35)[c]	9
Flow injection ICP-MS				
Dilution		0.1	6.0 (5)[c]	17
HR-ICP-MS				
Microwave digestion	1 mL	0.085	<10.0[b]	20
DRC-ICP-MS				
Proteins precipitation and dilution		0.38	3.8 (78)[c]	18
Dilution	100 µL	4.82		19
Dilution	500 µL	0.008[d]	1.7 (89)[c]	21
FAAS				
Ashing of the punched blood filter paper	20 µL	40[d]		22
ETAAS				
Extraction of the punched blood filter paper	50 µL	10.4	14.0 (125)[c]	23
Direct sampling of the punched blood filter paper	50–100 µL	2.5	<10.0[b]	26
LA-ICP-TOF-MS				
Direct sampling of the blood filter paper		9	3.0–13.0	32
This procedure/LA-ICP-MS				
Direct sampling	0.5 µL	0.1	<10.0[b]	

[a] ng g^{-1}.
[b] For all results.
[c] Concentration level at which the RSD value was obtained.
[d] Limit of quantification; HR, high resolution; DRC, dynamic reaction cell.

the additional advantage of direct sampling. Furthermore, most analytical techniques involved time-consuming sample preparation steps include removing a portion of the solid sample or digestion [5–8,11,12,20,22]. Although analysis of blood by ICP-MS after simple dilution is possible [9,17–19,21], the high content of organic components remaining in the samples may cause problems with carbon buildup in the interference, on cones and in the introduction system. Even when flow injection is used for sample introduction, daily cleaning of the torch is necessary [17]. Both matrix-matched calibration and self-prepared aqueous standard calibration method can be applied for this method, which makes it a throughput of 75 specimens in an 8 h daily work.

4. Conclusions

The analytical methodology proposed here allows a rapid Pb determination in blood samples using LA-ICP-MS without acid digestion or melting of the samples. Micro-droplet blood samples and standards were prepared onto a hydrophobic PTFE filter. Under appropriate LA-ICP-MS operational conditions, the small dried blood spots on the filter membrane surface can be completely ablated and analyzed. Effective LA-ICP-MS blood sample Pb measurements calibration was performed by preparing series diluted aqueous standard solutions or blood standard reference materials on the filter membranes. The aqueous standard solution could be used as an alternative calibration standard to replace the expensive blood standard reference materials. Compared with the traditional methods, the proposed method offers several benefits including shortened sample preparation time, reducing the possibility of sample contamination and decreasing the possibility of analyte loss before analysis. A detection limit of less than $ng\,mL^{-1}$ can be easily achieved for Pb with only $0.5\,\mu L$ of blood sample. This is not difficult to collect from children using a finger or hell stick. This proposed procedure is very attractive for the screening of children to detect those with blood lead levels above the present threshold of concern ($10\,ng\,mL^{-1}$).

Acknowledgements

References

[1] Agency for Toxic Substances and Disease Registry (ATSDR), Toxicological Profile for Lead, U.S. Department of Health and Human Services, Public Health Service, Atlanta, GA, 2007.
[2] T.I. Lidsky, J.S. Schneider, Brain 126 (2003) 5.
[3] T.P. Moyer, D.N. Nixon, K.O. Ash, Clin. Chem. 45 (1999) 2055.
[4] Centers for Disease Control and Prevention (CDC), Preventing Lead Poisoning in Young Children, U.S. Department of Health and Human Services, Public Health Service, Atlanta, GA, 1991.
[5] A. Viitak, A.B. Volynsky, Talanta 70 (2006) 890.
[6] E.J. Daftsis, G.A. Zachariadis, Talanta 71 (2007) 722.
[7] F. Kummrow, F.F. Silva, R. Kuno, A.L. Souza, P.V. Oliveira, Talanta 75 (2008) 246.
[8] Z.W. Zhang, S. Shimbo, N. Ochi, M. Eguchi, T. Watanabe, C.S. Moon, M. Ikeda, Sci. Total Environ. 205 (1997) 179.
[9] C.D. Palmer, M.E. Lewis, C.M. Geraghty, F. Barbosa, P.J. Parsons, Spectrochim. Acta Part B 61 (2006) 980.
[10] Y. Zhou, R.A. Zanão, F. Barbosa, P.J. Parsons, F.J. Krug, Spectrochim. Acta Part B 57 (2002) 1291.
[11] J.H. Wang, Y.L. Yu, Z. Du, Z.L. Fang, J. Anal. At. Spectrom. 19 (2004) 1559.
[12] Z. Wan, Z.R. Xu, J.H. Wang, Analyst 131 (2006) 141.
[13] S. Jaenicke, R.M. Sabarathinam, B. Fleet, H. Gunasingham, Talanta 45 (1998) 703.
[14] B.J. Feldman, J.D. Osterloh, B.H. Hata, A. D'Alessandro, Anal. Chem. 66 (1994) 1983.
[15] D. Jagner, L. Renman, Y.D. Wang, Electroanalysis 6 (1994) 285.
[16] H.T. Delves, M.J. Campbell, J. Anal. At. Spectrom. 3 (1988) 343.
[17] E. Barany, I.A. Bergdahl, A. Schütz, S. Skerfving, A. Oskarsson, J. Anal. At. Spectrom. 12 (1997) 1005.
[18] D.E. Nixon, K.R. Neubauer, S.J. Eckdahl, J.A. Butz, M.F. Burritt, Spectrochim. Acta Part B 59 (2004) 1377.
[19] W.J. McShane, R.S. Pappas, V. Wilson-McElprang, D. Paschal, Spectrochim. Acta Part B 63 (2008) 638.
[20] I. Rodushkin, F. Ödman, S. Branth, Fresenius' J. Anal. Chem. 364 (1999) 338.
[21] P. Heitland, H.D. Köster, J. Trace Elem. Med. Biol. 20 (2006) 253.
[22] K. Verebey, Y.M. Eng, B. Davidow, A. Ramon, J. Anal. Toxicol. 15 (1991) 237.
[23] S.T. Wang, H.P. Demshar, Analyst 117 (1992) 959.
[24] H.Y. Yee, T.G. Holtrop, J. Anal. Toxicol. 21 (1997) 142.
[25] M.T. Di Martino, A. Michniewicz, M. Martucci, G. Parlato, Clin. Chim. Acta 350 (2004) 143.
[26] M. Resano, L. Rello, E. García-Ruiz, M.A. Belarra, J. Anal. At. Spectrom. 22 (2007) 1250.
[27] D.F. El-Hajjar, K.H. Swanson, J.D. Landmark, D.F. Stickle, Clin. Chim. Acta 377 (2007) 179.
[28] R.E. Russo, X.L. Mao, H.C. Liu, J. Gonzalez, S.S. Mao, Talanta 57 (2002) 425.
[29] S.F. Durrant, N.I. Ward, J. Anal. At. Spectrom. 20 (2005) 821.
[30] N.S. Mokgalaka, J.L. Gardea-Torresdey, Appl. Spectrosc. Rev. 41 (2006) 131.
[31] F. Boué-Bigne, B.J. Masters, J.S. Crighton, B.L. Sharp, J. Anal. At. Spectrom. 14 (1999) 1665.
[32] J.V. Cizdziel, Anal. Bioanal. Chem. 388 (2007) 603.
[33] J.S. Becker, Spectrochim. Acta Part B 57 (2002) 1805.

Automated nucleic acids isolation using paramagnetic microparticles coupled with electrochemical detection

Dalibor Huska [a,b], Jaromir Hubalek [c], Vojtech Adam [a,d], David Vajtr [e],
Ales Horna [f], Libuse Trnkova [g], Ladislav Havel [b], Rene Kizek [a,*]

[a] Department of Chemistry and Biochemistry, Mendel University of Agriculture and Forestry, Zemedelska 1, CZ-613 00 Brno, Czech Republic
[b] Department of Plant Biology, Mendel University of Agriculture and Forestry, Zemedelska 1, CZ-613 00 Brno, Czech Republic
[c] Department of Microelectronics, Faculty of Electrical Engineering and Communication, Brno University of Technology, Udolni 53, CZ-602 00 Brno, Czech Republic
[d] Department of Animal Nutrition and Forage Production, Faculty of Agronomy, Mendel University of Agriculture and Forestry, Zemedelska 1, CZ-613 00 Brno, Czech Republic
[e] Department of Clinical Biochemistry and Pathobiochemistry, 2nd Faculty of Medicine, Charles University, V Uvalu 84, CZ-150 06 Prague 5, Czech Republic
[f] Faculty of Technology, Tomas Bata University, T.G. Masaryka 275, CZ-762 72 Zlin, Czech Republic
[g] Department Chemistry, Faculty of Science, Masaryk University, Kotlarska 2, CZ-611 37 Brno, Czech Republic

ARTICLE INFO

ABSTRACT

Easy, efficient and low demanding separation of mRNA from biological material is needed to study gene expression and to use in chip technologies. It is common knowledge that each mRNA molecule contains sequence of 25 adenines. This feature can be used for binding mRNA on the surface of the particles coated by thymine chains. The present work reports on suggesting and optimizing of mRNA separation and detection from biological material via paramagnetic microparticles coupled with electrochemical detection. Primarily we optimized cyclic and square wave voltammetric conditions to detect poly(A), which was used as standard to mimic behaviour of mRNA. Under the optimized square wave voltammetric conditions (frequency 280 Hz, accumulation time 200 s, supporting electrolyte and its temperature: acetate buffer 4.6 and 35 °C) we estimated detection limit down to 1 ng of poly(A) per ml. To enhance effectiveness and repeatability of isolation of nucleic acid automated approach for rinsing and hybridizing was proposed. We optimized the whole procedure and experimental conditions. Using automated way of isolation and under optimized conditions the yield of poly(A) (isolated concentration of poly(A)/given concentration of poly(A)*100) was approximately 75%. The suggested and optimized method for poly(A) isolation and detection was utilized for the analysis of brain tissues of patients with traumatic brain injury. The total amount of isolated mRNA varied from 40 to 760 g of mRNA per g of brain tissue. The isolation of mRNA from six samples per run was not longer than 2.5 h. Moreover, we applied the optimized procedure on fully automated pipetting instrument to isolate mRNA. The instrument was successfully tested on the analysis of extracts from roots of maize plants treated with cadmium(II) ions.

© 2009 Elsevier B.V. All rights reserved.

1. Introduction

Simple, rapid and reproducible isolation of nucleic acids with high purity is needed in a wide range of molecularly biological procedures. We are able to obtain nucleic acids with sufficient purity by the most commonly used method based on phenol–chloroform extraction; however, the whole procedure is laborious and time consuming. Due to this fact methods and approaches have been developing to shorten the time of isolation and to obtain nucleic acids with sufficient purity to be analysed by polymerase chain reaction and other molecularly biological methods [1–4]. Nucleic acids isolation using paramagnetic or superparamagnetic particles (MPs) represents promising tool for this purpose [5–7]. MPs, whose size is ranging from nm to mm, respond to external magnetic field and facilitate bioactive molecules binding because of their affinity for the MPs modified surface made of biological components [8–11]. The paramagnetic properties of the particles enable us to use magnetic force for transferring of the beads or for rinsing of nonbinding, otherwise commonly interfering substances. Among other advantages of MPs easy-to-use, non-laborious relatively rapid sample preparation without centrifugation and dialysis compared to conventional purification techniques belong. The time needed to get target biomolecule is also reduced due to the fact that binding of the biomolecule by MPs can protect it against physical and biological damage, e.g. denaturation [12]. Physico-chemical prop-

erties of MPs (e.g. their size, surface topography) are important to evaluate their usage in biology [13–21]. The mostly used MPs in biosensors applications are superparamagnetic nanoparticles composed of ferrous oxide or ferric oxide [22]. Small particles with size from 1 to 10 nm are paramagnetic, but larger particles (mm) are ferromagnetic.

Nanoparticles have a lot of physico-chemical advantages [23,24]. Their size can be adapted to the extension and kind of a biological sample, which is a source of target biomolecules (e.g. proteins 5–50 nm, viruses 20–450 nm, cells 10–100 μm) [15,25,26]. Nanoparticles from ferric oxide also provide surface suitable for biomolecules binding. Methods of magnetic particles synthesis are largely discussed [9]. There are two ways to find how MPs can be modified. The first way is based on electric envelope layer for electrostatic adsorption of biomolecules. This method compared to conventional methods enables to avoid organic solvents. Matsunaga et al. modified the surface of MPs using electrically positive amino groups. Isolation was based on mutual electrostatic activities between negatively charged DNA and positively charged MPs [27]. The second way of paramagnetic particles surface modification is based on biomolecules anchored on particles. These biomolecules specifically bind target biomolecules [28–30]. On this method it is based also mRNA isolation. Oligo(deoxythymine)$_{25}$ anchored on the surface of MPs can be hybridized to mRNA molecule due to the presence of single chain sequence of tens adenines at the very end of all mRNA molecules [29].

MPs are commonly coupled with optical detection including fluorescent dyes. In addition, the isolated molecules can also be detected by electrochemical methods [28,31–35]. The main aim of this work was to automate isolation of mRNA using paramagnetic microparticles and detect the isolated nucleic acids by cyclic and square wave voltammetry both coupled with adsorptive transfer technique.

2. Materials and methods

All chemicals of ACS purity used and parafilm were purchased from Sigma–Aldrich Chemical Corp. (Sigma–Aldrich, USA) unless noted otherwise. Synthetic polyadenylic acid (poly(A)) was used as a standard. Stock standard solution of poly(A) (100 μg/ml) was prepared from lyophilized poly(A) (0.5 mg/ml, Mr = 400,000) with water of ACS purity (Sigma–Aldrich) and stored in dark at $-20\,^{\circ}$C. The concentration of poly(A) was determined spectrophotometrically at 260 nm using spectrometer Spectronic Unicam (UK). The pH values were measured using WTW inoLab Level 3 with terminal Level 3 (Weilheim, Germany). All the chemicals used for the preparation of plant cultivation media were purchased from Duchefa (Netherlands).

2.1. Instrumentation for poly(A) isolation

Isolation of poly(A) and mRNA was carried out using paramagnetic particles Dynabeads Oligo (dT)25 (Invitrogen, USA) and magnetic stand Dynal Magnetic Particle Concentrator-S supplied by Dynal A.S (Norway). All experiments with paramagnetic particles were performed in RNA/DNA UV cleaner box UVT – S – AR (Biosan, Latvia). For centrifuging and vortexing of a sample multi-spin MSC-3000 centrifuge (Biosan, Latvia) placed in UV cleaner box was used. Denaturation was carried out at 85 $^{\circ}$C using the Thermomixer 5355 Comfort/Compact (Eppendorf, Germany).

The buffers used in our experiments were as follows: (a) phosphate buffer I: 0.1 M NaCl + 0.05 M Na_2HPO_4 + 0.05 M NaH_2PO_4; (b) phosphate buffer II: 0.2 M NaCl + 0.1 M Na_2HPO_4 + 0.1 M NaH_2PO_4; (c) acetate buffer: 0.2 M CH_3COOH + 0.2 M CH_3COONa. Hybridization solution: 100 mM Na_2HPO_4 + 100 mM NaH_2PO_4, 0.5 M NaCl,

0.6 M guanidinium thiocyanate, 0.15 M Trizma base adjusted by HCl on pH of 7.5.

2.2. Fully automated isolation of nucleic acids

Fully automated isolation was carried out on automated pipetting system epMotion 5075 (Eppendorf, Germany). The position of B4 is a magnetic separator (Promega). The positions of C1 and C4 can be thermostated (Epthermoadapter PCR96). The pipetting provides a robotic arm with adapters (TS50, TS300 and TS1000) and Gripper (TG-T). The samples are placed in the position B3 in adapter Ep0.5/1.5/2 ml. Module Reservoir is located in the position B1, where washing solutions and waste are available. The device is controlled by the ep*Motion* control panel. The tips are located in the A4 (ePtips 50), A3 (ePtips 300) and A2 (ePtips 1000) positions. PCR 96 plates are used. The resulting volumes of collected samples ranged from 10 to 30 μl depending on the procedure.

2.3. Electrochemical analysis

Electrochemical measurements were performed with AUTOLAB PGS30 Analyzer (EcoChemie, Netherlands) connected to VA-Stand 663 (Metrohm, Switzerland), using a standard cell with three electrodes. A hanging mercury drop electrode (HMDE) with a drop area of 0.4 mm^2 was employed as the working electrode. An Ag/AgCl/3 M KCl electrode served as the reference electrode. Glassy carbon electrode was used as the auxiliary electrode. For smoothing and baseline correction the software GPES 4.9 supplied by EcoChemie was employed. Cyclic voltammetric or square wave voltammetric measurements were carried out in the presence of acetate buffer pH 4 or 4.6. CV parameters were as follows: potential step 5 mV, scan rates 10, 20, 40, 80, 160 and 320 mV/s. Square wave voltammetry parameters: potential step 5 mV and frequency 280 Hz. The samples measured by cyclic and square wave voltammetry were deoxygenated prior to measurements by purging with argon (99.999%) saturated with water for 120 s. The temperature of supporting electrolyte was maintained by the flow electrochemical cell coupled with thermostat JULABO F12/ED (Labortechnik GmbH, Germany).

2.4. In vitro plants cultivation

Maize (*Zea mays* L.) F1 hybrid Gila was used in our experiments. Maize kernels were sterilized with sodium hypochlorite (5%, v/v), washed with water and germinated on wet filter paper in special vessels at 23 $\pm$ 2 $^{\circ}$C in dark. After seven days, each maize seedling was placed into glassy test-tube containing Murashige Skoog medium with gerlit [36] and with addition of Cd(II)-ethylenediaminetetraacetic acid (Cd(II)-EDTA, 0, 5, 10, 25, 50 and 100 μM). Plants grown without Cd(II)-EDTA (0 μM) were used as a control. These seedlings were cultivated in Versatile Environmental Test Chamber (MLR-350 H, Sanyo, Japan) for five days with 14 h long daylight per day (maximal light intensity was 70 lx) at a temperature 23.5–25 $^{\circ}$C and humidity 71–78%. Three plants each were harvested at certain time intervals (24, 48, 72, 96 and 120 h) during the experiment, and their roots were rinsed three times in distilled water and 0.5 M EDTA. In addition, each harvested plant was divided into leaves and roots. Fresh weight of the samples was measured immediately after the rinsing by using a Sartorius scale.

2.5. Preparation of plant tissues for mRNA isolation

Weighed plant tissues (approximately 0.2 g) were transferred to a test-tube, and liquid nitrogen was added. The samples were frozen to disrupt the cells. The frozen sample was transferred to mortar and grinding for 1 min. Then, 1000 μl of 0.2 M phosphate buffer (pH 7.2) was added to the mortar, and the sample was grinding

for 5 min. The homogenate was transferred to a new test-tube. The mixture was homogenised by shaking on a Vortex–2 Genie (Scientific Industries, New York, USA) at 4 °C for 30 min. The homogenate was centrifuged (14 000 × g) for 30 min at 4 °C using a Universal 32 R centrifuge (Hettich-Zentrifugen GmbH, Tuttlingen, Germany). Before the analysis the supernatant was filtered through a membrane filter (0.45 μm Nylon filter disk, Millipore, Billerica, Mass., USA).

2.6. Patients with brain disorders

We have investigated blood samples of patients with brain disorders. All patients ($n = 6$) received cranial computerized tomography (CT). Five patients were diagnosed as focal traumatic brain injury (TBI) according to the CT scan performed during admission, and one patient was diagnosed as cerebral stroke (sample 6CE). Four patients with TBI were submitted to neurosurgery (samples 1NM, 2SE, 3SEL, 4MA) due to expansive contusion with midline shift of more than 10 mm, and intra-cranial pressure elevation of more than 10 Torr, and one patient without expansive behaviour of contusion (sample 5HA) with suspicion on diffuse axonal injury. *Informed agreement:* The ethics committee at each institution approved this study Written informed consent was obtained from all patients. The group II of controls ($n = 6$) included patients with non-traumatic diagnosis.

2.7. Preparation of brain tissues for mRNA isolation

To the sample of brain tissue (approximately 200 mg of tissue, obtained from patients with serious brain injury) guanidinium thiocyanate (4 M, pH 7.5) was added. pH of this solution was adjusted by 1 M Tris–HCl to 7.5. The cells were lyzed by vortexing until the eye-observable precipitates disappeared. To the homogenate: (i) 50 μl 2 M of sodium acetate pH 4.1, (ii) 450 μl of phenol, (iii) 130 μl of chloroform:isoamyl alcohol (49:1, v/v) was added. This mixture was vortexed for 10–30 s until the emulsion was formed and then incubated for 15 min on ice. Then the sample was centrifuged for 15 min at 14,000 rpm, 4 °C. After the centrifugation the upper phase containing total RNA was collected. This phase was transferred to new test-tube prior to analysis by magnetic microparticles.

2.8. Statistical analyses

Data were processed using MICROSOFT EXCEL® (USA) and STATISTICA.CZ Version 8.0 (Czech Republic). Results are expressed as mean ± standard deviation (S.D.) unless noted otherwise (EXCEL®). Statistical significances of the differences between mRNA content in roots of plants treated with cadmium(II) ions and control plants were determined using STATISTICA.CZ. Differences with $p < 0.05$ were considered significant and were determined by using of one way ANOVA test (particularly Scheffeho test), which was applied for means comparison.

3. Results and discussion

More than 40 years ago Palecek discovered using oscillopolarography that nucleic acids gave two signals: (i) redox signal of adenine and cytosine, and (ii) oxidative signal of guanine [37–39]. Recently elimination voltammetry has been successfully utilized for resolution of reduction signal of adenine and cytosine [40–45]. Moreover it was published that cytosine, adenine, thymine and guanine gave signals at carbon electrodes [31,46,47]. Based on these promising milestones of electroanalysis of nucleic acids together with the fact that electrochemistry is still one of the most sensitive analytical technique, voltammetric methods can be considered as a suitable tool for the detection of nucleic acids [48–50].

3.1. Electrochemical optimization detection of poly(A)

3.1.1. Electrochemical behaviour of poly(A) investigated by adsorptive transfer technique in connection with cyclic voltammetry

Nucleic acids can be accumulated onto surface of HMDE easily. Therefore, it is possible to use adsorptive transfer technique for their detection. The description of this technique follows. A working electrode with well-defined surface due to unique physico-chemical properties of mercury is renewed (Fig. 1A,a). An analysed sample in very low volume (5 μl) is introduced onto parafilm (Fig. 1A,b). The working electrode is immersed into the sample and nucleic acid is adsorbed for the desired time of accumulation (Fig. 1A,c). Then the working electrode is rinsed in water of ACS purity and supporting electrolyte (Fig. 1A,d). Finally the working electrode with adsorbed nucleic acid is transferred into electrochemical cell with supporting electrolyte and analysed (Fig. 1A,e). The principle of poly(A) isolation by using of paramagnetic particles is shown in Fig. 1B. Nucleic acids with homo-adenine sequence (poly(A)) are captured by the particles with chains of homo-thymidine anchored on their surface. Due to the principle of complementarity of nucleic acid bases hybridization of poly(A) with homo-thymidines takes place (Fig. 1B,a). Non-specifically linked molecules due to other types of attractive forces are washed due to rinsing step. Hybridized poly(A) is cleaved by heat treatment (Fig. 1B,b). Then, the particles are forced by magnetic field and only poly(A) containing solution is collected (Fig. 1B,c). The collected solution is analysed (Fig. 1B,d).

Cyclic voltammetry is a commonly used method for the analysis of DNA [29,30,43]. The ammonium formiate is the most often used supporting electrolyte, but the mechanisms of electrode processes are still not clear. It is supposed that the supporting electrolyte provides proton, which is bound to DNA molecule and then the reduction of adenine and cytosine occurs. The dependence of the peak height of poly(A) (100 μg/ml) measured by cyclic voltammetry on scan rate was studied (Fig. 2A). The typical voltammograms of poly(A) measured at three scan rates (40, 80 and 160 mV/s) are shown in inset in Fig. 2A. The cyclic voltammetry gives well-developed symmetric reduction peaks within the potential range from −1.25 to −1.3 V. Peak height enhanced with increasing scan rate linearly according to the following equation $y = 74.943x + 6.0057$ and $R^2 = 0.9918$. Symmetry of the peak was poor at scan rate higher than 320 mV/s. Therefore we applied scan rate of 160 mV/s in the following experiments.

The time of nucleic acids accumulation onto the working electrode surface belongs to the one of the most important experimental conditions needs to be optimized. The sample (volume 5 μl) was accumulated onto the surface of HMDE for the 30, 60, 90, 120, 150, 180 and 210 s at open circuit. We found that the height of adenine peak enhanced with the time of accumulation up to 120 s, then gradually decreased (Fig. 2B). The observed decrease in adenine peak height at accumulation time higher than 120 s can be associated to length of poly(A) chains, which could form poly-layer structures on the surface of HMDE. The influence of the poly(A) concentration on the current response at the accumulation time of 120 s is shown in Fig. 2C. Redox signal of adenine was proportional to the concentration of poly(A) up to 35 μg/ml, then the signal enhanced slowly. The linear dependence was measured within the range from 0.4 to 25 μg/ml with equation $y = 1.204x + 888.5$, $R^2 = 0.992$ (Table 1). The obtained experimental data were repeatable very well with relative standard deviations 5.5% ($n = 5$).
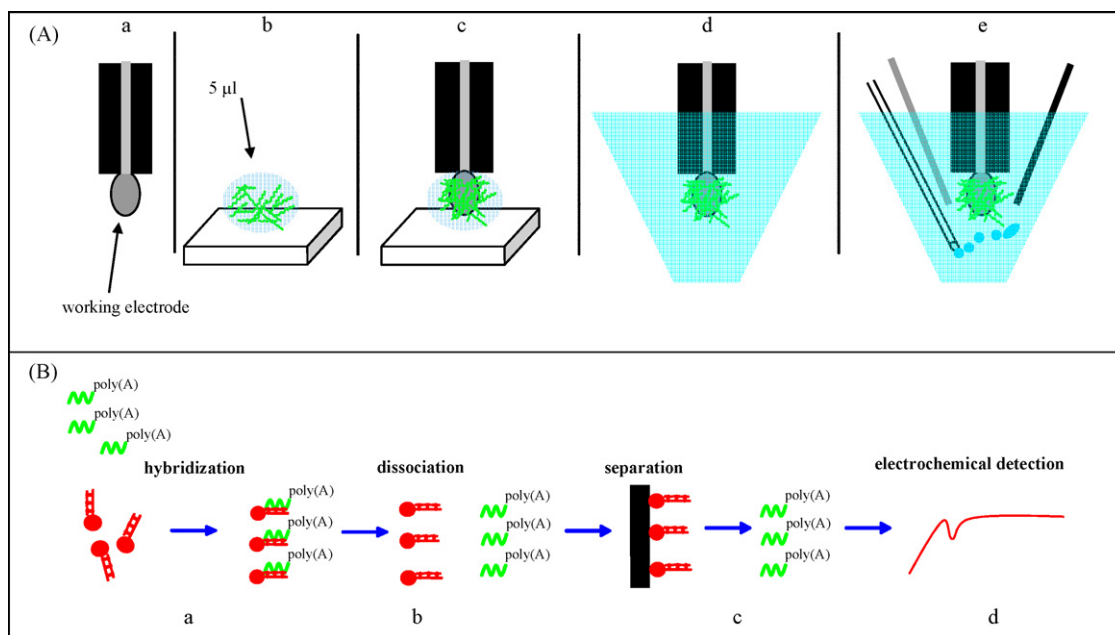
Fig. 1. (A) Electrochemical analysis of poly(A) and/or mRNA: (a) renewing of the hanging mercury drop electrode surface, (b) introducing of sample (5 µl) containing poly(A) and/or mRNA on parafilm, (c) adsorbing of poly(A) and/or mRNA in a drop onto the HMDE surface at open circuit, (d) rinsing electrode in water of ACS purity, (e) measuring in supporting electrolyte. (B) Scheme of poly(A) isolation by using of paramagnetic microparticles: (a) washing of the particles, adding of hybridization solution and a sample; (b) denaturation of hybridized nucleic acids chains at higher temperature; (c) forcing of the particles by magnetic field; (d) electrochemical detection an isolated nucleic acids.
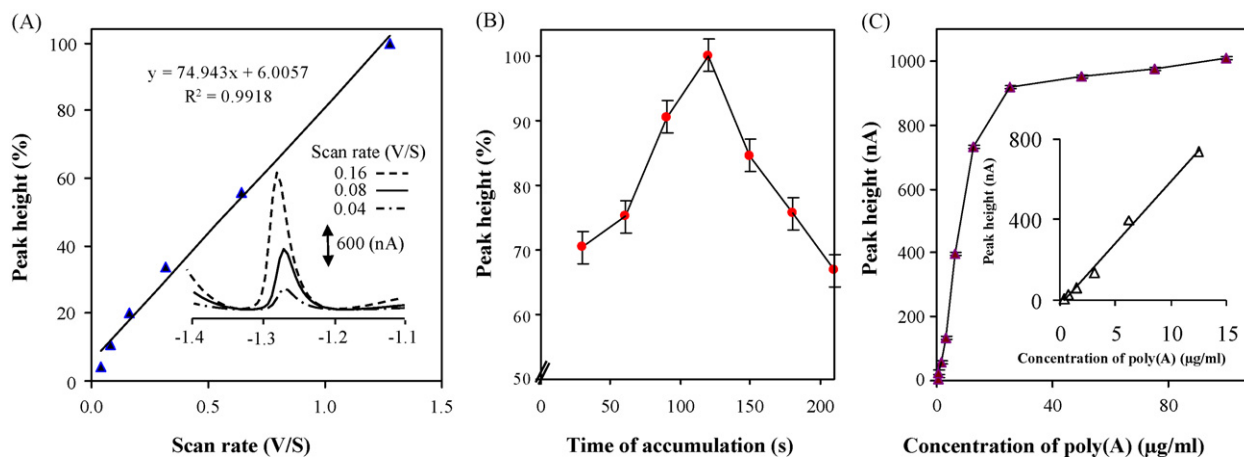
Fig. 2. Optimization of CV experimental parameters: the dependence of peak height on (A) scan rate, (B) time of accumulation and (C) concentration of poly(A). Concentration of poly(A): 100 µg/ml.

Table 1
Analytical parameters of poly(A) detection.

Data	Peak potential (V)[a]	Calibration curve (nA)	R^2	Linear dynamic range (µg/ml)	LOD (ng/ml)[b]	LOQ (ng/ml)[c]	R.S.D. (%)[d]
Poly(A)[e]	-1.4 ± 0.1	$I = 1.204c + 888.5$	0.9920	0.4–25	100	333	5.5
Poly(A)[120s][f,g]	-1.4 ± 0.1	$I = 56.91c + 7.14$	0.9973	0.2–25	1	3	3.9
Poly(A)[60s][f,g]	-1.4 ± 0.2	$I = 36.89c + 4.52$	0.9967	0.2–25	5	17	4.8
Poly(A)[30s][f,g]	-1.5 ± 0.2	$I = 19.86c + 6.67$	0.9917	0.2–25	10	33	6.8

I: peak current (in calibration curve).
c Poly(A) concentration (in calibration curve).
  [a] Measured vs. Ag/AgCl/3 M KCl electrode.
  [b] Limit of detection estimated (3 signal/noise, S/N) was calculated according to Long and Winefordner [56], whereas N was expressed as standard deviation of noise determined in the signal domain unless stated otherwise.
  [c] Limit of quantification estimated as (10 S/N) [56].
  [d] Relative standard deviation.
  [e] Poly(A) was measured by AdTS CV, time of accumulation 120 s.
  [f] Poly(A) was measured by AdTS SWV, time of accumulation as superscript.
  [g] Number of measurement ($n = 5$).

3.1.2. Electrochemical behaviour of poly(A) investigated by adsorptive transfer technique in connection with square wave voltammetry

Cyclic voltammetry is the most widely used technique for acquiring qualitative information about electrochemical reactions; however, it suffers from insufficient sensitivity and high detection limits. Therefore we selected much more sensitive method called square wave voltammetry (SWV) [51]. The comparison of poly(A) signals measured by CV and SWV is shown in Fig. 3A. The signal measured by CV was shifted for more than 50 mV to positive potentials. From the analytical point of view SWV signal was approximately two times higher compared to CV signal. Based on SW voltammetric analyses of DNA the highest current response was measured at 260 Hz [43,51]. We investigated the influence of frequency on poly(A) SWV signal (Fig. 3B). The highest signal was determined at a frequency of 280 Hz. Under higher frequencies the signal rapidly decreased. The difference between previously published value (260 Hz) and the optimized ones (280 Hz) can be probably associated with the influence of nucleic acids sequence. The dependence of peak height on accumulation time had similar trend compared to CV analyses with maximum measured at 200 s (Fig. 3C). Under higher accumulation times the peak height decreased. Further we focused our attention on studying the effect of temperature of supporting electrolyte on poly(A) signal. The highest peak was determined at 35 °C. Temperature higher than 40 °C resulted to the progressive destabilization of poly(A) molecule on the electrode surface. The increasing temperature enhances probability of irregular bases pairing (Fig. 3D). The significant role in nucleic acids detection also plays pH of supporting electrolyte. It clearly follows from the results obtained that the highest response

was measured in the presence of acetate buffer pH 4.6 (Fig. 3E). This phenomenon can be associated with the protonization of poly(A) molecule. Under the optimized conditions (frequency 280 Hz, accumulation time 200 s, supporting electrolyte and its temperature: acetate buffer 4.6 and 35 °C) we investigated the dependence of peak height on poly(A) concentration within the range from 0.02 to 12 μg/ml (Fig. 3F). The dependence was proportional to poly(A) concentration according to the equation $y = 56.91x + 7,14$, $R^2 = 0.9973$ with relative standard deviation 3.9% ($n = 5$). The detection limit of poly(A) was estimated as 1 ng/ml (2.5 pM). The other analytical parameters are shown in Table 1.

3.2. Semi-automated isolation of nucleic acids by using of paramagnetic particles

Analysis of nucleic acids represents still challenge for analytical chemistry and biochemistry especially in the field of RNA detection or determination of specific DNA sequences. From various types of RNAs mRNA is important due to the fact that relates with gene activity; however, their isolation is still laborious and time consuming. We utilized paramagnetic particles with homo-thymidine chain anchored on their surface for isolation of mRNA as it is shown in Fig. 1B. To enhance effectiveness and repeatability of isolation of nucleic acid automated approach for rinsing and hybridizing was proposed. The whole process is shown in Fig. 4. Paramagnetic particles (10 μl) are transferred with solution in which they are kept to a test-tube (A1). After this step the test-tube is placed to magnetic stand that separates paramagnetic particles from the solution of storage (A2). The solution is then pipetted away and 20 μl of washing solution (phosphate buffer I) is added (A3). Further the
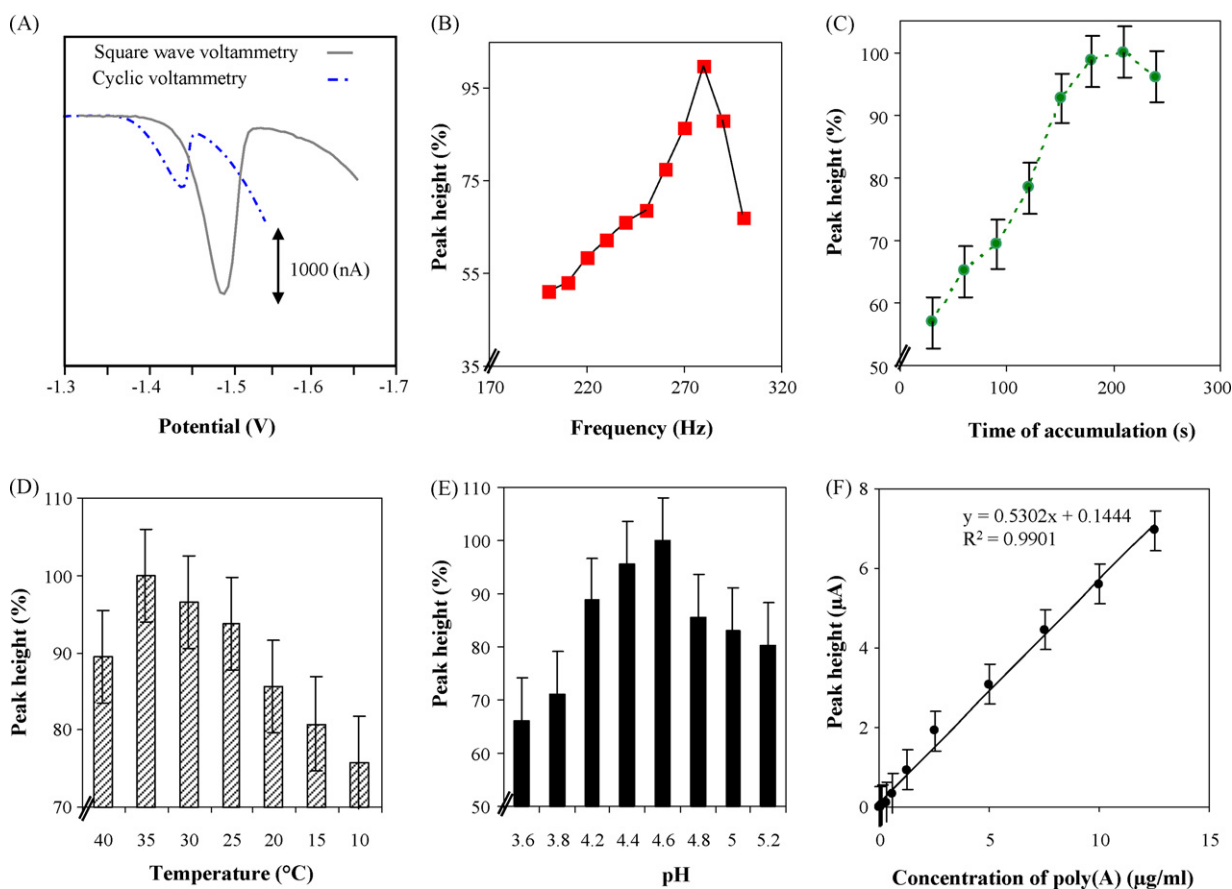
Fig. 3. (A) Cyclic and square wave voltammograms of poly(A). Optimization of SWV experimental parameters: the dependence of peak height on (B) frequency, (C) time of accumulation, (D) temperature of supporting electrolytes, (E) pH of acetate buffer and (F) concentration of poly(A). Concentration of poly(A) was 10 μg/ml except (F).
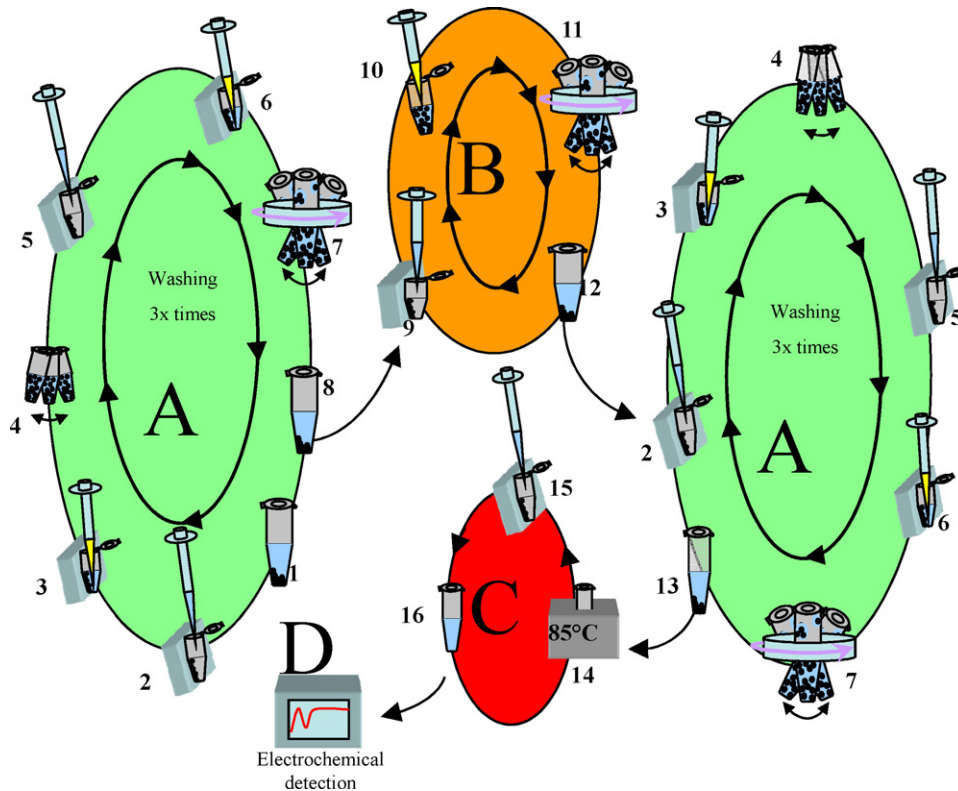
Fig. 4. Scheme of semi-automated isolation of poly(A): (A) rinsing before hybridization, (B) hybridization, (C) rinsing after hybridization, (D) denaturation and (E) detection.

test-tube is moved from magnetic stand and shortly shook in the hands so that the paramagnetic particles are equally dispersed in washing solution (A4). After this step the washing process is repeated (A5–A6). The washing with apparatus multi-spin MSC-3000, in which the centrifugation and shaking can be changed, follows. Shaking was set to level hard and lasted for 20 s; centrifugation proceeded at centrifugal force 285 g for 1 s (A7). Steps nos. A2–A7 are three times repeated. After paramagnetic particles being washed they are ready for nucleic acid isolation (process of hybridization). When the washing solution is removed (A8–B9), the hybridization solution is added to the paramagnetic particles. Total volume of the hybridization solution with the sample was 30 μl

(B10). The hybridization was proceeding on apparatus multi-spin MSC-3000 for the 40 min. The settings were as follows: 20 s of shaking (level soft) and centrifugation for 1 s at 285 g (B11). After the hybridization, the washing steps nos. A2–A7 were repeated three times. To the washed paramagnetic particles with bounded poly(A) phosphate buffer II (30 μl) was added (A13). Then the test-tube was placed in the Thermomixer 5355. Denaturation was carried out at 85 °C for 5 min (C14). Under heat treatment poly(A) is released from the particles. After this step, paramagnetic particles were forced using magnetic stand and the solution containing only mRNA was transferred into new test-tube (C15–C16). The solution is subsequently analysed (D).
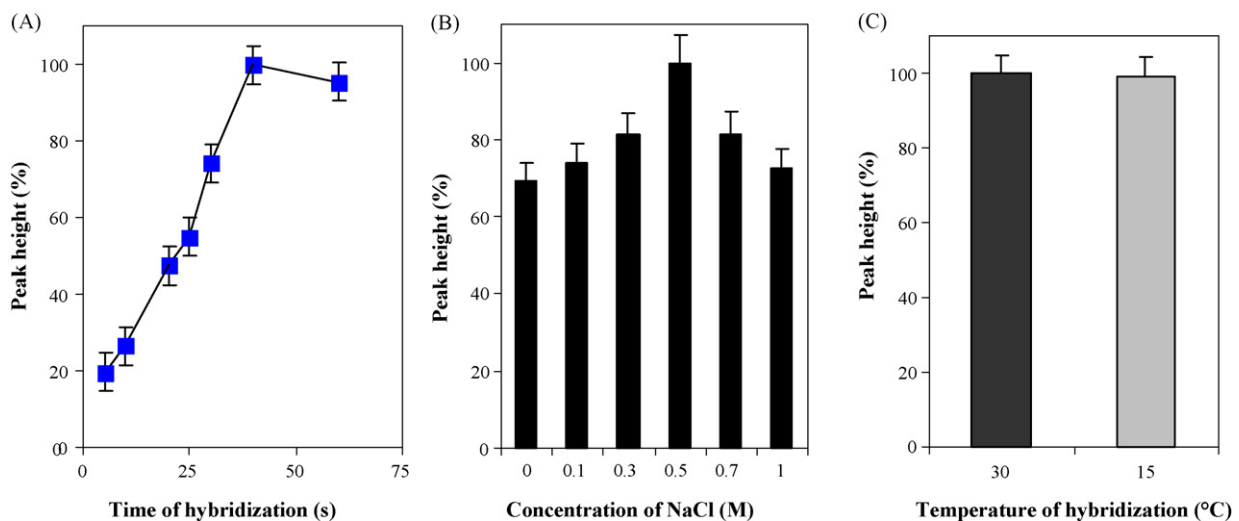
Fig. 5. Optimization of hybridization: (A) the dependence of hybridization time on poly(A) peak height, (B) the dependence of NaCl concentration on poly(A) peak height and (C) the dependence of temperature on poly(A) peak height.

3.2.1. Hybridization of poly(A) on paramagnetic particles

Hybridization of poly(A) to homo-thymine chains anchored on the surface of paramagnetic particles is the most important part of the whole isolation. Therefore we optimized experimental conditions to reach the highest yield of poly(A). There are many factors that affect the process of hybridization. The first parameter we investigated was length of hybridization. We found that the total amount of isolated poly(A) enhanced with increasing hybridization time. For the above-suggested semi-automated way of isolation (Fig. 4) the most suitable time for the most effective hybridization varied between 30 and 40 min (Fig. 5A). The yield of poly(A), which was defined as "isolated concentration of poly(A)"/"given concentration of poly(A)", was approximately 50% (n = 15). The ionic strength also markedly affects hybridization process. To mimic the influence of ionic strength on the hybridization we used NaCl. The highest peak was determined in the presence of 0.5 M NaCl (Fig. 5B). The differences in peaks measured in the presence of tested NaCl concentrations were not higher than 35%. Process of hybridization is also affected by temperature. In our experimental design it was possible to test two temperatures: 15 and 30 °C. Based on our results these two temperatures had no effect on the hybridization process (Fig. 5C).

Further we attempted to evaluate how the automation and optimization steps were effective (Fig. 6). The white columns show poly(A) (10, 50 and 90 μg/ml) detected without previous isolation. The development of peak heights corresponds to the typical concentration dependence shown in Fig. 3E. If we used the experimental procedure described by Palecek for poly(A) isolation [29], the yield was low (15%) with relative standard deviation 8%. Under the optimized conditions the yield of isolation enhanced up to 60% with relative standard deviation 10%. Using semi-automated way of isolation and under optimized conditions the yield was about 75% with the relative standard deviation below 6%. It clearly follows from the results obtained that automation step considerably reduced errors made by hand operating and thus enhanced yield of the isolation.

3.2.2. mRNA separation from samples of patients with traumatic brain injury

In many cases of traumatic injury there are no suitable markers available for the monitoring of brain damage and health state of the patients. S100B protein might be one of such markers [52–54]. Moreover, changes in gene expression profile a set of genes transcripts for cell cycle control, inflammation, cell proliferation and oxygen free radical scavenger proteins, growth inhibitory factor; metallothionein-III, p53 antigen, p53-induced protein, interleukins, TNF receptor associated death domain, and FAS soluble protein was shown in patients with traumatic brain injury [54]. To follow these changes sample of pure mRNA is needed. Not only the level of mRNA can be considered as one of the markers of traumatic brain injury, but also the isolated mRNA can be used for more specialized processing to detect specific sequence of a gene associated with traumatic brain injury. Moreover, the enhancing of mRNA level in few hours after traumatic brain injury was discussed [55]. The suggested and optimized methods for poly(A) isolation and detection was utilized for the analysis of brain tissues of six patients with traumatic brain injury. Traumatic damaging of brain tissue measured by nuclear magnetic resonance (abnormal signals are white-highlighted) is shown in inset in Fig. 7. mRNA was successfully isolated from all analysed samples by the semi-automated above-described method. Their quantity was determined by SWV. Well-developed peaks about −1.6 V were observed in the SW voltammograms shown in Fig. 7A. The total amount of the isolated mRNA varied from 40 to 760 μg of mRNA per g of brain tissue (Fig. 7B). Based on the spikes of poly(A) to real samples we investigated the influence of matrix on the electrochemical response of isolated mRNA. The recovery was within the interval from 94 to 115% (Table 2).

Fig. 6. The yield of isolation of various initial concentrations of poly(A) (10, 50 and 90 μg/ml).
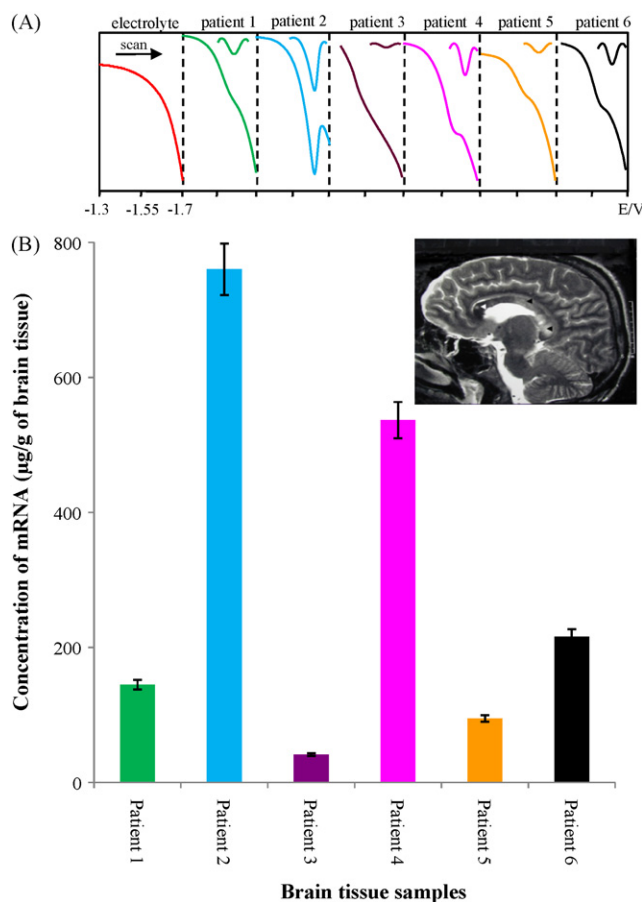
Fig. 7. mRNA separation from patients with traumatic brain injury. (A) Typical SW voltammograms of eluates (20 μl) obtained from the brain tissues. (B) The content of the isolated mRNA in brain tissues obtained from patients; inset: traumatic damaging of brain tissue measured by nuclear magnetic resonance.

Table 2
Detect mRNA vs. brain tissues.

Sample[a]	Peak current (nA)[b]	Peak potential (mV)[c]	Recovery (%)[d]
Patient 1	280 ± 20	−1.56 ± 0.02	105.5
Patient 2	205 ± 50	−1.59 ± 0.04	98.7
Patient 3	100 ± 5	−1.58 ± 0.03	94.6
Patient 4	1060 ± 20	−1.58 ± 0.02	110.8
Patient 5	220 ± 10	−1.56 ± 0.03	115.0
Patient 6	500 ± 20	−1.55 ± 0.02	108.8

[a] Each sample was measured in triplicates.
[b] The height of SWV signal after baseline correction (GPES 4.9, EcoChemie, Netherlands).
[c] Measured vs. Ag/AgCl/3 M KCl electrode.
[d] Addition of poly(A) (10 μg/ml) to a sample after isolation.

3.3. Fully automated separation of nucleic acids by using of paramagnetic particles

In the following experiments we have been carried out with fully automated isolation of poly(A) by using a robotic device epMotion (Fig. 8). Pipetting of liquids and moving of PCR plates provide *x*, *y*, *z* moving arm controlled by a microprocessor (Fig. 8A). The work sequence is shown in Fig. 8B. The eluate obtained is analysed electrochemically. For our purposes the following sequence was proposed: (i) paramagnetic microparticles (10 μl) are pipetted into the PCR plate; (ii) a washing cycle is three times repeated (50 μl); (iii) the sample (poly(A), (10 μl) and hybridization solution (30 μl) are pipetted into PCR plates with paramagnetic microparticles; (iv) 15 min long hybridisation is carried out at 25 °C; (v) a washing cycle is three times repeated (50 μl). The PCR plate is later on moved on thermostated position, where the denaturation of bound nucleic acid chain takes place. The yield of poly(A) separation (25 μg/ml) was 40% with R.S.D. 6.5% (*n* = 10). Fully automatic process leads to timesavings and, in particular, reduces experimental errors. Among the technical problems, which are still associated with the use of this procedure, the evaporation of the sample analysed belongs. We have been investigated the isolation of poly(A) on DBT and/or ROCHE magnetic microparticles by using of the fully automated technique. The yield of poly(A) isolated by DBT microparticles was approximately 40%. Using these microparticles the dependence of peak height on concentration of isolated poly(A) (0–100 μg/ml) was investigated and is shown in Fig. 9A. In inset of this figure, strictly linear part of this dependence is shown. The yield of poly(A) isolated by ROCHE microparticles was approximately 25%. Moreover the isolated amount of
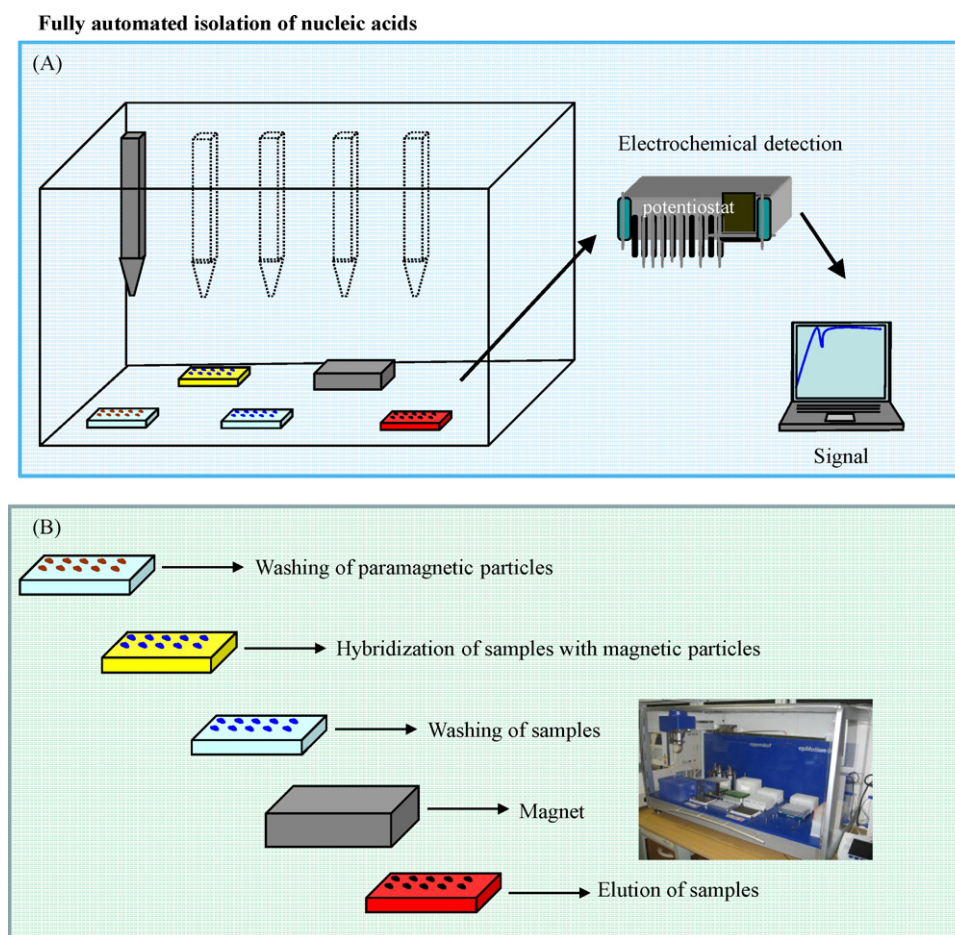
Fig. 8. Scheme of fully automated instrument for isolation of mRNA. (A) The arrangement of working tools. Electrochemical analyser is off-line connected. (B) Sequence of steps for the analysis of real samples.
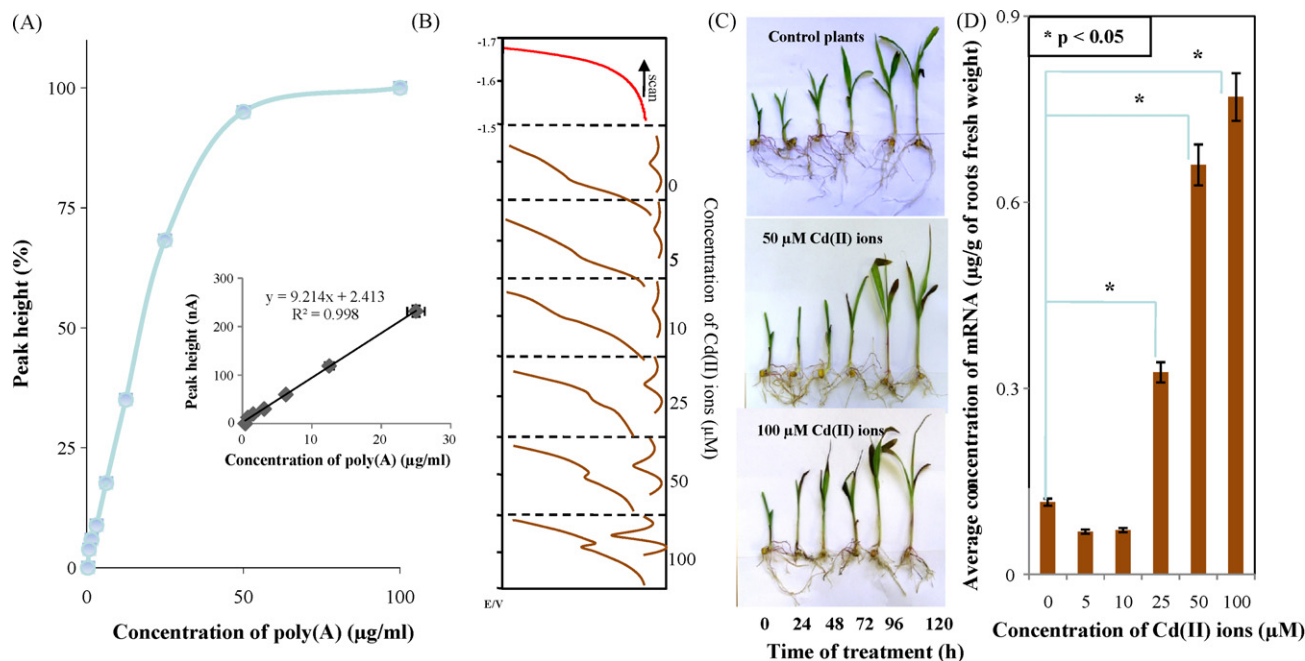
Fig. 9. (A) The dependence of height of poly(A) after its isolation by using fully automated instrument; inset: the linear part of this dependence. (B) Typical SW voltammograms of extracts from tissues of plants treated with cadmium(II) ions. (C) Photographs of maize plants treated with cadmium(II) ions (0, 50 and 100 μM). (D) The content of the isolated mRNA from roots extracts. *Differences with $p < 0.05$ were considered significant.

poly(A) was not proportional to the initial concentration of these molecules.

The method of fully automated isolation of mRNA was utilized for the analysis of tissues of maize plants exposed to cadmium(II) ions. Roots of the plants treated with particular concentration of cadmium(II) ions were sampling for five days. mRNA was isolated from the extract prepared from all roots belonging to one particular concentration of heavy metal. Typical voltammograms of the isolated mRNA are shown in Fig. 9B. In all samples it was possible to detect mRNA. Photographs of maize plants treated with cadmium(II) ions are shown in Fig. 9C. It follows from the photographs that plants are loosing weight in roots, leaf surface is reduced and content of chlorophyll is decreased with the increasing concentration of cadmium(II) ions and time of the exposition. All of these negative processes lead to the gradual exhaustion of a plant. We found that the average level of mRNA in samples decreased slightly in the lower concentrations applied. Since the applied concentration of 25 μM, the significant increase of mRNA levels was observed (Fig. 9D). The dramatic increase in mRNA levels can be associated with the increased metabolic activity in plants of maize to overcome the adverse effects of heavy metal ions.

4. Conclusion

We succeeded in suggestion, optimization and automation of the method for mRNA isolation using paramagnetic microparticles. The main advantage of our method is its rapidity. The isolation of mRNA from six samples per run is not longer than 2.5 h. The proposed method was tested on brain tissues and maize roots.

References

[1] M.J. Archer, B.C. Lin, Z. Wang, D.A. Stenger, Anal. Biochem. 355 (2006) 285.
[2] L. Cler, D.W. Bu, C. Lewis, D. Euhus, Mol. Cell. Probes 20 (2006) 191.
[3] S. Dubus, J.F. Gravel, B. Le Drogoff, P. Nobert, T. Veres, D. Boudreau, Anal. Chem. 78 (2006) 4457.
[4] J.S. Ki, K.B. Chang, H.J. Roh, B.Y. Lee, J.Y. Yoon, G.Y. Jang, J. Biosci. Bioeng. 103 (2007) 242.
[5] C. Becker, M. Hodenius, G. Blendinger, A. Sechi, T. Hieronymus, D. Muller-Schulte, T. Schmitz-Rode, M. Zenke, J. Magn. Magn. Mater. 311 (2007) 234.
[6] Z.J. Cao, Z.X. Li, Y.J. Zhao, Y.M. Song, J.Z. Lu, Anal. Chim. Acta 557 (2006) 152.
[7] C.H. Chiou, Y.Y. Huang, M.H. Chiang, H.H. Lee, G.B. Lee, Nanotechnology 17 (2006) 1217.
[8] N. Jaffrezic-Renault, C. Martelet, Y. Chevolot, J.P. Cloarec, Sensors 7 (2007) 589.
[9] D.K. Kim, Y. Zhang, W. Voit, K.V. Rao, M. Muhammed, J. Magn. Magn. Mater. 225 (2001) 30.
[10] T. Kinoshita, S. Seino, Y. Mizukoshi, T. Nakagawa, T.A. Yamamoto, J. Magn. Magn. Mater. 311 (2007) 255.
[11] E. Palecek, M. Fojta, Talanta 74 (2007) 276.
[12] S.W. Yeung, I.M. Hsing, Biosens. Bioelectron. 21 (2006) 989.
[13] M.A.M. Gijs, Microfluid Nanofluid 1 (2004) 22.
[14] R. Heer, M. Eggeling, J. Schotter, C. Nohammer, R. Pichler, M. Mansfeld, H. Bruckl, J. Magn. Magn. Mater. 311 (2007) 244.
[15] I.M. Hsing, Y. Xu, W.T. Zhao, Electroanalysis 19 (2007) 755.
[16] L. Lagae, R. Wirix-Speetjens, C.X. Liu, W. Laureyn, G. Borghs, S. Harvey, P. Galvin, H.A. Ferreira, D.L. Graham, P.P. Freitas, L.A. Clarke, M.D. Amaral, IEE Proc. Circ. Dev. Syst. 152 (2005) 393.
[17] N. Minc, C. Futterer, K. Dorfman, A. Bancaud, C. Gosse, C. Goubault, J.L. Viovy, Anal. Chem. 76 (2004) 3770.
[18] O. Mykhaylyk, D. Vlaskou, N. Tresilwised, P. Pithayanukul, W. Moller, C. Plank, J. Magn. Magn. Mater. 311 (2007) 275.
[19] P.I. Nikitin, P.M. Vetoshko, T.I. Ksenevich, J. Magn. Magn. Mater. 311 (2007) 445.
[20] L. Pichl, A. Heitmann, P. Herzog, J. Oster, H. Smets, V. Schottstedt, Transfusion 45 (2005) 1106.
[21] A. Revyakin, R.H. Ebright, T.R. Strick, Nat. Met. 2 (2005) 127.
[22] A.F. Ngomsik, A. Bee, M. Draye, G. Cote, V. Cabuil, C. R. Chim. 8 (2005) 963.
[23] T. Lund-Olesen, M. Dufva, M.F. Hansen, J. Magn. Magn. Mater. 311 (2007) 396.
[24] O. Lunov, S. Bespalova, V. Zablotskii, J. Magn. Magn. Mater. 311 (2007) 162.
[25] C.J. Xu, S.H. Sun, Polym. Int. 56 (2007) 821.
[26] C.H. Yu, C.C.H. Lo, K. Tam, S.C. Tsang, J. Phys. Chem. C 111 (2007) 7879.
[27] T. Matsunaga, M. Kawasaki, X. Yu, N. Tsujimura, N. Nakamura, Anal. Chem. 68 (1996) 3551.
[28] M. Fojta, L. Havran, S. Billova, P. Kostecka, M. Masarik, R. Kizek, Electroanalysis 15 (2003) 431.
[29] E. Palecek, S. Billova, L. Havran, R. Kizek, A. Miculkova, F. Jelen, Talanta 56 (2002) 919.
[30] E. Palecek, R. Kizek, L. Havran, S. Billova, M. Fojta, Anal. Chim. Acta 469 (2002) 73.
[31] V.C. Diculescu, A.M.C. Paquim, A.M.O. Brett, Sensors 5 (2005) 377.
[32] M. Fojta, L. Havran, R. Kizek, S. Billova, Talanta 56 (2002) 867.
[33] R. Kizek, L. Havran, M. Fojta, E. Palecek, Bioelectrochemistry 55 (2002) 119.
[34] O. Korbut, M. Buckova, J. Labuda, P. Grundler, Sensors 3 (2003) 1.

[35] J. Wang, A.N. Kawde, A. Erdem, M. Salazar, Analyst 126 (2001) 2020.
[36] T. Murashige, F. Skoog, Physiol. Plant 15 (1962) 473.
[37] E. Palecek, Collect. Czech. Chem. Commun. 25 (1960) 2283.
[38] E. Palecek, Naturwissenschaften 45 (1958) 186.
[39] E. Palecek, Biochem. Moscow 25 (1960) 619.
[40] R. Mikelova, L. Trnkova, F. Jelen, V. Adam, R. Kizek, Electroanalysis 19 (2007) 348.
[41] L. Trnkova, F. Jelen, J. Petrlova, V. Adam, D. Potesil, R. Kizek, Sensors 5 (2005) 448.
[42] L. Trnkova, F. Jelen, I. Postbieglova, Electroanalysis 18 (2006) 662.
[43] L. Trnkova, R. Kizek, O. Dracka, Electroanalysis 12 (2000) 905.
[44] L. Trnkova, R. Kizek, O. Dracka, Bioelectrochemistry 55 (2002) 131.
[45] L. Trnkova, I. Postbieglova, M. Holik, Bioelectrochemistry 63 (2004) 25.
[46] A.M.O. Brett, A.M. Chiorcea, Electrochem. Commun. 5 (2003) 178.
[47] F.C. Abreu, M.O.F. Goulart, A.M.O. Brett, Biosens. Bioelectron. 17 (2002) 913.
[48] D.F. Colgan, J.L. Manley, Genes Dev. 11 (1997) 2755.
[49] J.L. Manley, Biochim. Biophys. Acta 950 (1988) 1.
[50] N.J. Proudfoot, A. Furger, M.J. Dye, Cell 108 (2002) 501.
[51] M. Tomschik, F. Jelen, L. Havran, L. Trnkova, P.E. Nielsen, E. Palecek, J. Electroanal. Chem. 476 (1999) 71.
[52] M. Rothermundt, M. Peters, J.H.M. Prehn, V. Arolt, Microsc. Res. Tech. 60 (2003) 614.
[53] D. Vajtr, R. Prusa, J. Kukacka, L. Houstava, F. Samal, J. Pachl, J. Pazout, Cesk. Slov. Neurol. Neurochir. 70 (2007) 515.
[54] J. Kukacka, D. Vajtr, D. Huska, R. Prusa, L. Houstava, F. Samal, V. Diopan, K. Kotaska, R. Kizek, Neuroendocrinol. Lett. 27 (2006) 116.
[55] S.A. Dutcher, B.D. Underwood, P.D. Walker, F.G. Diaz, D.B. Michael, Neurol. Res. 21 (1999) 234.
[56] G.L. Long, J.D. Winefordner, Anal. Chem. 55 (1983) A712.

The use of Artificial Neural Networks for the selective detection of two organophosphate insecticides: Chlorpyrifos and chlorfenvinfos

Georges Istamboulie, Montserrat Cortina-Puig, Jean-Louis Marty, Thierry Noguer *

Université de Perpignan Via Domitia, IMAGES EA4218, Centre de Phytopharmacie, 52 Avenue Paul Alduy, 66860 Perpignan Cedex, France

ARTICLE INFO

ABSTRACT

Amperometric acetylcholinesterase (AChE) biosensors have been developed to resolve mixtures of chlorpyrifos oxon (CPO) and chlorfenvinfos (CFV) pesticides. Three different biosensors were built using the wild type from electric eel (EE), the genetically modified *Drosophila melanogaster* AChE B394 and B394 co-immobilized with a phosphotriesterase (PTE). Artificial Neural Networks (ANNs) were used to model the combined response of the two pesticides. Specifically two different ANNs were constructed. The first one was used to model the combined response of B394 + PTE and EE biosensors and was applied when the concentration of CPO was high and the other, modelling the combined response of B394 + PTE and B394 biosensors, was applied with low concentrations of CPO. In both cases, good prediction ability was obtained with correlation coefficients better than 0.986 when the obtained values were compared with those expected for a set of six external test samples not used for training.

© 2009 Elsevier B.V. All rights reserved.

1. Introduction

Organophosphosphate (OP) compounds are highly powerful neurotoxics that act by inhibiting acetylcholinesterase (AChE) [1]. They are commonly used as insecticides and chemical warfare agents. Due to their high acute toxicity and risk towards the population, some European directives have been established to limit their presence in water and food resources. For instance, the council directive 98/83/CE concerning the quality of water for human consumption has set a maximum admissible concentration of 0.1 ppb (μg L^{-1}) per pesticide and 0.5 ppb for the total amount of pesticides.

Early detection of OP neurotoxins is a very important challenge for protecting water resources and food supplies, but also for defence against terrorist activity, and for monitoring detoxification processes. For that purpose, biosensors have been described for many years as being good candidates as substitutive or complementary tools to these conventional methods, since they can provide real-time qualitative information about the composition of a sample with minimum preparation [2–5]. Biosensors based on the inhibition of AChEs have been widely used for the detection of OP compounds. Among the numerous sensors described, some of them involve the use of recombinant AChEs allowing enhancing dramatically the sensitivity of these devices. Such sensors have been recently described in our group for the highly sensitive detection of two insecticides of interest: chlorpyrifos (CPO) and chlorfenvinfos (CFV), which are included in a list of priority substances in the field of water policy (decision 2455/2001/EC) [6]. Although these devices show a high sensitivity, they have been shown to be poorly adapted to the selective detection of insecticides.

To overcome this problem, we have recently described a biosensor associating a highly sensitive genetically-modified *Drosophila melanogaster* AChE (B394) with a phosphotriesterase (PTE) [7]. This latter enzyme has the ability to hydrolyse organophosphate compounds. It has already been used in other works as a target enzyme for the detection of parathion [8–11]. The developed device has been shown to allow the discriminative detection of CPO and CFV in a wide range of concentrations, providing that these two substances were not both present in the same sample [7]. When both CPO and CFV were present, it was shown that CFV induced a competitive inhibition of PTE, which in turn was unable to react with CPO. Consequently, a dramatic increase of the sensor inhibition was observed due to the non-degradation of CPO [7]. This feature complicated dramatically the selective detection of these pesticides.

The aim of this work is therefore to improve the selectivity of the previously described sensors by employing sensor arrays and chemometric data analysis. Artificial Neural Networks (ANNs) were used to model the combined response of the two pesticides using sensors incorporating wild-type electric eel AChE and drosophila mutant AChE, associated or not with PTE. These two types of AChEs were selected according to their different sensitivities to OP insecticides [6,7].

---

* Corresponding author.
  E-mail address: noguer@univ-perp.fr (T. Noguer).

2. Materials and methods

2.1. Chemicals and stock solutions

Genetically-modified AChE from *D. melanogaster* type B394 was produced by Protein Bio Sensor (PBS, Toulouse, France) and AChE (EC 3.1.1.7) from electric eel (EE) (Type V-S, 1000 U/mg) was purchased from Sigma–Aldrich (Switzerland). Acetylthiocholine chloride (ATChCl), acetylthiocholine iodide (ATChI) and 5,5′-dithiobis(2-nitrobenzoic acid) (DTNB-Ellman's reagent) were provided by Sigma.

In order to minimize hydrolysis, ATChCl and ATChI solutions were prepared daily in 0.9% NaCl (Sigma–Aldrich, Switzerland) solution. Stock solutions of enzymes and DTNB were prepared in 0.1 M phosphate buffer (Na_2HPO_4/KH_2PO_4, Sigma–Aldrich, Switzerland) at pH 8. CPO, CFV and Paraoxon were purchased from Chem Service (West Chester, PA, USA). Pesticide stock solutions were prepared in acetonitrile (Carlo Erba, Italy) and working pesticide solutions were prepared daily in distilled water by dilution from the stock solution. Silver (Electrodag PF 410), graphite (Electrodag 423 SS) and silver/silver chloride (Electrodag 418SS) inks were obtained from Acheson (Plymouth, UK). Cobalt-phtalocyanine-modified carbon paste was purchased from Gwent Electronic Materials, Ltd. (Gwent, UK). Poly(vinyl)chloride (PVC) sheets (200 mm × 100 mm × 0.5 mm), supplied by SKK (Denzlingen, Germany), were used as support for the screen-printed electrodes. A glycerophthalic paint (Astral, France) was used as insulating layer. The photocrosslinkable polymer poly(vinyl alcohol) PVA-AWP (Toyo Gosei, Japan) was used for immobilization of enzymes.

2.2. Determination of enzymes activity

Spectrophotometric measurements were performed using a Hewlett Packard diode array 8451A spectrophotometer.

The AChE activities were measured spectrophotometrically as described previously [12]. PTE activity was measured in 10 mM phosphate buffer pH 8 using 1 mM of substrate (Paraoxon) by monitoring the formation of paranitrophenol at 405 nm [7].

2.3. Electrode preparation

Screen-printed three-electrode systems with Cobalt-phtalocyanine-modified carbon as working electrode, graphite as counter electrode and Ag/AgCl as reference electrode (on Ag conductive tracks), were fabricated using a DEK248 screen-printing system (Weymouth, UK).

The immobilization of enzymes was performed by physical entrapment in a poly(vinyl alcohol)-based photopolymer (AWP), as described in previous works [6,7]. AWP polymer was mixed with enzymatic solution in a ratio 70:30% (v/v). The mixture was vortex-mixed and briefly centrifuged to eliminate the foam. A volume of 3 μL was then spread onto the working electrode using a micropipette. The concentration of the initial AChE solutions was adjusted in order to obtain a final enzyme loading of 1 mU/biosensor. The electrodes were then exposed for 3 h under a neon lamp (15 W) at 4 °C to carry out photopolymerization and were ready to use after drying for 48 h at 4 °C.

Three different types of biosensors were fabricated by depositing wild AChE from EE, genetically modified AChE B394, and B394 co-immobilized with PTE (0.85 IU/biosensor).

2.4. Amperometric measurements

The activity of AChEs immobilized on the electrodes was determined by electrochemically monitoring the thiocholine formed upon enzymatic hydrolysis of ATChCl. Amperometric measurements were carried out using a 641VA potentiostat (Metrohm,

Switzerland), connected to a BD40 (Kipp & Zonen, The Netherlands) flatbed recorder. As described in previous works [6,7], the applied potential was 100 mV vs. a printed Ag/AgCl reference electrode, using cobalt-phtalocyanine as a mediator. In order to make amperometric measurements, the biosensor strip was vertically inserted into an analytical cell containing 10 mL of phosphate buffer pH 8 under constant magnetic stirring (250 rpm) at constant temperature (30 °C).

The pesticide detection was made in a three-step procedure as follows: first, the initial response of the electrode to the substrate ATCh (1 mM) was recorded three times, then the electrode was incubated for 10 min in a solution containing a known concentration of insecticides, and finally the residual response of the electrode was recorded again. Electrodes were cleaned between each measurement. The percentage of the inhibition was correlated with insecticide concentration.

2.4.1. Biosensor characterization and kinetic study of the immobilized enzyme

The stability of the sensors needs to be evaluated in order to ensure that the decrease in the signal during inhibition measurements is due to enzyme inactivation and not to enzyme leaking. The operational stability of immobilized AChE (EE, B394) was estimated by successively measuring the response of the same enzyme electrode to 1 mM ATCh, at 100 mV vs. Ag/AgCl. The PTE stability was estimated by measuring the sensor response to 1 mM paraoxon using the same enzyme electrode at 700 mV vs. Ag/AgCl. The sensors were washed between tests with distilled water. All three types of sensors were shown to be stable for at least 10 consecutive measurements. The biosensors based on AWP-entrapment presented a good reproducibility, with a signal maximum variation of 5%. The average response to 1 mM ATCh for $n = 5$ electrodes prepared in the same experimental conditions was 290 ± 15 nA for biosensors with B394 (without or with PTE) and 245 ± 10 nA for biosensors with EE. These reproducibility data refers to the mean value of 10 assays for each electrode.

2.4.2. ANN modelling

ANNs were used to model the combined response of the two pesticides studied from amperometric measurements. Calculations were made by developing the corresponding programs in MATLAB (MATLAB 6.1, Mathworks, USA) which employed its Neural Network Toolbox (Neural Network Toolbox 4.0.2, Mathworks, USA). The used ANNs were feedforward networks and were trained by employing back-propagation algorithms, viz. Bayesian Regularization (BR) [13].

In order to model the mixed response to CPO and CFV pesticides, a total amount of 66 mixed solutions were manually prepared, with values selected randomly. 33 of these mixed solutions were used with both EE and B394 + PTE biosensors, by using low concentrations of CFV together with high concentrations of CPO. The other 33 solutions were used with B394 and B394 + PTE biosensors, by using low concentrations of the two insecticides. The concentration ranges of these solutions were chosen according to results published in previous works [6,7]. Each set of 33 samples was divided into two subsets: (1) training: with 75% of total set (25 samples) which served to establish the response model; (2) test: with 25% of the set (8 samples) which served to evaluate the model's predictive ability.

3. Results and discussion

3.1. Amperometric inhibition measurements

Two different ANNs were constructed in order to evaluate different concentrations of CPO. On the one hand, the first ANN (ANN_1)

was used to model the combined response of the B394 + PTE and EE biosensors and was applied when the concentration of CPO was high. On the other hand, the combined response of B394 + PTE and B394 biosensors was modelled by means of the second ANN (ANN$_2$), used with low concentrations of CPO.

As previously specified, two sets of 33 mixed solutions of CFV and CPO were freshly prepared for the building of the two response models. In the first set, the range concentration for CFV was 0.01–1.01 nM and for CPO it was 3.00–303 nM. In the second set, concentrations ranged from 0.08 to 8.08 nM for CFV and 0.0018 to 0.35 nM for CPO. Each set of solutions was randomly subdivided in two different subsets (viz. training and test) needed for the correct training of the network. One single precaution was taken, which was to reserve the extreme values for the training subset, in order to avoid the adjusted ANN to extrapolate these points out of the obtained model.

The used ANN architecture was exhaustively studied from an initial configuration using a single hidden layer [14]. In each case, the percentage of inhibition after 10 min incubation in each mixed solution of pesticides was used as the input information to the ANN. Thus the number of neurons at the input layer equalled the number of biosensors used in each ANN, two. Analogously, as there were two concentrations sought, the output layer was formed by two output neurons. The number of neurons at the hidden layer was determined by trial and error seeking the optimal modelling ability of the ANN.

On basis of our previous experience, some configuration details were fixed a priori [15]. These details comprised the learning rate (α) and the momentum (β), which took the values of 0.1 and 0.4, respectively, the transfer functions used in the input and output layers were also set to be always linear. Furthermore, the data were range-scaled prior to training so that they had a value between -1 and 1, having demonstrated that this pre-processing facilitates the modelling process [15].

With the aim of obtaining the final response model for each ANN, the number of neurons used at the hidden layer was optimized in detail as well as the transfer functions used at this layer. All possible combinations of transfer functions (tansig and logsig) and number of neurons (between 3 and 10) at the hidden layer were tested. As criteria to choose the best ANN configuration, the root mean square error (RMSE) was considered as well as the modelling performance for each analyte. For this last purpose, the predicted values were represented with respect to those expected and the regression line of the comparison was calculated, the ideal case being with correlation coefficient close to 1, intercept close to 0 and slope close to 1. From the different tests, the best ANN$_1$ configuration had four neurons in its hidden layer using the tansig transfer function. On the other hand, the best ANN$_2$ model had also four neurons in the hidden layer but using the logsig transfer function, as can be seen in Fig. 1.

Fig. 2 shows the prediction ability of the models for the two pesticides with the optimal ANN configurations, for the external test subset.

Very good correlations were obtained for both the training and the external test data with comparison lines indistinguishable form the theoretical values, as can be seen in Table 1. Therefore, prediction capability of the two models could be considered as satisfactory for both considered pesticides.
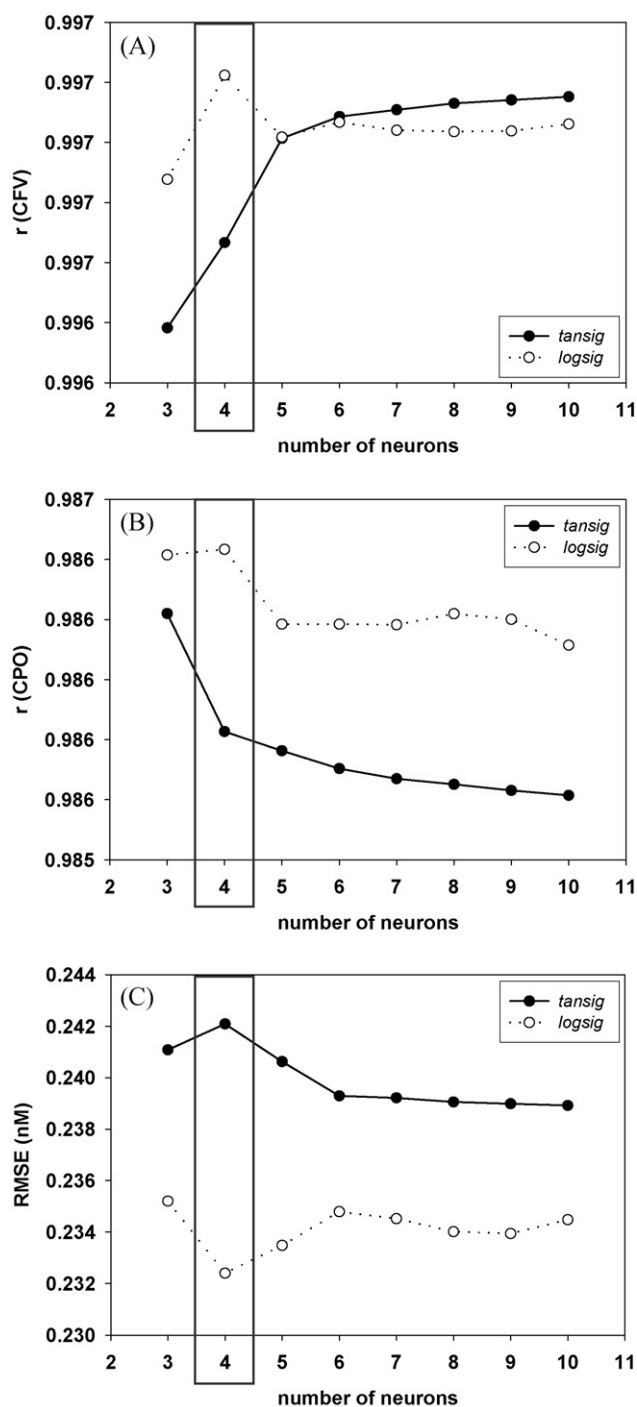
Fig. 1. Selection of the configuration of the final ANN$_2$ model. Obtained correlation coefficients for CFV (A) and CPO (B) and RMSE values (C) for different transfer functions and number of neurons in the hidden layer.

Table 1
Summary of the goodness of fits obtained for the two pesticides with training ($n = 25$) and external test ($n = 8$) sets.

		Slope	Intercept (nM)
ANN$_1$			
Training	CFV, $r = 0.996$	0.99 ± 0.04	$(0.5 \pm 2) \times 10^{-2}$
	CPO, $r = 0.995$	0.99 ± 0.04	1 ± 8
Test	CFV, $r = 0.998$	1.00 ± 0.06	$(0.8 \pm 3) \times 10^{-2}$
	CPO, $r = 0.995$	0.98 ± 0.09	3 ± 8
ANN$_2$			
Training	CFV, $r = 0.998$	0.99 ± 0.03	0.03 ± 0.13
	CPO, $r = 0.988$	1.00 ± 0.08	$(-0.7 \pm 0.9) \times 10^{-3}$
Test	CFV, $r = 0.997$	0.99 ± 0.08	0.2 ± 0.3
	CPO, $r = 0.986$	1.0 ± 0.2	$(0.4 \pm 2) \times 10^{-2}$

r is the correlation coefficient. Confidence intervals calculated at the 95% confidence level.
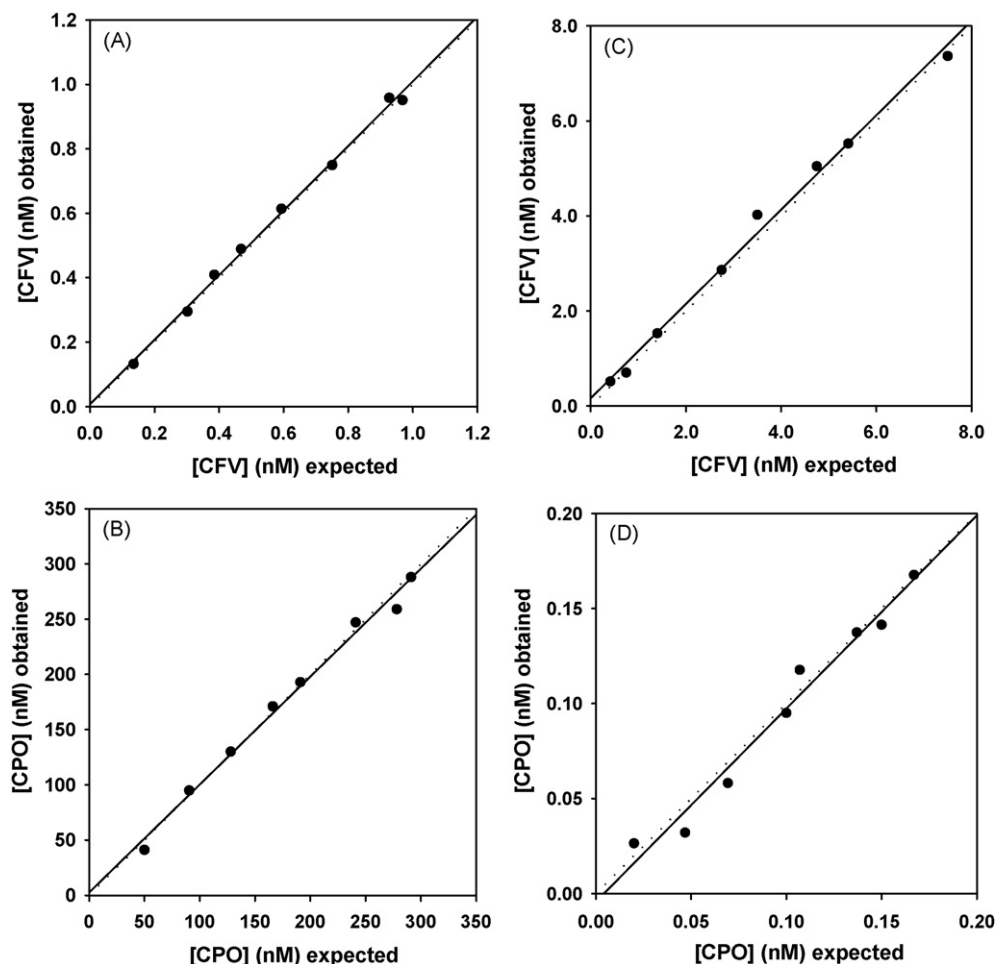
Fig. 2. Correlation between expected and obtained concentrations for CFV (A and C) and CPO (B and D) pesticides, pertaining to the external test subset. (A) and (B) were obtained with the ANN_1 model and (C) and (D) with the ANN_2. The dotted line represents the theoretical comparison line $y = x$.

3.2. Application to real samples

The proposed method was carried out in complex real samples to demonstrate its viability. Seven samples taken from a lake (Villeneuve-de-la-Raho, France) were analyzed directly and after spiking with CFV and CPO. All samples without added pesticide revealed no inhibitory effect, whereas the spiked ones showed some inhibition, which could be estimated with the previously trained ANN_2, since the amount of spiked pesticide was low. The obtained results are shown in Table 2.

As can be seen, the values found with the ANN_2 were consistent with the spiked concentrations. Average recovery yields, calculated as $(P_1/P_0)100$, where P_0 is the added quantity of pesticide and P_1 is the found quantity of it, were 98% for both pesticides.

These results suggested that the proposed method was able to resolve the considered pesticide mixtures in the tested real samples. A Student's t-test for paired samples was also applied to check that there were no significant differences between the obtained and expected values, significance being set at 95%. No significant differences ($t_{calc} < t_{tab} = 1.94$) were obtained for both pesticides ($t_{calc}(CFV) = 1.89$; $t_{calc}(CPO) = 0.53$).

4. Conclusions

This work shows that it is possible to selectively quantify mixtures of the pesticides CPO and CFV. The amperometric signal was generated from three biosensors built using the wild type AChE from EE, the genetically modified *D. melanogaster* AChE B394 and B394 co-immobilized with a PTE. The combined response of these biosensors was modelled by means of ANNs. Specifically, two different ANNs were constructed. The first one was used to model the combined response of B394 + PTE and EE biosensors and was applied when the concentration of CPO was high and the other, modelling the combined response of B394 + PTE and B394 biosensors, was applied with low concentrations of CPO. In both cases, the structure providing the best modelling was a single hidden layer containing four neurons. Finally, the developed system was applied to the determination of CPO and CFV pesticides in real water samples. Both pesticides could be quantified with low errors from a direct measurement step.

Table 2
Results obtained in the determination of CFV and CPO pesticides in spiked water samples taken from a lake (Villeneuve-de-la-Raho, France).

Sample	Spiked concentrations		Found values, ANN_2	
	CFV (nM)	CPO (nM)	CFV (nM)	CPO (nM)
A	0.28	0.30	0.32	0.32
B	1.00	0.05	1.00	0.05
C	2.00	0.15	2.08	0.14
D	3.00	0.10	2.95	0.10
E	4.00	0.10	3.50	0.11
F	5.00	0.15	4.47	0.16
G	6.00	0.05	5.62	0.03

References

[1] M. Maroni, J. Jarvisalo, F. La Ferla, Toxicol. Lett. 33 (1986) 115.
[2] A. Hildebrandt, R. Bragós, S. Lacorte, J.L. Marty, Sens. Actuators B 133 (2008) 195.
[3] S. Sotiropoulou, N.A. Chaniotakis, Anal. Chim. Acta 530 (2005) 199.
[4] S. Sotiropoulou, D. Fournier, N.A. Chaniotakis, Biosens. Bioelectron. 20 (2005) 2347.
[5] G. Valdés-Ramírez, D. Fournier, M.T. Ramírez-Silva, J.-L. Marty, Talanta 74 (2008) 741.
[6] G. Istamboulie, S. Andreescu, J.-L. Marty, T. Noguer, Biosens. Bioelectron. 23 (2007) 506.
[7] G. Istamboulie, D. Fournier, J.-L. Marty, T. Noguer, Talanta 77 (2009) 1627.
[8] A. Mulchandani, P. Mulchandani, W. Chen, J. Wang, L. Chen, Anal. Chem. 71 (1999) 2246.
[9] A. Mulchandani, S. Pan, W. Chen, Biotechnol. Progr. 15 (1999) 130.
[10] A. Mulchandani, W. Chen, P. Mulchandani, J. Wang, K.R. Rogers, Biosens. Bioelectron. 16 (2001) 225.
[11] R.P. Deo, J. Wang, I. Block, A. Mulchandani, K.A. Joshi, M. Trojanowicz, F. Scholz, W. Chen, Y. Lin, Anal. Chim. Acta 530 (2005) 185.
[12] G.L. Ellman, K.D. Courtney, V. Andres, R.M. Featherstone, Biochem. Pharmacol. 7 (1961) 88.
[13] H. Demuth, M. Beale, Neural Network Toolbox for Use with MATLAB, Mathworks Inc., Natick, MA, USA, 1992.
[14] M. Cortina, M. del Valle, J.-L. Marty, Electroanalysis 20 (2008) 54.
[15] J. Gallardo, S. Alegret, R. Muñoz, M. De-Román, L. Leija, P.R. Hernández, M. del Valle, Anal. Bioanal. Chem. 377 (2003) 248.

Design and application of a novel integrated electrochemical hydride generation cell for the determination of arsenic in seaweeds by atomic fluorescence spectrometry

Xian-Juan Jiang, Wu-Er Gan*, Su-Ping Han, Hong-Jing Zi, You-Zhao He

Department of Chemistry, University of Science and Technology of China, Hefei, Anhui 230026, PR China

ABSTRACT

An integrated electrochemical hydride generation cell, mainly composed of three components (a gas liquid separator, a graphite tube cathode and a reticulate Pt wire anode), was laboratory constructed and employed for the detection of arsenic by coupling to atomic fluorescence spectrometry. This integrated cell was free of ion-exchange membrane and individual anolyte, with the virtues of low-cost, easy assembly and environmental-friendly. Using flow injection mode, the sample throughput could come to 120 h^{-1} attributed to the small dimension of the cathode chamber. The operating conditions for the electrochemical hydride generation of arsenic were investigated in detail and the potential interferences from oxygen or various ions were also evaluated. Under the optimized conditions, no obvious oxygen quenching effects were observed. The limit of detection of As (III) for the sample blank solution was 0.2 ng mL^{-1} (3σ) and the relative standard deviation was 3.1% for nine consecutive measurements of 5 ng mL^{-1} As (III) standard solution. The calibration curve was linear up to 100 ng mL^{-1}. The accuracy of the method was verified by the determination of arsenic in the reference materials GBW08517 (*Laminaria Japonica* Aresch) and GBW10023 (*Porphyra crispata*) and the developed method was successfully applied to determine trace amounts of arsenic in edible seaweeds.

© 2009 Elsevier B.V. All rights reserved.

1. Introduction

Seaweeds have been used as a foodstuff in the Asian diet for centuries and are considered an under-exploited resource, and at present, edible seaweeds are being increasingly consumed in Europe countries [1–3]. Nevertheless, seaweeds or alga can accumulate high percentages of As. So many authors have been focused on As speciation analysis in this kind of samples during the last years [4–7]. Considerable efforts have also been made in developing simple and sensitive methods for As detection. The most popular and traditional of them are atomic absorption spectrometry (AAS) or atomic fluorescence spectrometry (AFS), in which chemical hydride generation (CHG) is usually employed [8,9]. However, the traditional tetrahydroborate (III)-based CHG methods are prone to interferences by transition metal ions, thus blocking its general applications [10–15]. For eliminating or reducing the interferences, many means have been developed, including increase the acid concentration or using masking agents [16,17]. Besides, photochemical vapor generation (photo-CVG), which had high tolerance to the presence of several

transition metals, such as Co^{2+} and Ni^{2+}, has also been reported [18,19].

As a suitable alternative approach to CHG techniques, electrochemical hydride generation (EC-HG) has been widely used as sample introduction technique for detection of As in atomic spectrometry [20–23]. The structure of conventional electrochemical hydride generators, published by different authors, is nearly identical [24,25]. The two half-cells, anode chamber and cathode chamber, are usually separated by an ion-exchange membrane [26–29], or simply a glass frit [30,31] or ceramic tube [32].

Recently, attentions were paid to mini-sized EC-HG cells. For example, a three-dimensional miniaturized electrolysis cell with a fibrous carbon cathode was adopted for optical emission spectrometric determination of As and Sb [33]. Two types of miniaturized non-membranes flow-through electrolytic cells for electrochemical hydride generation of Se were designed [34]. A miniaturized electrochemical flow cell with a porous glass carbon working electrode coupled to induced plasma atomic emission spectrometry was developed for Se determination [35].

In the present work, an integrated EC-HG cell was laboratory constructed and a small dimension (180 μl) graphite tube used as cathode chamber. This integrated cell had the virtues of low-cost, easy assembly and environmental-friendly due to its free of ion-exchange membrane and individual anolyte. A simple and sen-

sitive FI method for the detection of As was created by coupling this integrated EC-HG cell with AFS, and this developed method was successfully applied to determine trace amounts of As in edible seaweeds.

2. Experimental

2.1. Instrumentation

An AFS-230 double-channel non-dispersive atomic fluorescence spectrometer (Beijing Haiguang Instrument Co., Beijing, China) was employed throughout. A high intensity As hollow cathode lamp (General Research Institute for Nonferrous Metals, Beijing, China) with lamp current of 60 mA was used as a radiation source. Quartz tube (7 mm i.d. × 14 mm length) was used as atomizer.

A homemade integrated EC-HG cell was employed as hydride generator. A direct current (DC) constant current and voltage unit (Type DH1719A-3, Beijing Da Hua Wireless instrument Co., Beijing, China) operating at constant current mode was used as power supply. WX-3000 microwave oven (Shanghai EU Chemical Instruments Co., Ltd., China) was used for sample digestion.

Linear Sweep Voltammetric measurements were performed on an automated LK98BII electrochemical measurement system (Tianjin Lanlike Chemistry & Electron High Technology Co., Tianjin, China) equipped with Pt disc (1.5 mm diameter) working electrode, saturated calomel electrode (SCE) reference electrode and a Pb foil (4 mm^2 area) counter electrode.

2.2. Electrochemical hydride generation system

A schematic diagram of the analytical system is shown in Fig. 1. The integrated EC-HG cell is composed of the gas–liquid separation (GLS) chamber (20 mm i.d., 60 mm length), cathode chamber (6.4 mm i.d., 40 mm length) and anode chamber (6.4 mm i.d., 40 mm length). The graphite tube cathode (2.4 mm i.d., 2 mm thickness, 40 mm length) was put firmly into the cathode chamber and a reticulate Pt wire anode (0.25 mm diameter, 50 mm length) into

Fig. 1. Schematics of the integrated EC-HG cell and the EC-HG-AFS system, P: peristaltic pump; W: waste; S: sample; AFS: atomic fluorescence spectrometry.

the anode chamber. The angle between the GLS chamber and the anode chamber is 60°.

A tiny pore (0.5 mm i.d.) connecting the GLS chamber with the anode chamber was used to keep solution level of GLS chamber. A piece of rounded porous glass frit was fixed at the bottom of the GLS chamber for airflow dispersion.

2.3. Reagents and materials

Unless otherwise stated all reagents were of highest available purity, and of at least analytical grade. Doubly deionized water (DDW) was solely used. A series of standard solutions were prepared daily by stepwise diluting the stock solution of As (1000 g L^{-1}, Shanghai Institute of Measurement and Testing Technology) with 1 mol L^{-1} H$_2$SO$_4$ just before use.

Guarantee reagent H$_2$SO$_4$ was used to test the properties of electrolytic solutions. A mixture of 100 g L^{-1} thiourea and ascorbic acid solution was prepared by dissolving both thiourea and ascorbic acid in DDW. The reference materials GBW08517 (*Laminaria Japonica* Aresch) and GBW10023 (*Porphyra crispata*) obtained from China National Research Center for Certified Reference Materials were applied to evaluate the accuracy of the present method. Three common edible seaweeds, one brown (*L. japonica*) and two red (*Porphyra tenera* and *Sarcodia montagneana*) were bought at local public markets.

Argon (≥99.99%) was used as carrier gas; hydrogen gas (≥99.99%) was used to maintain a stable Ar–H$_2$ flame. Graphite tube and Pt wire were used as cathode and anode, respectively.

2.4. Sample preparation

The crude seaweeds were firstly cleaned thoroughly with tap water to remove the salt and dirt and further rinsed with DDW. The resulting seaweeds were oven dried at 40 °C to a constant weight prior to further preparation and then ground in an agate mortar and stored in a desiccator.

Digestion was carried out placing approximately 200 mg of samples or reference materials (GBW 08517 and GBW10023) in polytetrafluoroethylene vessels together with 4 mL concentrated HNO$_3$ and 1 mL H$_2$O$_2$, the vessels were sealed and placed in the microwave digestion oven. The digestion program consisted two stages, stage 1 (120 °C, 0.5 MPa, 5 min); stage 2 (140 °C, 1 MPa, 10 min). After digestion and cooled to room temperature, the solution in the vessels was transferred to a 50 mL beaker and gently heated to remove the residual HNO$_3$. Then, it was transferred into a 100 mL calibrated flask, added 10 mL of the mixture reducing agent (10% ascorbic acid + 10% thiourea) according to previous paper [36] and acidified with H$_2$SO$_4$ to an acid concentration of 1 mol L^{-1}.

2.5. Cathode pretreatment

The graphite tube cathode was rinsed by hot nitric acid (1:1) and DDW before assembly and then anodically activated at a constant current of 2 mA in 0.1 mol L^{-1} H$_2$SO$_4$ for 20 min. It was observed that the hydride-generating efficiencies decreased after the electrode was used more than 1 week. Therefore, the electrode should be treated every week with aforementioned method.

2.6. Analytic procedures

Firstly, the graphite cathode chamber, GLS chamber and anode chamber were successively introduced with 1 mol L^{-1} H$_2$SO$_4$ electrolyte by peristaltic pump. The working program of the integrated EC-HG system was as follows: open the power operating at a constant current of 1.5 A and then inject 0.7 mL sample into the electrolyte carrier stream. The generated H$_2$ and AsH$_3$ were swept to
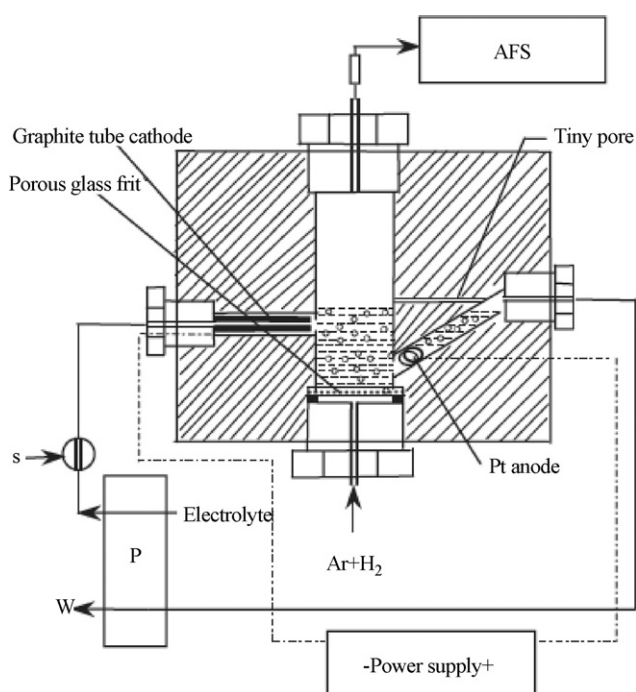
the quartz tube by working gas ($400\,\text{mL}\,\text{min}^{-1}$ Ar and $200\,\text{mL}\,\text{min}^{-1}$ H_2) for atomic fluorescence measurement in peak area mode with read time of 10 s. The total sample determination last about 30 s (sample introduction, 6 s; electrolyte introduction, 23 s; valve switch, 1 s) and the analytical throughput of $120\,\text{h}^{-1}$ was achieved.

3. Results and discussions

3.1. Electrochemical hydride generator design

The present integrated EC-HG cell was manufactured with a polytetrafluoroethylene (PTFE) body ($120\,\text{mm} \times 80\,\text{mm} \times 50\,\text{mm}$), mainly including graphite tube cathode, GLS chamber and reticulate Pt wire anode. The proposed device dispensed with ion-exchange membrane and individual anolyte.

The non-membrane setup enabled the electrolyte stream to be sequentially pumped through cathode chamber, GLS chamber and anode chamber acted as both catholyte and anolyte. Therefore, it had advantages of low-cost and environmental-friendly.

A tiny pore (0.5 mm i.d.) communicating the GLS chamber and the anode chamber was used to adjust solution level in GLS chamber. As the solution level in GLS chamber was lower than the tiny pore, the liquid in GLS chamber would stop draw off owing to the air pressure and while the liquid level go beyond the tiny pore, excessive liquid would be drawn out since the tiny pore was filled with liquid. The solution level in the GLS chamber was maintained within 2 mm around the tiny pore. A piece of porous glass frit fixed at bottom of GLS chamber was used for dispersing airflow and stabilizing both the liquid surface and the electrical current. In addition, the screw cap makeup for components seal makes assembling of EC-HG cell easy, and reduced the time required for cathode replacement or cleaning.

3.2. Potential effect of oxygen

It is well known that atomic fluorescence is prone to be quenched by oxygen [37]. The ion-exchange membrane is often used to separate the two compartments physically and to prevent the passing (diffusion) of anode products, especially the oxygen into the cathode compartment in the conventional EC-HG cell [24]. Considering non-membrane setting in the proposed EC-HG cell, it is critical to evaluate the potential effect of generated oxygen on fluorescence signal intensity.

The Linear Sweep Voltammetry was applied to detect oxygen content in mixed gas scanning between 0.2 and $-0.6\,\text{V}$ (vs. SCE) at $10\,\text{mV}\,\text{s}^{-1}$. Supporting electrolyte ($0.1\,\text{mol}\,\text{L}^{-1}$ NaOH) was deaerated with Ar for 20 min before use. The analytes were prepared by insufflating gases from GLS into the supporting electrolyte for 10 min. The results were shown in Fig. 2. Among them, Fig. 2a and b illustrate the results of supporting electrolyte alone before and after deaerated with Ar; Fig. 2c and d were those of the proposed EC-HG cell and the conventional EC-HG cell with ion-exchange membrane [36], respectively; Fig. 2e was the result of supporting electrolyte insufflated by air (diluted 1:10 with Ar) for 2 min.

The peak heights of oxygen reductive peak (ca. $-0.14\,\text{V}$) in Fig. 2b–d were almost the same and much lower than that of the saturated oxygen reductive peak (Fig. 2a). However, when air (diluted with Ar) was introduced for only 2 min (Fig. 2e), an obvious wave was seen at $-0.14\,\text{V}$. It was indicated that the oxygen generated in the anode chamber was fluently led to waste along with the electrolyte stream and the potential effect of oxygen on fluorescence signal intensity could be neglected; therefore, the ion-exchange membrane was unnecessary in this integrated EC-HG cell.
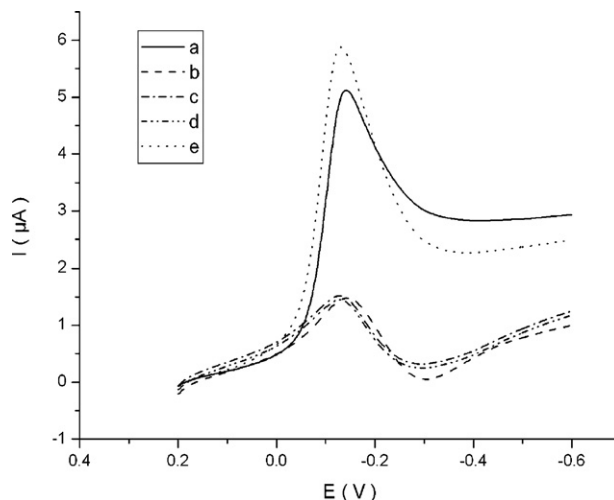
Fig. 2. Linear Sweep Voltammograms. (a) The supporting electrolyte before deaerated with Ar. (b) The supporting electrolyte deaerated with Ar for 20 min. (c) Gas mixtures from the integrated EC-HG cell were insufflated for 10 min. (d) Gas mixtures from ion-exchange membrane EC-HG cell were insufflated for 10 min. (e) Air (diluted 1:10 with Ar) was insufflated for 2 min.

3.3. Effect of working gas

The influence of working gas (Ar and H_2) on both the fluorescence signal intensity and repeatability were studied. In accordance with our previous work [36], gas mixtures of $400\,\text{mL}\,\text{min}^{-1}$ Ar and $200\,\text{mL}\,\text{min}^{-1}$ H_2 were employed as working gas for transferring hydride to the AFS and for maintaining the hydrogen–argon–air entrained flame in the quartz tube atomizer.

Firstly, the working gas ($400\,\text{mL}\,\text{min}^{-1}$ Ar and $200\,\text{mL}\,\text{min}^{-1}$ H_2) was divided into two portions. One portion, the sweeping gas, was introduced into the GLS chamber from bottom; the other portion was introduced to the cross-tube at the outlet of the integrated cell. As illustrated in Fig. 3, the fluorescence signal intensity of $5\,\text{ng}\,\text{mL}^{-1}$ As (III) increased along with the sweeping gas flow rate up to $600\,\text{mL}\,\text{min}^{-1}$ no matter with or without the porous glass frit. As a result, all of the working gas was introduced into the GLS chamber from bottom.

The results also indicated that the fluorescence signal intensity and its repeatability could be improved by using porous glass
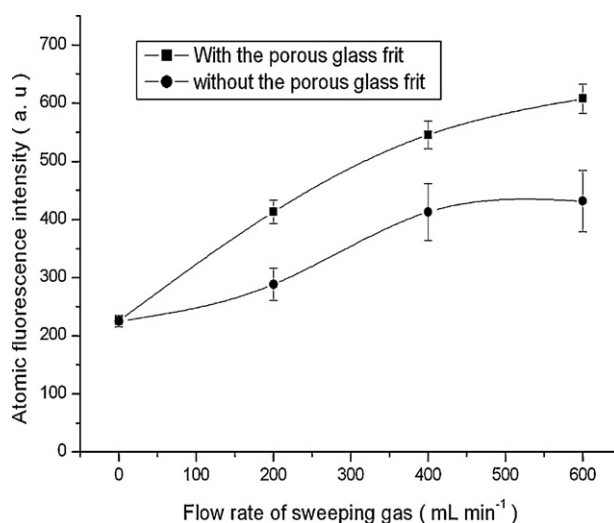
Fig. 3. Effect of working gas flow rate on the As (III) fluorescence signal intensity in the electrochemical hydride generation system. The analyte concentration was $5\,\text{ng}\,\text{mL}^{-1}$. Error bars represents standard deviations of three replicates.
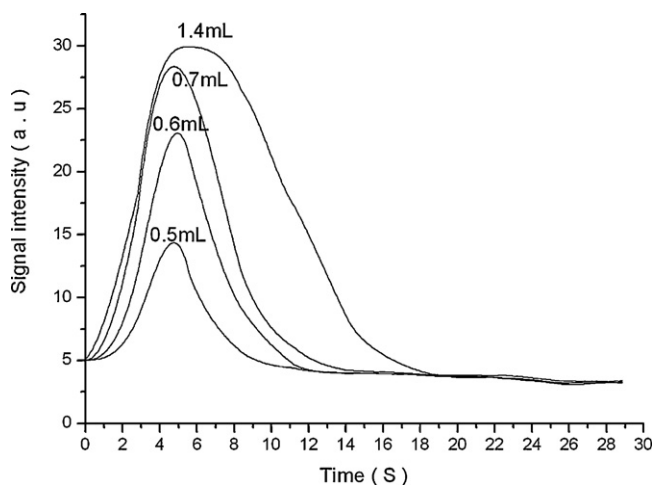
Fig. 4. Effect of sample volume on analytical performance of the system by detecting the atomic fluorescence intensity of $5\,ng\,mL^{-1}$ As (III) in peak height mode.

frit. In contrast, without the porous glass frit, the introduction of gas mixtures would produce big bubbles in the GLS chamber, make against the stability of liquid surface and electrolysis current and deteriorate the repeatability of the fluorescence signal intensity. Consequently, the gas mixtures of $400\,mL\,min^{-1}$ Ar and $200\,mL\,min^{-1}$ H_2 were totally introduced into the GLS chamber through the porous glass frit.

3.4. Optimization of the experimental conditions

3.4.1. Sample volume

Effect of sample volume on analytical performance was studied by detecting the atomic fluorescence signal intensity of $5\,ng\,mL^{-1}$ As (III) in peak height mode. It was found that the signal intensity increased as the sample volume increased from 0.5 to 1.4 mL (Fig. 4), i.e. increasing the sample volume would decrease the dispersion coefficient. On the other hand, when larger sample volume was introduced, longer time would be needed for the signal to return to near blank level and it would result in lower analytical throughput. Therefore, sample volume of 0.7 mL was chosen in the analytical procedure. In addition, it was observed in Fig. 4 (0.7 mL) that the atomic fluorescence signal intensity attenuated remarkably as read time exceeded 10 s. Considering both analytical throughput and method precision, measurement time of 10 s was adopted in our work.

3.4.2. Electrical current

The influence of applied electrolytic current on the fluorescence signal intensity of $5\,ng\,mL^{-1}$ As (III) in $1\,mol\,L^{-1}$ H_2SO_4 was investigated within the range of 0.25–2.25 A. It was found that fluorescence signal intensity increased along with electrolysis current, in agreement with the observations of other authors [38]. However, higher current values (>1.75 A) were unsuitable for prolonged measurements due to considerable electrolytes overheating. That would bring some water fog into the quartz tube atomizer, causing deterioration in the repeatability of the fluorescence signal intensity. Compromising fluorescence signal intensity and stability, constant current of 1.5 A was used throughout.

3.4.3. Electrolyte

Diluted H_2SO_4, HCl and H_3PO_4 were often used as electrolytes for the determination of As (III) in the EC-HG system; HNO_3 was not used because of its oxidation properties. HCl was not chosen in this work, considering that the poisonous $NH_2OH \cdot HCl$ was demand to inhibit the interference from resultant chlorine [39].

H_3PO_4 was also unsuitable owing to its weak acidity and resultant low conductivity. In general, H_2SO_4 was the appropriate electrolyte for the generation of arsine [24,40] and chosen in the present work.

Effect of H_2SO_4 concentration on the fluorescence signal intensity was examined. It was found that the fluorescence signal intensity of $5\,ng\,mL^{-1}$ As (III) increased slowly with increasing acidity of the electrolyte, and reached to maximum value at $1\,mol\,L^{-1}$. As a result, the solution of $1\,mol\,L^{-1}$ H_2SO_4 was selected in our work.

The effect of the electrolyte flow rate on the fluorescence signal intensity was investigated within 4–$12\,mL\,min^{-1}$. It was found that flow rate of $7\,mL\,min^{-1}$ was suitable and used throughout.

3.5. Interference

The effects of some representative potential interference on the determination of As (III) by EC-HG-AFS were examined, which were expressed as the recovery relating to the responses with and without interference ions as in Table 1. Variations less than 5% of recovery may be believed insignificant. It was found that large amounts of alkali and alkaline earth metal ions did not interfere with the determination. As for transition metal ions interference, it is usually assumed that transition metal ions were reduced to metals to bring catalytic effect on the decomposition of the hydrides [24]. In this work, the hydride generated in cathode chamber could be rapidly separated from solution, which means reducing hydride decomposition. In our experiments, there was no significant interference for ion concentrations as high as $2\,mg\,L^{-1}$ for Fe^{3+}, $1\,mg\,L^{-1}$ for Mn^{2+}, $0.5\,mg\,L^{-1}$ for Cr^{3+}, Cu^{2+}, Ni^{2+} and $0.05\,mg\,L^{-1}$ for Mo^{6+}, Co^{2+}, in a solution containing $50\,ng\,mL^{-1}$ As (III). Moreover, $2\,mg\,L^{-1}$ for Se^{4+}, $0.05\,mg\,L^{-1}$ for Sn^{4+} and 0.5% $NO_3{}^-$ also did not interfere with the detection of As (III).

It was found that the fluorescence signal intensity of As (V) was about 10% that of As (III) without the pre-reducing process. After being reduced by the mixed reducing agent (1% ascorbic acid + 1% thiourea), the As (V) reached the same intensities of the As (III). Therefore, the As (V) was pre-reduced to As (III) by the mixed reducing agent in this study.

Table 1
Interference of various ions on the determination of $50\,ng\,mL^{-1}$As.

Element	Concentration (mg L^{-1})	[M][a]/[X][b]	Recovery (%)
K$^+$	100	2000	102
	200	4000	93
Na$^+$	20	400	108
	200	4000	101
Ca^{2+}	20	400	96
Mg^{2+}	200	4000	99
Fe^{3+}	2	40	96
Mn^{2+}	1	20	104
	2	40	88
Cu^{2+}	0.5	10	101
	4	80	87
Se^{4+}	2	40	105
Co^{2+}	0.05	1	96
	0.5	10	64.6
Cr^{3+}	0.5	10	95
Ni^{2+}	0.5	10	103
Mo^{6+}	0.05	1	96
	0.5	10	74
Sn^{4+}	0.05	1	103
	0.5	10	91
NO$_3{}^-$	0.5%		97
	1%		83
	2%		51

[a] Interference ions.
[b] As (III).

X.-J. Jiang et al. / Talanta 79 (2009) 314–318

Table 2
Analytical results of As in edible seaweeds.

Samples	Found value[a] ($\mu g\,g^{-1}$)	Added value ($\mu g\,g^{-1}$)	Reclaimed ($\mu g\,g^{-1}$)	Recovery (%)
Laminaria japonica Aresch	11.54 ± 0.53	10.00	22.24 ± 0.82	107
Porphyra tenera	11.32 ± 0.58	10.00	21.82 ± 0.88	105
Sarcodia montagneana	16.25 ± 0.81	10.00	26.15 ± 0.96	99

[a] Mean value $\pm$ standard deviation ($n = 3$).

3.6. Analytical figures of merit

Regression lines between fluorescence signal response (I_F) and the concentration (C) can be expressed by $I_F = -4.01 + 122.37\,C_{As}/\mathrm{ng\,mL^{-1}}$ with the regression coefficient R of 0.9978. The limit of detection of As (III) for the sample blank solution is $0.2\,\mathrm{ng\,mL^{-1}}$ (3σ). The relative standard deviation (R.S.D.) was 3.1% for nine consecutive measurements of $5\,\mathrm{ng\,mL^{-1}}$ As (III) standard solution. The calibration curve was linear up to $100\,\mathrm{ng\,mL^{-1}}$. In this work, the hydride-generating efficiency was calculated as the method used in Ref. [36]. The highest hydride generation efficiency of As (III) was 96.4% compared with that of the KBH$_4$–acid system.

3.7. Method validation and analytical results of samples

The accuracy of the method was evaluated through the analysis of the reference materials GBW 08517 (*L. Japonica* Aresch) and GBW10023 (*P. tenera*) with a certified As concentration of 13.9 ± 2.4 and $27 \pm 6\,\mu g\,g^{-1}$, respectively. Results obtained for As were 12.88 ± 0.51 and $22.42 \pm 1.03\,\mu g\,g^{-1}$ and the results were in good agreement with certified values. The proposed method was applied to the analysis of three common edible seaweeds, brown (*L. japonica* Aresch) and two red (*P. tenera* and *S. montagneana*). The results were listed in Table 2 and their recoveries are satisfying.

4. Conclusions

In the present work, a novel integrated EC-HG cell was designed. A graphite tube with a small volume was used as cathode chamber and samples were introduced in flow injection mode. This integrated cell was free of ion-exchange membrane and individual anolyte, with the virtues of low-cost, easy assembly, environmental-friendly. In addition, the use of porous glass frit not only stabilized the EC-HG system but also enabled the hydride to be effectively driven out by the working gas from GLS chamber. The hydride generated in cathode chamber could be immediately separated with liquid and reduced losing in transferring process. The developed method, by coupling EC-HG with AFS, was successfully applied to determine trace amounts of As in edible seaweeds. The precision and accuracy of the method were satisfactory.

Acknowledgement

References

[1] P. Rupérez, F. Saura-Calixto, Eur. Food Res. Technol. 212 (2001) 349.
[2] A. Jiménez-Escrig, I. Jiménez-Jiménez, R. Pulido, F. Saura-Calixto, J. Sci. Food Agric. 81 (2001) 530.
[3] P. Rupérez, Food Chem. 79 (2002) 23.
[4] J. Moreda-Piñeiro, E. Alonso-Rodríguez, P. López-Mahía, S. Muniategui-Lorenzo, D. Prada-Rodríguez, A. Moreda-Piñeiro, P. Bermejo-Barrera, Anal. Chim. Acta 598 (2007) 95.
[5] S. García Salgado, M.A. Quijano Nieto, M.M. Bonilla Simón, Talanta 75 (2008) 897.
[6] S. Farías, P. Smichowski, D. Vélez, R. Montoro, A. Curtosi, C. Valdopívez, Chemosphere 69 (2007) 1017.
[7] S. García Salgado, M.A. Quijano Nieto, M.M. Bonilla Simón, Talanta 68 (2006) 1522.
[8] Z.L. Zhu, J.X. Liu, S.C. Zhang, X. Na, X.R. Zhang, Anal. Chim. Acta 607 (2008) 136.
[9] A.G. Howard, J. Anal. Atom. Spectrom. 12 (1997) 267.
[10] T. Näykki, P. Perämäki, J. Kujala, A. Mikkonen, Anal. Chim. Acta 439 (2001) 229.
[11] X.H. Li, Y.Y. Su, K.L. Xu, X.D. Hou, Y. Lv, Talanta 72 (2007) 1728.
[12] P. Pohl, W. Zyrnicki, Anal. Chim. Acta 468 (2002) 71.
[13] M. Yamamoto, M. Yasuda, Y. Yamamoto, Anal. Chem. 57 (1985) 1382.
[14] B. Welz, M. Sucmanova, Analyst 118 (1993) 1417.
[15] E. Bolea, D. Arroyo, G. Cepriá, F. Laborda, J.R. Castillo, Spectrochim. Acta, Part B 61 (2006) 96.
[16] N. Erdem, E. Henden, Anal. Chim. Acta 505 (2004) 59.
[17] J. Dedina, D.L. Tsalev, Hydride Generation Atomic Absorption Spectrometry, Wiley, Chichester, 1995, pp. 91–115.
[18] Y.H. He, X.D. Hou, C.B. Zheng, R.E. Sturgeon, Anal. Bioanal. Chem. 388 (2007) 769.
[19] C.B. Zheng, Y. Li, Y.H. He, Q. Ma, X.D. Hou, J. Anal. Atom. Spectrom. 20 (2005) 746.
[20] M.A. Amberger, N.H. Bings, P. Pohl, J.A.C. Broekaert, Int. J. Environ. Anal. Chem. 88 (2008) 625.
[21] M.H. Arbab-Zavar, M. Hashemi, Talanta 52 (2000) 1007.
[22] W.B. Zhang, W.E. Gan, X.Q. Lin, Talanta 68 (2006) 1316.
[23] M. Hashemi, M.H. Arbab-Zavar, A. Sarafraz-Yazdi, Talanta 64 (2004) 644.
[24] E. Denkhaus, A. Golloch, X.M. Guo, B. Huang, J. Anal. Atom. Spectrom. 16 (2001) 870.
[25] F. Laborda, E. Bolea, J.R. Castillo, Anal. Bioanal. Chem. 388 (2007) 743.
[26] Y. Lin, X. Wang, D. Yuan, P. Yang, B. Huang, Z. Zhuang, J. Anal. Atom. Spectrom. 7 (1992) 287.
[27] E. Denkhaus, A. Golloch, T.U. Kampen, M. Nierfeld, U. Telgheder, Fresenius' J. Anal. Chem. 361 (1998) 733.
[28] L.F.R. Machado, A.O. Jacintho, A.A. Menegário, E.A.G. Zagatto, M.F. Giné, J. Anal. Atom. Spectrom. 13 (1998) 1343.
[29] J. Šíma, P. Rychlovský, J. Dédina, Proceedings of XIVth Seminar on Atomic Spectrochemistry, High Tatras, Podbanske, September, 1998, p. 243.
[30] U. Pyell, A. Dworschak, F. Nitschke, B. Neidhart, Fresenius' J. Anal. Chem. 363 (1999) 495.
[31] D. Schaumlöffel, B. Neidhart, Fresenius' J. Anal. Chem. 354 (1996) 866.
[32] F. Laborda, E. Bolea, J.R. Castello, J. Anal. Atom. Spectrom. 15 (2000) 103.
[33] P. Pohl, I.J. Zapata, N.H. Bings, Anal. Chim. Acta 606 (2008) 9.
[34] J. Hraníček, V. Červený, P. Rychlovský, Chem. Listy 102 (2008) 200.
[35] S. Schermer, L. Jurica, J. Paumard, E. Beinrohr, F.M. Matysik, J.A.C. Broekaert, Fresenius' J. Anal. Chem. 371 (2001) 740.
[36] W.B. Zhang, W.E. Gan, X.Q. Lin, Anal. Chim. Acta 539 (2005) 335.
[37] I. Bergma, Nature 218 (1986) 396.
[38] E. Bolea, F. Laborda, J.R. Castillo, Anal. Sci. 19 (2003) 367.
[39] W.W. Ding, R.E. Sturgeon, J. Anal. Atom. Spectrom. 11 (1996) 225.
[40] X. Li, J. Jia, Z.H. Wang, Anal. Chim. Acta 560 (2006) 153.

Determination of senkirkine and senecionine in *Tussilago farfara* using microwave-assisted extraction and pressurized hot water extraction with liquid chromatography tandem mass spectrometry

Zhangjian Jiang[a], Feng Liu[a], Jennifer Jia Lei Goh[a], Lijun Yu[a], Sam Fong Yau Li[a,*], Eng Shi Ong[b,**], Choon Nam Ong[b]

[a] *Department of Chemistry, National University of Singapore, 3 Science Drive 3, Singapore 117543, Singapore*
[b] *Department of Epidemiology and Public Health, National University of Singapore, 16 Medical Drive, Singapore 117597, Singapore*

ARTICLE INFO

ABSTRACT

Tussilago farfara (*Kuan Donghua*) is an important Chinese herbal medicine which has been shown to contain many bioactive compounds and widely used to relieve cough and resolve phlegm. However, besides therapeutic bioactive compounds, this herb has been found to contain toxic pyrrolizidine alkaloids (PAs), mainly senkirkine and traces of senecionine. In this report, conditions for microwave-assisted extraction (MAE) and pressurized hot water extraction (PHWE) were optimized for the extraction of the PAs. The results were compared against heating under reflux. It was found that the binary mixture of MeOH:H_2O (1:1) acidified using HCl to pH 2–3 was the optimal solvent for the extraction of the PAs in the plant materials. Liquid chromatography (LC) with ultra-violet (UV) detection and electrospray ionization mass spectrometry (ESI-MS) in the positive mode was used for the determination and quantitation of senkirkine and senecionine in the botanical extract. The proposed extraction methods with LC/MS allow for the rapid detection of the major and the minor alkaloids in *T. farfara* in the presence of co-eluting peaks. With LC/MS, the quantitative analysis of PAs in the extract was done using internal standard calibration and the precision was found to vary from 0.6% to 5.4% on different days. The limits of detection (LODs) and limits of quantitation (LOQs) for MAE and PHWE were found to vary from 0.26 µg/g to 1.04 µg/g and 1.32 µg/g to 5.29 µg/g, respectively. The method precision of MAE and PHWE were found to vary from 3.7% to 10.4% on different days. The results showed that major and minor alkaloids extracted using MAE and PHWE were comparable to that by heating under reflux. Our data also showed that significant ion suppression was not observed in the analysis of senkirkine and senecionine in the botanical extracts with co-eluting peaks.

© 2009 Elsevier B.V. All rights reserved.

1. Introduction

Tussilago farfara (*Kuan Donghua*), the dried flower bud of *T. farfara* L., is an important Chinese herbal medicine which has been commonly used for the relief of coughs and as an expectorant, blood pressure raiser, platelet activating factor and anti-inflammatory [1]. It is also used for the treatment of asthma, silicosis, pulmonary tuberculosis, obesity, type 2 diabetes, and hepatitis [2–7]. However, besides therapeutic bioactive compounds present in the herb, it has been found to contain toxic pyrrolizidine alkaloids (PAs), mainly senkirkine and traces of senecionine (Fig. 1) [8]. The PAs can be hepatoxic, causing damage to the liver and may even cause liver cancer

when minute quantities are consumed [9–11]. As a result, in order to minimize the amount of toxic PAs ingested, the German health authorities have limited the daily intake of toxic PAs to 1 µg. And in Austria only drugs and preparations free of 1,2-unsaturated PAs have been authorised since 1994 [8]. Therefore, in order to reduce the risk presented to consumers, it is very important to develop a simple method for the isolation and quantification of the toxic PAs in this herb.

Usually, the bioactive or marker compounds of *T. farfara* are extracted by soxhlet extraction [8], or by heating under reflux [8,12–14]. However, these extraction methods are time-consuming and involve the use of large volumes of solvent. Recently, simpler and more environmental friendly extraction methods have been developed. These include supercritical fluid extraction (SFE), microwave-assisted extraction (MAE), pressurized fluid extraction (PFE) and so on. Their applicability in extraction of solid matrices and natural products has been discussed [15,16]. Among these

new methods, MAE is applied on the extraction of a variety of sample matrices due to its faster extraction time and better extraction yields. This is because the heating by microwaves is instantaneous and occurs in the heart of the sample, leading to rapid extractions. Moreover, as the radiation can be focused directly onto the sample, microwave heating is more efficient and thus homogeneity and reproducibility improve significantly [16]. Until recently, MAE has been widely applied on the extraction of bioactive compounds from natural products, such as isolation of alkaloids from *Rhizoma coptidis* [17], *Nelumbo nucifera* leaves [18], *Lycoris radiata* [19] and *Solanum nigrum* L. [20].

Pressurized hot water extraction (PHWE) is another extraction technique which can be applied for the isolation of bioactive or marker compounds from botanicals and medicinal plants while reducing or completely eliminating the use of organic solvents [21]. In PHWE, water is used as the extraction solvent at temperatures of 100–350 °C and at a pressure high enough to keep it as a liquid. At elevated temperatures and pressures, the dielectric constant of water will be similar to those of ethanol or acetone. As a result, it can be used with other organic solvents to extract medium- or low-polarity compounds [22]. Until recently, PHWE has already been successfully applied to the extraction of less polar organic compounds from the environmental samples and traditional herbal medicines [21,23–26].

For the analysis and separation of PAs in *T. farfara*, analytical techniques such as gas chromatography [8], high performance liquid chromatography [12,27], and capillary electrophoresis [12,13] have been used. Sometimes, only the major alkaloid senkirkine, but not the minor alkaloid senecionine in *T. farfara* could be determined [8,12,14]. LC/MS is able to detect low levels of target compounds in a complex matrix as MS provides a second dimension (mass to charge) which separates co-eluting components. With tandem mass spectrometry, characteristic fragmentation pattern required for the rapid identification of unknown compounds can be obtained. To the best of our knowledge, the isolation, quantitative analysis and effects of ion suppression on senkirkine and senecionine in medicinal plant extracts using LC/MS have not been reported. Furthermore, reports on the rapid detection of major and minor components in the presence of co-eluting peaks in botanical extracts have been limited.

For the determination of PAs present in medicinal plants, proper sample preparation is of utmost importance. Thus, the aim of the current work is to develop a method for the rapid extraction and analysis of alkaloids such as senkirkine and senecionine using MAE and PHWE for determination by LC and LC–MS. The extraction efficiency of MAE and PHWE will be compared with that of heating under reflux. Concurrently, the effect of ion suppression in the botanical extracts will be investigated.

2. Experimental

2.1. Chemicals and reagents

Methanol (HPLC Grade) and dichloromethane (HPLC Grade) were the products of Merck (Nordic European Center, Singapore). Absolute ethanol (HPLC Grade) was purchased from Fisher scientific (Loughborough, Leicestershire LE11 5RG, UK). Anhydrous ether (HPLC Grade) was obtained from Hayman (Witham, Essex, UK). Acetonitrile (HPLC Grade) was the product of Tedia (Fairfield, OH 45014, USA). Ultra-pure water was obtained by a NANOpure ultra-pure water system (Barnstead Int., Dubuque, IA, USA). Formic acid was obtained from Fluka (Sigma–Aldrich pte Ltd., Science Park II, Singapore). Ammonium formate, sand (white quartz, 50–70 mesh, suitable for chromatography) and chlorpheniramine maleate were purchased from Sigma (St. Louis, MO, USA). Ammonium acetate was the product of Merck (Darmstadt, Germany). Powdered and dried flowers of *T. farfara*, as well as crystallized standards of pyrrolizidine alkaloids were kindly provided by Health Sciences Authority, Singapore.

2.2. Preparation of reference standards

Stock solution of senkirkine at 3000 mg/L was prepared in methanol. Senecionine was prepared at 2500 mg/L in methanol. For the LC analysis of MAE, the working solutions of PAs were prepared in the calibration range of 5–200 mg/L in methanol. For the LC analysis of PHWE, the working solutions of PAs were prepared in the calibration range of 10–200 μg/L in methanol.

2.3. Extraction

2.3.1. Microwave-assisted extraction

A closed vessel system technique was employed using Marsx from CEM Corporation (Matthews, NC, USA). Powdered air-dried *T. farfara* flowers (1 g) were placed into a 100 mL Teflon extraction vessel with 40 mL of extraction solvent (Acidified to pH 2–3 with acid). Multiple extractions (2–3 samples simultaneously) were performed under different conditions. Samples were automatically stirred during the extraction process. The pressure in the vessel was set to be that of its own vapor pressure, and the temperature was set to be at boiling point of the binary mixture. After extraction, the vessel was allowed to cool to room temperature, extracts filtered, reduced to half volume, and extracted twice using dichloromethane, and twice using ether. The aqueous layer was then basified using 1 M NaOH (pH 8–9) before it was extracted thrice using dichloromethane. The combined extracts were then evaporated to dryness using rotary evaporator and residues were
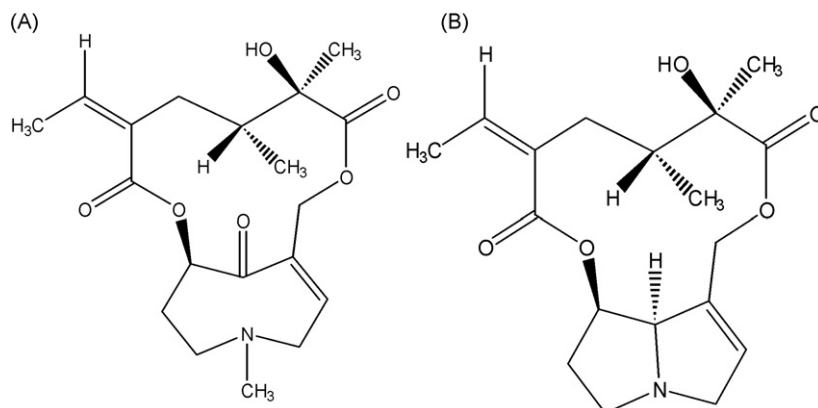
Fig. 1. Chemical structures of (A) senkirkine and (B) senecionine.

dissolved in 1 mL of methanol for analysis using HPLC and 5 mL for analysis using LC–MS. The mixture was centrifuged at 13,000 rpm for 15 min before it was analysed.

2.3.2. Pressurized hot water extraction

The instrumentation of PHWE was the same as the one used by Ong et al. [21]. Briefly, the dimensions of the stainless steel columns obtained from Phenomenex were 10.0 mm ID × 1/2 in OD × 25 cm. The high pressure was generated by an isocratic Shimadzu LC 10 series pump (Kyoto, Japan). The pump flow was set at 1.5 mL/min and the pressure in the system indicated by the HPLC pump was between 15 and 23 bars. The elevated temperature for PHWE was maintained by a HP5890 GC oven (Hewlett-Packard, CA, USA). And a CLIC miniature back pressure regulator (Switzerland) was used to control the outlet flow. Generally 0.25 g of the powdered and dried *T. farfara* was weighed directly in to a 50 mL plastic tube and mixed thoroughly with around 15 mL sand. The mixture was then transferred to the extraction cell, whose ends were filled with cotton. The cell was pre-filled with extraction solvent to check the possible leakage before setting the temperature to a certain value.

The extraction efficiency was investigated with extractions at various temperatures of 60 °C, 80 °C, 100 °C and 120 °C for 40 min. The extract collected was rota-evaporated or heated to less than 50 mL, followed by being transferred to a 50 mL volumetric flask. The kinetic study of PHWE was performed by collecting extracts at an interval of 10 min over a period of 80 min. In between runs, the system was washed with methanol in water (1:1) for 5 min.

2.3.3. Heating under reflux

Powdered air-dried *T. farfara* flowers (1 g) were placed in a 150 mL round bottom flask with 60 mL of solvent. 1 M of HCl was added such that the pH of the resulting solution fell to around 2–3. A condenser was fitted to prevent solvent loss from occurring and the mixture was refluxed for 60 min. The mixture was cleaned up in the same way as described in MAE section.

2.4. LC and LC/ESI-MS analyses of MAE extracts

HPLC analyses were performed on an Agilent 1100 HPLC instrument (Waldbronn, Germany) coupled to binary gradient pump, autosampler, column oven, and diode array detector. Detection wavelength was set at 220 nm.

For the analysis of MAE extracts by HPLC, the samples were separated on a Waters Xterra C_{18} column (5 μm, 3.9 mm × 150 mm, USA). The gradient elution involved a mobile phase consisting of (A) 0.1% formic acid in 20 mM ammonium acetate and (B) 0.1% formic acid in acetonitrile. The initial condition was set at 10% B, gradient up to 40% B in 20 min before returning to initial conditions for 10 min. The oven temperature was set at 40 °C and flow rate was set at 0.7 mL/min. For all experiments, volumes of 10 μL of the diluted standards and samples were injected.

For LC/ESI-MS analysis, the system comprised of an Agilent 1100 series (Waldbronn, Germany) binary gradient pump, autosampler, column oven, diode array detector and a LCQ-Duo ion trap mass spectrometer (ThermoFinnigan, San Jose, CA, USA).

ESI-MS was performed in the positive mode. The LCQ mass spectrometer was operated with the capillary temperature at 270 °C, sheath gas at 80 (arbitrary units) and auxillary gas at 20 (arbitrary units). The target was fixed at 2×10^7 ions and the automatic gain control was turned on. The electrospray voltage was set at 4.5 kV, the capillary voltage at 10 V and lens tube offset at 0 V. Mass spectra were recorded from m/z 100–800.

The ESI-MS spectrum was acquired in the positive mode. The instrument was operated in the selected ion monitoring (SIM) mode, where m/z of 336, m/z of 366 and m/z of 230 were isolated. The product ions from 100 to 800 were collected. The heated capil-

lary temperature was maintained at 350 °C, the flow rate of drying gas was set at 10 L/min and the pressure of nebulizer nitrogen gas was 50 psi, respectively. The target was set at 30,000, maximum accumulation time: 300 ms, the number of average scans was 5 spectra/s and Smart-Select™ was used.

Linearities for PAs were established between 5 mg/L and 200 mg/L (correlation coefficient ≥ 0.99). S/N was at least 3 for peak identification. To quantify the two compounds in the medicinal herb, a three-point calibration based on the linearity established was used. The R.S.D.s ($n=6$) for senkirkine and senecionine were found to be less than 5% on different days.

2.5. LC/ESI-MS analyses of PHWE extracts

For LC/ESI-MS analyses of PHWE extracts, the gradient elution consisted of mobile phase of (A) 30 mM ammonium formate with 0.1% formic acid and (B) acetonitrile with 0.1% formic acid. The initial condition was set at 5% B, gradient up to 100% B in 15 min before returning to initial condition for 10 min. Oven temperature was set at 50 °C and flow rate was set at 0.2 mL/min. For all experiments, 5 μL of standards and sample extracts were injected. The column used for separation was Luna 3u C18 (2) 100A, 100 mm × 2.0 mm (Phenomenex, Torrance, CA, USA). All the conditions for ESI-MS were the same as mentioned above. Linearitis of PAs were established between 10 μg/L and 200 μg/L for LC/MS with correlation coefficients of $r^2 \geq 0.99$. And the three-point calibration based on the linearity established was used to quantify the two compounds in the medicinal herb. The R.S.D.s ($n=6$) for senkirkine and senecionine was found to vary from 0.6% to 5.4% on different days.

3. Results and discussions

3.1. HPLC analysis for MAE

3.1.1. HPLC analysis with UV detector

The optimized separation conditions were applied to the MAE extracts of *T. farfara*. The content of senkirkine in samples of *T. farfara* was found to be present from 19.5 ppm to 46.6 ppm. For senecionine, it was either not detected or present in less than 1 ppm [8]. From the chromatograms obtained, co-eluting peaks were observed with the analyte, senkirkine, before any clean-up step was performed (Fig. 2A). In order to determine the amounts of PAs present in the plant extract, a clean-up step to remove co-eluting substances was performed to quantitate senkirkine accurately (Fig. 2B). Based on other reports, a clean-up step with solid phase extraction with diol or cation exchange cartridges was used [8,28–29]. For the current work, we used a liquid–liquid extraction clean-up step as reported earlier [12]. To check if the co-eluting peaks had been removed efficiently, UV spectra (not shown) were obtained for the senkirkine peak in the botanical extract and compared against that obtained using a standard. From the UV spectra obtained, it can be seen that the clean-up step has effectively removed the co-eluting components as the UV spectrum of the peak from the sample closely resembles that of the UV spectrum of the peak from the standard.

3.1.2. Optimization of MAE

As the pyrrolizidine alkaloids exist mainly in basic form, the alkaloids are usually extracted in acidified solution with weak acids such as acetic acid or other strong acids [8,12,28,29]. For the current work, two different acids, acetic acid and HCl in MeOH:H_2O (1:1) were tested with MAE under the identical experimental conditions. From the results obtained in Fig. 3A, it can be seen that extraction using HCl gives better extraction efficiency. Hence, all further extractions were done using solution acidified with HCl.

The amount of microwave radiation absorbed is dependant on the dielectric constants of the solvents used. For the extraction of

Z. Jiang et al. / Talanta 79 (2009) 539–546

Table 1
Comparison of MAE with heating under reflux for the analysis of senkirkine in *Tussilago farfara* by LC with UV detection.

Comparison between heating under reflux and MAE on 2 days	Heating under reflux ($n = 2$)		MAE ($n = 3$)	
Senkirkine (μg/g)	Mean ± S.D.	R.S.D. (%)	Mean ± S.D.	R.S.D. (%)
Senkirkine	94.0 ± 4.2	4.50	111.7 ± 11.3	9.66
Senkirkine	118.5 ± 0.04	0.04	123.6 ± 3.57	3.05

marker compounds in *T. farfara,* it was reported that a binary mixture of MeOH:H$_2$O (1:1) gave better extraction efficiency compared to using purely just water or methanol itself [8]. Two different solvent types namely MeOH:H$_2$O (1:1) and EtOH:H$_2$O (1:1) were evaluated under the same experimental conditions. From the result in Fig. 3B, MeOH:H$_2$O (1:1) was able to give better extraction efficiency. Hence, MeOH:H$_2$O (1:1) acidified with HCl was selected for all further works. Although the use of a closed vessel allowed the use of temperatures above the boiling point of the solvent, the boiling point of the binary mixture was chosen for the current work. This is to prevent any buildup of excessive vapor pressure in the vessel. An extraction time of 15 min was selected as it was reported that extraction using MAE could be completed in less than 15 min [16,30–33].

To determine the extraction efficiency of MAE, the amount of senkirkine present in the same medicinal plant was compared with that obtained by heating under reflux. From Table 1, the amount of senkirkine in the medicinal plant extracted by MAE was compara-ble to that obtained by heating under reflux. This shows that the conditions such as the extraction temperature and time of extraction for MAE were optimal. The recovery of the clean-up step using liquid–liquid extraction was found to be 103.1 ± 3.7% ($n = 3$).

Taking into account the number of steps in the proposed procedures, sample size used and the non-homogeneity of the medicinal plant samples, the method precision for the current work was comparable with other reports for the determination of marker or bioactive compounds in medicinal plants by LC with UV detection [34–37].

The main reasons for the enhanced performance when using MAE over reflux extraction are the higher solubility of analytes in solvent and higher diffusion rates as a result of a more homogenous heating due to the principle of microwave heating. A more homogenous heating resulted in the strong solute-matrix interaction caused by van der Waals forces, hydrogen bonding and dipole attractions between solute molecules and active sites on the matrix to be disrupted.

3.1.3. LC/ESI-MS analyses for MAE

For the positive ion ESI experiments, senkirkine and senecionine showed a very high tendency to form [M+H]$^+$ at 366.3 and 336.2 respectively. The two compounds were injected into the ESI/MS system and then fragmented in the ion trap up to MS^2 or MS^3 using the collision induced dissociation (CID). The advantage of multistage
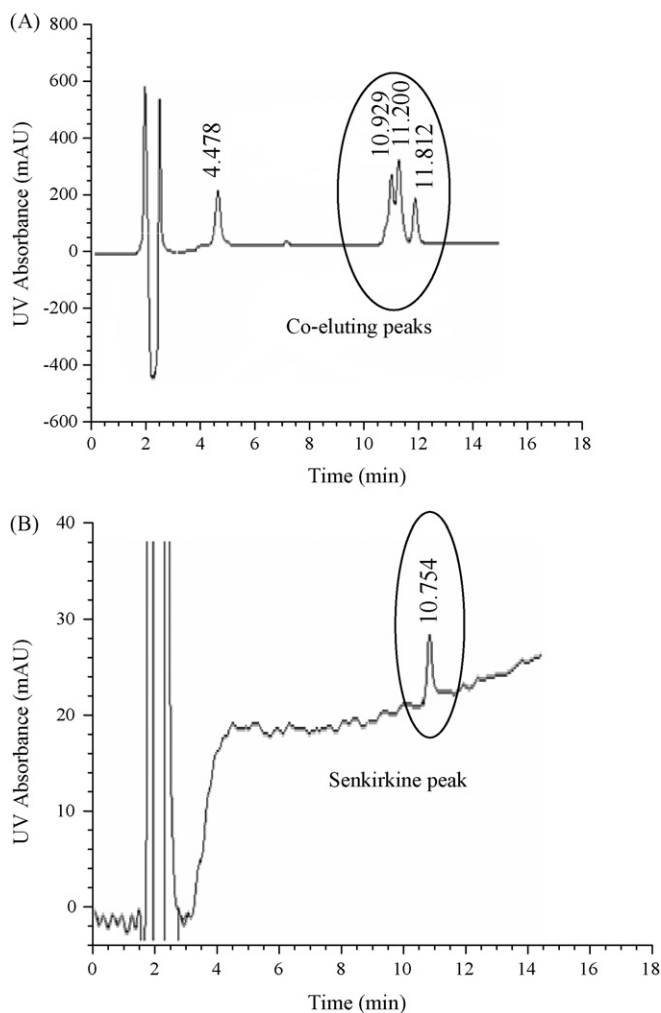
Fig. 2. Chromatogram of *Tussilago farfara* extract (A) before clean-up step, and (B) after clean-up step. Running conditions are as stated above.
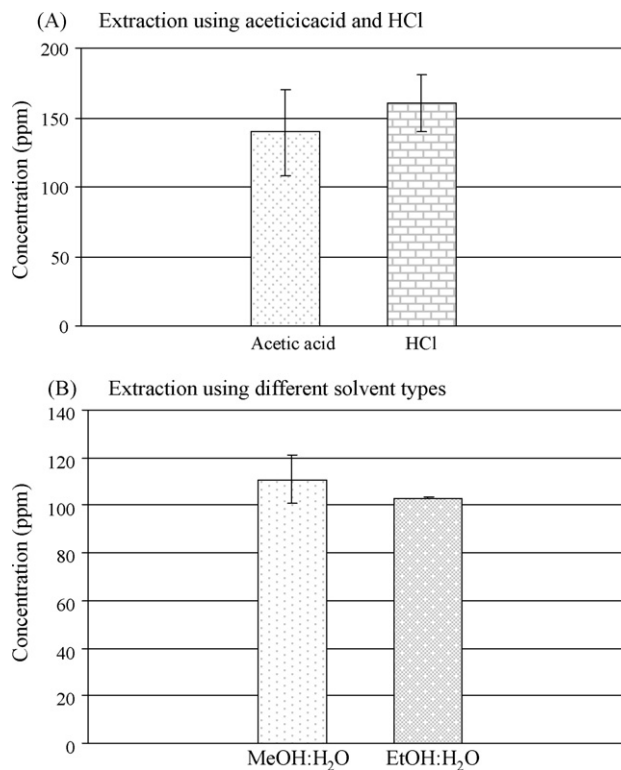
Fig. 3. Effect of different acids and solvents on microwave-assisted extraction for senkirkine using: (A) different acids with MeOH:H$_2$O (1:1) as solvent, and (B) MeOH:H$_2$O (1:1) and EtOH:H$_2$O (1:1) as solvents with HCl. Values expressed as means ± S.D. ($n = 2$).
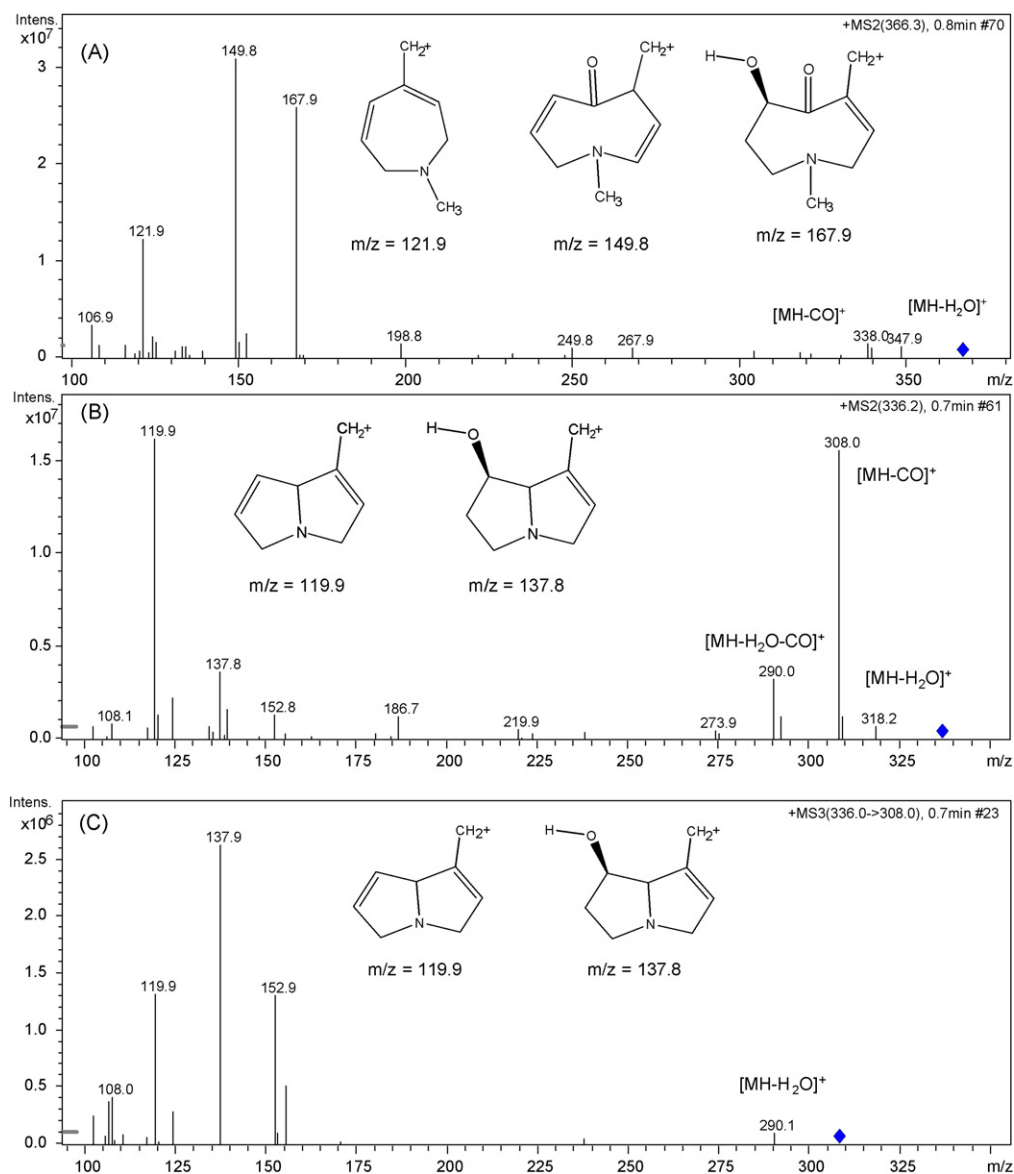
Fig. 4. MS^2 fragmentation pattern of (A) senkirkine, (B) senecionine, and (C) MS^3 fragmentation pattern of senecionine.

MS is that further fragmentation can be induced when significant fragmentation pattern cannot be observed from the ESI/MS^2 spectra. This can be seen for baicalin in *Scutellariae radix* and Salvinorin B in *Salvia divinorum* where significant fragmentation pattern was not observed with the MS^2 spectra and MS^3 was required to generate characteristic fragmentation pattern [38,39]. As seen from each fragmentation pathways in Fig. 4, the main losses were water and carbon monoxide. The losses of H_2O and CO have been observed in the MS^n spectra of natural occurring substances such as salvinorin A and others [38,40]. The MS/MS experiments of senkirkine and senecionine (Fig. 4A–C) provided characteristic fragmentation ions that were consistent with that of retrosine-type and otonecine-type alkaloids [28,41]. The otonecine-type PA, senkirkine, showed characteristic fragment ions at *m/z* 150, and 168. The retronecine-type PA, senecionine, showed characteristic fragment ions at *m/z* 138 and 120. The fragmentation pathways for both senkirkine and senecionine were consistent with other reports [28,41].

For senkirkine, only MS^2 spectra was collected as the abundance of daughter ions at *m/z* 347.9 [MH−H$_2$O]$^+$ and 338.0 [MH−CO]$^+$ were low. The selection of lower *m/z* for MS^3 did not give useful information. Thus, further fragmentation was not done for senkirkine. As for senecionine, the abundance of daughter ion at *m/z* 308.0 [MH−CO]$^+$ was high. From Fig. 4B and C, it can be seen that the daughter ions at *m/z* 119.9 decreased while other ions at *m/z* 137.9 and *m/z* 152.9 increased. Although both senkirkine and senecionine have similar chemical structures, the fragmentation patterns can differ significantly. Finally, the characteristic fragmentation patterns for both senkirkine and senecionine are required for the rapid identification of unknown compounds in botanical extracts with reference to pure standards.

For the determination of aristolochic acids in multi-components herbal remedies, a method without any clean-up or concentration steps with LC/MS^2 had been developed [42]. To the authors' best knowledge, reports on the use of LC/MS for identification of target compounds in the presence of co-eluting peaks in botanical extracts are rather limited. As seen in Fig. 2A and B, when HPLC was used, long and tedious clean-up step had to be employed to remove co-eluting peaks before senkirkine could be detected. However, by using LC/MS in the SRM mode where ions of *m/z* of 336 and 366 were isolated and detected, trace component senecionine as well as senkirkine could be detected successfully without the use of any clean-up step (Fig. 5). Despite the presence of co-eluting

Table 2
Comparison of MAE between heating under reflux and PHWE between heating under reflux.

Conc. of alkaloids on 2 days (μg/g)	Comparison between MAE and heating under reflux				Comparison between PHWE and heating under reflux			
	MAE ($n=3$)		Heating under reflux ($n=2$)		PHWE ($n=6$)		Heating under reflux ($n=2$)	
	Mean $\pm$ S.D.	R.S.D. (%)	Mean $\pm$ S.D.	R.S.D. (%)	Mean $\pm$ S.D.	R.S.D. (%)	Mean $\pm$ S.D.	R.S.D. (%)
Senkirkine (Day 1)	102.2 $\pm$ 10.6	10.4	109.6 $\pm$ 7.1	6.5	85.28 $\pm$ 5.00	5.9	84.78 $\pm$ 3.14	3.7
Senecionine (Day 1)	2.16 $\pm$ 0.08	3.7	2.65 $\pm$ 0.04	1.5	3.20 $\pm$ 0.19	5.9	3.05 $\pm$ 0.04	1.3
Senkirkine (Day 2)	112.8 $\pm$ 11.5	10.2	118.6 $\pm$ 8.3	7.0	80.95 $\pm$ 2.45	4.0	84.70 $\pm$ 3.73	5.8
Senecionine (Day 2)	2.57 $\pm$ 0.12	4.7	2.76 $\pm$ 0.15	5.4	3.18 $\pm$ 0.16	5.0	3.30 $\pm$ 0.18	5.5

peaks and possible ion suppression, the presence of low level of senecionine in the extract can be detected confidently. This shows that the proposed method using LC/MS was sensitive and selective. From Table 2, we can see that the comparable extraction efficiency was obtained between MAE and heating under reflux extraction. The limits of detection (LODs) and limits of quantitation (LOQs) of the MAE method developed were found to be 0.26 μg/g and 1.32 μg/g, 0.47 μg/g and 1.80 μg/g for senkirkine and senecionine respectively.

3.2. HPLC analysis for PHWE

3.2.1. LC/ESI-MS analysis for PHWE

A LC/ESI-MS method without the use of splitting was used for the analysis of senkirkine and senecionine in the herbal medicine. Linearities for senkirkine and senecionine were established between 10 μg/L and 200 μg/L (correlation coefficient $\geq$ 0.99). The relative standard deviation (R.S.D.) values of the peak heights for senkirkine and senecionine were observed to vary from 0.6% to 5.4% and 3.0% to 4.2% ($n=6$) respectively on different days.

3.2.2. Optimization of PHWE

The main parameters that can affect the extraction efficiency of PHWE are pressure, temperature, extraction time and addition of organic modifiers [21,43,44]. Generally, the pressure has little effect on the extraction efficiency since it is only for maintaining the extraction solvent in liquid state at elevated temperature [45–47]. For the current work, the optimal extraction solvent in MAE was also used in PHWE. As a result, temperature and extraction time were the main parameters considered. Since the physicochemical

properties of water such as viscosity, surface tension, diffusibility, and solvent strength could be changed at elevated temperature, they could affect the solubility of the target compound in water. Since significant changes in the extraction efficiency from 60 °C to 120 °C were not observed in Fig. 6, a temperature of 60 °C was chosen as the optimized temperature. Fig. 7 shows that most of the main PA, senkirkine, was extracted out after 50 min, while most of senecionie was extracted out after 20 min. As a result, 50 min was selected as the optimal extraction time.

The extraction efficiencies of pyrrolizidine alkaloids in *T. farfara* by PHWE were found to be comparable with heating under reflux extraction (Table 2). The method precision (R.S.D.) was found to vary from 4.0% to 5.9%. The LODs and LOQs of the PHWE method established were found to be 1.04 μg/g and 5.29 μg/g, 0.72 μg/g and 2.86 μg/g for senkirkine and senecionine respectively. From Table 2, we can also see that there are some differences between the two sets of results for heating under reflux extractions. This might be due to the batch to batch variation.

3.3. Matrix-induced interference

Ion suppression is one form of matrix effect that is a major concern in LC/MS techniques. It is typically observed in sample extracts from biological samples and is most possibly caused by the high
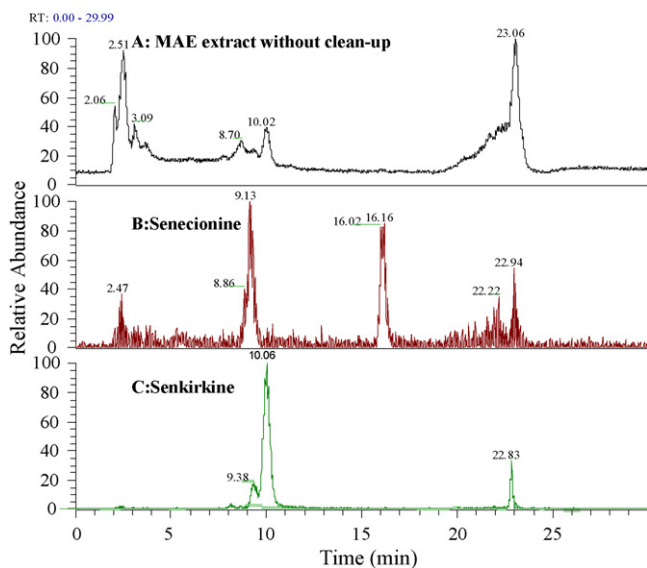
Fig. 5. (A) Total ion chromatogram (TIC) of *Tussilago farfara* extract before clean-up step. (B) Extracted ion chromatogram (EIC) of senecionine observed at *m/z* 336 and (C) EIC of senkirkine observed at *m/z* 366.
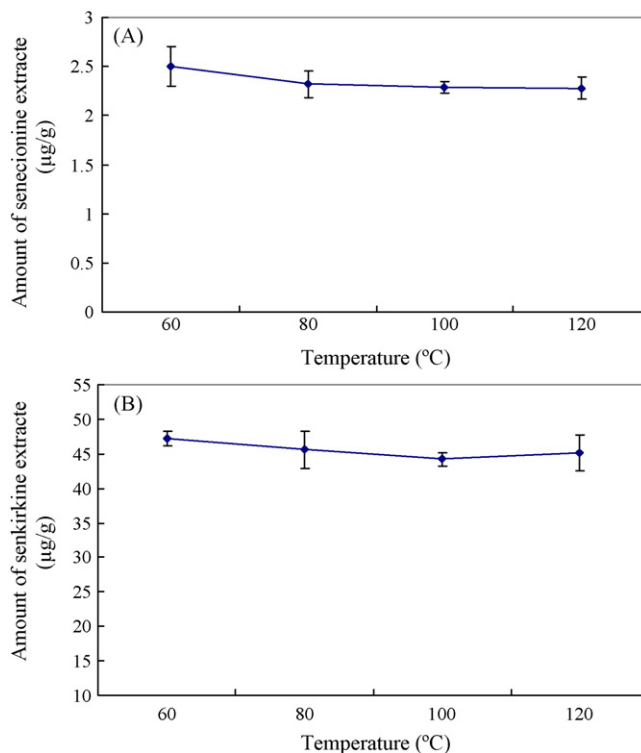
Fig. 6. Effect of different extraction temperatures on the recoveries of (A) senecionine and (B) senkirkine by PHWE ($n=3$) with flow rate: 1.5 mL/min for 40 min.
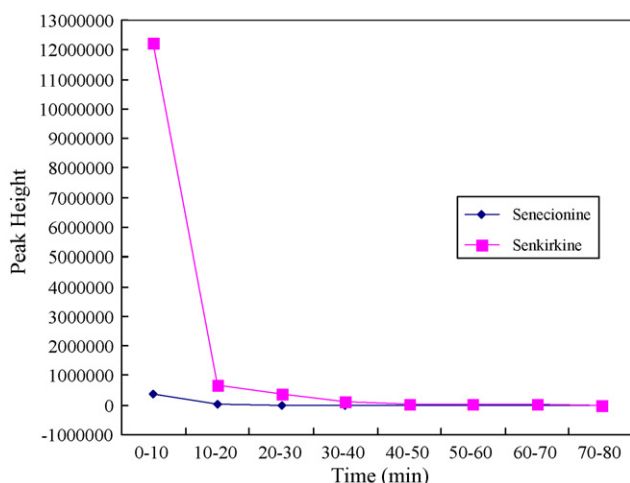
Fig. 7. Effect of extraction time on the recoveries of senecionine and senkirkine by PHWE.

concentration of nonvolatile materials present in the spray with the analyte. Any co-eluting nonvolatile solute such as salts may cause the suppression of ionization, giving rise to irreproducible results. Ion pairing agents, surface activities of the analyte and interfering compounds may also play an important role in ionization suppression [48]. Modifying instrumental components and parameters, chromatographic separation and sample preparation are strategies to reduce or eliminate ion suppression. Various calibration methods can be applied to compensating this effect. Standard addition is an effective method and is able to give good results even with variable matrices [49]. For the analysis of naturally occurring substances in botanical extracts, the effect of ion suppression was often not investigated [50–54]. As for the analysis of Toosendanin in the botanical extracts carried out using external standard calibration, the effect of matrix induced interference was investigated and significant ion suppression was not observed [55]. For plant analysis, standard addition experiments remained to be the most effective method for the evaluation of ion suppression in LC/MS. From the chromatograms obtained in Fig. 2B, the presence of senkirkine was confirmed by the retention time and the UV spectra with the standard compounds. The effect of ion suppression or matrix-induced interference in the botanical extracts was investigated using the standard addition method. For extracts obtained from MAE, the internal standard calibration plot ($y = 0.0024x − 0.035$, $y = 0.0031x + 0.075$) and the standard addition (with the use of internal standard) plot ($y = 0.0025x + 0.1831$, $y = 0.0031x + 0.4857$) were essentially parallel for both senecionine and senkirkine respectively. For extracts obtained from PHWE, the external standard calibration plot ($y = 4321.1x − 7089.6$, $y = 2774.9x − 4978.7$) and the standard addition (without the use of internal standard) plot ($y = 4112x + 97678$, $y = 2986.7x + 122142$) were also essentially parallel for both senecionine and senkirkine. Hence, it can be deduced that without the use of any sample clean-up steps, significant ion suppression was not present even for the analysis of low level of senecionine in the plant extract.

4. Conclusions

In this work, both the combination of MAE and PHWE with LC/MS allow for the simple, rapid isolation and quantification of the major and the minor pyrrolizidine alkaloids in *T. farfara*. Using LC/MS^n, characteristic fragmentation pattern for both senkirkine and senecionine were obtained and can be used for the rapid identification of unknown compounds in botanical extracts with reference to a pure standard. Accompanied with the use of internal

and external standard calibration, significant matrix-induced interferences or ion suppression in the presence of co-eluting peaks was not observed. As a result, the MAE and PHWE methods proposed in this work could be alternatives for the extraction of bioactive or marker compounds in medical plants.

References

[1] K.Y. Liu, T.J. Zhang, W.Y. Gao, H.X. Chen, Y.N. Zheng, Zhongguo Zhongyao Zazhi 31 (2006) 1837.
[2] C.L. Fan, Faming Zhuanli Shenqing Gongkai Shuomingshu, 2007.
[3] Y.M. Shi, Faming Zhuanli Shenqing Gongkai Shuomingshu, 2002.
[4] S.X. Wang, Faming Zhuanli Shenqing Gongkai Shuomingshu, 2002.
[5] H.S. Lee, M.C. Rho, Y.K. Kim, M.Y. Chung, S.W. Lee, H.R. Park, J.H. Choi, J.Y. Kang, D.H. Kim, Repub. Korean Kongkae Taeho Kongbo (2007).
[6] Awasthy, Narendra Kumar, Indian Patent Application (2006).
[7] H.R. Park, M.Y. Yoo, J.H. Seo, I.S. Kim, N.Y. Kim, J.Y. Kang, L. Cui, C.S. Lee, C.H. Lee, H.S. Lee, J. Agric. Food Chem. 56 (2008) 10493.
[8] R. Lebada, A. Schreier, S. Scherz, C. Resch, L. Krenn, B. Kopp, Phytochem. Anal. 11 (2000) 366.
[9] Environmental Health Criteria 80, Pyrrolizidine Alkaloids, World Health Organization, Geneva, 1988.
[10] P.P. Fu, Y.C. Yang, Q.S. Xia Xia, M.W. Chou, Y.Y. Cui, G. Lin, J. Food Drug Anal. 10 (2002) 198.
[11] P.P. Fu, Q. Xia, G. Lin, M.W. Chou, Drug Metab. Rev. 36 (2004) 1.
[12] L.J. Yu, S.F.Y. Li, Electrophoresis 26 (2005) 4360.
[13] H.T. Feng, S.F.Y. Li, J. Chromatogr. A 973 (2002) 243.
[14] T. Mroczek, K. Glowniak, A. Wlaszczyk, J. Chromatogr. A 949 (2002) 249.
[15] V. Camel, Analyst 126 (2001) 1182.
[16] B. Kaufmann, P. Christen, Phytochem. Anal. 13 (2002) 105.
[17] C. Sun, H.Z. Liu, Anal. Chim. Acta 612 (2008) 160.
[18] G.Q. Xiao, Y. Tian, X.Y. Lu, J. Fang, Anjisuan He Shengwu Ziyuan 29 (2007) 76.
[19] H.J. Fan, W. Luan, G.K. Li, Fenxi Ceshi Xuebao 25 (2006) 27.
[20] Q. Liu, X.Q. Chen, X.Y. Jiang, S.D. Wu, Tianran Chanwu Yanjiu Yu Kaifa 17 (2005) 65.
[21] E.S. Ong, J.S.H. Cheong, D. Goh, J. Chromatogr. A 1112 (2006) 92.
[22] R. Carabias-Martinez, E. Rodriguez-Gonzalo, P. Revilla-Ruiz, J. Hernandez-Mendez, J. Chromatogr. A 1089 (2005) 1.
[23] V. Fernandez-Gonzalez, E. Concha-Grana, S. Muniategui-Lorenzo, P. Lopez-Mahia, D. Prada-Rodriguez, J. Chromatogr. A 1196–1197 (2008) 65.
[24] C.C. Teo, S.N. Tan, J.W.H. Yong, C.S. Hew, E.S. Ong, J. Chromatogr. A 1182 (2008) 34.
[25] K. Hartonen, J. Parshintsev, K. Sandberg, E. Bergelin, L. Nisula, M. Riekkola, Talanta 74 (2007) 32.
[26] L. Dong, J.Y. Wang, C.H. Deng, X.Z. Shen, J. Sep. Sci. 30 (2007) 86.
[27] G. Hosch, H. Wiedenfeld, T.H. Dingermann, E. Roder, Phytochem. Anal. 7 (1996) 284.
[28] T. Mroczek, K. Ndjoko, K. Glowniak, K. Hostettmann, J. Chromatogr. A 1056 (2004) 91.
[29] T. Mroczek, K. Ndjoko-Ioset, K. Glowniak, A. Mietkiewicz-Capala, K. Hostettmann, Anal. Chim. Acta 566 (2006) 157.
[30] A. Brachet, P. Christen, J.L. Veuthey, Phytochem. Anal. 13 (2002) 162.
[31] X. Pan, G. Niu, H. Liu, J. Chromatogr. A 922 (2001) 371.
[32] V. Camel, Trends Anal. Chem. 19 (2000) 229.
[33] F. Zhang, B. Chen, S. Xiao, S. Yao, Sep. Purif. Technol. 42 (2005) 283.
[34] E.S. Ong, S.O. Woo, Y.L. Yong, J. Chromatogr. A 904 (2000) 57.
[35] E.S. Ong, S.M. Len, Anal. Chim. Acta 482 (2003) 81.
[36] E.S. Ong, S.M. Len, J. Chromatogr. Sci. 42 (2004) 211.
[37] A.T.W. Eng, M.Y. Heng, E.S. Ong, Anal. Chim. Acta 583 (2007) 289.
[38] C. Medana, C. Massolino, M. Pazzi, C. Baiocchi, Rapid Commun. Mass Spectrom. 20 (2006) 131.
[39] E.S. Ong, J. Chromatogr. B 812 (2004) 23.
[40] Y. Zhang, Q. Shi, P. Shi, W. Zhang, Y. Cheng, Rapid Commun. Mass Spectrom. 20 (2006) 2328.
[41] S. Pu, D. Xu, M. Zhang, H. Zhou, Z. Wang, G. Yu, Chin. J. Nat. Med. 2 (2004) 293.
[42] G.C. Kite, M.A. Yule, C. Leon, M.S.J. Simmonds, Rapid Commun. Mass Spectrom. 16 (2002) 585.
[43] J. Kronholm, K. Hartonen, M.L. Riekkola, Trends Anal. Chem. 26 (2007) 396.
[44] R.M. Smith, J. Chromatogr. A 975 (2002) 31.
[45] S.B. Hawthorne, Y. Yang, D.J. Miller, Anal. Chem. 66 (1994) 2912.
[46] M.S. Krieger, J.L. Wynn, R.N. Yoder, J. Chromatogr. A 897 (2000) 405.
[47] E.S. Ong, J. Sep. Sci. 25 (2002) 825.

[48] R. King, R. Bonfiglio, C. Fernandez-Metzler, C. Miller-stein, T. Olah, J. Am. Soc. Mass Spectrom. 11 (2000) 942.
[49] L.E. Jessome, D.A. Volmer, LC GC 24 (2006) 498.
[50] Y. Bao, C. Li, H. Shen, F. Nan, Anal. Chem. 76 (2004) 4208.
[51] R. Kaneko, S. Hattori, S. Furuta, M. Hamajima, Y. Hirata, K. Watanabe, H. Seno, A. Ishii, J. Mass Spectrom. 41 (2006) 810.
[52] D. Pigini, A.M. Cialdella, P. Faranda, G. Tranfo, Rapid Commun. Mass Spectrom. 20 (2006) 1013.
[53] T. Ligor, A. Ludwiczuk, T. Wolski, B. Buszewski, Anal. Bioanal. Chem. 383 (2005) 1098.
[54] P. Zou, H.L. Koh, Rapid Commun. Mass Spectrom. 21 (2007) 1239.
[55] E.S. Ong, C.N. Ong, Rapid Commun. Mass Spectrom. 21 (2007) 589.

A solid phase extraction using a chelate resin immobilizing carboxymethylated pentaethylenehexamine for separation and preconcentration of trace elements in water samples

Shigehiro Kagaya [a,*], Emiko Maeba [a], Yoshinori Inoue [b,c], Waka Kamichatani [b], Takehiro Kajiwara [a], Hideyuki Yanai [b], Mitsuru Saito [b], Koji Tohda [a]

[a] Graduate School of Science and Engineering for Research, University of Toyama, Gofuku 3190, Toyama 930-8555, Japan
[b] R&D Marketing Division, Nippon Filcon Co., Ltd., Ohmaru 2220, Inagi, Tokyo 206-8577, Japan
[c] Graduate School of Medicine, Osaka City University, Asahi-machi 1-4-3, Abeno, Osaka 545-8585, Japan

ARTICLE INFO

ABSTRACT

A chelate resin immobilizing carboxymethylated pentaethylenehexamine (CM-PEHA resin) was prepared, and the potential for the separation and preconcentration of trace elements in water samples was evaluated through the adsorption/elution test for 62 elements. The CM-PEHA resin could quantitatively recover various elements, including Ag, Cd, Co, Cu, Fe, Ni, Pb, Ti, U, and Zn, and rare earth elements over a wide pH range, and also Mn at pH above 5 and V and Mo at pH below 7. This resin could also effectively remove major elements, such as alkali and alkaline earth elements, under acidic and neutral conditions. Solid phase extraction using the CM-PEHA resin was applicable to the determination of 10 trace elements, Cd, Co, Cu, Fe, Mn, Mo, Ni, Pb, V, and Zn, in certified reference materials (*Enviro*MAT EU-L-1 wastewater and ES-L-1 ground water) and treated wastewater and all elements except for Mn in surface seawater using inductively coupled plasma atomic emission spectrometry. The detection limits, defined as 3 times the standard deviation for the procedural blank using 500 mL of purified water (50-fold preconcentration, $n = 8$), ranged from $0.003\,\mu g\,L^{-1}$ (Mn) to $0.28\,\mu g\,L^{-1}$ (Zn) as the concentration in 500 mL of solution.

© 2009 Elsevier B.V. All rights reserved.

1. Introduction

An evaluation of trace elements in treated wastewater and environmental water has value from the viewpoint of protecting and managing the environment as well as understanding the distribution of trace elements in the environment. For the determination of trace elements in water samples, inductively coupled plasma atomic emission spectrometry (ICP-AES) and inductively coupled plasma mass spectrometry (ICP-MS) are widely utilized because multi-elemental determination can be readily achieved. In the analyses of real water samples, such as treated wastewater and environmental water, however, large amounts of alkali and alkaline earth elements are often abundant and sometimes interfere with the determination of trace elements. In addition, ICP-AES has an insufficient detection power for some elements for the analyses of real water samples. To overcome these problems, the combination of a separation and preconcentration technique with ICP-AES and ICP-MS is useful.

The separation and preconcentration technique must effectively remove alkali and alkaline earth elements and concentrate targeted trace elements within detectable levels. Among the various separation and preconcentration techniques proposed up to now, a solid phase extraction using a chelate resin is one of the most practical ways to satisfy these requirements [1–5]; a variety of chelate resins have been studied from the viewpoint of the effective and/or selective adsorption of elements. The functional group immobilized on a chelate resin generally dominates the adsorption behavior of elements. Aminocarboxylic acids, such as iminodiacetic acid (IDA) [6–21], nitrirotriacetic acid (NTA) [20,22–29], ethylenediaminetetraacetic acid (EDTA) [30–32], diethylenetriaminepentaacetic acid (DTPA) [21,31–33], and triethylenetetraminehexaacetic acid (TTHA) [34], are the most popular functional groups for solid phase extraction. Chelate resins immobilizing IDA, such as Chelex 100 [6–13], Lewatit TP-207 [13], Muromac A-1 [14,15], and Toyopearl AF-Chelate 650 M [16], and those immobilizing NTA, such as NTA Superflow [28,29], are commercially available. Since the aminocarboxylic acid-type chelate resin can adsorb many elements simultaneously, solid phase extraction using these chelate resins is conveniently used for the separation and preconcentration of elements prior to their ICP-AES and ICP-MS determination. However, such aminocarboxylic acid-type chelate resins suffer at least

* Corresponding author. Tel.: +81 76 445 6865; fax: +81 76 445 6703.
E-mail address: kagaya@eng.u-toyama.ac.jp (S. Kagaya).

one serious disadvantage; alkaline earth elements, such as Mg and Ca, are significantly adsorbed even under weakly acidic conditions. Therefore, a washing process using a solution in which the pH is adjusted to appropriate values is needed after the adsorption of elements. Recently, a NOBIAS Chelate-PA1, in which both ethylene-diaminetriacetic acid and IDA are introduced as functional groups on a hydrophilic methacrylate resin, has become commercially available and has been applied to the separation and preconcentration of some trace elements, including Al, Cd, Co, Cu, Fe, Mn, Mo, Ni, Pb, Ti, U, and Zn [35–39]. It is noteworthy that NOBIAS Chelate-PA1 can remove considerable amounts of alkaline earth elements, such as Mg and Ca, at pH below 7 [36–39]. This exclusion ability for alkaline earth elements is attractive to the analyses of real water samples, particularly, treated wastewater and seawater, although the exclusion mechanism is not clear.

We studied a new aminocarboxylic acid-type chelate resin that can successfully remove major elements, such as alkali and alkaline earth elements, and effectively concentrate trace elements. The stability constant for a complex of a transition element with aminocarboxylic acid, including IDA, EDTA, DTPA, and TTHA, generally increases with increasing the number of ethyleneamine units in aminocarboxylic acids; IDA < EDTA < DTPA < TTHA [40]. The difference between the stability constant of Mg or Ca and that of other elements, such as Cd, Co, Cu, Fe, Ni, Pb, and Zn, also increase in that order. This information suggests that the use of polyaminocarboxylic acid as a functional group on a chelate resin possibly expands the range of pH within which trace elements can be effectively separated from major elements, such as alkaline earth elements, in treated wastewater and environmental

water. In this work, we prepared a new chelate resin immobilizing carboxymethylated pentaethylenehexamine (CM-PEHA resin) and found that the CM-PEHA resin is superior. The potential of CM-PEHA resin is comparable to that of NOBIAS Chelate-PA1 [35–39] for the exclusion of major elements and the concentration of trace elements. We here report the usefulness of the CM-PEHA resin to separate and concentrate trace elements in water samples. The results for the application of solid phase extraction using the CM-PEHA resin to analyze certified reference materials and some real water samples are also described.

2. Experimental

2.1. Apparatus

A Beckman Coulter Multisizer 3 Coulter Counter was used for measuring the particle size distribution of resin. The specific surface area and average pore diameter of the resin were measured using a Beckman Coulter SA3100 Surface Area Analyzer. Elemental analysis was carried out using a PerkinElmer 2400 Series II CHNS/O Elemental Analyzer System. Nuclear magnetic resonance (NMR) analysis was carried out using a JEOL JNM-α400. A PerkinElmer Optima 3000 DV inductively coupled plasma atomic emission spectrometer, equipped with a cross-flow nebulizer and a Scott-type spray chamber, and a Hitachi 180-80 polarized Zeeman atomic absorption spectrometer (flame-type) were used for the measurements of elements. The pH measurement was carried out using a Horiba F-22 pH meter. For the separation of the CM-PEHA resin in batch experiments, a Kubota Model 5400 centrifuge was used.
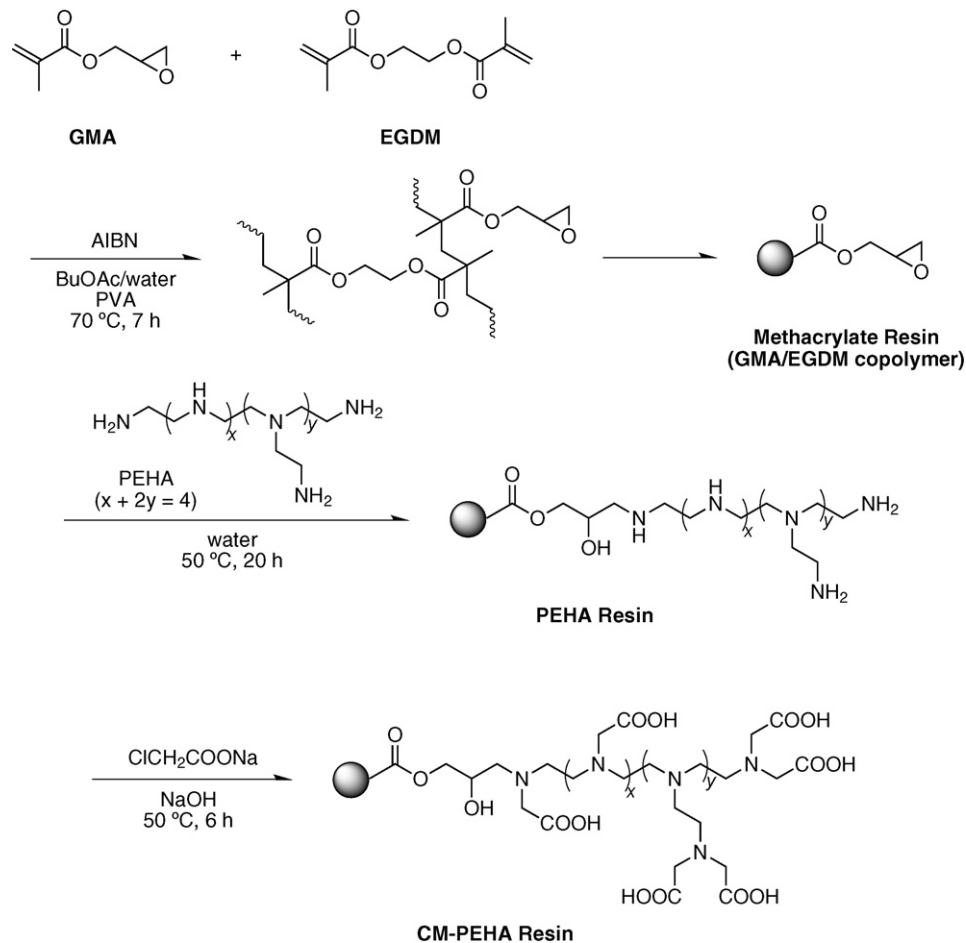
Fig. 1. Preparation scheme of CM-PEHA resin.

2.2. Reagents

For the preparation of the CM-PEHA resin, most reagents were purchased from Wako Pure Chemical Industries; all reagents were utilized without any further purification. Glycidylmethacrylate (GMA) and ethyleneglycoldimethacrylate (EGDM, Tokyo Chemical Industry) were used as a functional monomer and a cross-linker, respectively. Butylacetate (BuOAc) was chosen as an inert diluent for pore generation. As an initiator of radical polymerization, 2,2-azobis(isobutyronitrile)(AIBN) was utilized. Poly(vinyl alcohol) 500 (PVA) was used as a suspension stabilizer. Pentaethylenehexamine (PEHA) and sodium monochloroacetate were also used for the introduction of functional groups.

For the adsorption/elution study of elements, purified water (18.2 MΩ cm) obtained by a Millipore Simplicity UV was used. The commercially available ICP multi-element standard solution XVI (100 mg L^{-1} each of As, Be, Cd, Ca, Cr, Co, Cu, Fe, Li, Mg, Mn, Mo, Ni, Pb, Sb, Se, Sr, Tl, Ti, V, and Zn, Merck) and the PlasmaCAL multi-element standard (100 mg L^{-1} each of Ce, Dy, Er, Eu, Gd, Ho, Lu, Nd, Pr, Sm, Tb, Tm, U, Y, and Yb, SCP Science) were used. For the other elements, single-element stock solutions (1000 mg L^{-1}) were purchased from Acros Organics (Ir, Re Ru, and Hf) and Kanto Chemical (all others). These standard and stock solutions were diluted to a desired concentration in each experiment. For the estimation of the adsorption capacity, Mn(NO$_3$)$_2$·6H$_2$O (guaranteed reagent grade (GR), Wako Pure Chemical Industries), Cu(NO$_3$)$_2$·3H$_2$O (GR, Kanto Chemical), Y(NO$_3$)$_3$·6H$_2$O (99.99%, Kanto Chemical), and (NH$_4$)$_6$Mo$_7$O$_{24}$·4H$_2$O (GR, Wako Pure Chemical Industries) were used. The other reagents, including nitric acid, ammonium acetate, aqueous ammonia, and methanol, were of guaranteed or analytical reagent grade.

2.3. Preparation of CM-PEHA resin

The preparation scheme of CM-PEHA resin is shown in Fig. 1; CM-PEHA resin was prepared in 3 steps as follows.

2.3.1. Preparation of methacrylate resin

A methacrylate resin was first prepared by a suspension copolymerization of GMA and EGDM. A 1.0 g of AIBN was added to a mixture of 30 g of GMA, 70 g of EGDM, and 100 g of BuOAc. The mixture was added to 1000 mL of an aqueous solution dissolving 1 g of PVA. After the mixture was suspended with stirring at 400 rpm, the copolymerization of GMA and EGDM was performed at 70 °C for 7 h with stirring at 250 rpm. After cooling at room temperature, the obtained resin was washed with deionized water and methanol and then dried. The resin was classified at 45–90 μm of particle size by sieving.

2.3.2. Immobilization of PEHA on methacrylate resin

The methacrylate resin (20 g) was added to a mixture of 40 g of PEHA and 150 mL of deionized water. The suspension was stirred at 250 rpm for 20 h at 50 °C to immobilize PEHA on the resin. After cooling at room temperature, PEHA-immobilized resin (PEHA resin) was washed with deionized water and methanol.

2.3.3. Carboxymethylation of PEHA resin

All of the PEHA resin obtained by the reaction mentioned above was added to a solution prepared by dissolving 20 g of sodium chloroacetate in 200 mL of a 1 mol L^{-1} sodium hydroxide solution. The primary and secondary amines in PEHA on the resin were carboxymethylated at 50 °C for 6 h with stirring at 250 rpm. After cooling at room temperature, the CM-PEHA resin was washed with deionized water, methanol, and 1 mol L^{-1} nitric acid and was dried in vacuo.

2.4. Adsorption behavior of elements

The CM-PEHA resin (0.25 g as dry weight) was packed in 6 mL of a reservoir for solid phase extraction (Bond Elut Reservoir, Varian). The CM-PEHA resin was conditioned by passing 5 mL of methanol, 10 mL of 3 mol L^{-1} nitric acid, 20 mL of purified water, and 10 mL of a 0.1 mol L^{-1} ammonium acetate solution through the reservoir, in this order. The test solution (100 mL), which was prepared by adding a single element or several elements (10 μg each) to a 5 mmol L^{-1} ammonium acetate solution and adjusting the pH with nitric acid or aqueous ammonia, was then passed through the reservoir at a flow rate of 3 mL min^{-1}. After the CM-PEHA resin was washed using 20 mL of purified water, the adsorbed elements were eluted by passing 3 mL of 3 mol L^{-1} nitric acid and then 3 mL of purified water though the reservoir-packed CM-PEHA resin. The eluate was diluted to 10 mL with purified water, and the elements in the solution were determined by ICP-AES or flame atomic absorption spectrometry. The recovery of each element was calculated on the basis of the ratio of the amount of the element in the solution after adsorption/elution to that in the initial sample solution.

To investigate the adsorption capacity, the pH of the solution containing 5 mmol L^{-1} of Mn, Cu, Mo, or Y and 5 mmol L^{-1} of ammonium acetate was adjusted to 5.5 with nitric acid and aqueous ammonia. The CM-PEHA resin (0.10 g as dry weight) was added to 100 mL of the solution and then stirred at room temperature for 3 h. After the CM-PEHA resin was centrifuged at 3500 rpm for 5 min, the element in the supernatant solution was determined by ICP-AES. The adsorption capacity for each element was estimated on the basis of the decreased amount of the element in the solution.

2.5. Determination of trace elements in water samples

As the sample solution, treated wastewater in a wastewater treatment plant (Toyama Prefecture, Japan) was used; the sample solution was digested with nitric acid on heating [41] before use. A surface seawater sample, which was sampled at Iwase Port (Toyama Prefecture, Japan), was filtered through a membrane filter (Omnipore Membrane, Nihon Millipore, 0.45 μm of pore size), and the pH in the filtrate was adjusted to approximately 1 with nitric acid as soon as possible. For the recovery tests, 5 μg of Cd, Co, Cu, Fe, Mn, Mo, Ni, Pb, V, and Zn was spiked to an appropriate volume of the sample solution. Certified reference materials, *Enrivo*MAT EU-L-1 wastewater and ES-L-1 ground water (SCP Science), were also used to validate the solid phase extraction using the CM-PEHA resin combined with ICP-AES determination.

To 100–500 mL of the sample solution, 5–25 mL of 0.1 mol L^{-1} ammonium acetate was added, and the pH of the sample solution was then adjusted to 4.0 (for the surface seawater sample) or 5.5 (for certified reference materials and the treated wastewater sample) with aqueous ammonia using a pH meter. The sample solution was passed through the reservoir-packed CM-PEHA resin (0.25 g

Table 1
Operating conditions for ICP-AES.

Radio frequency output	1.3 (kW)
Argon gas flow rate	
Plasma gas	15 (L min^{-1})
Auxiliary gas	0.5 (L min^{-1})
Nebulizing gas	0.8 (L min^{-1})
Pump parameter	
Sample flush time	10 (s)
Sample flush flow rate	4.0 (mL min^{-1})
Sample flow rate	1.5 (mL min^{-1})
Read delay time	30 (s)
Reading time	Auto (minimum 0.01 s–maximum 20 s)

Table 2
Analytical wavelengths and ranges and correlation coefficients (R^2) of calibration curves for elements.

Element	Analytical wavelength (nm)	Calibration curve	
		Range[a]/μg in 10 mL	R^2
Cd	228.802	0.05–10	0.999
Co	230.786	0.05–10	0.999
Cu	327.393	0.5–10	0.999
Fe	238.204	0.1–10	0.999
Mn	257.610	0.01–10	0.999
Mo	202.031	0.5–10	0.999
Ni	231.604	0.05–10	0.999
Pb	220.353	0.1–10	0.999
V	309.310	0.05–10	0.999
Zn	206.200	0.5–10	0.997

[a] Amount in final solution (10 mL) after solid phase extraction using 100 mL of solution.

as dry weight) at a flow rate of 5 mL min^{-1} so that some elements could be adsorbed on the CM-PEHA resin. The adsorbed elements were eluted in the manner mentioned above. The 10 elements (Cd, Co, Cu, Fe, Mn, Mo, Ni, Pb, V, and Zn) were determined by ICP-AES under the operating conditions summarized in Tables 1 and 2; the emission intensities of the elements were measured in the axial view mode. Solutions for calibration curves were prepared using 100 mL of purified water spiked with the 10 elements in the same manner as for the sample solution. A blank test was also carried out using purified water at the same volume of the sample solution.

3. Results and discussion

3.1. Characteristics of the CM-PEHA resin

The methacrylate resin prepared by suspension copolymerization has a satisfactory-spherical shape with a macro-porous structure, which was confirmed using both optical and scanning electron microscopy. The median diameter based on the volume % size distribution was 70.9 μm after classification at 45–90 μm by sieving; the distribution, D_{75}/D_{25}, was 1.33. The specific surface

area and average pore diameter for the resin were 200 m^2 g^{-1} and 10.9 nm, respectively.

The result of the elemental analysis of the CM-PEHA resin was as follows: C, 52.08; H, 7.72; N, 4.71%. The N content in the CM-PEHA resin calculated from the result was 3.4 mmol g^{-1}, corresponding to 0.56 mmol g^{-1} as PEHA. PEHA can exist in some types of isomers, including linear and branched structures; these isomers are probably also contained in commercially available PEHA [42]. When an aqueous solution containing PEHA was titrated with hydrochloric acid, well-defined inflection points were not observed in the titration curve. This result suggests that the pK_a values of PEHA are closely spaced due to the presence of some types of isomers in the PEHA used for this study [42]. A ^{13}C NMR analysis of PEHA was carried out as indicated in the literature [43]; the obtained spectrum indicated the presence of tertiary amine as well as primary and secondary amines in PEHA. One of the primary or secondary amines in PEHA would react with the epoxide group on the resin because a large excess of PEHA was added in the PEHA-immobilization step. The primary and secondary amines in PEHA immobilized on the resin were carboxymethylated; however, a part of the amine possibly remained in the primary and secondary states.

3.2. Adsorption behavior of trace elements

The recoveries of 62 elements on the CM-PEHA resin were investigated at various pH. The obtained results are shown in Fig. 2. A chelate resin immobilizing PEHA is available for Cu adsorption [44,45]; however, the adsorption behavior of the other elements is not clear. The CM-PEHA resin was able to quantitatively recover various elements, such as Ti, Fe, Co, Ni, Cu, Zn, Ag, Cd, Pb, rare earth elements, and U, over a wide pH range. It is interesting to note that the CM-PEHA resin has excellent affinity to V and Mo, which are present as oxo anions in the sample solution, under acidic and neutral conditions. On the other hand, alkali elements, such as Li, Na, and K, were remarkably excluded at all of the pH investigated. Alkaline earth elements, such as Mg, Ca, Sr, and Ba, were also hardly recovered at pH below 7. The recoveries of large amounts of Na, K, Mg, and Ca were also investigated. When
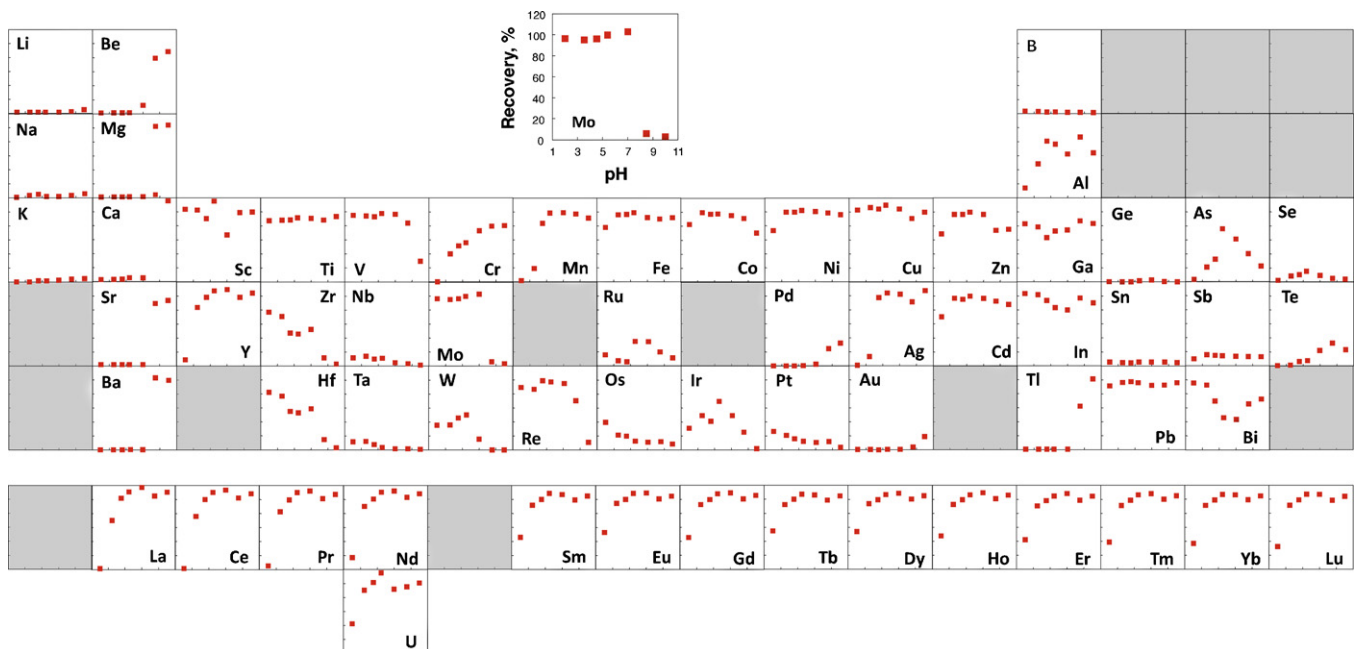
Fig. 2. Effect of pH on the recoveries of various trace elements.
Adsorption: sample volume 100 mL; element, 10 μg; flow rate, 3 mL min^{-1}. Elution: 3 mol L^{-1} HNO$_3$, 3 mL; final volume, 10 mL.
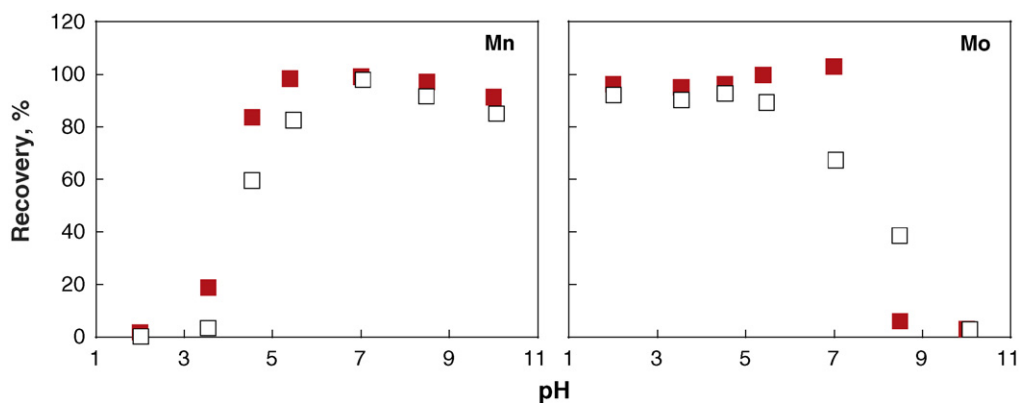
Fig. 3. Effect of the presence of Ca on the recoveries of Mn and Mo at various pH.
Adsorption: sample volume, 100 mL; Mn or Mo, 10 μg; Ca, 0.5 g L^{-1} (□) or not added (■); flow rate, 3 mL min^{-1}. Elution: 3 mol L^{-1} HNO$_3$, 3 mL; final volume, 10 mL.

100 mL of the solution containing 1200 mg of Na, 150 mg of Mg, or 50 mg of K or Ca, which is nearly equal to the amount contained in seawater [46], was passed through the reservoir-packed CM-PEHA resin, the recovered amount at pH 7 was 0.001 mg for Na, 0.002 mg for Mg, less than 0.001 mg for K, and 0.006 mg for Ca. The excellent ability for the exclusion of alkali and alkaline earth elements on the CM-PEHA resin makes it desirable for use in the separation and preconcentration of trace elements prior to their atomic spectroscopic determination because alkali and alkaline earth elements are generally present in large quantities in various samples and often interfere in atomic spectroscopic determination.

The adsorption capacities of the CM-PEHA resin for Mn, Cu, Y, and Mo, which achieved a quantitative adsorption under almost neutral conditions (Fig. 2), were then investigated at pH 5.5 in batch experiments. The amount of each element remaining in the solution nearly reached a constant after stirring for at least 1 h. The amounts of the elements that can be adsorbed on 1.0 g of CM-PEHA resin were estimated at 0.036 mmol (Mn), 0.34 mmol (Cu), 0.046 mmol (Y), and 0.35 mmol (Mo). The adsorption capacity of the CM-PEHA resin for Cu was larger than that of NOBIAS Chelate-PA1 [36–38].

The performance of the CM-PEHA resin for the separation and preconcentration of trace elements was comparable to those of NOBIAS Chelate-PA1 [35–39]. These results conclusively demonstrated that the CM-PEHA resin was useful for the separation and preconcentration of trace elements for atomic spectrometry.

3.3. Application to water analyses

The solid phase extraction using the CM-PEHA resin was applied to the separation and preconcentration of trace elements in various water samples for their ICP-AES determination. In this study, 10 elements (Cd, Co, Cu, Fe, Mn, Mo, Ni, Pb, V, and Zn), which were efficiently recovered using CM-PEHA resin, were selected as target elements.

3.3.1. Optimum conditions for the separation and preconcentration of trace elements

The conditions for the adsorption/elution of 10 elements were optimized. The effect of the presence of large amounts of Na, K, Mg, Ca, chloride, and sulfate on the recoveries of the elements was first investigated in the pH range of 2–10. An appropriate amount of NaNO$_3$ (12 g L^{-1} as Na), KNO$_3$ (0.5 g L^{-1} as K), Mg(NO$_3$)$_2$·6H$_2$O (1.5 g L^{-1} as Mg), Ca(NO$_3$)$_2$·4H$_2$O (0.5 g L^{-1} as Ca), NaCl (20 g L^{-1} as chloride), or Na$_2$SO$_4$ (1 g L^{-1} as sulfate) was added to the test solution. For the adsorption of Cd, Co, Cu, Fe, Ni, Pb, V, and Zn, a significant influence was not observed using the solution in the pH range of 3–10, whereas the recoveries of some elements decreased at pH 2. Fig. 3 shows the effect of the presence of Ca for Mn and Mo. The recovery of Mn slightly decreased in the presence of Ca; similar tendencies were observed in the presence of Na, K, Mg, and chloride. Mo was quantitatively recovered in the pH range of 2–4.5 when Na, K, Mg, Ca, chloride, or sulfate was present in the solution;

Table 3
Blank values and detection limits.

Element	Detection limit without SPE[a] (μg L^{-1})	SPE using 100 mL[b] ($n=8$)			SPE using 500 mL[b] ($n=8$)		
		Blank[c] (μg L^{-1})	Detection limit[d] (μg L^{-1})	Detection limit[d] (μg)	Blank[c] (μg L^{-1})	Detection limit[d] (μg L^{-1})	Detection limit[d] (μg)
Cd	0.50	0.078 ± 0.0172	0.052	0.005	N.D.	0.009	0.005
Co	0.90	N.D.	0.12	0.012	N.D.	0.013	0.007
Cu	2.4	N.D.	0.78	0.078	0.10 ± 0.036	0.11	0.055
Fe	0.23	0.29 ± 0.087	0.26	0.026	0.036 ± 0.0118	0.035	0.018
Mn	0.085	0.095 ± 0.0032	0.010	0.001	N.D.	0.003	0.001
Mo	2.0	N.D.	0.23	0.023	N.D.	0.069	0.035
Ni	1.5	N.D.	0.069	0.007	N.D.	0.063	0.032
Pb	5.2	N.D.	0.31	0.031	N.D.	0.089	0.044
V	6.0	N.D.	0.18	0.018	N.D.	0.087	0.043
Zn	0.95	N.D.	0.76	0.076	0.33 ± 0.092	0.28	0.14

N.D.: Not detected.

   [a] Three times standard deviation for 1 mol L^{-1} HNO$_3$ ($n=8$).

   [b] Solid phase extraction (SPE) was carried out using 100 mL or 500 mL of purified water; final volume was 10 mL (10- or 50-fold preconcentration). Values were given as concentration or amount in 100 mL or 500 mL of solution.

   [c] Mean ± standard deviation.

   [d] Three times standard deviation for procedural blank.

Table 4
Results for determination of 10 elements in certified reference materials.

Element	EU-L-1 (wastewater)[a] ($n = 3$)		ES-L-1 (ground water)[b] ($n = 3$)	
	Found[c] (mg L^{-1})	Certified value[d] (mg L^{-1})	Found[c] (mg L^{-1})	Certified value[d] (mg L^{-1})
Cd	0.06 ± 0.002	0.06 ± 0.002	0.010 ± 0.0000$_4$	0.010 ± 0.001
Co	0.20 ± 0.006	0.20 ± 0.003	0.051 ± 0.0001	0.051 ± 0.001
Cu	0.26 ± 0.008	0.26 ± 0.01	0.021 ± 0.0002	0.020 ± 0.002
Fe	0.10 ± 0.004	0.11 ± 0.01	0.017 ± 0.0000$_4$	0.021 ± 0.002
Mn	0.26 ± 0.012	0.30 ± 0.01	0.098 ± 0.0003	0.096 ± 0.003
Mo	0.10 ± 0.004	0.10 ± 0.003	0.010 ± 0.0001	0.011 ± 0.001
Ni	0.20 ± 0.005	0.20 ± 0.004	0.010 ± 0.0000$_2$	0.010 ± 0.0004
Pb	0.11 ± 0.005	0.10 ± 0.002	0.005 ± 0.0003	(0.002)[e]
V	0.11 ± 0.004	0.12 ± 0.004	0.010 ± 0.0001	0.010 ± 0.001
Zn	0.05 ± 0.004	0.06 ± 0.003	0.020 ± 0.0003	0.021 ± 0.001

Solution pH was adjusted to 5.5 for adsorption.

[a] Sample volume, 100 mL.

[b] Sample volume, 200 mL.

[c] Mean ± standard deviation.

[d] Confidence interval at the 95% confidence level.

[e] The value is not certified; it is listed for information only.

however, the recovery decreased with increasing the pH to above 5. These results indicate that (1) all elements except for Mn could be recovered simultaneously from a sample solution containing large amounts of Na, K, Mg, Ca, chloride, and sulfate, such as surface seawater, at pH below 5; and (2) all 10 elements, including Mn, could also be effectively separated and preconcentrated from the other sample solution in the pH range of 5–7. In this work, the pH was adjusted to pH 4.0 for surface seawater or 5.5 for the other samples.

The effects of the flow rate and the sample volume were then examined using the sample solution at pH 5.5. When the flow rate was varied in the range of 1.5–19 mL min^{-1}, all of the target elements were recovered at more than 89%. The recoveries of the target elements were scarcely affected by passing up to 1000 mL of the sample solution through the reservoir-packed CM-PEHA resin at a flow rate of 10 mL min^{-1}. From these results, the adsorption of elements was carried out using 100–500 mL of the sample solution at a flow rate of 5 mL min^{-1}.

For the elution of the adsorbed elements, nitric acid was chosen. When 3 mL of 0.1 mol L^{-1} nitric acid was used, Cd, Mn, and Zn were quantitatively eluted. However, the recoveries of Co, Fe, Ni, Pb, and V were insufficient, and Cu and Mo were hardly eluted under this condition. The recoveries of these elements increased with increasing the concentration of nitric acid; quantitative elution was achieved using 3 mol L^{-1} nitric acid. All of the target elements were eluted at almost 100% when more than 2 mL of 3 mol L^{-1} nitric acid was used. In further experiments, 3 mL of 3 mol L^{-1} nitric acid was used for the elution of the adsorbed elements.

3.3.2. Calibration curves and detection limits

The relationship between the emission intensity of each element and the amount of the element was investigated using 100 mL of purified water spiked with the elements. Straight lines were obtained for all of the elements over the ranges listed in Table 2; sub-µg L^{-1} levels of the elements can be determined with the combined method of solid phase extraction using CM-PEHA resin with ICP-AES when using 100–500 mL of the sample solution.

The detection limits in the method proposed here were evaluated as 3 times the standard deviation for the procedural blank. The blank values and the detection limits for 100 mL and 500 mL of purified water ($n = 8$) are shown, respectively, in Table 3 as the concentrations of the elements in 100 mL and 500 mL of solution. For Co, Mo, Ni, Pb, and V, the blank values in the final solution after the solid phase extraction were lower than the detection limits for ICP-AES without the solid phase extraction, which was defined as 3 times the standard deviation ($n = 8$) for

1 mol L^{-1} nitric acid (Table 3), whereas significant blanks were observed for Cd, Cu, Fe, Mn, and Zn. Therefore, a blank test was carried out using purified water at the same volume of the sample solution in this work. The detection limits as the absolute amounts of the elements are also appended in Table 3. A significant difference in the amounts for 100 mL and 500 mL of solution was not observed for the elements, except for Ni, V, and Zn, for which the amounts for 500 mL of solution were larger than those for 100 mL. In this work, the detection limits when using 200 mL or 300 mL of the sample solution were estimated on the basis of those for the procedural blanks using 500 mL of purified water.

3.3.3. Determination of trace elements in certified reference materials

To validate the solid phase extraction using CM-PEHA resin in combination with ICP-AES determination, 10 elements in the certified reference materials, EU-L-1 and ES-L-1, were determined. The obtained results are shown in Table 4. The values obtained in the proposed method were nearly equal to the certified values. These results indicate that the solid phase extraction using CM-PEHA resin combined with ICP-AES determination would be applicable to the analyses of these water samples.

Table 5
Results for analyses of treated wastewater and surface seawater samples.

Element	Treated wastewater[a,c] ($n = 3$)		Surface seawater[b,c] ($n = 3$)	
	Found (µg L^{-1})	Recovery[d] (%)	Found[c] (µg L^{-1})	Recovery[d] (%)
Cd	0.2 ± 0.02	93 ± 2.9	(0.03 ± 0.004)[e]	96 ± 1.7
Co	<0.033[f]	92 ± 3.7	(0.02 ± 0.012)[e]	96 ± 1.5
Cu	1.1 ± 0.13	104 ± 3.5	0.77 ± 0.017	112 ± 3.2
Fe	33 ± 3.3	114 ± 13.8	1.3 ± 0.05	94 ± 3.2
Mn	871 ± 75	64 ± 9.0	–[g]	–[g]
Mo	458 ± 9.3	98 ± 1.7	7.4 ± 0.07	100 ± 4.5
Ni	11 ± 0.2	101 ± 4.9	0.46 ± 0.017	100 ± 1.8
Pb	<0.22[f]	94 ± 2.7	0.09 ± 0.052	104 ± 2.0
V	<0.22[f]	92 ± 3.1	1.3 ± 0.05	96 ± 2.5
Zn	11 ± 3.1	83 ± 2.1	2.5 ± 0.24	102 ± 2.2

[a] Sample volume, 200 mL; pH 5.5.

[b] Sample volume, 300 mL; pH 4.0.

[c] Mean ± standard deviation.

[d] 5 µg of each element was added to the solution.

[e] The result was estimated by the extrapolation of the calibration curve.

[f] Estimated detection limit for 200 mL of solution.

[g] Not measured.

3.3.4. Determination of trace elements in treated wastewater and surface seawater

The target elements in some water samples were determined. Table 5 shows the result for the analysis of treated wastewater (200 mL), which was generated during the treatment of wastewater containing some elements using coagulation and sedimentation process with formation of metal hydroxides. The 6 elements, Cd, Cu, Fe, Mo, Ni, and Zn, could be determined. For Co, Pb, and V, the concentrations were lower than the detection limits for 200 mL of solution, which were estimated from the detection limits for 500 mL of solution in Table 3. The recovery test was also carried out using a sample solution spiked with 5 μg of the target elements. Although the recoveries of Mn and Zn were less than 90%, the other elements were recovered at 92–114%. For Mn, the low recovery seems to be due to the presence of a large amount of Mn in the treated wastewater compared with the spiked amount. The result for the analysis of surface seawater (300 mL) was also shown in Table 5. All elements except for Mn were detected; the recoveries of the elements from the spiked sample were within 94–112%.

4. Conclusion

The chelate resin immobilizing carboxymethylated pentaethylenehexamine shows excellent performance for the separation and preconcentration of trace elements in water samples. CM-PEHA resin could effectively remove alkali and alkaline earth elements and quantitatively concentrate some trace elements such as Cd, Co, Cu, Fe, Mo, Ni, Pb, V, and Zn even under acidic and neutral conditions. The solid phase extraction using the CM-PEHA resin was applicable to the analyses of certified reference materials and real water samples, such as treated wastewater and surface seawater, through the optimization of the adsorption/elution conditions. This method would contribute to the separation and preconcentration of trace elements in various water samples.

Acknowledgement

References

[1] K. Oshita, S. Motomizu, Bunseki Kagaku 57 (2008) 291.
[2] V. Camel, Spectrochim. Acta Part B 58 (2003) 1177.
[3] H. Matsunaga, Bunseki Kagaku 50 (2000) 89.
[4] B.S. Garg, R.K. Sharma, N. Bhojak, S. Mittal, Microchem. J. 61 (1999) 94.
[5] C. Kantipuly, S. Katragadda, A. Chow, H.D. Gesser, Talanta 37 (1990) 491.
[6] D. Rahmi, Y. Zhu, E. Fujimori, T. Umemura, H. Haraguchi, Talanta 72 (2007) 600.
[7] S. Ji, Y. Zhu, T. Yabutani, A. Itoh, H. Haraguchi, Bull. Chem. Soc. Jpn. 79 (2006) 588.
[8] Y. Zhu, A. Itoh, H. Haraguchi, Bull. Chem. Soc. Jpn. 78 (2005) 107.
[9] Y. Zhu, A. Itoh, E. Fujimori, T. Umemura, H. Haraguchi, Bull. Chem. Soc. Jpn. 78 (2005) 659.
[10] T. Yabutani, S. Ji, F. Mouri, H. Sawatari, A. Itoh, K. Chiba, H. Haraguchi, Bull. Chem. Soc. Jpn. 72 (1999) 2253.
[11] A. Itoh, K. Iwata, S. Ji, T. Yabutani, C. Kimata, H. Sawatari, H. Haraguchi, Bunseki Kagaku 47 (1998) 109.
[12] H. Sawatari, T. Toda, T. Saizuka, C. Kimata, A. Itoh, H. Haraguchi, Bull. Chem. Soc. Jpn. 68 (1995) 3065.
[13] M.B. Alvarez, M.E. Malla, D.A. Batiston, Anal. Bioanal. Chem. 378 (2004) 438.
[14] R.K. Katarina, N. Lenghor, S. Motomizu, Anal. Sci. 23 (2007) 343.
[15] S. Hirata, T. Kajiya, M. Aihara, K. Honda, O. Shikino, Talanta 58 (2002) 1185.
[16] K.W. Warnken, D. Tang, G.A. Gill, P.H. Santschi, Anal. Chim. Acta 423 (2000) 265.
[17] C.-C. Wang, C.-Y. Chen, C.-Y. Chang, J. Appl. Polym. Sci. 84 (2002) 1353.
[18] K.-H. Lee, M. Oshima, T. Takayanagi, S. Motomizu, Anal. Sci. 16 (2000) 731.
[19] H. Kumagai, Y. Inoue, T. Yokoyama, T.M. Suzuki, T. Suzuki, Anal. Chem. 70 (1998) 4070.
[20] H. Kumagai, M. Yamanaka, T. Sakai, T. Yokoyama, T.M. Suzuki, T. Suzuki, J. Anal. At. Spectrom. 13 (1998) 579.
[21] K. Inoue, K. Ohto, K. Yoshizuka, R. Shinbaru, Y. Baba, K. Kina, Bunseki Kagaku 42 (1993) 725.
[22] A. Baraka, P.J. Hall, M.J. Heslop, J. Hazard. Mater. 140 (2007) 86.
[23] Y. Inoue, H. Kumagai, Y. Shimomura, T. Yokoyama, T.M. Suzuki, Anal. Chem. 68 (1996) 1517.
[24] T. Yokoyama, S. Asami, M. Kanesato, T.M. Suzuki, Chem. Lett. (1993) 383.
[25] T. Yokoyama, M. Kanesato, T. Kimura, T.M. Suzuki, Chem. Lett. (1990) 693.
[26] T.M. Suzuki, T. Yokoyama, Polyhedron 3 (1984) 939.
[27] T.M. Suzuki, T. Yokoyama, Polyhedron 2 (1983) 127.
[28] J. de Jong, V. Schoemann, D. Lannuzel, J.-L. Tison, N. Mattielli, Anal. Chim. Acta 623 (2008) 126.
[29] M.C. Lohan, A.M. Aguilar-Islas, R.P. Franks, K.W. Bruland, Anal. Chim. Acta 530 (2005) 121.
[30] K. Inoue, K. Ohto, K. Yoshizuka, R. Shinbaru, K. Kina, Bunseki Kagaku 44 (1995) 283.
[31] K. Inoue, K. Yoshizuka, K. Ohto, Anal. Chim. Acta 388 (1999) 209.
[32] K. Inoue, K. Ohto, K. Yoshizuka, T. Yamaguchi, T. Tanaka, Bull. Chem. Soc. Jpn. 70 (1997) 2443.
[33] A. Baraka, P.J. Hall, M.J. Heslop, React. Fanct. Polym. 67 (2007) 585.
[34] L. Hou, F. Jiang, S. Wang, Annali di Chim. 97 (2007) 995.
[35] Y. Suzuki, Y. Endo, M. Ogawa, M. Matsuda, Y. Nakajima, N. Onda, M. Iwasaki, S. Tsugane, Anal. Sci. 24 (2008) 1049.
[36] Y. Sohrin, S. Urushihara, S. Nakatsuka, T. Kono, E. Higo, T. Minami, K. Noriyasu, S. Umetani, Anal. Chem. 80 (2008) 6267.
[37] S. Tamiya, J. Yoshinaga, Bunseki Kagaku 57 (2008) 99.
[38] K. Yamamoto, H. Sakamoto, A. Yonetani, T. Shirasaki, Nippon Kaisui Gakkaishi 61 (2007) 260.
[39] H. Sakamoto, K. Yamamoto, T. Shirasaki, Y. Inoue, Bunseki Kagaku 55 (2006) 133.
[40] L.G. Sillen, A.E. Martell, Stability Constants of Metal-Ion Complexes, 2nd ed., The Chemical Society, London, 1964.
[41] Japan Industrial Standards, Testing methods for industrial wastewater, K0102 (1998).
[42] O. Vesterberg, Acta Chem. Scand. 23 (1969) 2653.
[43] G.M. Lukovkin, V.S. Pshezhetsky, G.A. Murtazaeva, Eur. Polym. J. 9 (1973) 559.
[44] Z. Matejka, Z. Zitkova, React. Funct. Polym. 35 (1997) 81.
[45] C.-C. Wang, C.-C. Wang, React. Funct. Polym. 66 (2006) 343.
[46] C. Reimann, P. de Caritat, Chemical Elements in the Environment, Springer, Berlin, 1998.

Inductively coupled plasma atomic emission spectrometric determination of 27 trace elements in table salts after coprecipitation with indium phosphate

Shigehiro Kagaya*, Toshiyuki Mizuno, Koji Tohda

Graduate School of Science and Engineering for Research, University of Toyama, Gofuku 3190, Toyama 930-8555, Japan

ABSTRACT

The coprecipitation method using indium phosphate as a new coprecipitant has been developed for the separation of trace elements in table salts prior to their determination using inductively coupled plasma atomic emission spectrometry (ICP-AES). Indium phosphate could quantitatively coprecipitate 27 trace elements, namely, Be, Ti, Cr, Mn, Fe, Co, Ni, Cu, Zn, Cd, Pb, Sc, Y, La, Ce, Pr, Nd, Sm, Eu, Gd, Tb, Dy, Ho, Er, Tm, Yb, and Lu, in a table salt solution at pH 10. The rapid coprecipitation technique, in which complete recovery of the precipitate was not required in the precipitate-separation process, was completely applicable, and, therefore, the operation for the coprecipitation was quite simple. The coprecipitated elements could be determined accurately and precisely by ICP-AES using indium as an internal standard element after dissolution of the precipitate with 5 mL of 1 mol L^{-1} nitric acid. The detection limits (three times the standard deviation of the blank values, $n = 10$) ranged from 0.001 μg (Lu) to 0.11 μg (Zn) in 300 mL of a 10% (w/v) table salt solution. The method proposed here could be applied to the analyses of commercially available table salts.

1. Introduction

Salt takes on an important role as an ingredient of food and a carrier of food additives and/or nutrients. Evaporative crystallization combined with the concentration of seawater by electrodialysis using an ion-exchange membrane is a useful technique for table salt production [1–3]. Since seawater often contains various harmful elements as well as essential elements at a trace or ultra-trace level [4], some of these elements may be present in table salt. Therefore, determining the elements in table salt is significant from the viewpoints of quality control and food safety.

For the determination of trace elements, inductively coupled plasma atomic emission spectrometry (ICP-AES) is conveniently utilized because this method can determine many elements simultaneously. However, major elements, such as Na and K, often interfere with the determination of trace elements in table salt analysis using ICP-AES. A combination of a separation technique for trace elements with ICP-AES is a practical way to reduce the interference and obtain accurate and precise results.

Among a variety of separation techniques proposed so far, coprecipitation using inorganic precipitates [5–13] is a useful method for the separation of trace elements in table salt. For ICP-AES determi-

nation, the coprecipitation methods using magnesium hydroxide [10], hybrid hydroxides of ytterbium, gallium, and magnesium [11], and yttrium hydroxide [12] have been applied because of the potentials of these methods for the separation of trace elements and the scarce interference of the coprecipitants for the determination. However, these coprecipitation methods have some disadvantages, that is, the cumbersome operation in the precipitate-separation process due to the fine precipitate [10], the use of large amounts of carrier elements compared with those in other coprecipitation methods [11], and the restriction of the sample volume, which is correlated to the amount of table salt used for the analysis [12].

In this work, we studied a coprecipitation method that is useful for table salt analysis using ICP-AES and found that the method using indium phosphate, which is a new coprecipitant, was excellent. Indium is well recognized as a suitable carrier element for ICP-AES because the presence of indium scarcely interfered with the determination of many elements [14–16]. Indium phosphate could quantitatively coprecipitate 27 trace elements in 300 mL of a 10% (w/v) table salt solution; the formed precipitate had a good sedimentation property. Indium phosphate as a coprecipitant was also readily applicable to the rapid coprecipitation technique [12,17], in which complete recovery of the precipitate is not required in the precipitate-separation process. This paper describes the potential of the coprecipitation method using indium phosphate for the separation of 27 trace elements in table salt prior to their determination using ICP-AES.

* Corresponding author. Tel.: +81 76 445 6865; fax: +81 76 445 6703.
E-mail address: kagaya@eng.u-toyama.ac.jp (S. Kagaya).

2. Experimental

2.1. Apparatus

A PerkinElmer Optima 3000DV inductively coupled plasma atomic emission spectrometer was used for determining elements. The pH measurement was carried out using a Horiba F-22 pH meter. A Kubota Model 5400 centrifuge was used for separating the precipitate.

2.2. Reagents

Purified water obtained by a Simplicity UV (Millipore) was used for all experiments. An indium solution ($5\,g\,L^{-1}$) was prepared by dissolving indium chloride (99%, Mitsuwa Chemicals) in 5 mL of concentrated hydrochloric acid (for poisonous metal analysis, Kanto Chemical) and diluting to 100 mL with purified water. A commercially available ICP multi-element standard solution XVI (21 elements, including Be, Ti, Cr, Mn, Fe, Co, Ni, Cu, Zn, Cd, and Pb; $100\,mg\,L^{-1}$ each, Merck), a plasma CAL multi-element standard (15 elements, including Y, Ce, Pr, Nd, Sm, Eu, Gd, Tb, Dy, Ho, Er, Tm, Yb, and Lu; $100\,mg\,L^{-1}$ each, SCP Science), and standard solutions for Sc and La ($1000\,mg\,L^{-1}$, Kanto Chemical) were used. The standard solutions were diluted to a desired concentration in each experiment. The other reagents were of guaranteed or analytical reagent grade.

2.3. Procedures

2.3.1. Preparation of sample solutions

For the optimization of the operating conditions for coprecipitation, a 5–10% (w/v) sodium chloride or table salt solution was used as a sample solution. The solution was prepared by dissolving sodium chloride or a commercially available table salt (Fuji Salt, Ishikawa Prefecture, Japan), which contains $590\,mg\,g^{-1}$ of Na, $4.8\,mg\,g^{-1}$ of K, $0.83\,mg\,g^{-1}$ of Mg, and $0.68\,mg\,g^{-1}$ of Ca, with $0.1\,mol\,L^{-1}$ nitric acid and then adding the appropriate amount of the standard solutions for trace elements. A purified water-based solution spiked with trace elements was also used for the investigation. For determining trace elements in table salts, 30.00 g of each table salt was dissolved with 300 mL of $0.1\,mol\,L^{-1}$ nitric acid.

2.3.2. Coprecipitation of trace elements

To the sample solution (100–300 mL), 1 mL of the indium solution (5 mg) and 0.5 mL of $0.3\,mol\,L^{-1}$ phosphoric acid were added. The pH was then adjusted to 10 with an 8 or $1\,mol\,L^{-1}$ sodium hydroxide solution using a pH meter; trace elements were coprecipitated with the formed precipitate. After the solution had been allowed to stand for approximately 30 min, the supernatant solution was discarded by decantation; loss of a portion of the precipitate was permitted. The remaining solution, which contained most of the precipitate, was transferred to a 50 mL polypropylene centrifuge tube, and the precipitate was centrifuged at 3500 rpm for 5 min. After the supernatant solution was discarded, 10 mL of purified water was added to the centrifuge tube, which was then shaken by hand. The precipitate was re-centrifuged and dissolved with 5 mL of $1\,mol\,L^{-1}$ nitric acid. A blank test was also carried out using purified water at the same volume of the sample solution; in this case, the standing time for sedimentation of the precipitate and the centrifugation time were lengthened to approximately 60 min and 20 min, respectively.

For optimizing the coprecipitation conditions, filtration using a membrane filter (Nihon Millipore, Omnipore membrane, pore size of 0.2 μm) was utilized for the separation of the precipitate instead of the centrifugation. In this case, the precipitate was dissolved in

Table 1
Operating conditions for ICP-AES.

Radio frequency output	1.3 kW
Argon gas flow rate	
Plasma gas	$15\,L\,min^{-1}$
Auxiliary gas	$0.5\,L\,min^{-1}$
Neblizing gas	$0.8\,L\,min^{-1}$
Pump parameter	
Sample flush time	10 s
Sample flush flow rate	$4.0\,mL\,min^{-1}$
Sample flow rate	$1.2\,mL\,min^{-1}$
Read delay time	30 s
Reading time	Auto (minimum 0.2 s – maximum 20 s)
View mode	Axial

3 mL of approximately $6.5\,mol\,L^{-1}$ nitric acid and the solution was then diluted to 10 mL with purified water.

2.3.3. Determination of trace elements

The trace elements in the solution after the coprecipitation were determined by ICP-AES. The operating conditions for ICP-AES and analytical wavelength for each element are summarized in Tables 1 and 2, respectively. Indium added as a carrier element was also used as an internal standard element for the determination. Solutions for calibration curves were prepared using 100 mL of purified water spiked with trace elements in the same manner for the sample solution.

3. Results and discussion

3.1. Optimization of conditions for the coprecipitation of trace elements

The effect of the solution pH on the formation of the precipitate in the solution containing indium and phosphate was first investi-

Table 2
Analytical wavelengths, detection limits, and ranges of calibration curves for elements.

Element	Analytical wavelength (nm)	Detection limit[a] (μg in 300 mL)	Range of calibration curve (μg in 100 mL)
Be	313.107	0.001_3	0.005–50
Ti	334.940	0.015	0.05–50
Cr	267.716	0.005_0	0.02–50
Mn	257.610	0.014	0.05–50
Fe	239.562	0.061	0.3–50
Co	228.616	0.008_2	0.02–50
Ni	232.003	0.050	0.3–50
Cu	224.700	0.048	0.3–50
Zn	206.200	0.11	0.3–50
Cd	228.802	0.007_3	0.02–50
Pb	220.353	0.066	0.3–50
Sc	357.253	0.002_2	0.008–50
Y	360.073	0.052	0.1–50
La	379.478	0.098	0.3–50
Ce	418.660	0.037	0.1–50
Pr	390.844	0.032	0.1–50
Nd	406.109	0.048	0.1–50
Sm	359.260	0.017	0.05–50
Eu	412.970	0.004_6	0.02–50
Gd	342.247	0.031	0.1–50
Tb	350.917	0.022	0.08–50
Dy	353.170	0.016	0.05–50
Ho	345.600	0.024	0.08–50
Er	349.910	0.091	0.3–50
Tm	346.220	0.005_8	0.02–50
Yb	369.419	0.035	0.1–50
Lu	291.139	0.001_0	0.005–50
In[b]	230.606		

[a] Three times the standard deviation of the blank values ($n = 10$).
[b] Internal standard element.
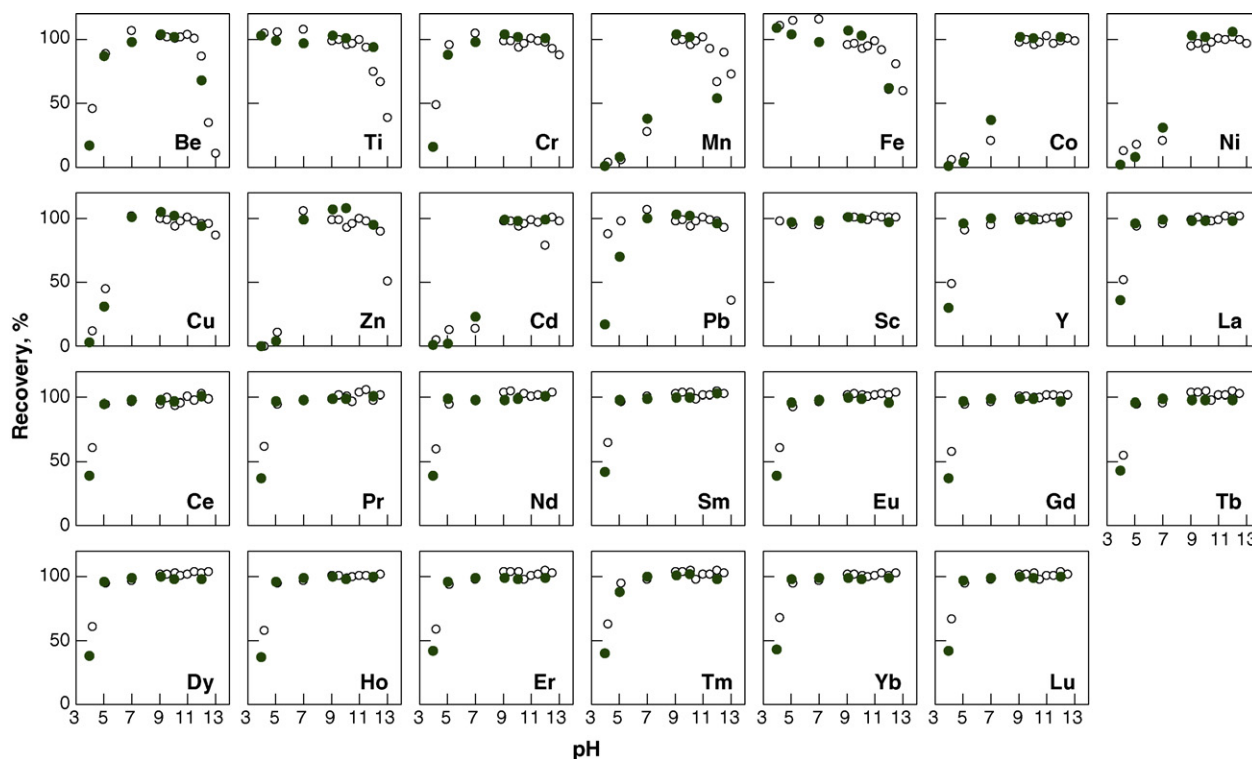
Fig. 1. Effect of pH on the recovery of trace elements from purified water-based solution (○) and 5% (w/v) sodium chloride solution (●). Solution volume, 100 mL; 2.0 mol L^{-1} HNO$_3$, 5 mL; In, 1 mg; 0.3 mol L^{-1} H$_3$PO$_4$, 0.5 mL; each element, 5 μg.

gated. When 1 mg of indium and 0.5 mL of 0.3 mol L^{-1} phosphoric acid were added to purified water or a 5% (w/v) sodium chloride solution spiked with trace elements and the pH of the solution was raised by adding a sodium hydroxide solution, the precipitate appeared at a pH of around 3; the added indium precipitated quantitatively at pH above 4 for the purified water-based solution and above 5 for the sodium chloride solution. The mole ratio of indium to phosphorus in the precipitate formed in the sodium chloride solution at pH 9–10 was 0.97–0.98. This result suggests that indium would be precipitated as phosphate in this pH range.

The potential of indium phosphate as a coprecipitant was then investigated using 100 mL of a purified water-based solution and a 5% (w/v) sodium chloride solution spiked with trace elements. Fig. 1 shows the recoveries of trace elements at various pH in the coprecipitation with indium phosphate. In the purified water-based solution, Ti, Fe, and Sc were quantitatively coprecipitated at pH above 4. The recoveries of the other elements increased with increasing pH; more than 90% of the recoveries were obtained in the pH range of 9–11.5 for all the 27 trace elements. A similar result was obtained using a 5% (w/v) sodium chloride solution spiked with the trace elements, as shown in Fig. 1; the quantitative recoveries of the 27 trace elements could be obtained in the pH range of 9–10. These results indicate that indium phosphate is a powerful coprecipitant for the separation of these 27 trace elements.

The coprecipitation was then investigated using 100 mL and 300 mL of a 5–10% (w/v) table salt solution spiked with the trace elements at pH 10. The recoveries of many trace elements from 300 mL of the solution were insufficient when 1 mg of indium was used. The recoveries increased with increasing the added amount of indium, and the quantitative coprecipitation of the 27 trace elements was achieved using more than 5 mg of indium. It is noteworthy that the sedimentation property of the precipitate formed in the table salt solution improved considerably. A large part of the formed precipitate could settle down for approximately 30 min, although in the sodium chloride solution more than 60 min was needed. The

precipitate formed in 300 mL of 10% (w/v) table salt solution contained 1.0 mg of Mg and 2.6 mg of Ca, which corresponded to 4.0% of Mg and 13% of Ca contained in the table salt solution, as well as indium and phosphate. The improvement of the sedimentation property would be due to the precipitation of Mg and Ca. When the coprecipitation was carried out using 300 mL of 5% (w/v) sodium chloride solution spiked with the trace elements, the recoveries of the trace elements, except for Fe and Zn, were quantitative at pH 10; however, Fe and Zn were recovered at 87% and 77%, respectively. This result indicates that the precipitate of Mg and Ca formed in the table salt solution also contributed to the coprecipitation of Fe and Zn. The amount of Mg and Ca precipitated increased with increasing the added amount of phosphoric acid, and the standing time required for the sedimentation significantly lengthened when using more than 1 mL of 0.3 mol L^{-1} phosphoric acid. For efficient sedimentation, 0.5 mL of 0.3 mol L^{-1} phosphoric acid was suitable.

3.2. Simplification of operation

To make the operation in the coprecipitation simple, the rapid coprecipitation technique [12,17] was applied. In general, the separation of the precipitate is troublesome and time-consuming in the coprecipitation method because complete recovery of the precipitate is required. The rapid coprecipitation technique permits a loss of a portion of the precipitate in the precipitate-separation process; a portion of the trace element coprecipitated was also lost together with the precipitate. However, the amount of trace element in the initial sample solution can be determined using the carrier element as an internal standard element. The following requirements must be satisfied in the rapid coprecipitation technique [12,17]: (1) the content of the carrier element in the sample solution must negligibly small, (2) the carrier element must be quantitatively precipitated, (3) the loss of the carrier element must be proportional to that of each trace element in the precipitate-separation process, and (4) the carrier element must be readily determined. Indium,
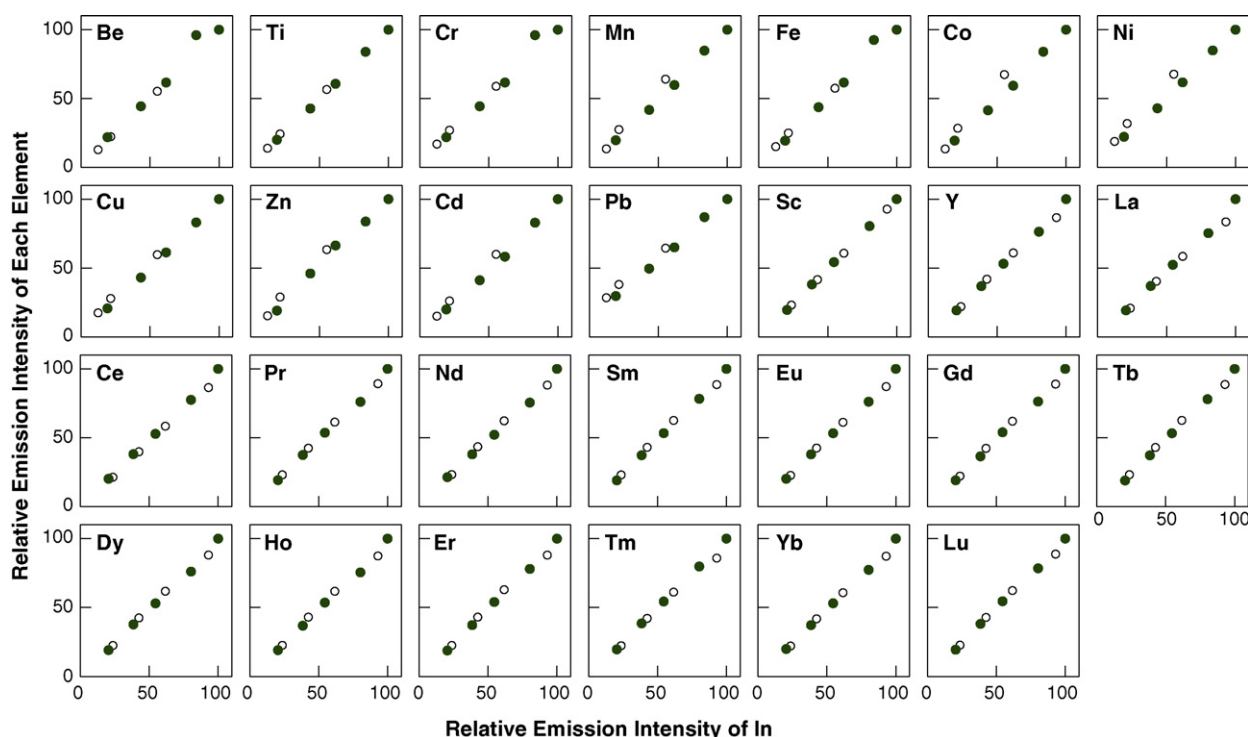
Fig. 2. Relationship between the emission intensity of indium and that of each element after coprecipitation. Solution, 300 mL of purified water-based solution (○) or 5% (w/v) table salt solution (●); 2.0 mol L^{-1} HNO$_3$, 15 mL; In, 5 mg; 0.3 mol L^{-1} H$_3$PO$_4$, 0.5 mL; each element, 5 μg; pH, 10.

which was used as a carrier element in this work, satisfied all of these requirements. The content of indium in table salt is a generally negligible level compared to the added amount in this work (5 mg). Indium could be precipitated over the wide pH range mentioned above and could be easily determined by ICP-AES. For requirement (3), the following investigation was carried out: a part of the suspended solution was discarded by decantation after each element was coprecipitated with indium phosphate at pH 10 using 300 mL of purified water-based and 5% (w/v) table salt solutions. The precipitate remaining in the solution was filtrated and then dissolved in nitric acid. The relationship between the emission intensity of indium and that of each trace element is shown in Fig. 2. The emission intensity of each element was proportional to that of indium. From these results, the rapid coprecipitation technique was applicable to the coprecipitation with indium phosphate.

In this work, centrifugation using a 50 mL polystyrene centrifuge tube (3500 rpm, 5 min) combined with decantation was used for the separation of the precipitate. After the formed precipitate had settled for 30 min, the supernatant solution was discarded by decantation. The precipitate remaining in the solution was centrifuged, and 70–90% of indium could be recovered. This operation was simple and rapid compared with the filtration.

The rapid coprecipitation technique using indium phosphate could efficiently remove Na and K, which are contained in large amounts in table salt; the recoveries of Na and K were 0.06% and 0.1%, respectively. A part of Mg and Ca in the table salt solution was precipitated with indium phosphate, as reported above. However, significant interference was not observed in the determination of trace elements. This would be due to use of indium as the internal standard element in the determination using ICP-AES.

3.3. Calibration curves and detection limits

The relationship between the amounts of trace elements in the sample solution and the emission intensity ratios of trace elements to indium were used for calibration curves in the method proposed

here. Straight lines were obtained over the ranges summarized in Table 2. The detection limits, which were defined as three times the standard deviations obtained from 10 replicate determinations of 300 mL of a blank solution, are also shown in Table 2. These results indicate that the 27 trace elements at sub μg g^{-1} to sub ng g^{-1} levels in table salt could be detected using the method proposed here. The detection limits for many trace elements were lower than those in the coprecipitation methods using hybrid hydroxides of ytterbium, gallium, and magnesium [11] and yttrium hydroxide [12]. The blank value for Lu was 0.071 ± 0.022 μg (mean ± standard deviation, n = 10); the values for the other elements were less than the detection limits.

3.4. Determination of trace elements in certified reference materials and table salts

To validate the method proposed here, some elements in the certified reference material, *Enviro* MAT ground water (ES-L-1, SCP

Table 3
Results for determination of trace elements in a certified reference material, ES-L-1 (ground water).

Element	Found[a] (mg L^{-1})	Certified value[b] (mg L^{-1})
Be	0.053 ± 0.0009	0.052 ± 0.001
Ti	N.D.	–
Cr	0.020 ± 0.0001	0.020 ± 0.0004
Mn	0.099 ± 0.0011	0.096 ± 0.003
Fe	0.021 ± 0.0002	0.021 ± 0.002
Co	0.052 ± 0.0005	0.051 ± 0.001
Ni	0.010 ± 0.0014	0.010 ± 0.0004
Cu	0.021 ± 0.0001	0.020 ± 0.002
Zn	0.021 ± 0.0004	0.021 ± 0.001
Cd	0.010 ± 0.0002	0.010 ± 0.001
Pb	0.004 ± 0.0007	(0.002)[c]

N.D., not detected.
[a] Mean ± standard deviation (n = 5).
[b] Confidence interval at the 95% confidence level.
[c] The value is not certified; it is listed for information only.

Table 4
Results for determination of trace elements in table salts.

Element	Salt 1		Salt 2		Salt 3	
	Found[a] ($\mu g\,g^{-1}$)	Recovery[b] (%)	Found[a] ($\mu g\,g^{-1}$)	Recovery[b] (%)	Found[a] ($\mu g\,g^{-1}$)	Recovery[b] (%)
Be	N.D.	102 ± 3	N.D.	92 ± 2	N.D.	96 ± 2
Ti	N.D.	103 ± 2	N.D.	92 ± 2	N.D.	97 ± 2
Cr	0.014 ± 0.001	103 ± 1	0.048 ± 0.002	92 ± 3	$0.10 \pm 0.00_4$	110 ± 3
Mn	0.042 ± 0.003	102 ± 3	$0.012 \pm 0.000_4$	$93 \pm 0._8$	$0.048 \pm 0.000_4$	94 ± 6
Fe	0.043 ± 0.008	106 ± 2	0.22 ± 0.02	95 ± 8	0.75 ± 0.04	106 ± 3
Co	N.D.	104 ± 2	N.D.	99 ± 2	$0.005 \pm 0.000_3$	97 ± 4
Ni	0.044 ± 0.004	103 ± 2	0.027 ± 0.002	$102 \pm 0._7$	0.080 ± 0.001	107 ± 10
Cu	0.32 ± 0.03	108 ± 5	$0.007 \pm 0.000_1$	93 ± 3	0.024 ± 0.006	96 ± 2
Zn	0.050 ± 0.006	108 ± 4	$(0.008 \pm 0.003)^c$	94 ± 3	0.032 ± 0.002	102 ± 1
Cd	$(0.0004 \pm 0.0001)^c$	104 ± 3	$(0.0007 \pm 0.0003)^c$	93 ± 2	$0.004 \pm 0.000_1$	95 ± 4
Pb	0.070 ± 0.007	107 ± 1	N.D.	93 ± 2	$(0.007 \pm 0.001)^c$	98 ± 3
Sc	N.D.	102 ± 1	N.D.	$104 \pm 0._6$	N.D.	$103 \pm 0._6$
Y	N.D.	$109 \pm 0._4$	N.D.	$109 \pm 0._7$	N.D.	$108 \pm 0._6$
La	N.D.	112 ± 2	N.D.	111 ± 4	N.D.	107 ± 5
Ce	N.D.	$111 \pm 0._7$	N.D.	109 ± 2	N.D.	$109 \pm 0._4$
Pr	N.D.	$109 \pm 0._6$	N.D.	107 ± 4	N.D.	109 ± 1
Nd	N.D.	$109 \pm 0._5$	N.D.	111 ± 2	N.D.	109 ± 2
Sm	N.D.	$109 \pm 0._9$	N.D.	$109 \pm 0._8$	$0.003 \pm 0.000_2$	109 ± 1
Eu	N.D.	$108 \pm 0._4$	N.D.	$109 \pm 0._7$	N.D.	$109 \pm 0._7$
Gd	0.043 ± 0.006	106 ± 2	0.076 ± 0.006	103 ± 3	0.10 ± 0.01	102 ± 4
Tb	0.004 ± 0.001	108 ± 1	0.004 ± 0.002	108 ± 3	0.003 ± 0.001	107 ± 2
Dy	N.D.	$110 \pm 0._4$	N.D.	$110 \pm 0._3$	$0.003 \pm 0.000_2$	109 ± 2
Ho	N.D.	$109 \pm 0._2$	N.D.	110 ± 1	N.D.	108 ± 2
Er	N.D.	$108 \pm 0._4$	N.D.	$109 \pm 0._6$	N.D.	$108 \pm 0._7$
Tm	N.D.	101 ± 2	N.D.	$102 \pm 0._1$	N.D.	$102 \pm 0._6$
Yb	N.D.	$108 \pm 0._5$	N.D.	$108 \pm 0._9$	N.D.	$108 \pm 0._6$
Lu	0.0003 ± 0.0001	$107 \pm 0._3$	0.0005 ± 0.0002	$106 \pm 0._8$	0.0005 ± 0.0001	106 ± 1

N. D.: not detected.

[a] Mean ± standard deviation ($n = 3$).

[b] Each element (5 μg) was added to the sample solution. Mean ± standard deviation ($n = 3$).

[c] The result was estimated by the extrapolation of the calibration curve.

Science), were determined. The results are shown in Table 3. All the obtained values were within the confidence intervals at the 95% confidence level. The proposed method had good accuracy and precision in the analysis of the certified reference material, although the contents of major elements such as Na and K were lower than those in the table salt solution.

The 27 trace elements in three kinds of commercially available table salts were also determined. As shown in Table 4, Cr, Mn, Fe, Ni, Cu, Zn, Cd, Gd, Tb, and Lu could be determined or detected in all the table salts, and Co, Pb, Sm, and Dy in some table salts. The recovery tests were carried out using a table salt solution spiked with the trace elements; 92–112% of recoveries were obtained in all the trace elements. These results indicate that the proposed method is applicable to analysis of table salt. The operation time required for the separation of trace elements in table salt was approximately 60 min, which was much shorter than that for the coprecipitation method using magnesium hydroxide [10].

4. Conclusion

The coprecipitation method using indium phosphate has been shown to be useful for the separation of 27 trace elements, namely, Be, Ti, Cr, Mn, Fe, Co, Ni, Cu, Zn, Cd, Pb, Sc, Y, La, Ce, Pr, Nd, Sm, Eu, Gd, Tb, Dy, Ho, Er, Tm, Yb, and Lu, in table salt. Indium phosphate could quantitatively coprecipitate the 27 trace elements even from 300 mL of a 10% (w/v) table salt solution. The operation for the precipitate-separation process after the coprecipitation was quite simple and rapid because complete recovery of the precipitate was not required by applying the rapid coprecipitation technique. The coprecipitated elements could be determined accurately and precisely by ICP-AES using indium as the inter-

nal standard element. The coprecipitation method using indium phosphate combined with ICP-AES was a powerful tool for table salt analysis and would contribute to the quality control of table salt.

References

[1] N. Yoshikawa, T. Fuchiwaki, Bull. Soc. Sea Water Sci., Jpn. 62 (2008) 79.
[2] M. Hasegawa, Bull. Soc. Sea Water Sci., Jpn. 57 (2003) 256.
[3] Y. Mizutani, J. Membr. Sci. 54 (1990) 233.
[4] C. Reimann, P. de Caritat, Chemical Elements in the Environment, Springer, Berlin, 1998.
[5] T. Tsaikov, Zh. Prikl. Khim. 58 (1985) 1230.
[6] A.N. Baklanov, V.T. Chuiko, F.A. Chmilenko, L.V. Shevchuk, Izv. Vyssh. Uchebn. Zaved., Khim. Khim. Tekhnol. 31 (1988) 39.
[7] N. Inoue, F. Sugimoto, Y. Maeda, T. Azumi, Bull. Soc. Sea Water Sci., Jpn. 42 (1989) 228.
[8] A.N. Baklanov, V.T. Chuiko, F.A. Chmilenko, Vopr. Khim. Khim. Tekhnol. 92 (1990) 20.
[9] F.A. Chmilenko, A.N. Baklanov, Izv. Vyssh. Uchebn. Zaved., Khim. Khim. Tekhnol. 34 (1991) 40.
[10] T. Yabutani, T. Kanazawa, A. Fukuda, J. Motonaka, Bull. Soc. Sea Water Sci., Jpn. 58 (2004) 36.
[11] S. Kagaya, T. Sagisaka, S. Miwa, K. Morioka, K. Hasegawa, Bull. Chem. Soc. Jpn. 79 (2006) 717.
[12] S. Kagaya, S. Miwa, T. Mizuno, K. Tohda, Anal. Sci. 23 (2007) 1021.
[13] D.S.K. Peker, O. Turkoglu, M. Soylak, J. Hazard. Mater. 143 (2007) 555.
[14] M. Hiraide, T. Ito, M. Baba, H. Kawaguchi, A. Mizuike, Anal. Chem. 52 (1980) 804.
[15] T. Fukaya, M. Takeya, Y. Sayama, Anal. Sci. 9 (1993) 727.
[16] K. Yamazaki, H. Tsuji, K. Chayama, Y. Tamari, Y. Kusaka, Bunseki Kagaku 42 (1993) 305.
[17] S. Kagaya, Y. Araki, K. Hasegawa, Fresenius J. Anal. Chem. 366 (2000) 842.

Preconcentration and determination of trace metals by flow injection micelle-mediated extraction using flame atomic absorption spectrometry

Derya Kara *

Department of Chemistry, Art and Science Faculty, Balikesir University, 10100 Balikesir, Turkey

ABSTRACT

Micelle-mediated extraction/preconcentration is incorporated on-line into a flow injection system used to determine low levels of Cd(II), Co(II), Cu(II), Mn(II), Ni(II), Pb(II) and Zn(II) present in various samples. The analyte is complexed with HBDAP (N,N′-bis(2-hydroxy-5-bromo-benzyl)1,2-diaminopropane). Under optimal conditions, a solution of 30% (m/v) NaCl and a sample solution containing 2.5 mL of 1% (m/v) sodium dodecyl sulfate (SDS), 0.5 mL of 1.8×10^{-3} M HBDAP and 2.5 mL of pH 8.5 borate buffer solution in 25 mL were pumped through the cotton filled mini-column; onto which the surfactant-rich phase containing the complex is collected. A solution of 0.5 M HNO_3 in 50% acetone is used as the eluent. The limits of detection are $(ng\,mL^{-1})$ Cd = 0.39, Cu = 3.2, Co = 7.5, Mn = 3.0, Ni = 3.4, Pb = 17.9 and Zn = 0.89 if the sample is allowed to flow for 30 s, but improved for extended preconcentration periods. Analysis of liquid and solid reference materials showed good agreement with the certified values. Complex formation constants between HBDAP and these metal ions were also determined potentiometrically.

© 2009 Published by Elsevier B.V.

1. Introduction

Ionic surfactants get adsorbed from solution on to interfaces and aggregates in solution to form charged micelles through a cooperative association process. The micellar formation takes place above a certain surfactant concentration, the so-called critical micelle concentration (CMC), below which surfactant molecules are present as monomers [1,3]. Such self-assembled systems have been examined for several decades; the most extensively studied surfactant being sodium dodecyl sulfate [4,5]. It is thus not surprising that the effect of different kinds of electrolytes, both with inorganic and organic counter ions, on the critical micelle concentration (CMC), aggregation number (N_{agg}) and micellar transition for surfactants has been examined in detail [2,3]. Inorganic salts decrease CMC, increase N_{agg} and favour sphere-to-rod transitions due to the condensation of counter ions on the charged micelles.

Most of the developed preconcentration methods were based on the cloud point phenomenon where an aqueous solution of some surfactant becomes turbid and separates into two isotropic phases if some condition such as temperature or pressure is changed or if an appropriate substance is added to the solution. Non-ionic micelles have been used extensively for the cloud point extraction of metal ions [6–8]. Some of the cloud point extraction (CPE) procedures have been developed using the mixture of non-ionic and anionic surfactants [9,10]. However, the use of only charged surfactants such as anionic surfactants is still rare for the preconcentration of metals [11–13]. There are, however, a few determination methods of metal ions based on to use of anionic surfactants [14,15].

The very small size and the dynamic properties of the micelle seem to promise the development of rapid and highly efficient micelle-based methodologies for concentrating analytes in water. In the literature, there are a few flow injection methods using micelle-mediated extraction and most of these methods are based on the cloud point extraction technique that uses non-ionic surfactants. Some of these methods are based on off-line merging of flow injection analyses. After the viscous surfactant-rich phase that contains metal chelates was decanted from aqueous solution, it is dissolved in an appropriate solution and delivered to the FIA stream of instrument [8,16–18]. Flow injection on-line cloud point extraction methods using non-ionic surfactants [19–21] or the mixture of non-ionic and anionic surfactants [9] have also been described in the literature. Furthermore, the on-line applications of CPE were described not only as a preconcentration scheme but also as an efficient way to deliver the sample to the detector device.

In this work, a flow injection on-line micelle-mediated extraction method has been developed to determine heavy metals in various samples using a chelating agent, N,N′-bis(2-hydroxy-5-bromo-benzyl)1,2-diaminopropane. Micelle media were produced using inexpensive anionic surfactant sodium dodecyl sulfate in aqueous solution. N,N′-bis(2-hydroxy-5-bromo-benzyl)1,2-diaminopropane has been used to preconcentrate metal ions by liquid–liquid extraction [22–26]. The micelle-mediated extrac-

* Tel.: +90 266 612 10 00; fax: +90 266 612 12 15.
E-mail address: dkara@balikesir.edu.tr.

tion method has some advantages over liquid–liquid extractions. Included in these advantages is the fact that surfactants are used instead of harmful organic solvents. The degree of formation of the metal–ligand complex and the success of extraction systems may be understood by determining the stability constants of the HBDAP metal ion complexes. The stability constants of HBDAP metal ion complexes have been determined using a program developed by Martell and co-worker [27] for potentiometric titration or by manual calculation [28].

2. Experimental

2.1. Reagents and chemicals

A multi-element stock solution containing $200\,mg\,L^{-1}$ of Cu, Ni, Co and Mn; $50\,mg\,L^{-1}$ of Cd and Zn and $500\,mg\,L^{-1}$ Pb were prepared from $10,000\,mg\,L^{-1}$ stock standard solutions (BDH, Aristar, Poole, UK). From this solution, other diluted standard solutions were prepared daily. Buffer solutions were prepared using pure boric acid and sodium tetraborate (BDH).

All reagents used were of the highest available purity. Doubly de-ionized water ($18.2\,M\Omega\,cm$) obtained from a Primar water system (Elga, Buckinghamshire, UK) was used throughout. Nitric acid for sample digestion was obtained from BDH. 5-Bromo-2-hydroxybenzaldehyde, 1,2-diaminopropane and ethanol were purchased from Fluka (Gillingham, Dorset, UK). N,N′-bis(2-hydroxy-5-bromo-benzyl)1,2-diaminopropane was synthesised according to the procedure given in the literature [22,23]. Ligand (0.2 g) was dissolved in 25 mL methanol and then the solution was diluted to 250 mL using 0.1 M NaOH. Four certified reference materials were used in this study: a high purity standard (QCS-19) (High Purity Standard, Charleston, USA), a river water sample (SLRS-4), hay leaves (IAEA V-10) and poplar leaves (NCS DC73350). Each of the CRMs were analyzed using the proposed method under optimal conditions in replicate ($n = 5$). Perchloric acid solution, prepared by the use of double distilled water, was standardized by titration using primary standard sodium carbonate, potentiometrically. Sodium hydroxide solutions were prepared in a (50:50) ethanol/water mixture containing 0.1 M sodium perchlorate and were standardized against the potassium hydrogen phthalate and solutions by the potentiometric method, and they were kept under nitrogen atmosphere.

2.2. Apparatus

2.2.1. FAAS system

A Varian SpectrAA 50 atomic absorption spectrometer (Oxford, UK) furnished with a hollow cathode lamp, and an air–acetylene flame ($9.0/3.0\,L\,min^{-1}$) as the atomiser was used as the detector throughout. The wavelengths (nm) selected for the determination of the analytes were as follows: Cd 228.8, Co 240.7, Cu 324.8, Mn 279.5, Ni 232.0, Pb 283.3 and Zn 213.9. The flow rate of the peristaltic pump was adjusted to be between 3.6 and $8.4\,mL\,min^{-1}$.

2.2.2. Potentiometric system

Potentiometric apparatus consisted of a water-jacketed glass reaction vessels as described in Ref. [29]. A solution of base (sodium hydroxide) was introduced into the measuring cell using a Titroline 96 automatic titrator; the solution in the measuring cell was stirred magnetically. The titration data were obtained in the form of milli-volts against milli-liters of base added. The temperature was maintained at $25 \pm 0.1\,°C$ and titrations were performed under nitrogen. Milli-volt values were recorded directly from the automatic titrator. The calibration of the cell used in the titrations was performed as described in the literature [30].
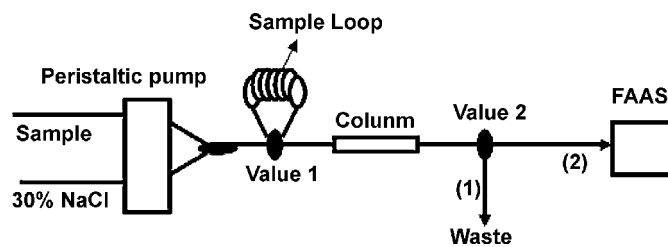
Fig. 1. The diagram of the flow injection micelle-mediated extraction. (1) Sample loading step and (2) elution and analysis step.

2.3. Measurement procedures

2.3.1. Determination of the complex formation constants of HBDAP metal ion complexes

The stability constants for the metal complexes were determined as described in the literature [31,32]. The analytical concentration of metal ion, perchloric acid, HBDAP and sodium perchlorate were 1.5×10^{-3}, 6×10^{-3}, 3×10^{-3} and 0.1 M, respectively. The stability constants were also determined by the use of formation curves ($\bar{n} - p$[HBDAP]) plotted by the use of potentiometric titration data [31] ($\bar{n}$ = the average number of HBDAP bound to each metal ion).

2.3.2. On-line FI preconcentration and elution procedure

A schematic diagram of the on-line preconcentration system is presented in Fig. 1. The system consists of a Gilson Minipuls 3 peristaltic pump (Anachem Ltd., Luton, UK), a four-way valve and a mini-column (5 cm × 3 mm, Omnifit, Cambridge, UK), packed with cotton wool. The 30% (m/v) NaCl solution and a sample solution that contains 2.5 mL of 1% sodium dodecyl sulfate (SDS), 0.5 mL of 1.8×10^{-3} M ligand and 2.5 mL of a pH 8.5 borate buffer solution in a 25 mL volumetric flask were transported using the peristaltic pump. The tubing carrying these two solutions was connected using a T-piece connector, post-peristaltic pump. The other side of the T-piece was connected to the mini-column via the four-way rotary valve. This valve also had a loop fitted that could be filled with the nitric acid prepared in acetone–water mixture as an eluent. The mini-column was also connected to a second valve so that one orientation of this valve directs the flow to waste whereas the other way enables the flow to be directed to the FAAS instrument. Transport lines were made using the minimum length necessary of 0.3 mm id PTFE tubing.

The FI system was operated as follows: during the 30 s sample loading period, with the valve in the 'fill' position, the micelle solution was produced by mixing the 30% NaCl solution with a sample or blank solution containing 2.5 mL 1% sodium dodecyl sulfate (SDS), 0.5 mL of 1.8×10^{-3} M ligand and 2.5 mL of pH 8.5 borate buffer solution diluted to a volume of 25 mL. Mixing was achieved using the T-piece. Both the NaCl and the sample solutions were pumped at a flow rate of $8.4\,mL\,min^{-1}$ through the mini-column containing the cotton wool. The micelles containing the metal complexes were adsorbed on the cotton within the mini-column and the sample matrix was allowed to pass through to waste. After preconcentration, valve 2 was turned to orient the flow towards the FAAS instrument and the 500 μL loop on valve 1 was filled with 0.5 M HNO₃ in a 50% acetone–water mixture. On turning this valve, the eluent was pumped in a stream of water at a rate of $8.4\,mL\,min^{-1}$ by the peristaltic pump to the FAAS instrument. After measuring the metal ions, de-ionised water was passed at a flow rate of $8.4\,mL\,min^{-1}$ for 30 s through the mini-column to re-equilibrate it prior to the next sample.

Table 1
The stability constants for metal complexes of HBDAP.

	$\log K_1$	$\log K_2$	$\log K_3$	$\log \beta$
Cu(II)	20.7	14.6		35.3
Mn(II)	28.5	14.2	10.7	53.4
Cd(II)	16.2	6.7	5.9	28.8
Pb(II)	18.7	11.1	9.4	39.2
Zn(II)	21.6	11.2	10.4	43.2
Ni(II)	23.7	9.5	7.9	41.1
Co(II)	17.9	10.1	9.6	37.6

3. Results and discussion

3.1. Stability constants for metal complexes of HBDAP

Potentiometric measurements have been used to determine stability constants (K) for the metal complexes of HBDAP. The stability constants of HBDAP with metal ions were determined by the use of formation curves ($\bar{n} - p[\text{HBDAP}]$) plotted by the use of potentiometric data [28,33]. Test solutions containing suitable amounts of metal ions, HBDAP and perchloric acid stock solutions were titrated with sodium hydroxide solution until a precipitate or opalescence was just observed in the titration cell. The degree of formation, $\bar{n}$ values were calculated, in order to find the number of ligands bound to each metal ion; then $\bar{n}$ values were plotted versus $p[L]$ values that were found from potentiometric titration results; however it is known that $\bar{n}$ cannot be deduced unless it reaches a limiting value metal:ligand system. The values of $\bar{n}$ (the average number of HBDAP bound to each metal ion) and $[L]$ (the concentration of the anionic form of free uncomplexed of HBDAP) were calculated based on the potentiometric data. The stability constants, $\log K_1$, $\log K_2$ and $\log K_3$, of metal complexes of HBDAP were determined by the use of $p[L]$ values where $\bar{n} = 0.5$, 1.5 and 2.5, respectively. The stability constants of the metal complexes of HBDAP were given in Table 1. As can be seen from Table 1, HBDAP produces very strong complexes with Cu, Cd, Co, Mn, Ni, Pb and Zn ions.

3.2. Analytical parameters of on-line micelle-mediated extraction system

Different experimental parameters (such as temperature, pH, ligand concentration, SDS and sodium chloride concentration, sample flow rate and elution flow rate) were investigated to determine the optimum conditions for the on-line micelle-mediated extraction system.

The most important parameter in the complexation reaction between the metal ion and a ligand is to select a pH at which the complexation rate is very high and very rapid. The effect of pH was studied using the flow injection system between pH values of 3 and 11. The concentrations of the analyte solutions were 2 mg L^{-1} for Cu, Co, Ni and Mn; 0.5 mg L^{-1} for Cd and Zn and 5 mg L^{-1} for Pb. These solutions were passed through the flow injection system shown in Fig. 1 at a flow rate of 7.2 mL min^{-1}. The adsorbed micelles on the mini-column were eluted using 0.5 M HNO$_3$ in a 50% acetone–water mixture at a flow rate of 7.2 mL min^{-1}. Absorbance signals for metals were recorded using the FAAS detector. The results indicated that the extraction ratio increased as the pH increased (Fig. 2). A similar result was found in previous work using the same reagent in a solvent extraction method [26]. Ionic surfactants such as SDS produce charged micelles that can attract ions. These experimental results also showed that metal complexes were produced at basic pH values and hence, have cationic charges. High absorbance signals were observed at pH 10. However, it was also noted that some precipitation reactions occurred at this pH. Since the aim of the work was to evaluate the complexation reaction effect of the ligand on the micelle-mediated extraction, pH 8.5 was selected as opti-
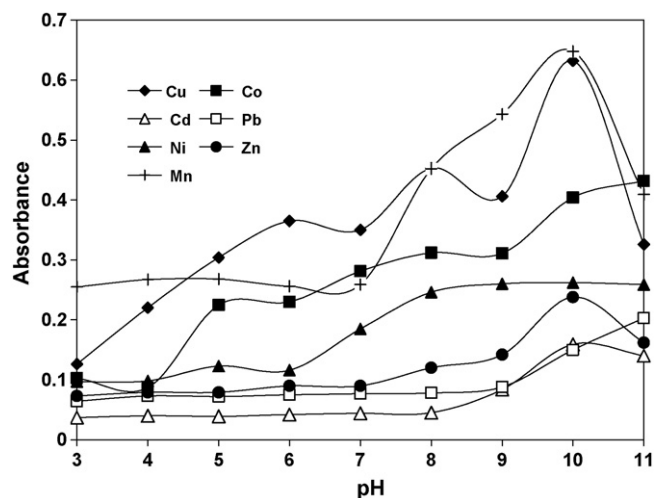
Fig. 2. The effect of the pH on the micelle-mediated extraction.

mum for all subsequent experiments. A borate buffer was selected to maintain the sample solutions at this pH.

Another analytical parameter requiring optimisation of the developed method is the concentration of the ligand in the solution. To determine the suitable ligand concentration, different concentrations of ligand up to 72 µM were used to prepare 25 mL of the solutions that also contain 0.3 ppm Cu, Ni and Co, 0.08 ppm Cd and Zn, 0.8 ppm Pb and 0.2 ppm Mn and analysed according to the procedure. As can be seen in Fig. 3, 36 µM of the ligand solution was sufficient to obtain maximum signal for all of the analytes. Since the extraction efficiency of the micelle-mediated extraction was highest using this concentration of the ligand, 36 µM was used for all subsequent experiments.

SDS was used to create the micelle media in the experiments and therefore the optimization of its concentration was also very important during the development of the method. Different volumes of 1% SDS were added to the 25 mL solution containing metal ions, buffer and ligand. The results showed that the highest signals were observed when the SDS volume was 2.5 mL. Greater volumes than this led to the absorbance signal decreasing slightly. In addition, when higher volumes of SDS were used, considerable foaming was produced and this caused some flow problems during the elution step of the flow injection system. Consequently a stable absorbance
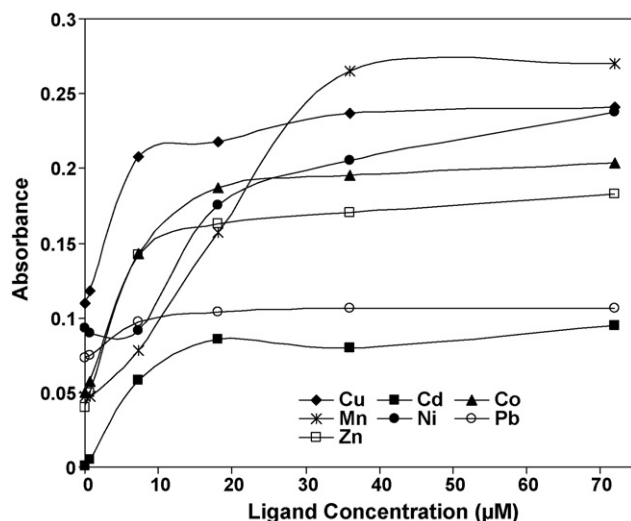
Fig. 3. The effect of ligand concentration on the absorbance signals of the metals.

signal could not be observed. For these reasons, the volume of 1% SDS used was 2.5 mL during subsequent experiments.

It is known that electrolytes such as NaCl decrease the critical micelle concentration. Addition of NaCl in the SDS solution facilitates micelle production to under the critical micelle concentration of the SDS solution alone. Different percentages of NaCl were therefore used in the flow injection system to find the optimal concentration. This solution was supplied separately *via* a peristaltic pump. The NaCl and the sample solution containing SDS were mixed using a flow system. This was possible because the micelles were produced very rapidly after the two solutions were mixed. Had they been mixed beforehand in a batch type system, some micelles and foam containing the metal chelates could stay within a volumetric flask and hence be lost analytically. Different percentages of NaCl were supplied to the system. The micelles adsorbed on the column were eluted and the absorbance signals were recorded. Absorbance signals were very low when the NaCl solutions were at 5 and 10%. This was attributed to low micelle formation. When the percentage of NaCl was increased, higher absorbance signals were observed as the micelle concentration increased. Subsequent experiments were performed using 30% NaCl solution. A higher percentage of NaCl was not tried because of the solubility problem of NaCl in water. Although a very high concentration of NaCl was used in these experiments, it is a very cheap and readily available chemical. It therefore does not increase the cost of the method significantly. In addition it is a chemical that can be obtained in very high purity, leading to low blanks and improved limits of detection.

The temperature effect on the micelle formation for sodium dodecyl sulfate was studied using sodium chloride that is used to decrease critical micelle concentration of sodium dodecyl sulfate. The experimental studies showed that the micelles of SDS which formed at room temperature rapidly disappear if the temperature increases. In addition, the critical micelle concentration was also found to increase as the temperature increased. Similar results have been found in the literature [34]. It is an advantage that the method can be optimised at room temperature with a low concentration of SDS. For these reasons, subsequent experiments were performed at room temperature.

Different eluents were tested to elute the metal ions from the cotton wool filled column. Different concentrations of nitric acid solutions in water (0.1, 0.5 and 1.0 M) as well as 0.5 M nitric acid in a 50% acetone–water mixture were used to determine the eluent that gives the highest desorption or absorbance values for
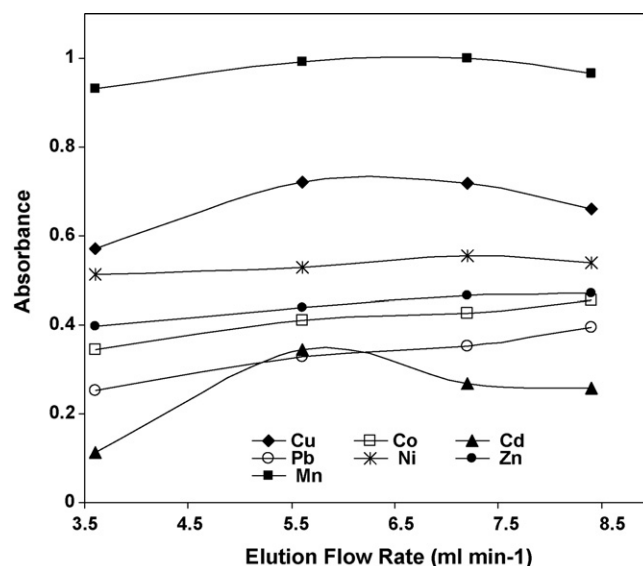
Fig. 5. The effect of the elution flow rate on the flow injection system.

the metal ions. As the concentration of the nitric acid increased, the absorbance signals did not change. The highest signals were obtained using 0.5 M nitric acid in 50% acetone. It is possible that the acetone helps to desorb the metal chelates from the cotton as well as increasing the absorbance signals for metals because of the improved transport efficiency associated with nebulisation of organic solvents.

Lastly, for flow injection analysis, the selection of the optimum flow rates is very important. Although the sample and elution flow rates should be rapid to increase sample throughput, they should not be too fast so that the adsorption and desorption characteristics become impaired. The effects of sample and elution flow rates were determined in the range between 3.6 and 8.4 mL min^{-1}. While the effect of sample flow rate was investigated, the eluent flow rate was kept constant at 7.2 mL min^{-1}. Similarly a constant flow rate of 7.2 mL min^{-1} was used for the sample flow rate when the eluent flow rate was changed between 3.6 and 8.4 mL min^{-1}. Figs. 4 and 5 show that the highest flow rate of 8.4 mL min^{-1} for both sample and eluent flows was suitable for obtaining higher signals for the required metal ions. Therefore, a cycle of preconcentration and elution was extremely rapid with the time required for one sample analysis being approximately 2 min.

Table 2
Effect of potentially interfering ions on the determination of Cd, Co, Cu, Mn, Ni, Pb and Zn using flow injection micelle-mediated extraction method by FAAS.

Ions	Tolerance limit of concentration (mg L^{-1})
Na$^+$, K$^+$, SO$_4^{2-}$, PO$_4^{3-}$, Cl$^-$	>10,000
Mg^{2+}	1300
CO$_3^{2-}$	>10,000 for Zn^{2+}, Ni^{2+}, Cu^{2+} and Cd^{2+}; 5000 for Co^{2+}, Mn^{2+} and Pb^{2+}
NH$_4^+$	>10,000 for Zn^{2+}, Mn^{2+}, Pb^{2+}, Cu^{2+} and Cd^{2+}; 5000 for Co^{2+}, Ni^{2+}
Ca^{2+}	500
Sn^{2+}, Al^{3+}	100
Ag$^+$	100 for Zn^{2+}, Ni^{2+}, Cu^{2+} Co^{2+}, Mn^{2+} and Pb^{2+}; 25 for Cd^{2+}
Ba^{2+}	100 for Ni^{2+} and Co^{2+}; 50 for Zn^{2+}, Cu^{2+}, Mn^{2+}, Cd^{2+} and Pb^{2+}
Cr^{3+}	100 for Zn^{2+}, Cu^{2+}, Cd^{2+} and Pb^{2+}; 50 for Ni^{2+}, Mn^{2+} and Co^{2+}
Fe^{3+}	100 for Cu^{2+}; 50 for Cd^{2+}, Zn^{2+}, Ni^{2+}, Mn^{2+}, Pb^{2+} and Co^{2+}

Fig. 4. The effect of the sample flow rate on the flow injection method.

Table 3
The results for the certified materials.

Trace element	HPS		SLRS-4		IAEA/V-10 HAY		NCS DC73350		t_{exp}
	Certified value (μg L^{-1})	Found value (μg L^{-1})	Certified value (μg L^{-1})	Found value (μg L^{-1})	Certified value (mg kg^{-1})	Found value (mg kg^{-1})	Certified value (mg kg^{-1})	Found value (mg kg^{-1})	
Cd	30	29.7 ± 2.5	0.012 ± 0.002	<LOD	0.03	<LOD	0.32 ± 0.07	0.4 ± 0.1	0.68
Co	30	30 ± 1	0.033 ± 0.006	<LOD	0.13	<LOD	0.42 ± 0.03	0.4 ± 0.1	0.8
Cu	30	29.6 ± 0.7	1.81 ± 0.08	1.8 ± 0.1	9.4	9.4 ± 0.5	9.3 ± 1.0	9.7 ± 0.9	0.08
Mn	30	29 ± 1	3.37 ± 0.18	3.3 ± 0.6	47	N/A	45 ± 4	N/A	1.08
Ni	30	31 ± 2	0.67 ± 0.08	<LOD	4.2	4.6 ± 0.3	1.9 ± 0.3	2.1 ± 0.2	2.16
Pb	30	29 ± 3	0.086 ± 0.007	<LOD	1.6	1.7 ± 0.1	1.5 ± 0.3	1.6 ± 0.1	0.74
Zn	30	31.1 ± 0.5	0.93 ± 0.10	0.9 ± 0.4	24	N/A[a]	37 ± 3	N/A[a]	0.98

[a] Not analysed because preconcentration was not necessary.

3.3. The effect of foreign ions

A list of tolerance limits for an assortment of foreign ions (expressed as mg L^{-1}) during the determination of the seven elements is given in Table 2. The effects of each potential interferent on every element were determined separately to make the study more complete. The concentrations of the analyte ions used during this experiment were 0.4 mg L^{-1} for Cu^{2+}, Ni^{2+}, Co^{2+} and Mn^{2+}, 0.1 mg L^{-1} for Cd^{2+} and Zn^{2+} and 1.0 mg L^{-1} for Pb^{2+}. The only significant interfering element appeared to be Fe^{3+} and only then if the sample contains more than 50 mg L^{-1}. The results indicate that this method may easily be applied for the determination of these seven elements in water samples as well as acid digests of solid samples that contain less than 50 mg L^{-1} Fe. If the sample contains more than 50 mg L^{-1} Fe, a masking agent such as fluoride should be added to the sample before determination. The method may also be used to determine these seven elements in sea water that contains very high concentrations of Na, K, Cl, etc. since these ions do not cause any interference.

3.4. Analytical characteristics

In order to evaluate the performance of the developed method, the linearity and detection limits for the seven analytes were determined. The standards and blanks were passed through the FI manifold shown in Fig. 1 using the optimum flow and experimental conditions determined. All solutions were prepared using ultra-pure water. The correlation coefficients of the calibration curves for the seven metals were typically close to 0.999. The detection limits were calculated using 3 s/slope (n = 15 runs of the blank). The limits of detection for a 30 s period of preconcentration were Cd = 0.39 ng mL^{-1}, Cu = 3.2 ng mL^{-1}, Co = 7.5 ng mL^{-1},

Mn = 3.0 ng mL^{-1}, Ni = 3.4 ng mL^{-1}, Pb = 17.9 ng mL^{-1} and Zn = 0.89 ng mL^{-1}. However, these improved to Cd = 0.29 ng mL^{-1}, Cu = 2.1 ng mL^{-1}, Co = 3.8 ng mL^{-1}, Mn = 1.5 ng mL^{-1}, Ni = 1.97 ng mL^{-1}, Pb = 7.8 ng mL^{-1} and Zn = 0.58 ng mL^{-1} if the flow time, i.e. the pre-concentration period, was doubled. These results were considered to be satisfactory considering the very short pre-concentration time.

3.5. Analyses of certified samples

The accuracy of the developed procedure was tested using certified reference materials. Two water certified materials, a high purity standard (QCS-19) (High purity standard, Charleston, USA) and a river water (SLRS-4) as well as two plant samples Hay (IAEA/V-10) and Poplar leaves (NCS DC73350) were analysed using the developed procedure. Acid digests of the vegetation samples were prepared by weighing material (0.25 g) into a pre-cleaned beaker, adding nitric acid (5 mL) and then heating on a hot plate. After an hour of boiling, the digests were allowed to cool and were then transferred quantitatively to clean 25 mL volumetric flasks. The other reagents (2.5 mL of 1% sodium dodecyl sulfate (SDS), 1.0 mL of 1.8×10^{-3} M ligand and 2.5 mL of pH 8.5 borate buffer solution) were then placed in the flask and the sample solution diluted to volume (25 mL) with water. The results of the analyses are given in Table 3. As shown in Table 3, the results obtained are in close agreement with the certified values. These results show that the method may readily be applied for the determination of these metals in water and vegetation samples. The iron concentrations are 177–190 and 274 ± 17 mg/kg in hay and poplar leaves, respectively. Therefore, the digested solutions contained less than 50 mg L^{-1} iron, which was below the concentration required to cause an interference.

Table 4
The results of the real natural water samples.

Analyte	Added value (μg L^{-1})	River water (μg L^{-1})	Recovery (%)	Sea water (μg L^{-1})	Recovery (%)
Cu	–	11 ± 1		18 ± 1	
	60	72.6 ± 0.7	102.7	80 ± 4	103.3
Cd	–	–		–	
	16	15.3 ± 0.9	95.6	16 ± 2	100
Ni	–	3.0 ± 0.6		3.4 ± 0.8	
	60	64 ± 2	101.7	63 ± 3	99.3
Pb	–	–		–	
	160	163 ± 6	101.9	167 ± 3	104.4
Zn	–	5.4 ± 0.4		28 ± 1	
	16	21.5 ± 0.7	100.6	45 ± 0.6	106.2
Mn	–	6 ± 1		22 ± 0.6	
	40	48 ± 2	105	63 ± 1	102.5
Co	–	–		–	
	60	63 ± 3	105	61 ± 1	101.7

Table 5
Characteristics of Micelle-mediated extraction—flow injection method for determination of metal ions in different samples.

Reagent (surfactant type)	Detection method	Samples	Temperature (°C)	Analysed metals	Preconcentration factor	Detection limits	Ref.
Luminol – H_2O_2 (SDS + Triton X114)	Chemiluminescence	Water	Room temperature	Cr	6	0.5 ng L^{-1}	[9]
Dithizone (Triton X-100)	Spectrophotometer	Water	60	Hg	6	0.014 µg mL^{-1}	[19]
2-(5-Bromo-2-pyridylazo)-5-diethylamino phenol (PONPE-7.5)	ICP-OES	Urine	Room temperature	Gd(III)	20	40 ng L^{-1}	[20]
Pyrrolidine dithiocarbamate (APDC) (Triton X-114)	ETAAS	Biological	Room temperature	Pb	22.5	44.6 ng L^{-1}	[21]
Chrome-Azurol-S (benzyldimethyl tetradecyl ammonium chloride + PONPE-7.5)	Spectrophotometer	Parenteral solutions	Room temperature	Al	50	3.024 µg L^{-1}	[36]
N,N′-bis (2-hydroxy-5-bromo-benzyl)1,2-diamino propane (SDS)	FAAS	Water and biological	Room temperature	Cd, Co, Cu, Mn, Ni, Pb and Zn	8.4	Cd = 0.39 ng mL^{-1}, Cu = 3.2 ng mL^{-1}, Co = 7.5 ng mL^{-1}, Mn = 3.0 ng mL^{-1}, Ni = 3.4 ng mL^{-1}, Pb = 17.9 ng mL^{-1}, Zn = 0.89 ng mL^{-1}	This work

Using the paired *t*-test, adopting the null hypothesis it is possible to determine whether or not there is a significant difference between the mean concentrations found using the proposed method and the certified values. The paired *t*-test was performed for every element and for each of the certified materials individually. The results show that the t values calculated using the equation $\bar{x}_d \sqrt{N}/s_d$, where $\bar{x}_d$, s_d and N show the mean difference, the standard deviation of differences and the number of samples, respectively, are smaller than the critical value of t at 95% confidence interval for all certified samples, indicating that there is no evidence of systematic error in the proposed method [35]. The critical values of t for 1, 2 and 3 number of degrees of freedom at 95% confidence interval are 12.71, 4.3 and 3.18, respectively. This confirms that the results obtained by the proposed method were in good agreement with the certified values.

3.6. Analysis of real samples

The proposed method was applied to river and sea water samples. The experiments were performed using river and sea water samples at natural analyte concentrations and with samples spiked with 16 µg L^{-1} of Cd(II), 40 µg L^{-1} of Mn(II), 60 µg L^{-1} of Co(II), Cu(II) and Ni(II) and 160 µg L^{-1} of Pb(II). The results of these spike/recovery experiments are given in Table 4. The recovery values obtained were very satisfactory. The procedure developed in this work is therefore an alternative method for the determination of very low concentrations of Cd(II), Co(II), Cu(II), Mn(II), Ni(II), Pb(II) and Zn(II) in fresh and sea waters.

3.7. Comparison with other flow injection micelle-mediated extraction methods

In the literature, although there are numerous applications of the off-line micelle-mediated extraction to determine metal ions in different samples, only a few applications have been developed that have used on-line flow injection for the purpose of micelle-mediated extraction. Comparative data using on-line flow injection methods given in Table 5 show that all the previous applications reported data only for a single element. The method presented in this work was applied to the determination of seven elements in water and biological samples. In addition, the method

proposed here needs only one surface active material, SDS, and could be applied at room temperature. Most surfactant-mediated procedures use one surface active compound, generally non-ionic surfactants. The combination of surfactants such as non-ionic and cationic or anionic surfactants is another aspect and it is used depending on the target analyte. Room temperature extraction can also be achieved with non-ionic surfactants like Triton X-45 or Triton X-114 in the presence of salts in the literature. All the methods except this work are based on the cloud point phenomenon. However, since SDS is an anionic surface active material, the micelles disappear as the temperature increases whereas a polar surface active materials such as Triton X-100, Triton X-114, etc. gives a cloud point temperature above which the micelles are produced. There appear few applications in the literature that have used only an anionic surface active material in flow injection micelle-mediated methods. An advantage of the method is that the presence of excess chelating agent does not reduce the extraction efficiency as may occur with other reagents. Instead, the presence of an excess of reagent helps to compensate for the competition from other metals present within the sample. From this perspective, this work is a new application of the on-line flow injection micelle-mediated extractions.

4. Conclusions

A micelle-mediated FI-FAAS preconcentration method has been developed to determine very low concentrations of Cd(II), Co(II), Cu(II), Mn(II), Ni(II), Pb(II) and Zn(II) in natural waters and foodstuffs. N,N′-bis(2-hydroxy-5-bromo-benzyl)1,2-diaminopropane (HBDAP) was used to complex Cd(II), Co(II), Cu(II), Mn(II), Ni(II), Pb(II) and Zn(II) at pH 8.5. The limits of detection for a 30 s period of preconcentration were Cd = 0.39 ng mL^{-1}, Cu = 3.2 ng mL^{-1}, Co = 7.5 ng mL^{-1}, Mn = 3.0 ng mL^{-1}, Ni = 3.4 ng mL^{-1}, Pb = 17.9 ng mL^{-1} and Zn = 0.89 ng mL^{-1}. However, these improved to Cd = 0.29 ng mL^{-1}, Cu = 2.1 ng mL^{-1}, Co = 3.8 ng mL^{-1}, Mn = 1.5 ng mL^{-1}, Ni = 1.97 ng mL^{-1}, Pb = 7.8 ng mL^{-1} and Zn = 0.58 ng mL^{-1} if the flow time, i.e. the preconcentration period, was doubled. These results were considered to be satisfactory considering the very short pre-concentration time. The method is very fast, cheap and does not use any hazardous solvents. The analysis time for one sample is less than 2 min.

References

[1] E. Fuguet, C. Rafols, M. Roses, E. Bosch, Anal. Chim. Acta 548 (2005) 95–100.
[2] O.R. Pal, V.G. Gaikar, J.V. Joshi, P.S. Goyal, V.K. Aswal, Langmuir 18 (2002) 6764–6768.
[3] P.A. Hassan, S.J. Candau, F. Kern, C. Manohar, Langmuir 14 (1998) 6025–6029.
[4] J. Mata, D. Varade, G. Ghosh, P. Bahadur, Colloids Surf. A: Physicochem. Eng. Aspects 245 (2004) 69–73.
[5] P. Mukerjee, K.J. Mysels, Critical Micelle Concentrations of Aqueous Surfactants Systems; National Standard Reference Data System 36, Nat. Bur. Stand. (U.S.), Washington, DC, 1971.
[6] S. Candir, I. Narin, M. Soylak, Talanta 77 (1) (2008) 289–293.
[7] A. Tang, G. Ding, X. Yan, Talanta 67 (2005) 942–946.
[8] D.L. Giokas, E.K. Paleologos, M.I. Karayannis, Anal. Bioanal. Chem. 373 (2002) 237–243.
[9] E.K. Paleologos, A.G. Vlessidis, M.I. Karayannis, N.P. Evmiridis, Anal. Chim. Acta 477 (2003) 223–231.
[10] X. Zhu, X. Zhu, B. Wang, J. Anal. Atom. Spectrom. 21 (2006) 69–73.
[11] E.K. Paleologos, D.L. Giokas, M.I. Karayannis, Trends Anal. Chem. 24 (5) (2005) 426–436.
[12] M. Almeida Bezerra, M.A. Zezzi Arruda, S.L. Costa Ferreira, Appl. Spectrosc. Rev. 40 (4) (2005) 269–299.
[13] M. Fernanda Silva, E. Soledad Cerutti, L.D. Martinez, Microchim. Acta 155 (3–4) (2006) 349–364.
[14] H. Khan, M.J. Ahmed, M.I. Bhanger, Anal. Sci. 21 (2005) 507–512.
[15] T. Saitoh, K. Hattori, M. Hiraide, Anal. Chim. Acta 543 (2005) 25–30.
[16] D.L. Giokas, E.K. Paleologos, S.M. Tzouwara-Karayanni, M.I. Karayannis, J. Anal. Atom. Spectrom. 16 (5) (2001) 521–526.
[17] D.L. Giokas, E.K. Paleologos, S.M. Tzouwara-Karayanni, M.I. Karayannis, Anal. Chim. Acta 458 (1) (2002) 241–248.
[18] G.M. Wuilloud, J.C.A. de Wuilloud, R.G. Wuilloud, M.F. Silva, R.A. Olsina, L.D. Martinez, Talanta 58 (4) (2002) 619–627.
[19] M. Garrido, M.S. Di Nezio, A.G. Lista, M. Palomeque, B.S. Fernández Band, Anal. Chim. Acta 502 (2004) 173–177.
[20] C. Ortega, M.R. Gomez, R.A. Olsina, M.F. Silva, L.D. Martinez, J. Anal. Atom. Spectrom. 17 (2002) 530–533.
[21] J. Nan, Y. Jiang, X.-P. Yan, J. Anal. Atom. Spectrom. 18 (2003) 946–950.
[22] D. Kara, M. Alkan, Talanta 55 (2001) 415–423.
[23] D. Kara, M. Alkan, Microchem. J. 71 (1) (2002) 29–39.
[24] D. Kara, M. Alkan, Ş. Güçer, Anal. Lett. 35 (15) (2002) 2577–2592.
[25] M. Alkan, D. Kara, J. Trace Microprobe Tech. 21 (3) (2003) 479–491.
[26] M. Alkan, D. Kara, Instrum. Sci. Technol. J. 32 (3) (2004) 291–301.
[27] J.R. Motekaitis, A.E. Martell, Can. J. Chem. 60 (1982) 2403–2409.
[28] A. Çetin, Master's thesis, Gazi University, Ankara, 1992.
[29] T. Gündüz, N. Gündüz, E. Kılıç, F. Köseoğlu, S.G. Öztaş, Analyst 113 (1988) 715–719.
[30] T. Gündüz, E. Kılıç, E. Canel, F. Köseoğlu, Anal. Chim. Acta 282 (1993) 489–495.
[31] N. Türkel, R. Aydın, U. Özer, Turk. J. Chem. 23 (1999) 139–152.
[32] A. Doğan, F. Köseoğlu, E. Kılıç, Anal. Biochem. 295 (2001) 237–239.
[33] H. Rossotti, The study of Ionic Equilibria, Longmans, London, 1978.
[34] H.U. Kim, K.H. Lim, Bull. Korean Chem. Soc. 24 (10) (2003) 1449–1454.
[35] J.C. Miller, J.N. Miller, Statistics for Analytical Chemistry, Third edition, Ellis Horwood Limited, 1993, p. 58.
[36] L. Sombra, M. Luconi, M. Fernanda Silva, R.A. Olsina, L. Fernandez, Analyst 126 (2001) 1172–1176.

Rapid analysis of captopril in human plasma and pharmaceutical preparations by headspace solid phase microextraction based on polypyrrole film coupled to ion mobility spectrometry

Akarm Karimi[a], Naader Alizadeh[b],*

[a] Department of Chemistry, Faculty of Science, Bu-Ali Sina University, Hamadan, Iran
[b] Department of Chemistry, Tarbiat Modares University, P.O. Box 14115-175, Tehran, Iran

ABSTRACT

A rapid, simple, and sensitive headspace solid phase microextraction coupled to ion mobility spectrometry (HS-SPME-IMS) method is presented for analysis of the highly specific angiotensin-converting enzyme (ACE) inhibitor, captopril (CAP). Positive ion mobility spectra of CAP were acquired with an ion mobility spectrometer equipped with a corona discharge ionization source. Mass-to-mobility correlation equation was used to identify product ions. A dodecylsulfate-doped polypyrrole (PPy-DS) coating was used as a fiber for SPME. The results showed that PPy-DS based SPME fiber was suitable for successfully extracting CAP from human blood plasma and pharmaceutical samples. The HS-SPME-IMS method provided good repeatability (R.S.D.s < 4%) for aqueous and spiked plasma samples. The calibration graphs were linear in the range of 10–300 ng mL^{-1} ($R^2 > 0.99$) and detection limits were 7.5 ng mL^{-1} for aqueous and 6.3 ng mL^{-1} for plasma blank samples. Finally, a standard addition calibration method was applied to HS-SPME-IMS technique for the analysis of blood plasma samples and tablets. Purpose method seemed to be suitable for the analysis of CAP in plasma samples as it is not time consuming (state total time from sample preparation to analysis), it required only small quantities of the sample, and no derivatization was required.

© 2009 Elsevier B.V. All rights reserved.

1. Introduction

Captopril, 1-[(2S)-3-mercapto-2-methylpropionyl]-L-proline (CAP), is a synthetic dipeptide serving as an orally active inhibitor of the angiontensin-converting enzyme and has been widely used as antihypertensive drug [1] to moderate heart failure [2]. After oral administration of therapeutic-doses of CAP, rapid absorption occurs with peak blood levels in about an hour period. The average minimal absorption is approximately 75%. Like other thiols, CAP undergoes rapid oxidation to disulfide metabolites both in vitro and in vivo [3]. Intracellularly, disulfide metabolites are reduced to the free thiol and can therefore act as a reservoir for free CAP [3]. Only the free CAP is pharmacologically active; however, the formation of the inactive disulfide is reversible; subsequently they may act as a reservoir of free CAP and contribute to a longer duration of action than predicted by the blood concentrations of free CAP [3]. Captopril with a thiol (SH) functional group was shown to act as a scavenger of free radicals in living systems [4] ameliorating toxic effect of arsenite when administered individually [5]. The structure of CAP is shown in inset of Fig. 1b.

Many analytical methods have been used for CAP determination in biofluids. The majority of published articles describe the use of HPLC [6–12], GC [13] or GC–MS [14] techniques, electrochemical oxidation of CAP using a modified carbon-paste electrode [15], spectrophotometry [16,17], fluorimetry [18], and chemiluminescence [19] for the analyzing CAP Recently, an LC-MS/MS method utilizing solid phase extraction (SPE) catridges, was developed for the analysis of catropril [20]. Most of the techniques reported so far for analyses of CAP have utilized the derivative of CAP. Analysis of analyte without derivatization would simplify the method and as a result reduce the analysis time. Furthermore, most extraction procedures, especially liquid–liquid extraction are based on a series of extraction/concentration steps. This can greatly increase time of analysis [21].

Ion mobility spectrometry refers to the principles, practice and instrumentation for characterizing chemical substances through their gas-phase ion mobilities. IMS is an analytical technique that distinguishes ionic species on the basis of the differences in the drift velocity through a gas under an applied electrostatic field. It is a rapid and sensitive technique for the detection of trace explosives [22,23], drugs [24,25] and illicit drugs [26,27], chemical warfare agents [28,29] and environmental pollutants [30,31] under atmospheric pressure conditions. The separation of ions in the drift region in an IMS is based on the mobility of ions. The mobility of an
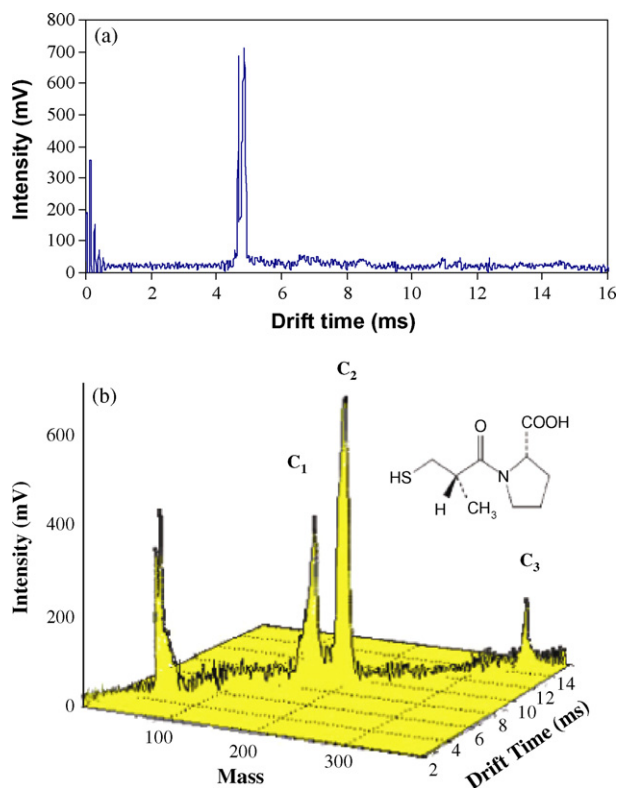
Fig. 1. The ion mobility spectrum obtained by HS-SPME-IMS using a PPy-DS fiber for pure solid drug; (a) background, (b) the 3D mass-to-mobility spectrum based on mass-ion mobility correlation equation sampling by PPy-DS fiber from the headspace above the heated pure solid sample.

ion is determined by the structure (size and shape), the mass and the charge of the analyte [32,33].

IMS provides fast, reliable, and sensitive response for many drugs. These instruments have low cost and power requirements. To achieve the necessary levels of sensitivity, enrichment and clean-up steps are needed before the analysis of drugs in the biological samples. Headspace solid phase microextraction (HS-SPME) with sampling from the headspace above the sample can especially offer a high potential in biomedical analysis, for producing neat spectra and protecting the fiber from irreversible damages by non-volatile concomitants present in the biological matrix [34]. The coupling of SPME to ion mobility spectrometry (IMS) is combines rapid sampling with rapid detection while improving sensitivity and selectivity.

To achieve selective determination for different classes of compounds, the number of available coating materials has increased in recent time. In our previous studies [27,35], the electrochemical fiber coating (EFC) technique was used for the preparation of dodecylsulfate-doped polypyrrole (PPy-DS), and applied as a fiber for HS-SPME procedures. To our knowledge there is no published HS-SPME method for the rapid and sensitive determination of CAP in human plasma or pharmaceutical dosage without derivatization. In continuation of our research activities, for the first time, the efficiency of PPy-DS as a fiber for extraction and determination of CAP by HS-SPME device coupled with IMS is described. The effects of the extraction parameters on the extraction efficiency have been studied. Analytical parameters of the method, i.e. linearity, detection limits and repeatability were established at low nanogram per milliliter level of concentration and quantitative aspects and matrix effects in human plasma were studied. The optimized method is proposed as an efficient alternative to more expensive, time consuming conventional methods. The performance of the proposed

method was applied to the analysis of CAP in positive human plasma and tablet.

2. Experimental

2.1. Reagents

Captopril (CAP) was obtained from Daro Pakhsh-co (Tehran, Iran). The stock solution of these compounds was prepared with concentration of $1\,mg\,mL^{-1}$ in water. These stock standard solutions were diluted with water to prepare stock solution with concentration of $0.1\,mg\,mL^{-1}$ for each compound. The model solutions containing the required amount of analyte ($5–300\,ng\,mL^{-1}$) were freshly prepared daily by diluting mixed standard solution in aqueous and plasma samples. Stock and working standards were stored at $4\,°C$ in the refrigerator. Pyrrole (Fluka, Buchs, Switzerland) was distillated before use. In SPME experiments, double distillated water was used as a solvent, pH was adjusted with hydrogen chloride from Merck (Darmstadt, Germany) and to saturate the samples, sodium chloride from Merck (Darmstadt, Germany) was used. Sodium dodecylsulfate (SDS) was of maximum purity available and obtained from Sigma–Aldrich (Deisenhofen, Germany).

2.2. Apparatus

The SPME holder for manual sampling was obtained from Azar Electrode (Ourumieh, Iran). Stirring the solution was carried out with a magnetic stirrer (Heidolph MR 3001 K) and a $2\,mm \times 5\,mm$ stirring bar. A circulating water bath (Frigomix B. Braun UM-S) with accuracy of $\pm0.1\,°C$ was used to keep the temperature of solutions constant. Also, a two-compartment-recirculating cell laboratory-made from glass was used for controlling the sample temperature. All pH measurements were performed at $25 \pm 0.1\,°C$ by use of a pH/ion-meter Metrohm 713 with a standard uncertainty of 0.1 mV (Metrohm, Switzerland).

Electrochemical polymerization of pyrrole was carried out using Behpajuh (BHP 2061-C model) potentiostat (Isfahan, Iran). An electrochemical cell including a platinum (Pt) working electrode ($2\,cm \times 200\,\mu m$ O.D.), a Pt counter electrode and a double junction saturated calomel (dj-SCE) electrode, as reference electrode was used for preparation of the polymer.

Detection and quantification of CAP were carried out using an ion mobility spectrometer (model 1000) constructed at Isfahan University of Technology. A GC injection port was equipped with a heating element and a digital temperature controller (TC14P, Alton-Ray, Tehran) was used for introduce the SPME in the IMS. The carrier gas passes through the port and carries the analyte vapor to the IMS cell. The main parts of the instrument and conditions were reported in our previous works [27,35]. The optimized experimental conditions for obtaining the ion mobility spectra of the compounds are listed in Table 1.

2.3. Electrochemical fiber coating

Polypyrrole film was prepared electrochemically using a three-electrode system. PPy-DS film was directly electrodeposited on the surface of platinum wire (as working electrode). The technique and other operating conditions are similar to our previous work [27,35].

2.4. HS-SPME/IMS of CAP

The blood samples were taken from both healthy and diseased humans and centrifuged at 3000 rpm for 20 min obtain plasma and was subsequently stored at $-20\,°C$ prior to analysis. Working plasma samples were prepared by combining 100 μL of blank plasma sample spiked with an appropriate amount of the CAP

Table 1
IMS operation parameters and reduced mobility values for reactant and CAP ions.

Parameter	Value	
Corona voltage (V)	2600	
Drift field voltage (V)	7200	
Drift gas flow, N_2 (mL/min)	450	
Carrier gas flow, N_2 (mL/min)	150	
Drift tube temperature (°C)	150	
Injection temperature (°C)	220	
Drift tube length cm	11	
Shutter grid pulse (μs)	380	
Calibrant ion	$(H_2O)nH^+$	
	$(H_2O)nH^+$	Product ions
Drift time (ms)	4.82 ± 0.06	$8.55 \pm 0.05, 9.27 \pm 0.08, 14.53 \pm 0.05$
Reduced ion mobility ($cm^2 V^{-1} s^{-1}$)	$2.37^a \pm 0.10$	$1.33 \pm 0.05, 1.23 \pm 0.05, 0.79 \pm 0.04$
Mass-to-mobility (amu)	52.2 ± 6.3	$181.3 \pm 10.9, 204.4 \pm 12.3, 346.1 \pm 16.6$
Number of hydration (n)	1–2	0–1, 0, 0–1
Ion mass (amu)	19.0	$171.6^b, 217.9^b, 343.2$

^a not used — see below

[a] Data from Ref. [25].
[b] Data from Ref. [21].

along with 400 μL of buffered solution (pH 4.0) in a 2 mL glass vial. After the addition of sodium chloride and a magnetic stirring bar, the vial was hermetically closed with a PTFE/silicon septum and tightly sealed with an aluminum cap to prevent sample loss due to evaporation. To achieve equilibrated samples, the vial was heated in a circulating water bath at 45 °C for 15 min before the start of HS-SPME analysis. Fibers were conditioned prior to the use by inserting them into the IMS injection port for 5 min. The PPy-DS fiber was exposed to the headspace over the stirring liquid sample for 5–30 min, depending on the experiment. After completion of sampling step, the fiber was withdrawn into the needle and removed from the sample vial. The fiber was then immediately inserted into the injection port of the IMS for thermal desorption and analysis. Tablets of CAP were prepared by Iran Daru Company (Tehran, Iran). Four, 25 mg CAP/tablet were grounded in an agate mortar. A sample equivalent to one tablet was carefully weighed and finally dissolved in de-ionized water, and the flask was sonicated for 10 min. The resulting solution was separated by filtration and the residue was washed three times with water. The filtrate was transferred quantitatively into a calibrated volumetric flask and diluted to a final volume of 100 ml with water. An aliquot of this solution was diluted with buffer solution (pH 4.0) to prepare different concentration levels (50 ng mL^{-1} and 70 ng mL^{-1}) and was analyzed by standard addition methods.

3. Result and discussion

3.1. Optimization of IMS conditions

In the positive mode of IMS, the analyte is ionized in ion-molecular exchange reactions with reactant ions. For identification purposes, reduced mobility (K_0) is often used instead of drift time. Reduced mobilities are calculated for positive ion mode using $(H_2O)nH^+$ as the calibrant. The reduced mobility is normalized to a standard pressure (760 torr) and temperature (273 K). Reduced mobility can be calculated using Eq. (1),

$$K_o(\text{unknown}) = K_o(\text{standard}) \times \frac{t_d(\text{standard})}{t_d(\text{unknown})} \qquad (1)$$

where K_o is the reduced mobility with the units of ($cm^2 V^{-1} s^{-1}$), and t_d is the drift time. Different mass–mobility correlation curves have been published in the last few years [36–40]. The regression equation of the mass-to-mobility correlation curve for corona discharge IMS as shown in Eq. (2) and agreement with investigations

of Bell et al. [36].

$$\log m = -0.52 K_o + 2.95 \qquad (2)$$

The peaks observed in the corona discharge IMS spectra can be assigned to ions formed by hydrogen abstraction and clustering with water. Therefore, in Eq. (2) m is the mass of product ions. The top spectrum of Fig. 1 shows the background signal of the IMS. The 3D mass-to-mobility spectrum based on mass-ion mobility correlation equation was calculated and shown in Fig. 1b. The right view spectrum of Fig. 1b shows IMS spectra of CAP sampling by PPy-DS fiber from the headspace above the heated pure solid sample. There are three distinct peaks, (C_1, C_2, C_3), that can be used as a fingerprint tool in the identification of CAP. The primary peak, labeled C1, has a drift of 8.55 ms ($K_o = 1.33$ cm^2 V^{-1} s^{-1}), and the other peak, labeled C_2 has drift times of 9.27 ms ($K_o = 1.23$ cm^2 V^{-1} s^{-1}). The third small product ion peak is observed with a drift time of 14.53 ms ($K_o = 0.79$ cm^2 V^{-1} s^{-1}). Considering the above-described findings, the peaks observed in the ion mobility spectra can be identified by mass–mobility correlation (left view of Fig. 1b). Peaks labeled C_1 and C_2 were identified as $C_8H_{14}NOS^+$, $C_9H_{16}NO_3S^+$. The peak labeled C_3 has a mass of 346 amu and is suggested to be a $C_{16}H_{28}N_2O_2S_2^+$ (dimer of C_1). These assignments were made on the basis of the mass spectrum analyses that have been previously reported in the literature [21]. The mass spectral analysis revealed that it contained two ions with m/z 171.26 and 218. In the mass spectrum, the peaks with mass 343 that corresponded to the drift time 14.53 ms in IMS spectra (it may be dimer of C_1) were not reported. The reduced mobility of ions together with their corresponding mass-to-mobility and standard deviations are listed in Table 1. The peak at 9.27 ms was integrated for all quantitative analysis.

The next step was the optimization of the desorption temperature. The efficient desorption of CAP from the fiber is critical for this technique to achieve good repeatability, high sensitivity, and to prevent excessive carryover between analysis. An SPME-IMS desorption temperature optimization study was conducted to determine the response vs. desorber temperature profile of CAP from the PPy-DS fiber. The sample concentration and extraction parameters were kept the same for each of the temperature studies conducted from 120 °C (m.p. of CAP) to 240 °C. The extraction temperature and the drift tube temperature remained constant throughout the experiments. Fig. 2 shows the results of the desorber temperature profiles at 120–240 °C. The response of CAP increased as the desorber temperature was raised from 120 °C to 200 °C and reaches a plateau. The carry over was measured with one blank injection following the initial desorption. At the desorption tem-
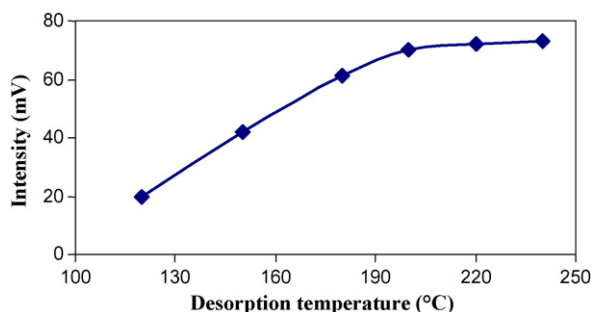
Fig. 2. Effect of desorption temperature on the response sensitivity of HS-SPME of CAP by PPy-DS. Concentration of CAP: 50 ng mL^{-1}; NaCl: 5 mol L^{-1}; extraction time, 20 min; pH 4.0; extraction temperature, 45 °C; stirring speed, 600 rpm; cell temperature, 150 °C.

perature of 220 °C CAP was fully desorbed from the fiber coating after a 60 s desorption period with no carry over's observed in blank injections.

In the IMS, cell temperature has a significant effect on both the kinetics and thermodynamics of the ion-molecular exchange process between reactant ions and analyte [41]. The influence of cell temperature in the ranges of 120–200 °C was investigated. The peak intensity of CAP was noticeably affected by the cell temperature, as shown in Fig. 3. This figure shows that the peak enhances with increasing cell temperature, and reaches a maximum intensity at 150 °C. With an additional increase in the cell temperature, peak intensity decreases. This behavior may be attributed to deprotonation of an analyte. According to these concepts, the mechanism for the ion-molecular exchange reaction may be written as

$$H_3O^+ + CAP \overset{K_{ex}}{\longleftrightarrow} H_2O + CAPH^+ \qquad (3)$$

$$CAPH^+ + M \overset{k_2}{\longrightarrow} CAP + MH^+ \qquad (4)$$

where K_{ex} and k_2 are the exchange equilibrium constant and deprotonation rate constant, respectively. M is competed species; CAPH$^+$ and MH$^+$ are the protonation form of analyte and competitor respectively. If the steady-state hypothesis is applied to the concentration of CAPH$^+$, the overall rate of reaction becomes

$$Rate = K_{ex} \frac{k_2[H_3O^+][CAP][M]}{[NH_3]} \qquad (5)$$

Therefore, the overall rate constant is the exchange equilibrium constant multiplied by the deprotonation rate constant of CAPH$^+$. The overall activation energy for the exchange and deprotonation
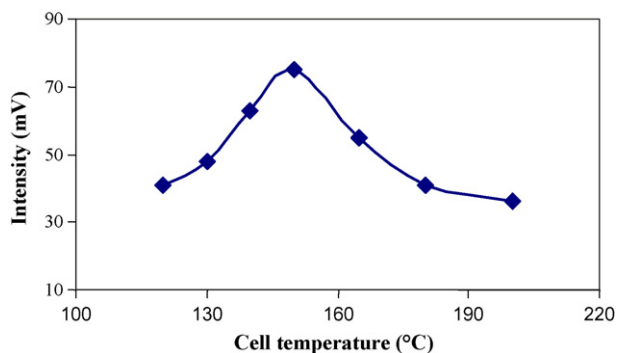
Fig. 3. Effect of cell temperature on the response sensitivity of HS-SPME of CAP by PPy-DS. Concentration of CAP: 50 ng mL^{-1}; NaCl: 5 mol L^{-1}; extraction time, 20 min; pH 4.0; extraction temperature, 45 °C; stirring speed, 600 rpm; desorption temperature, 220 °C.

process is given by

$$E = RT^2 \left(d \ln K_{ex} \frac{k_2}{dT} \right) = \Delta H_{ex}^\circ + E_2 \qquad (6)$$

where R, T, ΔH_{ex}°, and E_2 are the gas constant, absolute temperature, standard enthalpy of exchange process, and activation energy of deprotonation reaction, respectively. It is noted that as the temperature increases, the [CAPH$^+$] concentration decreases revealing that there is a shift in the equilibrium toward the deprotonaed form of analyte and a decreasing signal with the increase in temperature. The optimum temperature for CAPH$^+$ is about 150 °C.

Different IMS shutter widths were tested with SPME-IMS. Different shutter gate widths 50–500 μs were tested with SPME-IMS. It was observed that when the 380 μs shutter gate width was used, the best sensitivity, peak shape and separation between peaks could be obtained. Therefore, 380 μs was chosen as the optimal shutter gate width for all of the following experiments. In order to obtain a stable signal, corona voltages in the range of 2400–3000 V was investigated. The results indicated that the signal intensity increased with increasing the corona voltage, reaching a maximum at 2600 V. Therefore, all experiments were conducted by applying 2600 V between the corona electrodes. The optimized instrumental conditions for obtaining the IMS spectra of the analyte are listed in Table 1.

3.2. Optimization of HS-SPME conditions

In order to obtain the optimized extraction conditions and best extraction efficiency, we used the maximum of peak height of analyte as the IMS response to evaluate the extraction efficiency under different conditions. To optimize the method, all the microextractions were performed from the headspace of water solution spiked with CAP. The effect of the main extraction parameters, such as the sample pH, exposure time, sampling temperature, salt concentration, and stirring rate of the sample were studied.

The sample pH is an important factor, which may affect the recovery of CAP from water. To increase the extraction recovery of CAP, it was necessary to acidify the sample. To study the effect of sample pH on the extraction of CAP from water samples, the PPy-DS fiber was exposed to the headspace over the stirring liquid samples for 20 min with same concentration in the 50 ng mL^{-1} level at different pH values (2, 2.5, 3, 3.6, 3.9, 4, 4.2, 4.7, and 5.7).

Fig. 4 depicts the supplemented distribution curves calculated with the acidity constants [15,42,43] for the CAP system. The upper part (a) shows the distribution curves as a function of pH, while the lower part (b) gives the intensity of the CAP IMS peak at various pH values. The Fig. 4a clearly illustrates that the CAP exists in four different forms in the pH interval 1–12. The curves clearly demonstrate that the predominant species is the neutral CAP form at pH 4. Fig. 4b shows the IMS peak intensity obtained at different pH with the maximum recovery obtained at pH 4. At this pH, the acid–base equilibrium for the CAP shifts significantly toward the neutral forms which have higher vapor pressure, greater affinities toward the film, and therefore increased extraction efficiencies.

The time and temperature of extraction determines the maximum amount of analyte that can be extracted by the fibers which additionally controls the sensitivity of the method. The effect of extraction time was studied in the range of 5–30 min for spiked-water samples at same concentration in the 50 ng mL^{-1} level. Fig. 5a shows that the analytical signal increases quickly with sampling time in the range of 5–20 min. After 20 min, a decrease in adsorption capacity was observed with increasing extraction time. This was probably attributed to desorption.

Extraction temperature also plays an important role in the adsorption of analytes; it influences the rates of mass transfer, and the partition coefficients of the analyte. The extraction temperature
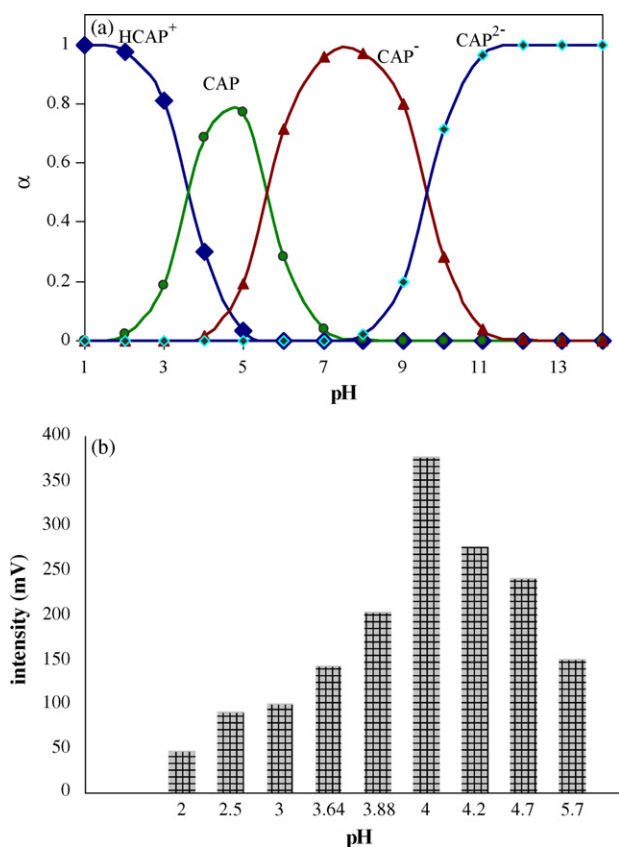
Fig. 4. Influence of pH on the distribution curves (a) and HS-SPME-IMS efficiency of CAP with PPy-DS (b). Concentration of CAP: $50 \, ng \, mL^{-1}$; NaCl: $5 \, mol \, L^{-1}$; extraction time, 20 min; extraction temperature, 45 °C; stirring speed, 600 rpm; desorption temperature, 220 °C; cell temperature, 150 °C.

profile for extraction efficiencies are shown in Fig. 5b. The extraction efficiency increases as the solution temperature is enhanced. However, a significant decrease in adsorption capacity was observed when temperature increased (>45 °C). Because adsorption is generally an exothermic process, the partition coefficient of analytes between headspace and fiber is expected to decrease. Thus, a significant decrease in adsorption capacity was observed when the temperature was increased from 45 °C. Finally, the time and temperature of extraction were selected at 20 min and 45 °C as optimized values of these parameters respectively.

The salting-out effect was assessed by the addition of NaCl to the extracting solution in a range of 0–5 mol L^{-1}. As expected, under the same conditions the extraction efficiency increases as the concentration of NaCl increases. Efficiency maximum was obtained with a $5 \, mol \, L^{-1}$ NaCl. The addition of salt has a significant effect on the extraction of CAP. Further analyses were conducted with the optimum $5 \, mol \, L^{-1}$ NaCl solution.

Fig. 5. Effect of extraction time (a) and extraction temperature (b) on the HS-SPME efficiency of CAP with PPy-DS. Concentration of CAP: $50 \, ng \, mL^{-1}$; NaCl: $5 \, mol \, L^{-1}$; stirring speed, 600 rpm; desorption temperature, 220 °C; cell temperature, 150 °C.

Agitation of the sample improves mass transfer in the aqueous phase and induces the convection in the headspace. Therefore, equilibrium between the aqueous and headspace can be achieved more rapidly. So, sample stirring reduces the time required to reach the equilibrium by enhancing the diffusion of the analyte towards the fiber. The results revealed that extraction efficiency increases as the stirring speed is enhanced and reaches a maximum and remains constant above 600 rpm. Thus, for all further experiments a stirring rate of 600 rpm was used.

3.3. Quantitative analysis

Dynamic linear range, correlation coefficient of calibration graph, reproducibility, and detection limit of CAP with proposed method are listed in Table 2. The linear ranges of the method were tested by extracting different aqueous and plasma standards with increasing concentrations. The precision of the method was determined by performing five consecutive fiber extractions from aqueous and plasma solution with a concentration level at $50 \, ng \, mL^{-1}$ under the optimal conditions. The R.S.D. using the PPy-DS fiber was 3.2% and 2.5% for aqueous and plasma solution respectively. The limits of detection for CAP in aqueous and plasma blank samples when using the optimized conditions were determined to be 7.5 and $6.3 \, ng \, mL^{-1}$, respectively, at a signal-

Table 2
Dynamic linear range (DLR), correlation coefficient (R^2), intra-/inter-day precision (R.S.D. %, $n = 5$) and limit of detections for the analysis of CAP in plasma sample with HS-SPME-IMS using PPy-DS fiber and comparison with several different methods.

Method	DLR ($ng \, mL^{-1}$)	Correlation coefficient (R^2)	Intra-day R.S.D.%	Inter-day R.S.D.%	LOD ($ng \, mL^{-1}$)
HPLC [8] [a]	20–4,000	0.9993	7.8	10.9	7
GC–MS [14] [a]	10–5,000	0.993	3.1–4.3	2.9–4	10
LC-MS-MS [21]	25–3,000	0.9995	2.6– 9.7	5–10	7.6
DPV [b] [15]	1,800–10,000	0.9991	2.5–3.5	–	760
HS-SPME-IMS [c]	10–300	0.9987	1.5–3.5	1.2	6.3–7.5[d]

[a] With derivatization.
[b] Differential pulse voltammetric.
[c] This work.

Table 3
Detremination of CAP in tablet and human plasma samples by multiple standard addition method in optimum condition with HS-SPME-IMS.

Sample	Concentration (ng mL^{-1})			Correlation coefficient (R^2)	Relative recovery (%)	R.S.D. %
	Level	Added standard	Found			
Tablet	50	10,20,50,100,150, 200	49.8 ± 1.7	0.9964	99	3.9
	70	10,20,50,100,150, 200	66.3 ± 2.5	0.9967	95	2.9
Human plasma	Intra-day	0, 70, 200	183.2 ± 2.2	0.9997	–	1.2
	Inter- day	0, 50, 100	179.6 ± 1.3	0.9996	–	1.0

to-noise ratio (S/N) of 3. Comparing the HS-SPME-IMS results for the extraction and determination of CAP using PPy-DS fiber with literature data from several methods [8,14,15,21] shows that the proposed method has very good analytical parameter for analyzing CAP (Table 2). However, the limited linear ranges were observed for this analysis. Fig. 6a displays the IMS spectrum obtained for non-spiked and spiked blank plasma samples using HS-SPME at optimal conditions.

3.4. Real samples

The applicability of HS-SPME-IMS method to real samples was investigated for a positive human plasma sample and tablet. Blood plasma sample was collected up to 80 min after oral administration of CAP tablet to an aged, female volunteer patient. Fig. 6b displays the IMS spectrum obtained for non-spiked and standard addition plasma samples using HS-SPME at optimal conditions. The concentration of CAP was determined by the standard addition method. The quantitation of CAP in this sample was determined by performing a linear regression analysis on the standard added sample. Table 3 shows the quantitative results of the intra-/inter-day precision of this method for the plasma samples. The comparative results of the two analyses did not reveal any significant difference within

a 95% confidence level with a global quantification error of ≤1.2% for determination of CAP in plasma samples.

Finally, HS-SPME-IMS method was applied to the determination of CAP in pharmaceutical sample by using the standard addition method. Experimental conditions for these measurements were similar to those described in Section 2.4. The precision of method for the determination of CAP in the pharmaceutical preparations, based on three replicates analysis, shows an R.S.D. < 4%. The analytical results are summarized in Table 3.

4. Conclusion

The HS-SPME-IMS method with dodecylsulfate-doped polypyrrole (PPy-DS) film as a fiber was introduced and evaluated to quantify CAP in human plasma and tablet samples as it is not time consuming, without sample cleanups and derivatization. The SPME-IMS combination possesses several attractive attributes such as the simplicity of sample preparation, minimized sample handling, and one step sample extraction/concentration directly from the complex matrices sample into the IMS. The technique offers good performance in terms of precision (R.S.D. < 4%), LOD (6–7.5 ng mL^{-1}) and because of simplicity and low equipment cost, is well suited for the quantification of CAP in real samples, make the HS-SPME-IMS method promising for routine analysis.

Fig. 6. The ion mobility spectrum obtained by HS-SPME-IMS using a PPy-DS fiber under optimum conditions for non-spiked and spiked blank plasma samples (a) and positive human plasma sample and standard addition with 70 and 200 ng mL^{-1} of CAP (b).

References

[1] K. Florey (Ed.), Analytical Profiles of Drug Substances, vol. 11, Academic Press, New York, 1982, pp. 81–136.
[2] A. Goodman, L.S. Goodman, in: T.W. Rall, F. Murad (Eds.), Les bases farmacologicas de la terapeutica, seventh ed., Panamericana, Madrid, 1989, pp. 616–620.
[3] K.L. Duchin, D.N. McKinstry, A.L. Cohen, B.H. Migdalof, Clin. Pharmacokinet. 14 (1988) 241.
[4] N. Aykin, R. Neal, M. Yusof, N. Ercal, Biomed. Chromatogr. 15 (2001) 427.
[5] K. Kalia, G.D. Narula, G.M. Kannan, S.J.S. Flora, Comp. Biochem. Physiol. Part C: Toxicol. Pharmacol. 144 (2007) 372.
[6] J. Klein, P. Colin, E. Scherer, M. Levy, G. Koren, Ther. Drug Monit. 12 (1990) 105.
[7] M. Bahmaei, A. Khosravi, C. Zamiri, A. Massoumi, M. Mahmoudian, J. Pharm. Biomed. Anal. 15 (1997) 1181.
[8] T. Huang, Z. He, B. Yang, L. Shao, X. Zheng, G. Duan, J. Pharm. Biomed. Anal. 41 (2006) 644.
[9] A. Engalytcheff, R. Debuyst, G.C. Vanhaelewyn, F.J. Callens, B. Tilquin, Radiat. Res. 162 (2004) 616.
[10] F. Tache, A. Farca, A. Medvedovici, V. David, J. Pharm. Biomed. Anal. 28 (2002) 549.
[11] A. Medvedovici, C. Mircioiu, V. David, D.S. Miron, Eur. J. Drug Metab. Pharmacokinet. 25 (2000) 91.
[12] R.J. Kok, J. Visser, F. Moolenaar, D. de Zeeuw, D.K. Meijer, J. Chromatogr. B: Biomed. Sci. Appl. 693 (1997) 181.
[13] M.S. Bathala, S.H. Weinstein, F.S. Meeker Jr., S.M. Singhvi, B.H. Migdalof, J. Pharm. Sci. 73 (1984) 340.
[14] M.E. Franklin, R.S. Addison, P.V. Baker, W.D. Hooper, J. Chromatogr. B: Biomed. Sci. Appl. 705 (1998) 47.
[15] S. Shahrokhian, M. Karimi, H. Khajehsharifi, Sens. Actuators B 109 (2005) 278.

[16] R. Karlicek, P. Solich, Pharmazie 53 (1998) 549.
[17] P.D. Tzanavaras, D.G. Themelis, A. Economou, G. Theodoridis, Talanta 57 (2002) 575.
[18] K. Imai, T. Toyo'oka, Y. Watanabe, Anal. Biochem. 128 (1983) 471.
[19] Z.D. Zhang, W.R.G. Baeyens, X.R. Zhang, G. van der Weken, J. Pharm. Biomed. Anal. 14 (1996) 939–945.
[20] K.R. Rezende, I.M. Mundim, L.S. Teixeira, W.C. Souza, D.R. Ramos, C.R.F. Cardoso, I.C. Souza, M. Grafao, K.B. Bellîorio, J. Chromatogr. B 850 (2007) 59.
[21] I.I. Salem, W.A. Saif, Y. Jmeian, J.I. Al Tamimi, J. Pharm. Biomed. Anal. 37 (2005) 1073.
[22] A.B. Kanu, H.H. Hill Jr., Talanta 73 (2007) 692.
[23] J.K. Lokhnauth, Ni.H. Snow, J. Chromatogr. A 1105 (2006) 33.
[24] Y. Wanga, S. Nacson, J. Pawliszyn, Anal. Chim. Acta 582 (2007) 50.
[25] M.T. Jafari, T. Khayamian, V. Shaer, N. Zarei, Anal. Chim. Acta 581 (2007) 147.
[26] N. Takayama, R. Iio, S. Tanaka, S. Chinaka, K. Hayakawa, Biomed. Chromatogr. 17 (2003) 74.
[27] N. Alizadeh, A. Mohammadi, M. Tabrizchi, J. Chromatogr. A 1183 (2008) 21.
[28] B.M. Kolakowski, P.A. D'Agostino, C. Chenier, Z. Mester, Anal. Chem. 79 (2007) 8257.
[29] R.P. Ericksona, A. Tripathib, W.M. Maswadehc, A.P. Snyderc, P.A. Smith, Anal. Chim. Acta 556 (2006) 455.
[30] T. Keller, A. Keller, E. Tutsch-Bauer, F. Monticelli, Forensic Sci. Int. 161 (2006) 130.
[31] R. Pozzi, F. Pinelli, P. Bocchini, G.C. Galletti, Anal. Chim. Acta 504 (2004) 313.
[32] F.W. Karasek, Anal. Chem. 46 (1974) 710A.
[33] E.W. McDaniel, E.A. Mason, The Mobility, Diffusion of Ions in Gases, John Wiley & Sons, New York, USA, 1973.
[34] S. Ulrich, J. Chromatogr. A 902 (2000) 167.
[35] A. Mohammadi, Y. Yamini, N. Alizadeh, J. Chromatogr. A 1063 (2005) 1.
[36] S.E. Bell, R.G. Ewing, G.A. Eiceman, J. Am. Soc. Mass Spectrom. 5 (1994) 177.
[37] H. Borsdorf, H. Schelhorn, J. Flachowsky, H.R. Döring, J. Stach, Anal. Chim. Acta 403 (2000) 235.
[38] F.W. Karasek, W.D. Kilpatrick, M.J. Cohen, Anal. Chem. 43 (1971) 1441.
[39] F.W. Karasek, Anal. Chem. 44 (1972) 1758.
[40] G.W. Griffin, I. Dzidic, D.I. Carroll, R.N. Stillwell, E.C. Horning, Anal. Chem. 45 (1973) 1204.
[41] G.A. Eiceman, Trends Anal. Chem. 21 (2002) 259.
[42] M. Remko, Chem. Pap. 61 (2007) 133.
[43] P.R. Riberio, A.O. Santini, H.R. Pezza, L. Pezza, Elect. Quim. 28 (2003) 39.

Determination of the phenolic-group capacities of humic substances by non-aqueous titration technique

Akira Kirishima *, Takashi Ohnishi [1], Nobuaki Sato, Osamu Tochiyama [2]

Institute of Multidisciplinary Research for Advanced Materials, Tohoku University, 1-1 Katahira, 2-Chome, Aoba-ku, Sendai 980-8577, Japan

ARTICLE INFO

ABSTRACT

The phenolic-group capacities of five humic substances, such as, the Aldrich humic acid, the humic and fulvic acids extracted from a soil, the humic and fulvic acids extracted from a peat have been precisely determined by the non-aqueous potentiometric titration technique. The titration by KOH in the mixed solvent of DMSO:2-propanol:water = 80:19.3:0.7 at $[K^+] = 0.02$ M enabled to measure the potential change in a wide range of pOH ($= -\log [OH^-]$), and thus to determine the capacities of phenolic groups which could not be precisely determined in the aqueous titration. The results of the titration revealed that the mean protonation constants of the phenolic groups were nearly the same for all humic substances and close to that of phenol in the same medium, indicating that each phenolic-group in the humic substances is rather isolated and is not electronically affected by other affecting groups in the humic macromolecule.

© 2009 Elsevier B.V. All rights reserved.

1. Introduction

Humic substances (HS) are heterogeneous mixtures of high-molecular weight organic materials formed by the decomposition and condensation of plant, animal and microbial materials, and are present as colloids in the aquatic environment such as sea, river, lake, and even in deep underground environments where the radioactive wastes are planned to be disposed of. It is commonly recognized that a humic substance having many functional groups in the macromolecule interacts strongly with a variety of metal cations to form complexes and affects the migration behavior of radionuclides released from the disposed radioactive waste [1–5]. For that reason, numerous attempts have been carried out to model and describe the interactions of a humic substance with cations quantitatively [6–20]. The proton exchange capacities of various functional groups in the humic substance are one of the fundamental parameters for the modeling of the cation–humic substance interaction and has been customarily determined by potentiometric acid–base titration in aqueous solution. This method is suitable for the determination of the capacity of carboxylic group which is the major contributor to the cation–humic substance inter-

actions. However, the phenolic groups cannot be titrated as an acid in aqueous solution because water is too acidic and present in too high a concentration to permit the phenolate ion to be formed stoichiometrically by titration with a base. Milne et al. [12] mentioned that the reliable analytical window of potentiometric titration using a glass electrode is $4 < pH < 10$ in aqueous solution, where less than 55% of phenol ($\log K_a = \log[HL]/[H][L] = 9.82$ at $I = 1.0$ [21]) could be dissociated. Titration data obtained in this pH range is insufficient to determine phenol or phenolic-group concentration and their protonation constants. Nevertheless, the development of precise determination method of the phenolic-group on HS is desired since the phenolic-group is known as the second important contributor next to the carboxylic group for cation–HS interaction [2] and the large uncertainty in the phenolic-group capacity is one of the main reasons to give the difficulty in describing this interaction quantitatively. It is known that, in less acidic non-aqueous solvents, this titration can be carried out readily with a stronger basic titrant. Therefore, to determine the total proton exchange capacities of HS, non-aqueous titrations in dimethylformamide (DMF) [22–24], dimethylsulphoxide (DMSO) [22,25], acetonitrile (AN) [24,26], isopropanol [26] and acetone [26] have been tried in an attempt to avoid the deprotonation effect of water. A good solvent for the titration should be sufficiently weak in acidity to permit titration of the most weakly acidic component and sufficiently weak in basicity to permit resolution of the most stronger acid components. Thus, by using DMSO as a medium and potassium hydroxide as a titrant, we have carried out a non-aqueous potentiometric titration for five kinds of humic substances, i.e., Aldrich humic acid, IHSS (Interna-

tional Humic Substances Society) soil humic acid, IHSS peat humic acid, IHSS soil fulvic acid and IHSS peat fulvic acid. The titration system consists of a glass electrode, a mixed solvent of DMSO:2-propanol:water = 80:19.3:0.7 and a titrant solution of potassium hydroxide (KOH) in 2-propanol, where 2-propanol was used as a solvent of KOH instead of DMSO since high concentration of KOH could form a slight precipitation in DMSO. Prior to the HS titration, the concentrations of benzonic acid and phenol in the above mentioned mixed solvent were determined by the same titration system to confirm the reliability of the system. The obtained titration curves for HS were analyzed by applying a simple protonation model which we have proposed previously to describe the protonation behavior of HS in aqueous solution [27,28]. The functional group capacities of carboxylic and phenolic groups thus determined were then compared with those determined by the aqueous titration.

2. Experimental

2.1. Reagents

Four humic substances were purchased from International Humic Substance Society (IHSS); humic acid extracted from soil (Cat. No. 1S102H) and peat (Cat. No. 1R107H), abbreviated to SHA and PHA, respectively; fulvic acids extracted from soil (Cat. No. 2S102F) and peat (Cat. No. 1R107F), abbreviated to SFA and PFA, respectively. Another humic sample purchased from Aldrich Inc. in sodium form was purified as described in the literature [29–31], which is abbreviated to ALHA. Phenol was purchased from Aldrich Inc. Other reagents, such as, benzonic acid, dimethylsulphoxide (DMSO), 0.1 M KOH in 2-propanol solution and KCl were purchased from Wako Pure Chemical Industries and were used without further purification.

2.2. Potentiometric titration

Potentiometric titration was conducted by using the "Wallingford" automated titration system [32] equipped with two automatic burettes (Metrohm 665 Dosimat), a water-jacketed glass vessel (Metrohm, 6.1418.220), a double-junction Ag/AgCl reference electrode (Metrohm, 6.0726.100) and a glass electrode (Metrohm, 6.0133.100). The reference electrode was filled with saturated lithium chloride ethanol solution. The non-aqueous medium for the titration sample was a mixture of DMSO:2-propanol:H_2O = 80:19.3:0.7 containing 0.02 M KCl. 0.7% of H_2O was added in order to keep H_2O activity constant in the sample solution during the titration process. The added hydroxide anion from the titrant forms water molecule with proton dissociated from humic substance, which would increase the H_2O activity in the sample solution. Since the relation between electrode potential (E/mV) and −log [OH^-] (=pOH) shown in Fig. 1 depends on the H_2O activity in the sample solution, this activity change should be minimized by coexisting certain amount of H_2O initially both in the titrant and sample solutions. There is a possibility that high concentration of KOH, like 0.1 M, would form a precipitate in DMSO. To avoid the formation of this precipitate in the titrant stock bottle, KOH and DMSO were added separately into the titration sample, i.e., two kinds of titrant solutions were supplied by using two respective automatic burettes in this titration system, where "titrant A" was pure DMSO and "titrant B" was a mixture of 2-propanol:H_2O = 29:1 containing 0.0966 M KOH and 0.0034 M KCl. The titrant A and B were added simultaneously from the two burettes by keeping a constant volume ratio of titrant A:titrant B = 4:1. Consequently, the final composition of added titrant solution was DMSO:2-propanol:H_2O = 80:19.3:0.7 containing 0.0193 M KOH and 0.0007 M KCl, which had the same
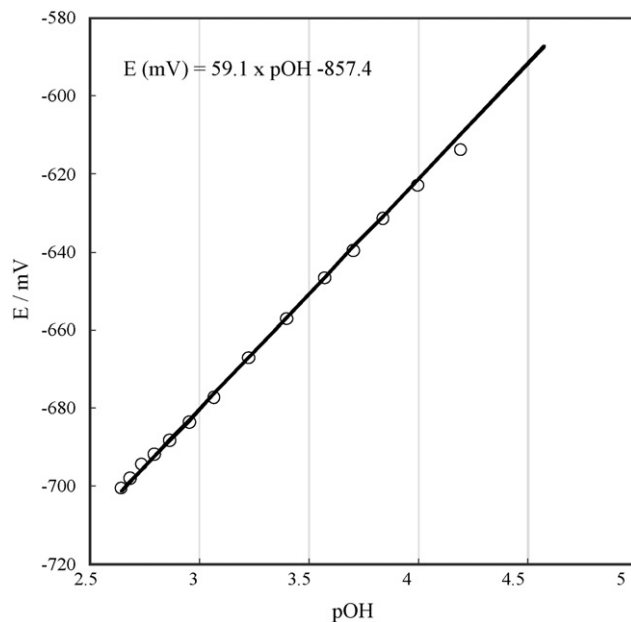
Fig. 1. The calibration curve of the glass electrode for the non-aqueous titration.

solvents ratio and K^+ concentration as the titration sample medium. These titrant and sample condition kept the composition of the mixed solvents in the titration vessel constant during the titration, so that the activity coefficient of proton could be regarded as constant. Since keeping constant K^+ concentration was also important to get a linear relationship between mV readings of glass electrode and pH or pOH especially in the non-aqueous titration, 0.02 M KCl was added to the medium for the titration sample. As the titrations were conducted in strong alkaline region, the titration vessel was covered by a plastic bag and N_2 gas was flowed continuously into the bag to prevent the dissolution of carbon dioxide to the sample solution from air.

The calibration of the glass electrode for the conversion of the mV readings into pOH was conducted by the blank titration using the above mentioned titrant and mixed non-aqueous medium. The mV readings of the glass electrode in this blank titration was compared with −log [OH^-] (=pOH) calculated from the added KOH concentration assuming KOH was dissociated completely in the titration condition.

To confirm the reliability of the employed titration system, 3.5 g dm^{-3} of benzonic acid solution and 1.0 g dm^{-3} of phenol solution in the mixed non-aqueous medium were titrated. In these titrations, the electrode potential was measured over a 0.5 min interval following an initial delay of 1 min to allow adequate mixing of the titrant after each addition of the titrant. The electrode reading was recorded when its drift was less than ± 0.5 mV/min. The drift of the mV reading of electrode potential tends to be larger in this non-aqueous titration than that in the normal aqueous titration system. When a stricter criterion was applied, the titration time was extended too much, raising another concern for CO_2 dissolution into the sample. Therefore, relatively lenient criterion i.e., ±0.5 mV/min was employed for the drift of the electrode reading in this work. When this criterion had not been satisfied over 0.5 min, electrode potential was measured over a 0.5 min interval again, and this process was repeated maximum 20 times. The volume of the titrant drop was automatically calculated at each titration step in order to shift the pOH in the vessel 0.17 by one injection.

40 mg of the humic substances (ALHA, SHA, PHA, SFA and PFA) in their acid form were dissolved in 30 ml of the mixed solvent medium, and then, these solutions were titrated from pOH ≅ 17 to 3

by the same titration system with the same criterion as the benzonic acid titration.

3. Results and discussion

3.1. Glass electrode calibration

For the calibration of the glass electrode, the titrant solutions containing 0.0193 M KOH were added to the blank medium of the titration sample. As mentioned in Section 2.2, the activity coefficient of proton in the sample solution was kept constant during the titration. Therefore, the glass electrode potential can be theoretically expressed by the following equation [33]:

$$E(\text{mV}) = -59.1\,\text{pH} + \text{constant}, \quad \text{at } T = 25\,^{\circ}\text{C} \tag{1}$$

The employed mixed solvent contains DMSO, 2-propanol and H_2O, therefore, the autoprotolysis reaction of this solvent is

$$(\text{mixed solvent}) \ \rightleftharpoons \ H^+_{\text{solvated}} + x(CH_3SOCH_2^-) + y(C_3H_7O^-)$$
$$+ z(OH^-) \tag{2}$$
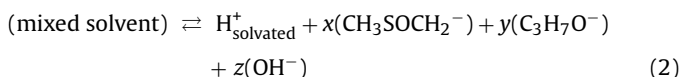
where $x + y + z = 1$. Therefore, the autoprotolysis constant K_{SH} is written by the following equation:

$$K_{SH} = [H^+][CH_3SOCH_2^-]^x[C_3H_7O^-]^y[OH^-]^z \tag{3}$$

The value of this pK_{SH} ($= -\log K_{SH}$) was unknown but was kept constant during the titration since the composition of the mixed solvents was constant during the titration. The pK_{SH} of pure H_2O is 14.0 [34] which is much smaller than those of pure DMSO (>33.3 [35]) and 2-propanol ($= 20.8$ [34]), meaning H_2O is extremely dissociable in comparison with DMSO and 2-propanol. For this reason, the coefficients in Eq. (2) can be regarded as

$$x + y \ll z \simeq 1. \tag{4}$$

Therefore, Eq. (3) can be approximated to

$$K_{SH} = [H^+][OH^-] \tag{5}$$

In consequence, pK_{SH} of the employed mixed solvent is expressed by

$$pK_{SH} = \text{pH} + \text{pOH} \tag{6}$$

By using Eq. (6), Eq. (1) is rewritten as

$$E(\text{mV}) = -59.1\,\text{pH} + \text{constant} = -59.1\,(pK_{SH} - \text{pOH}) + \text{constant}$$
$$= 59.1\,\text{pOH} + B \tag{7}$$

where, B is a constant parameter depending on the composition of the mixed solvents. Since KOH is considered to dissociate completely and the autoprotolysis of the employed mixed solvent is negligible under the applied titration window for the electrode calibration, pOH can be approximated to $-\log[\text{KOH}]_{\text{total}}$ in the calibration. Fig. 1 is a calibration curve of the employed glass electrode where the B value, that is the intercept of the fitted solid line by Eq. (7), was derived as $(-857.4 \pm 0.3)\,\text{mV}$.

3.2. The non-aqueous titration

To demonstrate the validity of the non-aqueous titration technique, the concentrations of benzonic acid and phenol were determined by the potentiometric titration in the mixed non-aqueous medium which is the same as that used in the titration of the humic substances. The titration curves of the benzonic acid solution and the phenol solution are shown in Fig. 2(a) and (b), respectively. The equivalence points of the both titrations can be reliably determined from the maximum points of differential curves (=dE/dml). The benzonic acid concentration determined
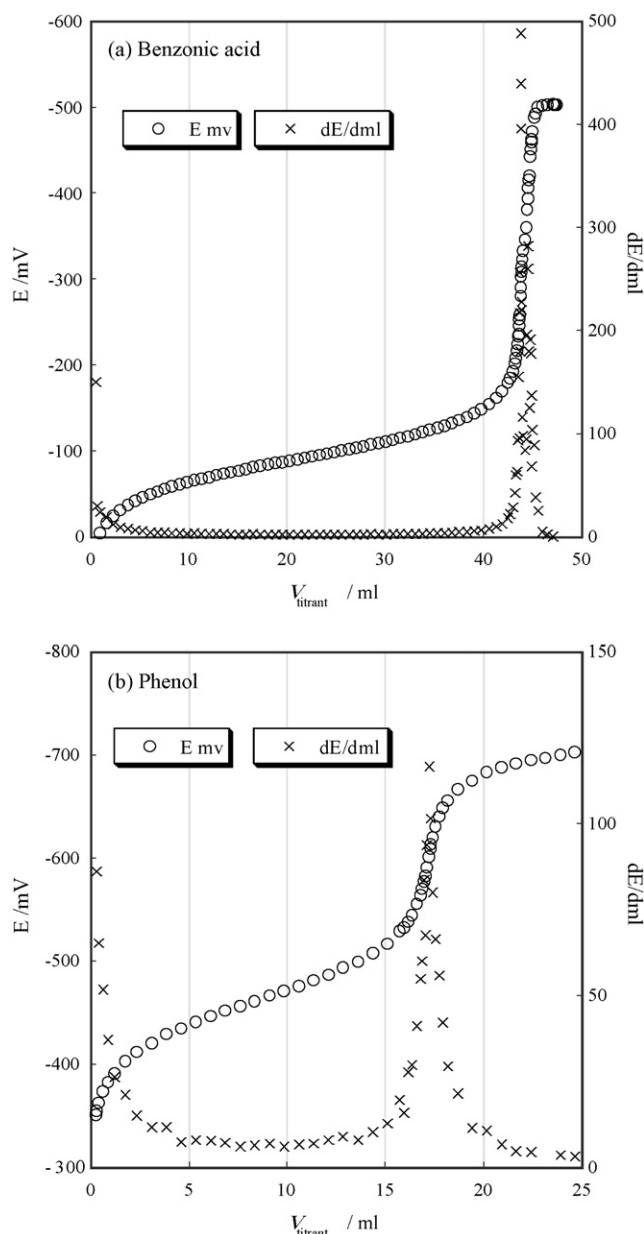
Fig. 2. Demonstrative non-aqueous titration curves of (a) benzonic acid, and (b) phenol.

from the titrant volume consumed before the equivalence point in Fig. 2(a) was 0.0287 M which agreed well with the real concentration 0.0288 M calculated from the measured weight of the benzonic acid powder used in the sample preparation. On the other hand, the phenol concentration determined from the titration curve shown in Fig. 2(b) was 0.0111 M which is 1.8% higher than the concentration calculated from the measured weight of the phenol. The reason of this "over estimation" is supposed to be the absorption of carbon dioxide to the sample from air. This effect was not observed in the benzonic acid titration. Since the pOH value of equivalence point of the benzonic acid titration was higher ($[OH^-]$ was lower) than those of the phenol titration, less amount of CO_2 was supposed to be absorbed in the sample. From the result of this phenol titration, it is expected that the phenol group capacities of humic substances might be overestimated about 2% by the non-aqueous titration due to CO_2 effect even when CO_2 gas is eliminated from the titration vessel as possible by N_2 gas flowing. By the analysis of the titration curves shown in Fig. 2, the $pOH_{1/2}$ values of benzonic acid and

phenol in this non-aqueous medium were determined as

$$pOH_{1/2}(\text{benzonic acid}) = 12.77 \pm 0.01 \qquad (8)$$

$$pOH_{1/2}(\text{phenol}) = 6.78 \pm 0.02 \qquad (9)$$

where the $pOH_{1/2}$ was the pOH value at α (the degree of dissociation) = 0.5.

3.3. Humic substance titration

The five humic substances, ALHA, SHA, SFA, PHA and PFA, in the mixed solvent medium were titrated by the above mentioned titrant solution containing KOH. The obtained titration curves are respectively shown in Fig. 3(a) ALHA, (b) SHA, (c) SFA, (d) PHA and (e) PFA. The vertical axes in Fig. 3 are the amount of the dissociated functional group equivalent, (R^-) (mequiv./g), that is derived from the charge balance equation.

$$[H^+] + [K^+] = [OH^-] + [Cl^-] + [R^-] \qquad (10)$$

where $[R^-]$ is the concentration of the dissociated functional group in mol/dm^3. Under the employed titration condition, $[H^+]$ is negligible due to $[H^+] \ll [OH^-]$. Thus, Eq. (10) can be described by

$$V_T[R^-] = (R^-)w_g \times 10^{-3} = -V_T 10^{-pOH} + C_{KOH}V_{titrant} \qquad (11)$$

where V_T, w_g, C_{KOH} and $V_{titrant}$ are the total volume of the solution in the titration vessel (dm^3), the weight of humic substance (g), the KOH concentration in the titrant (mol/dm^3) and the added titrant volume (dm^3), respectively. (R^-) can be calculated by Eq. (11). In our previous study [27], we have proposed a simple and approximate expression to describe the interaction of a humic substance with cations,

$$\log K_{app} = \log K + a \log \alpha - b \log[\text{Na}^+] - m \log[\text{M}] \qquad (12)$$

$$K_{app} = \frac{[\text{ML}]}{[\text{M}][R^-]} \qquad (13)$$

where $[\text{ML}]$ and $[\text{M}]$ are the concentrations of bound and free cation, $[\text{Na}^+]$ is the bulk sodium ion concentration in the background electrolyte solution, α is the degree of dissociation and $\log K$, a, b, m are constant parameters depending on the cation and HS. In the aqueous titration system, this equation was successfully applied to the protonation of the each functional group [28] in the form of

$$\log K_{i,app} = \log K_i + m_i pcH - b \log[\text{Na}^+], \qquad (14)$$

$$K_{i,app} = \frac{[\text{HR}]}{[\text{H}][R^-]}, \qquad (15)$$

where two groups of apparent protonation constants, $K_{1,app}$ and $K_{2,app}$, were employed for the protonation of carboxylic and phenolic groups which were considered to be contained in HS. From Eqs. (14) and (15), the degree of dissociation of each functional group is expressed by the following equation as a function of pH and [Na] with three parameters, $\log K_i$, m_i and b,

$$\alpha_i = \frac{1}{1 + [\text{H}]K_{i,app}} = \frac{1}{10^{\log K_i + (m_i-1)pH - b\log[\text{Na}^+]} + 1} \qquad (16)$$

The parameter b is taken as common to two acidic groups since this parameter is related to the charge and charge density of the macromolecule and not dependent on the kind of functional groups. Therefore, the sum of the dissociated functional groups (R^-), expressed in mmol per 1 g of humic substance, is given by

$$(R^-) = C_{R,1}^W \alpha_1 + C_{R,2}^W \alpha_2 = \frac{C_{R,1}^W}{10^{\log K_1 + (m_1-1)pH - b\log[\text{Na}^+]} + 1}$$

$$+ \frac{C_{R,2}^W}{10^{\log K_2 + (m_2-1)pH - b\log[\text{Na}^+]} + 1} \qquad (17)$$

where the first and second terms, represented by subscripts $i = 1$ and 2, describe the contribution from the carboxylic and the phenolic groups, respectively, and $C_{R,1}^W$ and $C_{R,2}^W$ mean the total carboxylic- and phenolic-group concentrations in mequiv./g. In the non-aqueous titration system adopted in this study, the measurable parameter is pOH instead of pH and the bulk cation concentration is constant. Thus, the apparent protonation constant is expressed in the form of

$$\log K_{i,app} = \log K_i' - m_i pOH \qquad (18)$$

Eq. (16) can be transformed to the following equation using Eq. (5) and (18),

$$\alpha_i = \frac{1}{1 + (K_{SH}/[OH])K_{i,app}} = \frac{1}{10^{\log K_{SH} + pOH + \log K_i' - m_i pOH} + 1}$$

$$= \frac{1}{10^{\log K_i'' + (1-m_i)pOH} + 1} \qquad (19)$$

where

$$\log K_i'' = \log K_i' + \log K_{SH} \qquad (20)$$

Consequently, Eq. (17) is transformed to describe (R^-) in the non-aqueous titration system as

$$(R^-) = C_{R,1}^W \alpha_1 + C_{R,2}^W \alpha_2 = \frac{C_{R,1}^W}{10^{\log K_i'' + (1-m_1)pOH} + 1}$$

$$+ \frac{C_{R,2}^W}{10^{\log K_i'' + (1-m_2)pOH} + 1} \qquad (21)$$

The titration curves in Fig. 3 were organized to give the relation of (R^-) versus pOH by Eq. (11) and were fitted to Eq. (21) by non-linear least-squares fittings. In Fig. 3, the red dot curve and blue dot curve are $C_{R,1}^W/(10^{\log K_1'' + (1-m_1)pOH} + 1)$ and $C_{R,2}^W/(10^{\log K_2'' + (1-m_2)pOH} + 1)$, respectively obtained by this fitting, expressing the dissociation of carboxyl group and phenol group in HS, while the black solid line is the summation of the dissociated carboxyl and phenol groups. The best set of the fitting parameters, $\log K_1''/(m_1 - 1)$, $\log K_2''/(m_2 - 1)$, m_1, m_2, $C_{R,1}^W$ and $C_{R,2}^W$ for each humic substance thus obtained are listed in Table 1. Here, it is noted that the values of $\log K_1''/(m_1 - 1)$ and $\log K_2''/(m_2 - 1)$ mean the pOH values at $\alpha_i = 0.5$ for the carboxylic and the phenolic groups, respectively, because of Eq. (19) and the following relation:

$$\alpha_i = \frac{1}{10^{\log K_i'' + (1-m_i)pOH} + 1} = \frac{1}{2}, \quad pOH = \frac{\log K_i''}{m_i - 1} \qquad (22)$$

As given in Table 1, the carboxylic-group and phenolic-group capacities of the humic substances were successfully determined with relatively small deviations. The phenolic-group capacity is always less than that of carboxylic-group for all the humic substances regardless of the kind of humic or fulvic acids. An interesting tendency is found in the comparison of $\log K_i''/(m_i - 1)$ values that correspond to the mean protonation constant of the functional group in the humic substance. The $\log K_2''/(m_2 - 1)$ values for the phenolic-group agree well for nearly all humic substances except SHA, and are close to the $pOH_{1/2}$ of phenol given in Eq. (9). This fact indicates that each phenolic-group in the humic substances is rather isolated and is not electronically affected by other affecting groups in the non-aqueous medium, so that its protonation behavior is similar to that of simple phenol molecule. The reason for the deviation of SHA from the other humic substances is not clear at present. The larger deviations in the estimated values in Table 1 and a slight difference in the shape of the curve for phenol groups in Fig. 3(b) may suggest some unknown experimental defect in the titration procedure. Since the mean protonation constant strongly depends on the nature of solvent medium, the determined
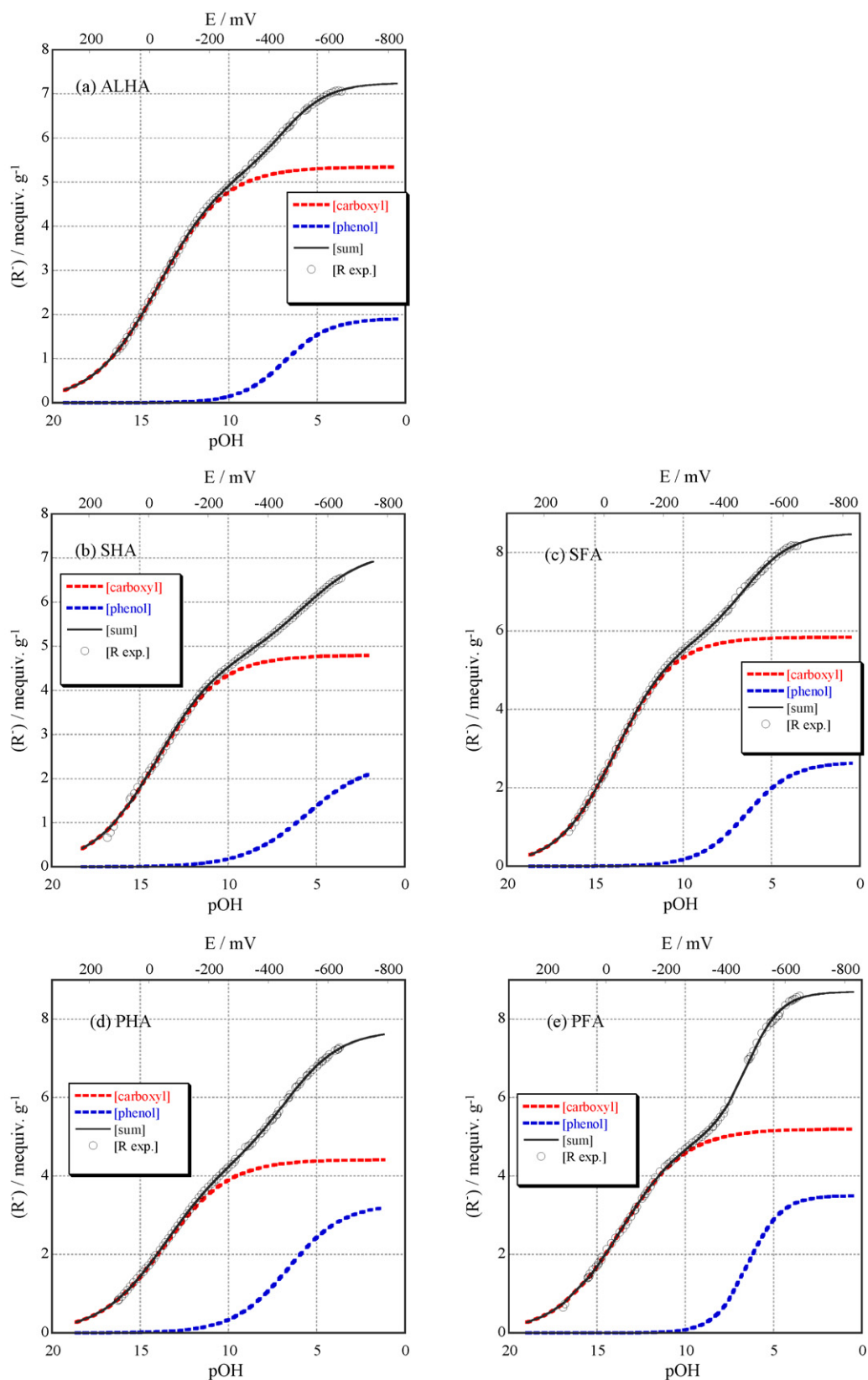
Fig. 3. Non-aqueous titration curves of the humic substances. (a) Aldrich humic acid, (b) soil humic acid, (c) soil fulvic acid, (d) peat humic acid and (e) peat fulvic acid. The red and blue dotted lines are fitting curves for the carboxylic and phenolic groups, respectively. The solid line is the summation of the both functional groups. (For interpretation of the references to color in this figure legend, the reader is referred to the web version of the article.)

Table 1
The obtained parameters for the protonation of humic substances from the non-aqueous titration.

	$C_{R,1}^{W}$ /mequiv. g^{-1}	$\frac{\log K_1''}{m_1-1}$	m_1	$C_{R,2}^{W}$ /mequiv. g^{-1}	$\frac{\log K_2''}{m_2-1}$	m_2
ALHA	5.34(4)	13.97(3)	0.77(1)	1.91(6)	6.81(4)	0.66(1)
SHA	4.80(12)	14.06(8)	0.76(1)	2.39(30)	5.55(22)	0.76(3)
PHA	4.42(7)	13.66(5)	0.76(1)	3.29(11)	6.62(4)	0.72(1)
SFA	5.84(5)	13.84(3)	0.74(1)	2.66(9)	6.45(4)	0.68(1)
PFA	5.20(6)	13.68(5)	0.76(1)	3.50(8)	6.46(4)	0.54(2)

The digits in the parentheses following numerical values represent the estimated standard deviations (σ) of those values in terms of the final listed digits.

Table 2
The obtained parameters for the protonation of humic substances from the aqueous titration.

	$C_{R,1}^{W}$ /mequiv. g^{-1}	$\frac{\log K_1}{1-m_1}$	m_1	b	$C_{R,2}^{W}$ /mequiv. g^{-1}	$\frac{\log K_2}{1-m_2}$	m_2
ALHA	4.93(15)	3.46(6)	0.65(2)	0.28(2)	1.86(29)	9.13(54)	0.64(4)
SHA	4.41(4)	3.57(3)	0.64(1)	0.28(1)	0.91(7)	8.77(8)	0.15(8)
PHA	4.46(16)	3.07(9)	0.65(3)	0.33(3)	2.19(42)	9.02(61)	0.63(5)
SFA	5.40(14)	3.06(6)	0.57(3)	0.20(1)	2.31(53)	9.49(99)	0.77(3)
PFA	5.20(4)	3.01(5)	0.66(2)	0.28(1)	1.69(25)	9.16(26)	0.48(6)

The digits in the parentheses following numerical values represent the estimated standard deviations (σ) of those values in terms of the final listed digits.

$\log K_2''/(m_2 - 1)$ values for the non-aqueous medium is not directly applicable for the protonation of the phenolic-group in aqueous media. Nevertheless, our result from the titrations of five humic substances reveals important information, that is, the mean protonation constant of the phenolic-group of humic substances can be approximated to that of simple phenol molecule in the non-aqueous medium. On the contrary, the $\log K_1''/(m_1 - 1)$ values of all the humic substances are much larger than the $pOH_{1/2}$ of benzonic acid given in Eq. (8), meaning that the carboxylic groups in the humic substance are electronically affected each other, so that their proton dissociation are rather promoted than that of simple benzonic acid in the same medium.

3.4. Comparison of non-aqueous and aqueous titration systems

To compare the capacities of the functional groups in the humic substances determined by the non-aqueous titration with those determined by the aqueous titration, the same humic substances were titrated in an aqueous titration system by using the same titration instrument, where NaCl and NaOH were used as the background electrolyte and the titrant, respectively. The obtained titration curves were organized to give the relation of (R$^-$) versus

pH by Eq. (10) and were fitted to Eq. (17). The obtained parameters were summarized in Table 2 where the values of $\log K_1/(1 - m_1)$ and $\log K_2/(1 - m_2)$ mean the pH values at $\alpha_i = 0.5$ for the carboxylic and the phenolic groups, respectively. In contrast to the parameters listed in Table 1, $\log K_2/(1 - m_2)$, m_2, and $C_{R,2}^{W}$ in Table 2 for the phenolic groups contain large uncertainties. When the titration curves of ALHA in the non-aqueous and the aqueous systems are compared as in Fig. 4, the reason of the large uncertainties for those obtained in the aqueous titration can be easily understood. In Fig. 4(b), from the comparison of (R$^-$) values at the end point of the titration (=5.54 mequiv./g) and calculated carboxylic and phenolic-group dissociation curves, it was regarded that almost 100% of carboxylic group ($\cong$4.93 mequiv./g) and less than 33% of phenolic-group (<0.61 mequiv./g) had been dissociated at the end point of aqueous titration, which was insufficient for the quantitative determination of the phenolic-group capacity. Contrary to this, it was regarded from Fig. 4(a) that more than 97% of phenolic-group had been dissociated at the end point of non-aqueous titration. As a result, the curve-fitting gave the phenolic-group capacity with relatively small uncertainties. It is commonly understood that the functional group capacity of polymer acid can be regarded as an independent quantity of the types of solvent media, therefore, the
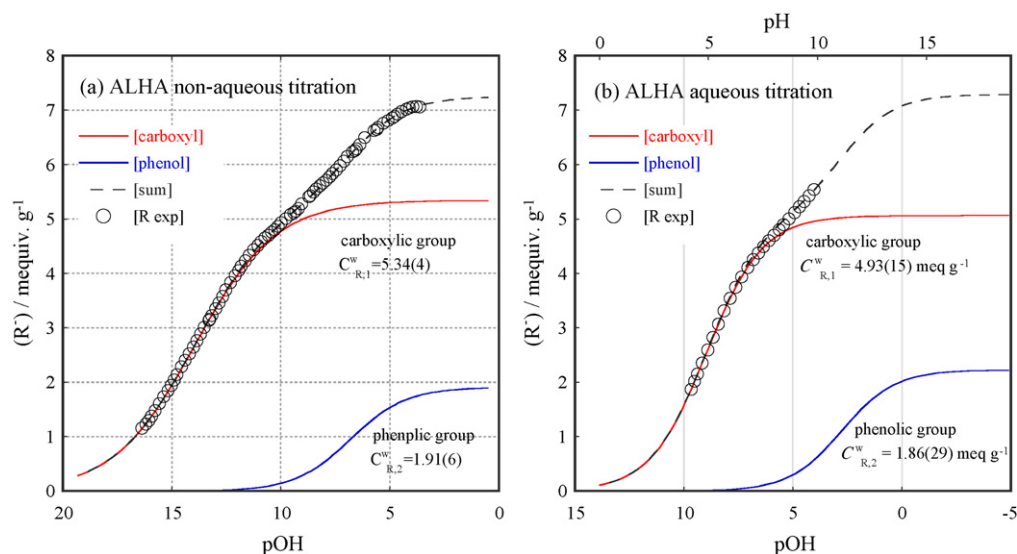
Fig. 4. The comparison of the titration curves for Aldrich humic acid between (a) non-aqueous titration, and (b) aqueous titration.
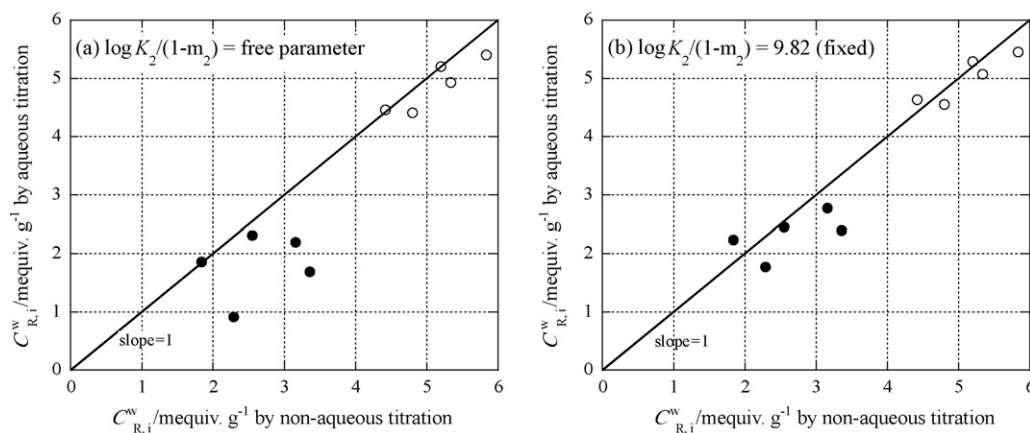
Fig. 5. The comparison of the functional group capacities for the five humic substances. (a) The aqueous titration curves were fitted without any fixed parameter, (b) the aqueous titration curves were fitted with a fixed parameter $\log K_2/(1 - m_2) = 9.82$. (○) The carboxylic group capacity, (●) the phenolic-group capacity.

phenolic-group capacities of the five kinds of humic substances obtained in this study are considered to be applicable to the study on the humic substance chemistry in aqueous solution system. Furthermore, the non-aqueous titration technique employed in this study coupled with the analysis by using the cation–humic interaction model equation proposed by the authors [27,28] is considered as an effective technique for the determination of the phenolic-group capacity of a variety of humic substances.

Based on the above mentioned hypothesis concerning the mean protonation constant of the phenolic-group in the humic substance, an approximate estimation method of the phenolic-group capacity from simple aqueous titration data is proposed here, that is, employing the protonation constant of phenol molecule in the aqueous media as the fixed parameter of $\log K_2/(1 - m_2)$ in Eq. (17), and then conducting the fitting of the aqueous titration curve of the humic substance in the same way. This simple approximation method works effectively as shown in Fig. 5. Fig. 5(a) is a simple comparison of functional groups capacities of the five humic substances between the non-aqueous titration result and the aqueous titration result shown in Tables 1 and 2, respectively, indicating that the phenolic-group capacities tend to be estimated to be lower by the aqueous titration than those by the non-aqueous titration, while no systematic difference is found in the carboxylic group capacities. Contrary to this, as shown in Fig. 5(b), when the protonation constant of phenol, i.e., $\log K = 9.82$ for $I = 1.0$ [21] is given to the Eq. (17) as the fixed parameter of the mean protonation constant of the phenolic-group ($= \log K_2/(1 - m_2)$), the calculated phenolic-group capacities by the fitting of the aqueous titration data get close to those calculated from the non-aqueous titration data. This simple approximation method is considered useful for the re-estimation of published titration data of humic substance, or for the rough estimation of the phenolic-group capacity only from the aqueous titration data. Generally, the functional group capacity is needed for the study on the complexation of humic substance with metal cations. If those reactions occur at pH < 5, the contribution of phenolic-group is regarded as meager comparing with that from the carboxylic group. Therefore, in such a case, the approximated phenolic-group capacity obtained by the above mentioned procedure seems to be enough for the study of complexation reaction between humic substance and cation.

4. Conclusion

The phenolic-group capacities of the five kinds of humic substances were successfully determined with small uncertainties by the non-aqueous potentiometric titration using a mixed solvent of DMSO:2-propanol:H_2O = 80:19.3:0.7 with KOH titrant solution. From the analysis of the titration curves, it was found that the mean protonation constants of the phenolic-group were close for nearly all humic substances, indicating that the each phenolic-group tends to be isolated and is not electronically affected by other affecting groups, so that its protonation behavior can be approximated to that of simple phenol molecule.

References

[1] F.J. Stevenson, Humus Chemistry—Genesis, Composition, Reactions, 2nd ed., John Wiley, Inc., New York, 1994.
[2] E. Tipping, Cation Binding by Humic Substances, Cambridge University Press, Cambridge, 2002.
[3] J. Buffle, Complexation Reactions in Aquatic Systems: An Analytical Approach, Ellis Harwood, New York, 1990.
[4] G.R. Choppin, Radiochim. Acta 44/45 (1988) 23.
[5] G.R. Choppin, Radiochim. Acta 58/59 (1992) 113.
[6] E. Tipping, Aquat. Geochem. 4 (1998) 3.
[7] D.G. Kinniburgh, W.H. van Riemsdijk, L.K. Koopal, M. Borkovec, M.F. Benedetti, M.J. Avena, Colloids Surf. A 151 (1999) 147.
[8] L.K. Koopal, T. Saito, J.P. Pinheiro, W.H. van Riemsdijk, Colloids Surf. A 265 (2005) 40.
[9] E. Compnays, J.L. Graces, J. Salvador, J. Galceran, J. Puy, F. Mas, Colloids Surf. A 306 (2007) 2.
[10] J.M. Garcia-Mina, J. Phys. Chem. B 111 (2007) 4488.
[11] J.I. Kim, K.R. Czerwinski, Radiochim. Acta 73 (1996) 5.
[12] C.J. Milne, D.G. Kinniburgh, J.C.M. de Wit, W.H. van Riemsdijk, L.K. Koopal, Geochim. Coschim. Acta 59 (1995) 1101.
[13] M.M. Nederlof, J.C.M. de Wit, W.H. van Riemsdijk, L.K. Koopal, Environ. Sci. Technol. 27 (1993) 846.
[14] J.C.M. de Wit, W.H. van Riemsdijk, L.K. Koopal, Environ. Sci. Technol. 27 (1993) 2015.
[15] J.C.M. de Wit, W.H. van Riemsdijk, L.K. Koopal, Environ. Sci. Technol. 27 (1993) 2005.
[16] J.D. Ritchie, E.M. Perdue, Geochim. Cosmochim. Acta 67 (2003) 85.
[17] E.M. Perdue, J.H. Reuter, R.S. Parrish, Geochim. Cosmochim. Acta 48 (1984) 1257.
[18] J.P. Gustafsson, J. Colloid Interface Sci. 224 (2001) 102.
[19] J.A. Marinsky, J.H. Ephraim, Environ. Sci. Technol. 20 (1986) 349.
[20] J.A. Marinsky, in: W. Stumm (Ed.), Aquatic Surface Chemistry: Chemical Processes at the Particle–Water Interface, John Wiley Inc., New York, 1987, p. 49.
[21] A.E. Martell, R.M. Smith, R.J. Motekaitis, NIST Critically Selected Stability Constants of Metal Complexes, version 7, Texas A&M University, Texas, 2003.
[22] J.M. Andres, C. Romero, J.M. Gavilan, Talanta 34 (1987) 583.
[23] J.H. Ephraim, Talanta 36 (1989) 379.
[24] J.C.G. Esteves da Silva, A.A.S.C. Machado, Talanta 41 (1994) 2095.
[25] J.H. Ephraim, H. Boren, C. Pettersson, I. Arsenie, B. Allard, Environ. Sci. Technol. 23 (1989) 356.
[26] J.M. Andres, C. Romero, Fuel 67 (1988) 1305.

[27] O. Tochiyama, Y. Nibbori, K. Tanaka, H. Yoshino, T. Kubota, A. Kirishima, B. Seti-awan, Radiochim. Acta 92 (2004) 559.
[28] J. Du, N. Sato, O. Tochiyama, J. Nucl. Radiochem. Sci. 6 (2005) 25.
[29] E.L. Bertha, G.R. Choppin, J. Inorg. Nucl. Chem. 40 (1978) 655.
[30] J.I. Kim, Radiochim. Acta 52/53 (1991) 71.
[31] J.I. Kim, G. Buckau, W. Zhuang, Mater. Res. Symp. Proc. 84 (1987) 747.
[32] D.G. Kinniburgh, C.J. Milne, P. Venema, Soil Sci. Soc. Am. J. 59 (1995) 417.
[33] D.R. Lide (Ed.), CRC Handbook of Chemistry and Physics, 73rd ed., CRC Press Inc., Boca Raton, 1992, section 8.
[34] C. Reichardt, Solvents and Solvent Effects in Organic Chemistry, John Wiley & Sons Ltd., Hoboken, 1988.
[35] K. Izutsu, Acid–base dissociation constants in dipolar aprotic solvents (IUPAC Chemical Data Series No. 35), Blackwell Scientific Publications, Oxford, 1990.

Analysis of aqueous pyrethroid residuals by one-step microwave-assisted headspace solid-phase microextraction and gas chromatography with electron capture detection

Hong-Ping Li [a,1], Chiu-Hua Lin [a,1], Jen-Fon Jen [b,*]

[a] *Residue Control Division, Taiwan Agricultural Chemicals and Toxic Substances Research Institute,*
Council of Agriculture (TACTRI/COA), Wu-Fong, Taichung County 413, Taiwan
[b] *Department of Chemistry, National Chung-Hsing University, Taichung 402, Taiwan*

ABSTRACT

A one-step microwave-assisted headspace solid-phase microextraction (MA-HS-SPME) has been applied to be a pretreatment step in the analysis of aqueous pyrethroid residuals by gas chromatography (GC) with electron capture detection (ECD). Microwave heating was applied to accelerate the vaporization of pyrethroids (bioallenthrin, bifenthrin, fenpropathrin, cyhalothrin, permethrin, cyfluthrin, cypermethrin, fluvalinate, fenvalerate and deltamethrin) into the headspace, and then being absorbed directly on a SPME fiber under the controlled conditions. Optimal conditions for the SPME sampling, such as the selection of sampling fiber, sample pH, sampling temperature and time, microwave irradiation power, desorption temperature and time were investigated and then applied to real sample analysis. Experimental results indicated that the extraction of pyrethroids from a 20-mL aquatic sample (pH 4.0) was achieved with the best efficiency through the use of a 100-μm PDMS fiber, microwave irradiation of 157 W and sampling at 30 °C for 10 min. Under optimum conditions, the detections were linear in the range of 0.05–0.5 μg/L with the square of correlation coefficients (R^2) of >0.9913 for pyrethroids except bifenthrin being 0.9812. Method detection limits (MDL) were found to be varied from 0.2 to 2.6 ng/L for different pyrethroids based on S/N (signal to noise) = 3. The coefficients of variation (CVs) for repeatability were 7–21%. A field underground water sample was analyzed with recovery between 88.5% to 115.5%. This method was proven to be a very simple, rapid, and solvent-free process to achieve the sample pretreatment before the analysis of trace pyrethroids in aqueous samples by gas chromatography.

© 2009 Elsevier B.V. All rights reserved.

1. Introduction

Synthetic pyrethroids are widely used as pest control agents in agricultural production and hygienic treatments in houses due to their advantage of low hazard to users and rather low environmental impact [1]. Chronologically, they were the fourth major group of insecticides developed (after organochlorines, organophosphates and carbamates) [2]. As a major group of insecticide widely used in the world, the residue analysis of pyrethroids in crops, foods and environmental matrices is of importance in agricultural and environmental sciences. Therefore, a rapid, convenient, accurate and sensitive method is required to monitor their concentrations in water samples.

Chromatographic techniques have been considered as the best methods to determine pyrethroids in different sample matrix [2–8]. Before carrying out the chromatographic analysis of samples, pretreatment and preconcentration are important steps for ultratrace analysis. Previous studies have set forth various extraction techniques for pyrethroids in samples, including the liquid–liquid extraction (LLE) [2,5,6,9], solid-phase extraction (SPE) [8,10], or matrix solid-phase dispersion [4,7,11]. Although such pretreatments efficiently yield precise results, they are tedious, time-consuming, hazardous to health due to the usage of organic solvents, and highly expensive with respect to the disposal of solvents.

In the past decades, the solid-phase microextraction (SPME) technique has been developed as a simple, rapid and less solvent consumption process [12] typically applied to pyrethroids sampling [13–17]. The headspace (HS) SPME sampling method has been applied to eliminate interference and aging problems of the fiber from complicate matrices [18–19] commonly found in the direct immersion (DI) approach. Sample heating has also been introduced in HS-SPME to accelerate the evaporation of analytes into

* Corresponding author. Tel.: +886 4 22853148; fax: +886 4 22862547.
  E-mail addresses: hplee@tactri.gov.tw (H.-P. Li), jfjen@dragon.nchu.edu.tw
(J.-F. Jen).
  [1] Tel.: +886 4 23302101x401; fax: +886 4 23324738.

headspace for sampling [19–21]. However, it was still unfavor to SPME sampling due to adsorption/absorption is an exothermic process [22–23]. Zhang and Pawliszyn [23] thus developed an interlay cooled solid-phase microextraction device to improve the HS-SPME efficiency. Ghiasvand et al. [24] also applied a cold-fiber HS-SPME device to decrease fiber temperature and increase extraction quantity of PAHs from sediment. Both offered efficient and precise results. However, the direct internal cooling at extremely low temperature with liquid CO_2 was suspected to affect the SPME fiber's physical properties and may lead to irreversibly damage to the SPME surface.

In this decade, microwave energy was investigated and widely applied in accelerating sample digestion, extraction and chemical reactions [25–26]. We have recently investigated use of microwave heating to enhance the vaporization of semi-volatile analytes (e.g. chlorophenols and organochlorine pesticides) for one-step HS-SPME sampling before GC analysis [27–29]. Huang et al. [30] also applied successfully the same technique to analyse semi-volatile organic compounds in aqueous samples. Therefore, MA-HS-SPME has the potential to become an alternative pretreatment method for collection of pyrethroids from aqueous sample before GC-ECD analysis.

Our primary aim in this study is to demonstrate the applicability of the one-step MA-HS-SPME coupled to GC-ECD, which combines the fast microwave heating and control of sampling temperature for HS-SPME sampling of pyrethroids in aqueous samples toward effective GC determination. Our results showed that this analytical procedure is a rapid, convenient, sensitive and eco-friendly way to analyze pyrethroids in aqueous samples.

2. Materials and methods

2.1. Reagents and solutions

A Millipore Milli-Q water purification system (Bedford, MA, USA) was used to produce deionized water for all aqueous solutions. All chemicals and solvents used were of ACS reagent grade. Pesticides (analytical-standards grade) including bioallenthrin, bifenthrin, fenpropathrin, cyhalothrin, permethrin, cyfluthrin, cypermethrin, fluvalinate, fenvalerate and deltamethrin purchased from Dr Ehrenstorfer (Augsburg, Germany) and Riedel-deHäen (Hannover, Germany), were used for preparing standard stock solutions without further purification (purity was >95% for all pesticides). Standard stock solutions of 1000 mg/L pesticides were prepared individually in n-hexane (Merck, Darmstadt, Germany), then diluted to 0.01 mg/L as working solution by adding n-hexane. All standards and working solutions were stored at 4 °C in silanized brown glass bottles with Teflon-lined caps. Disodium hydrogen phosphate (Na_2HPO_4) and citric acid monohydrate ($C_6H_8O_7 \cdot H_2O$) obtained from Merck (Darmstadt, Germany) were used to prepare various pH buffer solutions. Sodium chloride and sodium hydroxide were obtained from Riedel-dehäen. Hydrochloric acid (36.4%) was from J.T. Baker (Phillipsburg, USA). The high purity nitrogen gas (99.999%) as carrier gas was obtained from local supplier (Lien-Hwa, Taichung).

2.2. Apparatus

The GC used in this work was a Hewlett-Packard 6890 (Agilent Technologies, Palo Alto, CA, USA) equipped with a split/splitless injector and an electron capture detector (ECD, ^{63}Ni). The microwave oven used in this work was a modified version of the domestic NN-L520 inverter system (2450 MHz, Panasonic Canada Inc., Mississauga, ON, Canada) with a maximum power of 1100 W. It was equipped with a cooling system connected to

a water circulating machine (YIH DER BL-720, Taipei, Taiwan) to reduce the effective power of microwave irradiation. A headspace temperature-controlled sampling chamber located in a cooling water jacket was externally connected to a water circulating machine (temperature-control cooler) for temperature control. A microwave stirrer (Scienceware, Garner, NC, USA) was used for stirring the sample solution at 300 rpm during extraction. After modification, the effective powers of microwave irradiation of 67, 124, and 157 W for P2, P3, and P4, respectively, were used in this study. The assembly of MA-HS-SPME sampling system was similar to our previous study [29]. Aluminum foils were attached to the inner- and outer-walls of the microwave oven between the microwave body and the headspace sampling apparatus in order to prevent irradiation leakage. A MD-2000 microwave leak detector (Less EMF, Albany, NY, USA) was used to check the safety aspects of the equipment during the experiments.

The SPME device consisting of a holder (SUPELCO 57331) and fiber assembly for manual sampling was obtained from Supelco (Bellefonte, PA, USA) and was used without modification. Seven types of fibers with 1 cm in length were examined in this study including coatings of PDMS (100 and 30 μm), CW-DVB (65 μm), PDMS-DVB (65 μm), DVB-CAR-PDMS (50/30 μm), CAR-PDMS (75 μm) and PA (85 μm) (Supelco). Before use the fibers were conditioned under nitrogen in the hot injection port, according to the manufacturer's instructions. The needle on the SPME manual holder was set at its maximum length of 4 cm in the GC injection port. A desorption temperature of 290 °C held for 3 min was used to produce the highest sensitivity for pyrethroids. All analyses were performed with a 50-mL flask with ground-glass joints containing 20 mL aqueous sample with 2 mL buffer solution (pH 4.0). The flask was connected to water condenser through a 5-mL hollow glass tube (5 mm i.d.) having been silanized. Prior to the experiment, all the glassware were thoroughly cleaned in the order of soap solution, deionized water, acetone, and again in deionized water, before being dried continuously in the oven at 80 °C for about 4 h. Two sets of flasks and condensers were used alternately, because the inner surfaces of flasks and condensers should be thoroughly cleansed by acetone and deionized water between runs to prevent the carryover problem from the glassware setup.

2.3. Procedures

2.3.1. One-step MA-HS-SPME

20 mL aqueous sample containing pyrethroids was mixed with 2 mL buffer solution (pH 4.0) in a 50-mL flask with ground-glass joints. After swirling, the flask was placed in the microwave oven and connected to the HS-SPME system. A SPME device with a fiber was inserted into the hollow part of the condenser which was connected to a cooling system. The pyrethroids in sample solution, with stirring at 300 rpm, were vaporized with water into headspace and absorbed in-situ on the SPME fiber in the headspace by microwave irradiation at 157 W for 10 min. After collection of the pyrethroids, the SPME fiber was withdrawn from headspace and desorbed immediately in the GC injector for GC-ECD analysis.

2.3.2. GC-ECD analysis

After desorption from the SPME fiber in the hot GC injector (290 °C held for 3 min), pyrethroids were separated on a fused silica DB-608 capillary column (30 m × 0.25 mm i.d., 0.25 μm film thickness) (J&W Scientific, Folsom, CA, USA). Nitrogen was used as carrier gas and makeup gas at flow rates of 2.5 and 30 mL/min, respectively. The oven temperature was maintained at 190 °C for 1.0 min then programmed at 40 °C/min to 230 °C held for 3.0 min, and then at 20 °C/min to 270 °C which was held for 13 min. The separated species were measured by electron capture detector held at 300 °C.

3. Results and discussion

To attain the optimum extraction efficiency of the one-step MA-HS-LPME method for pyrethroids analysis by GC-ECD, the following parameters were investigated systematically. These parameters include selection of fiber coating, microwave irradiation power and irradiation time, pH of the sample solution, sampling temperature and the desorption condition.

3.1. Selection of SPME fiber coating

The extraction efficiency of a SPME method greatly depends on the polarity of fiber coating and the physiochemical properties of target analytes as well as the sample matrix. Although PDMS (100 μm) was recommended as the most appropriate fiber coating for the study of pyrethroids in water matrix [14,31], however, some new complex-polymer SPME fibers have been developed and commercial available. Therefore, seven commercial SPME fiber-coatings as described in the section of apparatus were evaluated. A fortified aqueous sample (20 mL water containing 0.5 μg/L of each pyrethroid) was analyzed triplicate by use of each fiber to sampling. After the MA-HS-SPME sampling at the power irradiation of 157 W for 10 min and GC-ECD determination, the results by use of different fibers are illustrated in Fig. 1(a). It can be seen that the PDMS fiber owns the highest extraction efficiency for bioallenthrin, cyhalothrin, cyfluthrin, cypermethrin and fenvalerate. The fiber coated with mixed PDMS/DVB polymer is also suitable for collecting bifenthrin, fenpropathrin, permethrin, fluvalinate and deltamethrin. Because the fiber coatings are examined to their relative absorption ability for all pyrethroids, the summation of normalized quantities of pyrethroids absorbed on the tested fiber

Fig. 2. Extraction efficiency of pyrethroid pesticides under different microwave powers MA-HS-SPME conditions: 20-mL sample containing 0.5 μg/L each pyrethroid pesticide, 10 min extraction at different microwave irradiation power with agitation.

by considering the highest peak area obtained to be 1 was evaluated [3], as demonstrated in Fig. 1(b). It can be seen, the PDMS (100 μm) is with the highest absorption quantity, and PDMS/DVB (65 μm) is next. Therefore, the PDMS (100 μm) fiber was recommended to headspace sampling of pyrethroids for compromising the extraction efficiency of all 10 pyrethroids.

3.2. Optimization of microwave irradiation conditions

In this study, microwave irradiation was applied to accelerate the vaporization of the pyrethroids from water sample into headspace for one-step MA-HS-SPME sampling. Microwave irradiation was optimized at effective powers of 67, 124 and 157 W for 6–12 min for sampling. Experimental results indicate that the effective irradiation power of 157 W resulted in better extraction efficiency than the others for all interested pyrethroids as demonstrated in Fig. 2. During the extraction, the relative extraction quantity of whole pyrethroids increased significantly at the beginning, reached maximum levels at 10 min, and leveled to constant after that. Therefore, microwave irradiation with effective irradiation power of 157 W for 10 min is recommended to the MA-HS-SPME sampling for pyrethroids in this study.

3.3. Selection of sampling temperature

In the present study, the microwave-assisted heating technique improves the release of analyte from the sample matrix into the headspace. A circulation cooling water system was designed to control the temperature of the sampling area to increase the partition coefficient of the analyte between the SPME fiber and headspace. The temperature in the sampling area was optimized from 10 to 50 °C for MA-HS-SPME sampling. Experimental results indicate that the temperature at 30 °C in the sampling area resulted in better extraction efficiency than the others for all interested pyrethroids, and was thus used in the MA-HS-SPME sampling for pyrethroids.

3.4. Influence of sample pH

Proper adjustment of sample pH is often applied to enhance the extraction efficiency in conventional LLE, SPE and immerse SPME due to the partition of analytes in their neutral (molecular) forms, which were considered favorable to the hydrophobic phase. In headspace sampling, the extraction efficiency can be enhanced also by keeping the target molecules in their non-ionized forms through the pH adjustment. The pH in the sample solution was optimized from 2.0 to 13.0 for MA-HS-SPME sampling. Experimental results indicate that the relative extraction quantity of all 10 pyrethroids increased significantly at the beginning with pH, reached max-

Fig. 1. (a) Extraction efficiency of pyrethroid pesticides with different SPME fibers. (b) Relative absorption quantity of individual fiber coating to the whole interested pyrethroids MA-HS-SPME conditions: 20-mL sample containing 0.5 μg/L of each pyrethroid pesticide, 10 min extraction at the power irradiation of 157 W with agitation. Pesticides: 1. bioallenthrin; 2. bifenthrin; 3. fenpropathrin; 4. cyhalothrin; 5. permethrin; 6. cyfluthrin; 7. cypermethrin; 8. fluvalinate; 9. fenvalerate; 10. deltamethrin.

Fig. 3. Influence of pH in sample matrix on the extraction efficiency.

imum levels at pH 4.0, and declined after that as illustrated in Fig. 3. Therefore, the pH of sample solution was adjusted to 4.0 before MA-HS-SPME to obtain the optimum extraction efficiency of pyrethroids.

3.5. Thermal desorption conditions in GC injection port

In general, desorption of analytes from the SPME fiber in the hot GC injector at a higher-temperature or a long-time is required to ensure all the analytes being completely desorbed and then injected into the separation column. However, thermal desorption of analytes at low temperature should extend desorption period which might decrease separation efficiency and worsen the resolution of vicinal peaks. Because the vapor pressures of pyrethroids are low relatively and they are unstable at high temperature, the thermal desorption temperature and time in the hot GC injection port were optimized to achieve sensitive quantification and prevent memory effects. After a series of tests, desorption of pyrethroids was optimum at 290 °C for 3 min. After desorption at this condition, no significant signals of pyrethroids appeared in the chromatogram after re-injection. Thus, no further regeneration of the fiber was required between runs.

3.6. Features of the proposed method

The applicability of the proposed method for quantitative determination of pyrethroids was examined by adding different concentrations of standard pyrethroids spiked in reagent water and subjecting them to the complete treatment process (i.e., MA-HS-SPME and GC-ECD analysis). A chromatogram obtained, under the conditions described in the section "GC-ECD analysis" from spiked aqueous samples (as 0.5 μg/L each) is presented in Fig. 4(a). Calibration plots for quantities of pyrethroids in the ranges listed in Table 1 were found to have good linearity with the square of correlation coefficients (R^2) being better than 0.9913 except bifenthrin being 0.9812. Calibration plot data are listed in Table 1. Method detection limits (MDLs) were calculated on the basis of three times the standard deviation of the detection signal for the lowest concentration ($n = 7$) in the calibration plot, divided by the detection sensitivity (slope of calibration plot) and then varied from 0.02 to 2.6 ng/L for interested pyrethroids. Precision was estimated by performing five extractions of sample solutions spiked with all studied pyrethroids at the concentration levels used for the calibration plots. Coefficients of variation (CVs) ranged from 7% to 21%, thereby showing satisfactory results for pyrethroids determination in samples. From the slope ratio of the correlation equation by the present method to that by direct injection method (pyrethroids prepared in organic solvent), pyrethroids being collected onto the SPME fiber ranged from 0.14% to 4.10%.

3.7. Analysis of real sample

To examine the applicability of the method for pyrethroids determination in an actual aqueous sample, a field underground water sample was collected from the agriculture area, Shi-Hu, Yun-Lin County, Taiwan, and subsequently analyzed with the use of the proposed method after adjusting the pH to 4.0. The chromatogram of pyrethroids in underground water is shown in Fig. 4(b), and all pyrethroids taken for this study were below the detection limits from the underground water sample. Recovery was tested to investigate the effect of the actual sample matrix by spiking 0.5 μg/L of each pyrethroid standard in the underground water sample before subjecting the spiked samples to the proposed MA-HS-SPME extraction and GC-ECD analysis. Fig. 4(c) illustrates the pyrethroids chromatogram in the spiked underground water sample. Recoveries of the pyrethroids were calculated from the measured quantity of spiked sample minus the measured quantity of sample, divided by the spiked quantity and then varied from 88.5% to 115.5%, as listed in Table 1. This accuracy is deemed acceptable in environmental analysis. When adding humic acid from 0% to 0.5% to a sample solution containing 0.5 μg/L of each pyrethroid standard, and subsequently analyzed with the use of the proposed method after adjusting the pH to 4.0, no considerable chance in the peak areas of pyrethroids in the chromatogram. Besides, no significant interference occurred when adding metal ions up to 300 μg/mL of Ca^{2+} and Mg^{2+} and 30 μg/mL of Fe^{3+} and Al^{3+}. The microwave irradiation apparently decreased the interaction forces between pyrethroids and humic acid or prospective aqueous metal ions (Ca^{2+}, Mg^{2+}, Fe^{3+} and Al^{3+}) from these results.

3.8. Comparison of the present method with the SPE and LLE/SPE methods

The present one-step MA-HS-SPME method was compared with the conventional LLE/SPE method [32] and SPE method [33] in the

Table 1
The calibration parameters for pyrethroids with the present MA-HS-SPME method.

	Pesticides	Linear range (μg/L)	n	Equation	R^2	CV (%)	Recovery (%)[a]	MDL (ng/L)
1	Bioallenthrin	0.05–0.5	5	$y = 272188x - 3967$	0.9960	21	115.5	0.4
2	Bifenthrin	0.05–0.5	5	$y = 432892x - 1527$	0.9812	17	89.8	0.2
3	Fenpropathrin	0.05–0.5	5	$y = 268879x - 4311$	0.9947	14	97.0	0.4
4	Cyhalothrin	0.05–0.5	5	$y = 370411x - 1265$	0.9986	20	88.9	0.2
5	Permethrin	0.05–0.5	5	$y = 88014x - 1294$	0.9913	13	102.3	1.2
6	Cyfluthrin	0.05–0.5	5	$y = 118251x - 1724$	0.9980	13	92.0	0.9
7	Cypermethrin	0.05–0.5	5	$y = 94692x - 704$	0.9990	15	91.4	1.0
8	Fluvalinate	0.05–0.5	5	$y = 47377x - 508$	0.9945	17	90.1	1.8
9	Fenvalerate	0.05–0.5	5	$y = 78799x - 731$	0.9981	7	88.5	1.3
10	Deltamethrin	0.05–0.5	5	$y = 39846x - 584$	0.9992	18	88.6	2.6

[a] Spiking 0.5 μg/L pyrethroids; R^2: square of correlation coefficient.
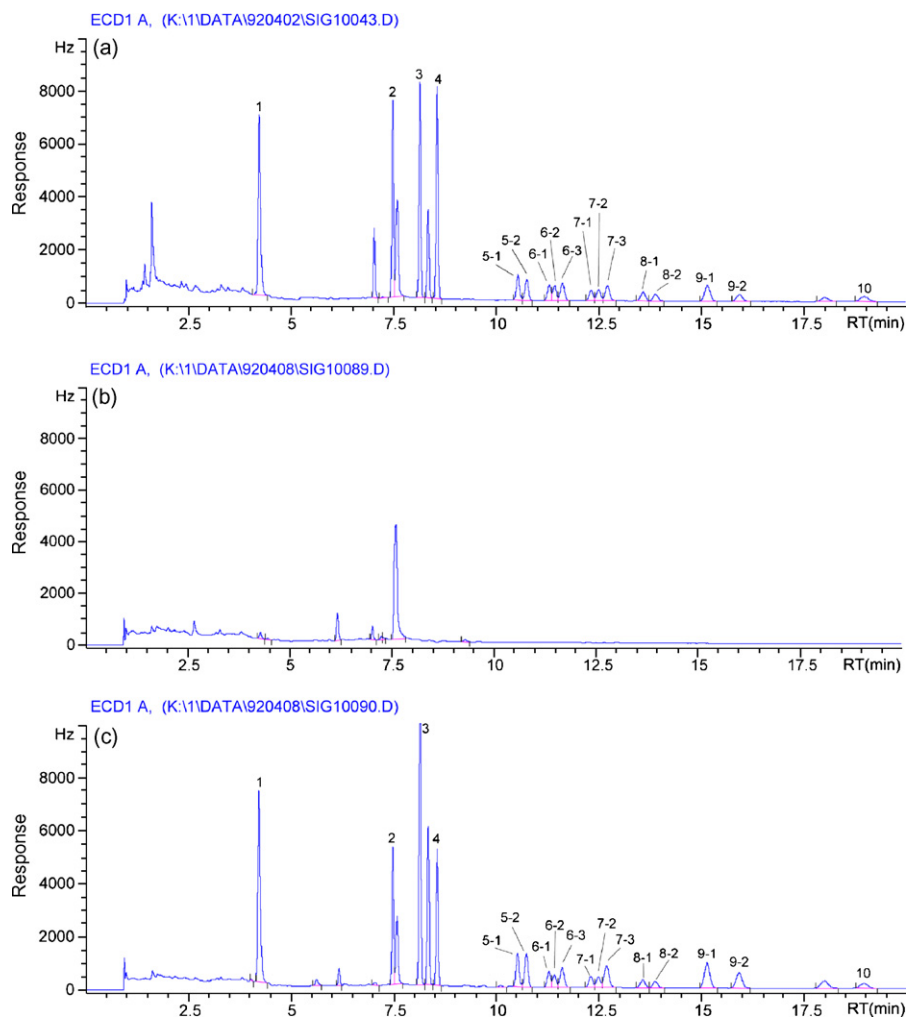
Fig. 4. GC-ECD chromatograms (a) standard pyrethroids spiked in water (0.5 μg/L); (b) field underground water sample; (c) spiked pyrethroids sample in field underground water sample (0.5 μg/L). Peaks: 1. bioallenthrin (4.185 min); 2. bifenthrin (7.457 min); 3. fenpropathrin (8.119 min); 4. cyhalothrin (8.540 min); 5. permethrin (10.505 and 10.722 min); 6. cyfluthrin (11.268, 11.402 and 11.587 min); 7. cypermethrin (12.294, 12.476 and 12.684 min); 8. fluvalinate (13.549 and 13.853 min); 9. fenvalerate (15.117 and 15.911 min); 10. deltamethrin (18.941 min).

determination of pyrethroids. The field underground water spiked with pyrethroid standards (0.5 μg/L of each) was as the fortified sample. After being pretreated by the procedures of these methods, pyrethroids were analyzed by GC-ECD. Table 2 lists the analytical results of these methods. It is obvious the extraction efficiency of the proposed one-step MA-HS-SPME method is much better than

that of the SPE method and is comparable to that of the LLE/SPE method. The detection limits of pyrethroids by the present method are thus lower than both conventional methods. Although the precisions of data by the present method are worsen than the LLE/SPE and slightly better than the SPE method, the levels are still acceptable in environmental analysis. Table 3 lists the comparison of the

Table 2
Comparison of the present MA-HS-SPME method with LLE/SPE and SPE methods.

	Methods	LLE/SPE			SPE			MA-HS-SPME		
	Sample quantity	89 mL + 11 mL buffer[*]			900 mL + 100 mL buffer[*]			18 mL + 2 mL buffer[*]		
	Sorbent	Florisil			C18			PDMS fiber		
		Recovery (%)	RSD (%)	MDL (ng/L)	Recovery (%)	RSD (%)	MDL (ng/L)	Recovery (%)	RSD (%)	MDL (ng/L)
1	Bioallenthrin	41.7	13	9	70.5	5	1	115.5	21	0.4
2	Bifenthrin	100.5	2.0	6	50.5	23	1	89.8	17	0.2
3	Fenpropathrin	96.4	1.4	6	59.9	10	1	97.0	14	0.4
4	Cyhalothrin	95.4	6.2	3	32.6	19	1	88.9	20	0.2
5	Permethrin	93.4	1.7	31	54.3	22	6	102.3	13	1.2
6	Cyfluthrin	87.0	4.7	8	34.4	20	2	92.0	18	0.9
7	Cypermethrin	87.6	6.8	9	34.1	20	2	91.4	15	1.0
8	Fluvalinate	92.9	14	5	49.9	28	1	90.1	17	1.8
9	Fenvalerate	89.9	5.9	5	30.2	23	1	88.5	7	1.3
10	Deltamethrin	97.4	6.3	3	49.4	30	1	88.6	18	2.6

[*] pH 4 buffer solution.

Table 3
Comparison of sources used between LLE/SPE and MA-HS-SPME.

Method characters	LLE/SPME	MA-HS-SPME
Sample size	20 mL	20 mL
Acetone	20 mL	No
Petroleum ether	30 mL	No
Methylene chloride	62 mL	No
Total solvent used	>127 mL (including washing)	No
10% NaCl	5 mL	No
Sodium sulfate	20 g	No
Total time-expense (including GC analysis)	3 h	25 min
Glassware	>10 items	Two items
Apparatus	SPE set-up, Sep. funnel, Filters, Roto-vaporator, N_2 evaporator	Microwave oven, SPME holder
Sorbent	Florisil SPE cartridge (Disposable)	SPME fiber (repeated use for 80–100 time)
Material cost (per sampling)	US$ 3.82	US$ 1.18

proposed method with the LLE/SPE method in sources-expense in each sample pretreatment. It is obvious that with the proposed MA-HS-SPME method, it took only 25 min to finish a sample analysis and no organic solvent and less sources were required in the sample pretreatment of pyrethroids before GC analysis.

4. Conclusion

In this study, a one-step microwave-assisted headspace solid-phase microextraction (MA-HS-SPME) is found to be an effective and much improved analytical procedure for pyrethroids analysis. From the results of the applicability test for pyrethroids determination in the field ground water sample, the present approach is found to be a simple, rapid, sensitive, inexpensive and eco-friendly procedure to collect analytes from aqueous samples.

Acknowledgements

References

[1] T. Roberts, D. Hutson, Metabolic Pathways of Agrochemicals. Part 2. Insecticides and Fungicides, The Royal Society of Chemistry, Cornwall, UK, 1999.
[2] T. Lopez-Lopez, M.D. Gil-Garcia, J.L. Martinez-Vidal, M. Martinez-Galera, Anal. Chim. Acta 447 (2001) 101.
[3] C. Goncalves, M.F. Alpendurada, J. Chromatogr. A 968 (2002) 177.
[4] E.M. Kristenson, E.G.J. Haverkate, C.J. Slooten, L. Ramos, R.J.J. Vreuls, U.A.Th. Brinkman, J. Chromatogr. A 917 (2001) 277.
[5] L. Elflein, E. Berger-Preiß, K. Levsen, G. Wünsch, J. Chromatogr. A 985 (2003) 147.
[6] A. Colume, S. Cardenas, M. Gallego, M. Valcarcel, Anal. Chim. Acta 436 (2001) 153.
[7] A. Di Muccio, P. Pelosi, D. Attard Barbini, T. Generali, A. Ausili, F. Vergori, J. Chromatogr. A 765 (1997) 51.
[8] J.W. Wong, M.G. Webster, C.A. Halverson, M.J. Hengel, K.K. Ngim, S.E. Ebeler, J. Agric. Food Chem. 51 (2003) 1148.
[9] S. Qin, J.J. Gan, J. Agric. Food Chem. 54 (2006) 9145.
[10] M.B. Woudneh, D.R. Oros, J. Agric. Food Chem. 54 (2006) 6957.
[11] Y.Y. Hu, P. Zheng, Y.Z. He, G.P. Sheng, J. Chromatogr. A 1098 (2005) 188.
[12] A.A. Body-Boland, J. Pawliszyn, Anal. Chem. 68 (1996) 1521.
[13] W. Liu, J.J. Gan, J. Agric. Food Chem. 52 (2004) 736.
[14] V. Casas, M. Llompart, C. García-Jares, R. Cela, T. Dagnac, J. Chromatogr. A 1124 (2006) 148.
[15] P. Parrilla Vázquez, A.R. Mughari, M. Martínez Galera, Anal. Chim. Acta 607 (2008) 74.
[16] M. Fernandez-Alvarez, M. Llompart, J. Pablo Lamas, M. Lores, C. Garcia-Jares, R. Cela, T. Dagnac, J. Chromatogr. A 1188 (2008) 154.
[17] P. Parrilla Vázquez, A.R. Mughari, M. Martínez Galera, J. Chromatogr. A 1188 (2008) 61.
[18] N. Campillo, R. Penalver, M. Hernandez-Cordoba, J. Chromatogr. A 1125 (2006) 31.
[19] J. You, M.J. Lydy, Int. J. Environ. Anal. Chem. 86 (2006) 381.
[20] R.A. Doong, S.M. Chang, Y.C. Sun, J. Chromatogr. A 879 (2000) 177.
[21] S. Waidyanatha, Y. Zheng, S.M. Rappaport, Chem. Biol. Interact. 145 (2003) 165.
[22] D.H. Cho, S.H. Kong, S.G. Oh, Water Res. 37 (2003) 402.
[23] Z.Y. Zhang, J. Pawliszyn, Anal. Chem. 67 (1995) 34.
[24] A.R. Ghiasvand, S. Hosseinzadeh, J. Pawliszyn, J. Chromatogr. A 1124 (2006) 35.
[25] A. Zlotorzynski, Crit. Rev. Anal. Chem. 25 (1995) 43.
[26] Q. Jin, F. Liang, H. Zhang, L. Zhao, Y. Huan, D. Song, Trends Anal. Chem. 16 (1999) 479.
[27] Y.I. Chen, Y.S. Su, J.F. Jen, J. Chromatogr. A 976 (2002) 349.
[28] M.C. Wei, J.F. Jen, J. Chromatogr. A 1012 (2003) 111.
[29] H.P. Li, G.C. Li, J.F. Jen, J. Chromatogr. A 1012 (2003) 129.
[30] Y. Huang, Y.-C. Yang, Y.Y. Shu, J. Chromatogr. A 1140 (2007) 35.
[31] J. Shen, Z. Xu, J. Cai, X. Shao, Anal. Sci. 22 (2006) 241.
[32] U.S. E.P.A., Method 525.2, Determination of Organic Compounds in Drinking Water by Liquid–Solid Extraction and Capillary Column Gas Chromatography/Mass Spectrometry, Environmental Monitoring and Support Laboratory, Cincinnati, 1995.
[33] B.M. McMahon, N. Hardin (Eds.), Pesticide Analytical Manual, Vol. 1: Multiresidue Methods, 3rd ed., U.S. Food and Drug Administration, Washington, DC, 1994.

Electrochemiluminescence from tris(2,2′-bipyridyl)ruthenium(II)–graphene–Nafion modified electrode

Haijuan Li [a,b], Jiuan Chen [a,b], Shuang Han [a,b], Wenxin Niu [a,b], Xiaoqing Liu [a,b], Guobao Xu [a,*]

[a] State Key Laboratory of Electroanalytical Chemistry, Changchun Institute of Applied Chemistry, Chinese Academy of Sciences, 5625 Renmin Street, Changchun, Jilin 130022, China
[b] Graduate University of the Chinese Academy of Sciences, Beijing 100864, China

ARTICLE INFO

ABSTRACT

An electrochemiluminescence (ECL) sensor based on $Ru(bpy)_3^{2+}$–graphene–Nafion composite film was developed. The graphene sheet was produced by chemical conversion of graphite, and was characterized by atomic force microscopy (AFM), scanning electron microscopy (SEM), and Raman spectroscopy. The introduction of conductive graphene into Nafion not only greatly facilitates the electron transfer of $Ru(bpy)_3^{2+}$, but also dramatically improves the long-term stability of the sensor by inhibiting the migration of $Ru(bpy)_3^{2+}$ into the electrochemically inactive hydrophobic region of Nafion. The ECL sensor gives a good linear range over 1×10^{-7} to 1×10^{-4} M with a detection limit of 50 nM towards the determination of tripropylamine (TPA), comparable to that obtained by Nafion-CNT. The ECL sensor keeps over 80% and 85% activity towards 0.1 mM TPA after being stored in air and in 0.1 M pH 7.5 phosphate buffer solution (PBS) for a month, respectively. The long-term stability of the modified electrode is better than electrodes modified with Nafion, Nafion–silica, Nafion–titania, or sol–gel films containing $Ru(bpy)_3^{2+}$. Furthermore, the ECL sensor was successfully applied to the selective and sensitive determination of oxalate in urine samples.

1. Introduction

Graphene, a flat monolayer of carbon atoms tightly packed into a two-dimensional (2D) honeycomb lattice, is the basic building block for graphitic materials of all other dimensionalities (wrapped up into 0D fullerenes, rolled into 1D nanotubes or stacked into 3D bulk graphite). It is a rapidly rising star in material science that exhibits unique nanostructure and extraordinarily electrical properties [1]. Its physical properties have been extensively studied; however, its analytical applications remain largely unexplored, despite the anticipated intriguing properties. Among various approaches for preparation, graphene produced by chemical conversion from graphite has received the most attention [2,3]. In this method, graphite is first exfoliated with strong acids and oxidative reagents to produce graphene oxide (GO), and then GO is converted to graphene by chemical reduction with amines [2,3]. The as-prepared graphene contains a variety of oxygen functionalities (–OH, –O–, and –COOH) and is negatively charged when dispersed in water [2,4]. The presence of negatively charged groups and the conductivity of graphene make it attractive matrix for the immobilization of positively charged molecules in electrochemistry, such as $Ru(bpy)_3^{2+}$.

$Ru(bpy)_3^{2+}$ electrogenerated chemiluminescence (ECL) has been given much concern in chemical analysis because of its wide applications, good electrochemical stability, and high ECL efficiency in aqueous media [5–11]. It is widely used in immunoassays [12] and DNA probe assays [13,14] as well as the determination of alkylamines [15,16], hydroxyl compounds [17–19], persulfate [20], oxalate, and organic acid [21] with high sensitivity and wide dynamic range. The immobilizations of $Ru(bpy)_3^{2+}$ onto a solid electrode surface are important for $Ru(bpy)_3^{2+}$ ECL applications because it can simplify experimental design and reduce the consumption of expensive reagent [22–26]. The cation-exchange polymer Nafion is effective for the immobilization of $Ru(bpy)_3^{2+}$ because of its high ion-exchange selectivity coefficients for $Ru(bpy)_3^{2+}$ and its electrochemical stability [27]. However, the migration of the $Ru(bpy)_3^{2+}$ into the electrochemically inactive hydrophobic region of Nafion results in poor long-term stability of the ECL sensor. Several materials have been introduced to $Ru(bpy)_3^{2+}$–Nafion film to improve performance, such as carbon nanotubes (CNT), silica, titania, and zirconia [28–33].

In this study, $Ru(bpy)_3^{2+}$ was incorporated into the graphene–Nafion composite film through the electrostatic interactions with negatively charged graphene and Nafion. The introduction of graphene facilitates the electron transfer of $Ru(bpy)_3^{2+}$ and retards the migration of the $Ru(bpy)_3^{2+}$ into the electrochemically inactive hydrophobic region of Nafion. The $Ru(bpy)_3^{2+}$–graphene–Nafion modified electrode showed good sensitivity and stability for the ECL determination of TPA.

---

* Corresponding author. Tel.: +86 431 85262747; fax: +86 431 85262747.
E-mail address: guobaoxu@ciac.jl.cn (G. Xu).

The detection limit was comparable to the ECL sensor based on Nafion–CNT composite [33]. The ECL sensor was further applied to the selective and sensitive determination of oxalate in urine samples.

2. Experimental

2.1. Reagents

Tris(2,2′-bipyridyl)ruthenium(II) chloride hexahydrate and TPA were purchased from Aldrich. Nafion (20 wt.%) was purchased from Sigma. $K_3Fe(CN)_6$ and sodium oxalate were purchased from Beijing Chemical Reagent (Beijing, China). Other reagents were of at least analytical grade and used as received. All solutions were prepared with doubly deionized water.

2.2. Apparatus

Cyclic voltammetry (CV) experiments and ECL detections were carried out with an MPI-A capillary electrophoresis ECL detector (Xi'an Remax Electronics Co. Ltd., Xi'an, China). A glassy carbon (GC, 3 mm in diameter) electrode, an Ag/AgCl electrode, and a platinum wire were used as working, reference, and counter electrode, respectively. Scanning electron microscope (SEM) measurements were carried out on a PHILIPS XL-30 ESEM at an accelerating voltage of 20 kV. Tapping-mode AFM imaging was performed on a Digital Instruments multimode AFM controlled by a Nanoscope IIIa apparatus (Digital Instruments, Santa Barbara, CA) equipped with an E scanner. A standard silicon cantilever tip from Digital Instruments was used. The scan rate was 1–1.5 Hz. Raman spectra were measured with a Renishaw 2000 model confocal microscopy Raman spectrometer with a CCD detector and a holographic notch filter (Renishaw Ltd., Gloucestershire, U.K.). Radiation of 514.5 nm from an air-cooled argon ion laser was used for the SERS excitation.

2.3. Preparation of GO

The oxidation of the graphite was carried out based on the Hummers method [34]. 1 g graphite and 0.75 g $NaNO_3$ were put into a flask with stirring in an ice bath, and 62.1 g H_2SO_4 was added. Then 4.5 g $KMnO_4$ was added gradually through a funnel within 1 h. After cooling for 1 h, the mixture was gently stirred at room temperature for 5 days. So-prepared mixture was gradually added into 100 mL 5 wt.% H_2SO_4 within 1 h with successively stirring, and then the mixture was further stirred for additional 2 h. After addition of 2.7 mL 30 wt.% H_2O_2, the mixture was stirred for another 2 h. The mixture was filtered and washed with a solution containing 3 wt.% H_2SO_4 and 0.5 wt.% H_2O_2 for several times, totally 200 mL. After that, the mixture was washed with deionized water three times to remove the remaining metal ions and acid. The resulted solid was dried in air and stored for use.

2.4. Preparation of graphene from GO

The reduction of GO to graphene was conducted according to Refs. [2,3]. Briefly, 12.8 mg GO was dispersed in 24.3 mL H_2O to create a 0.05 wt.% dispersion. Exfoliation of GO was achieved by the ultrasonication of the dispersion for 45 min with a 494 W power. The obtained homogeneous dispersion was mixed with 44 mL H_2O, 22 μL hydrazine solution and 154 μL 25 wt.% ammonia solution in a flask. After being vigorously shaken, the flask was put in a water bath (95 °C) for 1 h with consistently stirring. Graphene dispersions prepared according to the above procedure were used for further characterization and film fabrication in this work.

2.5. Preparation of Ru(bpy)$_3$$^{2+}$–graphene–Nafion modified electrode

1 μL 20 wt.% Nafion was added into 39 μL graphene sample solution with agitation to give a homogeneous solution (0.5 wt.%

Fig. 1. (A and B) Tapping mode AFM images of graphene sheet on mica, (C) SEM image of the graphene on ITO.

Nafion). Then 5 μL of 0.5% pure Nafion solution or graphene–Nafion solution was dipped on the clean GC surface and the solvents were allowed to evaporate under ambient condition. Finally, the resulting electrode was immersed in 1 mM $Ru(bpy)_3^{2+}$ solution for 30 min to obtain $Ru(bpy)_3^{2+}$ modified electrode.

3. Results and discussion

3.1. Characterizations of the as-synthesized graphene

Fig. 1A–C displays the AFM and SEM images of the graphene sheets. Distinctive layered structure can be observed from these images. The graphene sheet has lateral dimensions from a few hundred nanometers to several micrometers, and a thickness of ~1.2 nm. This height, larger than the value predicted by theory [35], is due to individual graphitic sheets bearing oxygen-containing groups on both faces. Similar results have also been reported [3,36]. Corrugated sheets overlapping each other can be readily observed in the SEM (Fig. 1C), because the sheet is soft and flexible, and electronic repulsion between layers leads to the bumps and wrinkles.

The structure changes occurring during the chemical reduction from GO to graphene are reflected in their Raman spectra (Fig. 2). The Raman spectrum of the GO (Fig. 2a) displays a prominent G peak at 1592 cm^{-1} and a D band at 1356 cm^{-1}. The G peak corresponds to an E_{2g} mode of graphite and is related to the vibration of sp^2-bonded carbon atoms in a 2D hexagonal lattice, such as in a graphite layer. The D band associates with vibrations of carbon atoms with dangling bonds in plane terminations of disordered graphite [37]. The Raman spectrum of the graphene (Fig. 2b) also displays both the G and D band (1601 cm^{-1} and 1344 cm^{-1}), but with an increased intensity ratio of D and G band compared with that in GO. The intensity ratio of the D and G band is a measure of the disorder, as expressed by the sp^3/sp^2 carbon ratio. The increase of D/G ratio suggests a decrease in the average size of the sp^2 domains upon reduction of the exfoliated GO.

3.2. Electrochemical characterization of graphene–Nafion film

Fig. 3 shows typical CV of 1 mM $K_3Fe(CN)_6$ at Nafion modified electrode (curve a) and graphene–Nafion modified electrode (curve b) in 0.1 M KCl electrolyte (pH 5.2) at a scan rate of 10 mV/s from −0.2 V to 0.6 V. The CV curve was obtained immediately after the modified electrodes had been immersed in solution, and the peak currents was not changed by increasing the immersion time

Fig. 3. CVs of 1 mM $K_3Fe(CN)_6$ at (a) Nafion modified electrode and (b) graphene–Nafion modified electrode in 0.1 M KCl. Scan rate, 10 mV/s.

for both Nafion modified electrode and graphene–Nafion modified electrode in the electrolyte from 0 to 60 min. The anodic and cathodic currents at the Nafion modified electrode were negligible (curve a), demonstrating that the one-electron redox behavior of $Fe(CN)_6^{3-/4-}$ was blocked by Nafion film. In contrast, a pair of well-defined oxidation and reduction peaks was observed at 0.3 and 0.15 V at the graphene–Nafion modified electrode (curve b), indicating that conductive graphene facilitates electron transfer.

3.3. Electrochemistry and ECL of $Ru(bpy)_3^{2+}$–graphene–Nafion composite film

Fig. 4 shows CV of the $Ru(bpy)_3^{2+}$–graphene–Nafion composite film in 0.1 M pH 7.5 PBS at different scan rates. A pair of redox wave characteristics of $Ru(bpy)_3^{2+}/Ru(bpy)_3^{3+}$ appears. The anodic peak current is proportional to the square root of the scan rate over the range of 20–400 mV/s, indicating that the immobilized $Ru(bpy)_3^{2+}$ undergoes a diffusion process.

The ECL behavior of $Ru(bpy)_3^{2+}$ encapsulated in the composite film-modified electrode is initially studied using TPA as a coreactant. The ECL emission of the $Ru(bpy)_3^{2+}$–TPA system resulted from the reaction between the deprotonated TPA radical (TPA$^\bullet$) and electrogenerated $Ru(bpy)_3^{3+}$ to form $[Ru(bpy)_3^{2+}]^*$, which then decays to produce orange emission (Eqs. (1)–(4)). TPA$^\bullet$ was formed via cat-

Fig. 2. The Raman spectra of (a) GO and (b) graphene.

Fig. 4. CVs of $Ru(bpy)_3^{2+}$–graphene–Nafion modified electrode at various scan rates (a) 20, (b) 50, (c) 100, (d) 150, (e) 200, (f) 300, and (g) 400 mV/s in 0.1 M pH 7.5 PBS. Inset was the relationship between the anodic peak current and the square root of scan rate.

Fig. 5. CVs of Ru(bpy)$_3$$^{2+}$–graphene–Nafion modified electrode in the absence (dash line) and presence (solid line) of 0.1 mM TPA in 0.1 M pH 7.5 PBS at a scan rate of 100 mV/s.
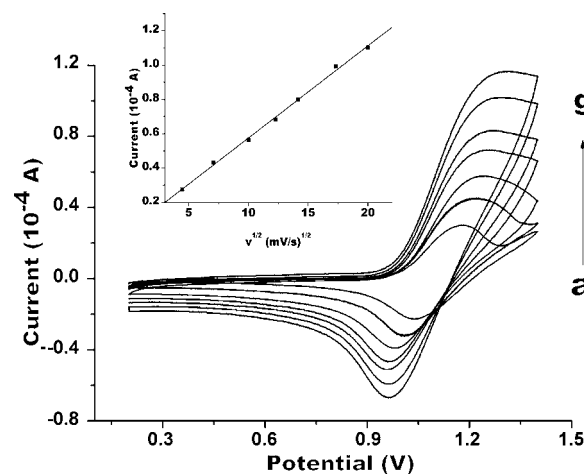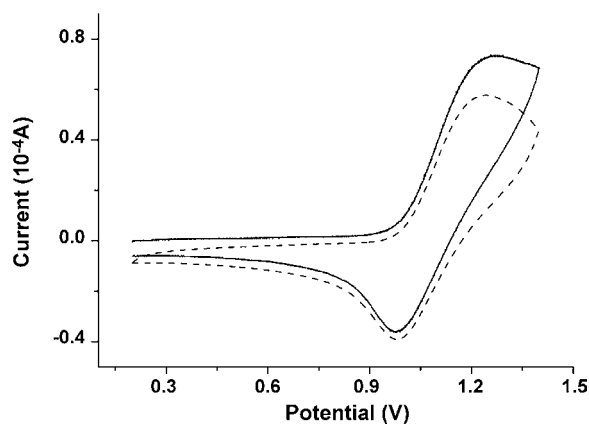
alytic oxidation by electrogenerated Ru(bpy)$_3$$^{3+}$ (Eq. (2a)) and direct electrode oxidation (Eq. (2b)) [38–43].

$$Ru(bpy)_3{}^{2+} \rightarrow Ru(bpy)_3{}^{3+} + e^- \tag{1}$$

$$Ru(bpy)_3{}^{3+} + TPA \rightarrow Ru(bpy)_3{}^{2+} + TPA^\bullet \tag{2a}$$

$$TPA \rightarrow TPA^\bullet + e^- \tag{2b}$$

$$Ru(bpy)_3{}^{3+} + TPA^\bullet \rightarrow Ru(bpy)_3{}^{2+*} \tag{3}$$

$$Ru(bpy)_3{}^{2+*} \rightarrow Ru(bpy)_3{}^{2+} + h\nu\,(610\,nm) \tag{4}$$

Fig. 5 shows CV of Ru(bpy)$_3$$^{2+}$ immobilized in the graphene–Nafion composite film-modified electrode in the absence (dash line) and presence (solid line) of 0.1 mM TPA. The presence of TPA results in increase in the anodic peak current and decrease in the cathodic peak current, indicating that the Ru(bpy)$_3$$^{2+}$–graphene–Nafion composite film electrochemically catalyze the oxidation of TPA. Meanwhile, the ECL signal increased considerably in the presence of TPA. The corresponding ECL-potential profile is shown in Fig. 6. The onset of luminescence occurred near 0.9 V and the ECL peak intensity occurred near 1.1 V, where Ru(bpy)$_3$$^{2+}$ is electrochemically oxidized.
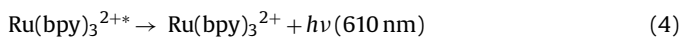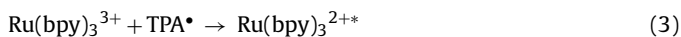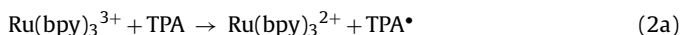
The ECL intensity decreased with increasing scan rate over 5–80 mV/s, and kept relatively constant in the range of 80–200 mV/s (Fig. 7A). The dependence of ECL intensity on the scan rate is attributed to the chemical kinetics of the ECL system and the rate of TPA diffusion in the solid host [39–43].
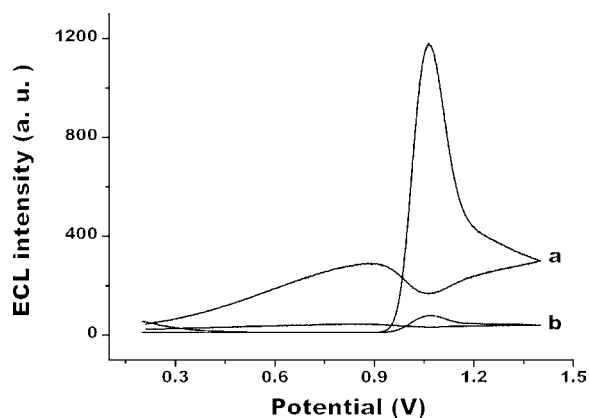
Fig. 6. ECL-potential curve for Ru(bpy)$_3$$^{2+}$–graphene–Nafion modified electrode in the absence (a) and presence (b) of 5 μM TPA in 0.1 M pH 7.5 PBS at a scan rate of 10 mV/s.

The ECL intensity for TPA was greatly affected by the pH of the buffer solution (Fig. 7B). It increased significantly from pH 4.0 up to pH 7.5 and slightly decreased at higher pH. This was similar to the results obtained at the Nafion–CNT, Nafion–silica and Nafion–titania composite film [28–30]. The Ru(bpy)$_3$$^{2+}$/TPA ECL reaction involves in the deprotonation of TPA and/or its radical cations [39–43]. At lower pH, lower ECL response is attributed to protonation of the TPA and/or its radical cations. The decrease in ECL at pH higher than 7.5 is ascribed to significant side reaction between OH$^-$ and electrogenerated Ru(bpy)$_3$$^{3+}$.

The linear experiments were carried out in 0.1 M PBS pH 7.5 at a scan rate of 100 mV/s. The ECL signal varies linearly with the concentration of TPA from 1.0×10^{-7} to 1.0×10^{-4} M. The regression equation was $I = 28.69 + 40.56\,C$ ($n = 7$) with a correlation coefficient of 0.9989, where I was ECL intensity and C was the concentration of TPA (μM). The detection limit (S/N = 3) is 50 nM. The detection limit is lower than that obtained from the Nafion–silica-, Nafion–titania-, or sol–gel-film modified ECL sensors, and comparable to the ECL sensor based on Nafion–CNT composite [26,29,30,33]. The relative standard deviation of the ECL intensity from the modified electrode under continuous potential scanning for six cycles from 0.2 to 1.4 V in 0.1 M pH 7.5 PBS containing 4×10^{-5} M TPA is 2.14%. The modified electrode kept over 80% and 85% activity towards 0.1 mM TPA after being stored in air and in 0.1 M pH 7.5 PBS for a month, respectively. It is more stable than the Nafion-, Nafion–silica-, Nafion–titania-, or sol–gel-film-modified ECL sensors, and is less stable than sol–gel-derived titania–Nafion composite films [26,27,29,30,33]. The decrease in the ECL signal in the present ECL sensor is probably due to the partition of Ru(bpy)$_3$$^{2+}$ to the more hydrophobic regions of Nafion in the graphene–Nafion composite films, as observed in the previous works with pure Nafion- and Nafion–titania-modified electrode [27,30].

3.4. ECL detection of urine oxalate based on Ru(bpy)$_3$$^{2+}$–graphene–Nafion modified electrode

Oxalate, a product of protein metabolism, is excreted by the kidney. High concentration of oxalate in urine accompanies many diseases and mostly the presence of kidney stones [44,45]. So that selective and precise detection oxalate is important for diagnosis analysis. A number of methods have been recommended for oxalate determination in clinical laboratory analyses mainly including chromatographic and enzymatic methods [44,45]. The chromatographic methods are complicated and time-consuming while the enzymatic methods are limited by the instability of reagents. The Ru(bpy)$_3$$^{2+}$ ECL, as a sensitive and selective method, has been used to detect oxalate in vegetable, synthetic urine, urine, and blood without coupling with separation techniques and any chemically pre-treated process [46–50]. The notable selectivity in the determination of oxalate is mainly because oxalate is a much more effective coreactant than amino acids and ascorbic acid in weakly acidic solution and neutral solution [51,52]. In this study, we use oxalate as a representative analyte to test the feasibility of sensitive ECL detection by Ru(bpy)$_3$$^{2+}$–graphene–Nafion modified electrode in real world sample.

The ECL peak intensity for oxalate reached a maximum value at pH 6.0 in PBS, consistent with that observed in solution-phase Ru(bpy)$_3$$^{2+}$ ECL detection [21]. The ECL reaction mechanism of Ru(bpy)$_3$$^{2+}$ and oxalate can be described as follows [21]:

$$Ru(bpy)_3{}^{2+} \rightarrow Ru(bpy)_3{}^{3+} + e^- \tag{5}$$

$$Ru(bpy)_3{}^{3+} + C_2O_4{}^{2-} \rightarrow Ru(bpy)_3{}^{2+} + C_2O_4{}^{-\bullet} \tag{6}$$

$$C_2O_4{}^{-\bullet} \rightarrow CO_2{}^{-\bullet} + CO_2 \tag{7}$$

Fig. 7. (A) The effect of scan rate on ECL intensity in 0.1 M pH 7.5 PBS containing 4.0 μM TPA and (B) the effect of buffer pH on ECL intensity in 0.1 M PBS containing 50 μM TPA at a scan rate of 100 mV/s.

$$Ru(bpy)_3^{3+} + CO_2^{-\bullet} \rightarrow Ru(bpy)_3^{2+*} + CO_2 \tag{8}$$

$$Ru(bpy)_3^{2+*} \rightarrow Ru(bpy)_3^{2+} + h\nu \,(610\,nm) \tag{9}$$
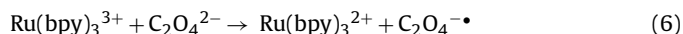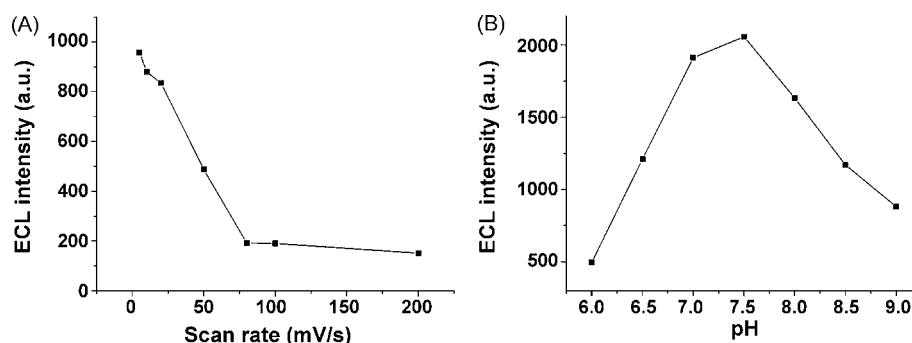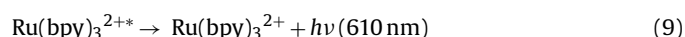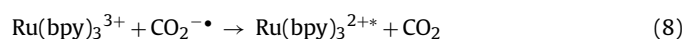
For oxalic acid, $pK_{a1} = 1.23$, $pK_{a2} = 4.19$, therefore the predominant form at lower pH values is $HC_2O_4^-$, which underwent a reaction sequence similar to that represented by Eqs. (5)–(9) with the reactive intermediate now being $CO_2H^\bullet$. $CO_2H^\bullet$ is a much weaker reducing agent than $CO_2^{-\bullet}$, accounting for the pH dependence of oxalate [21]. Oxalate was detected at a scan rate of 100 mV/s in 0.1 M pH 5.5 PBS to minimize interference from amino acids and ascorbic acid in urine [26,27]. The ECL signal varies linearly with the concentration of oxalate from 1.0×10^{-6} to 5.0×10^{-4} M. The regression equation was $I = 175.9 + 17.3\,C\,(n = 8)$ with a correlation coefficient of 0.999, where I was ECL intensity and C was the concentration of oxalate (μM). The RSD of six consecutive determinations of 1.0×10^{-5} M oxalate is 2.1%. The detection limit (S/N = 3) is 8×10^{-7} M, one order of magnitude lower than that at the pure Nafion-modified electrode, and comparable with those at the Nafion–silica- and Nafion–titania-composite-modified electrodes [27,29,30].

The concentration of oxalate in normal urine is range from about 1.6×10^{-4} to 5.5×10^{-4} M [47]. In our study, the urine sample was diluted to 50-fold. After dilution, oxalate concentrations in samples are in the range between 3.2 and 11 μM. Interference study indicated that 20 μM glycine and uric acid, 10 μM alanine, threonine, lysine, leucine, histidine, and serine, 2.5 μM asparagine, phenylalanine, tryptophan, and ascorbic acid, and 0.5 μM proline, isoleucine, glutamic acid, arginine, and cystine did not interfere with the determination of 3 μM oxalate (Table 1). The investigated concentrations of ascorbic acid, uric acid and amino acids were higher than their concentrations in 50-fold diluted normal urine samples, respectively. The tolerable limit of a foreign species was taken as a relative error less than 5%.

Table 1
Results of interference study.

Analytes[a]	Relative response	Analytes[a]	Relative response
Oxalate	100	Asparagine	101
Glycine	101.9	Phenylalanine	100
Uric acid	100	Tryptophan	100
Alanine	100	Ascorbic acid	100
Threonine	102.8	Proline	101
Lysine	100	Isoleucine	102.8
Leucine	100	Glutamic acid	102.8
Histidine	100	Arginine	100
Serine	102.8	Cystine	100

[a] Oxalate, 3 μM; glycine and uric acid, 20 μM; alanine, threonine, lysine, leucine, histidine, and serine, 10 μM; asparagine, phenylalanine, tryptophan, and ascorbic acid, 2.5 μM; proline, isoleucine, glutamic acid, arginine, and cystine, 0.5 μM.

The practicality of the proposed method was further demonstrated by the determination of oxalate in urine samples. The oxalate concentration in the urine sample of a health volunteer was determined to be 4.13×10^{-4} M with an RSD of 2.6%. This urine sample was also supplemented with various concentrations of oxalate (1.1, 1.8, and 2.7×10^{-4} M). The analytical recoveries and RSDs were 97.8–99.6% and 2.2–4.2%, respectively. All these data indicated the feasibility of the ECL sensor for real world sample analysis.

4. Conclusions

Graphene was used as new material for the immobilization of $Ru(bpy)_3^{2+}$ for the first time. The introduction of conductive graphene facilitates the electron transfer of $Ru(bpy)_3^{2+}$ and the interaction between negatively charged graphene and $Ru(bpy)_3^{2+}$ retards the migration of the $Ru(bpy)_3^{2+}$ into the electrochemically inactive hydrophobic region of Nafion. As a result, the $Ru(bpy)_3^{2+}$–graphene–Nafion modified electrode showed good sensitivity and stability for the ECL determination of TPA. Moreover, the sensor shows good selectivity and sensitivity for the determination of oxalate in urine. The study shows that graphene holds great promise for ECL applications.

References

[1] A.K. Geim, K.S. Novoselov, Nat. Mater. 6 (2007) 183.
[2] D. Li, M.B. Muller, S. Gilje, R.B. Kaner, G.G. Wallace, Nat. Nano 3 (2008) 101.
[3] S. Stankovich, A.D. Dmitriy, D.P. Richard, A.K. Kevin, G. Kleinhammes, Y.Y. Jia, Y. Wu, T.N. SonBinh, R.S. Ruoff, Carbon 45 (2007) 1558.
[4] Y.C. Si, E.T. Samulski, Nano Lett. 8 (2008) 1679.
[5] W.Y. Lee, Mikrochim. Acta 127 (1997) 19.
[6] W.J. Miao, Chem. Rev. 108 (2008) 2506.
[7] A.W. Knight, G.M. Greenway, Analyst 121 (1996) 101R.
[8] M.M. Richter, Chem. Rev. 104 (2004) 3003.
[9] A.W. Knight, G.M. Greenway, Analyst 119 (1994) 879.
[10] R.D. Gerardi, N.W. Barnett, S.W. Lewis, Anal. Chim. Aata 378 (1999) 1.
[11] B.A. Gorman, P.S. Francis, N.W. Barnett, Analyst 131 (2006) 616.
[12] M.M. Richter, A.J. Bard, W. Kim, R.H. Schmehl, Anal. Chem. 70 (1998) 310.
[13] W.J. Miao, A.J. Bard, Anal. Chem. 75 (2003) 5825.
[14] E.G. Hvastkovs, M. So, S. Krishnan, B. Bajrami, M. Tarun, I. Jansson, J.B. Schenkman, J.F. Rusling, Anal. Chem. 79 (2007) 1897.
[15] W.Y. Lee, T.A. Nieman, Anal. Chem. 67 (1995) 1789.
[16] S.N. Brune, D.R. Bobbitt, Anal. Chem. 64 (1992) 166.
[17] F. Li, H. Cui, X.Q. Lin, Anal. Chim. Acta 471 (2002) 187.

[18] X. Chen, L. Jia, X.R. Wang, G.L. Hu, M. Sato, Anal. Sci. 13 (1997) 71.
[19] H. Cui, F. Li, M.J. Shi, Y.Q. Pang, X.Q. Lin, Electroanalysis 17 (2005) 589.
[20] H.S. White, A.J. Bard, J. Am. Chem. Soc. 104 (1982) 6891.
[21] I. Rubinstein, A.J. Bard, J. Am. Chem. Soc. 103 (1981) 512.
[22] H. Wei, E.K. Wang, Trends Anal. Chem. 27 (2008) 447.
[23] T. Ying, Z.J. Lin, X.M. Chen, X. Chen, Progr. Chem. 20 (2008) 362.
[24] X. Zhang, A.J. Bard, J. Phys. Chem. 92 (1988) 5566.
[25] C.J. Miller, P. McCord, A.J. Bard, Langmuir 7 (1991) 2781.
[26] M.M. Collinson, B. Novak, S.A. Martin, J.S. Taussig, Anal. Chem. 72 (2000) 2914.
[27] T.M. Downey, T.A. Nieman, Anal. Chem. 64 (1992) 261.
[28] Z.H. Guo, S.J. Dong, Anal. Chem. 76 (2004) 2683.
[29] A.N. Khramov, M.M. Collinson, Anal. Chem. 72 (2000) 2943.
[30] H.N. Choi, S.H. Cho, W.Y. Lee, Anal. Chem. 75 (2003) 4250.
[31] S.N. Ding, J.J. Xu, H.Y. Chen, Electrophoresis 26 (2005) 1737.
[32] D.J. Kim, Y.K. Lyu, H.N. Choi, I.H. Min, W.Y. Lee, Chem. Commun. (2005) 2966.
[33] H.N. Choi, J.Y. Lee, Y.K. Lyu, W.Y. Lee, Anal. Chim. Acta 565 (2006) 48.
[34] W.S. Hummers, R.E. Offeman, J. Am. Chem. Soc. 80 (1958) 1339.
[35] H.C. Schniepp, J.L. Li, M.J. McAllister, H. Sai, M. Herrera-Alonso, D.H. Adamson, R.K. Car, R. Prud'homme, D.A. Saville, I.A. Aksay, J. Phys. Chem. B 110 (2006) 8535.
[36] C. Gómez-Navarro, R.T. Weitz, A.M. Bittner, M. Scolari, A. Mews, M. Burghard, K. Kern, Nano Lett. 7 (2007) 3499.
[37] A.C. Ferrari, Solid State Commun. 143 (2007) 47.
[38] X.Q. Liu, L.H. Shi, W.X. Niu, H.J. Li, G.B. Xu, Angew, Chem. Int. Ed 46 (2007) 421.
[39] W.J. Miao, J.P. Choi, A.J. Bard, J. Am. Chem. Soc. 124 (2002) 14478.
[40] R.M. Wightman, S.P. Forry, R. Maus, D. Badocco, P. Pastore, J. Phys. Chem. B 108 (2004) 19119.
[41] Y. Zu, A.J. Bard, Anal. Chem. 72 (2000) 3223.
[42] Y. Zu, A.J. Bard, Anal. Chem. 73 (2001) 3960.
[43] E.M. Gross, P. Pastore, R.M. Wightman, J. Phys. Chem. B 105 (2001) 8732.
[44] B.G. Keevil, S. Thornton, Clin. Chem. 52 (2006) 2296.
[45] R.H. Capra, M. Strumia, P.M. Vadgama, A.M. Baruzzi, Anal. Chim. Acta 530 (2005) 49.
[46] N. Egashira, H. Kumasako, Y. Kurauchi, K. Ohga, Anal. Sci. 8 (1992) 713.
[47] I. Rubinstein, C.R. Martin, A.J. Bard, Anal. Chem. 55 (1983) 1580.
[48] N. Egashira, H. Kumasako, K. Ohga, Anal. Sci. 6 (1990) 903.
[49] R.A. Forster, C.F. Hogan, Anal. Chem. 72 (2000) 5576.
[50] L.H. Shi, X.Q. Liu, H.J. Li, G.B. Xu, Electroanalysis 18 (2006) 1584.
[51] S.N. Brune, D.R. Bobbitt, Talanta 38 (1991) 419.
[52] M. Zorzi, P. Pastore, F. Magno, Anal. Chem. 72 (2000) 4934.

Electrophoretic separation with 2-mm inner diameter fused-silica microcolumn packed with quartz microncrystals and its application

Lian Li, You-Zhao He*, Wu-Er Gan, Xiao-Kui Wang, Hai-Yang Xie, Yong Gao

Department of Chemistry, University of Science and Technology of China, Hefei, Anhui 230026, China

ABSTRACT

The feasibility of a microcolumn electrophoresis technique was investigated with a 100 mm length, 2 mm I.D. fused-silica microcolumn packed with uniform quartz microncrystals prepared by hydrothermal synthesis. To evaluate the separation technique, tryptophan, phenylalanine and tyrosine were primarily separated by the microcolumn electrophoresis and detected at 216 nm without derivatization by an ordinary spectrophotometer. The separation conditions of the amino acids were optimized. With 1.5 mmol/L disodium phosphate buffer solution (pH 11.5) containing 25% (v/v) methanol and 10% (v/v) acetonitrile, the three amino acids were separated and the separation efficiency of tryptophan was 4.5×10^4 plates/m. The limits of detection were 0.035, 0.22 and 0.20 µmol/L, respectively. The sample capacity of the electrophoretic microcolumn achieved 35 µL. The proposed method was used to determine these amino acids in compound amino acid injection samples without derivatization. For the simplicity and portability of the microcolumn electrophoresis, it is studied as one of the high-performance separation techniques for an in situ and real-time electrokinetic flow analysis system. For its high detection sensitivity and large sample capacity, it can be developed for preparative electrophoresis.

© 2009 Elsevier B.V. All rights reserved.

1. Introduction

Electrophoresis is one of the efficient separation techniques in biochemical and clinical analysis. In particular, capillary electrophoresis (CE) has been employed widely owing to its high separation efficiency, fast analytical velocity, low sample consumption and multiform separation modes [1–7]. On the other hand, CE has its shortcomings too, such as low sample loadability and dissatisfactory detection sensitivity, resulting from its small sample volume and short light path of the separation capillary. However, large electrophoresis channel can enhance Joule heat and deteriorate the separation efficiency. The thermal broadening of analyte zones is proportional to the sixth power of inner diameter of electrophoretic channel [8]. Thus, the separation capillary larger than 0.2 mm I.D. is rarely adopted in CE. To improve detection sensitivity, reduce Joule heat and enhance sample capacity, millimeter monolith microcolumns filled with purchased fine quartz sand were proposed for electrochromatographic and chromatographic separations of an electrokinetic flow analysis (EFA) system by our group [9–11]. Although the thermal effect was reduced and the detection sensitivity was improved, the separation efficiencies of the monolithic microcolumns were not satisfactory because of the irregular shape and large size of the purchased quartz sand.

In this paper, the feasibility of an electrophoresis technique was investigated using a 2 mm I.D. fused-silica microcolumn packed with uniform quartz microncrystals prepared by hydrothermal synthesis. To evaluate the electrophoretic technique, three underivatized amino acids of tryptophan, phenylalanine and tyrosine were primarily separated by the proposed electrophoresis technique and detected at 216 nm by an ordinary spectrophotometer. The separation conditions were optimized. The electrophoretic technique was applied to the analysis of the three amino acids in compound amino acid injection samples successfully.

The microcolumn electrophoresis is studied as one of the high-performance separation techniques of the portable EFA system [9–14], and can develop to be preparative electrophoresis.

2. Experimental

2.1. Chemicals and materials

Methanol and acetonitrile were of chromatographic grade. Other reagents were of analytical grade. All the reagents were purchased from Sinopharm Chemical Reagent (Shanghai, China). Silica gel was obtained from Minuteness Nano-Technology (Shanghai, China). Compound amino acid injection samples were purchased from local drugstores. Distilled water was obtained from a tri-distilled

---

* Corresponding author. Tel.: +86 5513607072; fax: +86 5513603388.
E-mail address: yzhe@ustc.edu.cn (Y.-Z. He).
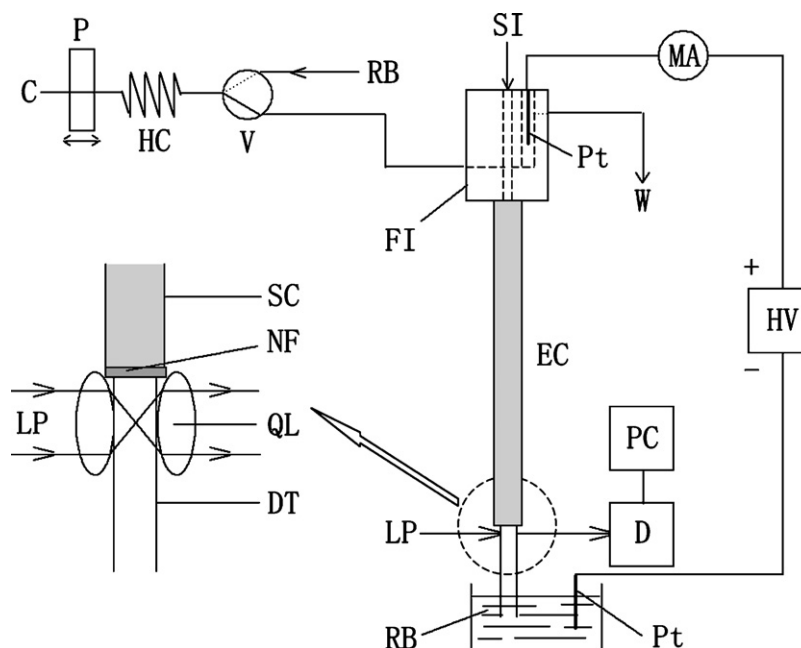
Fig. 1. Schematic diagram of electrokinetic flow analysis system. C, carrier; D, spectrophotometer; DT, detection tube; EC, electrophoretic microcolumn; FI, flow interface; GF, glass frit; HC, holding coil; HV, high-voltage power supply; LP, light path; MA, milliampere meter; NM, nylon membrane; P, electroosmotic pump; PC, personal computer; Pt, platinum electrodes; QL, quartz lens; RB, running buffer; SC, separation column; SI, sample injection; V, solenoid valve; W, waste.

water system (SZ-3 Huxi Analytical Instrument Factory, Shanghai, China).

Three stock solutions of 1.25 mmol/L tryptophan, 5.0 mmol/L phenylalanine and 5.0 mmol/L tyrosine were prepared by dissolving each reagent with distilled water and reserved at 4 °C. The mixed standard solutions were obtained by diluting the stock solutions with distilled water. 1.5 mmol/L disodium phosphate (pH 11.5) containing 25% (v/v) methanol and 10% (v/v) acetonitrile was used as the running buffer of the microcolumn electrophoresis, and 0.5 mmol/L hexamethylene tetramine was adopted as the electroosmotic pump carrier.

The fused-silica tubes of 2 and 1.5 mm I.D. were purchased from Lianyungang Dongxin Quartz Products (Jiangsu, China). Nylon membrane with 0.20 µm pore size was obtained from Millipore (Cork, Ireland).

2.2. Instrumentation

The EFA system consisted of one electrophoretic microcolumn unit, one laboratory-made electroosmotic pump, two electrophoretic power supplies (DYY-12C, 10–5000 V and DYY-III-4, 20–1600 V, Liuyi Instrument Factory, Beijing, China) providing the voltages for electrophoretic separation and electroosmotic pump respectively, one spectrophotometer (UV-9100, Rayleigh Analytical Instruments, Beijing, China), one personal computer, one three-way solenoid valve (161T031, Nreseach, Caldwell, NJ, U.S.A.) and 1–50 µL HPLC syringes (Gaoge Instruments, Shanghai, China), as shown in Fig. 1. The laboratory-made electrophoresis microcolumn unit was composed of one electrophoretic microcolumn made with a 100 mm × 2 mm I.D. fused-silica tube (separation column) jointed with a 20 mm × 1.5 mm I.D. fused-silica tube (detection tube) by fritting and packed with uniform quartz microcrystals, one on-column optical detection unit assembled with two quartz lenses of 4 mm focus and their brass holders fixed to the separation column, one PEEK flow interface installed on the top of the electrophoretic microcolumn and one waste buffer reservoir.

The flow interface was adopted to introduce the running buffer solution and mount a high potential electrode for the electrophoresis. The sample solutions were injected on the top of the microcolumn through a lockable hole of the interface by a microliter syringe. The running buffer was aspirated and propelled by the electroosmotic pump at 2.0 mL/min (−500 V) and 0.1 mL/min (25 V), respectively. The flow rate and direction of the pump were regulated by the working voltage and voltage polarity. The relative standard deviation (RSD) of the pump flow rate was 4.0%, measured each 10 min in 4 h. The pump and solenoid valve were controlled by a personal computer with a laboratory-made interface card and a Visual C program written by our group. In addition, the carrier solution inside the pump chambers should be replaced immediately after the pump was closed.

An ultrasonic cleaner (S-2200, 120 W, 35 kHz, J & L Technology, Shanghai, China) was used for degassing of the standard and buffer solutions. A high temperature oven (SG 2-3-10, 3 kW, 1000 °C, Lixin Electric Apparatus Factory, Shanghai, China) was employed for hydrothermal synthesis.

2.3. Preparation of quartz microncrystals

Referring to the preparation of quartz nanocrystals [15,16], quartz microncrystals were prepared by hydrothermal synthesis in a stainless steel autoclave with a nickel inner lining of 36 cm³. 1.8 g silica gel was mixed with 27 mL, 0.41 mol/L potassium hydroxide for 15 min by the ultrasonic cleaner and transferred into the nickel lining of the autoclave. The autoclave temperature was enhanced to 350 °C at 10 °C/min and kept at 350 °C for 2 h. After cooled to room temperature, the quartz microncrystals were washed with distilled water and ethanol by a centrifuge, and dried by a vacuum drier. The crystalline phase was identified by an X-ray diffractometer (Philips X'Pert Pro Super, Amsterdam, The Netherlands) with Cu Kα radiation (λ = 1.54056 Å) under the operation conditions of 40 kV and 40 mA. The morphology was observed by a scanning electron microscope (KYKY 1010B, KYKY Technical Development, Beijing, China) with a magnification of 2000, as shown
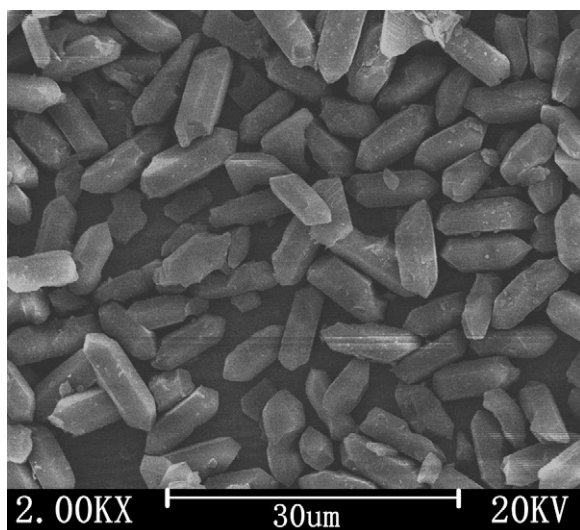
Fig. 2. Scanning electron micrograph of quartz microncrystals. The micrograph is observed with a magnification of 2000. The preparation conditions are 1.8 g silica gel mixed with 27 mL 0.41 mol/L KOH and synthesized at 350 °C for 2 h in an autoclave.

Fig. 3. Effect of electric field strength on electric current in electrophoretic microcolumns. Curve 1 and 2 represent the thermal effect in the microcolumns (100 mm length, 2 mm I.D. and 4 mm O.D.) packed without and with the quartz microncrystals, respectively. The running buffer is 1.5 mmol/L disodium phosphate (pH 11.5) containing 25% (v/v) methanol and 10% (v/v) acetonitrile.

in Fig. 2. The average dimension of the quartz microncrystals was $9 \, \mu m \times 3.8 \, \mu m$.

2.4. Electrophoretic microcolumn packed with quartz microncrystals

Before packing the quartz microncrystals, the separation tube was washed with 0.1 mol/L HCl, distilled water, 0.1 mol/L NaOH and distilled water in turn, and dried at 60 °C for 1 h; the quartz microncrystals were flushed with 0.01 mol/L HCl, distilled water and a packing buffer solution of 2 mmol/L sodium acetate (pH 3.0), and then soaked in the packing buffer for 6 h. Two pieces of nylon membrane with 0.20 μm pore size were placed between the separation and detection tube to hold the quartz microncrystals inside the microcolumn. The membrane was compatible to the organic solvents added in the running buffer (e.g. methanol and acetonitrile) and avoided the bubble formation better than a column frit. The slurry solution of the quartz microncrystals in the packing buffer was introduced into the separation column slowly by vibration. When the whole microcolumn was filled with the quartz microncrystals, it was further packed by both the effects of electroosmotic flow (EOF) at 500 V and vibration on the side column. The microcolumn should be packed compactly and homogeneously. After completed the microcolumn packing, its top was sealed with a piece of nylon membrane and a nylon filter plate of 0.5 mm thickness.

2.5. Separation procedure with microcolumn zone electrophoresis

The electrophoretic microcolumn was equilibrated with the running buffer before the separation, and the standard and buffer solutions were degassed for 5 min ultrasonically. The mixed standard solutions were injected on the top of the microcolumn by a syringe quantitatively. Three amino acids were separated in the electrophoretic microcolumn at 1200 V, detected at 216 nm by the spectrophotometer and recorded by the personal computer. Between the electrophoretic runs, the microcolumn was flushed with the running buffer for 5 min electrokinetically. A milliampere meter was employed to measure the electric current during the electrophoretic separation. When the separation efficiency of the electrophoretic microcolumn decreased to 50% of the original one, it should be washed with 0.1 mol/L HCl, 0.1 mol/L NaOH and the running buffer electrokinetically.

3. Results and discussion

3.1. Electrophoretic microcolumn unit

Joule heat of the electrophoretic microcolumn can be limited by packing the uniform quartz microncrystals. Curve 1 and 2 of Fig. 3 displayed the effect of electric field strength on electric current of the microcolumns packed without and with the quartz microncrystals, respectively. The data of the figures were the mean value obtained from three independent determinations. The electric current of the former was much higher and increased faster than that of the latter under the same electric field strength. For the slope of Curve 1 increased from 10 to 70 V/cm obviously, the excessive Joule heat occurred in the microcolumn without the quartz microncrystals. On the contrary, the slope of Curve 2 for the microcolumn packed with the quartz microncrystals kept almost constant by increasing the electric field strength to 140 V/cm. The experimental results indicated that the Joule heat was reduced by packing the quartz microncrystals in the electrophoretic microcolumn. With the electric field strength higher than 140 V/cm, a few small bubbles were formed in the microcolumn.

In addition, the separation efficiency and Joule heat of the electrophoretic microcolumn packed with purchased fine quartz sand were investigated with the average sizes of 45–360 μm. The experimental results showed that the separation efficiency was enhanced and the Joule heat was reduced by decreasing the size of the fine quartz sand. For example, the average sizes were reduced from 360 to 45 μm, the separation efficiencies of the microcolumn electrophoresis were increased from 3.0×10^3 to 7.0×10^3 plates/m. For the unsatisfactory separation efficiency, the microcolumn electrophoresis packed with regular quartz microncrystals prepared by hydrothermal synthesis was put forward.

3.2. Buffer system of electrophoretic separation

Amino acids can be used as the target compounds in the evaluation of electrophoretic techniques [17–20]. Tryptophan, phenylalanine and tyrosine are the only a few amino acids possessing UV absorption and can be detected by UV–vis spectrophotometry without derivatization. Their isoelectric points (pI) are close to each other at 5.89, 5.48 and 5.66, respectively. Therefore, the three amino acids were primarily chosen to evaluate the
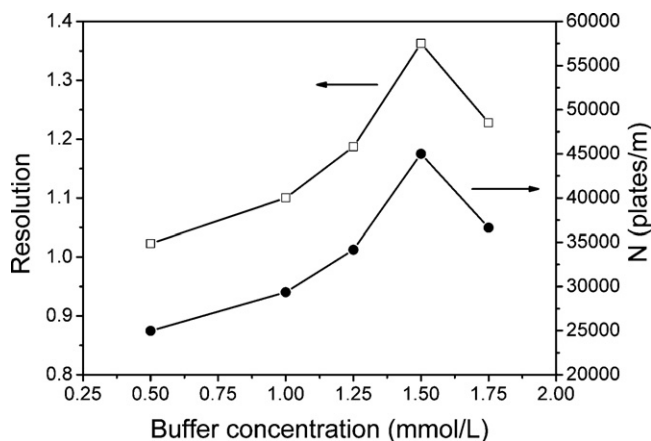
Fig. 4. Effect of disodium phosphate concentration on electrophoretic resolution between tryptophan and phenylalanine and separation efficiency of tryptophan. The electrophoretic separations are performed in disodium phosphate buffer solutions (pH 11.5) containing 25% (v/v) methanol and 10% (v/v) acetonitrile using a 100 mm × 2.0 mm I.D. separation microcolumn packed with the quartz microncrystals at 1200 V. 1-μL mixed standard solution of 0.125 mmol/L tryptophan, 0.50 mmol/L phenylalanine and 0.50 mmol/L tyrosine is injected into the electrophoretic microcolumn and detected at 216 nm.

Fig. 5. Effect of organic solvents on electrophoretic resolution. Curve 1 displays the influence of methanol concentration in 1.5 mmol/L disodium phosphate buffer solution (pH 11.5) containing 10% (v/v) acetonitrile and Curve 2 represents the influence of acetonitrile concentration in the same buffer solution containing 25% (v/v) methanol. Other conditions are the same as in Fig. 4.

separation properties of the microcolumn electrophoresis. For the resolution between tyrosine and two others was higher than that between tryptophan and phenylalanine, the subsequent discussion was focused on the separation of tryptophan and phenylalanine in the optimization of the separation conditions, including buffer pH, buffer concentration and organic additives, etc.

Running buffer system is an important condition for the electrophoretic separation. Two buffer systems of disodium phosphate–sodium hydroxide and sodium tetraborate–sodium hydroxide were investigated. Owing to the better electrophoretic resolution for the amino acids, disodium phosphate buffer solution was chosen in the following separations.

The effect of buffer pH on the electrophoretic resolution between tryptophan and phenylalanine was examined from pH 9.5 to 12.0 for 1.5 mmol/L disodium phosphate buffer solution containing 25% (v/v) methanol and 10% (v/v) acetonitrile. The experimental results indicated that the satisfactory separation efficiency and resolution of the amino acids were obtained with the pH value higher than 10.5 and 11.0, respectively. By considering the separation efficiency and resolution comprehensively, the pH value from 11.0 to 12.0 was examined particularly and the optimal resolution was obtained at pH 11.5. The migration time of the amino acids was prolonged and their apparent velocities were reduced with the increase of pH value and electrolyte concentration. On the other hand, the resolutions were reduced with the buffer solutions higher than pH 11.5, due to the high electrolyte concentration and thermal effect for the electrophoretic separation. As a result, pH 11.5 disodium phosphate solution was selected in the electrophoretic separation.

The effect of buffer concentration on the electrophoretic resolution between tryptophan and phenylalanine was investigated from 0.5 to 1.75 mmol/L disodium phosphate (pH 11.5) containing 25% (v/v) methanol and 10% (v/v) acetonitrile. As shown in Fig. 4, the optimal resolution between tryptophan and phenylalanine and separation efficiency of tryptophan were observed at 1.5 mmol/L disodium phosphate. By increasing the disodium phosphate concentration from 0.5 to 1.5 mmol/L, the improved resolution resulted from the reduction of the diffusion coefficient and resultant velocity. For the optimal separation efficiency of tryptophan was observed at 1.5 mmol/L disodium phosphate, it implied that the diffusion coefficient of the amino acids had the main effect on the separation efficiency by increasing the buffer con-

centration from 0.5 to 1.5 mmol/L. With the disodium phosphate concentration higher than 1.5 mmol/L, the thermal effect caused the reduction of the separation resolution and efficiency. So, 1.5 mmol/L was adopted as the running buffer concentration in this work.

Organic additives of methanol, acetonitrile and isopropyl alcohol were investigated in this work, respectively. It was found that methanol and acetonitrile were more effective on the separation resolution of tryptophan and phenylalanine. The optimal resolutions were observed at 25% (v/v) methanol in Curve 1 and 10% (v/v) acetonitrile in Curve 2 of Fig. 5.

3.3. Analytical characteristic of microcolumn electrophoresis

The sample capacity of the electrophoretic microcolumn was also investigated. According to the experimental results, the peak height of the amino acids increased almost linearly with the enhanced sample volume from 0.1 to 40 μL containing the same concentrations of the amino acids, and then changed slightly with the sample volume larger than 40 μL. Based on the chromatographic definition, the sample capacity is the sample volume to increase the standard deviation of chromatographic peak to 5%. After surveyed the peak widths, the sample capacity of the electrophoretic microcolumn was about 35 μL. Therefore, the sample capacity and detection sensitivity of the microcolumn electrophoresis could be improved.

The electropherogram of tryptophan, phenylalanine and tyrosine is illustrated in Fig. 6a. Three amino acids were separated by the microcolumn zone electrophoresis with a larger sample volume of 30 μL and lower sample concentrations of 2.5–10 μmol/L. The asymmetry factor of tryptophan, phenylalanine and tyrosine peak was 1.05, 0.96 and 1.03, respectively, and in the range from 0.95 to 1.05. It indicated that the analyte peaks were symmetric. The separation efficiencies of tryptophan, phenylalanine and tyrosine were 4.5×10^4, 4.0×10^4 and 3.7×10^4 plates/m, respectively. It manifested that the electrophoretic microcolumn packed with the uniform quartz microncrystals was able to limit Joule heat and achieve satisfactory separation efficiency. The linear concentration range of tryptophan, phenylalanine and tyrosine was 0.11–16, 0.70–100 and 0.60–90 μmol/L, respectively, with the correlative coefficients higher than 0.997. The RSDs of the peak height and migration time were less than 4.8% and 0.35%, respectively, which were obtained by five individual runs.

Table 1
LODs of amino acids by electrophoresis and HPLC with different detection techniques.

Separation method	Detection technique	LOD (µmol/L)
Column electrophoresis	Underivatized direct UV	0.035–0.22 (Trp, Tyr, Phe)
Capillary electrophoresis	Laser-induced fluorescence [21]	0.093–0.097 (Phe, Tyr)
	Mass spectrometry [22]	0.1–0.4 (Phe, Trp, Tyr)
	Contactless conductivity detection [23]	3.0–3.8 (Trp, Tyr, Phe)
	Indirect UV [24]	3.2–7.2 (Tyr, Phe, Trp)
	Derivatized direct UV [25]	2.0–39 (Tyr, Trp, Phe)
	Underivatized direct UV [26]	21–140 (other amino acids)
HPLC	Derivatized fluorescence [27]	0.016–0.031 (Phe, Tyr)
	Derivatized direct UV [28]	0.098–0.22 (Trp, Phe, Tyr)
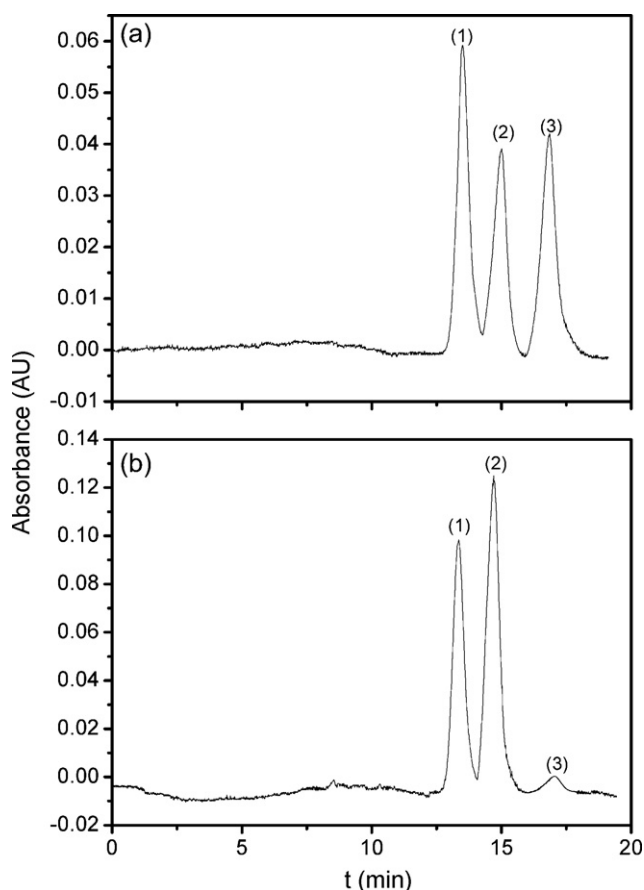
Fig. 6. Electropherogram of tryptophan (1), phenylalanine (2) and tyrosine (3) in a mixed standard solution (a) and a sample of compound amino acid injection (b). The buffer concentration of disodium phosphate is 1.5 mmol/L. The injection volume of the mixed standard solution is 30 µL, containing 2.5 µmol/L tryptophan, 10 µmol/L phenylalanine and 10 µmol/L tyrosine. Other conditions are the same as in Fig. 4.

The limits of detection (LODs) of the microcolumn electrophoresis were compared with different detection techniques of CE [21–26] and HPLC [27,28], as listed in Table 1. The LODs of tryptophan, phenylalanine and tyrosine were 0.035, 0.22 and 0.20 µmol/L, respectively obtained with 3-times signal-to-noise ratio. It was found that the LODs of the microcolumn electrophoresis with an ordinary UV–vis spectrophotometer were close to laser-induced fluorescence detection, and better than mass spectrometric and derivatized UV–vis spectrometric detection of CE. By comparing with HPLC, the LODs of the microcolumn electrophoresis with the underivatized UV spectrometric detection were similar to those of derivatized UV–vis spectrometric detection, but worser than fluorescence detection of HPLC.

3.4. Separation of compound amino acid injection samples

The underivatized tryptophan, phenylalanine and tyrosine in compound amino acid injection samples were analyzed to evaluate the proposed electrophoresis method. A typical electropherogram of tryptophan, phenylalanine and tyrosine in a compound amino acid injection sample is illustrated in Fig. 6b. The compound amino acid injection samples were diluted to 1:1000 with distilled water and then analyzed by the microcolumn electrophoresis directly. The analyte recoveries were obtained in the range of 91.3–105.8%. The analyte concentrations found in four compound amino acid injection samples are listed in Table 2. The results are close to the labelled concentrations. With high separation efficiency, large sample capacity, enhanced detection sensitivity and satisfactory analysis precision, the proposed microcolumn electrophoresis can be used in the sample analysis with low concentration and large volume. It can also be developed as preparative electrophoresis.

4. Conclusion

The experimental results indicated that the microcolumn electrophoresis with a 2 mm I.D. fused-silica microcolumn packed with the uniform quartz microncrystals was able to be employed as a high-performance separation technique. The electrophoretic technique not only can reduce Joule heat, but also improve LOD and sample capacity. From the analysis of diluted tryptophan, phenylalanine and tyrosine in four compound amino acid injection samples, it verified that trace analytes can be determined directly by the microcolumn electrophoresis coupled with an ordinary spectrophotometer without preconcentration. Compared with CE, the microcolumn electrophoresis is suitable for the analysis of low concentration and large volume samples. It can be developed for preparative electrophoresis. Compared with other

Table 2
Labelled concentrations, detected concentrations and recoveries of amino acids in four compound amino acid injection real samples.

Amino acids	Labelled concentration (g/L)	Detected concentration (g/L)[a]				Recovery (%)[a]
		1#	2#	3#	4#	
Tryptophan	0.90	0.90	0.84	0.92	0.87	96.5
Phenylalanine	5.33	5.43	5.35	5.22	5.29	105.8
Tyrosine	0.25	0.27	0.24	0.25	0.28	91.3

[a] The data were the mean value obtained from three independent determinations.

high-performance separation techniques, its simpleness and portability are the attractive trends of separation science, and the analytical technique can be employed in in situ and real-time analysis.

Acknowledgement

References

[1] J.W. Jorgenson, K.D. Lukacs, Anal. Chem. 53 (1981) 1298.
[2] J.W. Jorgenson, K.D. Lukacs, Science 222 (1983) 266.
[3] S. Hjerten, J. Chromatogr. 271 (1983) 1.
[4] S. Terebe, K. Otsuka, K. Ichikawa, A. Tsuchiya, T. Ando, Anal. Chem. 56 (1984) 111.
[5] S. Hjerten, J. Chromatogr. 347 (1985) 191.
[6] J.W. Jorgenson, K.D. Lukacs, J. Chromatogr. 218 (1981) 209.
[7] A. Manz, D.J. Harrison, E.M.J. Verpoorte, J.C. Fettinger, A. Paulus, H. Lüdi, H.M. Widmer, J. Chromatogr. 593 (1992) 253.
[8] J.H. Knox, I.W. Grant, Chromatographia 24 (1987) 135.
[9] Y.Z. He, X.K. Wang, N. Deng, L. Wang, F. Han, Chin. Pat. ZL200510038677.5 (2008).
[10] N. Deng, Y.Z. He, L. Wang, X.K. Wang, Q.D. Su, Anal. Chem. 77 (2005) 5622.
[11] L. Wang, Y.Z. He, N. Deng, X.K. Wang, G.N. Fu, Instrum. Sci. Technol. 34 (2006) 743.
[12] W.E. Gan, L. Yang, Y.Z. He, R.H. Zeng, M.L. Cervera, M. de la Guardia, Talanta 51 (2000) 667.
[13] L. Wang, Y.Z. He, G.N. Fu, Y.Y. Hu, X.K. Wang, Talanta 70 (2006) 358.
[14] F. Han, Y.Z. He, L. Li, G.N. Fu, H.Y. Xie, W.E. Gan, Anal. Chim. Acta 618 (2008) 79.
[15] J.F. Bertone, J. Cizeron, R.K. Wahi, J.K. Bosworth, V.L. Colvin, Nano Lett. 3 (2003) 655.
[16] K. Yanagisawa, Y. Zhu, A. Onda, K. Kajiyoshi, J. Mater. Sci. 39 (2004) 2931.
[17] Z.R. Xu, Y. Lan, X.F. Fan, Q. Li, Talanta 78 (2009) 448.
[18] M.M. Hsieh, S.M. Chen, Talanta 73 (2007) 326.
[19] A. Carrasco-Pancorbo, A. Cifuentes, S. Cortacero-Ramírez, A. Segura-Carretero, A. Fernández-Gutiérrez, Talanta 71 (2007) 397.
[20] W. Yang, Z. Zhang, W. Deng, Talanta 59 (2003) 951.
[21] K. Thongkhao-On, S. Kottegoda, J.S. Pulido, S.A. Shippy, Electrophoresis 25 (2004) 2978.
[22] T. Soga, Y. Kakazu, M. Robert, M. Tomita, T. Nishioka, Electrophoresis 25 (2004) 1964.
[23] P. Tůma, E. Samcová, K. Andělová, J. Chromatogr. B 839 (2006) 12.
[24] G. Žunić, Z. Jelić-Ivanović, M. Čolić, S. Spasić, J. Chromatogr. B 772 (2002) 19.
[25] F. Chen, S. Wang, W. Guo, M. Hu, Talanta 66 (2005) 755.
[26] N.V. Komarova, J.S. Kamentsev, A.P. Solomonova, R.M. Anufrieva, J. Chromatogr. B 800 (2004) 135.
[27] L. Bosch, A. Alegría, R. Farré, J. Chromatogr. B 831 (2006) 176.
[28] S. Gómez-Alonso, I. Hermosín-Gutiérrez, E. García-Romero, J. Agric. Food Chem. 55 (2007) 608.

Grafting of molecularly imprinted polymers from the surface of silica gel particles via reversible addition-fragmentation chain transfer polymerization: A selective sorbent for theophylline

Yong Li [a,b], Wen-Hui Zhou [a,b], Huang-Hao Yang [b,*], Xiao-Ru Wang [a,b,**]

[a] College of Chemistry and Chemical Engineering, Ocean University of China, Qingdao 266003, China
[b] The First Institute of Oceanography, SOA, Qingdao 266061, China

ABSTRACT

Molecularly imprinted polymers (MIPs) were grafted successfully from the surface of silica gel particles via surface initiated reversible addition-fragmentation chain transfer (RAFT) polymerization using RAFT agent functionalized silica gel as the chain transfer agent. The intrinsic characteristics of the controlled/living polymerization mechanism of RAFT allowed for the effective control of the grafting process. Thus the grafting copolymerization of methacrylic acid and divinyl benzene in the presence of template theophylline led to thin MIP film coating silica gel (MIP-Silica). The thickness of MIP film prepared in this study is about 1.98 nm, which was calculated from the nitrogen sorption analysis results. Measured binding kinetics for theophylline to the MIP-Silica and MIPs prepared by conventional bulk polymerization demonstrated that MIP-Silica had improved mass-transfer properties. In addition, the theophylline-imprinted MIP-Silica was used as the sorbent in solid-phase extraction to determine theophylline in blood serum with satisfactory recovery higher than 90%. Nonspecific adsorption of interfering compounds can be eliminated by a simple elution with acetonitrile, without sacrificing the selective binding of theophylline.

1. Introduction

Molecularly imprinted polymers (MIPs), first introduced by Mosbach and co-workers [1] and Wulff [2], are widely reported materials that can be used as biomimetic molecular recognition elements. The synthesis of MIPs involves the formation of a complex of a target molecule (template) with one or more functional monomers though either covalent or noncovalent bonds followed by a polymerization reaction with excess cross-linking agent. Upon removal of the template, the binding sits are produced that are complementary to the template in shape, size, and the position of the functional groups. The stability, ease of preparation and low cost of these MIPs make them particularly attractive [3–5]. However, the conventional techniques used to prepare MIPs most often result in materials exhibiting high affinity and selectivity but poor site accessibility for the target molecule [4–6].

Recently, a new molecular imprinting technique called "grafting from" technique has emerged to overcome this drawback [7–11]. In the "grafting from" technique, the initiating groups were immobilized on the surface of a solid support. During the course of polymerization, the grafted MIPs were propagated from the surface of the solid supports. Using the "grafting from" technique, MIP film with high graft density and nanometer thickness can be prepared on the surface of a solid support. The resulting MIP composites have the advantages of more accessible binding sites and faster mass transfer compared to the MIPs prepared by conventional bulk polymerization techniques. Recently, the "grafting from" technique has been used by several research groups to produce imprinted polymer films on various substrates, including silica gel [7–10] and silica nanoparticle [11].

In recent years, the use of surface initiated controlled/living radical polymerization (CRP) has proven to be the most versatile approach for producing a wide range of polymer chains on solid surfaces [12,13]. In CRP, the life-time of the growing radical can be controlled, resulting in the synthesis of polymer chains with predefined molar mass, low polydispersity, controlled composition, and functionality. In general surface initiated CRP can be achieved by stable free-radical polymerization, e.g. nitroxide-mediated processes (NMP), metal catalyzed atom transfer radical polymerization (ATRP) and degenerative transfer, e.g. reversible

addition-fragmentation chain transfer (RAFT). Recently, significant interest has been shown in the use of surface initiated CRP for the preparation of MIP composites [14–18].

This paper describes the use of surface initiated RAFT polymerization technique to functionalize silica gel with molecularly imprinted polymer films. RAFT has recently emerged as a promising CRP technique due to its versatility and simplicity, and the product polymer is free from the contamination of metal catalyst [19]. The RAFT technique is compatible with almost all of the conventional radical polymerization monomers. In our approach, the RAFT agents are directly immobilized on the surface of silica gel. The resulting thin MIP film coated silica can be applied in solid-phase extraction, HPLC as well as in capillary electrochromatography.

Theophylline has long been used to treat asthmatic symptoms in children and adults as well as apnea in premature infants. This drug is effective, however, over a narrow concentration range. At high concentrations, it is known to cause permanent neurological damage or death. Current measurement of theophylline levels are done by GC or LC method and by immunoassays. However, these approaches can be seriously disadvantaged in the presence of a complex sample matrix containing much interference such as blood serum. Thus using molecularly imprinted polymers to selectively extract theophylline from serum is very attractive [20,21].

2. Experimental

2.1. Reagents

4-(Chloromethyl) phenyltrimethoxysilane and phenylmagnesium bromide (PMB, 3 M in ether) were purchased from Alfa. Theophylline, theobromine and caffeine were purchased from Sigma. Methacrylic acid (MAA) was purchased from Alfa and distilled to remove the polymerization inhibitor before use. Divinylbenzene (DVB) containing 20% ethylvinylbenzene was purchased from Fluka and treated with basic alumina immediately prior to use to remove the polymerization inhibitor. Silica gel (particle size 35–70 μm, pore size 15 nm, pore volume $1.15\,cm^3/g$, surface area $300\,m^2/g$) was purchased from Aldrich.

2.2. Synthesis of chloromethyl-phenyl functionalized silica gel (Cl-Silica)

The silica gel was pretreated in order to eliminate any surface contaminants and to activate the surface silanol groups for silanization. In a typical experiment, silica gel were pretreated by reflux in 10% HCl solution for 8 h, rinsed by deionic water, and then dried in vacuum at 120 °C before use.

Dried silica gel (500 mg), 4-(chloromethyl)phenyltrimethoxysilane (2 mmol) and 10 mL absolutely dry toluene were introduced into a conical flask under the atmosphere of nitrogen. Keeping under constant temperature of 90 °C and with continuous stirring, the reaction was allowed to proceed for 24 h. The particles were then separated from the mixture via centrifugation. The product was washed with toluene for five times and then washed with methanol for five times in order to remove excess 4-(chloromethyl)phenyltrimethoxysilane. At the end, the obtained Cl-Silica was dried under vacuum at room temperature.

2.3. Synthesis of SC(S)Ph-Silica

PhC(S)SMgBr was prepared using phenylmagnesium bromide and carbon disulfide. The phenylmagnesium bromide solution (0.6 M in dry tetrahydrofuran) was warmed to 50 °C and carbon disulfide was added over 10 min, then the reaction mixture was kept at 50 °C for 1 h. To the resultant brown mixture was added Cl-Silica (500 mg) and the reaction temperature was kept at 50 °C

for 24 h. Ice hydrochloric acid (1 M, 50 mL) was then added. The product was washed with distilled water for five times and then washed with ether for five times. The RAFT agent functionalized silica gel (SC(S)Ph-Silica) obtained was dried under vacuum at room temperature.

2.4. Grafting of MIP film on silica gel (MIP-Silica)

The grafting was performed in a flask containing 300 mg of SC(S)Ph-Silica suspended in a polymerization mixture consisting of 1 mmol of theophylline, 12 mmol of MAA, 60 mmol of DVB and 4 mg of azobis (isobutyronitrile) (AIBN) dissolved in 20 mL of chloroform. After sealing, mixing, and sparging the mixture with nitrogen for 10 min, the flask was placed in a thermostated oil bath at 55 °C for 24 h. After polymerization, the product was extracted with ethanol containing 20% acetic acid using a Soxhlet apparatus for 24 h. Then the product was washed with ethanol for three times and dried under vacuum at room temperature. A similar procedure with no added template was used to prepare non-imprinted polymer composites (NIP-Silica) as control.

2.5. Synthesis of conventional MIP particles using conventional bulk technique (MIP)

To compare the binding ability of MIP-Silica materials to conventional MIP materials, we prepared the latter using the bulk synthesis technique. 1 mmol of theophylline was dissolved in a mixture of 12 mmol of MAA, 60 mmol of DVB, 0.6 mmol of AIBN and 10 mL of chloroform. The solution was sonicated for 5 min, sparged with nitrogen for 15 min, and then polymerized at 60 °C for 24 h. Following polymerization, the bulk polymer was dried overnight under vacuum at 50 °C. Next, it was ground with a mortar and pestle and sieved between 200 and 400 mesh screens to give particles with size dimensions between 38 and 75 μm. Fines were removed by sedimentation from ethanol. The product was extracted with ethanol containing 20% acetic acid using a Soxhlet apparatus for 24 h. Then the product was washed with ethanol for three times and dried under vacuum at room temperature.

2.6. Nitrogen sorption analysis

Nitrogen sorption measurements were performed on a Tristar3000 (Micromeritics Co., USA). Prior to measurements, the samples were heated at 60 °C under high vacuum for at least 12 h. The average pore diameter (dp) was evaluated using the BJH theory.

2.7. Elemental analysis

Elemental analysis was performed on Vario EL III universal CHNOS elemental analyzer (ELEMENTAR, Hanau, Germany).

2.8. Steady-state binding studies

5 mg of MIP-Silica, NIP-Silica, MIP, or NIP particles were contacted with 5 mL of theophylline solutions in acetonitrile with initial concentrations ranging from 0.005 to 0.1 mmol/L. The samples were placed in a constant temperature, reciprocating shaker bath at 35 °C and 80 rpm. Samples were taken at regular time intervals during incubation in order to measure the time needed to reach equilibrium. Initial and final theophylline concentrations were determined by HPLC using UV detection at 270 nm.

2.9. MIP-Silica SPE

Commercial SPE cartridges were emptied from their packing material. Next the cartridge tube and frits were thoroughly cleaned

and dried. 200 mg of MIP-Silica was packed dry in the cartridge and the upper frit was placed on top.

2.10. Serum analysis

To 1 mL of human plasma, 200 μL of a theophylline solution (in methanol) was added, followed with the addition of 200 μL of cold acetonitrile. The mixture was vortex mixed for 1 min and centrifuged at 3000 rpm for 5 min. The supernatant was diluted to 2 mL with addition of water and the mixture was loaded on the MIP-Silica SPE cartridge. The MIP-Silica SPE cartridge had been previously conditioned by adding successively 1 mL methanol and 1 mL water. After loading the sample, the cartridge was washed with 2 mL of acetonitrile. Theophylline was then eluted with 2 mL of acetonitrile containing 5% acetic acid. All the applied fractions were collected and evaporated to dryness (at 45 °C under a stream of N_2). The dry residue was reconstituted with 200 μL of mobile-phase solution (methanol/water, 20/80, v/v), and an aliquot was analyzed on HPLC. Extraction recovery was calculated using the constructed calibration curve.

3. Results and discussion

3.1. Characterization of RAFT agent modified silica gel and MIP-Silica

Previous research has shown that dense polymer films with tunable thickness can be easily grafted from the surfaces of solids with a controlled behavior via surface RAFT polymerization [15,17]. Dithiobenzoate is an excellent RAFT agent for living radical polymerization, and can be fixed onto silica gel for the preparation of MIP-Silica. Fig. 1 shows the method for fixing the

Table 1
Element analysis of silica samples following each functionalization step.

	C/%	S/%	Grafted amount (per g of silica)	Coverage (%)
Cl-Silica	7.37	0.00	0.62 mmol	24.8
SC(S)Ph-Silica	9.54	2.94	0.50 mmol	20.0
MIP-Silica	31.95	2.17		

RAFT agent onto silica gel, and the subsequent growth of MIP film from silica gel via surface RAFT polymerization. In this protocol, 4-(chloromethyl)phenyltrimethoxysilane was immobilized on the surface of silica gel, forming chloromethyl-phenyl functionalized silica gel (Cl-Silica). RAFT agent functionalized silica gel was subsequently produced by substitute reaction of Cl-Silica with PhC(S)SMgBr. In the final step, the initiator was activated to start the polymerization in the presence of template molecule.

Elemental analysis was used to confirm the grafting of MIP film. Table 1 summarizes elemental analysis results of the silica samples following each functionalization step. Amorphous silica gels prepared by myriad ways show similar values of silanol density (4.2–5.7 OH groups/nm^2) with the currently accepted mean value of 5 OH groups/nm^2). In this work, the silica gel had a surface area of 300 m^2/g, which gives an estimated 2.5 mmol/g capacity of silanol groups. The capacity of RAFT agent was 0.50 mmol/g, and thus, 20% of silanol groups were functionalized with RAFT agent. After polymerization, the carbon content of MIP-Silica was much higher than that of SC(S)Ph-Silica. This provides an evidence for the presence of grafted polymer.

Additional evidence for the grafted polymer films was obtained by nitrogen sorption analysis. The average pore diameters of silica samples were evaluated using the BJH theory. Fig. 2 shows the pore size distribution of the bare silica gel and MIP-Silica. The pore size
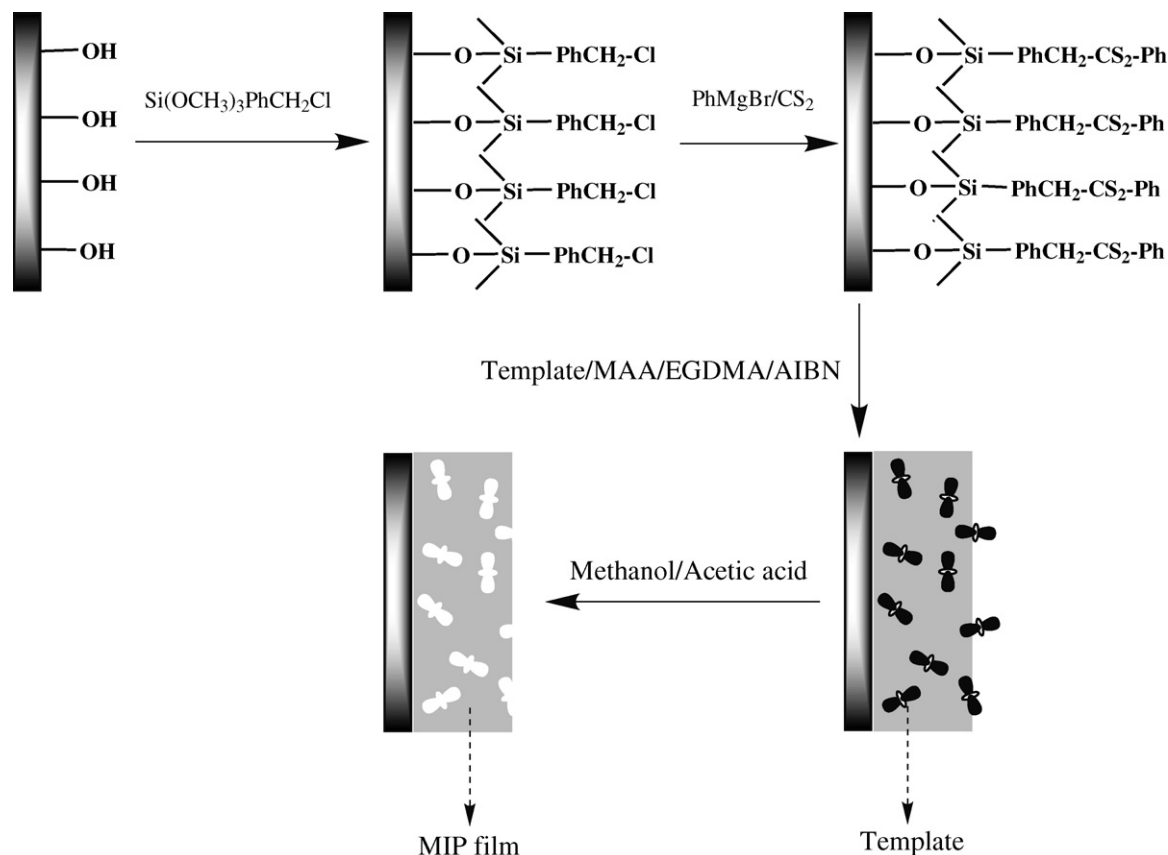
Fig. 1. Outlines of the fixation of RAFT agent onto silica gel and the growth of MIP film from silica gel via surface RAFT polymerization.
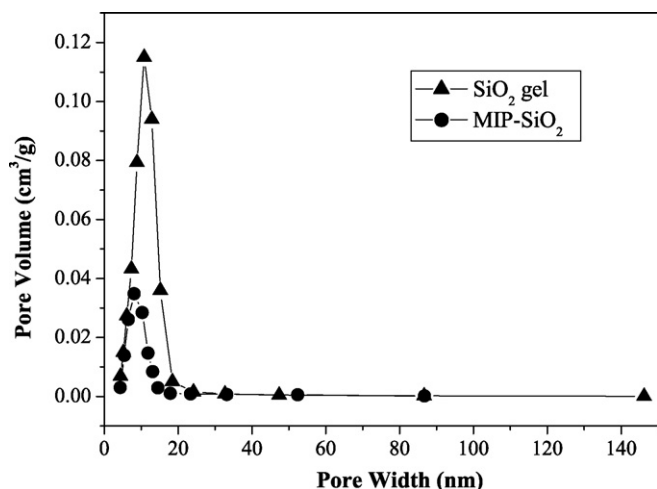
Fig. 2. Pore size distribution of the bare silica gel (▲) and MIP-Silica (●) calculated from the desorption branch of the isotherm obtained from nitrogen sorption measurements.

Fig. 4. Binding behaviors of different compounds on the theophylline imprinted MIP-Silica. Amount of MIP-Silica is 5 mg with sample solution volume 5 mL. The points represent mean values of three measurements.

of bare silica gel is about 12.02 nm. The pore size of MIP-Silica is about 8.06 nm. The thickness of the MIP films is about 1.98 nm. The presence of homogeneously grafted MIP films is obvious from the similar widths of the pore size distribution of the bare silica gel and MIP-Silica.

3.2. Molecular recognition property

The template theophylline recognition ability of the MIP-Silica was investigated by the steady-state binding method. As shown in Fig. 3, the MIP-Silica exhibits a higher capacity for theophylline than the NIP-Silica. The binding selectivity by MIP-Silica towards theophylline against its two structural analogs, theobromine and caffeine was compared. It can be seen from Fig. 4 that the MIP-Silica showed a higher adsorption to theophylline than its structural analogues. This result is similar to that obtained with bulk polymers [6].

Binding kinetics of the template theophylline with MIP-Silica and conventional MIP were evaluated. Fig. 5 shows the adsorption uptake polymer versus the incubation time. The MIP-Silica requires a shorter time to reach equilibrium than does the conventional MIP. Two factors contribute to the faster mass transfer in the MIP-Silica.

First, the MIP-Silica has a large average pore diameter of about 8 nm, which allows the template molecules to diffuse into the MIP-Silica pore rapidly during rebinding. Second, the ultrathin, grafted polymer films allow the template molecules to diffuse into the polymer more efficiently than thick MIP particles.

3.3. Solid-phase extraction of theophylline from serum

The MIP-Silica and corresponding NIP-Silica were packed individually into cartridges to compare their efficiency of extracting theophylline from serum. Fig. 6(a) is the HPLC chromatogram of serum after addition of 10 µg of theophylline, in which the complexity of the serum matrix background is evident. The extraction on MIP-Silica column can successfully clean up the serum matrix, thus allowing the extraction of theophylline with high selectivity (Fig. 6(b)). Contrary to this, NIP-Silica column showed no such selectivity (Fig. 6(c)). Hence MIP-Silica offers itself as a simple and straightforward technique for the direct analysis of theophylline in human serum without lengthy sample cleanup. The extraction recovery of 10 µg/mL theophylline was 90.3%. The relative standard deviation (n = 3) for quantitation was 5.1%, which is a good value for real sample analysis. A standard calibration curve for serum theophylline analysis was constructed, with excellent linearity (R^2 = 0.992) in the concentration range up to 100 µg/mL and a detection limit of 200 ng/mL. Note that this detection limit was bet-

Fig. 3. Amount of bound theophylline by MIP-Silica (▲) and NIP-Silica (●). Experiment was conducted by the addition of 5 mg of MIP-Silica in 5 mL of theophylline solution at room temperature.
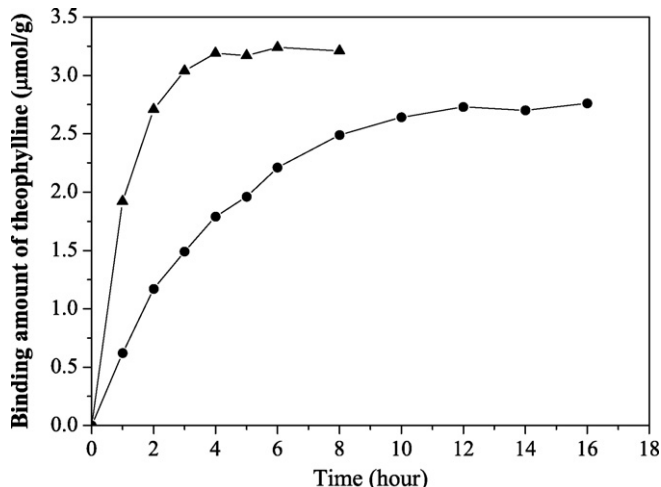
Fig. 5. Binding kinetics of theophylline on MIP-Silica (▲) and MIP (●).
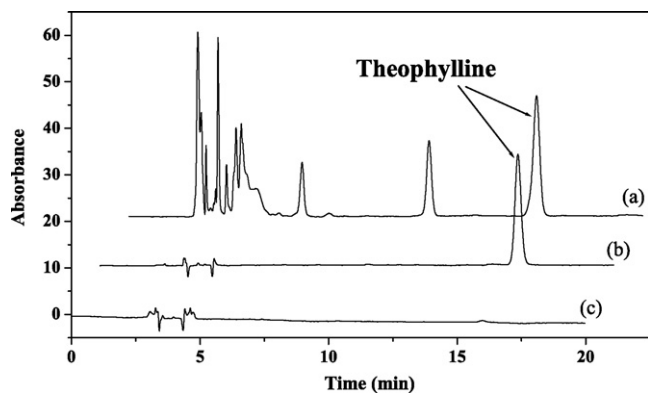
Fig. 6. HPLC chromatograms of (a) serum after addition of 10 μg of theophylline, (b) after extraction on MIP-Silica column and (c) after extraction on NIP-Silica column.

ter than the 500 ng/mL obtained using conventional MIP materials (data not shown). Method repeatability was evaluated by independent preparation and analysis of different serum samples, to produce an intra-assay precision of <7%.

4. Conclusions

This paper describes the use of surface initiated RAFT technique to graft thin MIP films from the silica gel particles. The intrinsic characteristics of the controlled/living polymerization mechanism of RAFT allowed an efficient control of the grafting process. The MIP-silica prepared in this study had improved mass-transfer properties compared with MIPs prepared by conventional bulk polymerization. In addition, MIP-Silica can be used as the sorbent in solid-phase extraction to determine theophylline in blood serum.

Furthermore, the MIP-silica can also be applied in HPLC and capillary electrochromatography.

References

[1] G. Vlatakis, L.I. Andersson, R. Müller, K. Mosbach, Nature 361 (1993) 645.
[2] G. Wulff, Angew. Chem. Int. Ed. 34 (1995) 1812.
[3] C. Alexander, H.S. Andersson, L.I. Andersson, R.J. Ansell, N. Kirsch, I.A. Nicholls, J. O'Mahony, M.J. Whitcombe, J. Mol. Recognit. 19 (2006) 106.
[4] K. Haupt, Anal. Chem. 75 (2003) 376A.
[5] L. Ye, K. Mosbach, Chem. Mater. 20 (2008) 859.
[6] E. Yilmaz, K. Haupt, K. Mosbach, Angew. Chem. Int. Ed. 39 (2000) 2115.
[7] B. Rückert, A.J. Hall, B. Sellergren, J. Mater. Chem. 12 (2002) 2275.
[8] C. Sulitzky, B. Rückert, A.J. Hall, F. Lanza, K. Unger, B. Sellergren, Macromolecules 35 (2002) 79.
[9] C. He, F. Liu, K. Li, W. Liu, Anal. Lett. 39 (2006) 275–286.
[10] M. Shamsipur, J. Fasihi, K. Ashtari, Anal. Chem. 79 (2007) 7116.
[11] N. Pérez-Moral, A.G. Mayes, Macromol. Rapid Commun. 28 (2007) 2170.
[12] S. Edmondson, V.L. Osborne, W.T.S. Huck, Chem. Soc. Rev. 33 (2004) 14.
[13] W. Senaratne, L. Andruzzi, C.K. Ober, Biomacromolecules 6 (2005) 2427.
[14] X. Wei, S.M. Husson, Biomacromolecules 6 (2005) 1113.
[15] M.M. Titirici, B. Sellergren, Chem. Mater. 18 (2006) 1773.
[16] H.J. Wang, W.H. Zhou, X.F. Yin, Z.X. Zhuang, H.H. Yang, X.R. Wang, J. Am. Chem. Soc. 128 (2006) 15954.
[17] C.H. Lu, W.H. Zhou, B. Han, H.H. Yang, X. Chen, X.R. Wang, Anal. Chem. 79 (2007) 5457.
[18] X. Wei, S.M. Husson, Ind. Eng. Chem. Res. 46 (2007) 2117.
[19] C.L. Mccormick, A.B. Lowe, Acc. Chem. Res. 37 (2004) 312.
[20] W.M. Mullett, E.P.C. Lai, Anal. Chem. 70 (1998) 3636.
[21] W.M. Mullett, E.P.C. Lai, J. Pharm. Biomed. Anal. 21 (1999) 835.

Polyaniline and poly(flavin adenine dinucleotide) doped multi-walled carbon nanotubes for p-acetamidophenol sensor

Ying Li, Yogeswaran Umasankar, Shen-Ming Chen*

Department of Chemical Engineering and Biotechnology, National Taipei University of Technology, No. 1, Section 3, Chung-Hsiao East Road, Taipei 106, Taiwan, ROC

ABSTRACT

A conductive biocomposite film (MWCNTs–P*ANIFAD*) which contains multi-walled carbon nanotubes (MWCNTs) along with the incorporation of poly(aniline) and poly(flavin adenine dinucleotide) co-polymer (P*ANIFAD*) has been synthesized on gold and screen printed carbon electrodes by potentiostatic methods. The presence of MWCNTs in the MWCNTs–P*ANIFAD* biocomposite film enhances the surface coverage concentration (Γ) of P*ANIFAD* and increases the electron transfer rate constant (k_s) to 89%. Electrochemical quartz crystal microbalance studies reveal the enhancements in the functional properties of MWCNTs and P*ANIFAD* present in MWCNTs–P*ANIFAD* biocomposite film. Surface morphology of the biocomposite film has been studied using scanning electron microscopy and atomic force microscopy. The surface morphology results reveal that P*ANIFAD* incorporated on MWCNTs. The MWCNTs–P*ANIFAD* biocomposite film exhibits promising enhanced electrocatalytic activity towards the oxidation of p-acetamidophenol. The cyclic voltammetry has been used for the measurement of electroanalytical properties of p-acetamidophenol by means of P*ANIFAD*, MWCNTs and MWCNTs–P*ANIFAD* biocomposite film modified gold electrodes. The sensitivity value of MWCNTs–P*ANIFAD* film ($88.5\,\mathrm{mA\,mM^{-1}\,cm^{-2}}$) is higher than the values which are obtained for P*ANIFAD* ($28.7\,\mathrm{mA\,mM^{-1}\,cm^{-2}}$) and MWCNTs films ($60.7\,\mathrm{mA\,mM^{-1}\,cm^{-2}}$). Finally, the flow injection analysis (FIA) has been used for the amperometric detection of p-acetamidophenol at MWCNTs–P*ANIFAD* film modified screen printed carbon electrode. The sensitivity value of MWCNTs–P*ANIFAD* film ($3.3\,\mathrm{mA\,mM^{-1}\,cm^{-2}}$) in FIA is also higher than the value obtained for MWCNTs film ($1.1\,\mathrm{mA\,mM^{-1}\,cm^{-2}}$).

© 2009 Elsevier B.V. All rights reserved.

1. Introduction

Electropolymerization is a simple but powerful method in targeting selective modification of different type electrodes with desired matrices. However, the materials on the matrices do not possess peculiar properties when compared with those materials which are chemically synthesized by traditional methods. The electroactive polymers and carbon nanotubes (CNTs) matrices have received considerable attraction in recent years. Numerous conjugated polymers have been electrochemically synthesized for their application in the fabrication of chemical and biochemical sensor devices [1]. These conjugated polymers for sensor devices exhibits interesting enhancement in the electrocatalytic activity towards the oxidation or reduction of several biochemical and inorganic compounds [2] where, some of the functional groups in polymers will act as catalyst [3–5]. In this article, the word "enhanced electrocatalytic activity" could be explained as both; increase in peak current and lower overpotential [6]. The wide variety of applica-

tions of matrices made of CNTs for the detection of inorganic and bioorganic compounds such as $IO_3{}^-$, ascorbic acid, etc., have already been reported in the literature [7–9].

Even though the electrocatalytic activity of conjugated polymers and CNTs matrices individually shows good results; some properties like mechanical stability, sensitivity for different techniques, and electrocatalysis for multiple compound detections are found to be poor. To overcome this difficulty, new studies have been developed in the past decade for the preparation of composite films composed of both CNTs and conjugated polymers. The rolled-up graphene sheets of carbon exhibit π-conjugative structure with highly hydrophobic surface. This unique property of the CNTs allows them to interact with organic aromatic compounds through π–π electronic and hydrophobic interactions to form new structures [10,11]. There were past attempts in the preparation of composite and sandwiched films made of polymer adsorbed on CNTs, and used them for electrocatalytic studies such as, selective detection of dopamine in the presence of ascorbic acid [12]. The sandwiched films were also been used in the designing of nanodevices with the help of non-covalent adsorption, electrodeposition, etc. [13].

Among conjugated polymers, polyaniline (P*ANI*) is one of the most widely used conducting polymer [14]. The synthesis of P*ANI*

* Corresponding author. Tel.: +886 2270 17147; fax: +886 2270 25238.
E-mail address: smchen78@ms15.hinet.net (S.-M. Chen).

was first reported by Letheby [15], where aniline was oxidized on Pt-sheet in acidic media. PANI layers have been used as gas sensors [16,17], electrode material for redox supercapacitor [18], shield material for electromagnetic interference control [19], corrosion control [20], etc. Similarly, flavin adenine dinucleotide (FAD) is a flavoprotein coenzyme that plays an important biological role in many oxidoreductases and in reversible redox conversions in biochemical reactions. FAD has an isoalloxazine ring as a redox-active component. The adsorption of FAD has been studied on Hg electrode and titanium electrodes [21,22], and the electrochemical reaction of FAD was also studied on various electrodes in aqueous solutions [23,24]. Further, the electropolymerization of FAD to form poly(flavin adenine dinucleotide) (PFAD) was also reported in the literature [25].

p-Acetamidophenol is a well-known drug which has extensive applications in pharmaceutical industries. It is an antipyretic and analgesic compound that has high therapeutic value. It is also used as a precursor in penicillin, and as stabilizer for hydrogen peroxide, photographic chemical, etc. Various studies were reported for the determination of p-acetamidophenol in drug formulations using different techniques [26–33]. Among these several methods of determination techniques, the electrochemical methods have more advantages over the other in sensing p-acetamidophenol. However in these reports, the same principle, that is, oxidation of p-acetamidophenol by metal ion oxidants has been used for the estimation.

The literature survey reveals that there were no previous attempts made for the synthesis of biocomposite film composed of CNTs, PANI and PFAD for the use in sensor application. In this article, we report about a novel biocomposite film (MWCNTs–PANIFAD) made of multi-walled carbon nanotubes (MWCNTs) which has been incorporated with PANIFAD co-polymer. MWCNTs–PANIFAD biocomposite film's characterization, enhancement in functional properties, peak current and electrocatalytic activity have also been reported along with its application in the determination of p-acetamidophenol. The film formation processing involves the modification of gold electrode with uniformly well dispersed MWCNTs, and which is then modified with PANIFAD co-polymer.

2. Experimental

2.1. Materials

Aniline, FAD, MWCNTs (OD = 10–20 nm, ID = 2–10 nm and length = 0.5–200 μm), potassium hydroxide and p-acetamidophenol obtained from Aldrich and Sigma–Aldrich were used as received. All other chemicals used were of analytical grade. The preparation of aqueous solution was done with twice distilled deionized water. Solutions were deoxygenated by purging with pre-purified nitrogen gas. Solutions were prepared from 1 M HClO$_4$ for the pH 2.28 aqueous solution.

2.2. Apparatus

Cyclic voltammetry (CV) was performed in analytical system models CHI-611, CHI-400 and CHI-1205A potentiostats. A conventional three-electrode cell assembly consisting of Ag/AgCl reference electrode and a Pt wire counter electrode were used for the electrochemical measurements. The working electrode was either an unmodified gold or a gold modified with PANI, PANIFAD, MWCNTs–PANI or MWCNTs–PANIFAD biocomposite films. In all experiments, the potentials are reported vs. the Ag/AgCl reference electrode. The working electrode used for EQCM measurements was an 8 MHz AT-cut quartz crystal coated with gold electrode. The diameter of the quartz crystal is 13.7 mm; the gold electrode diameter is 5 mm. The flow injection analysis (FIA) of the p-acetamidophenol at screen printed carbon electrode (SPCE) was done using Alltech 426 HPLC pump containing an electrochemical cell with electrodes. This above-mentioned electrochemical cell was connected with an inlet from the pump and an outlet, which were used for the carrier stream flow in the electrochemical cell. The morphological characterizations of the films were examined by means of scanning electron microscopy (SEM) (Hitachi S-3000H) and atomic force microscopy (AFM) (Being Nano-Instruments CSPM4000). All the measurements were carried out at 25 °C ± 2.

2.3. Preparation of MWCNTs dispersion and MWCNTs–PANIFAD modified electrode

There was an important challenge in the preparation of MWCNTs. Because of its hydrophobic nature, it was difficult to disperse it in any aqueous solution to get a homogeneous mixture. Briefly, the hydrophobic nature of the MWCNTs was converted in to hydrophilic nature by following the previous studies [34]. This was done by weighing 10 mg of MWCNTs and 200 mg of potassium hydroxide in to a ruby mortar and grained together for 2 h at room temperature. Then the reaction mixture was dissolved in 10 ml of double distilled deionized water and it was precipitated many times in to methanol for the removal of potassium hydroxide. Thus obtained MWCNTs in 10 ml water was ultrasonicated for 6 h to get uniform dispersion. This functionalization process of MWCNTs was done to get hydrophilic nature for the homogeneous dispersion, in water. This process not only converts MWCNTs to hydrophilic nature but this helps to breakdown larger bundles of MWCNTs in to smaller ones also. This process was confirmed using SEM, which is not shown in figures.

Before starting each experiment, gold electrodes were polished by BAS polishing kit with 0.05 μm alumina slurry and rinsed and then ultrasonicated in double distilled deionized water. The gold electrodes studied were uniformly coated with 50 μg cm^{-2} of MWCNTs and then dried at 35 °C. The concentrations of homogeneously dispersed MWCNTs were exactly measured using micro-syringe. The electropolymerization of aniline with FAD to form PANIFAD co-polymer was performed using the mixture 50 mM aniline and 1 mM FAD present in pH 2.28 aqueous solution by consecutive CV over a suitable potential region of −0.35 to 1.0 V. Then the MWCNTs–PANIFAD modified gold electrode was carefully washed with double distilled deionized water. For detailed study, comparison of different modified gold electrodes such as PANI, PANIFAD, MWCNTs–PANI and MWCNTs–PANIFAD have been performed. These characterization studies were done to reveal the obvious necessity for the usage of MWCNTs and PANIFAD in the MWCNTs–PANIFAD biocomposite film. For the FIA of p-acetamidophenol oxidation (at 726 mV), carrier stream used was pH 2.28 aqueous solution with the flow rate of 2 ml min^{-1}, and the volume of p-acetamidophenol injected at each cycle was 10 μl at the time interval of 50 s.

3. Results and discussions

3.1. Electrochemical synthesis of MWCNTs–PANIFAD biocomposite film and its characterization

The electropolymerization of aniline (50 mM) with FAD (1 mM) mixture on MWCNTs modified gold electrode present in pH 2.28 aqueous solution has been performed by consecutive CVs for the preparation of MWCNTs–PANIFAD biocomposite film. Fig. 1(a) shows the reduction and electropolymerization of aniline and FAD at MWCNTs modified gold electrode. Four redox couples (formal potential $E^{0'}$ = −14.8, 202.15, 511.9 and 718.4 mV vs. Ag/AgCl) are
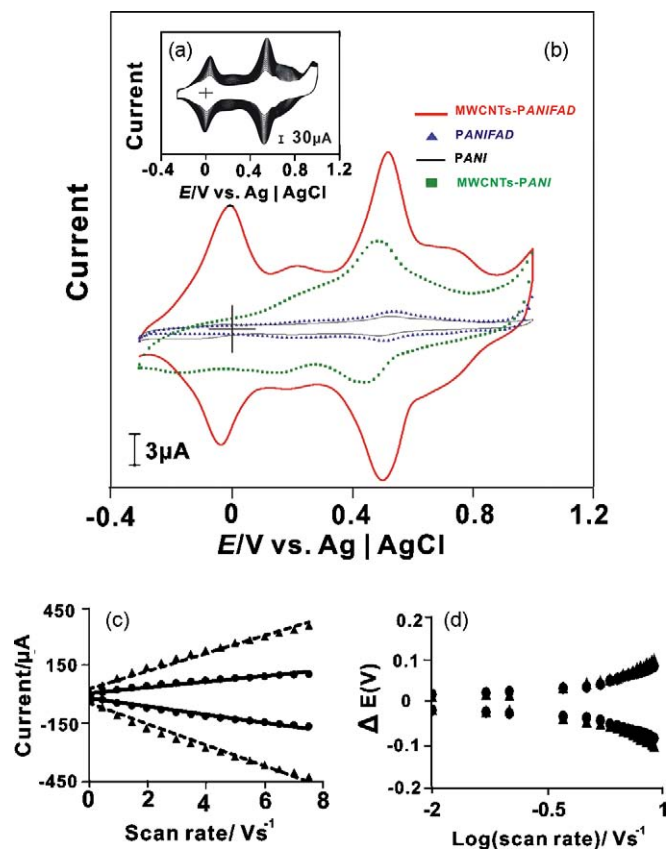
Fig. 1. (a) Repetitive CVs of MWCNTs–gold electrode modified from 50 mM aniline with 1 mM FAD present in pH 2.28 aqueous solution, scan rate 100 mV s^{-1}. (b) Comparison of CVs of PANI, PANIFAD, MWCNTs–PANI and MWCNTs–PANIFAD biocomposite films at gold electrode in pH 2.28 aqueous solution, scan rate 20 mV s^{-1}. (c) The plot of I_{pa} and I_{pc} vs. different scan rate for PANIFAD (continuous line) and MWCNTs–PANIFAD (dotted line) present in pH 2.28 aqueous solution and (d) the plot of ΔE vs. log scan rate for the same films.

Table 1
Surface coverage concentration (Γ) of various species present in PANIFAD at different gold modified electrodes.

Modified films [a]	Γ (nmol cm^{-2})			
	b	c	d	e
PANI	–	–	0.13	–
PANIFAD	0.37	0.03	0.15	–
MWCNTs–PANI	–	–	0.92	–
MWCNTs–PANIFAD	1.82	0.18	2.03	0.93

Species b, c, d, and e representing redox couples at $E^{0\prime}$ = −14.8, 202.15, 511.9 and 718.4 mV, respectively.

[a] Studied using CV technique in pH 2.28 aqueous solution.

obtained for PANIFAD during electropolymerization, which represents the electrochemical redox reactions of PANIFAD co-polymer present in MWCNTs–PANIFAD biocomposite film. The increase in peak current of the same redox couples at each cycle reveals the continuous deposition of PANIFAD during cycling. The electropolymerization has been carried out at a suitable potential range of −0.3 to 1 V. In Fig. 1(a) result, the $E^{0\prime}$ at −14.8 and 202.15 mV represents PFAD redox reactions, then the $E^{0\prime}$ at 511.9 mV represents PANI redox reaction, and then the $E^{0\prime}$ at 718.4 mV represents the redox reaction of PANIFAD co-polymer. In the following experiments, each newly prepared MWCNTs–PANIFAD biocomposite film on gold electrode has been washed carefully in deionized water to remove the loosely bounded aniline and FAD on the modified gold electrode. It was then transferred to pH 2.28 aqueous solution for other electrochemical characterizations.

Fig. 1(b) represents the electrochemical redox signals of PANI, PANIFAD, MWCNTs–PANI and MWCNTs–PANIFAD modified gold electrodes present in pH 2.28 aqueous solution; scan rate 20 mV s^{-1}. Among these four films, PANI has a redox couple at $E^{0\prime}$ = 511.9 mV vs. Ag/AgCl, where as for PANIFAD two new redox couples appear at $E^{0\prime}$ = 202.15 and 718.4 mV along with the enhancement in the redox couple's peak current at $E^{0\prime}$ = 511.9 mV. Similarly in MWCNTs–PANI film, the presence of MWCNTs abruptly enhances the PANI's redox couple at $E^{0\prime}$ = 511.9 mV. These above results show that the presence of PFAD and MWCNTs in the film enhances the redox reaction of PANI. In the same figure, MWCNTs–PANIFAD biocomposite film have four redox couples at $E^{0\prime}$ = −14.8, 202.15, 511.9 and 718.4 mV. These four redox couple for MWCNTs–PANIFAD biocomposite

film represents the redox reactions of the compounds as we discussed above for Fig. 1(a). Among these four redox couples, $E^{0\prime}$ at −14.8 mV do not appear for other three films, and the peak currents of each redox couple in MWCNTs–PANIFAD biocomposite film is higher than the other films. From these CVs in Fig. 1(b), the surface coverage concentration (Γ) values have been calculated and given in Table 1. In this above calculation, the charge involved in the reaction (Q) has been obtained from CVs and it has been applied in the equation $\Gamma = Q/nFA$, where the number of electron transfer involved in PANIFAD redox reactions are assumed as two. These values in Table 1 indicates that the concentration increase of MWCNTs increases the Γ of PANIFAD. The Γ increase can be explained as, the concentration of MWCNTs directly proportional to the geometric area, where the MWCNTs modified gold electrode contains more surfaces to hold PANIFAD when comparing bare gold electrode surface. In general, the geometric area of nanomaterials is higher than the bulk materials. The slope value obtained from Table 1 reveals the increase in Γ of PANI and PFAD per μg of MWCNTs is ≈16 and 29 pmol cm^{-2} μg^{-1} respectively.

The CVs of PANIFAD and MWCNTs–PANIFAD biocomposite films on gold electrode in pH 2.28 aqueous solution at different scan rates have been studied (CVs not shown). In these results, the redox peaks intensity increases linearly with the increase of scan rates up to 7.8 V s^{-1}. The scan rate vs. PANI redox couple peak current in Fig. 1(c) shows that, the ratio of I_{pa}/I_{pc} remains almost in unity as expected for surface type behavior. These above results demonstrate that the redox process is not controlled by diffusion up to 7.8 V s^{-1}. From the slope values of ΔE_p vs. log scan rate given in Fig. 1(d) plot, by assuming the value of $\alpha \approx 0.5$, the electron transfer rate constant (k_s) has been calculated based on Laviron theory [35]; and the k_s for PANI redox reaction at PANIFAD and MWCNTs–PANIFAD biocomposite films are ≈6.1 and 11.5 s^{-1} respectively. From these k_s values, we have calculated the increase in the ability of electron transfer between the electrode surface and PANIFAD in presence of MWCNTs, and it is ≈89%. These results show the enhanced functional property of MWCNTs–PANIFAD biocomposite film in the presence of MWCNTs.

3.2. EQCM and pH studies of MWCNTs–PANIFAD biocomposite film

The EQCM experiments have been carried out by modifying the gold electrochemical quartz crystal with and without uniformly coated MWCNTs, which was then dried at 35° C. Fig. 2(a) and (b) shows the consecutive CVs from EQCM studies for the PANIFAD formation at MWCNTs modified and unmodified gold coated quartz crystal electrodes respectively. In these results, increase in the voltammetric peak currents of PANIFAD redox couples and the frequency decrease, or mass increase (figure not shown) are found to be consistent with the growth of PANIFAD film on both modified and unmodified gold electrode. From the frequency change, change in the mass of PANIFAD and MWCNTs–PANIFAD biocom-
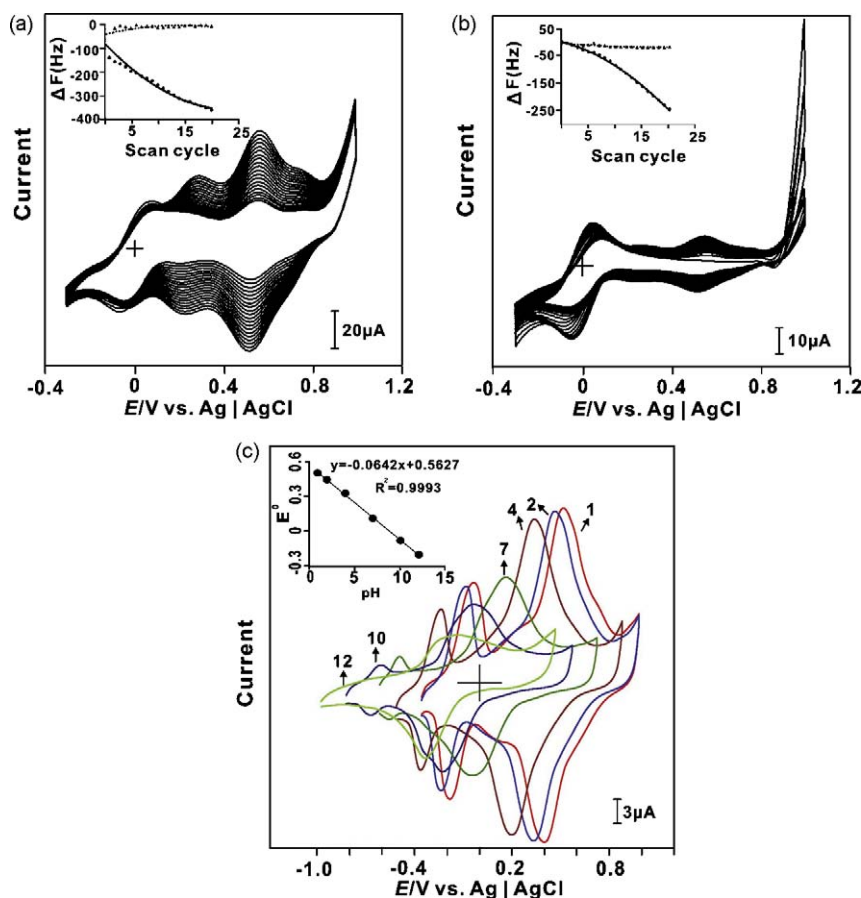
Fig. 2. Consecutive potential CVs of electrochemical quartz crystal gold electrode modified with P*ANIFAD* at 1.0 to −0.3 V (scan rate 20 mV s^{-1}), where (a) and (b) is the presence and absence of MWCNTs on the gold electrode respectively. Insets in both (a) and (b) are the variation of frequency change with the increase of scan cycles (continuous line) and every cycle frequency change with the increase of the scan cycles (dotted line). (c) CVs of MWCNTs–P*ANIFAD* biocomposite film synthesized at pH 2.28 on gold electrode and transferred to various pH solutions; inset shows formal potential vs. pH.

posite film at gold coated quartz crystal has been calculated using Sauerbrey equation. From this calculation for the above-mentioned experimental conditions, it has been found that 1 Hz frequency change is equal to 1.4 ng of mass change [36–39]. Therefore, mass change during P*ANIFAD* incorporation on the MWCNTs modified and unmodified gold electrodes for total cycles are 504 and 341 ng cm^{-2} respectively. The insets in Fig. 2(a) and (b) indicates the every cycle frequency change with the increase of the scan cycles (dotted lines) and variation of frequency change with the increase of scan cycles (continuous lines) for MWCNTs–P*ANIFAD* biocomposite and P*ANIFAD* films respectively. From these plots, it is clear that there is a higher deposition of P*ANIFAD* in presence of MWCNTs, which is similar to the Γ results given in Table 1. These results show that the deposition of P*ANIFAD* on MWCNTs film and bare gold electrode is stable and homogeneous. Previous studies on CNT composites have shown also the necessity of CNTs for improving the functional properties such as orientation, enhanced electron transport, high capacitance, etc. [40,41]. Fig. 2(c) shows the CVs of MWCNTs–P*ANIFAD* on gold electrode at various pH aqueous solutions in which the aniline and FAD are absent. In these experiments, the MWCNTs coated gold electrode has been modified with P*ANIFAD* using pH 2.18 aqueous solution, and it has been washed with deionized water and then transferred to various pH aqueous solutions for CV measurements. These CV results show that the P*FAD* present in the film is stable in the pH range between 1 and 10, and the E_{pa} and E_{pc} values of both P*ANI* and P*FAD* present in the film depends on the pH value of the aqueous solution. The decrease of P*FAD* peak current in pH 7 or greater could be due to

the decomposition of P*FAD* in higher pH, which in turn affects the P*ANI* redox peak current also. The inset in Fig. 2(c) shows the formal potential of P*ANI* redox couple present in MWCNTs–P*ANIFAD* plotted over the pH range of 1–12. The response shows a slope of −64 mV pH^{-1}, which is close to that given by Nernstian equation for equal number of electrons and protons transfer [42,43].

3.3. Topographic characterization of MWCNTs–PANIFAD biocomposite film

Three different films MWCNTs, P*ANIFAD* and MWCNTs–P*ANIFAD* have been prepared on gold electrode with similar conditions and similar potential as mentioned in the previous sections, and were characterized using SEM and AFM. It is a well-known fact that the prolonged exposure to electron beam will damage the P*FAD* present in P*ANIFAD* and MWCNTs–P*ANIFAD* films, so an at most care has been taken to measure these images. Comparison of Fig. 3(a) and (b) SEM images reveals significant morphological difference between P*ANIFAD* and MWCNTs–P*ANIFAD* films. The top views of nanostructures in Fig. 3(a) on the gold electrode surface show grains of P*ANIFAD* deposited on the electrode. The MWCNTs–P*ANIFAD* biocomposite film in Fig. 3(b) shows that the plateaus of P*ANIFAD* deposited over MWCNTs to form MWCNTs–P*ANIFAD* biocomposite modified gold electrode. Similarly, (a′) and (b′) represents bare gold electrode and only MWCNTs, where MWCNTs are more visible in (b′) when comparing (b). The same modified gold electrodes have been used to measure the AFM topography images shown in Fig. 4(a) P*ANIFAD* and (b) MWCNTs–P*ANIFAD*, where (a′) is the bare
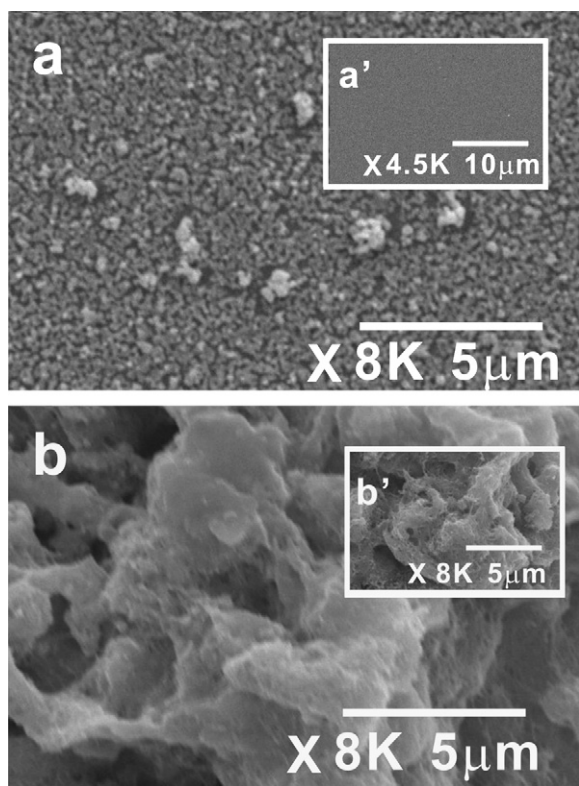
Fig. 3. SEM images of (a) PANIFAD and (b) MWCNTs–PANIFAD biocomposite films, where (a′) is bare gold electrode and (b′) is only MWCNTs.

gold electrode. The higher magnification ($10\,\mu m \times 10\,\mu m$) of AFM images when comparing SEM images reveal that disk shaped grain structures of PANIFAD formed on the gold electrode. However in Fig. 4(b), elongated deposition of PANIFAD formed over MWCNTs instead of disk shaped grain structure. This result reveals that higher concentration of PANIFAD has been deposited on MWCNTs modified gold electrode, which is consistent with the Γ values given in Table 1. Further, the thicknesses of PANIFAD and MWCNTs–PANIFAD obtained from AFM results are 300 and 1500 nm respectively. These values too show MWCNTs–PANIFAD is thicker than PANIFAD, which is due to the presence of MWCNTs covered under PANIFAD film. These SEM and AFM results reveal the coexistence of MWCNTs and PANIFAD in the biocomposite film.

3.4. Electroanalytical response of p-acetamidophenol at MWCNTs–PANIFAD biocomposite film

The MWCNTs–PANIFAD biocomposite film has been synthesized on gold electrode at similar conditions as given in experimental section. Then the MWCNTs–PANIFAD biocomposite film modified electrode has been washed carefully in deionized water and transferred to pH 2.28 aqueous solution for the electrocatalysis of p-acetamidophenol. All the CVs have been recorded at the constant time interval of 1 min with nitrogen purging before the start of each experiments. Fig. 5 shows the electrocatalytic oxidation of p-acetamidophenol ($60\,\mu M$) at various film modified and unmodified gold electrodes; scan rate $20\,mV\,s^{-1}$. The various film modified electrodes are PANIFAD, MWCNTs and MWCNTs–PANIFAD biocomposite films, where the MWCNTs–PANIFAD biocomposite film is shown with highest concentration ($60\,\mu M$) and also in the absence of p-acetamidophenol (blank). The schematic representation of p-acetamidophenol electrochemical oxidation at MWCNTs–PANIFAD biocomposite film is given in Scheme 1. The CVs for MWCNTs–PANIFAD biocomposite film exhibits reversible
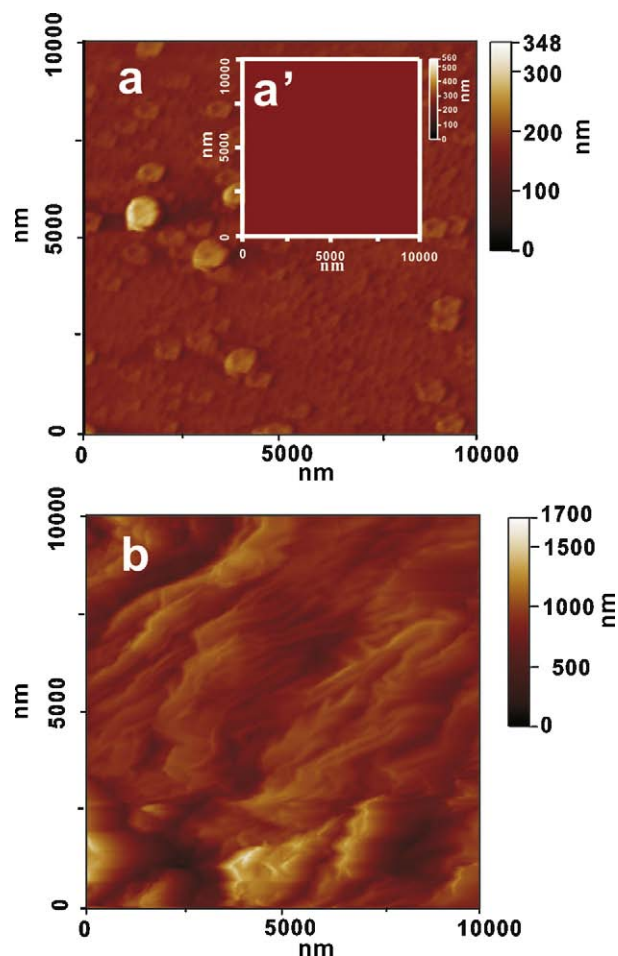
Fig. 4. AFM images of (a) PANIFAD and (b) MWCNTs–PANIFAD biocomposite films, where (a′) is bare gold electrode.

redox couples in the absence of p-acetamidophenol, and upon addition of p-acetamidophenol a new growth in the oxidation peak of p-acetamidophenol appeared at $E_{pa} = 726\,mV$. This above said anodic peak shows that the electrocatalytic oxidation of
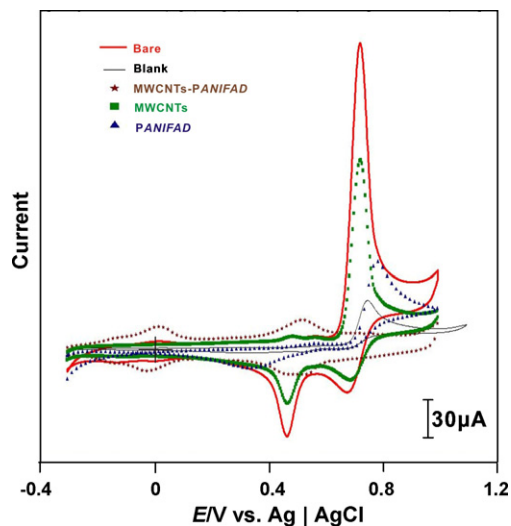
Fig. 5. CVs of p-acetamidophenol ($60\,\mu M$) at bare, PANIFAD, MWCNTs and MWCNTs–PANIFAD biocomposite film modified gold electrodes using pH 2.28 aqueous solution at $20\,mV\,s^{-1}$, where MWCNTs–PANIFAD biocomposite film is shown with both the absence and presence of $60\,\mu M$ p-acetamidophenol.
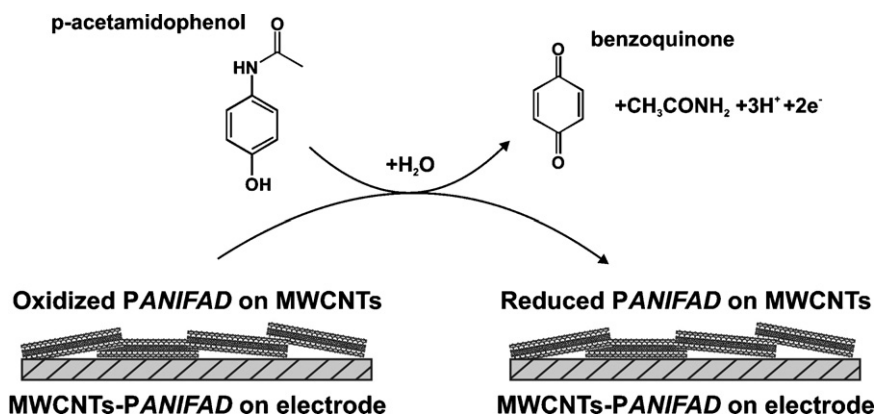
Scheme 1. Electrochemical oxidation of p-acetamidophenol at MWCNTs–P*ANIFAD* biocomposite film modified electrode.

p-acetamidophenol takes place at P*ANIFAD* co-polymer's redox couple $E^{0\prime}$ = 718.4 mV. In these above electrocatalysis experiment, an increase in concentration 2–60 μM of p-acetamidophenol simultaneously produces a linear increase in the oxidation peak current of p-acetamidophenol with good film stability at P*ANIFAD*, MWCNTs and MWCNTs–P*ANIFAD* biocomposite films. However, there is no increase at bare gold electrode. The anodic peak current is linear with the concentration of p-acetamidophenol for all the three films.

It is obvious that the MWCNTs–P*ANIFAD* biocomposite film shows higher electrocatalytic activity for p-acetamidophenol. More specifically, the enhanced electrocatalytic activity of MWCNTs–P*ANIFAD* biocomposite film can be explained in terms of both lower in overpotential and higher peak current than that of P*ANIFAD* film, MWCNT film and bare gold electrode. These results can be observed from the I_{pa} and E_{pa} values given in Table 2. Where, the increase in peak current and decrease in overpotential; both are considered as the electrocatalytic activity [6]. In detail, the enhancement in electrocatalytic activity at MWCNTs–P*ANIFAD* biocomposite film is due to presence of both MWCNTs and P*ANIFAD*, where the anodic peak potential is lowered by MWCNTs, and the peak current is enhanced by both MWCNTs and P*ANIFAD*. From the slopes of linear calibration curves, the sensitivities of P*ANIFAD*, MWCNTs and MWCNTs–P*ANIFAD* biocomposite film modified gold electrodes and their correlation co-efficient have been calculated and given in Table 3. It is obvious that the sensitivity of MWCNTs–P*ANIFAD* biocomposite film is higher for p-acetamidophenol when comparing P*ANIFAD* and MWCNTs films. The overall view of these results reveals that MWCNTs–P*ANIFAD* biocomposite film is efficient for p-acetamidophenol analysis.

3.5. FIA of p-acetamidophenol at MWCNTs–PANIFAD biocomposite film

The MWCNTs–P*ANIFAD* biocomposite film has been synthesized on SPCE at similar conditions to that of gold electrode. Then the modified electrode has been washed carefully in deionized water and used for FIA of p-acetamidophenol as shown in Fig. 6. The

Table 2
Comparison of E_{pa} and I_{pa} of p-acetamidophenol in electrocatalytic oxidation reaction using CV technique at different modified electrodes in pH 2.28 aqueous solution.

Modified films [a]	E_{pa} (mV)	I_{pa} (μA)
Bare gold electrode	753.5	36.91
P*ANIFAD*	765.3	69.88
MWCNTs	728.2	152.1
MWCNTs–P*ANIFAD*	726.0	246.1

[a] Modified at gold electrode.

Table 3
Sensitivities and correlation coefficient of different modified electrodes for p-acetamidophenol oxidation in pH 2.28 aqueous solution using various techniques.

Modified films	Sensitivity (mA mM^{-1} cm^{-2}) [correlation coefficient]	
	CV[a]	FIA[b]
P*ANIFAD*	28.7 [0.9976]	–
MWCNTs	60.7 [0.8941]	1.1 [0.9326]
MWCNTs–P*ANIFAD*	88.5 [0.7843]	3.3 [0.9957]

[a] Films modified at gold electrode.
[b] Films modified at SPCE.

carrier stream used was pH 2.28 aqueous solution with the flow rate of 2 ml min^{-1}, and the volume of p-acetamidophenol injected at each cycle was 10 μl at the time interval of 50 s. Fig. 6 shows the successive addition of p-acetamidophenol in the concentration range from 10 μM to 0.1 M at the potential of 726 mV. This above-mentioned potential is the optimized potential obtained from CV study. The rapid amperometric response of the MWCNTs and MWCNTs–P*ANIFAD* biocomposite film is proportional to the respective analytes concentration. From the slopes of linear calibration curves, sensitivities of MWCNTs and MWCNTs–P*ANIFAD* biocomposite film modified SPCE and their correlation co-efficient have been calculated and given in Table 3. The comparison of slope values of both the films show that the MWCNTs–P*ANIFAD* biocom-
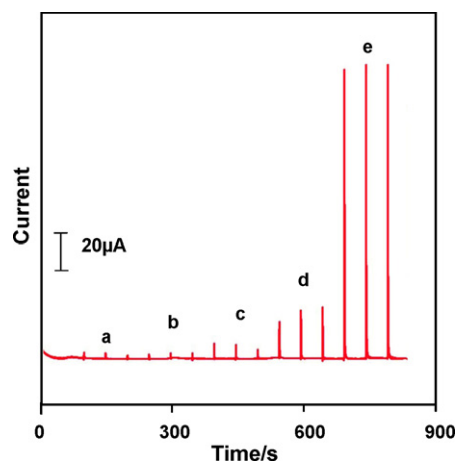
Fig. 6. FIA of p-acetamidophenol at MWCNTs–P*ANIFAD* biocomposite film with five different concentrations of p-acetamidophenol = (a) 1×10^{-5}; (b) 1×10^{-4}; (c) 1×10^{-3}, (d) 1×10^{-2} and (e) 1×10^{-1} M; potential = 726 mV, where the carrier stream used was pH 2.28 aqueous solution; flow rate = 2 ml min^{-1} and injected volume = 10 μl.

Table 4
Electroanalytical values obtained for the p-acetamidophenol tablet's determination using FIA in pH 2.28 aqueous solution at MWCNTs–P*ANIFAD* biocomposite film modified SPCE.

Added (mM)	Found (mM)	RSD (%)	Recovery (%)
0.01	0.0102	1.94	102
0.1	0.107	2.61	107
1	1.08	2.78	108
10	10.86	1.28	109
100	109.49	1.71	109

posite film possess good reproducibility with higher sensitivity for p-acetamidophenol.

3.6. Analysis of p-acetamidophenol tablet

The performance of MWCNTs–P*ANIFAD* biocomposite film modified SPCE has been tested by applying it to the determination of the p-acetamidophenol present in p-acetamidophenol tablets. The technique used for the determination was FIA. These p-acetamidophenol tablets were obtained from GlaxoSmithKline Dungarvan Ltd., Ireland. The tablet's labeled composition is 500 mg of acetamidophenol and 65 mg of caffeine. In these experiments, the concentration added, found and the relative standard deviation (RSD) are given in Table 4. From these results in Table 4, the recovery of p-acetamidophenol is ≈107%. These above results show that MWCNTs–P*ANIFAD* biocomposite film is efficient for p-acetamidophenol detection.

4. Conclusions

We developed a novel biocomposite material using MWCNTs and P*ANIFAD* (MWCNTs–P*ANIFAD*) at gold electrode and SPCE, which are more stable in pH 2.28 aqueous solution. The developed MWCNTs–P*ANIFAD* biocomposite film for the electrocatalysis combines the advantages of ease of fabrication, high reproducibility and sufficient long-term stability. The EQCM results confirmed the incorporation of P*ANIFAD* on MWCNTs modified gold electrode. The SEM and AFM results have shown the difference between P*ANIFAD* and MWCNTs–P*ANIFAD* biocomposite films morphology. Further, it has been found that MWCNTs–P*ANIFAD* biocomposite film has excellent functional properties along with good electrocatalytic activity on p-acetamidophenol. The experimental methods of CV and FIA with MWCNTs–P*ANIFAD* biocomposite film sensor integrated into the gold electrode and SPCE which are presented in this article provide an opportunity for qualitative and quantitative characterization. Therefore, this work establishes and illustrates in principle and potential, a simple and novel approach for the development of a voltammetric and amperometric sensor which is based on modified gold electrode and SPCE.

References

[1] C.P. McMahon, G. Rocchitta, S.M. Kirwan, S.J. Killoran, P.A. Serra, J.P. Lowry, R.D. O'Neill, Biosens. Bioelectron. 22 (2007) 1466.
[2] I. Becerik, F. Kadirgan, Synth. Met. 124 (2001) 379.
[3] T. Selvaraju, R.R. Ramaraj, J. Electroanal. Chem. 585 (2005) 290.
[4] M. Mao, D. Zhang, T. Sotomura, K. Nakatsu, N. Koshiba, T. Ohsaka, Electrochim. Acta 48 (2003) 1015.
[5] M. Yasuzawa, A. Kunugi, Electrochem. Commun. 1 (1999) 459.
[6] C.P. Andrieux, O. Haas, J.M. SavGant, J. Am. Chem. Soc. 108 (1986) 8175.
[7] J. Wang, M. Musameh, Anal. Chim. Acta 511 (2004) 33.
[8] H. Cai, X. Cao, Y. Jiang, P. He, Y. Fang, Anal. Bioanal. Chem. 375 (2003) 287.
[9] A. Erdem, P. Papakonstantinou, H. Murphy, Anal. Chem. 78 (2006) 6656.
[10] Q. Li, J. Zhang, H. Yan, M. He, Z. Liu, Carbon 42 (2004) 287.
[11] J. Zhang, J.K. Lee, Y. Wu, R.W. Murray, Nano Lett. 3 (2003) 403.
[12] M. Zhang, K. Gong, H. Zhang, L. Mao, Biosens. Bioelectron. 20 (2005) 1270.
[13] R.J. Chen, Y. Zhang, D. Wang, H. Dai, J. Am. Chem. Soc. 123 (2001) 3838.
[14] M. Trojanowicz, Microchim. Acta 143 (2003) 75.
[15] H. Letheby, J. Chem. Soc. 15 (1862) 161.
[16] D. Nicolas-Debarnot, F. Poncin-Epaillard, Anal. Chim. Acta 475 (2003) 1.
[17] J. Huang, S. Virji, B.H. Weiller, R.B. Kaner, J. Am. Chem. Soc. 125 (2003) 314.
[18] V. Gupta, N. Miura, Electrochem. Solid-State Lett. 8 (2005) A630.
[19] S.K. Dhawan, N. Singh, S. Venkatachalam, Synth. Met. 125 (2002) 389.
[20] D. Sazou, M. Kourouzidou, E. Pavlidou, Electrochim. Acta 52 (2007) 4385.
[21] V.I. Birss, S. Guha-Thakurta, C.E. McGarvey, S. Quach, P. Vanysek, J. Electroanal. Chem. 456 (1998) 71.
[22] R. Garjonyte, A. Malinauskas, L. Gorton, Bioelectrochemistry 61 (2003) 39.
[23] M.M. Kamal, H. Elzanowska, M. Gaur, D. Kim, V.I. Birss, J. Electroanal. Chem. 318 (1991) 349.
[24] L.T. Kubota, L. Gorton, A.R. Lanzilotta, A.J. McQuillan, Bioelectrochem. Bioenerg. 47 (1998) 39.
[25] S.A. Kumar, S.M. Chen, J. Solid State Electrochem. 11 (2007) 993.
[26] J.E. Wallace, Anal. Chem. 39 (1967) 531.
[27] F.M. Plakogiannis, A.M. Saad, J. Pharm. Sci. 64 (1975) 1547.
[28] K.K. Verma, A.K. Gulati, S. Palod, P. Tyagi, Analyst 109 (1984) 735.
[29] S.M. Sultan, I.Z. Alzamil, A.M. Aziz Alrahman, S.A. Altamrah, Y. Asha, Analyst 111 (1986) 919.
[30] F.A. Mohamed, M.A. AbdAllah, S.M. Shammat, Talanta 44 (1997) 61.
[31] J.F. van Staden, M. Tsanwani, Talanta 58 (2002) 1095.
[32] M. Oliva, R.A. Olsina, A.N. Masi, Talanta 66 (2005) 229.
[33] M.K. Srivastava, S. Ahmad, D. Singh, I.C. Shukla, Analyst 110 (1985) 735.
[34] Y. Yan, M. Zhang, K. Gong, L. Su, Z. Guo, L. Mao, Chem. Mater. 17 (2005) 3457.
[35] E. Laviron, J. Electroanal. Chem. 101 (1979) 19.
[36] S.M. Chen, M.I. Liu, Electrochim. Acta 51 (2006) 4744.
[37] S.M. Chen, C.J. Liao, V.S. Vasantha, J. Electroanal. Chem. 589 (2006) 15.
[38] U. Yogeswaran, S.M. Chen, Electrochim. Acta 52 (2007) 5985.
[39] U. Yogeswaran, S.M. Chen, S.H. Li, Electroanalysis 20 (2008) 2324.
[40] J. Wang, J. Dai, T. Yarlagadda, Langmuir 21 (2005) 9.
[41] M. Tahhan, V.T. Truong, G.M. Spinks, G. GWallace, Smart Mater. Struct. 12 (2003) 626.
[42] T. Komura, G.Y. Niu, T. Yamaguchi, M. Asano, A. Matsuda, Electroanalysis 16 (2004) 1791.
[43] U. Yogeswaran, S. Thiagarajan, S.M. Chen, Carbon 45 (2007) 2783.

Salicylaldehyde hydrazones as fluorescent probes for zinc ion in aqueous solution of physiological pH

Na Li, Yu Xiang, Xiaotong Chen, Aijun Tong*

The Key Laboratory of Bioorganic Phosphorus Chemistry & Chemical Biology, Department of Chemistry, Tsinghua University, Beijing 100084, China

ARTICLE INFO

ABSTRACT

Salicylaldehyde hydrazones of **1** and **2** were synthesized and their potential as fluorescent probes for zinc ion was investigated in this paper. Both of the probes were found to show fluorescence change upon binding with Zn^{2+} in aqueous solutions, with good selectivity to Zn^{2+} over other metal ions such as alkali/alkali earth metal ions and heavy metal ions of Pb^{2+}, Cd^{2+} and Hg^{2+}. They showed 1:2 metal-to-ligand ratio when their Zn^{2+} complex was formed. By introducing pyrene as fluorophore, **2** showed interesting ratiometric response to Zn^{2+}. Under optimal condition, **2** exhibited a linear range of 0–5.0 μM and detection limit of 0.08 μM Zn^{2+} in aqueous buffer, respectively. The detection of Zn^{2+} in drinking water samples using **2** as fluorescent probe was successful.

© 2009 Elsevier B.V. All rights reserved.

1. Introduction

Zinc ion, which serves as an essential ingredient for various enzymes, is a very important ion species in many biological activities [1,2]. It is the second most abundant heavy metal ion after iron in human body with its total content of 2–3 g in whole body and concentration as high as 10 μM in serum [3]. Because of these, as well as the simple instrumentation and visible signal advantages of fluorescence technology, the quantification of Zn^{2+} by artificial fluorescent probes in environmental or biological samples has attracted much attention in recent years [4–9].

There have been many excellent Zn^{2+}-selective fluorescent probes reported during the latest two decades. However, most of them give fluorescence enhancement response upon the interaction with Zn^{2+} [10–18], with only a few of them that could sense Zn^{2+} ratiometrically [19–22]. It is generally believed that fluorescent probes of ratiometric type exhibit advantages of better resistance to variation of sensor concentration, higher sensitivity, and signal of color change [23]. Thus, the design and development of these probes are of great concern and challenge.

In this paper, we investigated the potential of some salicylaldehyde hydrazones (**1** and **2**) as fluorescent probes for Zn^{2+}, because it was reported that salicylaldimines underwent fluorescence enhancement upon chelating with Zn^{2+} [24–26]. The salicylaldehyde hydrazone moiety [27,28] served as both receptor

and reporter in Zn^{2+} sensing, with its advantage of high selectivity toward Zn^{2+} over other metal ions. These salicylaldehyde hydrazones showed 1:2 metal-to-ligand ratio, respectively, when their Zn^{2+} complex formed. Moreover, by introducing pyrene as donor, ratiometric fluorescent probe (**2**) for Zn^{2+} was also constructed. The application of probe **2** for determination of Zn^{2+} in water samples by fluorescence ratiometry was also successful.

2. Experimental

2.1. Reagents

Absolute ethanol of analytical grade and deionized water (distilled) were used throughout the experiment as solvents. All the materials for synthesis were purchased from commercial suppliers and used without further purification. The solutions of metal ions were prepared from their nitrate salts of analytical grade, and then subsequently diluted to prepare working solutions. Tris–HCl buffer solutions of different pH were prepared using proper amount of Tris and HCl (all of analytical grade) under adjustment by a pH meter.

2.2. Apparatus

Absorption spectra were determined on a JASCO V-550 UV-VIS spectrophotometer. Fluorescence spectra measurements were performed on a JASCO FP-6500 spectrofluorimeter equipped with a xenon discharge lamp, 1 cm quartz cells. All pH measurements were made with a Model pHS-3C pH meter (Shanghai, China). NMR spectra were recorded using a JOEL JNM-ECA300 spectrometer operated

* Corresponding author. Tel.: +86 10 62782485; fax: +86 10 62782485.
E-mail address: tongaj@mail.tsinghua.edu.cn (A. Tong).
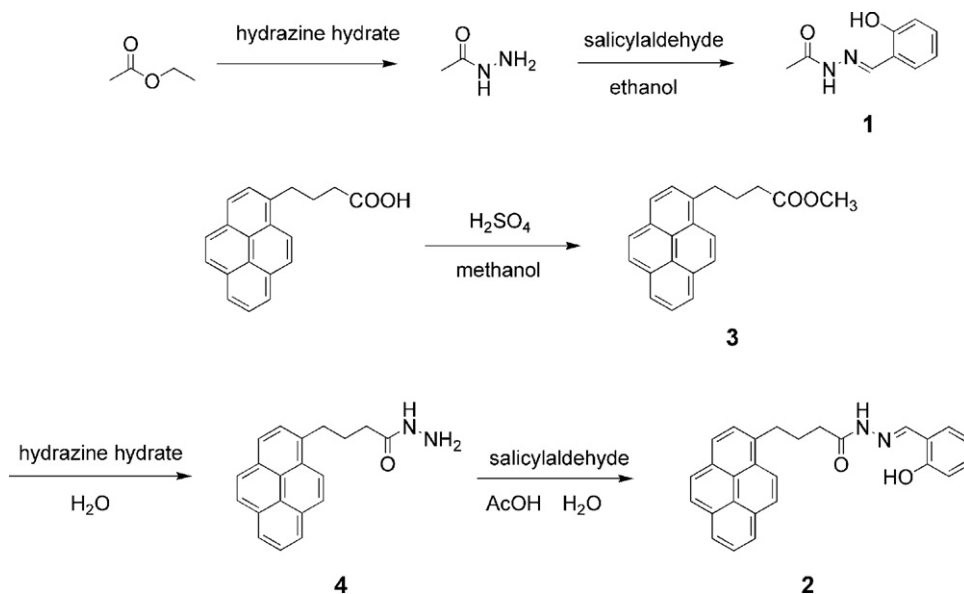
Scheme 1. Synthesis of compounds **1** and **2**.

at 300 MHz. ESI-MS spectra were obtained on an API3000 LC-MS spectrometer. Elemental analysis was carried out on a FLASH EA1112 elemental analyzer. Fluorescence lifetime was measured on a FLSP920 spectrophotometer (Edinburgh Instruments). All of the measurements were operated at room temperature at about 298 K.

2.3. Synthesis of 1 and 2 (Scheme 1)

2.3.1. Synthesis of salicylaldehyde acetic hydrazone (1) [29]

To a 25 mL flask were added 10 mL ethyl acetate (100 mmol) and 5 g hydrazine hydrate (85%, 85 mmol). The flask was allowed to stand in a 90 °C oil bath for 4 h. After cooled to room temperature, the excess ethyl acetate was removed under reduced pressure. 5.95 g colorless oil was obtained as rough product of acetic hydrazide.

0.74 g acetic hydrazide (about 10 mmol) prepared by the above method and 1.05 mL salicylaldehyde (1.17 g/mL, 10 mmol) were added to 20 mL absolute ethanol in a 50 mL flask. The mixture was stirred at room temperature for 30 min, and the resulting precipitate was filtered. After washing the solid for three times by 20 mL absolute ethanol and dried under reduced pressure, 0.96 g **1** (yield 54%) was obtained as white solid. ESI mass spectrometry: m/z 179.0 (20% [M+H]$^+$), 201.0 (80% [M+Na]$^+$); M$^+$ calculated 178.1. ^{1}H NMR (CD$_3$OD), δ (ppm): 8.25 (s, 1H), 7.36 (m, 1H), 7.28 (m, 1H), 6.89 (m, 2H), 2.07 (s, 3H). Elemental analysis: N 15.73%, C 60.62%, H 5.58%, calculated: C$_9$H$_{10}$N$_2$O$_2$, N 15.72%, C 60.66%, H 5.66%.

2.3.2. Synthesis of salicylaldehyde 4-pyren-1-yl-butyric hydrazone (2)

To a 50 mL flask were added 2.0 g 4-pyren-1-yl-butyric acid (7 mmol), 20 mL methanol and 2 mL concentrated H$_2$SO$_4$. The mixture was allowed to reflux for 2 h in a 70 °C oil bath. After cooled to room temperature, saturated Na$_2$CO$_3$ solution was added to neutralize the excess acid. Then the mixture was extracted two times by 20 mL dichloromethane. The organic phase was separated out and dried by anhydrous MgSO$_4$, and the solvent was removed under reduced pressure. 1.7 g **3** (yield 87%) was obtained as brown oil. ^{1}H NMR (DMSO–d$_6$), δ (ppm): 8.50–7.80 (m, 9H, pyrene-H), 3.64 (s, 3H), 3.33 (t, 2H), 2.46 (t, 2H), 2.04 (m, 2H). ^{13}C NMR (DMSO–d$_6$), δ (ppm): 173.2, 136.1, 138.9, 130.4, 129.3, 128.1, 127.4 (2C, 127.39,

127.40), 127.2, 126.5, 126.0, 124.9, 124.9, 124.8, 124.2, 124.1, 123.3, 51.2, 32. 9, 31.8, 26.7.

1.5 g **3** (5 mmol), 10 mL hydrazine hydrate (85%) and 10 mL water were added to a 50 mL flask. The mixture was heated in an oil bath at 100 °C overnight. The resulting precipitate was filtered out and washed three times by 20 mL water. After dried under reduced pressure, 1.2 g **4** (yield 80%) was obtained as white solid. ^{1}H NMR (DMSO–d$_6$), δ (ppm): 9.10 (s, 1H), 8.50–7.80 (m, 9H, py-H), 4.32 (s, 2H), 3.34 (t, 2H), 2.27 (t, 2H), 2.07 (m, 2H). ^{13}C NMR (DMSO–d$_6$), δ (ppm): 171.5, 136.5, 130.9, 130.4, 129.3, 128.2, 127.4 (2C, 127.43, 127.44), 127.2, 126.5, 126.1, 124.9, 124.8, 124.2, 124.2, 123.5, 33.2, 33.1, 27.5.

0.8 g **4** (2.6 mmol), 0.312 mL salicylaldehyde (1.17 g/mL, 3 mmol), 20 mL glacial acetic acid and 10 mL water were added to a 100 mL flask. The mixture was heated in an oil bath at 80 °C for 50 min, and the resulting precipitate was filtered out. The solid was washed three times by 20 mL water and dried under reduced pressure. 0.720 g **2** (yield 67%) was obtained as offwhite solid. ESI mass spectrometry: m/z 407.2 (43% [M+H]$^+$), 429.2 (57% [M+Na]$^+$); M$^+$ calculated 406.2. ^{1}H NMR (DMSO–d$_6$), δ (ppm): 8.60–7.90 (m, 10H, py-H and NH), 7.02–6.80 (m, 2H, Benz-H), 6.38 (d, 1H, Benz-H), 6.11 (m, 1H, Benz-H), 3.36 (t, 2H), 2.40 (t, 2H), 2.10 (m, 2H). ^{13}C NMR (DMSO–d$_6$), δ (ppm): 170.5, 151.6, 138.2, 137.9, 133.1, 133.0, 131.4, 130.9, 129.6, 128.6, 128.0 (2C), 127.6, 126.9, 126.6, 125.4, 125.3, 125.2, 124.7, 124.6, 124.3, 122.0 (2C, 122.4, 122.3), 109.6, 33.2, 31.8, 29.9. Elemental analysis: N 6.94%, C 79.76%, H 5.57%, calculated: C$_{27}$H$_{22}$N$_2$O$_2$, N 6.89%, C 79.78%, H 5.46%.

2.4. Absorption and fluorescence measurements

Absorption and fluorescence titrations were performed by addition of small aliquots of one of **1** and **2** and metal ion working solutions to 3.0 mL buffered water/ethanol of different pH and ethanol fractions in a 1 cm quartz cell. After well mixed, the solutions were allowed to stand at ambient condition for 2 min, and absorption or fluorescence spectra were recorded.

Absorption and fluorescence spectra measurement of Zn^{2+} containing water samples was carried out by adding proper amount of one of **1** and **2**, buffer stock solution and ethanol to sample solutions, and then well mixed for 2 min before test.
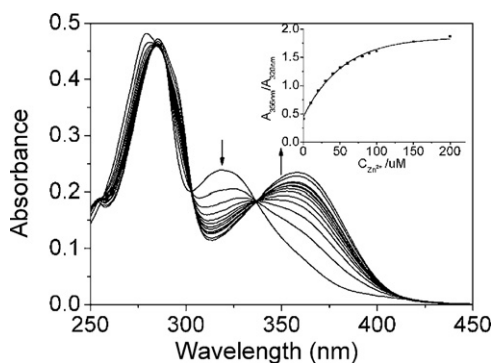
Fig. 1. Absorption spectra of **1** (50 μM) in the absence and presence of Zn^{2+} in water buffered by 10 mM Tris–HCl at pH 7.03. [Zn^{2+}] changes from 0 to 200 μM as indicated by arrows. Inset shows ratio of absorbance at 356 and at 320 nm as a function of Zn^{2+} concentration.

3. Results and discussion

3.1. Binding of **1** and **2** with Zn^{2+}

We first examined the simple probe **1**. In aqueous solution of 10 mM Tris–HCl buffer at pH 7.03, **1** (50 μM) exhibited absorption bands at 280 and 320 nm respectively. Upon the addition of Zn^{2+}, a clear red shift from 320 to 360 nm in absorption spectra was observed, with absorbance decreased in 305–335 nm while enhanced in 340–400 nm (Fig. 1). Two isobestic points at 303 and 337 nm could be found. In its fluorescence spectra under the same condition, obvious fluorescence enhancement (more than 4-fold) occurred, with mild blue shift of peak wavelength from 470 to 460 nm, upon the addition of Zn^{2+} (Fig. 2). The change in both absorption and fluorescence spectra of **1** upon Zn^{2+} binding suggested there was strong interaction between **1** and Zn^{2+}. To investigate the stoichiometry of the complex formed by **1** and Zn^{2+}, Job's method [30] and ESI-MS measurements [31] were carried out. With a total concentration of 50 μM **1** and Zn^{2+} in 10 mM Tris–HCl buffer at pH 7.03, the maximum of absorbance at 360 nm was reached when the molar fraction of Zn^{2+} was about 1/3, indicating the 1:2 metal-to-ligand ratio for the complex of **1**–Zn^{2+} (Fig. 3). ESI-MS spectra of **1** in the absence and presence of Zn^{2+} also supported this binding mode, with peaks at $m/z = 179.0$ ([1+H]$^+$) and $m/z = 419.1$ ([2**1**+Zn–H]$^+$) for **1** and **1**–Zn^{2+}, respectively. Moreover, the fluorescence enhancement signal was selective toward Zn^{2+} over other common metal ions (Fig. 4), with only interference from Fe^{3+}, Co^{2+}, Ni^{2+}, and Cu^{2+} in the metal ions measured, mainly because these metal ions exhibited comparable chelating affinity

Fig. 3. Job's plot data for evaluating the stoichiometry of **1**–Zn^{2+} complex. The total concentration of **1** and Zn^{2+} was 50 μM. The wavelength of absorbance is 360 nm.
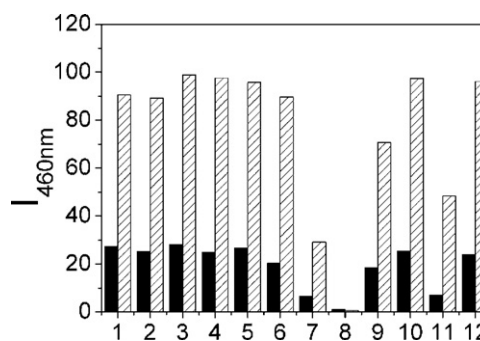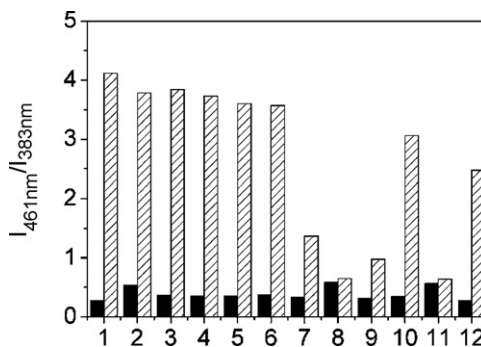

Fig. 4. Fluorescence intensity at 460 nm of **1** (50 μM) in 10 mM Tris–HCl buffer at pH 7.03 with different metal ions (50 μM) in the absence (black bar) and presence (white bar) of 50 μM Zn^{2+}. Excitation was performed at 337 nm. 1: dye only; 2: Na^+; 3: Mg^{2+}; 4: Ca^{2+}; 5: Ba^{2+}; 6: Pb^{2+}; 7: Ni^{2+}; 8: Cu^{2+}; 9: Fe^{3+}; 10: Cd^{2+}; 11: Co^{2+}; 12: Hg^{2+}.

to **1** and Zn^{2+}. The stoichiometry and binding constant (K) of **1** with different metal ions were summarized in Table 1.

The satisfactory character of **1** as a fluorescent probe for Zn^{2+} encouraged us to explore its derivatives for more promising Zn^{2+} probes. Thus, compound **2** was synthesized. It was designed as a candidate for ratiometric fluorescent probe for Zn^{2+} by displaying fluorescence of pyrene and that of hydrazone-Zn^{2+} (similar to that of **1**–Zn^{2+}) moiety in the absence and presence of Zn^{2+}, respectively. In a solution of 30% (v/v) ethanol/water with 10 mM Tris–HCl at pH 7.03, probe **2** (10 μM) alone exhibited strong absorption bands at 326 and 342 nm, which underwent red shift to 351 and 376 nm in the presence of 5 μM Zn^{2+} (Fig. 5). Two isobestic points at 332 and 347 nm could be clearly observed. When excited at its isobestic point of 347 nm, compound **2** free of metal ions showed the characteristic fluorescence of pyrene monomer around 400 nm, with also some mild fluorescence in 450–550 nm range due to either

Fig. 2. Fluorescence spectra of **1** (50 μM) in the absence and presence of Zn^{2+} in water buffered by 10 mM Tris–HCl at pH 7.03. Excitation was performed at 337 nm. [Zn^{2+}] changes from 0 to 300 μM as indicated by arrow. Inset shows fluorescence intensity at 460 nm as a function of Zn^{2+} concentration.

Table 1
Stoichiometry and binding constant (K) of the probe with different metal ions.

Metal ions	Stoichiometry of **1**–metal ratio[a]	log K with **1**[b]	Stoichiometry of **2**–metal ratio[c]	log K with **2**[d]
Zn^{2+}	2:1	9.1	2:1	11.0
Cu^{2+}	1:1	6.6	1:1	6.7
Co^{2+}	2:1	9.1	2:1	11.0
Ni^{2+}	1:1	5.1	1:1	5.0
Fe^{3+}	2:1	7.4	2:1	9.6

[a] According to Job's method (a total concentration of 50 μM **1** and metal ion in 10 mM Tris–HCl buffer at pH 7.03) and ESI-MS measurements.

[b] Tris–HCl aqueous buffer (pH 7.03).

[c] According to Job's method (a total concentration of 20 μM **2** and metal ion in 30% (v/v) ethanol/water solutions) and ESI-MS measurements.

[d] 30% (v/v) ethanol/water buffered by 10 mM Tris–HCl at pH 7.03.
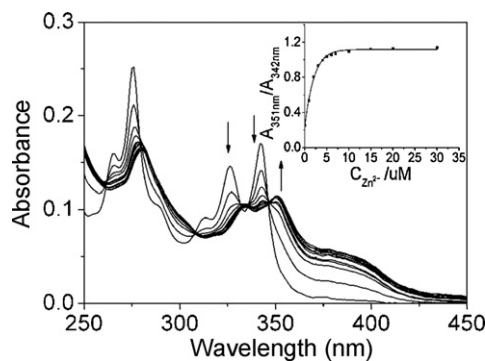
Fig. 5. Absorption spectra of **2** (10 μM) in the absence and presence of Zn^{2+} in 30% (v/v) ethanol/water buffered by 10 mM Tris–HCl at pH 7.03. [Zn^{2+}] changes from 0 to 30 μM as indicated by arrows. Inset shows ratio of absorbance at 351 and at 342 nm as a function of Zn^{2+} concentration.
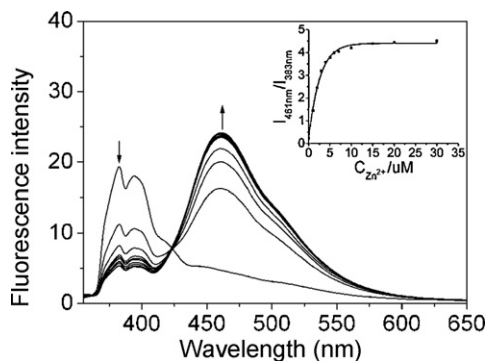
Fig. 6. Fluorescence spectra of **2** (10 μM) in the absence and presence of Zn^{2+} in 30% (v/v) ethanol/water buffered by 10 mM Tris–HCl at pH 7.03. Excitation was performed at 347 nm. [Zn^{2+}] changes from 0 to 30 μM as indicated by arrows. Inset shows the ratio of fluorescence intensity at 461 and 383 nm as a function of Zn^{2+} concentration.

the weak emission of hydrazone moiety or trace pyrene excimer [32] (Fig. 6). However, upon the addition of Zn^{2+}, the characteristic fluorescence of pyrene decreased while a new band centered at 461 nm appeared and enhanced simultaneously. This new fluorescence band could be ascribed to the fluorescence of hydrazone-Zn^{2+} moiety but not pyrene excimer, because we further confirmed that the fluorescence lifetime of **2**–Zn^{2+} (3.8 ns) and **1**–Zn^{2+} (4.2 ns) were very similar and much lower than typical excimer lifetime of pyrene (40 ns) [33]. The fluorescence intensity ratio of I_{461}/I_{383} increased from 0.20 to 4.53 for 10 μM **2** upon stepwise addition of up to 20 μM Zn^{2+}. Similar to **1**, the results of Job's method [30] and ESI-MS measurement [31] also indicated that the binding mode of **2**–Zn^{2+} complex exhibited a 1:2 metal-to-ligand ratio (Scheme 2): (1) with a total concentration of 10 μM **2** and Zn^{2+} in 30% (v/v) ethanol/water with 10 mM Tris–HCl buffer at pH 7.03, the maximum of absorbance
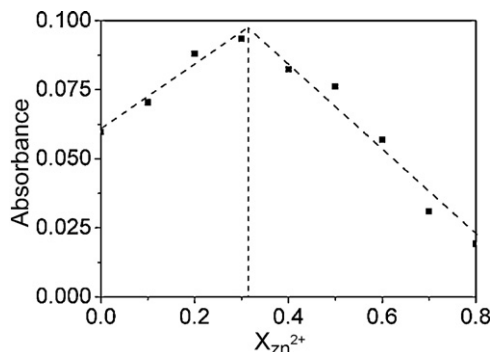
Fig. 7. Job's plot data for evaluating the stoichiometry of **2**–Zn^{2+} complex. The total concentration of **2** and Zn^{2+} was 10 μM. The wavelength of absorbance is 351 nm.

Fig. 8. Ratio of fluorescence intensity at 461 and 383 nm of **2** (10 μM) in 30% (v/v) ethanol/water buffered by 10 mM Tris–HCl at pH 7.03 with different metal ions (10 μM) in the absence (black bar) and presence (white bar) of 10 μM Zn^{2+}. Excitation was performed at 347 nm. 1: dye only; 2: Na^+; 3: Mg^{2+}; 4: Ca^{2+}; 5: Ba^{2+}; 6: Pb^{2+}; 7: Ni^{2+}; 8: Cu^{2+}; 9: Fe^{3+}; 10: Cd^{2+}; 11: Co^{2+}; 12: Hg^{2+}.

at 351 nm was achieved when the molar fraction of Zn^{2+} was near 1/3 (Fig. 7); (2) ESI-MS spectra of **2** in the absence and presence of Zn^{2+} exhibited ion peaks at $m/z = 407.2$ ([**2**+H]$^+$) and $m/z = 834.9$ ([**22**+Zn−H]$^+$) for **2** and **2**–Zn^{2+}, respectively. The selectivity of the ratiometric fluorescence response of **2** to Zn^{2+} was also very satisfactory according to the competitive measurement. Except for Fe^{3+}, Co^{2+}, Ni^{2+}, and Cu^{2+}, the metal ions investigated showed very mild interference to the sensing of Zn^{2+} using **2** by monitoring the fluorescence intensity ratio of I_{461}/I_{383} (Fig. 8). Owing to the satisfactory characters of **2** as a ratiometric fluorescent probe for Zn^{2+}, **2** was applied for the determination of Zn^{2+} concentration in water samples.

3.2. Optimizing the condition for fluorescent determination of Zn^{2+} by **2**

For an optimal condition for the determination of Zn^{2+} by **2** in aqueous solution, the pH of buffer and ethanol fraction used were
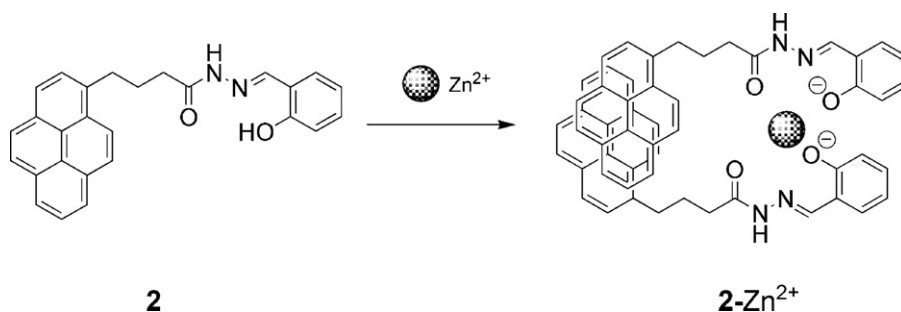
Scheme 2. The proposed 1:2 metal-to-ligand ratio binding model of **2** with Zn^{2+}.
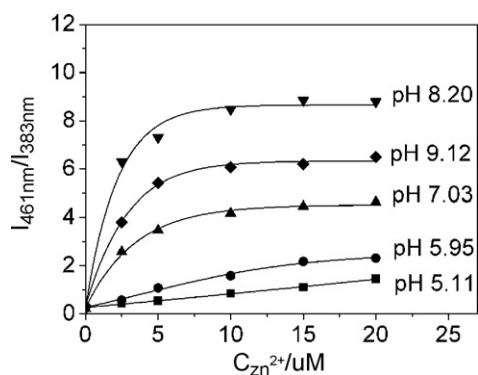
Fig. 9. Effect of pH on the fluorescence intensity ratio I_{461}/I_{383} of **2** upon the addition of Zn^{2+} using 10 μM **2** in 30% (v/v) ethanol/water. The concentration of Tris was fixed to 10 mM. Excitation was performed at 347 nm.

Fig. 11. Fluorescence spectra of **2** (10 μM) in the absence and presence of Zn^{2+} in ethanol. Excitation was performed at 347 nm. [Zn^{2+}] changes from 0 to 40 μM as indicated by arrows. Inset shows the ratio of fluorescence intensity at 461 and 383 nm as a function of Zn^{2+} concentration.

investigated. Because the binding of 10 μM Zn^{2+} to 10 μM **2** could complete within 2 min, all the absorption and fluorescence spectra were recorded after equilibration for 2 min.

3.2.1. Effect of buffer pH

pH might affect the binding of **2** and Zn^{2+} because **2** deprotonized when **2**–Zn^{2+} formed. To investigate the effect of pH on the response of **2** to Zn^{2+}, 10 mM Tris–HCl solutions of 30% ethanol/water (v/v) at pH 5.11, 5.95, 7.03, 8.20 and 9.12 were used as buffer media, respectively (Fig. 9). pH referred that of buffer solutions before they were mixed with ethanol. It was found that in solutions of higher pH, **2** showed more significant increase in I_{461}/I_{383}, which was of benefit for obtaining a good signal/noise ratio upon the addition of Zn^{2+}. However, most samples for Zn^{2+} analysis were neutral, thus the media for Zn^{2+} quantification was then buffered by 10 mM Tris–HCl at pH 7.03.

3.2.2. Effect of ethanol fraction

Ethanol was chosen as a cosolvent for facilitating the binding of **2** and Zn^{2+} because it was a clean and inexpensive solvent compared to many other organic solvents such as acetone, DMF, DMSO, methanol, tetrahydrofuran and acetonitrile. We investigated the determination of Zn^{2+} by **2** in 10 mM Tris–HCl aqueous buffers containing different fractions of ethanol (10, 25, 30, 35, 50%, v/v) at pH 7.03 (Fig. 10). In buffer of low ethanol fraction (10%), I_{461}/I_{383} ratio of **2** was already high even in the absence of Zn^{2+} due to the formation of aggregates of **2** which emitted excimer fluorescence in such a poor solvent. However, if the fraction of ethanol was too high (50%), the binding of **2** and Zn^{2+} could only cause mild increase in fluorescence ratio of I_{461}/I_{383}, which was most probably because the pyrene moiety in solvent of high ethanol fraction was much

more emissive around 383 nm than that in low ethanol fraction buffers and thus decreased the I_{461}/I_{383} ratio. For the largest fold of I_{461}/I_{383} enhancement upon the addition of Zn^{2+} from 0 to 5 μM to **2** (10 μM), the ethanol fraction of buffer was selected as 30% (30%, 20-fold; 25%, 14-fold; 35%, 4-fold). Fluorescence spectra of **2** in the absence and presence of Zn^{2+} in pure ethanol were shown in Fig. 11.

3.3. Analytical figures of merit

According to the above optimized condition of 10 μM **2** in 30% (v/v) ethanol/buffer with Tris–HCl buffer (10 mM) at pH 7.03, the calibration curve for the determination of Zn^{2+} by **2** was constructed. The relationship between fluorescence intensity ratio of I_{461}/I_{383} and concentration of Zn^{2+} in μM (C) was as $I_{461}/I_{383} = 0.8037C + 0.2928$. The linear range of the method was found to be at least 0–5.0 μM Zn^{2+} with a correlation coefficient of $R^2 = 0.9951$ ($n = 21$) (Fig. 12). The detection limit, based on the definition by IUPAC ($C_{DL} = 3S_b/m$) [34], was found to be 0.08 μM from 10 blank solutions. The relative standard deviation (R.S.D.) for three repeated measurements of 2.5 μM Zn^{2+} was 3.3%.

3.4. Tolerance of **2** to Zn^{2+} over other metal ions

The interference experiment using 10 μM **2** in 30% (v/v) ethanol/buffer with 10 mM Tris–HCl at pH 7.03 in the presence of 3 μM Zn^{2+} and proper concentration of other metal ions suggested that, within 5% error, 1000-fold concentration of Na$^+$, K$^+$, Mg^{2+}, Ca^{2+}, more than 5-fold that of Pb^{2+}, Cd^{2+}, Ba^{2+}, more than 0.5-fold of Hg^{2+}, and less than 0.1-fold of Fe^{3+}, Co^{2+}, Ni^{2+}, Cu^{2+} could be tolerant for the analysis. The addition of Fe^{3+}, Co^{2+}, Ni^{2+} and

Fig. 10. Effect of ethanol volume fraction on the fluorescence intensity ratio I_{461}/I_{383} of **2** upon the addition of Zn^{2+} using 10 μM **2** buffered by 10 mM Tris–HCl at pH 7.03. Excitation was performed at 347 nm.
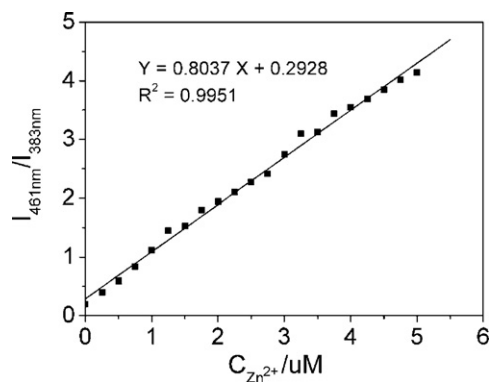
Fig. 12. Fluorescence intensity ratio I_{461}/I_{383} of **2** (10 μM) as a function of Zn^{2+} concentration within its linear range of 0–5 μM in 30% (v/v) ethanol/water buffered by 10 mM Tris–HCl at pH 7.03. Excitation was performed at 347 nm.

Table 2
Determination of Zn^{2+} by **2** in water samples[a].

Sample	Zn^{2+} added (μM)	Zn^{2+} found (μM)	Recovery (%)	R.S.D.[b] (%)
Drinking water	0.00	0.00		
	0.80	0.82	102	3.9
Synthesized water[c]	0.00	0.37	93	5.4
	2.00	2.48	104	4.3

[a] The concentration values are those in 30% (v/v) ethanol/water solutions.

[b] $n = 3$.

[c] Synthesized by: drinking water, 0.40 μM Zn^{2+}, 1.0 μM Cd^{2+}, Ba^{2+}, Pb^{2+}, 5.0 μM Na^+, K^+, Mg^{2+}, and Ca^{2+}. Conditions: 10 μM **2** in 30% (v/v) ethanol/water buffered by 10 mM Tris–HCl at pH 7.03.

Cu^{2+} induced fluorescence quenching of **2** due to their high affinity to probe **2** (Table 1). However, these metal ions did not lead to the change of the fluorescence intensity ratio of I_{461}/I_{383}. Therefore, adding more **2** to the solution could further decrease the interference from Fe^{3+}, Co^{2+}, Ni^{2+} and Cu^{2+}, though a new calibration curve for Zn^{2+} should be constructed. For example, in the presence of Fe^{3+}, Co^{2+}, Ni^{2+} and Cu^{2+} (each 0.5 μM) in 30% (v/v) ethanol/buffer with 12 μM **2**, the calibration curve for the determination of Zn^{2+} by **2** was also constructed. The relationship between fluorescence intensity ratio of I_{461}/I_{383} and concentration of Zn^{2+} in μM (C) was as $I_{461}/I_{383} = 0.7951C + 0.2910$. The linear range was found to be at least 0–4.0 μM Zn^{2+} with a correlation coefficient of $R^2 = 0.9922$ ($n = 17$).

3.5. Application of **2** for Zn^{2+} analysis in water samples

Drinking water (no Zn^{2+}) and synthesized water (with Zn^{2+} and other metal ions in drinking water) were analyzed using **2** under optimized condition (Table 2). The results suggested the successful quantification of Zn^{2+} by **2**, even in the presence of Na^+, K^+, Ca^{2+}, Pb^{2+}, Cd^{2+} and Ba^{2+}.

4. Conclusion

A ratiometric fluorescent probe **2** for Zn^{2+} in aqueous solution of 30% (v/v) ethanol/buffer with 10 mM Tris–HCl buffer at pH 7.03 was reported in this paper. It exhibited the fluorescence of pyrene unit (383 nm) and its zinc complex (461 nm) in the absence and presence of Zn^{2+}, respectively. By monitoring the fluorescence intensity ratio of I_{461}/I_{383}, the probe showed a linear range of 0–5.0 μM and detection limit of 0.08 μM Zn^{2+} in optimized condition. Alkali/alkali earth metal ions and heavy metal ions such as Pb^{2+}, Cd^{2+} and Hg^{2+} showed very mild interference to the method. The detection of Zn^{2+} in drinking water and zinc-containing water samples was also successful. However, Fe^{3+}, Co^{2+}, Ni^{2+} and Cu^{2+} could interfere the analysis by quenching the fluorescence of **2**, and new calibration curves were needed for Zn^{2+} detection under these conditions.

References

[1] J.M. Berg, Y. Shi, Science 271 (1996) 1081.
[2] J.H. Weiss, S.L. Sensi, J.Y. Koh, Trends Pharmacol. Sci. 21 (2000) 395.
[3] R.M. Roat-Malone, Bioinorganic Chemistry: A Short Course, John Wiley & Sons, NJ, 2002.
[4] A.P. de Silva, H.Q.N. Gunaratne, T. Gunnlaugsson, A.J.M. Huxley, C.P. McCoy, J.T. Rademacher, T.E. Rice, Chem. Rev. 97 (1997) 1515.
[5] L. Prodi, F. Bolletta, M. Montalti, N. Zaccheroni, Coord. Chem. Rev. 205 (2000) 59.
[6] P.D. Beer, P.A. Gale, Angew. Chem. Int. Ed. 40 (2001) 487.
[7] L. Pu, Chem. Rev. 104 (2004) 1687.
[8] G.W. Gokel, W.M. Leevy, M.E. Weber, Chem. Rev. 104 (2004) 2723.
[9] V. Amendola, L. Fabbrizzi, F. Forti, M. Licchelli, C. Mangano, P. Pallavicini, A. Poggi, D. Sacchi, A. Taglieti, Coord. Chem. Rev. 250 (2006) 273.
[10] T. Hirano, K. Kikuchi, Y. Urano, T. Higuchi, T. Nagano, J. Am. Chem. Soc. 122 (2000) 12399.
[11] T. Hirano, K. Kikuchi, Y. Urano, T. Nagano, J. Am. Chem. Soc. 124 (2002) 6555.
[12] K. Komatsu, K. Kikuchi, H. Kojima, Y. Urano, T. Nagano, J. Am. Chem. Soc. 127 (2005) 10197.
[13] S.C. Burdette, C.J. Frederickson, W. Bu, S.J. Lippard, J. Am. Chem. Soc. 125 (2003) 1778.
[14] F. Zapata, A. Caballero, A. Espinosa, A. Tarraga, P. Molina, Org. Lett. 9 (2007) 2385.
[15] H.H. Wang, Q. Gan, X.J. Wang, L. Xue, S. Liu, H. Jiang, Org. Lett. 9 (2007) 4995.
[16] Y. Liu, N. Zhang, Y. Chen, L.H. Wang, Org. Lett. 9 (2007) 315.
[17] T. Bo, H. Huang, K. Xu, L. Tong, G. Yang, X. Liu, L. An, Chem. Commun. 34 (2006) 3609.
[18] A.E. Dennis, R.C. Smith, Chem. Commun. 44 (2007) 4641.
[19] C.C. Woodroofe, S.J. Lippard, J. Am. Chem. Soc. 125 (2003) 11458.
[20] C.J. Chang, J. Jaworski, E.M. Nolan, M. Sheng, S.J. Lippard, Proc. Natl. Acad. Sci. U.S.A. 101 (2004) 1129.
[21] A. Ajayaghosh, P. Carol, S. Sreejith, J. Am. Chem. Soc. 127 (2005) 14962.
[22] K. Komatsu, Y. Urano, H. Kojima, T. Nagano, J. Am. Chem. Soc. 129 (2007) 13447.
[23] G. Grynkiewicz, M. Poenie, R.Y. Tsien, J. Biol. Chem. 260 (1985) 3440.
[24] M.E. Germain, T.R. Vargo, P.G. Khalifah, M.J. Knapp, Inorg. Chem. 46 (2007) 4422.
[25] M.E. Germain, M.J. Knapp, J. Am. Chem. Soc. 130 (2008) 5422.
[26] L. Gao, Y. Wang, J. Wang, L. Huang, L. Shi, X. Fan, Z. Zou, T. Yu, M. Zhu, Z. Li, Inorg. Chem. 45 (2006) 6844.
[27] Y. Xiang, A. Tong, P. Jin, Y. Ju, Org. Lett. 8 (2006) 2863.
[28] Y. Xiang, N. Li, X. Chen, A. Tong, Talanta 74 (2008) 1148.
[29] S.C. Chan, L.L. Koh, P.H. Leung, J.D. Ranford, K.Y. Sim, Inorg. Chim. Acta 236 (1995) 101.
[30] W.C. Vosburgh, G.R. Cooper, J. Am. Chem. Soc. 63 (1941) 437.
[31] V.B. Di Marco, G.G. Bombi, M. Tubaro, P. Traldi, Rapid Commun. Mass Spectrom. 17 (2003) 2039.
[32] Y. Shiraishi, K. Ishizumi, G. Nishimura, T. Hirai, J. Phys. Chem. A 111 (2007) 8812.
[33] P. Conlon, C.Y.J. Yang, Y.R. Wu, Y. Chen, K. Martinez, Y.M. Kim, N. Stevens, A.A. Marti, S. Jockusch, N.J. Turro, W.H. Tan, J. Am. Chem. Soc. 130 (2008) 336.
[34] H.M.N.H. Irving, H. Freiser, T.S. West (Eds.), IUPAC compendium of analytical nomenclature, Definitive Rules, Pergamon Press, Oxford, 1981.

Characterization of PDMS-modified glass from cast-and-peel fabrication

Ke Liu[a], Yu Tian[a], Rajesekar Pitchimani[b], Michael Huang[a], Hawa Lincoln[a], Dimitri Pappas[a],[*]

[a] *Department of Chemistry and Biochemistry, Texas Tech University, Lubbock, TX 79409-1061, United States*
[b] *Department of Chemical Engineering, Texas Tech University, Lubbock, TX 79409-3121, United States*

ARTICLE INFO

ABSTRACT

In glass/poly(dimethylsiloxane) (PDMS) hybrid microfluidic chips, two different fabrication approaches are used: photolithographic or solid ink molds, or cast-and-peel methods. In the latter, a thin slab of PDMS is laid down and fluid channels are cut manually or by machine. The cast-and-peel approach has been used successfully for low-shear culture devices, among other applications. The main drawback, not reported to date, of cast-and-peel methods is that removal of PDMS (exposing the glass substrate) results in nanoscopic domains of PDMS still attached to the surface. This residual PDMS is not observable by eye, but affects the hydrophobicity of the device. Using contact angle measurement, atomic force and fluorescence microscopy, the changes in glass surfaces from the cast-and-peel technique were elucidated. This study demonstrates the enhanced protein (NeutrAvidin) adsorption on PDMS treated glass surfaces, and the potential influence of altered glass properties on microfluidic applications has been discussed as well.

© 2009 Elsevier B.V. All rights reserved.

1. Introduction

Poly(dimethylsiloxane) (PDMS) devices have proved to be versatile and popular microfluidic systems for a variety of analytical applications. The methods of producing PDMS chips are versatile, and many take advantage of the elastomeric properties of the material. In particular, the ability to cut and remove large sections of PDMS to form wells, pools, and other structures (henceforth referred to as "cast-and-peel" methods) allows devices to be realized in PDMS that cannot be fabricated in other materials. The material properties of PDMS, however, must be considered in full when designing microfluidic systems. When material is cut from a PDMS slab to form a well, fluid interconnects, etc, the glass underneath the PDMS (upon which PDMS prepolymer was cured) will have an increased hydrophobicity and roughness. Hydrophobicity of a surface is critical for protein attachment [1] (wanted or unwanted) in the device. The manipulation of surface properties—ranging from hydrophobic to hydrophilic, charged or uncharged, smooth to rough—are important in defining biocompatibility [2]. In some cases, modification of glass after the cast-and-peel process may result in unwanted side effects, such as excessive dye or protein adhesion to the device or interruption of glass conjugation chemistry by residual PDMS domains. However, this type of PDMS-modified glass may also serve as a useful, biocompatible surface for protein and cell analysis. To date,

surface modification for biocompatibility has been based on self-assembled monolayers (SAMs) [3,4], polyelectrolyte multilayers (PEMs) [2,5,6], spin-coating [7], microcontact printing (stamping) [8,9], and carbon nanotube (CNT) deposition [10,11]. Although, these techniques have been successful in significantly improving device performance in relevant biological studies, they may not be the best choices to reach these goals, especially with regard to reagent and time management [12], structure quality and surface coverage control [12–14], storage and instrument access [15].

Since the early 1990s, PDMS has been extensively used in either clinic or laboratory for medical implants, biomedical devices, microfluidic channels, and optical components on the basis of its unique advantages. These advantageous properties include good biocompatibility and gas (O_2 and CO_2) permeability, nontoxicity, high oxidative and thermal stability, optical transparency (240–1100 nm), and so on [16]. The above mentioned attributes, in addition to the elastic nature of PDMS, have made PDMS suitable and favorable for studies of cell-based assays [16–20]. Despite these intriguing merits, PDMS still has shortcomings, among which the intrinsic hydrophobicity has been criticized as a major limitation in quantitative analysis due to unwanted protein adsorption. Although many efforts have already been made to render the PDMS surface more hydrophilic, like plasma treatment, anionic surfactant coating, silica particle modification [17], the reported strategies for preparing a more biocompatible (hydrophobic) glass surface are exclusively based on aforementioned technologies (SAM, PEM, spin-coating, stamping, and CNT). None of these methods have been fully proposed for applying PDMS to this particular purpose.

* Corresponding author. Tel.: +1 806 742 3142.
  E-mail address: d.pappas@ttu.edu (D. Pappas).

Protein adhesion is significant for biocompatible material determination. At most substrates, this dynamic process relies on hydrophobic interactions, electrostatic attractions, van der Waals force and hydrogen bonding, among which the hydrophobic interaction is the governing factor that leads to more proteins absorb on hydrophobic surfaces than on hydrophilic (–OH) surfaces [20–22]. Many PDMS–glass hybrid devices feature separate chemical properties (e.g. cell culture on the glass substrate, while PDMS serves as a structural material). Glass is typically chosen in these cases because of its thermal and chemical stability, excellent optical properties, and cost efficiency [23]. Furthermore, the ability to conjugate with numerous biomolecules and the well-established protocols to precisely pattern the surface make glass an attractive candidate for the fabrication of PDMS hybrid microdevices.

In our previous work, a cast-and-peel approach was used to fabricate circular culture wells in a low-shear chip design [16]. The main benefit of removing PDMS from the substrate in a cast-and-peel manner is that larger structures can be fabricated than by photolithography. The cursory experiments reported in that paper indicated that the introduction of methyl functional termini from residual PDMS domains altered the expected functionality of the chip. After removing portions of the PDMS slab from glass during the fabrication process the culture chips exhibited a bioactive interface for interacting with adherent cell culture. Favorable cell growth was possible without adhesion promoting materials such as fibronectin, collagen, and poly-L-lysine. However, we only showed preliminary results of the surface properties on a PDMS-modified glass. In some circumstances, this surface modification format is preferable, when more hydrophobic surfaces are needed but the rigidity of glass is desired. This paper presents an expanded investigation of the surface alteration. The residual PDMS domains left on glass can chemically or physically alter the properties of the substrate. To better elucidate the modification process and its consequent impact toward the changes in surface hydrophobicity and topography, this study focuses on the increased hydrophobicity of PDMS-modified glass. Glass surfaces were modified by physically peeling off a cured PDMS layer from the microscope slide. Surface characterization was carried out via water contact angle measurement, atomic force microscopy and fluorescence detection of protein adhesion.

2. Experimental

2.1. Chemicals and materials

All reagents and materials were used as received unless otherwise noted. Poly(dimethlysiloxane (PDMS) elastomer and crossing-linking agent were purchased from Ellesworth Adhesives (Dow Sylgard 184). Microscope glass slides (76.2 mm × 25.4 mm × 1 mm) were obtained from VWR International and used for substrates in all the experiments. Phosphate buffer saline (PBS, Ph 7.4) was acquired from Gibco Invitrogen (Grand Island, NY). Biotin-Rhodamine 110 (BR110) and NeutrAvidin were purchased from Biotium and Pierce, respectively. Ethanol and isopropyl alcohol were obtained from Fisher Scientific. Deionized water was prepared with a Millipore purification system and Rhodamine B dye was purchased as solids from Sigma (St. Louis, MO).

2.2. Preparation of the glass surface and water contact angle measurement

The glass surfaces were rinsed subsequently with ethanol and DI water, dried with a stream of air, and stored in desiccators for further use. The preparation of the PDMS mixture was previously described elsewhere [16]. In short, PDMS was thoroughly mixed
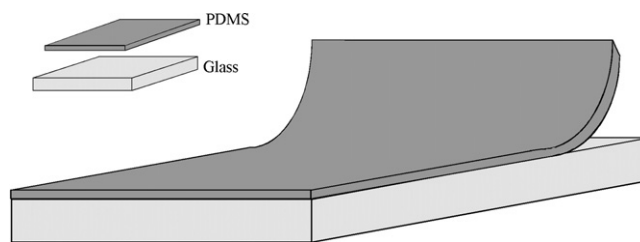
Fig. 1. Schematic representation of fabrication for PDMS-modified glass surface.

in a 10:1 mass ratio of prepolymer and curing agent according to the manufacturers directions and degassed under vacuum. Prior to decanting PDMS onto the glass substrates, the slides were checked using water contact angle, a small contact angle (<15°) indicated the sufficient cleanliness on the surfaces and thus ensured the quality of PDMS modification [24]. Fluorescence background of cleaned glass slides was minimal. The PDMS mixture was then cured against the glass substrate at $90 \pm 5\,^{\circ}C$ for 60 min and subsequently peeled to yield the modified surface (Fig. 1). For contact angle measurements, two types of glass surfaces were examined to assess the changes in hydrophobic character from PDMS modification: sample surface with PDMS coating and control surface (bare glass) without PDMS coating. The measurements were performed with the sessile drop technique and the values were determined from the average of at least 3 or 4 separated droplets through Drop-Analysis plugin in imageJ (National Institutes of Health). The measured contact angle of PDMS slabs and pristine glass controls were in good agreement with previously reported data obtained under the same conditions [25], which demonstrated reasonable accuracy in our observation. All the contact angle images were acquired using a CCD digital camera (SONY-DSC-W7) at different time scales on distinct sample surfaces in order to examine the stability of PDMS coating, and the measurements were repeated by different personnel ($n = 4$) to reduce the subjectivity in statistical analysis.

The stability of the PDMS surface was assessed by repeat contact angle measurements. In cases where PDMS-modified glass will be exposed to non-aqueous solvents, the swelling of PDMS may affect the surface stability. Surface stability will affect wettability; therefore, contact angle can also serve as a gauge of surface stability after exposure to different solvents.

2.3. Fluorescence imaging and measurement

An inverted epifluorescence microscope (Olympus IX71) equipped with a charge-coupled-device CCD camera (Hamamatsu C4742-95) was used to collect the fluorescent images of adsorbed Rhodamine B dye on the surfaces. PDMS treated and cleaned glass slides were immersed in 480 µM Rhodamine B/ethanol solution, placed at 37 °C in the dark and allowed to react for one hour to enable the completely hydrophobic/electrostatic interaction between glass surfaces and Rhodmine B molecules. Afterwards, the surfaces were gently washed with DI water to remove excess Rhodamine B and dried in a stream of air. Rhodamine B-labeled surfaces were excited through an appropriate bandpass filter. A 100W mercury lamp was chosen as the excitation source. Multiple images ($n > 12$) were taken from different spots on sample and control surfaces. The fluorescence intensities had been measured using the same NIH image software and normalized by the overall maximum value obtained from one of the modified surfaces. All Rhodamine B fluorescence images were captured with 10× objective at 100 ms exposure time to eliminate experimental deviation; graphs were generated by Origin 6.0 (OriginLab, USA).

2.4. Protein adsorption determination

NeutrAvidin was used as a model of protein adsorption onto PDMS-modified and pristine glass surfaces. NeutrAvidin has a high binding association constant for biotin ($K_a \approx 10^{15}\,M^{-1}$) [26] and forms stable complexes.

Biotin-Rhodamine 110 was used to image NeutrAvidin adsorption via fluorescence microscopy. In this approach, a half-treated glass surface was exposed to dilute NeutrAvidin solution (100 nM in PBS) for 30 min, carefully rinsed with PBS, and placed in BR110 PBS solution (400 nM) for another 30 min. The slide was then transferred into bulk PBS solution and immediately imaged through appropriate filter set coupled with the identical 10× objective mounted on the microscope. The untreated portion of the slide served as the control. All the reactions were performed at room temperature.

2.5. Atomic force microscopy

The morphologies of modified and untreated surfaces were characterized by using atomic force microscopy (AFM) (model PSIA XE-100, Park Scientific) in ambient environment. The surface imaging was operated in non-contact (tapping) mode with a standard silicon cantilever and the scan rates were optimized to minimize hysteresis between forward and backward traces of cantilever probe. For determination of topography properties, randomly selected regions ($2\,\mu m \times 2\,\mu m$) on both surfaces were visualized. Comparisons were made with AFM images to examine the compositional and physical variations in surface features. Previous observations have shown that the resulting root-mean-square (RMS) roughness of an obtained topography image can reach a relatively higher level by the coverage of trace amount PDMS [16]. Since 10:1 PDMS had been reported to yield optimal cross-linking density between silicon elastomer and curing agent [13], only this ratio was tested.

3. Results and discussion

3.1. Surface characterization

Fig. 2 shows the AFM phase images of modified and plain glass substrates. The phase values of untreated glass are low, indicating a lack of the more elastic PDMS domains found on the treated slide. The glass surface exhibits a drastic change in heterogeneity due to the chemical modification of residual PDMS. The displayed white microdomains on the modified surface represent presumably residual PDMS, while the localized features on bare glass surface indicate the inevitable defects and contaminants found in glass. The PDMS adsorption on glass substrate can be used to account for the observation of more hydrophobic nature and rougher surface. Various explanations had been proposed for the formation of these micro-sized PDMS features on silica surfaces. Galliano and co-workers described this process as the result of both adherence and friction behaviors in cross-linked polymer on a porous surface [24]. Another alternative hypothesis is based on cohesive failure mechanism, in which the physical detachment of hydrogen-bonded siloxane (Si–O–Si) groups between the PDMS chains and glass surface contributes to the generation of PDMS adsorbed substrate [25,27].

The effect of surface modification on the water contact angle was investigated in this approach. Fig. 3 presents a water droplet on the glass surface before and after the PDMS treatment, and on a flat 10:1 PDMS slab. As one can see, PDMS coated surfaces have significantly increased water contact angle values. The comparable values of contact angle of PDMS-modified glass and bulk PDMS indicate that the
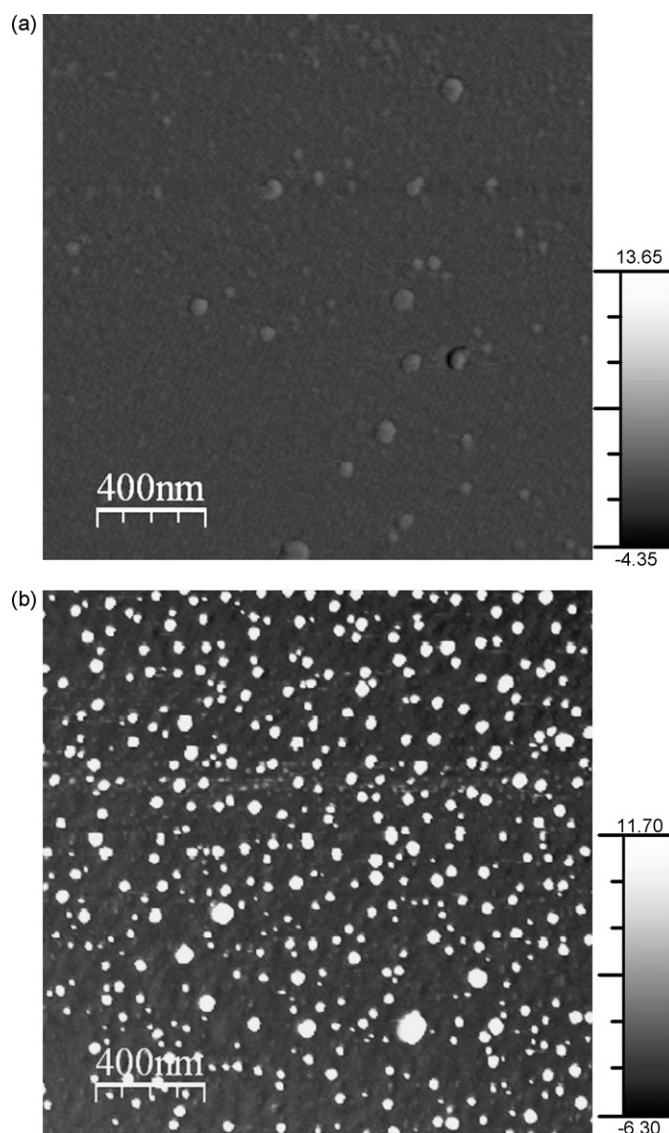
Fig. 2. AFM phase images of untreated glass slide (a) and glass slide coated with PDMS (b). The white features (higher phase) represent the PDMS on the surface.
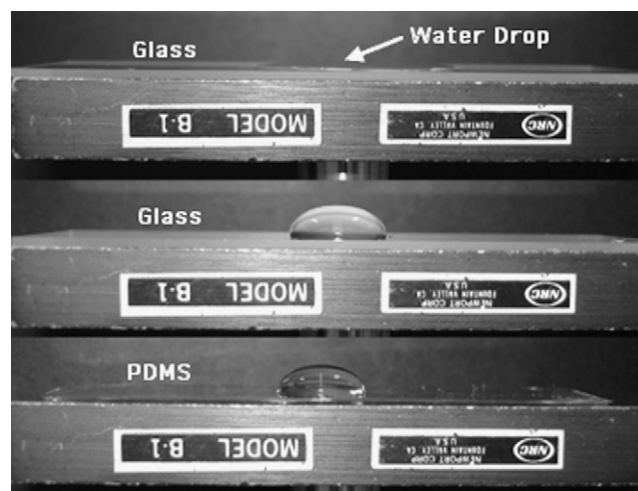
Fig. 3. Photographs of water droplet on a regular glass slide (a), on a slide coated with 10:1 PDMS (b), and on a 10:1 PDMS slab (c). An inverted optic mount was used to hold the glass slide.
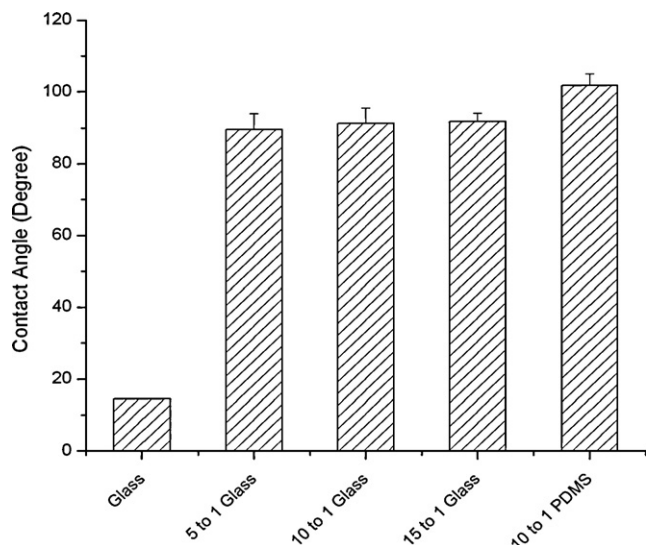
Fig. 4. Contact angle measurements on non-modified glass surfaces, glass surfaces treated with different ratios of PDMS, and 10:1 PDMS surfaces. The value of contact angle on the PDMS slab is slightly higher (10–15%) than modified glass surfaces, which show little differences with each other. The t-test was applied to confirm the statistical difference between PDMS-modified glasses and PDMS slab.

surfaces have similar hydrophobicities and surface energies. As the prepolymer-cross linker ratio increases, the hydrophobicity of the PDMS-peeled glass does not vary significantly (Fig. 4).

To analyze the effects of time and chemical exposure on surface hydrophobicity, we measured the contact angles between the glass slides immersing in widely used solvent (ethanol or isopropyl alcohol) and placing in vacuum after 72 h. The shapes of water drops
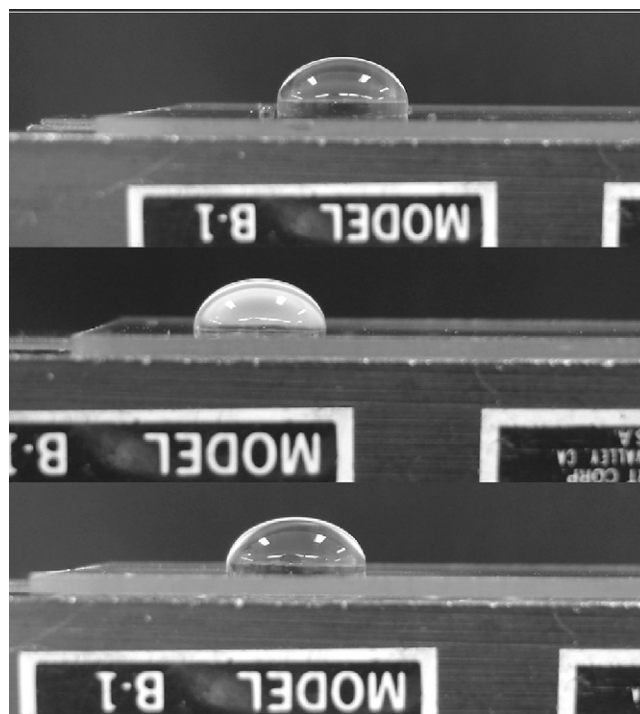
Fig. 5. Images of water drop on PDMS treated glass surfaces acquired after 72 h exposure to vacuum (a), ethanol (b), and isopropyl alcohol (c).
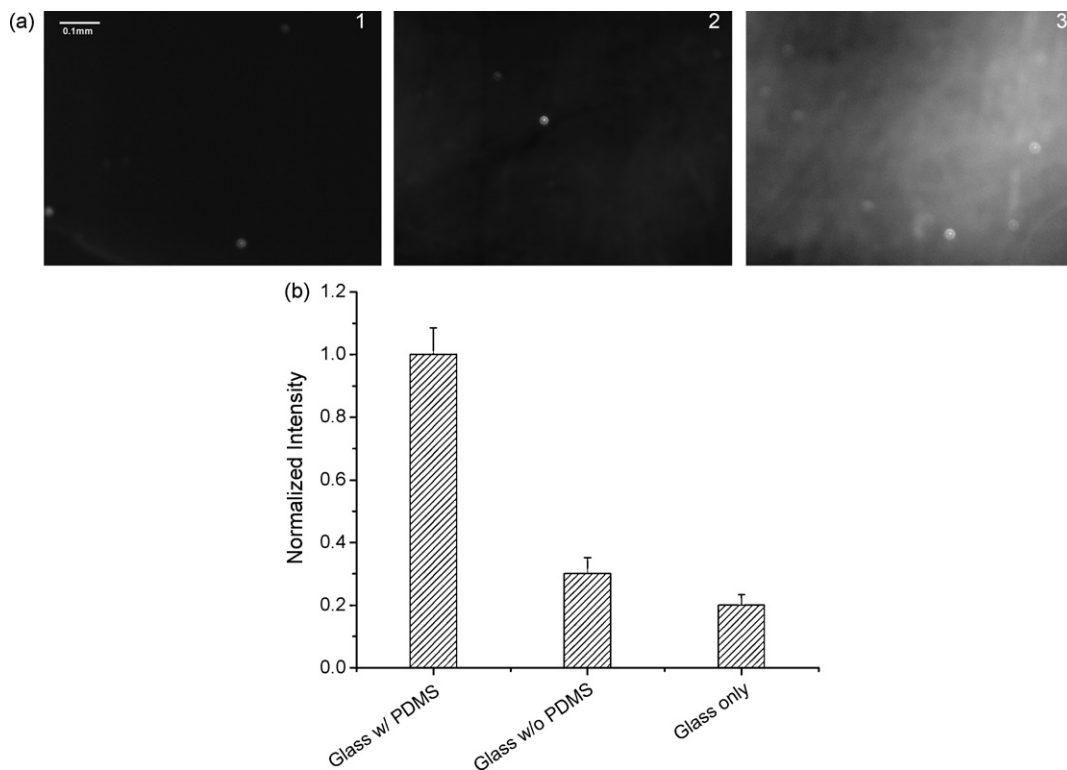
Fig. 6. Fluorescent images of the PDMS coated (C) and blank glass (B) surfaces after 60 min immersion in 480 μM ethanol-based Rhodamine B at a fixed exposure time for 100 ms. The background fluorescence intensity is evaluated using original glass slide (A). These images reveal the corresponding enhancement of Rhodamine B adsorption on a PDMS-modified surface due to its hydrophobic property. Bright spots could be induced by the fluorescent impurities existing in glass; the discrepancy in fluorescence intensity across the glass surface may arise from the uneven distribution of PDMS modification. Scale bar = 100 μm. B: Corresponding profile of normalized intensity showing the enhanced adsorption of Rhodamine B on a more hydrophobic surface. The error bar denotes the standard deviations.

are similar to those in Fig. 3, which reveals the absence of dramatic increase or decrease of contact angles (Fig. 5).

Since the combination of chemical composition and microstructures of the surface plays an important role in defining its wettability, we believe that the noticed shift to a hydrophobic appearance confirms the presence of PDMS on the glass surface. The fabricated surface also possesses an increased roughness of 1 nm compared to 0.5 nm for a clean glass; thus more air can be trapped in the spaces between the structural features on surface. In conjunction with previous observations that a water droplet can be speculated as partially sitting on entrapped air on a surface [28], this levitation reduces the contact area of water with the support surface, and directly influences the value of contact angle in our study. The quantitative determination of apparent contact angle on a solid and air composite surface can be described by the following equation [29].

$$\cos \theta^c = f(\cos \theta + 1) - 1$$

where θ^c and θ are apparent and equilibrium contact angles on heterogeneous and planar surfaces, respectively, and f is the area fraction of the solid substrate. Due to the inversely proportional dependence, with the decreasing of contact area f, the θ^c will be accordingly increased. Using the mean water contact angle (15 °C) and the measured contact angle for PDMS-modified glass (10:1 PDMS mix), the area fraction can be estimated to be 0.5, and this calculated number is observed to be consistent with the effect resulted from the increase of root mean square (RMS) roughness.

3.2. Adsorption of rhodamine B on PDMS-modified glass

Recently, fluorescence imaging of Rhodamine B has been successfully used for dynamic flow characterization and temperature studies in microfluidic and lab-on-a-chip devices [30–32]. Although, many researchers have also reported the problem of specific adsorption and diffusion of small hydrophobic fluorophores (e.g. Rhodamine B) within PDMS based channels [32], this compatibility issue has been exploited in this case for monitoring the trace amount PDMS on the sample surface. As shown in Fig. 6, the fluorescent intensity of PDMS-treated glass is much higher than glass without PDMS modification. The blank slide indicates the base level of background luminescence common to glass slides excited at the wavelengths used with rhodamine B (540–550 nm). A residual amount of rhodamine B on untreated glass increases the fluorescence from 19% of the normalized scale to 29%, whereas the adsorption of rhodamine B on PDMS-treated glass is 3.4 times larger. In comparison, rhodamine absorption to PDMS slabs was measured to be 25 times larger than PDMS treated glass. The adhesion or partition of this low molecular weight hydrophobic dye can therefore be used as a marker of surface modification, particularly when the cast-and-peel features are too small for AFM access or contact angle analysis. In addition, this method is useful in finished devices, where fluorescence imaging may be the only method to assay surface modification.

3.3. Biotin-neutravidin labeling of PDMS-modified surface

Protein adsorption is especially meaningful in cell-based assays. It is commonly accepted that cell adhesion is mediated by the interaction with preadsorbed proteins during implant integration [21]. To quantitatively evaluate whether modification of glass surfaces with PDMS is beneficial for the fabrication of a more bio-friendly interface, adhesion of NeutrAvidin was investigated. As shown in Fig. 7A, the portion of the surface with PDMS domains has higher fluorescence intensity, which is the evidence that more NeutrAvidin protein molecules were immobilized at defined location due
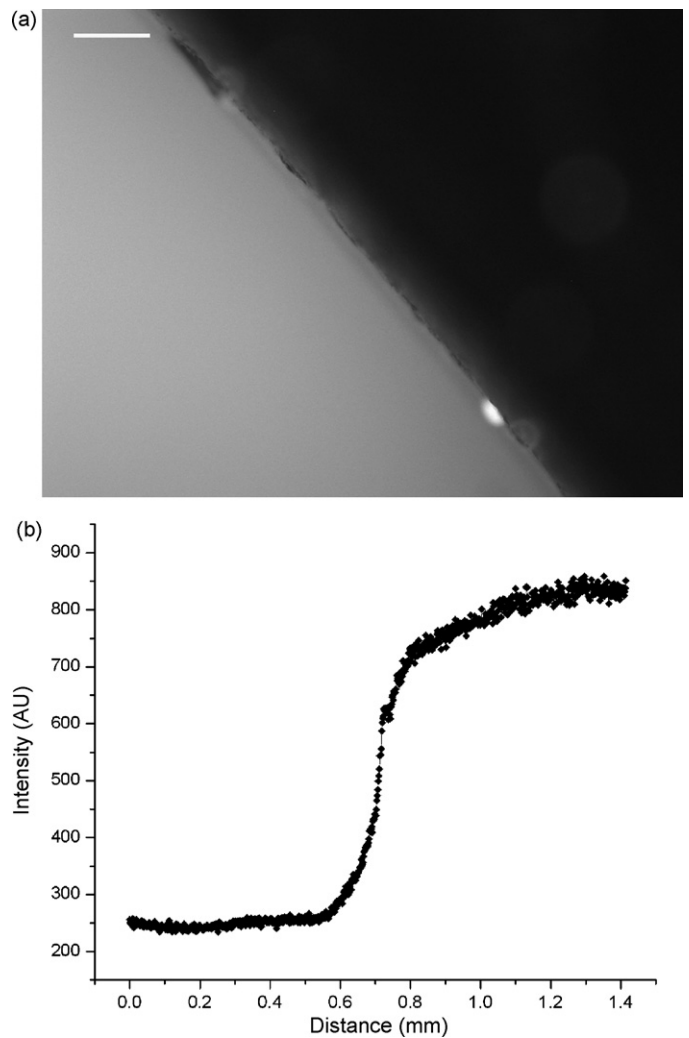
Fig. 7. A: Fluorescence images at the edge of PDMS-modified and original surfaces on the same glass slide. The PDMS-modified portion is on the left; untreated glass is on the right. The increased hydrophobicity results in increased NeutrAvidin adsorption (visualized using biotinylated rhodamine 110, scale bar = 100 μm. B: Fluorescent intensity profile of a randomly selected line across the boundary showing the difference in signal amplitude.

to the hydrophobic interaction. Fig. 7B illustrates the corresponding fluorescence intensity profile across the edge of two separate areas. Experiments with the biotin-rhodamine 110 probe only (no protein) showed minimal adhesion to glass and PDMS-modified glass when compared with experiments where both protein and biotinylated fluorophore were present.

4. Conclusion

PDMS-modified glass results as an artifact from a cast-and-peel fabrication method. Microfluidic devices using this fabrication approach must therefore be careful to assure that the desired operation matches the real functionality of the device. Alternatively, this method can intentionally be performed to generate rigid surfaces with greater hydrophobicity than bare glass. The water contact angle and fluorescence measurements revealed a profound increase in water contact angle (∼90°) on the treated glass surface. Our future work will focus on controlling of PDMS residual density on surfaces by means of varying the ratio of PDMS prepolymer or the curing time and temperature between the slab and the surface, achieving a more uniform modification on various surfaces. We will also investigate different polymeric materials and metals, and

improving the reproducibility from chip to chip. A greater understanding of PDMS–glass interactions, including investigation into the mechanism of PDMS adhesion after peeling, will aid in producing a new class of microfluidic devices with tailored surface properties.

Acknowledgements

References

[1] L. Yu, C.-M. Li, Q. Zhou, J.H.-T. Luong, Bioconj. Chem. 18 (2007) 281–284.
[2] D.S. Salloum, S.G. Olenych, T.C.S. Keller, J.B. Schlenoff, Biomacromolecules 6 (2005) 161–167.
[3] S. Chen, L. Liu, S. Jiang, Langmuir 22 (2006) 2418–2421.
[4] A. Revzin, R.G. Tompkins, M. Toner, Langmuir 19 (2003) 9855–9862.
[5] S.P. Forry, D.R. Reyes, M. Gaitan, L.E. Locascio, Langmuir 22 (2006) 5770–5775.
[6] S. Kidambi, I. Lee, C. Chan, J. Am. Chem. Soc. 126 (2004) 16286–16287.
[7] H. Zheng, M.C. Berg, M.F. Rubber, P.T. Hammond, Langmuir 20 (2004) 7215–7222.
[8] M. Schaeferling, S. Schiller, H. Paul, M. Kruschina, P. Pavlickova, M. Meerkamp, C. Giammasi, D. Kambhampati, Electrophoresis 23 (2002) 3097–3105.
[9] N.D. Gallant, J.R. Capadona, A.B. Frazier, D.M. Collard, A.J. García, Langmuir 18 (2002) 5579–5584.
[10] M.P. Mattson, R.C. Haddon, A.M. Rao, J. Mol. Neurosci. 14 (2000) 175–182.
[11] H. Hu, Y. Ni, V. Montana, R.C. Haddon, V. Parpura, Nano. Lett 4 (2004) 507–511.
[12] J.C. Love, L.A. Estroff, J.K. Kriebel, R.G. Nuzzo, G.M. Whitesides, Chem. Rev. 105 (2005) 1103–1170.
[13] M. Godin, P.J. Williams, V. Tabard-Cossa, O. Laroche, L.Y. Beaulieu, R.B. Lennox, P. Grutter, Langmuir 20 (2004) 7090–7096.
[14] C. O'Dwyer, G. Gay, B. Viaris de Lesegno, J. Weiner, Langmuir 20 (2004) 8172–8182.
[15] K. Jans, K. Bonroy, R. De Palma, G. Reekmans, H. Jans, W. Laureyn, M. Smet, G. Borghs, G. Maes, Langmuir 24 (2008) 3949–3954.
[16] K. Liu, R. Pitchimani, D. Dang, K. Bayer, T. Harrington, D. Pappas, Langmuir 24 (2008) 5955–5960.
[17] R. Mukhopadhyay, Anal. Chem. A 79 (09) (2007) 3248–3253.
[18] J.W. Hong, T. Fujii, M. Seki, T. Yamamoto, I. Endo, Electrophoresis 22 (2001) 328–333.
[19] R. Gomez-Sioberg, A.A. Layrat, D.M. Pirone, C.S. Chen, S.R. Quake, Anal. Chem. 79 (2007) 8557–8563.
[20] J.N. Lee, X. Jiang, D. Ryan, G.M. Whitesides, Langmuir 20 (2004) 11684–11691.
[21] P. Roach, D. Farrar, C.C. Perry, J. Am. Chem. Soc. 127 (2005) 8168–8173.
[22] D.O.H. Teare, N. Emmison, C. Ton-That, R.H. Bradley, Langmuir 16 (2000) 2818–2824.
[23] H. Zheng, M.C. Berg, M.F. Rubner, P.T. Hammond, Langmuir 20 (2004) 7215–7222.
[24] A. Galliano, S. Bistac, J. Schultz, J. Colloid Interf. Sci. 265 (2003) 372–379.
[25] Z. Zheng, O. Azzaroni, F. Zhou, W.T.S. Huck, J. Am. Chem. Soc. 128 (2006) 7730–7731.
[26] P. Vermette, T. Gengenbach, U. Divisekera, P.A. Kambouris, H.J. Griesser, L. Meagher, J. Colloid Interf. Sci. 259 (2003) 13–26.
[27] K.G. Marinova, D. Christova, S. Tcholakova, E. Efremov, N.D. Denkov, Langmuir 21 (2005) 11729–11737.
[28] S.M. Kim, S.H. Lee, K.Y. Suh, Lab. Chip. 8 (2008) 1015–1023.
[29] A.B.D. Cassie, S. Baxter, Trans. Faraday Soc. 40 (1944) 546–551.
[30] T. Glawdel, Z. Almutairi, S. Wang, C. Ren, Lab. Chip. 9 (2009) 171–174.
[31] R. Samy, T. Glawdel, C.L. Ren, Anal. Chem. 80 (2008) 369–375.
[32] J.L. Pittman, C.S. Henry, S. Douglass Gilman, Anal. Chem. 75 (2003) 361–370.

Solid phase extraction of Co ions using L-tyrosine immobilized on multiwall carbon nanotubes

Pablo H. Pacheco [a,b], Patricia Smichowski [b,c], Griselda Polla [d], Luis D. Martinez [a,b,*]

[a] Instituto de Química de San Luis (INQUISAL-CONICET), Chacabuco y Pedernera, CP 5700, San Luis, Argentina
[b] Consejo Nacional de Investigaciones Científicas y Técnicas (CONICET), Rivadavia 1917, CP C1033AAJ, Ciudad de Buenos Aires, Argentina
[c] Comisión Nacional de Energía Atómica, Gerencia Química, Av. Gral. Paz 1499, B1650KNA, San Martín, Argentina
[d] Comisión Nacional de Energía Atómica, Gerencia de Investigación y Aplicaciones, Av. Gral. Paz 1499, B1650KNA, San Martín, Argentina

ABSTRACT

A study was performed to assess the performance of aminoacids immobilized on carbon nanotubes (CNTs) for their employment as a sorbent for solid phase extraction systems. An immobilization method is introduced and the aminoacid L-tyrosine was chosen as a case study. A spectrophotometric study revealed the amount of aminoacid immobilized on CNTs surface, and it turned to be of 3174 μmol of L-tyr g^{-1}. The material was tested for Co retention using a minicolumn inserted in a flow system. At pH 7.0, the amount of Co retained by the column was of 37.58 ± 3.06 μmol Co g^{-1} of CNTs. A 10% (v/v) HNO$_3$ solution was chosen as eluent. The pH study revealed that Co binding increased at elevated pH values. The calculation of the mol ratio (moles of Co bound at pH 9 to moles of L-tyr) turned to be 3:1. The retention capacity was compared to other bivalent cations and showed the following tendency: Cu^{2+} > Ni^{2+} > Zn^{2+} $\gg$ Co^{2+}. The analytical performance was evaluated and an enrichment factor of 180 was obtained when 10 mL of 11.37 μg L^{-1} Co solution was loaded onto the column at pH 9.0; reaching a limit of detection (LoD) of 50 ng L^{-1}. The proposed system was successfully applied to Co determination in QC-LL2 standard reference material (metals in natural water).

© 2009 Elsevier B.V. All rights reserved.

1. Introduction

Some heavy metals like copper and cobalt are necessary for human life, while some heavy metals such as lead and cadmium are problematic for humans [1]. Metal ions determination at trace levels is very important in the context of environmental protection, food and agricultural chemistry as well as high purity materials [2]. Metals are introduced into the environment by natural and anthropogenic sources [3]. The major man-made sources of these heavy metals are soils and dusts from traffic, industry and weathered materials.

The direct determination of metal ions in complex matrices is limited due to their usually low concentrations and matrix interferences [1]. In trace analysis, therefore, preconcentration and/or separation of analytes are necessary to improve sensitivity and selectivity of analysis. Solid phase extraction (SPE) has been developed as a convenient and low cost alternative in comparison to other extraction techniques, and is widely used for separation and preconcentration purposes [4]. SPE is an effective means for extending detection limits and solving problem referred to matrix interferences. The methods based on sorbent extraction have proven to be the most attractive ones due to their specificity and high preconcentration efficiency [5,6].

Many materials have been employed by our research group for SPE like activated carbon [7] and more recently different aminoacids immobilized on controlled pore glass (CPG) like L-methionine [8]. Nowadays, carbon nanotubes (CNTs) have been proposed as a novel solid phase extractant for various inorganic and organic compounds/elements at trace levels [1,9–11]. The hexagonal arrays of carbon atoms in graphite sheets of CNTs surface are ideal for strong interactions with other molecules. In addition, their large surface areas make them a promising solid sorbent for preconcentration procedures [12–14]. In this context, many molecules have been immobilized onto CNTs surface, like DNA and different proteins [15–21]. In order to create synergy between nanotubes and biomolecules, these must be connected to CNTs. The best stability, accessibility and selectivity, however, will be achieved through covalent binding because of its capability to control the location of the biomolecule, improving stability, accessibility and selectivity; reducing leaching [22].

Aminoacids appear as promising molecules to be immobilized on nanomaterials [23]. They possess different functional groups with different metal binding capacities. Selectivity, strong binding

* Corresponding author at: Instituto de Química de San Luis (INQUISAL-CONICET), Chacabuco y Pedernera, CP 5700, San Luis, Argentina. Fax: +54 2652 430224.
E-mail address: ldm@unsl.edu.ar (L.D. Martinez).

capacity and environmental innocuity [24–27] are some properties that aminoacids present turning them into ideal molecules for trace element preconcentration.

L-Tyrosine is an aromatic, low polar aminoacid with a phenolic group on its side chain. Many complexes have been described involving L-tyrosine and metals such as Al [28], Cu [29], Fe [30], Hg [31] even with Co [32]. The noncovalent binding forces involved in these complexes are cation–π interactions [33]

This paper describes a new immobilization method to link the aminoacid L-tyrosine to CNTs. The number of aminoacid molecules immobilized onto the CNTs was determined. Cobalt was selected as a key element to assess L-tyrosine-CNTs as a new sorbent for SPE procedures. Influent concentration, pH, influent flow rate and a comparison with other bivalent cations were used as parameters for characterization. Analytical features were also studied. For validation, Co was determined in QC-LL2 standard reference material. To the best of our knowledge this is the first time that an aminoacid immobilized on CNTs has been employed for analytical purposes.

2. Experimental

2.1. Instrumentation

The determination of metal concentrations was carried out on a Shimadzu Model AA-6800 atomic absorption spectrometer (Tokyo, Japan), equipped with an air/acetylene flame. A deuterium background corrector was used for every elemental determination. The wavelengths of Co, Ni, Cu and Zn used were 228.616, 221.647, 324.754 and 213.856 nm, respectively.

A Beckman, Model DU 520, UV/Vis spectrophotometer (California, USA) was employed to determine the number of L-tyr molecules immobilized onto CNTs surface.

A Minipulse 3 peristaltic pump Gilson (Villiers-Le-Bell, France) was also used. Sample injection was achieved using a Rheodyne (Cotati, CA, USA) Model 50, four-way and of six ports, two positions, rotary valves. Instrumental details and experimental conditions adopted for the FI system are the same reported previously [34].

The conical minicolumn was prepared by placing 10 mg of L-tyrosine-CNTs into an empty conical tip using the dry packing method. The minicolumn has an internal diameter of 0.5–3 mm and 1 cm length. To avoid filling losses when the sample solution passed through the conical minicolumn, a small amount of quartz wool was placed at both the ends. The column was then connected to an eight-roller peristaltic pump with PTFE tubing to form the preconcentration system. Tygon type pump tubing with an internal diameter of 1.52 mm (Ismatec, Cole Parmer, Vernon Hills, IL, USA) was employed to propel the sample, reagents and eluent.

2.2. Reagents

Unless otherwise stated, the chemicals used were of analytical grade, and therefore no further purification was required. Working standard solutions were prepared immediately before use by stepwise dilution from 1000 mg L^{-1} Co, Ni, Zn and Cu stock standard solution (Flucka, Steinheim, Switzerland). Commercial multiwall CNTs were obtained from Sunnano (Jiangxi, China). L-Tyrosine was obtained from MP Biomedicals Inc (Chicago, IL, USA).

2.3. Immobilization procedure

About 10 mg of commercial multiwall CNTs were treated with concentrated HNO$_3$ to clean them and eliminate possible Fe residues present in CNTs due to the generation process. This procedure also allowed the generation of –COOH and –OH groups on CNTs surface, improving their solubility [35]. After this, CNTs were centrifuged, filtrated and dried.
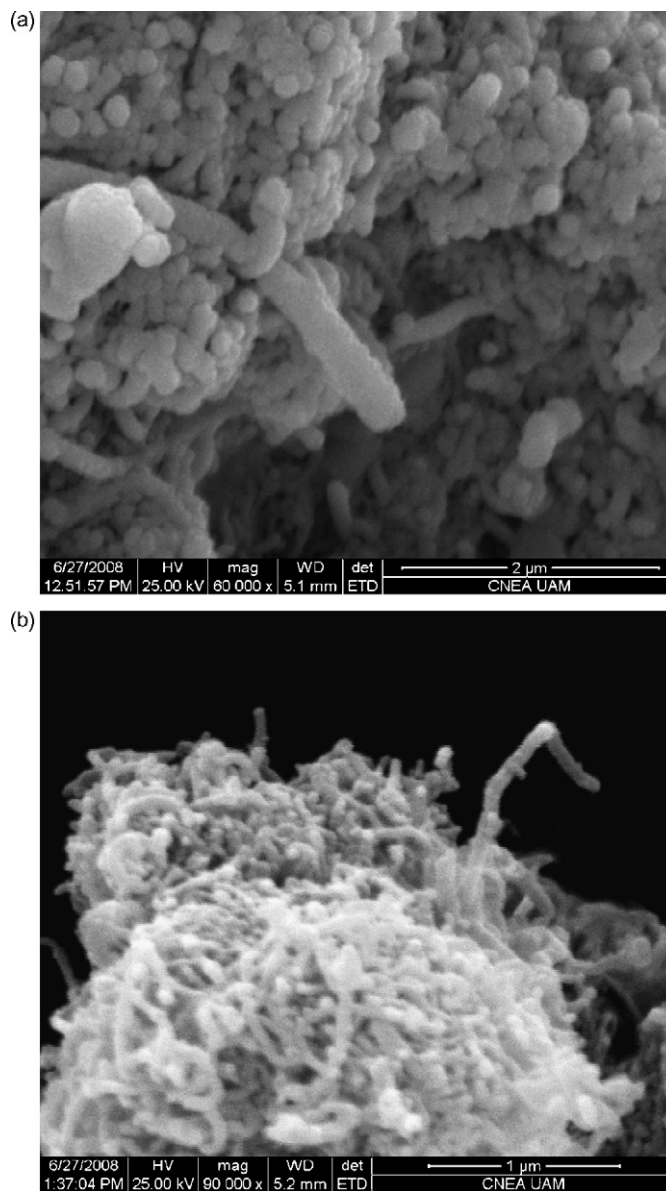
Fig. 1. Electron micrographs of (a) CNTs and (b) L-tyrosine immobilized on CNTs.

The resultant powder was suspended in phosphate buffer pH 7.0 and an aliquot of 10 mg of the aminoacid (L-tyr) was added to the buffer solution. After this, the solution was heated for 48 h at 45 °C. Finally, it was filtered, and CNTs were dried at room temperature. Fig. 1 shows a scanning electron microscopy (SEM) photograph of CNTs previous and after the immobilization.

2.4. Metal binding studies

2.4.1. Procedure

The uptake and release of Co by L-tyr immobilized on CNTs were studied with respect to pH, influent flow rate, influent concentration and compared with other bivalent cations (Zn, Ni, and Cd) using an on line procedure. Before starting the experiments, a cleaning step of 5 min with 10% HNO$_3$ was performed. After that, a 0.05 mol L^{-1} ammonium acetate solution (pH 7.0) was pumped through the column for 2 min at 1 mL min^{-1} to recondition the column to the neutral pH. The different solutions were prepared by dilution from metal standard into 0.05 mol L^{-1} ammonium acetate. Different volumes of 11.4 mg L^{-1} ammonium acetate–metal
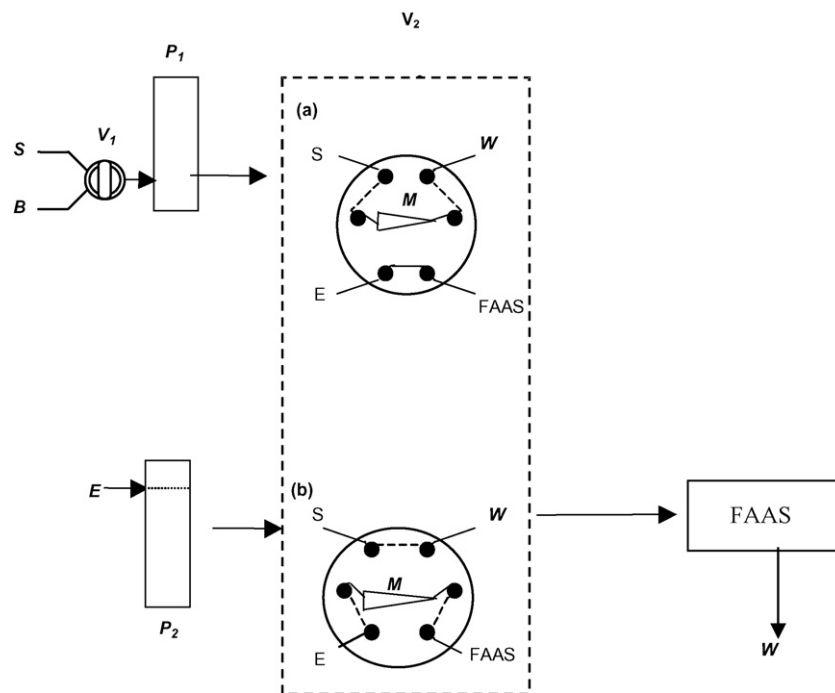
Fig. 2. Schematic diagram of the instrumental setup: S, sample (flow rate, 1 mL min^{-1}); B, buffer; E, eluent (flow rate, 1.0 mL min^{-1}); A, Ar (flow rate, 0.7 mL min^{-1}); W, waste; P_1 and P_2, peristaltic pumps; C, minicolumn packed with L-tyr-CNTs; V, injection valve. Valve positions: (a) sample loading and (b) injection.

solution were then passed through the column at a flow rate of 1 mL min^{-1}. The end of the column was connected directly to the FAAS instrument and Co signal was registered. Once the effluent concentration reached the influent concentration, the sample flow was stopped.

After that, metals were eluted from the column with a 10% HNO$_3$ solution and collected in 25 mL glass flasks. It was probed that acids can cause a reversible change in the tertiary structure of aminoacids providing efficient and rapid release of metals from the binding cavity [8]. Other eluents such as HCl were tested and no significant differences were obtained. Finally, the column was reconditioned and the process started again.

An Origin® 7.0 program was used to perform calculations related to the amount of metal bound to the column, from breakthrough curves.

2.5. Analytical performance studies

2.5.1. Preconcentration procedure
Analytical performance studies were carried out employing an on line system. The flow injection manifold used for preconcentra-
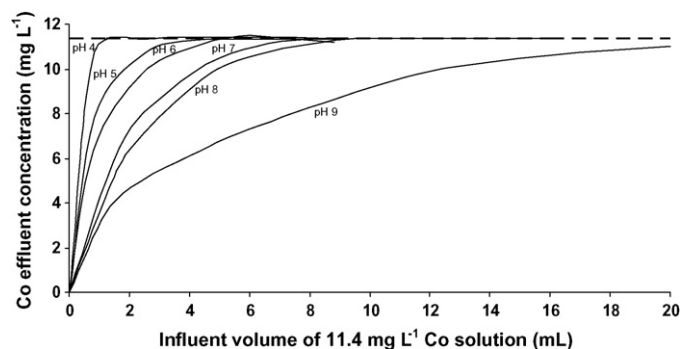
Fig. 3. Breakthrough curves on L-tyr-CNTs for 11.4 mg of Co L^{-1} solution loaded at 1.00 mL min^{-1}. The discontinued upper line corresponds to the initial influent concentration.

tion, separation and subsequent determination of Co is shown in Fig. 2. Before loading, the column was conditioned at the desired pH with a 0.05 mol L^{-1} ammonium acetate buffer (valve V_1 in position B). A volume of sample was then loaded on the conical minicolumn (M) at flow rate of 1 mL min^{-1} with valve V_1 in position S and valve V_2 in load position (a). Finally, valve V_2 was switched to the injection position (b) and Co retained was eluted with 10% HNO$_3$ solution at 1 mL min^{-1}. After that, the eluate was introduced into FAAS. The operation conditions were established and the determinations were carried out.

3. Results and discussion

3.1. Determination of L-tyr immobilized on CNTs

The amount of L-tyr immobilized on CNTs was spectrophotometrically determined. In a first step, the maximum absorption line of L-tyr was searched using a 125 mg L^{-1} solution. Accordingly to Cvijovic et al. [28], L-tyr intensively absorbs in the near-UV region. The spectra obtained showed that the maximum absorption of L-tyr occurs at 290 nm. Every other determination was performed at this wavelength value.

The analyzed solution was the residue obtained after the filtration of the heated solution, where the remained un-immobilized aminoacid was collected. Then, the amount of aminoacid determined corresponds to that one not retained by the column. The amount of immobilized aminoacid on CNTs was calculated by the difference with the initial concentration of aminoacid added (10 mg).

The results showed that 4 mg L^{-1} of the aminoacid remained in the filtrated solution. Then, the amount of immobilized aminoacid on 10 mg of CNTs was of 6 mg of L-tyr (60% immobilization). It is plausible to think that at this concentration levels, CNTs were saturated with the aminoacid. This value corresponds to 3173 μmol of L-tyr g^{-1} of CNTs with a surface coverage of 2.2–8.5 × 10^{15} L-tyr residues cm^{-2} CNTs, assuming a surface area of 90–350 m^2 g^{-1} CNTs (value provided by Sunnano). These results

Table 1
Effective Co retention capacities for L-tyr-CNTs.

pH	Co bound (μmol g^{-1} of CNTs)	Co recovered (%)
4	6.22 ± 0.49	110.41
5	15.33 ± 1.59	110.07
6	22.05 ± 2.74	104.67
7	37.58 ± 3.06	79.96
8	43.08 ± 3.52	109.66
9	101.9 ± 6.94	101.0

demonstrate that the immobilization procedure adopted is highly efficient.

3.2. Column capacity

The L-tyr-CNTs column capacity was determined for pH values ranging from 4.0 to 9.0, using a 11.4 mg L^{-1} Co influent solution pumped through the column at a flow rate of 1.00 mL min^{-1}.

The total amount of Co bound, expressed in μmol g^{-1} of L-tyr-CNTs, was determined by integration of the breakthrough curves in Fig. 3 and it was verified by comparison to the amount of Co recovered in the 25 mL 10% nitric effluent solution (Table 1). The total Co recovered in the effluent was in good agreement with calculations from the breakthrough curves. The analysis of Table 1 shows that L-tyr-CNT has a high retention capacity for Co, considering the mass present in the column, only 10 mg. If we consider that typical sorbent materials such as resin beads, porous glasses and carbon-based powders have diameters in the μm–mm range while nanoparticle have diameter in 10–100 nm range, for a given mass of media, the particle density increases with the nanoparticles falling between 10^6 and 10^{15} [23].

The un-functionalized CNTs binding capacity for Co was evaluated at pH 7.0 and it turned to be of 20.17 ± 2.58 μmol Co g^{-1} of CNTs. As shown in Table 1, L-tyr-CNTs has a binding capacity of 37.58 ± 3.06 μmol Co g^{-1} of CNTs, then the functionalized CNTs improves Co retention capacity compared to un-functionalized CNTs with an enhancement factor of ~2.

3.3. Effect of pH on Co binding

It has been reported that pH is a very important factor for the adsorption process of metals on aminoacids [8,23]. It is related to protonation and deprotonation processes on aminoacids, and with the metal specie present in solution [8].

As it can be seen in Fig. 3, the retention of Co by L-tyr-CNTs is more effective at higher pH values. The Co species present in solution at these pH values and concentration levels that could be interacting with L-tyr-CNTs are CoOH$^+$ and HCoO$_2$$^-$ [36].

The discontinued upper line indicates the influent concentration. Every effluent solution reaches the influent concentration except for pH 9.0. This could be attributed to the presence of weaker binding sites [37]. Also at this pH value a remarkable different behavior appears, with an acute increment in Co retention, with 101.8 ± 6.9 μg of Co g^{-1} of L-tyr-CNTs as it can be seen in Table 1. This increase in Co adsorption onto L-tyr-CNTs at pH 9.0 coincides with the deprotonation of NH$_3$ group in L-tyr which occurs at pH 9.11. The calculation of the mol ratio (moles of Co bound at pH 9 to moles of L-tyr) turned to be 3:1.

3.4. Comparison with other bivalent metals

The adsorption behavior of Co on L-tyr-CNTs was compared with that of Ni, Zn and Cu. The pH was fixed at 7 for comparative purposes. These elements were chosen because they are bivalent cations, immediately close to Co and a comparison with respect to cation size could be made. The retention capacities for Cu, Ni, Zn and

Fig. 4. Breakthrough curves on L-tyr-CNTs for 5.7, 11.4 and 22.7 mg of Co L^{-1} solution (pH 7.0) loaded at 1.00 mL min^{-1}. The discontinued upper line corresponds to the initial influent concentration.

Co obtained from the integrations of the breakthrough curves are 155.0 ± 3.3, 100.5 ± 1.5, 78.8 ± 1.1 and 37.6 ± 0.84 μmol g^{-1} of CNTs, respectively.

It is plausible to think that smallest cations should be more retained on the sorbent. As it can be observed, the adsorption trend is Cu > Ni > Zn $\gg$ Co. This tendency shows that bigger cations are more absorbed on L-tyr-CNTs. Analyzing the metal species present in solution at this pH value and concentration it can be seen that the major Co specie present is Co^{2+}. However, for the most retained metals (Cu and Ni) the predominant species are CuOH$^+$ and NiOH$^+$, respectively [36]. In conclusion, metal size is an important parameter to evaluate the adsorption process, but the metal specie present at a determined pH value and the element concentration should be considered for a correct evaluation as well.

3.5. Effect of influent concentration

Different Co influent concentrations were loaded on line onto the column at pH 7.0, at a flow rate of 1 mL min^{-1} to assess the Co uptake capacity of L-tyr-CNTs. The influent concentrations tested were 22.7 and 5.7 mg L^{-1} and the amount of metal bound was 82.64 and 35.31 μmol of Co g^{-1} L-tyr-CNTs, respectively. Results were obtained by integration of the breakthrough curves shown in Fig. 4.

When a Co concentration of 11.4 mg L^{-1} was tested, the column retained 37.58 μmol of Co g^{-1} of L-tyr-CNTs at pH 7.0. This experiment showed that at low influent concentrations (5.7 mg L^{-1}) no substantially changes in Co retention occurred. At higher Co concentrations, the amount of metal bound to the sorbent was proportional to the amount of Co loaded. This could be related to an improved accessibility of Co ions to L-tyr-CNTs binding sites when low concentration rates of the influent were passed through the column. At higher concentrations, Co retention by L-tyr-CNTs could be reaching a saturation level.

3.6. Effect of influent flow rate

It is expected that sample solutions can be passed through the column at higher flow rates with constant recoveries. Influent flow rate is a very important parameter to consider in this kind of studies because it is directly related to sample throughput. The influent flow rate effect on Co binding by L-tyr-CNTs was studied by loading a 11.4 mg L^{-1} Co solution at 0.5 and 2.0 mL min^{-1} at pH 7.0. These results were compared with the breakthrough curve at 1.0 mL min^{-1}, as it can be seen in Fig. 5.

By integration of the breakthrough curves the amount of Co bound to the column at 0.5 and 2.0 mL min^{-1} turned to be of 50.32 and 25.44 μmol of Co g^{-1} L-tyr-CNTs, respectively. The absorption capacity of the column decreases at higher flow rates, but not proportionally, keeping in mind that 37.58 μmol of Co g^{-1} L-tyr-CNTs are retained at a flow rate of 1 mL min^{-1}. This could be indica-
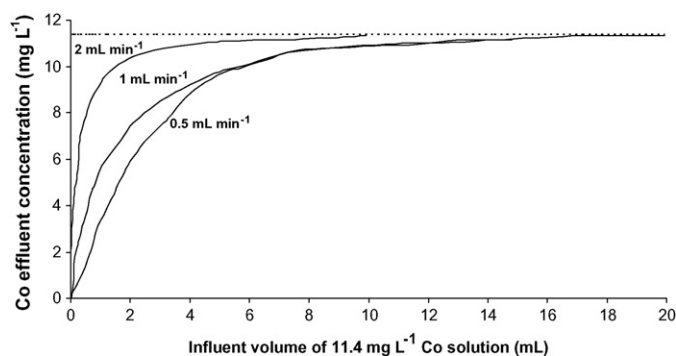
Fig. 5. Breakthrough curves on L-tyr-CNTs for 11.375 mg of Co L^{-1} solution (pH 7.0) loaded at 0.5, 1.00 and 2.00 mL min^{-1}. The discontinued upper line corresponds to the initial influent concentration.

tive that at flow rates higher than 1.0 mL min^{-1} L-tyr-CNTs are not binding Co under equilibrium conditions.

3.7. Analytical performance

The potential of this new sorbent for a SPE extraction system was evaluated by applying it to Co determination in the standard reference material (SRM), QC METAL LL2 (metals in natural water). Different analytical parameters were evaluated and they can be seen in Table 2.

The analytical performance was studied by loading 10 mL of 11.37 μg L^{-1} Co solutions on the column. The study was performed at pH 9.0 because the retention was maximal. As it can be seen in Table 2, an enrichment factor as high as 180-fold can be obtained. Previous studies demonstrated that metals retained by aminoacids were released with a quantitative recovery and that elevated enrichment factors can be reached [8]. This is possible because a quantitative release can be achieved by simply lowering the pH of the solution and the target metal can be easily released enhancing the preconcentration ratio. Also the presence of the active sites on the surface, inner cavities and inter-nanotube space contributes to the high metal removal capability of CNTs.

The effects of potential interference species at the concentration levels at which they may occur in the studied sample were tested. For this purpose, synthetic Co solutions were prepared and the signal was monitored, after the preconcentration procedure, in the presence of cations such as Na$^+$, K$^+$, Ca^{2+} and they were tolerated up to at least 1000 mg L^{-1}. On the other hand, the effects of anions such as CO$_3$$^{2-}$, SO$_4$$^{2-}$, Cl$^-$ and NO$_3$$^-$ were tolerated up to at least of 1000 mg L^{-1}.

In order to validate the proposed method, Co was determined in the standard reference material (SRM), QC METAL LL2 metals in natural water with a Co certified concentration of 50 μg L^{-1}. The standard addition technique was applied to Co determination. Three aliquots of 20 mL of the SRM at pH 9.0 were added with 10, 50 and 100 μg L^{-1} of Co solution and diluted with distilled water into glass flasks to 25 mL. Using the proposed method, the content of Co found was 51 ± 1.26 μg L^{-1} (95% confidence interval; n = 10).

Table 2
Analytical performance of the preconcentration system.

Preconcentration time (s)	600
Calibration range (μg L^{-1})	$\sim$DL − 250
Sample consumption (mL) (sample flow rate = 1 mL min^{-1})	10
Relative standard deviation (%) [n = 10, at 10.0 μg L^{-1} Co (II) level]	2.7–3.4
Detection limit (ng L^{-1})	50
Enrichment factor (EF)	180

DL, detection limit.

4. Conclusion

This work presents a method for aminoacids immobilization on CNTs. The performance was verified by the determination of the amount of L-tyr immobilized on the nanomaterial surface.

The new substrate demonstrated a high retention capacity for metals combined with a high CNTs specific surface for aminoacids immobilization.

The analytical features were correlated with aminoacids behavior on SPE systems. A 100% of Co retention was reached in a wide pH range. The fast kinetic adsorption/desorption process, allowed a high enrichment factor, reaching a very low detection limit. These results will be extended to other elements in order to evaluate the speciation possibility, another characteristic of aminoacids immobilized on solid supports.

Acknowledgements

References

[1] M. Tuzen, K.O. Saygi, M. Soylak, J. Hazard. Mater. 152 (2008) 632.
[2] A. Stafiej, K. Pyrzynska, Microchem. J., doi:10.1016/j.microc.2007.11.001.
[3] S. Esakku, A. Selvam, K. Joseph, K. Palanivelu, Chem. Spec. Bioavail. 17 (2005) 95.
[4] N.J.K. Simpson, Solid-phase Extraction, Principles, Techniques and Applications, Marcel Dekker, New York, 2000, p. 7.
[5] M. Soylak, A.U. Karatepe, L. Elci, M. Dogan, J. Chem. 27 (2003) 235.
[6] C. Arpa, S. Bektas, Anal. Sci. 22 (2006) 1025.
[7] R.A. Gil, S. Cerutti, J.A. Gásquez, R.A. Olsina, L.D. Martinez, Talanta 68 (2006) 1065.
[8] P.H. Pacheco, R.A. Olsina, P. Smichowski, L.D. Martinez, Talanta 74 (2008) 593.
[9] R.A. Gil, S.N. Goyanes, G. Polla, P. Smichowski, R.A. Olsina, L.D. Martinez, J. Anal. At. Spectrom. 22 (2007) 1290.
[10] M. Tuzen, K.O. Saygi, C. Usta, M. Soylak, Bioresour. Technol. 99 (2008) 1563.
[11] M. Tuzen, M. Soylak, J. Hazard. Mater. 147 (2007) 219.
[12] M. Biesaga, K. Pyrzynska, J. Sep. Sci. 29 (2006) 2241.
[13] Q.L. Li, D.X. Yuan, Q.M. Lin, J. Chromatogr. A 1026 (2004) 283.
[14] G. Liu, J. Wang, Y. Zhu, X. Zhang, Anal. Lett. 37 (2004) 3085.
[15] S.C. Tsang, J.J. Davis, M.L.H. Green, H.A.O. Hill, Y.C. Leung, P.J. Sadler, Chem. Commun. 17 (1995) 1803.
[16] F. Balavoine, P. Schultz, C. Richard, V. Mallouh, T.W. Ebbesen, C. Mioskowski, Angew. Chem. Int. Ed. 38 (1999) 1912.
[17] R.J. Chen, Y. Zhang, D. Wang, H. Dai, J. Am. Chem. Soc. 123 (2001) 3838.
[18] W. Huang, S. Taylor, K. Fu, Y. Lin, D. Zhang, T.W. Hanks, A.M. Rao, Y.P. Sun, Nano Lett. 2 (2002) 311.
[19] B.R. Azamian, J.J. Davis, K.S. Coleman, C.B. Bagshaw, M.L.H. Green, J. Am. Chem. Soc. 124 (2002) 12664.
[20] K. Besteman, J.O. Lee, F.G.M. Wiertz, H.A. Heering, C. Dekker, Nano Lett. 3 (2003) 727.
[21] B.F. Erlanger, B.-X. Chen, M. Zhu, L. Brus, Nano Lett. 1 (2001) 465.
[22] K. Jiang, L.S. Schadler, R.W. Siegel, X. Zhang, H. Zhang, M. Terrones, J. Mater. Chem. 14 (2004) 37.
[23] B.R. White, B.T. Stackhouse, J.A. Holcombe, J. Hazard. Mater. 161 (2009) 848.
[24] L. Malachowski, J.L. Stair, J.A. Holcombe, Pure Appl. Chem. 76 (2004) 777.
[25] G.G. Wildgoose, H.C. Leventis, I.J. Davies, A. Crossley, N.S. Lawrence, L. Jiang, T.G.J. Jones, R.G. Compton, J. Mater. Chem. 15 (2005) 2375.
[26] S.A. Sayed, S.M. Saleh, E.E. Hasan, Mansoura Sci. Bull. A: Chem. 32 (2005) 1.
[27] C.C. Huang, C.C. Su, J.L. Hsieh, C.P. Tseng, P.J. Lin, J.S. Chang, Enzyme Microb. Technol. 33 (2003) 379.
[28] P. Djurdjevic, R. Jelic, D. Dzajevic, M. Cvijovic, Metal Based Drugs 8 (2002) 5.
[29] T. Toyomi Tominaga, H. Imasato, O. Range Nascimento, M. Tabak, Anal. Chim. Acta 315 (1995) 217.
[30] M. Lanznaster, A. Neves, A.J. Bortoluzzi, A.M.C. Assumpcüao, I. Vencato, S.P. Machado, S.M. Drechsel, Inorg. Chem. 45 (2006) 1005.
[31] S. Majid, M. El Rhazi, A. Aminea, C.M.A. Brett, Anal. Chim. Acta 464 (2002) 123.
[32] D.U. Miodragovic, Z.M. Miodragovica, D. Skalab, M.J. Malinara, D.M. Minicc, K. Andjelkovic, Thermochim. Acta 436 (2005) 90.
[33] C. Ruan, M.T. Rodgers, J. Am. Chem. Soc. 126 (2004) 14600.
[34] P.H. Pacheco, R.A. Gil, P. Smichowski, G. Polla, L.D. Martinez, Microchem. J. 89 (2008) 1.
[35] P. Liang, E. Zhao, Q. Ding, D. Du, Spectrochim. Acta, Part B 63 (2008) 714.
[36] F. Burriel Marti, Química Analítica Cualitativa, Paraninfo, Madrid, 1994.
[37] H.A. Jurbergs, J.A. Holcombe, Anal. Chem. 69 (1997) 1893.

A self-assembled fusion protein-based surface plasmon resonance biosensor for rapid diagnosis of severe acute respiratory syndrome

Tae Jung Park[a], Moon Seop Hyun[b], Hye Jin Lee[c], Sang Yup Lee[a,d], Sungho Ko[e,*]

[a] BioProcess Engineering Research Center, Center for Systems & Synthetic Biotechnology, Institute for the BioCentury, KAIST, 335 Gwahangno, Yuseong-gu, Daejeon 305-701, Republic of Korea
[b] National NanoFab Center, 335 Gwahangno, Yuseong-gu, Daejeon 305-806, Republic of Korea
[c] Department of Chemistry, Kyungpook National University, 1370 Sankyuk-dong, Buk-gu, Daegu 702-701, Republic of Korea
[d] Department of Chemical & Biomolecular Engineering (BK21 program), Department of Bio & Brain Engineering, Department of Biological Sciences, Bioinformatics Research Center, KAIST, 335 Gwahangno, Yuseong-gu, Daejeon 305-701, Republic of Korea
[e] Korea Food Research Institute, 516 Baekhyun-dong, Bundang-gu, Seongnam 463-746, Republic of Korea

ARTICLE INFO

ABSTRACT

A surface plasmon resonance (SPR)-based biosensor was developed for simple diagnosis of severe acute respiratory syndrome (SARS) using a protein created by genetically fusing gold binding polypeptides (GBPs) to a SARS coronaviral surface antigen (SCVme). The GBP domain of the fusion protein serves as an anchoring component onto the gold surface, exploiting the gold binding affinity of the domain, whereas the SCVme domain is a recognition element for anti-SCVme antibody, the target analyte in this study. SPR analysis indicated the fusion protein simply and strongly self-immobilized onto the gold surface, through GBP, without surface chemical modification, offering a stable and specific sensing platform for anti-SCVme detection. AFM and SPR imaging analyses demonstrated that anti-SCVme specifically bound to the fusion protein immobilized onto the gold-micropatterned chip, implying that appropriate orientation of bound fusion protein by GBP resulted in optimal exposure of the SCVme domain to the assay solution, resulting in efficient capture of anti-SCVme antibody. The best packing density of the fusion protein onto the SPR chip was achieved at the concentration of $10 \, \mu g \, mL^{-1}$; this density showed the highest detection response (906 RU) for anti-SCVme. The fusion protein-coated SPR chip at the best packing density had a lower limit of detection of $200 \, ng \, mL^{-1}$ anti-SCVme within 10 min and also allowed selective detection of anti-SCVme with significantly low responses for non-specific mouse IgG at all tested concentrations. The fusion protein provides a simple and effective method for construction of SPR sensing platforms permitting sensitive and selective detection of anti-SCVme antibody.

© 2009 Elsevier B.V. All rights reserved.

1. Introduction

Severe acute respiratory syndrome (SARS) is a newly emerged disease of global significance because of its highly contagious nature. Extensive human worldwide travel, and contact with animals [1,2], contribute to the SARS problem. Early detection and identification of SARS coronavirus (CoV)-infected patients, and actions to prevent transmission, are absolutely critical in prevention of another SARS outbreak [1,3]. Although enzyme-linked immunosorbent assays (ELISAs) and real-time PCR-based diagnostic tests for SARS have been valuable for early identification of infections, they are still laborious and expensive and require skilled personnel [3–5]. Therefore, in terms of public health measures in response to epidemics, a rapid recognition of emerging SARS

infections urgently requires new diagnostic tools that are portable, sensitive, and easy to use, to assure (as much as possible) "in-field" detection.

Recently, surface plasmon resonance (SPR)-based biosensors have been developed for the direct monitoring of antigen–antibody interactions. Such sensors offer several advantages: there is no need for labeling; real-time detection is possible; curtailment of non-specific binding is achievable; and detection of nanomolar concentrations of proteins of molecular weights larger than 180 Da is possible [6,7]. In principle, a surface plasmon oscillation is a localized wave that propagates along the interface between the gold film and the ambient medium and is very sensitive to changes in the refractive index near the gold surface when biomolecules bind to that surface [7,8].

One of the main issues in the development of biosensors is efficient immobilization of biomolecules on the sensor surface. Many protein immobilization techniques, based on both physical adsorption and covalent linkage, have been developed in the past few

* Corresponding author. Tel.: +82 31 780 9320; fax: +82 31 780 9228.
E-mail address: shko7@kfri.re.kr (S. Ko).

years [9]. However, the physical attachment to surface is likely to be heterogeneous, weak, and randomly oriented, and the covalent attachment also can lead to random immobilization of proteins, resulting in a reduction of biological activity. Such techniques are cumbersome and time-consuming. Therefore, a simple method to immobilize target proteins, with retention of biological activity, is urgently required.

A gold binding polypeptide (GBP) containing triple repeats of a particular 14 amino acid sequence is able to bind metallic gold [10]. Interestingly, none of these 14 amino acid residues is cysteine, generally considered to form a thiol linkage with gold [11], thus offering a new way of interaction between proteins and gold surfaces. Polar side-chains of peptides rich in serine and threonine seem to interact with the gold surface. The adsorption kinetics of GBP onto the gold surface were explored using SPR spectroscopy [12]. Furthermore, proteins and peptides of interest can be fused to the GBP for immobilization on the gold surface [13]. These findings led us to develop protein immobilizations of biological sensors using GBP as a fusion partner.

In this paper, we developed a simple protein immobilization method employing genetically engineered GBP-fused proteins as both biolinkers and ligands, to create a SARS diagnosis technique employing an SPR detection system. The GBP-fusion proteins consist of two domains of the GBP fused to SARS-CoV membrane-envelope (SCVme) protein. The fusion proteins can be directly self-assembled onto the SPR gold surfaces via the GBP portions without complicated chemical modification of the gold surface, and the SCVme portion serves as a capture ligand for anti-SCVme antibody.

2. Experimental

2.1. Chemicals and reagents

Unless otherwise stated, all chemical reagents were purchased from Sigma–Aldrich (St. Louis, MO, USA). Rabbit anti-SCVme polyclonal antibody was prepared by immunization with a peptide corresponding to residues 58–75 (COOH-CVYSRVKNLNSSEGVPDLL-NH₂) of the envelope protein, according to the manufacturer's procedures (Peptron, Daejeon, Korea). All restriction enzymes were purchased from New England Biolabs (Beverly, MA, USA). Phosphate-buffered saline (PBS, pH 7.4) from BD Biosciences (San Jose, CA, USA) was used as a flow solution and dilution buffer for SPR analysis. Distilled water (18 MΩ cm) was obtained using an ultrapure water system (Milli-Q; Millipore, Billerica, MA, USA).

2.2. Preparation of SARS-CoV envelope gene

Antigenic regions were predicted by analyzing the primary structure of the SARS-CoV envelope protein. Oligonucleotides encoding the SARS-CoV envelope protein were synthesized by design of gene sequence from the envelope amino acid sequence, employing the DNAWorks program [14]. The sequence encoding the SARS-CoV envelope protein was obtained from GenBank (accession number AY274119.3). The relevant gene was located from base pairs 26,117–26,347 in the SARS genomic sequence, and encoded 76 amino acids [1]. The codon frequency was chosen to represent *Escherichia coli* class II, and the following parameters were employed: maximum oligonucleotide length, 50 nt; annealing temperature, 58 °C; codon frequency threshold, 50; number of solutions, 50. Synthetic assembly of the intact envelope gene using component oligonucleotides was performed with a single-step assembly protocol [15]. We describe the approach only in general. Polymerase chain reaction (PCR) experiments for gene assembly were carried out under the following cycling conditions: initial
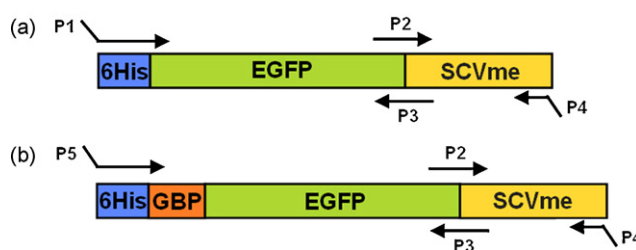
Fig. 1. Synthesis of (a) E-SCVme and (b) GBP-E-SCVme fusion genes by overlap PCR. Abbreviations are: 6His, six histidines; EGFP, enhanced green fluorescent protein; GBP, gold binding polypeptide; SCVme, the SARS-CoV membrane-envelope chimera protein.

denaturing step at 94 °C for 5 min to avoid any possible mispriming; 30 cycles of denaturing at 94 °C for 30 s; annealing at various temperatures (depending on the melting temperatures indicated by the DNAWorks program); extension at 72 °C for 1 min; and a final extension at 72 °C for 7 min. For gene amplification, 1 μL of the mixture from the gene assembly reaction was used as a template, with the outermost oligonucleotides used as primers. As in a previous report [2], PCR experiments were performed using a Thermal Cycler (Bio-Rad, Hercules, CA, USA) and high-fidelity Taq polymerase (Takara Bio, Shiga, Japan) for the cloning of the SARS-CoV envelope gene in *E. coli*. All DNA manipulations including restriction digestion, ligation, and agarose gel electrophoresis, were standard procedures [16]. The DNA sequence of the clone was confirmed by automatic DNA sequencing (ABI Prism 377, PerkinElmer, Grove, IL, USA).

2.3. Preparation of GBP-EGFP-SCVme fusion proteins

Bifunctional fusion proteins were created by genetically fusing GBP and SCVme to enhanced green fluorescent protein (EGFP), allowing for two specific interactions between GBP and gold substrates, and the capture of SCVme and anti-SCVme antibodies by SCVme. EGFP from the jellyfish *Aequorea victoria* was used as a model protein for soluble expression of the fusion proteins and offered convenient monitoring of soluble fractions, and a six-histidine (6His) was tagged to easily purify the fusion proteins. The DNA fragment encoding 6His-EGFP was first amplified by PCR with the primers P1 (5′-GCGAATTCCATGGT-GCACCATCACCATCACCATAGCAAGGGCGAGGAG-3′) and P3 (5′-ACAAAAACCTGTTCCGATTCTTGTACAGCTCGTCCATGCC-3′), using the plasmid pEGFP (BD Biosciences) as a template. Then, the fusion of the DNA fragment encoding incomplete SCVme to 6His-EGFP was achieved by PCR amplification with the primers P2 (5′-GGCATGGACGAGCTGTACAAGAATCGGAACAGGTTTTTGT-3′) and P4 (5′-CGGAATTCAAGCTTTTAGACCAGAAGATCAGGAAC-3′), using pTrc-6HSCVme::AfBD [2] as a template. Finally, the complete 6His-EGFP-SCVme (E-SCVme) fusion gene fragment was amplified with the primers P1 and P4 using the PCR products encoding 6His-EGFP and SCVme as templates (Fig. 1(a)). The PCR product was digested with NcoI and HindIII, and ligated into the NcoI–HindIII fragment of pTrc99A (GE Healthcare, Piscataway, NJ, USA) to construct pTESCVme expressing E-SCVme fusion protein.

For the cloning of 6His-GBP-EGFP-SCVme (GBP-E-SCVme) fusion gene (Fig. 1(b)), DNA fragments encoding EGFP and the SCVme fusion gene were amplified by PCR as previously reported [2]. The DNA fragment encoding 6His-GBP-EGFP was first amplified by PCR with the primers P3 and P5 (5′-GCGAATTCCATGGGC-*CACCATCACCATCACCAT*GGCAAAACCCAGGCGACCA-3′) using the plasmid pTGE as a template. A DNA fragment encoding SCVme was amplified using primers P2 and P4. Finally, the GBP-E-SCVme fusion gene was amplified with primers P4 and P5 using the above PCR products as templates. The amplified GBP-E-SCVme

fusion gene was digested with NcoI and HindIII, and ligated into the NcoI–HindIII fragment of pTrc99A to construct pTGESCVme expressing GBP-E-SCVme fusion protein.

For expression of the fusion proteins, plasmids were consecutively introduced into *E. coli* XL1-Blue strain (*recA1, endA1, gyrA96, thi, hsdR17, suppE44, relA1, l⁻, lac⁻,* F′[*proAB lacIq* lacZΔM15, Tn*10* (tet)ʳ]), from Stratagene, La Jolla, CA, USA using a Gene Pulser electroporator (Bio-Rad) in accordance with the manufacturer's instructions. The *E. coli* transformants harboring pTESCVme and pTGESCVme were cultivated in Luria–Bertani (LB) medium (tryptone $10\,g\,L^{-1}$, yeast extract $5\,g\,L^{-1}$, NaCl $5\,g\,L^{-1}$) with ampicillin ($100\,\mu g\,mL^{-1}$) at $37\,°C$ in a shaking incubator (200 rpm). Cell growth was monitored by measuring optical density at 600 nm (OD_{600}) using a spectrophotometer (DU®650, Beckman, Fullerton, CA, USA). When cultures reached OD_{600} values of 0.6, the expression of the *trc* promoter was induced by adding 1 mM (final concentration) isopropyl-β-D-thiogalactopyranoside (IPTG) to culture broth. After further cultivation for 6 h, cells were harvested by centrifugation at $10,000 \times g$ for 10 min at $4\,°C$ and disrupted by sonication (Braun Ultrasonics, Danbury, CT, USA) for 1 min at 40% of output power. After centrifugation at $16,000 \times g$ for 10 min at $4\,°C$, the supernatant containing soluble proteins was obtained for further analysis. Because of the 6His tags, the E-SCVme and GBP-E-SCVme fusion proteins were simply purified using Ni-chelating resin (Qiagen, Valencia, CA, USA).

2.4. Fabrication of gold micropatterns

To prepare gold-patterned chips, glass slides were washed with piranha solution (75% H_2SO_4/25% H_2O_2, v/v) to enhance gold adhesion onto the glass substrate. An AZ9260 positive photoresist (SU-8, Microchem, Newton, MA, USA) master was made on the slide by even pouring and spin-coating at 2000 rpm for 60 s. To remove volatile organics, the slide was cured in a convection oven at $110\,°C$ for 3 min. After slow cooling, the slide was exposed to ultraviolet (UV) light for 75 s at a temperature below $30\,°C$, which was very useful to prevent the photoresist cracking. UV-exposed slides were then treated with AZ9260 developer for about 5 min, and then UV-exposed photoresist was removed, but SU-8-negative photoresist was retained. A thermal evaporation unit was used to deposit the chromium and gold onto the slide glass, in which height was controlled to be 5 and 40 nm, sequentially. Following gold deposition, the slides were soaked in acetone to remove the AZ9260 photoresist over 4 h. Finally, the gold patterns of 50-μm circle in diameter remained only on the developed region, where no photoresist existed after development.

2.5. Atomic force microscopy (AFM) imaging analysis

The GBP-E-SCVme fusion protein was immobilized onto the gold-micropatterned substrate by dipping the substrate into a solution of GBP-E-SCVme ($100\,\mu g\,mL^{-1}$) for 30 min at $25\,°C$, followed by washing with distilled water and drying with nitrogen gas. Anti-SCVme antibodies ($100\,\mu g\,mL^{-1}$) were sequentially treated onto the substrate surface by dipping in antibody solution for 30 min at $25\,°C$. Following washing and drying of the prepared chip, the surface morphology and the height of each layer formed were investigated by AFM. The AFM analyses were performed using an XE-100 Scanning Probe Microscope system (Park Systems, Suwon, Korea) in the non-contact mode, employing a Tap300Al cantilever (Budget Sensors, Sofia, Bulgaria) with an aluminum reflex coating on the reverse side of the cantilever. The spring constant and the resonance frequency of the cantilever were typically $40\,N\,m^{-1}$ and 300 kHz, respectively. The AFM images of the gold micropatterns were acquired in an ambient atmosphere (40–50% relative humidity) at a speed of 1.0 Hz and a resolution of 512×512 pixel. To analyze surface roughness, and to verify the height of each layer on the surface of glass slides, sample surfaces were scanned in an AFM feedback loop in a manner permitting changes in cantilever vibrational amplitude to be recorded. Feedback signals were used to generate a topographic image. The phase lag was monitored while each topographic image was being taken so that several topographic images could be simultaneously collected.

2.6. Binding properties of GBP-E-SCVme fusion proteins onto SPR chip surfaces

The binding of GBP-E-SCVme fusion protein onto the surface of the SPR bare gold chip was characterized by SPR measurement using a BIAcore3000™ instrument (Biacore AB, Uppsala, Sweden) with an automatic flow injection system. A fresh SPR sensor chip was attached to a separate chip carrier for easy assembly in the SPR system. After the SPR chip was docked and primed, PBS was used to flush the activated surface, to minimize non-specific binding and any unbound sites by removing loosely bound material and dust. Fifty microliters of GBP-E-SCVme fusion protein ($0.1\,mg\,mL^{-1}$) or E-SCVme fusion protein (negative control, $0.1\,mg\,mL^{-1}$) were injected onto the chip surface for 10 min using a liquid-handling micropipette in the SPR system, and the surface was then washed and equilibrated with PBS. The SPR responses are indicated in resonance units (RUs). All SPR experiments in this study were conducted in PBS at a flow rate of $5\,\mu L\,min^{-1}$ at $25\,°C$, and all sensorgrams were fitted globally using BIA evaluation software.

2.7. Sensitivity and selectivity of the GBP-E-SCVme-coated SPR biosensor

To examine the sensitivity of the GBP-E-SCVme-coated SPR chip, various anti-SCVme antibody concentrations (0.1, 0.2, 1, 10, 50, and $100\,\mu g\,mL^{-1}$) were applied to the chip surface covered with the GBP-E-SCVme, at optimal packing density determined above, for 10 min after blocking of non-specific binding with BSA for 10 min. Then, the chip was rinsed with PBS. The limit of detection (LOD) was determined by measuring the lowest anti-SCVme concentration showing a significant change in signal over the baseline obtained with the PBS. As tests for selective detection, solutions of 1 and $10\,\mu g\,mL^{-1}$ of mouse IgG (negative controls) were allowed to flow over fresh SPR chips coated with GBP-E-SCVme, at the optimal packaging density, for 10 min,

2.8. SPR imaging (SPRi) analysis

The gold-micropatterned chip was loaded onto an SPRi apparatus (SPR*i*, K-MAC, Daejeon, Korea) using an incoherent light source (a 150 W quartz tungsten-halogen lamp; Schott, Mainz, Germany) for excitation. Briefly, ρ-polarized collimated white incident light on a prism/gold/thin film/buffer flow cell assembly was set at a fixed incident angle. Reflected light from this assembly was passed via a bandpass filter centered at a wavelength of 830 nm and collected by a CCD camera (Sony, Tokyo, Japan). Data images were collected digitally via a B/W frame grabber. Scion Image release Beta 4.0.3 software (Scion Corp., Frederick, MD, USA) was used to analyze the images.

3. Results and discussion

3.1. Surface morphology for binding of GBP-E-SCVme and anti-SCVme onto the gold surface

Fabrication processes for homogeneous stable monolayer structures have been developed to control the surface orientations
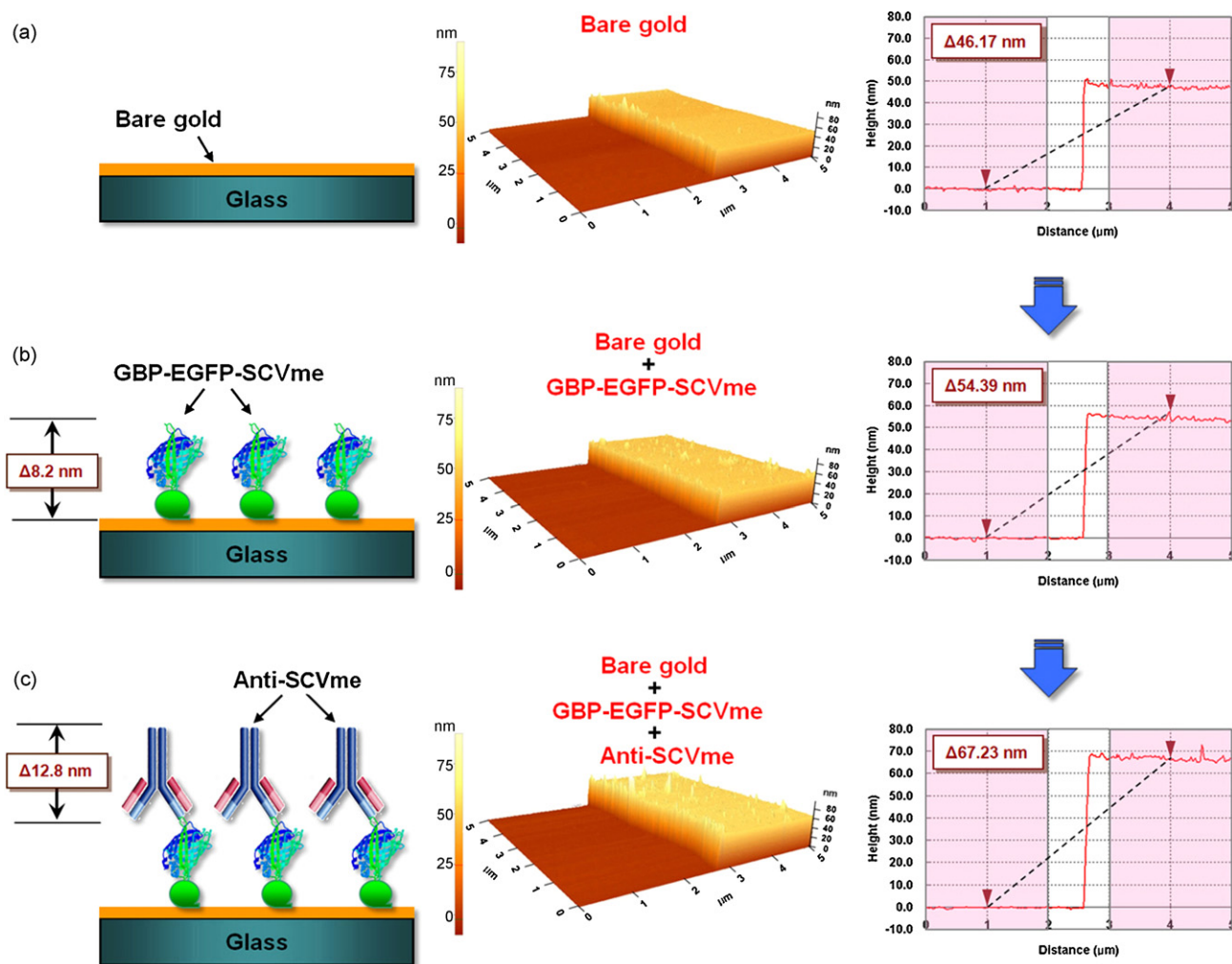
Fig. 2. AFM images of the sequential binding of GBP-E-SCVme and anti-SCVme on the gold-micropatterned surface. (a) Bare gold surface, (b) binding of the GBP-E-SCVme fusion proteins onto the gold surface, and (c) subsequent binding of the anti-SCVme antibodies on the GBP-E-SCVme layer. Left, schematic diagrams for the successive binding of GBP-E-SCVme and anti-SCVme on the gold micropatterns; middle, three-dimensional topological images; right, the cross-sectional contours of samples a–c, sequentially (these are average height differences of the individual scan lines from each area).

of biomolecules [17,18]. However, such fabrications require surface chemical modifications involving reactive functional groups or charged materials. Uniformly oriented immobilization of the GBP-E-SCVme fusion protein onto the gold chip was easily achieved without any surface chemical modification because of the gold binding property of the protein. To examine whether protein monolayers and protein molecular interactions might develop on the gold chip surface, we analyzed, at the molecular level, alterations in surface morphologies caused by sequential binding of GBP-E-SCVme and anti-SCVme antibodies onto a gold surface, employing high-resolution AFM analysis. After the specific immobilization of the GBP-E-SCVme ($100 \mu g \, mL^{-1}$) onto the gold-micropatterned surface, the subsequent binding of anti-SCVme antibodies ($100 \mu g \, mL^{-1}$) onto the GBP-E-SCVme layer was observed (Fig. 2). GFP has a 4.2 nm long cylindrical structure with a MW of ∼27 kDa [19]. As GBP-E-SCVme fusion protein has a MW of ∼57 kDa, the length of GBP-E-SCVme can be estimated to be ∼8.87 nm. The line profile of the GBP-E-SCVme bound onto the micropatterned gold surface was measured as approximately 8.2 nm as a height difference from the gold surface (Fig. 2(a) and (b)). The height difference after binding with anti-SCVme antibodies was about 12.8 nm, which shows specific interaction of antibodies with the monolayer of GBP-E-SCVme immobilized onto the gold substrate (Fig. 2(b) and (c)). Furthermore, roughness increases

caused by sequential binding of GBP-E-SCVme and anti-SCVme onto the gold surface were observed with different surface properties. Three-dimensional images show distinct well-shaped and well-defined peaks on the gold surface, and the gradual rise in peak numbers of Fig. 3(b) and (c) also indicates an increase in binding of biomolecules, suggesting that the GBP-E-SCVme and anti-SCVme antibodies were sequentially and specifically immobilized on the gold surface as ordered monolayers with a uniform thickness.

3.2. SPR analysis of GBP-fusion protein binding

The binding properties of the GBP-E-SCVme onto the gold surface were examined as shown in Fig. 3. The dynamic and specific binding of GBP-E-SCVme onto the SPR gold chip was directly monitored in real-time. A sharp increase in the SPR signal up to about 3060 RU was observed upon introducing GBP-E-SCVme solution onto the chip surface, and about 98% of the GBP-E-SCVme remained to the surface even after washing with PBS, which showed that most of the fusion protein was strongly immobilized onto the chip surface. The 3000 RU value obtained implies that about 3 ng of GBP-E-SCVme was immobilized onto a gold surface area of $1 \, mm^2$. One RU is determined as $0.0001°$ of resonance angle shift and equivalent to a mass change of the $1 \, pg \, mm^{-2}$ on the sensor surface [20,21]. However, the SPR signal of 3057 RU generated from the binding of
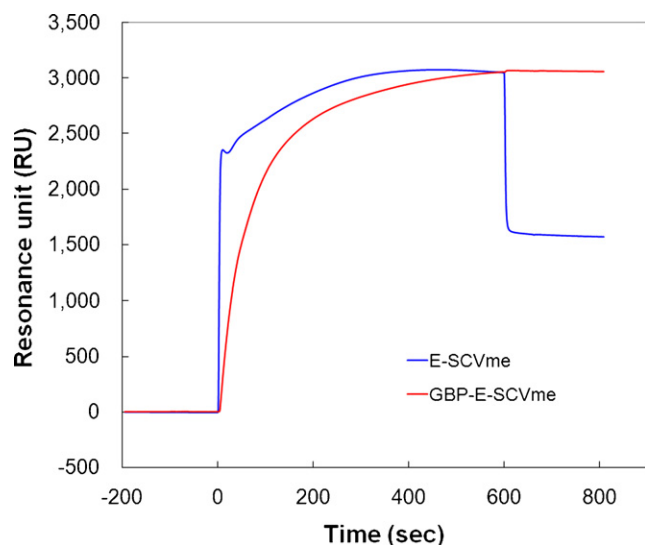
Fig. 3. SPR sensorgrams showing the specific immobilization of GBP-E-SCVme fusion proteins onto the gold chip. Red line, GBP-E-SCVme of 100 μg mL^{-1} (3057 RU); blue line, E-SCVme of 100 μg mL^{-1} (1574 RU) as a negative control. (For interpretation of the references to color in this figure legend, the reader is referred to the web version of the article.)

Fig. 4. (a) SPR sensorgrams showing the specific immobilization of GBP-E-SCVme fusion proteins onto the gold chip at various concentrations (1, 5, 10, 25, and 50 μg mL^{-1}). Each SPR phase was explored: (i) before immobilization, (ii) after binding of GBP-E-SCVme fusion proteins, and (iii) after washing with PBS. (b) Optimal concentration of GBP-E-SCVme immobilized onto the SPR gold chip, showing the highest signal from subsequent binding of anti-SCVme antibodies.

E-SCVme (control) onto the chip surface immediately decreased up to around 50% on rinsing with PBS, indicating that about 50% of E-SCVme was non-specifically bound to the gold surface. Positive surface charges of the amine groups in E-SCVme proteins may be irregularly coupled with negative charges of the gold surface by electrostatic force [22,23]. This showed that the electrostatic binding force was even weaker than the specific binding between GBP and the gold surface, and that GBP-E-SCVme fusion proteins could be strongly immobilized onto the gold surface by the GBP domain. Previous work also reported that the binding of GBP onto the gold surface is stronger than that of self-assembled monolayers of alkanethiol molecules due to the lower standard Gibbs free energy of GBP [12]. Therefore, it is clear that strong binding or adsorption of GBP-fusion protein onto the SPR chip can assist in studies on various protein–protein interactions.

3.3. Optimal packing density of GBP-E-SCVme onto the gold surface

In the study of the immunosensors, it is crucial to optimize the packing density of a recognition element immobilized onto a sensing surface in order to attain maximal sensitivity [24,25]. The amount of GBP-E-SCVme fusion protein immobilized onto the gold chip will affect the sensitivity of the SPR biosensor. To determine the optimal packing density, GBP-E-SCVme was immobilized onto the gold surface at various concentrations (1, 5, 10, 25, and 50 μg mL^{-1}), followed by washing out with PBS. Then, BSA (100 μg mL^{-1}) was injected onto the GBP-E-SCme-coated chips to block non-specific bindings. Finally, anti-SCVme antibody (100 μg mL^{-1}) was applied to the GBP-E-SCVme-layered surface in order to examine specific binding between GBP-E-SCVme and anti-SCVme by SPR biosensor response.

As shown in Fig. 4(a), the immobilization of GBP-E-SCVme onto the gold surface increased progressively from 950 to 2250 RU as GBP-E-SCVme concentration increased, indicating that GBP portion played an important role in surface self-immobilization of GBP-E-SCVme. Fig. 4(b) shows the interaction between the GBP-E-SCVme layer and subsequent applied anti-SCVme. When anti-SCVme was permitted to flow over the GBP-E-SCVme layer, SPR

signals increased until the concentration of GBP-E-SCVme reached to 10 μg mL^{-1}, but they began to decrease as the concentration was over 10 μg mL^{-1}. Less than 10 μg mL^{-1}, 1 and 5 μg mL^{-1} concentrations of GBP-E-SCVme resulted in low levels of the fusion protein immobilized on the gold surface, resulting in insufficient interaction between GBP-E-SCVme and anti-SCVme. Moreover, lower signals of 680 and 480 RU compared to that (900 RU) observed at the concentration of 10 μg mL^{-1} GBP-E-SCVme were obtained at 25 and 50 μg mL^{-1} concentrations, respectively, because the GBP-E-SCVme was densely immobilized on the surface and thus steric hindrance between closely packed GBP-E-SCVme molecules may have occurred. These results indicate that the best packing density of GBP-E-SCVme was obtained using a 10 μg mL^{-1} solution concentration. This particular packing density of the GBP-E-SCVme likely reduced steric hindrance, provided sufficient binding sites for anti-SCVme antibody, and avoided loss of biological activity. Ko et al. [24,25] have shown similar trends that insufficiently or densely immobilized antibodies on sensing surfaces can lead to a reduced detection signal, and Kolotilov et al. [26] also showed that a nanoparticle with immobilized protein A could not anchor sufficient IgG molecules to its surface due to steric hindrances. The best packing density of GBP-E-SCVme determined here was used in subsequent experiments.
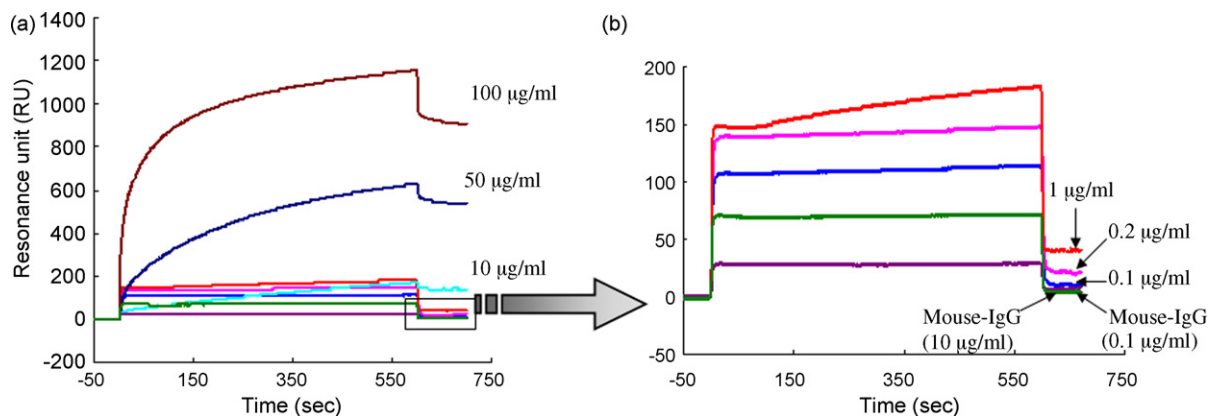
Fig. 5. SPR sensorgrams for (a) sensitive and (b) selective detection of anti-SCVme using the GBP-E-SCVme immobilized gold sensor chip at various concentrations (0.1, 1, 10, 50, and 100 μg mL^{-1}) of anti-SCVme and (1 and 10 μg mL^{-1}) of mouse IgG as negative controls.

3.4. Sensitivity and selectivity for SARS diagnosis

To investigate the sensitivity and selectivity of the SPR biosensor system using GBP-E-SCVme for detection of anti-SCVme antibody, the best concentration of GBP-E-SCVme (10 μg mL^{-1}) determined above was applied onto the gold surface to simply construct a sensitive SPR chip. The binding signal of anti-SCVme to the GBP-E-SCVme layer progressively increased from 11.3 to 905 RU as the anti-SCVme concentration increased from 0.1 to 100 μg mL^{-1}, respectively (Fig. 5(a)).

In addition, the selectivity of the GBP-E-SCVme-coated SPR sensor chip for detection of anti-SCVme was examined using mouse IgG (1 and 10 μg mL^{-1}) as negative controls (Fig. 5(b)). As expected, little SPR responses of 5.8 and 6.7 RU were observed by the non-specific binding of mouse IgG at 1 and 10 μg mL^{-1}, respectively. These SPR responses were much lower than those (43 and 142 RU) obtained when the anti-SCVme of 1 and 10 μg mL^{-1} concentrations, respectively, were used. Also, the slight difference between SPR signals of 5.8 and 6.7 RU means that the binding of mouse IgG was independent of concentration since it was only a negative control. It means that the GBP-E-SCVme-coated SPR chip selectively detects anti-SCVme antibodies.

Meanwhile, the lowest SPR response value (11.3 RU) by the binding of 0.1 μg mL^{-1} anti-SCVme among various concentrations was even differentiable from the control signal (6.7 RU) for 10 μg mL^{-1} of mouse IgG. However, low detection limit is normally the signal that is three times higher than the background signal [27,28]. The SPR signal of 25.2 RU at the anti-SCVme concentration of 0.2 μg mL^{-1} meets this requirement. Therefore, it was determined that the LOD of the GBP-E-SCVme immobilized sensor chip for detection of anti-SCVme in PBS was 0.2 μg mL^{-1}. It is considered that the best packing density of GBP-E-SCVme fusion proteins used in fabrication of the sensor chip may contribute to this low LOD. These results show that development of a sensitive and selective immunoassay system for SARS diagnosis was possible using a GBP-E-SCVme fusion protein-immobilized SPR chip.

3.5. SPRi analysis for detection of anti-SCVme antibodies on the gold micropatterns

After we determined that AFM imaging and SPR spectroscopy analyses could successfully be used to study biomolecular interactions on the gold surface, we visually confirmed the successive binding of GBP-E-SCVme and anti-SCVme antibodies onto the gold-micropatterned chip using an SPRi analysis system. The SPRi difference images produced by subtracting a reference image from a post-binding image contribute to visual confirmation of bind-

ing [29,30]. The gold-micropatterned chip was cleaned for 5 min in piranha solution and next washed with distilled water. After drying under nitrogen, the chip sequentially bound GBP-E-SCVme fusion proteins and anti-SCVme antibodies. The GBP-E-SCVme fusion proteins (from a 100 μg mL^{-1} solution) were immobilized onto the gold-micropatterned chip by dipping for 30 min at 25 °C. After the GBP-E-SCVme-treated chip was washed with distilled water and dried under nitrogen, the chip was dipped into a solution of anti-
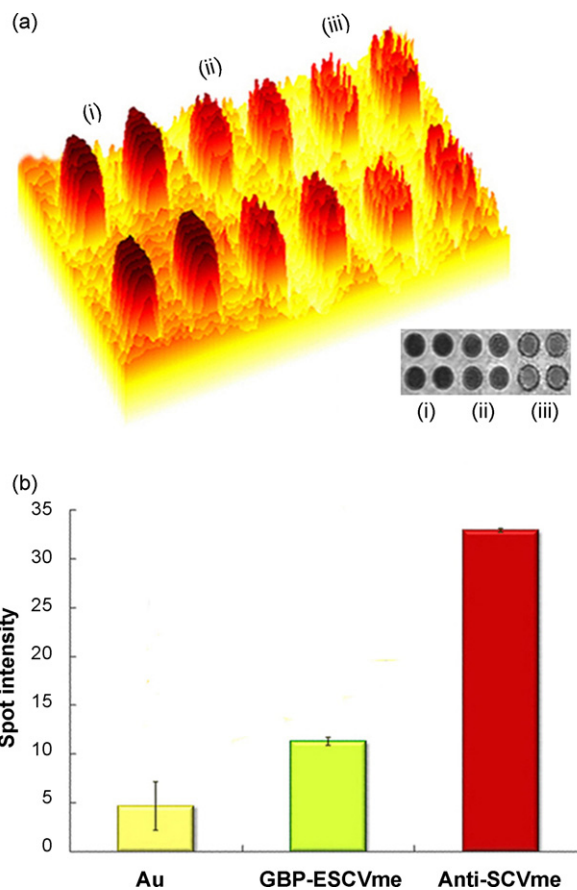
Fig. 6. SPRi analysis of the sequential binding of GBP-E-SCVme and anti-SCVme onto gold micropatterns composed of 50-μm diameter circles. (a) Three-dimensional and two-dimensional (inset) images of bare gold micropatterns as controls (sample (i)); binding of GBP-E-SCVme fusion proteins onto the gold patterns (sample (ii)); and successive binding of GBP-E-SCVme and anti-SCVme onto the gold patterns (sample (iii)). (b) Spot intensities of the three samples shown in scanned images were measured through the gold circle micropatterns.

SCVme ($100\,\mu g\,mL^{-1}$) for 30 min at 25 °C. Following washing and drying, the prepared chip was analyzed. The brighter spots indicate binding of the target proteins onto gold substrates, because reflectivity increases when binding occurs. As shown in Fig. 6(a), the brighter spots shown in samples (ii) and (iii) (compared to sample (i)) indicate the successive binding of GBP-E-SCVme and anti-SCVme antibodies onto the gold micropatterns. The brighter spots indicate the binding of target proteins onto gold substrates. Moreover, spot brightness is shown as spot intensity in Fig. 6(b). The spot intensity increased to 11.2 RU when GBP-E-SCVme was specifically bound to a gold-patterned chip showing background spot intensities of 4.6 RU, and subsequent binding of anti-SCVme to the resulting GBP-E-SCVme layer yielded a stronger spot intensity of 32.8 RU. These SPRi images show that the binding of GBP-E-SCVme, through the GBP domain, onto the gold substrate, was highly specific, and the fusion protein remained functional for further specific interaction between the SCVme domain and anti-SCVme, after immobilization onto the gold surface.

4. Conclusion

The emergence of SARS has resulted in several outbreaks worldwide. Therefore, in this study, a rapid diagnostic method of SARS was developed using a new strategy for effective immobilization of a recognition element onto an SPR gold sensor chip. The recognition element (SCVme) for detecting anti-SCVme was genetically fused to GBP. SPR analysis demonstrated that the fusion proteins were directly and simply self-immobilized onto the gold chip surface via the GBP domain which has a strong gold binding affinity, without surface modifications. The fusion protein-coated SPR chip offers a stable and specific sensing platform maintaining its anti-SCVme binding activity. Moreover, AFM analyses demonstrated specific binding of the fusion protein onto the gold surface and subsequent binding of anti-SCVme to the SCVme domain of the fusion protein layer. Using the fusion protein described here as an anchoring and recognition element, the SPR chip for rapid diagnosis of SARS infections was easily constructed and contributed to the sensitive and selective detection of anti-SCVme within 10 min. In future study, the system needs to be combined with a signal-enhancing method to obtain a more sensitive detection response. Furthermore, GBP-fusion proteins with other functional groups may open an avenue for the development of various gold substrate-based biosensor systems.

Acknowledgments

References

[1] M.A. Marra, S.J. Jones, C.R. Astell, R.A. Holt, A. Brooks-Wilson, Y.S. Butterfield, J. Khattra, J.K. Asano, S.A. Barber, S.Y. Chan, A. Cloutier, S.M. Coughlin, D. Freeman, N. Girn, O.L. Griffith, S.R. Leach, M. Mayo, H. McDonald, S.B. Montgomery, P.K. Pandoh, A.S. Petrescu, A.G. Robertson, J.E. Schein, A. Siddiqui, D.E. Smailus, J.M. Stott, G.S. Yang, F. Plummer, A. Andonov, H. Artsob, N. Bastien, K. Bernard, T.F. Booth, D. Bowness, M. Czub, M. Drebot, L. Fernando, R. Flick, M. Garbutt, M. Gray, A. Grolla, S. Jones, H. Feldmann, A. Meyers, A. Kabani, Y. Li, S. Normand, U. Stroher, G.A. Tipples, S. Tyler, R. Vogrig, D. Ward, B. Watson, R.C. Brunham, M. Krajden, M. Petric, D.M. Skowronski, C. Upton, R.L. Roper, Science 300 (2003) 1399.
[2] S.J. Lee, J.P. Park, T.J. Park, S.Y. Lee, S. Lee, J.K. Park, Anal. Chem. 77 (2005) 5755.
[3] Y.J. Tan, P.Y. Goh, B.C. Fielding, S. Shen, C.F. Chou, J.L. Fu, H.N. Leong, Y.S. Leo, E.E. Ooi, A.E. Ling, S.G. Lim, W. Hong, Clin. Diagn. Lab. Immunol. 11 (2004) 362.
[4] P.-R. Hsueh, C.-L. Kao, C.-N. Lee, L.-K. Chen, M.-S. Ho, C. Sia, X.-D. Fang, S. Lynn, T.-Y. Chang, S.-K. Liu, A.-M. Walfield, C.-Y. Wang, Emerg. Infect. Dis. 10 (2004) 1558.
[5] L.F.P. Ng, M. Wong, S. Koh, E.-E. Ooi, K.-F. Tang, H.-N. Leong, A.-E. Ling, L.V. Agathe, J. Tan, E.T. Liu, E.-C. Ren, L.-C. Ng, M.L. Hibberd, J. Clin. Microbiol. 42 (2004) 347.
[6] Y. Mizuta, T. Onodera, P. Singh, K. Matsumoto, N. Miura, K. Toko, Biosens. Bioelectron. 24 (2008) 191.
[7] Y. Sun, Y. Bai, D. Song, X. Li, L. Wang, H. Zhang, Biosens. Bioelectron. 23 (2007) 473.
[8] E. Kretschmann, H. Raether, Z. Naturforsch. 23 (1968) 2135.
[9] F. Rusmini, Z. Zhong, J. Feijen, Biomacromolecules 8 (2007) 1775.
[10] S. Brown, Nat. Biotechnol. 15 (1997) 269.
[11] M. Sarikaya, C. Tamerler, A.K. Jen, K. Schulten, F. Baneyx, Nat. Mater. 2 (2003) 577.
[12] C. Tamerler, E.E. Oren, M. Duman, E. Venkatasubramanian, M. Sarikaya, Langmuir 22 (2006) 7712.
[13] R.G. Woodbury, C. Wendin, J. Clendenning, J. Melendez, J. Elkind, D. Bartholomew, S. Brown, C.E. Furlong, Biosens. Bioelectron. 13 (1998) 1117.
[14] D.M. Hoover, J. Lubkowski, Nucleic Acids Res. 30 (2002) e43.
[15] W.P. Stemmer, A. Crameri, K.D. Ha, T.M. Brennan, H.L. Heyneker, Gene 164 (1995) 49.
[16] J. Sambrook, D.W. Russell, Molecular Cloning: A Laboratory Manual, 3rd edn., Cold Spring Harbor Laboratory Press, Cold Spring Harbor, NY, 2001.
[17] T. Kawaguchi, D.R. Shankaran, S.J. Kim, V.K. Gobi, K. Matsumoto, K. Toko, N. Miura, Talanta 72 (2007) 554.
[18] L.A. Ruiz-Taylor, T.L. Martin, F.G. Zaugg, K. Witte, P. Indermuhle, S. Nock, P. Wagner, Proc. Natl. Acad. Sci. U.S.A. 98 (2001) 852.
[19] M. Ormo, A.B. Cubitt, K. Kallio, L.A. Gross, R.Y. Tsien, S.J. Remington, Science 273 (1996) 1392.
[20] J. Lahiri, L. Isaacs, J. Tien, G.M. Whitesides, Anal. Chem. 71 (1999) 777.
[21] Subramanian, J. Irudayaraj, T. Ryan, Sens. Actuators B: Chem. 114 (1) (2006) 192–198.
[22] K.C. Grabar, R.G. Freeman, M.B. Hommer, M.J. Natan, Anal. Chem. 67 (1995) 735.
[23] J. Schmitt, P. Machtle, D. Eck, H. Mohwald, C.A. Helm, Langmuir 15 (1999) 3256.
[24] S. Ko, S.A. Grant, Biosens. Bioelectron. 21 (2006) 1283.
[25] S. Ko, B. Kim, S.-S. Jo, S.Y. Oh, J.-K. Park, Biosens. Bioelectron. 23 (2007) 51.
[26] S.V. Kolotilov, P.N. Boltovets, B.A. Snopok, V.V. Pavlishchuk, Theor. Exp. Chem. 42 (2006) 211.
[27] P.B. Richard, E. Lindner, Pure Appl. Chem. 66 (1994) 2527.
[28] R. Ekins, P. Edwards, Clin. Chem. 43 (1997) 1824.
[29] Y. Li, A.W. Wark, H.J. Lee, R.M. Corn, Anal. Chem. 78 (2006) 3158.
[30] D. Peelen, V. Kodoyianni, J. Lee, T. Zheng, M.R. Shortreed, L.M. Smith, J. Proteome Res. 5 (2006) 1580.

Detection of polycyclic aromatic hydrocarbon (PAH) compounds in artificial sea-water using surface-enhanced Raman scattering (SERS)

Olivier Péron[a], Emmanuel Rinnert[a,*], Michel Lehaitre[a], Philippe Crassous[b], Chantal Compère[a]

[a] IFREMER, Service Interfaces et Capteurs, BP 70, 29280 Plouzané, France
[b] IFREMER, Laboratoire Environnement Profond, BP 70, 29280 Plouzané, France

ABSTRACT

This paper reports an accurate synthesis of surface-enhanced Raman scattering (SERS) active substrates, based on gold colloidal monolayer, suitable for *in situ* environmental analysis. Quartz substrates were functionalized by silanization with (3-mercaptopropyl)trimethoxysilane (MPMS) or (3-aminopropyl)trimethoxysilane (APTMS) and they subsequently reacted with colloidal suspension of gold metal nanoparticles: respectively, the functional groups SH and NH_2 bound gold nanoparticles. Gold nanoparticles were prepared by the chemical reduction of $HAuCl_4$ using sodium tricitrate and immobilized onto silanized quartz substrates. Active substrate surface morphology was characterized with scanning electron microscopy (SEM) measurements and gold nanoparticles presented a diameter in the range 40–100 nm. Colloidal hydrophobic films, allowing nonpolar molecule pre-concentration, were obtained. The surfaces exhibit strong enhancement of Raman scattering from molecules adsorbed on the films. Spectra were recorded for two PAHs, naphthalene and pyrene, in artificial sea-water (ASW) with limits of detection (LODs) of 10 ppb for both on MPMS silanized substrates.

© 2009 Elsevier B.V. All rights reserved.

1. Introduction

Since the discovery by Fleischmann et al. in 1974 [1] of an abnormally intense enhancement of the Raman signal of pyridine molecules adsorbed on the roughened surfaces of silver electrodes, the scientific community has shown an ever increasing interest in the surface-enhanced Raman scattering (SERS) effect. SERS is a very sensitive technique which has been extensively employed in the study of a wide range of molecules and using different types of surfaces like colloidal metal nanoparticles, roughened metal foils, island crystal films... In SERS measurements, huge Raman enhancements, up to 10^6-fold [2–4] the normal Raman signal of non-adsorbed molecules, have been observed when molecules are adsorbed on active metallic surfaces (Au, Ag, Cu...) which exhibit high optical reflectivity. More recently, enhancement factors of up to 10^{14} to 10^{20} were obtained in single-molecule detection experiments [5–8]. Two theories help to explain the Raman enhancement origin: the short-range chemical model and the long-range electromagnetic model [9–11]. The first one is related to a charge transfer between the roughened surface and the target molecule

via an increase in adsorbed molecule polarisability. The second one is linked to the excitation of surface plasmons (free electrons oscillations) leading to an increase in the local electromagnetic field. A final Raman enhancement of an adsorbed molecule can be considered as the coupling of both mechanisms. However, the electromagnetic one is known to contribute predominantly to the Raman enhancement compared to chemical one which is much smaller (10^2) [12].

SERS can be considered as an alternative to the inherent low cross-section of normal Raman scattering. In the investigation of chemical pollutions, such as PAH low concentration (ppm) or trace concentration (ppb) in sea-water, SERS effect reveals an immense potential regarding the marine environment. In this study, SERS-active substrates able to act as pre-concentrate hydrophobic compounds were developed. The strategy for obtaining SERS-sensitive substrates was to graft silanes with terminal function groups, such as —SH or —NH_2, having an affinity for metal particles. Gold is bound to the surface through covalent interactions if the functional group is a thiol or an amine [13–15]. Although silver presents a higher SERS response with an enhancement factor 10–100-fold greater than gold, Au was chosen here on account of AgCl formation on silver surfaces in the marine medium [16]. The silanes are bound chemically to the substrate via hydroxyl groups which are already present at the SiO_2 surface

---

[17]. With (3-mercaptopropyl)trimethoxysilane (MPMS) and (3-aminopropyl)trimethoxysilane (APTMS) silanizations, the quartz surface properties are modified and the nonpolar $-CH_2$ groups give hydrophobic surfaces. Consequently nonpolar molecules, such as PAHs, are preferentially adsorbed on the substrate surface. Previous studies have already been undertaken works were on PAH detection based on sol–gel process with Au or Ag particles embedded in a methyl/ethyl-tetraethoxysilane (MTEOS/ETEOS) precursor [18,19] through the EU funded MISPEC project. In Lucht et al. [19], LODs of 430 ppb naphthalene concentration were notified with a 785-nm Raman excitation. More recently within the scope of screening development, a solution of five PAHs in sea-water with LODs of 37.5 and 0.1 μM for naphthalene and pyrene respectively, was analyzed by Schmidt et al. [20]. Besides, published literature has reported the influence of adsorption and complexation with PAHs on host calixarenes (nonpolar cavities) [21,22].

There are further studies on such functionalization for which SERS measurements were recorded. For example, APTMS silanization was used to detect bi-ethylene-pyridine [23] and tetrakis(methyl-pyridyl)porphyrin [24]. As for MPMS, mercaptoundecanol SERS spectra were recorded [25], benzenethiol as a molecular probe was detected in Jung et al. [26] and Rhodamine 6G detection was carried out [27]. Moreover, ppm levels of PAHs were detected thanks to the alkyl chain of propanethiol by Costa et al. [28]; MPMS was used as a link to build self-assembly monolayers (SAMs). Furthermore, MPMS plays a role in various application fields: chelating ligands for use in the removal of heavy metal ions in solution [29], electroless plating of silver on SAMs [30], free DNA biosensors characterized with electrochemical impedance spectroscopy [31] or silanized-protection versus steel corrosion [32].

This article demonstrates the interest of developing sensitive sensors for sea-water analyses with the aim of detecting PAHs. As far as we know, this paper relates for the first time PAHs pre-concentration onto APTMS or MPMS.

2. Experimental

2.1. Instrumentation

SERS spectra of naphthalene and pyrene solutions were recorded at room temperature with a Raman spectrometer (Labram HR800-Jobin Yvon) using the 632.8 nm excitation line of a He–Ne laser (power ~0.1 mW at the sample) in retrodiffusion geometry. The laser beam was focused through a water immersion lens (100×, NA = 1) to a spot of around 1 μm². Scattered radiation was collected at 180° relative to the excitation beam and detected with an Andor CCD cooled by the Peltier effect. A 300-g/mm grating coupled to a 800-mm spectrograph allows a spectral resolution of around 2 cm⁻¹. Spectral calibration was performed on silicium samples (at 520 cm⁻¹). Two stage edge filters allow Raman Stokes studies. The accumulation times were 1, 10 or 20 s.

A visible JenWay-6400 spectrometer was used to record the extinction spectra of colloidal solutions in the spectral region between 400 and 900 nm (resolution 0.2 nm). Analyzed solutions were diluted in distilled water (25%, v/v). Water spectrum was used as the baseline. A tungsten light was employed as the exciting source.

Concerning colloidal film extinction spectra, a Raman spectrometer, without any edge filter, was used with a white exciting light through a lens (50×, NA = 0.75). In order to record the spectrum baseline, the bare substrate was illuminated.

Scanning electron microscopy (SEM) measurements were done with a field emission scanning electron microscope (FEI-Quanta200). Before loading into the observation chamber, the

samples were coated with a thin Au film (~10–15 nm) by sputtering to avoid a surface charging effect.

2.2. Chemicals and materials

$HAuCl_4\cdot3H_2O$ and (3-aminopropyl)trimethoxysilane (APTMS, 95%) were purchased from Acros Organics. Hydrochloric acid (37%) and (3-mercaptopropyl)trimethoxysilane (MPMS, 95%) were obtained from Sigma–Aldrich. Sodium tricitrate was purchased from Prolabo, nitric acid (65%) was from Merck, hydrogen peroxide (30%) was from J.T. Baker, ammonium hydroxide (33%) was from Riedel-de-Haën, methanol and ethanol were of analytical grade from Fisher. Naphthalene from Fisher and pyrene from Cerilliant were used as analytical molecular references.

The quartz substrates were tailored with 8 mm diameter and 0.8 mm thickness from Heraeus. Quartz were cleaned using aqua regia (25% HCl, 25% HNO₃, 50% distilled water v/v) and afterwards a base "piranha" solution (75% NH₄OH, 25% H₂O₂ v/v) to eliminate organic compounds and to promote hydroxylated surfaces.

2.3. Colloidal suspension of gold nanoparticles and PAH solutions

Colloidal suspensions of gold nanoparticles were prepared according to the method described by Frens [33]. Such a metal preparation technique has been used in different studies [15,23,34,35] and consists in the reduction of $HAuCl_4$ or $AgNO_3$ by sodium tricitrate. After the addition of a reducing agent, the gold particles start to form during a process known as nucleation and subsequently grow. Here, 10 mL of sodium tricitrate at 8×10^{-3} M was slowly added to 10 mL of boiling tetrachloroauric acid at 2×10^{-3} M while stirring. The reactor was placed on a hot plate and magnetically stirred. The mixture of both solutions was refluxed for 1 h. Temperature mixture was controlled with a thermometer (~90 °C). The initially dark-grey solution turned to a red-violet hue following 2–3 min of continued boiling. After 1 h boiling, the mixture was cooled at room temperature under stirring.

The naphthalene solution was prepared by dissolving PAH in methanol wherein it is more soluble and diluted in distilled water. Naphthalene in pure water at 25 °C is soluble at 31.8 mg L⁻¹. A 25-ppm naphthalene solution was prepared from 390 μL of 0.05 mol L⁻¹ naphthalene methanol solution and the corresponding blank composed by 390 μL of methanol completed by 100 mL of pure water.

PAH solutions in artificial sea-water (ASW) were also obtained. A 10-ppm naphthalene solution and a 0.10-ppm pyrene solution both diluted to 10 ppb were achieved. Pyrene in pure water at 25 °C is soluble at 0.13 mg L⁻¹. The 10 ppm pyrene solution was prepared from 5 μL of 0.005 mol L⁻¹ pyrene methanol solution and the corresponding blank composed by 5 μL of methanol completed by 50 mL of ASW. ASW was prepared according to the ASTM D1141-90 norm [36].

2.4. Silanization—SERS substrates

Clean disk quartz substrates were vertically immersed in a 5% (v/v) methanol solution of MPMS or APTMS for 4 h according to the results obtained by Seitz et al. [23]. After silanization, the substrates were rinsed several times in methanol, sonicated in methanol for 20 min to remove silane excess and dried for 1 h at 100 °C in an air oven. Then, the silanized quartz was vertically dipped for 1 h into the colloidal suspension of gold nanoparticles for the purpose of preparing Au nanoparticle films. In order to reach the most favorable conception recipe, some substrates were kept 2 days in the air before immersion in the colloidal solution. Finally, SERS-active substrates were dried for 10 min at 100 °C. Suitable substrates for adsorbed hydrophobic molecule species and SERS measurements
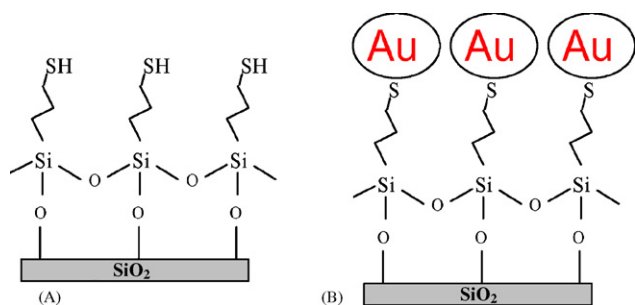
Scheme 1. Schematic representation of the SERS substrate fabrication procedure. (A) silanization step and (B) after immersion in gold colloidal suspension.

were thus synthesized. Scheme 1 presents a schematic representation of the SERS substrate fabrication procedure.

3. Results and discussion

3.1. Plasmon band (evolution)

After the silanized substrates were dipped in colloidal suspension, the extinction spectra were recorded in order to check the potential SERS activity (Fig. 1A). On the one hand, the samples which Au nanoparticles were deposited immediately after APTMS and MPMS silanization (case (i)) show extinction spectra with a plasmon band centered around 540–548 nm. On the other hand, the extinction spectrum of the samples which Au nanoparticles were immobilized 2 days after MPMS silanization (case (ii)) reveals a red shift around 554–557 nm of the plasmon band and a broad plasmon band (600–700 nm). Such a broad plasmon band has already been observed by Hajdukova et al. [24] in the course of different

preparation procedures. The colloidal solution used for the SERS substrate fabrication presents a plasmon band centered around 530 nm. We noted that such a colloidal suspension leads to samples with extinction spectra centered around 540–548 or 554–557 nm. These results seem to indicate that particle self-organization and the interaction between themselves are slightly modified. Fig. 1B and C respectively shows SEM images of APTMS and MPMS samples obtained following an immersion in colloidal suspension in case (i). As expected, no significant difference appears between APTMS and MPMS functionalization. Fig. 1D presents the SEM image of a MPMS sample kept in the air for 2 days before immersion (case (ii)). The latter shows a dense nanoparticle distribution with a couple of nanoparticles of large diameters. Size particles are in the range of 40–100 nm. When comparing both MPMS extinction spectra, such results are in agreement with the shoulder of up 700 nm.

3.2. Spectroscopic characterization

A neat MPMS (95%) Raman spectrum and a MPMS active substrate SERS spectrum were collected (Fig. 2). The laser beam was focused through a conventional lens regarding SERS-active substrate and neat MPMS in order to avoid the silanization of the water immersion lens for the latter one. The neat MPMS (95%) Raman spectrum presents a S—H stretching mode of around $2580\,cm^{-1}$ while in the SERS spectrum of active substrate, S—H vibration is not observed around the Au particles. This result is due to a thiol interaction process with Au particles. Such phenomena have already been observed and correspond to the S—H bond cleavages with the formation of a S—Au bond [37,38]. Consequently during the silanized substrate immersion stage into the colloidal suspension of gold nanoparticles, most of the S—H bond was cleaved and Au nanoparticles adhered to the substrate surface by a S—Au bond.
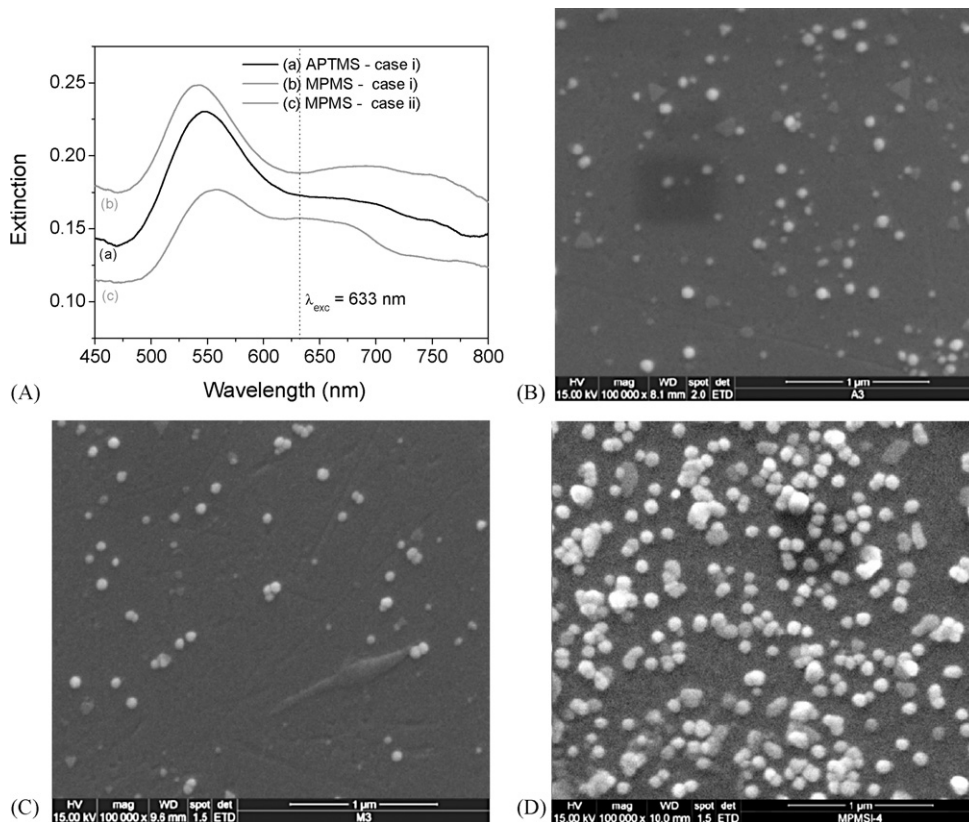
Fig. 1. (A) Extinction spectra of Au-colloidal films deposited immediately (case (i)) after (a) APTMS silanization, (b) MPMS silanization and deposited 2 days later (case (ii)) after (c) MPMS silanization. All spectra were smoothed by adjacent averaging (250 points). SEM images (100,000×) of Au-colloidal films deposited immediately (case (i)) after (B) APTMS silanization, (C) MPMS silanization and (D) 2 days later (case (ii)) after MPMS silanization.
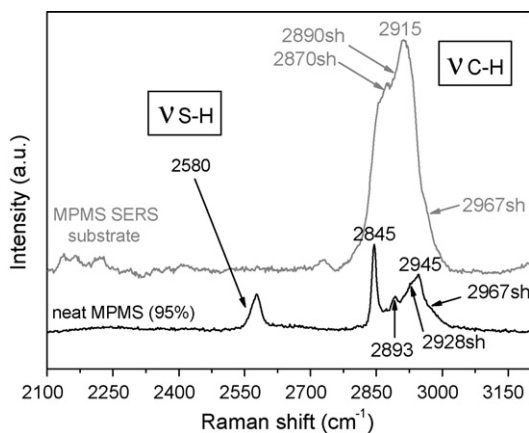
Fig. 2. Neat MPMS (95%) Raman spectrum and MPMS active substrate SERS spectrum. Integration time of 10 s.

Table 1
Raman shifts and assignments in the spectral region from 2750 to 3100 cm^{-1} for neat MPMS and MPMS SERS substrate.

Raman shift (cm^{-1})		Assignment
Neat MPMS	MPMS SERS substrate	
2580	–	$\nu(SH)$
2845	sh	$\nu_s(CH_3)$
–	2870	$\nu_s(CH_2)$
2893	2890sh	$\nu_a(CH_2)$
2928sh	2915	$\nu_s(CH_2)/\nu_a(CH_2)$
2945	sh	$\nu_s(CH_3)$
2967sh	2967sh	$\nu_a(CH_3)/\nu_a(CH_2)$

sh = shoulder.

Besides, the spectral region from 2750 to 3100 cm^{-1} gives information about ν_{C-H} vibrations regarding the methyl and methylene groups. The spectra do not have the same features. In the spectrum of neat MPMS, the intensity of the symmetric $\nu_s(CH_3)$ vibrations at 2845 and 2945 cm^{-1} are substantial. In contrast concerning the spectrum of the MPMS SERS substrate, these modes assigned to the methoxy groups disappear and only $\nu(C-H)$ associated to the methylene groups of the propyl chain exist. The Raman shifts and the assignments are summarized in Table 1. The hydrolysis and the condensation of self-assembled monolayer films of MPMS on Au surfaces could explain Raman spectrum evolution [39]. In our case, hydrolysis and condensation occur during the silanization process (see Scheme 1).
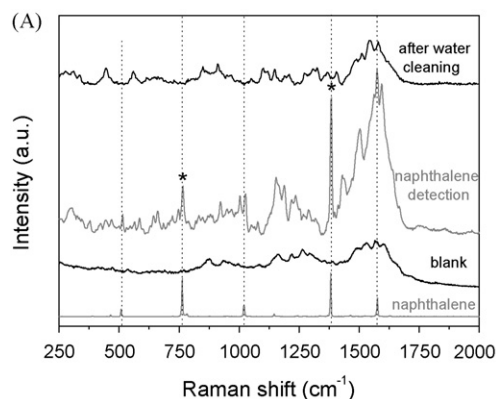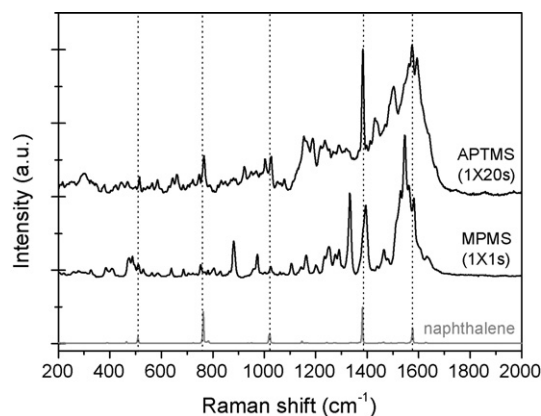
Fig. 4. SERS spectra of naphthalene solution (25 ppm) adsorbed on APTMS and MPMS surfaces with respectively 20 and 1 s as integration times. For comparison Raman spectrum of solid-state naphthalene is also given.

3.3. Hydrophobic surface behavior—SERS activity

In order to evaluate the detection reversibility of sensors and optimal organosilane functionalization, tests were conducted on APTMS and MPMS SERS-active substrates. SERS spectra were recorded after naphthalene molecules were adsorbed onto the surface by depositing a drop of solution. The SERS substrates were then immersed for 10 min in 10 mL of distilled water and SERS blank measurements were made. In the case of MPMS silanization, another rinsing in 10 mL of ethanol for 10 min is required to eliminate totally the hydrophobic molecules. Results are presented in Fig. 3A and B. Hydrophobic molecule pre-concentrations on nonpolar surfaces result in a physisorption process. Physical adsorption is a type of adsorption in whereby the adsorbate is weakly linked to the surface only through Van der Waals interactions. More precisely here, London dispersion forces arise between nonpolar molecules. Concerning APTMS silanization, the functional amine group, with the free doublet, confers a sizeable polarity to the substrate surface. According to such results, we suggest that APTMS substrates allow reversible detection after water cleaning, whereas ethanol cleaning is necessary on MPMS substrates. MPMS substrates may be more sensitive towards hydrophobic molecule pre-concentrations due to stronger hydrophobic interactions.

With a view to obtaining a complete study, naphthalene detection was acquired with different integration times of SERS spectra from different spots on the substrate surface (Fig. 4): 20 and 1 s respectively for APTMS and MPMS silanization. The

Fig. 3. (A) SERS spectra of naphthalene solution (25 ppm) adsorbed on APTMS surface, after water cleaning and blank. For comparison Raman spectrum of solid-state naphthalene is also given. (B) SERS spectra of naphthalene solution (25 ppm) adsorbed on MPMS surface, after water and ethanol cleaning and blank. For comparison Raman spectrum of solid-state naphthalene is also given. Integration time of 10 s. *Naphthalene detection.

Fig. 5. (A) SERS spectra of artificial sea-water naphthalene solutions from 0 to 10 ppm, blank and for comparison Raman spectrum of solid-state naphthalene is also given. (B) SERS spectra of artificial sea-water pyrene solutions from 0 to 0.1 ppm, blank and for comparison Raman spectrum of solid-state pyrene is also given. Integration time of 10 s.

response of MPMS SERS-active substrate is much higher than that of APTMS. With respect to previous hypotheses, the high MPMS substrate predisposition in detecting and preconcentrating hydrophobic molecules was demonstrated. Even though Hajdukova et al. [24] underline the better efficiency of APTMS in binding Au nanoparticles, they detected adsorbed tetrakis(1-methyl-4-pyrydil)porphyrin (TMPyP) which are hydrophilic molecules. In our case, MPMS allows at the same time: quartz substrate silanization, Au nanoparticle binding and pre-concentration of hydrophobic molecules. As regards PAH detection in ASW, MPMS silanization is more relevant than that of APTMS.

3.4. PAH detection

Here, SERS substrate sensitivity was investigated by SERS measurements in ASW of naphthalene and pyrene solutions. The experiments were conducted on MPMS silanized substrates kept in the air for 2 days during their preparation before being immersed in colloidal suspension (case (ii)). These SERS-active substrates present: extinction spectra with a broad plasmon band (600–700 nm) and a suitable pre-concentration of hydrophobic molecules for this study. With a 632.8-nm excitation line, such SERS substrates match the required conditions for detecting hydrophobic molecule traces. SERS spectra were recorded at different PAH concentrations. Between each concentration test, the samples were rinsed with ethanol and blank measurements were achieved in order to confirm sensor reversibility. The spectra were recorded from different spots on the substrate surface to promote SERS response homogeneity.

Thanks to the SERS spectra (Fig. 5A and B), four points must be emphasized here: (i) both PAHs, naphthalene and pyrene dissolved in ASW solution, exhibit a random intensity variation of the main characteristic Raman peaks, (ii) under excitation the organic part of the active substrate seems to continually evolve, (iii) adsorbed PAHs onto gold surface can be damaged and (iv) LODs of these PAHs in ASW.

Concerning the first point a well known theory [40], which stipulates that the vibrational parallel modes to the plane of the surface are the least enhanced modes, could explain the peak intensity variations. According to the surface selection rule and the adsorbate vibrational mode, different orientations and tilts of PAH molecules on substrate surface could occur [41]. Moreover, Nie and Emory [5] have shown that the SERS signal also depends on how nanoparticles are oriented with respect to the light polarisation axis.

Concerning the evolution of the organic part under laser excitation, the origin remains uncertain but during the reduction process of gold nanoparticles, sodium tricitrate excess and oxidation prod-

ucts still remain in the colloids. The displacement of these species arising from competitive adsorption on the metal surface could be responsible for changes in the spectra features [42].

In addition, chemical oxidation phenomena of PAHs could occur in the case of PAH adsorption on gold island films [28]. Here, SERS substrate surfaces present a different catalytic activity as regards chemical species with free spaces on their surfaces. Moreover in our case, the intensity of the extinction spectra and of the laser power are lower.

As shown in Fig. 5A and B, LODs of 10 ppb for both PAHs, naphthalene and pyrene in ASW, were performed. Concerning naphthalene trace detection, the main peaks centered on 760 and 1380 cm^{-1} are preferentially considered. In the pyrene case, peaks centered on 590 and 1406 cm^{-1} with a higher intensity were preferentially studied. The peaks at 1575 cm^{-1} for naphthalene, 1594 and 1630 cm^{-1} for pyrene cannot be easily analyzed since the organic part, i.e. MPMS and sodium tricitrate excess, presents Raman signals in this spectral region. Such results confirm SERS MPMS substrate performance in relation to hydrophobic sensitivity and sensors. We cannot draw any conclusions on the evolution of the spectral intensity of the Raman peaks versus PAH concentration in so far as isolated sites on the surface, called hot spots, give rise to intense local plasmon fields. Moreover, 10 ppb LODs in ASW for both PAHs with an integration time of 10 s could lead to a more sensitive detection by increasing the integration time of the experiment. In this way a sub-ppb detection sensor may be obtained with a reasonable resolution of signal/noise >10 on the main characteristic Raman peaks.

4. Conclusions

This present study has demonstrated that Au-colloidal hydrophobic films synthesized by quartz silanization provide, PAH pre-concentration and as well as a SERS effect. Surfaces exhibit a strong enhancement of Raman scattering from nonpolar molecules adsorbed on the films and PAH detection in ASW was performed. A LOD of 10 ppb was found for naphthalene and pyrene ASW solutions. Such results were obtained with MPMS surfaces which exhibit a broad plasmon band and a red shift. These MPMS SERS-active substrates are very interesting for future in situ applications. The geometry and the chemical stability of the substrates match with our home-made in situ Raman spectrometer [20].

otechnologie et d'Instrumentation Optique (LNIO) - Université de Technologie de Troyes (UTT).

References

[1] M. Fleischmann, P.J. Hendra, A.J. McQuillan, Chem. Phys. Lett. 26 (1974) 163.
[2] M. Fleischmann, P.J. Hendra, A.J. McQuillan, R.L. Paul, E.S. Reide, J. Raman Spectrosc. 4 (1976) 269.
[3] D.J. Jeanmaire, R.P. Van Duyne, J. Electroanal. Chem. 84 (1977) 1.
[4] M.G. Albrecht, J.A. Creighton, J. Am. Chem. Soc. 99 (1977) 5215.
[5] S. Nie, S.R. Emory, Science 275 (1997) 1102.
[6] K. Kneipp, Y. Wang, H. Kneipp, L.T. Perelman, I. Itzkan, R.R. Dasari, M.S. Feld, Phys. Rev. Lett. 78 (1997) 1667.
[7] K. Kneipp, H. Kneipp, G. Deinum, I. Itzkan, R.R. Dasari, M.S. Feld, Appl. Spectrosc. 52 (1998) 175.
[8] K. Kneipp, H. Kneipp, I. Itzkan, R.R. Dasari, M.S. Feld, Chem. Phys. 247 (1999) 155.
[9] M. Moskovits, Rev. Mod. Phys. 57 (1985) 783.
[10] A. Otto, J. Raman Spectrosc. 22 (1991) 743.
[11] A. Otto, I. Mrozek, H. Grabhorn, W. Akemann, J. Phys. Condens. Matter 4 (1992) 1143.
[12] J.E. Ivanecky III, C.M. Child, A. Campion, Surf. Sci. 325 (1995) 428.
[13] R.G. Nuzzo, B.R. Zegarski, L.H. Dubois, J. Am. Chem. Soc. 109 (1987) 733.
[14] K.C. Grabar, K.J. Allison, B.E. Baker, R.M. Bright, K.R. Brown, R.G. Freeman, A.P. Fox, C.D. Keating, M.D. Musick, M.J. Natan, Langmuir 12 (1996) 2353.
[15] C.D. Keating, M.D. Musick, M.H. Keefe, M.J. Natan, J. Chem. Educ. 76 (1999) 949.
[16] T. Murphy, H. Schmidt, H.D. Kronfeldt, SPIE 3107 (1997) 281.
[17] M. Hu, S. Noda, T. Okubo, Y. Yamaguchi, H. Komiyama, Appl. Surf. Sci. 181 (2001) 307.
[18] T. Murphy, H. Schmidt, H.D. Kronfeldt, Appl. Phys. B 69 (1999) 147.
[19] S. Lucht, T. Murphy, H. Schmidt, H.D. Kronfeldt, J. Raman Spectrosc. 31 (2000) 1017.
[20] H. Schmidt, N. Bich Ha, J. Pfannkuche, H. Amann, H.D. Kronfeldt, G. Kowalewska, Mar. Pollut. Bull. 49 (2004) 229.
[21] P. Leyton, S. Sanchez-Cortes, J.V. Garcia-Ramos, C. Domingo, M. Campos-Valette, C. Saitz, R.E. Clajivo, J. Phys. Chem. B 108 (2004) 17484.
[22] P. Leyton, C. Domingo, S. Sanchez-Cortes, M. Campos-Valette, J.V. Garcia-Ramos, Langmuir 21 (2005) 11814.
[23] O. Seitz, M.M. Chehimi, E. Cabet-Deliry, S. Truong, N. Felidj, C. Perruchot, S.J. Greaves, J.F. Watts, Colloids Surf. A: Physicochem. Eng. Aspects 218 (2003) 225.
[24] N. Hajdukova, M. Prochazka, J. Stepanek, M. Spirkova, Colloids Surf. A: Physicochem. Eng. Aspects 301 (2007) 264.
[25] G. Chumanov, K. Solokov, B.W. Gregory, T.M. Cotton, J. Phys. Chem. 99 (1995) 9466.
[26] H.Y. Jung, Y.-K. Park, S. Park, S.K. Kim, Anal. Chim. Acta 602 (2007) 236.
[27] H. Chen, Y. Wang, S. Dong, E. Wang, Spectrochim. Acta Part A 64 (2006) 343.
[28] J.C.S. Costa, A.C. Sant'Ana, P. Corio, M.L.A. Temperini, Talanta 70 (2006) 1011.
[29] B. Lee, Y. Kim, H. Lee, J. Yi, Micropor. Mesopor. Mater. 50 (2001) 77.
[30] Z.-C. Liu, Q.-G. He, P.-F. Xiao, B. Liang, J.-X. Tan, N.-Y. He, Z.-H. Lu, Mater. Chem. Phys. 82 (2003) 301.
[31] Y. Fu, R. Yuan, L. Xu, Y. Chai, X. Zhong, D. Tang, Biochem. Eng. J. 23 (2005) 37.
[32] U. Bexell, T.M. Grehk, Surf. Coat. Technol. 201 (2007) 4734.
[33] G. Frens, Nature, Phys. Sci. 241 (1973) 20.
[34] P.C. Lee, D. Meisel, J. Phys. Chem. 86 (1982) 3391.
[35] O. Siiman, L.A. Bumm, R. Callaghan, C.G. Blatchord, M. Kerker, J. Phys. Chem. 87 (1982) 1014.
[36] ASTM Standard D1141-98, (2008), Standard Practice for the Preparation of Substitute Ocean Water, ASTM International, West Conshohocken, PA, 2008, doi:10.1520/D1141-98R08, www.astm.org.
[37] R.L. Sobocinski, M.A. Bryant, J.E. Pemberton, J. Am. Chem. Soc. 112 (1990) 6177.
[38] F. Osterloch, H. Hiramatsu, R. Porter, T. Guo, Langmuir 20 (2004) 5553.
[39] W.R. Thompson, M. Caei, M. Ho, J.E. Pemberton, Langmuir 13 (1997) 2291.
[40] J.A. Creighton, Surf. Sci. 124 (1983) 209.
[41] T.G. Lee, K. Kim, M.S. Kim, J. Phys. Chem. 95 (1991) 9950.
[42] S. Sanchez-Cortés, J.V. Garcia-Ramos, J. Raman Spectrosc. 29 (1998) 365.

Self-modeling curve resolution method applied for the evaluation of dissolution testing data: A case study of meloxicam–mannitol binary systems

Róbert Rajkó [a,*], Parya Reisi Nassab [b], Piroska Szabó-Révész [b]

[a] Department of Mechanical and Process Engineering, Faculty of Engineering, University of Szeged, Moszkvai krt. 5-7, H-6725 Szeged, Hungary
[b] Department of Pharmaceutical Technology, Faculty of Pharmacy, University of Szeged, Eötvös u. 6., H-6720 Szeged, Hungary

ARTICLE INFO

ABSTRACT

This paper introduces some chemometric methods, *i.e.*, self-modeling curve resolution (SMCR), multivariate curve resolution-alternating least squares (MCR-ALS) and parallel factor analysis (PARAFAC and PARAFAC2), which are used to evaluate *in vitro* dissolution testing data detected by a UV–vis spectrophotometer on meloxicam–mannitol binary systems. These systems were chosen because of their relative simplicity to apply as part of the validation process illustrating the effectiveness of the developed and applied chemometric method. The paper illustrates the failure of PARAFAC methods used before for pharmaceutical data evaluations as well, and we suggest application of the feasible band form given by SMCR as a more general procedure.

Steps to improve the dissolution behavior of drugs have become among the most interesting aspects of pharmaceutical technology, and our results show that a larger particle size of meloxicam is advantageous for dissolution. Instead of the use of only one characteristic wavelength, appropriate chemometric methods can furnish more information from dissolution testing data, *i.e.*, the individual dissolution rate profiles and the individual spectra for all the components can be obtained without resorting to any separation techniques such as HPLC.

© 2009 Elsevier B.V. All rights reserved.

1. Introduction

In the pharmaceutical industry, the development of a new drug involves not only the discovery of a new biologically active agent, but also the physico-chemical development of a stable form of the active ingredient and the pharmaceutical development of an effective pharmaceutical dosage form. The determination of dissolution properties is one of the most commonly performed solid dosage form assays in the pharmaceutical industry and is used to establish the release profiles of solid dosage forms (tablets or capsules) in an *in vitro* system. In traditionally performed dissolution tests using baskets (apparatus 1) and paddles (apparatus 2), a dosage form unit is placed in a stirred, thermostated vessel and samples are removed at regular intervals and analyzed by a standard analytical chemistry method, *e.g.*, spectrophotometrically at a suitable chosen wavelength in the UV–vis region [1].

The history of dissolution testing processes started in 1897 with the paper of Noyes and Whitney [2]. They established that "the rate at which a solid substance dissolves in its own solution is proportional to the difference between the concentration of that solution and the concentration of the saturated solution" and gave the first mathematical expression of a diffusion-controlled dissolution process.

There are several factors that are known to influence the rate of dissolution of a pharmaceutical product *in vitro* [3], including pH, temperature, agitation, etc. Since 1967, USP has regularly standardized dissolution tests, prescribing the appropriate parameters and recommending the two apparatuses [4]. As an indication of the progress that has been made, computerized and automated systems have been developed [5,6]. Through the use of simple or multiple fiberoptic probes [7–11] and multi-wavelength sensors [12,13], chemometric methods can be applied for data analysis [14–19].

Wiberg and Hultin [20] recently reported on the application of chemometric methods to fiberoptic dissolution testing data on glibenclamide tablets enclosed in hard gelatin capsules. Their study did indeed contain applications of several chemometric methods (PLS, MCR-ALS, and GRAM) which all gave quite accurate estimations of the pure spectra and dissolution profiles. However, in their PARAFAC application some discrepancies seemed to be found, below we discuss the possible reason and the solution.

In the present case study, meloxicam–mannitol binary systems were used to investigate how chemometric methods can be used to evaluate dissolution testing data. The systems were chosen because of their relative simplicity. We used them as proper controlling systems to validate our developed and used chemometric methods.

First we tried PARAFAC (because Wiberg and Hultin [20] reported its usefulness for dissolution studies) to evaluate the data measured with the standard condition, *i.e.*, using juice in the reference cell. In that case negative absorbances occurred, thus self-modeling curve resolution (SMCR) method could not be used; the minimal non-negativity condition for SMCR was not fulfilled. We replaced the reference material to distilled water, and in that case only non-negative absorbances were obtained, thus PARAFAC and SMCR methods could become comparable. This paper is a natural continuation of our previous study [21]. The theme of this paper is not intended to be industrial, we prepared all substances under laboratorial circumstances.

2. Theoretical background

2.1. Meloxicam and mannitol as model materials

Meloxicam (ME; 4-hydroxy-2-methyl-N-(5-methyl-2-thiazolyl)-2H-benzothiazine-3-carboxamide-1,1-dioxide) is one of the enolic acid class compounds of nonsteroidal anti-inflammatory drugs (NSAIDs). ME selectively inhibits COX-2 more than COX-1 [22], and it has recently been used in the treatment of rheumatoid arthritis, osteoarthritis, Alzheimer's disease and cancers (mainly colorectal cancers) [23].

Because of the very low solubility of ME in acidic media, it can cause few adverse local gastrointestinal events [22] and this is one of its main advantages (other advantages such as good renal tolerability have been reported) [24]. One way to improve solubility is to disperse a drug in a carrier, either as a eutectic mixture or as a simple solid dispersion (physical mixtures, PMs) [25].

Mannitol ($C_6H_{14}O_6$), a sugar alcohol, is widely used in the pharmaceutical and food industries [26]. Mannitol is a water-soluble material: according to US Pharmacopoeia (USP) [1] 1 g dissolves in 5.5 ml of water. In the present experiment, β-D-mannitol was used as a carrier to increase the solubility of ME.

2.2. Self-modeling curve resolution with non-negativity constraints

SMCR, one of the oldest chemometric procedures, was introduced for two-component systems by Lawton and Sylvestre [27] (LS) in 1971 to deconvolve raw spectroscopic data into the product of two physically interpretable profile matrices, provided that both concentrations and absorbances are non-negative, accepting both as minimal constraints. Unfortunately, the solution is not unique; without further restrictions, the method can give only feasible regions for the pure component profiles. Later, Borgen et al. [28,29] generalized the LS method for three-component systems with the same minimal constraints. The concepts of Borgen seemed to be rather difficult to understand and to implement, and hence several chemometricians turned to the development of approximation methods [30]. Rajkó and István [31] recently have revisited Borgen's method, gave a clearer interpretation and used computational geometry tools to find inner and outer polygons. Rajkó [32] has subsequently extended the duality concept to the minimal constrained SMCR making a simpler algorithm possible.

2.3. Decomposing two-way bilinear data

The spectroscopic data can be collected into a two-way data type, *i.e.*, the response matrix $\underset{I \times J}{\boldsymbol{R}}$. Every *i*th row represents an object (the spectrum of a sample) and every *j*th column a variable (generally, a composition profile). According to the Bouguer–Lambert–Beer Law, the matrix will be the product of two matrices, $\underset{I \times N}{\boldsymbol{C}}$ (concentration profile matrix) and $\underset{J \times N}{\boldsymbol{S}}$ (spectral profile

matrix), built up with the profiles of the individual *N* components:

$$\underset{I \times J}{\boldsymbol{R}} = \underset{I \times N}{\boldsymbol{C}} \underset{N \times J}{\boldsymbol{S}^{\mathrm{T}}} = \sum_{n=1}^{N} \underset{I \times 1}{\boldsymbol{c}_n} \underset{1 \times J}{\boldsymbol{s}_n^{\mathrm{T}}} \tag{1}$$

Of course, we cannot know the concentration profiles in advance; in fact the task is to exploit them from the measured data with the help of SMCR methods, presuming only minimal restrictions, but without any estimation of parameters of any predefined model functions. Singular value decomposition (SVD) [33] can be regarded as the basic procedure of the chemometric methods and SMCR methods are also based on SVD.

The bilinear data matrix $\underset{I \times J}{\boldsymbol{R}}$ can be decomposed into orthogonal product matrices by SVD or principal component analysis (PCA) [34,35]:

$$\underset{I \times J}{\boldsymbol{R}} = \left(\underset{I \times N}{\boldsymbol{U}} \underset{N \times N}{\boldsymbol{D}} \right) \underset{N \times J}{\boldsymbol{V}^{\mathrm{T}}} = \underset{I \times N}{\boldsymbol{X}} \underset{N \times J}{\boldsymbol{V}^{\mathrm{T}}}, \tag{2}$$

where **U** is the matrix with the left eigenvectors of **R** in its columns, **D** is the diagonal matrix of the singular values, **V** is the matrix with the right eigenvectors of **R** in its columns, and in terms of the PCA: **UD** = **X** is the score matrix and **V** is the loading matrix.

The suitably chosen initial estimations of **S** or **C** are optimized by solving Eq. (1) iteratively by alternating least squares (ALS) optimization:

$$\begin{aligned} \underset{N \times I}{\boldsymbol{C}^+} \cdot \underset{I \times J}{\boldsymbol{R}} &= \underset{N \times J}{\boldsymbol{S}^{\mathrm{T}}} \\ \underset{I \times J}{\boldsymbol{R}} \cdot \underset{J \times N}{(\boldsymbol{S}^{\mathrm{T}})^+} &= \underset{I \times N}{\boldsymbol{C}} \end{aligned} \tag{3}$$

where $^+$ means the pseudoinverse [36].

Unfortunately, this decomposition is often not unique because of the rotational and intensity (scaling) ambiguities [27–31,35,37]. The rotational ambiguities can be moderated or even eliminated if convenient constraints can be used [38–41]. Tauler and de Juan developed a Matlab code for MCR-ALS [42] with some constraints, *i.e.*, non-negativity, unimodality, equality and closure. The same algorithm has been implemented in the PLS_Toolbox [43], offering only non-negativity and equality constraints. Gemperline and Cash presented another method, called GUIPRO P-ALS, using least squares penalty functions [44] to implement constraints in an ALS algorithm.

In this paper, acronym SMCR is used for the algorithm with which analytical band solution can be obtained, and acronym MCR-ALS is used for the approximation method which can provide "unique" solution (at least in mathematical sense: after the convergence, the solution will be the same using different initial values; of course this "unique" solution will be only one from the feasible regions/band solution).

2.4. Decomposing three-way trilinear data

When several dissolution tests of related samples are analyzed, the data can be arranged in a three-way data cube. Parallel factor analysis (PARAFAC) [35,45–48] can decompose this data cube (dissolution times by wavelengths by samples) if the data are trilinear and the dissolution rate profiles and spectral profiles to be calculated remain the same in every run. According to this, the working equation of PARAFAC is:

$$\underset{J \times K}{\boldsymbol{R}_i} = \underset{J \times N}{\boldsymbol{S}} \cdot \underset{N \times N}{\boldsymbol{Q}_i} \cdot \underset{N \times K}{\boldsymbol{E}^{\mathrm{T}}} \quad \underset{N \times N}{\boldsymbol{Q}_i} = Diag\left(\boldsymbol{c}_{i,1:N}\right) \quad i = 1 \ldots I \tag{4}$$

where $\mathbf{R}_i$ is the matrix of the *i*th slice of the data cube $\underline{\mathbf{R}}$, **E** is the matrix of dissolution rate profiles, **S** is the matrix of spectra, and $\mathbf{Q}_i$ is a diagonal matrix with the elements of the *i*th row of matrix **C** in its diagonal, whereas **C** is the matrix of concentration profiles

Table 1
Contents of the samples analyzed.

Samples	Meloxicam (mg)	Mannitol (mg)
ME1-PM 1:10	15	150
ME1-PM 3:7	15	35
ME2-PM 1:10	15	150
ME2-PM 3:7	15	35
Mannit1 (1:10)	–	150
Mannit2 (3:7)	–	35
ME1	15	–

(the outer product of the three matrices **C**, **S** and **E** yields the data cube **R**). It may be noted that this decomposition is unique under mild mathematical conditions (concerning the special ranks of the profile matrices) [48], the only indeterminacy in the least squares solution being the sequence of the components (permutation) and the scaling of the loading vectors (*i.e.*, the columns of the profile matrices) [47].

Alternatively, it is possible to define a model that does not require the dissolution rate profiles to be identical from sample to sample, but allows for some sort of deviation. The PARAFAC2 model [35,47–50] offers a way of doing this. In this case, only the covariance (or cross-product) matrix of the profile loading matrices should be the same to conform to the PARAFAC2 model:

$$\underset{J \times K}{\boldsymbol{R}_i} = \underset{J \times N}{\boldsymbol{S}} \cdot \underset{N \times N}{\boldsymbol{Q}_i} \cdot \underset{N \times K}{\boldsymbol{E}^{\mathrm{T}}} \quad \underset{K \times N}{\boldsymbol{E}_l} \cdot \underset{N \times K}{\boldsymbol{E}_l^{\mathrm{T}}} = \underset{K \times N}{\boldsymbol{E}_h} \cdot \underset{N \times K}{\boldsymbol{E}_h^{\mathrm{T}}} \quad 1 \le l, \ h \le I \tag{5}$$

This is naturally a less stringent condition than requiring that the profiles be identical as in the PARAFAC model.

3. Materials and methods

3.1. Raw materials

ME samples with different particle sizes (ME1 and ME2) were supplied by EGIS Ltd. (Budapest, Hungary). β-D-Mannitol was from Hungaropharma Ltd. (Budapest, Hungary). All other reagents and solvents were of analytical grade.

3.2. Determination of particle size

The particle sizes of the MEs and the mannitol were measured by laser diffraction (Malvern Mastersizer 2000, Malvern Ltd., Worcestershire, UK). For the measurements, the materials were dispersed with air and deagglomerated at an air pressure of 0.5 bar. The particle size was determined in the range 0.02–2000 μm. The measurements were repeated three times. The d(90%) values were 206.20 μm, 5.97 μm and 239.45 μm for ME1, ME2 and mannitol, respectively. The specific surface areas of the samples were calculated from the particle size data: $0.071 \, \mathrm{m^2 \, g^{-1}}$, $2.514 \, \mathrm{m^2 \, g^{-1}}$ and $0.226 \, \mathrm{m^2 \, g^{-1}}$ for ME1, ME2 and mannitol, respectively.

3.3. Preparation of solid binary systems

PMs of ME1 and ME2 and mannitol (ME1-PM and ME2-PM) in ratios of 3:7 (w/w) and 1:10 (w/w) were prepared by mixing the individual components for 10 min at 50 rpm in a Turbula mixer (Turbula WAB, Systems Schatz, Switzerland). For the PM binary systems, because the therapeutic dose of ME is between 7 mg and 15 mg, 15 mg of ME and the appropriate amount of mannitol were filled into hard gelatine capsules (No. 2) by hand, on a digital balance (4 digits). Two different pure samples of mannitol were used: Mannit1 (amount as in the mixture with a ratio of 1:10) and Mannit2 (amount as in the mixture with a ratio of 3:7). In Table 1 the contents of the samples analyzed are collected.

3.4. Dissolution studies

Dissolution tests were performed by using Pharmatest equipment (Hainburg, Germany) with one vessel at a paddle speed of 100 rpm. Artificial enteric juice (900 ml) with a pH of 7.5 (±0.1) at 37 °C (±0.5 °C) was used according to the composition of standard phosphate puffer solution described in USP [1]. The sampling was made after 5 min, 10 min, 20 min, 30 min, 60 min and 90 min, and the samples were measured spectrophotometrically in UV–vis range, *i.e.*, from 200 nm to 800 nm in steps of 4 nm (Helios α Spectronic, Unicam, Cambridge, UK). After concentrated investigation, for most of the cases, we selected the range of 220–436 nm which contained the most relevant spectroscopic information. The UV–vis spectra of pure components were not measured because, *e.g.*, meloxicam is weakly solvable in water. From the dissolution studies the samples must contain juice as well.

3.5. Data evaluation by chemometric methods

The SMCR method was implemented in the MATLAB computational environment [51], as an in-house development, based on the algorithm published by Rajkó and István [31]. MCR-ALS, PARAFAC and PARAFAC2 calculations were carried out through the use of PLS_Toolbox [43]. For PARAFAC 46 (wavelengths) × 6 (dissolution times) × 7 (samples) and 55 × 6 × 8 data cubes were used according to the juice and distilled water in reference cell, respectively. 55 (wavelengths) × 31 (6 × 5 dissolution times by each sample + 1 juice sample) data matrices were applied for SMCR and MCR-ALS calculations.

4. Results and discussion

For the first spectrophotometric measurements, the reference cell contained the artificial enteric juice, which is the usual and tested practice. These measurements were evaluated by PARAFAC. Because PARAFAC can provide real unique solution under relatively mild conditions and its successful application has been reported recently in the literature [20], we discuss the results in some detail. In Fig. SM-1 in the Supplementary Material the exploited spectra of the three components can be seen: the blue line possible belongs to mannitol, the red one to ME and the green one to the juice. The juice has a negative part in its spectrum in the range 220–250 nm, but the absorbances are close to zero in the remainder of the spectrum. The mannitol and ME have absolute maximum absorbances at 364 nm. About the exploited dissolution rate profiles (Fig. SM-1b): the juice has an almost constant "dissolution rate" (of course the solvent cannot be dissolving, however the concentration of the solvent is changing because of the dissolution of the other components), while mannitol can dissolve much better than ME, so its dissolution curve has a much steeper slope. After 60 min, however, the curve decreases slightly. The exploited concentration profiles contain some contradictory elements (Fig. SM-1c). Three pure samples were used: Mannit1, Mannit2 and ME1. The results for the samples Mannit1 and ME1 are appropriate. In Mannit1, the amount of ME is zero and the amount of mannitol is the largest. In ME1, the amount of the mannitol is zero and the amount of ME is the largest. However, Mannit2 appears to contain some ME, which is impossible. It seems ME2-PM 1:10 does not contain any ME, which is again impossible. In addition a high peak appeared for mannitol at around 360 nm (Fig. SM-1a), however it is known that mannitol has very weak absorbance in this region. The unacceptable results stem from the fact that the dissolution rates of ME and/or mannitol are not the same from sample to sample, and trilinearity is not fulfilled, thus PARAFAC cannot be used for data evaluation. In some
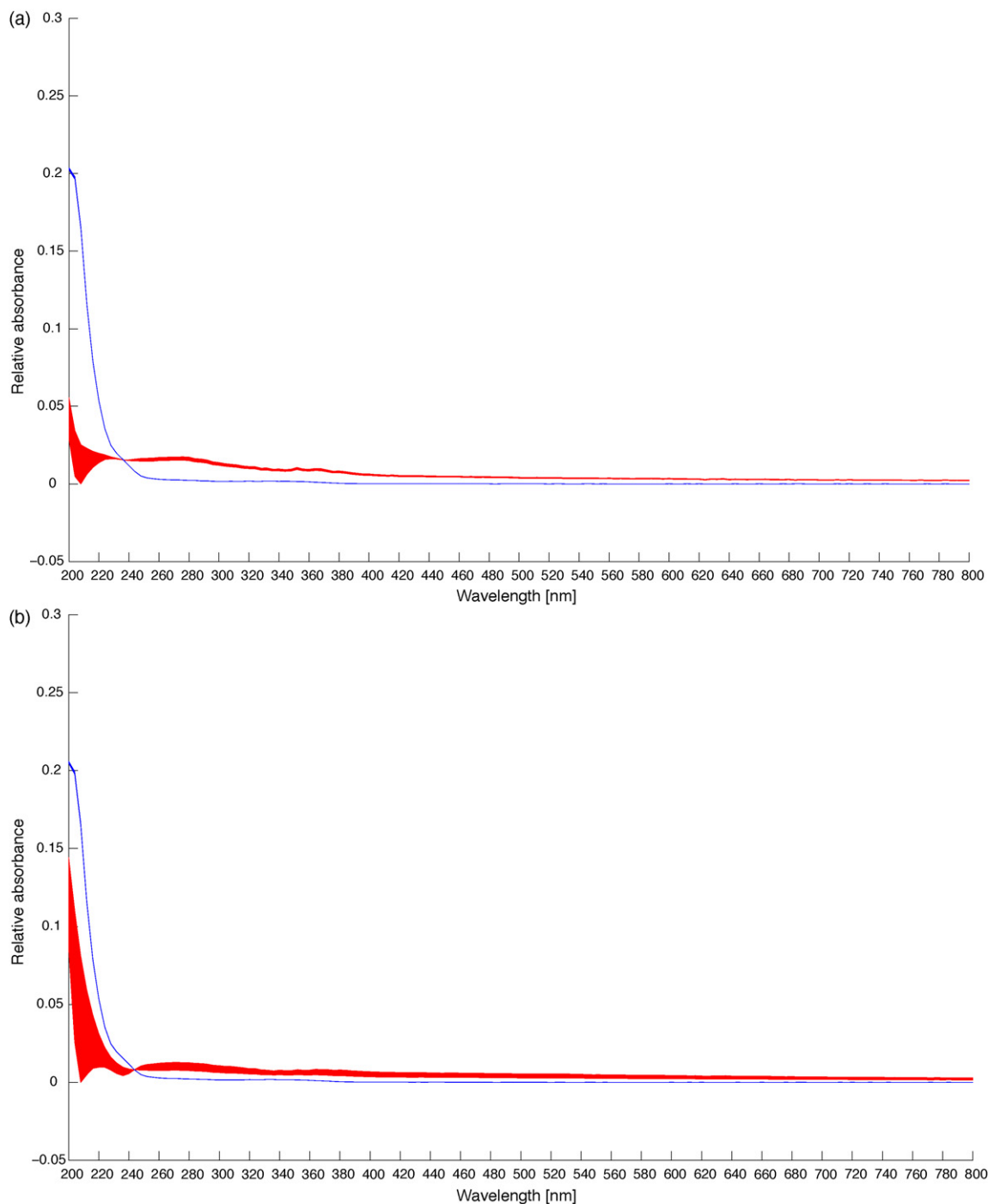
Fig. 1. Based on the two-component systems, *i.e.*, mannitol and capsule separately in juice, the spectral band of mannitol is very similar to one of the capsule. (a) Blue (narrower) band is for juice, red band is for mannitol. (b) Blue (narrower) band is for juice, red band is for the capsule. (For interpretation of the references to colour in this figure legend, the reader is referred to the web version of the article.)

of these cases, PARAFAC2 can give consistent results. Unfortunately, the calculations showed that the use of PARAFAC2 did not help, the concentration profiles again exhibiting the uninterpretable properties (not shown). It might be worth to mention that the similar limitation of use of PARAFAC and PARAFC2 was met in a previously published paper [52].

Because of the above-mentioned discrepancies, another experiment was designed, *i.e.*, in order to obtain non-negative absorbances, the reference material being changed from juice to distilled water. PARAFAC with non-negativity constraint provided the same contradictory outcome as before. In Fig. SM-1d the red

curve suggests that pure meloxicam sample should contain mannitol. Based on the green curve, one should conclude that juice contains mannitol and meloxicam. Investigating the blue curve, pure mannitol sample should involve meloxicam. Because these reasoning are impossible, we had to choose other chemometric method to evaluate data.

Taking out PARAFAC, the SMCR and MCR-ALS methods with non-negativity constraint were applied. First we realized that both mannitol and the capsule in juice have very similar spectral bands based on studying two-component systems as Fig. 1 demonstrates this fact.
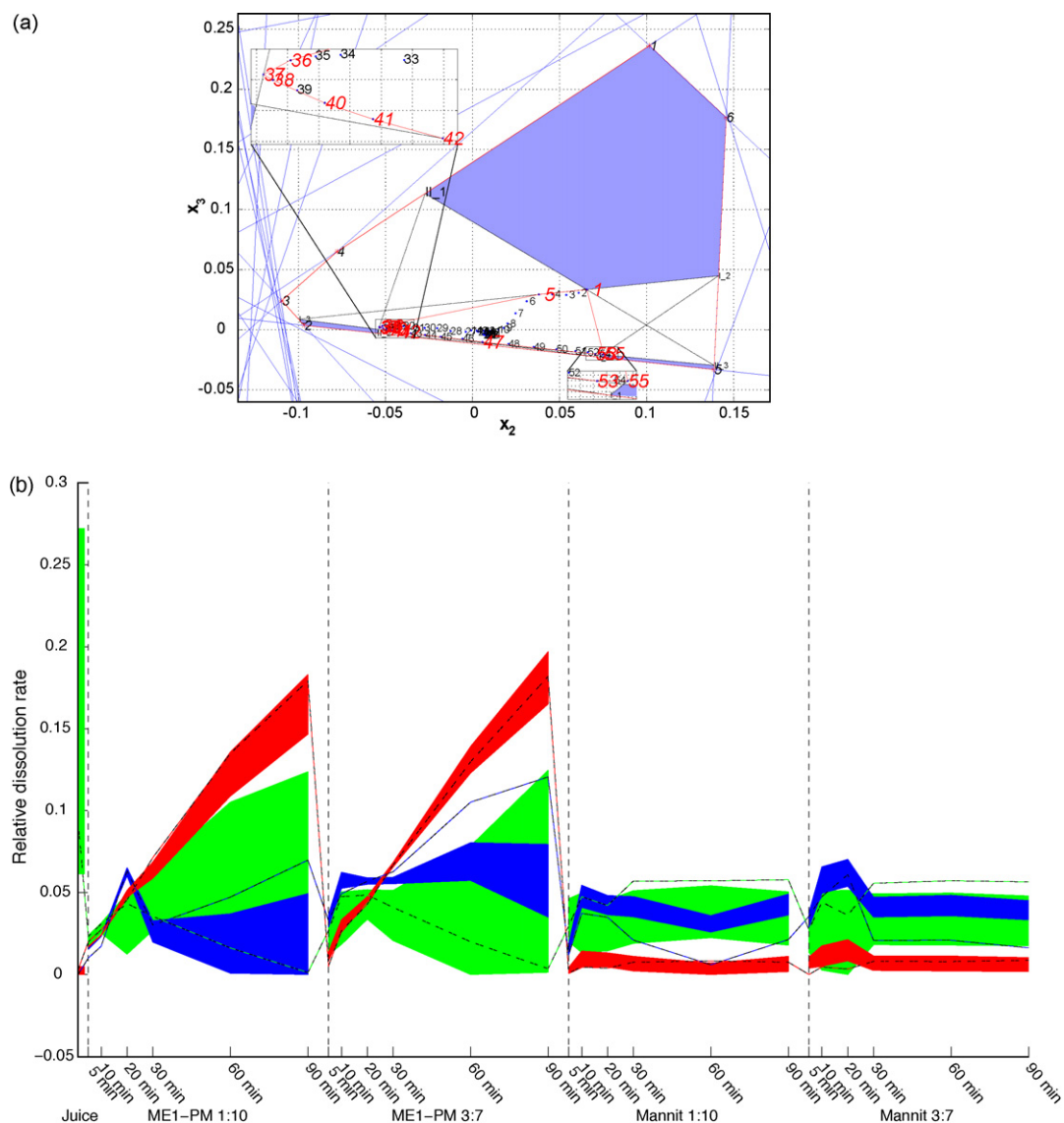
Fig. 2. SMCR results of dissolution tests using samples containing juice, ME1 and mannitol. (a) Borgen plot. The two inserts magnify the areas where the red figures are unclear. (b) Bands for the dissolution rate profiles of the three components: juice (green), ME1 (red) and mannitol (blue). The dashed lines are the unique solutions given by MCR implemented in PLS_Toolbox. (For interpretation of the references to colour in this figure legend, the reader is referred to the web version of the article.)

Then the measurement data were split into two groups. Besides juice and mannitol-capsule, one contained ME1-related data, and the others were related to ME2 data.

Figs. 2–4 show the dissolution profiles calculated by SMCR method. Fig. 2 shows the results of dissolution tests in which samples containing juice, ME1 and mannitol were used. Fig. 2a is one of the two Borgen plots [28,29,31,32] of the data, *i.e.*, the analytically calculated feasible regions of the transformed dissolution rate profile points. (The other Borgen plot having the feasible regions for the transformed spectral profiles is not shown here.) In the inner polygon, there are as many points as wavelengths used. There are one large and two smaller feasible regions. The largest one is near the farthest UV part to vis for points 1–5 with wavelengths of 220–236 nm in steps of 4 nm. This area must relate to the juice (cf. Fig. SM-2 where the green band is above the others). The smaller feasible region on left the must belong to ME1, the red band is above the others in the region of 360–384 nm in steps of 4 nm (points 36–42) in Fig. SM-2. The remaining feasible region must relate to mannitol-capsule (points 53–55, *i.e.*, 428–436 nm in steps of 4 nm); the blue band is above the others in Fig. SM-2. It is interesting that

the MCR-ALS method gave curves which were frequently outside the analytically calculated bands (cf. dashed lines in Figs. 2b and 3), which can ascribe to the effect of the mild measurement noise (SMCR can suffer from noise, however, in this investigation the noise level was tolerable for the algorithm of SMCR and maybe not by MCR-ALS).

Figs. 2b and 3 allow the conclusion that the dissolution rate of pure ME (its physical mixture with mannitol was investigated) in the given juice differs for the two forms, *i.e.*, ME1 and ME2. ME1, *i.e.*, the material with the larger particle size, displays a lower dissolution rate (see Fig. 2b) under the circumstances used, but it seems that the dissolution is independent of the concentration of ME1. Pure ME2 (its physical mixture with mannitol was investigated) exhibits better dissolution properties, but surprisingly, the dissolution rate worsened when the concentration of ME2 in the mixture was increased (see Fig. 3).

The dissolution profiles of ME1 in Fig. 2b reveal larger maxima than those for ME2 in PMs in Fig. 3 (see the red bands in both figures). However this is only a virtual difference, because these profiles are normalized to unit area. If we wish to compare the
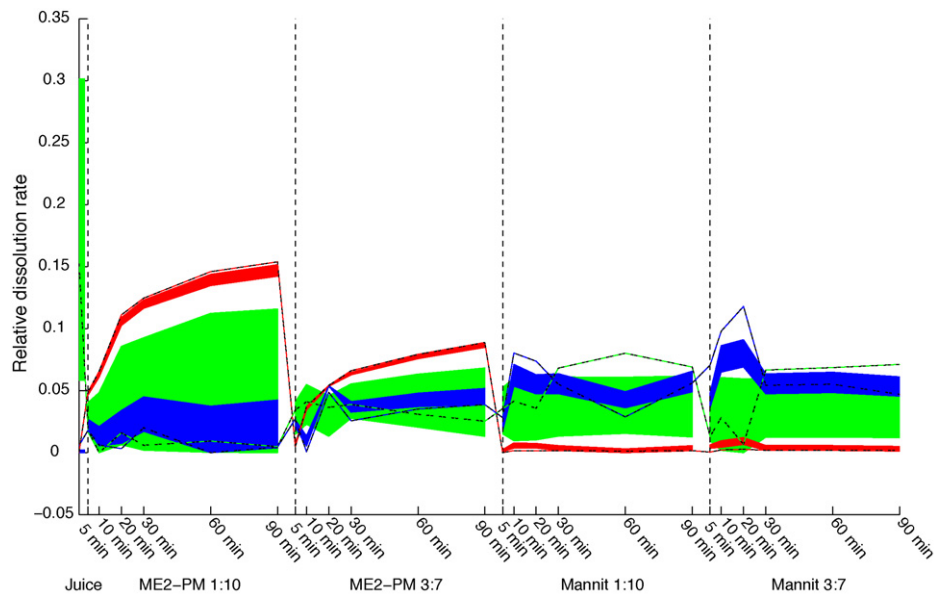
Fig. 3. SMCR results of dissolution tests using samples containing juice, ME2 and mannitol; bands for the dissolution rate profiles of the three components: juice (green), ME2 (red) and mannitol (blue). The dashed lines are the unique solutions given by MCR implemented in PLS_Toolbox. (For interpretation of the references to colour in this figure legend, the reader is referred to the web version of the article.)

dissolution profiles properly, we should consider those obtained by normalization of the spectra for unit area. The correction ratio was calculated by using MCR-ALS; Fig. 4 shows the physically comparable bands. It is clear that ME2 with a concentration ratio of 1:10 gives the largest maximum; the other three dissolution curves have more or less the same maximum.

The calculated bands for the spectra of the pure components are very similar to the two partitions of the data (compare Fig. SM-2a and -2b), proving the consistency between the parts of the measurements. If only one characteristic wavelength, *i.e.*, 364 nm in this case, is used, which is the practice nowadays, the conclusion may be drawn from Fig. SM-3: the ME2-PM with

a concentration ratio of 1:10 dissolves better than the ME2-PM with a concentration ratio of 3:7 and also better than ME1-PM, in accordance with previous findings [21]. These latter characteristic wavelength investigations were used as the validation step for our exerted SMCR-based method. The comparison of Fig. 4 and Fig. SM-3 verifies that the SMCR-based method worked correctly. However, using our method, not even the dissolution curves were provided, but the spectral profiles as well. Another point of view, if the meloxicam concentration is low enough, then the *one characteristic wavelength method* can fail because of the comparable absorbance of the mannitol-capsule pair at 364 nm.
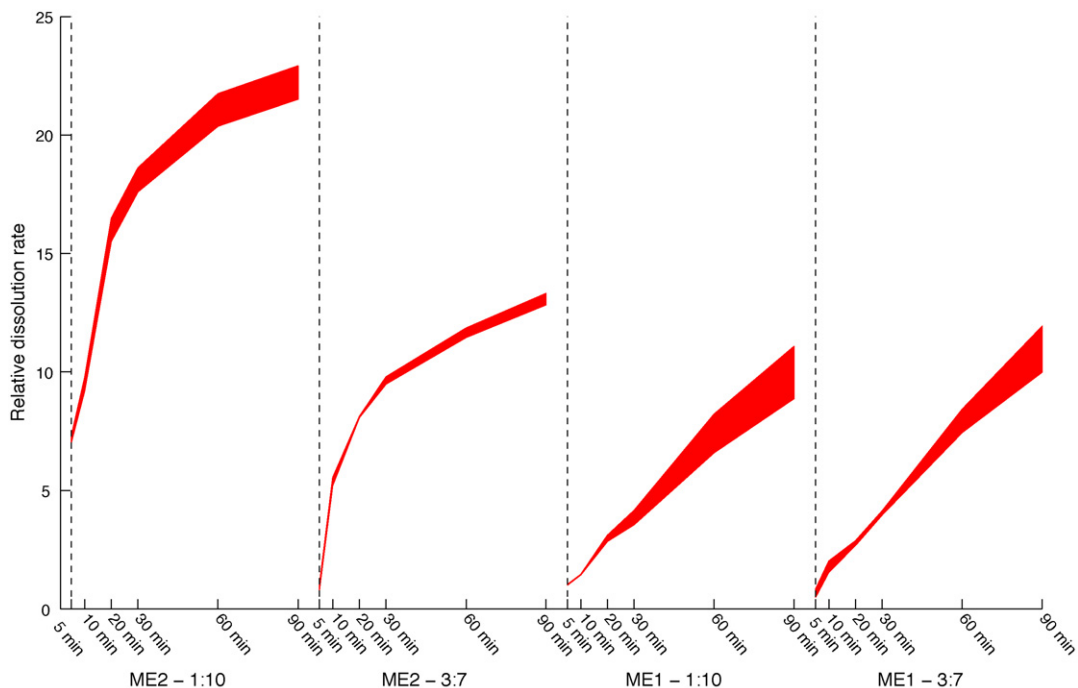
Fig. 4. The comparable relative dissolution bands for ME2 and ME1 given by SMCR and corrected by using the MCR results.

It is of interest to consider the phenomenon of the weakening of the dissolution of ME2 when the ME concentration was increased, *i.e.*, to the concentration ratio 3:7. The micronized form (ME2) was agglomerated even in the PM of mannitol and ME2, because the ME particles preserved their strong cohesive force to each other and this effect decreased the wetting surface of both the mannitol and the ME crystals. The decrease in the surface area is more significant when ME2 is at higher concentration. To verify this, scanning electron microscopy (SEM) investigation was carried out; the pictures (not shown) clearly demonstrated the particle habits of ME1 and mannitol, which have larger particles than those of ME2. The micronized ME2 resulted in agglomerates because of the very small particle size (about 6 μm on average). The arrangement of the components in the PMs was also studied by SEM and the results have been published in an accompanying paper [53]. In the sample of ME1-PM 1:10, the components with the same particle size are seen side by side, with only the small crystals adhering on the surface of the larger crystals and *vice versa* (Fig. 5A and B in Ref. [53]). However, in the case of ME2-PM 1:10, many small adherent crystals could be observed (Fig. 5E and F in Ref. [53]).

5. Conclusions

We have established that the absorbance of the artificial enteric juice is not negligible, and thus the juice should be regarded as a component. For the spectrophotometric measurements, we changed the material in the reference cell from juice to distilled water, obtaining non-negative absorbances. Next, chemometric methods were used to calculate data from the dissolution testing of ME–mannitol binary systems.

We found that PARAFAC could not be used for these data, because the trilinearity condition was not fulfilled, *i.e.*, the dissolution rate profiles changed from one sample to another. This might hold for the measurements and data evaluations of Wiberg and Hultin [20] too. From Fig. 7c in Ref. [20], the estimated (relative) concentrations are about 0 and 18, thus their ratio is far from the expected 1/2. Fig. 7a in Ref. [20] demonstrates that the dissolution profile of glibenclamide is negative at 3 min, which means that glibenclamide produced instead of dissolving at that time.

To the best of our knowledge, this is the first reported use of the SMCR method for the analytical calculation of the feasible regions and the bands of the profiles for three-component dissolution systems. Naturally, the band solutions can give only a qualitative picture, but in most of the cases the bands are narrow enough to provide a quantitative outcome within the measurement error.

Our investigation leads us to suggest use of the spectra instead of only one characteristic wavelength during the evaluation of dissolution testing data, as in that case the individual dissolution rate profiles for all the components can be exploited by using suitable chemometric methods without applying time-consuming separation techniques such as liquid chromatography. It provides an opportunity to investigate the correlation between the individual dissolution rates of the active components in complex formulations too (*in vitro* testing) and the *in vivo* bioavailability, yielding bioequivalence results faster and more cheaply.

It would be interesting to investigate some industrial aspects corresponding to the dissolution study reported above, however, it is out of the scope of the present paper.

Acknowledgments

Appendix A. Supplementary data

Supplementary data associated with this article can be found at doi:10.1016/j.talanta.2009.03.068.

References

[1] United States Pharmacopeia (USP), 28 NF23 S1.
[2] A.A. Noyes, W.R. Whitney, J. Am. Chem. Soc. 19 (1987) 930.
[3] J.A. Miller, Pharm. Technol. 1 (1977) 19.
[4] J.L. Cohen, B.B. Hubert, L.J. Leeson, C.T. Rhodes, J.R. Robinson, T.J. Roseman, E. Shefter, Pharm. Res. 7 (1990) 983.
[5] F.J. Cioffi, H.M. Abdou, A.T. Warren, J. Pharm. Sci. 65 (1976) 1234.
[6] Z.-Q. Zhang, Y. Tang, Anal. Bioanal. Chem. 381 (2005) 932.
[7] M. Josefson, E. Johansson, A. Torstensson, Anal. Chem. 60 (1988) 2666.
[8] J.H. Cho, P.J. Gemperline, A. Salt, D.S. Walke, Anal. Chem. 67 (1995) 2858.
[9] P.K. Aldridge, D.W. Melvin, B.A. Williams, K. Bratin, L.J. Kostek, S.S. Sekulic, J. Pharm. Sci. 84 (1995) 909.
[10] P.J. Gemperline, J.H. Cho, B. Baker, B. Batchelor, D.S. Walker, Anal. Chim. Acta 345 (1997) 155.
[11] J. Johansson, M. Cauchi, M. Sundgren, J. Pharm. Biomed. Anal. 29 (2002) 469.
[12] C.W. Brown, J. Lin, Appl. Spectrosc. 47 (1993) 615.
[13] C.-S. Chen, C.W. Brown, Pharm. Res. 11 (1994) 979.
[14] E. Adams, R. De Maesschalck, B. De Spiegeleer, Y. Vander Heyden, J. Smeyers-Verbeke, D.L. Massart, Int. J. Pharm. 212 (2001) 41.
[15] E. Dinç, C. Serin, F. Tuğcu-Demiröz, T. Doğanay, Int. J. Pharm. 250 (2003) 339.
[16] C.K. Markopoulou, E.T. Malliou, J.E. Koundourellis, J. Pharm. Biomed. Anal. 37 (2005) 249.
[17] M.C.F. Ferraro, P.M. Castellano, T.S. Kaufman, Anal. Bioanal. Chem. 377 (2003) 1159.
[18] P.M. Castellano, S.E. Vignaduzzo, R.M. Maggio, T.S. Kaufman, Anal. Bioanal. Chem. 382 (2005) 1711.
[19] S.E. Vignaduzzo, R.M. Maggio, P.M. Castellano, T.S. Kaufman, Anal. Bioanal. Chem. 386 (2006) 2239.
[20] K.H. Wiberg, U.-K. Hultin, Anal. Chem. 78 (2006) 5076.
[21] P.R. Nassab, R. Rajkó, P. Szabó-Révész, J. Pharm. Biomed. Anal. 41 (2006) 1191.
[22] S. Altinöz, E. Nemutlu, S. Kir, Il Farmaco 57 (2002) 463.
[23] R.N. Rao, S. Meena, A.R. Rao, J. Pharm. Biomed. Anal. 39 (2005) 349.
[24] N. Seedher, S. Bhatia, J. Pharm. Biomed. Anal. 39 (2005) 257.
[25] P. Luger, K. Daneck, W. Engel, G. Trummlitz, K. Wagner, Eur. J. Pharm. Sci. 4 (1996) 175.
[26] Á. Gombás, P. Szabó-Révész, G. Regdon Jr., I. Erős, J. Therm. Anal. Cal. 73 (2003) 615.
[27] W.H. Lawton, E.A. Sylvestre, Technometrics 13 (1971) 617.
[28] O.S. Borgen, B.R. Kowalski, Anal. Chim. Acta 174 (1985) 1.
[29] O.S. Borgen, N. Davidsen, Z. Mingyang, Ø. Øyen, Microchim. Acta II (1986) 63.
[30] A. de Juan, R. Tauler, Crit. Rev. Anal. Chem. 36 (2006) 163.
[31] R. Rajkó, K. István, J. Chemometr. 19 (2005) 1.
[32] R. Rajkó, J. Chemometr. 20 (2006) 164–169.
[33] G. Stewart, SIAM Rev. 35 (1993) 551.
[34] S. Wold, Chemom. Intell. Lab. Syst. 2 (1987) 37.
[35] E.R. Malinowski, Factor Analysis in Chemistry, 3rd edn., Wiley, New York, USA, 2002.
[36] G.H. Golub, C.F. Van Loan, Matrix Computations, 2nd edn., The John Hopkins University Press, Baltimore, USA, 1989.
[37] R. Tauler, A. Smilde, B.R. Kowalski, J. Chemometr. 9 (1995) 31.
[38] R. Tauler, J. Chemometr. 15 (2001) 627.
[39] A. de Juan, Y. Vander Heyden, R. Tauler, D.L. Massart, Anal. Chim. Acta 346 (1997) 307.
[40] R. Bro, N.D. Sidiropoulos, J. Chemometr. 16 (2002) 613.
[41] M.H. Van Benthem, M.R. Keenan, D.M. Haaland, J. Chemometr. 16 (2002) 613.
[42] R. Tauler, A. de Juan, Multivariate Curve Resolution Homepage. http://www.ub.edu/mcr/welcome.html, 2005–2007 (17 May 2008).
[43] B.M. Wise, N.B. Gallagher, R. Bro, J.M. Shaver, PLS_Toolbox 3.0 for use with MATLAB™, Eigenvector Research, Manson (WA), USA, 2003.
[44] P.J. Gemperline, E. Cash, Anal. Chem. 75 (2003) 4236.
[45] R.A. Harshman, UCLA Working Papers in Phonetics 16 (1970) 1.
[46] J.D. Carroll, J. Chang, Psychometrika 35 (1970) 283.
[47] R. Bro, Multi-way Analysis in the Food Industry, Ph.D. Thesis, Amsterdam, The Netherlands, 1998.
[48] A. Smilde, R. Bro, P. Geladi, Multi-way Analysis. Applications in the Chemical Sciences, Wiley, Chichester, UK, 2004.
[49] R.A. Harshman, UCLA Working Papers in Phonetics, 22 (1972) 30.
[50] H.A.L. Kiers, J.M.F. Ten Berge, R. Bro, J. Chemometr. 13 (1999) 275.
[51] The Mathworks Inc. MATLAB™, Version 6.1 (R12.1), User's Guide, Natick (MA), USA, 2000.
[52] K. István, R. Rajkó, G. Keresztury, J. Chromatogr. A 1104 (2006) 154.
[53] P.R. Nassab, Zs. Tüske, P. Kása Jr., A. Bashiri-Shahroodi, P. Szabó-Révész, J. Adhes. 83 (2007) 799.

Admicelle-enhanced synchronous fluorescence spectrometry for the selective determination of polycyclic aromatic hydrocarbons in water

Tohru Saitoh*, Hiroto Itoh, Masataka Hiraide

Department of Molecular Design and Engineering, Graduate School of Engineering, Nagoya University, Chikusa-ku, Nagoya 464-8603, Japan

ABSTRACT

A simple and rapid method for the highly sensitive determination of polycyclic aromatic hydrocarbons (PAHs) in water was developed. Benzo[a]pyrene, benzo[k]fluoranthene, perylene, and pyrene in water were concentrated into sodium dodecyl sulfate (SDS)-alumina admicelles. The collection was performed by adding SDS and alumina particles into the sample solution at pH 2. After gentle mixing, the resulting suspension was passed through a membrane filter to collect the SDS admicelles containing highly concentrated PAHs. The filter was placed on a slide glass and then covered admicellar layer with a fused silica glass plate before setting in a fluorescence spectrometer. Benzo[a]pyrene, benzo[k]fluoranthene, perylene, and pyrene were selectively determined by the synchronous fluorescence scan (SFS) analysis with keeping wavelength intervals between excitation and emission to 98, 35, 29, and 45 nm, respectively. Because of the minimum spectral overlapping, $1–40 \, ng \, l^{-1}$ of benzo[a]pyrene, benzo[k]fluoranthene, and perylene as well as $10–150 \, ng \, l^{-1}$ of pyrene were selectively determined with eliminating the interferences of other 12 PAHs. The detection limits were $0.3 \, ng \, l^{-1}$ for benzo[a]pyrene, benzo[k]fluoranthene, and perylene, and $1 \, ng \, l^{-1}$ for pyrene. They were 2–3 orders of magnitude lower than the detection limits in normal aqueous micellar solutions. The application to water analysis was studied.

© 2009 Elsevier B.V. All rights reserved.

1. Introduction

Polycyclic aromatic hydrocarbons (PAHs) are ubiquitous environmental pollutants resulting from the combustion of fossil fuels and the cremation of waste products. They can be transfer from gas to aqueous phases such as rain, river, and ground waters. Because of their toxic, carcinogenic, mutagenic, and bioaccumulative properties, PAHs in environmental water have to be frequently monitored. The analysis of traces of PAHs in water samples have generally been performed by the pre-concentrating by liquid–liquid extraction or solid-phase extraction and the subsequent determination by gas or liquid chromatography [1–5]. However, cumbersome and time-consuming procedures are necessary in the conventional analytical methods. The use of harmful and flammable organic solvents potentially damages to user's health and environment.

We have designed a simple and efficient extraction method using admicelles for the concentration of hydrophobic organic compounds and metal chelates in the aqueous solution [6–14]. An anionic surfactant such as sodium dodecyl sulfate (SDS) can sorb on positively charged surfaces of alumina to form micelle-like aggregates (hemi-micelles or admicelles) [15–19]. Hydrophobic

compounds in water are predominantly incorporated into the admicelles depending on their hydrophobic properties. The method (termed hemi-micelle/admicelle-mediated extraction by some researchers) has been extensively applied to the extraction of varieties of compounds [6–14,20–28]. For example, hydrophobic PAHs were quantitatively collected to the admicelles by passing the solution through the solid-phase extraction cartridge filling with SDS-coated alumina [11]. PAHs were easily eluted by washing the admicelle cartridge with small amount of organic solvent. The method was compatible to their HPLC analysis by fluorometric detection without reducing its performance. Since the fluorescent spectra of PAHs are extensively overlapping, HPLC separation is necessary for the simultaneous analysis. However, considerable time is required for their chromatographic separation.

An attractive alternative may be the determination by a synchronous fluorescence scan (SFS). The SFS is known to be a choice for simultaneous determination of multi-component samples without a preseparation [29]. In this method, both excitation and emission monochromaters are scanned simultaneously with keeping constant interval to obtain a simpler and narrower spectrometric peak. Because of sharp and narrow spectrum, the SFS serves as a very simple, selective, and sensitive method for the simultaneous analysis of PAHs in solution or solid media [30–34]. Recently, it was found that the fluorescence intensity obtained by

---

SFS was sensitized in the micellar media [35,36]. In addition, our previous observation indicated that the fluorescence intensity of pyrene in the conventional fluorescence scan was enhanced by incorporating to SDS-alumina admicelles [37]. Thus, the combination of admicelle-mediated extraction and SFS could be a simple, rapid, and sensitive method for the simultaneous determination of PAHs in water samples.

In the present study, PAHs in water was collected to admicelles that were prepared just by pouring surfactant and solid particle to the sample solution. Then the admicelles were collected on a membrane filter for measuring the fluorescence of PAHs. The conditions including kind or/and amount of surfactant and solid particle were investigated for achieving efficient collection and sensitive detection. Some PAHs were selectively determined by SFS without any procedures of elution or separation.

2. Experiment

2.1. Reagents

PAHs including anthracene, benzo[a]anthracene, benzo[k]fluoranthene, benzo[a]pyrene, benzo[e]pyrene, chrysene, coronene, fluoranthene, phenanthrene, naphtharene, naphtha[2,3a]pyrene, perylene, and pyrene were purchased from Sigma–Aldrich (St. Louis, MO, USA). They were used as 0.1 mM ethanol solutions. Sodium dodecyl sulfate (SDS, for biochemistry, Wako Pure Chemical, Tokyo, Japan) and cetyltrimethylammonium chloride (CTAC, Kanto Chemical, Tokyo, Japan) were used without further purification. Alumina (B-0, for TLC, containing no binder, Wako Pure Chemical) and silica gel (for TLC, containing no binder, Kanto Chemical, Tokyo, Japan) were employed. Other reagents used were of analytical grade. Milli-Q purified water was used for all experiments.

2.2. Procedures

To 500 ml of water sample (pH 2) containing PAHs were added 10 mg of alumina and 150 mg of SDS. The water sample was precedently filtrated with an aluminum oxide membrane filter (Anodisk^{TM}, filter size: 47 mm, pore size: 0.1 μm, Whatman plc, Maidstone, UK) to remove particulate materials. After mixing with a magnetic stirrer (ca. 120 rpm) for 10 min, the solution was passed through a membrane filter (Omnipore^{TM}, hydrophilic PTFE, filter size: 25 mm, pore size: 0.45 μm, Millipore, Billerica, MA, USA) to collect the admicelles. The membrane filter was precedently set to a glass filter holder having 16 mm of inner diameter. The filtration was performed by suction at a flow rate of ca. 200 ml min^{-1}. Immediately after the completion of the filtration, the farther suction should be avoided. The membrane filter was carefully detached from the holder, placed on a slide glass (35 mm × 26 mm × 1 mm), and subsequently covered with a fused silica glass plate (25 mm × 25 mm × 1 mm). The gap of the glass plates was sealed with a flexible paraffin film (Parafilm®, Pechiney Plastic Packaging, Chicago, IL, USA). The procedures of sample preparation (Fig. 1) were performed in a dark room for minimizing the photo-bleaching of PAHs. The sample was directly placed in the front surface accessory for solid samples in a Perkin-Elmer LS-50B luminescence spectrometer. The incidence angle of the excitation radiation was set at 60° to ensure that reflected light, scattered radiation, and depolarization phenomena are minimized. The wavelength intervals between excitation and emission ($\Delta\lambda$) in the synchronous fluorescence scan were set to 98 nm for benzo[k]fluoranthene, 35 nm for benzo[a]pyrene, 29 nm for perylene, and 45 nm for pyrene. Slit widths were 2.5 nm for both of excitation and emission. The temperature was maintained at 25 ± 1 °C.
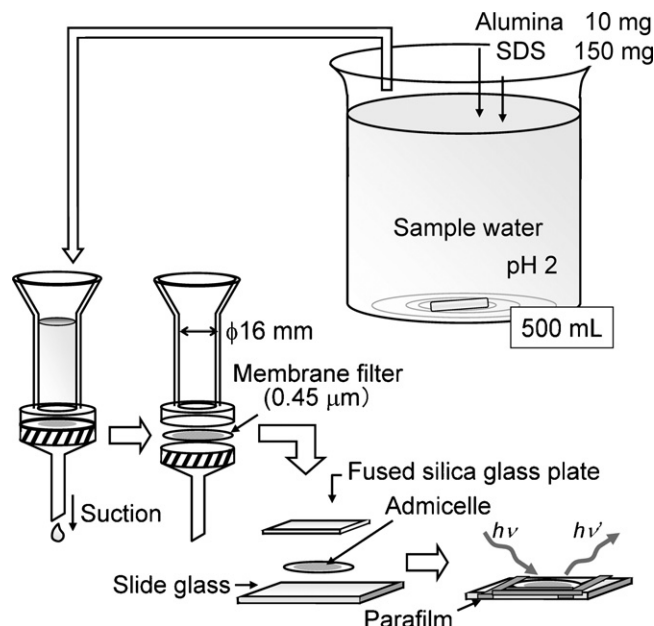
Fig. 1. Schematic illustration of experimental procedures.

3. Results and discussion

3.1. Collection of PAHs

Fig. 2 shows the effect of the amount of SDS on the collection of PAHs. The SDS dependent increase in the collection is explained by gradual formation of SDS-alumina admicelles. The extent of the collection was more than 97% by adding 50–150 mg of SDS for 500 ml of sample water when 10 mg of alumina was used. On the other hand, the collections decreased by adding further amount of SDS, being ascribable to the distribution of PAHs to normal SDS micelles formed in the bulk aqueous solution. In the present study, the addition of 150 mg of SDS was recommended.

In the extraction of analytes from large volume of water to very small amount of sorbents, the mixing or the stirring of the solution for considerable time is usually necessary for the complete collection. This is due to small area of the interface between solid sorbents and bulk aqueous solution. Low water-permeability of conventional hydrophobic solid-phase extraction media may be another reason
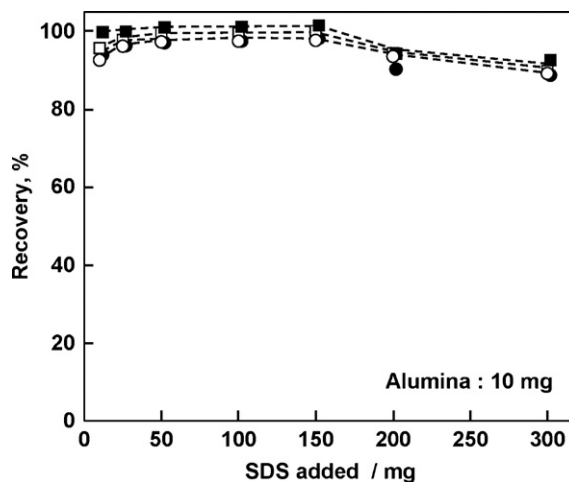
Fig. 2. Effect of the amount of SDS added on the collection of benzo[a]pyrene (□), benzo[k]fluoranthene (●), perylene (■), and pyrene (○) from 500 ml of water to admicelles composing of 10 mg of alumina.

for slow mass transfer. However, the mixing of the solution for 2 min was enough to achieve more than 97% recoveries of pyrene and benzo[a]pyrene. Such rapid collection can be ascribed to high water-permeability of admicelles. Dynamic sorption of surfactant molecules on solid surfaces may be another reason for the rapid collection. The mixing for 10 min with a magnetic stirrer (ca. 120 rpm) is recommended for the complete collection of PAHs.

The amount of alumina can also influence to the collection of PAHs. By using more than 5 mg of alumina, however, the recoveries of pyrene and benzo[a]pyrene were almost quantitative (>97%). On the other hand, the fluorescence intensities of PAHs were largely dependent on the amount of admicelles (Fig. 3). Low and less-reproducible intensity was obtained by adding alumina below 10 mg, owing to the difficulty in the preparation of uniform admicelle layer. The fluorescence intensity also decreased with increasing the amount of alumina more than 10 mg. The increasing thickness of admicellar layer diminished the incident excitation radiant power. The addition of 150 mg of SDS and 10 mg of alumina was optimum for the quantitative collection and the maximum fluorescence intensity.

In the present study, CTAC-silica gel admicelle was also tested for the collection and fluorescence detection of PAHs, because it is also useful for the rapid and efficient collection of hydrophobic analytes in water [12]. However, the fluorescence intensity
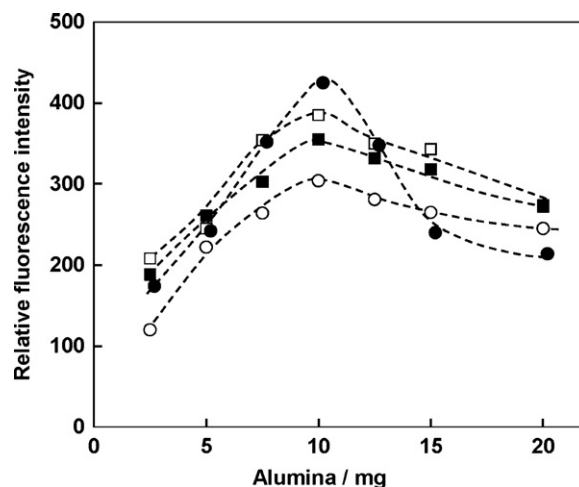
Fig. 3. Effect of amount of admicelles on the fluorescence intensities of PAHs. The marks are the same as those defined in Fig. 2.
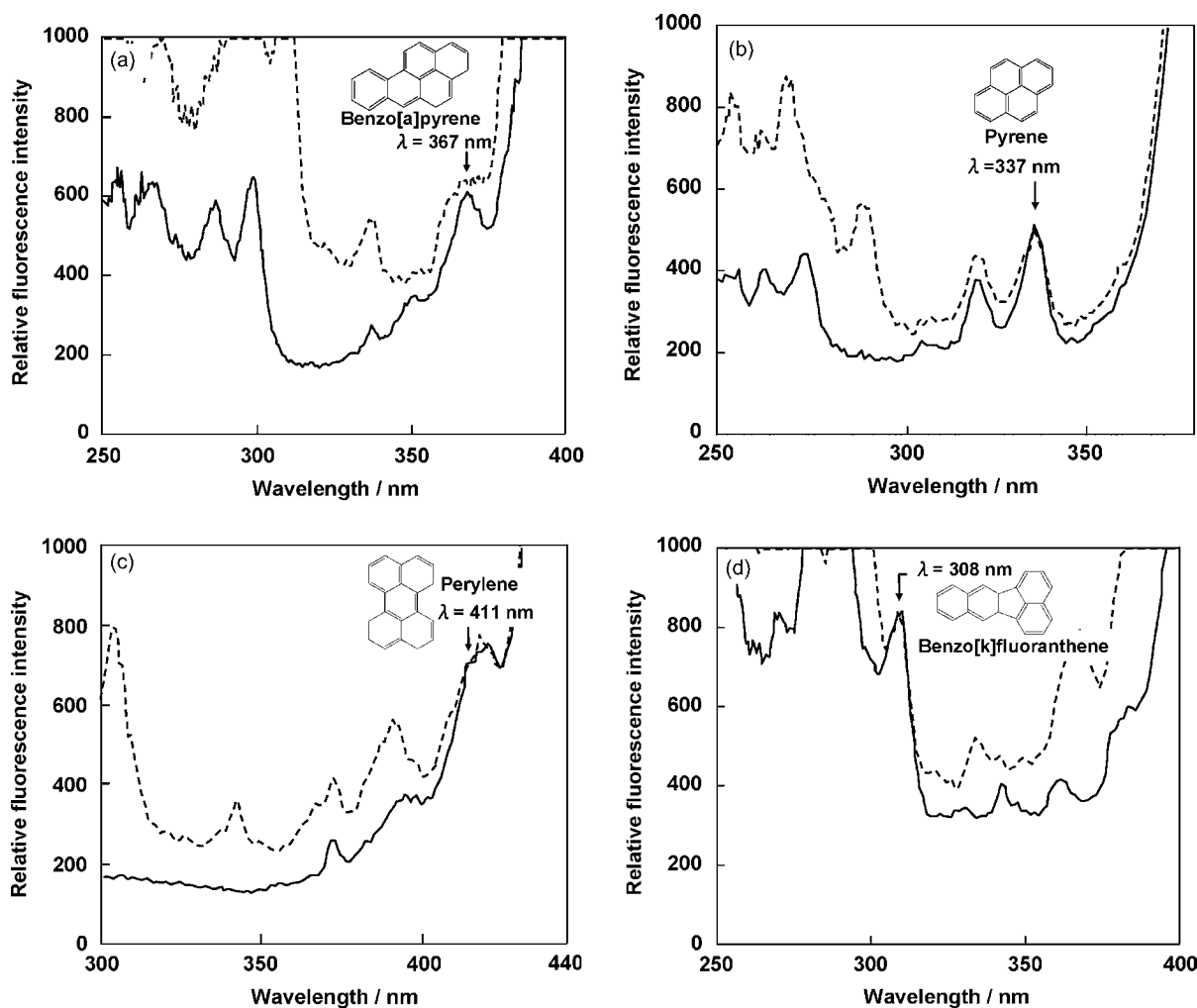
Fig. 4. Normal excitation spectra of 20 ng l^{-1} of benzo[a]pyrene (a), pyrene (b), perylene (c), and benzo[k]fluoranthene (d) in the absence (solid line) and the presence of 50 ng l^{-1} other 12 PAHs (broken line) obtained by the concentration to admicelles composing of 10 mg alumina. Other 12 PAHs include anthracene, benzo[a]anthracene, benzo[k]fluoranthene, benzo[a]pyrene, benzo[e]pyrene, chrysene, coronene, fluoranthene, phenanthrene, naphtharene, naphtha[2,3a]pyrene, perylene, and pyrene except a PAH of interest. Emission wavelengths are 402 nm for benzo[a]pyrene, 382 nm for pyrene, 441 nm for perylene, and 408 nm for benzo[k]fluoranthene. Arrows indicate detection wavelengths.
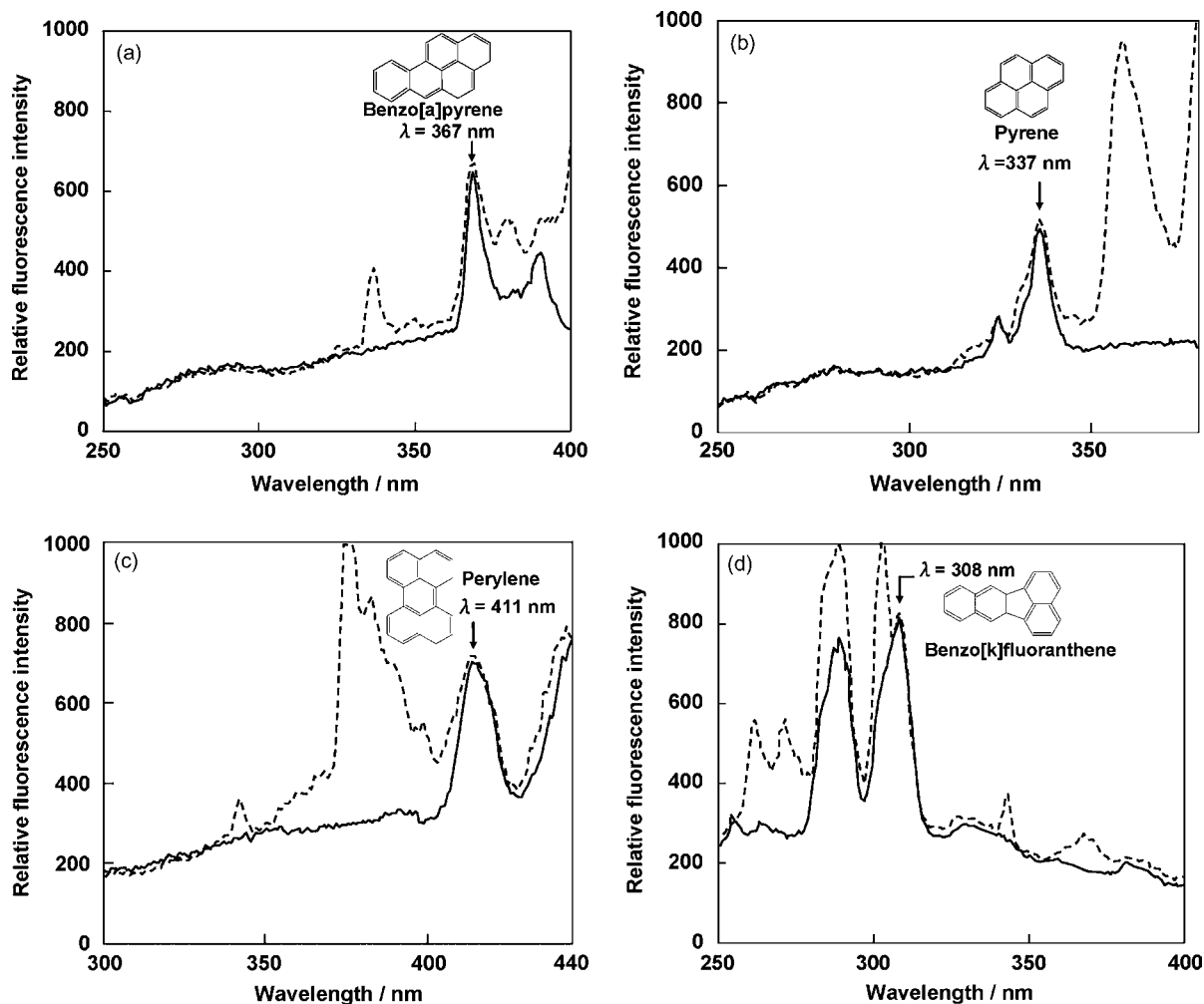
Fig. 5. Synchronous excitation spectra of 20 ng l^{-1} of benzo[a]pyrene (a), pyrene (b), perylene (c), and benzo[k]fluoranthene (d) in the absence (solid line) and the presence of 50 ng l^{-1} other 12 PAHs (dotted line) obtained by the concentration to admicelles composing of 10 mg alumina. The values of $\Delta\lambda$ are 35 nm for benzo[a]pyrene, 45 nm for pyrene, 29 nm for perylene, and 98 nm for benzo[k]fluoranthene. Arrows indicate detection wavelengths.

of benzo[k]fluoranthene on CTAC-silica gel admicelles was only approximately a one-eighth of the intensity on SDS-alumina admicelles. He et al. [36] reported that SDS micelles sensitized synchronous fluorescence intensity of PAHs rather than other micelles including CTAB micelles. It can be assumed that SDS-admicelles sensitize the fluorescence intensity of PAHs rather than CTAC-admicelles do. Difference in the light transmittance of the solid materials may be another reason for the different fluorescence intensity. Therefore, the use of CTAC-silica gel admicelle was eliminated in the present study.

3.2. Selective measurement in SFS mode

In the conventional scan mode, benzo[a]pyrene gave a peak at 367 nm in the excitation spectrum (solid line in Fig. 4a). However, huge background signals also appeared because of light scattering on admicelle layer. Additionally, background signal increased in the presence of other PAHs (broken line in Fig. 4a). The signals of pyrene, perylene, and benzo[k]fluoranthene were also indistinct and thus could not be used for the respective determination (Fig. 4b–d). In contrast, simple and sharp peaks of benzo[a]pyrene were obtained in the SFS measurement (solid line in Fig. 5a). The wavelength interval between excitation and emission ($\Delta\lambda$) for the highest ratio of signal intensity to background was 35 nm. The attempt of the SFS measurement was performed by setting $\Delta\lambda$ in 1 nm intervals

around the optimal values (19 and 43 nm) in the aqueous solution of normal SDS micelles [36]. The smaller $\Delta\lambda$ was not available due to the significant background owing to the light scattering on the particulate admicelles. The value of $\Delta\lambda$ was slightly different from that ($\Delta\lambda = 43$ nm [36]) in the normal SDS micelles, suggesting difference in the property as extracting media. In the presence of other 12 PAHs, some additional peaks also appeared in the spectrum (broken line in Fig. 5a). However, only benzo[a]pyrene gave a peak at 367 nm in the excitation spectrum. Therefore, benzo[a]pyrene can be selectively determined based on the fluorescence intensity at 367 nm. The SFS measurement was also useful for the determination of pyrene, perylene, and benzo[k]fluoranthene (Fig. 5b–d). The optimum $\Delta\lambda$ (nm) values for obtaining the maximum ratio of signal to interferences were 45 for pyrene, 29 for perylene, and 98 for benzo[k]fluoranthene. In the presence of other PAHs, they were selectively determined based on the signal intensities at 337, 411, and 308 nm, respectively.

Linear correlations between PAH concentration and fluorescence intensity were obtained in the concentration range of 1–40 ng l^{-1} for benzo[a]pyrene, benzo[k]fluoranthene, and perylene. The concentration range on the linear calibration was 10–150 ng l^{-1} for pyrene. The standard deviation in the determination of 10 ng l^{-1} of benzo[a]pyrene was ca. 10%. The detection limits (S/N = 3) of benzo[a]pyrene, benzo[k]fluoranthene, and perylene were 0.3 ng l^{-1}, while that of pyrene was 1 ng l^{-1}. They are

Table 1
Determination of four PAHs in water samples.

Sample	Exp. no.		PAH (ng l^{-1})		Exp. no.		PAH (ng l^{-1})	
			Added	Found			Added	Found
Milli-Q water	1	B[a]P	0	2 ± 1	3	B[a]P	0	2 ± 1
		B[k]F	0	<0.5		B[k]F	0	<1
		Perylene	0	<0.5		Perylene	0	2 ± 1
		Pyrene	0	~3		Pyrene	0	~3
	2	B[a]P	10	11 ± 1	4	B[a]P	10	13 ± 1
		B[k]F	10	10 ± 1		B[k]F	5	7 ± 3
		Perylene	10	12 ± 2		Perylene	10	10 ± 2
		Pyrene	10	12 ± 1		Pyrene	50	67 ± 5
					5	B[a]P	20	23 ± 2
						B[k]F	10	12 ± 2
						Perylene	20	19 ± 1
						Pyrene	100	120 ± 18
Groundwater	6	B[a]P	0	~1	8	B[a]P	0	2 ± 1
		B[k]F	0	<1		B[k]F	0	2 ± 1
		Perylene	0	~1		Perylene	0	~1
		Pyrene	0	~2		Pyrene	0	13 ± 5
	7	B[a]P	10	11 ± 1	9	B[a]P	10	13 ± 2
		B[k]F	10	9 ± 1		B[k]F	5	7 ± 2
		Perylene	10	13 ± 1		Perylene	10	10 ± 1
		Pyrene	10	13 ± 2		Pyrene	50	62 ± 4
					10	B[a]P	20	21 ± 2
						B[k]F	10	12 ± 2
						Perylene	20	21 ± 3
						Pyrene	100	111 ± 8
Rainwater	11	B[a]P	0	3 ± 1	13	B[a]P	0	3 ± 1
		B[k]F	0	2 ± 1		B[k]F	0	3 ± 1
		Perylene	0	2 ± 1		Perylene	0	2 ± 1
		Pyrene	0	10 ± 2		Pyrene	0	11 ± 8
	12	B[a]P	10	12 ± 1	14	B[a]P	10	11 ± 2
		B[k]F	10	11 ± 1		B[k]F	5	8 ± 1
		Perylene	10	13 ± 1		Perylene	10	9 ± 1
		Pyrene	10	19 ± 1		Pyrene	50	49 ± 11
					15	B[a]P	20	16 ± 3
						B[k]F	10	11 ± 2
						Perylene	20	16 ± 3
						Pyrene	100	71 ± 16

Average of 5 experiments. B[a]P: benzo[a]pyrene, B[k]F: benzo[k]fluoranthene. Nos. 1, 2, 6, 7, 11, 12: 10 ng l^{-1} each of other 9 PAHs added. Nos. 3–5, 8–10, 13–15: 50 ng l^{-1} each of other 9 PAHs added. Other 9 PAHs: anthracene, benzo[a]anthracene, benzo[e]pyrene, chrysene, coronene, fluoranthene, phenanthrene, naphtharene, and naphtha[2,3a]pyrene.

2–3 orders of magnitude lower than the detection limits in normal aqueous micellar solutions (0.0055 µg l^{-1} [33], 24.9 µg l^{-1} [34], 0.34 µg l^{-1} [36] for perylene and 0.14–2.4 µg l^{-1} [33,34,36] for other PAHs).

3.3. Application to water samples

Table 1 summarizes the analytical results of four PAHs in some water samples. Benzo[a]pyrene, benzo[k]fluoranthene, and perylene spiked were selectively determined with very small interference of other PAHs. Because of selective detection by SFS measurement, only small signal from other PAHs were observed in the determination of the objective PAHs. On the other hand, the determination of pyrene was somewhat interfered by coexisting PAHs, probably due to the spectral overlapping of pyrene with other PAHs. Relatively lower sensitivity of pyrene than other PAHs is another reason for the interference. Slightly lower value in the analysis of rainwater may be due to the adsorption of PAHs on some dissolved or colloidal materials including in rainwater.

The present method can be compared with the front-face fluorometry on solid sorbents such as alkylated silica gel [38], Sephadex G-25 gel [39], or commercial C$_{18}$ Empore^{TM} membrane disk [40,41]. The combination of solid-phase extraction with synchronous fluorometric analysis enables the determination of PAHs at µg l^{-1}-level without chromatographic separation. However, considerable time (e.g. 60 min [41]) is required for the equilibrium extraction to the

solid-phase materials. This is explained by slow mass transfer from bulk aqueous solution to hydrophobic solid materials having low water-permeability. Slow diffusion in gel matrices may be another reason for slow collection. Additionally, the use of large amount of solid materials or thick extraction disks can reduce the excitation and the emission light strengths. In the present method, PAHs in large volume of water can rapidly be collected into very small amount of admicelles having high water-permeability and extraction ability. Because of the combination of highly efficient concentration with the selection of suitable media for sensitive SFS analysis, the sensitivity of the present method is two or three orders of magnitude greater than those of other methods including micellar sensitized SFS analysis in the bulk aqueous solution (µg l^{-1}-levels [33,34,36]). On the other hand, very small amount of organic components were also highly concentrated and thus significantly interfered to the detection of fluorescent signals. For example, the recoveries of PAHs were lowered in the application to highly contaminated rainwater samples that had been collected at the time of just beginning or from the surfaces of road. The reduced recoveries of PAHs may be ascribed to dissolved materials or fine particles that could not be removed with membrane filters. In the application to river water, the signal intensities of PAHs were significantly lowered. The admicelles were colorized to light blown. Humic substances containing in river water tend to predominantly sorb onto SDS-alumina admicelles [42]. Such organic components can reduce the light intensity for the excitation of PAHs and the emission to be detected. The use of effective sample pretreatment

method will extend the applicability of the present method to the analysis of wide range of environmental water.

4. Conclusions

The combination of admicelle-mediated extraction with synchronous fluorescence scan was a powerful technique for the determination of ng l^{-1}-levels of PAHs without chromatographic separation. Four PAHs in water samples were quite rapidly collected to highly water-permeable SDS-alumina admicelles. Because of extreme extraction ability of the admicelles, PAHs were highly concentrated into very small quantities of admicelles. Additionally, SDS-alumina admicelles were suitable for the sensitive fluorescence measurement of PAHs. Further studies about surfactants and solid sorbents as well as solution conditions will be valuable for improving the sensitivity and selectivity in the analysis of PAHs.

Acknowledgements

References

[1] G.A. Jungclaus, L.M. Games, R.A. Hites, Anal. Chem. 48 (1976) 1894.
[2] U.S. EPA method 610, SW-846, Ch4.3.3, Electronic version, September 1, 1986.
[3] V. Leoni, G. Puccetti, A. Grella, J. Chromatogr. 106 (1975) 119.
[4] R.K. Symons, I. Crick, Anal. Chim. Acta 151 (1983) 237.
[5] E. Manoli, C. Samara, Trac-Trends Anal. Chem. 18 (1999) 417.
[6] M. Hiraide, M.H. Soroundin, H. Kawaguchi, Anal. Sci. 10 (1994) 125.
[7] M. Hiraide, Y. Ohta, H. Kawaguchi, Fresenus' J. Anal. Chem. 350 (1994) 648.
[8] M. Hiraide, J. Iwasawa, H. Kawaguchi, Talanta 44 (1997) 231.
[9] T. Saitoh, Y. Nakayama, M. Hiraide, J. Chromatogr. A 972 (2002) 205.
[10] T. Saitoh, S. Matsushima, M. Hiraide, J. Chromatogr. A 1040 (2004) 185.
[11] T. Saitoh, S. Matsushima, M. Hiraide, J. Chromatogr. A 1069 (2005) 271.
[12] T. Saitoh, T. Kondo, M. Hiraide, Bull. Chem. Soc. Jpn. 79 (2006) 748.
[13] T. Saitoh, T. Kondo, M. Hiraide, J. Chromatogr. A 1164 (2007) 40.
[14] H. Matsumiya, Y. Yatsuya, M. Hiraide, Anal. Chim. Acta 588 (2007) 82.
[15] K.T. Valsaraj, Sep. Sci. Technol. 24 (1989) 1191.
[16] K.T. Valsaraj, Sep. Sci. Technol. 27 (1992) 1633.
[17] L.K. Koopal, E.M. Lee, M.R. Böhmer, J. Colloid Interface Sci. 170 (1995) 85.
[18] P. Somasundaran, L. Huang, Adv. Colloid Interface Sci. 88 (2000) 179.
[19] T. Behrends, R. Herrmann, Colloid Surf. A: Physicochem. Eng. Aspects 162 (2000) 15.
[20] K.R. Reid, L.J. Kennedy, E.W. Crick, E.D. Conte, J. Chromatogr. A 975 (2002) 135.
[21] S. Rubio, D. Pérez-Bendito, Trac-Trends Anal. Chem. 22 (2003) 470.
[22] F. Merino, S. Rubio, D. Pérez-Bendito, Anal. Chem. 75 (2003) 6799.
[23] F. Aloulou, S. Boufi, D. Beneventi, J. Colloid Interface Sci. 280 (2004) 350.
[24] Q. Zhao, R.T. Philpott, T.D. Oakes, E.D. Conte, Analyst 130 (2005) 750.
[25] F. Merino, S. Rubio, D. Pérez-Bendito, J. Sep. Sci. 28 (2005) 1613.
[26] M. Cantero, S. Rubio, D. Pérez-Bendito, J. Chromatogr. A 1067 (2005) 161.
[27] A. García-Prieto, L. Lunar, S. Rubio, D. Pérez-Bendito, Analyst 131 (2006) 407.
[28] A. Moral, M.D. Sicilia, S. Rubio, D. Pérez-Bendito, Anal. Chim. Acta 569 (2006) 132.
[29] D. Patra, A.K. Mishra, Trac-Trends Anal. Chem. 21 (2002) 787.
[30] T. Vodinh, R.B. Gammage, P.R. Martinez, Anal. Chem. 53 (1981) 253.
[31] J.L. Vilchez, M. Delolmo, R. Avidad, L.F. Capitanvallvey, Analyst 119 (1994) 1211.
[32] T. Vo-Dinh, J. Fetzer, A.D. Campiglia, Talanta 47 (1998) 943.
[33] D. Patra, A.K. Mishra, Talanta 55 (2001) 143.
[34] M.A. Lage-Yusty, J. López-González, J. Simal-Lozano, Anal. Sci. 21 (2005) 1203.
[35] J.H. Ayala, A.M. Afonso, V. Gonzalez, Talanta 44 (1997) 257.
[36] L.-F. He, D.-L. Lin, Y.-Q. Li, Anal. Sci. 21 (2005) 641.
[37] T. Saitoh, K. Taguchi, M. Hiraide, Anal. Chim. Acta 454 (2002) 203.
[38] J.W. Carr, J.M. Harris, Anal. Chem. 60 (1988) 698.
[39] L.F. Capitan-Vallvey, M.D. Fernandez, I. de Orbe, J.L. Vilchez, R. Avidad, Analyst 119 (1994) 351.
[40] E.J. Poziomek, D. Eastwood, R.L. Lidberg, G. Gibson, Anal. Lett. 24 (1991) 1913.
[41] M. Algarra, V. Jiménez, P.F. de Violet, M. Lamotte, Anal. Bioanal. Chem. 182 (2005) 1103.
[42] M. Hiraide, A. Ishikawa, Anal. Sci. 18 (2002) 199.

Identification of reaction compounds in micrometric layers from gothic paintings using combined SR-XRD and SR-FTIR

Nati Salvadó [a,*], Salvador Butí [a], James Nicholson [b], Hermann Emerich [c], Ana Labrador [d], Trinitat Pradell [e]

[a] Dpt. d'Enginyeria Química, EPSEVG, Universitat Politècnica de Catalunya, Av. Víctor Balaguer s/n, 08800 Vilanova i la Geltrú, Barcelona, Spain
[b] STFC, Daresbury Laboratory, Kecwick Lane, Warrington WA4 4AD, UK
[c] BM01-ESRF, BP 220, 38043 Grenoble Cedex, France
[d] LLS, BM16-ESRF, BP 220, 38043 Grenoble Cedex, France
[e] Dpt. Física i Enginyeria Nuclear, ESAB, Universitat Politècnica de Catalunya, ESAB, Campus del Baix Llobregat, Avda. del Canal Olímpic 15, 08860 Castelldefels, Barcelona, Spain

ARTICLE INFO

ABSTRACT

Synchrotron radiation X-ray diffraction (μ-SR-XRD) and Fourier transform infrared spectroscopy (μ-SR-FTIR) are used in the non-destructive identification of reaction and aging compounds from micrometric ancient painting layers. The combination of the micrometer size and non-destructive nature of the techniques together with the high resolution and brilliance of the synchrotron radiation has proved to be a procedure most advantageous for the study of reaction, aging and degradation processes. Copper, lead and calcium carboxylates and oxalates are determined in the chromatic, preparation and alteration layers from 15th century egg tempera and oil paintings. Their nature and crystallinity have been assessed. Some hypothesis about the mechanisms of development of both carboxylates and oxalates are presented.

1. Introduction

The identification of aged binders [1] and of the reaction compounds formed by the interaction between the binding media and the pigments is a subject of the highest interest in the chemical stability and conservation of ancient paintings. However, the identification of pigments, binders, reaction and alteration compounds presents great technical difficulties since most of them appear in extremely small amounts. In addition most of these substances lack a good crystallographic order since some of them are soluble in the binders and the solid state reactions and aging processes involved are kinetically controlled. The art works studied correspond to 15th century Catalan Gothic paintings. In this period, oil-based binders started being used and coexisted with the preceding tempera techniques that used egg yolk and animal glue. Sometimes different binders were used in the same paint and due to the micrometer size layered structure of the paint this makes the study more interesting but at the same time more difficult.

The samples extracted from an artwork are necessarily small; a few hundred micrometers surface area, which gives a measurable volume of only 10^{-3} mm^3. The identification of the organic fraction when present in very small proportion can be obtained by chemical separation techniques after a process of dissolution of the sample [2,3]. However, using this methodology information the exact location of the different compounds is lost. The use of spatially resolved low level detection non-destructive techniques is a good option, although the sensitivity is moderate. Thus a special and careful preparation of the samples is required. Analytical techniques sensitive down to the 10 μm level must be used. High resolution X-ray diffraction (XRD) and Fourier transform infrared spectroscopy (FTIR) techniques are non-destructive and a good combination for the identification of compounds present in the painting layers. Synchrotron radiation has a clear advantage with respect to conventional radiation sources because it has a high brilliance, low noise and tuneable monochromatic and highly collimated light with footprints down to the micrometers size [4–6]. In this study we demonstrate the capability and potentiality of combined μ-SR-FTIR and μ-SR-XRD techniques in the detection and identification of those compounds in micrometric painting layers. When μ-SR-FTIR is used, separation of the compounds can only be achieved by first a previous mechanical separation of

layers under the stereomicroscope, followed by the thinning out of small fragments taken from each layer in a diamond cell. When the technique employed is μ-SR-XRD thin cross-sections are prepared and measurement points are focused with a video microscope. The combination of μ-FTIR and μ-XRD allows for the identification of compounds and information to be gathered on the distribution of these highly heterogeneous samples.

The drying oils used in the 15th century are either linseed or walnut oils. They include two poly-unsaturated fatty acids containing 18 carbon atoms, linoleic and linolenic acids, as well as, the mono-unsaturated oleic acid. They contain also about 8% of saturated acids, palmitic and stearic (C16 and C18 straight-chain monocarboxylic fatty acids) [7–9]. The drying and aging process results in a polymerization by uptake of oxygen that free fatty acids may be produced [2,7,8,10–12].

Dried egg yolk contains two thirds of lipids and one third of proteins, resulting in different drying and aging processes from those that work with oil. The lipids are made up of one third phospholipids and two thirds triglycerides. These triglycerides contain two thirds unsaturated acids (∼60% oleic, ∼25% linoleic) and one third saturated acids, such as stearic and palmitic acids. Aging of the lipids in the egg yolk is the same as in the drying oil; an oxidative polymerization and, consequently, similar reaction compounds are formed [7,13]. Consequently, drying and aging will produce similar free fatty acids in the egg yolk and in the drying oil.

The simultaneous presence of free fatty acids in the binders and metals, such as lead, calcium, copper or tin from the pigments and ground layers makes the formation of metal soaps predictable. In fact they are part of the drying process of the paint and therefore, they are always expected to form. In some cases those compounds affect the artwork to a large extend (formation of protrusions), and it is in these cases that they have been identified [10,11,14–16]. However, in most of the cases, and in particular, when they are not aggregated, their presence is hard to detect [17]. In this study we identify the lead, calcium and copper carboxylates formed in different paint and ground layers from both 15th century paintings both with egg yolk and oil-based binders. The presence of metal carboxylates has been reported in other studies, in particular in oil painting [2,10,14–16,18], in this study they have been non-destructively identified and isolated in ancient egg yolk paintings. Moreover, it is the first time that these compounds have been identified by means of micro-XRD directly on ancient painting layers.

Oxalates are a type of salts usually found on the surfaces of artworks [18–20]. However, their relationship to the degradation/weathering processes, although suspected, is still unknown. In this study, we determine the nature of the oxalates formed, in particular of lead, calcium and copper oxalates and their distribution in the different chromatic, preparation and alteration layers. This is the first step necessary in order to ascertain origin of their oxalates and to establish the mechanisms responsible for their development and to relate their presence to specific degradation processes.

2. Experimental

2.1. Samples and reference materials

The samples analysed belong to altarpieces painted by the most important masters of the Crown of Aragó: *Sant Vicenç de Menàrguens* dated 1438–1440 by Bernat Martorell (1400?–1452), *Sant Vicenç de Sarrià* dated between 1455 and 1460 and *El Conestable* dated 1464 both by Jaume Huguet (141?–1492), *La Mare de Déu dels Consellers* dated 1443–1445 by Lluís Dalmau's (1428–1461) and *L'aparició de la Mare de Déu a Sant Francesc a la Porciúncula* by Mestre de la Porciúncula dated around 1450. They are on exhibit at the Museu Nacional d'Art de Catalunya in Barcelona [21]. Finally, the

Fig. 1. Detail of the scene of the Crucifixion in the altarpiece of the Conestable from the chapel of Saint Àgata in Barcelona by the painter Jaume Huguet, 15th century. Photo: Carles Aymerich, Centre de Restauració de Bens Mobles de Catalunya (CRBMC).

altarpiece *El Conestable* dated 1464 by Jaume Huguet is placed in the chapel of Santa Àgata in Barcelona (Fig. 1).

The paints were applied over a ground preparation, mixing the pigments with an organic binder, either egg yolk or animal glue and water (tempera technique) or a drying oil (oil technique). The ground preparation was made of several layers of gypsum mixed with animal glue and applied over the wood surface. The paintings are formed by a sequence of layers including a ground layer (few millimetres), several paint layers (between 10 and 100 μm thick each) and superficial layers of alteration of varnishes and contamination (less than 2 μm thick).

Organic binders and pigments react and age, therefore some naturally aged materials are also analysed. Egg yolk (chicken), drying oils (linseed oil) and some pigments mixed with the binders applied over a glass slide and allowed to age naturally in the laboratory for at least 8–10 years are also studied.

The mixtures were prepared blending binding media with pigments or gypsum in a weight proportion of 25–30% binding media and applying it over a glass slide in layers of between 60 and 150 μm in thickness.

2.2. Specific sample preparation

The samples taken were small in size (surface area of a few hundred micrometers side), from which two preparations are made, fresh-fractured fragments and polished cross-sections. For

the cross-sections, the samples are embedded in polyester resin polymerized by a peroxo organic catalyser under low humidity conditions. After polymerization, cross-sections were obtained; a first cut with a diamond saw was afterwards polished with 1 μm size diamond paste and, then, the block cut again in a slice about 200 μm thick.

2.3. Analytical techniques

μ-SR-XRD is a good solution to resolve complex mixtures of crystalline compounds, and the small amount of each compound makes the brilliance and collimation of the synchrotron beam fundamental for their study [5,22,23]. However, since the size of these compounds is often comparable to the size of the layers themselves, the use of a microbeam is only adequate if the beam size is not too small. A beam size of about 10–50 μm is an adequate compromise between the typical size of crystals and the thickness of the layers. A smaller beam may lead to a spotty single crystal-like X-ray diffraction pattern, dominated by only some of the compounds, and therefore a full identification of the whole layer will not be visible. If bigger, it is not possible to separate the compounds present in the different layers. A map of compounds was obtained from cross-sections of the layered paintings by using a XYZ motorized goniometer head as sample support in combination with a video microscope with a motorized zoom 12×. For this, beam footprints of 30 μm were used. XRD patterns were obtained at station BM16 of the European Synchrotron Radiation Facility (ESRF) in transmission geometry, 12.7 keV X-rays (0.98 Å) and an ADSC Q210r CCD detector, pixel size 102 μm. The angular range is limited by the size of the detector and if organic and inorganic compounds are present at the same time, the experimental conditions adequate for their identification are different. Therefore, different angular ranges have been measured. For adequate separation and unambiguous identification of the inorganic compounds high angular

Table 1
Wavenumbers of the characteristics bands of egg yolk and lead carboxylates (Figs. 2 and 3).

Egg yolk	
3286 cm^{-1}	ν(N–H)
3069 cm^{-1}	NH bending overtone
3008 cm^{-1}	ν(CH), olefinic C=C–H
2955, 2923, 2853 cm^{-1}	ν(CH) methylene and methyls groups
1744 cm^{-1}	ν(C=O) ester linkage
1710 cm^{-1}	ν(C=O) free fatty acids
1656 cm^{-1}	ν(C=O) amide I
1542 cm^{-1}	δ(N–H) and ν(C–N) amide II
1465 cm^{-1}	δ(CH) methylene and methyls groups
1233 cm^{-1}	νC–O in ester
1170 cm^{-1}	νC–O
721 cm^{-1}	CH$_2$ rocking
Lead carboxylates	
2955, 2919, 2849 cm^{-1}	ν(CH) methylene and methyls groups
1540, 1513 cm^{-1}	ν_{as}(COO$^-$)
1472, 1462 cm^{-1}	δ(CH$_2$)
1419 cm^{-1}	ν(COO$^-$)
1350–1180 cm^{-1}	Vibrations from hydrocarbon chains
930 cm^{-1}	
730 cm^{-1}	
719 cm^{-1}	
706 cm^{-1}	

resolution SR-XRD measurements were also performed at station BM01 (ESRF). For these measurements, small fragments of the sample were put in a glass capillary to allow spinning of the sample in a two circle diffractometer with three line detectors 5° measuring angle. Measurements were taken in transmission geometry at 24.9 keV (0.50 Å). A 2θ range of 25° was collected during 15 h.

μ-SR-FTIR analysis is also performed to extract chemical and structural information on the different compounds present. The accurate separation of the different compounds is necessary to obtain unambiguous identification even for the compounds present in very small amounts. Separation of the different compounds is accomplished thanks to the small spot of 10 μm × 10 μm used and the high quality spectra obtained measuring one of the sides of pressed small fresh-fractured fragments extracted from the different paint and ground layers of the samples in a diamond cell [4]. μ-SR-FTIR measurements were performed at station 11.1 of the Synchrotron Radiation Source (SRS Daresbury Laboratory). The NEXUS FTIR Spectrophotometer is equipped with a Nicolet Continuμm microscope, MCT detector, measuring range 4000–700 cm^{-1}. Spectra were obtained in transmission mode. For each measurement, 128 scans were recorded with a resolution of 4 cm^{-1}.

Fig. 2. μ-SR-FTIR spectra corresponding to (a) egg yolk naturally aged for 8 years; (b) proteins partially separated from the egg yolk naturally aged for 8 years; (c) lipids separated from the egg yolk naturally aged for 8 years; (d) lead carboxylates obtained from a mixture of lead white and egg yolk naturally aged for 8 years.
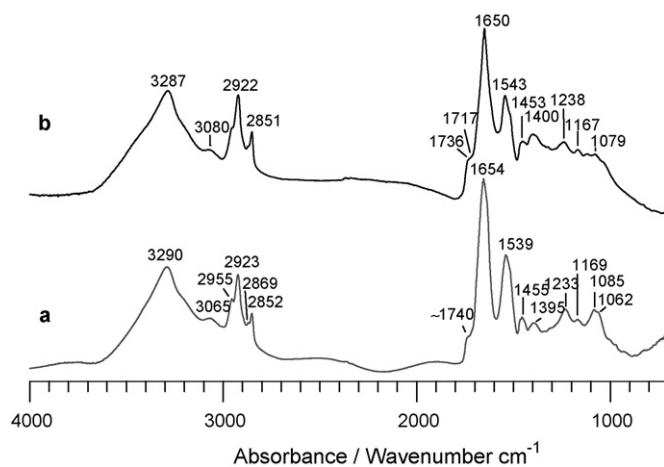
Fig. 3. μ-SR-FTIR spectra corresponding to (a) proteins partially separated from an egg yolk naturally aged for 8 years (b) proteins partially separated from a paint layer from the altarpiece *Sant Vicenç de Sarrià* which is related to egg yolk.

Finally, as the pigments appear normally as powders, the analyses also include Optical Microscopy (OM) and Scanning Electron Microscopy (SEM), Cambridge S-120, with elemental analysis using the PCXA LINK EDS (25 keV, 1 nA) microanalyzer in order to obtain information of the composition, size distribution and homogeneity of the particles.

3. Results and discussion

The paintings studied belong to the same historical period; they were painted within a period of 30 years, and all share, broadly speaking, the same painting technique: the paints are applied in several layers over a gypsum based ground surface. The diversity of binders and pigments used, as well as, all their possible combinations make analysis of these paintings particularly valuable for the study of the differences and sim-

ilarities in the aging process between oil and egg yolk based paintings.

In these samples which are small in size (a few hundreds of micrometers), structured in thin layers (of some tens of micrometers) and of heterogeneous composition, the identification of the compounds is complex. The use of various complementary techniques such as OM, SEM, μ-SR-FTIR and μ-SR-XRD and further comparison of the data with reference materials and naturally aged laboratory prepared samples allows us to obtain reliable conclusions. The strategy consists of extracting a micrometer size particle from the layer under study using a microscope and placing it in a diamond cell and applying pressure so that it is evenly spread over the surface of the diamond cell. Focusing on 10 μm spot size at different points compounds can be separated. μ-SR-FTIR spectra are shown in Fig. 2 obtained from reference samples of egg yolk and a mixture of egg yolk and lead white both naturally aged in the
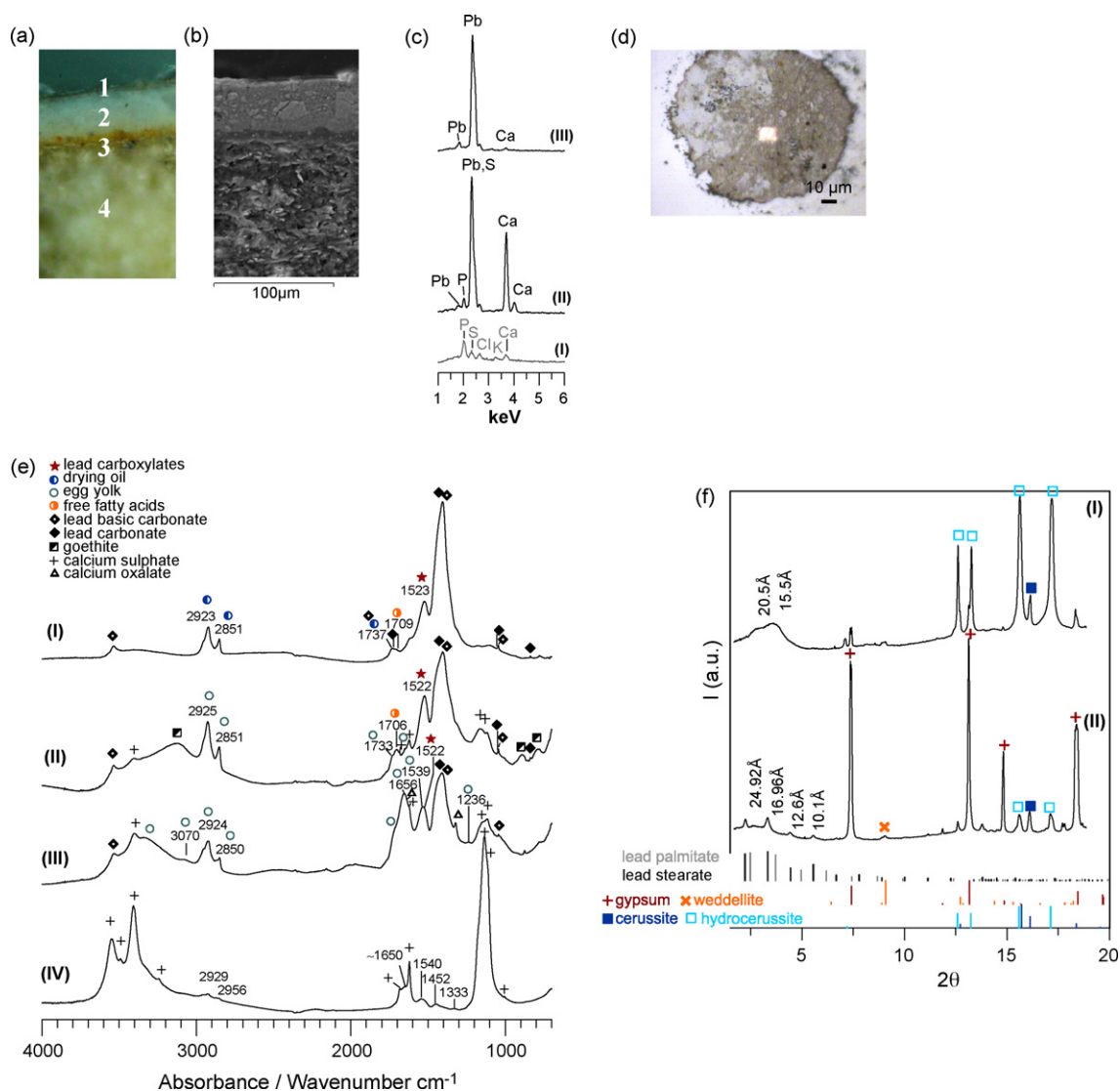
Fig. 4. (a) Optical image and (b) SEM image from polished cross-section of a white sample from *L'aparició de la Mare de Déu a Sant Francesc a la Porciúncula*. (1) Superficial layer, (2) white paint layer with drying oil, (3) ocher paint layer with egg yolk and (4) ground layer. (c) SEM-EDS spectra, 25 kV and 1 nA, corresponding to (I) reference egg yolk, (II) layer 3 and (III) layer 2. Phosphorous are identified in spectrum I and II related to egg yolk. (d) Optical image of the material from layers 3 and 4 spread over the diamond cell, as well as, the 10 μm spot used for the analyses. (e) μ-SR-FTIR spectra corresponding to (I) layer 2, (II/III) from different points on layer 3 and (IV) layer 4. (f) μ-SR-XRD patterns corresponding to (I) layer 2 and (II) layer 3. Lead white (JCPDF patterns from cerussite and hydrocerussite, 13-0131 and 70-2052, respectively) and lead carboxylates are identified in both layers (diffraction patterns from lead stearate and palmitate are obtained from Ref. [31]). Layer 2 shows the IR bands corresponding to drying oil. Layer 3 shows egg yolk, goethite and also gypsum and calcium oxalates, weddellite, corresponding to the ground layer (JCPDF patterns 74-1905 and 75-1314, respectively). (For interpretation of the references to color in this figure legend, the reader is referred to the web version of the article.)

laboratory. μ-SR-FTIR spectra of the different components, proteins, lipids and carboxylates, are obtained thanks to the high focusing capability and brilliance of the synchrotron beam. In Table 1 wavenumbers of the characteristic bands of egg yolk and lead carboxylates are shown. Fig. 3 shows a comparison between the μ-SR-FTIR corresponding to the proteins component separated from the naturally aged egg yolk and from a paint sample. When the different parts of a layer of paint from an original sample are focused on, besides to determine carboxylates, areas where mostly proteins are found are also isolated. A shoulder at about 1740 cm^{-1} which is related to the lipids is always found coexisting with the proteins. The simultaneous presence of proteins and lipids combined with the presence of phosphorous (determined by SEM-EDX) points toward the use of egg yolk. Conversely, the presence of lipids and absence of proteins indicates the use of a drying oil.

Five altarpieces were selected that cover both egg tempera and oil techniques. *Sant Vicenç de Menàrguens* by Bernat Martorell, is painted with egg tempera, *Sant Vicenç de Sarrià* and *El Conestable* by Jaume Huguet, painted with egg tempera with the exception of the green pigment which is mixed with a linseed oil, *L'aparició de la Mare de Déu a Sant Francesc a la Porciúncula* by "Mestre de la Porciúncula" painted with a mixed egg tempera and oil technique (oil painting layer applied over an egg tempera layer, as shown in Fig. 4), and, finally, *Mare de Déu dels Consellers* by Lluís Dalmau painted with oil.

The paint samples are made up of a sequence of ground, chromatic and surface alteration layers. For each of these layers SEM-EDS and the corresponding μ-SR-FTIR spectra and μ-SR-XRD pattern were obtained. Fig. 4 shows OM and SEM image of a typical cross-section, an image of the material spread over the diamond cell, and the corresponding μ-SR-FTIR spectra and μ-SR-XRD pattern of a sample from a white area from *L'aparició de la Mare de Déu a Sant Francesc a la Porciúncula*. The ground layer (>500 μm thick) contains gypsum (CaSO$_4$·2H$_2$O), protein related to animal glue and some calcium oxalates (calcium oxalate di-hydrate, CaC$_2$O$_4$·2H$_2$O, weddellite). The ochre paint layer (5–7 μm thick), contains, lead white (mixture of hydrocerussite, 2·PbCO$_3$·Pb(OH)$_2$ and cerussite, PbCO$_3$) , a small amount of iron oxides (FeOOH goethite) and some particles of yellow (lead stannate Pb$_2$SnO$_4$) and as binding media egg yolk containing free fatty acids and lead carboxylates. The white paint layer (50 μm thick) contains, lead white, with drying oil, free fatty acids and lead carboxylates. The finishing layer (2–5 μm thick) contains some carbon pigment particles (carbon black).

Fig. 5. At the bottom and in grey the μ-SR-FTIR spectrum obtained from a mixture of egg yolk and gypsum naturally aged for 8 years. (a) μ-SR-FTIR spectra and (b) μ-SR-XRD patterns corresponding to (I) contact area between ground layer (gypsum and animal glue) and red layer (cinnabar and egg yolk) from the altarpiece *Sant Vicenç de Menàrguens*. (II) Adhesive applied between ground layer and silver foil from the altarpiece *Sant Vicenç de Sarrià*. JPDF files for cinnabar, AgCl, Ag$_2$S, metal silver, calcium stearate and calcium palmitate are 80-2192, 85-1355, 71-0996, 4-0862, 5-0010, 5-0012, respectively. The rest of the reference files are the same as in Fig. 4. (For interpretation of the references to color in this figure legend, the reader is referred to the web version of the article.)

Fig. 6. Identification of lead carboxylates in oil paints. μ-SR-FTIR spectra corresponding to (a) yellow paint layer (lead tin oxide and drying oil) from the altarpiece *L'aparició de la Mare de Déu a Sant Francesc a la Porciúncula*. (b) White paint layer (lead white and drying oil) from the altarpiece *La Mare de Déu dels Consellers*. (c) Blue paint layer (azurite, lead white and drying oil) from the altarpiece *La Mare de Déu dels Consellers*. (For interpretation of the references to color in this figure legend, the reader is referred to the web version of the article.)
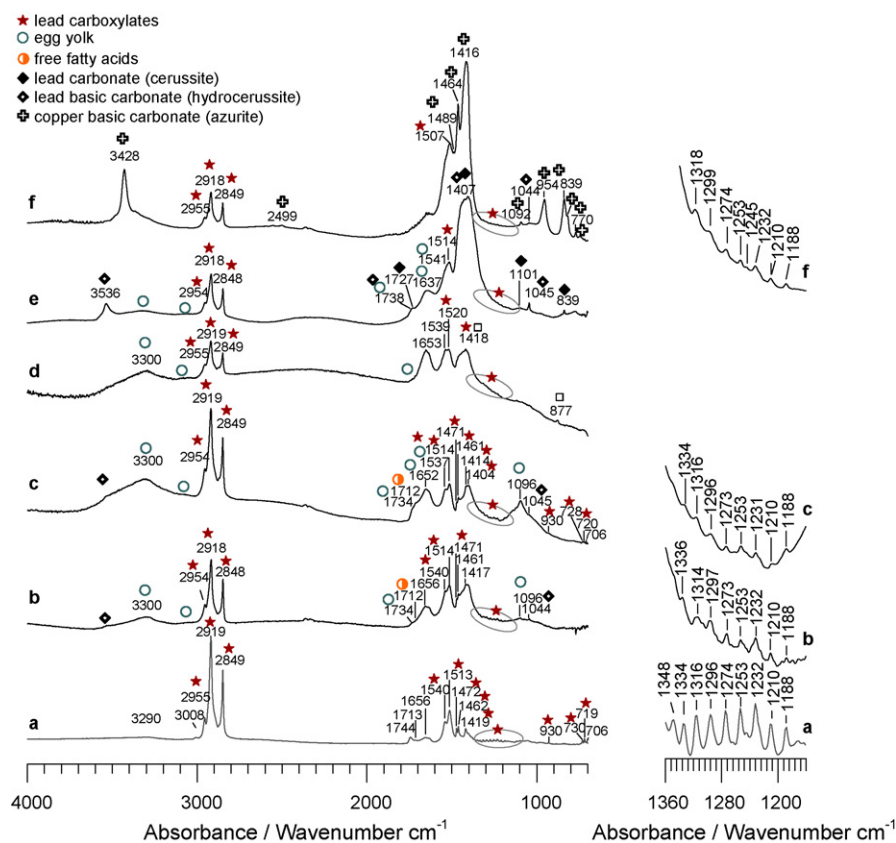
Fig. 7. Identification of lead carboxylates in egg yolk paints; the μ-SR-FTIR spectra, at the left, and an enlargement of the 1160–1360 cm^{-1} region at the right, corresponding to (a) lead carboxilates from a mixture of lead carbonate and egg yolk naturally aged for 8 years. (b) Black paint (carbon black, lead white and egg yolk). (c) Red paint (cinnabar, lead white and egg yolk). (d) Yellow paint (lead tin oxide and egg yolk). (e) White paint (lead carbonate/lead basic carbonate and egg yolk). (f) Blue paint (azurite, lead white and egg yolk). (b, c, e and f) Correspond to the altarpiece *Sant Vicenç de Menàrguens* and (d) to the altarpiece *Sant Vicenç de Sarrià*. (For interpretation of the references to color in this figure legend, the reader is referred to the web version of the article.)

Although this information is extremely interesting, and is being published elsewhere [22] in this paper we will concentrate on the identification of the reaction and degradation compounds formed by the reaction of the metals from the painting materials and the binders. However, the nature of the pigments is also very important and a summary of the compounds identified in the paint layers is presented herewith. The sample selection (46 samples) included painting layers containing all the colors: green, blue, red, red lake, yellow and white. Different greens are identified, a synthetic green following a recipe similar to *viridi salso* described by Theophilus in *De Diversis Artibus* [4,5,24], and formed by a complex mixture of copper compounds such as hydrated copper acetate and copper hydroxychlorides were used by Martorell and Huguet [4,5,24]. A synthetic green made of basic copper acetate x-hydrate was used by the other artists [22]. Two different blues are identified, both of mineral origin, azurite, $Cu_3(CO_3)_2(OH)_2$, and lapis lazuli, a rock formed by a mixture of sodium aluminosilicates containing SO_4^{2-} and S groups. This second pigment was used only by Dalmau [22]. The reds are mainly made of cinnabar, HgS, although iron oxides and minium, Pb_3O_4, are sometimes used. Red lakes of natural origin were also used either alone or mixed with white and/or with cinnabar. Two different yellows are identified, lead stannates of type I and II, Pb_2SnO_4 and $Pb_2(Sn,Si)_2O_6$, respectively. Type II is used only by Martorell. In all the altarpieces, a synthetic lead white, formed by a mixture of cerussite and hydrocerussite, $PbCO_3$ and $2PbCO_3 \cdot Pb(OH)_2$, respectively, is found.

This study is dedicated to the identification of the compounds produced by the reaction of the binding media and the other mate-rials present in the paint layers, as well as in the environment; that is the nature of the carboxylates and oxalates produced.

3.1. Identification of lead, calcium and copper carboxylates

The formation of free fatty acids in both drying oil and egg yolk is confirmed. The μ-SR-FTIR spectrum shows the C=O stretching band from a triglyceride ester linkage at about 1740 cm^{-1} and a carboxylic acid band related to the free fatty acids at about 1710 cm^{-1}. In the μ-SR-FTIR spectra corresponding to the drying oil and the egg yolk paint layers from the white sample from *L'aparició de la Mare de Déu a Sant Francesc a la Porciúncula* shown in Fig. 4e the bands appear at 1737 and 1710 cm^{-1} and 1733, 1706 cm^{-1}. Metal carboxylates are expected to form from the reaction of these free fatty acids with the metals from the paint; for instance, the μ-SR-FTIR spectra, Fig. 4e, corresponding to the paint layers show the presence of lead carboxylates formed from the reaction between the free fatty acids with the lead white in both drying oil and egg yolk. The important absorption band corresponding to C=O stretching is observed at about 1520 cm^{-1} for both drying oil and egg yolk. Fig. 4f shows the XRD patterns corresponding to both the white paint layer and ocher paint layer which contain lead white mixed with oil and egg yolk, respectively. The XRD spot size of 30 μm in thickness is thicker than the ochre paint layer. Therefore, the XRD measurement shown in Fig. 4f(II) includes part of the gypsum ground layer below, but excludes the white paint layer from above. The gypsum preparation layer is mixed with animal glue in all the paint samples studied and carboxylates have not been determined in the gypsum ground layer. The figure shows the pres-

ence of lead carboxylates in both the white paint layer and ochre paint layer containing oil and egg yolk, respectively. However, the carboxylates formed in the egg yolk are very crystalline and show all the reflections unlike the ones formed in the drying oil which show broad peaks corresponding to the two main reflections.

Calcium carboxylates are determined by μ-SR-FTIR but not always by μ-SR-XRD, due to the lack crystalline order. The μ-SR-FTIR spectra obtained from egg yolk mixed with calcium sulphate and aged 8 years in the laboratory and original 15th century samples are shown in Fig. 5a. In all the cases IR bands characteristic of a calcium carboxylate (2914, 2847, 1576, 1539, 1471, 720 cm^{-1}) are obtained. The absorption bands appearing in the region 3000–2800 cm^{-1} are due to CH stretching vibrations from methylene and terminal methyl groups from fatty acids chains; the doublet appearing around 1576 and 1540 cm^{-1} is related to COO$^-$ asymmetric stretching vibrations and the band at 720 cm^{-1} to CH$_2$ rocking band related to fatty acids. These absorption bands are similar to the bands given in the literature for both calcium stearate and palmitate [25–27]. Fig. 5a(I) and b(I) shows respectively μ-SR-FTIR and μ-SR-XRD data corresponding to the contact region between a red paint layer, consisting of cinnabar and egg yolk, and the ground layer, formed by gypsum and protein related to animal glue from the altarpiece *Sant Vicenç de Menàrguens*. Although the calcium carboxylates are clearly shown by FTIR, they are not detected by XRD. In the silver areas of the altarpiece from *Sant Vicenç de Sarrià*, the silver foil was adhered to the ground (gypsum and small amount of calcite, CaCO$_3$) with egg yolk. Fig. 5a(II) and b(II) shows the corresponding μ-SR-FTIR and μ-SR-XRD data from a silver sample from this altarpiece; calcium carboxylates are determined, but in this

case, by both μ-SR-FTIR and μ-SR-XRD. The large amount of egg yolk used to adhere the silver foil, could favour the crystallisation of the calcium carboxylates. The XRD-peak positions determined correspond neither to calcium stearate nor to calcium palmitate, but show intermediate values. These results indicate that calcium carboxylates are formed by the reaction of the fatty acids with the calcium from the ground layer. Neither the cinnabar (HgS) nor the silver atmospheric corrosion compounds (silver sulphides and chlorides) produces other metal carboxylates.

If lead is present in the painting layers, either in the form of lead white, PbCO$_3$/2PbCO$_3$·Pb(OH)$_2$, or yellow, either Pb$_2$SnO$_4$ or Pb(Si,Sn)O$_3$, lead carboxylates are always formed. μ-SR-FTIR data corresponding to lead containing painting layers mixed with both drying oil and egg yolk are shown in Figs. 6 and 7, respectively. The lead carboxylates are particularly difficult to isolate in the oil paints. Fig. 6 shows a single band at about 1520 cm^{-1} and Fig. 7 shows a doublet at about 1540 and 1513 cm^{-1}, these bands are related to a COO$^-$ asymmetric stretching vibration. The band at 1407 and 1419 cm^{-1}, Figs. 6 and 7, respectively, corresponds to a COO$^-$ symmetric stretching vibration. The doublet at 1472 and 1462 cm^{-1} corresponds to CH$_2$ bending absorption. Finally, a group of bands related to vibrations from hydrocarbon chains of the fatty acids are observed between 1350 and 1180 cm^{-1}. These results indicate the presence of lead stearates and palmitates [10,11,28–30] but also some bands that have intermediate values. Moreover, the results
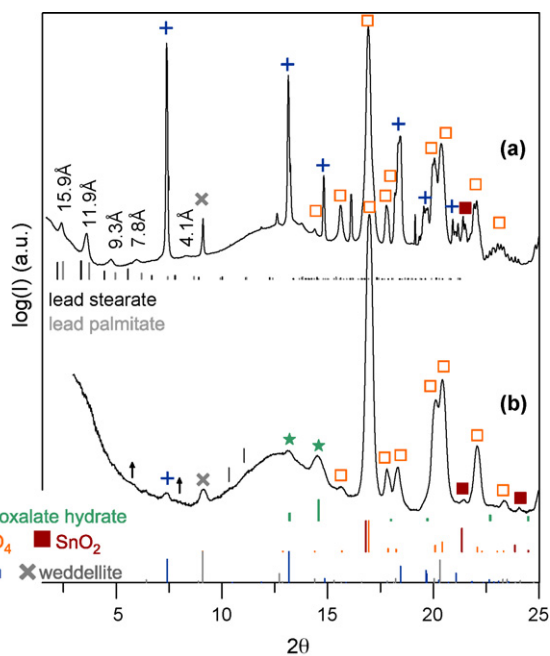
Fig. 8. μ-SR-XRD patterns from (a) yellow and (b) green paints from the altarpiece *Sant Vicenç de Sarrià*. The yellow paint is lead stannate (Pb$_2$SnO$_4$, JPDF file 29-0589) mixed with egg yolk. The green paint is made of a mixture of green (copper based pigment *veride salsum*) mixed with oil and yellow mixed with egg yolk. We can see that the green copper pigment is dissolved/decomposed into the binders, and only small traces of copper acetate hydrate (marked with an arrow) and Cu$_2$(OH)Cl$_3$, atacamite (marked with a thin line) may be identified. Broad diffraction peaks corresponding to the formation of copper oxalate hydrate (JCPDF file 48-1054) are clearly seen. The presence of some small amounts of cassiterite (SnO$_2$, JPDF file 77-0448) may be related to either the synthesis or to the degradation of the lead stannate. The presence of gypsum from the ground layer and weddellite is also shown in both paint layers. Same JCPDF files as in Fig. 4. (For interpretation of the references to color in this figure legend, the reader is referred to the web version of the article.)
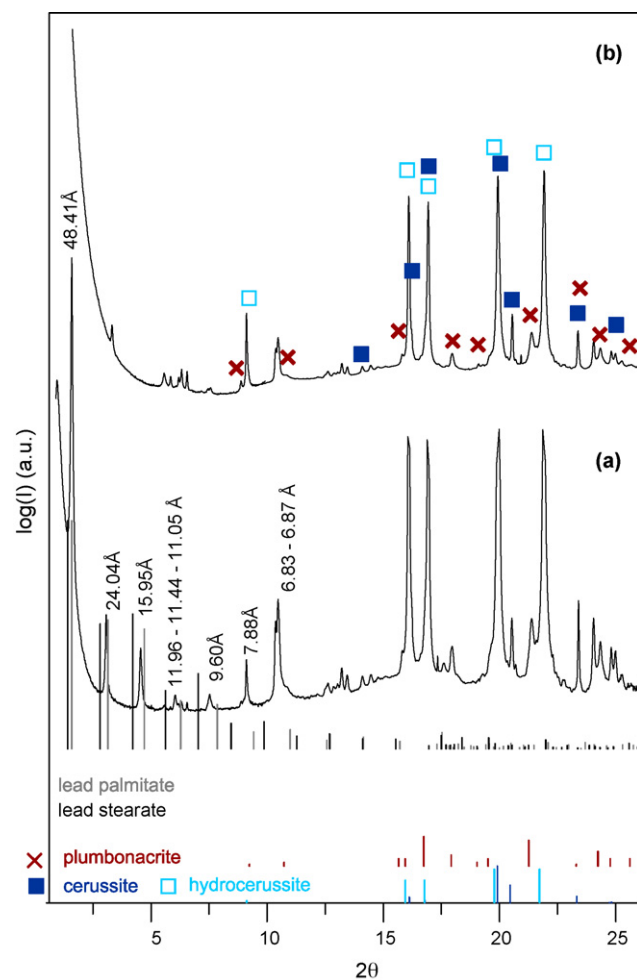

Fig. 9. μ-SR-XRD patterns from lead white (hydrocerussite/cerussite) mixed with either (a) egg yolk and (b) linseed oil naturally aged for 8 and 10 years, respectively. The formation of plumbonacrite (3·[2·PbCO$_3$·Pb(OH)$_2$]·PbO, JPDF file19-0680) and the crystallisation of a lead carboxylate are shown. Same reference patterns as in Fig. 4.

indicate that the crystallinity of the lead carboxylates is higher in the egg yolk than in the oil. Lead carboxylates are also determined in all the yellow paints studied, but they are more crystalline in the yellow paints mixed with egg yolk; Fig. 8a shows a yellow paint layer
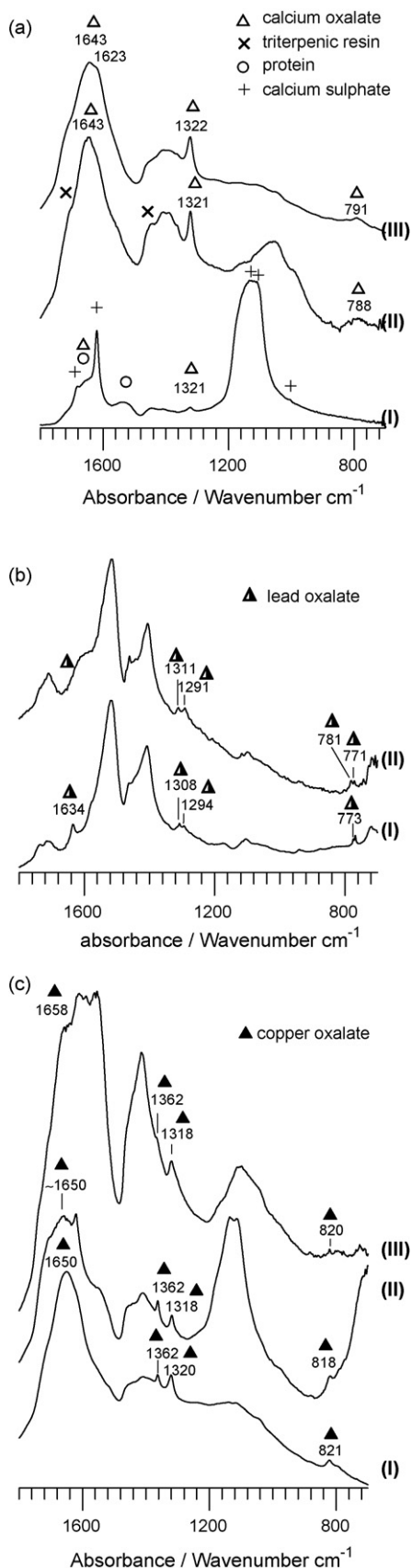
from the altarpiece *Sant Vicenç de Sarrià*. However, tin carboxylates are not determined in any case either by μ-SR-FTIR or μ-SR-XRD. In all the cases where the lead carboxylates are well crystallised (mixed with egg yolk) the XRD peak positions measured correspond neither to lead palmitate nor to lead stearate, but show intermediate values [31]. The XRD patterns from 8 years old linseed oil and egg yolk mixed with lead white are shown in Fig. 9. A well crystallised lead carboxylate with intermediate peak positions similarly to the ones determined in the ancient paintings is also formed in the egg yolk. The crystallinity of the lead carboxylates is also higher in the egg yolk than in the linseed oil in good agreement with the results obtained in the study of the ancient paintings. All these results suggest the formation of mixed lead carboxylates from the reaction of the egg yolk with the lead of the pigment in good agreement with the FTIR and XRD data corresponding to the lead carboxylates and also the results obtained for the calcium carboxylates.

The presence of plumbonacrite, $3[2PbCO_3 \cdot Pb(OH)_2] \cdot PbO$, formed by the degradation of hydrocerussite has been found in the aged oil and egg yolk mixed with lead white and is shown in Fig. 9, and also in some ancient lead white containing paint layers. Its presence suggests that the lead carboxylates may form from the reaction of the PbO with the free fatty acids. In the case of the yellow paints high resolution XRD has revealed the presence of SnO_2 and of PbO either from the decomposition or the synthesis of the yellow pigment. The reaction of these compounds with the fatty acids could lead to the formation of the corresponding carboxylates. However, although lead carboxylates are always formed, tin carboxylates have not been determined by either μ-SR-XRD or μ-SR-FTIR.

When a green copper based pigment is present, made either of copper acetates or basic copper chlorides, the formation of copper carboxylates is preferred even if lead based pigments are also present. These carboxylates have already been identified by μ-SR-FTIR in previous studies [4]; bands corresponding to both COO⁻ asymmetric and symmetric stretching appearing at about 1585 and 1411 cm⁻¹, respectively, and a CH_2 deformation vibration band appearing at 1470 cm⁻¹. However, the copper carboxylates are not crystalline, the corresponding XRD pattern show a large background but no crystalline carboxylates. Fig. 8b shows the corresponding XRD pattern of a green paint layer from the altarpiece *Sant Vicenç de Sarrià*. Due to the bluish color shown by the copper acetates, the green pigment is normally mixed with yellow. In Fig. 8 the XRD patterns obtained from the green (containing yellow) and the yellow paint layers from the altarpiece *Sant Vicenç de Sarrià* are compared. In the yellow paint, well crystallised lead carboxylates are determined, however in the green, an amorphous background and the presence of well crystallised copper oxalate hydrated is determined instead.

Copper acetate hydrate has the structure of a carboxylate and when mixed with the binders it partially decomposes and transforms. Some of the IR bands are lost and some split into two at the same time the diffraction patterns become more amorphous, although some big crystallites can survive. These transformations are somehow related to the formation of copper carboxylates and also of copper oxalates.

Fig. 10. Identification of oxalate salts in the paint layers. μ-SR-FT-IR spectra corresponding to (a) calcium oxalates in (I) ground layer and (II) superficial layer from the altarpiece *Sant Vicenç de Menàrguens* and (III) superficial layer from the altarpiece *El Conestable*. (b) Lead oxalates in yellow paints from the altarpiece (I) *L'aparició de la Mare de Déu a Sant Francesc a la Porciúncula* and (II) *La Mare de Déu dels Consellers*. (c) Copper oxalates in green paints from the altarpiece (I) *El Conestable*, (II) *L'aparició de la Mare de Déu a Sant Francesc a la Porciúncula* and (III) *Sant Vicenç de Sarrià*. (For interpretation of the references to color in this figure legend, the reader is referred to the web version of the article.)

The formation of copper carboxylates in the blue copper containing pigment azurite, $Cu_3(CO_3)_2(OH)_2$, is very limited. On the one hand because in most of the cases the azurite is mixed with lead white either with egg yolk or oil and then, the lead carboxylates are preferably formed. On the other hand, when azurite is not mixed with lead white the binder used is the animal glue and therefore carboxylates cannot form.

3.2. Identification of lead, calcium and copper oxalates

The formation of calcium oxalates has been proved to happen mainly close to the surface of the paint, and in particular when old varnishes are present (Fig. 10a(II) and (III)). However, they have also been observed in the paint layers and in the ground layer (Fig. 10a(I)) [5]. The infrared absorption bands related to calcium oxalate are seen; both COO asymmetric and symmetric stretching bands at 1643 and 1322 cm^{-1}, respectively. XRD data shows also the presence of calcium oxalate dihydrate, $CaC_2O_4 \cdot 2H_2O$, weddellite (as shown in Figs. 4f, 5b and 8), and, in few cases, whewellite, calcium oxalate monohydrate, $CaC_2O_4 \cdot H_2O$ has been determined. The calcium oxalates formed in the surface layers are related to the atmospheric exposure of old varnishes and their reaction with the calcium from the gypsum deposited from the environment. The presence of cracks on the surface of the paint favours the penetration of the varnishes and gypsum inside the paint layers and the development of calcium oxalates. Finally, in the ground layer, gypsum is mixed with animal glue, both materials are hygroscopic and again calcium oxalates appear to be the main degradation product.

Apart from the calcium oxalates, in the paint layers of both, egg tempera and oil paintings, copper and lead oxalates have also been determined. Lead oxalates are determined in the yellow and minium-red (Pb_3O_4) paint layers, copper oxalates in the green copper paint layers, see Fig. 8b, and also in some copper containing blue paint layers. The μ-SR-FTIR spectra corresponding to the lead and copper oxalates identified in the painting layers are shown in Fig. 10b and c, respectively. For the lead oxalate a doublet about 1311 and 1290 cm^{-1} is related to COO symmetric stretching band and the OCO deformation vibration bands at 781 and 773 cm^{-1} as shown in Fig. 10b. These bands are coincident with FTIR spectrum from lead oxalate synthesized in our laboratory. For the copper oxalates, Fig. 10c shows the infrared absorption bands corresponding to COO asymmetric stretching at about 1650 cm^{-1}, COO symmetric stretching at about 1362 and 1320 cm^{-1} and the OCO deformation vibration band at 820 cm^{-1} [32,33]. The oxalates are crystalline and may be determined by μ-SR-XRD. However, they show broad diffracting peaks and a reduced number of reflections that may overlap with the diffracting peaks corresponding to other compounds.

4. Conclusion

The formation of calcium, lead and copper carboxylates in oil and egg yolk tempera from 15th century paintings has been demonstrated. These substances are part of the expected evolution and reactivity of the materials in the paintings. The non-destructiveness, high brilliance and small footprint of synchrotron radiation and the combination of μ-SR-FTIR and μ-SR-XRD techniques have demonstrated to be particularly powerful for the study. Copper carboxylates are formed in copper based green paint layers, lead carboxylates in all lead containing paints and calcium carboxylates only when both, copper and lead are absent. The lead and calcium carboxylates formed are more crystalline with the egg yolk than with the drying oil.

The same metals, calcium, lead and copper also produce oxalates. Calcium oxalates are widespread on the surface, in the paint and ground layers. Their presence may be related to the degradation of the organic matter and reaction with the calcium from the environment or ground layer. Lead oxalates are formed in the yellow paints and copper oxalates in the green paints and, to a lesser extent, in the copper blue paint layers; they are also crystalline. The possible connection between their development and the formation of the corresponding carboxylates is still not clear. What is demonstrated is that calcium, copper and lead are the most reactive elements of the paint layers, forming both carboxylates and oxalates. The location, type and amount of carboxylates formed are consequence of the natural drying out of the paint. However, if a link between the formation of carboxylates and of oxalates is demonstrated, it may be one of the mechanisms of degradation that affects the paint preservation.

References

[1] M.T. Doménech-Carbó, Anal. Chim. Acta 621 (2008) 109.
[2] I. Surowiec, I. Kaml, E. Kenndler, J. Chromatogr. A 1024 (2004) 245.
[3] J.V. Gimeno, R. Mateo, M.T. Doménech, F. Bosch, A. Doménech, M.J. Casas, L. Osete, J. Chromatogr. A 922 (2001) 385.
[4] N. Salvadó, S. Butí, M.J. Tobin, E. Pantos, J.N.W. Prag, T. Pradell, Anal. Chem. 77 (2005) 3444.
[5] N. Salvadó, T. Pradell, E. Pantos, M.Z. Papiz, J. Molera, M. Seco, M. Vendrell-Saz, J. Synchrotron Radiat. 9 (2002) 215.
[6] D. Creagh, in: D. Bradley, D. Creagh (Eds.), Physical Techniques in the Study of Art, Archaeology and Cultural Heritage, vol. 2, Elsevier, 2007, p. 1.
[7] J.S. Mills, R. White, The Organic Chemistry of Museum Objects, Butterworth, London, 1987.
[8] D. Erhardt, in: V. Dorge, F.C. Howlett (Eds.), Painted Wood: History and Conservation, The Getty Conservation Institute, Los Angeles, 1998, p. 17.
[9] J.D.J. van den Berg, N.D. Vermist, L. Carlyle, M. Holčapek, J.J. Boon, J. Sep. Sci. 27 (2004) 181.
[10] C. Higgitt, M. Spring, D. Saunders, National Gallery Technical Bulletin, vol. 24, National Gallery Company Limited, London, 2003, p. 75.
[11] M.J. Plater, B. De Silva, T. Gelbrich, M.B. Hursthouse, C.L. Higgitt, D.R. Saunders, Polyhedron 22 (2003) 3171.
[12] J. Mallégol, J. Lemaire, J.-L. Gardette, Prog. Org. Coat. 39 (2000) 107.
[13] R. Newman, in: V. Dorge, F.C. Howlett (Eds.), Painted Wood: History and Conservation, The Getty Conservation Institute, Los Angeles, 1998, p. 33.
[14] M. Cotte, E. Checroun, J. Susini, P. Walter, Appl. Phys. A (2007) 841.
[15] J.J. Boon, E. Gore, K. Keune, A. Burnstock, in: M. Picollo (Ed.), Proceedings of the Sixth Infrared and Raman Users Group Conference (IRUG6), Florence, 2005, p. 66.
[16] K. Keune, J.J. Boon, Anal. Chem. 76 (2004) 1374.
[17] R.J. Meilunas, J.G. Bentsen, A. Steinberg, Stud. Conserv. 35 (1990) 33.
[18] M. Cotte, J. Susini, V.A. Solé, Y. Taiguchi, J. Chillida, E. Checron, P. Walter, J. Anal. At. Spectrom. 23 (2008) 820.
[19] A. Lluveras, S. Boularand, J. Roqué, M. Cotte, P. Giraldez, M. Vendrell, Appl. Phys. A 90 (2008) 23.
[20] N. Salvadó, S. Butí, E. Pantos, F. Bahrami, A. Labrador, T. Pradell, Appl. Phys. A 90 (2008) 67.
[21] http://www.mnac.cat/, 2008.

[22] N. Salvadó, S. Butí, F. Ruiz-Quesada, H. Emerich, T. Pradell, Butlletí del MNAC 9 (2008).
[23] E. Pantos, N. Salvadó, S. Butí, M.J. Tobin, T. Pradell, Proceedings G8 Workshop on Qumran, Jerusalem, 2006, p. 239.
[24] N. Salvadó, Ph.D. thesis, Universitat de Barcelona, Barcelona, 2001. http://www.tdx.cat/TDX-0718102-104305.
[25] J.P. Henichart, J.L. Bernier, Clin. Chim. Acta 118 (1982) 279.
[26] Y. Lu, J.D. Miller, J. Colloid Interface Sci. 256 (2002) 41.
[27] H. Dong, B. Meng, N. Zhu, F. Cui, Mater. Sci. Eng. C 26 (2006) 670.
[28] L. Robinet, M.C. Corbeil, Stud. Conserv. 48 (2003) 23.
[29] R. Mazzeo, S. Prati, M. Quaranta, E. Joseph, E. Kendix, M. Galeotti, Anal. Bioanal. Chem. 392 (2008) 65.
[30] M. Cotte, P. Dumas, G. Richard, R. Breiaux, Ph. Walter, Anal. Chim. Acta 553 (2005) 105.
[31] M.C. Corbeil, L. Robinet, Powder Diffr. 17 (2002) 52.
[32] K. Takata, S. Yamaguchi, S. Nishiyama, S. Tsuruya, J. Mol. Catal. A: Chem. 225 (2005) 125.
[33] C. Higgitt, R. White, National Technical Bulletin, vol. 26, National Gallery Company Limited, London, 2005, p. 88.

A new high-speed hollow fiber based liquid phase microextraction method using volatile organic solvent for determination of aromatic amines in environmental water samples prior to high-performance liquid chromatography

A. Sarafraz-Yazdi [a,*], F. Mofazzeli [b], Z. Es'haghi [c]

[a] Department of Chemistry, Faculty of Sciences, Ferdowsi University of Mashhad, Iran
[b] Department of Chemistry, Quchan Branch, Islamic Azad University, Quchan, Iran
[c] Department of Chemistry, Faculty of Sciences, Payame Noor University, Iran

ARTICLE INFO

ABSTRACT

A new and fast hollow fiber based liquid phase microextraction (HF-LPME) method using volatile organic solvents coupled with high-performance liquid chromatography (HPLC) was developed for determination of aromatic amines in the environmental water samples. Analytes including 3-nitroaniline, 3-chloroaniline and 4-bromoaniline were extracted from 6 mL basic aqueous sample solution (donor phase, NaOH 1 mol L^{-1}) into the thin film of organic solvent that surrounded and impregnated the pores of the polypropylene hollow fiber wall (toluene, 20 μL), then back-extracted into the 6 μL acidified aqueous solution (acceptor phase, HCl 0.5 mol L^{-1}) in the lumen of the two-end sealed hollow fiber. After the extraction, 5 μL of the acceptor phase was withdrawn into the syringe and injected directly into the HPLC system for the analysis. The parameters influencing the extraction efficiency including the kind of organic solvent and its volume, composition of donor and acceptor phases and the volume ratio between them, extraction time, stirring rate, salt addition and the effect of the analyte complexation with 18-crown-6 ether were investigated and optimized. Under the optimal conditions (donor phase: 6 mL of 1 mol L^{-1} NaOH with 10% NaCl; organic phase: 20 μL of toluene; acceptor phase: 6 μL of 0.5 mol L^{-1} HCl and 600 mmol L^{-1} 18-crown-6 ether; pre-extraction and back-extraction times: 75 s and 10 min, respectively; stirring rate: 800 rpm), the obtained EFs were between 259 and 674, dynamic linear ranges were 0.1–1000 μg L^{-1} ($R > 0.9991$), and also the limits of detection were in the range of 0.01–0.1 μg L^{-1}. The proposed procedure worked very well for real environmental water samples with microgram per liter level of the analytes, and good relative recoveries (91–102%) were obtained for the spiked sample solutions.

© 2009 Elsevier B.V. All rights reserved.

1. Introduction

Aromatic amines such as aniline and other substituted derivatives are widely used in industry and may be released from the manufactures of medicine, cosmetic, dyestuff and as by products of energy technologies [1,2]. Generally, this class of compounds is considered hazardous to the human health and implicated in inducing cancer of the bladder [3,4], because they can be readily converted to carcinogenic *n*-nitroamines through the reactions with nitrosylating agents in the environment [5,6]. These compounds can enter into the environment and experience complex environmental transformations at trace level. Therefore with the growing use of these compounds in the different industries, mon-

itoring of their levels in environmental waters is very important for the protection of health and the environment. Thus, it is important to develop a simple, rapid and sensitive analytical method for the determination of these compounds in the environmental water samples.

Two of the most conventionally used sample preparations, preconcentration and clean-up methods are solid phase extraction (SPE) [7,8] and liquid–liquid extraction (LLE) [9], which are used prior to gas chromatography (GC), high-performance liquid chromatography (HPLC) and capillary electrophoresis (CE) [7]. However, the main drawback of SPE or LLE is that they are time- and labour-intensive procedures and require large amount of high purity organic solvents, which are expensive, toxic and considered as environmental pollutants [10]. Moreover, both techniques require the evaporation of solvent to dryness and the reconstitution of the dry residue in a suitable solvent for the HPLC and CE. One noticeable trend in the development of sample preparation techniques has been miniaturization. In recent years, miniaturized techniques such

* Corresponding author. Tel.: +98 511 8797022; fax: +98 511 8796416.
E-mail address: asyazdi@ferdowsi.um.ac.ir (A. Sarafraz-Yazdi).

as: solid phase microextraction (SPME) [11], supported liquid membrane (SLM) extraction [12,13] and liquid phase microextraction (LPME) [14] have been reported as alternatives to the conventional ones.

In 1990, Arthur and Pawliszyn introduced SPME [15] as a solvent-free extraction method, which has been used for the analysis of volatile and semi-volatile analytes [16]. But this method has some disadvantages like; SPME fibers are still comparatively expensive and have a limited lifetime which tends to degrade with increased usages. On the other hand, the coatings currently available for SPME are either nonpolar or slightly polar; hence, SPME cannot be satisfactorily used for highly polar analytes. Furthermore, when SPME is coupled to HPLC, a special SPME–HPLC interface device has to be used for the solvent desorption.

By using the LLE at the miniaturized scale, i.e. liquid phase microextraction [17–19], the disadvantages of SPME can be overcome. In this method, the extracted analytes in the acceptor phase are injected directly in to the analytical instruments and the problems in SPME are omitted here. LPME is not an exhaustive extraction procedure, and only a small fraction of the analytes is extracted. It can be classified into two-phase and three-phase microextraction methods.

In the two-phase LPME, the analytes are extracted from an aqueous sample matrix into a microdrop organic solvent as an acceptor phase, which is suspended on the needle tip of a microsyringe immersed in the stirred aqueous sample solution [20]. Acceptor phase may also be contained inside the lumen of a hollow fiber and immobilized inside the wall pores of the hollow fiber [21,22]. After extraction, the acceptor phase is directly introduced to gas chromatography or high-performance liquid chromatography for further analysis.

In three-phase LPME, the ionizable analytes are first extracted from an aqueous sample matrix into an organic solvent and then back-extracted into an aqueous acceptor phase. The organic phase in this method is a thin layer of organic solvent which is held between two aqueous solutions [23] or inside the wall pores of a polypropylene hollow fiber [14,24,25]. Analytical techniques such as HPLC and CE are used for the analysis of the aqueous acceptor phase in this procedure.

In our present study, a new microextraction technique using a microporous membrane and volatile organic solvent was developed. The microporous hydrophobic hollow fiber membrane is used to separate the aqueous donor sample solution and aqueous acceptor phase. In the conventional hollow fiber microextraction method, use of volatile organic solvent with low viscosity which leads to the high extraction efficiency is impracticable. Because, the solvent cannot remain in the pores of the hollow fiber for more than a few seconds due to the high volatility. Therefore, throughout the transfer of the fiber from organic solvent into donor sample solution, vaporization of organic solvent will occur leaving nearly nothing inside the pores. In addition to be non-volatile, the organic solvent which is used in hollow fiber based liquid phase microextraction (HF-LPME) should be easily immobilized in the pores of the hollow fiber and immiscible with water because it serves as a barrier between two aqueous donor and acceptor phases. Based on these parameters, the numbers of used organic solvent in HF-LPME is limited to the high viscose solvent which has low solubility and volatility. But in our work, we used a new modification of HF-LPME method which allows us to use of the organic solvents with a wide range of viscosity and volatility values.

In this method, first a low amount of volatile organic solvent is added to the top of the aqueous donor phase as a spot and then the mixture is stirred for a short time to extract the analytes. The fiber which is closed from both ends is placed in the center of this organic spot. This two-end sealed hollow fiber contains aqueous acceptor phase inside the lumen. Then, the solution is stirred again and the

analytes are back-extracted from organic solvent into the aqueous acceptor phase very quickly. This modification has three important advantages over the conventional ones. Firstly, the extraction equilibrium is very fast. Because, one of the parameters which influences the mass transfer is the viscosity of the organic solvent, thus, by reducing the viscosity of the solvent the mass transfer is increased. Therefore, by the use of the organic solvent with low viscosity and also the free movement of the fiber, the mass transfer process will be contributed. Secondly, in this work the volatile organic solvents can be used and we have no limitation for selection of the organic solvent. Thirdly, the extraction efficiency is very high at a specific extraction time in comparison with conventional HF-LPME method.

2. Experimental

2.1. Standards and reagents

Analytical reagents grade methanol, benzene, toluene, *o*-xylene, *n*-heptane, hydrochloric acid and also 3-chloroaniline (3-CA), 4-bromoaniline (4-BA) and sodium chloride were supplied by Merck (Darmstadt, Germany). 3-Nitroaniline (3-NA, analytica standard) and 18-crown-6 ether ($C_{12}H_{24}O_6$) were obtained from Riedel de Haën (Steinheim, Germany). 1-Octanol was purchased from Fluka (Buchs, Switzerland). These compounds were all HPLC-grade and were used without further purification. Sodium hydroxide was from Farabi (Tehran, Iran).

A stock solution of $100\,\mu g\,mL^{-1}$ of each analyte was prepared in methanol and stored at $4\,^{\circ}C$. Standard sample solutions which contain the three target compounds were provided daily at different concentrations by diluting the stock standard solutions with triple-distilled water. The used water was purified on a Milli-Q ultra-pure water purification system (Millipore, Bedford, MA, USA).

The Q 3/2 Accurel PP polypropylene microporous hollow fiber membrane (200 μm wall thickness, 600 μm inner diameter, 0.2 μm pore size, and 75% porosity) was obtained from Membrana (Wuppertal, Germany).

2.2. Instrumentation

The HPLC system consisted of a Waters 600 E (Millipore Co. Milford, MA, USA), LC-600 pump, C1 Cheminert injector valve equipped with a 20 μL sample loop (Switzerland), a Waters 486 tune-able UV-VIS detector and a Waters 746 integrator. A C_8 (125 mm length, 4.0 mm diameter, 5 μm particle size) column was used for separation. This column was packed in our laboratory with a KNAUER packing system including a KNAUER pneumatic HPLC pump (Germany) using packing material (Eurospher 100, C_8). The degassed mobile phase was a mixture of methanol–pure water optimized on (40:60, v/v). The mobile phase flow-rate was $1\,mL\,min^{-1}$ and the UV detection wavelength was set at 240 nm. The column was used at ambient temperature ($22 \pm 0.5\,^{\circ}C$).

2.3. Preparation of the hollow fiber

The hollow fiber was cut into segments with a length of 2.5 cm. The approximate internal volumes of these segments were ~6 μL. The hollow fiber segments were sonicated for 5 min in HPLC-grade acetone to remove any contaminants in the fiber. After sonication, the fibers were removed from the acetone, and the solvent was allowed to evaporate completely. These hollow fiber segments were used for subsequent extractions. A 25 μL flat-cut HPLC microsyringe (Hamilton, Reno, NV, USA) was used to introduce the aqueous acceptor phase (HCl $0.5\,mol\,L^{-1}$, pH 0.3) into the hollow fiber. It also served as a sample introduction device for the HPLC. A 6 μL volume of acceptor solution was withdrawn into the HPLC microsyringe and the needle of the syringe was inserted into the hollow fiber
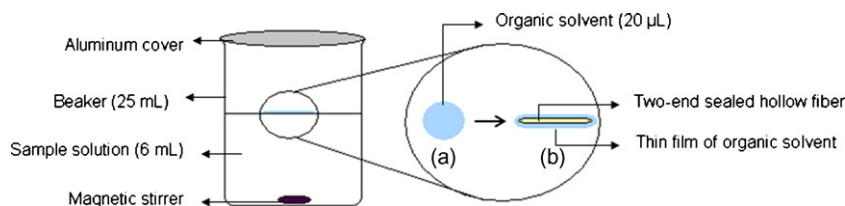
Fig. 1. Illustration of the microextraction apparatus for new HF-LPME: (a) 20 μL of organic solvent as spot over the sample solution; (b) organic solvent which is surrounded by the two-end hollow fiber as a thin film.

segment. The acceptor solution was introduced carefully without penetration into the wall of the hollow fiber; otherwise, it would be lost during the extraction. Then, the two ends of the hollow fiber segment were heat-sealed.

2.4. Extraction procedure

The extraction was performed according to the following procedure. Sample solution (6 mL, adjusted to pH 14 with NaOH) was placed in a 25 mL beaker, along with a 7 mm × 3 mm stirring bar. A heating-magnetic stirrer (0–1200 rpm) was used to stir the extraction mixture. Organic solvent (20 μL, toluene) was added to the sample solution by a 100 μL syringe (KNAUER, USA). Then the mixture was agitated for 75 s at 1200 rpm. Thereafter, the mixture was allowed to be quiescent for few seconds till the tiny droplets of organic solvent were gathered and a spot of organic solvent which was enriched by the analytes was produced over the aqueous sample solution. Afterwards, the two-end sealed hollow fiber which was filled with the acceptor phase was placed in the center of this spot for impregnation of its pores. At the same time, the magnetic stirrer was switched on to start the extraction. By placing of the hollow fiber in the organic spot, it was surrounded by a thin film of organic solvent which remained around the hollow fiber throughout the extraction process. An aluminum foil was used to cover the beaker during the extraction procedure to prevent the evaporation of the volatile organic solvent. The basic experimental apparatus was shown in Fig. 1.

When the magnetic stirrer was switched on, the two-end sealed hollow fiber can rotate around a symmetrical axis and intensify the mass transfer process. After a prescribed time, the magnetic stirrer was switched off and the hollow fiber was removed from the sample solution. One end of the hollow fiber was cut carefully with a sharp blade and the needle tip of the microsyringe was carefully inserted into the lumen. The acceptor solution in the hollow fiber lumen was withdrawn back into the syringe. Only 5 μL of acceptor solution was injected into the HPLC system for separation and identification. The used fiber was discarded, and a fresh one was used for the next experiment.

3. Results and discussion

3.1. Basic principle

Liquid–liquid–liquid phase microextraction techniques involve two processes and three phases. Extraction from donor phase into an organic phase and then back-extraction from organic phase into an aqueous acceptor phase for an analyte (A) may be represented by the equation:

$$A_{P1} \leftrightarrow A_O \leftrightarrow A_{P2}$$
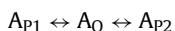
When a hollow fiber is used for extraction the subscript P1 represents the aqueous donor phase, O represents the organic phase which is immobilized within the pores of the hollow fiber and P2 represents the aqueous acceptor phase inside the lumen of the hollow fiber.

In such cases, the pH of the sample solution is adjusted to make the analytes neutral and thus extractable into the organic solvent. After reaching the equilibrium of phase separation, the analytes which are mostly transferred into the organic phase are back-extracted into the acceptor aqueous phase set to a pH at which the analytes are charged. This back-extraction step introduces extra selectivity since neutral compounds will preferably stay in the organic phase. The theory of the method is well defined by the others [24,26,27]. To have an appropriate analyte pre-concentration, it is necessary to convert the analytes in the acceptor phase by such reactions as protonation, complexation, etc. to the species that have very slight affinity for the organic phase [26]. It is also necessary to prevent the reverse extraction from the acceptor phase to the donor phase. In the current study, both protonation and complexation processes are applied to obtain large enrichment factor and also to prevent the reverse extraction.

3.2. Optimization method

To obtain the optimal extraction efficiency, various parameters that potentially affect sample extraction were studied which can be discussed respectively.

3.2.1. Selection of organic solvent

In three liquid phase microextraction, the type of organic solvent has an important role in the extraction efficiency and the analyte pre-concentration. When the hollow fiber is used for the extraction, there are several requirements for selection of organic solvent. Firstly, it should be non-volatile to prevent solvent loss during the extraction. Secondly, the appropriate organic solvent should be easily immobilized in the hollow fiber and immiscible with water because it serves as a barrier between two aqueous donor and acceptor phases. Lastly, the solubility of analytes in the organic solvent should be lower and higher than that of the donor and acceptor phases, respectively. This causes to promote analyte migration from the donor phase through the pores of the hollow fiber finally to the acceptor phase. Based on the above parameters, 1-octanol and di-*n*-hexyl ether are usually selected as organic solvents for hollow fiber based liquid phase miroextraction. But other organic solvents such as: toluene, *o*-xylene, benzene, etc. with low viscosity and high extraction efficiencies are not selected as organic phases in conventional HF-LPME due to their high volatilities and solvent loss during the extraction process. In the present work, we used a new design of hollow fiber microextraction which allowed us to use these volatile organic solvents without considerable loss of them during the extraction process.

Six organic solvents with different viscosities and volatilities have been examined in this work. These extracting solvents were: 1-octanol, toluene, benzene, *o*-xylene, ethyl benzene and *n*-heptane. All of these solvents were easily immobilized in the pores of the hollow fiber. As shown in Fig. 2, toluene has the highest analyte enrichment among the others, and it was selected as the organic solvent for further studies.
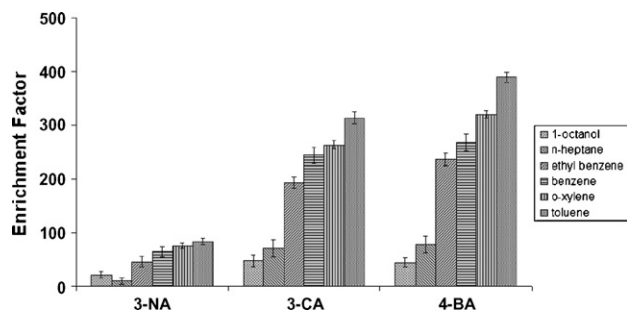
Fig. 2. The effect of organic solvent on the extraction efficiency; P1, 6 mL of pH 14 water sample; O, 20 μL toluene; P2, 6 μL, HCl 0.5 mol L^{-1} receiving aqueous phase. Time for the extraction is 75 s; for back-extraction, 10 min.

3.2.2. Volume ratio of donor to acceptor phase

In the current work, the phase ratio of donor and acceptor phases was changed in the range of 600:1 to 1000:1, by changing the volume of the donor phase while the volume of acceptor phase was kept constant at 6 μL. In LLLME, the enrichment factor can be improved by increasing the volume ratio of donor and acceptor phases. Therefore, when the volume of acceptor phase was 6 μL, the results indicate that the best extraction efficiency was obtained when 6 mL of donor phase was used (i.e. donor/acceptor ratio of 1000:1). Hence, these were chosen as donor and acceptor phase volumes.

3.2.3. Volume of organic solvent

In the conventional HF-LPME method use of the volatile organic solvents like toluene is impossible; because, before placing the hollow fiber in the sample solution, the organic solvent is evaporated from the pores of the hollow fiber. In this work, a new modification of hollow fiber microextraction using volatile organic solvents was applied. Through this process, the impregnation of hollow fiber pores should occur inside the extraction device above the sample solution. Therefore, the solvent loss before and during the extraction procedure was highly minimized. Thus, the volume of the organic phase was too important due to the special design of extraction method and must be carefully optimized. The range of organic solvent volume was between 100 and 10 μL. The results indicate that the best volume of the organic solvent was found to be 20 μL. Lower volumes of organic solvent tend to solvent loss during agitation because of its high volatility, and higher volumes cause lower enrichment factor. Consequently, a 20 μL volume of the organic solvent was chosen for the subsequent extractions.

3.2.4. Extraction time

Like the other techniques of microextraction, LLLME is a type of equilibrium extraction. Maximum efficiency is obtained at the equilibrium, and usually it takes too long and a further increase in extraction time does not affect the amount of the extracted analytes. Therefore, the extraction time is expected to be an important factor in the extraction efficiency of the process. According to the theoretical model of mass transfer for solvent microextraction [28], increase of the stirring speed caused an increase in mass transfer coefficient. In this work, we used toluene (very low solubility in water, 0.5 g L^{-1}) as extractant. First, the stirring speed for agitating the donor sample solution and organic phase was fixed at 1200 rpm. Afterwards, the mixture was allowed to be quiescent for few seconds to gather the tiny drops of organic solvent on the surface of the sample solution. Therefore, a spot of organic solvent which was enriched by the analytes was produced (Fig. 1(a)). The range of extraction times investigated here was between 15 and 90 s. When 1200 rpm of stirring speed was applied, the changes of

HPLC signals became steady after 75 s, and the increase of signals with elapsed extraction time was very slow. After extraction process, the two-end sealed hollow fiber filled with aqueous acceptor phase was placed inside the spot of organic solvent for impregnation of its pores. By placing the two-end sealed hollow fiber in the organic spot a thin film of enriched organic solvent surrounded the hollow fiber (Fig. 1(b)) and the magnetic stirrer was switched on simultaneously, to start the back-extraction procedure.

The back-extraction occurred from the enriched organic solvent (toluene in the pores of hollow fiber) into the aqueous acceptor phase (6 μl, HCl 0.5 mol L^{-1}, inside the hollow fiber lumen), with a large rate constant. It took only 10 min for the back-extraction to attain equilibrium. The enrichment factor did not increase significantly after 10 min. Thus, the equilibrium time of 10 min was chosen for back-extraction.

3.2.5. Stirring rate

The effect of stirring speed on the extraction efficiency was also examined. As described before, higher stirring speed causes an increase in the mass transfer process and also the kinetic rates. In the current work, the two-end sealed hollow fiber was laid above the sample solution, inside the organic solvent spot and it can rotate around a symmetrical axis when the magnetic stirrer was switched on. The free movement of the fiber will contribute to the mass transfer process. Therefore, the stirring speed was also optimized for better extraction, while back-extraction was performed. The stirring speed was in the range of 360–960 rpm. Agitation increased the extraction efficiency but in very high speed (more than 800 rpm) a vortex was created in sample solution and the fiber started rotating rather than stirring and escaped from the symmetrical axis at the surface of the sample solution due to centrifugal force and stuck the wall of the beaker. Consequently, the stirring speed of 800 rpm was selected.

3.2.6. The pH of donor and acceptor phases

The compositions of both donor and acceptor phases are very important parameters which affect the extraction efficiency in three liquid phase microextraction. The pH of the donor phase is adjusted to deionize the analytes and the acceptor phase adjusted to ionize them. The difference in pH between the donor and acceptor phases is one of the major parameters which can promote the transfer of analytes from donor to acceptor phase. Hence, a series of the experiments was carried out to find the optimal compositions of the donor and acceptor phases. Since, the target compounds are weak base with low pK_a {3-NA (pK_a = 2.47), 3-CA (pK_a = 3.52), 4-BA (pK_a = 4.02) [29,30]}, protonation is an important reaction. At first, we investigated the donor phase, which was adjusted to deionize aromatic amines by various concentrations (0.001–1 mol L^{-1}) of NaOH. The results, shown in Table 1 indicate that increase of NaOH concentrations provides some but not significant enhancement of the extraction efficiencies. The enrichment factors for 1 mol L^{-1} NaOH were better than the others, therefore, 1 mol L^{-1} NaOH was used as donor media.

While the pH of donor sample solution was not a critical factor, the extraction efficiency was more dependent on the pH of acceptor solution. As shown in Table 1, the HCl concentrations were studied in the range of 0.001–0.5 mol L^{-1}. The higher concentration was not used to avoid possible problems with the column and injector. The results show that the pH of acceptor phase inside the hollow fiber is a very important factor and influences the EFs, especially for 3-NA which has the lowest pK_a value. Finally, 0.5 mol L^{-1} HCl was used as acceptor phase because it provided highest EF for the target compounds. After each injection, rinsing the HPLC injector with pure water should be carried out to prevent possible acid erosion of the stainless steel injector.

Table 1
Effect of pH on enrichment factors.[a]

Analytes	0.1 mol L^{-1} HCl as acceptor phase[b]				1 mol L^{-1} NaOH as donor phase[c]			
	0.001 mol L^{-1} NaOH	0.01 mol L^{-1} NaOH	0.1 mol L^{-1} NaOH	1 mol L^{-1} NaOH	0.001 mol L^{-1} HCl	0.01 mol L^{-1} HCl	0.1 mol L^{-1} HCl	0.5 mol L^{-1} HCl
3-NA	28.5	32.9	38.9	5.7	6.2	10.8	45.7	129.6
3-CA	198.6	209.5	327.3	285.9	25.6	76.3	285.9	517.8
4-BA	322.5	329.8	373.6	428.6	41.3	128.3	428.6	603.9

[a] The concentration of analytes were 1 μg mL^{-1} and SD ≤10 for three replicates.
[b] The concentration of HCl in the acceptor phase is fixed, the concentration of NaOH in donor phase is varied.
[c] The concentration of NaOH in the donor phase is fixed, the concentration of HCl in acceptor phase is varied.
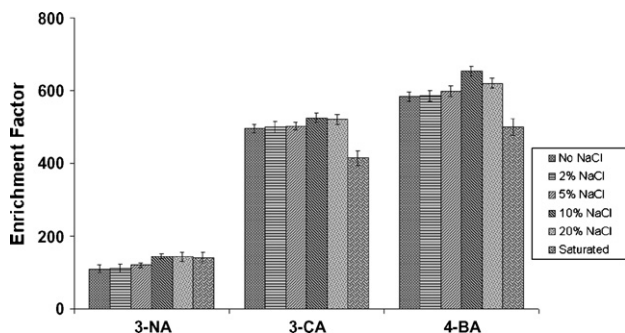
Fig. 3. The effect of salt added in the aqueous donor phase on the extraction efficiency for the aromatic amines; P1, 6 mL of pH 14 water sample solution containing NaCl in different concentrations; O, 20 μL toluene as a spot on the surface of the donor phase; P2, 6 μL, HCl 0.5 mol L^{-1} receiving aqueous phase; extraction and back-extraction times: 75 s and 10 min.

3.2.7. Addition of salt to the donor phase

Addition of a salt can often improve extraction efficiency when the extraction methods are used. For this purpose, sodium chloride is normally used [31]. To evaluate the effect of salt in this work, NaCl was added into the donor sample solution and the effect was studied from 0% to saturation. The results indicate an initial increase in the enrichment factors with increasing salt concentration, along with a maximum being reached at 10%, followed by a decrease in EFs with further increase in salt concentration to saturation (Fig. 3). These results can be explained by two simultaneously occurring processes as described by Lord and Pawliszyn [32]. Initially, extraction efficiency was enhanced due to salting out effect, whereby water molecules form hydration spheres around the ionic salt molecules. These hydration spheres reduce the amount of water available to dissolve analyte molecules in water [33], thus, it is expected that the target compounds will drive into the organic solvent. On the other hand, with increase of salt concentration and ionic strength, salting in effect occurred. Whereby, polar molecules may participate in electrostatic interactions with the salt ions in solution; therefore, the mass transfer is reduced. With salt addition, at first, the predominant process is the interaction of salt with water (salting out effect). With increasing salt concentration, salt molecules start interacting with analytes (salting in effect). Thus, it is reasonable that the initial improvement in extraction efficiencies with increasing salt concentration is followed by a decrease as concentration is increased further. According to the results in Fig. 3, the optimal concentration of NaCl in donor phase was 10% and selected for the future studies.

3.2.8. Addition of crown ether to the acceptor phase

As described before, to have an appropriate analyte preconcentration, it is necessary to convert the analytes in the acceptor phase by such reactions as protonation or complexation to reduce the affinity for the organic phase. In the current study, besides protonation, the influence of analyte complexation to obtain higher extraction efficiency was investigated. Protonated aniline can form complex with crown ether in solutions [34]. Crown ethers are heterocyclic chemical compounds that consist of a ring containing several ether groups. The characteristic chemistry of the crown ethers involves complexation of the ether oxygens with various ionic species. This is termed "host–guest" chemistry, with the ether as host and the ionic species as guest. Apart from its high affinity for potassium cations, 18-crown-6 can also bind to protonated amines [($-NH_3^+$) as guest] and form very stable complexes in both solutions and the gas phases [35]. Therefore, the addition of 18-crown-6 ether (soluble in water) in aqueous acceptor phase was used to study of the effect of complexation on extraction efficiency. For this purpose, 18-crown-6 ether was added in 0.5 mol L^{-1} HCl solution as acceptor phase and the concentration was varied from 100 to 600 mmol L^{-1}. The results indicate that no significant effect on extraction was achieved at lower concentrations (100–300 mmol L^{-1}). However, increases were obtained at higher concentration of 18-crown-6 ether. Therefore, the concentration of 18-crown-6 ether in the acceptor phase inside the hollow fiber lumen was 600 mmol L^{-1}.

3.3. Comparison with the conventional HF-LLLME

New high-speed HF-LPME and conventional HF-LPME were performed for comparison of their respective efficiencies. Identical conditions for both procedures were used: donor phase— 6 mL of 1 mol L^{-1} NaOH consisting 1 μg mL^{-1} of each aromatic amines, 1-octanol as organic solvent; acceptor phase—6 μL of 0.5 mol L^{-1} HCl and 600 mmol L^{-1} 18-crown-6 ether solution, stirring rate 800 rpm, and extraction time 10 min. In conventional HF-LPME the organic solvent is immobilized in the pores by immersing the hollow fiber for 5 s in it but in new high-speed HF-LPME, 20 μL of 1-octanol is placed at the surface of the sample solution as a spot. The hollow fiber was then inserted in the center of this spot to impregnate the pores. As shown in Table 2, higher enrichment factors were achieved for our method (new HF-LPME) compared to conventional HF-LPME in the same organic solvent and extraction time.

Another comparison was performed between organic solvents with different viscosities and volatilities by using our developed method. For this purpose, 1-octanol (viscosity = 6.49) and toluene (viscosity = 0.778) were selected as organic solvents. A 20 μL vol-

Table 2
Comparison of new HF-LPME and conventional HF-LPME.

Analytes	Conventional HF-LPME using 1-octanol Enrichment factor	New HF-LPME using 1-octanol Enrichment factor	New HF-LPME using toluene Enrichment factor
3-NA	52.3 ± 5.1	98.9 ± 6.8	258.9 ± 5.9
3-CA	69.5 ± 8.6	104.3 ± 11.8	598.5 ± 11.5
4-BA	83.3 ± 7.9	119.2 ± 11.2	674.2 ± 10.8

Table 3
Analytical performance of the proposed extraction procedure.

Analytes	RSD% ($n = 5$)	Correlation coefficient, r	Linear range ($\mu g\,L^{-1}$)	Limit of detection, LOD ($\mu g\,L^{-1}$)	Enrichment factor, EF
3-NA	4.11	0.9991	1.0–1000	0.1	258.9 ± 5.9
3-CA	3.8	0.9994	0.5–1000	0.05	598.5 ± 11.5
4-BA	4.34	0.9996	0.1–1000	0.01	674.2 ± 10.8
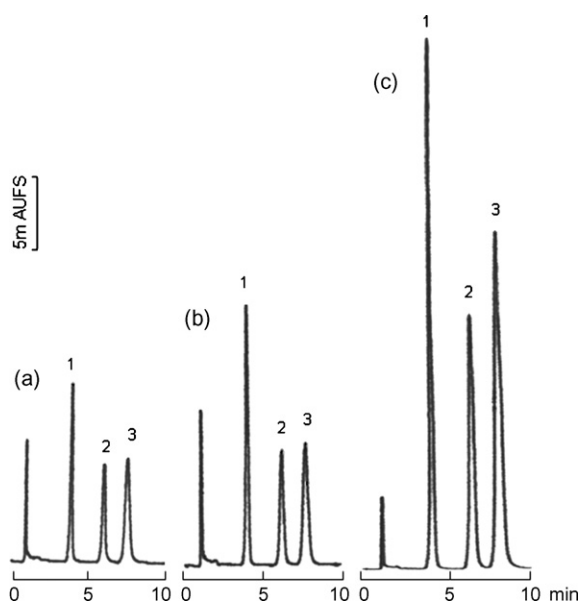
Fig. 4. The chromatograms which were obtained after extraction of aromatic amines: (a) conventional HF-LPME using 1-octanol as extractant; (b) new HF-LPME using 1-octanol as extractant; (c) new HF-LPME using toluene as extractant. Peaks identified as: (1) 3-nitroaniline, (2) 3-chloroaniline, (3) 4-bromoaniline.

Table 4
The relative recoveries of target compounds in real environmental water samples at 2.5 $\mu g\,L^{-1}$ spiking level ($n = 3$).

Samples	3-NA	3-CA	4-BA
Tap water	99 ± 8	92 ± 11	91 ± 9
Groundwater	96 ± 7	101 ± 9	94 ± 10
River water	102 ± 6	98 ± 7	101 ± 8

ume of each solvent was laid above the sample solution as a spot and impregnation of pores occurred as described before. According to the results in Table 2, the extraction by using toluene has very higher enrichment factors compared to the use of 1-octanol as organic solvent. As expected from the theory, by decreasing the viscosity of the organic solvent, the rate of mass transfer process has been increased. These comparisons were also shown better in Fig. 4.

3.4. Quantitative consideration

Under optimal extraction conditions, enrichment factors, repeatability, the linearity, the limits of detection and relative recoveries were determined by utilizing standard solutions of three
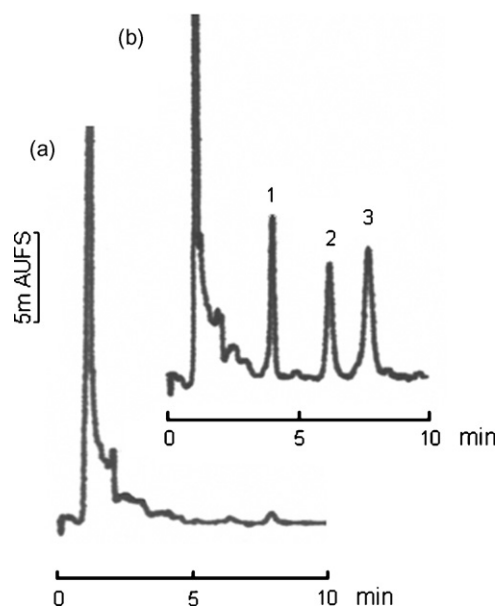
Fig. 5. Chromatograms generated after new HF-LPME of a groundwater sample, (a) 6 mL groundwater, (b) 6 mL groundwater was spiked with 2.5 $\mu g\,L^{-1}$ each analyte under the optimal conditions. The pH of the water sample was adjusted to 14 using 1 mol L^{-1} NaOH and contained 10% NaCl. Organic phase was 20 μL of toluene which surrounded and impregnated the pores of the 2.5 cm hollow fiber segments; acceptor phase is 6 μL, HCl 0.5 mol L^{-1} containing 600 mmol L^{-1} of 18-crown-6 ether. Time for the extraction is 75 s; for back-extraction is 10 min. Peaks identified as: (1) 3-nitroaniline, (2) 3-chloroaniline, (3) 4-bromoaniline.

aromatic amines in water. The repeatability in peak areas was studied for five replicate experiments. The relative standard deviations (RSDs) were lower than 4.34 for all the three analytes. By plotting peak areas versus concentrations of analytes in the sample solution, calibration curves were obtained which showed that correlation coefficient (r), were all above 0.9991. The limits of detection (LODs at S/N = 3) ranged from 0.01 to 0.1 $\mu g\,L^{-1}$ and the aromatic amines could be pre-concentrated up to 670-fold. Analytical data are summarized in Table 3.

3.5. Real water analysis

Three real environmental water samples including tap water, river water and groundwater were studied using the developed method. Tap water was collected from Mashhad (Iran), river and groundwater were collected from Kardeh, a village near Mashhad. No target compounds could be detected in the sample, however. Therefore, separate samples were spiked with 2.5 $\mu g\,L^{-1}$ of each aromatic amine. In Fig. 5, the chromatograms obtained after enrich-

Table 5
Comparison of figures of merit of the proposed method with conventional HF-LPME applied for the analysis of 4-BA (proposed [14]) and 4-NA [25].

Method	Organic solvent	LOD ($\mu g\,L^{-1}$)	Linearity range ($\mu g\,L^{-1}$)	EF	Time (min)	Ref.
Proposed	Toluene	0.01	0.1–1000	674 ± 11	10	–
HF-LPME	di-n-hexyl ether	0.05	0.5–500	510 ± 10	30	[14]
HF-LPME	di-n-hexyl ether	1.5	5–200	745 ± SD[a]	80	[25]

[a] SD was not reported.

ing of 6 mL of groundwater without and with spiking 2.5 μg L^{-1} of each aromatic amine were shown, respectively, using our proposed method.

The relative recoveries which were defined as the ratios of the peak areas of the analyses in real samples and the peak areas of analyses in pure distilled water sample spiked with same amount of analytes are listed in Table 4.

Table 5 compares the figures of merit generated by the proposed method and alternative HF-LPME method for the extraction of aromatic amines like 4-bromoaniline and 4-nitroaniline from water samples. The linearity range of the proposed method shows a wider value in comparison with conventional HF-LPME. On the other hand, our proposed method has higher sensitivity (lower LOD) and higher enrichment factor along with a very low extraction time.

4. Conclusion

In the present study, a new mode of liquid phase microextraction, using a microporous membrane and volatile organic solvent was developed for the extraction of aromatic amines in water samples. The extraction was carried out by the use of volatile organic solvent which has low viscosity that leads to increase of mass transfer and extraction efficiency along with a decrease in extraction time. On the other hand, this method is very easy and simple and the eluted analytes are directly determined with HPLC. Using this technique, the aromatic amines can be extracted from real water samples quantitatively with a good linearity and reasonable relative recoveries.

Acknowledgement

References

[1] H. Kataoka, J. Chromatogr. A 733 (1996) 19.
[2] R.D. Voyksner, R. Straub, J.T. Keever, H.S. Freeman, W.N. Hsu, Environ. Sci. Technol. 27 (1993) 1665.
[3] S. Laha, R.G. Luthy, Environ. Sci. Technol. 24 (1990) 363.
[4] A. Dasgupta, J. Chromatogr. B 716 (1998) 354.
[5] R.J. Lewis, Sax's Dangerous Properties of Industrial Materials, 8th ed., Van Nostrand Reinhold, New York, 1992.
[6] K.T. Chung, Ecotoxicol. Rev. C 18 (2000) 51.
[7] M.-C. Hennion, C. Cau-Dit-Coumes, V. Pichon, J. Chromatogr. A 823 (1998) 147.
[8] M.G. Knize, C.P. Salmon, E.C. Hopmans, J.S. Felton, J. Chromatogr. A 763 (1997) 179.
[9] D.K. Lloyd, J. Chromatogr. A 735 (1996) 29.
[10] H. Prosen, L. Zupančič-Kralj, Trends Anal. Chem. 18 (1999) 272.
[11] D. Louch, S. Motlagh, J. Pawliszyn, Anal. Chem. 64 (1992) 1187.
[12] M. Sandahl, L. Mathiasson, J.Å. Jönsson, J. Chromatogr. A 893 (2000) 123.
[13] M. Khrolenko, P. Dżygiel, P. Wieczorek, J. Chromatogr. A 975 (2002) 219.
[14] L. Zhao, L. Zhu, H.K. Lee, J. Chromatogr. A 963 (2002) 239.
[15] C.L. Arthur, J. Pawliszyn, Anal. Chem. 62 (1990) 2145.
[16] A. Peñalver, E. Pocurull, F. Borrull, R.M. Marcé, Trends Anal. Chem. 18 (1999) 557.
[17] E. Psillakis, N. Kallogerakis, Trends Anal. Chem. 21 (2002) 53.
[18] T.S. Ho, S. Pedersen-Bjergaard, K.E. Rasmussen, J. Chromtogr. A 963 (2002) 3.
[19] C. Basheer, H.K. Lee, J.P. Obbard, J. Chromatogr. A 968 (2002) 191.
[20] L. Xu, C. Basheer, H.K. Lee, J. Chromatogr. A 1216 (2009) 701.
[21] S. Pedersen-Bjergaard, K.E. Rasmussen, J. Chromtogr. A 1184 (2008) 132.
[22] T. Barri, J.Å. Jönsson, J. Chromtogr. A 1186 (2008) 16.
[23] H. Ebrahimzadeh, Y. Yamini, A. Gholizade, A. Sedighi, S. Kasraee, Anal. Chim. Acta 626 (2008) 193.
[24] Y. Tao, J.F. Liu, T. Wang, G.B. Jiang, J. Chromatogr. A 1216 (2009) 756.
[25] A. Sarafraz Yazdi, Z. Es'haghi, J. Chromatogr. A 1082 (2005) 136.
[26] M. Ma, F.F. Cantwell, Anal. Chem. 70 (1998) 3912.
[27] S. Pedersen-Bjergaard, K.E. Rasmussen, Anal. Chem. 71 (1999) 2650.
[28] M.A. Jeannot, F.F. Cantwell, Anal. Chem. 69 (1997) 2935.
[29] http://ull.chemistry.uakron.edu/erd/chemicals/20001/20688.html.
[30] P.H. Howard, W.M. Meylan, Handbook of Physical Properties of Organic Chemicals, CRC Press/Lewis Publishers, Boca Raton, FL, USA, 1997.
[31] H.L. Lord, J. Pawliszyn, Anal. Chem. 69 (1997) 3899.
[32] H. Lord, J. Pawliszyn, J. Chromatogr. A 902 (2000) 17.
[33] A.A. Boyd-Boland, J.B. Pawliszyn, J. Chromatogr. A 704 (1995) 163.
[34] H.J. Buschmann, L. Mutihac, K. Jansen, E. Schollmeyer, An. Quim., Int. Ed. 94 (1998) 211.
[35] http://en.wikipedia.org/wiki/Crown_ether.

Sugar determination via the homogeneous reduction of Au salts: A novel optical measurement

Matteo Scampicchio, Carlos Alberto Fuenmayor, Saverio Mannino*

Department of Food Science and Microbiology, University of Milan Via Celoria, 2, 20133 Milan, Italy

A B S T R A C T

A novel optical assay for sugar determination based on the catalytic and biocatalytic growth of gold nanoparticles (AuNPs) is presented. The reaction of carbohydrates with these Au salts in alkaline media generates AuNPs at room temperature (RT) without the need for Au seeds in the solution or fibrous mesh. The optical properties of the resulting AuNPs relates to the total reducing sugar content of the samples analyzed. The development of such inexpensive optical assay was evaluated qualitatively and quantitatively on food beverages and honey samples. Its application can be of help to control the glucose content of the diet or easily extended in a host of industrial, biomedical and clinical fields.

© 2009 Elsevier B.V. All rights reserved.

1. Introduction

Metal nanoparticles of different compositions and dimensions have been used in recent years as versatile and sensitive tracers for the electronic, optical, and microgravimetric transduction of different biomolecular recognition events [1–3]. An elegant example, is by Willner et al. who developed an amplified biocatalytic optical assay in connection to enzymatically induced particle-growth processes [4]. Such biocatalytic enlargement of gold nanoparticles (AuNPs) involved the reduction and deposition of a metal onto a nanoparticle by an enzymatically generated reducing agent. Recently, colorimetric detection processes, based on AuNPs growth, have been used for the sensing of antioxidants in food [5]. Such protocols rely on the quantitative formation of AuNPs by the intrinsic reducing power of the analyte in question.

Herein, we develop a novel colorimetric assay for the sensing of sugars based on the growth of AuNPs from a solution containing Au salts. The reaction of carbohydrates with these Au salts in alkaline media generates AuNPs at room temperature (RT) without the need for Au seeds in the solution or fibrous mesh (see Scheme 1 of Fig. 1). The optical properties of the resulting AuNPs relates to the total reducing sugar content of the samples analyzed. The development of such inexpensive assay can be of help to control the glucose content of the diet, especially in diabetics, or easily extended in a host of industrial, biomedical and clinical fields.

2. Experimental

2.1. Apparatus, reagents and samples

Absorbance measurements were performed using a UV spectrophotometer (Cary V, Varian). Electrochemical measurements were conducted using a CHI 1010. Electrochemical Analyzer (CH Instruments, Austin, TX) with a three-electrode set-up. This consisted of an Ag/AgCl (3 M) reference electrode, a platinum wire counter-electrode and a glassy carbon electrode coated with a film of copper. A mass of $0.2\,mg\,cm^{-2}$ of copper was deposited on the glassy carbon surface by electrodeposition, applying a fixed potential of $-0.3\,V$ in $5 \times 10^{-2}\,M$ $CuSO_4$ [6].

All chemicals were received from Aldrich and Sigma and used without further purification. 1 g of honey samples was dissolved in 10 mL of distilled water. Enzyme suspension contained $4\,mg\,mL^{-1}$ (5–7 U/mL) of invertase in distilled water.

2.2. Gold nanoparticles procedure

The AuNPs growth solution consisted of $HAuCl_4 \cdot 3H_2O$ ($1 \times 10^{-3}\,M$), CTAC ($3.7 \times 10^{-3}\,M$), in NaOH 0.1 M, along with different levels of sugars. The reaction was conducted at RT. The absorbance spectra were recorded between 900 and 350 nm.

2.3. Invertase reaction

Invertase enzyme solution was added to increasing concentration of sucrose in acetate buffer 0.1 M, pH 4.6. After 30 min (in the
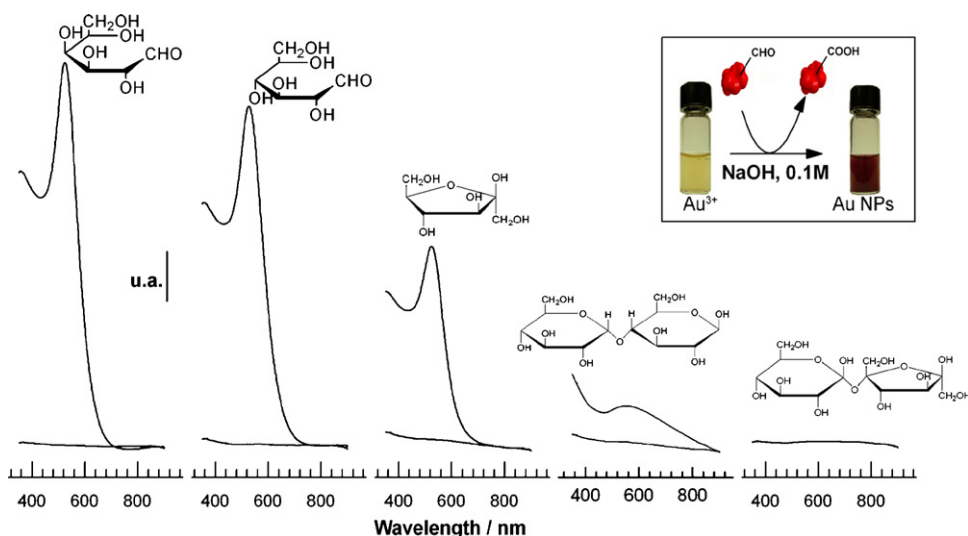

Fig. 1. Absorbance spectra of Au NPs formed in the presence of 0.3×10^{-4} M of (from left to right) galactose, glucose, fructose, maltose and sucrose. Experimental conditions: buffer composed of 3.7×10^{-3} M CTAC; 0.1 M NaOH; 1×10^{-3} M AuCl$_4{}^-$. Both samples have been heated up to 50 °C during 4.5 min and then scanned (starting 5 min after the addition of the AuCl$_4{}^-$). Also shown as inset the reaction scheme of gold nanoparticles growth from reducing sugars.

dark), the reaction was stopped by adding NaOH to a final concentration of 0.1 M. The resulting solution was used in the gold nanoparticles assay.

3. Results and discussion

Preliminary studies focused on understanding the growth of AuNPs in the presence of various sugars in alkaline media (NaOH, 0.1 M). Fig. 1 details the resulting absorbance spectra obtained when different reducing sugars were added to solutions containing HAuCl$_4$ and the CTAC surfactant. In the absence of any sugar no absorbance peaks are observed, however addition of sugar to the solution, results in a characteristic sharp particle plasmon absorption band at 540 nm, indicative of AuNPs growth. Such generation of AuNPs proceeds without addition of AuNPs seeds, at RT, and involves the reduction of gold(III) to gold(0) by the reducing sugar.

It can be expected that the rate of growth and the optical properties of the AuNPs will depend significantly on the reducing power of the corresponding aldose or ketose used. Such correlation is expected since the ability of these compounds to reduce Au(III) reflect their tendency to donate electrons, and therefore to reduce gold ions. Fig. 1 shows that the absorbance maxima obtained at 540 nm is dependent on the variety of sugars introduced into a solution containing 1×10^{-3} M HAuCl$_4$ and 3.7×10^{-3} M CTAC surfactant. It can be clearly seen that absorbance decreases in the order: galactose > glucose > fructose > maltose > sucrose. In order to prove that this trend is related to the reducing power of the sugar, amperometric experiments of the different reducing sugars (1×10^{-3} M) at a fixed potential of +0.3 V were thus been performed. The corresponding anodic current followed the trend: fructose (65 µA cm^{-2}) > galactose (32 µA cm^{-2}) > glucose (20 µA cm^{-2}) > maltose (7 µA cm^{-2}) > sucrose (1 µA cm^{-2}), in agreement with previous studies [7]. The reasons for this trend can thus be related to the different availability of the free aldehyde group (see Scheme 1 of Fig. 1). This is also consistent with Fig. 1 where the absorbance of the AuNPs decreased in the same order of sugars, with the exception of fructose which was found to be less prone to reduce gold ions in solution. Fructose produced the highest current response but the lowest plasmon absorption band among the monosaccharides analyzed. The discrepancy of fructose can be explained easily. The homogeneous reaction of fructose with gold ions occurs only after its conversion to glucose

and mannose. This was confirmed in a control experiment, where fructose (2×10^{-4} M) was left in alkaline media until completely converted to the free aldehyde form, and then added to the gold solution: the plasmon absorption band obtained was comparable with the one obtained with an equivalent concentration of glucose and gold. The fact that sucrose showed the minimum absorbance and current is due to the unavailability of free aldehyde groups limiting its reaction with the gold salt. As expected the growth of AuNPs is pH limited was only observed in alkaline media (NaOH, 0.1 M), where transformation, of the non-reducible cyclic hemiacetal form of the sugar to the aldehyde form is favored. Next the analytical capabilities of using this reaction process to determine sugar concentrations in homogeneous solutions were analyzed.

The analytical capabilities of the detection methodology will depend on relevant reaction conditions, like concentration of the gold salt and CTAC components (affecting the stability and growth of AuNPs) and pH. All these factors were optimized using a linear multivariate analysis where the absorption peak generated by glucose (3×10^{-4} M) was the output to maximize. Results of this variance analysis revealed that all of the components are essential to stimulate growth of the AuNPs. The most favorable NPs spectral plasmon changes corresponded to AuCl$_4{}^-$ and CTAC concentrations, of 1×10^{-3} M and 3.7×10^{-3} M respectively, consistent with previous studies [6].

As the interaction of the sugar with Au salts is a chemical reaction it will have a defined rate constant, and it can be predicted that the quantity of AuNPs and hence analytical signal will increase with time. This would have beneficial effects when examining media with low sugar concentrations, as longer reaction times will produce lower limits of detection. This was observed performing the assay at a reaction time of 1 and 5 min, with different solutions of glucose in the concentration range up to 3×10^{-4} M. As expected, the limit of detection lower from 4.02×10^{-5} M to 2.45×10^{-5} M, with the limit of detection calculated by the propagation of error approach [7]. Also, longer reaction times affected the sensitivity and the coefficient of determination (linearity) of the assay. This is shown in Fig. 2a where the variation in sensitivity and the coefficient of determination is displayed *vs.* time. The results indicate that the longer the time of reaction the more sensible is the assay. This can be caused by the larger amount of particles produced in solution. Anyway, the growing of AuNPs is not linear over time, since
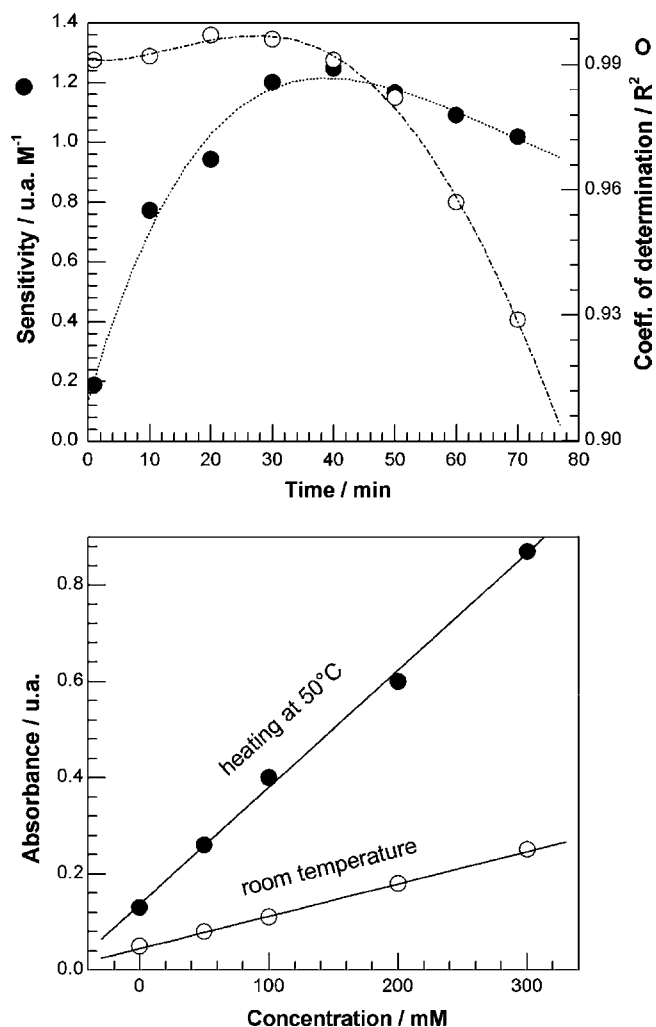
Fig. 2. (A) Effect of the reaction time on the sensitivity and coefficient of determination. Experimental: each point is pointed out from the regression analysis performed on five glucose solutions (from 0 to 3×10^{-4} M) at RT. (B) Effect of the reaction temperature on two regression analysis, performed on glucose solutions at RT and at 50 °C, after 5 min of reaction time. Other conditions as in Fig. 1.

Fig. 3. Effect of different pretreatment strategies. Experimental conditions: buffer composed as in Fig. 1. Samples of 1.5×10^{-4} M of glucose have been (A) heated up to 50 °C during 4.5 min and then cooled in ice bath; (B) heated up to 50 °C during 4.5 min and then cooled at 23 °C; (C) heated up to 50 °C during 4.5 min and then directly measured; (D) reaction at 23 °C.

the aggregation of AuNPs to form clusters can become significant and difficult to foresee.

To facilitate more rapid analysis time without affecting the assay linearity, the effect of temperature on the analytical signal was next investigated. It can be foreseen that the homogeneous reaction of the sugar with the gold salts would increase with elevated temperature. This is summarized in Fig. 2(b) where the calibration plot of the reaction of glucose with gold is shown. With a reaction time of 5 min, the slope of the calibration plot triples as the temperature rose from RT to 50 °C (0.7 u.a./mM and 2.4 u.a./mM, respectively). The rise in temperature can affect the limit of detection as well, this lowered at 9.7×10^{-6} M. It can be envisaged however that sampling at elevated temperatures is difficult and the method by which the sample is treated prior to recording may have an effect on the analytical signal. This was evident by leaving glucose solutions (up to 3×10^{-4} M) at 50 °C for 30 and 60 min. In this case, the relationship between sugar concentration and absorbance loses its linearity at concentration higher than 1×10^{-4} M. The nature of this effect can be partially related to the faster consumption of the gold salt in solution. Furthermore, at higher temperature for longer period of time, other components of the buffer (CTAC) can contribute to the growth of AuNPs.

Fig. 3 examines these issues, as it shows the sensitivity change for four different pretreatment strategies of the sample. In particular, glucose and gold ions were allowed to react (1) at 50 °C (4.5 min) and then cooled in ice bath; (2) at 50 °C (4.5 min) and then cooled at RT; (3) at 50 °C (4.5 min) and then measured; (4) at 23 °C and measured. Fig. 3 confirms how heating the reaction enhances analytical signal but it also shows that there is little deviation in the sensitivity when using the various heating/cooling strategies. Also, the more steps involved during the (1–3) experiments result in a higher variance of the assay than the (4) experiment, as highlighted by the error bars.

The effect of the reducing sugar on the hydrodynamic radius (Hr) of the AuNPs was next monitored using dynamic light scattering. It was found that the scattering intensity of gold nanoparticles solutions varied linearly with the concentration of glucose, indicating the presence of more AuNPs in the solution, however the Hr of the AuNPs was found to be independent of glucose concentrations and was 30 ± 5 nm. Furthermore, the radius was virtually independent of the reducing sugar used with average Hr of 35 ± 10 nm found when using glucose, fructose and galactose. This is consistent with the strength of CTAC capping agent being dominant force on the ultimate size of the AuNPs.

As mentioned above the scattering intensity of the AuNPs varied linearly with the sugar concentration in solution, therefore it would be expected that the absorbance maxima at 540 nm would follow the same trend. Fig. 4 shows how the AuNPs absorbance maxima enhances as a linear function of the glucose concentration, after 5 min of reaction ($y = 0.2360$ °C (u.a./mM), $R^2 = 0.999$). Specifically it displays the absorbance spectra of the AuNPs in the presence of variable concentrations of glucose (up to 1×10^{-3} M). It can be clearly seen that the peak wavelength is independent of glucose concentration and hence the particle size is concentration independent as discussed above.

This protocol can be easily extended for the sensing of disaccharides through the incorporation of enzymes into the sampling procedure. In this case, the disaccharide is enzymatically converted to the corresponding monosaccharide in acetate buffer (see inset
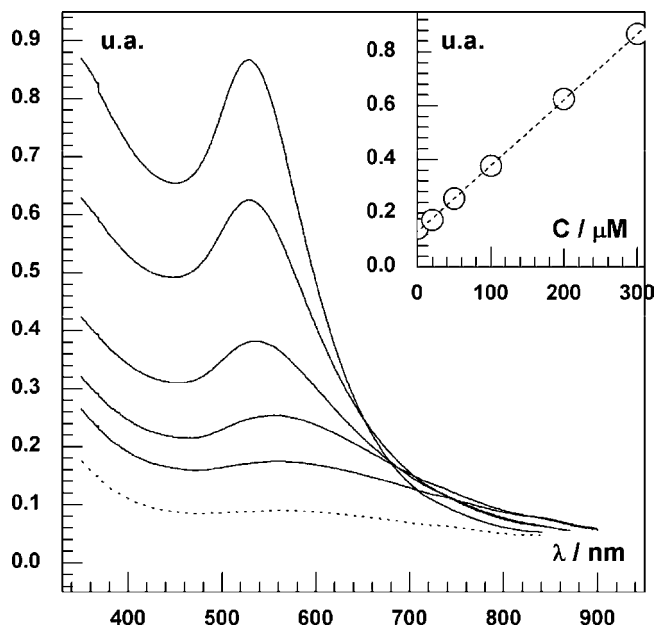
Fig. 4. Absorbance spectra for gold nanoparticles formed in the presence of different concentrations of glucose (0, 0.15, 0.5, 1, 2, and 3×10^{-4} M) after 5 min treatment at 50 °C. Also shown (inset) the corresponding calibration plots. Dotted line corresponds to the blank.

of Fig. 5). After addition of NaOH the enzymatic reaction stops, and the growth of gold nanoparticles proceeds. In the absence of invertase no analytical signal is observed, however in its presence, an absorbance wave is observed which increases with sucrose concentration. Fig. 5 shows the response of increasing concentrations of sucrose before and after its reaction with invertase.

The analytical utility of the homogeneous generation AuNPs by reducing sugars was evaluated qualitatively and quantitatively. Fig. 6 shows the qualitative sensorial assay performed on commercial food beverages. In detail, 20 honeys samples, 15 Coca-Cola
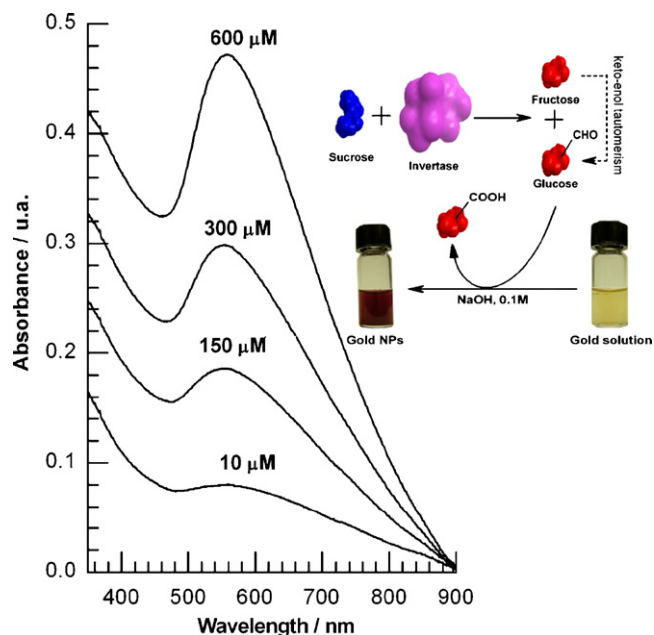
Fig. 6. Colour images of vials containing a blank solution of gold (A); Coca-Cola Zero (B); Coca-Cola Classic (C); honey (D). Photographs were taken after a 10-min reaction at RT. All samples were diluted 1:100. Other conditions as in Fig. 1.

Classic drink samples containing glucose (both used as known positives) and 12 diet Coca-Cola Zero drinks samples (used as known negatives) were added into an alkaline solution containing Au salt. The subsequent appearance of the purple color in less than 10 min was identified as a positive test. A negative test was identified when the sample remained uncolored. Negative or positive test were identified by the comparison of a blank solution, consisting of gold salt dissolved in NaOH 0.1 M. All the samples were diluted 1:100 with NaOH 0.1 M. The results obtained gave a sensitivity rate of 100% and a specificity rate of 92%, calculated as in Ref. [9].

The growth of AuNPs was also evaluated quantitatively, by comparison with the Fehling reference protocol for the analysis of honey samples. Fig. 7 shows the absorbance scan of different samples containing increasing amount of honey content after 5 min of reaction at RT. As inset, the corresponding mass calibration plot is shown. The absorption bands obtained are linearly related to the amount of honey introduced into the solution ($R^2 = 0.992$). The recovery was also calculated as relative difference between this assay and the Fehling reference protocol [8]. The result of $92 \pm 9\%$ ($n = 6$) demonstrates the suitability of the method for the rapid estimation of reducing sugars in complex matrices. Furthermore, the AuNPs assay

Fig. 5. Absorbance spectra for gold nanoparticles formed in the presence of different concentrations of sucrose subsequent to 20 min reaction with invertase at 25 °C. Also shown as inset the biocatalytic reaction scheme of the gold nanoparticles growth from sucrose and invertase.
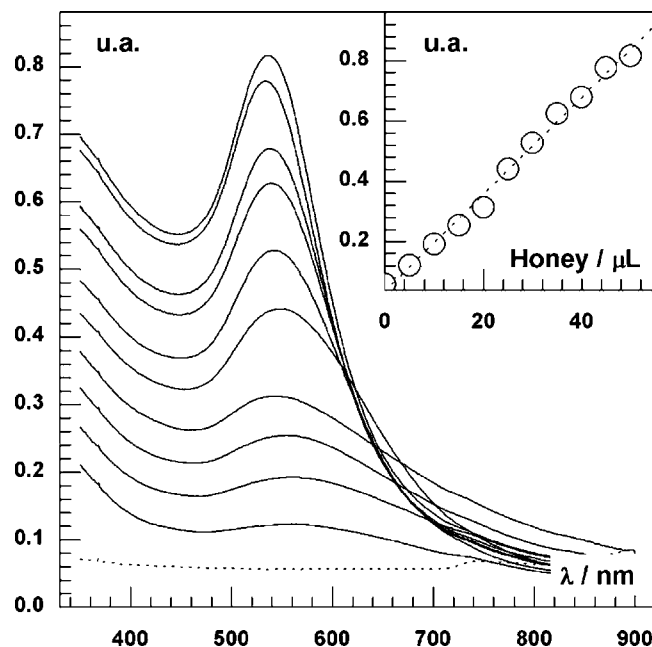
Fig. 7. Absorbance spectra for AuNPs formed in the presence of different volumes of honey (5 μL each) after 5 min treatment at 50 °C. As inset, also shown the corresponding calibration plot.

is faster then the Fehling since the heating step is not mandatory (in contrast with the Fehling). Also, the small amount of reagents consumption is a further advantage of the AuNPs assay.

4. Conclusion

In conclusion, we described a novel optical assay for the rapid and efficient detection of reducing sugars. The underlying chemistry behind the growth of AuNPs by some reducing sugars has been examined, where it was found that reducing sugars can generate AuNPs without the need for Au seeds. The ease of analysis using this facile homogenous reaction makes this technique promising strategy for use in sugar determinations in a wide range of industrial, biomedical and clinical applications. Further research is under development in our laboratory for manufacturing a disposable optical nanoprobe based on this assay.

References

[1] E.E. Connor, J. Mwamuka, A. Gole, C.J. Murphy, M.D. Wyatt, Small 1 (2005) 325.
[2] T. Pellegrino, S. Kudera, T. Liedl, A.M. Javier, L. Manna, W.J. Parak, Small 1 (2005) 48.
[3] J. Wang, Small 1 (2005) 1036.
[4] I. Willner, R. Baron, B. Willner, Adv. Mater. 18 (2006) 1109.
[5] M. Scampicchio, J. Wang, A.J. Blasco, A.S. Arribas, S. Mannino, A. Escarpa, Anal. Chem. 78 (2006) 2060.
[6] H. Mohammadi, A. Amine, M. El Rhazi, C.M.A. Brett, Talanta 62 (2004) 951.
[7] G.L. Long, J.D. Winefordner, Anal. Chem. 55 (1983) 712A.
[8] Kenneth Helrich, Official Methods of Analysis of the AOAC, 15th edition, 1990, Protocol 960.64.
[9] E. Trullols, I. Ruisánchez, X.F. Rius, TrAC 23 (2004) 137.

Short communication

Colorimetric and fluorescent sensing of biologically important fluoride in physiological pH condition based on a positive homotropic allosteric system

Jie Shao[a], Xudong Yu[a], Xiufang Xu[a], Hai Lin[b,*], Zunsheng Cai[a], Huakuan Lin[a,**]

[a] Department of Chemistry, Nankai University, Tianjin 300071, PR China
[b] Key Laboratory of Functional Polymer Materials of Ministry of Education, Nankai University, Tianjin 300071, China

ARTICLE INFO

ABSTRACT

A novel positive homotropic allosteric system 1 based on 3-methylpyrozole-5-one-4-one-2′,4′-dinitrophenylhydrazone was designed, synthesized and characterized. Colorimetric and fluorescent sensing of anions was achieved in physiological condition (pH 7.4), resulting from the positive homotropic allosterism of 1 induced by anions tested. In particular, the compound 1 exhibited a two-step response to the strong basic anions such as F⁻. In the first step, the hydrazone form of 1 interacted with anions through hydrogen bonding with an obvious color change from yellow to orange upon addition of 0.3 equiv. of anions. In the second step, with further addition of anions, the hydrazone form of 1 was shifted to the azophenol form, whose anion binding was accompanied with an orange-to-purple color change. In addition, the receptor 1 exhibited a fluorescent enhancement response to anions exploiting two possible signaling transduction mechanisms: (1) inhibition of photoinduced electronic transfer (PET) and (2) binding-induced rigidity of the host molecule.

1. Introduction

Anion recognition is an area of growing interest in supramolecular chemistry due to its important role in a wide range of environmental, clinical, chemical, and biological applications, and considerable attention has been focused on the design of host molecules that are able to selectively recognize and sense anion species [1,2]. Among the biologically important anions, halide ions are important analytes from biological and environmental aspects. For example, it has been well documented for some time that fluoride is associated with dental heath, and a great deal of interest has focused on its potential in treatment of osteoporoses [3]. Fluoride is easily absorbed but is excreted slowly from body, resulting in chronic poisoning. Acute gastric and kidney problems also result from overexposure to fluoride. The total number of people suffering from fluorosis (a debilitating bone disease) is not known, but a conservative estimate would number in the tens of millions [4]. As a result of these diversities, there is still an urge for design and synthesis of the artificial sensors for such anions.

Although large numbers of artificial receptors for anionic species have been reported, most of them work only in dry organic medium

not in aqueous medium [5–7]. The possible reasons are that (1) any electrostatic binding interactions are less effective due to anions are larger than their respective isoelectronic cations and hence possess a lower charge to radius ratio; (2) H_2O molecule would compete with anions for binding sites of the host owing to anions possess high solvation energy [8]. Particularly, a crucial issue is that anions would be protonated at low pH or be deprotonated at high pH [9]. For example, Hamachi and co-workers reported a series of chemosensors for nucleoside polyphosphates based on Zn(II) complex, which could effectively sense presence of analytes in the physiological pH conditions [10–12]. Consequently, there would still be a significant challenge for development of new neutral host molecules working in the physiological pH conditions [13,14].

In general, anion binding events could be translated into the output signals such as fluorescence, electrochemistry and UV–vis spectrum resulting from hydrogen binding interaction, anion-induced deprotonation of the host and/or chemical reaction of anion with the host [15–17]. There are rather few reports about colorimetric sensing of anions based on anion-induced tautomerism of the host molecules [18,19], although such tautomerism of the host induced by the guest has been applied on naked-eye detection of cations. As an example, Chung and co-workers [20,21] showed highly sensitive chromogenic sensors for Hg^{2+} ion based on calix[4]arenes derivatives. Before interactions with Hg^{2+} ion, the hosts existed as azophenol form and would be tautomerized into quinone–hydrazone form upon binding Hg^{2+} ion in a methanol–chloroform (v/v, 1/399) cosolvent. In particular, the biomimetic design of allosteric systems is of great importance, as
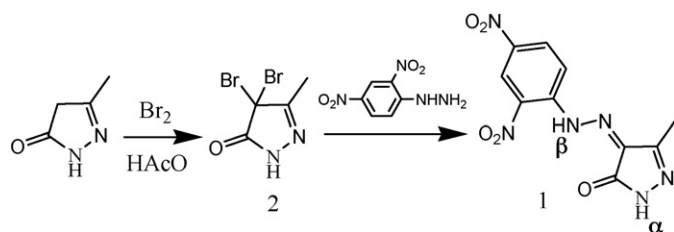
Scheme 1. Synthetic route to the compound 1.

they are readily applicable to the efficient regulation of capture and release of analytes, catalytic reactions, and information transduction to the remote site that are frequently seen in biological systems. From the viewpoint of constructing a molecular sensory system, the methodology is very useful to amplify, integrate, and convert the weak chemical or physical signals into other signals so that we can readily read out and record [22]. But it is very unlucky that the methodology is rarely applicable to design and synthesis of anion receptors [23].

With these in mind, we designed and synthesized a simple host compound 1 with pyrazole moiety as binding sites. Just as expected, the compound 1 could act as a colorimetric and fluorescent probe for anions. Upon exposure to excess strong basic anions such as F$^-$, the hydrazone form of the receptor 1 would be promoted to the azophenol form accompanying a color change from orange to purple. Interestingly, the receptor could succeed in colorimetric sensing of anions in the physiological conditions (pH 7.4), which could be rationalized on basis of the positive homotropic allosterism of 1.

2. Experimental

2.1. Apparatus

^{1}H NMR spectra and ^{13}C NMR spectra were obtained on a Varian UNITY Plus-400 MHz and a Varian UNITY Plus-300 MHz Spectrometer, respectively. ESI-MS was performed with a MARINER apparatus. C, H, N elemental analyses were made on an elementar vario EL. UV–vis spectra were recorded on a Shimadzu UV2450 Spectrophotometer with quartz cuvette (path length = 1 cm) and Fluorescent spectra were recorded on a Shimadzu RF-5301PC Spectrophotometer at 298.2 ± 0.1 K and the width of the slits used is 5 nm.

2.2. Chemicals

All reagents for synthesis obtained commercially were used without further purification. In the titration experiments, all the anions were added in the form of tetrabutylammonium (TBA) salts, which were purchased from Sigma–Aldrich Chemical, stored in a vacuum desiccator containing self-indicating silica and dried fully before using. DMSO was dried with CaH$_2$ and then distilled in reduced pressure. HEPES (4-(2-hydroxyerhyl)piperazine-1-erhanesulfonic acid) is used as a buffer reagent.

2.3. Synthesis

2.3.1. 4,4-Dibromo-3-methyl-pyrazol-5-one (2)

The compounds 1 and 2 were synthesized according to Scheme 1. The compound 2 was synthesized according to the procedure reported [24]. To a solution of 3-methyl-pyrazol-5-one (1.96 g, 0.01 mol) in CH$_3$COOH (8 ml) was added dropwise a solution of Br$_2$ (3.2 g, 0.02 mol) in CH$_3$COOH (4 ml) when stirring. The resulting mixture was stirred and refluxed at 60 °C for 4 h. After that, the

reaction mixture was poured into the ice-cold water and the precipitate was filtered, washed by water and then recrystallized from ethanol to give the white solid. ^{1}H NMR (400 MHz, DMSO-d_6, 25 °C, TMS): δ 2.21 (s, 3H, –CH$_3$), 10.97 (s, 1H, –NH).

2.3.2. 3-Methylpyrozole-5-one-4-one-2′,4′-dinitrophenylhydrazone (1)

4,4-Dibromo-3-methyl-pyrazol-5-one (2.52 g, 0.01 mol) and 2,4-dinitrophenylhydrazine (1.98 g, 0.01 mol) were dissolved in ethanol (50 ml) and then refluxed for 24 h under magnetic stirring. Ethanol was removed under reduced pressure and the resulting mixture was neutralized with 5% NaHCO$_3$ to give the precipitate and the pure product was obtained by recrystallizing from methanol. ^{1}H NMR (400 MHz, DMSO-d_6, TMS): δ 2.22 (s, 3H, –CH$_3$), 8.28 (d, 1H, J = 9.2 Hz, H–Ar), 8.58 (m, 1H, H–Ar), 8.92 (d, 1H, J = 2.8 Hz, H–Ar), 11.96 (s, 1H, –NH), 14.49 (s, 1H, H–Py). ^{13}C NMR (75 MHz, DMSO-d_6, TMS,): δ 11.7, 117.3, 122.2, 130.2, 133.3, 135.6, 141.2, 142.5, 147.2 and 159.1. Elemental analysis calcd for C$_{10}$H$_8$N$_6$O$_5$: C, 41.10; H, 2.76; N, 28.76. Found: C, 41.10; H, 2.75; N, 28.79. ESI-mass: m/z calcd. for C$_{10}$H$_8$N$_6$O$_5$ [M−H]$^-$: 291.06, found 291.70 [M−H]$^-$.

3. Results and discussion

3.1. UV–vis titrations in organic medium

The anion binding ability of the receptor 1 was evaluated through UV–vis titrations by adding a standard solution of the tetrabutylammonium salt of anions to a dry DMSO solution of the sensor at 298.2 ± 0.1 K. The acidity of –NH group was greatly improved because of two –NO$_2$ electron-withdrawing substituents and thus the hydrazone form of the receptor 1 would be easily shifted to the azophenol form upon presence of the strong basic anions. Fig. 1 demonstrated UV–vis spectral changes of 1 (1×10^{-5} M) in absence and presence of fluoride ions (or see S1 in supporting information). As expected, UV–vis fluoride titration spectra of the compound 1 indeed exhibited stepwise changes. First, with the addition of F$^-$ up to 0.3 molar equiv, the absorption band at 356 nm decreased gradually and a new absorption band at 552 nm appeared, accompanied with a color change of the solution from yellow to orange (see Fig. 2). The 196 nm red-shifted band (from 356 to 552 nm) could be ascribed to intramolecular charge-transfer between the electron rich –NH group bond anion and the electron deficient –NO$_2$ moiety [25]. In addition, there was a well-defined isosbestic point at 461 nm indicating the stable complex was obtained with a certain stoichiometric ratio between the hydrazone form and F$^-$ [26]. The Job plots indicated that 1:1 host–guest complex was formed between the azophenol form and F$^-$ With Origin program, non-linear fitting analyses of the titration curves gave the $K_{ass}^1 = 2.93 \times 10^6$ M^{-1} for the first-step changes (the association constant of the hydrazone form with F$^-$). Second, with further addition of F$^-$ (up to 8 equiv. F$^-$), there was an increase in the intensity of absorption band at 459 nm and meanwhile color of the solution changed from orange to purple. The results demonstrated the presence of fluoride ion induced the configurational change of the sensor 1 from the hydrazone form to the azophenol form, which would be discussed further in ^{1}H NMR titrations. And the azophenol form of 1 could interact with F$^-$ ion through six-member intermolecular hydrogen bonding (see Scheme 2). In this step, the Job plots (Fig. 3) indicated that 1:1 host–guest complex was formed between the azophenol form and F$^-$. With the same method, the second-step association constant (the association constant of the azophenol form with F$^-$) was determined to be $K_{ass}^2 = 1.36 \times 10^4$ M^{-1}. In the case of the other strong basic anions tested such as AcO and H$_2$PO$_4$$^-$, similar spectral changes were observed during the titration experiment (see SX in supporting
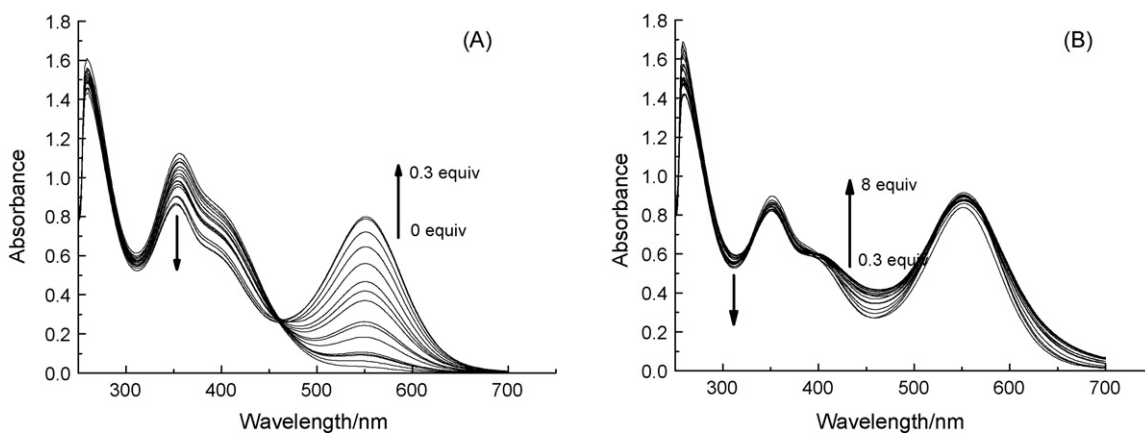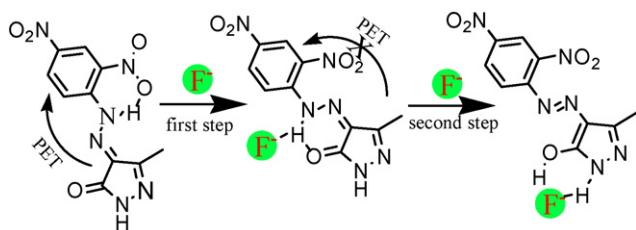
Fig. 1. Changes in the UV–vis spectra for the receptor 1 (1×10^{-5} M) in DMSO solution with addition of (A) from 0 to 0.3 equiv. and (B) from 0.3 to 8 equiv.

Scheme 2. The anion binding behaviors of the receptor 1 and its signaling transduction mechanism.

Fig. 2. The color changes of the receptor 1 (1×10^{-5} M) with different fluoride concentrations in DMSO. From left to right: (a) only 1; (b) 0.05 equiv. of F^-; (c) 3 equiv. of F^-.
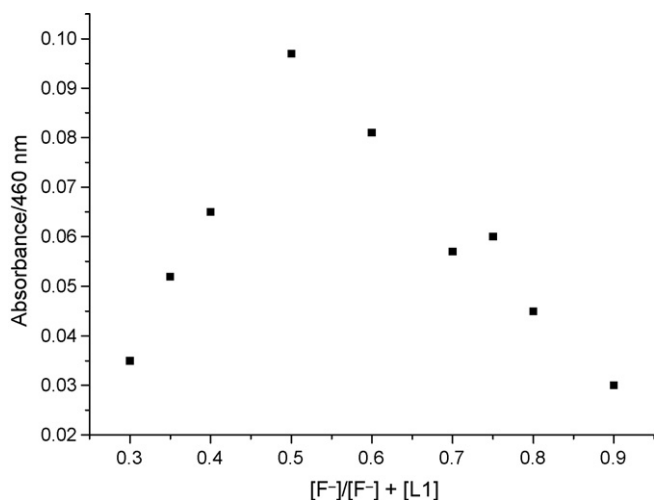

Fig. 3. Job plots of the receptor 1 with fluoride ($[F^-] + [L1] = 1 \times 10^{-5}$ M).

information). However, the spectral changes resulting from the configurational change of the compound 1 were in disorder so that the K_{ass}^2 could not be obtained, which could be attributed to absence of the stable complex with a certain stoichiometric ratio between the azophenol form and AcO^- and $H_2PO_4^-$. Unlike F^-, AcO^- and $H_2PO_4^-$ could not interact with 1 through stable six-member intermolecular H-bond. In particular, the receptor 1 was insensitive to excess equiv of the weak basic anions such as Cl^-, Br^- and I^- (see Fig. 4).

3.2. Titration of F^- from aqueous medium

It is well known that most anions exist in aqueous solution and therefore it is very important the host molecule has anion sensing ability in aqueous solution, especially in the physiological conditions (pH 7.4). In order to examine the potential application for analytical chemistry, the receptor 1 was applied in detection of biologically important anions in the physiological pH conditions. HEPES (20 mM) is used as buffer reagent. Obviously seen from Fig. 5A, there was a decrease in the absorption band at 356 nm and formation of a new band at 546 nm upon addition of 3 equiv. of fluoride. In this step, the association constant of the hydrazone form with F^- in aqueous solution was obtained to be $1.00 \times 10^4\ M^{-1}$. With further addition of fluoride, the spectrum of the receptor 1 exhibited slight changes, which were not similar with spectral changes in the first step (see Fig. 5B), so that the second-step asso-
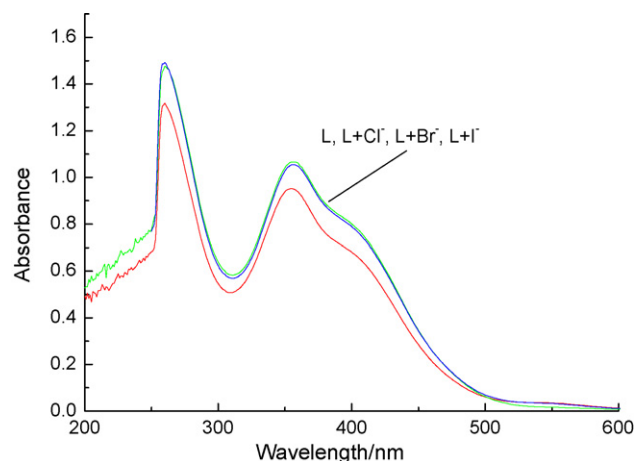
Fig. 4. UV–vis spectral changes of the receptor 1 (1×10^{-5} M) induced by addition of excess equiv of the other anions tested such as Cl^-, Br^- and I^- in DMSO.
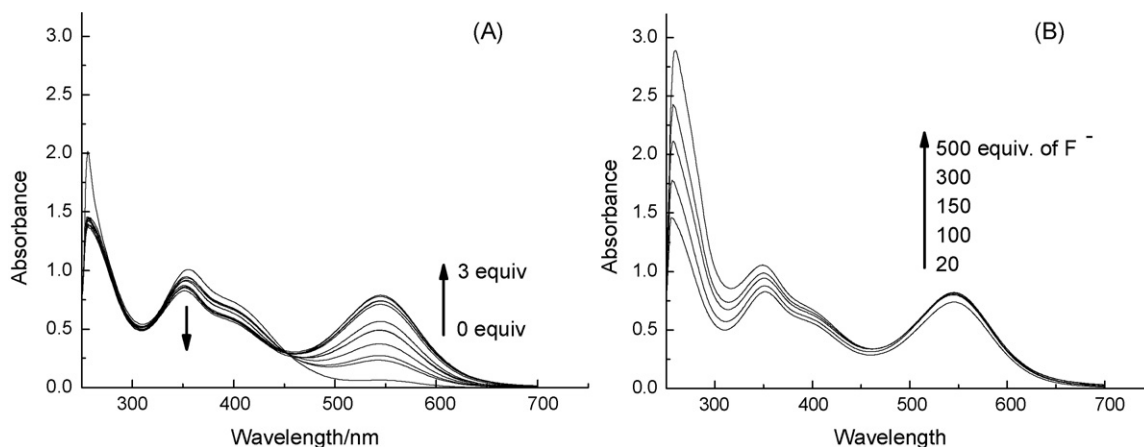
Fig. 5. Changes in the UV–vis spectra for the receptor 1 (1×10^{-5} M) in aqueous solution (DMSO/H$_2$O = 90:10, v:v; buffer solution: HEPES 20 mM) with addition of (A) from 0 to 3 equiv. and (B) from 3 to 500 equiv.

ciation constant was not calculated. The possible explanation for this result might be as follow. There were two possible intramolecular hydrogen bonding between the –NH unit and the –NO$_2$ unit or the –NH moiety and the –C=O moiety in the configuration of 1 (see Scheme 2). To support further occurrence of two type of intramolecular H-bond, unconstrained optimization for the receptor 1 were calculated at B3LYP/6-31G* by using Guassian 03 program. The result indicated that it was prone to form intramoleclar hydrogen bonding between –NH and the oxygen atom of –NO$_2$ not between –NH and the oxygen atom of –C=O, because the distance between –NH and the oxygen atom of –NO$_2$ (1.849 Å) is shorter than that between –NH and the oxygen atom of –C=O (1.926 Å, see Supporting information). Upon addition of F$^-$, the hydrazole form interacted with F$^-$ through hydrogen bonding, which resulted in increase in the electron density of the nitrogen atom linking the binding site and as a result the hydrazole form would be shifted to the azo form. The configuration of the azophenol form is coplanar, which would promote intramolecular charge transfer. However, such positive homotropic allosteric effect was not involved in interactions between the azophenol form and F$^-$, and therefore, the association constant of the hydrazone form with F$^-$ was larger than that of the azophenol form not only in organic medium but also in aqueous medium.

3.3. Fluorescent titrations

The anion binding behavior of the probe 1 was investigated by fluorescent titrations in DMSO. Obviously, the compound 1 exhibited two weak fluorescent emission peaks at 377 and 396 nm, respectively, with a shoulder emission band at 418 nm (see Fig. 6) upon excitation at 340 nm. Upon addition of fluoride ions, there was a significant increase in the emission intensity of 1. Such fluorescent enhancement could be rationalized on basis of two possible signaling transduction mechanisms: (1) inhibition of photoinduced electronic transfer (PET) [27,28] and (2) binding-induced rigidity of the host molecule [29,30]. Before complexation with anions, there was a photoinduced electronic transfer from the pyrazole unit (a fluorophore) to the electron-withdrawing substituent (–NO$_2$), resulting in a weak emission. Upon binding anions, the above-mentioned PET would be inhibited and as a result, a fluorescent enhancement was observed. In addition, it has been well shown that complexation-induced rigidity of a fluorescent receptor has been reported to result in a large increase in emission intensity because of inhibiting vibrational and rotational relaxation modes of non-radiative decay (see Scheme 2).

3.4. ^{1}H NMR titrations

To shed a light on the nature of the interaction between anions tested and the receptor, ^{1}H NMR titrations were carried out in DMSO-d_6. Fig. 7 showed ^{1}H NMR spectral changes of the receptor 1 (5×10^{-3} M) in DMSO-d_6 in the absence and presence of different equiv of fluoride ions. Obviously, before addition of 0.3 equiv. of F$^-$, the proton signal of the hydrazone group at 11.96 ppm broadened gradually, however, no change was observed in the proton signal of the pyrazole group at 14.49 ppm, which demonstrated that the receptor 1 complexed F$^-$ through hydrogen bonding interactions with the hydrazone –NH$_\beta$ not the pyrazole –NH$_\alpha$ [31]. With further addition of F$^-$, the resonance signal of the hydrazone moiety broadened further and disappeared and the resonance signal of the pyrazole –NH$_\alpha$ also broadened gradually. In particular, a new signal peak at 10.47 ppm appeared, being ascribed to the signal of –OH of the isomer of 1. Obviously, the proton signals at 8.28, 8.58 and 8.92 ppm shifted upfield, which resulted from disappearance of the hydrazone moiety when excess F$^-$ ions were added [31]. The resulted showed that the compound 1 exhibited a configurational change from the hydrazone form to the azophenol form and finally –OH of the azophenol form and –NH$_\alpha$ of the pyrazole cooperatively interacted with F$^-$ ions through hydrogen bonding (see Scheme 2), which also supported the hypothesis obtained according to the results of UV–vis titrations.
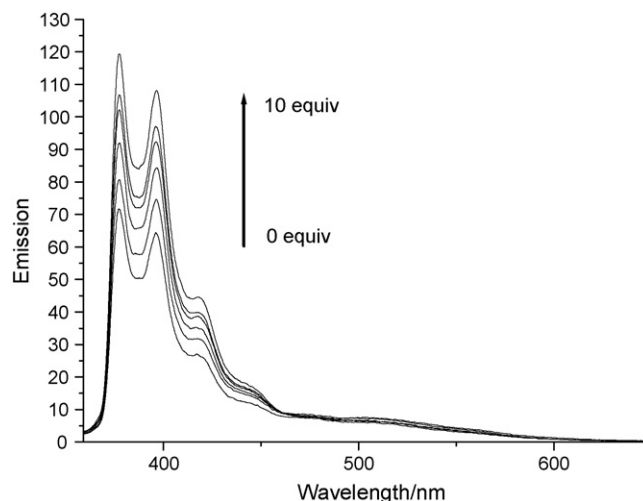

Fig. 6. Evolution of fluorescent emission spectra of the receptor 1 (1.0×10^{-5} M in DMSO) during the titration with F$^-$ (excitation at 340 nm and slit width is 5 nm).
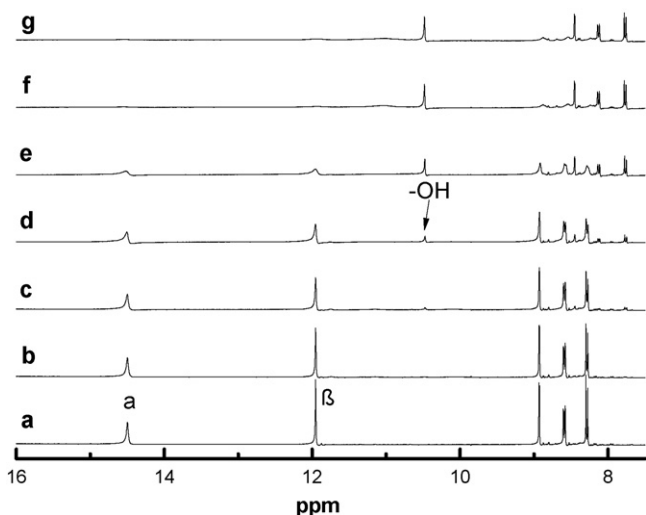
Fig. 7. Changes in the ^{1}H NMR spectra with gradual addition of F$^-$ in DMSO-d_6. (a) Only 1 equiv, (b) 0.1 equiv, (c) 0.2 equiv, (d) 0.3 equiv, (e) 1 equiv, (f) 2 equiv and (g) 3 equiv. of F$^-$.

4. Conclusions

In conclusion, a positive homotropic allosteric system has been successfully exploited for colorimetric and fluorescent detection of biological important anions in physiological pH condition. The biomimetic design of allosteric systems for anion sensing not only can significantly improve the affinity of the host for anionic guest but also can make the weak chemical or physical signals to be amplified so that we can readily read out and record. As a result, the receptor 1 based on a positive homotropic allosteric system have successfully detected anions in physiological pH condition. Such methodology would be expected to help to extend the development of colorimetric and fluorescent sensors for biologically anions in aqueous medium.

Acknowledgements

References

[1] S.O. Kang, R.A. Begum, K. Bowman-James, Angew. Chem. Int. Ed. 47 (2006) 7882.
[2] V. Luxami, N. Sharma, S. Kumar, Tetrahedron Lett. 49 (2008) 4265.
[3] J. Shao, M. Yu, H. Lin, H.K. Lin, Spectrochim. Acta A 70 (2008) 1217.
[4] E. Galbraith, T.M. Fyles, F. Marken, M.G. Davidson, T.D. James, Inorg. Chem. doi:10.1021/ic800204q.
[5] J. Shao, H. Lin, H.K. Lin, Talanta 77 (2008) 273.
[6] W. Yang, Z. Yin, C.H. Wang, C. Huang, J. He, X. Zhu, J.P. Cheng, Tetrahedron 64 (2008) 9244.
[7] T. Gunnlaugsson, M. Glynn, G.M. Tocci (née Hussey), P.E. Kruger, F.M. Pfeffer, Coordin. Chem. Rev. 250 (2006) 3094.
[8] E. Galbraith, T.M. Fyles, F. Marken, M.G. Davidson, T.D. James, Inorg. Chem. 47 (2008) 6236.
[9] A. Ojida, I. Takashima, T. Kohira, H. Nonaka, I. Hamachi, J. Am. Soc. Chem. 130 (2008) 12095.
[10] A. Ojida, Y. Miyahara, J. Wongkongkatep, S. Tamaru, K. Sada, I. Hamachi, Chem. Asian J. 1 (2006) 555.
[12] A. Ojida, H. Nonaka, Y. Miyahara, S. Tamaru, K. Sada, I. Hamachi, Angew. Chem. Int. Ed. 45 (2006) 5518.
[13] J. Shao, H. Lin, H.K. Lin, Talanta 75 (2008) 1015.
[14] J. Shao, H. Lin, M. Yu, Z.S. Cai, H.K. Lin, Talanta 75 (2008) 551.
[15] T. Mizuno, W.H. Wei, L.R. Eller, J.L. Sessler, J. Am. Chem. Soc. 124 (2002) 1134.
[16] V. Amendola, D. Esteban-Gomez, L. Fabbrizzi, M. Licchelli, Acc. Chem. Res. 39 (2006) 343.
[17] D.G. Cho, J.H. Kim, J.L. Sessler, J. Am. Chem. Soc. 130 (2008) 12163.
[18] J. Shao, Y.H. Wang, H. Lin, J.W. Li, H.K. Lin, Sens. Actuators B: Chem. 234 (2008) 849.
[19] J. Shao, H. Lin, H.K. Lin, Dyes Pigments 80 (2009) 259.
[20] T.L. Kao, C.C. Wang, Y.T. Pan, Y.J. Shiao, J.Y. Yen, C.M. Shu, G.H. Lee, S.M. Peng, W.S. Chung, J. Org. Chem. 70 (2005) 2912.
[21] I.T. Ho, G.H. Lee, W.S. Chung, J. Org. Chem. 72 (2007) 2434.
[22] M. Takeuchi, M. Ikeda, A. Sugasaki, S. Shinkai, Acc. Chem. Res. 34 (2001) 865.
[23] L. Nie, Z. Li, J. Han, X. Zhang, R. Yang, W.X. Liu, F.Y. Wu, J.W. Xie, Y.F. Zhao, Y.B. Jiang, J. Org. Chem. 69 (2004) 6449.
[24] S. Singh, K. Husain, F. Athar, A. Azam, Eur. J. Pharm. Sci. 25 (2005) 255.
[25] J. Shao, H. Lin, X.F. Shang, H.M. Chen, H.K. Lin, J. Incl. Phenom. Macrocycl. Chem. 59 (2007) 371.
[26] K.A. Connors, Binding Constants, 1st edn., John Wiley & Sons, New York, 1987.
[27] J. Shao, Y.H. Qiao, H. Lin, H.K. Lin, J. Lumin. 128 (2008) 1985.
[28] T. Gunnlaugsson, A.P. Davis, J.E. O'Brien, M. Glynn, Org. Lett. 4 (2002) 2449.
[29] S. Watanabe, O. Onogawa, Y. Komatsu, K. Yoshida, J Am. Chem. Soc. 120 (1998) 229.
[30] S.A. McFarland, N.S. Finney, J. Am. Chem. Soc. 123 (2001) 1260.
[31] Z.H. Lin, Y.G. Zhao, C.Y. Duan, B.G. Zhang, Z.P. Bai, Dalton Trans. (2006) 3678.

An approach by using near-infrared diffuse reflectance spectroscopy and resin adsorption for the determination of copper, cobalt and nickel ions in dilute solution

Nan Sheng, Wensheng Cai, Xueguang Shao*

Research Center for Analytical Sciences, College of Chemistry, Nankai University, Tianjin, 300071, PR China

ABSTRACT

Near-infrared spectroscopy (NIRS) has been proved to be a powerful analytical tool and used in various fields, it is seldom, however, used in the analysis of metal ions in solutions. A method for quantitative determination of metal ions in solution is developed by using resin adsorption and near-infrared diffuse reflectance spectroscopy (NIRDRS). The method makes use of the resin adsorption for gathering the analytes from a dilute solution, and then NIRDRS of the adsorbate is measured. Because both the information of the metal ions and their interaction with the functional group of resin can be reflected in the spectrum, quantitative determination is achieved by using multivariate calibration technique. Taking copper (Cu^{2+}), cobalt (Co^{2+}) and nickel (Ni^{2+}) as the analyzing targets and D401 resin as the adsorbent, partial least squares (PLS) model is built from the NIRDRS of the adsorbates. The results show that the concentrations that can be quantitatively detected are as low as 1.00, 1.98 and 1.00 mg L^{-1} for Cu^{2+}, Co^{2+} and Ni^{2+}, respectively, and the coexistent ions do not influence the determination.

© 2009 Elsevier B.V. All rights reserved.

1. Introduction

Near-infrared spectroscopy (NIRS) in combination with chemometrics has been proved to be a convenient, fast and non-destructive quantitative method for complex samples [1–8]. Therefore, NIRS has been widely adopted in the fields of agriculture [9–11], petrochemicals [12,13] and pharmaceuticals [14–17]. This technique, however, has the disadvantage not suitable for micro-analysis or trace analysis because of the low molar absorptivity of NIRS signals. Recently, quantitative analysis of the adsorbates by diffuse reflectance FT-IR [18], UV–vis [19] and NIR [20] spectroscopy with preconcentration of the analytes in a dilute solution has been reported. In our previous work, near-infrared diffuse reflectance spectroscopy (NIRDRS) in combination with the preconcentration procedure has also investigated for the determination of low concentration analytes in beverage [21]. In these combination techniques, the extracted analytes are directly determined. As no elution step is required, analyte dilutions and consumption of organic solvents are avoided. Moreover, these techniques simplify and speed up the analytical procedures.

Metal contamination in water is a problem of global concern because it can usually accumulate to toxic levels [22]. Determination of metal content serves as an important step in ecosystem condition monitoring and pollution control [23–25]. Frost et al. [26–28] estimated the contents of some transition metals in minerals with NIRS originated from the d–d transitions. Theoretically, however, most of inorganic compounds cannot give a direct signature in NIR spectra, especially in solution or low content samples. Therefore, NIRS is seldom used in quantitative analysis of metal ions. Nevertheless, prediction of metal ion contents can still be performed by NIRS because the interaction of metal ions and organic compounds or hydrated inorganic molecules can be reflected in NIR spectra [29–34]. Therefore, the estimation of metals by NIRS is generally dependent on the mixture generated by certain function bonds between those elements and organic or hydrated compounds, which can be detected in the spectral range of NIRS [29,30]. For instance, several elements in wine were successfully determined by NIRS [35–37]. In these works, determination of metals in solution by using NIRS is due to the changes in the localized hydrogen bonding around the metal cations in solution [35].

In this study, a method for quantitative analysis of metal ions is proposed. The ions are preconcentrated onto an adsorbent from a complex solution, and then the adsorbent is analyzed by NIRDRS. Although the information of the ions cannot been obviously seen in the spectra, their contents can be quantitatively predicted by a multivariate model, because both the spectral information of the ions and their interaction with the adsorbent is included in the spectra. Metal ions Cu^{2+}, Co^{2+} and Ni^{2+} are used as the analyzing targets. Commercially available D401 resin is used as the adsorbent for collecting the analytes. Partial least squares (PLS) regression [38,39] is

---

* Corresponding author. Tel.: +86 22 23503430; fax: +86 22 23502458.
E-mail address: xshao@nankai.edu.cn (X. Shao).

adopted as the calibration tool due to the complexity of the spectra. The main purpose of this work is to investigate the feasibility of the quantitative determination of metal ions in complex dilute solution by using NIRDRS.

2. Experimental

2.1. Reagents and adsorbent

All chemical reagents are of analytical purity grade. Doubly distilled water was used to prepare the samples. Macroporous styrene iminodiacetic acid chelating resin D401 was purchased from Nankai Hecheng Chemical Co., Ltd. (Tianjin, China), its functional group is $-N(CH_2COONa)_2$, bead size is 0.315–1.25 mm, moisture content is 45–55%, maximum operating temperature is 100 °C, and pH range is 1.0–14.0.

2.2. Samples preparation

42 mixtures of Cu^{2+}, Co^{2+} and Ni^{2+} were prepared with doubly distilled water as solvent. The concentration ranges of Cu^{2+}, Co^{2+} and Ni^{2+} were 1.00–32.97, 1.98–37.07 and 1.00–36.02 mg L^{-1}, respectively. Zn^{2+}, Pb^{2+}, Ca^{2+}, Mg^{2+}, K^+ and Li^+ with concentration range of 2.00–50 mg L^{-1} was added to the solution as interfering ions. The 42 samples were taken as calibration set for building the PLS models.

Then, 12 mixtures of Cu^{2+}, Co^{2+} and Ni^{2+} were prepared with river water as solvent. The pH of local river water was around 6.0 and there were some laurel-green suspended solids which were filtered before use. The Cu^{2+}, Co^{2+} and Ni^{2+} contents of raw river water were found to be 0.056, 0.25 and 2.73 mg L^{-1} by using inductively coupled plasma-atomic emission spectrometry (ICP-AES ICP-9000 (N + M), USA Thermo Jarrell-Ash Corp.). Meanwhile, there are large amounts of coexisting elements in raw river water such as Na^+ 244.9 mg L^{-1}, K^+ 24.44 mg L^{-1}, Ca^{2+} 100.8 mg L^{-1}, Mg^{2+} 59.19 mg L^{-1}. Different levels of Cu^{2+}, Co^{2+} and Ni^{2+} are added to the 12 river water samples so that they can be detected by the proposed method. The total concentration ranges of Cu^{2+}, Co^{2+} and Ni^{2+} were 8.05–30.04, 9.24–34.22 and 6.53–34.58 mg L^{-1}. The 12 river water samples were taken as validation set. The statistics of the Cu^{2+}, Co^{2+} and Ni^{2+} content of the samples are listed in Table 1.

2.3. Adsorption operation

The adsorption operation was performed with 100 mL of the aforementioned solutions and ca. 2.0 g D401 resin in a flask at room temperature (ca. 26 °C) for 20 min with the aid of ultrasonic vibration. After the adsorption, the cloudy solutions were filtered with the aid of vacuum pump. The solid surface moisture was carried away by adding 15 mL ethanol at the end of the filtration. Finally, the resin with the adsorbates was used for NIR spectral measurement. It should be noted that a large variety of resins and other adsorbents should be used for this study, D401 resin was adopted because it is a commonly used adsorbent.

Table 1
Statistics of the concentrations (mg L^{-1}) of the calibration and validation samples.

Analyte	Calibration				Validation			
	n[a]	Range	Mean	S.D.[b]	n	Range	Mean	S.D.
Cu^{2+}	42	1.00–32.97	19.65	9.54	12	8.05–30.04	19.88	6.75
Co^{2+}	42	1.98–37.07	22.05	10.91	12	9.24–34.22	24.06	8.54
Ni^{2+}	42	1.00–36.02	21.11	10.84	12	6.53–34.58	24.07	9.83

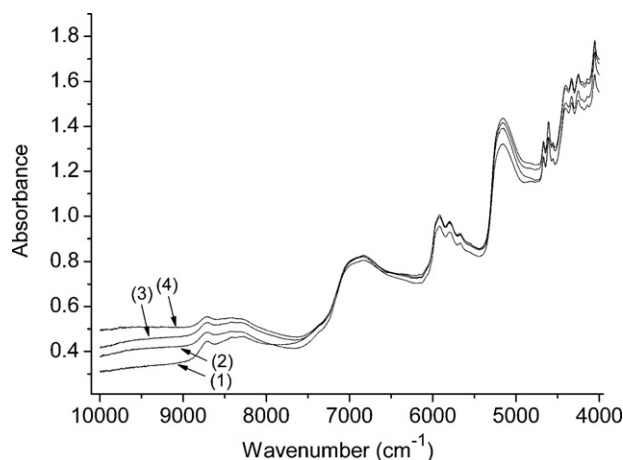[a] n = sample numbers.
[b] S.D. = standard deviation.

Fig. 1. NIR spectra of a blank resin sample (1) and three arbitrarily selected samples (2, 3 and 4).

2.4. NIR spectral measurement

All NIR spectra were measured from 4000 to 10,000 cm^{-1} with a Vertex 70 spectrometer (Bruker, Ettlingen, Germany) in diffuse reflectance mode with a near-infrared integrating sphere diffuse reflection accessory (Bruker, Ettlingen, Germany). The spectra are digitalized with ca. 2 cm^{-1} interval in the Fourier transform, so each spectrum is composed of 3111 data points. A reference spectrum was taken before the measurement of each sample with the standard material provided within the spectrometer, i.e., the gold-coated background. To increase signal to noise ratio, both reference and sample spectra were measured with scan number 64, and each spectrum was averaged from three parallel measurements. The temperature was balanced at ca. 26 °C for 12 h before the measurements. Fig. 1 shows the measured NIR spectra of a blank resin sample without the adsorbate and three arbitrarily selected samples. Nine ions of Cu^{2+}, Co^{2+}, Ni^{2+}, Zn^{2+}, Pb^{2+}, Ca^{2+}, Mg^{2+}, K^+ and Li^+ are included in the samples. 13.98, 23.72, 31.51; 14.98, 33.12, 32.02; 31.47, 33.61, 32.52 mg L^{-1} Cu^{2+}, Co^{2+}, Ni^{2+} and different concentration of the interfering ions mentioned above are included in the adsorption solution for three selected samples, respectively. From Fig. 1 it can be seen that there is no obvious change in the spectra after the adsorption of the ions. It is difficult to use the ordinary calibration method for quantitative analysis. Therefore, multivariate calibration was used in this study.

2.5. PLS modeling

PLS regression was used for modeling and prediction. The modeling was performed with the software package OPUS 6.0 (Bruker, Ettlingen, Germany). 42 samples were taken as calibration set for building the PLS models, the 12 artificial river water samples were used for validation of the practicability of the method for analyzing the samples with complex matrix.

The performance of the PLS regression model was evaluated in terms of the correlation coefficients (R), and root mean square error of cross validation (RMSECV), which were determined by leave-one-out cross validation (LOO-CV). For the validation set, correlation coefficients (R) and standard deviation (S.D.) between the reference and prediction concentration was used to estimate the prediction of the developed models. The factor number for PLS model was determined by using the LOO-CV with F-test [40]. Furthermore, due to the drifting baseline or background in the spectra (Fig. 1), signal processing techniques such as straight line subtraction, derivative calculation, standard normal variate (SNV)
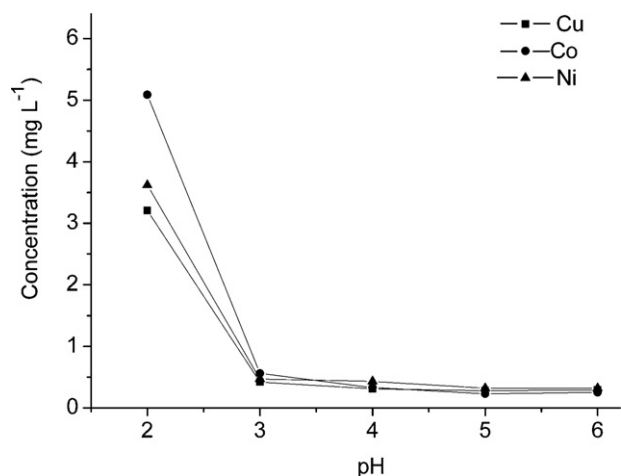
Fig. 2. Effect of pH on the adsorption of Cu^{2+}, Co^{2+} and Ni^{2+} onto 2.0 g resin with 20 min adsorption time.

Fig. 3. Effect of time on the adsorption of Cu^{2+}, Co^{2+} and Ni^{2+} onto 2.0 g resin at pH 5.5.

and multiplicative scatter correction (MSC) were used to obtain an optimized PLS model.

3. Results and discussion

3.1. Effect of sorbent dosage

Sorbent dosage affects not only the spectral reproducibility, but also the quantity of absorptive solutes. Three parallel spectra were recorded for the blank resin samples of different quantity (ca. 0.5, 1.0, 1.5 and 2.0 g), respectively. The mean squared error (MSE) of the three parallel spectra with their mean spectrum was calculated for evaluation of reproducibility. The MSEs of the parallel spectra for the four different resins quantity were 1.36×10^{-3}, 1.16×10^{-3}, 1.12×10^{-3} and 1.10×10^{-3}, respectively. It can be seen that there is a slight improvement in the reproducibility with the increase of the sorbent dosage from 0.5 to 2.0 g. Therefore, 2.0 g sorbent was used in this study.

3.2. Effect of adsorption conditions

In order to investigate the effects of pH on adsorption efficiency, experiments are conducted in the pH range from 2.0 to 6.0, which was adjusted with diluted hydrochloric acid and diluted

sodium hydroxide. In the experiment, 2 g adsorbent, 20 min adsorption time and 100 mL 14.97 mg L^{-1} Cu^{2+}, 15.03 mg L^{-1} Co^{2+} and 15.07 mg L^{-1} Ni^{2+} solution were used, respectively. Fig. 2 shows the variation of the Cu^{2+}, Co^{2+} and Ni^{2+} concentrations, respectively, of the solution after adsorption under different pH conditions. The concentrations were determined with ICP-AES as mentioned in Section 2. It is clear that almost all the analyte in the solutions is adsorbed onto the adsorbent at pH 3.0–6.0. Therefore, the pH of the raw solutions (ca. 5.5) is used for the adsorption without adjusting.

For understanding the effect of adsorption time on the adsorption efficiency, the variation of the adsorbate quantity with different adsorption time was investigated at pH 5.5. Fig. 3 shows the variation of the Cu^{2+}, Co^{2+} and Ni^{2+} concentrations, respectively, of the solution after different adsorption time. In the experiment, adsorption time varies from 5 to 40 min, 2 g adsorbent and 100 mL 14.97 mg L^{-1} Cu^{2+}, 15.03 mg L^{-1} Co^{2+} and 15.07 mg L^{-1} Ni^{2+} solution were used, respectively. It is clear that the concentration of the solutions decreases significantly with the increase of adsorption time, and after 20 min, almost all the analyte is adsorbed onto the adsorbent. The adsorption rates for the three ions were found to be 97.80%, 97.41% and 96.89%, respectively. Therefore, 20 min was adopted for adsorption in this study.

Table 2
PLS models and the results of cross validation.

Analyte	Preprocessing	PLS factors	Wavelength regions (cm^{-1})	R	RMSECV
Cu^{2+}	Raw spectra	12	9997.4–4248.5	0.9548	2.74
	Straight line subtraction	11	9997.4–4248.5	0.9579	2.64
	First derivative	10	9997.4–6099.9	0.9461	2.97
			4601.4–4248.5		
	SNV	11	9997.4–4248.5	0.9654	2.39
	MSC	10	9997.4–4248.5	0.9647	2.42
Co^{2+}	Raw spectra	11	9997.4–6099.9	0.9394	3.72
			5451.9–4248.5		
	Straight line subtraction	11	9997.4–4248.5	0.9475	3.46
	First derivative	11	9997.4–4248.5	0.9283	4.02
	SNV	9	9997.4–6099.9	0.9378	3.76
			4601.4–4248.5		
	MSC	11	9997.4–4248.5	0.9338	3.88
Ni^{2+}	Raw spectra	10	9997.4–6099.9	0.9294	4.00
			5451.9–4248.5		
	Straight line subtraction	9	9997.4–4248.5	0.9415	3.63
	First derivative	11	9997.4–6099.9	0.9411	3.65
			5451.9–4248.5		
	SNV	10	9997.4–4248.5	0.9363	3.81
	MSC	10	9997.4–4248.5	0.9438	3.57

3.3. Quantitative model

The quantitative PLS models were built with "OPUS-QUANT" program in the OPUS 6.0 software package. Spectral preprocessing methods, factor numbers and the wavelength regions for the PLS calibration models are optimized combinatorially by using LOO-CV. For obtaining the optimized model, straight line subtraction, derivative calculation, standard normal variate (SNV), and multiplicative scatter correction (MSC) are used, respectively, in the Cu^{2+}, Co^{2+} and Ni^{2+} models.

Table 2 summarized the results obtained by LOO-CV with different signal processing techniques. From both the correlation coefficient (R) and the RMSECV in the table, it can be found that both the background removal (straight line subtraction and MSC) and the background correction (SNV and MSC) techniques can significantly improve the PLS models. With the criterion to gain a minimal RMSECV, SNV, straight line subtraction and MSC are used for the PLS models of Cu^{2+}, Co^{2+}, and Ni^{2+}, respectively. The optimal factor numbers for the three models are found to be 11, 11 and 10, respectively. In some respects, the factor number seems too big for quantitative PLS models, it should be reasonable, however, because the samples in calibration set are interfered with several extra added ions. For all the three models, the wavelength regions 9997.4–4248.5 cm^{-1} were selected. Generally, it is difficult to assign wavelengths to specific molecular absorptions in the NIR region. This is especially true in the case of this study, where the NIR absorption includes the responses of the metal ions, the adsorbent (resin) and the interaction of the ions with the chelating functional groups.

3.4. Validation of the method

In order to test the feasibility of the method, external validation is further done with the 12 validation samples. In the validation, the same conditions were used for the adsorption and the spectral measurements, and the optimized PLS models were used for prediction. Fig. 4 shows the relationship of the predicted and the reference concentrations of the samples in the validation sets. In the figure, the reference concentrations were calculated by the contents of the ions contained in the river water, which were determined by ICP-AES, plus the contents added into the samples, and the predicted concentrations were predicted by the PLS models obtained above. It can be found that, in the concentration range of 8.05–30.04 mg L^{-1} for Cu^{2+}, 9.24–34.22 mg L^{-1} for Co^{2+} and 6.53–34.58 mg L^{-1} for Ni^{2+}, a good linearity was obtained. With linear regression of these points,

the correlation coefficient (R) and standard deviation (S.D.) are found to be 0.9708 and 1.5853 for Cu^{2+} model, 0.9581 and 2.3560 for Co^{2+} model and 0.9735 and 2.2083 for Ni^{2+} model, respectively. The recoveries of Cu^{2+}, Co^{2+} and Ni^{2+} were found to be 87.0–129.8%, 85.1–114.6% and 86.6–115.8%, respectively. However, a bias can be clearly found in Fig. 4, which makes the recoveries slightly biased above 100%. This may be caused by random errors because there are only 12 samples. If enough samples are used, the error may be corrected.

4. Conclusion

A combined method was proposed for quantitative determination of the metal ions in dilute solution by using resin adsorption and NIRDRS. In the method, the analytes are, at first, concentrated onto an adsorbent, then NIRDRS is measured, and the quantitative analysis is achieved by using multivariate calibration, such as PLS regression. Due to the concentration, the sensitivity or the detection limit can be improved, and due to the usage of multivariate calibration, the effect of interfering components can be avoided. Furthermore, large variety of absorbents can be used for NIRDRS, which makes the method practicable for the analysis of real samples. With samples prepared with pure reagent and river water, the method is proved to be workable and the concentrations that can be quantitatively detected can be as low as 1.00, 1.98 and 1.00 mg L^{-1} for Cu^{2+}, Co^{2+} and Ni^{2+}, respectively. Therefore, the NIRDRS in combination with resin adsorption technique can provide a feasible way for the determination of metal ions in complex real samples. However, there is still an obvious bias in the recoveries, and the feasibility of the method still needs further validation with more real world samples.
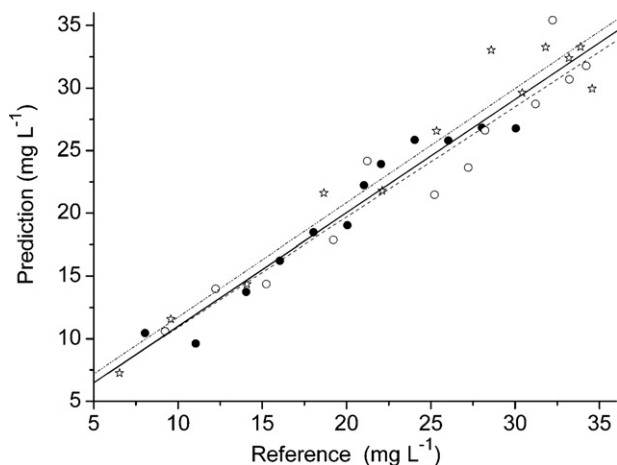
Fig. 4. Relationship of the predicted concentrations with the reference values for Cu^{2+} (●), Co^{2+} (○) and Ni^{2+} (☆), respectively. The straight lines are obtained by linear regression.

References

[1] C. Tan, M.L. Li, X. Qin, Anal. Bioanal. Chem. 389 (2007) 667–674.
[2] A.M.K. Pedro, M.M.C. Ferreira, Anal. Chem. 77 (2005) 2505–2511.
[3] L.O. Rodrigues, L. Vieira, J.P. Cardoso, J.C. Menezes, Talanta 75 (2008) 1356–1361.
[4] M. Ito, T. Suzuki, S. Yada, A. Kusai, H. Nakagami, E. Yonemochi, K. Terada, J. Pharm. Biomed. Anal. 47 (2008) 819–827.
[5] R. Cantero, T. Canals, H. Iturriaga, Talanta 71 (2007) 1690–1695.
[6] Q.J. Han, H.L. Wu, C.B. Cai, L.J. Tang, R.Q. Yu, Talanta 76 (2009) 752–757.
[7] N. Labbe, S.H. Lee, H.W. Cho, M.K. Jeong, N. Andre, Bioresour. Technol. 99 (2008) 8445–8452.
[8] W. Fan, Y.Z. Liang, D.L. Yuan, J.J. Wang, Anal. Chim. Acta 623 (2008) 22–29.
[9] D. Cozzolino, M.J. Kwiatkowski, M. Parker, W.U. Cynkar, R.G. Dambergs, M. Gishen, M.J. Herderich, Anal. Chim. Acta 513 (2004) 73–80.
[10] I. Esteban-Diez, J.M. Gonzalez-Saiz, C. Saenz-Gonzalez, C. Pizarro, Talanta 71 (2007) 221–229.
[11] M. Uddin, E. Okazaki, H. Fukushima, S. Turza, Y. Yumiko, Y. Fukuda, Food Chem. 96 (2006) 491–495.
[12] E.D. Gaiao, S.R.B. dos Santos, V.B. dos Santos, E.C.L. do Nascimento, R.S. Lima, M.C.U. de Araujo, Talanta 75 (2008) 792–796.
[13] H.L. Fernandes, I.M. Raimundo Jr., C. Pasquini, J.J.R. Rohwedder, Talanta 75 (2008) 804–810.
[14] J. Rantanen, H. Wikstrm, R. Turner, L.S. Taylor, Anal. Chem. 77 (2005) 556–563.
[15] J. Luypaert, D.L. Massart, Y.V. Heyden, Talanta 72 (2007) 865–883.
[16] C. Abrahamsson, J. Johansson, S. Andersson-Engels, S. Svanberg, S. Folestad, Anal. Chem. 77 (2005) 1055–1059.
[17] H. Liu, H.B. Gao, L.B. Qu, Y.P. Huang, B.R. Xiang, Spectrochim. Acta A 71 (2008) 1228–1233.
[18] J. Sirita, S. Phanichphant, F.C. Meunier, Anal. Chem. 79 (2007) 3912–3918.
[19] M.A. Zanjanchi, H. Noei, M. Moghimi, Talanta 70 (2006) 933–939.
[20] Q. Zhou, Y. Xi, H.P. He, R.L. Frost, Spectrochim. Acta A 69 (2008) 835–841.
[21] Y. Hao, W. Cai, X. Shao, Spectrochim. Acta A 72 (2009) 115–119.
[22] N.S. Chary, C.T. Kamala, D.S.S. Raj, Ecotoxicol. Environ. Saf. 69 (2008) 513–524.
[23] H. Vanhoe, C. Vandecasteele, J. Versieck, R. Dams, Anal. Chem. 61 (1989) 1851–1857.
[24] K.X. Yang, K. Swami, Spectrochim. Acta B 62 (2007) 1177–1181.
[25] P. Verma, K.L. Ramakumar, Anal. Chim. Acta 601 (2007) 125–129.

[26] R.L. Frost, B.J. Reddy, D.L. Wain, W.N. Martens, Spectrochim. Acta A 66 (2007) 1075–1081.
[27] R.L. Frost, B.J. Reddy, S.J. Palmer, Polyhedron 27 (2008) 1747–1753.
[28] B.J. Reddy, R.L. Frost, M.J. Dickfos, Spectrochim. Acta A 71 (2009) 1762–1768.
[29] J.S. Shenk, M.O. Westerhaus, M.R. Hoover, J. Dairy Sci. 62 (1979) 807–812.
[30] D.H. Clark, H.F. Mayland, R.C. Lamb, Agron. J. 79 (1987) 485–490.
[31] I. Gonzalez-Martin, N. Alvarez-Garcia, C. Gonzalez-Perez, V. Villaescusa-Garcia, Talanta 69 (2006) 711–715.
[32] D.F. Malley, P.C. Williams, Environ. Sci. Technol. 31 (1997) 3461–3467.
[33] J. Moros, I. Llorca, M.L. Cervera, A. Pastor, S. Garrigues, M. de la Guardia, Anal. Chim. Acta 613 (2008) 196–206.
[34] C. Petisco, B. Garcia-Criado, B.R.V. de Aldana, I. Zabalgogeazcoa, S. Mediavilla, A. Garcia-Ciudad, Anal. Bioanal. Chem. 382 (2005) 458–465.
[35] L. Sauvage, D. Frank, J. Stearne, M.B. Millikan, Anal. Chim. Acta 458 (2002) 223–230.
[36] D. Cozzolino, M.J. Kwiatkowski, R.G. Dambergs, W.U. Cynkar, L.J. Janid, G. Skouroumounis, M. Gishen, Talanta 74 (2008) 711–716.
[37] H.Y. Yu, Y. Zhou, X.P. Fu, L.J. Xie, Y.B. Ying, Eur. Food Res. Technol. 225 (2007) 313–320.
[38] D. Chen, B. Hu, X.G. Shao, Q.D. Su, Anal. Bioanal. Chem. 381 (2005) 795–805.
[39] S.P. Reinikainen, A. Hoskuldsson, Anal. Chim. Acta 595 (2007) 248–256.
[40] D.M. Haaland, E.V. Thomas, Anal. Chem. 60 (1988) 1193–1202.

Rapid IC–ICP/MS method for simultaneous analysis of iodoacetic acids, bromoacetic acids, bromate, and other related halogenated compounds in water

Honglan Shi [a,b], Craig Adams [a,b,c,*]

[a] Environmental Research Center, Missouri University of Science and Technology, Rolla, MO, 65409, United States
[b] Dept. of Chemistry, Missouri University of Science and Technology, Rolla, MO, 65409, United States
[c] Dept. of Civil, Environmental & Architectural Engineering, University of Kansas, Lawrence, KS, 66045, United States

ARTICLE INFO

ABSTRACT

Haloacetic acids (HAAs) and bromate are toxic water disinfection by-products (DBPs) that the U.S. Environmental Protection Agency has regulated in drinking water. Iodoacetic acids (IAAs) are the emerging DBPs that have been recently found in disinfected drinking waters with higher toxicity than their corresponding chloro- and bromo-acetic acids. This study has developed a new rapid and sensitive method for simultaneous analysis of six brominated and four iodinated acetic acids, bromate, iodate, bromide, and iodide using ion chromatography–inductively coupled plasma-mass spectrometry (IC–ICP-MS). Mono-, di- and tri-chloroacetic acids are not detected by this method because the sensitivity of ICP-MS analysis for chlorine is poor. Following IC separation, an Elan DRC-e ICP-MS was used for detection, with quantitation utilizing m/z of 79, 127, and 74 amu for Br, I, and Ge (optional internal standard) species, respectively. Although the primary method used was an external standard procedure, an internal standard method approach is discussed herein as well. Calibration and validation were done in a variety of natural and disinfection-treated water samples. The method detection limits (MDLs) in natural water ranged from 0.33 to 0.72 $\mu g\,L^{-1}$ for iodine species, and from 1.36 to 3.28 $\mu g\,L^{-1}$ for bromine species. Spiked recoveries were between 67% and 123%, while relative standard deviations ranged from 0.2% to 12.8% for replicate samples. This method was applied to detect the bromine and iodine species in drinking water, groundwater, surface water, and swimming pool water.

© 2009 Elsevier B.V. All rights reserved.

1. Introduction

Haloacetic acids (HAAs), including chloroacetic acids (CAAs), bromoacetic acids (BAAs), and iodoacetic acids (IAAs), are toxic DBPs that are potentially formed during drinking water disinfection treatment. The potential adverse health effects from exposure to HAAs include increased cancer risk, spontaneous abortions, and birth defects [1–3]. The five haloacetic acids (HAA5) regulated by the U.S. Environmental Protection Agency (USEPA) include mono-chloroacetic acid (MCAA), di-chloroacetic acid (DCAA), tri-chloroacetic acid (TCAA), monobromoacetic acid (MBAA), and dibromoacetic acid (DBAA). The HAA5 regulatory limit under the Stage 2 DBP Rule is 60 $\mu g\,L^{-1}$ maximum contaminant level (MCL) for the sum of the five HAAs [4].

A significant fraction of the unregulated BAAs was found in some water treatment systems [5,6]. Similarly, IAAs were also reported to be present in some of the drinking waters in the U.S. in treatment plants using chloramination [7,8]. In a recent occurrence and mammalian cell toxicity study of iodinated DBPs in drinking water [9], monoiodoacetic acid (MIAA) and bromoiodoacetic acid (BIAA), together with three lower levels of other iodoacids, were found in the chloraminated drinking water in most of the 23 cities studied in the USA and Canada. MIAA was found to be at the highest level (1.7 $\mu g\,L^{-1}$) in the chloraminated drinking water, as compared with levels of other iodoacids [9]. Iodoacetic acid was also the most cytotoxic and genotoxic DBP analyzed in a mammalian cell system [9,10]. Further, chloroiodoacetic acid (CIAA) was reported to be formed when municipal chlorinated tap water reacted with iodized table salt during cooking [11]. Recent interest in IAAs has greatly increased because of the fact that they are reported to be much more cytotoxic and genotoxic than the regulated CAAs and BAAs. It is possible, though not certain, that these currently unregulated BAAs and IAAs may be included in future drinking water regulations. Thus, the detection of these emerging iodoacetic acids and bromoiodoacetic acids in drinking water and other waters is

---

* Corresponding author at: Dept. of Civil, Architectural & Environmental Engineering, Kansas University in Lawrence, 1530 W 15th St., Room 2150, Lawrence, KS, 66045, United States. Tel.: +1 785 864 1921.
E-mail address: cadams@ku.edu (C. Adams).

crucial in order to assess the potential public health risks posed, particularly by drinking water.

Bromate is a DBP formed primarily during ozonation when the bromide ion is present [12,13]. Ozonation of water containing bromide ion (Br^-) results in the oxidation of Br^- to hypobromous acid (HOBr) and further oxidation of the hypobromite ion (BrO^-) to (BrO_3^-) [13,14]. The degree of bromate formation depends on ozone concentration, pH, and contact time. Bromate is a possible human carcinogenic [12,13]. The USEPA current regulation MCL for bromate is $10 \, \mu g \, L^{-1}$ in drinking water. In the near future, water treatment systems will need to have a bromate running annual average (RAA) of $2.5 \, \mu g \, L^{-1}$ (or less), based on 1 year of monthly data, to qualify for reduced bromate monitoring [4]. In a background document for bromate in drinking water, the World Health Organization (WHO) has indicated that the health-based value of bromate concentration in drinking water is $2 \, \mu g \, L^{-1}$ [13]. However, due to the higher attainable practical quantification level (PQL) in many laboratories, a provisional guideline value of $10 \, \mu g \, L^{-1}$ is currently recommended in *Guidelines for Drinking-water Quality* (GDWQ) [15].

The standard analytical method for the CAAs and BAAs is gas chromatography with electron capture detection (GC-ECD), after time-consuming extraction and derivatization [16]. Guo et al. have analyzed BAAs and bromate using ion chromatography–inductively coupled plasma-mass spectrometry (IC–ICP-MS) and achieved very good sensitivity [17]. A direct liquid chromatography/electrospray tandem mass spectrometry method has been developed for determination of MIAA with a negative ion detection mode [18]. A new GC–MS method, using negative ionization method, was also recently developed for detecting iodoacids [9]. There are some advantages and limitations for each of these methods, both of which utilize a variety of different instruments. With increasing health concern for iodinated and bromated DBPs, a rapid and simple analytical method is desirable.

Several USEPA standard methods have been used for detecting bromate in drinking water, including EPA Method 321.8, an IC–ICP-MS method [19]; EPA Method 300.1, an ion chromatography (IC) method with conductivity detection [20]; EPA Method 317.0, revision 2.0 [21]; and EPA Method 326.0 [22], ion chromatography (IC) methods with post-column reagent addition and UV/vis absorbance detection.

EPA Method 300.1, with a practical quantification level (PQL) of approximately $5 \, \mu g \, L^{-1}$, will not be sufficient for analyze drinking water for reduced bromated monitoring to a lowered RAA of $2.5 \, \mu g \, L^{-1}$ in the near future [4]. Sensitive and simple detection methods will assist in the analysis of bromate at lower levels in drinking water.

In addition to the toxic HAAs and bromate, the detection of other related halogenated compounds, bromide, iodide, and iodate, are also important in raw water and finished water because they play a critical role as DBP precursors or competitive products in the water. It is a great advantage if a method can be used to detect all of these compounds simultaneously.

In this study, a new fast, sensitive and simultaneous detection method for iodo- and bromo-acetic acids, bromate, iodate, bromide, and iodide, has been developed by coupling ion chromatography with ICP-MS. Specifically, the method allows separation and detection of MIAA, diiodoacetic acid (DIAA), MBAA, DBAA, tribromoacetic acid (TBAA), chloroiodoacetic acid (CIAA), BIAA, bromochloroacetic acid (BCAA), bromodichloroacetic acid (BDCAA), dibromochloroacetic acid (DBCAA), bromate, bromide, iodide, and iodate. No complex sample preparation is required except for the filtration of the water sample with a membrane filter. However, the method does not detect mono-, di- and tri-chloroacetic acid because ICP-MS does not discern well the chlorine atom.

This method was validated and applied to drinking water, groundwater, surface water, and swimming pool water. These compounds are the important regulated DBPs and their precursors in drinking water, swimming pool water, aquaria water, and marine water. The other iodoacids, such as triiodoacetic acid (TIAA) and iodo-propenoic acid, were not tested due to their unstable nature, and reportedly very low levels in drinking water [9].

2. Experimental

2.1. Reagent and preparation

Three IAAs – CIAA, BIAA, and DIAA – were purchased from Orchid Cellmark (New Westminster, BC, Canada). MIAA and all of the bromoacetic acids – MBAA, BCAA, DBAA, BDCAA, DBCAA, and TBAA – were purchased from Sigma–Aldrich (St. Louis, MO, USA). All of these chemicals were of the highest purity available. All the other ACS certified reagent grade chemicals were purchased from Fisher Scientific (Pittsburgh, PA, USA) and Sigma–Aldrich. Deionized (DI) water ($18.2 \, M\Omega \, cm$) was prepared with a Milli-Q water purification system (Millipore, Bedford, MA, USA).

The DI water used for standards and mobile phase preparations was pre-degassed by vacuum filtration and/or ultrasonication to prevent any possible oxidation of iodide and bromide. Continuous online degas of mobile phases was also performed during the IC–ICP-MS analysis. Stock standard solutions were prepared by dissolving the chemicals in freshly degassed DI water at a concentration of 100–1000 mg/L, except iodide, which was prepared by dissolving sodium iodide in 0.5% ammonium hydroxide at pH 10 to minimize the possible oxidation of the iodide. All standard solutions were stored in amber glass vials, capped with Teflon-lined caps, in a freezer or refrigerator. The GeO_2 stock solution (used as an optional internal standard) was prepared in DI water at 500 mg/L. All of the standards were freshly prepared monthly. The more diluted working standard solutions were freshly prepared daily by dilution with DI water.

IC mobile phase A was DI water, and mobile phase B was 200 mM ammonium nitrate in DI water. Both mobile phases were filtered through a 0.22-μm nylon membrane filter, and degassed prior to use.

2.2. Instruments and operation conditions

IC separation was conducted using a PerkinElmer 200 Series high pressure liquid chromatography (HPLC) system composed of a 200 Series pump and autosampler (PerkinElmer, Norwalk, CT, USA). An automated switching valve was used between the HPLC and ICP-MS nebulizer to direct the mobile phase to the waste or ICP-MS. The tubing and sample loop were PEEK material. The analytical column was an AS11-HC high capacity ion exchange column ($4.0 \, mm \times 250 \, mm$), with an AG11-HC guard column ($4.0 \, mm \times 50 \, mm$) (Dionex, Sunnyvale, CA). The elution flow rate was 1.0 mL/min, and the injection volume was 100 μL. Amber glass sampler vials were used for all samples. Both the autosampler and column were kept at room temperature ($\sim20\,^{\circ}C$). The binary gradient elution for the separation was programmed as: 15% B for 3 min; increased to 50% B over 5 min; increased to 100% B over 18 min; maintained at 100% B for 10 min; decreased to 15% B over 5 min; and equilibrated at 15% B for 2 min, prior to the next injection. The total run time was 43 min.

The detection system was a Model Elan DRC-e ICP-MS (PerkinElmer SCIEX, Norwalk, CT, USA). Chromaria software was used to control the IC–ICP-MS systems for analysis. Table 1 lists the important ICP-MS instrumental conditions and method parameters used for this method.

Quantitation was performed at a mass/charge (m/z) ratio of 79 and 127 amu for Br and I, respectively. (*Note*: An isomeric m/z of 81 amu was sometimes also monitored for additional confirmation for the bromo-compounds.)

Table 1
Inductively coupled plasma-mass spectrometry (ICP-MS) operational conditions.

Parameter	Operation setting
ICP RF power	1500 W
Plasma gas flow	15 L/min
Auxiliary gas flow	1.20 L/min
Nebulizer gas flow	1.01 L/min
Sample introduction system	Cyclonic spray chamber with Meinhard nebulizer
Detector mode	Dual
AutoLens	Enabled
Lens voltage	6.5 V
Analog stage voltage	−1600 V
Pulse stage voltage	850 V
Sampler cone	Platinum, 1.1 mm orifice
Skimmer cone	Platinum, 0.9 mm orifice
Mass resolution	0.7 amu
Operating vacuum pressure	6×10^{-6} Torr
Number of replicates	3
Dwell time	250 ms
m/z for Br	79 amu
m/z for I	127 amu
m/z for Ge	74 amu

2.3. Water samples

Several types of water samples were tested, including laboratory reagent (DI) water, finished drinking water from a groundwater source, surface water, and swimming pool water. Water samples were collected in pre-cleaned amber glass bottles, prefiltered through a 0.22-μm nylon membrane filter, and stored cold in the dark until analysis. The drinking water (DW) was collected from tap water (Rolla, MO, USA) that utilized local groundwater as its source, with chlorine added for disinfection. Missouri River water (MRW) was collected from the Missouri River (near Jefferson City, MO, USA). Mississippi River water (MSW) was collected from the Mississippi River (near St. Louis, MO, USA). Maramec Spring water (MSW) was collected at Maramec Spring Park (MO, USA). Schuman Pond water (SPW) was collected in Rolla, MO (USA). An indoor swimming pool water sample was obtained from a local recreational swimming pool that had been treated using free chlorine (Rolla, MO, USA). All of the water samples were analyzed directly for halogenated compounds by IC–ICP-MS, after filtration, without any other sample preparation.

3. Results and discussion

3.1. Separation

A total of 14 different bromo- and iodo-compounds (plus an optional internal standard, GeO$_2$) were separated and detected
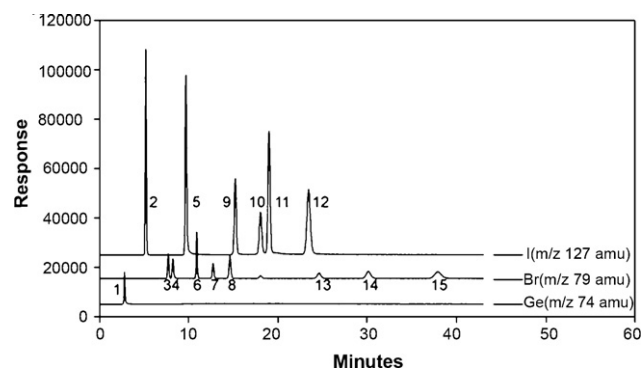
Fig. 1. Chromatograms of 14 halogenated compounds (and GeO$_2$ internal standard) analyzed using the new IC–ICP-MS method. Peak identification is per Table 2.

within 39 min using this method. A representative chromatogram for these 15 compounds is shown in Fig. 1. Peak identification, retention time, and precision within the same day and between days are listed in Table 2. All of the 15 compounds were well separated chromatographically and peaks showed very good symmetry. The neutral species, GeO$_2$, eluted at ~2.8 min, had a very sharp peak. Each of the other peaks eluted with retention times of 5.1–38 min. Excellent reproducibility of retention time was observed with a relative standard deviation ranging from 0.03% to 0.28% for the same day, and 0.39% to 1.46% for between days, over nine non-continuous days within 1 month of testing time.

3.2. Calibration linearity

Calibration curves at concentration ranges of 1–1000 and 2.5–1000 μg L^{-1} for iodo- and bromo-compounds, respectively, exhibited good linearity ($R^2 > 0.999$) with the external standard method.

3.3. Instrument and method detection limits

Estimated instrument detection limits (IDLs) and method detection limits (MDLs) for all bromo- and iodo-compounds in surface water are shown in Table 3 for a 100 μL injection volume. At a signal-to-noise ratio of 3, IDLs in DI water were 0.5–2.5 and 0.1–0.3 μg L^{-1} for the bromo- and iodo-compounds, respectively, using the external standard method. MDLs for Missouri River water samples were determined following the USEPA standard method. Specifically, seven spike replicates were analyzed at a spiked concentration of 2–5 times the estimated instrument detection limit, with MDLs calculated as the product of the standard deviation (s) and Student's

Table 2
Peak identification, retention time, and repeatability of retention (percent R.S.D.) for same day and between day replicates.

Compound	Abbreviation or formula	Peak #	Minutes	Retention Same day R.S.D. (%) ($n = 10$)	Time Between day R.S.D. (%) ($n = 9$)
Germanium dioxide	GeO$_2$	1	2.76		
Iodate	IO$_3^-$	2	5.17	0.16	1.10
Bromate	BrO$_3^-$	3	7.69	0.15	0.79
Monobromoacetic acid	MBAA	4	8.19	0.15	1.24
Monoiodoacetic acid	MIAA	5	9.66	0.03	0.97
Bromide	Br$^-$	6	10.88	0.03	0.51
Bromochloroacetic acid	BCAA	7	12.71	0.15	0.63
Dribromoacetic acid	DBAA	8	14.59	0.10	0.56
Chloroiodoacetic acid	CIAA	9	15.19	0.04	0.56
Bromoiodoacetic acid	BIAA	10	18.04	0.05	0.39
Iodide	I$^-$	11	18.98	0.06	1.46
Diiodoacetic acid	DIAA	12	23.40	0.09	0.42
Bromodichloroacetic acid	BDCAA	13	24.57	0.19	0.56
Dibromochloroacetic acid	DBCAA	14	30.11	0.04	0.43
Tribromoacetic acid	TBAA	15	37.92	0.28	0.77

Table 3
Estimated instrument detection limit (IDL) and method detection limits (MDL) in Missouri River water (MRW) using external standard method.

Compound	IDL (at S/N = 3) in DI water (μg L^{-1})	MDL in Missouri River water (μg L^{-1})
IO$_3$$^-$	0.1	0.33
MIAA	0.1	0.40
CIAA	0.2	0.44
BIAA	0.3	0.72
I$^-$	0.1	0.70
DIAA	0.2	0.36
BrO$_3$$^-$	0.7	1.65
MBAA	0.7	2.54
Br$^-$	0.5	NM
BCAA	1.0	2.63
DBAA	0.7	1.36
BDCAA	2.5	3.28
DBCAA	2.0	2.15
TBAA	1.0	2.01

NM = not measured.

t (α = 0.01, d.f. = 6). In surface water samples, the MDLs (without an internal standard) ranged from 1.36 to 3.28 and 0.33 to 0.72 μg L^{-1} for bromo- and iodo-compounds, respectively.

These data demonstrated that this method is a sensitive and useful method for IAAs, iodide, and iodate without sample pre-concentration or extraction. The sensitivity was also good for bromate at 1.65 μg L^{-1}, which should satisfy the USEPA new regulatory limit level of 2.5 μg L^{-1} in the near future [4]. All MDLs were more than an order of magnitude below the MCL for HAA5 of 60 μg L^{-1}. If greater sensitivity is desired, a larger injection volume could be used (e.g., 500 μL, depending on instrument configuration).

3.4. Precision

The precision of the method was tested by multiple spiked sample analysis for three natural waters under different concentration ranges (Table 4). For drinking water from a groundwater supply spiked with 20 and 80 μg L^{-1} of the iodo- and bromo-compounds, respectively, R.S.D.s ranged from 0.7% to 10.9%, with a median of 3.4%. For filtered Missouri River water (MRW), a spike of 5 and 10 μg L^{-1} of the iodo- and bromo-compounds, respectively, resulted in R.S.D.s ranging from 1.1% to 12.8%, with a median of

3.5%. For the same MRW, a higher spike of 50 and 100 μg L^{-1} of the iodo- and bromo-compounds, respectively, resulted in R.S.D.s ranging from 0.4% to 6.4%, with a median of 2.8%. Method precision was also tested in pond water (SPW) at 100 and 400 μg L^{-1} of the iodo- and bromo-compounds, respectively, resulting in R.S.D.s ranging from 0.2% to 2.8%, with a median of 1.1%. These results indicated that this method is highly reproducible and meets the USEPA quality control precision criteria [16].

3.5. Spike recovery

To test method accuracy, spike recoveries for different levels of analyte spikes were conducted and are summarized in Table 4 for the external standard method. For drinking water from a groundwater supply spiked with 20 and 80 μg L^{-1} of the iodo- and bromo-compounds, respectively, spiked recoveries ranged from 76.3% to 123.1%, with a median of 100.8%. For MRW, a spike of 5 and 10 μg L^{-1} of the iodo- and bromo-compounds, respectively, resulted in spiked recoveries ranging from 67.4% to 101.9%, with a median of 94%. For the same MRW, a higher spike of 50 and 100 μg L^{-1} of the iodo- and bromo-compounds, respectively, resulted in spiked recoveries ranging from 90.7% to 106.3%, with a median of 99.1%. Method accuracy was also tested in pond water at 100 and 400 μg L^{-1} of the iodo- and bromo-compounds, respectively, resulting in spiked recoveries ranging from 91.4% to 115.3%, with a median of 102%. With a single exception (of 67.4% for the 5 μg L^{-1} spike of TBAA in drinking water), these recoveries are well within the commonly accepted range of 70–130% indicated in the USEPA method [16].

3.6. Water samples analysis

Each of the sources waters (i.e., DW, MRW, MSW, SPW, RSW, and MPIW) was tested for the occurrence of all 14 compounds using the external standard method. Only iodate, iodide, MBAA, and bromide were detected in amounts above the method detection limits. The results are tabulated in Table 5.

For the waters tested, the TOC ranged from 2.3 mg/L (for the Rolla finished drinking water from a groundwater source) to 12.8 mg/L (for the Rolla swimming pool water) (Table 5). Of all the samples tested, the Missouri River water (MRW) sample contained the highest bromide and iodide concentrations of 75.6 and 0.86 μg L^{-1},

Table 4
Precision and spike recovery (%) for drinking water (DW), Missouri River water (MRW) and Schuman Pond water (SPW) using external standard method.

	Drinking water (DW)			Missouri River water (MRW)			Missouri River water (MRW)			Schuman Pond water (SPW)		
	20 I or 80 Br (μg L^{-1}) (n=4)			5 I or10 Br (μg L^{-1}) (n=5)			50 l or l00 Br (μg L^{-1}) (n=3)			100 I or 400 Br (μg L^{-1}) (n=3)		
	Mean recovery	R.S.D. (%)	Recovery (%)	Mean recovery	R.S.D. (%)	Recovery (%)	Mean recovery	R.S.D. (%)	Recovery (%)	Mean recovery	R.S.D. (%)	Recovery (%)
Iodate	21.0	0.7	105.2	5.4	0.71	101.9	48.7	3.1	96.8	101.5	0.4	101.5
Iodide	15.3	7.2	76.3	5.7	2.0	95.3	48.4	0.4	96.8	115.2	0.4	115.2
MIAA	24.6	6.2	123.1	4.5	2.6	90.5	48.7	5.8	97.4	115.3	2.8	115.3
DIAA	20.5	4.8	102.4	4.8	2.8	96.6	49.5	1.4	99.0	91.4	2.8	91.4
CIAA	17.6	6.2	87.7	4.7	3.5	94.0	49.6	3.6	99.3	96.2	2.5	96.2
BIAA	23.8	10.9	119.6	4.6	1.1	92.6	49.1	2.7	98.2	105.5	0.2	105.5
Bromate	80.7	2.5	100.9	9.8	3.5	97.8	103.5	6.4	103.5	422.2	1.3	105.6
Bromide	74.4	2.4	94.4	NM	NM	NM	90.7	3.0	90.7	398.0	1.2	99.5
MBAA	80.6	3.2	100.7	7.6	12.8	76.2	106.3	3.210	106.3	430.6	0.6	107.7
DBAA	80.3	2.4	100.4	7.6	5.9	76.0	101.3	3.6	101.3	401.8	1.9	100.5
TBAA	82.3	2.2	102.9	6.7	9.9	67.4	98.5	0.4	98.5	407.0	0.8	101.8
BCAA	80.0	4.0	100.0	9.9	4.01	98.8	100.4	2.6	100.4	409.1	1.0	102.3
BDCAA	79.8	3.6	99.7	8.4	12.4	83.5	99.2	1.7	99.2	412.5	1.2	103.1
DBCAA	84.2	1.2	105.3	9.8	5.2	98.4	101.8	1.2	101.8	404.5	0.5	101.1

NM = not measured.

Table 5
Total organic carbon (TOC) and all detected halogenated compounds in natural water and drinking water determined using external standard method ($n = 2$ or 3).

Sample ID	TOC (mg/L) (R.S.D.,%)	Iodate ($\mu g\,L^{-1}$) (R.S.D.,%)	Iodide ($\mu g\,L^{-1}$) (R.S.D.,%)	MBAA ($\mu g\,L^{-1}$) (R.S.D.,%)	Bromide ($\mu g\,L^{-1}$) (R.S.D.,%)
DW—drinking (tap) water	2.30(0.07)	8.92(16.9)	<0.7	<2.54	10.1(6.12)
MRW—Missouri River water	10.2(0.29)	0.2(3.87)	0.86(3.56)	<2.54	75.6(2.95)
MSW—Meramec Spring Park water	7.34(0.19)	0.62(9.60)	<0.7	<2.54	60.6(1.22)
SPW—Schuman Pond water	11.7(0.09)	0.74(2.72)	<0.7	<2.54	27.0(0.45)
RSW—Rolla swimming pool water	12.8(0.19)	24.7(0.87)	<0.7	192(0.19)	12.8(3.35)
MSW—Mississippi River water	11.0(0.11)	0.29(0)	<0.7	<2.54	66.2(1.84)

respectively. The highest iodate, at a concentration of 24.7 $\mu g\,L^{-1}$, was observed in the Rolla swimming pool water (RSW). The only haloacetic acid observed in any of the waters was 192 $\mu g\,L^{-1}$ of MBAA observed in the same chlorinated swimming pool water (RSW). All of the surface water samples tested were untreated natural waters and should not contain significant levels of HAAs. The drinking water tested was from groundwater with a low concentration of TOC and also should not have high levels of HAAs.

3.7. Alternative internal standard method

As shown above, the IC–ICP-MS method was successfully developed using an external standard method (that is, without use of an internal standard). An internal standard method was also tested that utilized GeO$_2$ as the internal standard. The selection of GeO$_2$ was based on work by Eickhorst et al. [23]. The purpose of including internal standards is to increase the robustness of a method, and to correct for injection and instrument variability. Preliminary results for the internal standard method resulted in calibration curves with good linearity (R^2 ranged from 0.996 to 0.999). It is suggested that if an internal standard is required for a given application, use of GeO$_2$ is likely a good candidate.

4. Conclusion

A rapid and sensitive simultaneous detection method for iodide, iodate, bromide, bromate, four iodoacetic acids, and six bromoacetic acids was successfully developed, validated and applied to natural and treated waters. The method is simple with no sample preparation required, except for prefiltration.

This is the first single method reported to date to incorporate these bromo- and iodo-compounds in a single separation and detection run, including all of the regulated bromoacetic acids, bromate, and emerging iodoacetic acids, as well as their precursors. Due to the high toxicity of bromo- and iodo-compounds, there are many applications of interest for the method, including occurrence monitoring, treatability, disinfection byproduct formation and control, and human exposure studies in drinking water, groundwater, surface water, and swimming pool water. The method was also applied and validated in salt water and seawater systems (data not shown). The method is especially valuable for monitoring the highly toxic IAAs in treated drinking water that have been found recently in most of the finished drinking water in the USA and Canada [9]. It is also a very useful method for detecting the lower level of bromate (2.5 $\mu g\,L^{-1}$ running annual average) [4].

While the MDLs are sufficiently low for most drinking water applications, lower detection limits could likely be achieved using a larger injection volume, if needed (though this was not tested in this work). Immediate application of the method is needed, especially in studies to assess the exposure of the general public to these toxic DBPs of new and emerging concern.

References

[1] U.S. Environmental Pretection Agency, National Primary Drinking Water Regulations: Stage 2 Disinfectants and Disinfection Byproducts Rule, Fed. Reg. 71 (2006) 387–493 (www.epa.gov, National Primary Drinking Water Standards).
[2] M. Nieuwenhuijsen, M. Toledano, N. Eaton, J. Fawell, P. Elliott, Occup. Environ. Med. 57 (2000) 73.
[3] K. Waller, S. Swan, S. Windham, L. Fenster, J. Exp. Anal. Environ. Epidemiol. 11 (2001) 522.
[4] http://www.epa.gov/safewater/disinfection/stage2/pdfs/guide_stage2_stateimplementationguide.pdf.
[5] D. Shoaf, P. Singer, J. Am. Water Works Assoc. 99 (2007) 69.
[6] S.D. Richardson, A.D. Thruston Jr., C. Rav-Acha, L. Groisman, I. Popilevsky, O. Juraev, V. Glezer, A.B. McKague, M.J. Plewa, E.D. Wagner, Environ. Sci. Technol. 37 (2003) 3782.
[7] H.S. Weinberg, S.W. Krasner, S.D. Richardson, A.D. Thruston, Jr., U.S. Environmental Protection Agency, National Exposure Research Laboratory: Athens, GA, 2002, EPA/600/R-02/068, www.epa.gov/athens/publications/EPA_600_R02_068.pdf.
[8] M. Plewa, E. Wagner, S.D. Richardson, A. Woo, Y. Thruston, A. McKague, Environ. Sci. Technol. 38 (2004) 4713.
[9] S.D. Richardson, F. Fasano, J.J. Ellington, F.G. Crumley, K.M. Buettner, J.J. Evans, B.C. Blount, L.K. Silva, T.J. Waite, G.W. Luther, A.B. McKague, R.J. Miltner, E.D. Wagner, M.J. Plewa, Environ. Sci. Technol. 42 (2008) 8330.
[10] E. Cemeli, E. Wagner, D. Anderson, S.D. Richardson, M. Plewa, Environ. Sci. Technol. 40 (2006) 1878.
[11] A. Becalski, B.P.-Y. Lau, T.J. Schrader, S.W. Seaman, W.F. Sun, Food Addit. Contam. 23 (2006) 957.
[12] US EPA Toxicological review of bromate in support of Integrated Risk Information System (IRIS), Washington, DC, US Environmental Protection Agency, http://www.epa.gov/iris/toxreviews/1002-tr.pdf.
[13] Bromate in drinking-water, WHO/SDE/WSH/05.08/78, 2005, www.who.int/water_sanitation_health/dwq/chemicals/bromate030406.pdf.
[14] W.R. Haag, J. Holgne, Environ. Sci. Technol. 17 (1983) 261.
[15] WHO Guidelines for drinking-water quality, Chemical aspects, www.who.int/water_sanitation_health/dwq/gdwq0506_8.pdf.
[16] EPA Method 552.2—determination of haloacetic acids and dalapon in drinking water by liquid–liquid extraction, derivatization and gas chromatography with electron capture detection, revision 1.0, 1995.
[17] Z. Guo, Q. Cai, C. Yu, Z. Yang, J. Anal. Atom. Spectrom. 18 (2003) 1396.
[18] P.-Y. Lau, A. Benjamin, Becalski, Rapid Commun. Mass Spectrom. 22 (2008) 1787.
[19] EPA Method 321.8, http://www.epa.gov/microbes/m_321_8.pdf, 1997.
[20] EPA Method 300.1, http://www.epa.gov/ogwdw/methods/pdfs/methods/met300.pdf, 1997.
[21] EPA Method 317.0, revision 2.0, http://www.epa.gov/ogwdw/methods/pdfs/methods/met317rev2.pdf, 2001.
[22] EPA Method 326.0 http://www.epa.gov/ogwdw/methods/analyticalmethods_ogwdw.html, 2002.
[23] T. Eickhorst, A. Seubert, J. Chromatogr. A 1050 (2004) 103.

Correction of self-absorption effect in calibration-free laser-induced breakdown spectroscopy by an internal reference method

Lanxiang Sun [a,b,1], Haibin Yu [a,*]

[a] *Key Laboratory of Industrial Informatics, Shenyang Institute of Automation, Chinese Academy of Sciences, Shenyang 110016, China*
[b] *Graduate School of the Chinese Academy of Sciences, Beijing 100039, China*

ARTICLE INFO

ABSTRACT

A simplified procedure for correcting self-absorption effect was proposed in calibration-free laser-induced breakdown spectroscopy (CF-LIBS). In typical LIBS measurement conditions, the plasma produced is often optically thick, especially for the strong lines of major elements. The selection of self-absorption lines destroys the performance of CF-LIBS, and the familiar correction method based on the curve of growth is complex in implementation. The procedure we proposed, named internal reference for self-absorption correction (IRSAC), first chose an internal reference line for each species, then compared other spectral line intensity of the same species with the reference line to estimate the self-absorption degrees of other spectral lines, and finally achieved an optimal correction by a regressive algorithm. The self-absorption effect of the selected reference line can be ignored, since the reference line with high excitation energy of the upper level is slightly affected by the self-absorption. Through the IRSAC method, the points on the Boltzmann plot become more regular, and the evaluations of the plasma temperature and material composition are more accurate than the basic CF-LIBS.

© 2009 Elsevier B.V. All rights reserved.

1. Introduction

Laser-induced breakdown spectroscopy (LIBS) is an analytical technique of atomic emission spectroscopy (AES) that laser-generated plasma is used as the emitting source. In LIBS, a pulsed laser beam is focused by a lens on the target material, of which a small volume is intensely heated and thus brought to a transient plasma state. With high temperature and high electron density, the plasma state, in which the sampled material is broken down, vaporized, atomized, and partially ionized, releases energy by emission of radiation across a broad spectral range between 200 and 980 nm [1]. The atomic and ionic spectra are obtained by means of a spectrograph, thereby allowing elemental components of the target to be identified and quantified.

Since the first analytical use of laser plasma for the spectrochemical analysis of surfaces was published in 1963, the LIBS technique has demonstrated its potential in qualitative and quantitative analysis of elemental composition [2]. Compared with other atomic emission spectral analysis techniques, the LIBS has many benefits, such as the capability of multi-element simultaneous analysis, applicability to all sample types like solids, liquids, and gases, less

sample requirement, lack of sample preparation, and quickness of data acquisition. During the last two decades, the applications of LIBS have increased considerably, including industrial production control and quality assurance [3–5], environmental protection [1,6–8], explorations of outer space [9], cultural heritage conservation [10], and medicinal studies [11].

Commonly, LIBS is used to determine the elemental composition of materials by calibration curves that require several reference samples with the same matrices [12–14]. This method requires that the measurement conditions of the reference samples match with the measurement conditions of the objects analyzed. Moreover, sometimes making the reference samples that have the absolutely same matrices as the samples analyzed is difficult or even impossible [9]. Consequently, the approach of calibration curves is appropriate to laboratorial analysis and not compatible with field analysis for variable circumstances or priori unknown samples.

In order to correct the matrix effect on the calibration curves, a number of methods have been proposed [15–17]. The procedure based on normalization with respect to a reference line can provide higher accuracy and reproducibility of the analytical results than methods using simple line intensity [15]. Panne et al. propose a model which includes the equilibrium Saha and Boltzmann relationships to correct the pulse-to-pulse variability of the plasma electron temperature and density [16]. Chaleard et al. describe the emission intensity of a line by using a model considering the electron temperature and total mass vaporized in the plasma plume

* Corresponding author. Tel.: +86 24 23970043.
E-mail addresses: sunlanxiang@sia.cn (L. Sun), yhb@sia.cn (H. Yu).
[1] Tel.: +86 24 23970173.

[17]. In their experimental conditions, they demonstrated that the acoustic signal emitted by the plasma is proportional to the vaporized mass. Therefore, a correction for the matrix effect was accomplished by measuring the vaporized mass and plasma temperature [17].

Another analytical approach of LIBS for quantifying the elemental composition of materials is the calibration-free LIBS (CF-LIBS) proposed by Ciucci et al. in 1999 [18]. The CF-LIBS determines the concentration of elements by using the mathematic models that describe the plasma emission, not requiring any calibration curves and reference samples. Hence, the CF-LIBS avoids the matrix effect caused by the different matrices between the reference samples and the objects analyzed, and is more suitable to field and on-line applications. The calculation of plasma temperature is a crucial point of the procedure. To increase the reliability of temperature calculation, Saha–Boltzmann method can be used [19,20]. In Saha–Boltzmann method, lines from atoms and ions of the same element are included in the linear regression for enlarging the difference in the excitation energies of upper levels thus improving the statistics. However, the CF-LIBS method is often affected by the self-absorption effect, especially for the major elements. In CF-LIBS, many spectral lines must be chosen, including some strong lines of major elements, to draw a Boltzmann or Saha–Boltzmann plot. The self-absorption effect makes the intensity of selected lines at low excitation energies of upper levels lower than its theoretical value, and thus the calculated plasma temperatures are higher and the intercepts are lower than expected. Therefore, the accuracy of the quantitative results of the CF-LIBS method may be extremely destroyed by the self-absorption effect.

With the purpose for correcting the self-absorption effect, the CF-LIBS procedure has been updated by Bulajic et al., in which a self-absorption correction step is implemented by using a recursive algorithm based on the curve of growth (COG) [21]. In order to correct the self-absorption effect, the COGs of all the analytical lines in the Boltzmann plot should be constructed. The construction of the COGs requires calculating the plasma temperature, electron density, Gaussian broadening, Lorentzian broadening and optical path length. The authors introduce a recursive algorithm to obtain the Lorentzian broadening since it is difficult to calculate in theory. Through the correction procedure, the quantitative results show a significant improvement with respect to those obtained without self-absorption correction. However, this procedure is complex and time consuming, for it requires calculating theoretical values of many variables and measuring the observed half-widths of all analytical lines. Furthermore, some theoretical values like Lorentzian broadening are not easy to accurately calculate, and sometimes the line half-widths are difficult to observe especially when line overlaps exist.

In this paper, for CF-LIBS we propose a method called internal reference for self-absorption correction (IRSAC) to correct self-absorption effect. In this method, we select an internal reference line for each species in order to evaluate the self-absorption degrees of other spectral lines. The selected internal reference line with high excitation energy of the upper level is slightly affected by the self-absorption effect, and thus the self-absorption can be negligible. Based on the self-absorption degrees obtained, other spectral line intensity can be iteratively corrected.

2. Theoretical

2.1. Calibration-free LIBS

The procedure of CF-LIBS has been described in detail by Ciucci et al. [18]; therefore, we only introduce the basic characteristics of this method for better depicting the procedure of IRSAC. Assuming the plasma is optically thin and in local thermodynamic equilibrium (LTE) in the temporal window of signal acquisition, the measured integral line intensity can be expressed as:

$$I_\lambda^{ij} = FC_s A_{ij} \frac{g_i}{U_s(T)} e^{-E_i/k_B T} \tag{1}$$

where λ is the wavelength corresponding to the transition between two energy levels, E_i and E_j, of an atomic or ionic species s; C_s is the number concentration of the emitting species s; A_{ij} is the transition probability for the given line; g_i is the degeneracy of the i level; F is a constant that takes into account the optical efficiency of the collection system as well as the total plasma number density and volume; k_B is the Boltzmann constant; T is the plasma temperature; $U_s(T)$ is the partition function for the emitting species.

The spectral parameters of A_{ij}, g_i and E_i can be obtained from spectral databases, and the values of F, C_s and T must be determined from the experimental data. By defining the following quantities

$$y_i = \ln \frac{I_\lambda^{ij}}{g_i A_{ij}}, \quad x_i = E_i, \quad m = -\frac{1}{k_B T}, \quad q_s = \ln \frac{C_s F}{U_s(T)}, \tag{2}$$

and taking the logarithms of the both sides, Eq. (1) can be rewritten in a linear form:

$$y_i = mx_i + q_s. \tag{3}$$

According to Eq. (3), each line intensity can be represented as a point in the Boltzmann plot with the above defined x and y coordinates. For all species, these points lie on several parallel straight lines with the same slope m and different intercepts q_s. Since the sum of the relative concentration of all species equal unity, the experimental factor F can be determined using the following normalization relation,

$$\sum_s C_s = \frac{1}{F} \sum_s U_s(T) e^{q_s} = 1 \tag{4}$$

and the concentration of all the species in the sample can be obtained by

$$C_s = \frac{1}{F} U_s(T) e^{q_s}. \tag{5}$$

The initial CF-LIBS method compensates for the matrix effect by applying the basic equations derived from the LTE and optically thin plasma assumptions, avoiding the need for any comparison with calibration curves or reference samples. The plasma created by laser ablation, however, is often optically thick for some special wavelengths, and thus causes the spectral self-absorption and pronounced nonlinearity in the Boltzmann plot. In the following section, we will present a method for self-absorption correction to improve the quantitative performance of the CF-LIBS.

2.2. Model of the IRSAC

In order to consider the self-absorption effect, we introduce a self-absorption coefficient to correct the model of spectral line intensity described in Eq. (1) as follows:

$$I_\lambda^{ij} = f_\lambda^b FC_s A_{ij} \frac{g_i}{U_s(T)} e^{-E_i/k_B T} \tag{6}$$

where f_λ^b is defined as the self-absorption coefficient at the wavelength λ, with the value between 0 and 1. $f_\lambda^b = 0$ denotes the spectral line is absolutely reabsorbed along the optical path, while $f_\lambda^b = 1$ denotes the spectral line is not affected by self-absorption effect.

Generally, the self-absorption effect is strong for the lines with low excitation energies of upper levels and high transition probabilities, especially for the resonant lines; otherwise, the self-absorption effect is weak for the lines with high excitation energies

of upper levels. Therefore, an approximate measurement of the self-absorption coefficient can be obtained by the intensity ratios of other emission lines to an internal reference line for each species:

$$\frac{f_\lambda^b}{f_{\lambda_R}^b} = \frac{I_\lambda^{ij}}{I_{\lambda_R}^{mn}} \frac{A_{mn}g_m}{A_{ij}g_i} e^{-E_m - E_i/k_B T} \tag{7}$$

where λ_R, $I_{\lambda_R}^{mn}$ and $f_{\lambda_R}^b$ are the wavelength, spectral line intensity and self-absorption coefficient of the internal reference line, and the A_{mn}, g_m and E_m are the spectral parameters related to the transition between energy levels of m and n.

If we select the internal reference line with a low transition probability A_{mn} or a high excitation energy level E_m, the self-absorption effect of the internal reference line can be negligible, and thus $f_{\lambda_R}^b \approx 1$. Therefore, the self-absorption coefficient of other emission lines can be evaluated based on the following equation,

$$f_\lambda^b = \frac{I_\lambda^{ij} A_{mn} g_m}{I_{\lambda_R}^{mn} A_{ij} g_i} e^{-E_m - E_i/k_B T}. \tag{8}$$

Consequently, the corrected spectral line intensities that the lines would have in the absence of self-absorption can be approximated from the ratios of the measured line intensities to the self-absorption coefficient:

$$\hat{I}_\lambda^{ij} = \frac{I_\lambda^{ij}}{f_\lambda^b} = \frac{I_{\lambda_R}^{mn} A_{ij} g_i}{A_{mn} g_m} e^{E_m - E_i/k_B T}. \tag{9}$$

By Eq. (9), the self-absorption correction for each line can be obtained. When these corrections are applied to each point in the Boltzmann plot, the spread of points from each species around the best fit line will be reduced, and thus more accurate quantitative results will be obtained.

2.3. Algorithm description of the IRSAC

According to Eq. (8), the calculation of the self-absorption coefficients requires the plasma temperature, which can be preliminarily evaluated from the Boltzmann plot without any correction. The line intensities corrected by the previous temperature are used to calculate a new temperature. Since the evaluation of the temperatures interacts with the evaluation of the self-absorption coefficients, the optimal self-absorption coefficients can be determined by an iterative procedure until the convergence of the correlation coefficients on the Boltzmann plot. When the correlation coefficients come into convergence, the corrected points will well linearly lie on the Boltzmann plot, and the temperatures calculated from two iterations will change little.

Assuming that there is a good linear relation between x_i and y_i defined as Eq. (2) on the Boltzmann plot, when the self-absorption does not exist for all lines, three cases are possible after the iterative process: (1) if all lines do not need correction, the iterative process will little modify the intensity of all lines, thus keeping the corrected fitting line nearly same as the one before correction; (2) if only some lines need correction, the iteration will greatly correct these scattered points on the Boltzmann plot, and accordingly improve the temperature and intercepts estimation; (3) if most or even all lines need to be corrected, though the correlation coefficients come into convergence, the corrected fitting line is not our expected. In case 3, the corrected temperature will still be higher than the real value, at the same time the intercept will still be lower than expected. This case generally happens on the matrix element. We can determine whether this case has happened by judging if the fitting lines of all species are nearly parallel after the previous iterative correction. If they are not nearly parallel, for the species with the highest temperature estimated, we suggest setting the initial

temperature of this specific species as the mean value of the temperatures determined by all species, and then repeating iterative correction until all fitting lines are nearly parallel. By this manner, we finally obtain the stable plasma temperature and intercepts.

The determination of the internal reference line is another crucial point of the procedure. Selecting one single reference line to correct other lines reflects in a large uncertainty on the results, due to statistical fluctuations or possible unrecognized systematic bias affecting the intensity. Therefore, we use the fitted value of the reference line on the Boltzmann plot instead of the actual value obtained by experiments. The fitted value is defined as the value on the position of the energy level E_m on the fitting line based on Eq. (3). The fitted value is an integration of lines with the energy levels close to the energy level of the reference line, and thus is relatively stable. Based on the fitted value, the correction of other lines is not sensitive to the selection of the reference line, as long as the energy level of the reference line is not extremely low for avoiding the self-absorption of the reference line.

We should note that, some self-absorption coefficients determined by Eq. (8) are bigger than one. There are many possible reasons for this situation, such as the self-absorption of the reference line, the statistical fluctuation of the transition probability, and the measurement errors of the line intensity. Anyway, the integrated effect of these reasons makes the self-absorption of the lines with self-absorption coefficients more than one negligible. Therefore, we will not change the intensity of these lines. The outline of the IRSAC is described in Fig. 1.

2.4. Experimental

A schematic representation of the instrument set-up is shown in Fig. 2. The laser source is a Q-switched Nd:YAG laser (CFR200 Nd:YAG from Big Sky Laser) with maximum pulse energy of 200 mJ, pulse width of 10 ns, wavelength of 1064 nm, and repetition rate of 1–15 Hz. The sample is placed on an x-y-z manually controlled stage, and the laser beam is focused on the sample surface by a convergent lens of 75 mm focal length. The optical radiation is collected by a 7-fiber bundle and sent to the LIBS2500-7 spectrometers (from Ocean Optics, Inc.) for analysis. With seven 2048-pixel linear CCD array detectors, the LIBS2500-7, which has a wide broadband (200–980 nm) corresponding to seven high-resolution (~0.1 nm at FWHM) spectrometers, is connected to a PC that is used for storage and analysis of spectral signal.

An aluminum-based alloy, an iron–chromium alloy, and an iron–chromium–nickel alloy sample of known compositions were used to test the IRSAC method to the CF-LIBS procedure. In our experiments, the laser power is fixed at 200 mJ for the aluminum alloy and 130 mJ for the iron–chromium and iron–chromium–nickel alloys. For each position of the sample surface, 50 laser shots were used for cleanness before data acquisition.

At the initiation of the laser-induced plasma, continuum background is very intense and unfavorable for quantitative analysis. In order to obtain a maximum signal-to-noise ratio (SNR), the acquisition gate and the time delay between the laser pulse and the beginning of the acquisition should be set at proper values. Limited by our detectors, the integration gate width was fixed at 1 ms, which is the minimal value of the detectors. This integration time is much wider than the life time of plasma, which is generally between one microsecond to tens of microseconds. With the integration time of 1 ms, the temperatures determined by Boltzmann plots are meaningless, since the line intensities are almost integrated over the whole life time of plasma. In order to solve this restriction, for each sample we collected two groups of spectrum under two different time delays. For the aluminum alloy sample, the two time delays are 2.5 μs and 5.0 μs, and for the iron–chromium and iron–chromium–nickel alloy samples are
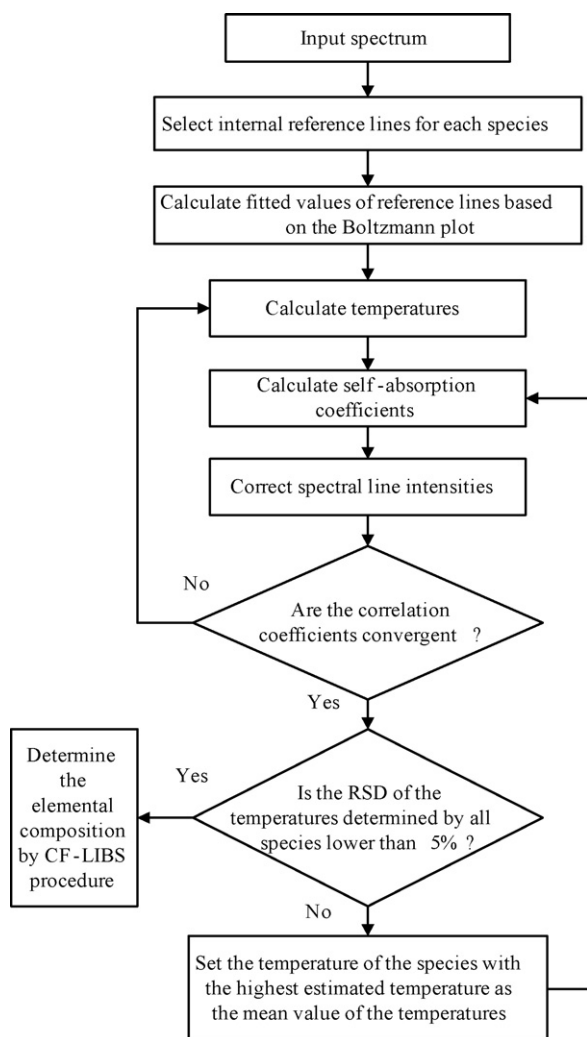
Fig. 1. Flow diagram of the proposed internal reference for self-absorption correction algorithm.

0.83 μs and 4.17 μs. Each of groups included 100 spectra obtained at 5 different positions of the sample surface. After averaging the 100 spectra, we used the difference of the average values of the two groups as the final analytical spectrum. By this manner, the time delay is corresponding to 2.5 μs for the aluminum alloy and 0.83 μs for the iron–chromium and iron–chromium–nickel alloys, and the acquisition gate is corresponding to 2.5 μs and 3.34 μs, respectively.
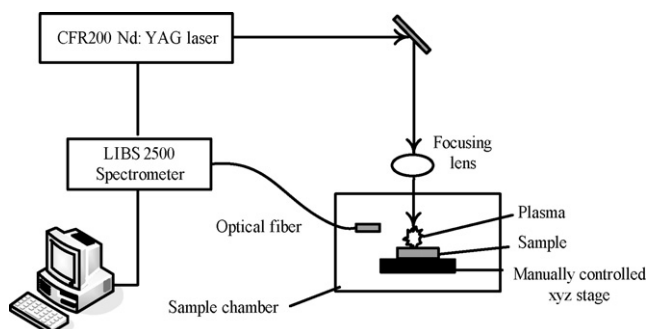
Fig. 2. Schematic experimental setup.
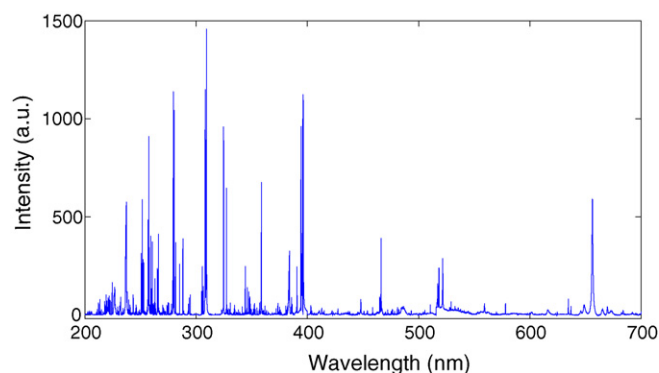
Fig. 3. One hundred shots averaged LIBS spectrum of the aluminum alloy sample obtained after 50 laser shots surface preparation.

3. Results and discussion

3.1. Selection of analytical lines

Figs. 3 and 4 show the typical processed LIBS spectrum of the aluminum alloy and the iron–chromium alloy samples. In typical LIBS measurement conditions, only neutral atomic species and singly ionized species are present to a significant degree, and accordingly we only considered the two kinds of species. The selected analytical lines for the three samples are listed in Tables 1–3, and the boldfaced numbers in tables represent the selected reference lines.

For the aluminum alloy sample, the energy levels of the observed ionic lines of Cu and Al elements were very convergent, and thus were not suitable to build their fitting lines on the Boltzmann plot. Therefore, we did not list the ionic lines of the two elements. For other species, we chose many lines in order to better reveal the correction process and reduce the effect of some specific lines with large fluctuation. In fact, we need not use all of the listed as analytical lines. The reference lines are not restricted to the selected, and other lines can be chosen only if they have near excitation energies of upper levels.

3.2. Boltzmann plots before and after self-absorption correction

The Boltzmann plots, determined by the basic CF-LIBS method and IRSAC method, are shown in Figs. 5–10. From Figs. 5, 7 and 9, before correction, the self-absorption lines make the points on Boltzmann plots very scattered. Moreover, for the matrix elements, Al, Cr, Fe, and Ni, most of their analytical lines with low excitation energies of upper levels exhibit strong self-absorption. The self-absorption effect causes their plasma temperature calculated higher than real values, the intercepts lower than expected, and finally large errors in the quantitative results.
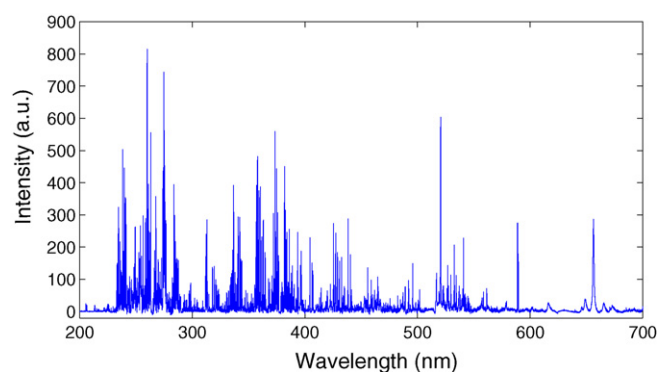
Fig. 4. One hundred shots averaged LIBS spectrum of the iron-chromium alloy sample obtained after 50 laser shots surface preparation.

Table 1
List of spectral lines used for building the Boltzmann plot for the aluminum-based alloy sample.

Species	Wavelength (nm)							
Al I	226.35	226.91	236.71	237.31	257.51	265.25	266.04	**305.47**
	305.71	306.43	306.61	308.22	309.27	394.40	396.15	669.60
Cu I	217.90	**219.98**	324.75	327.40	330.79	360.20	510.55	521.82
Mn I	279.83	322.81	354.78	356.95	357.79	380.67	403.08	403.31
	404.14	423.53	445.16	446.20	476.24	478.34	482.23	
Mn II	255.86	259.37	260.57	261.81	262.56	263.82	267.26	270.17
	270.57	**270.84**	271.03	288.96	293.31	293.93	294.92	344.20

The boldfaced number is the reference line used for correcting the self-absorption effect.

After correction based on our proposed IRSAC method (see Figs. 6, 8 and 10), points on the Boltzmann plots linearly stretch, and all the fitting lines are almost parallel. As above described, in the correction process three cases happened for different species. For Cu I and Mn I, because lines of them are not affected by self-absorption, the correction process only slightly changed their line intensities, and the slops and intercept of their fitting lines are nearly not changed. For Mn II, Cr II and Fe I, some lines are strongly affected by self-absorption while some lines not. The correction process greatly regulates those scattered points on the Boltzmann plots, and attains expected plasma temperatures and intercepts by these species themselves. Nevertheless, for the species Al I, Cr I, Fe II, Ni I and Ni II, because almost all lines at low energy levels encounter seriously self-absorption, their correction process should fall back on the temperature information from other species. Since almost

Table 2
List of spectral lines used for building the Boltzmann plot for the iron–chromium alloy sample.

Species	Wavelength (nm)							
Fe I	248.33	248.81	249.06	252.28	271.90	278.81	305.74	305.91
	306.72	322.78	328.68	330.64	**339.93**	342.71	344.06	346.59
	347.55	349.06	349.78	351.38	352.13	353.32	353.66	355.49
	355.85	356.54	357.01	358.12	358.53	361.88	363.15	364.04
	364.78	367.99	368.75	370.56	370.92	371.99	372.26	372.76
	373.49	373.71	374.34	374.56	374.83	374.95	375.82	376.38
	376.72	378.79	379.50	379.75	379.85	379.95	380.53	380.67
	381.30	381.58	382.04	382.59	382.78	383.42	384.10	385.00
	385.99	387.25						
Fe II	225.18	232.74	233.13	233.28	233.80	234.35	234.83	235.45
	235.91	236.20	236.48	236.86	237.37	238.20	238.86	239.56
	239.92	240.49	240.67	241.05	241.33	241.79	242.41	242.84
	243.29	243.47	243.50	243.93	244.45	245.46	245.88	246.19
	246.49	247.07	247.24	248.27	249.33	249.89	250.33	251.18
	251.44	251.90	252.54	252.95	253.36	253.90	254.87	256.25
	256.69	258.26	258.59	259.94	260.71	261.19	261.38	261.76
	262.17	262.57	262.83	263.13	**266.47**	266.66	268.48	269.26
	270.40	271.44	272.75	273.70	273.95	274.32	274.65	274.93
	275.57	278.37	294.44	300.26				
Cr I	278.07	288.92	289.67	291.11	298.86	300.09	301.49	301.76
	302.16	303.70	304.08	325.78	343.36	357.87	359.35	360.53
	385.76	391.92	397.67	**398.39**	399.00	399.11	417.93	425.43
	427.48	428.97	433.94	435.18	520.45	520.60	520.84	
Cr II	203.99	205.56	206.16	206.55	212.99	224.36	225.60	225.77
	229.72	230.72	231.94	265.36	265.86	266.34	266.60	266.87
	267.18	267.72	268.71	269.10	269.87	271.23	272.27	274.20
	274.36	275.77	276.65	279.22	280.08	281.20	281.84	282.24
	283.05	283.56	284.00	284.32	284.98	285.57	285.89	286.09
	286.26	286.51	286.67	287.04	287.35	287.62	288.09	289.85
	292.12	292.37	**292.81**	293.51	295.33	296.17	297.19	297.97
	298.53	302.66	311.86	312.04	312.50	312.87	313.67	314.72
	318.07	319.71	320.92	321.74	323.41	323.88	326.43	327.01
	329.54	332.83	333.63	333.98	334.26	334.78	335.85	336.03
	336.80	338.27	339.43	340.33	340.88	342.27		

The boldfaced number is the reference line used for correcting the self-absorption effect.

Table 3
List of spectral lines used for building the Boltzmann plot for the iron–chromium–nickel alloy sample.

Species	Wavelength (nm)							
Fe I	305.74	305.91	306.72	322.78	328.68	330.64	**339.93**	342.71
	344.06	346.59	347.55	349.06	349.78	351.38	352.13	353.32
	353.66	355.49	355.85	356.54	357.01	358.12	358.53	361.88
	363.15	364.04	364.78	367.99	368.75	370.56	370.92	371.99
	372.26	372.76	373.49	373.71	374.34	374.56	374.83	374.95
	375.82	376.38	376.72	378.79	379.50	379.75	379.85	379.95
	380.53	380.67	381.30	381.58	382.04	382.59	382.78	383.42
	384.10	385.00	385.99	387.25				
Fe II	225.18	232.74	233.13	233.28	233.80	234.35	234.83	235.45
	235.91	236.20	236.48	236.86	237.37	238.20	238.86	239.56
	239.92	240.49	240.67	241.05	241.33	241.79	242.41	242.84
	243.29	243.47	243.50	243.93	244.45	245.46	245.88	246.19
	246.49	247.07	247.24	248.27	249.33	249.89	250.33	251.18
	251.44	251.90	252.54	252.95	253.36	253.90	254.87	256.25
	256.69	258.26	258.59	259.94	260.71	261.19	261.38	261.76
	262.17	262.57	262.83	263.13	**266.47**	266.66	268.48	269.26
	270.40	271.44	272.75	273.70	273.95	274.32	274.65	274.93
	275.57	278.37	294.44	300.26				
Cr I	300.09	301.49	301.76	302.16	303.70	304.08	325.78	343.36
	357.87	359.35	360.53	385.76	391.92	397.67	**398.39**	399.00
	399.11							
Cr II	302.66	311.86	312.04	312.50	312.87	313.67	314.72	318.07
	319.71	320.92	321.74	323.41	323.88	326.43	327.01	**329.54**
	332.83	333.63	333.98	334.26	334.78	335.85	336.03	336.80
	338.27	339.43	340.33	340.88	342.27			
Ni I	298.16	300.36	301.20	303.79	305.08	305.43	306.46	310.16
	313.41	320.21	322.13	328.28	336.96	338.06	339.30	341.48
	342.37	344.63	345.85	346.16	347.25	348.38	349.30	351.03
	351.50	351.62	351.86	352.45	356.64	359.77	361.94	**388.97**
	391.23	394.41	397.05	397.46				
Ni II	210.80	211.35	216.56	216.91	217.47	217.71	218.46	220.14
	221.32	331.65	222.04	222.30	226.45	227.88	228.71	229.71
	229.83	230.01	230.30	231.60	234.12	234.53		

The boldfaced number is the reference line used for correcting the self-absorption effect.

all measured line intensities of Al I, Cr I, Fe II, Ni I and Ni II have been corrected based on theoretical values determined by Eq. (9), almost all points of Al I and Fe II are on the fitting lines.

3.3. Calculation of elemental concentration

The concentration of neutral atoms and singly charged ions can be both deduced by q_s in Eq. (2). In this manner, we need find many
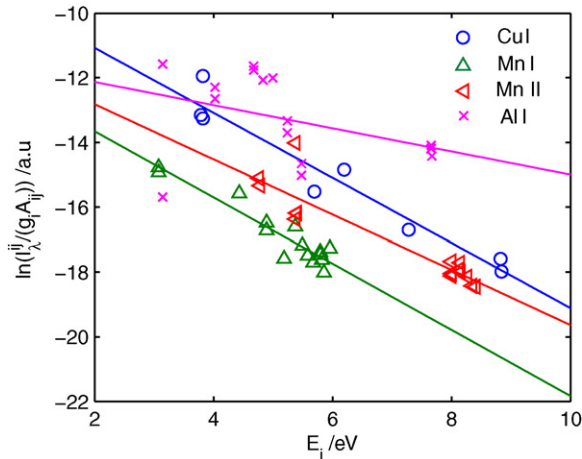

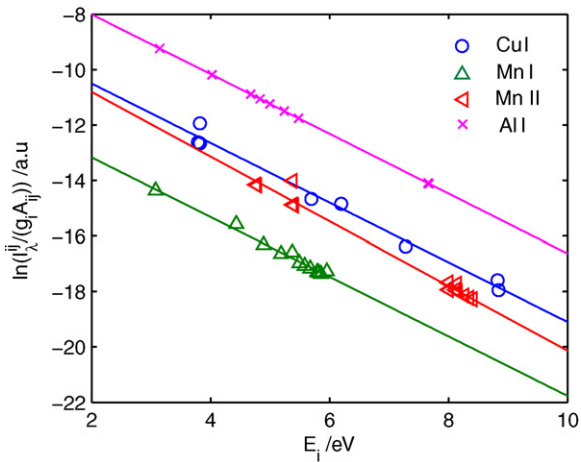**Fig. 5.** Initial Boltzmann plot derived from the raw line intensity of the aluminum alloy sample.

Fig. 6. Boltzmann plot corrected by the IRSAC for the aluminum alloy sample.

Fig. 8. Boltzmann plot corrected by the IRSAC for the iron–chromium alloy sample.

analytical lines with large difference in the excitation energies of upper levels for both neutral atoms and singly charged ions. In experiments, we found not all elements satisfy this condition. For the aluminum alloy sample, the energy levels of the ionic lines of Cu and Al elements were very convergent, and thus were not suitable to build their fitting lines. Therefore, we used another manner to calculate the ionic concentration of the two elements, and did not consider their ionic lines. We estimated the concentration of singly
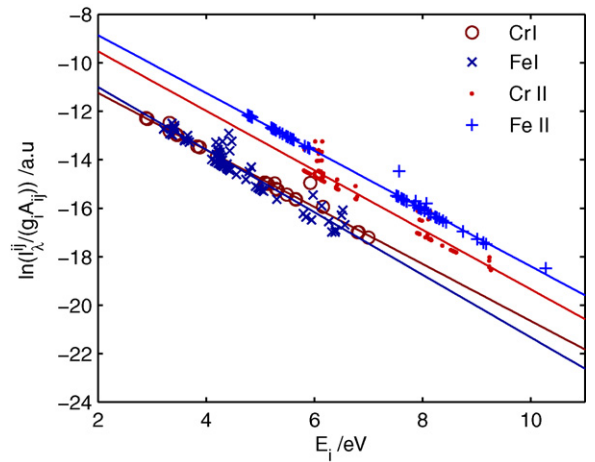
charged ions by Saha equation, which relating the number density of neutral and singly ionized species can be written as

$$n_e \frac{n^{II}}{n^{I}} = \frac{(2\pi m_e k_B T)^{3/2}}{h^3} \frac{2U^{II}(T)}{U^{I}(T)} e^{-E_{ion}/k_B T} \tag{10}$$

where n_e is the plasma electron density (cm^{-3}), n^{I} and n^{II} are the number densities of neutral atomic species and single ionized species, respectively, m_e is the electron mass (g), h is Planck's con-
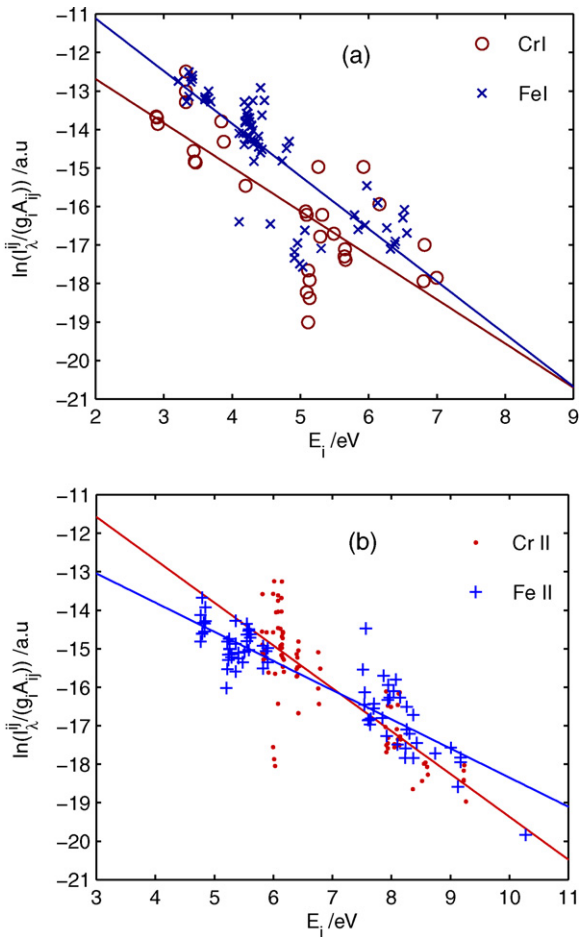
Fig. 7. Initial Boltzmann plot derived from the raw line intensity of the iron–chromium alloy sample (a) for neutral species, and (b) for singly ionized species.
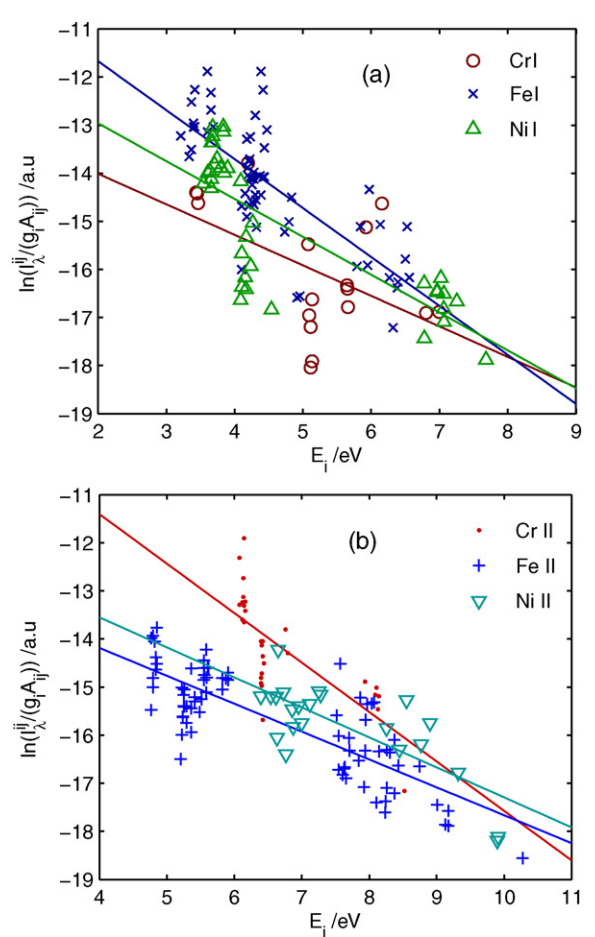
Fig. 9. Initial Boltzmann plot derived from the raw line intensity of the iron–chromium–nickel alloy sample (a) for neutral species, and (b) for singly ionized species.
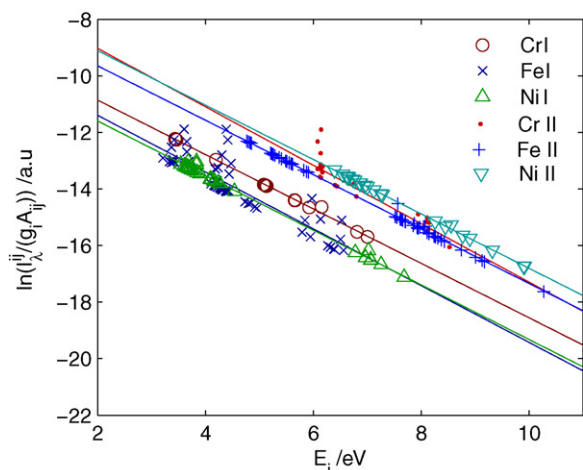
Fig. 10. Boltzmann plot corrected by the IRSAC for the iron–chromium–nickel alloy sample.

stant (eV s), E_{ion} is the ionization energy of the element, and the other symbols were defined above.

The plasma electron density, which must be known before using Saha equation, can be calculated through the determination of the Stark broadening of the H_α line as follows [22]:

$$n_e(H_\alpha) = 8.02 \times 10^{12} \left(\frac{\Delta\lambda_{1/2}}{\alpha_{1/2}} \right)^{3/2} \text{cm}^{-3} \qquad (11)$$

where $\Delta\lambda_{1/2}$ is the full width at half maximum (FWHM) of the H_α line, and $\alpha_{1/2}$ is the half width of the reduced Stark profiles and is a weak function of electron density and temperature. The values of $\alpha_{1/2}$ can be found in Ref. [23].

In order to obtain the Stark broadening, we used the Voigt function to fit the H_α, and then deconvoluted the Doppler and instrumental components. In this experimental condition, the Doppler broadening at the temperature of 10,000 K approximated to 0.08 nm, and the instrumental broadening approximated to 0.07 nm. Therefore, we finally obtained the electron density, n_e, approximating to 1.3×10^{17} cm^{-3} for the two samples. Knowing the electron density and concentration of neutral species, the concentration of singly ionized species can be obtained from the above Saha equation, Eq. (10).

The quantitative results determined by the basic CF-LIBS and our proposed IRSAC method are given in Table 4. Before self-absorption

correction, the intercepts of Al I, Fe II and Ni II are largely lower than real values, inducing huge errors in the calculation of the concentration. Because the CF-LIBS method utilizes the relation that the sum of the concentration of all elements equals one, the quantitative result of a certain species will affect the results of other elements. Therefore, for the element Al, Fe and Ni, the concentration calculated based on the basic CF-LIBS is extremely small, and for the other elements is exceptionally large.

By IRSAC method, the quantitative results of all elements except Mn acquire a notably improvement. Since all these quantitative results are based on the calibration-free method, the calculation errors of one element will affect the quantitative results of other elements. For example, though only a relative error of 0.5% is brought by the matrix element Al, this error will produce a fatal effect for the concentration estimation of minor elements. Consequently, though the IRSAC method can greatly improve the quantitative results based on CF-LIBS, we can just utilize them as a semi-quantitative method for minor elements. However, if the concentration of the matrix element is known beforehand and the concentrations of other elements have same orders of magnitude, then more accuracy quantitative results will be obtained.

4. Conclusion

In laser-induced breakdown spectroscopy, the plasma produced is often optically thick, especially for the strong lines of major elements. The measured spectral intensities of self-absorbed lines are lower than expected, which induces low concentration predictions for the elements analyzed. In order to correct the self-absorption effect, we proposed a recursive algorithm called IRSAC, which selects an internal reference line for each species as a standard line, estimates self-absorption levels of other lines based on the reference line, and finally obtains an optimal correction by a regressive procedure.

After the execution of the IRSAC, the corrected points on the Boltzmann plot are more regular, and consequently the plasma temperature and quantitative results are more accurate than the ones obtained by the basic CF-LIBS. Compared with the procedure of the self-absorption correction based on COG, the proposed IRSAC method does not require the values of quite so many quantities, like the Gaussian and Lorentzian broadenings of analytical lines, and thus can be more easily implemented.

Table 4
Quantitative results for the aluminum-based alloy, iron–chromium alloy and iron–chromium–nickel alloy studied in present work.

Element	Concentration (wt%)			Relative standard deviation (%)
	Certified value	Basic CF-LIBS	IRSAC	IRSAC
Aluminum alloy				
Cu	3.99	89.54	4.79	20.05
Mn	0.81	0.45	0.47	41.98
Al	83.89	4.40	83.46	0.51
Other elements	11.31	–	–	
Iron–chromium alloy				
Cr	14.26	28.07	13.32	6.59
Fe	84.54	71.93	86.68	2.53
Other elements	1.2	–	–	
Iron–chromium–nickel alloy				
Cr	28.24	68.92	29.90	5.88
Fe	40.57	21.25	41.61	2.56
Ni	24.28	2.91	21.59	11.08
Other elements	6.91	–	–	

References

[1] R.S. Harmon, F.C. DeLucia, C.E. McManus, N.J. McMillan, T.F. Jenkins, M.E. Walsh, A. Miziolek, Appl. Geochem. 21 (2006) 730–747.
[2] B. Sallé, P. Mauchien, S. Maurice, Spectrochim. Acta B 62 (2007) 739–768.
[3] R. Noll, H. Bette, A. Brysch, M. Kraushaar, I. Monch, L. Peter, V. Sturm, Spectrochim. Acta B 56 (2001) 637–649.
[4] J. Gruber, J. Heitz, N. Arnold, D. Bauerle, N. Ramaseder, W. Meyer, J. Hochortler, F. Koch, Appl. Spectrosc. 58 (2004) 457–462.
[5] S. Palanco, S. Conesa, J.J. Laserna, J. Anal. Atom. Spectrom. 19 (2004) 462–467.
[6] A. Ciucci, V. Palleschi, S. Rastelli, R. Barbini, F. Colao, R. Fantoni, A. Palucci, S. Ribezzo, H.J.L. van der Steen, Appl. Phys. B 63 (1996) 185–190.

[7] G. Arca, A. Ciucci, V. Palleschi, S. Rastelli, E. Tognoni, Appl. Spectrosc. 51 (1997) 1102–1105.

[8] M.A. Gondal, T. Hussain, Talanta 71 (2007) 73–80.

[9] B. Sallé, J.L. Lacour, P. Mauchien, P. Fichet, S. Maurice, G. Manhes, Spectrochim. Acta B 61 (2006) 301–313.

[10] V. Tornari, V. Zafiropulos, A. Bonarou, N.A. Vainos, C. Fotakis, Opt. Laser Eng. 34 (2000) 309–326.

[11] A. Kumar, P.C. Sharma, Uses of LIBS technology in biological media, in: Advanced Environmental, Chemical, and Biological Sensing Technologies IV, SPIE, Boston, MA, United States, 2006, 637701.

[12] J. Vrenegor, R. Noll, V. Sturm, Spectrochim. Acta B 60 (2005) 1083–1091.

[13] A.K. Rai, H. Zhang, Y. Fang Yu, J.P. Singh, A. Weisburg, Spectrochim. Acta B 56 (2001) 2371–2383.

[14] L. Fornarini, F. Colao, R. Fantoni, V. Lazic, V. Spizzicchino, Spectrochim. Acta B 60 (2005) 1186–1201.

[15] C. Aragon, J.A. Aguilera, F. Penalba, Appl. Spectrosc. 53 (1999) 1259–1267.

[16] U. Panne, C. Haisch, M. Clara, R. Niessner, Spectrochim. Acta B 53 (1998) 1957–1968.

[17] C. Chaleard, P. Mauchien, N. Andre, J. Uebbing, J.L. Lacour, C. Geertsen, J. Anal. Atom. Spectrom. 12 (1997) 183–188.

[18] A. Ciucci, M. Corsi, V. Palleschi, S. Rastelli, A. Salvetti, E. Tognoni, Appl. Spectrosc. 53 (1999) 960–964.

[19] J.A. Aguilera, C. Aragon, Spectrochim. Acta B 59 (2004) 1861–1876.

[20] E. Tognoni, G. Cristoforetti, S. Legnaioli, V. Palleschi, A. Salvetti, M. Mueller, U. Panne, I. Gornushkin, Spectrochim. Acta B 62 (2007) 1287–1302.

[21] D. Bulajic, M. Corsi, G. Cristoforetti, S. Legnaioli, V. Palleschi, A. Salvetti, E. Tognoni, Spectrochim. Acta B 57 (2002) 339–353.

[22] A.M. El Sherbini, H. Hegazy, T.M. El Sherbini, Spectrochim. Acta B 61 (2006) 532–539.

[23] H.R. Griem, Spectral Line Broadening by Plasmas, Academic Press, Inc., New York, United States, 1974.

Investigation on enhanced chemiluminescence reaction systems with bis(hydrogenperiodato) argentate(III) complex anion for fluoroquinolones synthetic antibiotics

Hanwen Sun*, Peiyun Chen, Fei Wang, Haifang Wen

College of Chemistry and Environmental Science, Hebei University, Key Laboratory of Analytical Science and Technology of Hebei Province, Wusi Road 188, Baoding, 071002, China

ARTICLE INFO

ABSTRACT

A novel chemiluminescence (CL) reaction system with bis(hydrogenperiodato) argentate(III) complex anion (Ag(III) complex, $[Ag(HIO_6)_2]^{5-}$), for the first time, is developed for the determination of lomefloxacin (LMFX), enrofloxacin (ENLX) and pefloxacin (PFLX). The possible CL emission mechanism was discussed by comparing the fluorescence emission with CL spectra. The CL conditions of $[Ag(HIO_6)_2]^{5-}$–H_2SO_4–LMFX/ENLX/PFLX systems were investigated and optimized. Under the optimized experimental conditions, the CL intensity is proportional to the concentration of the drugs in the range 0.2994–36.80×10^{-7} g mL^{-1} for LMFX, 4.00–30.0×10^{-7} g mL^{-1} for ENLX and 1.54–27.64×10^{-7} g mL^{-1} for PFLX. The limit of detection ($s/n = 3$) was 9.1×10^{-9} g mL^{-1} for LMFX, 3.1×10^{-9} g mL^{-1} for ENLX and 4.4×10^{-9} g mL^{-1} for PFLX. The recovery of LMFX, ENLX and PELX from the spiked pharmaceutical preparations was in the range of 92.3–105% with the RSDs of 0.5–2.7%. For urine, serum and milk samples the recoveries of the three drugs were in the range of 85.1–107% for LMFX with the RSDs of 2.3–3.4%. 80.2–112% for ENLX with the RSDs of 1.4–2.8%, and 87.8–114% for PFLX with the RSDs of 1.6–2.7%. The proposed method was applied successfully to the determination of these compounds in real samples.

© 2009 Elsevier B.V. All rights reserved.

1. Introduction

Chemiluminescence (CL) is known to be a powerful analytical technique that promises high sensitivity, wide linear range and simple instrumentation and has been applied for biomedical, pharmaceutical, clinical and food analysis [1–5]. A series of CL reagents were utilized, including acidic potassium permanganate, manganese(III) and manganese(IV) [6–8], Ce(IV) [9,10], luminol [11–13], peroxyoxalate [14] and Ru(bipy)$_3^{3+}$ [15–17]. Some reagents, such as formaldehyde [2], peroxynitrous acid [18], lanthanide ions [10,19,20] and gold nanoparticle [21], were selected as a sensitizing reagent in a CL system. In the recent years several electrogenerated oxidants were applied for the CL analysis of drugs [22–26].

Several CL method with different reaction systems were used for the analysis of lomefloxacin (LMFX), such as KIO$_4$-isoniazid system [27], luminol–KIO$_4$–calcein system [28], Ce(IV)–rhodamine 6G system [29], gold nanoparticles–luminol–hydrogen peroxide system [30] and terbium–Ce(IV)–H$_2$SO$_3$ system [31]. The detection limit of these methods was in the range from 3.0×10^{-7} g mL^{-1} to 7.0×10^{-9} g mL^{-1}. An electrogenerate CL method was presented for

the determination of pefloxacin (PFLX) with a detection limit of 8.0×10^{-9} g mL^{-1} [32]. There is few report for the determination of enrofloxacin (ENLX) by using CL method.

In our previous works CL methods for the determination of LMFX were reported by using Ce(IV)–sulfite system with a limit of detection (LOD) of 3×10^{-9} g mL^{-1} [33]. Capillary electrophoresis with CL detection was described for simultaneous determination of lomefloxacin, proline and lidocaine in human urine with a LOD of 6×10^{-8} g mL^{-1} for LMFX [34]. Otherwise, mechanistic insights into the reaction between bis(hydrogenperiodato) argentate(III) complex anion (Ag(III) complex, $[Ag(HIO_6)_2]^{5-}$) and some medicines under alkaline medium has been performed [35–38]. To our knowledge, there is no report using the Ag(III) complex to CL. This work focuses on researching and developing a new and sensitive Ag(III) complex CL reaction systems for fluoroquinolones synthetic antibiotics, their CL mechanism and application in pharmaceutical preparation, biological fluid and milk samples.

2. Experimental

2.1. Chemicals and solution

The following reagents were used: sodium periodate (NaIO$_4$, 99.5%) was purchased from Tianjin Kermel Chemical Reagent Com-

* Corresponding author. Tel.: +86 312 5079719; fax: +86 312 5079739.
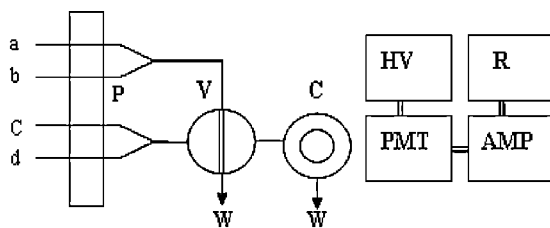*E-mail address:* hanwenhbu@yahoo.com.cn (H. Sun).

Fig. 1. Schematic diagram of flow injection CL analysis system. P, peristaltic pump; V, sampling inlet valve; C, flowing cell; PMT, photomultiplier tube; AMP, amplifier; HV, high voltage; R, recorder; W, waste; a, sample solution; b, H_2SO_4 solution; c, $[Ag(HIO_6)_2]^{5-}$ solution.

pany (Tianjin, China); potassium peroxydisulfate ($K_2S_2O_8$, 99.5%) was purchased from Beijing Chemical Reagent Company (Beijing, China). Silver nitrate ($AgNO_3$, 99.8%) and potassium hydroxide (KOH, 82%) were purchased from Tianjin Damao Chemical Reagent Company (Tianjin, China). All chemicals were of analytical reagent grade and used without further purification, and deionized water was used throughout.

The Ag(III) complex, $[Ag(HIO_6)_2]^{5-}$, was prepared by oxidizing Ag(I) in the alkaline medium according the known method [39]. The complex was characterized by UV/vis spectrum, which exhibits two absorb peak at 362 ± 1 nm and 252.6 ± 0.4 nm. The concentration of Ag(III) complex solutions prepared is determined accord to the literature [40].

LMFX, ENLX and PFLX were purchased from Institute of Medicinal Biotechnology (Beijing, China). Stock standard solution of LMFX, ENLX and PFLX (5.0×10^{-4} g mL^{-1}) alone was prepared by dissolving 25.0 mg the compound in 1 mL of 0.2 M HCl and diluting with deionized water to 50 mL. The $[Ag(HIO_6)_2]^{5-}$–H_2SO_4 working solutions were prepared daily and diluted as required.

2.2. Apparatus

The FI system, as shown in Fig. 1, is a MPI-B-FICL analysis system (Xi'an Remex Electronic Science Tech Co. Ltd., Xi'an, China) consisted of two peristaltic pumps working at a constant flow rate (70 rpm) and a six-way injection valve with a sample loop (120 μL), which is automatically operated by a computer equipped operation system of MPI-B flow injection analysis. PTFE tubing (0.8 mm i.d.) was used to connect all components in the flow system. The flow cell is a twisted glass tube, with a large surface area exposed to the adjacent photomultiplier tube (PMT, operated at −800 V).

Fluorescence spectra were recorded with an RF-5301PC Spectrofluorometer (Shimadzu, Japan) for studying CL mechanism. CL spectra were recorded by using a CL analyzer with 10 light filters in the range of 400–650 nm (Biophysics Institute of Chinese Academy of Science, Beijing, China). UV data were measured with an UV-265 spectrophotometer (Shimadzu, Japan).

2.3. Sample treatment

2.3.1. Procedure for dosage forms
Ten tablets were weighed and pulverized. An accurately weighed amount of the powder equivalent to 10.0 mg of the drug was dissolved with 3 mL of 0.1 M HCl in a small beaker and transferred into a 100-mL volumetric flask and diluted to the mark with deionized water. It was sonicated for 20 min, then filtered and the residue was washed with deionized water several times, then it was transferred into a 100-mL volumetric flask and diluted to the mark with deionized water. The working solutions were prepared by appropriate dilutions so that the final concentration was in the linear range. The nominal content of the tablets was calculated either from a previously plotted calibration graph.

The sample of LMFX injection was confected by mixing five bottles of the injections selected randomly from same group. The working solution was directly diluted with deionized water. The injection sample of ENLX and PELX was made in the same way as LMFX.

2.3.2. Procedure for urine and serum
Urine and serum samples were provided by Hospital of Hebei University. 1.0 g PbO_2 powder was added in 5.0 mL of blank urine, and followed by stirring for 10 min to eliminate urine acid, thiourea and ascorbic acid, etc. After centrifugation for 10 min at 10,000 rpm, the supernatant was filtrated, then the filtrate was applied to a cation exchange column (4 cm × 1.2 cm) for clean up. The clear liquid was diluted with deionized water to make different concentrations of fluoroquinolones in the linear range. The protein of a 1-mL volume of serum sample was removed by adding 4.0 mL 10% trichloroacetic acid (CCl_3COOH) in a centrifuge tube, which was shaken for 5 min, then centrifuged for 10 min at 10,000 rpm. The supernatant was diluted with deionized water to make different concentrations of fluoroquinolones in the linear range.

2.3.3. Procedure for milk
Milk samples were purchased from market. 30 mL 1% trichloroacetic acid (CCl_3COOH) and 1 mL 2.2% lead acetate were added in 3.0 g of blank milk in a centrifuge tube. The mixed solution was treated through the sonication for 20 min for eliminating proteins and extracting fluoroquinolones, then centrifuged for 10 min at 10,000 rpm. The supernatant was diluted with deionized water so as to make different concentrations of fluoroquinolones in the linear range.

2.4. Analytical procedure

The investigation of the CL intensity–time profiles was performed with the static CL analysis. In a 10-mL calibrated flask, 0.2 mL fluoroquinolones and 0.2 mL H_2SO_4 were mixed, then 1 mL $[Ag(HIO_6)_2]^{5-}$ (1.4×10^{-4} mol L^{-1}) was injected into the reaction
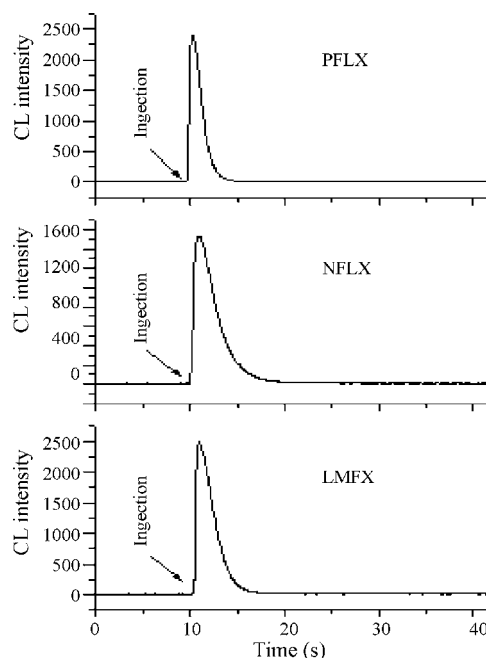

Fig. 2. Kinetic characteristic of the CL reaction of $[Ag(HIO_6)_2]^{5-}$–H_2SO_4–fluoroquinolone. $[Ag(HIO_6)_2]^{5-}$, 1.4×10^{-4} M; H_2SO_4, 1.0 M; LMFX, 3.0×10^{-7} g mL^{-1}; ENLX, 3.8×10^{-7} g mL^{-1}; PFLX, 3.2×10^{-7} g mL^{-1}.
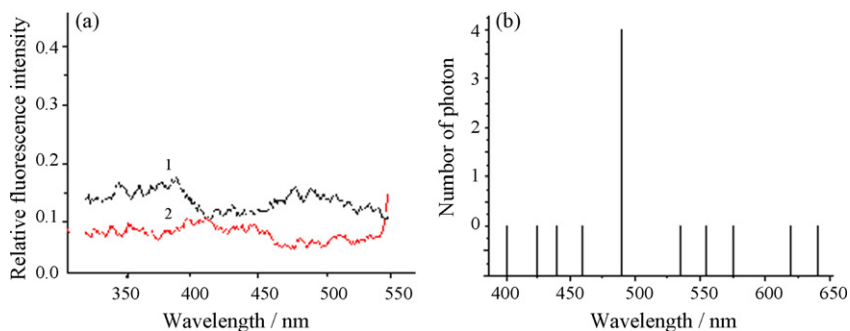
Fig. 3. Fluorescence emission spectra (a) of $[Ag(HIO_6)_2]^{5-}$ (1) and $[Ag(HIO_6)_2]^{5-}-H_2SO_4$ (2) and CL spectra (b) of $[Ag(HIO_6)_2]^{5-}-H_2SO_4$. (a) $\lambda ex = 290$ nm; $[Ag(HIO_6)_2]^{5-}$, 2.8×10^{-5} M; H_2SO_4, 4×10^{-2} M. (b) $[Ag(HIO_6)_2]^{5-}-H_2SO_4$; $[Ag(HIO_6)_2]^{5-}$, 1.4×10^{-4} M; H_2SO_4, 1.0 M.
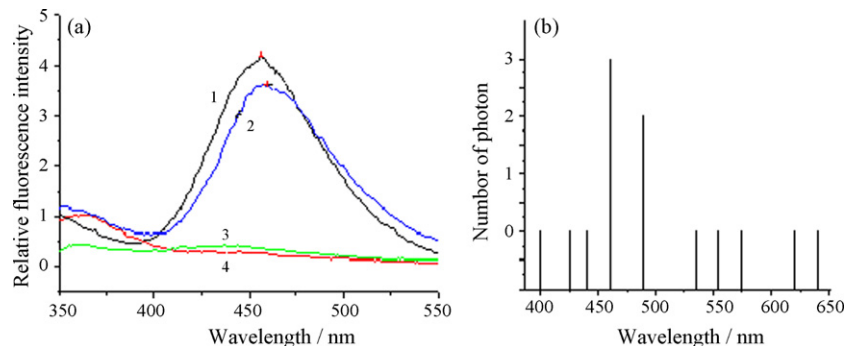
Fig. 4. Fluorescence emission spectra (a) and CL spectra (b). (a) (1) LMFX, (2) LMFX–H_2SO_4, (3) $[Ag(HIO_6)_2]^{5-}$–LMFX, and (4) $[Ag(HIO_6)_2]^{5-}$–H_2SO_4–LMFX; $\lambda ex = 290$ nm; LMFX, 1.26×10^{-8} g mL^{-1}; $[Ag(HIO_6)_2]^{5-}$, 2.8×10^{-5} M; H_2SO_4, 4×10^{-2} M. (b) $[Ag(HIO_6)_2]^{5-}$–H_2SO_4–LMFX; $[Ag(HIO_6)_2]^{5-}$, 1.4×10^{-4} M; H_2SO_4, 1.0 M; LMFX, 1.57×10^{-5} g mL^{-1}.
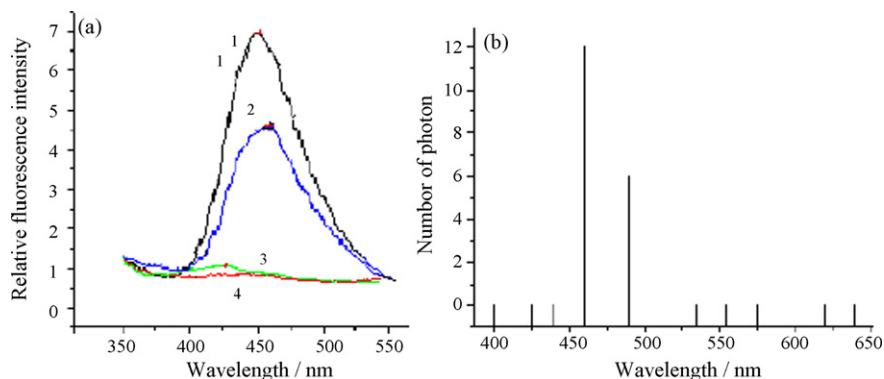
Fig. 5. Fluorescence spectra (a) and CL spectra (b). (a) (1) ENLX, (2) ENLX–H_2SO_4, (3) $[Ag(HIO_6)_2]^{5-}$–ENLX, and (4) $[Ag(HIO_6)_2]^{5-}$–H_2SO_4–ENLX; $\lambda ex = 270$ nm; ENLX, 1.26×10^{-8} g mL^{-1}; $[Ag(HIO_6)_2]^{5-}$, 2.8×10^{-5} M; H_2SO_4, 4×10^{-2} M. (b) $[Ag(HIO_6)_2]^{5-}$–H_2SO_4–ENLX; $[Ag(HIO_6)_2]^{5-}$, 1.4×10^{-4} M; H_2SO_4, 1.0 M; ENLX, 1.0×10^{-5} g mL^{-1}.
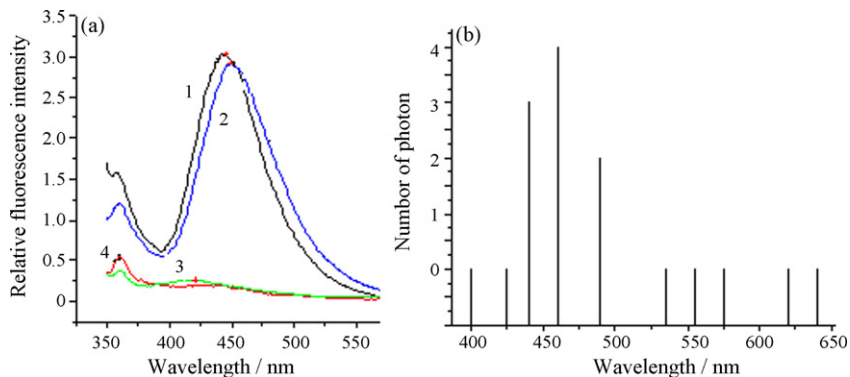
Fig. 6. Fluorescence spectra (a) and CL spectra (b). (a) (1) PFLX, (2) PFLX–H_2SO_4, (3) $[Ag(HIO_6)_2]^{5-}$–PFLX, and (4) $[Ag(HIO_6)_2]^{5-}$–H_2SO_4–PFLX; $\lambda ex = 320$ nm; PFLX, 3.20×10^{-9} g mL^{-1}; $[Ag(HIO_6)_2]^{5-}$, 2.8×10^{-5} M; H_2SO_4, 4×10^{-2} M. (b) $[Ag(HIO_6)_2]^{5-}$–H_2SO_4–PFLX; $[Ag(HIO_6)_2]^{5-}$, 1.4×10^{-4} M; H_2SO_4, 1.0 M; PFLX, 4.0×10^{-6} g mL^{-1}.

Table 1
Fluorescence and CL emission of different reaction systems.

Analyte	Reaction system	Fluorescence (nm)	CL emission (nm)
	$[Ag(HIO_6)_2]^{5-}$		
	$[Ag(HIO_6)_2]^{5-}$–H_2SO_4		490
LMFX	LMFX	457	
	LMFX–H_2SO_4	460	
	$[Ag(HIO_6)_2]^{5-}$–LMFX	440	
	$[Ag(HIO_6)_2]^{5-}$–H_2SO_4–LMFX		460, 490
ENLX	ENLX	452	
	ENLX–H_2SO_4	460	
	$[Ag(HIO_6)_2]^{5-}$–ENLX	425	
	$[Ag(HIO_6)_2]^{5-}$–H_2SO_4–ENLX		460, 490
PFLX	PFLX	445	
	PFLX–H_2SO_4	449	
	$[Ag(HIO_6)_2]^{5-}$–PFLX	421	
	$[Ag(HIO_6)_2]^{5-}$–H_2SO_4–PFLX		440, 460, 490

tube by a quantitative injector and the CL intensity was measured without stirring.

The procedure of FIA is shown in Fig. 1. The flow lines a and b were inserted into fluoroquinolones and H_2SO_4 solution, respectively, and then mixed with $[Ag(HIO_6)_2]^{5-}$ to produce CL when the injection valve was switched to the position of injection. The concentration of fluoroquinolones was quantified by the peak height of the CL signals.

3. Results and discussion

3.1. Investigation of enhanced CL system

An attempt was made to research and develop a new and sensitive CL system that could be applied for the CL determination. The kind of acid used in the reaction has a very significant influence on the CL emission intensity. Therefore, several acids, such as HCl, H_2SO_4, HNO_3, H_3PO_4 and $H_6P_4O_{13}$, were added in the $[Ag(HIO_6)_2]^{5-}$ solution to test the effect of acidic medium on the CL signal, respectively. The results indicated that CL signal could be produced by the direct CL reaction of H_2SO_4 and Ag(III) complex, with the highest and stable emission. The reason why H_2SO_4 could have best result compared to other acids tested needs to be researched further. When LMFX, ENLX and PFLX were added separately to the

Table 2
Tolerable content of foreign species for quantitative determination.

Additive	Tolerable concentration ($\times 10^{-7}$ g mL^{-1})		
	LMFX[a]	ENLX[b]	PFLX[c]
Polyglycol	345	38	339.2
Sodium benzoate	36	38	48
Amylum	15	95	80
Dextrin	180	380	192
Glucose	6	22.8	6.4
Lactose	15	11.4	96
Sucrose	36	41.8	32
Vitamin C	6	7.2	7.36
Ca^{2+}	15	11.4	249.6
Mg^{2+}	45	95	44.8
EDTA	30	19	32
Zn^{2+}	72	114	70.4
Cu^{2+}	42	38	80
Co^{2+}	84	102.6	80
Ba^{2+}	12	19	16
Fe^{3+}	6	3.8	6.4

[a] 3.0×10^{-7} g mL^{-1}.
[b] 3.8×10^{-7} g mL^{-1}.
[c] 3.2×10^{-7} g mL^{-1}.

$[Ag(HIO_6)_2]^{5-}$–H_2SO_4 system, the CL signal was enhanced significantly.

3.2. Kinetic characteristics of CL reaction systems

The CL kinetic characteristics of the reactions of three systems were investigated in detail. The result is shown in Fig. 2. It was shown that the reaction rate in solution was very fast, from reagent mixing to peak maximum only 0.7 s was needed for $[Ag(HIO_6)_2]^{5-}$–H_2SO_4–LMFX system, and it took 8 s for the signal to return to zero again, only 1 and 10 s for $[Ag(HIO_6)_2]^{5-}$–H_2SO_4–NFLX system, and only 0.6 and 6.5 s for $[Ag(HIO_6)_2]^{5-}$–H_2SO_4–PFLX system. The kinetic curve indicated the CL method is sensitive enough and suitable to perform the determination of LMFX, ENLX and PFLX.

3.3. Fluorescence and CL spectra

The fluorescence was examined in order to obtain more information about CL mechanism. The fluorescence emission spectra of different systems were observed, as shown in Figs. 3a–6a. The CL spectra were examined by using a CL analyzer, as shown in Figs. 3b–6b. The centre wavelength of fluorescence and CL emission is listed in Table 1.

From Fig. 3a it is shown that no fluorescence emission of Ag(III) complex with and without H_2SO_4 was observed in the range of 350–550 nm. Figs. 4a–6a show the three fluoroquinolones alone could produce fluorescence emission with a broad peak at 457 nm for LMFX, 452 nm for ENLX, and 445 nm for PFLX. When fluoroquinolone mixed with H_2SO_4, the fluorescence emission shows a broad peak at 460 nm for LMFX and ENLX, and 449 nm for PFLX. For fluoroquinolone–$[Ag(HIO_6)_2]^{5-}$ systems, since a complex to be formed, a very weak peak was observed at about 425 nm. For fluoroquinolone–$[Ag(HIO_6)_2]^{5-}$–H_2SO_4 systems, the fluorescence was disappeared.

From Figs. 4b–6b and Table 1 it is seen that a same CL peak at 490 nm was observed for each CL system. For $[Ag(HIO_6)_2]^{5-}$–H_2SO_4–LMFX/ENLX/PELX systems, a CL peak at 460 nm also was observed. Otherwise, for $[Ag(HIO_6)_2]^{5-}$–H_2SO_4–PFLX system, third CL peak was observed at 440 nm.

3.4. Possible mechanism of the CL system

It is shown that $[Ag(HIO_6)_2]^{5-}$ with and without H_2SO_4 could not produce fluorescence emission, and when added with $[Ag(HIO_6)_2]^{5-}$–H_2SO_4, fluorescence of fluoroquinolone would be saddened, but $[Ag(HIO_6)_2]^{5-}$ with H_2SO_4 could produce CL emission at 490 nm, it might be caused by the excited state $(O_2)_2^*$ [41,42]. Otherwise, the CL emission at 460 nm and 440 nm might be produced through an intermolecular energy transfer. The fluoroquinolone molecule received energy from $(O_2)_2^*$ to be excited, then, de-excited to its ground state, producing the CL emission at 460 nm, which is corresponding to fluorescence emission at 460 nm. The CL emission at 440 nm produced from $[Ag(HIO_6)_2]^{5-}$–H_2SO_4–PFLX system was suggested via the intermolecular energy transfer from $(O_2)_2^*$ to a complex of $[Ag(HIO_6)_2]^{5-}$ and PELX, then, the excited complex de-excited to its ground state, producing the CL emission. The reason on the difference of CL peak number between LMFX, ENLX and PELX needs to be researched further.

Our previous test had shown that Ag(III) complex ion has two forms, $[Ag(HIO_6)_2]^{5-}$ and $[Ag(HIO_6)(OH)(H_2O)]^{2-}$, and the latter could be active centre and could take place complex reaction [37]. Otherwise, the observed CL spectra at 490 nm for $[Ag(HIO_6)_2]^{5-}$–H_2SO_4 system suggested that $O_2^{-\bullet}$ to be produced in the reaction systems. The recombination of part of $O_2^{-\bullet}$ may generate energy-rich precursors of excited molecules $(O_2)_2^*$ which decompose to O_2, and a bright luminescence appeared with a 490-
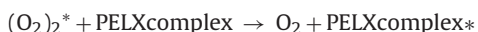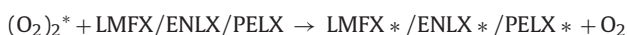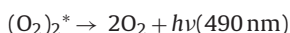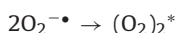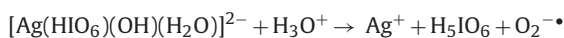
Table 3
Performance data for the CL determination of LMFX, ENLX and PFLX.

Analyte	Linear range ($\times 10^{-7}$ g mL^{-1})	Calibration equation	Correlation coefficient	LOD ($\times 10^{-9}$ g mL^{-1})	RSD% ($n = 11$)
LMFX	0.2994–36.80	$I = 6.410C + 17.8$	0.9992	9.1	2.0
ENLX	4.000–30.00	$I = 23.56C - 43.6$	0.9987	3.1	2.7
PFLX	1.536–27.64	$I = 28.96C + 2.14$	0.9977	4.4	2.1

Table 4
Determination results of recovery of LMFX, ENLX and PFLX from tablet and injection.

Sample	Analyte	Content ($\times 10^{-7}$ g mL^{-1})	Added ($\times 10^{-7}$ g mL^{-1})	Found ($\times 10^{-7}$ g mL^{-1})	Recovery (%)	RSD% ($n = 7$)
Tablet	LMFX	0.712	0.883	1.619	103	0.7
			2.355	3.019	98.0	2.2
			3.533	4.050	94.5	1.7
Tablet	ENLX	6.00	6.000	12.50	109	1.1
			12.00	17.60	97.0	0.5
			18.00	24.80	104	1.0
Injection	LMFX	1.38	2.397	3.671	95.7	2.4
			3.964	5.572	106	1.9
			7.905	9.345	101	2.3
Injection	ENLX	9.00	4.000	12.70	92.3	0.5
			12.00	21.00	99.8	1.1
			16.00	24.20	95.0	1.8
Injection	PFLX	4.22	3.186	7.259	95.4	2.2
			9.779	14.50	105	2.7
			15.00	18.64	96.1	1.4

nm maximum wavelength. Based on the discussion above, the possible CL mechanism for the three systems can be described as follows:

$$[Ag(HIO_6)_2]^{5-} + H_2O \rightarrow [Ag(HIO_6)(OH)(H_2O)]^{2-} + H_2IO_6{}^{3-}$$

$$[Ag(HIO_6)(OH)(H_2O)]^{2-} + \text{analyte} \rightarrow \text{complex} + H_2O$$

$$[Ag(HIO_6)(OH)(H_2O)]^{2-} + H_3O^+ \rightarrow Ag^+ + H_5IO_6 + O_2{}^{-\bullet}$$

$$2O_2{}^{-\bullet} \rightarrow (O_2)_2{}^*$$

$$(O_2)_2{}^* \rightarrow 2O_2 + h\nu(490\,\text{nm})$$

$$(O_2)_2{}^* + \text{LMFX/ENLX/PELX} \rightarrow \text{LMFX} * / \text{ENLX} * / \text{PELX} * + O_2$$

$$\text{LMFX} * / \text{ENLX} * / \text{PELX} * \rightarrow \text{LMFX/ENLX/PELX} + h\nu(460\,\text{nm})$$

$$(O_2)_2{}^* + \text{PELXcomplex} \rightarrow O_2 + \text{PELXcomplex}*$$

$$\text{PELXcomplex}* \rightarrow \text{PELXcomplex} + h\nu(440\,\text{nm})$$

3.5. Optimization of CL conditions

The concentration of $[Ag(HIO_6)_2]^{5-}$ and H_2SO_4 was an important factor for CL emission. In this CL system, $[Ag(HIO_6)_2]^{5-}$ was used as the oxidant, its concentration not only influenced the sensitivity, but also influenced the linear range for the assay. Therefore, the dependence of the $[Ag(HIO_6)_2]^{5-}$ concentration on the CL intensity was investigated for 1.0×10^{-6} g mL^{-1} analyte. The CL intensity increased remarkably with the increase of $[Ag(HIO_6)_2]^{5-}$ concentration in the range from 0.025 mM to 0.14 mM for LMFX and ENLX systems, and in the range from 0.025 mM to 0.11 mM for PFLX system, then decreased obviously with further increase of $[Ag(HIO_6)_2]^{5-}$ concentration. So optimized concentration of $[Ag(HIO_6)_2]^{5-}$ was 0.14 mM and 0.11 mM, respectively. The concentration of H_2SO_4 used in the reaction has a very significant influence

on the CL emission intensity. The CL intensity increased remarkably with the increase of concentration of H_2SO_4 in the range from 0.5 M to 1.0 M, but decreased over 1.0 M. So 1.0 M H_2SO_4 was selected as optimal concentration for the three CL systems.

The role of sample volume and flow rate is critical, for instance, if sample volume was too small or too large, CL maximum could not be obtained. The highest emission was produced when the injected sample volume was 120 μL. The CL intensity increased with increasing flow rate. However, a flow rate of 3.0 mL min^{-1} for all solutions is recommended because of greater precision and economy in the use of reagents.

3.6. Analytical performance of CL systems

The interfering effects from foreign species were investigated. The tolerance content was defined as the amount of coexisting species that produced an error not exceeding ±5% in the determination of LMFX, ENLX and PELX. The results are listed in Table 2. The data show that there was few interference.

Under the optimized conditions, the linearity was evaluated for each pharmaceutical by using the proposed systems. The regres-
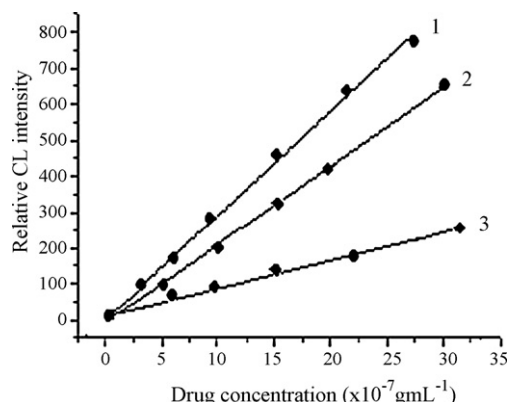

Fig. 7. Calibration graph of ENLX (1), LMFX (2) and PFLX (3).

Table 5
Analytical results of LMFX, ENLX and PFLX in tablet and injection samples.

Analyte	Sample	Labeled	Proposed method[a]	UV-method[a]
LMFX	Tablet (mg/tablet)	100	98.48 ± 1.10	97.83 ± 0.75
	Injection (mg/10 mL)	100	102.35 ± 2.05	99.31 ± 0.79
ENLX	Tablet (mg/tablet)	100	105.46 ± 3.08	101.11 ± 0.95
	Injection (mg/5 mL)	150	148.91 ± 2.85	145.38 ± 1.08
PFLX	Injection (mg/5 mL)	100	100.25 ± 1.02	98.45 ± 0.89

[a] Mean ± S.D. ($n = 5$).

sion equations are listed in Table 3. Coefficients of correlation were higher than 0.9977 thus confirming the linearity of the method.

The LOD was determined as the sample concentration that produces a peak with a height three times of the level of baseline noise. The LOD and RSD obtained also are listed in Table 4. The LOD was 9.1×10^{-9} g mL^{-1} for LMFX, 3.1×10^{-9} g mL^{-1} for ENLX and 4.4×10^{-9} g mL^{-1} for PFLX, which is lower than those for the methods described in the literature [27–34]. The RSD was found to be 2.0–2.7% for 11 determinations of 3.0×10^{-7} g mL^{-1} of each analyte. It is indicated that the proposed enhanced CL systems with $[Ag(HIO_6)_2]^{5-}$–H_2SO_4 has satisfactory linearity, sensitivity and precision.

3.7. Sample analysis

In order to evaluate the validity of the proposed method for the determination of the studied drugs in pharmaceutical, recovery studies were carried out on real samples to which known amounts of drugs were added. The results are given in Table 4. The recovery values for LMFX, ENLX and PELX were in the range of 92.3–105% with the RSDs of 0.5–2.7%.

Table 6
Recovery of LMFX, ENLX and PFLX in serum, urine and milk samples.

Analyte	Sample	Added ($\times 10^{-7}$ g mL^{-1})	Found ($\times 10^{-7}$ g mL^{-1})	Recovery (%)	RSD ($n = 5$) (%)
LMFX	Urine	1.472	1.290	87.6	2.3
		2.944	2.744	93.2	2.7
		6.930	5.933	85.6	3.4
	Serum	1.472	1.563	106	2.5
		2.944	2.571	87.3	2.6
		7.360	6.288	85.4	3.0
	Milk	1.420	1.208	85.1	2.9
		2.944	3.134	107	2.7
		7.360	6.642	90.2	2.7
		9.696	8.429	86.9	2.7
ENLX	Urine	16.16	15.76	97.5	2.8
		22.62	20.84	92.1	2.5
	Serum	9.696	10.81	112	2.3
		16.16	16.83	104	1.6
		22.62	23.41	104	2.5
	Milk	8.574	7.451	86.9	1.4
		16.16	12.96	80.2	2.7
		20.08	17.81	88.7	1.7
PFLX	Urine	3.200	2.811	87.8	3.2
		6.400	5.745	89.8	2.3
		16.00	13.92	87.0	2.1
	Serum	3.200	3.640	114	2.6
		6.400	5.694	89.0	2.7
		16.00	14.06	87.9	2.4
	Milk	3.200	3.487	109	2.5
		6.400	5.899	92.2	1.6
		16.00	13.91	86.9	1.9

Calibration curves were prepared for each compound by plotting the peak height versus the analyte concentration (Fig. 7). The proposed method was applied for the determination of LMFX, ENLX and PELX in three pharmaceutical preparations. The result is given in Table 5 along with the result obtained using the UV-method [43]. The results obtained by the proposed method agree with the labeled contents. Statistical analysis of the results using Student's t-test and the variance ratio F-test showed no significant difference at $p = 0.05$ between the performance of the two methods as regards to accuracy and precision.

The recovery tests were performed to evaluate the accuracy of this method. The results of recovery tests are listed in Table 6.

For urine and serum samples the recoveries of the three drugs were in the range of 85.4–106% for LMFX with the RSDs of 2.3–3.4%. 92.1–112% for ENLX with the RSDs of 1.6–2.8%, and 87.0–114% for PFLX with the RSDs of 2.1–2.7%. For milk sample the recoveries of the three drugs were in the range of 80.2–109% with the RSDs of 1.4–2.7%.

4. Conclusion

An $[Ag(HIO_6)_2]^{5-}$ complex–H_2SO_4 solution, for the first time, was used in CL emission system. The possible CL mechanism for $[Ag(HIO_6)_2]^{5-}$–H_2SO_4–fluoroquinolone is based on emission of the excited $(O_2)_2{}^*$ produced in the reaction system and intermolecular energy transfer from $(O_2)_2{}^*$ to analyte and complex of analyte and $[Ag(HIO_6)_2]^{5-}$. The proposed enhanced CL systems have good linearity, high sensitivity, precision for the determination of trace amount of LMFX, ENLX and PELX. The proposed method has potential capability for the analysis of studied analytes in pharmaceutical and biological samples.

Acknowledgement

References

[1] C. Dodeigne, L. Thunus, R. Lejeune, Talanta 51 (2000) 415.
[2] H.W. Sun, L.Q. Li, J. Anal. Chem. 63 (2008) 485.
[3] N. Kenichiro, Bunseki Kagaku 49 (2000) 135.
[4] L.J. Kricka, Anal. Chim. Acta 500 (2003) 279.
[5] M.J. Navas, A.M. Jiménez, Food Chem. 55 (1996) 7.
[6] H.W. Sun, L.Q. Li, X.Y. Chen, Anal. Bioanal. Chem. 384 (2006) 1314.
[7] J.L. Adcock, P.S. Francis, N.W. Barnett, Anal. Chim. Acta 601 (2007) 36.
[8] A.J. Brown, P.S. Francis, J.L. Adcock, K.F. Lim, N.W. Barnett, Anal. Chim. Acta 624 (2008) 175.
[9] P.S. Francis, J.L. Adcock, Anal. Chim. Acta 541 (2005) 3.
[10] H.W. Sun, L.Q. Li, X.Y. Chen, Anal. Chim. Acta 576 (2006) 192.
[11] H. Yoshida, R. Nakao, H. Nohta, M. Yamaguchi, Dyes Pigments 47 (2000) 239.
[12] H.N. McMurray, B.P. Wilson, J. Phys. Chem. A 103 (1999) 3955.
[13] S.F. Li, X.Z. Li, J. Xu, X.W. Wei, Talanta 75 (2008) 32.
[14] M. Tsunoda, K. Imai, Anal. Chim. Acta 541 (2005) 13.
[15] F.A. Aly, S.A. Al-Tamimi, A.A. Alwarthan, Talanta 53 (2001) 885.
[16] H.Y. Han, Z.K. He, Y.E. Zeng, Wuhan Univ. J. Nat. Sci. 5 (2000) 93.
[17] A. Nawal, A. Alarfaj, Anal. Sci. 19 (2003) 1145.
[18] Y.D. Liang, J.F. Song, X.F. Yang, Anal. Chim. Acta 510 (2004) 21.
[19] N. Lian, H.C. Zhao, C.Y. Sun, S.L. Chen, Y. Lu, L.P. Jin, Microchem. J. 74 (2003) 223.
[20] M. Elbanowski, B.M. kowska, K. Staninski, M. Kaczmarek, J. Photochem. Photobiol. A: Chem. 130 (2000) 75.
[21] A. Safavi, G. Absalan, F. Bamdad, Anal. Chim. Acta 610 (2008) 243.
[22] B.X. Li, Z.J. Zhang, M.L. Wu, Microchem. J. 70 (2001) 85.
[23] K.A. Fähnrich, M. Pravda, G.G. Guilbault, Talanta 54 (2001) 531.
[24] B.X. Li, Z.J. Zhang, W. Liu, Talanta 55 (2001) 1097.
[25] H.Z. Zheng, Y.B. Zu, J. Phys. Chem. B 109 (2005) 12049.
[26] D.J. Vinyard, S. Su, Richter S M.M., J. Phys. Chem. A 112 (2008) 8529.
[27] B.X. Li, Z.J. Zhang, W. Liu, Talanta 54 (2001) 697.
[28] J. Zhou, J.J. Li, L.B. Qu, J. Shi, Chin. J. Anal. Lab. 23 (2004) 46.
[29] J.J. Li, J. Zhou, X. Zhang, J. Shi, L.B. Qu, Chin. J. Anal. Sci. 21 (2005) 295.
[30] L. Wang, P. Yang, Y.X. Li, H.Q. Chen, M.G. Li, F.B. Luo, Talanta 72 (2007) 1066.
[31] J. Shi, K.L. Zhao, Q.G. Song, L. Li, F.P. Cao, Chin. J. Pharm. 36 (2005) 298.
[32] H.Y. Ma, X.W. Zheng, Z.J. Zhang, Chem. Res. Appl. 16 (2004) 713.
[33] L.Q. Li, H.W. Sun, X.Y. Chen, Curr. Anal. Chem. 4 (2008) 152.

[34] H.W. Sun, L.Q. Li, M. Su, Chromatographia 67 (2008) 399.
[35] H.M. Shi, S.G. Shen, H.W. Sun, Z.F. Liu, L.Q. Li, J. Inorg. Biochem. 101 (2007) 165.
[36] S.G. Shen, H.M. Shi, H.W. Sun, S.Y. Huo, Trans. Metal Chem. 32 (2007) 167.
[37] S.G. Shen, H.M. Hong, H.W. Sun, Acta Phys.-Chim. Sin. 23 (2007) 409.
[38] H.W. Sun, H.M. Hong, S.G. Shen, W.J. Kang, Z.F. Guo, Chin. J. Chem. 26 (2008) 615.
[39] A. Blaikungeri, M. Pelletier, D. Monnier, J. Inorg. Chim. Acta 22 (1997) 7.
[40] A. Blikungeri, M. Pelletier, J. Inorg. Chim. Acta 29 (1978) 141.
[41] H. Cui, Z.F. Zhang, M.J. Shi, J. Phys. Chem. B 109 (2005) 3099.
[42] S.X. Liang, L.X. Zhao, B.T. Zhang, J.M. Lin, J. Phys. Chem. A 112 (2008) 618.
[43] H. Chen, D.H. Zheng, J. Taizhou Univ. 26 (2004) 64.

Variable selection using probability density function similarity for support vector machine classification of high-dimensional microarray data

Li-Juan Tang, Jian-Hui Jiang*, Hai-Long Wu, Guo-Li Shen, Ru-Qin Yu*

State Key Laboratory of Chemo/Biosensing and Chemometrics, College of Chemistry and Chemical Engineering, Hunan University, Changsha 410082, PR China

ABSTRACT

One problem with discriminant analysis of microarray data is representation of each sample by a large number of genes that are possibly irrelevant, insignificant or redundant. Methods of variable selection are, therefore, of great significance in microarray data analysis. To circumvent the problem, a new gene mining approach is proposed based on the similarity between probability density functions on each gene for the class of interest with respect to the others. This method allows the ascertainment of significant genes that are informative for discriminating each individual class rather than maximizing the separability of all classes. Then one can select genes containing important information about the particular subtypes of diseases. Based on the mined significant genes for individual classes, a support vector machine with local kernel transform is constructed for the classification of different diseases. The combination of the gene mining approach with support vector machine is demonstrated for cancer classification using two public data sets. The results reveal that significant genes are identified for each cancer, and the classification model shows satisfactory performance in training and prediction for both data sets.

© 2009 Elsevier B.V. All rights reserved.

1. Introduction

With the development of microarray technology, it is possible to simultaneously monitor the levels of thousands of genes expressed in various organisms. Since expression changes accurately reflect the status of disease [1,2], the large amount of microarray data generated in even a single experiment may provide the insights into diseases on a genome-wide scale. Nowadays, gene expression profiles have found proliferated applications in biomedical studies, especially in cancer research field.

To mine the ability of gene expression profiles for distinguishing cancers, many classification methods have been developed for microarray data analysis, such as *k*-nearest neighbors [3], linear discriminant analysis [4], classification and regression tree (CART) [5], logitboost [6], artificial neural network (ANN) [7] and support vector machine (SVM) [8]. However, the implementation of most classification approaches is frequently baffled by the difficulty in handling enormous microarray data, since the analysis of relevant genes will be interfered by the inconsequential or detrimental information provided by a great deal of genes which are irrelevant to the study events. Although there are procedures such as SVM and CART with inherent capacity in treating a large number of variables, the extremely high gene dimension and relatively small sample size in microarray applications may still bring about a prohibitive compu-

tational burden and a lapsable model that is rather unstable to the errors. Reducing the dimension of the original data by gene selection is considered to be an efficient way to combat the difficulty. It has been demonstrated that with the aid of variable selection, the performance of most classifiers can be improved [9]. By removing the redundant variables, it is possible to highlight those genes that are the most relevant for certain events, and the classification models will become more interpretable regarding the biological significance. Essentially, variable selection is a process of gene identification and biomarker discovery. As well, hunting for a small set of highly significant genes for certain disease is the requirement for cost-saving in clinical disease diagnosis.

Variable selection is traditionally based on the analysis of between-class dissimilarity and within-class similarity. In the context, *t*-test [10], the ratio of between classes sum of squares to within class sum of squares (BSS/WSS) [11], analysis of variance [12] and significance analysis of microarray (SAM) [13] have been widely used in various gene selection approaches. Most of these approaches seek for variables that maximize the separability of all the classes rather than an individual class of interest with regard to the others. Though there are applications demonstrating the feasibility of these methods, they still suffer from pitfalls. To address the model variability the number of selected variables is frequently too large with reference to the number of samples, for instances, 1000 genes used in NCI60 data set for 60 samples [14] and 94 genes used in acute leukemia data for 38 samples [15]. A large variable number coupled with a small sample size is generally not advisable, not only resulting in a more complex classification

* Corresponding authors. Tel.: +86 731 8822577; fax: +86 731 8822782.
E-mail addresses: jianhuijiang@hnu.cn (J.-H. Jiang), rqyu@hnu.cn (R.-Q. Yu).

model and computationally intensive, but also increasing the risk of overfitting. Moreover, the significant genes related to certain disease might be masked by inconsequential or detrimental information and hardly be identified. According to this consideration, an entropy-based discretization method [16] is further developed to identify the genes for each individual class based on the boundaries of the expression levels for the disease states [17]. This method can substantially reduce the number of selected genes while achieve desirable discrimination using a traditional distance-based classifier. Nevertheless, it cannot identify the genes relevant to the disease states that each may have different subtypes, and then give a multi-mode expression pattern. It is recognized that the mining of these genes could offer fundamental insight into the assignment of patients to specific risk groups (subtypes) so as to administrate proper treatments.

A novel gene mining approach is proposed based on the discriminative information of each gene for a class of interest in the present study. The discriminative information of a gene for a class is measured in terms of the similarity between probability density functions on the gene for the class with respect to the others. In contrast with traditional gene selection methods with an attempt to maximize the separability of all classes, this approach identifies the significant genes that are more discriminative for each individual class rather than all classes. Because the binary discriminative power of each gene for belonging or not belonging to the class of interest is substantially enhanced as compared to the general discriminative power for all the classes, this enables the proposed approach to generate an ideal classifier using only very small number of genes. Also, the use of probability density function similarity as the measure of discriminative information allows the ascertainment of the genes with various complicated expression patterns, whatever up-regulated, down-regulated or multimodal. To exploit the information discriminative for a specific class, a classifier, support vector machine (SVM) with local kernel transform (LKT-SVM), is also developed. SVM is a relatively new algorithm from the machine learning community, boasting its structural risk minimization (RSM) principle and desirable performance both in solving classification and regression problems from various fields. For example, very recently Varol et al. successfully applied SVM to forecast thermodynamic features resulted from convection [18,19]; our previous studies also have shown that SVM and its extended patterns works well in quantitative structure–activity relation studies and tumor classification [20–23]. Rather than a traditional SVM using global kernel transform, the strategy of local kernel transform is developed in this study. The local kernel transform extracts the feature variables separately using the genes selected for an individual class instead of using all the selected ones, which offers the possibility of eliminating the interference between the redundant genes from different classes. Then, the local kernel transform is expected to generate an ideal feature mapping in which the resulting feature variables give large values for the corresponding class, while have small values for the others. The performance of the gene mining approach and the local kernel transform-based SVM has been demonstrated using two public gene expression data sets for diagnosis of multiple cancer types, a DNA profiling data for acute leukemia [24] and a RNA profiling data for eleven familiar cancers [25].

2. Methods

2.1. Gene mining using probability density function similarity

The probability density function (PDF) provides a straightforward description of the sample distribution for a certain class. Well-separated classes give PDFs with small convolution or large dissimilarity. Then, the PDFs' similarity (PDFS) is a natural measure for the discriminative information of a gene, thereby offering an effective approach for gene mining in microarray data classification.

Considering a microarray data set with P genes and I samples, x_{ip} ($i = 1, \ldots, I$; $p = 1, \ldots, P$) represents the expression level of the ith sample ($\mathbf{x}_i$) on the pth gene ($\mathbf{g}_p$). The data of each sample consists of a vector of expression profile, $\mathbf{x}_i = (x_{i1}, \ldots, x_{ip})$ and a K-dimensional vector of category label $\mathbf{y}_i = (y_{i1}, \ldots, y_{iK})$ with 1 in the kth coordinate and 0 elsewhere if the sample falls into class k ($k = 1, \ldots, K$). To evaluate the discriminative information of a gene p for a specified class k, the other classes except class k are merged into one class, and two PDFs, one for class k and the other for the merged class, can be calculated using the kernel method [26]. These two PDFs are discretized at I sample values as two vectors $\mathbf{f}_p^1(k) = (f_{1p}^1(k), \ldots, f_{Ip}^1(k))$ and $\mathbf{f}_p^0(k) = (f_{1p}^0(k), \ldots, f_{Ip}^0(k))$, where $\mathbf{f}_p^1(k)$ and $\mathbf{f}_p^0(k)$ represent the PDF of class k and the merged one, respectively, on gene p. The entries, $f_{ip}^s(k)$ ($s = 0$ and 1, $i = 1, \ldots, I$), are calculated as follows:

$$f_{ip}^s(k) = \sum_{j=1}^{I} \varphi(y_{jk} = s) \exp\left(-\frac{|x_{ip} - x_{jp}||^2}{2\sigma_{kp}^2}\right) \tag{1}$$

where $\varphi(\cdot)$ is the indicator function taking value 1 if $y_{jk} = s$ ($s = 0$ or 1) and value 0 otherwise, σ_{kp} is the standard deviation of the expression level on gene p for samples belonging to class k. Then, the PDFS for class k and the merged class on gene p is measured by

$$S_p(k) = \frac{\mathbf{f}_p^1(k)^T \mathbf{f}_p^0(k)^T}{\left\|\mathbf{f}_p^1(k)^T\right\| \left\|\mathbf{f}_p^0(k)^T\right\|} \tag{2}$$

Note that $S_p(k)$ is essentially the correlation coefficient between $\mathbf{f}_p^1(k)$ and $\mathbf{f}_p^0(k)$ that measures the angle between two PDF vectors. In other words, for genes with the smallest $S_p(k)$, the angle between two PDF vectors for class k and the others reaches the maximum, implying that these genes are the most discriminative between class k and the others. Thus, the genes with the smallest $S_p(k)$ are identified as the most significant genes for class k. In general cases, several significant genes, say J, are selected for each class, and the optimal number of significant genes can be determined by trying varying number of significant genes and identifying the model with the best classification as well as the least significant genes. In contrast to traditional gene selection methods based on the between-class dissimilarity, within-class similarity and two-end distribution, the proposed method based on PDFS can not only select the genes that are absolutely up-regulated or down-regulated, but also ascertain the genes with complicated multi-modal expression patterns.

2.2. Support vector machine with local kernel transform (LKT-SVM)

SVM is a relatively novel machine learning technique with comprehensive theoretical implications [27]. As an ideal refill of traditional classification and regression methods, SVM exhibits desirable performance in many applications. Standard SVM utilizes a global kernel transform, which is applied to all the input variables, for nonlinear feature extraction. Because the proposed gene mining approach selects a series of gene sets that respectively have discriminative information for each individual class, it is would be not a good strategy to use a global kernel transform here. Therefore, a Gaussian local kernel transform is used for SVM in the present study to transform the data from the original variables space to the feature one.

The Gaussian local kernel transform is applied separately to each gene set selected for an individual class, as given below:

$$o_{in}(k) = \exp\left(-\frac{||\mathbf{x}_i(k) - \mathbf{c}_n(k)||^2}{2\sigma_n^2(k)}\right) \tag{3}$$

where $\mathbf{x}_i(k)$ denotes the expression level vector of the ith sample on the genes selected for class k, and $o_{in}(k)$ ($n = 1, \ldots, N$; $k = 1, \ldots, K$; $i = 1, \ldots, I$) is the output of the nth kernel transform for class k at a center $\mathbf{c}_n(k)$ with a kernel width $\sigma_n(k)$ for sample i. The center $\mathbf{c}_n(k)$ is the nth cluster center of samples belonging to class k, which can be obtained using the standard hierarchical clustering algorithm. The kernel width $\sigma_n(k)$ is determined by the distance between $\mathbf{c}_n(k)$ and the mean vector of the class that is the nearest to $\mathbf{c}_n(k)$ among all classes other than class k. Note that samples belonging to class k have smaller distance from one of the kernel centers of class k than from centers of other classes, then the local kernel transform for class k is expected to give larger output values for samples belonging class k than those from other classes. As the output values offer more immediate information for discriminating the classes, it is clear that the proposed local kernel transform is very effective in feature extraction and is able to substantially enhance the classification performance of SVM.

The outputs $o_{in}(k)$ ($n = 1, \ldots, N$; $k = 1, \ldots, K$; $i = 1, \ldots, I$) obtained with the local kernel transform for all classes are then combined together, $\mathbf{o}_i = (\mathbf{o}_i(1), \ldots, \mathbf{o}_i(K))$ and $\mathbf{o}_i(k) = (o_{i1}(k), \ldots, o_{iN}(k))$, as the feature variables to be modeled using a linear SVM regression. That is, a regression-based classifier is constructed using SVM to relate the output vector $\mathbf{o}_i$ ($i = 1, \ldots, I$) to the corresponding category label y_{ik} using the following linear model:

$$y_{ik} = \mathbf{w}_k^T \times \mathbf{o}_i + b_k \tag{4}$$

where $\mathbf{w}_k$ and b_k are the weight vector and the bias, respectively, for the kth model ($k = 1, \ldots, K$). The optimal model parameters are estimated via minimizing the following cost function Φ_k of SVM:

$$\Phi_k = \frac{1}{2}\mathbf{w}_k^T\mathbf{w}_k + C\frac{1}{I}\sum_{i=1}^{I}L_{\varepsilon k}(\widehat{y}_{ik} - y_{ik}) \tag{5}$$

where

$$L_{\varepsilon k}(\widehat{y}_{ik} - y_{ik}) = \begin{cases} \left|\widehat{y}_{ik} - y_{ik}\right| - \varepsilon & \left|\widehat{y}_{ik} - y_{ik}\right| \geq \varepsilon \\ 0 & \text{otherwise} \end{cases} \tag{6}$$

is the ε-insensitive loss function measuring the error between the given category label y_{ik} ($i = 1, \ldots, I$) and calculated values $\widehat{y}_{ik}$ ($i = 1, \ldots, I$) and ε is the tolerance zone, $1/2\mathbf{w}_k^T\mathbf{w}_k$ is used as a measure of the model complexity. C is the penalty constant that is introduced to control the trade-off between the empirical error and the model complexity. This parameter can be determined by sensitivity analysis [20,21] and the tolerance zone ε as a desired precision band is given 10^{-2} in this study. It has been shown that the optimal regression parameters can be solved using the standard quadratic programming algorithm. With estimated model parameters, the classifier can be constructed immediately according to the calculated values $\widehat{y}_{ik}$ ($k = 1, \ldots, K$) for sample i: the sample is allocated into the hth class, where h is the number at which $\widehat{y}_{ih}$ reaches the maximum among all $\widehat{y}_{ik}'s$ ($k = 1, \ldots, K$).

3. Results and discussion

3.1. Data sets

The proposed strategy was evaluated by two microarray data sets, the leukemia data [24] available at http://www.broad.mit.edu/cgi-bin/cancer/datasets.cgi and a RNA profiling data for molecular classification of eleven familiar cancers [25] available at

Table 1
The description of five highly significant genes of each class in the leukemia data identified by PDFS.

Related class	S	Gene description
ALLB	0.1333	MB-1 gene
	0.2511	CST3 Cystatin C (amyloid angiopathy and cerebral hemorrhage)
	0.2668	IGHM Immunoglobulin mu
	0.2704	IGB Immunoglobulin-associated beta (B29)
	0.2973	ADPRT ADP-ribosyltransferase (NAD+; poly (ADP-ribose) polymerase)
ALLT	0.0002	TCF7 Transcription factor 7 (T-cell specific)
	0.0003	CD3E T-cell surface glycoprotein CD3 epsilon chain precursor
	0.0010	GB DEF = T-cell antigen receptor gene T3-delta
	0.0081	GB DEF = T-lymphocyte specific protein tyrosine kinase p56lck (lck) abberant mRNA
	0.0399	T-cell antigen CD7 precursor
AML	0.0949	Zyxin
	0.1695	CST3 Cystatin C (amyloid angiopathy and cerebral hemorrhage)
	0.1996	FAH Fumarylacetoacetate hydrolase
	0.2370	Cytoplasmic dynein light chain 1 (hdlc1) mRNA
	0.2813	FTL Ferritin, light polypeptide

http://www.gnf.org/cancer/epican. It was revisited here that the leukemia data were a three-class classification problem for myeloid leukemia (AML) and acute lymphoblastic leukemia (ALL) that was further divided into B-cell and T-cell ALLs (ALLB and ALLT). The data consisted of 38 samples (19 ALLB, 8 ALLT and 11 AML) in the training set and 34 samples (19 ALLB, 1 ALLT and 14 AML) in the test set with each sample represented by 7129 human genes. The second data set was used to demonstrate the performance of the proposed method for complex multi-classification problems. The data comprised 174 samples including carcinomas of prostate (PR), breast (BR), colorectum (CO), lung (adenocarcinomas and squamous cell carcinoma), liver (LI), gastroesophagus (GA), pancreas (PA), ovary (OV), kidney (KI) and bladder/ureter (BL), which collectively accounted for about 70% of all cancer-related deaths in the United States. The samples represented by 12,533 genes were randomly split into a training set of 132 samples and a test set of 42 samples. The training and the test sets both included the 11 kinds of cancers.

Before using PDFS to identify gene subsets whose expression typifies each cancer class, additional preprocessing steps [11] were taken to the two data sets: (1) thresholding (floor of 100 and ceiling of 16,000), (2) filtering (exclusion of genes with max/min ≤ 5 and max−min ≤ 500 across the samples) and (3) base 10 logarithmic transformation and standardization.

3.2. Significant gene mining for each disease class

3.2.1. Data set 1

The filtering resulted in 3571 genes for the data. Then, PDFS was used to mine significant genes for each cancer class. The identified genes are summarized in Table 1, in which five genes with the smallest PDFS values for each class, 15 genes in total, are listed. One notices in Table 1 that eight genes including MB-1 gene, CST3 Cystatin C, B29, ADPRT, T3-delta, zyxin, FAH and FTL are also referred to as important genes by previous studies of the data [9,24].

The five genes in the top of Table 1 are ideal variables for discriminating ALLB from ALLT and AML. Fig. 1A depicts the expression levels of these five highly significant genes of ALLB in the training set. It is clear from the heat map that the five genes selected by PDFS are very informative in discriminating cancer ALLB from ALLT or AML. Almost all samples of ALLB in the training set reveal great differences in expression levels, much higher on gene MB-1, IGHM, B29 and ADPRT and much lower on gene CST3 Cystatin C, as com-
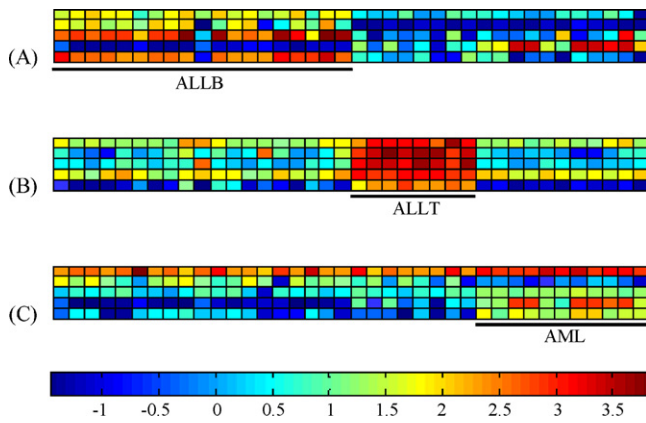
Fig. 1. The heat maps show the expression levels of the five highly significant genes identified for ALLB (A), ALLT (B) and AML (C) for the training samples standardized according to the preprocessing steps, respectively.

pared to samples of the other cancers. It was reported that these genes encoded functional proteins responsible for ALLB. MB-1 was investigated to be a marker for ALLB by Buccheri et al. [28]. Because of the products of B29, ALLB typically exhibited low or undetectable surface Ig [29]. The gene ADPRT was conjectured by Pero et al. to be a useful marker for the pathophysiology associated to AML [30], but it seemed from Fig. 1A that the ADPRT activity was by far more related to ALLB. The average expression level of ALLB samples in the training set was 1976.80, much higher than those of ALLT (624.75) and AML (546.64).

As shown in Fig. 1B, the expression levels of ALLT samples in the training set are uniformly higher than samples of the other cancers on the five genes (in the middle of Table 1) selected by the proposed method. Referring to the descriptions of the genes and previous studies [31–35], one realized that these genes were all T-cell specific, and TCF7 encoded the transcription factor 7, while the functional proteins encoded by CD3E, T3-delta, lck, CD7 antigen were responsible for the development of ALLT.

The five most significant genes selected for AML by PDFS are zyxin, CST3, FAH, hdlc1 and FLT (in the bottom of Table 1). Zyxin gene was shown to encode a LIM domain protein that was important in cell adhesion in fibroblasts [36], but there was no report concerning the gene about its role in hematopoiesis. The biological function of CST3 gene related to AML/ALL pathogenesis was also not documented in previous studies. Nevertheless, it was shown that zyxin, CST3, FAH and FTL genes were useful for classification of leukaemia [9]. Actually, it can be observed from their expression level map over the samples in the training set in Fig. 1C that AML demonstrates a distinct expression level on these four genes from ALL, indicating that zyxin, CST3, FAH and FTL genes might be of considerable significance in discriminating AML from ALLT and ALLB. Especially, the expression level on gene CST3 exhibited the most significant difference for the three cancer samples: samples of AML have the highest expression levels of 7423.50 on the average, samples of ALLT give a middle level of expression with an average of 560.38, and samples of ALLB show the lowest expression with an average of −30.68. Gene hdlc1 had not been considered as a significant gene in leukemia classification. However, the heat map in Fig. 1C reveals that this gene has much lower expression level in samples of AML than that for ALL, the average expression level being 328.00 for AML samples and 1707.80 for ALL samples, evidencing that hdlc1 gene also has close implication in the discrimination between AML and ALL.

3.2.2. Data set 2

After preprocessing 5536 genes were retained for the data. The selection of significant genes was implemented using PDFS. Table 2

lists the four genes with the smallest PDFS for each cancer class. The expression levels of the selected genes are shown in the heat map Fig. 2. For cancers of prostate, bladder, ovarian and pancreas, the expression of some selected genes exhibited an ideal two-end distribution. However, for other cancers such as breast, lung adenocarcinomas (LA) and lung squamous cell carcinoma (LS), it was impossible to obtain significant genes with ideal two-end distribution, and the expression of most of the significant genes had either a multi-modal distribution or a mono-modal one centering in the middle of the expression levels of other classes.

Most of genes with ideal two-end distribution were shown to be potential biomarkers for the related cancers. X05332 and X07730 encode mature human prostate specific antigens and then are specific genes for prostate cancer [37,38]. Keratin 13 (X14640) was identified to be differentially expressed in fresh cancers and normal urothelium of bladder cancer patients [39]. Interleukin-13 (U31120) was considered as a typical marker in the bladder of allergic cystitis bearing patients. It was proved that the liver was the main organ of plasma S protein (X03168) synthesis [40]. Significant decrease of S protein could be observed in liver diseases. Protein encoded by Il-TMP (U31449) was shown to be produced in the human intestinal epithelium and liver, and could regulate cell density-dependent proliferation [41]. It was demonstrated that U40434 was a differentiation antigen present in ovarian cancers [42]. Elastase III A gene was firstly found in human pancreas [43]. This gene might be a significant indicator of pancreas cancer, because it gave an extremely small PDFS of 1.6882×10^{-8}. Although no report gave direct evidence for DEPP (AB022718) and VEGF (AF022375) as significant genes of kidney cancer, it was found that samples of kidney cancer had much higher expression on these two genes than those from the others. The RNA of HSWT1 gene (X51630) was reported to be expressed with high level in fetal kidney, which was related to the development of kidney [44]. Surprisingly, a close inspection of HSWT1 revealed that the expression levels on HSWT1 for ovarian cancer samples in the training set were uniformly higher (5036.00 on the average) than that for samples from the other cancers (996.15 on the average) including kidney cancer (39.63 on the average).

Genes with multi-modal distribution or mono-modal distribution centering in the middle of the expression levels of other classes also had implications to the related cancers. TACC1 (transforming acidic coiled-coil, AF049910) was thought to be important gene in the evolution of breast cancer, which was expressed at high levels in human cancer cell lines [45]. It was observed that the expression level of TACC1 in breast samples was between 250 and 600 with an average of 445. Some studies reported that TACC1 was also associated with the androgen-independent stage in human prostate carcinoma samples [46]. Interestingly, it was found that the expression level of TACC1 in prostate tumor was uniformly higher than that in breast tumor. The average expression of prostate tumor samples was in range from 650 to 1600 with an average of 1069. Therefore, it might be possible to use TACC1 gene for discriminating prostate from breast cancers in clinical diagnosis. The possession of the (HLA)-DQB1 gene (M60028) was thought to significantly reduce the risk of disease progression or persistent diffuse of lung abnormalities during the first follow-up years [47]. And a risk reduction percentage in (HLA)-DQB1 carriers was estimated to be ~65%. It was observed that this gene was expressed at three different levels in lung adenocarinoma samples in the training data set: higher than 400 but lower than 600, higher than 950 but lower than 1400, and higher than 2350. This multi-modal expression of (HLA)-DQB1 in LA might have implication to the progression state of the tumor. Additionally, the expression of (HLA)-DQB1 was also inspected in sample of lung squamous, and lower expression was observed in LS samples than LA ones. The average expression level in LS was 322.90, and the samples were mainly distributed in two domains, [−100, 50] and [140, 390]. Gene hRVP1 (AB000714), whose product

RVP1 was detected to have abundant expression in lung [48], was expressed at two levels in LS samples, around 500 and at a level as low as <150. In LA samples, hRVP1 was expressed at three separate regions, [−100, 100], [800, 2100] and >3500.

3.3. Classification using local kernel transform-based SVM

The genes selected by PDFS were invoked for classification using the local kernel transform-based SVM. The centers of the kernel transform were identified using hierarchical clustering method. To balance the training performance and the generalization capability of the model, the number of the subclasses N in each class was determined based on the "parsimony" principle, that is, if the training errors were the same for different models of varying subclass number N, then the model with the minimum N was the best. The parameter C in SVM was determined by sensitivity analysis. In other words, different values were used for C in SVM leaning, and the training error was plotted versus the value of C. This plot typically showed that the training error firstly deceased with increasing value of C, and then became flat gradually as C values increased further. Therefore, C could be determined by the value that first gave the minimum training error.

As a comparison, k-nearest neighbors algorithm (k-NN) and traditional SVM with a global Gaussian kernel transform were also used to the two data sets. The parameters of k-NN and traditional SVM were determined by cross-validation.

3.3.1. Data set 1

The leukemia data set was used for classification with varying number of genes selected for each class $l = \{1, 2, 3, 6, 10, 20\}$. The classification results are summarized in Table 3. The first column is the number, l, of selected genes in each class. With l genes picked

Table 2
The description of four highly significant genes of each class in the second data set identified by PDFS.

Related class	S	Gene description
PR	3.2629×10^{-134}	X05332: Human mRNA for prostate specific antigen
	3.4419×10^{-82}	X07730: HSPSA human mRNA for prostate specific antigen
	1.7320×10^{-22}	S39329: Glandular kallikrein-1 {alternatively spliced} [human, prostate, mRNA, 1541 nt]
	5.6319×10^{-22}	AA658877: nt84c12.s1 Homo sapiens cDNA
BL	0.0566	X14640: Human mRNA for keratin 13
	0.2010	U31120: Human interleukin-13 (IL-13) precursor gene
	0.2289	AA131149: zo16d05.r1 homo sapiens cDNA
	0.3230	L19872: Human AH-receptor mRNA
BR	0.4653	AF061741: Homo sapiens retinal short-chain dehydrogenase/reductase retSDR1 mRNA
	0.6087	D13666: HUMOSF2OS homo sapiens osf-2 mRNA for osteoblast specific factor 2 (OSF-2os)
	0.6403	M55153: Human transglutaminase (TGase) mRNA
	0.6583	AF049910: Homo sapiens TACC1 (TACC1) mRNA
CO	0.0340	AB006781: Homo sapiens mRNA for galectin-4
	0.1400	X53463: Human mRNA for glutathione peroxidase-like protein
	0.1577	L20826: Human I-plastin mRNA
	0.1942	M35252: Human CO-029
GA	0.4742	M26683: HUMIFNIND human interferon gamma treatment inducible mRNA
	0.4993	U09510: Human glycyl-tRNA synthetase mRNA
	0.5093	AF002697: Homo sapiens E1B 19K/Bcl-2-binding protein Nip3 mRNA, nuclear gene encoding mitochondrial protein
	0.5488	D87433: Human mRNA for KIAA0246 gene, partial cds
KI	0.0233	AF022375: Homo sapiens vascular endothelial growth factor mRNA (VEGF)
	0.0248	AB022718: Homo sapiens mRNA for DEPP (decidual protein induced by progesterone)
	0.0303	AF024710: Homo sapiens vascular endothelial growth factor (VEGF) mRNA
	0.0312	D14874: Homo sapiens mRNA for adrenomedullin precursor
LI	0.0031	X03168: Human mRNA for S-protein
	0.0048	U31449: Human intestinal and liver tetraspan membrane protein (il-TMP) mRNA
	0.0134	U26209: Human renal sodium/dicarboxylate cotransporter (NADC1) mRNA
	0.0294	U37055: Human hepatocyte growth factor-like protein gene, complete cds
OV	0.0291	X51630: HSWT1 human Wilms cancer WT1 mRNA for zinc finger protein
	0.1588	U40434: Human mesothelin or CAK1 antigen precursor mRNA
	0.3414	X63187: Homo sapiens HE4 mRNA for extracellular proteinase inhibitor homologue
	0.4132	AI800499: tc11f11.x1 homo sapiens cDNA, 3 end
PA	1.6882×10^{-8}	M18700: Human elastase III A gene
	0.0013	U66061: Trypsinogen C
	0.0013	AB011112: Homo sapiens mRNA for KIAA0540 protein
	0.0127	U31449: Human intestinal and liver tetraspan membrane protein (il-TMP) mRNA
LA	0.2773	Z46629: Homo sapiens SOX9 mRNA
	0.4425	M60028: Human MHC class II HLA-DQ-beta (DQB1, DQw9)
	0.4519	U17760: Human laminin S B3 chain (LAMB3) gene
	0.4758	J05581: Human polymorphic epithelial mucin (PEM) mRNA
LS	0.2995	X14487: Human gene for acidic (type I) cytokeratin 10
	0.3112	U14550: Human sialyltransferase SThM (sthm) mRNA
	0.4252	AB000714: Homo sapiens hRVP1 mRNA for RVP1
	0.4417	AA675900: g02504r Homo sapiens cDNA, 5 end
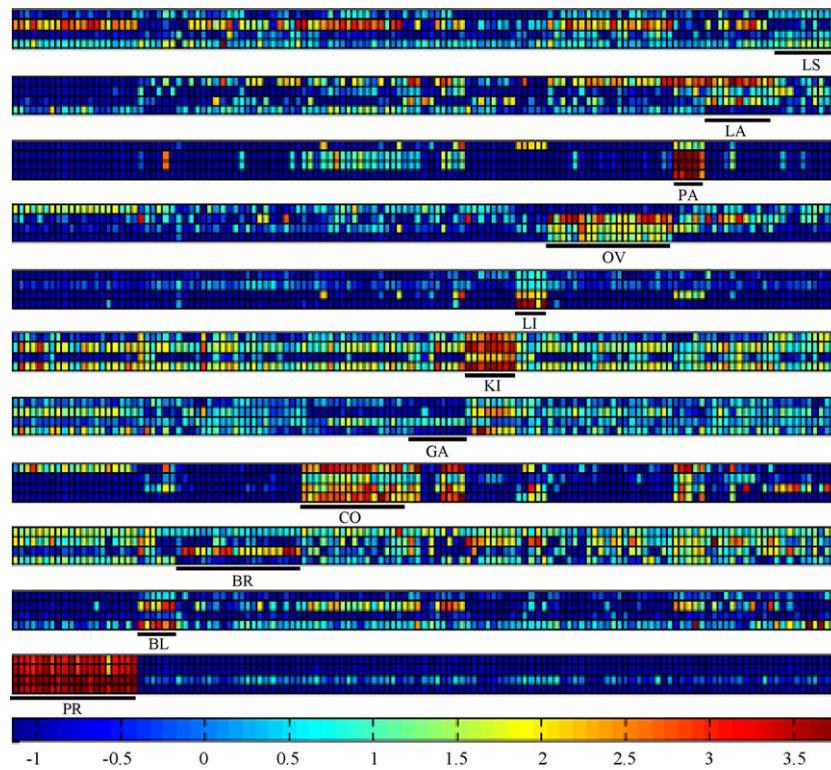
Fig. 2. The heat map shows the expression levels of the four most important genes identified for each class for the training samples of the data set 2 standardized according to the preprocessing steps.

out for each class, there were $l \times K$ genes in total in the classification model (here K was the number of classes). The misclassification counts of the training samples are given in the second column. It revealed that two or even less misclassified samples out of the 38-object training set were obtained. The training error decreased with increasing number of selected genes in cases when the selected genes were not excessive. The model with three genes for each class yielded a misclassification error of one sample, and with six genes for each class, the model yield perfect training and prediction. This conclusion seemed statistically straightforward, since a model with more variables would exhibit improve learning ability. With excessive selected genes (more than six genes for each class), the training error increased, on the contrary. The model with 10 genes for each class misclassified one training sample and one test object, which was worse than that with 6 genes for each class. This peculiar observation might be due to that the local kernel transform was distance-dependent, then inclusion of non-discriminative variables might mask the contribution of discriminative genes to the distance calculation and make the local kernel transform less discriminative. Therefore, it is clear that with proper number of selected genes, the proposed method is able to offer the best classification with only quite a few discriminative genes. It is noteworthy that such desirable results for AML/ALL problem have not reported yet. A misclassification rate of two samples was reported for the test

set with 44 genes selected [49]. Also, one sample was misclassified in the test set with 40 genes selected [50]. A prediction error of one sample was obtained by using 15 genes selected [51].

Fig. 3 reveals the best classification results obtained by different methods for the leukemia data. Six test errors were obtained by k-NN. The prediction accuracy for the 34 test samples is 82.35%. A traditional SVM using a global Gaussian kernel transform did not improve the classification accuracy. The prediction accuracy for the training set is 100.00%, but for the test set, the prediction accuracy is 85.29%. A good many irrelevant, insignificant or redundant genes among the 3571 variables increased the risk of overfitting of the classification model. Then, the performance of a traditional SVM model built using the top ranked genes identified by PDFS was examined. The classification model using the eighteen high

Table 3
Classification results for leukemia data obtained by LKT-SVM combined with PDFS method when different number of top ranked genes were used.

No. of genes for each class, l	Training errors	Test errors
1	1	2
2	0	2
3	0	1
6	0	0
10	1	1
20	1	1
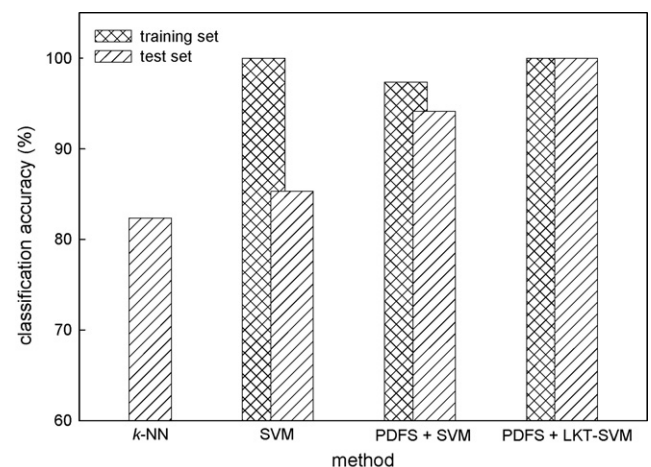
Fig. 3. The best classification accuracy of leukemia data obtained by different methods.

Table 4
Classification results for the second data set obtained by LKT-SVM combined with PDFS or standard kernel transform-SVM with BSS/WSS when different number of top ranked genes were used.

Total no. of genes	Training error rate (%)		Prediction error rate (%)	
	Method 1[a]	Method 2[b]	Method 1[a]	Method 2[b]
11	6.06	42.25	14.29	52.38
33	0	14.08	4.76	26.19
55	0.76	7.04	0	11.90
77	1.52	2.11	0	11.90
99	0	0.70	0	16.67

[a] LKT-SVM combined with PDFS method.
[b] Standard kernel transform-SVM combined with BSS/WSS.

related genes provides an improved prediction result. The classification accuracy for the training set is 97.37% and for the test set is 94.12%. One can conclude that PDFS is very effective in identifying significant genes. Compared with k-NN and SVM as shown in Fig. 3, LKT-SVM provides the same good performance for the training set but better performance for the test set, exhibiting that the proposed method has good precision in modeling and superior generalization in prediction. Key genes of leukemias were well addressed by PDFS, and local kernel transform-based SVM eliminated the interference from different classes, contributing to the supper performance of a classification model.

3.3.2. Data set 2

Table 4 is a summary of training and prediction accuracy for the 11-class cancer classification problem with varying number of selected genes. To demonstrate the advantage of the proposed method over traditional one, the results obtained using the BSS/WSS-based method [11] are also given in Table 4. The number of genes selected for each class is listed in the first column, implying that the number of variables included in different models is 11, 33, 55, 77 and 99, respectively. One observes from Table 4 that with equal number of selected genes, the proposed method demonstrates much better performance not only in the training but also in the generalization than the BSS/WSS-based strategy. With five genes selected for each class, the proposed method gave a training error of 0.76% and a perfect prediction, while the BSS/WSS-based protocol yielded a training error of 7.04% and a prediction error of 11.90%. Even with nine genes selected for each class, the BSS/WSS-based procedure still had a training error of 0.70% and a prediction error of 16.67%. These observations implied that the genes selected using the BSS/WSS-based procedures were less discriminative than those selected by the proposed PDFS-based method. A close inspection of the selected genes obtained by the proposed method, found that several significant genes such as X05332, X14640, U31120, U31449, U40434, AB022718, AF022375, AF049910, M60028 and AB000714 were not identified by the BSS/WSS-based procedure. As described in the preceding section, these genes contained useful information for discriminating a certain cancer class from the others. However, because these genes only possessed discriminative information for a certain class rather than maximizing the separability of all the classes, these genes would be ignored by the BSS/WSS-based strategy. One also noticed that the genes AF049910, M60028 and AB000714 with multi-mode distributions were also included in the model. It is theoretically apparent that these genes would be overlooked by all the existing gene mining approaches, since these methods are traditionally based on the statistics of between-class dissimilarity and within-class similarity that are generally derived from mono-modal distributions. Therefore, one could conclude that the proposed method could effectively select genes with enhanced discriminative power and the resulting model had improved learning and generalization ability with fewer variables.
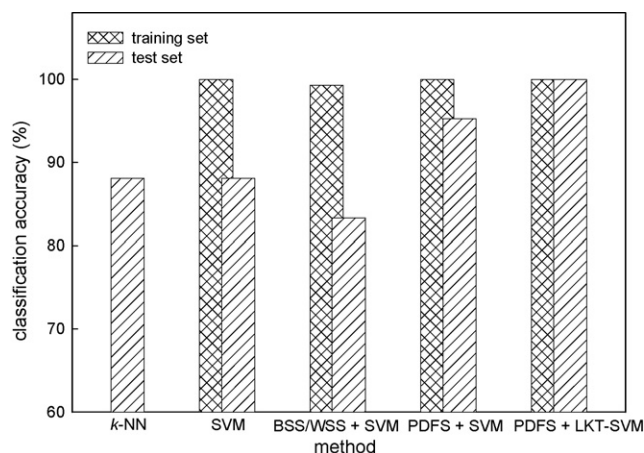
Fig. 4. The best classification accuracy of the second data set obtained by different methods.

Different classification methods were also used to this data set. Fig. 4 shows the best classification results obtained by k-NN, traditional SVM and LKT-SVM. The classification accuracy obtained by k-NN is 88.10% for the test set, a not satisfactory result. A traditional SVM model without variable selection gives classification accuracy 100.00% for the training set and 88.10% for the test set. The model endured serious overfitting problem. The best results provided by SVM combined with BSS/WSS are 99.30% for the training set and 83.33% for the test set when 99 variables were included in the model, as shown in Table 4. Due to limited variable selection ability of a BSS/WSS basis variable selection method, the overfitting problem of the classification model is still serious, exposed by the low prediction accuracy for the test set. Compared with the SVM model without variable selection and the SVM model using the BSS/WSS-based variable selection method, SVM combined with PDFS improves the results greatly. The classification accuracy for the test set is 95.24% when 99 top ranked genes were used, indicating that PDFS is helpful to improve the generalization ability of a model built by traditional SVM. In addition, LKT-SVM again provides even better classification performance than SVM. The classification accuracy for the training and test sets is both 100.00%. It reveals that LKT-SVM combined with PDFS has desirable generalization ability in prediction due to the incorporation of LKT.

4. Conclusion

In the present study a novel approach for significant gene mining has been proposed based on the probability density function similarity. Also, a local kernel transform-based support vector machine algorithm has been developed to tackle the multi-class problem. It has been demonstrated that the proposed gene mining approach is very flexible and efficient in significant gene identification for multi-class discrimination with complicated multi-modal distributions or mono-modal distribution with a center located among other classes. The local kernel transform of SVM extracts the feature variables separately using the significant genes identified for each class. This offers the possibility of eliminating the interference from different classes. The results reveal that the combination of the gene mining approach with the support vector machine algorithm is able to give desirable classification for both the training data and the testing set with a small set of significant genes. Therefore, the proposed approach is expected to hold great promise in gene marker discovery and expression profile-based clinical diagnosis.

Acknowledgements

References

[1] J. Derisi, L. Penland, P.O. Brown, M.L. Bittner, P.S. Meltzer, M. Ray, Y. Chen, Y.A. Su, J.M. Trent, Nat. Genet. 14 (1996) 457.
[2] L. Zhang, W. Zhou, V.E. Velculescu, S.E. Kern, R.H. Hruban, S.R. Hamilton, B. Vogelstein, K.W. Kinzler, Science 276 (1997) 1268.
[3] R.O. Duda, D.G. Stork, Pattern Classification, Wiley, New York, 2001.
[4] J.H. Cho, D. Lee, J.H. Park, K. Kim, I.B. Lee, Bitotechnol. Prog. 18 (2002) 847.
[5] A.L. Boulesteix, G. Tutz, K. Strimmer, Bioinformatics 19 (2003) 2465.
[6] M. Dettling, P. Bühlmann, Bioinformatics 19 (2003) 1061.
[7] W. Penny, D. Frost, Med. Decision Making 16 (1996) 386.
[8] Y.J. Liu, Chem. Inf. Comput. Sci. 44 (2004) (1936).
[9] K.E. Lee, N. Sha, E.R. Dougherty, M. Vannucci, B.K. Mallick, Bioinformatics 19 (2003) 90.
[10] J. Devore, R. Peck, Statistics: The Exploration and Analysis of Data, Duxbury Press, Pacific Grove, CA, 1997.
[11] S. Dudoit, J. Fridlyand, T. Speed, J. Am. Stat. Assoc. 97 (2002) 77.
[12] M.K. Kerr, M. Martin, G.A. Churchill, Analysis of Variance for Gene Expression Microarray Data, Technical Report, The Jackson Laboratory, Bar Harbor, ME, 2000.
[13] V.G. Tusher, R. Tibshirani, G. Chu, Proc. Natl. Acad. Sci. 98 (2001) 5116.
[14] C.H. Ooi, P. Tan, Bioinformatics 19 (2003) 37.
[15] D.V. Nguyen, D.M. Rocke, Bioinformatics 18 (2002) 1216.
[16] U. Fayyad, K. Irani, Proceedings of the Thirteenth International Joint Conference on Artificial Intelligence, Morgan Kaufmann, San Francisco, 1993, pp. 1022–1029.
[17] H.J. Li, J.R. Downing, A.E.J. Yeoh, W. Limsoon, Bioinformatics 19 (2003) 71.
[18] Y. Varol, H.F. Oztop, E. Avci, Int. Comm. Heat Mass Transfer 35 (2008) 928.
[19] Y. Varol, H.F. Oztop, A. Koca, E. Avci, Expert Syst. Appl. 36 (2009) 5813.
[20] W.Q. Lin, J.H. Jiang, Y.P. Zhou, H.L. Wu, G.L. Shen, R.Q. Yu, J. Comput. Chem. 28 (2007) 519.
[21] L.J. Tang, Y.P. Zhou, J.H. Jiang, H.L. Wu, G.L. Shen, R.Q. Yu, J. Chem. Inf. Model 47 (2007) 1438.
[22] Y.P. Zhou, J.H. Jiang, W.Q. Lin, H.Y. Zou, H.L. Wu, G.L. Shen, R.Q. Yu, Eur. J. Pharmaceut. Sci. 28 (2006) 344.
[23] Q. Shen, W.M. Shi, W. Kong, B.X. Ye, Talanta 71 (2007) 1679.
[24] T.R. Golub, D.K. Slonim, P. Tamayo, C. Huard, M. Gaasenbeek, J.P. Mesirov, H. Coller, M.L. Loh, J.R. Downing, M.A. Caligiuri, C.D. Bloomfield, E.S. Lander, Science 286 (1999) 531.
[25] A.I. Su, J.B. Welsh, L.M. Sapinoso, S.G. Kern, P. Dimitrov, H. Lapp, P.G. Schultz, S.M. Powell, C.A. Moskaluk, H.F. Frierson, J.M. Hampton, Cancer Res. 61 (2001) 7388.
[26] P. Smyth, in: S.J. Hanson, T. Petsche, M. Kem (Eds.), Computational Learning Theory and Natuml Learning Systems 2, The MIT Press, 1994, pp. 233–248.
[27] V. Vapnik, Statistical Learning Theory, Wiley, New York, 1998.
[28] V. Buccheri, B. Mihaljević, E.M. Matutes, J.S. Dyer, D.Y. Mason, D. Catovsky, Blood 82 (1993) 853.
[29] A. Alexis, A. Thompson, H.N. Jeaniene, H.L. Talley Do, L. Kagan, J. Kunkel, Berenson, Blood 90 (1997) 1387.
[30] R.W. Pero, T. Olofsson, A. Gustavsson, E. Kjellén, Carcinogenesis 6 (1985) 1055.
[31] M. Wetering, M. Oosterwegel, D. Dooijes, H. Clevers, EMBO J. 10 (1991) 123.
[32] H.C. Clevers, S. Dunlap, T.E. Wileman, C. Terhorst, Proc. Natl. Acad. Sci. 85 (1988) 8156.
[33] A. Tunnacliffe, J.E. Sims, T.H. Rabbitts, EMBO J. 5 (1986) 1245.
[34] L.B. Vogel, R. Arthur, D.J. Fujita, Biochim. Biophys. Acta 1264 (1995) 168.
[35] R. Stillwell, B.E. Bierer, Immunol. Res. 24 (2001) 31.
[36] H. Dunphy, Cherie, Arch. Pathol. Lab. Med. 130 (2006) 483.
[37] A. Lundwall, H. Lilja, FEBS Lett. 214 (1987) 317.
[38] P. Schulz, R. Stucka, H. Feldmann, G. Combriato, H.G. Klobeck, F. Fittler, Nucleic Acids Res. 16 (1988) 6226.
[39] Y.E. Guan, Y.H. Zhang, R.M. Breyer, L. Davis, M.D. Breyer, Neoplasia 1 (1999) 330.
[40] M.B. Kemkes, K.T. Preissner, F. Langenscheidt, K.J. Matthes, B.G. Muller, Eur. J. Haematol. 39 (1987) 161.
[41] B.M. Wice, J.I. Gordon, J. Biol. Chem. 270 (1995) 21907.
[42] K. Chang, I. Pastan, Proc. Natl. Acad. Sci. 93 (1996) 136.
[43] T. Tani, J. Ohsumi, K. Mita, Y. Takiguchi, J. Biol. Chem. 263 (1988) 1231.
[44] M. Gessler, A. Poustka, W. Cavenee, R.L. Neve, S.H. Orkin, G.A. Bruns, Nature 343 (1990) 774.
[45] B. Lauffart, S.J. Howell, J.E. Tasch, J.K. Cowell, I.H. Still, Biochem. J. 363 (2002) 195.
[46] E. Devilard, F. Bladou, O. Ramuz, G. Karsenty, J.P. Dalès, G. Gravis, C. Nguyen, F. Bertucci, L. Xerri, D. Birnbaum, BMC Cancer 6 (2006) 272.
[47] H. Sato, J.C. Grutters, P. Pantelidis, A.N. Mizzon, T. Ahmad, A.J.V. Houte, J.W.J. Lammers, J.M.M. Bosch, K.I. Welsh, R.M. Bois, Am. J. Resp. Cell Mol. Biol. 27 (2002) 406.
[48] J. Katahira, H. Sugiyama, N. Inoue, Y. Horiguchi, M. Matsuda, N. Sugimoto, J. Biol. Chem. 272 (1997) 26652.
[49] F. Martella, Bioinformatics 22 (2006) 202.
[50] Y. Lee, C.K. Lee, Bioinformatics 19 (2003) 1132.
[51] K.Y. Yeung, R.E. Bumgarner, A.E. Raftery, Bioinformatics 21 (2005) 2394.

Automated stopped-in-dual-loop flow analysis system for catalytic determination of vanadium in drinking water

Norio Teshima [a,*], Masami Kuno [a], Minoru Ueda [a], Hisashi Ueda [a], Shinsuke Ohno [b], Tadao Sakai [a]

[a] Department of Applied Chemistry, Aichi Institute of Technology, 1247 Yachigusa, Yakusa-cho, Toyota 470-0392, Japan
[b] Mitsubishi Chemical Analytech Co., Ltd., 370 Enzo, Chigasaki 253-0084, Japan

ARTICLE INFO

ABSTRACT

An automated stopped-in-dual-loop flow analysis (SIDL-FA) system is proposed for the determination of vanadium in drinking water. The chemistry is based on the vanadium-catalyzed oxidation reaction of p-anisidine by bromate in the presence of Tiron as an activator to produce a dye (λ_{max} = 510 nm). A SIDL-FA system basically consists of a selection valve, three pumps (one is for delivering of standard/sample, and others are for reagents), two six-way injection valves, a spectrophotometric detector and a data acquisition device. A 100-μL coiled loop around a heated device is fitted onto each six-way injection valve. A well-mixed solution containing reagents and standard/sample is loaded into the first loop on a six-way valve, and then the same solution is loaded into the second loop on another six-way valve. The solutions are isolated by switching these two six-way valves, so that the catalytic reaction can be promoted. The net waste can be zero in this stage, because all pumps are turned off. Then each resulting solution is dispensed to the detector with suitable time lag. A touchscreen controller is developed to automatically carry out the original SIDL-FA protocol. The proposed SIDL-FA method allows vanadium to be quantified in the range of 0.1–2 μg L^{-1} and is applied to the determination of vanadium in drinking water samples.

© 2009 Elsevier B.V. All rights reserved.

1. Introduction

Vanadium has recently attracted much attention for its potential role against diabetes [1,2]. Heyliger et al. reported that vanadate (vanadium in pentavalent state) appeared to have an insulin-like action in the *in vivo* experiments on diabetic rats [3]. Vanadyl (vanadium in tetravalent state) *in vitro* and in animal models of diabetes has been shown to reduce hyperglycemia and insulin resistance [4]. Some clinical trials with human have also shown that vanadium improved insulin sensitivity in patients with diabetes mellitus [5]. A recent study revealed that vanadium administration in impaired glucose tolerance patients increased triglyceride concentrations without changes in insulin sensitivity [6].

Nowadays prevalence of diabetes is a global issue [7], and the Japanese government enacted the Health Promotion Act (Act No. 103 of 2002) to raise health awareness by Japanese people. We have now various kinds of bottled mineral waters as drinking waters. Some of them contain naturally occurring vanadium, and it was reported that the consecutive administration of such drinking water (containing approximately 65 μg L^{-1} vanadium) resulted in a significant reduction of blood glucose levels in human diabetes [8]. Although devotees may benefit from such mineral waters

with respect to their health, the exact role of vanadium has yet to be established. Therefore the concentration of vanadium in bottled mineral waters must be strictly controlled, and an affordable and sensitive analytical method for vanadium determination is required.

Kinetic methods based on catalytic reactions are among the most sensitive for trace metal analysis [9,10]. Various catalytic reactions have heretofore been utilized as indicator reactions for the determination of trace vanadium [11–15].

Flow injection analysis (FIA) is one of the promising techniques to obtain highly sensitive methods, provided that suitable chemical reactions are introduced into FIA [16]. Since Yamane and Fukasawa first adapted a catalytic effect of vanadium into an FIA system [17], several workers have described FIA methods for catalytic determination of vanadium with spectrophotometric [18–24] and chemiluminescent [25,26] detections. However, basically FIA techniques need to establish a baseline continuously, which leads to continuous waste generation.

Since Ruzicka and Hansen conceived FIA [27], some highly sophisticated flow-based analytical systems have been proposed: air-carrier continuous analysis system [28], sequential injection analysis [29], multi-commutation in flow analysis [30], multi-syringe flow injection analysis [31], all injection analysis [32], multi-pumping in flow analysis [33] and hybrid flow analyzer [34]. These techniques are capable of lower reagent(s) consumption and lower waste generation than traditional FIA. A multi-pumping flow

system was demonstrated in relation to a spectrophotometric catalytic determination of iron and vanadium [35].

Stopped flow injection (FI) technique allows longer reaction time with minimization of dilution and without a long reaction coil, yielding higher sensitivity as well as lower waste generation. However, conventional stopped FI systems are subject to continuous contact of the resulting solution to the cell window. This may cause violation of cleanliness on the window; especially it would be a serious problem in spectrophotometric flow-based analysis. Another concept for stopped FI procedure was proposed by Grudpan [36]: the flow is stopped at a mixing coil (not at a flow cell) for a period before allowing to flow further to the flow-through cell in a simple colorimeter as a detector. Indeed the procedure does not expose continuously the cell window to the colored product, but the reagent solution continues to exist inside the cell during the stopping time.

In our previous paper [37], we proposed an alternative stopped flow technique called stopped-in-loop flow analysis (SIL-FA) and demonstrated an SIL-FA method for the catalytic determination of vanadium. The SIL-FA system allowed its own detection window to be washed (no continuous exposure to the reaction product and the reagents) when the reactant stayed at the stationary coiled loop on a six-way injection valve. However, the SIL-FA protocol containing switching of two six-way valves and control of three pumps (ON/OFF) were all carried out manually. Also, a produced dye in the loop was dispensed to the detector by the mixed solution containing carrier and all reagents solutions. Furthermore the applicability was limited due to only one loop in where the reaction took place.

In the present paper, two coiled loops are set in a SIL-FA system, and we call it stopped-in-dual-loop FA (SIDL-FA). A programmable touchscreen controller for a SIDL-FA system is newly designed, and the controller successfully accomplishes a SIDL-FA protocol for the catalytic determination of vanadium. A diluted nitric acid solution (not all reagents) is used to dispense a reaction product to the detector, so that it can be possible to minimize the consumption of reagents.

2. Experimental

2.1. Reagents

All reagents were of analytical grade and were used without further purification. Deionized water used to prepare solutions was obtained from an Advantec GSH-210 apparatus.

A commercially available vanadium(V) standard solution for atomic absorption spectrometry (Wako, Osaka) containing $1000\,\mathrm{mg\,L^{-1}}$ vanadium (ammonium metavanadate in 0.45 M sulfuric acid) was used as a stock solution. Each working solution was prepared by serial dilution of the standard solution with 10 mM nitric acid.

A 0.25 M *p*-anisidine stock solution was prepared by dissolving 6.16 g of *p*-anisidine (99%, FW = 123.16, Alfa Aesar Johnson Matthey Japan, Tokyo) in 200 mL of 3 M hydrochloric acid. A 2 M acetate buffer solution (pH 3.3) was prepared from solutions of acetic acid (Nacalai Tesque, Kyoto) and sodium acetate trihydrate (Nacalai Tesque). These stock solutions were daily mixed to prepare a solution containing 80 mM *p*-anisidine and 1 M acetate buffer, and the mixed solution was adjusted to pH 3.3 with 10 M sodium hydroxide (Nacalai Tesque). The mixed solution constituted RS_1 referred to in the section describing the procedure.

A 50 mM bromate solution was daily prepared by dissolving 0.418 g of potassium bromate (FW = 167, Wako) in 50 mL of water.

A 0.15 M Tiron solution was daily prepared by dissolving 2.49 g of 1,2-dihydroxy-3,5-benzenedisulfonic acid disodium salt monohydrate (FW = 332, Dojindo Laboratories, Kumamoto, Japan) in 50 mL of water.
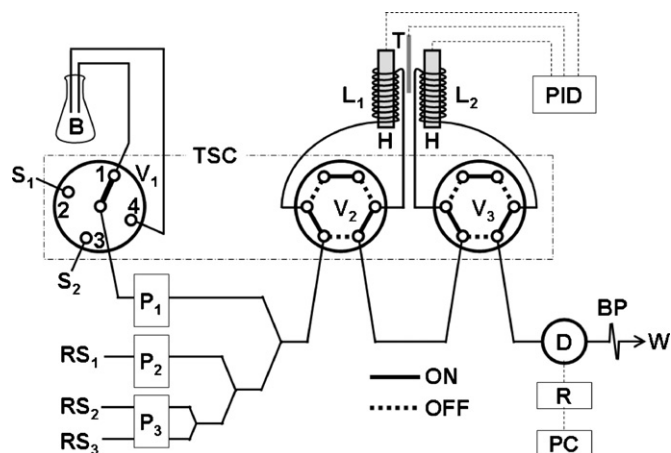
Fig. 1. Schematic flow diagram of the SIDL-FA system. B, 10 mM HNO_3; S_1 and S_2, sample; RS_1, mixed solution of 80 mM *p*-anisidine and 1 M acetate buffer (pH 3.3); RS_2, 50 mM $KBrO_3$; RS_3, 0.15 M Tiron; V_1, four-port selection valve; V_2 and V_3, six-way injection valves; P_1, P_2 and P_3, double plunger pumps (P_1, $0.90\,\mathrm{mL\,min^{-1}}$; P_2, $0.15\,\mathrm{mL\,min^{-1}}$; P_3, $0.20\,\mathrm{mL\,min^{-1}}$); H, heater; T, thermocouple; PID, proportional–integral–derivative controller (set at 105 °C); L_1, first loop (100 μL); L_2, second loop (100 μL); D, spectrophotometer (510 nm); R, recorder; PC, personal computer; BP, backpressure restrictor (0.25 mm i.d., 45 cm long).

2.2. Apparatus

The SIDL-FA system is shown schematically in Fig. 1. Three double plunger micro pumps were used to deliver solutions: P_1 and P_3 were of F·I·A Instruments, Tokyo (Dual Pump 201), and P_2 was of Soma Optics, Tokyo (Intelligent Pump 301 M). A homemade touchscreen controller (TSC) possesses a four-port selection valve and two six-way injection valves. A proportional–integral–derivative (PID) digital controller (SR91, Shimaden, Tokyo) was employed to control two cartridge heaters (C3JX4A, Watlow Japan, Tokyo) and a thermocouple (type K chromel–alumel, Sakaguchi E.H VOC, Tokyo). Each heater was installed into a tubular brass which Teflon tubing was coiled to compose a heated loop. A double beam spectrophotometer (S-3250, Soma Optics) fitted with a flow-through cell (8 μL volume, 10 mm path length) was used for absorbance measurement. The detector output was acquired on a PC through a recorder (FIA monitor, Ogawa & Co., Kobe, Japan). All flow lines were made from 0.5 mm i.d. Teflon tubing except for a backpressure restrictor (BP) that consisted of 0.25 mm i.d. Teflon tubing (45 cm long).

2.3. Procedure

A 10 mM nitric acid solution (B) for uncatalyzed reaction (blank measurement) or a standard/sample solution (S_1 or S_2) for catalyzed reaction was delivered by pump 1 (P_1) at a flow rate of $0.90\,\mathrm{mL\,min^{-1}}$. This diluted nitric acid (B) was also used as a carrier solution (for dispensing a reaction product to the detector, *vide infra*). Pump 2 (P_2, $0.15\,\mathrm{mL\,min^{-1}}$) was used to deliver a mixed solution (RS_1) of 80 mM *p*-anisidine and 1 M acetate buffer (pH 3.3). The oxidant (RS_2, 0.05 M $KBrO_3$) and the activator (RS_3, 0.15 M Tiron) solutions were delivered by pump 3 (P_3) at a flow rate of $0.1\,\mathrm{mL\,min^{-1}}$, respectively.

As shown in Fig. 2, TSC controlled three pumps (P_1, P_2 and P_3), three valves (V_1, V_2 and V_3) and a recorder (R) using a built-in programmable logic controller (PLC). The temporal operation and each function of the SIDL-FA system are depicted in Table 1. This protocol was automatically carried out to obtain two peaks derived from two loops (L_1 and L_2). When a couple of peaks for uncatalyzed reaction (namely blank peaks) was obtained, the port no. of V_1 was fixed at 1 through one protocol (see Table 1). For a couple of peaks for catalyzed reaction, several ports of V_1 were selected.
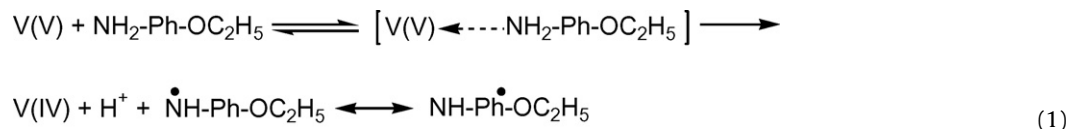
Table 1
Temporal operation of the SIDL-FA system.

Step	Port no. of V_1		V_2	V_3	P_1	P_2	P_3	R	Time s^{-1}	Function
	Uncatalyzed	Catalyzed								
1	1	2	ON	OFF	ON	ON	ON	OFF	75	Loading reagents and B or S_1 into L_1
2	1	3	OFF	ON	ON	ON	ON	OFF	75	Reaction in L_1, and loading reagents and B or S_2 into L_2
3	1	4	OFF	OFF	ON	OFF	OFF	OFF	40	Reaction in both loops and washing line
4	1	4	OFF	OFF	OFF	OFF	OFF	OFF	25	Reaction in both loops (net waste = 0)
5	1	4	OFF	OFF	ON	OFF	OFF	OFF	20	Reaction in both loops and establishing baseline
6	1	4	OFF	OFF	ON	OFF	OFF	ON	20	Reaction in both loops and starting data acquisition
7	1	4	ON	OFF	ON	OFF	OFF	ON	75	Reaction in L_2, signal monitoring for L_1 peak
8	1	4	ON	ON	ON	OFF	OFF	ON	40	Signal monitoring for L_2 peak

Abbreviations (V_1, V_2, V_3, P_1, P_2, P_3, R, B, S_1, S_2, L_1, and L_2) as in Fig. 1.

Here a typical sequence of operation for catalyzed reaction is described. Steps 1 and 2 involve the loading of a well-mixed solution of standard/sample and reagents into L_1 and L_2. The catalyzed reaction at 105 °C occurs in L_1 (steps from 2 to 6) and L_2 (steps from 3 to 7) for 180 s, respectively. While the reaction occurs in each loop, the flow-through cell and the flow line are washed with a diluted nitric acid (B) to prevent continuous exposure to the reaction product and the reagents (step 3). The net waste is zero in step 4 (all pumps are turned off).

In step 5, a baseline is established by pumping only B (only P_1 is turned on). In step 6, a trigger is sent to the recorder to acquire data. Finally, a peak for L_1 is obtained in step 7, followed by step 8 for signal monitoring of a peak for L_2. The overall measurement cycle for the two peaks is therefore 370 s.

The absorbance of the reaction product was measured at 510 nm.

3. Results and discussion

3.1. Absorption spectra

The chemistry relied on the catalytic effect of vanadium on the oxidation reaction of p-anisidine by bromate in the presence of Tiron as an activator. Preliminary batchwise experiments have been conducted to obtain absorption spectra. The procedure was as follows: to 5 mL of 50 mM p-anisidine in a 25-mL of volumetric flask, 0.5 mL of 2 M acetate buffer, 4 mL of 2.5 µg L^{-1} vanadium(V) in 10 mM nitric acid (or same volume of 10 mM nitric acid for blank) and 1 mL of 0.25 M Tiron were added. Then after adjusting pH 3.3, the solution was kept at 65 °C in a thermostated bath for about 5 min to attain thermal equilibrium. To initiate the catalytic reaction, 1 mL of 0.25 M bromate heated at 65 °C was added, and diluted

to the mark with water. At 30 min after the initiation of the reaction, a portion of the sample solution was immersed in an ice bath about 30 s for quenching. The result is shown in Fig. 3. The red colored product has an absorption maximum at 510 nm.

Bontschev and Jeliazkowa [38] fully investigated the catalytic oxidation of p-phenetidine (NH_2-Ph-OC_2H_5) by chlorate with vanadium(V) as catalyst. They reported that vanadium(V) forms a charge transfer complex with NH_2-Ph-OC_2H_5, an electron from the arylamine is completely localized in an atomic orbital of vanadium, and two arylamine radicals are formed:

$$V(V) + NH_2\text{-}Ph\text{-}OC_2H_5 \rightleftharpoons \left[V(V) \blacktriangleleft \text{-}\text{-}\text{-}\cdot NH_2\text{-}Ph\text{-}OC_2H_5 \right] \longrightarrow$$

$$V(IV) + H^+ + \overset{\bullet}{N}H\text{-}Ph\text{-}OC_2H_5 \longleftrightarrow NH\text{-}P\overset{\bullet}{h}\text{-}OC_2H_5 \tag{1}$$

Finally N-(4-ethoxyphenyl)-quinoneimine (λ_{max} = 510 nm) is produced by the recombination of two radicals with hydrolysis [38]. Vanadium(IV) produced is oxidized by bromate and thus returns in the cyclic reaction.

In this study we employed p-anisidine as substrate for a vanadium-catalyzed reaction. According to the obtained absorption spectra as shown in Fig. 3, the catalytic oxidation of p-anisidine can proceed by similar homolytic mechanism mentioned above. Therefore we concluded that the most expected product in this study was N-(4-methoxyphenyl)-quinoneimine:
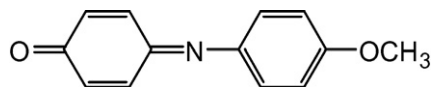
3.2. Design of touchscreen programmable controller for SIDL-FA

It is self-evident that sophisticated flow-based analyses have been developed by automatic controls of gas and/or liquid handling devices such as pumps and valves. Although it is easy for advanced users to accomplish such controls, a user-friendly ubiquitous control system is still required to have flow-based analyses widespread. As mentioned in Section 2, the proposed TSC (Fig. 4) controls three pumps (ON/OFF), port selection of V_1, valve switching of V_2 and V_3 and a recorder. As can be seen in Fig. 4(c), one can start analysis with a touch on the screen panel which displays the current states of three valves and three pumps in real time. Also, the analytical protocol can be easily modified by touching to "CONFIG." on the display area.

3.3. Optimization

The protocol depicted in Table 1 was temporarily modified in the optimization study. We omitted operation with respect to L_1 from the whole protocol, i.e. we measured the absorbance of the uncatalyzed and catalyzed reaction products from only L_2.
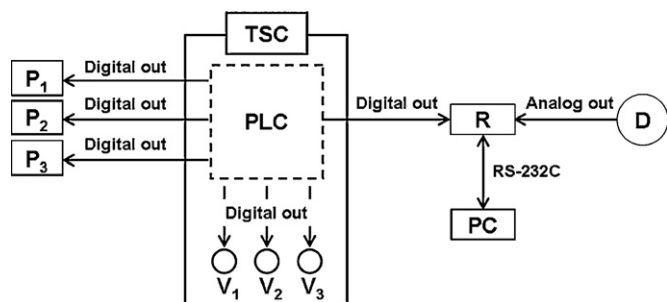
Fig. 2. Schematic diagram of control system with touchscreen controller (TSC). PLC, programmable logic controller. Other abbreviations as in Fig. 1.
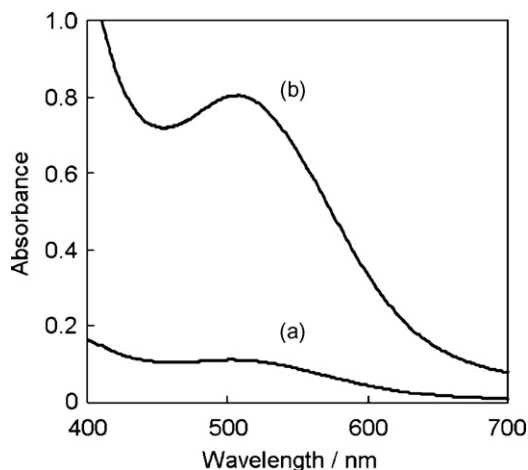
Fig. 3. Absorption spectra of the reaction product. C_V in $\mu g\,L^{-1}$: (a) 0; (b) 0.4. $C_{p\text{-anisidine}}$, 10 mM; $C_{\text{acetate buffer}}$, 40 mM (pH 3.3); C_{Tiron}, 10 mM; C_{bromate}, 10 mM; temperature, 65 °C; reaction time, 30 min.
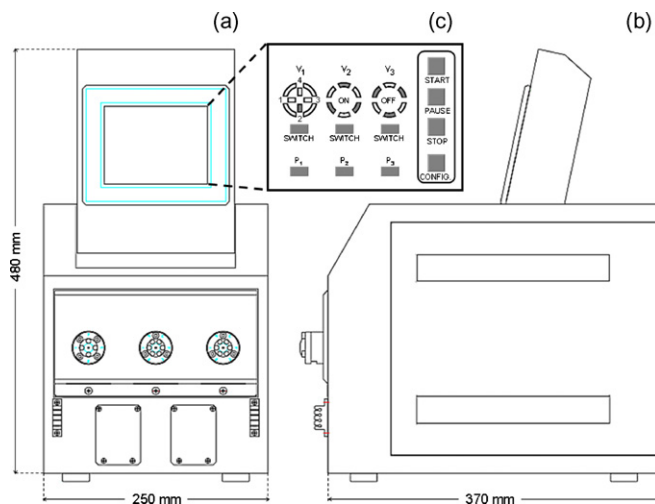
Fig. 4. Touchscreen controller. (a) Side view; (b) front view; (c) example of indication on the touchscreen panel.

3.3.1. Effect of stopping time in loop

Stopping time in L_2 was varied from 2 to 5 min. The symbols in Fig. 5 denote absorbance values of uncatalyzed (○), catalyzed
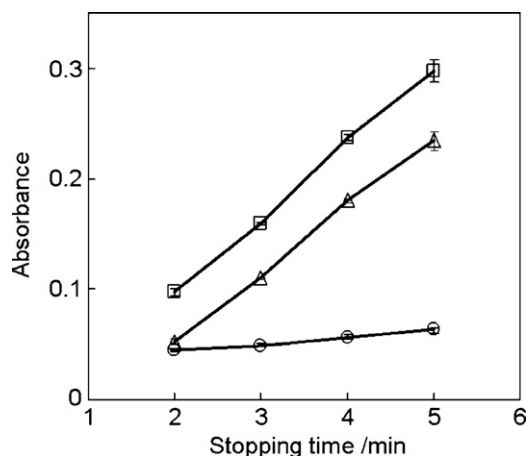
Fig. 5. Effects of stopping time in L_2 on uncatalyzed (○) and catalyzed (□) reactions. (△) Net absorbance; C_V, 1.0 $\mu g\,L^{-1}$. Other conditions as in Fig. 1.
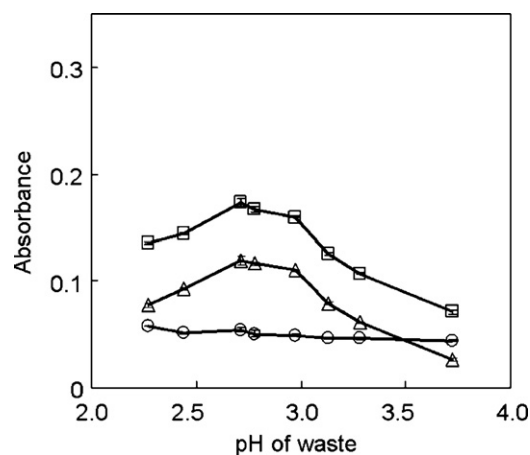
Fig. 6. Effects of pH on uncatalyzed (○) and catalyzed (□) reactions. (△) Net absorbance; C_V, 1.0 $\mu g\,L^{-1}$. Other conditions as in Fig. 1.

(□) and the net (△). The uncatalyzed reaction was little affected by an increase in stopping time. The catalyzed reaction, on the contrary, was dramatically enhanced. Taking into account sample throughput, a stopping time of 3 min was chosen.

3.3.2. Effect of temperature

Temperature setting of the PID controller was varied from 80 to 105 °C. The absorbance of uncatalyzed reaction was constant in this temperature range. The response of catalyzed reaction increased with raising temperature. At temperature higher than 105 °C, we encountered bubble-induced detector problems. We chose therefore a temperature setting of 105 °C.

3.3.3. Effect of pH

Fig. 6 shows the effect of pH on the responses. The *x*-axis of Fig. 6 stands for pH of the waste solution. The response of catalyzed reaction had a plateau in the range of 2.7–3.0, and the response of uncatalyzed reaction slightly decreased in the examined pH range. Although the net absorbance was highest at pH 2.7, we chose a reaction pH of 3.0, because the blank response at pH 3.0 was a little bit lower than that at pH 2.7. The pH value of RS_1 containing acetate buffer was adjusted at pH 3.3 to obtain the chosen pH 3.0 for the waste solution.

3.3.4. Effect of p-anisidine concentration

The effect of *p*-anisidine concentration on the responses was studied over the range from 40 to 90 mM in RS_1. The response of catalyzed reaction increased monotonically with *p*-anisidine concentration, but that of uncatalyzed reaction also increased slightly. Hence, *p*-anisidine concentration of 80 mM was chosen.

3.3.5. Effect of bromate concentration

Both catalyzed and uncatalyzed reactions accelerated with increasing bromate concentration over the range from 10 to 200 mM. We chose a bromate concentration of 50 mM.

3.3.6. Effect of Tiron concentration

The use of properly selected activators for catalytic reactions offers an improvement in the sensitivity and/or the selectivity [39]. There have been numerous reports on vanadium-catalyzed indicator reactions in which some ligands acted as activators: oxine [40], oxalic, citric [41] and sulfosalicylic acids [22,41], Tiron [14,19,23], tartrate [15], gallic acid [21] and hydrogen carbonate [25]. We employed Tiron as the activator for the proposed catalytic oxidation of *p*-anisidine. The effect of Tiron concentration on the responses was shown in Fig. 7. The response of catalyzed reaction remained
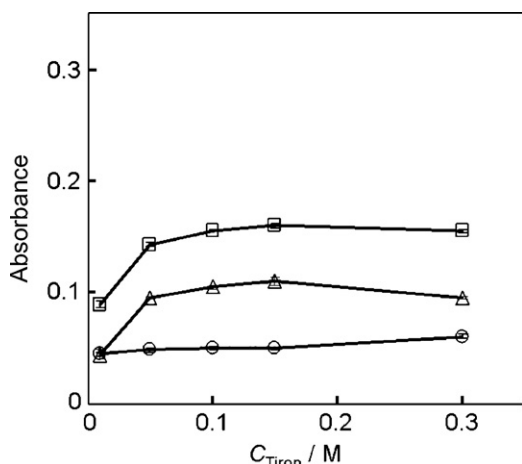
Fig. 7. Effects of Tiron concentration on uncatalyzed (○) and catalyzed (□) reactions. (△) Net absorbance; C_V, 1.0 µg L^{-1}. Other conditions as in Fig. 1.

almost constant at Tiron concentrations higher than 0.1 M. The net value was highest at 0.15 M, so we chose this concentration.

Bontschev [39] reported that hydroxy acids, such as oxalic, citric and gallic acids, acted as activator for vanadium-catalyzed oxidation of *p*-phenetidine by chlorate. Such activators (A) are oxidized easily by vanadium(V) to radicals (A$^\bullet$),

$$V(V) + A \rightarrow A^\bullet + V(IV) \tag{2}$$

which then react with the coexisted *p*-phenetidine (S) to produce its radical (S$^\bullet$),

$$A^\bullet + S \rightarrow A (\text{or } A') + S^\bullet \tag{3}$$

followed by the recombination of S$^\bullet$ as described in Section 3.1. Tiron has two hydroxyl groups to be easily reduced. Hence the similar pathway as mentioned above can be thought to proceed in the present catalytic reaction, although there are several possible mechanisms.

3.4. Analytical characteristics

The typical system output is shown in Fig. 8. As described in Section 2.3, the SIDL-FA protocol depicted in Table 1 gave two peaks for two loops; for example (a) and (a′) in Fig. 8 are of peaks for uncatalyzed reaction obtained from L$_1$ and L$_2$, and (b) and (b′) are of peaks for 1 µg L^{-1} vanadium from L$_1$ and L$_2$. As can be seen in Fig. 8, a negative peak was observed in each measurement. This is
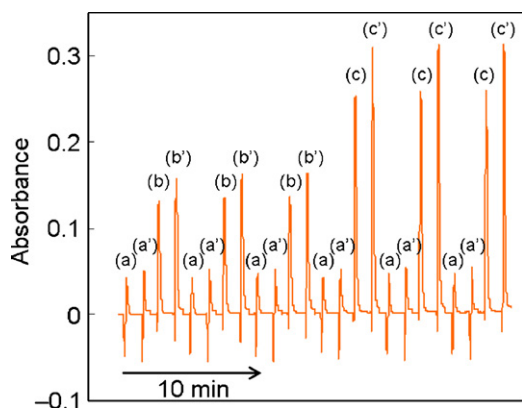
probably due to the differences in refractive indices between the resulting solution from each loop and the carrier stream (10 mM nitric acid). These negative peaks due to Schlieren effect could be neglected in this system because acceptable calibration curves for L$_1$ and L$_2$ in the range of 0–2.0 µg L^{-1} vanadium(V) were obtained from only positive peaks without any compensation:

$$\text{Net absorbance} = 0.104[V(V), \ \mu g\,L^{-1}] - 0.00504$$

$$\text{for } L_1 \ (r^2 = 0.993) \tag{4}$$

$$\text{Net absorbance} = 0.128[V(V), \ \mu g\,L^{-1}] - 0.00678$$

$$\text{for } L_2 \ (r^2 = 0.993) \tag{5}$$

The lower slope value of L$_1$ was caused by the longer distance between L$_1$ and the detector than that for L$_2$. However the 3σ limit of detection for L$_1$ (0.038 µg L^{-1}) was comparable to that for L$_2$ (0.037 µg L^{-1}). Therefore we can obtain analytical values of two unknown samples using L$_1$ and L$_2$ for 370 s. The sample throughput is therefore approximately 20 samples h^{-1}. In our previous study on SIL-FA with a single loop [37], 280 s was needed to obtain an analytical value of one unknown sample (the sample throughput was approximately 13 samples h^{-1}). The proposed SIDL-FA with two loops is superior to sample throughput. The R.S.D. values ($n = 5$) in the present study were 0.81% (L$_1$) and 1.1% (L$_2$) for responses at 1.0 µg L^{-1}.

3.5. Interferences

The effects of various foreign ions on the response of 1.0 µg L^{-1} vanadium(V) obtained from L$_2$ were studied. The results are summarized in Table 2. The tolerance limit was defined as the interference that yielded a relative error less than or equal to ±5%. Among the tested foreign ions, iron(III) gave the largest positive interference. In our previous paper [42], the oxidation of *p*-anisidine by hydrogen peroxide was catalyzed by iron. Hence iron(III) may act as a catalyst for the oxidation reaction in this study. Although 50 µg L^{-1} iron(III) is tolerable for the determination of 1.0 µg L^{-1} vanadium(V) by the proposed method, the applicability of this method to natural water analysis would be limited by this value. It was reported that 40–80 µg L^{-1} iron existed in well water [43]. However the proposed method is allowed to be applied to vanadium-rich water analysis.

3.6. Application

The proposed SIDL-FA method was applied to the determination of vanadium in commercial bottled water samples (Table 3). A paired *t*-test was performed on the data obtained by the proposed method and ICP-MS. The experimental *t*-value was 1.538 which is less than the critical *t*-value at the 95% confidence level for three degrees of freedom (3.182). The statistical analysis revealed that

Table 2
Tolerance limits of foreign ions on the determination of 1.0 µg L^{-1} vanadium(V).

Tolerance limit/µg L^{-1}	Ion added
50,000	Mg(II), Na(I), Ca(II), Cd(II), K(I), Rb(I), Cl$^-$, Br$^-$, F$^-$, NO$_3$$^-$, SO$_4$$^{2-}$
20,000	Ni(II), Mn(II), Pb(II)
10,000	Zn(II), Sn(IV)
5,000	Se(IV)
2,000	Al(III), Co(II), Si(IV)
500	Ti(IV)
200	Cr(VI)
100	Cu(II)
50	Fe(III)

Fig. 8. Typical system output for response to standard vanadium(V) obtained from L$_1$ ((a), (b) and (c)) and L$_2$ ((a′), (b′) and (c′)). C_V in µg L^{-1}: (a) and (a′) 0; (b) and (b′) 1.0; (c) and (c′) 2.0. Other conditions as in Fig. 1. The abscissa does not stand for the total analysis time, but stands for the data acquisition time (steps 6–8, see Table 1).

Table 3
Determination of vanadium in bottled mineral water.

Sample	Found/μg L^{-1}			Labeled/μg L^{-1}
	Proposed		ICP-MS	
	Loop 1	Loop 2		
1[a]	92 ± 0.9	–	92 ± 1.7	91
2[b]	–	50 ± 0.4	49 ± 0.6	50
3[b]	62 ± 1.5	–	60 ± 4.0	62
4[c]	–	0.97 ± 0.3	1.0 ± 0.05	1

[a] The water was diluted to 200 times with 10 mM nitric acid before measurement.
[b] The water was diluted to 100 times with 10 mM nitric acid before measurement.
[c] The water was diluted to 2 times with 10 mM nitric acid before measurement.

there is no significant difference between the two methods. In addition, the analytical values were in fair agreement with the labeled values.

4. Conclusion

We have proposed here an automated SIDL-FA system for kinetic-catalytic determination of vanadium in bottled drinking water. The designed touchscreen controller could successfully perform the SIDL-FA operation sequence. The SIDL-FA technique provides smaller reagent consumption than conventional FIA system. Such automated SIDL-FA technique is expected to be applicable to any kinetic-catalytic methods of analysis.

Acknowledgement

References

[1] M.D.V. Badmaev, P. Subbalakshmi, M. Muhammed, J. Altern. Complement. Med. 5 (1999) 273.
[2] H. Ueki, Yakugaku Zasshi 123 (2003) 633.
[3] C.E. Heyliger, A.G. Tahiliani, J.H. McNeill, Nature 227 (1985) 1474.
[4] K. Cusi, S. Cukier, R.A. Defronzo, M. Torres, F.M. Puchulu, J.C.P. Redondo, J. Clin. Endocrinol. Metab. 86 (2001) 1410.
[5] A.B. Goldfine, D.C. Simonson, F. Folli, M.-E. Patti, C.R. Kahn, Mol. Cell. Biochem. 153 (1995) 217.
[6] O. Jacques-Camarena, M. González-Ortiz, E. Martínez-Abundis, J.F.P. López-Madrueño, R. Medina-Santillán, Ann. Nutr. Metab. 53 (2008) 195.
[7] S. Wild, G. Roglic, A. Green, R. Sicree, H. King, Diabetes Care 27 (2004) 1047.
[8] T. Kitta, S. Yamada, T. Asakawa, K. Ishihara, N. Watanabe, H. Ishiyama, Y. Watanabe, Oyo Yakuri/Pharmacometrics 64 (2003) 77.
[9] S.R. Crouch, A. Scheeline, E.S. Kirkor, Anal. Chem. 72 (2000) 53R.
[10] T. Kawashima, N. Teshima, S. Nakano, in: R.A. Meyers (Ed.), Encyclopedia of Analytical Chemistry, John Wiley & Sons, Chichester, 2000, p. 11034.
[11] P.R. Bontschev, Microchim. Acta 50 (1962) 577.
[12] G.D. Christian, Anal. Lett. 4 (1971) 187.
[13] M.L. Camacho, M.T. Rodriguez, M.C. Mochón, A.G. Perez, Anal. Chim. Acta 244 (1991) 89.
[14] J. Gao, X. Zhang, W. Yang, B. Zhao, J. Hou, J. Kang, Talanta 51 (2000) 447.
[15] A.A. Mohamed, K.F. Fawy, J. Trace Microprobe Tech. 20 (2002) 29.
[16] T. Sakai, N. Teshima, Anal. Sci. 24 (2008) 855.
[17] T. Yamane, T. Fukasawa, Anal. Chim. Acta 119 (1980) 389.
[18] T. Fukasawa, S. Kawakubo, T. Okabe, A. Mizuike, Bunseki Kagaku 33 (1984) 609.
[19] S. Nakano, M. Tago, T. Kawashima, Anal. Sci. 5 (1989) 69.
[20] A.A. Ensafi, A. Kazemzadeh, Microchem. J. 53 (1996) 139.
[21] S. Kawakubo, K. Kajihara, M. Iwatsuki, Anal. Sci. 12 (1996) 237.
[22] T. Shiobara, N. Teshima, M. Kurihara, S. Nakano, T. Kawashima, Talanta 49 (1999) 1083.
[23] S. Nakano, E. Tanaka, Y. Mizutani, Talanta 61 (2003) 203.
[24] S. Nakano, N. Teshima, M. Kurihara, T. Kawashima, Bunseki Kagaku 53 (2004) 255.
[25] S. Nakano, K. Sakamoto, A. Takenobu, T. Kawashima, Talanta 58 (2002) 1263.
[26] J.A.P. Pérez, J.S.D. Alegría, P.F. Hernando, A.N. Sierra, Anal. Chim. Acta 536 (2005) 115.
[27] J. Ruzicka, E.H. Hansen, Anal. Chim. Acta 78 (1975) 145.
[28] K. Petersen, P.K. Dasgupta, Talanta 36 (1989) 49.
[29] J. Ruzicka, G.D. Marshall, Anal. Chim. Acta 237 (1990) 329.
[30] B.F. Reis, M.F. Giné, E.A.G. Zagatto, J.L.F.C. Lima, R.A. Lapa, Anal. Chim. Acta 293 (1994) 129.
[31] V. Cerda, J.M. Estela, R. Forteza, A. Cladera, E. Becerra, P. Altimira, P. Sitjar, Talanta 50 (1999) 695.
[32] H. Itabashi, H. Kawamoto, T. Kawashima, Anal. Sci. 17 (2001) 229.
[33] R.A.S. Lapa, J.L.F.C. Lima, B.F. Reis, J.L.M. Santos, E.A.G. Zagatto, Anal. Chim. Acta 466 (2002) 125.
[34] N. Amornthammarong, J. Jakmunee, J. Li, P.K. Dasgupta, Anal. Chem. 78 (2006) 1890.
[35] P.R. Fortes, S.R.P. Meneses, E.A.G. Zagatto, Anal. Chim. Acta 572 (2006) 316.
[36] K. Grudpan, Talanta 64 (2004) 1084.
[37] N. Teshima, S. Ohno, T. Sakai, Anal. Sci. 23 (2007) 1.
[38] P.R. Bontschev, B.G. Jeliazkowa, Microchim. Acta 55 (1967) 116.
[39] P.R. Bontschev, Talanta 19 (1972) 675.
[40] P.R. Bontchev, B.G. Jeliazkowa, Inorg. Chim. Acta 1 (1967) 249.
[41] P.R. Bontchev, G.S. Nikolov, J. Inorg. Nucl. Chem. 28 (1966) 2609.
[42] K. Watla-iad, T. Sakai, N. Teshima, S. Katoh, K. Grudpan, Anal. Chim. Acta 604 (2007) 139.
[43] S. Ohno, M. Tanaka, N. Teshima, T. Sakai, Anal. Sci. 20 (2004) 171.

Letter to the Editor

Comments on "Determination of *S*-nitrosoglutathione and other nitrosothiols by *p*-hydroxymercurybenzoate derivatization and reverse phase chromatography coupled with chemical vapor generation atomic fluorescence detection" by Bramanti et al.

Dear Editor,

Nitric oxide (NO) is one of the most potent endogenous vasodilators and a very short-lived species in blood. Half-life and concentration of NO in human circulation are estimated to be below 0.1 s and 1 nM, respectively. Other longer-lived NO-derived species, notably *S*-nitrosothiols (RSNO) and nitrite, are believed to be storage and transport forms of NO bioactivity within the vasculature. Endogenous high-molecular-mass (HMM) RSNO include *S*-nitrosohaemoglobin (SNOHb) and *S*-nitrosoalbumin (SNOALB). Putative endogenous low-molecular-mass (LMM) RSNO are *S*-nitrosoglutathione (GSNO), *S*-nitrosocysteinylglycine (SNOCG) and *S*-nitrosocysteine (SNOC).

Accurate quantitative determination of RSNO in biological samples represents a big challenge for chemist analysts. Presumably, there are no further analytes for which an almost five-order of magnitude concentration range has been reported for the basal state. The analytical problems associated with the analysis of RSNO in biological fluids are well-known and recognized and have been reviewed and discussed by different groups [1–4]. Many factors may compromise accurate quantitative determination of RSNO in biological fluids. Most important and difficult to control factors include low concentration (pM/nM range), lacking stability, abundant artifactual formation, and need for indirect measurement. A considerable amount of responsibility may also be attributed to the rather hesitant preparedness of scientists for adequate validation of their analytical methods for RSNO prior to application in basic and clinical research.

Bramanti et al. [5] recently reported on the development and application of an indirect HPLC method to quantify LMM-RSNO in human plasma. This investigators group detected in plasma of 8 healthy volunteers practically all putative LMM-RSNO and determined mean concentrations of 1460 nM for SNOC, 1000 nM for *S*-nitrosohomocysteine (SNOhC) and 320 nM for GSNO (in the presence of the γ-glutamyl transferase inhibitor SBC, a serine–borate complex), whereas SNOCG was below the LOQ value of the method (presumably 80 nM). In the absence of SBC, the respective concentrations were 1850 nM, 1100 nM, 80 nM and 200 nM in plasma of 4

healthy volunteers. To the best of my knowledge, this is the first report on such high concentrations of LMM-RSNO in plasma of healthy humans. Their total concentration sums up to about 3 μM. This concentration is about ten times higher than that reported for the first time by Stamler et al. [6] for the sum of LMM-RSNO which is however questioned in the literature [1,2,4]. Considering that the concentration of HMM thiols in human plasma is about 500 μM and that RSNO are in equilibrium with their thiols [7], the study of Bramanti et al. [5] suggests that the concentration of HMM-RSNO in human plasma (i.e. SNOALB) would be about 100–200 times higher than the LMM-RSNO concentration, i.e. 300 μM. Such dramatic conditions have not been reported and would be incompatible with human life.

It is worth mentioning that the concentration of the LMM thiol ʟ-homocysteine in plasma of healthy humans is about 100 nM [8]. The plasma concentration of about 1000 nM of SNOhC reported by Bramanti et al. [5] would be about 10 times higher than the plasma concentration of its precursor. Such an imbalance for thiol/*S*-nitrosothiol systems is reportedly unknown and highly unlikely.

Considering the present knowledge in the NO/RSNO area of research, one may be very surprised about the extremely high concentrations of LMM-RSNO reported by Bramanti et al. [5]. In addition to analytical issues, measuring of such unlikely high RSNO concentrations should prompt to a critical evaluation of the findings with respect to potential physiological and pathological consequences that would indispensably arise from such dramatically high LMM-RSNO concentrations in human plasma. There is no doubt that the quality of analytical measurements should be tested by purely analytical criteria. However, the status of a biological system, as reflected by the concentrations of relevant representatives of the system in the basal state, should be an additional criterion – on the part both of the investigators themselves and of the reviewers – to test the reliability of the analytical procedures being proposed. From this perspective as well as from the pure analytical point of view, i.e. improper method-validation and lacking method-specificity, there is reasonable objection to the validity of the LMM-RSNO concentrations measured in plasma of

healthy humans and to the dependability of the analytical method used by Bramanti et al. [5].

References

[1] P.H. MacArthur, S. Shiva, M.T. Gladwin, J. Chromatogr. B 851 (2007) 93.
[2] D. Giustarini, A. Milzani, I. Dalle-Donne, R. Rossi, J. Chromatogr. B 851 (2007) 124.
[3] A. Gow, A. Doctor, J. Mannick, B. Gaston, J. Chromatogr. B 851 (2007) 140.
[4] D. Tsikas, Anal. Biochem. 379 (2008) 139.
[5] E. Bramanti, K. Jacovozzi, L. D'Ulivo, C. Vecoli, R. Zamboni, Z. Mester, A. D'Ulivo, Talanta 77 (2008) 684.
[6] J.S. Stamler, O. Jaraki, J. Osborne, D.I. Simon, J. Keaney, J. Vita, D. SIngel, C.R. Valeri, J. Loscalzo, Proc. Natl. Acad. Sci. U.S.A. 89 (1992) 7674.
[7] D. Tsikas, J. Sandmann, S. Rossa, F.M. Gutzki, J.C. Frölich, Anal. Biochem. 270 (1999) 231.
[8] R.H. Williams, J.A. Maggiore, R.D. Reynolds, C.M. Helgason, Clin. Chem. 47 (2001) 1031.

Dimitrios Tsikas*
*Institute of Clinical Pharmacology,
Hannover Medical School, Carl-Neuberg-Strasse 1,
30625 Hannover, Germany*

* Tel.: +49 511 532 3959; fax: +49 511 532 2750.
E-mail address: tsikas.dimitros@mh-hannover.de

28 November 2008

Available online 25 March 2009

A single standard calibration module for flow analysis systems based on solenoid microdevices

Łukasz Tymecki*, Kamil Strzelak, Robert Koncki

University of Warsaw, Department of Chemistry, Pasteura 1, 02-093 Warsaw, Poland

ARTICLE INFO

ABSTRACT

Only two computer-controlled microsolenoid devices, namely two micropumps or one micropump and one microvalve, are sufficient for the construction of on-line dilution modules useful in several flow analytical systems for the calibration using single standard. Three simple constructions of such modules were tested and compared. The most promising is the one based on the concept of a microvalve controlling dilution ratio of the standard and a solenoid micropump playing a double role: solution pumping device and mixing segments homogenizer. All investigated modules were tested with paired emitter detector diode (PEDD) as photometric flow-through detector and bromothymol blue as a model analyte. The best module was implemented into more advanced flow-injection system dedicated for optical detection of alkaline phosphatase activity using UV-PEDD-based flow-through detector for the enzyme reaction product.

© 2009 Elsevier B.V. All rights reserved.

1. Introduction

The final goal of flow analysis (FA) is the automation or at least mechanization of whole analytical procedure from sampling to analytical results acquisition. Indispensable step of each FA method is calibration. The set of standards method is the most popular method of calibration. According to the FA idea this step should also be automated. For the analyst convenience off-line preparation of standard solutions should be simplified and therefore several FA systems requiring only one standard have been developed [1–8].

The mentioned approach can be realized by special units of FA manifolds dedicated for controlled dilution of single standard like the mixing chamber [1], system of dilution loops of different dimensions [2], fully rotating valve with set of dilution loops [3,4] etc. SIA approach exploits an additional loop to generate concentration gradient of standard [5]. Several calibration procedures in FA are based on either merging zones approach [6] in which segments of standard can be superimposed and merged in a controlled way in the FA system, or zone sampling approach [7] where a small portion of dispersed standard zone can be injected into another carrier stream. Similar possibilities are offered by modern, more or less sophisticated multi-pumping [9–11] and multi-commutation [12–14] FA systems, reviewed recently.

In this study, simple FA modules (composed of only two computer-controlled solenoid devices) dedicated for a single standard calibration procedures, are investigated. The main goal of this study is the development of module useful for further applications in more sophisticated FA systems. The utility of investigated modules will be tested with newly developed PEDD-based photometric detectors [15–17] designed for FA needs.

2. Experimental

Alkaline phosphatase isolated from bovine intestinal mucosa (ALP, EC 3.1.3.1, powder $15\,U\,mg^{-1}$) and *p*-nitrophenyl phosphate (NPP) were obtained from Sigma–Aldrich (USA). Bromothymol blue (BTB), *p*-nitrophenol (NP) and other reagents of analytical grade were obtained from POCh (Poland).

Microsolenoid devices were purchased from Bio-ChemValve Inc. (Boonton, USA). The solenoid pumps (product no.120SP1210-4TE) operated with 2 Hz frequency as recommended (http://www.biochemfluidics.com/) and indicated stroke volume of $16\,\mu L$. Moreover, three-way solenoid valves (product no.100T3MP12-62-5) were applied. Both devices were PC-controlled by the KSP Measuring System (Poland) [18]. Flow manifolds were arranged with PTFE Microbore tubings (ID 0,8 mm) from Cole-Palmer (USA). Architecture of investigated manifolds is shown in next section of this paper.

Fabrication and analytical performance of flow-through PEDD detectors was reported elsewhere [15–17]. Red, blue an UV light emitting diodes (LEDs, diameter: 5 mm; lens: transparent, flat front; view angle: 140°) were obtained from Optosupply (Hong Kong). Flow-PEDD for BTB detection was constructed using home-made polycarbonate cell (10 mm optical pathlength, $90\,\mu L$ dead volume)

* Corresponding author.
E-mail address: luktym@chem.uw.edu.pl (Ł. Tymecki).

where two identical red LEDs [15,16] were applied. Voltage signals generated by this PEDD were recorded using a precise pH-meter (Radelkis, model OP-208/1, Hungary) coupled with data storage PC via RS232 interface [15]. UV-PEDD for NP detection was constructed using UV-LED and blue LED, as the light emitter and detector, respectively [17]. Signals generated by this PEDD were recorded with Axiomet multimeter (model AX-18B, China) used as voltmeter connected with data storage PC via USB interface [16].

3. Results and discussion

The use of multi-pumping systems for on-line dilution is quite often reported in the analytical literature [9–11]. The primary investigated module consisting of two solenoid micropumps coupled with mixing coil and PEDD detector is depicted in Fig. 1A. The PEDD consisting of two red LEDs enables fast photometric detection of BTB. Voltage signal generated by the detector is directly proportional to the absorbance of solution and thus to BTB concentration [15]. In this module, the on-line dilution of standard is controlled by the ratio of pumps actuation. Pumps switching program dedicated for the on-line calibration of FA system using a single standard is shown in Fig. 1B

Results for calibration performed in the set-up without mixing coil, shown in Fig. 1C, clearly demonstrate a significant role of this part of the module. Immediately after Y-connector the separate series of segments of the calibrant (BTB standard) and the diluter (0.05 M borate buffer pH of 9.2) are formed and it is recorded as an apparent noise of detector (shaded recording C1). Obviously, "noise-free" signals for border calibrations standards (the highest and the lowest analyte concentrations, obtained for the undiluted standard or diluter) clearly confirm that the detector works correctly. The recording C2 obtained in the set-up with additional 1.10 mL mixing coil is free from these inexpedient effects. Comparison of recordings C1 and C2 clearly confirms that in the two-pumps module mixing coil is necessary for the effective mixing and homogenization of standard and diluter segments. It leads to the formation of well-defined zones of diluted standard exhibiting the requested concentration. The linear calibration graph corresponding to recording C2 is shown in Fig. 1D (curve D1).

Instability of solenoid micropumps parameters (mainly the decalibration observed as internal volume changes) is the Achilles heel of reported module. Thus frequent calibration of these devices is necessary, because negligible volume differences cause significant changes in resulted dilutions. This drawback is well illustrated
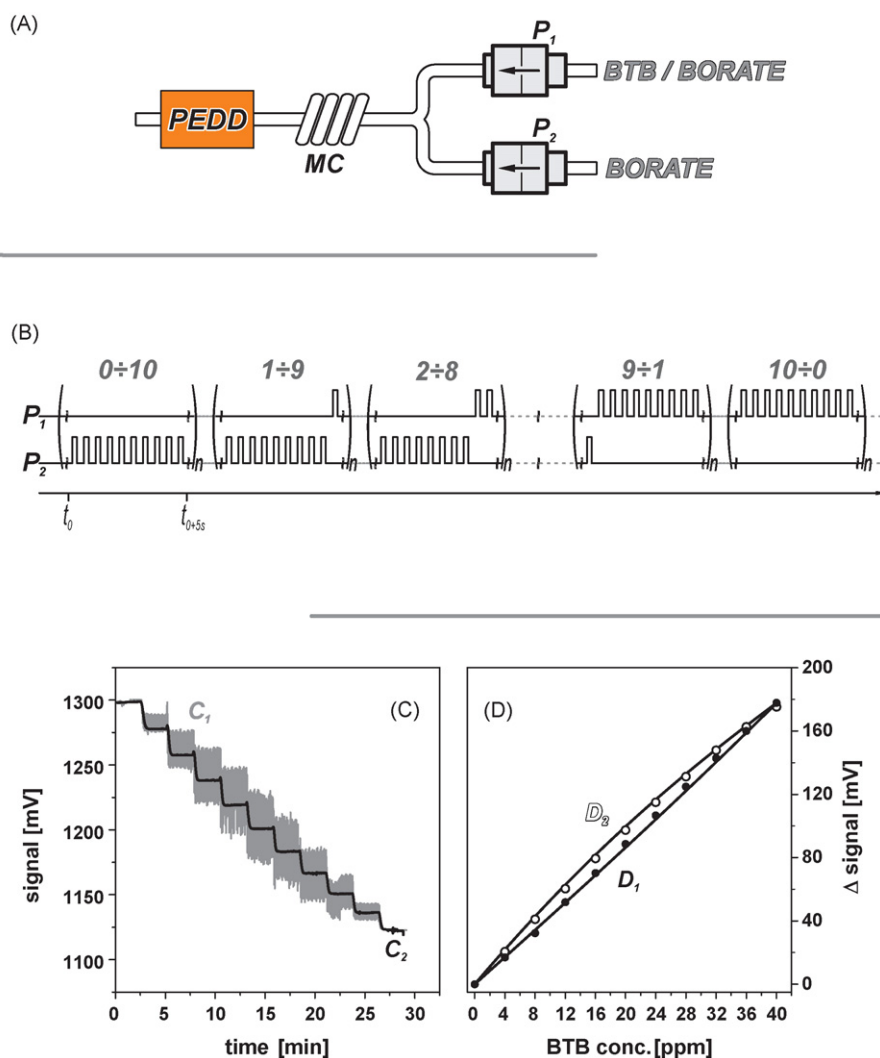
Fig. 1. The scheme of calibration module (A) consisted of two pumps (P1, P2,), mixing coil (MC) and detector (PEDD) Depiction of program for solenoid devices (B). Recordings of detector response in the course of calibration (C) performed without (C1) and with (C2) mixing coil it the manifold. Calibration plots (D) before (D1) and after (D2) pump replacement.
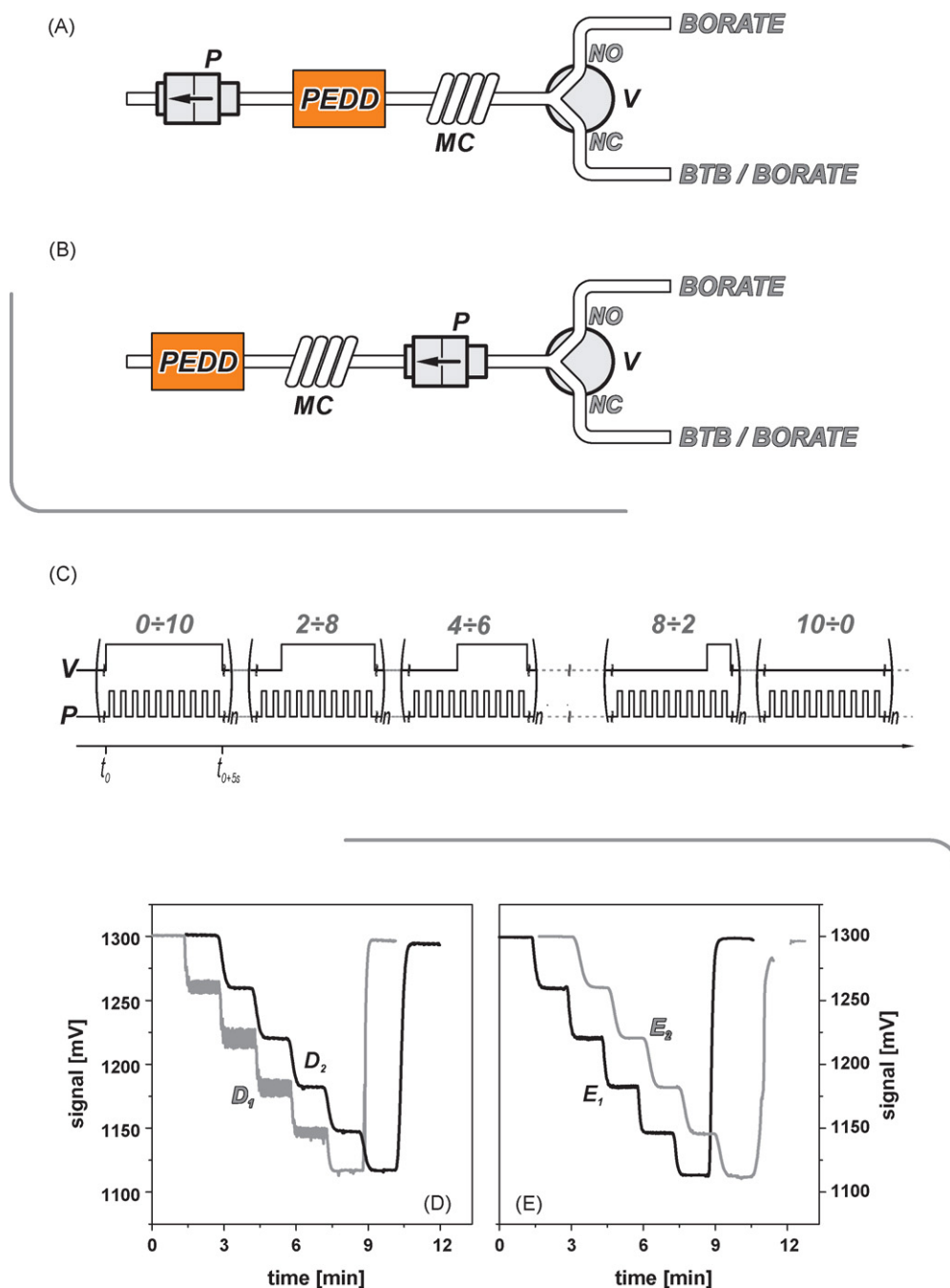
Fig. 2. The schemes of calibration modules (A,B) consisted of valve (V), pump (P), mixing coil (MC) and detector (PEDD). Depiction of program for solenoid devices (C). Recordings of detector response in the course of calibration performed in module A (D) and B (E) without (D_1, E_1) and with (D_2, E_2) presence of mixing coil in the manifolds.

by the D2 calibration graph shown in Fig. 1D, obtained under the same experiment conditions as D1 graph, after changing places of micropumps apparently exhibiting the same volumes only.

The role of device controlling on-line dilution ratio can be played by the microsolenoid valve. The scheme of single standard calibration module working according to this concept is shown in Fig. 2A. The device switching program realizing the on-line calibration is shown in Fig. 2C. The synchronization of electric pulses actuating the pump and valve is a key factor for the proper operation of the module. Because of mechanical nature and differences in the construction between solenoid devices, the pump should be actuated a few milliseconds earlier than the valve. Independent operation of

valve and pump could be possible only when pump generates continuous flow (e.g. peristaltic pump) not the pulsed flow (as solenoid pump).

The superiority of valve–pump module over two-pumps set-up is evident. The problem of valve decalibration does not exist, because the valve volume is not significant in this system. On the other hand, the ratio of calibrant/diluter mixing defined only by the valve operation is independent of internal volume of solenoid pump.

Similarly as in previous set-up shown in Fig. 1A, the presence of mixing coil in the module before the detector is necessary. The effect of mixing coil length on the recordings of calibration procedure (Fig. 2D) is explained as previously. The increase of its volume
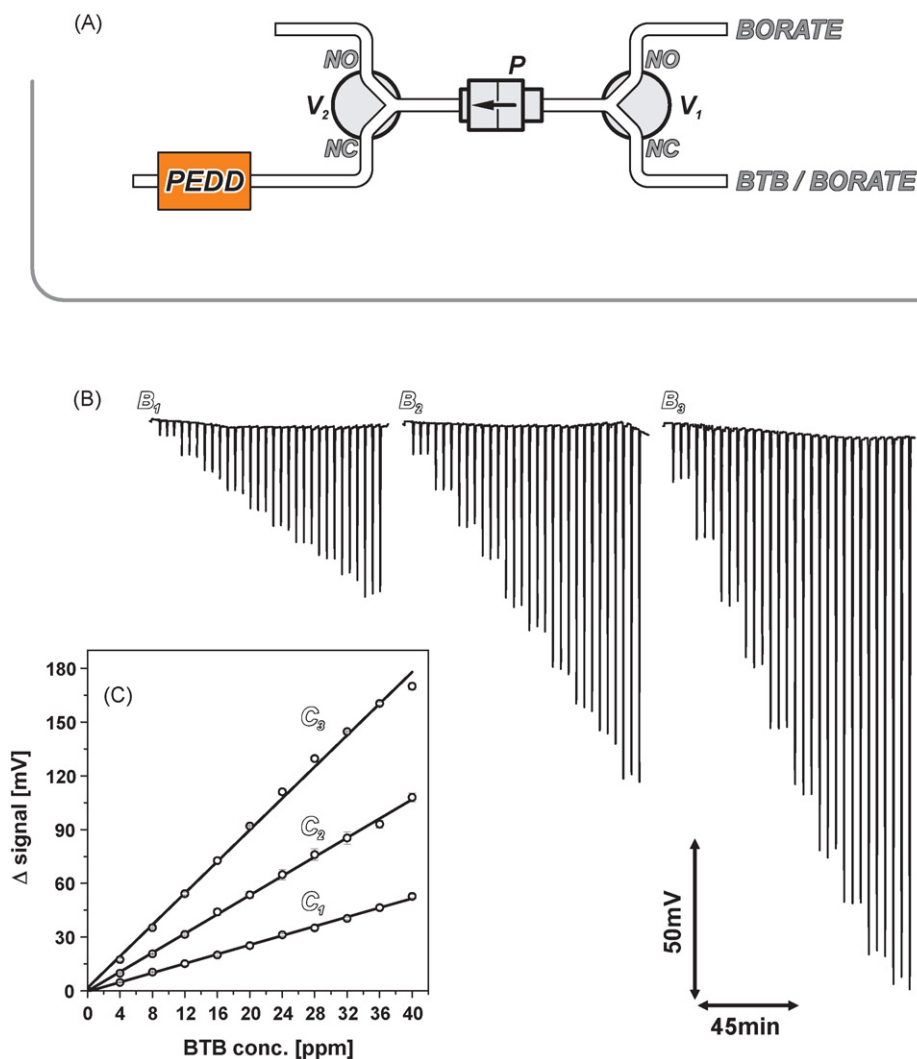
Fig. 3. The scheme of calibration module for FIA (A) consisted of pump (P), two valves (V$_1$ and V$_2$), mixing coil (MC) and detector (PEDD). FIAgrams (B) obtained with the set-up controlled by the program where V$_2$ valve allowed injection of the diluted standard. Injection was performed by opening of V$_2$ for 10 (B$_1$), 20 (B$_2$) or 40 (B$_3$) pulses (equivalents of 160 μL, 320 μL, 640 μL volumes of diluted standard, respectively) Calibration graphs C$_1$–C$_3$ correspond to FIAgrams B$_1$–B$_3$, respectively.

improves homogeneity of consecutive calibrant zones. Another drawback of presented module is closed architecture (detector located between valve and pump), so the build-up of flow system is difficult. Finally, the location of pumping device at the end flow system and the aspiration of stream is less recommended than its propelling, because in some cases it promotes the formation of gas bubbles in flow system.

From the practical point of view, the most promising seems to be the calibration module shown in Fig. 2B. Contrary to similar set-up shown in Fig. 2A, in this module the micropump is located directly at the microvalve. The solenoid devices actuation program is identical as previously (Fig. 2C). Recording of calibration cycle is shown in Fig. 2E. The valve function is the same as in previous set-up, whereas the pump plays a double role: pumps the solution and additionally homogenizes the segment series of calibrant and diluter generated by the operating valve. In other words, the pump additionally fulfils the task of mixing coil. Additional mixing coil causes needless dispersion of homogeneous segments only (recording E$_2$ in Fig. 2E). The set-up with relocated pump is more compact. Moreover, as the pump is located before the detector, the module has open architecture, so its implementation into more sophisticated flow analysis manifolds is simple.

Calibration modules dedicated for the single standard use, depicted in Figs. 1 and 2 Figs. 1A, 2A and 2B, have been developed for continuous flow measurements. They are able to generate the calibration recordings in the common form of step sequence, where each step is a stationary analytical signal for the consecutive concentration of standard. The most effective module (shown in Fig. 2B) can be easily adapted for the needs of flow injection analysis (FIA). For such purposes only one additional solenoid valve is required (Fig. 3A). The role of this valve is to separate a short segment from the stream of diluted standard and direct it to flow-through detector. The architecture of developed module is still compact. It is worth to notice, that the manifold shown in Fig. 3A allows to select the injection volume of generated segment and thus to control the sensitivity and frequency of measurements performed under FIA conditions. Three FIAgrams obtained for three different injection volumes and corresponding calibration graphs are shown in Fig. 3B and C, respectively.

Second valve incorporated into manifold dedicated for FIA measurements not only offers the separation of diluted standard segment and choice of its volume, but also its stopping before the detector independently of module operation. Such possibility is especially attractive for the automation of kinetic methods of anal-
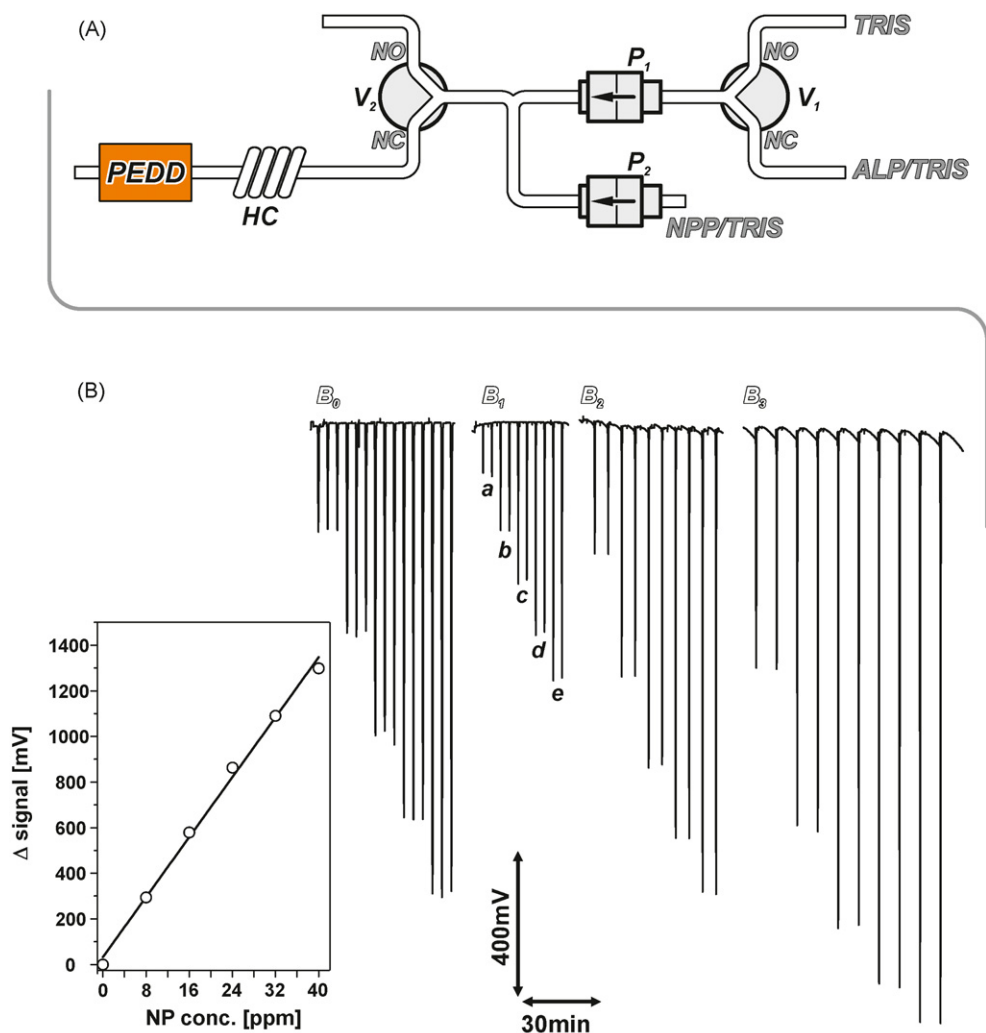
Fig. 4. The scheme of system for kinetic detection of ALP with implemented module for enzyme standard dilution (A) The manifold consists of two pumps (P_1,P_2), two valves (V_1,V_2), holding coil (HC) and detector (PEDD). FIAgrams obtained with the system (B) FIAgram of on-line dilution of NP standard (B_0) and corresponding calibration graph in inset (P_2 was not used; only synchronized operation of V_1 and P_1 was responsible for NP dilution). FIAgrams B_1, B_2, and B_3 for ALP were recorded for 0, 2 and 5 min stopped-flow, respectively. Each automatically diluted ALP standard (a–e) was injected twice.

ysis. For the demonstration of this feature the UV-PEDD dedicated for bioanalytical uses [17] coupled with simple multimeter as signal recorder [16] was mounted into manifold shown in Fig. 3A. This detector enables photometric detection of NP produced in the course of several enzyme reactions. FIAgram for NP and corresponding calibration graph are shown in Fig. 4 (recording B_0 and inset), whereas the manifold dedicated for enzyme activity assays is depicted in Fig. 4A.

The manifold can be applied for the photometric detection of ALP activity. The dilution module of manifold enables on-line dilution of single ALP standard. Second pump delivers the enzyme substrate (NPP). For saving the reagent, the dosing of NPP is synchronized with ALP pumping. Second valve separates defined volume of reaction segment and directs it into detector line. Reaction segment can be stopped before the detector for required reaction time. The stopped-flow mode of measurement allows elongation of this time without significant segment dispersion. Summarizing, the operation of second valve defines the sensitivity of method as well as the flow-throughput of FIA manifold. FIAgrams B_1–B_3 recorded for three different stopped-times are shown in Fig. 4B. In nearly all cases the dilutions of ALP standard are proportional as expected. Only signals for the highest enzyme activities and longest reaction

times (final peaks in recording B_3) are smaller than expected, what can be explained by the depletion of substrate concentration in the reaction segment and thus the slowdown of enzyme reaction rate.

4. Conclusion

Only two microsolenoid devices are sufficient for the construction of FA modules enabling calibration with the use of single standard. The most effective, robust and easily adaptive to more sophisticated FA systems is the module consisted of valve directly connected with pump. Introduction of second valve allows the use of module for FIA measurements. Such module enables the selection of standard injection volume as well as its controlled stopping, what is especially important in bioanalytical systems dedicated for enzyme activity measurements.

Finally, it is worth to notice a wide potential utility of FIA system developed for bioanalytical uses. This manifold with UV-PEDD-based detector for NP detection could be applied for activity measurements of many enzymes catalyzing reactions producing NP, like other phosphoesterases, lipases, α-chymotrypsin, carbonic anhydrase, etc. On the other hand this manifold could be easily adapted for FIA determinations of some enzyme inhibitors,

similarly as it has been recently demonstrated for conventional potentiometric FIA systems [19].

Acknowledgements

References

[1] J.F. Tyson, J.M.H. Appleton, Talanta 31 (1984) 9.
[2] J.F. Tyson, C.E. Adeeyinwo, J.M.H. Appleton, S.R. Bysouth, A.B. Idris, L.L. Sarkissian, Analyst 110 (1985) 487.
[3] P. Koscielniak, Anal. Chim. Acta 438 (2001) 323.
[4] P. Koscielniak, M. Wieczorek, J. Kozak, M. Herman, Anal. Chim. Acta 600 (2007) 6.
[5] A. Baron, M. Guzman, J. Ruzicka, G.D. Christian, Analyst 117 (1992) 1839.
[6] E.A.G. Zagatto, F.J. Krug, H.F. Bergamin, S.S. Jorgensen, B.F. Reis, Anal. Chim. Acta 104 (1979) 279.
[7] B.F. Reis, A.O. Jacintho, J. Mortatti, F.J. Krug, E.A.G. Zagatto, H.F. Bergamin, L.C.R. Passenda, Anal. Chim. Acta 123 (1981) 221.
[8] P. Koscielniak, J. Kozak, Crit. Rev. Anal. Chem. 34 (2004) 25.
[9] R.A.S. Lapa, J.L.F.C. Lima, B.F. Reis, J.L.M. Santos, E.A.G. Zagatto, Anal. Chim. Acta 466 (2002) 125.
[10] J.L.F.C. Lima, J.L.M. Santos, A.C.B. Dias, M.F.T. Ribeiro, E.A.G. Zagatto, Talanta 64 (2004) 1091.
[11] J.L.M. Santos, M.F.T. Ribeiro, A.C.B. Dias, J.L.F.C. Lima, E.A.G. Zagatto, Anal. Chim. Acta 600 (2007) 21.
[12] F.R.P. Rocha, B.F. Reis, E.A.G. Zagatto, J.L.F.C. Lima, R.A.S. Lapa, J.L.M. Santos, Anal. Chim. Acta 468 (2002) 119.
[13] A.F. Lavorante, M.A. Feres, B.F. Reis, Spectrosc. Lett. 39 (2006) 631.
[14] F.R.P. Rocha, C.M.C. Infante, W.R. Melchert, Spectrosc. Lett. 39 (2006) 651.
[15] L. Tymecki, P. Pokrzywnicka, R. Koncki, Analyst 133 (2008) 1501.
[16] L. Tymecki, R. Koncki, Anal. Chim. Acta 639 (2009) 73.
[17] L. Tymecki, L. Brodacka, B. Rozum, R. Koncki, Analyst, DOI:10.1039/B822025E.
[18] http://moskit.uwm.edu.pl/~kalinow/ksp/index.html.
[19] B. Rozum, R. Koncki, Talanta 77 (2008) 507.

DNA hybridization electrochemical biosensor using a functionalized polythiophene

Aysegul Uygun*

Suleyman Demirel University, Faculty of Arts and Science, Department of Chemistry, 32260 Isparta, Turkey

ARTICLE INFO

ABSTRACT

A simple and label-free electrochemical sensor for recognition of the DNA sensor event was prepared by electrochemical polymerization of 4-hydroxyphenyl thiophene-3-carboxylate. Poly(4-hydroxyphenyl thiophene-3-carboxylate) (PHPT) was synthesized electrochemically onto glassy carbon electrode and characterized by cyclic voltammetry, FTIR and AFM measurements. An ODN-probe was physisorbed onto PHPT film and tested on hybridization with complementary ODN segments. A biological recognition can be monitored by comparison with electrochemical signal (cyclic voltammogram) of single and double strand state oligonucleotide. The oxidation current of double strand state oligonucleotide is lower than that of single strand, that is corresponding to the decrease of electroactivity of PHPT with the increase of stiffness of polymer structure. Physisorbed ODN-probe and its hybridization were observed morphologically onto ITO electrodes using AFM. The sensitivity of the electrochemical sensor is 0.02 μA/nmol, detection limit is 1.49 nmol and it has good selectivity.

© 2009 Elsevier B.V. All rights reserved.

1. Introduction

There is a great interest in the development of easy-to-use DNA sensors. Detection of specific DNA sequences is of great importance in numerous applications, such as medical research and clinical diagnosis. Although fluorescent label or surface plasmon resonance was widely used as hybridization transduction systems, these methods may be lengthy and costly [1,2]. Recently, electrochemical gene sensors have attracted increasing attention because of their simplicity, high selectivity and sensitivity. Nanoparticles [3,4], metal complexes [5], enzymes [6] and organic redox indicators [7] have been used for the electrochemical detection of DNA hybridization.

The intrinsically conducting polymers are a relatively new class of polymeric materials and are sensitive to changes in the polymeric chain environment [8–10]. Therefore, they may be used as active substrates that can sensitively report a biological recognition event, such as DNA hybridization [11]. Immobilization of oligonucleotide (ODN) probes onto conducting polymer would be expected to provide a simple and direct way to detect hybridization events, which perturb the electrochemical response of the polymer. Conducting polymers deposited on electrodes provide effective sensors where they provide an interface for entrapment or attachment of DNA probes, and also act as an electronic transducer of obtained signal [12].

The performance of electrochemical biosensors generally depends on the physic-chemical properties of the electrode materials, as well as the sensing element immobilized over the electrode surface [13]. Most of the reported electrochemical biosensors must apply a high positive charge potential on the working electrode, which minimizes the interference effects from reducing species [14].

Among conducting polymers, many functionalized thiophenes have been synthesized in the past due to their favorable properties [15,16]. Bauerle and Emge introduced nucleobase functionalized polythiophenyl derivatives. They observed changes of absorption maximum and the decrease of electrochemical activities as well due to the hydrogen bond formation with complementary [17].

This paper shows the procedure used for the novel synthesis of thiophenyl monomer and electropolymerization, the specificity of the immobilization and ability of the probe ODN physisorbed onto the PHPT compound to be hybridized. The ODN/PHPT film has been characterized using cyclic voltammetry, FTIR spectroscopy and atomic force microscopy (AFM). The advantageous features of this biosensor include a low price, ease preparation, high sensitivity and good selectivity.

2. Experimental

2.1. Materials

3-Thiophenecarboxylic acid, thionyl, hydrokinon, diethylether, sodiumbicarbonate, anhydrous magnesium sulfate and acetonitrile (99.8%, anhydrous) were purchased from Aldrich. Phosphate buffer

* Tel.: +90 246 2114082; fax: +90 246 2371106.
  E-mail address: aysegul@fef.sdu.edu.tr.

(pH 7.4) was obtained from Sigma. An electrochemical grade tetra-butylammonium perchlorate (TBAClO$_4$) was purchased from Fluka. Integrated DNA Technologies (IDT), Inc. synthesized the ODNs including probe NH$_2$-GAT GAG TAT TGA TGC CGA-3′, complementary target 5′-TCG GCA TCA ATA CTC ATC-3′ and noncomplementary 5′-TAT GCT GGT GCG TCG CAC-3′. All aqueous solutions were prepared using Milli-Q water (18.2 MΩ cm).

2.2. Synthesis of 4-hydroxyphenyl thiophene-3-carboxylate (HPT)

A reaction mixture of 3-thiophenecarboxylic acid (7.81 mmol), of thionyl (220.50 mmol) and of hydrokinon (10 mmol) was stirred for 24 h under reflux. Then the reaction mixture was cooled and extracted with diethylether. The combined organic layer was washed with water, sodiumbicarbonate and dried with anhydrous magnesium sulfate. Finally, the solvent was removed by rotary evaporation. 4-Hydroxyphenyl thiophene-3-carboxylate solid was obtained in a 43% yield (M.p. 240 °C) ^{1}H NMR (400 MHz, CDCl$_3$, δ-ppm): 8.32 (m, α-2H, Th), 7.61 (m, β-2H, Th), 7.48 (m, α-2H, Th), 6.67 (m, 2H, aromatic), 6.46 (m, 2H, aromatic), 3.1 (s, 1H, hydroxyl); IR V_{max}^{KBr} cm^{-1}: 3207 (aromatic C–H), 3188, 3170, 3030, 2956, 2922, 2850, 1880, 1517, 1452, 1361, 1246, 1195, 1095, 833 (β-H), 758 (α-H).

2.3. Electropolymerization of HPT, immobilization ODN and detection of hybridization

The electropolymerization was carried out by cyclic voltammetry from 0 to 1.7 V at a scan rate of 50 mV/s using a Gamry 300 Model potentiostat. PHPT was performed onto glassy carbon electrode in acetonitrile solution containing 5 mM monomer and 5 mM TBAClO$_4$ using a three-electrode cell comprising Ag/AgCl reference electrode and using Pt counter electrode. Prior to electropolymerization, glassy carbon electrode was polished with 0.5 μM alumina slurry and then washed with acetone, ethanol, and Milli-Q water.

For the FTIR and experiments, the polymer was electrochemically deposited on an indium tin oxide (ITO)-coated glass electrode. FTIR spectra were recorded on a Perkin Elmer, Spectrum BX II spectrophotometer. The surface topology of the electrodes was characterized using an AFM in contact mode under a constant force (NanoSurf), the roughness was obtained from the 9.8 μm × 9.8 μm scan.

The PHPT/glassy carbon electrode was upturned and 10 μL of ODN-probe (1.35 nmol) was pipetted over the electrode surface and kept at room temperature for 1 h. The resulting ODN probed PHPT/glassy carbon bioelectrode was thoroughly washed with a phosphate buffer solution (PBS) of 7.4 to rinse off any loosely bound ODN-probe from the electrode. The hybridization reaction was carried out by pipetting 10 μL of target ODN (1.49 nmol) in PBS solution (pH 7.4). After hybridization, the electrode was washed with PBS to remove any nonhybridized ODNs. The similar procedure was adopted for both a different molar concentration of target ODN and the mismatched target ODN.

3. Results and discussion

The HPT can be electropolymerized in the electrolyte acetonitrile/TBAClO$_4$ to the corresponding PHPT. A typical polymerization voltammogram is presented in Fig. 1 and an anodic oxidation wave is obtained at 1.2 V vs. Ag/AgCl.

This cycle shows the "nucleation loop" where the scan is reversed on the rising part of the peak, which is typical for a voltammogram of monomers yielding conducting polymer [18]. The color of the polymer changed from brown to dark green-red with increasing film thickness. Unlike alkyl substituted polythiophene [19], the PHPT was not soluble in common organic solvents such as acetonitrile and chloroform.
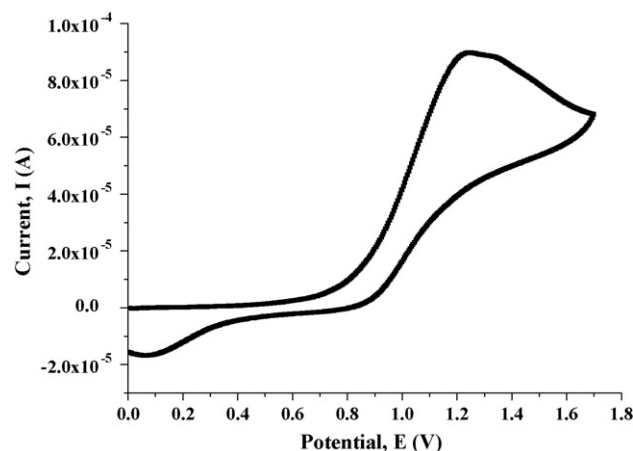
Fig. 1. Electropolymerization cyclic voltammogram of HPT on a glassy carbon electrode at 50 mV/s in 5 mM acetonitrile/TBAClO$_4$.

After repeated scans, the coated electrode was removed from the monomer solution and rinsed with acetonitrile to remove the monomer and oligomeric species. Then, electrode was placed in monomer-free electrolytic solution containing 5 mM TBAClO$_4$ into acetonitrile. The polymer film exhibited a high electroactivity in acetonitrile/TBAClO$_4$ media with an almost reversible oxidation wave at 1.2 V (vs. Ag/AgCl Fig. 2a) and a linear dependence of peak current of CV with scan rate. The anodic (Iac) peak current responses
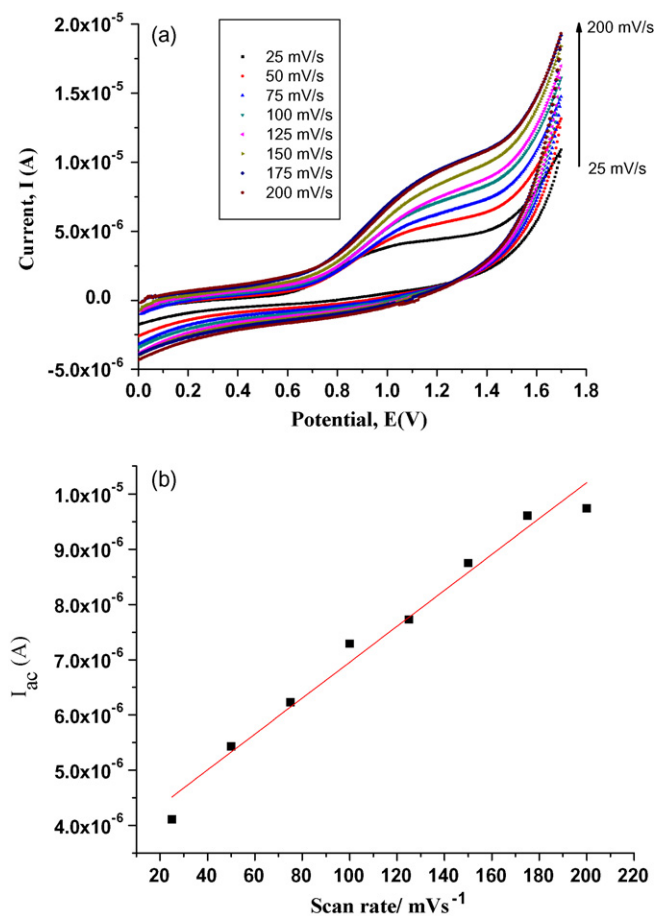
Fig. 2. (a) Cyclic voltammogram of PHPT film in acetonitrile/TBAClO$_4$ with different scan rates between 25 and 200 mV/s and (b) relationship of anodic current peaks as a function of scan rate for PHPT film in acetonitrile/TBAClO$_4$.
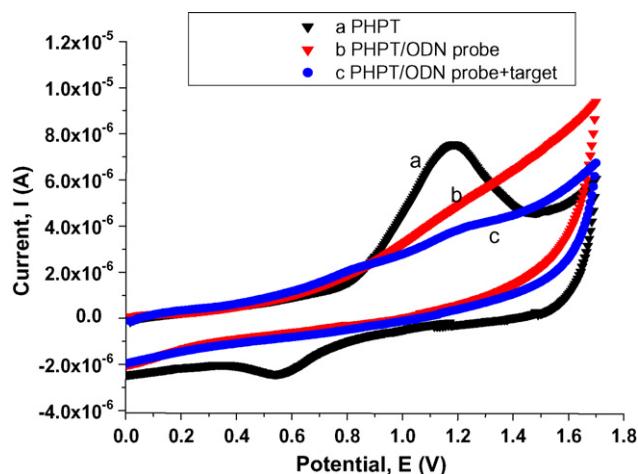
Fig. 3. Cyclic voltammograms of the (a) PHPT, (b) PHPT/ODN and (c) ODN hybridized PHPT/ODN electrodes in acetonitrile/TBAClO$_4$ (scan rate: 50 mV/s).
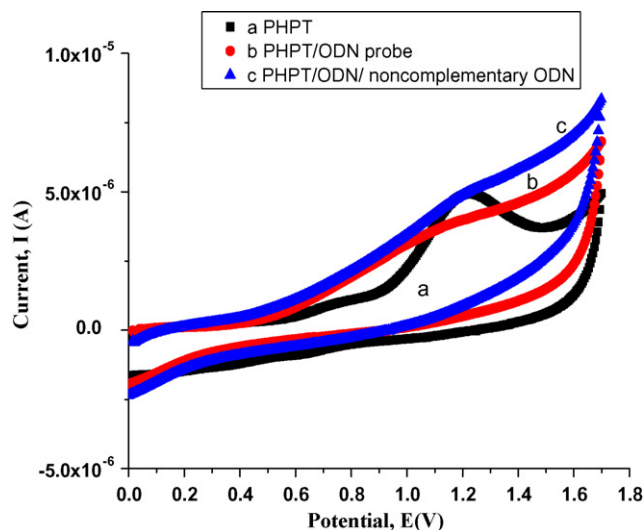

Fig. 5. Cyclic voltammograms of the (a) PHPT, (b) PHPT/ODN-probe and (c) after immobilization of noncomplementary ODN onto PHPT/ODN electrodes in acetonitrile/TBAClO$_4$ (scan rate: 50 mV/s).

were recorded and it was found that anodic current responses increase linearly as the scan rate increases (Fig. 2b). It was clear that the redox process was non-diffusional and the electroactive polymer was well adhered to the working electrode surface [20].

Fig. 3 shows the electrochemical characteristics of bare, ODN-probe immobilized, and ODN target hybridized PHPT/glassy carbon electrodes. The PHPT/glassy carbon electrodes illustrated admirable electrochemical performance. It was observed that the intensities of the oxidation current of ODN-probe and ODN target immobilized electrodes decreased, which could be attributed to prompt redox behavior of probe ODN [21]. The probe ODN and target ODN with hybridization could form a potential barrier of the rotation of polymer backbone and bulky conformational modifications made along the conjugated polymer backbone. The decrease in the peak current measured with the ODN hybridization PHPT/glassy carbon electrode may be related to the electrostatic repulsion between the polyanionic hybridized ODN on the cationic PHPT electrode and the anionic redox couple ions [22,23]. This can be explained by the formation of ODN duplexes that further distort the electronic properties of the polymer backbone and/or a additional increase in the amount of electrostatic changes and thus the repulsion of the oppositely charged redox probe (Fig. 4). Addi-

tionally, the voltammogram of PHPT in the presence of target ODN indicated a shift in the peak position.

The selectivity of the biosensor was investigated by the hybridization of the probe ODN immobilized PHPT/glassy carbon bioelectrode with noncomplementary ODN sequences. After incubation with noncomplementary ODN sequences, the bioelectrode indicated increasement in the oxidation current at 1.2 V, indicating that the biosensor had good selectivity only for the target ODN (Fig. 5). Also, one can see that the oxidization current of the bioelectrode that was incubated in the solution of noncomplementary ODN does not differ significantly from initially obtained than that of PHPT/glassy carbon electrode.

To investigate sensitivity of the sensor, different amounts of target ODN varying 1.49 and 7.45 nmol were incubated with electrochemical sensors. Fig. 6 exhibits cyclic voltammograms of PHPT/ODN bioelectrode with increasing target ODN concentration and the variation of oxidation peak current as a function of the amount of target ODN physisorbed onto PHPT film using cyclic voltammetry technique. It was found that the peak oxidation current observed at about 1.2 V decreased with an increasing concentration of the target ODN. This result indicates that binding

Fig. 4. Schematic presentation of the fabrication of PHPT/ODN bioelectrode.
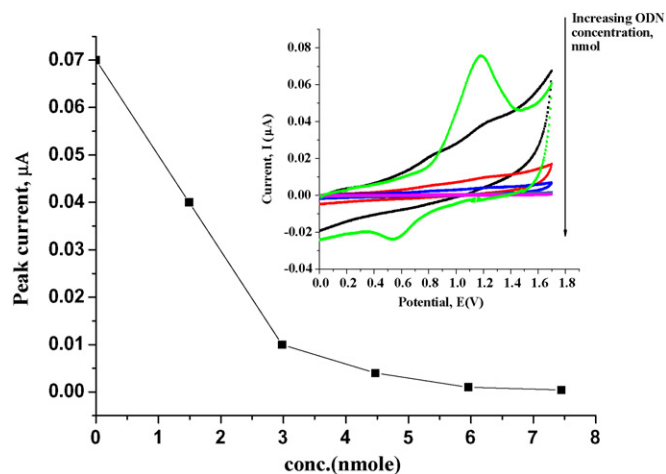
Fig. 6. Variation of electrode current at constant potential $E = 1.2$ V, as a function of concentration of target ODN (inset: cyclic voltammograms of PHPT/ODN bioelectrode with increasing target ODN concentration, mmol).

(a)

(b)

(c)
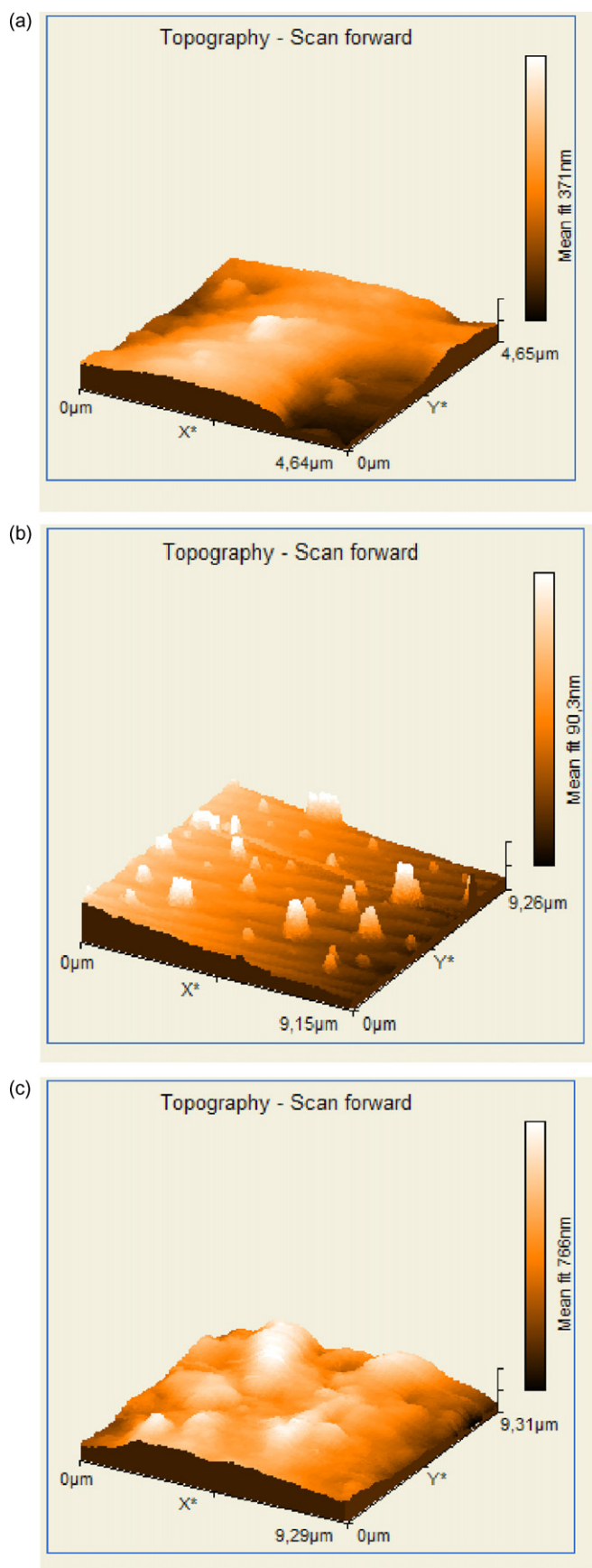
Fig. 7. AFM micrographs of the (a) PHPT, (b) PHPT/ODN-probe and (c) ODN hybridized PHPT/ODN electrodes onto ITO.
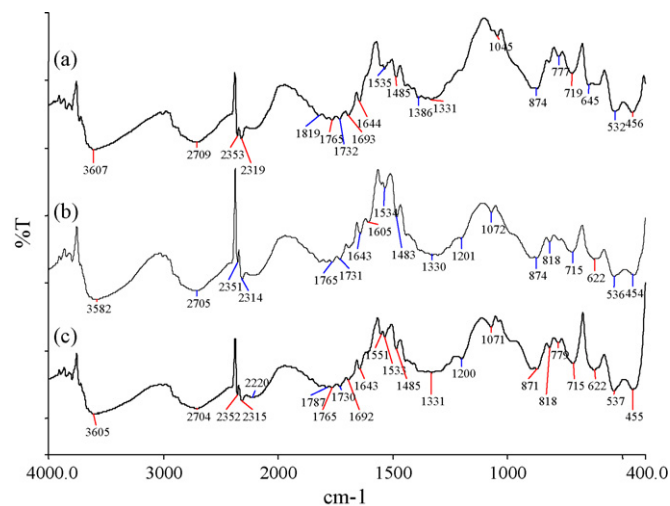
Fig. 8. FTIR spectra of the (a) PHPT (b) PHPT/ODN-probe and (c) ODN hybridized PHPT/ODN electrodes onto ITO.

of probe ODN with the target ODN at the probe PHPT/ODN electrode surface had occurred. From Fig. 6, the sensitivity of electrochemical sensor was evaluated 0.02 μA/nmol from the slope at the origin of this curve. The detection limit for the system is 1.49 nmol of ODN in solution. Compared to the detection limit of 10 nmol by Park et al. [24], 1 and 0.5 nmol by Peng et al. [25], 1 nmol by Cha et al. [20] and 2 nmol by Garnier et al. [26], the value of 1.49 nmol by ours appears promising for application.

Fig. 7a–c shows the AFM pictures obtained for bare PHPT/ITO electrode, after immobilization of probe ODN in the case of PHPT/ITO and after the hybridization of the target ODN in the case of probe ODN/PHPT/ITO electrodes, respectively. It may be noted that the roughness in PHPT/ITO surface is due to the immobilization of ODN-probe. The network structure of bioelectrode seen in Fig. 7c arises due to the hybridization of the target ODN to electrode resulting in the rougher topography of the polymeric surface [27].

Fig. 8a–c shows FTIR spectra of PHPT, ODN/PHPT and the ODN hybridized PHPT/ODN films coated onto ITO electrodes. In the spectrum of pure PHPT (Fig. 8a), the bands between 1500 and 1300 cm^{-1} originated from the stretching modes of C=C and C–C in the thiophene ring [28]. The bands at 1066 and 1045 cm^{-1} are assigned to stretching of the C–O–C bonds of PHPT. Vibrations from the C–S bond in the thiophene ring of PHPT are shown at 893 and 871 cm^{-1} [29,30]. The peaks at 1692, 1644 and 1534 cm^{-1} are assigned to the stretching and bending modes of benzene ring in the structure of PHPT. A strong absorption peak at 1732 cm^{-1} is characteristic of the stretching vibration of the carbonyl group of PHPT. FTIR spectrum of the ODN/PHPT and the ODN hybridized PHPT/ODN (Fig. 8b and c) showed additional peaks at 1602, 1200, 1072 and 982 cm^{-1} due to the attachment of ODN-probe and ODN target with PHPT polymer [31].

4. Conclusions

In this work, novel functionalized thiophene monomer was synthesized and characterized by FTIR, CV and AFM measurements. It was shown that ODN can be physisorbed onto electrochemically deposited PHPT film onto glassy carbon and ITO electrodes. The PHPT/ODN bioelectrode was employed for the hybridization of the target ODN, with detection limit of 1.49 nmol and showed good sensitivity and selectivity. The sensitivity of the biosensor was 0.0059 μA/nmol. The PHPT bioelectrode is advantageous of low price, ease of preparation without using any grafting agent, good

sensitivity and selectivity. Our further improvement in sensitivity and selectivity will be to prepare nanocomposites of PHPT.

References

[1] J.R. Epstein, I. Biran, D.R. Walt, Anal. Chim. Acta 469 (2002) 3.
[2] E.K. Wilson, 1998 Instant DNA detection C&EN25, 47.
[3] J. Wang, Anal. Chim. Acta 500 (2003) 247.
[4] H. Cai, Y. Wang, P. He, Y. Fang, Anal. Chim. Acta 469 (2002) 165.
[5] S. Takenaka, K. Yamashita, M. Takagi, Y. Uto, H. Kondo, Anal. Chem. 72 (2000) 1334.
[6] K. Hashimoto, K. Ito, Y. Ishimori, Anal. Chem. 66 (1994) 3830.
[7] G. Carpini, F. Lucarelli, G. Marrazza, M. Mascini, Biosens. Bioelectron. 20 (2004) 167.
[8] M. Gerard, A. Chaubey, B.D. Malhotra, Biosens. Bioelectron. 17 (2002) 345.
[9] A. Tiwari, S. Gong, Electroanalysis 20 (19) (2008) 2119–2126.
[10] A. Tiwari, S. Gong, Electroanalysis 10 (16) (2008) 1775–1781.
[11] E. Katz, I. Willner, Electroanalysis 15 (2003) 913.
[12] S. Reisberg, B. Piro, V. Nobel, M.C. Pham, Bioelectrochemistry 69 (2006) 172.
[13] M. Yang, Y. Yang, H. Yang, G. Shen, R. Yu, Biomaterials 27 (2006) 246.
[14] S.J. Updike, G.P. Hicks, Nature 214 (1967) 986.
[15] B. Fang, S. Jiao, M. Li, X. Jiang, Biosens. Bioelectron. 23 (7) (2008) 1175.
[16] L. Zhang, H. Sun, D. Li, S. Song, C. Fan, S. Wang, Macromol. Rapid Commun. 29 (17) (2008) 1489.
[17] P. Bauerle, A. Emge, Adv. Mater. 3 (1998) 3.
[18] A.J. Downard, D. Pletcherz, J. Electroanal. Chem. Interf. Electrochem. 206 (1986) 147.
[19] K. Buga, R. Pokrop, A. Majkowska, M. Zagorska, J. Planes, F. Genoud, J Mater. Chem. 16 (2006) 2150.
[20] J. Cha, J.I. Han, Y. g Choi, D.S. Yoon, K.W. Oh, G. Lim, Biosens. Bioelectron. 18 (2003) 1241.
[21] C.M.H. Yaua, H.L. Chana, S.F. Suib, M. Yang, Thin Solid Films 413 (2002) 218.
[22] I.O.K. Owino, A.O. Sadik, Electroanalysis 17 (2005) 2101.
[23] J.T. Sejdic, H. Peng, P.A. Kilmartin, M.B. Cannell, G.A. Bowmaker, R.P. Cooney, C. Soeller, Synth. Met. 152 (2005) 37.
[24] S.-J. Park, T.A. Taton, C.A. Mirkin, Science 295 (2002) 1503.
[25] H. Peng, C. Soeller, J. Sejdic, Macromolecules 40 (2007) 909.
[26] F. Garnier, B. Bouabdallaoi, P. Srivastava, B. Mandrand, C. Chaix, Sens. Actuators B: Chem. B 123 (1) (2007) 13.
[27] K. Arora, A. Chaubey, R. Singhal, R.P. Singh, M.K. Pandey, S.B. Samanta, B.D. Malhotra, S. Chad, Biosens. Bioelectron. 21 (2006) 1777.
[28] K.I. Seo, I.J. Chung, Polymer 41 (2000) 4491.
[29] G. Inzelt, M. Pineri, J.W. Schultze, M.A. Vorotyntsev, Electrochim. Acta 45 (2000) 2403.
[30] A. Gok, M. Omastova, A.G. Yavuz, Synth. Met. 157 (1) (2007) 23.
[31] A. Tiwari, S. Gong, Talanta 77 (2009) 1217.

Determination of free captopril in human plasma by liquid chromatography with mass spectrometry detection

Szende Vancea [a,*], Silvia Imre [a], Gabriella Donáth-Nagy [a], Tőkés Béla [a], Mária Nyulas [b], Teofil Muntean [b], Réka Borka-Balás [b]

[a] Faculty of Pharmacy, University of Medicine and Pharmacy, Gheorghe Marinescu 38, RO-540139, Târgu Mureş, Romania
[b] Analytical Laboratory PharmaQuest LTD., Râtul Morii 1295, RO-547530, Sângeorgiu de Mureş, Romania

ARTICLE INFO

ABSTRACT

A new simple, sensitive and selective liquid chromatography coupled with mass spectrometry (LC/MS) method for quantification of captopril after precolumn derivatization with p-bromo-phenacyl-bromide in human plasma was validated. Plasma samples were analysed on a monolithic column (Cromolith Performance-RP 18e, 100 mm × 4.6 mm I.D., 3 μm) under isocratic conditions using a mobile phase of a 40:60 (v/v) mixture of acetonitrile and 0.1% (v/v) formic acid in water. The flow rate was 1 mL/min at the column temperature of 30 °C. In these chromatographic conditions, the retention time was 4.4 min for captopril derivative. The detection of the analyte was in MRM mode using an ion trap mass spectrometer with electrospray positive ionisation. The monitored ions were 216, 253, 255, 268, 270 m/z derived from 415 m/z for derivatized captopril. The sample preparation was very simple and consisted in plasma protein precipitation from 0.2 mL plasma using 0.3 mL methanol after the derivatization reaction was completed. Calibration curves were generated over the range of 10–3000 ng/mL with values for coefficient of correlation greater than 0.993 and by using a weighted ($1/y^2$) quadratic regression. The values for precision (CV %) and accuracy (relative error %) at quantification limit were less than 9.9% and 3.9%, for within- and between-run, respectively. The mean recovery of the analyte was 99%. Derivatized samples demonstrated good short-term, long-term, post-preparative and freeze–thaw stability. This is the first reported LC–MS/MS method for analysis of captopril in human plasma that uses protein precipitation as sample processing procedure. The method is very simple and allows obtaining a very good recovery of the analyte. The validated LC–MS/MS method has been applied to a pharmacokinetic study of 50 mg captopril tablets on healthy volunteers.

© 2009 Elsevier B.V. All rights reserved.

1. Introduction

Captopril (CAP) (2S)-1-[(2S)-2-methyl-3-sulphanylpropanoyl] pyrrolidine-2-carboxylic acid, is a highly specific, competitive inhibitor of angiotensin-I converting enzyme (ACE inhibitors). The beneficial effects of ACE inhibitors appear to result primarily from the suppression of the plasma renin–angiotensin–aldosterone system. Captopril is an orally active agent that does not require biotransformation for activity. The average minimal absorption is approximately 75%. Peak plasma concentrations are reached within 60–90 min. The presence of food in the gastrointestinal tract reduces absorption by about 30–40%. Approximately 25–30% of the circulating drug is bound to plasma proteins. The apparent elimination half-life of unchanged captopril in blood is about 2 h, more of 95% of the absorbed dose being eliminated in the urine within 24 h, 40–50% is unchanged drug and the remainder are inactive disulphide metabolites (captopril disulphide and captopril cysteine disulphide) [1].

Captopril contains a sulphydryl group and forms disulphides and endogeneous thiol-containing compounds (cysteine, glutathione), as well as disulphide dimmer of parent compound [2]. The analysis of aliphatic thiols of biological importance such as natural products involved in metabolic processes (cysteine and reduced glutathione) and thiol drugs (acetylcysteine, captopril, etc.) often presents difficulties largely due to the absence of strong chromophores and fluorophores and their instability [3].

Therefore, the measurement of free or unchanged captopril concentration needs to be preceded by chemical stabilizer addition and molecule derivatization of biological samples in order to prevent captopril disulphide formation [2]. Stabilizer agents often used like N-(1-pyrenyl)maleimide (NPM) [2], p-bromo-phenacyl bromide (p-BPB) [2,4,5], monobrombimane [6,7], 2-bromo 2-acetonaphtone [8], o-phthaldialdehyde (OPA) [7,9], 1-benzyl-2-chloropyridinium bromide (BCPB) [10–12], ethacrynic

acid [3], 1,1′-[ethenylidene bis sulphonyl]bis-benzene [13], etc. are suitable to the applied (fluorescence or UV) detection methods.

Other methods involve a reduction of the disulphide bonds with agents such dithiothreitol (DTT) [2,14,15] and other chemical stabilizers to revert the converted disulphides dimmer (or conjugates) into captopril, as well as to prevent the formation of the disulphides dimmers during the sample preparation and analysis, in order to enable the determination of the total captopril content in biological samples.

Several methods for determination of free or total captopril concentration in human plasma have been reported. LC-based methods with UV detection have been employed for determination of captopril [3–5,8–13], and some LC methods with fluorescence detection have been described [6,7], but usually liquid–liquid or solid-phase extraction is necessary in order to concentrate or sample clean-up in both cases, these sample treatments supposing a time consuming work.

LC/MS has been widely accepted as the main tool in the identification, structure characterization and quantitative analysis of drugs and its metabolites owing to its superior sensitivity, specificity and efficiency. The analysis must be carried out in complex biological matrices and therefore efficient sample preparation and liquid chromatography are often required to achieve good specificity of the analysis. LC/MS grows in popularity, despite the equipment costs, and in the case of captopril determination in plasma there are only a few published articles [2,14,15] and in all cases the sample clean-up and concentration by liquid–liquid or solid-phase extraction were applied.

In the present study, we attempted to develop a fast LC–MS/MS method able to quantify free captopril in human plasma after oral administration of a single dose of 100 mg captopril by applying a simple protein precipitation. Despite the sensitivity of the LC–MS/MS method, prior derivatization is needed in order to prevent captopril disulphide formation during sample processing and storage. Finally, the developed and validated method was used for bioequivalence investigation of two oral medicinal products containing 50 mg captopril.

2. Experimental

2.1. Reagents

Captopril was a European Pharmacopoeia certified reference standard, the derivatization reagent (RD), p-bromophenacyl bromide (p-BPB) was from Fluka, Luckenwalde, Germany (purity ≥ 99%). Acetonitrile, methanol, formic acid were Merck products (Merck KgaA, Darmstadt, Germany). Ultrapure, deionised water was produced by a Millipore Simplicity (Millipore SA, Molsheim, France) water system. The human blank plasma was supplied from healthy volunteers.

2.2. Standard solutions

Two stock solutions of captopril and p-BPB, respectively, with concentration of 1 mg/mL were prepared by dissolving appropriate quantities of reference substances (weighed on an analytical balance from Radwag) in 10 mL ultrapure water, respectively, 10 mL methanol. Ten calibration working solutions of 0.06–18 μg/mL captopril were then obtained by diluting specific volumes of stock solutions with ultrapure water. Then these were used to spike 0.16 mL blank plasma, providing finally 10 plasma standards with the concentrations ranged between 10 and 3000 ng/mL. Accuracy and precision of the method were verified using plasma standards with concentrations of 30, 1500 and 2500 ng/mL. Quality control (QC) samples with the same concentrations 30 ng/mL (QCA), 1500 ng/mL (QCB) and 2500 ng/mL (QCC) analyte were used during clinical samples analysis.

2.3. Chromatographic and mass spectrometry systems and conditions

The LC system was an 1200 series model (Agilent Technologies) consisted of a binary pump, an in-line degasser, an autosampler, a column thermostat, and an 1100 series model Ion Trap SL mass spectrometer detector (Agilent Technologies). Chromatograms were processed using QuantAnalysis software.

The detection of the analyte was in the multiple reaction monitoring mode (MRM) using an electrospray positive ionisation (ESI positive). The monitored ions were m/z 216, 253, 255, 268, 270 m/z derived from 415 m/z for derivatized captopril. Other detector parameters: dry temperature 350 °C, nebulizer 60 psi, dry gas–nitrogen at 12 L/min.

Chromatographic separation was performed at 30 °C on a Cromolith Performance-RP 18e, 100 mm × 4.6 mm, 3 μm column (Merck), protected by an in-line filter.

2.4. Mobile phase

The mobile phase consisted of a mixture of water containing 0.1% formic acid and acetonitrile (60:40, v/v), each component being degassed, before elution, for 10 min in a Clifton 64426 ultrasonic bath. The pump delivered the mobile phase at 1 mL/min.

2.5. Sample preparation

Standard and test plasma samples were prepared as follows in order to be chromatographically analyzed. In an Eppendorf tube 0.2 mL plasma with 40 μL RD solution was vortex-mixed for 30 s. After 30 min, while the derivatization reaction being completed (Fig. 1), the tube was shaken again for 30 s with 0.3 mL methanol, and then centrifuged for 10 min at 14,000 rpm. The supernatant was
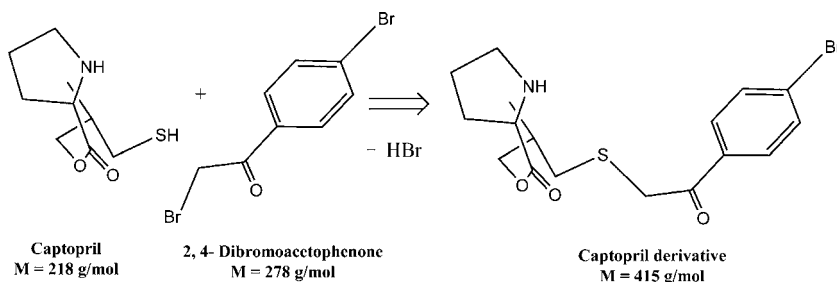

Fig. 1. Derivatization reaction of captopril.

transferred in an autosampler vial and 20 μL were injected into the LC–MS system.

2.6. Validation

As a first step of method validation [16–18], specificity was verified using eight different plasma blanks (normal, hyperlipemic and hemolyzed) obtained from healthy human volunteers who had not previously taken any medication.

The concentration of analytes was determined automatically by the instrument data system using the external standard method. Calibration was performed using singlicate calibration standards on five different occasions. The calibration curve model was determined by the least squares analysis. The applied calibration model was a quadratic one: $y = ax^2 + bx + c$, weight $1/y^2$, where y-peak area and x-concentration. Distribution of the residuals (% difference of the back-calculated concentration from the nominal concentration) was investigated. The calibration model was accepted, if the resid-

Fig. 2. Chromatograms of a blank (a), the LLOQ plasma standard with 10 ng/mL captopril (b) and a calibration standard – STD$_3$ (c).

uals were within ±20% at the lower limit of quantification (LLOQ) and within ±15% at all other calibration levels and at least 2/3 of the standards met this criterion, including highest and lowest calibration levels.

The lower limit of quantification was established as the lowest calibration standard with an accuracy and precision less than 20%.

The within- and between-run precision (expressed as coefficient of variation, CV%) and accuracy (expressed as relative difference between obtained and theoretical concentration, Bias%) of the assay procedure were determined by analysis on the same day of five different samples at each of the lower (30 ng/mL), medium (1500 ng/mL), and higher (2500 ng/mL) levels of the considered concentration range and one different sample of each on five different occasions, respectively.

The relative recoveries at each of the previously three levels of concentration and limit of quantification were measured by comparing the response of the treated plasma standards with the response of standards in solution with the same concentration of analytes as the prepared plasma sample.

The stability of the analytes in human plasma was investigated in four ways, in order to characterize each operation during the process of bioequivalence studies: room-temperature stability (RTS), post-preparative stability (PPS) in the autosampler, freeze–thaw stability (FTS) and long-term stability (LTS) below −20 °C. For all stability studies, plasma standards at each of the lower (30 ng/mL), medium (1500 ng/mL), and higher (2500 ng/mL) levels were used. Five plasma standards at each of the three levels were prepared and let at room temperature 2 h before processing (RTS study). Other five pairs were prepared, immediately processed and stored in the thermostated autosampler (15 °C) (PPS study). The samples were injected after 20 h, the expected longest storage times of the samples in autosampler before injection. For the FTS, aliquots at the same low, medium and high concentrations were prepared. These samples were subjected to three cycles of freeze–thaw operations in three consecutive days. After the third cycle the samples were analyzed against calibration curve of the day. The mean concentration calculated for the samples subjected to the cycles and the nominal ones were compared. For long-term stability (LTS), in the first validation day, there were injected and analyzed five samples at each of low, medium and high concentrations, and values were calculated against calibration curve of the day. Other two sets with the same plasma concentrations were stored in freezer below −20 °C and analyzed together with calibration samples after 3 weeks. The values were calculated against calibration curve of the day and the mean values for the stored samples and nominal concentrations were compared. The requirement for stable analytes was that the difference between mean concentrations of the tested samples in various conditions and nominal concentrations had to be in ±15% range.

The ability to dilute samples with concentrations above the upper limit of quantification was also investigated. Plasma standards ($n = 5$) with 5000 ng/mL captopril were six times diluted with plasma then processed and analyzed. The mean found concentration was compared with the nominal value. The accuracy and precision had to be within ±15% range.

2.7. Clinical application and in-study validation

The validated method was applied in a bioequivalence study of two dosage forms – tablets containing 50 mg captopril. The collecting times were 0, 0.33, 0.67, 1, 1.5, 2, 2.5, 3, 4, 5, 6, 8, 10, 12 h after oral administration of $2\times$ 50 mg = 100 mg captopril. The accuracy and precision of the validated method were monitored to ensure that it continued to perform satisfactorily during analysis of volunteer samples. To achieve this objective, a number of QC samples prepared in duplicate at three concentration levels were analyzed
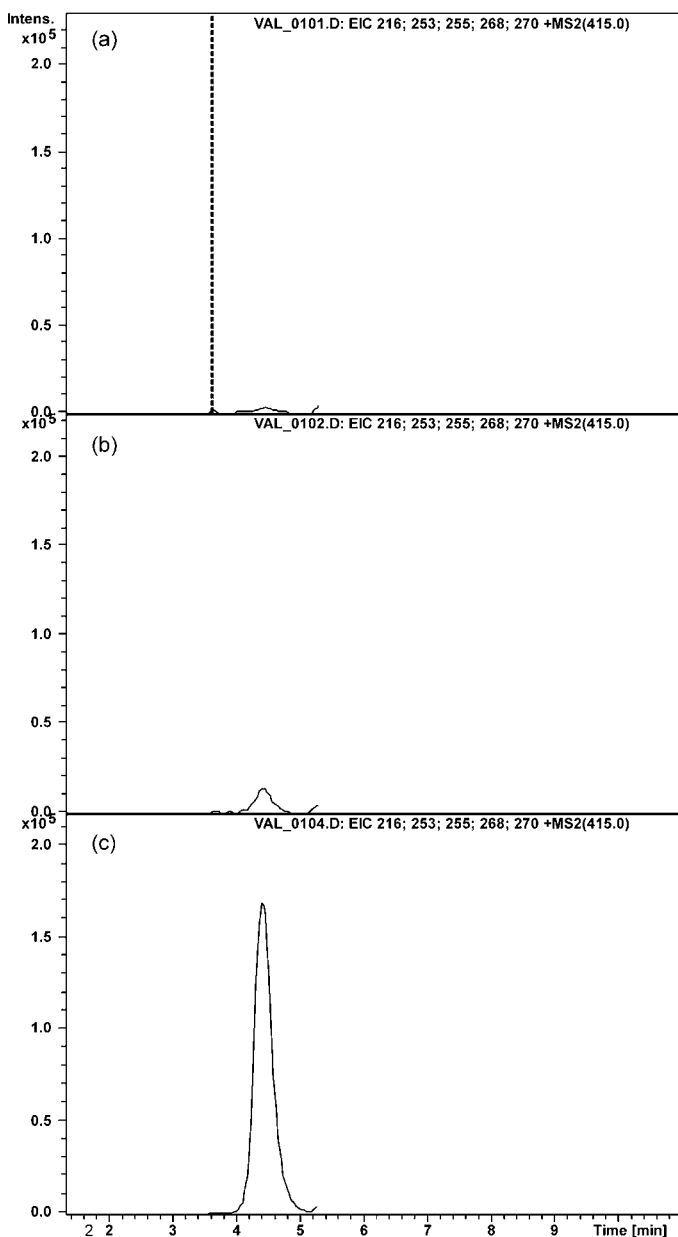
Table 1
Within-run accuracy and precision results.

Level	LLOQ		QCA		QCB		QCC	
Replicate	10 (ng/mL)	%nominal	30 (ng/mL)	%nominal	1500 (ng/mL)	%nominal	2500 (ng/mL)	%nominal
1	8.20	82.0	29.8	99.3	1336	89.0	2478	99.1
2	8.10	81.0	27.5	91.7	1339	89.3	2428	97.1
3	9.50	95.0	29.9	99.7	1242	82.8	2341	93.6
4	9.40	94.0	30.0	100.0	1284	85.6	2371	94.9
5	9.20	92.0	28.9	96.3	1232	82.3	2450	98.0
6	9.10	91.0	–	–	–	–	–	–
7	7.50	75.0	–	–	–	–	–	–
8	7.40	74.0	–	–	–	–	–	–
Mean	8.55		29.2		1287		2414	
S.D.		0.85		1.1		50		56
Accuracy	85.5		97.4		85.8		96.6	
%R.S.D.		10		3.6		3.9		2.3

Table 2
Between-run accuracy and precision results.

Level	LLOQ		QCA		QCB		QCC	
Replicate	10 (ng/mL)	%nominal	30 (ng/mL)	%nominal	1500 (ng/mL)	%nominal	2500 (ng/mL)	%nominal
1	10.0	99.7	29.2	97.4	1287	85.8	2414	96.5
2	10.0	100.0	31.7	105.7	1418	94.6	2575	103.0
3	10.7	106.6	29.3	97.7	1607	107.2	2578	103.1
4	10.7	106.7	28.0	93.3	1359	90.6	2598	103.9
5	9.9	99.4	30.1	100.5	1546	103.1	2706	108.2
Mean	10.3		29.7		1443		2574	
S.D.		0.4		1.4		132		104
Accuracy	102.6		98.9		96.2		102.9	
%R.S.D.		3.9		4.6		9.1		4.1

in each assay run and the results compared with the corresponding calibration curve. At least 67% (four out of six) of the QC samples should be within 15% of their respective nominal values; 33% of the QC samples (not all replicates at the same concentration) can be outside ±15% of the nominal value.

3. Results and discussion

No significant interference at the retention time of captopril (4.4 min) was observed in different plasma blank samples chromatograms due to the specificity of selected signals (Fig. 2).

The analyte carryover was verified using a blank injection made right after an injection of the most elevated level of concentration from calibration curve. No interference at retention time of analyte due to carryover was observed.

The applied calibration curve model proved to be accurate over the concentration range 10–3000 ng/mL for captopril, with a correlation coefficient greater than 0.993. The mean calibration curve,

$y = a\,(\pm\text{S.D.})\,x^2 + b\,(\pm\text{S.D.})\,x + c\,(\pm\text{S.D.})$ with S.D. standard deviation, was $y = -3.571\,(\pm0.486)\,x^2 + 61{,}007\,(\pm5044)\,x - 294{,}603\,(\pm65{,}474)$, $n = 10$ calibration points, $n = 5$ determinations for each calibration point. The residuals had no tendency of variation with concentration.

The method had within- and between-run accuracy and precision (Tables 1 and 2), in agreement to international regulations regarding bioanalytical methods validation [16–18]. The lower limit of quantification was established at 10 ng/mL captopril, respectively, with accuracy and precision less than 20% (Tables 1 and 2).

The recovery was consistent and repeatable (Table 3).

The analytes proved their stability under various conditions (Table 4), the Bias% of found concentration being less than 15%, the maximum accepted value for method's accuracy.

The sample dilution could be made with accuracy within ±9.4% range and precision less than 9.4%, both for within- and between-assay.

Table 3
Recovery results.

Nominal	30 (ng/mL)	1500 (ng/mL)	2500 (ng/mL)
Replicate	Rec A	Rec B	Rec C
1	2,216	55,160	102,455
2	2,077	58,102	94,672
3	1,930	67,246	101,770
4	1,896	72,388	82,419
5	2,075	69,841	91,767
Mean	2,039	64,547	94,617
QC	1,404	71,820	113,389
Rec. mean%		99.9	

Table 4
Results of the stability studies ($n = 4$).

$c_{nominal}$, ng/mL CAP	RTS			PPS			FTS			LTS		
	30	1500	2500	30	1500	2500	30	1500	2500	30	200	400
Bias%	17.01	−8.57	−11.27	−7.82	−3.56	−2.31	22.55	−0.03	17.55	−20.51	−0.64	16.00

RTS—room-temperature stability (23 °C, 2 h), PPS—post-preparative stability (15 °C, 20 h), FTS—freeze–thaw stability (3 freeze–thaw cycles), LTS—long-term stability (−20 °C, 3 weeks).

The validated method was verified during analysis of clinical samples from a bioequivalence study of two medicines containing 50 mg captopril. Fig. 3 shows typical chromatograms of the plasma samples from a volunteer and Fig. 4 shows a concentration profile of captopril obtained for a volunteer after oral administration of 100 mg captopril.
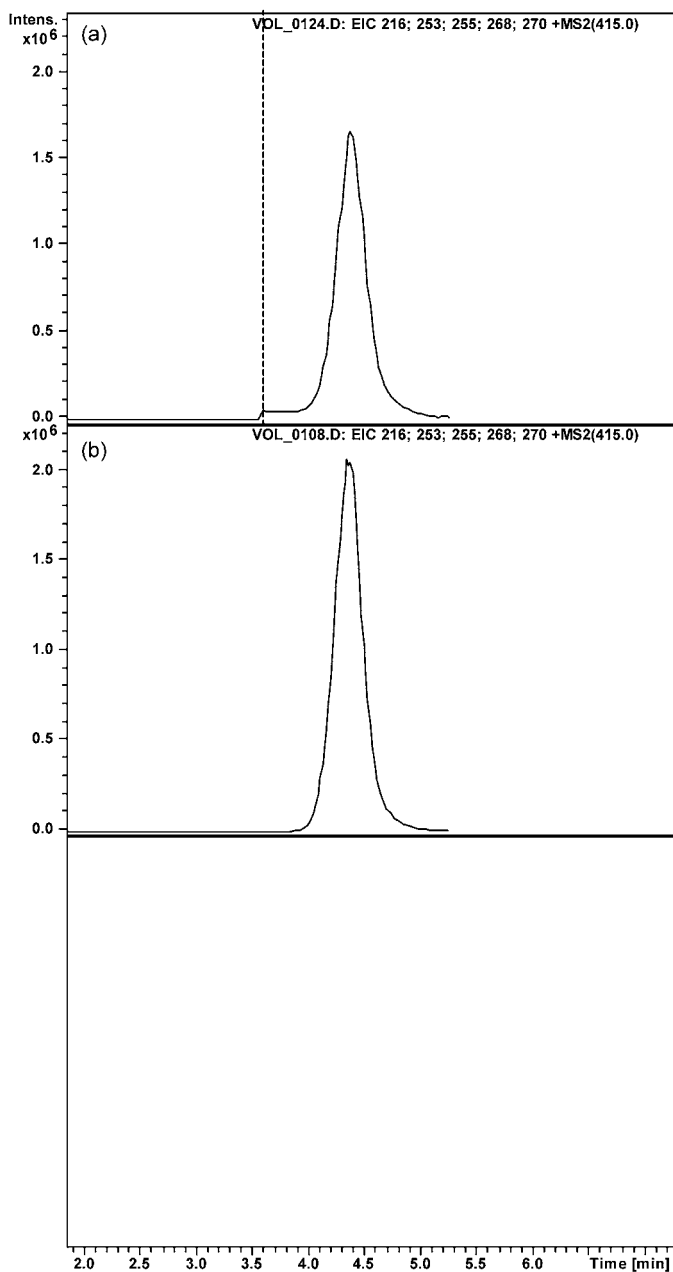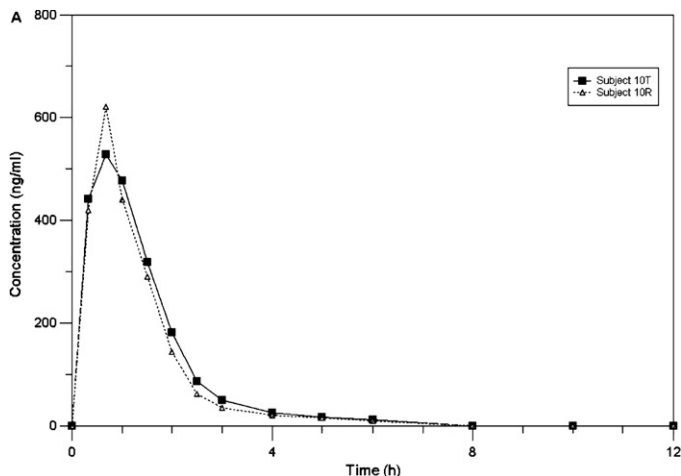
Fig. 4. Concentration profiles of captopril test (■) and reference (△) products after oral administration of 100 mg captopril – Subject 10.

The method continued to perform in terms of accuracy, in each analytical run not more than two out of six QC samples being outside of ±15% nominal value, but not all two at the same concentration.

In comparison with previously published LC–MS methods, the sensitivity of the proposed method (LLOQ 10 ng/mL) is equal as those in which liquid–liquid or solid-phase extraction was applied. But the main advantage is the sample preparation by protein precipitation and besides its simplicity, that sample treatment allows obtaining a good recovery of the analyte.

The method was successfully applied to accurately measure free captopril concentration on a large number of human plasma samples from a bioequivalence study.

4. Conclusions

The proposed method provides accuracy and precision for quantitative determination of free captopril in human plasma after oral administration of 100 mg captopril. The simple sample preparation by protein precipitation, while using less organic solvent with small amounts of sample plasma volume; the relatively short run time and the selected signals for monitoring allowed a specific and efficient analysis of plasma samples, making the method more productive and thus more cost effective. As far as we are aware, this is the first LC–MS method for captopril quantification in human plasma after protein precipitation. The method is suitable for captopril plasma level monitoring after oral administration of 100 mg captopril.

References

[1] K.L. Duchin, D.N. McKinstry, A.I. Cohen, B.H. Migdalof, Clin. Pharmacokinet. 14 (1988) 241.
[2] K.R. Rezende, I.M. Mundim, L.S. Teixeira, W.C. Souza, D.R. Ramos, C.R.F. Cardoso, I.C. Souza, M.Z. Gratao, K.B. Bellorio, J. Chromatogr. B: Biomed. Sci. Appl. 850 (2007) 59.
[3] V. Cavrini, R. Gatti, A.M. DiPietra, M.A. Raggi, Chromatographia 23 (1987) 680.

Fig. 3. The plasma sample chromatograms obtained from a healthy volunteer at 1.5 h after oral administration of 100 mg captopril (a) a calibration standard – STD$_7$ (b).

[4] A. Jankowski, A. Skorek, K. Krzysko, P.K. Zarzycki, R.J. Ochocka, H. Lamparczyk, J. Pharm. Biomed. Anal. 13 (1995) 655.

[5] T. Huang, Z. He, B. Yang, L. Shao, X. Zheng, G. Duan, J. Pharm. Biomed. Anal. 41 (2006) 644.

[6] F. Tache, A. Farca, A. Medvedovici, V. David, J. Pharm. Biomed. Anal. 28 (2002) 549.

[7] R.J. Kok, J. Visser, F. Moolenaar, D. de Zeeuw, D.K.F. Meijer, J. Chromatogr. B: Biomed. Sci. Appl. 693 (1997) 181.

[8] S.M. Foroutan, A. Zarghi, A.R. Shafaati, A. Khoddam, Arch. Iran. Med. 6 (2003) 44.

[9] M.R. Hadjmohammadi, K. Kamel, F. Khajooeinezhad, J. Iran. Chem. Soc. 5 (2008) 324.

[10] E. Bald, S. Sypniewski, J. Drzewoski, M. Stepien, J. Chromatogr. B: Biomed. Sci. Appl. 681 (1996) 283.

[11] E. Bald, S. Sypniewski, Fresenius J. Anal. Chem. 358 (1997) 554.

[12] S. Sypniewski, E. Bald, J. Chromatogr. A 729 (1996) 335.

[13] V. Cavrini, R. Gotti, V. Andrisano, R. Gatti, Chromatographia 42 (1996) 515.

[14] N.C.C. Borges, M.A.G. Heleno, R.A. Moreno, Revista Brasileira de Medicina 63 (2006) 518.

[15] I.I. Salem, W.A. Saif, Y. Jmeian, J.I.A. Tamimi, J. Pharm. Biomed. Anal. 37 (2005) 1073.

[16] The European Agency for the Evaluation of Medicinal Products, Note for Guidance on the Investigation of Bioavailability and Bioequivalence, CPMP/EWP/QWP/1401/98, July 2001, London, UK, http://www.emea.europa.eu/pdfs/human/qwp/140198enfin.pdf.

[17] U. S. Department of Health and Human Services, Food and Drug Administration, Center for Drug Evaluation and Research. Guidance for Industry. Bioavailability and Bioequivalence studies for orally administered drug products – general considerations, March 2003, Rockville, USA, http://www.fda.gov/cder/guidance/5356fnl.pdf.

[18] U.S. Department of Health and Human Services, Food and Drug Administration, Guidance for Industry–Bioanalytical Method Validation, May 2001, http://www.fda.gov/cder/guidance/4252fnl.pdf.

Copolypeptide-doped polyaniline nanofibers for electrochemical detection of ultratrace trinitrotoluene

Feng Wang [a,b], Wenbo Wang [a,b], Bianhua Liu [a], Zhenyang Wang [a], Zhongping Zhang [a,*]

[a] Key Laboratory of Biomimetic Sensing & Advanced Robot Technology, Institute of Intelligent Machines, Chinese Academy of Sciences, Hefei, Anhui 230031, China
[b] Department of Chemistry, University of Science & Technology of China, Hefei, Anhui 230026, China

ARTICLE INFO

ABSTRACT

This paper demonstrates a new electrochemical method for the detection of ultratrace amount of 2,4,6-trinitrotoluene (TNT) with synthetic copolypeptide-doped polyaniline nanofibers. The copolypeptide, comprising of glutamic acid (Glu) and lysine (Lys) units, is *in situ* doped into polyaniline through the protonation of the imine nitrogen atoms of polyaniline by the free carboxylic groups of Glu segments, resulting in the formation of polyaniline nanofibers of emeraldine salt. The free amino groups of Lys segments at the surface of nanofibers provide the receptor sites of TNT through the formation of charge–transfer complex between the electron-rich amino groups and the electron-deficient aromatic rings. Adsorptive stripping voltammetry results demonstrate that the poly(Glu-Lys)-doped nanofibers confined onto glassy carbon electrodes exhibit a remarkable enriching effect and thus sensitive electrochemical response to TNT with a linear dynamic range of 0.5–10 μM and a detection limit down to 100 nM. Moreover, other kinds of nitro compounds show different redox behaviors from TNT at the doped nanofibers, and thus do not interfere with the electrochemical detection of TNT. This study essentially offers a new and simple method for electrochemical detection of ultratrace TNT.

© 2009 Elsevier B.V. All rights reserved.

1. Introduction

The detection of nitroaromatic explosives has attracted considerable research efforts in recent years, due to the pressing needs in public security and environmental protection [1,2]. The methods currently used for the detections of nitroaromatics are usually time-consuming with the employment of cumbersome and expensive gas chromatography coupled with a mass spectrometry, ion mobility spectrometry, and neutron activation analysis. Therefore, there has been a great driving force in the development of ultrasensitive chemosensors for the detection of nitroaromatics by various approaches such as fluorescence [3–5], infrared [6], molecular imprinting [7–11] and electrochemistry [12–18], of which electrochemical sensors are particularly suited for the detection of nitroaromatics because, on one hand, the electron-deficient nitro compounds are easily electrochemically reduced and, on the other hand, electrochemical sensors can be made into inexpensive and portable devices, which can largely reduce the cost of detection and readily meet the requirements of a high-speed and on-spot detection.

The sensitivity and selectivity of electrochemical sensors are mainly dependent on the sensory materials used. Of various sensory materials reported so far, nanostructured materials have recently found a wide range of applications in the construction of electrochemical sensors, and such kind of nanostructure-based electrochemical sensors have demonstrated many remarkable advantages over traditional ones, such as sensitivity, selectivity and ability against electrode fouling [12–21]. As one example, the large surface-to-volume ratio and the high dispersivity of the nanostructured materials essentially provide a large surface area not only for the adsorption and thus the enrichment of analyte, but also for the stable immobilization of a large amount of molecular recognition elements, of which both could lead to the remarkable improvement of the sensitivity and selectivity of electrochemical sensors and biosensors [5,18]. As another example, low-dimensional inorganic nanomaterials have widely been used in electrochemical sensors for the detections of various analytes. For example, carbon nanotubes and their composites have been recently used for the detections of nitroaromatics [12], neurotransmitters [19], glucose [20], and organophosphate pesticides [21].

Recently, the electrochemical detections of TNT have also been explored by molecularly imprinted Au nanoparticles [13], metal nanoparticle/carbon nanotube composites [14], triphylene-modified carbon nanotubes [15], mesoporous silica nanoparticles [16] and TiO$_2$/metal nanoparticles [17]. Meanwhile, there has recently been much interest in conductive-polymer-based electrochemical sensors for the detections of organic or biological analytes [18,19,22–24]. Among all conductive polymer materials, polyaniline (PANI) may be the most extensively studied sensory materials for electrochemical sensors, mainly due to its easy preparation, good

* Corresponding author. Tel.: +86 551 5591654; fax: +86 551 5591156.
E-mail address: zpzhang@iim.ac.cn (Z. Zhang).
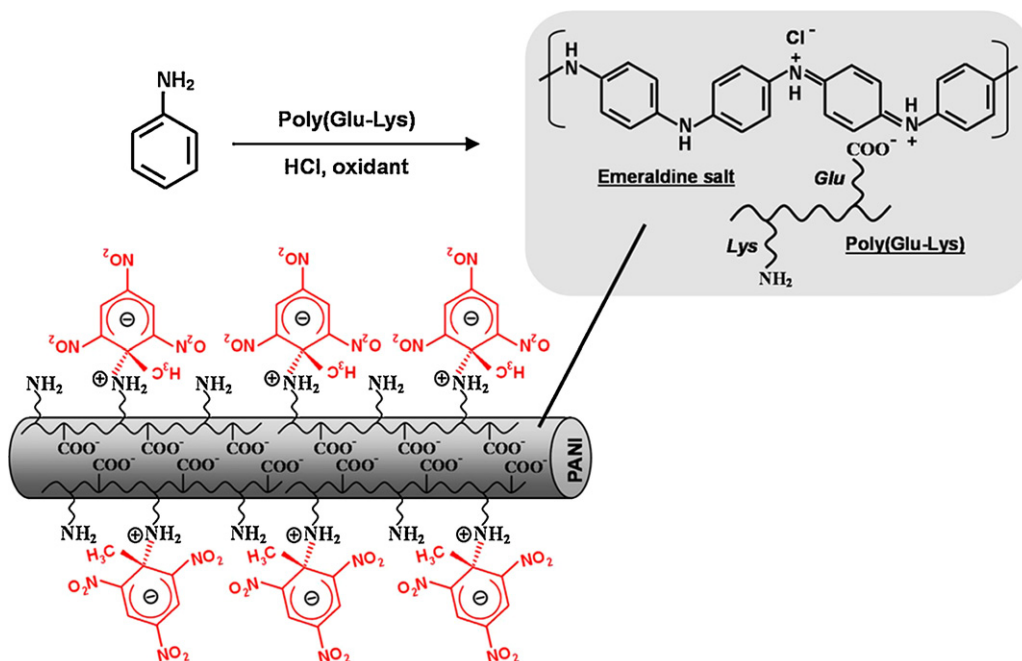
Scheme 1. Schematic illustrations for synthesis and structure of poly(Glu-Lys)-doped PANI nanofibers. The bottom-left inset shows the specific interaction between the doped nanofiber and TNT molecules through the formation of charge–transfer complex.

biocompatibility and high electrocatalytic activity. PANI nanomaterials as electrode materials have several remarkable advantages over inorganic counterparts in: (1) ready task-specific functionalization with copolymers and composites and so forth [19], (2) easy combination with enzyme or antibody with a good biocompatibility [18,22,23], and (3) high electrocatalytic activity towards many kinds of organic/biological molecules [24]. These properties substantially make the PANI nanomaterials to be quite promising in the development of various kinds of chemo/biosensors [25,26,27].

It has been reported that the doping of protonic acid (HCl) is a prerequisite process for transforming PANI emeraldine into the form of conductive emeraldine salt by the formation of radical ions at PANI backbone [28]. Recent studies have shown that organic carboxylic acids [29,30] or sulfonic acids [31] are also good acid dopants and can efficiently improve the processibility of emeraldine salt. In this work, we investigate the possibility of preparing the copolypeptide-doped PANI nanofibers for the electrochemical detection of nitroaromatic compounds. Poly(Glu-Lys) with two kinds of functional units is *in situ* doped into PANI nanofibers, where the free carboxylic groups of glutamic segments play a role of protonic dopants to drive the copolypeptide into the formed PANI nanofibers during the oxidant polymerization of aniline (Scheme 1). Meanwhile, the free amino groups of lysine segments residue at the surface of the nanofibers due to its high hydrophilic nature, and thus provide the selective binding sites of TNT through the interactions between the electron-rich amine and the electron-deficient aromatic rings. When poly(Glu-Lys)-doped PANI nanofibers are modified onto glassy carbon electrode, adsorptive stripping voltammetry demonstrates that the doped nanofibers with receptor sites exhibit a high electrochemical sensitivity and rapid response to TNT.

2. Experimental

2.1. Materials

Poly(D-Glu-D-Lys)   ($M_W = 2$–5×10^4 g mol^{-1},   glu:lys = 6:4, mol/mol) and poly(D-Glu) ($M_W = 7$–15×10^4 g mol^{-1}) were pur-

chased from Aldrich. 2,4,6-Trinitrotoluene (TNT) was supplied by National Security Department of China and recrystallized with ethanol before use. 2,4-Dinitrotoluence (DNT, from Merch-Schuchardt), trinitrobenzene (TNB, from Aldrich) and ammonium persulfate (99.99%, from Shanghai Chem. Ltd.) were used as received. Aniline was purified by vacuum distil before used. *Caution:* TNT is highly explosive and harmful to human health and should be used with extreme caution and handled only in a small quantity.

2.2. Copolypeptide-doped PANI nanofibers

Poly(Glu-Lys)-doped PANI nanofibers were prepared by oxidative polymerization of aniline with ammonium persulfate, according to a procedure similar to the doping of amino acids in PANI [27]. The oxidative polymerization was carried out in a weak acidic solution containing aniline and poly(Glu-Lys). Typically, a stock solution of 0.1 mg/mL of poly(Glu-Lys) was first prepared with Milli-Q water. A 10 μL of the distilled aniline was added into 1.5 mL of 0.1 mg/mL poly(Glu-Lys) solution to make a mixing solution of reactive precursors. Simultaneously, 30 mL of 1×10^{-4} M HCl aqueous solution was purged with nitrogen for 30 min and cooled in an ice bath. The above precursor solution was gradually added into the cooled acidic solution under stirring, and the pH value was further adjusted to 4.0 with diluted HCl solution. Then, the oxidative polymerization of aniline was initiated by adding 24 mg of ammonium persulfate into the reaction system. After the polymerization for 12 h at 0–5 °C, the dark-green poly(Glu-Lys)-doped nanofibers were collected by centrifugation and washed several times with distilled water. For comparison, poly(Glu)-doped PANI nanofibers were also synthesized according to the identical procedure and pure PANI nanofibers were prepared in the absence of polypeptides.

2.3. Modification of glassy carbon (GC) electrode

Commercial GC electrodes were carefully polished with 0.3-μm alumina powder, and rinsed in an ultrasonication bath before use. 2 mg of polypeptide-doped PANI nanofibers was dispersed into

0.5 mL of Milli-Q water, and sonicated for 5 min to obtain a dark-green nanofiber solution. A drop of the above solution was directly added onto the fresh surface of GC electrode and allowed to dry at room temperature. After water evaporation, a thin film of PANI nanofibers was formed on the electrode surface.

2.4. Apparatus and measurements

Electrochemical measurements were carried out using a LK 2005 workstation. A conventional three-electrode electrochemical cell was employed with the modified GC electrodes as working electrode, a saturated calomel electrode (SCE) as reference electrode, and a platinum foil as counter electrode. 60 mL of 0.5 M NaCl solution, deoxygenated thoroughly by bubbling high-purity nitrogen gas, was used as the supporting electrolyte for the electrochemical measurements. Nitro analytes were first dissolved in acetonitrile, and then added into the electrolyte. Adsorptive stripping voltammetry began with a deposition at the potential of 0.0 V for different period under stirring. After the deposition step, the stirring was stopped and the solution was equilibrated for 15 s. The potential was then linearly scanned from 0.0 to -1.0 V at a rate of 20 mV/s.

The morphology of poly(Glu-Lys)-doped PANI nanofibers was examined by a FEI Sirion-200 field-emission scanning electron microscope (FE-SEM). XPS analysis was carried out using a Thermo ESCALAB 250 equipped with a monochromatic microspot X-ray beam originating from the Al anode (Kα, X-ray at 1486.6 eV) with a spot diameter of 500 μM. The data were recorded at room temperature and under a pressure below 10^{-6} Pa. To compensate for charging effects, the binding energies were corrected with covalent C1s at 284.6 eV. The curve fitting and peak integration were carried out by the Avantage (Version 3.25) software through assuming a Gaussian–Lorentizian line shape.

3. Results and discussion

3.1. Synthesis of poly(Glu-Lys)-doped PANI nanofibers

Scheme 1 schematically illustrates the synthetic procedure and chemical structure of copolypeptide-doped PANI nanofibers, and the specific interactions between the doped nanofibers and TNT molecules. The poly(Glu-Lys) is highly soluble in water, and is thus well suited for the *in situ* doping into PANI during the oxidative polymerization of aniline in water. An aqueous diluted HCl solution with a relative high pH value (4.0) was used as a polymerization media, as the reported dopings of organic acids [29,30]. Detailed experiments revealed that the pH value of 4.0 could ensure both the protonic doping of Glu segments and the conductivity of the formed emeraldine salt. In general, the emeraldine salt of conductive PANI was synthesized at a lower pH value (1–2) by the protonic doping. When the pH value is higher than 5.0, the conductivity of PANI will reduce obviously, due to a low doping ratio of protons. At the pH < 3.0, however, the copolypeptide is very difficult to dope into the formed PANI, due to a high acidity. Thus, we found that the pH value of 4.0 is the most suitable for obtaining both a relative high conductivity and a high doping ratio of copolypeptide. The imine nitrogen atoms of the oxidative units on PANI chains are protonated in part by the carboxylic groups of Glu segment, and in part by hydrogen chloride. Therefore, poly(Glu-Lys) can be *in situ* doped into the formed PANI nanofibers through the protonation mechanism, and the free amino groups of lysine segments are inclined to stay at the surface of nanofibers due to its hydrophilic nature, resulting in the amine-capped PANI nanofibers, as drawn in Scheme 1.
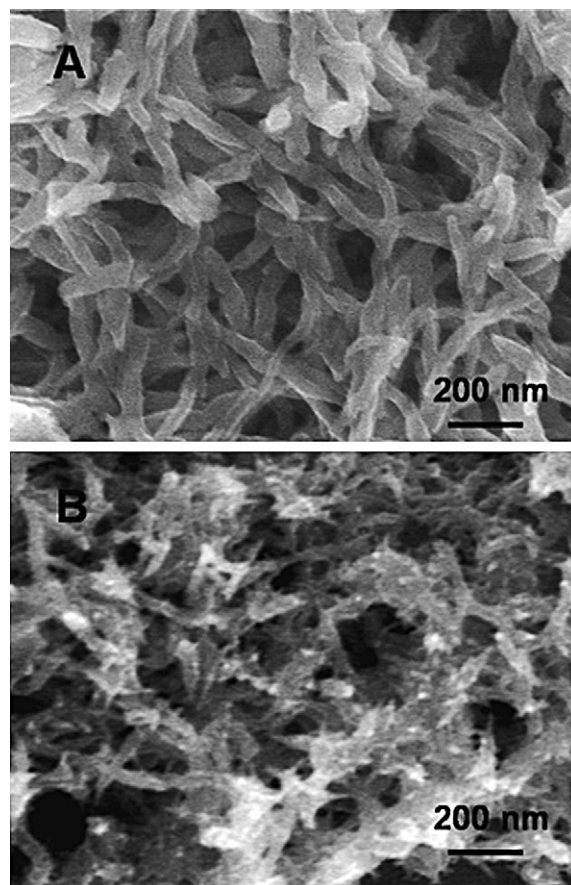
Fig. 1. SEM images of: (A) poly(Glu-Lys)-doped PANI nanofibers and (B) pure PANI nanofibers.

3.2. Interactions between poly(Glu-Lys)-doped PANI nanofibers and TNT

The bottom-left inset of Scheme 1 illustrates the interaction between the doped PANI nanofibers and TNT molecules. A strong charge–transfer interaction, as a predominant process, occurs between the electron-deficient aromatic ring of TNT and the electron-rich amino ligands at the surface of nanofibers. The electron-rich primary amine is nucleophilic group, and the center of TNT molecule exhibits an electrophilic property due to the three electron-withdrawing nitro groups, which allow for the formation of charge–transfer Meisenheimer complex, as demonstrated by our recent work [32] and other studies [33,34]. The zwitterion complex is a resonance-stabilizing form due to three electron-withdrawing nitro groups. On the other hand, TNT molecule is a Bronsted-Lowry acid and may also be deprotonated at the methyl group by basic amino ligands [35,36]. Therefore, the free amino ligands at the surface of the copolypeptide-doped nanofibers play a role of TNT receptors through the charge–transfer or acid–base pairing interactions, exhibiting a remarkable enriching effect to TNT species.

3.3. Characterization of poly(Glu-Lys)-doped PANI nanofibers

The poly(Glu-Lys)-doped PANI nanofibers are a dark green emeraldine salt containing the alternating reduced and oxidized repeat units, as confirmed by UV–vis and infrared spectral measurements (data not shown), suggesting a good conductivity of nanofibers. The diameter of the doped nanofibers is about 50 nm, as shown in the SEM image of Fig. 1A. However, the undoped PANI nanofibers are obviously irregular in morphology (Fig. 1B). The dif-
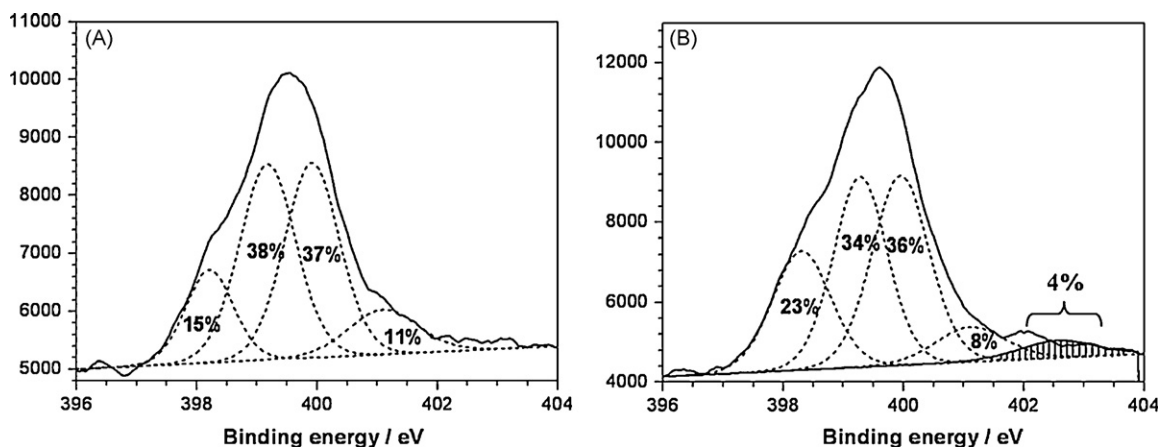
Fig. 2. N1s X-ray surface photoelectron spectra of: (A) PANI and (B) poly(Glu-Lys)-doped PANI nanofibers.

ference clearly reveals that the doped nanofibers have a better uniformity in shape and diameter than pure PANI nanofibers due to the addition of copolypeptide in the reaction systems. The observations also suggest that the copolypeptide may also play a role of growth-mediator of nanofibers while doping into the formed nanofibers, through the strong hydrogen bond or acid–base-pairing interactions between copolypeptide and aniline monomers.

To further confirm the doping of poly(Glu-Lys) in the PANI nanofibers, the N1s X-ray surface photoelectron spectra were measured to distinguish the different structural nitrogen atoms at the surface of nanofibers. Fig. 2A shows that, after a deconvolution treatment of Avantage software, the four peaks of N1s were detected for pure PANI nanofibers, centered at 398.25 ± 0.1, 399.23 ± 0.1, 399.92 ± 0.1, and 401.1 ± 0.1 eV, respectively. They were attributed to the imine nitrogen (–N=), the amino nitrogen (–NH–), the radical cation nitrogen (–NH$_2^+$–) and the iminium ion (–NH$^+$=), respectively [27]. With the doping of poly(Glu-Lys) in nanofibers, a new shoulder peak appeared at 402.56 eV, as shown in Fig. 2B. This new peak could be attributed to the acylamino nitrogen (–CONH–) at the main chains of poly(Glu-Lys) by the comparison with pure polypeptide [37,38]. Here, the physical adsorption is not almost possible because the synthesized nanofibers were fully washed with water to remove the residual of copolypeptide. Meanwhile, we could see that the area fraction of this peak is about 4%, which is higher than the theoretic nitrogen content of 1% estimated from the ratio of copolypeptide to aniline in the reactive materials. With further increase of the copolypeptide in the reaction system, XPS spectra did not detect the corresponding enhance-

ment of copolypeptide concentration in the nanofibers, suggesting a maximum doping of copolypeptide in the PANI. The surface photoelectron spectra reveal that poly(Glu-Lys) was successfully doped into PANI nanofibers and mainly distributed at the surface of PANI nanofibers, due to the thin diameter of the doped nanofibers and the highly hydrophilic nature of Lys segments. Thus, a number of primary amino groups of Lys segments residue at the surface of the nanofibers, as illustrated in Scheme 1.

3.4. Enriching effect of doped nanofibers on TNT analyte

To evaluate the electrochemical sensitivity of the copolypeptide-doped PANI nanofibers to TNT, poly(Glu)-doped PANI nanofibers without Lys units and pure PANI nanofibers were also prepared under the same conditions. Poly(Glu-Lys)-doped nanofibers, pure PANI nanofibers and poly(Glu)-doped nanofibers were individually modified onto GC electrodes for studying their electrochemical responses to TNT. Fig. 3 compares three parallel voltammetry measurements of 2.5 μM TNT with increasing the deposition time at the potential of 0.0 V. Before the deposition (0s), three reduction peaks of TNT at −0.49, −0.65 and −0.80 V were recorded at the three modified electrodes, which correspond to the stepwise reductions of three nitro groups into amino groups by the conversion of the hydroxylamines through the 6e$^-$ transfer process [16,39]. Meanwhile, the first reduction peak at −0.49 V is stronger than the second and third reduction ones at −0.65 and −0.80 V, respectively, which is similar to other electrochemical detection of TNT [12–16]. Furthermore, it is clear that before the deposition, the first
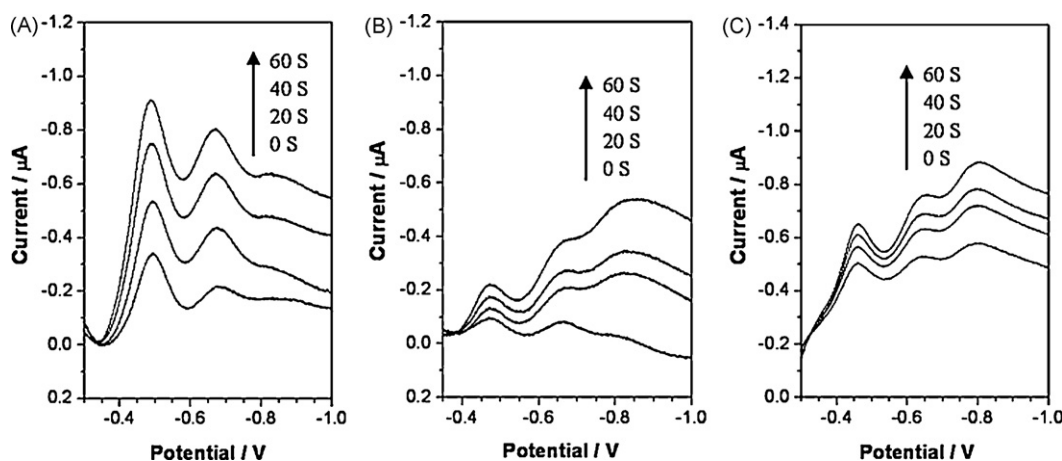
Fig. 3. Adsorptive stripping voltammograms of 2.5 μM TNT after different deposition time at the potential of 0.0 V with GC electrodes modified with (A) poly(Glu-Lys)-doped PANI, (B) pure PANI and (C) poly(Glu)-doped PANI nanofibers. The background current in the absence of TNT was subtracted for all curves.

reduction peak at the poly(Glu-Lys)-doped nanofibers is stronger than the first peaks at the poly(Glu)-doped nanofibers and the pure nanofibers, suggesting a higher sensitivity of the poly(Glu-Lys)-doped nanofibers towards TNT. With the increase of deposition period from 0 to 60 s, the first peak current (at −0.49 V) and the second peak current (at −0.65 V) were obviously enhanced at the GC electrode modified with poly(Glu-Lys)-doped nanofibers (Fig. 3A). In the case of pure PANI and poly(Glu)-doped PANI nanofibers, however, the two corresponding peak currents were only slightly enhanced with increasing the deposition time, as shown in Fig. 3B and C. Meanwhile, we can also see that the first peak current at the poly(Glu)-doped nanofibers is only slightly higher than that at the pure PANI nanofibers with prolonging the deposition time. These comparisons clearly indicate that the poly(Glu-Lys)-doped nanofibers exhibit a much stronger enriching capacity of TNT than the poly(Glu)-doped nanofibers and the pure nanofibers. This property may be elucidated by the fact that the primary amino ligands at the surface of the poly(Glu-Lys)-doped nanofibers provide a recognition receptor of TNT through the charge–transfer complexing interactions, as illustrated in the bottom-left inset of Scheme 1. The specific adsorption together with the large surface-to-volume ratio of nanofibers greatly amplifies the electrochemical response to TNT species. Moreover, the doped PANI-modified electrode has a high reliability in the supporting electrolyte for electrochemical detection of TNT.

We chose the first reduction peak of TNT at −0.49 V for quantitative evaluation on the sensitivity of electrode materials because this peak is the most separated and intense. Fig. 4 shows the plots of this peak area versus the deposition time for (a) poly(Glu-Lys)-doped nanofibers, (b) poly(Glu)-doped nanofibers and (c) pure nanofibers. The peak area of TNT at the poly(Glu-Lys)-doped nanofibers rapidly increases from 23 nA V at the initial stage to a maximum value of 56 nA V after 120 s of deposition, which is faster than the enriching rate of the previously reported carbon nanotubes [12] and metallic nanoparticles [14]. Meanwhile, the corresponding peak areas at the poly(Glu)-doped nanofibers and the pure nanofibers increase only from 11 to 15 nA V and from 5 to 9 nA V during the same time period, respectively. Thus, the increasing rate of the peak area at the poly(Glu-Lys)-doped nanofibers is about eightfold those at poly(Glu)-doped nanofibers and pure nanofibers. The data analysis clearly demonstrates that the short deposition period can lead to a rapid enhancement of electrochemical response to TNT at the poly(Glu-Lys)-doped nanofibers. The high sensitivity and
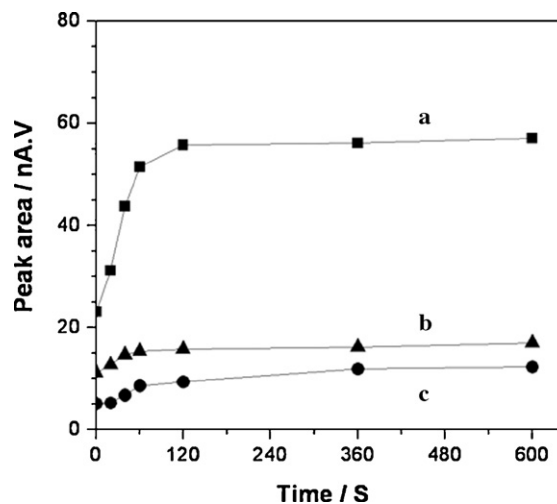
Fig. 4. Plots of the area of the first reduction peak (at −0.49 V for 2.5 μM TNT) versus the deposition time: (a) poly(Glu-Lys)-doped nanofibers, (b) poly(Glu)-doped nanofibers and (c) pure PANI nanofibers.

rapid response to TNT are two desirable features of the poly(Glu-Lys)-doped nanofibers, which holds a promising and significant implication for the fast detection of ultratrace TNT analyte.

3.5. Electrochemical response to different TNT concentrations

The electrochemical adsorptive effect of the poly(Glu-Lys)-doped nanofibers has further been confirmed by testing their electrochemical response to TNT with different concentrations. Fig. 5A shows the adsorptive stripping voltammograms of TNT with the 0.5 μM step of concentration after the deposition time of 200 s. Three reduction peaks of TNT were clearly recorded, and the peak currents were significantly enhanced with increasing the TNT concentration. Especially, the first reduction peak at −0.49 V is most obviously detected even at the 0.5 μM concentration. The plots of the areas of the three reduction peaks versus TNT concentrations were shown in Fig. 5B. The peak areas of the first peak have the highest slope and the largest correlation coefficient with TNT concentrations. The peak area is proportional to TNT concentration with a highly linear calibration plot of $R^2 = 0.998$, and a linear
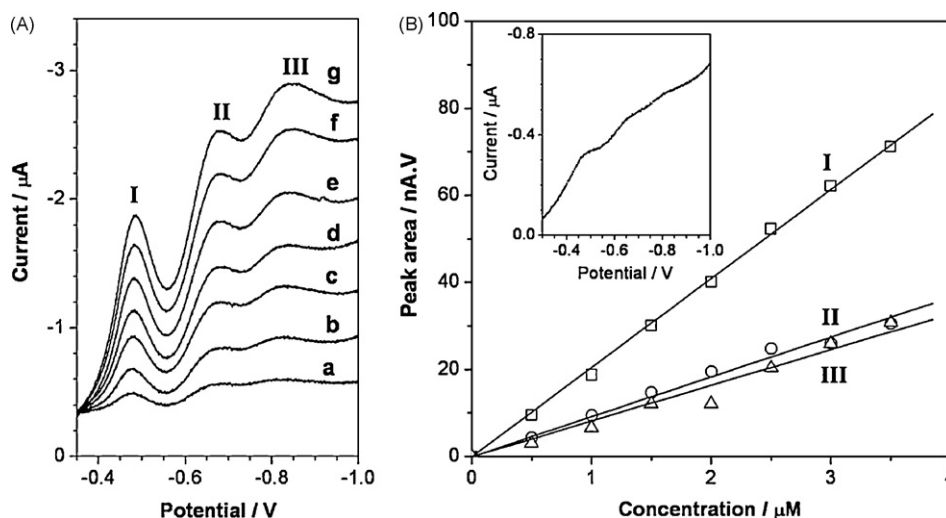
Fig. 5. (A) Adsorptive stripping voltammograms of (a) 0.5 μM, (b) 1.0 μM, (c) 1.5 μM, (d) 2.0 μM, (e) 2.5 μM, (f) 3.0 μM and (g) 3.5 μM TNT at the poly(Glu-Lys)-doped nanofibers-modified GC electrode after the deposition period of 200 s (the background current in the absence of TNT was subtracted for all curves). (B) The plots of the areas of the three reduction peaks versus TNT concentrations (the inset is the voltammogram of 100 nM TNT).
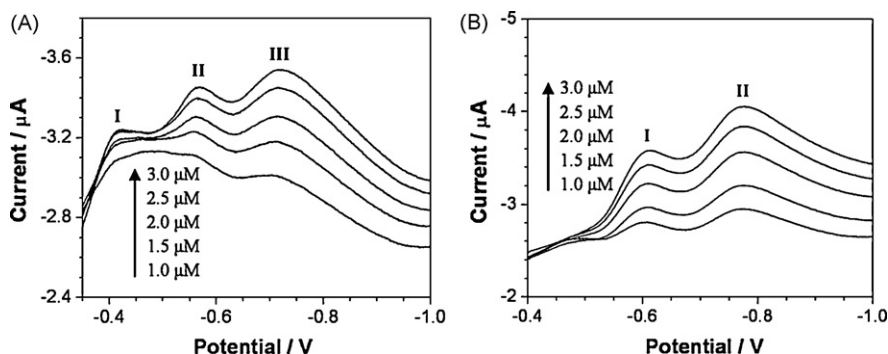
Fig. 6. Adsorptive stripping voltammograms of (A) TNB and (B) DNT with increasing analyte concentrations in 0.5 μM step at the poly(Glu-Lys)-doped nanofibers-modified GC electrode after the deposition period of 200 s.

slop of 20.4 nA/(V μM). The linear dynamic range (LRD) of the electrochemical sensor is about in the range of 0.5–10 μM. Therefore, the first peak is well suited as a representative peak for the TNT determination in a low concentration range.

Meanwhile, we can determine the detection limit by gradually reducing the concentration of TNT analyte in the solution. The strongest reduction signal of the nitro group at −0.49 V became weaker with the decrease of TNT concentration. When the TNT concentration approached to 100 nM, the reduction signal was still detected, as shown in the inset of Fig. 5B. However, when TNT concentration was lower than 50 nM, the reduction signal was not detected. Therefore, we can estimate that detection limit is about 100 nM.

3.6. Electrochemical response to analogous nitroaromatics

Moreover, it is very interesting that poly(Glu-Lys)-doped nanofibers as the electrode materials can distinguish TNT from other nitroaromatic analogues, such as TNB and DNT, not only by the peak potentials, but also by the evolution of reduction signals with analyte concentrations. TNB usually generates three well-defined redox signals at −0.34, −0.51 and −0.71 V in normal electrochemical detections, corresponding to the stepwise reduction of three nitro groups to the corresponding amine [16,39]. Fig. 6A shows that the first reduction peak of 1 μM TNB is almost invisible at the poly(Glu-Lys)-doped nanofibers-modified GC electrode. Until the TNB concentration rise up to 2.5 μM, the first reduction signal was just detected in a very small peak at −0.42 V. We can clearly see that the first reduction signal of TNB was very weak and was not enhanced with TNB concentration, which is quite different from that of TNT. However, the second reduction peak at −0.56 V was detected at the concentration of 1.5 μM. The third reduction peak at −0.72 V can most clearly be detected at low analyte concentration, and exhibits the obvious enhancement with the increase of TNB concentration. The unexpected reduction characteristic of TNB at poly(Glu-Lys)-doped nanofibers-modified GC electrode can roughly be understood as follows. The significant enhancements of the second and third signals of TNB suggest the strong deposition of TNB at the surface of the amine-capping nanofibers. However, the reduction manner of TNB at the surface of the doped nanofiber may be different from that of TNT. It is well known that TNB without methyl group is a more electron-deficient and symmetrical structure than TNT molecule. A very strong charge–transfer interaction should exclusively occur from amino ligands to TNB molecules, and thus leads to the highly homogeneous distribution of the accepted charge on three nitro groups, as shown in Fig. 7. Therefore, the reduction of the first nitro group for disrupting the highly symmetrical structure and charge distribution may become more difficult than TNT [39]. The assumption can roughly be con-

firmed by the reduction potential of the first signal of TNB. The first reduction signal appears at a more negative position (−0.42 V) than the corresponding potential by the other electrochemical reduction (−0.34 V) [16,39], while the third reduction potential at −0.72 V appears almost at the same position as the corresponding potential by other normal reduction [16].

On the other hand, DNT with two nitro groups is a Lewis acid much weaker than TNT, and therefore exhibits a weak interaction with the free amino ligands at the surface of the poly(Glu-Lys)-doped nanofibers. Fig. 6B shows that 1.0 μM DNT solution can clearly generate two reduction signals of nitro groups at −0.61 and −0.78 V, respectively. The second reduction signal is stronger than the first one at the beginning concentration of 1 μM, and exhibits a greater enhancement with the increase of DNT concentration. Therefore, these above results confirm that different nitro compounds show a distinct evolution of redox signals at the poly(Glu-Lys)-doped nanofiber-modified electrode. Fig. 8 shows the plots of the areas of the first reduction peaks versus the concentrations of TNB and DNT together with TNT. The linear slops of the peak area to concentration can be ordered as: TNT » DNT » TNB. Therefore, the first reduction signal exhibits the highest sensitivity for TNT and the lowest sensitivity for TNB. The evolution of redox signals at different peak potentials with analyte concentration may provide a new indicator for distinguishing different kinds of nitroaromatics.

3.7. Determination of TNT in different matrix samples

Fig. 9 shows the determination of TNT (3.5 μM) by adsorptive stripping voltammetry (200-s deposition time at 0.0 V) with different matrix samples. The river water and tap water were used directly to prepare the electrolyte solution (0.5 M NaCl) without filtering or any pretreatment. Seawater was artificially prepared by dissolving 26.66 g/kg NaCl and 0.73 g/kg KCl in river water. In the tap water sample, the three characteristic signals of TNT can most clearly be distinguished. However, the second and third peaks overlap each other to form a very wide peak for the sea and river
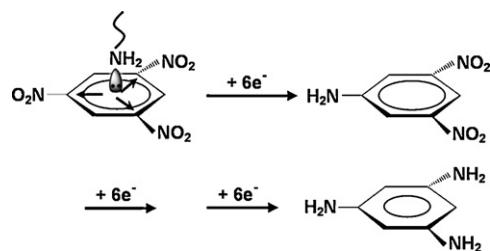

Fig. 7. Schematic illustration for the electrochemical reduction process of TNB at poly(Glu-Lys)-doped nanofibers.
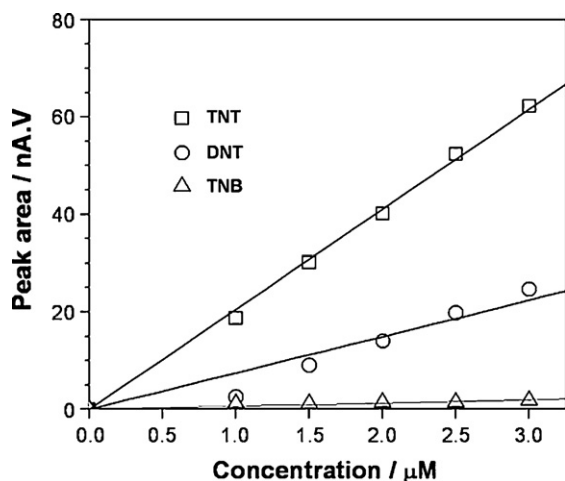
Fig. 8. The plots of the areas of the first reduction peaks versus the concentrations of TNT, DNT and TNB for poly(Glu-Lys)-doped nanofibers.
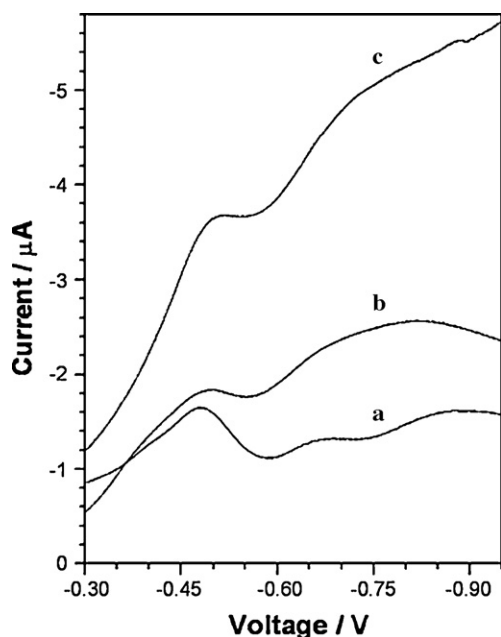

Fig. 9. Determination of TNT (3.5 μM) by adsorptive stripping voltammetry (200-s deposition time at 0.0 V) with different matrix samples: (a) tap water, (b) sea water, and (c) river water (the background current in the absence of TNT was subtracted for all curves).

samples. The first reduction signal at about −0.49 V is the most intense and separated for all three samples. Thus, the determination of TNT is feasible in all samples tested by the most reliable peak.

4. Conclusions

In summary, we have demonstrated that the copolypeptide with free carboxylic and amino units can *in situ* be doped into the polyaniline nanofibers through the protonation of the imine nitrogen atoms at polyaniline chains by the free carboxylic groups of copolypeptide. The resultant conductive nanofibers with surface amino ligands can electrochemically detect 2,4,6-trinitrotoluene with high sensitivity and fast response by the specific interaction between electron-rich amino groups and electron-deficient aromatic rings. It is particularly important that different nitro compounds show a distinct electrochemical response at the copolypeptide-doped nanofibers-modified electrode. Although the redox mechanism of different nitro compounds at the doped polyaniline nanofibers has to be fully understood, the resultant evolution of redox signals can distinguish different nitro analytes. On the other hand, it can be expected that the copolypeptide-doped polyaniline nanofibers can further be modified with antibody or enzyme for the detection of biological analytes. These main characteristics together with the simplicity of preparation suggest that the copolypeptide-doped polyaniline nanofibers are widely applicable in electrochemical sensors.

References

[1] J.I. Steinfeld, J. Wormhoudt, Annu. Rev. Phys. Chem. 49 (1998) 203.
[2] J.W. Gardner, J. Yinon, Electronic Nose & Sensors for the Detection of Explosives, Kluwer Academic Publishers, London, 2003.
[3] A. Rose, Z. Zhu, C.F. Madigan, T.M. Swager, V. Bulovic, Nature 434 (2005) 876.
[4] H. Sohn, M.J. Sailor, D. Magde, W.C. Trogler, J. Am. Chem. Soc. 125 (2003) 3821.
[5] R.Y. Tu, B.H. Liu, Z.Y. Wang, D.M. Gao, F. Wang, Q.L. Fang, Z.P. Zhang, Anal. Chem. 80 (2008) 3458.
[6] M.B. Pushkarsky, I.G. Dunayevskiy, M. Prasanna, A.G. Tsekoun, R. Go, C.K.N. Patel, Proc. Natl. Acad. Sci. 103 (2006) 19630.
[7] J.H. Li, C.E. Kendig, E.E. Nesterov, J. Am. Chem. Soc. 129 (2007) 15911.
[8] D.M. Gao, Z.P. Zhang, M.H. Wu, C.G. Xie, G.J. Guan, D.P. Wang, J. Am. Chem. Soc. 129 (2007) 7859.
[9] G.J. Guan, Z.P. Zhang, Z.Y. Wang, B.H. Liu, D.M. Gao, C.G. Xie, Adv. Mater. 19 (2007) 2370.
[10] C.G. Xie, B.H. Liu, Z.Y. Wang, D.M. Gao, G.J. Guan, Z.P. Zhang, Anal. Chem. 80 (2008) 437.
[11] C.G. Xie, Z.P. Zhang, D.P. Wang, G.J. Guan, D.M. Gao, J.H. Liu, Anal. Chem. 78 (2006) 8339.
[12] J. Wang, S.B. Hocevar, B. Ogorevc, Electrochem. Commun. 6 (2004) 176.
[13] M. Riskin, R. Tel-Vered, T. Bourenko, E. Granot, I. Willner, J. Am. Chem. Soc. 130 (2008) 15911.
[14] S. Hrapovic, E. Majid, Y. Liu, K. Male, J.H.T. Luong, Anal. Chem. 78 (2006) 5504.
[15] H.X. Zhang, J.S. Hu, C.J. Yan, L. Jiang, L.J. Wan, Phys. Chem. Chem. Phys. 8 (2006) 3567.
[16] H.X. Zhang, A.M. Cao, J.S. Hu, L.J. Wan, S.T. Lee, Anal. Chem. 78 (2006) 1967.
[17] B. Filanovsky, B. Markovsky, T. Bourenko, N. Perkas, R. Persky, A. Gedanken, D. Aurbach, Adv. Funct. Mater. 17 (2007) 1487.
[18] Z. Naal, J.H. Park, S. Bernhard, J.P. Shapleigh, C.A. Batt, H.D. Abruña, Anal. Chem. 74 (2002) 140.
[19] S.R. Ali, Y.F. Ma, R.R. Parajuli, Y. Balogun, W.Y.C. Lai, H.X. He, Anal. Chem. 79 (2007) 2583.
[20] M.W. Shao, Y.Y. Shan, N.B. Wong, S.T. Lee, Adv. Funct. Mater. 15 (2005) 1478.
[21] G. Liu, Y. Lin, Anal. Chem. 77 (2005) 5894.
[22] Y. Fan, X. Chen, A.D. Trigg, C.H. Tung, J.M. Kong, Z.Q. Gao, J. Am. Chem. Soc. 129 (2007) 5437.
[23] V.V.R. Sai, S. Mahajan, A.Q. Contractor, S. Mukherji, Anal. Chem. 78 (2006) 8368.
[24] X.L. Luo, A.J. Killard, M.R. Smyth, Chem. Eur. J. 13 (2007) 2138.
[25] S. Yunus, A. Attout, P. Bertrand, Langmuir 25 (2009) 1851.
[26] T. Tiwari, S. Gong, Talanta 77 (2008) 1217.
[27] N. Zhou, T. Yang, C. Jiang, M. Du, K. Jiao, Talanta 77 (2009) 1021.
[28] A.G. MacDiarmid, Angew. Chem. Int. Ed. 40 (2001) 2581.
[29] L.J. Zhang, Y.Z. Long, Z.J. Chen, M.X. Wan, Adv. Funct. Mater. 14 (2004) 693.
[30] L.J. Zhang, H. Peng, Z.D. Zujovic, P.A. Kilmartin, J. Travas-Sejdic, Marcomol. Chem. Phys. 208 (2007) 1210.
[31] A.G. MacDiarmid, J. Power Source 126 (2004) 214.
[32] D.M. Gao, Z.Y. Wang, B.H. Liu, L. Ni, M.H. Wu, Z.P. Zhang, Anal. Chem. 80 (2008) 8545.
[33] T.H. Lowry, K.S. Richardson, Mechanism and Theory in Organic Chemistry, Benjamin-Cummins, New York, 1987.
[34] J. Meisenheimer, Justus Liebigs Ann. Chem. 323 (1902) 205.
[35] N.R. Walker, M.J. Linman, M.M. Timmers, S.L. Dean, C.M. Burkett, J.A. Lloyd, J.D. Keelor, B.M. Baughman, P.L. Edmiston, Anal. Chim. Acta 593 (2007) 82.
[36] C.F. Bernasconi, J. Org. Chem. 36 (1971) 1671.
[37] J. Russat, Surf. Interf. Anal. 11 (1988) 414.
[38] K.L. Cheng, J.C. Carver, T.A. Carlson, Inorg. Chem. 12 (1973) 1702.
[39] A. Esteve-Núñez, A. Caballero, J.L. Ramos, Microbiol. Mol. Biol. Rev. 65 (2001) 335.

Interdigitated array microelectrode based impedance immunosensor for detection of avian influenza virus H5N1

Ronghui Wang [a], Yun Wang [a], Kentu Lassiter [a], Yanbin Li [a,b,*], Billy Hargis [b], Steve Tung [c], Luc Berghman [d], Walter Bottje [b]

[a] Department of Biological & Agricultural Engineering, University of Arkansas, Fayetteville, AR 72701, USA
[b] Department of Poultry Science, University of Arkansas, Fayetteville, AR 72701, USA
[c] Department of Mechanical Engineering, University of Arkansas, Fayetteville, AR 72701, USA
[d] Departments of Poultry Science and Veterinary Pathobiology, Texas A&M University, College Station, TX 77843, USA

ABSTRACT

Continuous outbreaks of avian influenza (AI) in recent years with increasing threat to animals and human health have warranted the urgent need for rapid detection of pathogenic AI viruses. In this study, an impedance immunosensor based on an interdigitated array (IDA) microelectrode was developed as a new application for sensitive, specific and rapid detection of avian influenza virus H5N1. Polyclonal antibodies against AI virus H5N1 surface antigen HA (Hemagglutinin) were oriented on the gold microelectrode surface through protein A. Target H5N1 viruses were then captured by the immobilized antibody, resulting in a change in the impedance of the IDA microelectrode surface. Red blood cells (RBCs) were used as biolabels for further amplification of the binding reaction of the antibody–antigen (virus). The binding of target AI H5N1 onto the antibody-modified IDA microelectrode surface was further confirmed by atomic force microscopy. The impedance immunosensor could detect the target AI H5N1 virus at a titer higher than 10^3 EID_{50}/ml (EID_{50}: 50% Egg Infective Dose) within 2 h. The response of the antibody–antigen (virus) interaction was shown to be virus titer-dependent, and a linear range for the titer of H5N1 virus was found between 10^3 and 10^7 EID_{50}/ml. Equivalent circuit analysis indicated that the electron transfer resistance of the redox probe $[Fe(CN)_6]^{3-/4-}$ and the double layer capacitance were responsible for the impedance change due to the protein A modification, antibody immobilization, BSA (bovine serum albumin) blocking, H5N1 viruses binding and RBCs amplification. No significant interference was observed from non-target RNA viruses such as Newcastle disease virus and Infectious Bronchitis disease virus. (The H5N1 used in the study was inactivated virus.)

1. Introduction

Avian influenza (AI) is a significant human and animal health problem worldwide. In recent years, continuous outbreaks of highly pathogenic avian influenza H5N1 and cases of human infection have caused increasing international concerns that the current virus could become capable of human to human transmission, triggering a global pandemic. The AI H5N1, discovered in the late 1990s, is a rod-shaped, negative-strand RNA virus with a segmented genome that belongs to type A in the family *Orthomyxoviridae*. It has been reported in more than 46 countries for animal cases and in 15 countries for human infection with 387 people infected and 245 died since 2003 [1]. It is estimated by FAO (2006) that 150 million chick-

ens and waterfowls died or were destroyed during containment efforts due to H5N1 outbreaks and that the related economic loss is beyond $ 10 billion. Consequently, rapid and sensitive technology for detection of AI H5N1 is urgently needed to help contain the spread of H5N1.

Current techniques employed to detect AI virus, such as virus isolation culture, ELISA, rapid influenza diagnostic test kits, RT-PCR and microarray technology "Flu Chip" [2–10], are either poor in specificity, low in sensitivity, time consuming, too expensive, or require a laboratory and a highly trained technician. Biosensor technologies provide promising opportunities to meet the new challenges and demands for rapid and reliable testing of influenza with minimal sample handling and laboratory skill requirements [11]. Various biosensors have been studied as alternatives to conventional methods for the detection of influenza viruses. Examples include non-labeling technologies surface plasmon resonance (SPR) and quartz-crystal microbalance (QCM), that show great potential in the area of sensor research but have had limited success in specificity [12–16]. Another promising method is colorimetric

* Corresponding author at: Department of Biological & Agricultural Engineering, University of Arkansas, Fayetteville, AR 72701, USA. Tel.: +1 4795752881/2424; fax: +1 4795752846.
E-mail address: yanbinli@uark.edu (Y. Li).

sensors [17,18], but these require the development and synthesis of a "smart" material with desirable physical, optical or electrical properties that respond to an environmental stimulus. An interferometric biosensor based on antibody–antigen interaction was reported for detection of purified AI H7 and H8 in buffer solution [19].

Compared to surface plasmon resonance, quartz-crystal microbalance and interferometric biosensors, electrochemical methods appear very promising due to the relatively simple and compact equipment required. Impedance biosensors are more sensitive than electrochemical biosensors that employ amperometry, where the signal depends critically on the relative proximity of the active site and the electrode surface [20]. At the same time, interdigitated array (IDA) microelectrodes have their advantages in impedance measurement. For example, IDA microelectrodes can maximize the impedance change at the surface, lower the detection time, minimize interfering effects of non-target analytes in the solution and have high signal/noise ratio [21,22]. In particular, IDA microelectrodes enable the detector device and sample volume to be miniaturized while sustaining its sensitivity and selectivity [23]. To the best of our knowledge, there was no report on IDA microelectrode based impedance immunosensor applied to the detection of AI H5N1.

In this study, we demonstrated an IDA microelectrode based impedance immunosensor as a new approach for the detection of AI H5N1 (inactivated). The immunosensor was fabricated using protein A of *Staphylococcus aureus* to modify the microelectrode surface followed by immobilization of specific antibodies on protein A. Target H5N1 viruses in different titers were captured by the immobilized antibody, resulting in a change in the impedance of IDA microelectrode surface. Red blood cells were used as biolabels for further amplification of the binding reaction of the antibody–antigen (virus). The capture of target AI H5N1 virus onto the IDA microelectrode was further confirmed by atomic force microscopy.

2. Experimental

2.1. Materials

Phosphate buffered saline (PBS, 10 mM, pH 7.4) and protein A (from *S. aureus*) were purchased from Sigma–Aldrich (St. Louis, MI). Three types of polyclonal HA (Hemagglutinin) antibodies specific for H5 protein of AI H5N1 were used in the assay: (1) rabbit polyclonal HA antibody raised against a synthetic peptide corresponding to 14 amino acids in the middle region of HA (Biodesign International, Saco, Maine); (2) rabbit polyclonal HA antibody raised against a synthetic peptide corresponding to 14 amino acids within residues 300–350 of HA (Abcam, Cambridge, MA); and (3) rabbit polyclonal HA antibody raised against a synthetic peptide corresponding to 15 amino acids at the amino terminus of HA (ProSci Incorporated, Poway, CA). Recombinant AIV (H5N1) HA (83 μg/ml) was obtained from Protein Sciences Corporation with purity greater than 90%. Bovine serum albumin (BSA) from EM Science (Gibbstown, NJ) was prepared in PBS (1.0%, w/v) as a blocking solution. All solutions were prepared with deionized water from Millipore (Milli-Q, 18.2 MΩ cm, Bedford, MA).

Avian influenza A/H5N1 virus (Scotland 59) was provided by USDA-APHIS National Veterinary Services Laboratory (NVSL, Ames, IA). The AI H5N1 viruses were inactivated with β-propiolactone similar to the procedure of Sever et al. [24] where viral infectivity was eliminated while maintaining hemagglutination ability [25]. The original titer of AI H5N1 was approximately 1×10^7 EID$_{50}$/ml. Newcastle/Infectious bronchitis (NCD/IB) combination vaccine was diluted for spray vaccination according to label recommendations. The vaccine was used as a competitive virus for specificity study of

the biosensor in the detection of AI H5N1. Chicken red blood cells (RBC) were prepared in isotonic dextrose at a concentration of 0.05% (w/v).

2.2. Dot Blot analysis

Immuno-Dot Blot analysis was employed as a conventional immunoassay method for checking the quality of the anti-H5N1 antibodies used in the immunosensor. Detailed procedure was the same as described in the report by Wang et al. [26]. 100 μl of the positive control (1:100,000 dilution of primary antibody in PBS), negative control (PBS only) and recombinant AI (H5N1) HA (10,000 dilution) were loaded into the Dot Blot system as directed. Secondary antibody used here was peroxidase-labeled and diluted 1:2500 with blocking buffer. After treating with substrate (Supersignal West Dura Extended Duration), the chemiluminescence dots were detected using a charge-coupled device (CCD) camera (LAS 1000 plus) (Fuji Photo Co., Tokyo, Japan).

2.3. Interdigitated array microelectrode and impedance measurement

Gold interdigitated array (IDA) microelectrodes were purchased from ABtech Scientific Inc. (Richmond, VA). Each electrode had 50 digital pairs with 15 μm digit width, 15 μm interdigit space, and a digit length of 4985 μm. The electrode area was calculated as 14.88 mm^2.

Impedance measurements were performed using an IM-6 impedance analyzer (BAS, West Lafayette, IN) with IM-6/THALES software. All impedance measurements were conducted in the presence of 10 mM [Fe(CN)$_6$]$^{3-/4-}$ (1:1) mixture in PBS (pH 7.4) as a redox probe. The tested frequency range was from 1 Hz to 1 MHz with an amplitude of 5 mV. Bode (impedance and phase vs frequency) and Nyquist (imaginary impedance vs real impedance) diagrams were recorded. Simulation was performed using the SIM program. 45 points of data from each measured spectrum were automatically selected by the software for input into an equivalent circuit to generate a fitting spectrum.

2.4. Procedure of biosensor fabrication and detection

The whole experimental procedure contains four steps: electrode cleaning, surface immobilization, AI virus detection, and RBC amplification. Step (1) The IDA microelectrode was cleaned by immersing in 1 M NaOH for 5 min, rinsed with deionized water, immersing in 1 M HCl for 2 min, rinsed with deionized water, and then wiped gently with alcohol wetted lens paper. After final rinsing with deionized water, the electrode was dried with a stream of nitrogen and it was ready for surface modification and antibody immobilization. Step (2) The clean IDA microelectrode was incubated with 50 μl of protein A solution (0.75 mg/ml) at room temperature (22–25 °C) for 2 h. Following the incubation, the microelectrode was rinsed with deionized water and dried with nitrogen stream, and then incubated with 0.1 mg/ml antibody (50 μl) for further 3 h at 4 °C. After rinsing with deionized water and drying with nitrogen, the microelectrode was incubated with 1% BSA (50 μl) as a blocking solution at room temperature for 30 min. After another rinsing with deionized water and drying with nitrogen stream, the microelectrode was ready for use in detection tests. Step (3) AI detection was performed by dropping 50 μl of inactivated AI H5N1 virus onto the IDA microelectrode surface coated with the antibody, and incubating it at room temperature for 1 h. After incubation, the microelectrode was rinsed with deionized water and dried with nitrogen. The impedance change caused by the target AI virus was calculated by subtracting the impedance measured at the end of step 2 (antibody immobilization) from the

impedance measured at the end of step 3 (virus binding). Step (4) 50 µl of 0.05% RBC, as biolabel for further amplification of the binding reaction of the antibody–antigen (virus), was added and incubated for 40 min at room temperature.

The microelectrode was reusable. After biomaterial immobilization and virus detection, the microelectrode was cleaned using the procedure described in Step (1). Then, it was observed under magnification to check for irregular features, damaged microelectrode, or foreign objects on the microelectrode. If no irregular feature was observed, impedance could be measured for the microelectrode in the presence of 10 mM $[Fe(CN)_6]^{3-/4-}$ (1:1) mixture in PBS (pH 7.4). This impedance value would be compared to the previous impedance value measured for a bare electrode. If a similar value was obtained, new antibodies can be immobilized, whereas if the value is different, the cleaning step should be repeated.

3. Results and discussion

3.1. Dot Blot analysis to select H5N1 antibody

The sensitivity and specificity of an immunosensor is greatly dependent on the immobilized antibodies. Prior to the use of antibodies for a biosensor, it is necessary to perform some tests to ensure the quality of antibodies. Several affinity-purified polyclonal HA antibodies specific for AI H5N1 H5 protein were commercially available, and the antibodies were raised against different regions of HA protein; e.g. at the amino terminus of HA or in the middle of HA. In order to select the antibodies with high affinity and high avidity interactions for our target H5N1 virus, conventional immuno-Dot Blot analysis was employed to check the immuno-interaction between antibody and antigen. Three types of commercial rabbit polyclonal anti-H5 antibodies were used in the assay: (1) antibody raised against a synthetic peptide in the middle region of HA; (2) antibody raised against a synthetic peptide within residues 300–350 of HA; and (3) antibody raised against a synthetic peptide at the amino terminus of HA [33]. Recombinant AI (H5N1) HA protein with purity >90% was used as target antigen in the Dot Blot analysis. The Dot Blot results shown in Fig. 1 indicated that antibodies raised against different regions of the H5 protein produced different binding affinities between the antibody and antigen. Among the three antibodies tested, antibody 1 (antibody to the mid region of HA) showed the best binding affinity with the biggest dot size and the highest intensity, and therefore was selected for use in the biosensor tests.
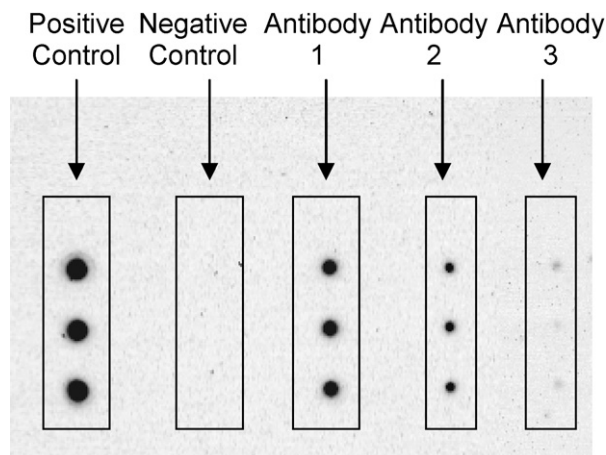
Fig. 1. Immuno-Dot Blot analysis of polyclonal HA antibodies raised against different regions of AI virus (H5N1) HA protein. *Antibody 1*: rabbit polyclonal HA antibody raised against a synthetic peptide corresponding to 14 amino acids in the middle region of HA; *Antibody 2*: rabbit polyclonal HA antibody raised against a synthetic peptide corresponding to 14 amino acids within residues 300–350 of HA; and *Antibody 3*: rabbit polyclonal HA antibody raised against a synthetic peptide corresponding to 15 amino acids at the amino terminus of HA.

3.2. Preparation and characterization of the IDA microelectrode based immunosensor

The stepwise modification of IDA microelectrode, AI detection, and RBC amplification is schematically presented in Fig. 2. The IDA microelectrode based immunosensor was fabricated through protein A. Protein A was directly adsorbed onto the gold surface of the IDA microelectrode. Then, affinity-purified anti-H5N1 antibodies were immobilized on the sensor surface due to Protein A's natural affinity towards the F_c region of antibody molecules [27]. The F_{ab} binding sites of the antibodies were thus oriented away from the protein A-modified solid support. As a result, protein A-mediated antibodies immobilization could lead to a highly efficient immunoreaction. Then, BSA blocking solution was applied to block uncoated surface sites and reduce non-specific adsorptions. Target H5N1 viruses were captured by the immobilized antibody, resulting in an impedance change. The change in the impedance caused by AI samples was correlated to the concentration or different titer of H5N1 AI virus present in the solution. Red blood cells (RBCs) were used as biolabels for further specifically amplifying the binding reaction of the antibody–antigen (virus), because they have
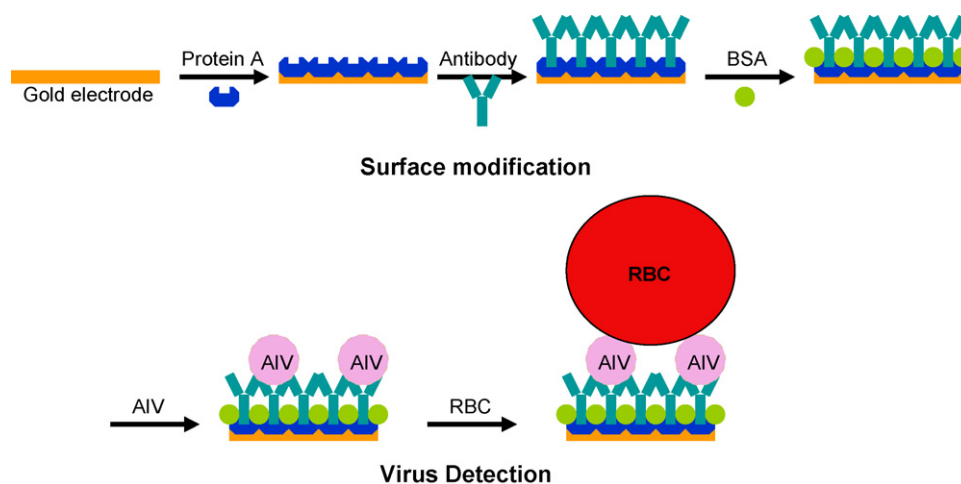

Fig. 2. Schematic representation of the stepwise modification of interdigitated array (IDA) microelectrode, AI virus detection, red blood cell (RBC) amplification.

specific and strong binding receptors for influenza viruses through the surface sialic acid-binding sites on the viruses [34] and they have relatively large diameter (7–12 μm) [35] compared to AI virus (80–120 nm) [36,37]. Although RBCs have common receptors for all subtypes of influenza virus, and do not only bind to subtype H5N1, the specificity of the biosensor was achieved by using the antibodies against H5 subtype. In the test, target H5 subtype was captured by the antibody immobilized on the IDA microelectrode surface, while other non-target subtypes of viruses were washed away. The intention of employing RBCs in this study to form a sandwich assay was to amplify the immunoreaction signal generated by antibody–antigen (virus) binding, since our detection target is nanoscale sized AI virus.

Fig. 3 shows the typical Nyquist diagram of impedance spectra of the bare IDA microelectrode, protein A modification, antibody immobilization, BSA blocking, H5N1 (1×10^5 EID$_{50}$/ml) binding and RBC amplification with [Fe(CN)$_6$]$^{3-/4-}$ as a redox probe in the frequency range from 1 Hz to 1000 kHz. The semicircle portion observed at high frequencies corresponds to the electron transfer limited process, whereas the linear part represents the diffusion limited process. The increased diameters of the semicircle portions on the spectra were observed, and the corresponding electron transfer resistances of bare IDA electrode, protein A, antibodies, BSA, viruses and RBC were 3.4, 28.3, 45.4, 61.7, 71.9, and 82.5 Ω, respectively. The result clearly indicated that the interdigitated array microelectrode based impedance biosensor with specific antibodies was feasible for rapid detection of AI H5N1 virus. Detection time is defined as the time from dropping a sample to obtaining an impedance reading, and in our experiments the detection time was 1 h. The result also demonstrated that RBC (red blood cell) could be used as a biolabel for specific amplification of the binding reaction between antibody and antigen.

The transduction principle of the impedance immunosensor is based on measurements of Faradaic impedance in the presence of [Fe(CN)$_6$]$^{3-/4-}$ as a redox probe [28,29]. The electron transfer of [Fe(CN)$_6$]$^{3-/4-}$ can be blocked by the formation of biolayers on the electrode surface, which results in an increase of the electron
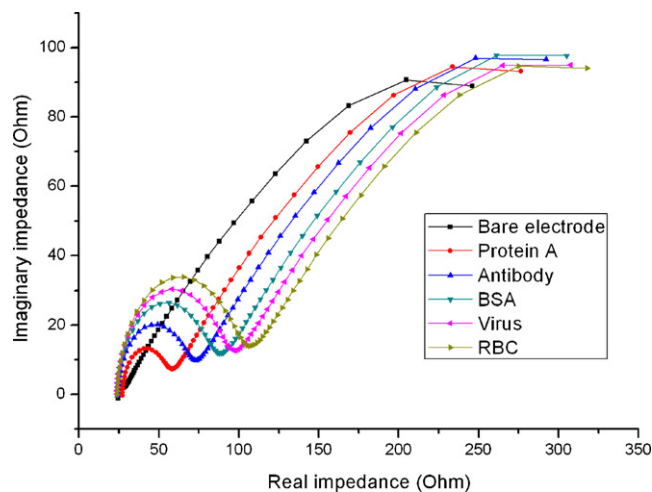
Fig. 3. The typical Nyquist diagram of impedance spectra for the bare IDA microelectrode, protein A modification (0.75 mg/ml), antibody immobilization (0.1 mg/ml), BSA blocking (1%), H5N1 (1×10^5 EID$_{50}$/ml) binding and RBC amplification (0.05%) with 10 mM [Fe(CN)$_6$]$^{3-/4-}$ as a redox probe in the frequency range from 1 Hz to 1000 kHz. Data points from left to right correspond to decreasing frequency. Amplitude voltage is 5 mV.

transfer resistance of [Fe(CN)$_6$]$^{3-/4-}$ probe. Since the number of viruses captured by the immobilized antibodies is related to the titer of target viruses in the solution, the detection of AI virus can be performed by measuring the change of the electron transfer resistance of [Fe(CN)$_6$]$^{3-/4-}$ probe on the IDA microelectrode before and after the AI virus binding using electrochemical impedance spectroscopy.

3.3. Equivalent circuit of the impedance immunosensor system

Electrochemical impedance measurements were obtained following simulation with a general equivalent circuit in the presence
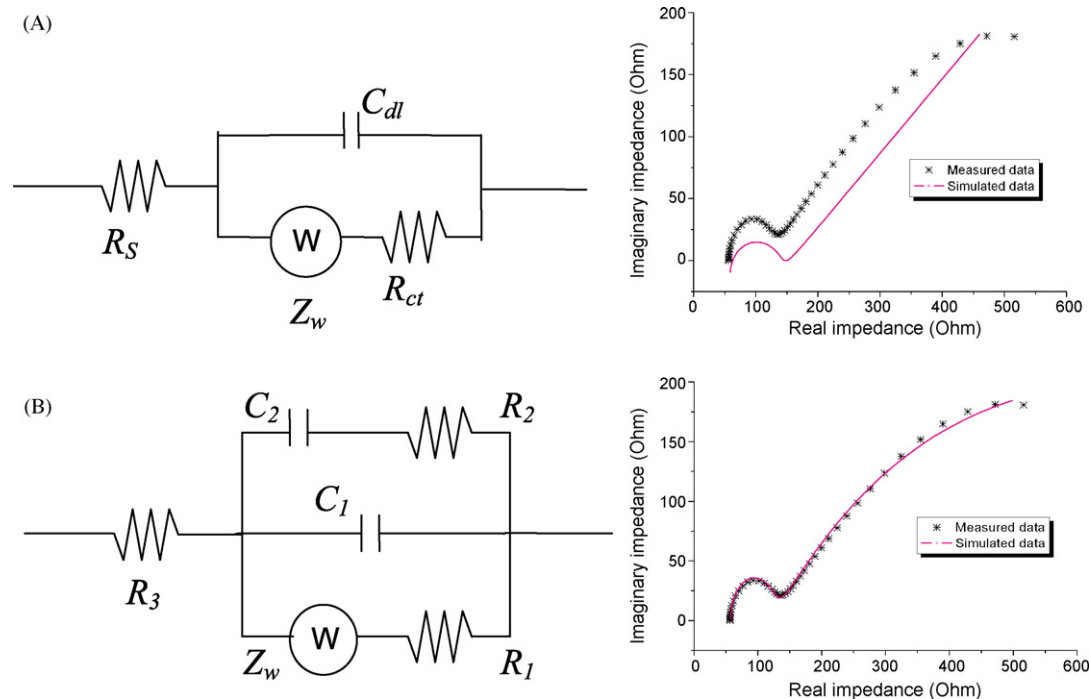
Fig. 4. Equivalent circuits for the impedance spectroscopy measurement with the IDA microelectrode and Nyquist plots of the simulated and measured data. (A) Unmodified model, and (B) modified model.
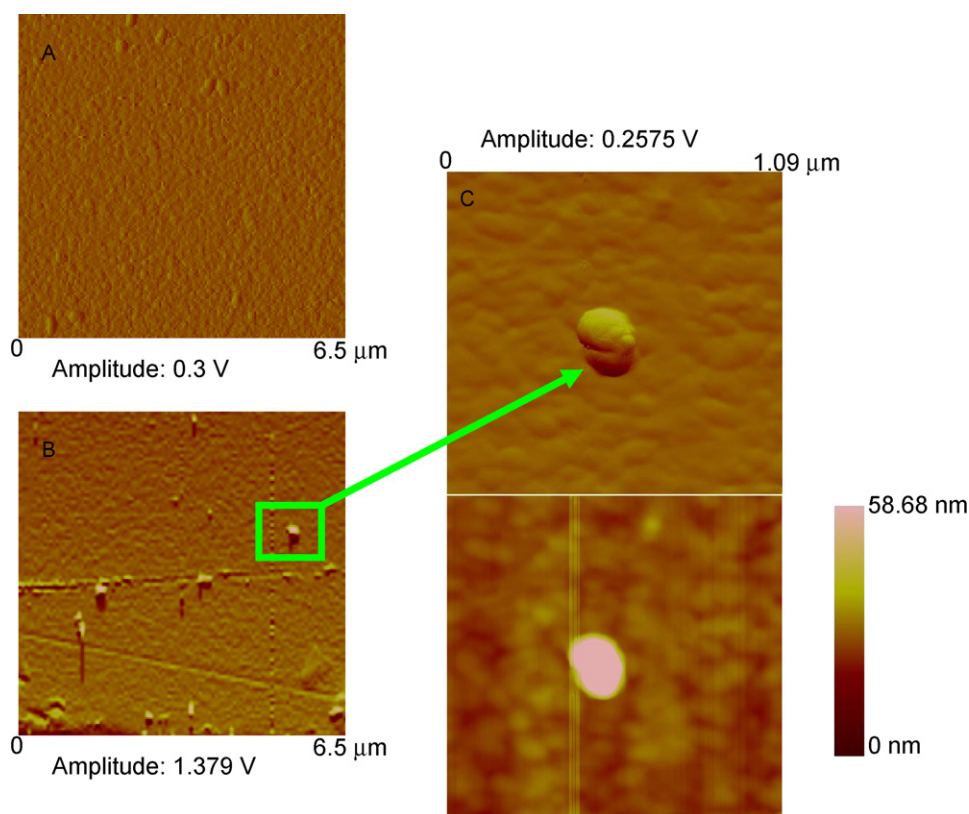
Fig. 5. Top view of AFM images of IDA gold electrode surface. (A) The image before virus binding; (B) the image after virus binding; (C) the image of zooming in one virus particle.

of a redox probe (Randles model shown in Fig. 4A), a model that has been well-documented [28,30–32]. The circuit includes the ohmic resistance of electrolyte solution, R_s, the Warburg impedance, Z_W, which resulted from the diffusion of ions to the electrode interface from the bulk of the electrolyte, the double layer capacitance, C_{dl}, and the electron transfer resistance, R_{ct}. However, slight differences between the simulated data and measured data at low frequencies were observed suggesting that there was an unsatisfied fitting of the equivalent circuit (Fig. 4A). Since the impedance at low frequencies is mostly affected by the double layer capacitor, some modification of the capacitor part in the equivalent circuit was needed.

Fig. 4B shows the modified equivalent circuit. One capacitor (C2) and one resistance (R2) are connected in series, and then another capacitor (C1) is added in parallel. With this modified equivalent circuit, a better fit was achieved with the average error of 0.3% and the maximum error of 4%, comparing with the average error of 0.8% and the maximum error of 9.1% when using the unmodified circuit for the same spectrum. Possibly, for the IDA microelectrode in this study, there were two poles; One of the poles was connected to the test-sense probe and the other was connected to the counter-reference probe. There were also double layer capacitors on both sides of one electrode, that could be modeled by two paralleled connected capacitors in the equivalent circuit. R2 connected to one of the capacitors in series here probably represented another process that might be related to polarization processes or to the electrode roughness.

3.4. Atomic force microscopy (AFM) imaging

Atomic force microscopy (AFM) was used to further confirm the binding of the target AI H5N1 virus onto the antibody immobilized microelectrode surface. The AFM experiments were performed using a Nanoscope III AFM (Digital Instruments, Santa Barbara,

CA). The Digital Instruments Nanoscope Software (V5.30r3.sr3) was used to analyze the AFM images. Fig. 5 shows the top view of AFM images for IDA gold microelectrode surface before (A) and after (B and C) binding of AI H5N1 virus. It can be seen from Fig. 5B that there were several virus particles captured on the IDA microelectrode surface. A single virus was clearly observed (Fig. 5C) with the height of 60 nm, which was lower than the diameter of typical AI viruses (80–120 nm). This was possibly due to the loss of an amount of liquid content inside the virus during killing virus process and/or sample preparation process (e.g. drying).

3.5. Detection of AI H5N1 (inactivated) by an IDA microelectrode based impedance immunosensor

Effective loading of active antibodies is important for the sensitivity of biosensors. The antibodies at different concentrations (0.025, 0.05, 0.1 and 0.5 mg/ml) were investigated to optimize the performance of the biosensor. The corresponding changes of impedance were observed to be 26.6 ± 3.9, 109.8 ± 10.3, 144.2 ± 9.8 and $154.6 \pm 6.9\,\Omega$, respectively, showing the increase of impedance along with the increase of antibody's concentration. The relative steady state was obtained when the concentration of antibodies was ≥ 0.1 mg/ml.

Considering the biosafety issue, only inactivated AI H5N1 virus with titers in the range of 1×10^0–1×10^7 EID$_{50}$/ml (EID$_{50}$: 50% Egg Infective Dose) in buffer solution was tested using the IDA microelectrode based impedance immunosensor. The electron transfer resistance was considered as the signal characterizing the viral detection, and the value of electron transfer resistance was calculated by using the SIM program in IM-6/THALES software and applying the modified equivalent circuit. The results were shown in Fig. 6. Triplicate tests were done for each measured titer, and the Standard Deviations (SDs) shown as error bars in the figure. A linear
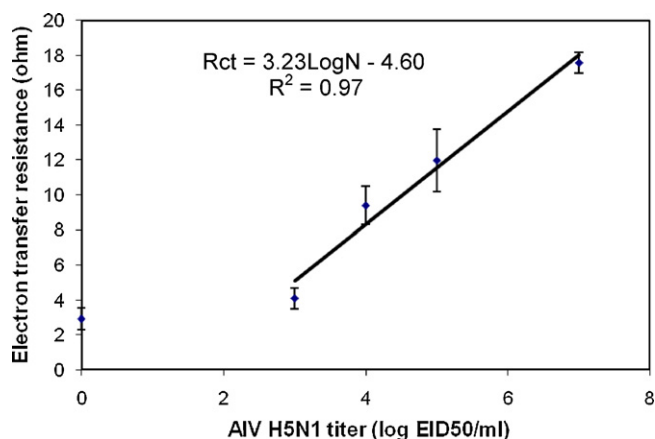
Fig. 6. Linear relationship between the logarithmic value of AI virus titers and the change in electron transfer resistance.

relationship was found in the H5N1 virus titer range between 10^3 and 10^7 EID$_{50}$/ml, and a corresponding equation was described as: $R_{ct} = 3.23 \log N - 4.60$ ($R^2 = 0.97$) where R_{ct} (electron transfer resistance) was expressed in Ω and N (virus titer) in EID$_{50}$/ml. The result showed that the impedance immunosensor could detect the target H5N1 virus at a titer higher than 10^3 EID$_{50}$/ml. The sensitivity and reproducibility of the IDA microelectrode based biosensor could be further improved by system optimization, for example, screening of different medium and their concentration, blocking solution and volume, the concentration of antibody, and more.

3.6. Specificity study

The IDA microelectrode based impedance immunosensor was investigated for its specificity in the detection of AI H5N1 virus by testing non-target RNA viruses such as Newcastle disease virus (NCD) and Infectious Bronchitis disease virus (IB). The signal resulting from these non-specific viruses was negligible, and the corresponding electron transfer resistances of bare IDA electrode, protein A, antibodies, BSA, and NCD/IB viruses were 3.2, 27.9, 44.8, 58.3, and 58.1 Ω, respectively.

The specificity of the immunosensor is mainly dependent upon the antibodies that are immobilized on the electrode surface. Therefore, the combination of monoclonal antibodies against unique epitopes on the H5N1 virus Hemagglutinin (HA) and Neuraminidase (NA) antigens is a logical approach for highly specific detection of AI H5N1, minimizing interferences from other AI virus subtypes.

4. Conclusions

The objective of this study was to develop an IDA microelectrode based impedance immunosensor for a new application of sensitive, specific and rapid detection of AI virus H5N1. It was based on the combination of IDA microelectrode with specific capture antibodies, red blood cell biolabel and impedance measurement. The results demonstrated that the IDA microelectrode based impedance immunosensor was able to detect target AI H5N1 virus (inactivated) within 2 h at a titer higher than 10^3 EID$_{50}$/ml, and a linear range was found up to 10^7 EID$_{50}$/ml. The binding of target AI H5N1 virus onto the antibody-modified IDA microelectrode surface was further confirmed by atomic force microscopy. Chicken RBC's further

amplified the binding reaction of the antibody–antigen (virus) due to its relatively large diameter as well as its specific and strong binding receptor for AI H5N1 virus. Future research on the IDA microelectrode based impedance immunosensor should focus on system parametric optimization and AI virus in poultry swab samples.

References

[1] WHO, http://www.who.int/csr/disease/avian_influenza/country/cases_table_2008_09_10/en/index.html (accessed September 10th, 2008).
[2] D. Stamboulian, P.E. Bonvehi, F.M. Nacinovich, N. Cox, Infect. Dis. Clin. North Am. 14 (2000) 141.
[3] A.C. Boon, A.M. French, D.M. Fleming, M.C. Zambon, J. Med. Virol. 65 (2001) 163.
[4] N.J. Montalto, Am. Fam. Physician 67 (2003) 111.
[5] K.A. Poehling, M.R. Griffin, R.S. Dittus, Y.W. Tang, K. Holland, H. Li, K.M. Edwards, Pediatric 110 (2002) 83.
[6] L.F. Ng, I. Barr, T. Nguyen, S.M. Noor, R.S. Tan, L.V. Agathe, S. Gupta, H. Khalil, T.L. To, S.S. Hassan, E.C. Ren, BMC Infect. Dis. 6 (2006) 40.
[7] Z. Xie, Y.S. Pang, J. Liu, X. Deng, X. Tang, J. Sun, M.I. Khan, Mol. Cell. Probes 20 (3–4) (2006) 245.
[8] M.B. Townsend, E.D. Dawson, M. Mehlmann, J.A. Smagala, D.M. Dankbar, C.L. Moore, C.B. Smith, N.J. Cox, R.D. Kuchta, J. Clin. Microbiol. 44 (8) (2006) 2863.
[9] M. Mehlmann, E.D. Dawson, M.B. Townsend, J.A. Smagala, C.L. Moore, C.B. Smith, N.J. Cox, R.D. Kuchta, K.L. Rowlen, J. Clin. Microbiol. 44 (8) (2006) 2857.
[10] R.H. Liu, M.J. Lodes, T. Nguyen, T. Siuda, M. Slota, H.S. Fuji, A. McShea, Anal. Chem. 78 (12) (2006) 4184.
[11] Y. Amano, Q. Cheng, Anal. Bioanal. Chem. 381 (1) (2005) 156.
[12] D.J. Schofield, N.J. Dimmock, J. Virol. Methods 62 (1) (1996) 33.
[13] A.A. Kortt, E. Nice, L.C. Gruen, Anal. Biochem. 273 (1) (1999) 133.
[14] P. Critchley, N.J. Dimmock, Bioorg. Med. Chem. 12 (10) (2004) 2773.
[15] T. Sato, M. Ishii, F. Ohtake, K. Nagata, T. Terabayashi, Y. Kawanishi, Y. Okahata, Glycoconj. J. 16 (3) (1999) 223.
[16] T. Sato, T. Serizawa, Y. Okahata, Biochim. Biophys. Acta 1285 (1) (1996) 14.
[17] D.H. Charych, J.O. Nagy, W. Spevak, M.D. Bednarski, Science 261 (5121) (1993) 585.
[18] K. Dore, S. Dubus, H.A. Ho, I. Levesque, M. Brunette, G. Corbeil, M. Boissinot, G. Boivin, M.G. bergeron, D. Boudreau, M. Leclerc, J. Am. Chem. Soc. 126 (13) (2004) 4240.
[19] J. Xu, D. Suarez, D.S. Gottfried, Anal. Bioanal. Chem. 389 (2007) 1193.
[20] J. Wang, J.A. Profitt, M.J. Pugia, I.I. Suni, Anal. Chem. 78 (2006) 1769.
[21] S.M. Radke, E.C. Alocilja, Biosens. Bioelectron. 20 (8) (2005) 1662.
[22] J.H. Thomas, S.K. Kim, P.J. Hesketh, H.B. Halsall, W.R. Heineman, Anal. Biochem. 328 (2) (2004) 113.
[23] M.S. Harrington, L.B. Anderson, Anal. Chem. 62 (1990) 546.
[24] J.L. Sever, G.A. Castellano, W. Peron, R.J. Huebner, F. Wolman, J. Lab. Clin. Med. 64 (1964) 983.
[25] M.A. Goldstein, N.M. Tauraso, Appl. Microbiol. 19 (2) (1970) 290.
[26] R. Wang, C. Ruan, D. Kanayeva, K. Lassiter, Y. Li, Nano Lett. 8 (9) (2008) 2625.
[27] A. Cemalettin, Immunol. Lett. 85 (2003) 231.
[28] C. Ruan, L. Yang, Y. Li, Anal. Chem. 74 (2002) 4814.
[29] L. Yang, Y. Li, G. Erf, Anal. Chem. 76 (2004) 1107.
[30] A.J. Bard, L.R. Faulkner, Electrochemical Methods: Fundamentals and Applications, Wiley, New York, 1980.
[31] L. Yang, Y. Li, Biosens. Bioelectron. 20 (2005) 1407.
[32] H. Tang, J. Chen, L. Nie, Y. Kuang, S. Yao, Biosens. Bioelectron. 22 (6) (2007) 1061.
[33] Y. Ha, D. Stevens, J. Skehel, D. Wiley, EMBO J. 21 (5) (2002) 865.
[34] L. Glaser, J. Stevens, D. Zamarin, I.A. Wilson, A. Garcia-Sastre, T.M. Tumpey, C.F. Basler, J.K. Taubenberger, P. Palese, J. Virol. 79 (17) (2005) 11533.
[35] Cell Size Database, the subset of Animal Genome Size Database, available at http://www.genomesize.com/cellsize/birds.htm.
[36] B.R. Murphy, R.G. Webster, Orthomyxoviruses, 1996, pp. 1397–1445. In Fields Virology, 3rd ed., B.N. Fields, D.M. Knipe and P.M. Howley (eds.), Lippincott-Raven, Philadelphia, PA.
[37] R.A. Lamb, R.M. Krug, Orthomyxoviridae, 2001, pp. 1487–1531 (Chapter 46). In Field Virology, D.M. Knipe, P.M. Howley (eds.), Lippincott William & Wilkins Publisher, Philadelphia, PA.

Determination of indole-3-acetic acid and indole-3-butyric acid in mung bean sprouts using high performance liquid chromatography with immobilized Ru(bpy)$_3$$^{2+}$–KMnO$_4$ chemiluminescence detection

Zhijun Xi, Zhujun Zhang *, Yonghua Sun, Zuolong Shi, Wei Tian

College of Chemistry and Materials Science, Shaanxi Normal University, Xi'an 710062, China

ABSTRACT

A novel method for determination of indole-3-acetic acid (IAA) and indole-3-butyric acid (IBA) in an extract from mung bean sprouts using high performance liquid chromatography (HPLC) with chemiluminescence (CL) detection is described. The method is based on the CL reaction of auxin (indole-3-acetic acid and indole-3-butyric acid) with acidic potassium permanganate (KMnO$_4$) and tris(2,2′-bipyridyl)ruthenium(II), which was immobilized on the cationic ion-exchange resin. The chromatographic separation was performed on a Nucleosil RP-C18 column (i.d.: 250 mm × 4.6 mm, particle size: 5 μm, pore size: 100) with an isocratic mobile phase consisting of methanol–water–acetic acid (45:55:1, v/v/v). At a flow rate of 1.0 mL min^{-1}, the total run time was 20 min. Under the optimal conditions, the linear ranges were 5.0×10^{-8} to 5.0×10^{-6} g mL^{-1} and 5.0×10^{-7} to 1.0×10^{-5} g mL^{-1} for IAA and IBA, respectively. The detection limits were 2.0×10^{-8} g mL^{-1} and 2.0×10^{-7} g mL^{-1} for IAA and IBA, respectively. The relative standard deviation (RSD) of intra-day were 3.1% and 2.3% (n = 11) for 2×10^{-6} g mL^{-1} IAA and 2×10^{-6} g mL^{-1} IBA; The relative standard deviations of inter-day precision were 6.9% and 4.9% for 2×10^{-6} g mL^{-1} IAA and 2×10^{-6} g mL^{-1} IBA. The proposed method had been successfully applied to the determination of auxin in mung bean sprouts.

1. Introduction

Phytohormones are regulators produced by plants themselves, which control the physiological processes. As a minor component of the metabolome, phytohormones are of particular significance given their role in the regulation of germination, growth, reproduction and the protective responses of plants against stress [1].

Auxins are a class of phytohormones which are involved in many aspects of growth and development of plants. In recent years it has become more clear that besides the 'classical' auxin indole-3-acetic acid (IAA) (Fig. 1A) and other auxin-like substances exist in plants such as indole-3-butyric acid (IBA) (Fig. 1B). The indole-3-acetic acid was the first plant hormone that was used to stimulate rooting of cuttings. IAA is known to regulate processes such as division, elongation and differentiation of cells, too. It was discovered that a second auxin indole-3-butyric acid also promoted rooting and was even more effective than IAA [2,3]. IBA is now used commercially worldwide to root many plant species [4]. The greater ability of IBA to promote adventitious root formation compared with IAA has been attributed to the higher stability of IBA versus IAA both

in solution and in plant tissue [5]. It has been found that IBA also occurs naturally in a number of plant species from maize (*zea mays*) and pea (*pisum sativum*) toarabidopsis [5–7]. Furthermore, some microorganisms such as *azospirillum brasilense* UAP 154 found in the soil are able to produce IBA [8].

Auxins are present in natural plant at the ng g^{-1} level and the difficulties associated with the analysis of extracts are severe because it is essential to distinguish the compound of interest. So it is very important to develop a simple and reliable separation and enrichment procedures, and a rapid and sensitive detection means for the accurate determination of the auxin (including IAA and IBA). Several ordinary methods for the determination of IAA or IBA have been described such as high performance liquid chromatography (HPLC) with different detectors [9–12], liquid chromatography–electrospray tandem mass spectrometry [13,14], capillary electrophoresis [15,16], gas chromatography–mass spectrometry [17,8], etc. Although these methods have been successfully applied to analysis of auxin in a variety of plants, they suffer from tedious procedure, time consumption or high cost. Therefore, the development of a simple, rapid, inexpensive and sensitive analytical method for determination auxin in complex matrices was still significative.

In recent years, chemiluminescence (CL) as a detection technique of high performance liquid chromatography is very attractive
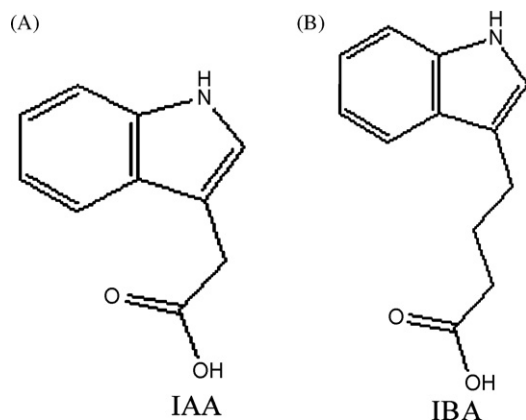

Fig. 1. Chemical structure of auxin.

due to higher sensitivity, wide linear dynamic ranges and simpler instrumentation [18,19]. The advance of CL detection has greatly catalyzed the growth and popularity of HPLC–CL application, and made trace analysis possible owing to its capability of measuring picogram or femtogram quantities of compounds in the column eluate. Al-Arfaj and Townshend had devised flow injection chemiluminescence methods for determination of metoclopramide hydrochloride and cephalosporins using tris(2,2′-bipyridyl)ruthenium(II)–potassium permanganate system [20,21]. However, there is no sample separation and all of FIA-CL reagents are preformed in solution, these methods face two problems: sample disturbance and spend some expensive luminescence reagents. For the first problem, high performance liquid chromatography has been used. In order to overcome the other one, the immobilized $Ru(bpy)_3^{2+}$ have received much attention and appeared in the literature in recent years including Langmuir–Blodgett [22,23], self-assembled techniques [24,25], Nafion films [26,27], ion-exchange resin [28] and sol–gel [29,30] techniques. However, to the best of our knowledge, no report for the simultaneous separation and determination of indole-3-acetic acid and indole-3-butyric acid using high performance liquid chromatography with immobilized reagent chemiluminescence detection has been found.

In this paper, a new kind of HPLC–CL method by immobilizing $Ru(bpy)_3^{2+}$ on resin for the simultaneous separation and determination indole-3-acetic acid and indole-3-butyric acid was developed. A strong chemiluminescence was observed during the reaction of auxin with tris (2,2′-bipyridyl)ruthenium(II) $(Ru(bpy)_3^{2+})$ in resin and potassium permanganate $(KMnO_4)$ under acidic conditions. The new CL detection need not deliver $Ru(bpy)_3^{2+}$ to CL reaction zone, would cut the consumption of expensive reagent, and would not require addition tubing, mixing chamber and pump. Compared with the use of continuously delivered $Ru(bpy)_3^{2+}$ reagents to CL reaction zone, present method with immobilized reagent are advantageous not only expensive reagent saving and resource considerations but also for operational convenience and instrumental simplification. Because the relative CL intensity decreased only from 100% to 97% during 6 months, the $Ru(bpy)_3^{2+}$ immobilized on cationic ion-exchange resin is stable, which can be used at least for 6 months when it reacts with the dilute $KMnO_4$ solution. The proposed method has been applied to determine auxin in mung bean sprouts with satisfactory results.

2. Experimental

2.1. Materials and reagents

Methanol was of HPLC grade (Tianjin Kermel Chemical Reagent Co., Ltd., China). All other chemicals were analytical-reagent grade

and solutions were prepared with distilled and deionised water.

IAA and IBA were purchased from the Alfa-aesar Company (Ward Hill, MA, USA). Stock standard solutions of IAA and IBA were prepared in methanol at $1 \, mg \, mL^{-1}$. The stock solutions were diluted with the mobile phase before use.

Potassium permanganate and sulfuric acid were obtained from Xi'an Chemical Reagent Factory (Xi'an, China). A stock standard solution of $KMnO_4$ $0.01 \, mol \, L^{-1}$ was prepared daily by dissolving 158.0 mg of $KMnO_4$ in 100 mL of water; a sulfuric acid stock solution $(5.0 \, mol \, L^{-1})$ was also prepared. Tris(2,2′-bipyridyl)ruthenium(II) $(Ru(bpy)_3^{2+})$ was purchased from the Alfa-aesar Company (Ward Hill, MA, USA). 732-type cationic ion-exchange resin was a product of Xi'an resin Company (Xi'an, China).

The HPLC mobile phases consisted of methanol–water–acetic acid (45:55:1, v/v/v). They were prepared fresh daily, filtered through a 0.22 μm membrane filter (Xinya, Shanghai, China), and then degassed prior to use.

2.2. Apparatus

The experimental setup for the HPLC–CL is shown in Fig. 2. High performance liquid chromatography was a LC-6A (Shimadzu, Tokyo, Japan) liquid chromatography equipped with a Rheodyne 7725i syringe-loading sample injector valve (20 μL-loop Cotati, CA, USA) and a Nucleosil C18 column (i.d.: 250 mm × 4.6 mm, particle size: 5 μm, pore size: 100 Å, Macherey-Nagel, Germany). Batch model IFFM-D luminescence analyzer (Ruimai Company, Xi'an, China) was employed to study the characteristics of the CL reaction. The CL detection was conducted on a flow injection chemiluminescence system comprising of a peristaltic pump (Ruimai Company, Xi'an, China), PTFE tubing (0.8 mm i.d.) which was used as connection material in the flow system and cationic ion-exchange column. The change of CL signal in the cationic ion-exchange column was detected and recorded with a computerized IFFM-D luminescence analyzer. Data acquisition and treatment were performed with IFFM software running under Windows XP.

2.3. Sample preparation procedures

Sample treatment was performed as follows. Auxins were extracted as described by Lu and co-workers [31] with some modifications. Briefly, Seeds of mung bean were soaked in tap water for 6 h and germinated in trays in a growth chamber. Then refresh the water periodically everyday. After 5 days, accurately weighed shoot apices were collected and ground to powder, hydrogenized in 5 mL 80% (v/v) aqueous methanol using a high-speed blender, and then maintained overnight at 4 °C in darkness. The extract was centrifuged at 4 °C (5000 rpm for 10 min). The supernatant was collected, and the residue was further extracted with cold 80% (v/v) aqueous methanol. A 1 mL extract was dried by blowing with N_2 gas, and then dissolved in 200 μL Na_2HPO_4 (pH 9.2) buffer. The solution was extracted three times with equal volume of ethyl acetate. It was further extracted with ethyl acetate, after adjusting solution buffer acidity to pH 2.5. All aliquots of ethyl acetate phase were collected, dried with N_2 gas, and finally dissolved in 1 mL mobile phase before use.

2.4. Cationic ion-exchange column preparation

732-type resin was regenerated with $2 \, mol \, L^{-1}$ HCl. Then washed with NaCl and H_2O. A 2.0 mL of resin was added into a 5 mL of $1.0 \, mmol \, L^{-1}$ $Ru(bpy)_3^{2+}$ solution. After 6 h, a 0.3 mL of resin was filled into the glass tube (20 mm × 3.0 mm i.d.), and some glass wool was inserted at both ends to prevent loss of resin.

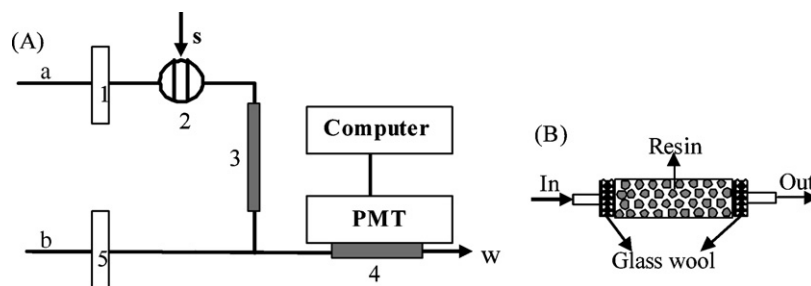**Fig. 2.** (A) Schematic diagram of HPLC–CL detector of auxin: (a) Mobile phase; (b) KMnO$_4$ + H$_2$SO$_4$ solution; (1) Reciprocating pump; (2) injector; (3) HPLC column; (4) cationic ion-exchange column; (5) peristaltic pump; (S) sample solution; (W) waste; PMT, photomultiplier tube. (B) The structure of the cationic ion-exchange column.

2.5. Procedure

Flow lines were inserted into the acidic potassium permanganate solution and mobile phase, respectively. The mobile phase was pumped through the column at a flow rate of 1.0 mL min^{-1}. The 20 μL standard solution or sample was injected into the mobile phase. This stream mixed with acidic potassium permanganate at a mixing-tee and then flowed into cationic ion-exchange column, which was placed close to the window of photomultiplier tube (Fig. 2), producing CL emission. The concentration of sample was quantified by the relative CL intensity I, $\Delta I = I_S - I_0$, where I_S is the CL intensity of auxin, and I_0 is the CL intensity of the blank.

3. Results and discussion

3.1. Optimization of the CL system

To obtain the maximal relative CL intensity, the effects of the concentration of sulfuric acid and potassium permanganate were investigated. The effects of flow rate on the relative CL intensities of auxin were also studied.

The effect of the type and concentration of the acidic medium, for example HCl, HNO$_3$, PPA (polyphosphoric acid), H$_3$PO$_4$ and H$_2$SO$_4$ on CL intensity was investigated. The results showed that sulfuric acid was a more suitable medium for all analytes since it gave the strongest light intensity and the highest signal-to-noise ratio (S/N). The effect of sulfuric acid concentration in the range of 0.06–1.2 mol L^{-1} was further studied and the results are shown in Fig. 3. Sulfuric acid solution 0.6 mol L^{-1} was chosen as the optimum sulfuric concentration in KMnO$_4$ solution.

The concentration of KMnO$_4$ had a very important effect on the relative CL intensity for the determination of auxin. The effect of

KMnO$_4$ concentration on the relative CL intensities was investigated from 8.0×10^{-6} mol L^{-1} to 8.0×10^{-4} mol L^{-1} and the results are in Fig. 4. When the concentration of KMnO$_4$ was lower or higher than 6.0×10^{-5} mol L^{-1}, the relative CL intensity for all the tested auxin decreased. Therefore, the optimum concentration of KMnO$_4$ was 6.0×10^{-5} mol L^{-1}.

The flow rates of luminescence solutions are very important to CL reactions and should be regulated. Under the optimum conditions described above, the effects of flow rate on the relative CL intensities of auxin were studied over the range 0.8–2.5 mL min^{-1} and the results are in Fig. 5. The CL intensities for auxin increased
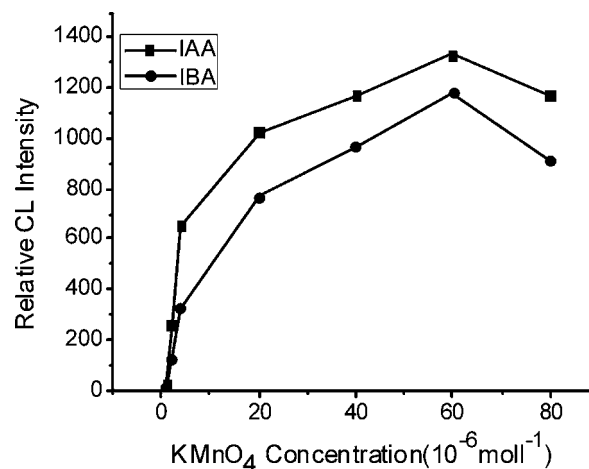

Fig. 4. Effect of KMnO$_4$ concentration on CL signal, H$_2$SO$_4$: 0.6 mol L^{-1}; flow rate: 2.0 mL min^{-1}.

Fig. 3. Effect of sulfuric acid concentration on CL signal, KMnO$_4$: 1.0×10^{-4} mol L^{-1}; flow rate: 2.0 mL min^{-1}.
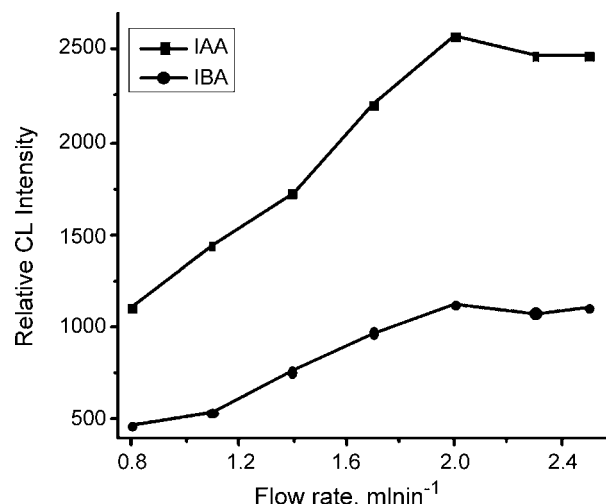

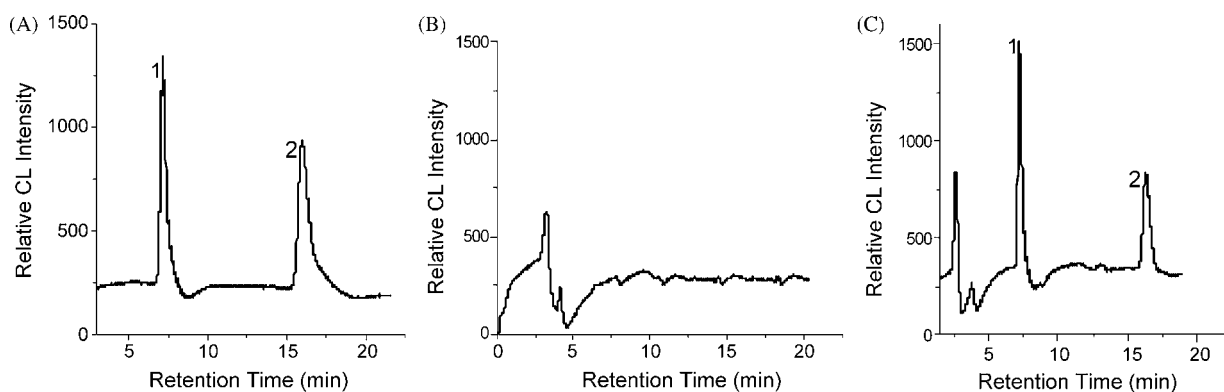**Fig. 5.** Flow rate on the relative CL intensity for the HPLC–CL detection.

Fig. 6. Typical chromatograms obtained with (A) a standard mixture solution of auxin; (B) a blank auxin sample; (C) auxin in mung bean sprouts. Peaks: (1) IAA (7.5 min); (2) IBA (16.5 min).

with increasing flow rate up to 2.0 mL min^{-1}. Above that value, the CL intensities decreased. Therefore, a flow rate of 2.0 mL min^{-1} was maintained throughout the current investigation.

3.2. Optimization of HPLC system

As for HPLC–CL detection, the composition of the mobile phase and its flow rate were optimized as a compromise between the resolution and the CL intensity. Methanol and acetonitrile are often used as mobile phases, so acetonitrile and methanol have been examined as the organic part of the mobile phase in our experiment. We tested the CL behavior of some mobile phases and found that although isocratic elution with acetonitrile–acetic acid–water or methanol–acetic acid–water enabled almost complete separation of auxin, use of a mobile phase containing acetonitrile greatly quenched the CL signal and produced serious background noise whereas methanol resulted in lower background emission and the baseline was fairly smooth. Methanol was therefore chosen as the organic part mobile phase for further study. The concentration of methanol in the mobile phase was initially optimized by varying the methanol–water composition in the range of 30–70% (v/v) methanol at a constant flow rate of 1.0 mL min^{-1}; 45% methanol proved to enable the best separation. In order to improve the peak shape and separate completely these compounds, water was then replaced with aqueous acetic acid. The effect of mobile phase flow rate was also tested. By use of the optimized conditions methanol–water–acetic acid (45:55:1, v/v/v) as mobile phase at a flow rate of 1.0 mL min^{-1} the maximum CL intensities of the auxin and good resolution could be achieved.

Under these optimum conditions, HPLC was used to separate auxin in mung bean sprouts. Fig. 6A shows an HPLC–CL chromatogram obtained from a standard mixture solution of auxin; Fig. 6B shows the chromatogram obtained from a blank auxin sample and Fig. 6C shows the chromatogram obtained from auxin in mung bean sprouts. From Fig. 6, it can be seen that auxin can be well separated without the interference of other compounds in mung bean sprouts. The retention times of IAA and IBA were 7.5 min and 16.5 min, respectively. Peak identification was carried out by the standard addition method and the retention time of auxin. These chromatograms revealed that the application of HPLC–CL to the determination of auxin in mung bean sprouts was possible.

3.3. Method validation

In the present work, the HPLC–CL method for the determination of auxin was validated by determining their performance characteristics regarding linearity, limit of detection (LOD), limits of quantification (LOQ) and precision. To test the CL response linearity, a series of auxin standard solutions at concentrations ranging from 1.0×10^{-8} g mL^{-1} to 1.0×10^{-5} g mL^{-1} for IAA, 1.0×10^{-7} g mL^{-1} to 1.0×10^{-4} g mL^{-1} for IBA were determined. Linear regression analysis of the results are summarized in Table 1. From these calibration curves, the limits of detection at a signal-to-noise of three were 0.02 μg mL^{-1} for IAA, 0.2 μg mL^{-1} for IBA and the limits of quantification at a signal-to-noise of 10 were 0.05 μg mL^{-1} for IAA, 0.5 μg mL^{-1} for IBA, respectively. From the above result, it indicates that the proposed method has lower detection limit than those of the methods HPLC–MS and HPLC with fluorescence detection [9,10]. Moreover, compare with HPLC–MS, the analytical instruments of the method are cheaper and more simple; the method do not need to derive in comparison to HPLC with fluorescence detection.

The intra-day precision was tested with 11 repeated injections of two sample solutions containing auxin at the concentration level of 1 μg mL^{-1}. The relative standard deviations (RSDs) were always less than 3.1%. The inter-day precision of the proposed method was studied by analyzing the identical sample (auxin at 1 μg mL^{-1}), injected six times every day, on five consecutive days. The relative standard deviations were 6.9% for IAA and 4.9% for IBA, respectively.

In order to check the influence of matrix element, Fig. 6B was established using the extracted samples obtained from the maturation of mung bean sprouts. By comparing Fig. 6B with Fig. 6C, no significant interference existed in the extract of mung bean sprouts after sample treatment and peaks of IAA and IBA were well resolved. Therefore, the present method does offer an alternative, sensitive, and simple approach to the simultaneous detection of IAA and IBA by HPLC.

3.4. Application of the method

Following the procedure for determination of auxin detailed in Section 2, the proposed method was applied to determinate auxin in mung bean sprouts. The typical chromatograms with CL detection obtained with a standard mixture of auxin and auxin in mung bean

Table 1
Calibration curves, detection limits and precisions of auxin.

Compounds	Linear range (μg mL^{-1})	LOD (μg mL^{-1})	LOQ (μg mL^{-1})	Calibration equation (μg mL^{-1})	Correlation coefficient	Precision (RSD)	
						Intra-day (%)	Inter-day (%)
IAA	0.05–5	0.02	0.05	$I = 223c + 48.4$	0.9976	3.1	6.9
IBA	0.5–10	0.2	0.5	$I = 62.9c + 26.0$	0.9963	2.3	4.9

Table 2
Determination of IAA and IBA in mung bean sprout.

Samples	Auxin	Detected (μg g^{-1})	Added (μg g^{-1})	Found (μg g^{-1})	Recovery (%)	RSD (%)
1	IAA	0.91	0.20	1.12	105.0	4.8
	IBA	0.59	0.20	0.78	95.0	3.2
2	IAA	0.83	0.40	1.24	102.5	4.3
	IBA	0.61	0.40	1.01	100.0	2.0
3	IAA	0.76	0.80	1.52	95.0	3.9
	IBA	0.57	0.80	1.35	97.5	3.3

Fig. 7. The CL spectra curve (A) KMnO$_4$–Ru(bpy)$_3$$^{2+}$–IAA; (B) KMnO$_4$–Ru(bpy)$_3$$^{2+}$–IBA.

sprouts are shown in Fig. 5. From Fig. 5 it can be seen that IAA and IBA were simultaneously detected in mung bean sprouts. The auxin content of mung bean sprout were calculated by the calibration formula. The results of auxin contents in mung bean sprout were shown in Table 2.

In order to evaluate the validity of the proposed method for the determination of auxin in mung bean sprouts, a recovery experiment was carried out by adding the known amounts of auxin into the extracted samples, and analyzed by using the described method. The mean recovery percentages and the RSDs of the samples were showed in Table 2. The RSDs of the quantitative results were below 4.8% with triplicate measurements. It could be concluded from above experiments, the proposed HPLC–CL approach could be used for the sensitive quantification for auxin in mung bean sprouts.

3.5. Possible CL reaction mechanism

It has been reported that the CL method containing Ru(bpy)$_3$$^{2+}$ is a particularly sensitive detection system for compounds which contain a secondary or tertiary amine functionality [32]. The studied auxin contained the secondary amine groups, thus we assumed that the proposed reaction mechanism is presumably similar to that reported previously for amine determination utilizing its electrogenerated CL reaction with Ru(bpy)$_3$$^{2+}$ [32,33]. The proposed mechanism involves the oxidation of Ru(bpy)$_3$$^{2+}$ and the secondary amine present on auxin by potassium permanganate. The oxidation product of amine undergoes deprotonation to form a radical. This reduces the Ru(bpy)$_3$$^{3+}$ to the excited state that subsequently emits light. The CL spectrum generated from the reaction was examined by using a series of interference filters to obtain an idea about the reaction product and is shown in Fig. 7. From Fig. 7, it can been seen that the peak of chemiluminescence spectrum is at 630 nm, which

is very similar to that of Ru(bipy)$_3$$^{2+}$ chemiluminescence, so it can be concluded that the above assumption. And the possible reaction mechanism is suggested as following:

$$Ru(bpy)_3{}^{2+} + MnO_4{}^- + 8H^+ \rightarrow Ru(bpy)_3{}^{3+} + Mn^{2+} + 4H_2O \quad (1)$$

$$Auxin + MnO_4{}^- + 8H^+ \rightarrow auxin*^+ + Mn^{2+} + 4H_2O \quad (2)$$

$$Auxin*^+ \rightarrow auxin* + H^+ \quad (3)$$

$$Ru(bpy)_3{}^{3+} + auxin* + H_2O \rightarrow [Ru(bpy)_3{}^{2+}]*$$
$$+ auxin fragment + H^+ \quad (4)$$

$$[Ru(bipy)_3{}^{2+}]* \rightarrow Ru(bipy)_3{}^{2+} + h\nu(630\,nm) \quad (5)$$
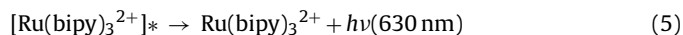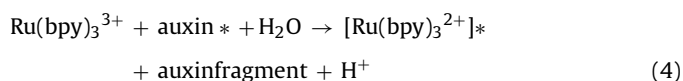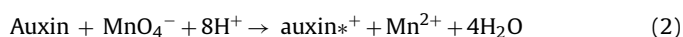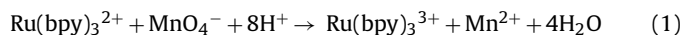
4. Conclusion

This is a first report for the simultaneous and sensitive detection of IAA and IBA in mung bean sprouts using reversed-phase high performance liquid chromatography with immobilized reagent chemiluminescence detection. In this method for determination IAA and IBA, luminescence reagent Ru(bpy)$_3$$^{2+}$ was immobilized on cationic ion-exchange resin, which made this method very simple, reagent saving and sensitive. Moreover, the CL reaction is also highly compatible with the mobile phase used for HPLC. The method can be used to determine auxin in mung bean sprouts and there is no interference from other compounds in this sample.

References

[1] P.J. Davies, in: P.J. Davies (Ed.), Plant Hormones: Physiology, Biochemistry and Molecular Biology, second ed., Kluwer, Dordrecht, Netherlands, 1995, pp. 1–12.
[2] E. Epstein, J. Ludwig-Müller, Physiol. Plant. 88 (1993) 382–389.
[3] J. Riov, S.F. Yang, Plant Growth Regul. 8 (1989) 131–141.
[4] H.T. Hartmann, D.E. Kester, F.T. Davies, Plant Propagation: Principles and Practices, Prentice-Hall, Englewood Cliffs, NJ, 1990, p. 246.
[5] A.C. Nordstrom, F.A. Jacobs, L. Eliasson, Plant Physiol. 96 (1991) 856–861.
[6] J. Ludwig-Muller, E. Epstein, J. Plant Growth Regul. 14 (1994) 7–14.
[7] J. Ludwig-Muller, J. Plant Growth Regul. 32 (2000) 219–230.
[8] L.J. Martinez-Morales, L. Soto-Urzua, B.E. Baca, J.A. Sanchez-Ahedo, FEMS Microbiol. Lett. 228 (2003) 167–173.
[9] F. García Sánchez, A. Navas Díaz, A. García Pareja, J. Chromatogr. A 723 (1996) 227–233.
[10] Z. Ma, L. Ge, A.S.Y. Lee, J.W.H. Yong, S.N. Tan, E.S. Ong, Anal. Chim. Acta 610 (2008) 274–281.
[11] F. Mattivi, U. Vrhovšek, G. Versini, J. Chromatogr. A 855 (1999) 227–235.
[12] G. Absalan, M. Akhond, L. Sheikhian, Talanta 77 (2008) 407–411.
[13] X. Pan, R. Welti, X. Wang, Phytochemistry 69 (2008) 1773–1781.
[14] S.J. Hou, J. Zhu, M.Y. Ding, G.H. Lv, Talanta 76 (2008) 798–802.
[15] X.B. Yin, D.Y. Liu, J. Chromatogr. A 1212 (2008) 130–136.
[16] J. Olsson, K. Claeson, B. Karlberg, A.C. Nordström, J. Chromatogr. A 824 (1998) 231–239.
[17] E. Fallik, Y. Okon, E. Epstein, A. Goldman, M. Fischer, Soil Biol. Biochem. 21 (1989) 147–153.
[18] M. Yamaguchi, H. Yoshida, H. Nohta, J. Chromatogr. A 950 (2002) 1–19.

[19] Y. Lv, S. Zhang, G. Liu, M. Huang, X. Zhang, Anal. Chem. 77 (2005) 1518–1525.
[20] N.A. Al-Arfaj, Talanta 62 (2004) 255–263.
[21] C. Thongpoon, B. Liawruangrath, S. Liawruangrath, R.A. Wheatley, A. Townshend, Anal. Chim. Acta 553 (2005) 123–133.
[22] X. Zhang, A.J. Bard, J. Phys. Chem. 92 (1988) 5566–5569.
[23] C.J. Miller, P. McCord, A.J. Bard, Langmuir 7 (1991) 2781–2787.
[24] Y.S. Obeng, A.J. Bard, Langmuir 7 (1991) 195–201.
[25] Y. Sato, K. Uosaki, J. Electroanal. Chem. 384 (1995) 57–66.
[26] L.L. Shultz, J.S. Stoyanoff, T.A. Nieman, Anal. Chem. 68 (1996) 349–360.
[27] T.M. Downey, T.A. Nieman, Anal. Chem. 64 (1992) 261–268.
[28] J.M. Lin, F. Qu, M. Yamada, Anal. Bioanal. Chem. 374 (2002) 1159–1164.
[29] M.M. Collinson, B. Novak, S.A. Martin, J.S. Taussig, Anal. Chem. 72 (2000) 2914–2918.
[30] H.Y. Wang, G.B. Xu, S.J. Dong, Analyst 126 (2001) 1095–1099.
[31] B.F. Liu, X.H. Zhong, Y.T. Lu, J. Chromatogr. A 945 (2002) 257–265.
[32] G.M. Greenway, S.J.L. Dolman, Analyst 124 (1999) 759–762.
[33] A.W. Knight, G.M. Greenway, E.D. Chesmore, Anal. Proc. 32 (1995) 125–127.

Label-free aptamer-based chemiluminescence detection of adenosine

Xiluan Yan[a], Zhijuan Cao[a], Masaaki Kai[b], Jianzhong Lu[a],*

[a] *School of Pharmacy, Fudan University, 826 Zhangheng Road, Shanghai 201203, China*
[b] *Faculty of Pharmaceutical Sciences, Graduate School of Biomedical Sciences, Nagasaki University, 1-14 Bunkyo-Machi, Nagasaki 852-8521, Japan*

ARTICLE INFO

ABSTRACT

We have developed a novel sensitive chemiluminescence (CL) aptasensor for the target assay as exemplified by using adenosine as a model target. In this work, we have demonstrated the signaling mechanism to make detection based on magnetic separation and 3,4,5-trimethoxyl-phenylglyoxal (TMPG), a special CL reagent as the signaling molecule, which reacts instantaneously with guanine nucleobases (G) of adenosine-binding aptamer strands. Briefly, amino-functioned capture DNA sequences are immobilized on the surface of carboxyl-modified magnetic beads, and then hybridized with label-free G-rich (including 15 guanine nucleobases) adenosine-binding aptamer strands to form our CL aptasensor. Upon the introduction of adenosine, the aptamer on the surface of magnetic beads is triggered to make structure switching to the formation of the adenosine/aptamer complex. Consequently, G-rich aptamer strands are forced to dissociate from magnetic beads sensing interface, resulting in a decrease of CL signal. The decrement of peak signal is proportional to the amount of adenosine. The effects of the amounts of capture DNA, aptamer, magnetic beads are investigated and optimized. It was found that the CL intensity had a linear dependency on the concentration of adenosine in the range of 4×10^{-7} to 1×10^{-5} M. With a low detection limit of 8×10^{-8} M and simplicity in CL detection, this novel technique will offer a great promise for future target/aptamer analysis.

© 2009 Elsevier B.V. All rights reserved.

1. Introduction

DNA aptamers are synthetic single-strand nucleic acids with high specificity and affinity to some given targets ranging from small molecules to large proteins and even cells [1]. Three-dimensional structures have been determined for a number of aptamers in complex with their cognate ligands. Structures of aptamer complexes reveal the key molecular interactions conferring specificity to the aptamer–ligand association, including the precise stacking of flat moieties, specific hydrogen bonding, and molecular shape complementarity [1]. Aptamers have been demonstrated to have advantages over antibodies with regard to chemical stability, readily availability, simple modifiability, and high flexibility in biosensor design for analyte detection [2–8]. In the last decade, aptamers have been widely reported as highly promising recognition probes for disease diagnosis, new drug selection, protein analysis, biosensor and molecular switch development, etc. Oncoprotein platelet-derived growth factor, cocaine and IgE, for example, can be sensitively determined by fluorescence anisotropy, electrogenerated chemiluminescence (CL) and affinity probe capillary electrophoresis, respectively [9–11]. In addi-

tion, aptamer-based thrombin assay was also performed by using electrogenerated CL based on $Ru(bpy)_3{}^{2+}$-doped silica nanoparticle aptasensor *via* target protein-induced strand displacement [12].

The above mentioned advances in developing aptasensors are impressive. However, some disadvantages should be concerned. Most of these existing methods need to label the aptamers or capture probes or the targets. Such a labeling process would not only make experiments relatively more complex and expensive, but also affect the binding affinity between the targets and their aptamers to a greater or lesser degree [13,14]. Many researchers have been trying to construct a protocol without the need of complex labeling process. Consequently, some label-free detection methods of small molecules have been successfully developed [15], such as the detection of adenosine based on electrochemical impedance spectroscopy [16].

CL has been exploited for a wide range of applications in various fields owing to its extremely high sensitivity along with its other advantages, such as simple instrumentation, wide calibration ranges and suitability for miniaturization in analytical chemistry [17–19]. As far as we know, there is no demonstration of an analytical paradigm that applies aptamers for the label-free CL analysis of small molecules. And it is of particular interest to us, because the interactions between oligonucleotides and small molecule have been well studied [8,20]. Upon that, we design a label-free CL aptasensor for the sensitive detection of small molecule using adenosine as a model analyte. It is well-known that adenosine

* Corresponding author. Tel.: +86 21 51980058; fax: +86 21 51980058.
E-mail address: jzlu@shmu.edu.cn (J. Lu).
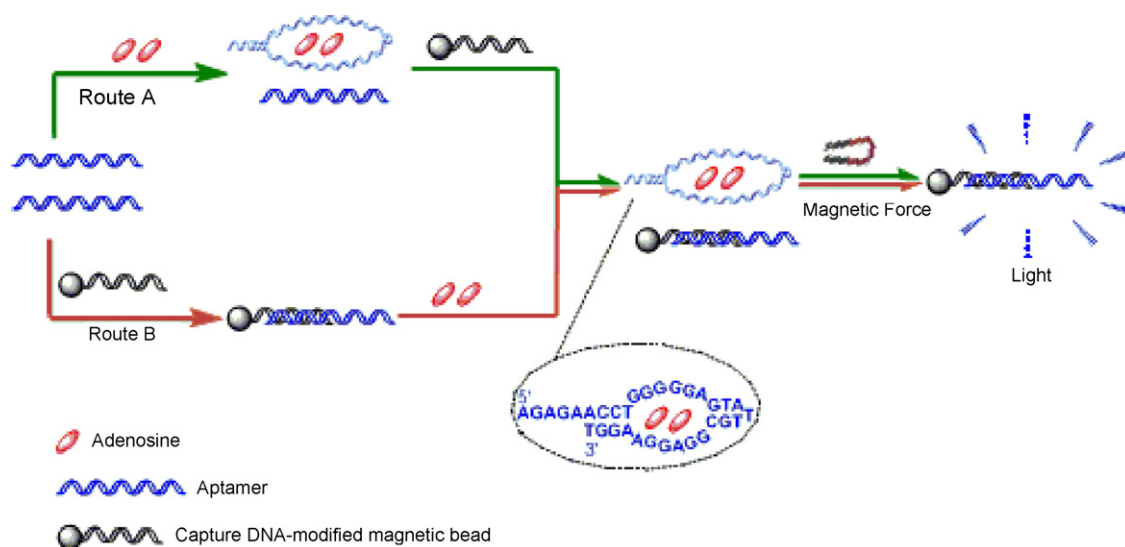
Scheme 1. Schematic presentation of two routes of analytical protocol.

is an endogenous nucleoside with potent vasodilator and anti-arrhythmic activities. Due to its crucial signaling functions in both the peripheral nervous system and the central nervous system, adenosine has always received much attention [21–24] and the detection of adenosine therefore is of great value. In addition, magnetic beads as special biomolecule immobilizing carrier offer a promising alternative to conventional methodology. Magnetic beads have been used in immunoassays, enzyme, DNA, and protein immobilization, DNA purification, and magnetically controlled transport of anticancer drugs [25]. So we also employ magnetic bead as our special DNA immobilizing carrier for the development of our CL aptasensor by simple magnetic separation process.

Herein, a CL biosensing platform for the sensitive detection of adenosine was developed based on a structure-switching aptamer without any label. The CL signal was obtained via an instantaneous derivatization reaction between 3,4,5-trimethoxyl-phenylglyoxal (TMPG) as the signal molecule, which reacts specially and instantaneously with guanine (G) nucleobases by our group as demonstrated previously [26,27], and the G nucleobases in the adenosine aptamers. Using this system, the adenosine could be specifically detected, and a relatively low detection limit as well as a wide linear dynamic range could be achieved. The optimal conditions for the detection of adenosine were investigated and optimized.

2. Experimental

2.1. Materials

All chemicals were of analytical grade and were used as received. All of the solutions were prepared with ultrapure water from a Millipore system. Carboxyl-terminated magnetic beads (1.5 μm, 20 mg/mL) were purchased from Polysciences (Warrington, PA). Oligonucleotides were acquired from Invitrogen Biotechnology Co. Ltd. (Shanghai, China) and had the following sequences: amino-modified capture probe: 5′-CCCAIITTCTCTAAAAAAAAAAA-NH₂-3′, the sequence of aptamer: 5′-AGA GAA CCT GGG GGA GTA TTG CGG AGG AAG GT-3′. TMPG was synthesized as described previously [28]. 1-Ethyl-3-(3-dimethylaminopropyl) carbodiimide (EDC), imidazole and tris(hydroxymethyl) aminomethane (Tris) were purchased from Sigma–Aldrich. Adenosine, guanosine, uridine, and cytidine were purchased from Aizite Biological Technology Corporation (Shanghai, China). Bovine serum albumin (BSA) was bought from Sino-American Biotechnology Co. and other

reagents were bought from Sinopharm Chemical Reagent Co. Ltd. (Shanghai, China). Human plasma was supplied by Zhongshan Hospital, Fudan University.

Buffer A (20 mM Tris–HCl, pH 8.0 and 0.5 M NaCl), wash buffer (7 mM Tris–HCl, pH 8.0, 0.17 M NaCl and 0.05% Tween 20), buffer X (20 mM Tris–HCl, pH 8.3, 300 mM NaCl, 5 mM MgCl₂ and 0.05% Tween 20).

2.2. Formation of self-assembled capture probes on magnetic beads

In a typical experiment, 2 μL of the carboxyl-terminated magnetic beads were washed three times with 0.1 M imidazole buffer (pH 6.0) and resuspended in 0.1 M imidazole buffer containing 0.1 M EDC for 30 min with gentle shaking. The activated magnetic beads were mixed with 60 pmol of capture probe and incubated for 1 h at 37 °C with gentle shaking. The bead-captured probes were magnetically separated and the supernatants were aspirated and discarded. So the self-assembled capture probes on magnetic beads were formed. Then 10% BSA was added as a blocking agent for 1 h at 37 °C with gentle shaking in order to minimize the nonspecific adsorption.

2.3. The assay procedures of detecting adenosine

As shown in Scheme 1, two different experimental routes for assay were employed. Route A (green line in Scheme 1) 10 pmol of the aptamers first reacted with different amount of adenosine in buffer X at 37 °C for 1 h with gentle shaking, leading to the formation of an adenosine–aptamer complex. Then the above-synthesized self-assembled capture probes on magnetic beads were added to the adenosine–aptamers reaction pool to hybridize with the aptamer at 37 °C for 1 h with gentle shaking. Magnetic beads were then washed and separated for direct CL analysis. Route B (brown line in Scheme 1) 10 pmol of the aptamers first hybridized with the self-assembled capture probes on magnetic beads in buffer A and then reacted with varied quantities of adenosine in buffer X at 37 °C for 1 h. Finally the magnetic beads were washed and separated for direct CL detection.

2.4. Chemiluminescence detection

The CL was performed in a homemade glass cell (14 mm × 40 mm) at room temperature with a BPCL analyzer (Bei-

jing, China). 100 μL of TMPG (40 mM in N,N-dimethlformamide) was mixed with the resultant magnetic beads and then shifted to the glass cell before the detection. 10 μL of tetrabutylammonium hydroxide-phosphate buffer (pH 8.5) was then injected and the CL signal was displayed immediately and then integrated 10 s for every signal.

3. Results and discussion

3.1. Analytical performance of the adenosine aptasensor

The schematic diagram of the principle of the present CL aptasensor protocol was depicted in Scheme 1. The CL aptasensor carrier, carboxyl-terminated magnetic beads, with large surface area could bind a large number of NH_2-modified 22-mer capture DNA oligonucleotides via the strong COOH–NH_2 bond under the EDC activation. Route A: (green line in Scheme 1) the adenosine aptamers first reacted with adenosine in buffer X and formed an adenosine–aptamer complex. The capture DNA, immobilized on magnetic beads, was then added to the reaction pool to hybridize with the aptamer in buffer A. Due to the formation of three-dimensional structure, the adenosine-binding aptamers could not hybridize with the capture DNA consequently. Only free aptamers were bound on the surface of magnetic beads through hybridization force and separated by magnetic force for direct CL analysis. From the experimental results, we could speculate that the stereo-conformation of the aptamers has a greater binding power and can effectively resist disintegrating from the competition combination of the addition of capture DNA. Route B: (brown line in Scheme 1) the aptamers first hybridized with capture DNA immobilized on magnetic beads in buffer A and then reacted with adenosine in buffer X. The aptamer could hybridize with the capture DNA–magnetic bead conjugates in the absence of adenosine. When adenosine as a specific competitor appeared, the aptamer preferred to form an adenosine–aptamer complex rather than an aptamer–capture DNA duplex. As a result, adenosine–aptamer complex was compelled to take apart from the magnetic beads, resulting in less aptamer remaining on the surface of magnetic beads and thus a lower CL intensity. As a whole, data further proved that the binding affinity of the aptamers toward their target adenosine is stronger than that of the aptamer–complementary DNA.

Note that the 32-mer specific aptamer sequence (5′-AGA AAA CCT GGG GGA GTA TTG CGG AGG AAG GT-3′) comprises the hybridizing segment and adenosine-binding segment, with seven nucleotides overlapping between them. Route A illustrates that binding of adenosine to aptamer results in the formation of three-dimensional DNA/adenosine complex, where the aptamer will not bind with capture DNA. Route B explains the switching structure from DNA/DNA duplex to DNA/adenosine complex. It is obvious that Route B process contains the competition between the DNA/adenosine complex and DNA/DNA duplex whereas this competition would not happen in Route A process due to the first appearance of the stronger binding pair DNA/adenosine complex. So the greater CL sensitivity would be obtained in Route A.

In the study, a solution of aptamer sequence was heated to 95 °C for 10 min, and then immersed into 4 °C water immediately to unwind the single-strand oligonucleotide before use. Each aptamer could enclose two adenosine molecules [29]. In addition, a special CL reagent TMPG was added to react with guanine nucleobases and then emit transient CL light, due to the formation of an unstable CL intermediate. Quantitative analysis of adenosine could be simply achieved by determining CL signal of the hybridized aptamers remaining on magnetic beads. With increasing the amount of adenosine, the increased amount of adenosine–aptamer complexes was formed and thus the aptamers remaining on the magnetic
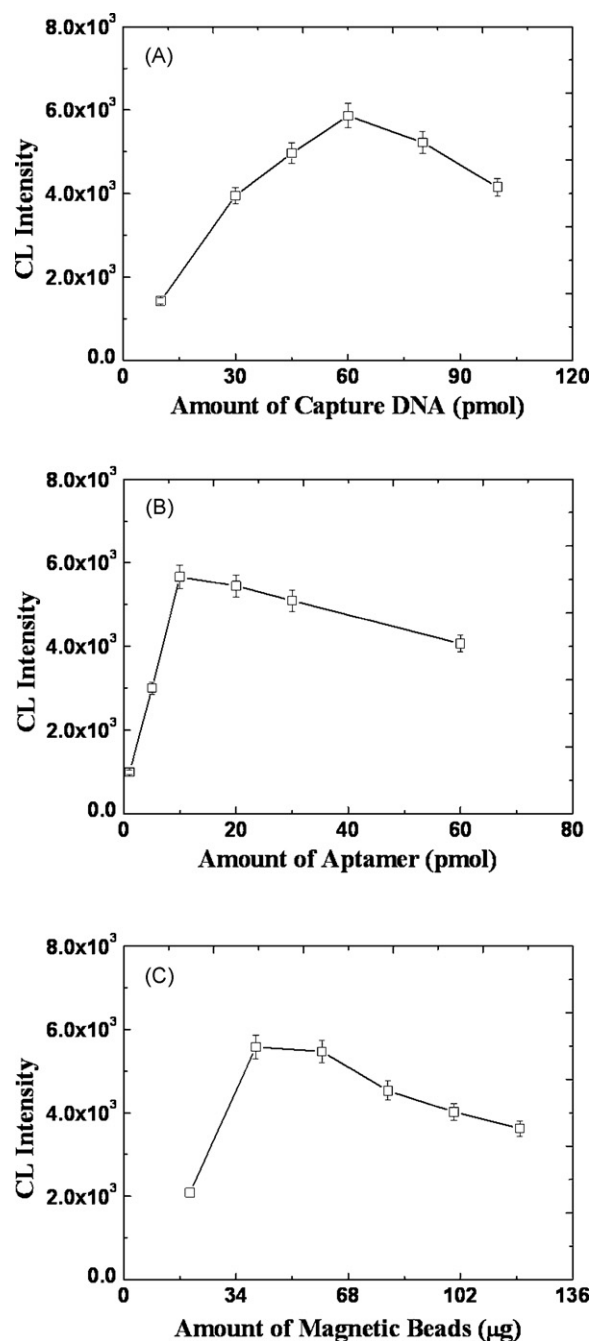

Fig. 1. CL intensity vs. the amounts of capture DNA, aptamer, magnetic beads in A, B, and C, respectively. Experimental conditions: (A) 10 pmol of aptamer, 60 μg of magnetic beads and 0.1 mM adenosine; (B) 60 pmol of capture DNA, 60 μg of magnetic beads and 0.1 mM adenosine; (C) 60 pmol of capture DNA, 10 pmol of aptamer, and 0.1 mM adenosine. Every data point was the mean of three measurements.

beads were gradually decreased, resulting in a lower CL signal. Therefore, the amount of adenosine was inversely correlated with the CL intensity. Moreover, it was noteworthy that two guanines in our capture DNA were substituted by inosines in order to minimize the background interference.

3.2. Optimization of experimental conditions

In order to obtain a higher sensitivity of the CL aptasensor, the optimal experimental conditions for the detection of adenosine were investigated. Firstly, to assess the optimal coverage for hybridization, a series of experiments with varying amounts of cap-
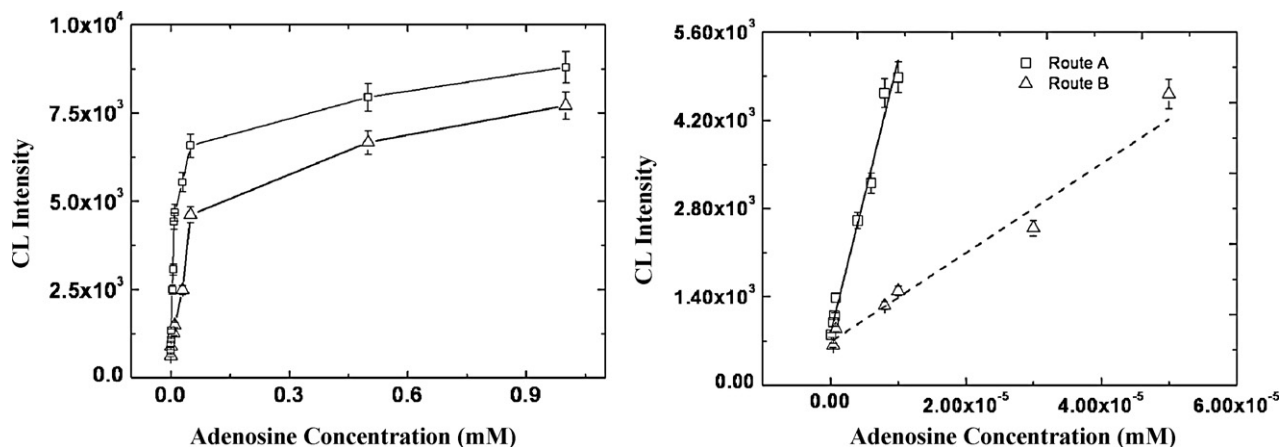
Fig. 2. Response of the CL sensor to different concentrations of adenosine for the two different experimental routes: Route A (□); Route B (△). Experimental conditions: 40 μg of magnetic beads, 60 pmol of capture DNA and 10 pmol of aptamer, respectively. Every data point was the mean of three measurements.

ture DNA for magnetic beads were conducted. As shown in Fig. 1A, with the amount of capture DNA increased, the CL intensity was also observed to increase at the beginning and reach maximum at a 60-pmol capture DNA. Further increasing capture DNA, however, decreased the hybridization efficiency and got a lower CL intensity [27,30]. We attribute this CL decrease to steric and electrostatic hindrances arising from the more tightly packed capture DNA, such that the aptamer cannot approach the surface-bound capture DNA, thus decreasing the number of duplexes formed on the carrier. Hence, subsequent work employed a capture DNA amount of 60 pmol.

Secondly, the amount of aptamer, a vital parameter for adenosine detection, was then explored. From the CL signal intensities of six different amounts of aptamer (1, 5, 10, 20, 30, 60 pmol), the optimal amount of aptamer was found to be 10 pmol (Fig. 1B), which was then used in the subsequent work.

For the same detection protocol, the amount of magnetic beads was also optimized thereafter. We could see in Fig. 1C that 40 and 60 μg of magnetic beads had the almost same CL intensity. Being cost-considered, 40 μg of magnetic beads was chosen for further studies. Note also that the above works were done following the experimental Route A.

We also noticed that the addition of $MgCl_2$ in the binding reaction has great impact on CL intensity. With and without $MgCl_2$, the results had the obvious difference (the data not shown). It was possible that the participation of Mg^{2+} was critical to the stabilization of the aptamer complex's stereo-structure [31]. At the same time, we made the binding buffer solution including 0.05% BSA, which would help to decrease the background noise.

3.3. The calibration curve of adenosine detection

We then tested the linear correlation of our novel detection method under the optimal experimental conditions. Using the method here, the detection limit could reach 8×10^{-8} M and the detection range could extend up to 10^{-3} M, with the most sensitive response range between 10^{-7} and 10^{-5} M. As shown in Fig. 2, with Route A, adenosine could be detected in a concentration ranged from 1×10^{-5} to 4×10^{-7} M in a linear pattern ($y = 363775x + 753.55$; $R^2 = 0.9852$). With Route B, adenosine could be detected in a shorter range from 5×10^{-5} to 4×10^{-7} M ($y = 74515x + 665.02$; $R^2 = 0.9764$). It is concluded that Route A is preferable to Route B, which could be explained that there are some competitive reaction between adenosine and capture DNA in Route B process. The results obtained were competitive with or better than those from adenosine and adenosine phosphate detection methods employing other technologies (Table 1). Compared with other methods for adenosine detection, this assay time is speedy and simple to manipulate. Except for some references [32,33] where no detailed information about the time for assay was included, other adenosine detection methods generally need more than 9 h for assay [16,34–37]. Overall, this assay technique is an attractive alternative due to features such as low cost, accessible biosensor and simple manipulation, and has the potential to measure other analytes when corresponding aptamers are used. Therefore, this simple and homogeneous technique will offer a new direction in design of high-performance CL biosensors for the sensitive and selective detection of a wide spectrum of analytes.

Table 1
Comparison of sensitivity for adenosine and adenosine phosphate assay methods.

| Analytical method	Label	Analyte	Detection limit	linear dynamic range	Reference
ISFET	Label-free	AMP	5×10^{-5} M	10^{-6} to 10^{-2} M	[8]
Electrochemical Detection	Label-free	Adenosine	10^{-7} M	10^{-6} to 10^{-4} M	[16]
Colorimetric detection	Label-free	AMP	4×10^{-6} M	4×10^{-6} to 1.5×10^{-3} M	[38]
Fluorescence detection	Label-free	Adenosine	10^{-5} M	1×10^{-5} to 5×10^{-4} M	[33]
Electrochemical Detection	Label-free	Adenosine	10^{-9} M	5×10^{-9} to 1×10^{-6} M	[34]
CL	Label-free	Adenosine	8×10^{-8} M	4×10^{-7} to 1×10^{-5} M	This work
FRET	Fluorophores-labeled aptamer	Adenosine	5×10^{-6} M	5×10^{-6} to 1×10^{-3} M	[32]
SERS	Tetramethylrhodamine-labeled complementary ss-DNA	Adenosine	1×10^{-8} M	2×10^{-8} to 2×10^{-6} M	[35]
Colorimetric detection	Au-nanoparticles-labeled aptamer	Adenosine	2×10^{-5} M	2×10^{-5} to 2×10^{-3} M	[36]
MS	Au-nanoparticles-labeled aptamer	ATP	4.8×10^{-7} M	2.5×10^{-6} to 5×10^{-5} M	[39]
SPR	Au-nanoparticles-tagged complementary ss-DNA	Adenosine	10^{-9} M	10^{-9} to 10^{-6} M	[37]
FRET	Quantum dot-tagged aptamer	ATP	2.4×10^{-5} M	10^{-4} to 10^{-3} M	[40]
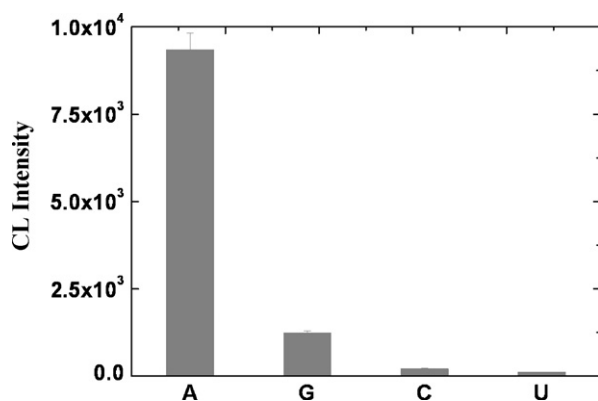
Fig. 3. CL signals vs. different nucleosides: 1 mM adenosine (A), guanosine (G), uridine (U), and cytidine (C). Experimental conditions: 40 µg of magnetic beads, 60 pmol of capture DNA and 10 pmol of aptamer respectively. Every data point was the mean of three measurements.

3.4. Selectivity of CL biosensor for detection of adenosine

To investigate the specificity of this aptamer to adenosine, we further examined the aptamer binding reaction with other nucleosides such as guanosine, uridine and cytidine. We can see in Fig. 3 that CL intensity was determined with 1 mM adenosine, guanosine, uridine, and cytidine under the same experimental conditions, respectively. The much higher CL intensity was gotten while adenosine was added as the binding target, which indicated that the aptamer has a higher specificity with adenosine, and is able to discriminate adenosine from its analogues under the same experimental conditions.

3.5. Analysis of serum sample

To assess the CL biosensor's ability to detect small molecule in complex samples, we tested the stability of adenosine aptamer-linked biosensor in the presence of biological fluids such as serum of normal human blood. Human blood serum 10-fold diluted with buffer X was used to prepare adenosine solution instead of buffer X alone and other experimental conditions were the same as described in Section 2. The recoveries of 0.1 and 1 mM adenosine in the 10-fold diluted serum were 97.71~95.95%. This result suggested that the sensor can still work in the complex serum matrix and is also promising for the determination of specific target by using this novel technique.

4. Conclusions

In summary, the CL sensor designed here is based on the adenosine competing reaction between adenosine and part complementary strand. In this protocol, it will no more be encountered of the time-consuming labeling process, cost-ineffective enzymes, and multistep experimental procedure as reported in other fluorescence/luminescence assays. The assay process can be completed in 4 h. Given the simplicity in CL detection, it is fairly easy to generalize this strategy to detect a spectrum of targets based on aptamers. Our novel CL technique, coupled the high sensitivity of CL methods with effective discrimination against adenosine, will offer a great promise for future target/aptamer analysis. This study may pave a facile and general way to the development of aptamer-based CL sensors.

References

[1] T. Hermann, D.J. Patel, Science 287 (2000) 820.
[2] F. He, Y. Tang, S. Wang, Y. Li, D.J. Zhu, J. Am. Chem. Soc. 127 (2005) 12343.
[3] J. Liu, Y. Lu, Angew. Chem. Int. Ed. 45 (2005) 90.
[4] H. Ueyama, M. Takagi, S. Takenaka, J. Am. Chem. Soc. 124 (2002) 14286.
[5] C. Fan, K.W. Plaxco, A.J. Heeger, Trends Biotechnol. 23 (2005) 186.
[6] Y. Ohtani, Y.K. amana, H. Nakano, Nucleic Acids Res. (Suppl.) (2002) 169.
[7] S.D. Jhaveri, R. Kirby, R. Conrad, E.J. Maglott, M. Bowser, R.T. Kennedy, G. Glick, A.D. Ellington, J. Am. Chem. Soc. 122 (2000) 2469.
[8] M. Zayats, Y. Huang, R. Gill, C.A. Ma, I. Willner, J. Am. Chem. Soc. 128 (2006) 13666.
[9] X.H. Fang, Z.H. Cao, T. Beck, W.H. Tan, Anal. Chem. 73 (2001) 5752.
[10] I. German, D.D. Buchanan, R.T. Kennedy, Anal. Chem. 70 (1998) 4540.
[11] Y. Li, H.L. Qi, Y.G. Peng, J. Yang, C.X. Zhang, Electrochem. Commun. 9 (2007) 2571.
[12] X.Y. Wang, J.M. Zhou, W. Yun, S.S. Xiao, Z. Chang, P.G. He, Y.Z. Fang, Anal. Chim. Acta 598 (2007) 242.
[13] J.S. Haveri, M. Rajendran, A.D. Ellington, Nat. Biotechnol. 18 (2000) 1293.
[14] H.A. Ho, M. Leclerc, J. Am. Chem. Soc. 126 (2004) 1384.
[15] Y.X. Jiang, X.H. Fang, C.L. Bai, Anal. Chem. 76 (2004) 5230.
[16] B. Li, Y. Du, H. Wei, S.J. Dong, Chem. Commun. (2007) 3780.
[17] A.M. Garcia-Campana, W.R.G. Baeyens, Chemiluminescence in Analytical Chemistry, Marcel Dekker, New York, 2001.
[18] R.A. Agbaria, P.B. Oldham, M. McCarroll, L.B. McGown, I.M. Warner, Anal. Chem. 74 (2002) 3952.
[19] A.M. Powe, K.A. Fletcher, N.N. St Luce, M. Lowry, S. Neal, M.E. McCarroll, P.B. Oldham, L.B. McGown, I.M. Warner, Anal. Chem. 76 (2004) 4614.
[20] X.L. Zuo, S.P. Song, J. Zhang, D. Pan, L.H. Wang, C.H. Fan, J. Am. Chem. Soc. 129 (2007) 1042.
[21] J.W. Phillis, Cerebrovasc. Brain Metab. Rev. 1 (1989) 26.
[22] M. Portellos, C.E. Riva, S.D. Cranstoun, B.L. Petrig, A. Brucker, J. Invest. Ophthalmol. Vis. Sci. 36 (1995) 1904.
[23] M.R. McMillan, G. Burnstock, S.G. Br.Haworth, J. Pharmacol. 28 (1999) 543.
[24] T.V. Dunwiddie, S.A. Masino, Annu. Rev. Neurosci. 24 (2001) 31.
[25] U. Hafeli, W. Schutt, J. Teller, M. Zborowski, Scientific and Clinical Applications of Magnetic Carriers, Plenum, New York, 1997.
[26] J.Z. Lu, C.Y. Lau, M. Kai, Chem. Commun. (2003) 2888.
[27] J.R. Miao, Z.J. Cao, Y. Zhou, C.Y. Lau, J.Z. Lu, Anal. Chem. 80 (2008) 1606.
[28] E. Kojima, Y. Ohba, M. Kai, Y. Ohkura, Anal. Chim. Acta 280 (1993) 157.
[29] J.W. Liu, Y. Lu, J. Am. Chem. Soc. 129 (2007) 8634.
[30] H. Li, C.W. Lau, J.Z. Lu, Analyst 133 (2008) 1229.
[31] E.J. Cho, J.R. Collett, A.E. Szafranska, A.D. Ellington, Anal. Chim. Acta 564 (2006) 82.
[32] H. Urata, K. Nomura, S.I. Wada, M. Akagi, Biochem. Biophys. Res. Co. 360 (2007) 459.
[33] X.H. Cheng, T. Bing, X.J. Liu, D.H. Shangguan, Anal. Chim. Acta 633 (2009) 97.
[34] K.J. Feng, C.H. Sun, Y. Kang, J.W. Chen, J.H. Jiang, G.L. Shen, R.Q. Yu, Electrochem. Commun. 10 (2008) 531.
[35] J.W. Chen, X.P. Liu, K.J. Feng, Y. Liang, J.H. Jiang, G.L. Shen, R.Q. Yu, Biosens. Bioelectron. 24 (2008) 66.
[36] W.J. Zhao, W. Chiuman, J.C.F. Lam, S.A. McManus, W. Chen, Y.G. Cui, R. Pelton, M.A. Brook, Y.F. Li, J. Am. Chem. Soc. 130 (2008) 3610.
[37] J.L. Wang, H.S. Zhou, Anal. Chem. 80 (2008) 7174.
[38] D. Li, B. Shlyahovsky, J. Elbaz, I. Willner, J. Am. Chem. Soc. 129 (2007) 5804.
[39] Y.F. Huang, H.T. Chang, Anal. Chem. 79 (2007) 4852.
[40] Z. Chen, G. Li, L. Zhang, J.F. Jiang, Z. Li, Z.H. Peng, L. Deng, Anal. Bioanal. Chem. 392 (2008) 1185.

Simultaneous determination of silicate and phosphate in environmental waters using pre-column derivatization ion-pair liquid chromatography

Yukio Yokoyama*, Takenobu Danno, Mizuki Haginoya, Yukari Yaso, Hisakuni Sato

Department of Analytical Chemistry, Faculty of Engineering, Yokohama National University, 79-7 Tokiwadai, Hodogaya, Yokohama 240-8501, Japan

ABSTRACT

A highly sensitive HPLC method for the simultaneous determination of soluble silicate and phosphate in environmental waters was developed, using ion-pair liquid chromatography preceded by the formation of their yellow α-heteropolymolybdates. The moderate-pH mobile phase enabled to use a highly efficient reversed-phase silica column. The pre-column coloring reactions at moderate-pH were reproducible for both silicate and phosphate in all quantification ranges with R.S.D.s less than 2% and 5%, respectively. The linear calibration lines between concentrations (mg-SiO_2/L and mg-PO_4/L) and peak area intensities were obtained for silicate and phosphate both with acceptable determination coefficients (r^2) of 0.9999. The limits of determination for both analytes were 0.007 mg-SiO_2/L and 0.003 mg-PO_4/L, which were calculated theoretically using 10σ/slope. The four-digit dynamic ranges were obtained for 0.007–10 mg-SiO_2/L and 0.003–20 mg-PO_4/L. The developed method was applied for the analysis of tap water, river water, coastal seawater, well water, hot-spring water, commercial mineral water, and laboratory water. The results were very reasonable and acceptable from the environmental viewpoints, which were well correlated with those confirmed by the molybdenum-blue spectrophotometry.

© 2009 Elsevier B.V. All rights reserved.

1. Introduction

Determinations of silicate and/or phosphate in environmental waters particularly in industrial waters or waste waters are very important to recognize the global elemental cycling and to understand their movements in our surroundings, because phosphorus, silicon, and nitrogen are eutrophic elements in water environments.

In general, soluble silicates and phosphate in water samples can be determined separately by means of visible-wavelength spectrophotometric methods based on the formation of yellow or blue heteropolymolybdates, called molybdenum-yellow method or molybdenum-blue method, respectively. The yellow complexes are analyzed at 410–450 nm usually despite the peak maxima around 320 nm, due to high UV-background by the residual molybdate [1–8]. Therefore, the molybdenum-yellow method, through direct measurements without any preliminary separation such as solvent extraction [8], is in general less sensitive than the blue method. The blue complexes produced by the reduction of yellow complexes using tin (II) chloride or ascorbic acid are analyzed at 725–882 nm [9–12], in which the wavelength can depend on the reductant used. Anyhow, such traditional spectrophotometric methods are still important in environmental analyses.

On the other hand, as simple and rapid methods alternative to such traditional methods, many flow injection analysis (FIA) procedures for the determination of phosphate [13–19] or silicate [20–27] or for both [28–31] have been proposed by many workers. However, the molybdenum-yellow procedures have been less frequently used because of the high background UV-absorbability due to residual molybdate. In the latest years, first-derivative spectrophotometric method [32] and ion-exclusion chromatography techniques with conductivity detection [33] or with post-column derivatization [34,35] have been proposed for their simultaneous quantifications.

It is known that the yellow chromophores can provide two possible forms of α- and β-heteropolymolybdates [36], depending on the reaction conditions such as acid concentration (pH), molybdate concentration, reaction temperature, and reaction times. The α- and β-molybdosilicic acids can be produced at pH around 3.8–4.8 and 1–1.8, respectively [37,38], and β-acids are often preferred rather than α-acids because of their high UV-absorbability [5,37,38]. However, the unstable β-form spontaneously transforms to the stable α-form [5,6]. In any case, the spectrophotometric determination of silicates and phosphates may be difficult simultaneously without any solvent extraction process [9,39,40], due to providing similar heteropoly chromophores.

Koshiishi and Imanari [41] have proposed an HPLC separation and simultaneous determination of the β-heteropolymolybdates under a very low-pH eluting condition less than pH 1, where the analytes and residual molybdate have been separated chro-

---

* Corresponding author. Tel.: +81 45 339 3939; fax: +81 45 339 3939.
E-mail address: yokyuk@ynu.ac.jp (Y. Yokoyama).

matographically. However, we can find few application and/or further improvement in chromatography, despite the poor chromatographic resolution. This is probably due to the use of a less efficient glass-column packed with a styrene co-polymer material of low-pH resistance. In addition to this, the reaction condition has not been detailed.

This paper describes a highly sensitive simultaneous determination of silicate and phosphate as their yellow α-heteropolymolybdates using an ion-pair HPLC. Based on the earlier HPLC method [41], the chromatographic procedure including the pre-column reaction was substantially improved into a new instrument-friendly and highly efficient HPLC method, in which the pre-column reaction and the subsequent separation were operated under moderate-pH conditions in order to enable to use a high-resolution reversed-phase silica column. The sensitivities for silicate and phosphate were considerably increased up to 20-times higher than those provided by molybdenum-blue spectrophotometric methods, and the improved method could give wide dynamic ranges for the analytes comparing to those given in earlier papers.

2. Experimental

2.1. Chemicals and materials

Hexaammonium heptamolybdate tetrahydrate ((NH_4)$_6$Mo$_7$O$_{24}$·4H$_2$O, FW = 1235.86, 99.0%, super special grade), silicon dioxide (99.9%), sodium carbonate (for pH standard), potassium dihydrogenphosphate (for pH standard), acetic acid (super special grade), and sodium acetate (guaranteed grade) were purchased from Wako Pure Chemical Ind. (Osaka, Japan). Ultrapure water made and bottled by Kurita Analysis Services (Tsukuba, Japan) was furnished by courtesy of the company, which was used for the solvent of all reaction agents. Acetonitrile of HPLC gradient-grade was purchased from Sigma–Aldrich Japan (Tokyo, Japan). Tetrabutylammonium (TBA$^+$) hydrosulfate of ion-pair reagent grade was purchased from Tokyo Chemical Ind. (Tokyo, Japan). Water used for the chromatographic eluent was purified through a Nihon Millipore (Tokyo, Japan) Direct-Q water purification system, having a resistance of 18.2 MΩ.

All plastic laboratory wares, such as volumetric flasks and reservoir bottles, made of polypropylene (PP), polymethylpentene (PMP), polytetrafluoroethylene (PTFE), or perfluoroalkoxyalkane (PFA), were used throughout the experiment.

Snap-capped 1.5 mL PP micro-tubes of conical type were used for the coloring reaction. Several kinds of micro-tubes with screw cap with O-ring and/or with surface treatment were unsuitable for the reaction because of serious contamination by breeding of silicate. Careful purchase is necessary.

2.2. Instrumentation

The HPLC system consisted of a Shimadzu (Kyoto, Japan) LC-10ADvp solvent delivery pump, a Rheodyne (Cotati, CA, USA) 7125 syringe-loading sample injector with a 100-μL sample loop, a Sugai (Tokyo, Japan) U-620 column heater, a Shimadzu (Kyoto, Japan) SPD-10Avp UV-VIS detector, and a SIC (Tokyo, Japan) Chromatocorder 11 chromatographic integrator. The chromatographic data were simultaneously acquired and processed, via an Advantest (Tokyo, Japan) R6441A digital multimeter used as an analog-to-digital converter through an RS232C interface, by using a personal computer installed with a data acquisition program laboratory-written with Visual BASIC working under Microsoft-Windows environments. A set of chromatographic data acquired as "dat" file can be transferred to Microsoft-Excel to draw a chromatogram.

A Metter-Toledo (Greifensee, Switzerland) AT20 microbalance was used for weighing the standard materials.

A Shibata Scientific Technology (Tokyo, Japan) BI-1200 dry-block-bath having 6×6 holes for 1.5 mL conical tubes was used for the coloring reaction. The vertical shape of the hole should be fit to the micro-tube to establish the thermal contact.

Several kinds of Metter-Toledo VoluMate micropipettes were used for pipetting solution less than 1 mL, with checking volumes at regular intervals.

2.3. Standard and reacting agents

The preparation of standard solutions and reaction reagents was based on the methods prescribed in Japanese Industrial Standard.

Silicate standard solution: A portion of SiO$_2$ powder reagent was allowed to stand heating at 700–800 °C in a platinum crucible for 1 h, and then to stand cooling in a desiccator. The dried 0.25311 g SiO$_2$ was weighed and mixed with 2 g Na$_2$CO$_3$ in a platinum crucible, and heating for 40 min fused the mixture. The resulting fused-salt was transferred into a 250-mL PMP volumetric flask and diluted to 250 mL by adding water, which led to the standard silicate (1 mg-SiO$_2$/mL) as stock solution stored in a PFA bottle.

Phosphate standard solution: A 71.62-mg portion of KH$_2$PO$_4$, dried at 105 °C for 2 h in advance, was dissolved in a 500-mL of water, corresponding to the standard of 0.1 mg-PO$_4$/mL.

In this paper, analytical concentrations are indicated by "mass/volume" like mg/L in accordance with the expression often seen in environmental analyses. The concentration in mg/L is convertible into molarity as occasion demands by those divided by formula weights of SiO$_2$: 60 and of PO$_4$: 95.

Reactant molybdate solution was prepared by dissolving 4.22 g of (NH_4)$_6$Mo$_7$O$_{24}$·4H$_2$O in 500 mL of water, corresponding to 8 g/L molybdate (6.8 mM).

1 M acetate buffer (pH 4) was prepared by mixing 1.0 M HOAc and 1.0 M NaOAc in volume ratio of 5:1, which led to pH 4.06 by theoretical calculation.

2.4. Separation column

A Tosoh (Tokyo, Japan) TSKgel super octyl (carbon loadings: 5%, 100 mm × 4.6 mm ID) reversed-phase column was finally selected and used for the separation column. Several kinds of reversed-phased columns examined were a Tosoh TSKgel super ODS (carbon loadings: 6%, 100 mm × 4.6 mm ID), a GC Sciences (Tokyo, Japan) Inertsil C8-3 (carbon loadings: 9%, 150 mm × 4.6 mm ID), and a Chemical Evaluation and Research Institute (Saitama, Japan) L-column C8 (carbon loadings: 10%, 150 mm × 4.6 mm ID), which were selected in consideration of lower hydrophobicity and column efficiency.

2.5. Chromatographic conditions

The chromatography was carried out on an isocratic elution mode. The mobile phase optimized was 65% (v/v) acetonitrile–water mixture, containing 12 mM TBA$^+$ and 20 mM acetate buffer (pH 4.76), which led to apparent pH 5.2. The mobile phase was degassed by sonicating for 10 min before use. The flow rate was 0.5 mL min^{-1}; the detection wavelength was 310 nm; and the column temperature was 35 °C.

2.6. Sample preparation

A 400-μL aliquot of the target solution of silicate standard, phosphate standard, or application sample was transferred into the 1.5-mL micro-tube, and in succession a 50-μL aliquot of the pH 4 acetate buffer and a 50-μL aliquot of the 8-g/L molybdate coloring

Table 1

Chromatographic column performances for molybdenum-yellow complexes. The data were obtained by the mobile phase: 60% (v/v) CH_3CN/H_2O containing 12 mM TBA^+.

Column brand	Carbon loading (%)	Pore size (nm)	Retention factor (k)		Plate number (N)	
			Si–Mo	P–Mo	Si–Mo	P–Mo
TSKgel super octyl	5	10	5.15	9.95	7,900	13,600
TSKgel super ODS	6	10	11.9	29.7	8,100	10,500
Inertsil C8-3	9	10	24.3	>50	7,300	–
L-column C8	10	10	21.4	42.2	6,400	9,400

agent were added to the solution. The capped tube was then set into a hole of the block-bath and allowed to stand heating at 75 °C for 45 min. After cooling the tube to a room temperature, a 500-μL aliquot of acetonitrile was added to the aqueous reactant to avoid forming precipitation of the aggregates when injecting, and then the mixture was degassed by sonicating. A 100-μL aliquot of the final solution was injected into the HPLC. When salt precipitation appeared in the final solution, due to the salt-abundant sample such as seawater, 0.2 μm filtration or centrifugation should be required in advance of the injection.

3. Results and discussion

3.1. Column selection

Since the yellow heteropolymolybdates can form hydrophobic ionic aggregates with tetrabutylammonium cations, a reversed-phase ion-pair chromatography has been successfully carried out in the earlier paper [41], where a styrene-divinylbenzene co-polymer reversed-phase column has been used because of the use of highly acidic eluent of less than pH 1. Since the column efficiency of those packed with such kind of materials may be poor, the separation of the analytes from the residual molybdate has not been so good. This can affect the simultaneous determination of trace amounts of the analytes, especially in silicate.

In this study, a highly efficient silica-based reversed-phase column was optimized for use with a moderate-pH eluent buffered by acetate. The separation column was selected from the viewpoints of high column resolution and acceptable retention factor. Since the hydrophobicity of stationary phase can depend on carbon loadings, several candidates of reversed-phase columns enough to separate the analytes from the residual molybdate. Table 1 lists the retention and separation parameters for four commercially available reversed-phase columns. Considering the chromatographic duration time and the column efficiency, TSKgel super octyl of 4.6 mm ID × 100 mm in length was selected for the separation. Some other reversed-phase columns of low carbon loadings may be useful for the purpose, if commercially available.

3.2. Eluting condition

The mobile phase condition was optimized by studying several ion-pair HPLC parameters, using a 60% (v/v) acetonitrile–water containing 12 mM TBA^+ as the starting composition. The column temperature and the flow rate were fixed to 35 °C and 0.5 mL min^{-1}, respectively, throughout the experiment.

The acetonitrile concentration should be more than 50% (v/v); otherwise, the molybdenum-yellow aggregates with TBA^+ will be precipitates in the column as described in the literature [41]. Effects of the acetonitrile concentration on the retention times are shown in Fig. 1. The peaks of the analytes were well separated each other in the acetonitrile concentration between 55 and 65% (v/v). In the cases using the super octyl column, 60 or 65% (v/v) acetonitrile was adequate for acceptable chromatographic duration time.

Effects of the concentration of the ion-pairing agent on the retention times when acetonitrile concentration is 60% (v/v) are shown
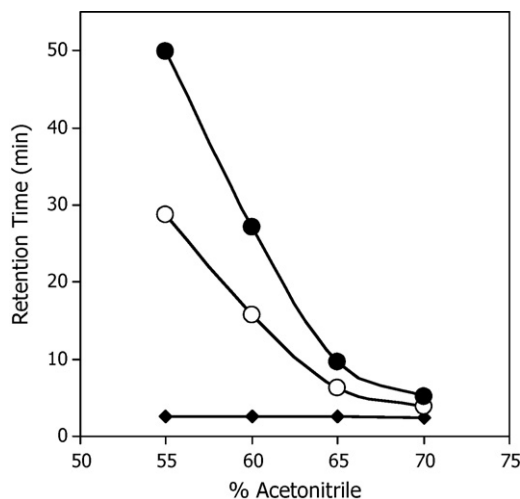

Fig. 1. Effects of acetonitrile % (v/v) concentration in eluent containing 12 mM TBA^+ at pH 5.2 (apparent) on the retention times for silicomolybdate (○), phosphomolybdate (●), and residual molybdate (♦).

in Fig. 2. The retention times of the two analytes increased with increase in the concentration of TBA^+. 8 or 12 mmol/L of TBA^+ was acceptable practically.

The eluent pH effected both on the retention time and on the chromatographic peak intensity. As the apparent pH of eluent was increased, the retention time was slightly decreased as shown in Fig. 3. In addition, the peaks due to the residual molybdate eluted around column void became further intense and broad in the chromatogram when eluting by an acidic eluent less than pH 5, which could affect the peak of silicomolybdate. In addition, the UV-absorbability of the yellow β-acids was seriously dependent on
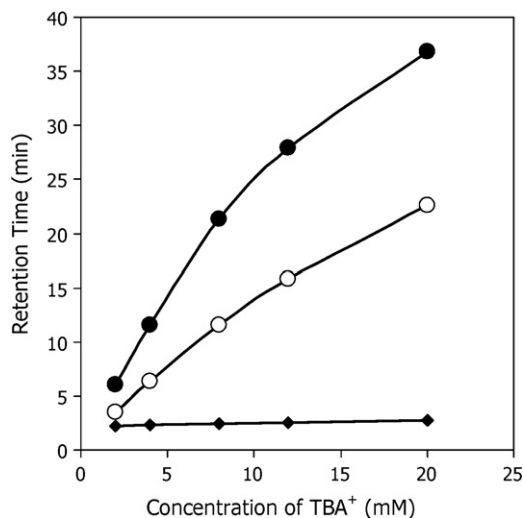

Fig. 2. Effects of concentration of ion-pair agent in eluent mixture of 60% (v/v) acetonitrile–water at pH 5.2 (apparent) on the retention times for silicomolybdate (○), phosphomolybdate (●), and residual molybdate (♦).
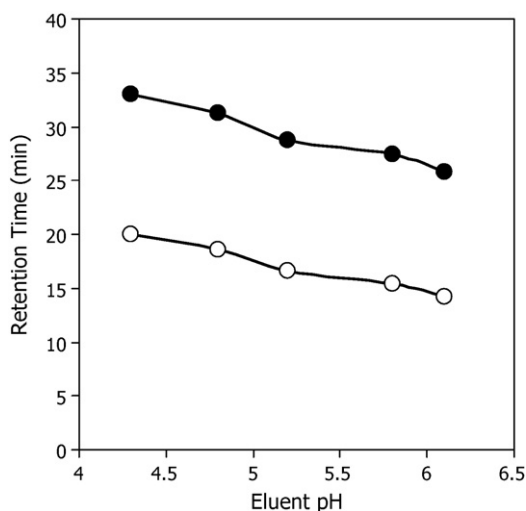
Fig. 3. Effects of apparent pH of eluent mixture of 60% (v/v) acetonitrile–water containing 12 mM TBA$^+$ on the retention times for silicomolybdate (○) and phosphomolybdate (●).

the surrounding acidity around pH 1 [37], but the UV-detectability of the α-acids was little affected in moderate-pH solutions [37,38]. Therefore, the pH of the mobile phase was adjusted apparently to pH 5.2, which was established by adding pH 4.7 acetate buffer into 60 or 65% (v/v) acetonitrile–water mixture.

The retentions of the analytes were relatively decreased by increasing acetonitrile contents or by decreasing TBA$^+$ concentration, as shown in Figs. 1 and 2. Comparing chromatograms obtained by changing the two possible parameters, the separation between the residual molybdate and the silicomolybdate was found better by increasing acetonitrile than by decreasing TBA$^+$. From the time-saving viewpoint, therefore, the acetonitrile concentration was set to 65% (v/v) in this work. Fig. 4 shows a typical chromatogram of standard silicate and phosphate obtained under the optimized chromatographic conditions as described in Section 2.

3.3. Coloring reaction

Although the heteropolymolybdates of silicate and phosphate can provide quite similar absorption spectra, the reaction conditions are considerably different between the two analytes. In particular, the reactivity of molybdosilicic acids has been well studied [37,38], depending greatly on acidity and molybdate concentration in the reaction mixtures. The formation of α-
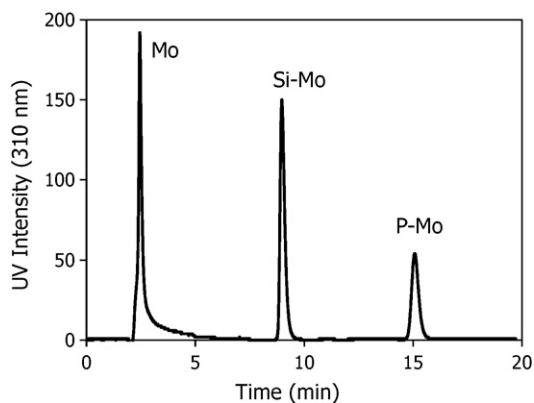
Fig. 4. An optimized chromatogram for standard silicate and phosphate by 65% (v/v) acetonitrile–water mixture containing 12-mM TBA$^+$ at pH 5.2 (apparent), corresponding to 0.5 mg/L both of SiO$_2$ and PO$_4$.

molybdosilicic acids around pH 4 is relatively fast even at room temperature when molybdate concentration is 3.2 mM in the reaction mixture [38]. In the present pre-column derivatization, the molybdate concentration had to be reduced to one-fifth of those often used in traditional spectrophotometric methods; otherwise the residual molybdate would give considerably large tailing peaks effectible on the peak of silicomolybdate, which could be seen in the earlier chromatogram [41]. However, the coloring reaction rate is strongly dependent both on the molybdate concentration and the solution pH. Under highly acidic conditions, the reaction can complete relatively fast at room temperatures, if the molybdate concentration in reaction mixtures is 3.2 mM or over as used in the earlier method [41]. After several rate studying, we found the fact that the coloring reaction of both analytes could be completed by heating at 75 °C even when the molybdate concentration was less than 1 mM in the reaction mixtures at pH 4. For the chromatography means, the reaction was carried out at 75 °C for 45 min as described in Section 2, although the time dependence was relatively small.

3.4. Interfering species

It is known that arsenate, As (V), can provide similar yellow heteropolymolybdates [28]. Since, however, such yellow acid was little produced under the present reaction condition at pH 4, few interfering peaks were observed in fact in the chromatograms for real waters.

On the one hand, arsenite, As (III), cannot react with molybdate. UV-absorbable hydrophilic anions such as bromide and chromate may give more or less chromatographic peaks under the eluting conditions; they little affected the separation and determination of the analytes because they were probably eluted as fast as residue molybdate.

Since reasonable data were obtained for seawaters, the salt problem was probably negligible in the coloring reaction.

The pre-column coloring reaction for both analytes at pH 4 was considerably affected by the presence of organic acids. The yellow phosphomolybdate was completely discolored by the presence of 1.25 g/L of oxalate (14 mM) or 1 g/L of citrate (5.2 mM). Similarly, the formation of yellow silicomolybdate was thoroughly inhibited by 0.75 g/L oxalate (8.3 mM) or 0.75 g/L citrate (3.9 mM) under the present coloring condition. It seems therefore at this point difficult to apply the present method to the direct analysis of beverages and/or foods without any dilution processes. Since such method problem can arise from the deficiency in reactivity, further studies for overcoming the matrix effects are now underway and the details will be presented in due course.

3.5. Quantification data

The preliminary sample treatments including the coloring reaction and the dilution for the standard silicate (0.001–10 mg-SiO$_2$/L or 17 nM to 170 μM) and phosphate (0.005–20 mg-PO$_4$/L or 53 nM to 210 μM) were five times replicated and a 100-μL aliquot of each resultant solution was subjected to the analyses.

The chromatographic reproducibility for both analytes is listed in Table 2. The relative standard deviation (R.S.D.) for their retention times (t_R) were less than 0.1% in all concentration levels. The R.S.D.s for peak area responses were within 5% in all ranges, probably showing acceptable precision for environmental analyses.

The calibration data are listed in Table 3. Although the linear regression lines were obtained for both analytes with acceptable coefficient of determination (r^2), it seemed better to calibrate separately in low and in high concentration regions as given in Table 3. In the case of silicate, the slope of line for the range between 0 and 0.02 mg/L was nearly equal to that between 0.02 and 10 mg/L, but r^2 for the lower concentration region was somewhat poor.

Table 2
Reproducibility data of retention time and peak area for silicate and phosphate.

	Reproducibility ($n = 5$)			
	t_R (min)		Peak area[a]	
	Average	R.S.D.	Average	R.S.D.
Silicate (mg/L)				
0[b]			4.034E+04	2.59
0.001	9.01	0.042	4.293E+04	2.86
0.002	9.02	0.038	4.460E+04	1.70
0.005	9.02	0.046	4.950E+04	3.55
0.01	9.03	0.065	5.695E+04	1.43
0.02	9.03	0.037	7.328E+04	3.24
0.05	9.03	0.048	1.189E+05	1.36
0.1	9.02	0.059	1.955E+05	0.76
0.2	9.03	0.034	3.532E+05	0.57
0.5	9.03	0.098	8.168E+05	1.09
1	9.11	0.070	1.645E+06	1.51
2	9.09	0.150	3.231E+06	1.92
5	9.03	0.047	8.081E+06	0.65
10	8.95	0.075	1.648E+07	2.23
20			Over range	
Phosphate (mg/L)				
0.002	ND			
0.005	14.35	0.049	1.330E+03	9.37
0.01	14.36	0.098	3.296E+03	4.76
0.02	14.34	0.112	8.705E+03	1.47
0.05	14.33	0.114	2.585E+04	2.19
0.1	14.33	0.061	5.438E+04	3.71
0.2	14.34	0.168	1.257E+05	2.42
0.5	14.32	0.053	3.366E+05	1.04
1	14.41	0.117	8.105E+05	4.40
2	14.44	0.058	1.606E+06	1.13
5	14.55	0.064	4.207E+06	1.51
10	14.17	0.042	8.743E+06	0.80
20	14.35	0.020	1.747E+07	0.22
50	14.59	0.156	3.342E+07[c]	1.00

[a] Integration unit.
[b] Reagent blank.
[c] Out of order.

This may be due to the unavoidable reagent blank standing out close to the limit of quantification. In the case of phosphate, the slope for 0.005–0.1 mg/L was considerably different from that for 0.1–20 mg/L. In contrast to this, the concentration and the integration response were well correlated in both ranges with good r^2. Anyway, linear regression lines with 0.9999 of r^2 were obtained for both analytes through four-digit dynamic ranges.

Table 4 shows the quantification limits for the two analytes, obtained by calculating 10-times standard deviation of blank signals divided by the slope of calibration lines around the limits (10σ/slope). The limit concentrations from the present method were expressed by mg/L and mmol/L, in comparison with those from the conventional molybdenum-blue method. The limit of silicate was established when using the ultrapure water for the pre-column reactions as described in Section 2. The HPLC method can provide considerably high-sensitivity for the analytes.

Table 3
Calibration data for silicate and phosphate.

Analyte	Linear regression lines $y = ax + b$			
	Range (mg/L)	Slope	Intercept	r^2
Silicate	0.007–0.02	1.613E+06	4.105E+04	0.9988
	0.02–10	1.640E+06	5.003E+03	0.9999
	0.007–10	1.638E+06	2.096E+04	0.9999
Phosphate	0.003–0.1	5.635E+05	−2.137E+03	0.9996
	0.1–20	8.780E+05	−8.882E+04	0.9999
	0.003–20	8.755E+05	−5.391E+04	0.9999

Table 4
Limits of quantification estimated by 10σ/slope.

Analyte	mg/L	mmol/L
SiO$_2$	0.007[a]	0.12[a]
	0.2[b]	3.3[b]
PO$_4$	0.003	0.03
	0.1[b]	1.1[b]

σ: standard deviation of blank signals and slope: slope of calibration line around LOD.
[a] Close to reagent blank.
[b] By spectrophotometric molybdenum-blue method.

Table 5
Amounts of silicate and phosphate found in real waters.

Sample water	SiO$_2$ (mg/L)	%R.S.D., $n = 5$	PO$_4$ (mg/L)	%R.S.D., $n = 5$
Laboratory water (from ion-exchange system)[a]	0.570	6.3	ND[d]	–
Laboratory water (from Millipore water purification system)[a]	0.028	3.3	ND	–
Seawater (Sakanoshita, Kamakura, Japan)[a]	0.267	1.4	0.006	6.7
Seawater (Inamuragasaki, Kamakura, Japan)[a]	0.438	2.0	0.003	17
Tap water (from Yokohama city)[b]	23.2	3.0	ND	–
River water (Katabira river, Yokohama)[b]	22.7	0.8	0.137	7.0
Well water (Kamakura, Japan)[b]	44.4	0.2	0.763	9.7
Mineral water (from USA)[b]	52.5	0.9	0.485	6.7
Mineral water (from France)[b]	28.4	0.4	0.460	9.5
Hot-spring water (Oomachi spa, Oomachi, Japan)[c]	78.6	0.7	ND	–
Hot-spring water (Toi spa, Izu, Japan)[c]	24.9	0.3	ND	–

[a] Determined without dilution.
[b] Determined with 5-times dilution.
[c] Determined with 10-times dilution.
[d] Not detected.

3.6. Application to surrounding waters

The developed chromatographic method was applied to the simultaneous determination of molybdenum-yellow active silicates and phosphates in several surrounding waters such as river water, coastal seawater, well water, hot-spring water, tap water, mineral water, and laboratory water. Fig. 5 shows a chromatogram for well water, and Table 5 lists the application results. Since the concentration of silicate in natural waters is relatively high, appro-
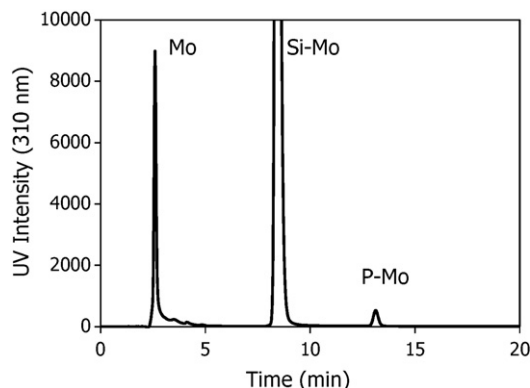
Fig. 5. A chromatogram for well water by 65% (v/v) acetonitrile–water mixture containing 12 mM TBA$^+$ at pH 5.2 (apparent). The difference in retention times is due to column lot.

priate dilution was required before the coloring reaction. The results for reactive silicates were reproducible with good R.S.D.s, and were very reasonable from the viewpoint of lithospheric substances.

The concentration levels of phosphates in natural waters seem to be relatively low unless there is any artificial pollution. The results are thought to be very convincing.

The chromatographic results were confirmed by analyzing some of the same samples using the traditional colorimetric molybdenum-blue method, based on the procedures described in the Japanese official method involving the reduction with ascorbic acid and the detection at 815 nm for silicate and at 880 nm for phosphate. The results by the chromatography and by the spectrophotometry were well correlated, giving 0.995 of r^2 for SiO_2 and 0.865 for PO_4. Since the concentrations of phosphate were fairly low in natural waters, the determination coefficient was somewhat poor. In addition to this, the data for phosphate acquired by the spectrophotometry were higher than those by the chromatography. Such positive bias is probably caused by the influence of large amount of coexisting silicate, because such traditional method is based on the kinetic difference in the formation of the heteropolymolybdates without any separating procedure; that is, the yellow phosphomolybdate can be formed faster than the yellow silicomolybdate under a high-acidity condition. We therefore concluded that the present HPLC method can provide more accurate and reliable results than the colorimetric method in the water analyses.

4. Conclusion

The developed ion-pair HPLC method for the simultaneous determination of silicate and phosphate preceded by the formation of yellow α-heteropolymolybdates is very sensitive and quantitative. The eluting condition is instrument-friendly and the yellow complexes are stable during the chromatography. In addition, the amount of coloring agents consumed in the pre-column derivatization was considerably reduced comparing to those in post-column derivatization methods [34,35].

The LOQ of silicate was almost equal to the reagent blank as minimized as possible, which seemed to be unavoidable limitation in the trace analysis of silicates. Since the silicate concentrations in environmental waters are relatively high, some laboratory water purified through a commercially available water purification system is acceptable for use in place of expensive ultrapure water as used in this work. The HPLC method could provide four-digit dynamic ranges for both analytes and thus the detection limits seemed to be further low.

At the present time, we can say that the improved HPLC method is highly sensitive and reliable rather than earlier methods and will contribute much to the environmental studies or surveillance.

References

[1] M.C. Schwarz, Ind. Eng. Chem. Anal. Ed. 14 (1942) 893.
[2] D.T.-W. Chow, R.J. Robinson, Anal. Chem. 25 (1953) 646.
[3] M.A. DeSesa, L.B. Rogers, Anal. Chem. 26 (1954) 1278.
[4] J.B. Mullin, J.P. Riley, Anal. Chim. Acta 12 (1955) 162.
[5] H.E. Garret, A.J. Walker, Analyst 89 (1964) 642.
[6] R.A. Chalmers, A.G. Sinclair, Anal. Chim. Acta 33 (1965) 384;
    R.A. Chalmers, A.G. Sinclair, Anal. Chim. Acta 34 (1966) 412.
[7] J.D. Ingle Jr., S.R. Crouch, Anal. Chem. 43 (1971) 7.
[8] C. Wadelin, M.G. Mellon, Anal. Chem. 25 (1953) 1668.
[9] A.B. Carlson, C.V. Banks, Anal. Chem. 24 (1952) 472.
[10] D.F. Boltz, M.G. Mellon, Anal. Chem. 19 (1947) 873.
[11] C.H. Lueck, D.F. Boltz, Anal. Chem. 28 (1956) 1168.
[12] J. Murphy, J.P. Riley, Anal. Chim. Acta 27 (1962) 31.
[13] J. Růžička, H. Hansen, Anal. Chim. Acta 78 (1975) 145.
[14] K.S. Johnson, R.L. Petty, Anal. Chem. 54 (1982) 1185.
[15] D.J. Halliwell, I.D. McKelvie, B.T. Hart, R.H. Dunhill, Analyst 121 (1996) 1089.
[16] S. Auflitsch, D.M. Peat, I.D. McKelvie, P.J. Worsfold, Analyst 122 (1997) 1477.
[17] X.D. Wang, T.J. Cardwell, R.W. Cattrall, R.P. Dyson, G.E. Jenkins, Anal. Chim. Acta 368 (1998) 105.
[18] G. Hanrahan, M. Gledhill, P.J. Fletcher, P.J. Worsfold, Anal. Chim. Acta 440 (2001) 55.
[19] A.J. L-Meaney, P.S. Ellis, P.J. Worsfold, E.C.V. Butler, I.D. McKelvie, Talanta 58 (2002) 1043.
[20] T. Yokoyama, Y. Hirai, N. Yoza, T. Tarutani, S. Ohashi, Bull. Chem. Soc. Jpn. 55 (1982) 3477.
[21] J.T. Thomsen, K.S. Johnson, R.L. Petty, Anal. Chem. 55 (1983) 2378.
[22] O.K. Borggaard, S.S. Jφrgensen, Analyst 110 (1985) 177.
[23] R. Kuroda, I. Ida, H. Kimura, Talanta 32 (1985) 353.
[24] P. Linares, M.D. Luque de Castero, M. Valcarcel, Anal. Chim. Acta 177 (1985) 263.
[25] M.L. Balconi, F. Sigon, M. Borgarello, R. FerraRoli, F. Realini, Anal. Chim. Acta 234 (1990) 167.
[26] M.C. Giacomelli, O. Largiuni, G. Piccardi, Anal. Chim. Acta 396 (1999) 285.
[27] M. Burguera, J.L. Burguera, P. Carrero, C. Rondon, Talanta 58 (2002) 1157.
[28] A.G. Fogg, N.K. Bsebsu, Analyst 106 (1981) 1288.
[29] A.G. Fogg, G.C. Cripps, Analyst 108 (1983) 1485.
[30] Y. Narusawa, Anal. Chim. Acta 204 (1988) 53.
[31] N. Lacy, G.D. Christian, J. Ruzicka, Anal. Chem. 62 (1990) 1482.
[32] A.Y. EI-Sayed, Y.Z. Hussein, M.A. Mohammed, Analyst 126 (2001) 1810;
    A.Y. EI-Sayed, Y.Z. Hussein, M.A. Mohammed, Anal. Sci. 17 (2001) 1461.
[33] H.-B. Li, F. Chen, J. Chromatogr. A 874 (2000) 143.
[34] M. Ikedo, M. Mori, K. Kurachi, W. Hu, K. Tanaka, Anal. Sci. 22 (2006) 117.
[35] N. Nakatani, D. Kozaki, W. Masuda, N. Nakagoshi, K. Hasebe, M. Mori, K. Tanaka, Anal. Chim. Acta 619 (2008) 110.
[36] J.D.H. Strickland, J. Amer. Chem. Soc. 74 (1952) 862;
    J.D.H. Strickland, J. Amer. Chem. Soc. 74 (1952) 868;
    J.D.H. Strickland, J. Amer. Chem. Soc. 74 (1952) 872.
[37] V.W. Truesdale, C.J. Smith, Analyst 100 (1975) 203.
[38] K. Kato, Anal. Chim. Acta 82 (1976) 401.
[39] M.A. DeSesa, L.B. Rogers, Anal. Chem. 26 (1954) 1381.
[40] J. Paul, Anal. Chim. Acta 23 (1960) 178.
[41] I. Koshiishi, T. Imanari, Anal. Sci. 1 (1985) 253.

Metabolomic profiling of rat serum associated with isoproterenol-induced myocardial infarction using ultra-performance liquid chromatography/time-of-flight mass spectrometry and multivariate analysis

Hong-yang Zhang[a,b], Xi Chen[b], Ping Hu[a,*], Qiong-lin Liang[b], Xiao-ping Liang[a,b], Yi-ming Wang[b], Guo-an Luo[a,b,**]

[a] School of Chemistry and Molecular Engineering, East-China University of Science and Technology, Shanghai 200237, China
[b] The Key Laboratory of Bioorganic Phosphorus Chemistry and Chemical Biology, Department of Chemistry, Tsinghua University, Beijing 100084, China

ARTICLE INFO

ABSTRACT

An ultra-performance liquid chromatography/time-of-flight mass spectrometry (UPLC/TOF-MS)-based metabolomic approach was developed to characterize the metabolic profile associated with isoproterenol (ISO)-induced myocardial infarction (MI). Analysis of the serum samples revealed distinct changes in the biochemical patterns of ISO-induced rats. A multivariate statistical method, supervised partial least squares-discriminant analysis (PLS-DA), was then used for screening of potential biomarkers. As a result, 13 lipid biomarkers, including lysophosphatidylcholines (Lyso-PCs) and fatty acids were identified by the accurate mass measurement of TOF-MS. The relationship between abnormal lipid metabolism and the formation of MI were also studied. This work demonstrates the utility of UPLC/TOF-MS-based metabolic profiling combined with multivariate analysis as a powerful tool to further investigate the pathogenesis of cardiovascular diseases.

1. Introduction

Metabolomics, refers to the comprehensive analysis of small-molecule metabolites present in a biological system, is an emerging technology of systems biology in studies of either clinical diagnosis or pharmaceutical industry [1,2]. The goal of metabolomics is to capture non-targeted, global metabolite profiles of complex samples such as biofluids and tissues [3]. Additionally, multivariate statistical methods, including principle component analysis (PCA) or partial least squares (PLS), are used to identify the potential biomarkers [4]. Such investigations thus generate metabolic phenotypes and, by studying these, it may well be possible to obtain new and unexpected insights into biological processes.

The analytical challenges in metabolomics lie in the fact that endogenous metabolites comprise a large number of diverse chemical structures, which are present in a wide concentration range [5]. Recently, metabolic profiling has gained popularity using a number of techniques, including high-field nuclear magnetic resonance (NMR) [6,7], gas chromatography/mass spectrometry (GC/MS) [8,9], and liquid chromatography/mass spectrometry (LC/MS) [10,11]. However, despite of some limitations, LC/MS can be accepted as the most useful platform for untargeted metabolic profiling. While NMR demonstrates its advantages in highly selective and non-destructive analysis, LC/MS possesses much better sensitivity and resolution. Unlike GC/MS, LC/MS can detect non-volatile compounds complementarily, which make up a large proportion of metabolites. Currently, the development of ultra-performance liquid chromatography (UPLC) has made it possible to achieve higher resolutions, higher sensitivities, and rapid separations as compared to those achieved using conventional HPLC [12,13]. This system combined with orthogonal acceleration time-of-flight mass spectrometry (TOF-MS), which enables the exact measurement of mass, is undoubtedly a suitable system for metabolomic study [14].

Cardiovascular diseases, including atherosclerosis and cardiac tissue injury after myocardial infarction (MI), are the most prevalent cause of death and disability worldwide. The World Health Organization (WHO) estimates that 17 million people die of cardiovascular disease annually [15]. MI is associated with ischaemic necrosis of cardiac muscles due to a decrease in the supply of

* Corresponding author. Tel.: +86 21 64252844.
** Corresponding author. Tel.: +86 10 62781688; fax: +86 10 62781688.
E-mail address: luoga@mail.tsinghua.edu.cn (G.-a. Luo).

blood to a portion of the myocardium below a critical level necessary for viability and proper physiological function [16]. The rat model of isoproterenol (ISO)-induced MI is considered as one of the most widely used experimental model to evaluate several cardiac dysfunctions. Previous studies have shown that the pathophysiological changes following ISO administration are comparable to those taking place in human MI [17,18]. To date, several biomarkers of MI (such as troponin I and T) have been identified and successfully incorporated into clinical practice. However, new biomarkers are still needed to augment the information obtained from traditional indicators and to illuminate disease mechanisms [19]. The application of metabolomics to allow systematic characterization of variations in metabolites associated with MI is therefore available.

Here, we developed an UPLC/TOF-MS-based metabolic profiling method for the analysis of endogenous metabolites in rat serum samples. Partial least squares-discriminant analysis (PLS-DA) was then performed to identify the characteristic metabolic variations associated with ISO-induced MI. Potential biomarkers were identified from the exact TOF-MS data. This work combined with other functional genomic studies may provide new insights into the pathogenesis of cardiovascular diseases.

2. Experimental

2.1. Chemicals

The DL-isoproterenol hydrochloride (ISO, batch no. 15627) was obtained from Shanghai Hefeng Pharmaceutical Company (Shanghai, China). The assay kits for lactate dehydrogenase (LDH), creatine kinases (CK), superoxide dismutase (SOD), and malondialdehyde (MDA) were purchased from Nanjing Jiancheng Bio-engineering Institute (Nanjing, China). The following compounds were obtained from Sigma–Aldrich (St. Louis, MO, USA): docosahexaenoic acid (C22:6), arachidonic acid (C20:4), linoleic acid (C18:2), palmitic acid (C16:0), oleic acid (C18:1), stearic acid (C18:0). 1-Palmitoyl-2-hydroxy-sn-glycero-3-phosphocholine (Lyso PC, C16:0) was purchased from Avanti Polar Lipids (Alabaster, AL, USA). HPLC-grade acetonitrile and methanol were purchased from J. T. Baker (Phillipsburg, NJ, USA). Ultrapure water (18.2 MΩ) was purified with a Milli-Q system (Millipore, MA, USA). All other chemicals used were of analytical grade.

2.2. Animal studies

Male Sprague–Dawley rats (200 ± 20 g) were obtained from the Centre of Laboratory Animals, Tsinghua University (Beijing, China). Animals were bred in a breeding room with temperature of 23 ± 2 °C, relative humidity of $60 \pm 5\%$, and 12 h dark–light cycle. They were given tap water and fed normal food *ad libitum* and were maintained in polypropylene cages (each cage containing a maximum of four animals). The animal facilities and protocols were approved by the Institutional Animal Care and Use Committee, Tsinghua University. All procedures were in accordance with the National Institute of Health's Guidelines regarding the principles of animal care (2004). The experiment animals were housed under the above conditions for 1-week acclimation.

2.3. Physiology

The animals were randomly divided into two groups as follows: the model group ($n = 13$) and the control group ($n = 10$), and were anesthetized with urethane (1.3 g/kg, i.p.). All the rats were fixed on pad in position on back and two-lead electrocardiograms (ECGs) were recorded by MPA 2000 bio-signal analytical system (Shanghai

Alcott Biotech Co. Ltd., Shanghai, China). Before starting the injections, normal ECG recordings were made for at least 5 min until they were well balanced. The ECGs in both groups after newly injection (the model group, received an i.p. injected ISO in a dose of 30 mg/kg; the control group, received the same volume of vehicle) at 0.5, 1, 2, 5, 10, 15, and 20 min were recorded and compared [20]. After ECG measurements, the blood was collected from the inferior caval vein and then centrifuged at 3000 rpm for 5 min at 4 °C. The supernatant obtained were frozen immediately and stored at −20 °C, and thawed before analysis. Serum concentrations of LDH, CK, SOD, and MDA were measured by UV 1100 ultraviolet spectrophotometer (Beijing Rayleigh Analytical Instrument Corp., Beijing, China).

2.4. Liquid chromatography

Chromatographic separation was performed using a Waters ACQUITY UPLC^{TM} system (Waters Corp., Milford, USA), equipped with a binary solvent delivery system and an auto-sampler. A Waters 100 mm × 2.1 mm ACQUITY C$_{18}$ 1.7 μm column was used to separate the endogenous metabolites. The mobile phase consisted of (A) 0.1% formic acid in water and (B) acetonitrile. A linear gradient was optimized as follows (flow rate, 0.4 mL/min): 0–3 min, 5% B to 50% B; 3–20 min, 50% B to 95% B; 20–21 min, 95% B to 5% B; 21–23 min, equilibration with 5% B. The column and auto-sampler were maintained at 50 and 4 °C, respectively.

Prior to the analysis, 400 μL of methanol was added to 100 μL aliquots of serum. The mixture was vortex mixed for 2 min followed by centrifugation at 6000 rpm for 15 min at 4 °C. The clear supernatant was transferred and diluted at a ratio of 1:10 with methanol before analysis. A 4 μL injection of sample was made onto the column in each run.

2.5. Mass spectrometry

Mass spectrometry was performed using a Micromass LCT Premier^{TM} orthogonal acceleration time-of-flight mass spectrometer (Waters Corp., Manchester, UK). The system was operated in "W" optics mode and the optimized conditions were as follows: negative ion (ESI−) mode, capillary voltage 2500 V, sample cone voltage 50 V, desolvation temperature 350 °C, source temperature 120 °C, cone gas flow 40 L/h, desolvation gas flow 700 L/h, and MCP detector voltage 2200 V. The data acquisition rate was set to 0.1 s, with a 0.05 s interscan delay using dynamic range enhancement (DRE). All analyses were acquired using the lock spray to ensure accuracy and reproducibility; leucine–enkephalin was used as the lock mass (m/z 554.2615) at a concentration of 50 pg/mL and an infusion flow rate of 5 μL/min. Data were collected in centroid mode from 50 to 1000 m/z. For accurate mass measurement, the TOF mass spectrometer was calibrated routinely using sodium formate solution infused at a flow rate of 5 μL/min.

2.6. Analytical method validation

To ensure the reproducibility of the newly developed UPLC/TOF-MS method, validation tests of both precision and repeatability were performed. Considering their relatively high abundance levels and wide retention time distribution range in the chromatogram, the extracted ions of m/z 564.3 (Lyso-PC, C18:2), 588.3 (Lyso-PC, C20:4), 540.3 (Lyso-PC, C16:0), 568.4 (Lyso-PC, C18:0), 327.2 (docosahexaenoic acid), 279.2 (linoleic acid), 281.2 (oleic acid), and 283.3 (stearic acid) were selected as the representative components in rat serum for validation.

Precision of injection was carried out by six replicated analyses of the same serum sample. Sample preparation before UPLC/MS analysis should also be performed carefully to ensure the stability of metabolomic analysis. Therefore, six parallel samples were
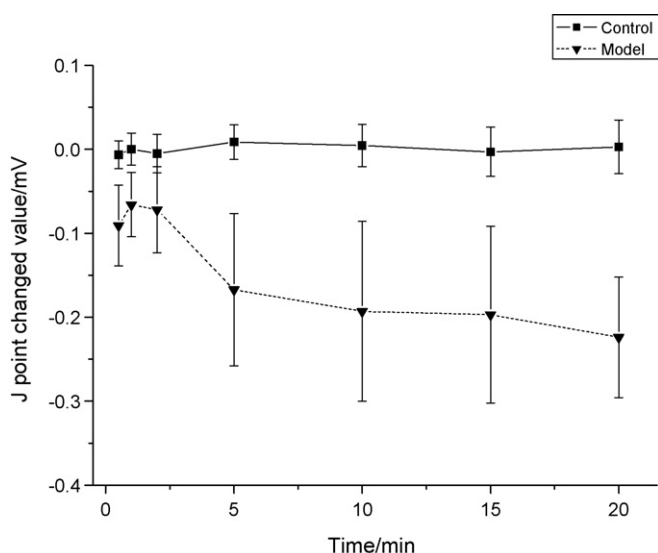
Fig. 1. Effect of isoproterenol on the J point of electrocardiogram (ECG) in rats.

prepared using the same preparation protocol to examine the repeatability of sample preparation.

2.7. Data analysis

The UPLC/MS data of control and model rat sera were analyzed to identify potential discriminant variables. The peak finding, peak alignment, and peak filtering of the raw data were carried out with the MarkerLynx applications manager Version 4.1 (Waters Corp., Manchester, UK). The parameters used were as follows: minimum retention time 0.50 min, maximum retention time 20.00 min, mass range 50–1000 m/z, mass tolerance 0.05 Da, intensity threshold 10 counts, retention time tolerance 0.01 min; noise elimination level was set at 6.00, and isotopic peaks were excluded for processing. A list of the ion intensities of all components with their corresponding retention time and m/z as identifier was generated. The ion intensities for each peak detected were then normalized, within each sample, to the sum of the peak intensities in that sample. The resulting 3D data set was then exported for multivariate statistical analysis by using PLS-DA in the software SIMCA-P+ 11.5 (Umetrics, Umea, Sweden).

3. Results and discussion

3.1. Electrocardiograms and serum enzymes

The effect of ISO on the J point of rats' ECG is shown in Fig. 1. The ECG alterations, especially the degree of J point alterations, are generally considered as a main index to evaluate animals' MI [21]. In this study, we also found that the J point of ECG in MI model rats elevated slowly for 1 min after ISO injection, and then continuously decreased within 20 min. The J point at each time points within 20 min were significantly different from those in control

rats ($P < 0.05$). Furthermore, serum enzyme activities have also been cited as important parameters in the assessment of myocardial injury [22]. As shown in Table 1, compared with control rats, the concentrations of LDH ($P < 0.01$), CK ($P < 0.01$), and MDA ($P < 0.001$) in model rats were significantly increased, while the levels of SOD ($P < 0.05$) were remarkably decreased. These alterations are consistent with the previously reported results [22]. All together, the ECG and enzymatic results presented here demonstrated that both myocardial tissue and cell in model rats have damaged.

3.2. Metabolic profiling of rat serum

Serum is a complex matrix containing a wide variety of compounds with diverse chemical structures. While metabolomics being a non-targeted analysis of the global system for changes in endogenous metabolites, sample pretreatment by conventional methods, such as solid-phase extraction or liquid–liquid extraction, may result in loss of potential biomarkers. Therefore, minimal sample preparation steps were employed in this experiment in order to avoid the loss of endogenous metabolites. The serum samples were deproteinized with methanol, centrifuged and diluted before analysis.

The UPLC system provided a rapid, sensitive, and convenient analytical method for a wide range of metabolites present in rat serum. The major benefit expected from the use of sub-2 μm particles is the increased column efficiency and concomitant increased resolution. Theoretically, a higher flow rate promises a good separation on the UPLC column, whereas the flow rate recommended for electrospray source is below 0.3 mL/min so as to guarantee the best ionization efficiency. Taking sensitivity and resolution into consideration together, the ultimate flow rate was optimized at 0.4 mL/min throughout this study. Column temperature was set at 50 °C to reduce the column pressure resulting from a higher flow rate, which can improve chromatographic separation and peak shape. Furthermore, to obtain better separation within a reasonable time, gradient elution and 0.1% formic acid in the mobile phase were also used. The base peak intensity (BPI) chromatograms of control or model rat serum obtained from the analysis in ESI− mode is shown in Fig. 2. Under these conditions, the UPLC system generated peak widths in the order of 5 s wide at the base, giving a peak capacity in excess of 200 for the 20 min separation. Further examination of these serum chromatograms indicated the presence of thousands of ions corresponding to a wide range of molecular species.

A large number of peaks could be detected using the ESI− mode as compared to using the ESI+ mode. Therefore, considering the sensitivity on the single mode, full-scan detection was set as ESI− mode. The desolvation gas flow and temperature were set at 700 L/h and 350 °C, respectively, so as to remove redundant solvent resulting from a higher flow rate of 0.4 mL/min for mass spectrometer. Accurate mass measurement was rendered possible by the simultaneous but independent acquisition of reference ions of leucine–enkephalin via the lock spray interface. This configuration avoids several problems such as ion suppression and mass interference, and therefore is suitable for non-targeted metabolic profiling.

Table 1
Concentrations of major serum enzymes in dosed and control groups.

Group	LDH (U/L)	CK (U/mL)	SOD (U/mL)	MDA (μmol/L)
Control	115.30 ± 61.70[**]	212.40 ± 71.64[**]	50.90 ± 3.96[*]	2.18 ± 0.80[***]
Model	271.00 ± 123.92	424.44 ± 178.80	44.55 ± 6.09	5.51 ± 1.30

LDH, lactate dehydrogenase; CK, creatine kinases; SOD, superoxide dismutase; MDA, malondialdehyde.

[*] $P < 0.05$.
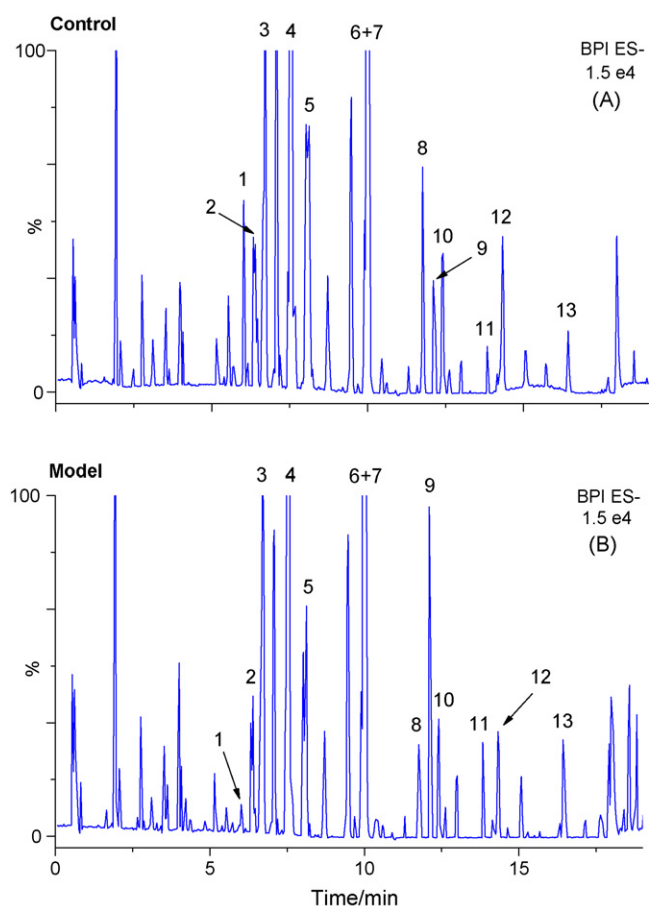[**] $P < 0.01$.
[***] $P < 0.001$.

Fig. 2. Typical UPLC/TOF-MS base peak intensity (BPI) chromatograms of rat serum from (A) control or (B) model group. Peak numbers are consistent with those in Table 3.

3.3. UPLC/MS method validation

The data of precision and repeatability tests of the proposed method are listed in Table 2. For the precision test, a stable retention time of the ion peaks was observed, with the variations less than 0.28% RSD. In addition, the RSD values of peak area for the main ions were varied from 2.21 to 6.33%. The precision of injection reflected the stability of UPLC/MS analysis, which was of great importance to guarantee the reliability of the acquired metabolomic data.

The repeatability data showed that the repeatability of sample preparation was acceptable. Almost all the corresponding ion peaks were presented at the same retention times, and RSD values of the peak area for the main ions were varied from 3.47 to 11.37%. The pro-

posed UPLC/MS profiling method is therefore highly reproducible and could be used for metabolomic studies.

3.4. Multivariate analysis

PLS-DA is a sophisticated supervised method in metabolomics, which can establish the optimal position to place a discriminant surface that separates classes best and generate the matrices of scores and loadings. In this work, a well-fitting two-component PLS-DA model ($R^2Y = 0.991$, $Q^2Y = 0.952$) was constructed to identify and reveal the differential metabolites in response to different groups. Mean-centered and par-scaled (scaled to square root of standard deviation) mathematical methods were performed to pretreat the chromatographic data sets. The obtained PLS-DA scores plot is shown in Fig. 3(a). Clear separation of the control and model rats could be observed, indicating that there was significant difference in serum samples collected from the two groups.

The loadings plot indicates that the most influential ions are responsible for separation between sample classes: the ions having the greatest influence in the PLS-DA scores plot are those farthest away from the main cluster of ions. In turns, these compounds might be the candidates for biomarkers. Fig. 3(b) indicates that the possible biomarkers (totally 14) are the ions with m/z 568.4, 540.3, 588.3, 564.3, 566.3, 612.3, 480.3, 327.2, 640.3, 279.2, 281.2, 283.3, 303.2, and 255.2 in the ESI– mode. Identification of these marker ions was then carried out by the TOF-MS accurate mass measurement with available standards.

3.5. Identification of potential biomarkers

Benefit from the increased resolving power, TOF-MS generates exact mass information and thus provides elemental compositions of unknown ions with limited accuracy (routinely within 10 ppm). Using MarkerLynx software, the potential calculated masses, mass accuracy, DBE (total number of rings and double bonds in a molecule), i-FIT value (the likelihood that the isotopic pattern of the elemental composition matches a cluster of peaks in the spectrum), and elemental compositions associated with the measured mass of the marker ions (metabolites) were generated and studied. Here, we take m/z 540.3263 Da (Fig. 4a) as an example to illustrate the marker ion identification process. The isotopic pattern of the ion indicates that it is a singly charged ion. Using a mass tolerance of 15 ppm, four possible candidates were produced with the elemental composition analysis software implemented in the MarkerLynx. The calculated masses/mDa/ppm/DBE/i-FIT/elemental compositions of the four candidates were 540.3301/−3.8/−7.0/2/19.1/$C_{25}H_{51}NO_9P$, 540.3243/2.0/3.7/11/363.3/$C_{32}H_{47}NO_4P$, 540.3325/−6.2/−11.5/11/444.7/$C_{32}H_{46}NO_6$, and 540.3266/−0.3/−0.6/20/1575.4/$C_{39}H_{42}NO$, respectively. Taking mass accuracy (mDa and ppm), DBE and i-FIT value into consideration, the confidence of the tentative marker

Table 2
Precision and repeatability data of the proposed method.

Peak no.[a]	m/z	Precision of injection ($n = 6$)				Repeatability of sample preparation ($n = 6$)			
		R. T. (min)		Peak area		R. T. (min)		Peak area	
		Mean	RSD (%)	Mean	RSD (%)	Mean	RSD (%)	Mean	RSD (%)
1	564.3	6.37	0.21	598	6.19	6.34	0.31	613	9.63
3	588.3	6.75	0.20	1148	3.78	6.72	0.20	1059	6.52
4	540.3	7.58	< 0.10	5309	2.21	7.53	0.22	5221	3.47
7	568.4	10.04	0.28	3906	3.55	9.98	0.22	3860	3.73
8	327.2	11.87	< 0.10	822	4.83	11.75	0.11	864	8.68
10	279.2	12.46	0.26	567	6.33	12.39	0.10	546	4.14
12	281.2	14.43	< 0.10	686	5.72	14.32	< 0.10	684	3.92
13	283.3	16.54	< 0.10	474	4.66	16.43	< 0.10	483	11.27

[a] Peak numbers are consistent with those in Fig. 2 and Table 3.
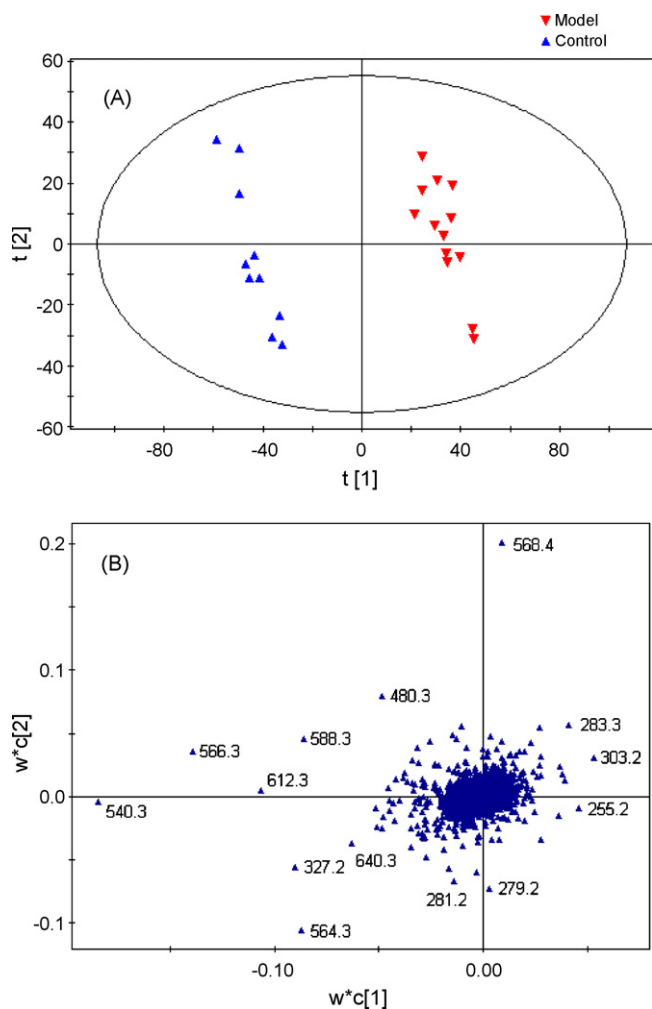
Fig. 3. PLS-DA results of the entire metabolites from 0.5 to 20 min. (A) Scores plot of control (blue triangle) and model (red inverted triangle) groups, (B) loadings plot obtained using Pareto scaling with mean centering.

assignment to the first candidate was enhanced by the high mass accuracy obtained (−3.8 mDa or −7.0 ppm), fulfillment of two DBE (two double bonds), and low i-FIT value (19.1). Results from data mining further suggested the candidate as Lyso-PC (C16:0), which was confirmed by its authentic standard. Noticed that the lysophosphatidylcholines (Lyso-PCs) all have a choline group at the polar head and these species tend to be detected as the formate adduct $[M + HCOO]^-$.

Fig. 4. Structures and spectra of representative marker compounds. (A) Lyso-PC (C16:0) and (B) arachidonic acid.

Using this iterative approach, 13 lipid species, including Lyso-PCs and fatty acids (e.g., arachidonic acid (Fig. 4b) as potential biomarkers of control and ISO-induced rats were identified (Table 3). The biochemical mechanisms of those relevant metabolites as well as the formation of MI were then investigated. However, it should be noted that the metabolite ion at m/z 640.3 (eluted at 9.5 min) was unidentified in the present experiment. Analyses of high-resolution MS data and isotope patterns of the ion matched an elemental composition of $C_{38}H_{42}NO_8$, which indicated that the compound did not belong to a certain class of lipid. Further study on this potential biomarker is needed for its structure elucidation.

Table 3
Identification results of potential biomarkers using TOF-MS accurate mass measurement.

No.	R. T. (min)	Selected ion	Exact mass (Da)	Elemental composition	Metabolites identification[a]
1	6.3	$[M + HCOO]^-$	564.3301	$C_{27}H_{51}NO_9P$	Lyso-PC, C18:2 (↓)
2	6.5	$[M + HCOO]^-$	612.3301	$C_{31}H_{51}NO_9P$	Lyso-PC, C22:6 (↓)
3	6.7	$[M + HCOO]^-$	588.3301	$C_{29}H_{51}NO_9P$	Lyso-PC, C20:4 (↓)
4[*]	7.5	$[M + HCOO]^-$	540.3301	$C_{25}H_{51}NO_9P$	Lyso-PC, C16:0 (↓)
5	8.0	$[M + HCOO]^-$	566.3458	$C_{27}H_{53}NO_9P$	Lyso-PC, C18:1 (↓)
6	9.9	$[M - H]^-$	480.3090	$C_{23}H_{47}NO_7P$	Lyso-PC, C15:1 (↓)
7	10.0	$[M + HCOO]^-$	568.3614	$C_{27}H_{55}NO_9P$	Lyso-PC, C18:0 (↑)
8[*]	11.8	$[M - H]^-$	327.2329	$C_{22}H_{31}O_2$	Docosahexaenoic acid (↓)
9[*]	12.1	$[M - H]^-$	303.2329	$C_{20}H_{31}O_2$	Arachidonic acid (↑)
10[*]	12.4	$[M - H]^-$	279.2329	$C_{18}H_{31}O_2$	Linoleic acid (↓)
11[*]	13.8	$[M - H]^-$	255.2339	$C_{16}H_{31}O_2$	Palmitic acid (↑)
12[*]	14.3	$[M - H]^-$	281.2486	$C_{18}H_{33}O_2$	Oleic acid (↓)
13[*]	16.4	$[M - H]^-$	283.2637	$C_{18}H_{35}O_2$	Stearic acid (↑)

[a] "↑" means a higher level of metabolites in model group as compared to the control, whereas "↓" represents a lower level of metabolites.

[*] Compounds confirmed with authentic standards.

3.6. Disorders of lipid metabolism

The metabolomic analysis conducted in the present study revealed ISO-induced changes in the profiles of certain endogenous metabolites. Correspondingly, the physiology study, including ECG and serum enzyme analyses confirmed the presence of substantial MI after administration of high ISO doses. In Table 3, the most of Lyso-PCs were downregulated by ISO intervention, while the levels of fatty acids were changed variously. These results suggested that an impaired lipid metabolism plays a deleterious role in the formation of MI.

Lyso-PCs, as endogenous phospholipids, are very important and participate in the pathophysiological change of myocardial tissue [23]. Fatty acids are important constituents of all cell membranes, including endothelial and myocardial cells [24]. As shown in Table 3, a decrease in Lyso-PCs and various alterations in fatty acids in ISO-treated rats might have been due to the breakdown of membrane phospholipids. Accelerated phospholipids degradation resulting in myocardial injury in ISO-treated rats has been reported previously [25]. These alterations may ascribe to the activation of phospholipase A$_2$, which mediates the release of specific fatty acids from Lyso-PCs [26]. It could be presumed that several biological factors, such as the activation of protein kinase C (PKC) pathway, enhance the activity of phospholipase A$_2$ and make the decrease of Lyso-PC generation [27]. Several studies have also been demonstrated that the phospholipase A$_2$ in heart was selective for arachidonic acid containing phospholipids [28,29]. The elevations of arachidonic acid in serum may have more contribution to the lipotoxicity in myocardium [30]. In any event, the various disorders of fatty acids as well as Lyso-PC degradation indicate an underlying lipid disturbance is present in ISO-induced rat model that are well associated with the formation of MI.

4. Conclusion

In this paper, a metabolomic approach based on UPLC/TOF-MS profiling and multivariate statistical method was developed to study ISO-induced MI. Metabolic profiles obtained from UPLC/TOF-MS as well as the physiological results revealed distinct biochemical changes in ISO-induced rats. The supervised PLS-DA analysis indicated clear differentiation of the control and ISO-induced rats and potential biomarkers were then screened. 13 lipid biomarkers, including Lyso-PCs and fatty acids were then identified by the TOF-MS accurate mass measurement. These results will be very helpful for further investigation of the pathogenesis of cardiovascular diseases. This study also demonstrates the metabolomic approach is a potentially powerful tool in the area of biological research.

References

[1] J.K. Nicholson, E. Holmes, J.C. Lindon, I.D. Wilson, Nat. Biotechnol. 22 (2004) 1268.
[2] W. Weckwerth, K. Morgenthal, Drug Discov. Today 10 (2005) 1551.
[3] G. Theodoridis, H.G. Gika, I.D. Wilson, Trac-Trends Anal. Chem. 27 (2008) 251.
[4] J. Trygg, E. Holmes, T. Lundstedt, J. Proteome Res. 6 (2007) 469.
[5] J.C. Lindon, J.K. Nicholson, Trac-Trends Anal. Chem. 27 (2008) 194.
[6] A.W. Nicholls, R.J. Mortishire-Smith, J.K. Nicholson, Chem. Res. Toxicol. 16 (2003) 1395.
[7] I.F. Duarte, E.G. Stanley, E. Holmes, J.C. Lindon, A.M. Gil, H.R. Tang, R. Ferdinand, C.G. McKee, J.K. Nicholson, H. Vilca-Melendez, N. Heaton, G.M. Murphy, Anal. Chem. 77 (2005) 5570.
[8] Q. Zhang, G.J. Wang, Y. Du, L.L. Zhu, A. Jiye, J. Chromatogr. B 854 (2007) 20.
[9] H.J. Major, R. Williams, A.J. Wilson, I.D. Wilson, Rapid Commun. Mass Spectrom. 20 (2006) 3295.
[10] J. Yang, G.W. Xu, W.F. Zheng, H.W. Kong, C. Wang, X.J. Zhao, T. Pang, J. Chromatogr. A 1084 (2005) 214.
[11] U. Lutz, R.W. Lutz, W.K. Lutz, Anal. Chem. 78 (2006) 4564.
[12] L. Novakova, D. Solichova, P. Solich, J. Sep. Sci. 29 (2006) 2433.
[13] A. Nordstrom, G. O'Maille, C. Qin, G. Siuzdak, Anal. Chem. 78 (2006) 3289.
[14] E.C.Y. Chan, S.L. Yap, A.J. Lau, Rapid Commun. Mass Spectrom. 21 (2007) 519.
[15] J. MacKay, G. Mensah, The Atlas of Heart Disease and Stroke, World Health Organization, Geneva, 2004.
[16] A. Chattopadhyay, S. Biswas, D. Bandyopadhyay, C. Sarkar, A.G. Datta, Mol. Cell. Biochem. 245 (2003) 43.
[17] B.C. Wexler, J.T. Judd, Br. J. Exp. Pathol. 51 (1970) 646.
[18] B.C. Wexler, Am. Heart J. 96 (1978) 70.
[19] R.E. Gerszten, T.J. Wang, Nature 451 (2008) 949.
[20] S.Y. Xu, R.L. Bian, X. Chen, Experimental Methodology of Pharmacology, second ed., People's Health Publishing House, Beijing, 1991, 897.
[21] G.L. Jia, P.Z. Dong, Acta Lab. Anim. Sci. Sin. 13 (2005) 106.
[22] S.Y. Zheng, J. Sun, X. Zhao, J.G. Xu, Am. J. Chin. Med. 32 (2004) 209.
[23] Y. Xu, Y.J. Xiao, K. Zhu, L.M. Baudhuin, J. Lu, G. Hong, K.S. Kim, K.L. Cristina, L. Song, F.S. Williams, P. Elson, M. Markman, J. Belinson, Curr. Drug Targets 3 (2003) 23.
[24] U.N. Das, Lipids Health Dis. 7 (2008) 19.
[25] S. Al Makdessi, J.L. Andrieu, H. Herilier, G. Faucon, J. Mol. Cell. Cardiol. 19 (1987) 141.
[26] J. Starkopf, T.V. Andreasen, E. Bugge, K. Ytrehus, Cardiovasc. Res. 37 (1998) 66.
[27] A.L. Fuly, A.L. Machado, P. Castro, Toxicon 50 (2007) 400.
[28] R.A. Wolf, R.W. Gross, J. Biol. Chem. 260 (1985) 7295.
[29] D.A. Ford, Prog. Lipid Res. 41 (2002) 6.
[30] L.E. Hjelte, A. Nilsson, J. Nutr. 135 (2005) 2271.

Solid-state electrochemiluminescence sensor based on the Nafion/poly(sodium 4-styrene sulfonate) composite film

Libing Zhang [a,b], Jing Li [a], Yuanhong Xu [a], Yueming Zhai [a], Yunhui Li [b,*], Erkang Wang [a,**]

[a] State Key Laboratory of Electroanalytical Chemistry, Changchun Institute of Applied Chemistry, Chinese Academy of Sciences, Changchun, Jilin, 130022, PR China
[b] School of Chemistry and Environmental Engineering, Changchun University of Science and Technology, Changchun, Jilin, 130022, PR China

ARTICLE INFO

ABSTRACT

An effective electrochemiluminescence (ECL) sensor based on Nafion/poly(sodium 4-styrene sulfonate) (PSS) composite film-modified ITO electrode was developed. The Nafion/PSS/Ru composite film was characterized by atomic force microscopy, UV–vis absorbance spectroscopy and electrochemical experiments. The Nafion/PSS composite film could effectively immobilize tris(2,2′-bipyridyl)ruthenium(II) ($Ru(bpy)_3^{2+}$) via ion-exchange and electrostatic interaction. The ECL behavior of $Ru(bpy)_3^{2+}$ immobilized in Nafion/PSS composite film was investigated using tripropylamine (TPA) as an analyte. The detection limit (S/N = 3) for TPA at the Nafion/PSS/Ru composite-modified electrode was estimated to be 3.0 nM, which is 3 orders of magnitude lower than that obtained at the Nafion/Ru modified electrode. The Nafion/PSS/Ru composite film-modified indium tin oxide (ITO) electrode also exhibited good ECL stability. In addition, this kind of immobilization approach was simple, effective, and timesaving.

1. Introduction

Electrochemiluminescence (ECL) is a means to convert electrochemical energy into radiative energy at the surface of an electrode via an applied potential [1,2]. ECL has been paid considerable attention during the past decades due to its versatility, simplified optical setup, low background signal, and good temporal and spatial control. As a sensitive detection method, ECL has been used in high-performance liquid chromatography (HPLC), flow injection analysis, capillary electrophoresis (CE), and microchip CE [3–8]. Among various ECL systems, tris(2,2′-bipyridyl)ruthenium(II) ($Ru(bpy)_3^{2+}$)-based ECL has been extensively investigated due to its superior properties including high sensitivity and good stability under moderate conditions in aqueous solution [9].

The oxidation–reduction reaction mechanism for $Ru(bpy)_3^{2+}$-based ECL has been well postulated by Rubinstein and Bard elucidates that $Ru(bpy)_3^{2+}$ can be regenerated in situ at the electrode surface during the ECL reaction [10]. Compared with the solution-phase ECL procedure, the immobilization of $Ru(bpy)_3^{2+}$ can provide several advantages, for example, reducing the consumption of expensive reagent, enhancing the ECL signal, and simplifying experimental design [11]. Many approaches, such

as sol–gel entrapment [12], electrostatic attachment, layer-by-layer self-assembly [13], and the Langmuir–Blodgett technique [14], etc., have been adopted to fabricate solid-state ECL sensors by immobilizing $Ru(bpy)_3^{2+}$ on a solid surface. Quite a lot of new materials, including cation exchange polymers [15–17], silica nanoparticles [18–20], carbon nanotubes [11,21], and metal nanoparticles have also been developed for solid-state ECL. However, the analytical applications of these solid-state ECL sensors are very limited because they easily desorbed in organic solvent and are unstable in positively biased potential [22]. Developing new materials and immobilization approaches still remains significant and challenging in order to improve sensitivity and the long-term stability of solid-state ECL sensor [23].

Nafion, as an ion-exchangeable, discriminative and biocompatible polymer, has inspired enormous research interests. Especially, Nafion has been found increasing use as a membrane material because it is very resistant to chemical attack, even by strong oxidants at elevated temperature [24]. However, due to the compact film construction and the slow rate of charge transfer, the analytical applications of Nafion are limited [21]. Recently, the researchers found that many efforts have been made to overcome the existent drawbacks via doping some nanoparticles into the pure Nafion film, for example, CNT–Nafion composite film [15,21], Nafion–silica composite film [16,25], and TiO$_2$–Nafion composite film [26]. Therefore, the Nafion-contained composite films with good properties still need further investigation.

* Corresponding author.
** Corresponding author. Tel.: +86 431 85262003; fax: +86 431 85689711.
E-mail addresses: liyh@cust.edu.cn (Y. Li), ekwang@ciac.jl.cn (E. Wang).

Scheme 1. Schematic illustration of preparation and enhanced ECL intensity of the proposed sensor.

In this work, the interfusion of poly(sodium 4-styrene sulfonate) (PSS) into the Nafion film was developed to fabricate the solid-state ECL sensor on the surface of indium tin oxide (ITO) electrode (Scheme 1). In this composite film, on one hand, Nafion is an effective matrix to incorporate $Ru(bpy)_3^{2+}$; on the other hand, the interfusion of negative charge and cation exchange polyelectrolyte PSS into the Nafion film not only enhances the amount of the $Ru(bpy)_3^{2+}$ incorporated into the film but also accelerates the rates of charge transfer. The Nafion/PSS/Ru composite film-modified ITO electrode showed a high sensitivity for the ECL determination of tripropylamine (TPA), and the detection limit (S/N = 3) was estimated to be 3.0 nM, which was 3 orders of magnitude lower than that obtained at the Nafion/Ru modified electrode. The Nafion/PSS/Ru composite film-modified ITO electrode also exhibited a good ECL stability. In addition, this kind of immobilization approach was simple, effective, and timesaving.

2. Experimental

2.1. Chemicals and materials

Tris(2,2′-bipyridyl)ruthenium chloride ($Ru(bpy)_3Cl_2(6H_2O)$), TPA, procyclidine, poly(sodium 4-styrene sulfonate) (PSS, molecular weight = 70,000), hexaammineruthenium(III) chloride 98% and Nafion (perfluorinated ion-exchange powder, 5 wt% solution in a mixture of lower aliphatic alcohols and water) were purchased from Sigma–Aldrich Chemical Co. (Milwaukee, WI). Arginine, proline and bovine serum albumin (BSA) were purchased from Dingguo Biotechnology Co., Ltd. (Beijing, China). ITO-coated glass (150-nM thick and <15 Ω^{-2}-resistant) was purchased from HIVAC Technology Co., Ltd. (Shenzhen, China). All the chemicals were of analytical reagent grade and were used as received without further purification. Solutions were prepared with deionized water processed with a Milli-Q ultra-high purity water system (Millipore, Bedford, MA, USA).

2.2. Apparatus and equipments

Cyclic voltammetric experiments were performed with a CH Instruments 800 workstation (Shanghai, China). The ECL signal produced in the electrolytic cell was detected by a model MPI-A capillary electrophoresis electrochemiluminescence system (Xi'an Remax Electronics Inc., Xi'an, China, and Changchun Institute of Applied Chemistry, Chinese Academy of Sciences, Changchun, China). ECL intensities were measured through the bottom of the cell with a photomultiplier tube (PMT) window, and all of them were enclosed in a light-tight box. The PMT was operated in current mode unless noted, and the PMT was biased at 800 V. The working electrode was ITO modified with the Nafion/PSS/Ru composite film. Ag/AgCl (saturated KCl) reference electrode and platinum counter electrode were used for all the electrochemical and ECL measurements. UV–vis absorbance spectra were recorded on a Cary 500 scan UV–vis-NIR spectrophotometer (Varian, Harbor City, CA) at room temperature. Atomic force microscopy (AFM) images were obtained by using a SPI3800N microscope (Seiko Instruments) operating in the tapping mode.

2.3. Preparation of the ECL sensor

The process of preparation of the ECL sensor mainly includes two steps. Firstly, the ITO electrodes with constant area were prepared. Secondly, the modification of the prepared ITO electrodes with 0.5% pure Nafion solution and Nafion/PSS suspension, respectively, and subsequent ion-exchange in $Ru(bpy)_3^{2+}$ aqueous solution were performed. Finally, the needed ECL sensors were obtained.

To obtain the ITO electrodes with constant area, a photolithographic method was adopted to fabricate the electrodes, and the preparation was according to the literature with a little modification [7]. Briefly, a piece of ITO-coated glass was first sliced into small slides (5 cm × 1.5 cm). Before use, these slides were sonicated sequentially for 20 min each in acetone, 10% KOH in ethanol, and distilled water. After rinsing with ethanol, the ITO electrode was dried under a stream of nitrogen. Positive photoresist (RZJ-390) was applied to the ITO surface with Spin Coater (KW-4A Model) at 2500 rpm for 30 s. Hot plates at 100 °C were used to prebake the slides for 100 s. A photoresist mask containing the desired electrode pattern was first designed in a computer and printer onto a transparent film by a commercial print service with a high-resolution laser printer (3000 dpi). The pattern was transferred onto the photoresist layer by Lithography System (JKG-2A Model). After removing the exposed photoresist, the plates were baked at 130 °C for 120 s. A wet chemical etching procedure was carried out with mixed solutions ($HCl:FeCl_3:H_2O = 1:3:1$). After removing the remained photoresist, the prepared ITO electrode was cleaned by sonicating sequentially for 20 min each in acetone, 10% KOH in ethanol, and distilled water. After that the ITO electrode was dried under a stream of nitrogen and stored for use.

The ECL sensor was fabricated as following. Typically, a 1.0 mg/mL sample of PSS was dispersed in the same volume of 1.0 wt% Nafion solution with ultrasonication for 20 min to obtain a homogeneous, well-dispersed solution of Nafion/PSS mixture. Two of the prepared ITO electrodes were coated by spin-coating with the same volume of 0.5% pure Nafion solution and Nafion/PSS suspension, respectively, and the solvents were allowed to evaporate under an infrared lamp heating for 60 s. Both of the modified ITO electrodes were then placed in 5.0 mM $Ru(bpy)_3^{2+}$ aqueous solution for incorporation of $Ru(bpy)_3^{2+}$ for 30 min (referred as Nafion/Ru and Nafion/PSS/Ru, respectively). The prepared electrodes were removed from the solution and rinsed thoroughly with deionized water, and then were allowed to dry in a nitrogen stream for further characterization and application.

3. Results and discussion

3.1. The characterization of the Nafion/PSS composite film

The preparation of Nafion film and Nafion/PSS composite film was according to the above-mentioned method. To characterize the property of the composite film, $Ru(NH_3)_6^{2+}$ was chosen as a probe to investigate its electrochemical behavior at different electrodes (as shown in Fig. 1). The potentials of oxidation and reduction peak of $Ru(NH_3)_6^{2+}$ are at near −0.1 V and −0.2 V, respectively, which are consistent with the previous report [27]. At the bare ITO electrode, only a very small current peak could be observed (Fig. 1a). The peak current obtained at the pure Nafion-modified electrode was about 2-fold greater than that obtained at bare ITO electrode (Fig. 1b), illustrating that Nafion was an effective medium for the preconcentration of $Ru(NH_3)_6^{2+}$. Furthermore, the peak current obtained at the Nafion/PSS composite film-modified electrode was almost 13-fold greater than that obtained at the pure Nafion-modified electrode. These phenomena may be explained by the strong cation exchange capacity of the Nafion/PSS composite film. The observed
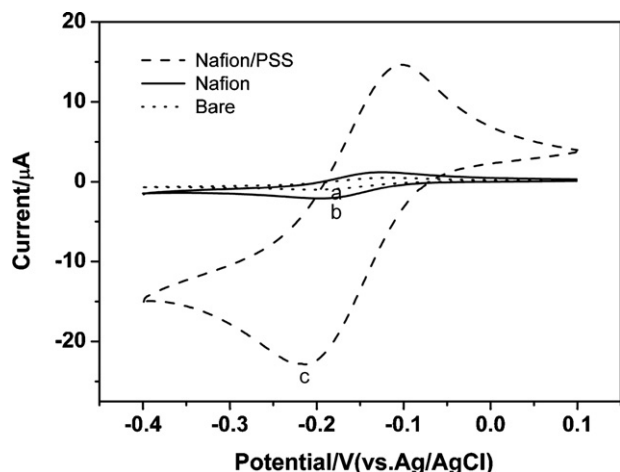
Fig. 1. Cyclic voltammograms of 1.0 mM $Ru(NH_3)_6^{2+}$ in 0.1 M phosphate buffer solution (pH 7.5) at the bare ITO electrode (a), the pure Nafion-modified electrode (b), and the Nafion/PSS composite film-modified electrode (c). The scan rate was 50 mV/s.

distinct current changes of $Ru(NH_3)_6^{2+}$ at the three electrodes may be due to the difference of the preconcentration of $Ru(NH_3)_6^{2+}$ in the different film as they were placed in the same solution. Thus, it can be seen that the Nafion/PSS composite film possibly improved the compact film construction of Nafion and accelerated the rate of charge transfer. The morphologies of Nafion film and Nafion/PSS film formed on the ITO electrode surfaces were characterized by AFM (Fig. 2). As a standard nanometer-scale imaging tool, AFM can give reliable topographical information for the Nafion film and Nafion/PSS film formed on the ITO electrode surfaces. As shown in Fig. 2, it can be seen that the structure of Nafion film is compact. Compared with the pure Nafion film, the interfusion of PSS into Nafion induced an evident change of the compact construction, and the structure of Nafion/PSS film is loose and porous, which is favorable for the construction of solid-state ECL sensor.

To confirm the accelerated charge transfer, the diffusion coefficients, at which rates the electro-active molecules diffuse to the surface of an electrode [28], were measured in $Ru(NH_3)_6^{2+}$ solution at the Nafion composite film-modified electrode and the Nafion/PSS composite film-modified electrode, respectively. The results are shown in Table 1. Plots of i_{pa} versus the square root of the scan rate ($v^{1/2}$) for 1.0 mM $Ru(NH_3)_6^{2+}$ at both modified electrodes are linear, indicating that the oxidation of $Ru(NH_3)_6^{2+}$ in aqueous solution is diffusion controlled. The diffusion coefficients at the Nafion composite film-modified ITO electrode (0.196 cm^2) and at the Nafion/PSS composite film-modified ITO electrode (0.196 cm^2) are estimated to be 1.16×10^{-7} cm^2 s^{-1} and 10.3×10^{-8} cm^2 s^{-1}, respectively, which apparently means that the diffusion rate of $Ru(NH_3)_6^{2+}$ to the surface of the Nafion/PSS composite film-modified ITO electrode is accelerated.

3.2. The characterization of the Nafion/PSS/Ru composite film

The fabrication of the sensor was used according to the above-mentioned method. To verify that the $Ru(bpy)_3^{2+}$ was veritably incorporated into the Nafion/PSS composite film, the UV–vis absorbance spectroscopy experiment was employed and the result is depicted in Fig. 3. A characteristic absorption band at 456 nm is observed in the spectrum, which is in good agreement with previous works and confirms the successful incorporation of $Ru(bpy)_3^{2+}$ [29]. It is worthy to note that the band at 456 nm should be the characteristic metal-to-ligand electron transfer band of $Ru(bpy)_3^{2+}$ [30].

To check the electrochemical behavior of Nafion/PSS/Ru composite film-modified electrode, the cyclic voltammograms (CV) were recorded after the electrodes had reached a steady-state response in the solution. As shown in Fig. 4a, almost no electrochemical response was observed for the bare ITO electrode. Compared with the bare ITO electrode, distinguishable responses appeared at the Nafion/Ru modified electrode and at the Nafion/PSS/Ru composite-modified ITO electrode (Fig. 4b and c), and the corresponding charge current obtained at these two electrodes were obviously larger than that obtained at the bare ITO electrode, indicating that Nafion was an effective medium for the incorporation of $Ru(bpy)_3^{2+}$. Fig. 4c exhibits a large redox wave with oxidation peak at near 1.25 V, which was the characteristic redox wave of $Ru(bpy)_3^{2+}$. This result further indicated that a large
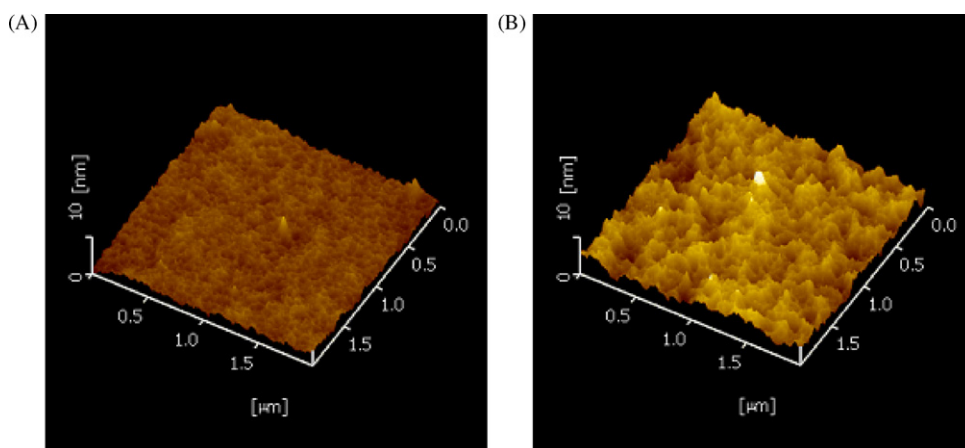

Fig. 2. Typical AFM images of Nafion film (A) and Nafion/PSS film (B) formed on the surfaces of ITO electrode.

Table 1
Diffusion coefficients of 1.0 mM $Ru(NH_3)_6^{2+}$ at the Nafion composite film-modified ITO electrode and the Nafion/PSS composite film-modified ITO electrode.

Electrode	Diffusion coefficients (cm^2 s^{-1})	Regression correlation	Correlation coefficients (R^2)
Nafion	1.16×10^{-7}	$y = 1.79 \times 10^{-6} \times +0.503 \times 10^{-6}$	0.992
Nafion/PSS	10.3×10^{-7}	$y = 5.36 \times 10^{-6} \times +0.277 \times 10^{-6}$	0.998

Electrode area: 0.196 cm^2.
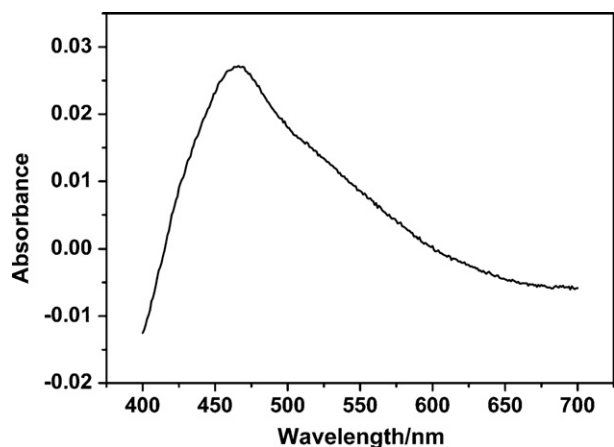
Fig. 3. UV–vis absorbance spectra of the Nafion/PSS/Ru composite-modified ITO electrode.
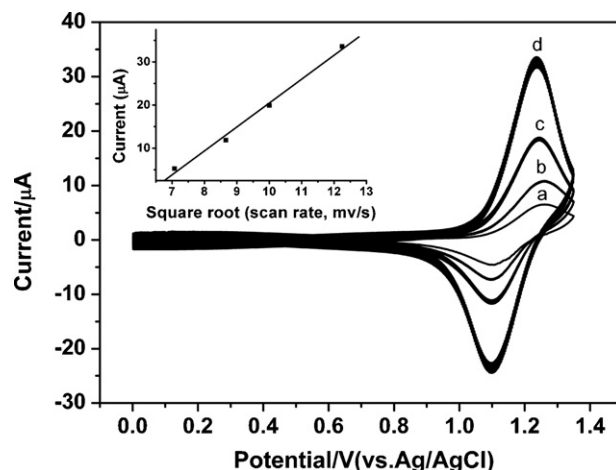

Fig. 5. Cyclic voltammograms of Nafion/PSS/Ru modified electrode at various scan rates: (a) 50 mV/s, (b) 75 mV/s, (c) 100 mV/s, and (d) 150 mV/s in 0.1 M phosphate buffer solution (pH 7.5). The inset is the relationship between the anodic peak currents and the square root of the scan rates.

amount of $Ru(bpy)_3^{2+}$ had been incorporated into the Nafion/PSS composite film after immersing in the $Ru(bpy)_3^{2+}$ aqueous solution. Nafion contains a hydrophobic domain or phase composed of fluorocarbon skeleton and an ionized sulfonate group [21], meanwhile PSS is a negative charge and cation-exchangeable polyelectrolyte. Thus, a hydrophobic cation such as $Ru(bpy)_3^{2+}$ can be easily incorporated into the composite film composed of Nafion and PSS via an ion-exchange process and electrostatic adsorption. Moreover, the strong interaction between $Ru(bpy)_3^{2+}$ and PSS leads to the formation of a large ion-association complex, which can avoid the leaching of $Ru(bpy)_3^{2+}$ from the composite matrix [31].

Meanwhile, compared with the Nafion/Ru modified electrode, the oxidation potential of $Ru(bpy)_3^{2+}$ was positively shifted by ca. 10 mV at the Nafion/PSS/Ru composite film-modified electrode. This phenomenon is consistent with that observed in the previous work [21,26,32], which should be attributed to the huge iR effects resulting from the resistance of Nafion film and the large area of Nafion/PSS composite film.

Subsequently, the CVs of Nafion/PSS/Ru modified electrode at different scan rates in 0.1 M phosphate solution were recorded (Fig. 5), and the relationship between the oxidation peak currents and the square root of scan rates is shown in the inset of Fig. 5. It can be seen that the anodic peak currents are proportional to the square root of the scan rates in the range of 50–150 mV, indicating

that the electrochemical behavior of $Ru(bpy)_3^{2+}$ was controlled by diffusion in the Nafion/PSS composite film. Similar diffusion control phenomena of $Ru(bpy)_3^{2+}$ in surface layers have been reported for pure Nafion film [33] and CNT/Nafion composite film [21].

The $Ru(bpy)_3^{2+}$–TPA system has been well studied in solution, which usually gives ca. 10-fold higher ECL signals compared with other commonly used reductants, such as oxalate [34,35]. Here, the ECL–potential curves of Nafion/PSS/Ru modified electrode in the presence and absence of 1.0 μM TPA in 0.1 M phosphate buffer solution (pH 7.5) are shown in Fig. 6. The onset of luminescence occurs near 1.1 V, and then the ECL intensity rises steeply until it reaches a maximum near 1.25 V, which is consistent with the oxidation potential of $Ru(bpy)_3^{2+}$. The ECL intensity is high up to ca. 2700 a.u., and the ECL response at the composite film-modified electrode is very fast. It may be attributed to the special structure of the Nafion/PSS composite film, and in which $Ru(bpy)_3^{2+}$ could scatter equably [36]. The corresponding ECL–time curves of Nafion/PSS/Ru modified electrode were recorded in the presence and absence of TPA (as shown in the inset of Fig. 6). It can be clearly seen that the ECL signal of $Ru(bpy)_3^{2+}$ increases greatly in the presence of TPA, and the intensity is almost 15-fold greater than that obtained in the absence of TPA, owing to the ECL reaction of $Ru(bpy)_3^{2+}$ with TPA.

Fig. 4. Cyclic voltammograms of the bare ITO electrode (a), the Nafion/Ru modified ITO electrode (b), and the Nafion/PSS/Ru composite film-modified ITO electrode (c) in 0.1 M phosphate buffer solution (pH 7.5) with a scan rate of 50 mV/s.
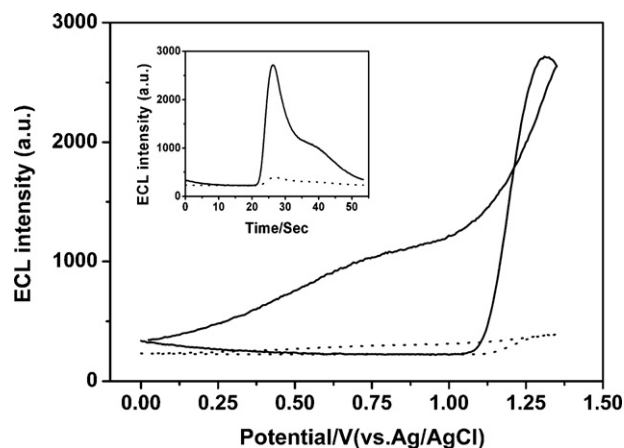

Fig. 6. The ECL–potential curves of Nafion/PSS/Ru modified electrode in the absence (dot line) and presence (solid line) of 1.0 μM TPA in 0.1 M phosphate buffer solution (pH 7.5), and the inset are their corresponding ECL–time curves. The scan rate was 50 mV/s.
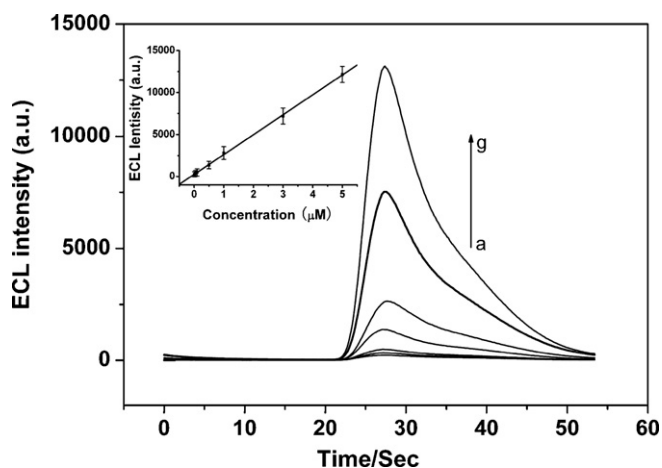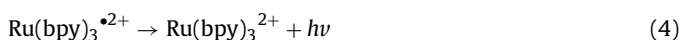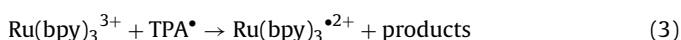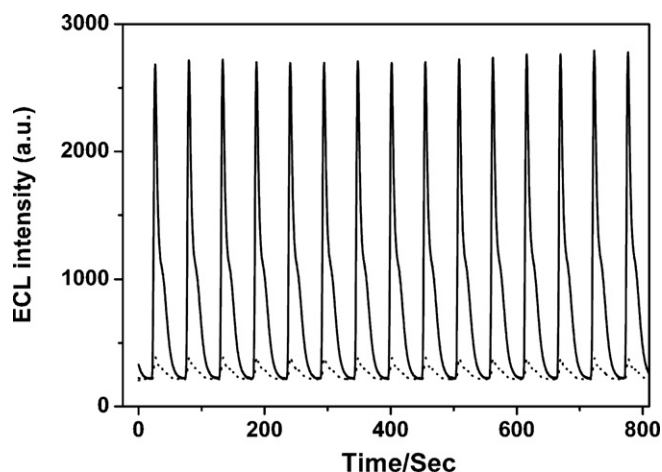
Fig. 7. The ECL behavior of Nafion/PSS/Ru modified electrode in presence of (a) 0.01 μM, (b) 0.05 μM, (c) 0.10 μM, (d) 0.50 μM, (e) 1.0 μM, (f) 3.0 μM, and (g) 5.0 μM TPA at the scan rate of 50 mV/s. The inset is the calibration curve of TPA.

A simplified reaction scheme is given below [14].

$$Ru(bpy)_3^{2+} - e^- \rightarrow Ru(bpy)_3^{3+} \tag{1}$$

$$TPA - e^- \rightarrow [TPA^\bullet]^+ \rightarrow TPA^\bullet + H^+ \tag{2}$$

$$Ru(bpy)_3^{3+} + TPA^\bullet \rightarrow Ru(bpy)_3^{\bullet 2+} + products \tag{3}$$

$$Ru(bpy)_3^{\bullet 2+} \rightarrow Ru(bpy)_3^{2+} + h\nu \tag{4}$$

3.3. Sensitivity, selectivity and stability

For the sensitivity study, the Nafion/PSS composite film-based solid-state ECL sensor was used to determine TPA. The ECL responses of the sensor in different concentration of TPA were recorded (Fig. 7). Calibration curves for TPA are also shown in the inset of Fig. 7. Such data are an average of ECL signals obtained by three times cyclic potential scans (50 mV/s) at a given TPA concentration. The linear range is from 10 nM to 5.0 μM ($R^2 = 0.996$) and the detection limit (S/N = 3) is estimated to be 3.0 nM, which is 3 orders of magnitude lower than that obtained at the Nafion/Ru modified electrode [33].

In order to realize what other compounds can be detected by this sensor, some experiments were performed to determine the selectivity or reveal potential analytes. All the following samples, including tripropylamine, oxalate, arginine, proline, procyclidine,
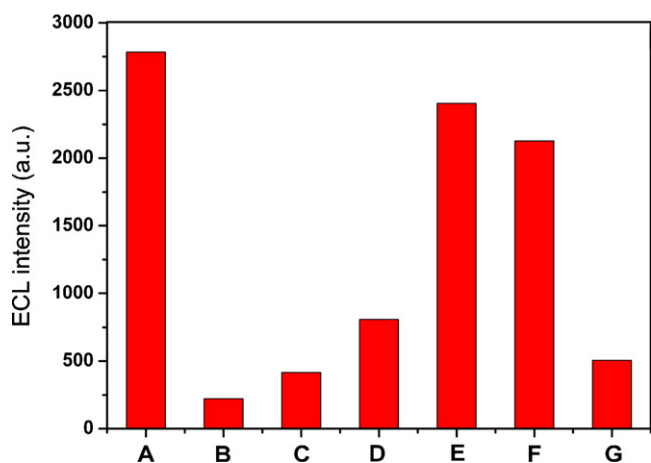

Fig. 8. ECL intensities observed for compounds (0.1 μM) in selectivity study with PMT biased at 800 V. (A) TPA, (B) oxalate, (C) arginine, (D) proline, (E) procyclidine, (F) lidocaine and (G) BSA.

Fig. 9. The ECL intensity–time curves of Nafion/PSS/Ru modified electrode in the absence (dot line) and presence (solid line) of 1.0 μM TPA at room temperature. The scan rate was 50 mV/s.

lidocaine and bovine serum albumin were prepared in the concentration of 1.0 μM in 0.1 M phosphate buffer solution (pH 7.5). The results are listed in Fig. 8, from which we can sum up a conclusion, generally speaking, compounds containing tertiary amino group can be detected by this ECL sensor.

Fig. 9 shows the ECL intensity–potential curves of the Nafion/PSS composite film-based solid-state ECL sensor in 0.1 M phosphate buffer solution (pH 7.5) with and without 1.0 μM TPA under continuous CV for 15 cycles. The relative standard deviation of ECL peak height is 1.38%, which reflects the good stability of the Nafion/PSS composite film-based solid-state ECL sensor. This result is possibly attributed to the synergetic effect of Nafion and PSS. Furthermore, the electrostatic interaction between negatively charged PSS and positively charged $Ru(bpy)_3^{2+}$ may have a certain effect on the stability of this sensor.

4. Conclusions

The coupling of organic cation exchange polymer (Nafion) with negative polyelectrolyte (PSS) provides an effective approach to immobilize ECL reagent–$Ru(bpy)_3^{2+}$ to fabricate the solid-state sensor. Herein, both Nafion and PSS can incorporate $Ru(bpy)_3^{2+}$ by ion-exchange, moreover, the negative charge PSS could immobilize $Ru(bpy)_3^{2+}$ by virtue of electrostatic interactions. Compared with the pure Nafion film, the interfusion of PSS into Nafion takes some advantages. On one hand, it could enhance the stability of ECL sensor due to the strong ability of ion-exchange; on the other hand, it could greatly overcome the drawback of slow mass transfer due to changing the compact construction of Nafion film, which results in the improvement of detection sensitivity. The solid-state ECL sensor based on the Nafion/PSS composite film also enhanced the ECL intensity of $Ru(bpy)_3^{2+}$ and exhibited good ECL stability, because the composite film immobilized a large amount of $Ru(bpy)_3^{2+}$. Furthermore, the present ECL sensor has great potentials in applications for CE, HPLC, and microfluidics.

References

[1] A.J. Bard, Electrogenerated Chemiluminescence, Marcel Dekker, NY, USA, 2004.
[2] M.M. Richter, Chem. Rev. 104 (2004) 3003.
[3] D.R. Skotty, W.Y. Lee, T.A. Nieman, Anal. Chem. 68 (1996) 1530.
[4] J.S. Ridlen, G.J. Klopp, T.A. Niemana, Anal. Chim. Acta 341 (1997) 195.
[5] J. Liu, J. Yan, X. Yang, E. Wang, Anal. Chem. 75 (2003) 36.
[6] M.T. Chiang, C.W. Whang, J. Chromatogr. A 934 (2001) 59.
[7] H. Qiu, J. Yan, X. Sun, J. Liu, W. Cao, X. Yang, E. Wang, Anal. Chem. 75 (2003) 5435.
[8] Y. Du, H. Wei, J. Kang, J. Yan, X. Yin, X. Yang, E. Wang, Anal. Chem. 77 (2005) 7993.
[9] R.A. Potyrailo, R.C. Conrad, A.D. Ellington, G.M. Hieftje, Anal. Chem. 70 (1998) 3419.
[10] I. Rubinstein, A.J. Bard, J. Am. Soc. 103 (1981) 512.
[11] J. Li, Y. Xu, H. Wei, T. Huo, E. Wang, Anal. Chem. 79 (2007) 5439.
[12] H. Wang, G. Xu, S. Dong, Electroanalysis 14 (2002) 853.
[13] Z. Guo, Y. Shen, M. Wang, F. Zhao, S. Dong, Anal. Chem. 76 (2004) 184.
[14] H. Wei, E. Wang, Trends Anal. Chem. 27 (2008) 447.
[15] Z. Liu, G. Chen, Talanta 70 (2006) 111.
[16] X. Hun, Z. Zhang, J. Pharm. Biomed. Anal. 47 (2008) 670.
[17] B. Qin, Y. Yan, X. Yang, Microchim. Acta 162 (2008) 211.
[18] C. Zhao, N. Egashira, Y. Kurauchi, K. Ohga, Anal. Sci. 14 (1998) 439.
[19] M. Sykora, T.J. Meyer, Chem. Mater. 11 (1999) 1186.
[20] H. Wang, G. Xu, S. Dong, Analyst 126 (2001) 1095.
[21] Z. Guo, S. Dong, Anal. Chem. 76 (2004) 2683.
[22] J.K. Herr, J.E. Smith, C.D. Medley, D. Shangguan, W. Tan, Anal. Chem. 78 (2006) 2918.
[23] A. Khramov, M. Collinson, Anal. Chem. 72 (2000) 2943.
[24] I. Rubinstein, A.J. Bard, Am. Chem. Soc. 102 (1980) 6642.
[25] A.N. Khramov, M.M. Collinson, Anal. Chem. 72 (2000) 2943.
[26] H.N. Choi, S.H. Cho, W.Y. Lee, Anal. Chem. 75 (2003) 4250.
[27] X. Liu, H. Bai, W. Huang, L. Du, X. Yang, E. Wang, Electrochim. Acta 51 (2006) 2512.
[28] S. Workman, M.M. Richter, Anal. Chem. 72 (2000) 5556.
[29] L. Fang, Z. Lü, H. Wei, E. Wang, Biosens. Bioelectron. 23 (2008) 1645.
[30] M. Miao, A.J. Bard, Anal. Chem. 75 (2003) 5825.
[31] J. Jia, Y. Cao, Z. Wang, Electroanalysis 19 (2007) 1845.
[32] Y. Deng, C.J. Seliskar, W.R. Heineman, Anal. Chem. 69 (1997) 4045.
[33] T.M. Downey, T.A. Nieman, Anal. Chem. 64 (1992) 261.
[34] W.Y. Lee, T.A. Nieman, Anal. Chem. 67 (1995) 1789.
[35] J.B. Noffsinger, N.D. Danielson, Anal. Chem. 59 (1987) 865.
[36] L.S. Rocha, J.P. Pinheiro, H.M. Carapuca, Langmuir 22 (2006) 8241.

Ni(II)–baicalein complex modified multi-wall carbon nanotube paste electrode toward electrocatalytic oxidation of hydrazine

Li Zheng [a,b], Jun-feng Song [a,*]

[a] Institute of Analytical Science, Northwest University, Xi'an, 710069, PR China
[b] College of Chemistry and Chemical Engineering, Xi'an Shiyou University, Xi'an, 710065,PR China

ARTICLE INFO

ABSTRACT

A modified electrode Ni(II)–BA–MWCNT-PE has been fabricated by electrodepositing nickel(II)–baicalein [Ni(II)–BA] complex on the surface of multi-wall carbon nanotube paste electrode (MWCNT-PE) in alkaline solution. The Ni(II)–BA–MWCNT-PE exhibits the characteristic of improved reversibility and enhanced current responses of the Ni(III)/Ni(II) couple compared with Ni(II)–BA–CPE. It also shows good electrocatalytic activity toward the oxidation of hydrazine. Kinetic parameters such as the electron transfer coefficient α, rate constant k_s of the electrode reaction, the diffusion coefficient D of hydrazine and the catalytic rate constant k_{cat} of the catalytic reaction are determined. Moreover, the catalytic currents present linear dependence on the concentration of hydrazine from 2.5 μM to 0.2 mM by amperometry. The detection limit and sensitivity are 0.8 μM and 69.9 μA mM^{-1}, respectively. The modified electrode for hydrazine determination is of the property of simple preparation, good stability, fast response and high sensitivity.

© 2009 Elsevier B.V. All rights reserved.

1. Introduction

Hydrazine and its derivatives are familiar reducing agents. They are widely used in industry and agriculture as fuel cells, insecticides, explosives, rocket propellants, metal film manufactures and photographic chemicals [1]. Hydrazine also has carcinogenic and hepatotoxic effect and can be absorbed through skin, affects blood production, causes liver and kidney damages [2]. Therefore, the determination of hydrazine is of practical importance. Hitherto, various methods including titrimetry [3], potentiometry [4], fluorimetry [5], spectrophotometry [6] and chemiluminescence [7] have been reported for the determination of hydrazine. Voltammetric method possesses many advantages as high sensitivity, good selectivity, rapid response and simple operating procedure, it is a competitive alternative for the determination of hydrazine. Because of the large overpotential of hydrazine at conventional electrodes, various inorganic and organic materials have been modified on the electrode surface to enhance the electron transfer rate and to reduce the overpotential for the oxidation of hydrazine [8–14].

Considering that nickel macrocyclic complexes can be easily electropolymerized onto an electrode surface in alkaline solution to form modified electrodes. This kind of modified electrode shows high catalytic activity toward electro-oxidation of organics containing OH and NH$_2$ groups, such as methanol, carbohydrates and

amino acids [15–17]. Additionally, baicalein (BA, structure shown in Scheme 1), a flavonoid, possesses biological activities including antioxidant, anti-tumor, anti-HIV and anti-neurotoxicity [18–21]. It is also known to complex with various metal cations including Ni(II) to form stable compounds [22]. So far, few reports investigate the redox behavior of BA. Zhu et al. investigated the oxidation behavior and some biological activities of BA at a glassy carbon electrode [23]. Vestergaard et al. investigated the redox behavior and copper-chelating properties of BA at disposable pencil graphite electrodes [24]. However, to our knowledge, there is no report about metal–baicalein complex modified electrode.

On the other hand, carbon nanotubes (CNT) have been widely applied as electrode material due to their high surface area and outstanding ability to mediate fast electron-transfer kinetics for a wide range of electroactive species [25–27]. CNT composite materials can further enhance electrode's electrocatalytic ability. For example, meldola's blue functionalized carbon nanotube electrode for the oxidation of NADH [28], nano-ZnO/MWCNT/chitosan nanocomposite for the detection of sequence-specific of PAT gene [29], and so on [30,31]. These composite materials have gained growing interest in the electroanalytical field.

Thus, in the present work, Ni(II)–BA complex and multi-wall carbon nanotubes (MWCNT) were both employed to prepare a composite material chemically modified electrode Ni(II)–BA–MWCNT-PE by electrodepositing Ni(II)–BA complex on the surface of multi-wall carbon nanotube paste electrode (MWCNT-PE). The electrochemical behavior of Ni(II)–BA–MWCNT-PE and the electrocatalytic activity to the oxidation of hydrazine were investigated by cyclic voltammetry and chronoamperometry.

* Corresponding author. Tel.: +86 29 8830 3448; fax: +86 29 8830 3448.
E-mail address: songjunf@nwu.edu.cn (J.-f. Song).
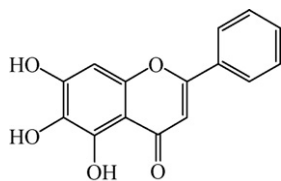
Scheme 1. Structure formula of baicalein.

2. Experimental

2.1. Materials

BA (purity > 98%) was purchased from Panya Chemical Co. Ltd. (Shanghai, China). 1.0 mM BA was prepared by 0.1 M NaOH solution. The stock solution of 10 mM Ni(II) ion was prepared by 2.5% ammonia solution and was diluted to 0.5 mM with 0.1 M NaOH solution before experiment. MWCNT (diameter: 10–20 nm, length: 1–2 μm, purity: >95%) was purchased from Shenzhen Nanotech Port Co. Ltd. (Shenzhen, China) and used without further purification. Graphite powder (spectral pure) was purchased from Beijing Chemical Reagent Factory (Beijing, China). All the chemicals used were of analytical-reagent grade. Twice-distilled water was used throughout the experiments.

2.2. Apparatus

Electrochemical measurements were carried out on CHI 660A electrochemical workstation (Chenhua Instrumental Company, Shanghai, China) controlled by a personal computer. A conventional three-electrode system was employed, including a homemade Ni(II)–BA–MWCNT-PE working electrode, a saturated calomel reference electrode (SCE) and a platinum wire counter electrode. All the potentials quoted in the present work were referred to SCE. All experiments were carried out at room temperature.

2.3. Electrode preparation

The MWCNT-PE was prepared by mixing MWCNT and paraffin oil in a ratio of 3:2 (w/w) in a mortar. A portion of the resulting paste was packed firmly into the cavity (1.6 mm diameter) of a PTFE tube. The conventional carbon paste electrode (CPE) was prepared in a similar way by mixing graphite powder with paraffin oil. The electric contact was established via a copper wire. The surface of electrode was smoothed on a weighing paper and rinsed with water. The efficient area of the MWCNT-PE was about 1.9 times as large as that of the CPE using $K_3Fe(CN)_6$ as a probe according to Randles–Sevcik equation.
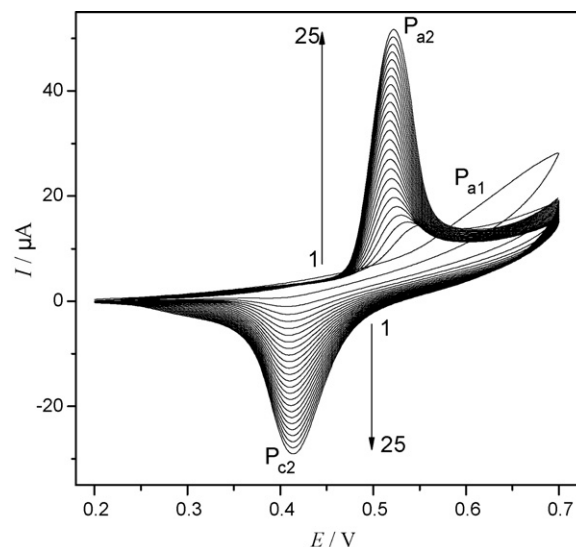

Fig. 1. Multicycle voltammograms of MWCNT-PE in 0.1 M NaOH solution containing 1.0 mM BA and 0.5 mM Ni(II) ion. Scan rate: 0.1 V s^{-1}, potential range: 0.2–0.7 V.

Ni(II)–BA–MWCNT-PE was prepared by the following procedure: MWCNT-PE was placed in 0.1 M NaOH solution containing 1.0 mM BA and 0.5 mM Ni(II) ion and scanned consecutively between 0.2 and 0.7 V at scan rate of 0.1 V s^{-1} for 25 cycles. BA–MWCNT-PE and Ni(II)–MWCNT-PE were prepared by the same way as Ni(II)–BA–MWCNT-PE in 1.0 mM BA or 0.5 mM Ni(II) ion, respectively. Also, the Ni(II)–BA–CPE was prepared by the same way as Ni(II)–BA–MWCNT-PE but the substrate electrode was a CPE.

3. Results and discussion

3.1. The preparation and electrochemical behavior of Ni(II)–BA–MWCNT-PE

Consecutive cyclic voltammograms of MWCNT-PE in 0.1 M NaOH solution containing 1.0 mM BA and 0.5 mM Ni(II) ion are shown in Fig. 1. On the first cycle, an oxidation peak P_{a1} at +0.60 V corresponding to the oxidation of BA [23,24] was observed. On the second cycle, peak P_{a1} disappeared. Concomitantly, an anodic peak P_{a2} at 0.51 V and a cathodic peak P_{c2} at 0.37 V were observed. While continuous scanning, peak currents of P_{a2} and P_{c2} increased gradually, and a uniform adherent blue polymer film was observed on the electrode surface. Moreover, SEM images of MWCNT-PE and Ni(II)–BA–MWCNT-PE (Fig. 2) also show the different surface morphologies of the two electrodes. These facts indicated that poly-
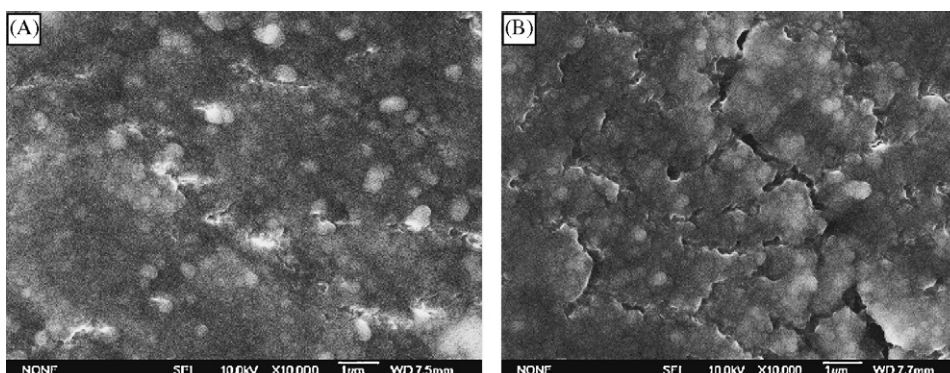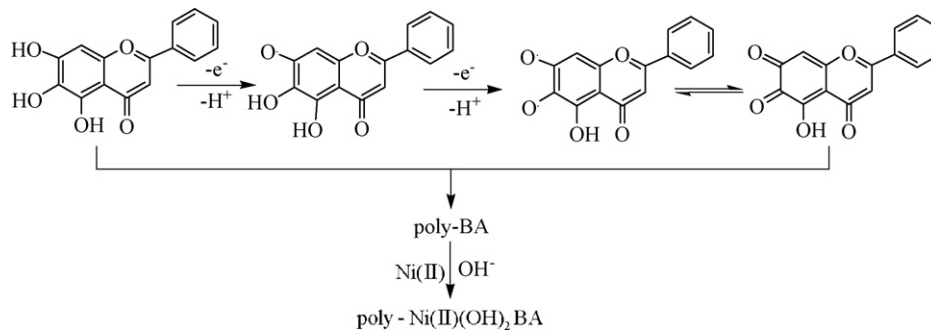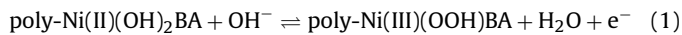

Fig. 2. SEM images of MWCNT-PE (A) and Ni–BA–MWCNT-PE (B).

Scheme 2. The possible deposition process of poly-[Ni(II)–BA].

[Ni(II)–BA] film was deposited on the surface of MWCNT-PE, and Ni(II)–BA–MWCNT-PE was prepared. The possible deposition process of poly-[Ni(II)–BA] and redox process of the modified electrode are expressed as Scheme 2 and Eq. (1):

$$\text{poly-Ni(II)(OH)}_2\text{BA} + \text{OH}^- \rightleftharpoons \text{poly-Ni(III)(OOH)BA} + \text{H}_2\text{O} + \text{e}^- \quad (1)$$

In other words, the mechanism of film formation was probably that BA was first oxidized to a corresponding *o*-quinone derivative of BA (peak P_{a1}) [23,24]. The *o*-quinone derivative and the intermediate free radicals of BA could undergo a variety of intermolecular reactions, leading to a polymeric structure [32] and deposited on the MWCNT-PE surface. And then the complexation of Ni(II) ion in the structure made the film conductive (peaks P_{a2} and P_{c2}) and allowed the growth of a multi-layer system.

Moreover, the voltammetric behavior of Ni(II)–BA–MWCNT-PE was examined and compared with those of BA–MWCNT-PE and Ni(II)–BA–CPE. Fig. 3 shows cyclic voltammograms of BA–MWCNT-PE (a), Ni(II)–BA–MWCNT-PE (b) and Ni(II)–BA–CPE (c) in 0.1 M NaOH solution at scan rate of 0.1 V s^{-1}. At BA–MWCNT-PE, no electrochemical response was observed. This was due to the passivation of the electrode surface by the irreversibly adsorbed oxidation product of BA. At Ni(II)–BA–MWCNT-PE, a pair of well-defined redox peaks with large peak current response ($I_{pa} = 46.6\,\mu A$) and small peak potential separation ($\Delta E_p = 106\,mV$) were observed. However, at Ni(II)–BA–CPE, the current response was smaller ($I_{pa} = 22.3\,\mu A$) and the peak potential separation was larger ($\Delta E_p = 129\,mV$). These
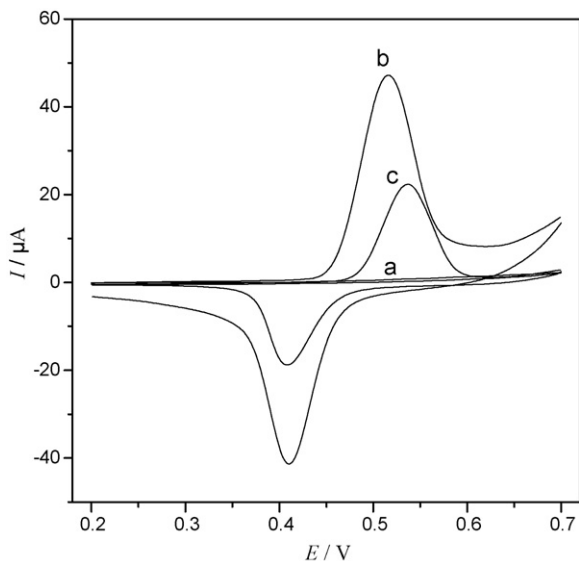

Fig. 3. Cyclic voltammograms of BA–MWCNT-PE (a), Ni(II)–BA–MWCNT-PE (b) and Ni(II)–BA–CPE (c) in 0.1 M NaOH solution at scan rate of 0.1 V s^{-1}.

results indicated that the anodic and cathodic peaks observed were from the redox reaction of the Ni(III)/Ni(II) couple in the electrode surface. Also, the reversibility and electrochemical response of Ni(III)/Ni(II) couple in Ni(II)–BA–MWCNT-PE were improved. These characters of Ni(II)–BA–MWCNT-PE resulted from the following contributions. Both BA and its oxidation product acted as ligand for immobilizing Ni(II) ions on the electrode surface. And the presence of MWCNT supplied larger surface area to allow more deposition of poly-[Ni(II)–BA] and to accelerate electron transfer between poly-[Ni(II)–BA] and the substrate electrode.

The influence of scan rate ν in a wide range of 0.01–1.8 V s^{-1} to the electrochemical behavior of Ni(II)–BA–MWCNT-PE was also investigated (Fig. 4A). As shown, the peak current I_p increased with the increase of scan rate and were proportional to scan rate ν below 0.1 V s^{-1} (Fig. 4B), which indicated a surface confined redox process. According to the following equation [33]:

$$I_p = \frac{n^2 F^2 \nu A \Gamma_c}{4RT} \quad (2)$$

where I_p was the peak current, A the electrode surface area, the other symbols had their usual meanings, the surface coverage concentration (Γ_c) of poly-[Ni(II)–BA] was calculated to be $2.1 \times 10^{-8}\,mol\,cm^{-2}$, corresponding to the presence of multi-layer of surface species. When $\nu > 0.1\,V\,s^{-1}$, the peak currents became proportional to the square root of scan rate ν (Fig. 4C), signifying the dominance of a diffusion process, which reflected the relatively slower diffusion process of OH$^-$ rather than the charge-transfer process of Ni(III)/Ni(II) couple [16,17].

Moreover, at higher scan rates, peak-to-peak separation increased evidently, and the peak potential E_p was proportional to the logarithm of scan rate for $\nu \geq 0.6\,V\,s^{-1}$ (Fig. 4D), indicating the limitation of charge-transfer kinetics. Based on the Laviron theory [34], the electron transfer coefficient α could be calculated. For cathodic and anodic peaks, the slopes of E_p versus log ν were -0.080 and 0.136, respectively. The calculated value of α was 0.65. According to the following equation:

$$\log\,k_s = \alpha \log(1-\alpha) + (1-\alpha)\log\,\alpha - \log\frac{RT}{nF\nu} - \frac{\alpha(1-\alpha)nF\Delta E_p}{2.3RT} \quad (3)$$

where k_s was the rate constant of electrode reaction, other symbols had their conventional meanings, k_s was calculated to be 2.21 s^{-1}.

3.2. Electrocatalytic oxidation of hydrazine at Ni(II)–BA–MWCNT-PE

The voltammetric behaviors of Ni(II)–BA–MWCNT-PE, MWCNT-PE, BA–MWCNT-PE, Ni(II)–MWCNT-PE and Ni(II)–BA–CPE in the absence and the presence of 2.0 mM hydrazine are shown in
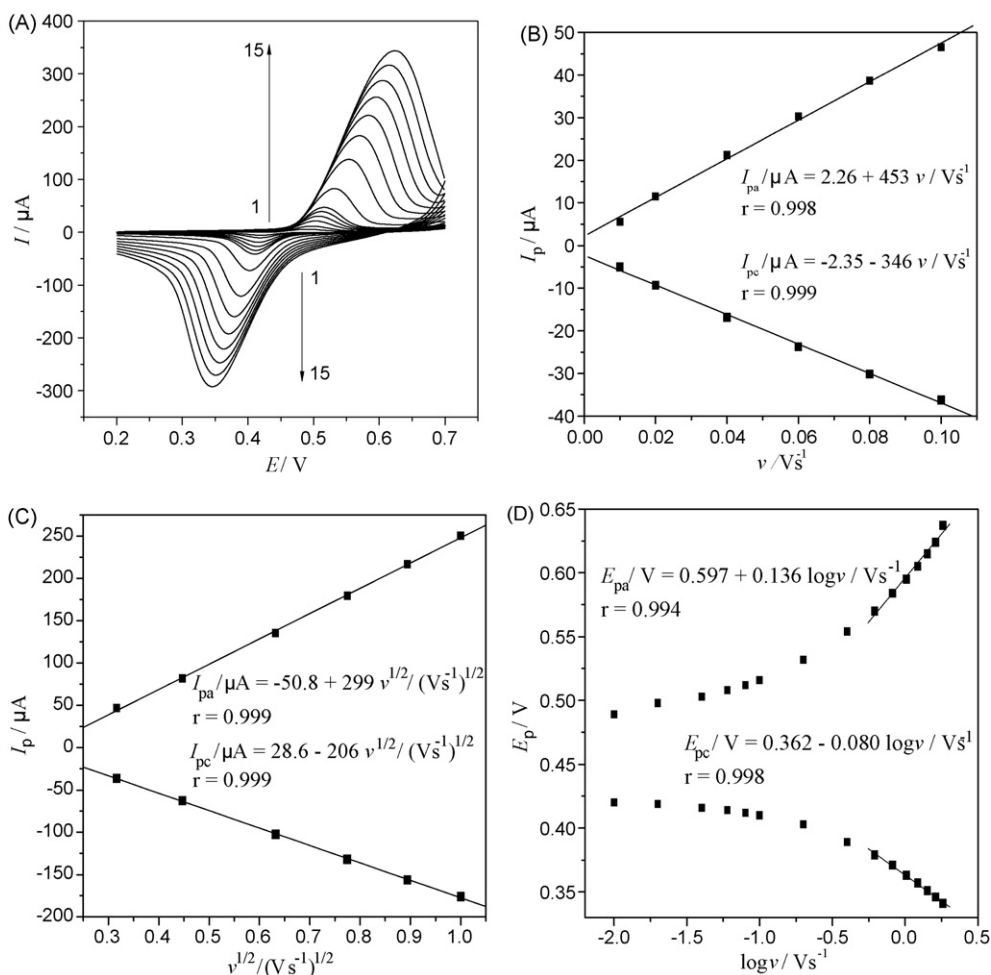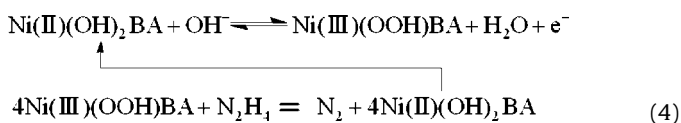
Fig. 4. (A) Cyclic voltammograms of Ni(II)–BA–MWCNT-PE in 0.1 M NaOH solution at various scan rates (from inner to outer): 0.01, 0.02, 0.04, 0.06, 0.08, 0.1, 0.2, 0.4, 0.6, 0.8, 1.0, 1.2, 1.4, 1.6, 1.8 V s^{-1}. (B) Plot of I_p vs. v. (C) Plot of I_p vs. $v^{1/2}$. (D) Plot of E_p vs. log v.

Fig. 5. At Ni(II)–BA–MWCNT-PE, a pair of redox peaks corresponded to the Ni(III)/Ni(II) couple was observed in the absence of hydrazine (Fig. 5A, curve a). After addition of 2.0 mM hydrazine, the anodic peak current increased noticeably accompanied by a decrease in cathodic peak current (Fig. 5A, curve b), and the anodic peak current was linear with hydrazine concentration in the range of 0.05–2.5 mM (Fig. 6). These facts indicated that Ni(II)–BA–MWCNT-PE had catalytic activity toward the oxidation of hydrazine. Under the same experimental conditions, the oxidation of hydrazine at MWCNT-PE and BA–MWCNT-PE involved increase in the background current but no defined anodic peaks were observed (Fig. 5B and C). The peak current of the electrocatalytic oxidation of hydrazine at Ni(II)–MWCNT-PE and Ni(II)–BA–CPE was 6.09 μA (Fig. 5D, curve h) and 51.5 μA (Fig. 5E, curve j), respectively, which were much lower than that at Ni(II)–BA–MWCNT-PE (118 μA, Fig. 5A, curve b). These results clearly indicated that poly-[Ni(II)–BA] and MWCNT composite material could improve the characteristic of hydrazine oxidation. The catalytic center was the Ni(III)/Ni(II) couple in the poly-[Ni(II)–BA]. And the oxidation process of hydrazine at Ni(II)–BA–MWCNT-PE could be expressed as follows:

$$\mathrm{Ni(II)(OH)_2\,BA + OH^- \rightleftharpoons Ni(III)(OOH)BA + H_2O + e^-}$$

$$4\,\mathrm{Ni(III)(OOH)BA + N_2H_4 = N_2 + 4\,Ni(II)(OH)_2\,BA} \qquad (4)$$

In order to get more information about the catalytic mechanism, cyclic voltammetry and chronoamperometry were conducted.

Cyclic voltammograms of 2.0 mM hydrazine at different scan rates v (Fig. 7A) show that the anodic peak currents were proportional to the square root of scan rate v (Fig. 7B). It indicated that at sufficient potential, the electrocatalytic process was controlled by hydrazine diffusion to the electrode/solution interface and depended on the hydrazine concentration in bulk solution, which was fit for quantitative applications. The peak potential for the catalytic oxidation of hydrazine shifted to more positive values with the increase of scan rate v, suggesting that there was a kinetic limitation in the reaction between the redox sites of poly-[Ni(II)–BA] and hydrazine.

Furthermore, chronoamperometry was used to estimate the diffusion coefficient of hydrazine (Fig. 8). For an electroactive material with a diffusion coefficient D, the current response under diffusion control was described by Cottrell equation [35]:

$$I = nFAD^{1/2}c\pi^{-1/2}t^{-1/2} \qquad (5)$$

where D and c were the diffusion coefficient (cm^2 s^{-1}) and bulk concentration (mol cm^{-3}) of hydrazine, respectively; A was the electrode area; n was the total number of electrons transfer in the oxidation of hydrazine (n = 4 [1,14]); I was the current controlled by the diffusion of hydrazine. From the slopes of I versus $t^{-1/2}$ relationship (Fig. 8B), the average value of D was calculated to be 3.58×10^{-5} cm^2 s^{-1}.
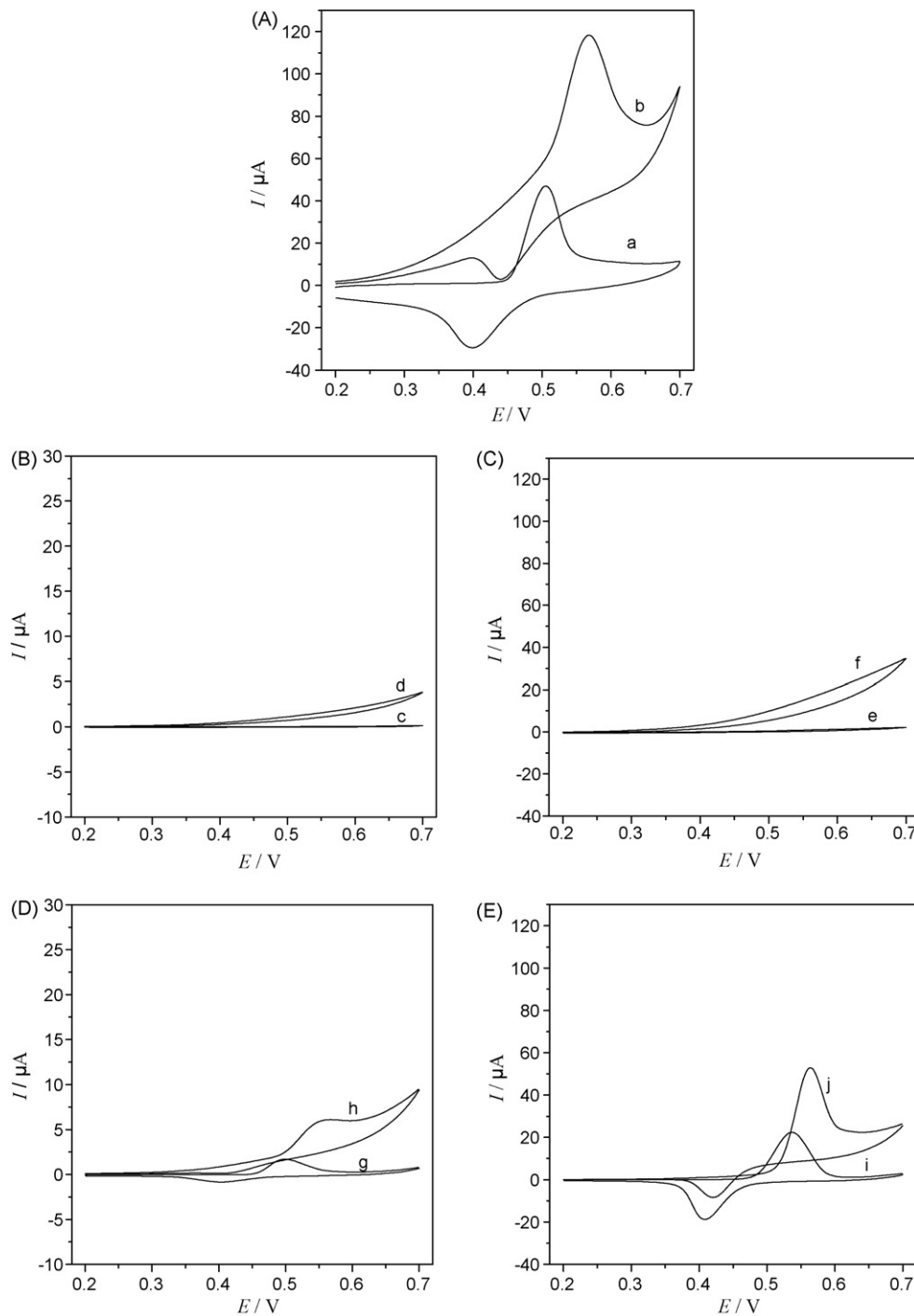
Fig. 5. Cyclic voltammograms of (A) Ni(II)–BA–MWCNT-PE, (B) MWCNT-PE, (C) BA–MWCNT-PE, (D) Ni(II)–MWCNT-PE and (E) Ni(II)–BA–CPE in the absence (a, c, e, g, i) and the presence (b, d, f, h, j) of 2.0 mM hydrazine in 0.1 M NaOH solution at scan rate of 0.1 V s^{-1}.

Chronoamperometry was also used for the evaluation of the catalytic rate constant k_{cat} [8,13]. At intermediate time, when the oxidation current was dominated by the rate of the electrocatalytic reaction of hydrazine, the catalytic current I_{cat} could be written as follows:

$$\frac{I_{cat}}{I_L} = \pi^{1/2}(k_{cat}c_0t)^{1/2} \tag{6}$$

where I_{cat} and I_L were the oxidation currents in the presence and the absence of hydrazine, respectively. k_{cat}, c_0 and t were the catalytic rate constant (M^{-1} s^{-1}), the bulk concentration (M) of hydrazine

and time elapsed (s). From the slope of I_{cat}/I_L versus $t^{1/2}$ relationship (Fig. 8C), k_{cat} was calculated to be 4.78×10^4 M^{-1} s^{-1} for the concentration of 1.0 mM hydrazine, which was higher than those reported [8,13].

3.3. Amperometric detection of hydrazine at Ni(II)–BA–MWCNT-PE

Based on the voltammetric results described above, amperometric current–time response was recorded to estimate the calibration curve and the detection limit for hydrazine determination at
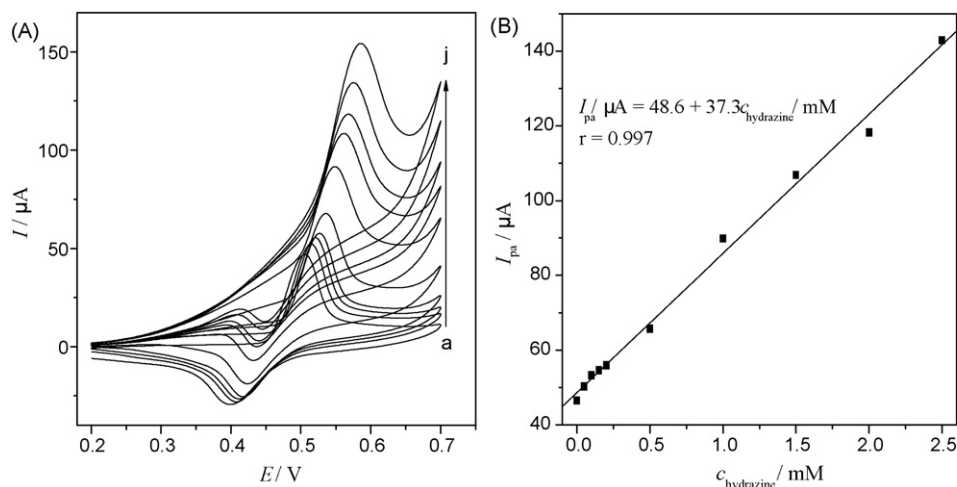
Fig. 6. (A) Cyclic voltammograms of Ni(II)–BA–MWCNT-PE at scan rate of 0.1 V s^{-1} in 0.1 M NaOH solution containing different concentration of hydrazine: (a) 0.00 mM, (b) 0.05 mM, (c) 0.10 mM, (d) 0.15 mM, (e) 0.20 mM, (f) 0.50 mM, (g) 1.0 mM, (h) 1.5 mM, (i) 2.0 mM and (j) 2.5 mM. (B) Plot of I_{pa} vs. $c_{hydrazine}$.

Ni(II)–BA–MWCNT-PE. The typical hydrazine amperogram during the successive addition of 2.5 μL of 5.0 mM hydrazine into continuously stirred 5.0 mL 0.1 M NaOH solution is shown in Fig. 9. As shown, a well-defined amperometric response with the response time less than 5 s was observed, demonstrating stable and efficient catalytic ability of Ni(II)–BA–MWCNT-PE. The response current was linear with the hydrazine concentration from 2.5 μM to 0.2 mM with a slope of 69.9 μA mM^{-1} and linear correlation coefficient of 0.999. The detection limit was 0.8 μM (3 σ/s, where σ was the standard deviation of the intercept and s was the slope of the calibration curve). The analytical characteristics of Ni(II)–BA–MWCNT-PE were compared with those reported in the literature, as shown in Table 1.

3.4. Interferences

In order to evaluate the selectivity of the proposed method, the influence of various substances on the determination of hydrazine was studied under the optimum conditions. The tolerable limit was defined as the concentrations of interfering substances that caused an error less than ±5.0% for the determination of 10 μM

of hydrazine. The results showed that 100-fold K$^+$, Ba^{2+}, Ca^{2+}, F$^-$, SO$_4^{2-}$, PO$_4^{3-}$; 50-fold Mg^{2+}, Al^{3+}, NO$_3^-$, Cl$^-$, SCN$^-$; 10-fold Pb^{2+}, Fe^{2+}, Co^{2+}, Zn^{2+}, NO$_2^-$, CO$_3^{2-}$ did not interfere with the determination. The results proved that the proposed method had acceptable selectivity.

3.5. Application to real sample analysis

In order to further elucidate the application of the proposed method, the amount of hydrazine in wet preservation solution of boiler was determined. The samples were also analyzed by a standard method based on p-dimethylamino benzaldehyde reaction [36] for comparison. The results obtained by the proposed method were in good agreement with those obtained by the standard method (Table 2).

3.6. Stability and reproducibility

The stability and the reproducibility of Ni(II)–BA–MWCNT-PE were studied in 0.1 M NaOH solution. A set of 15 replicate measurements for 2.5 μM hydrazine yielded a relative standard
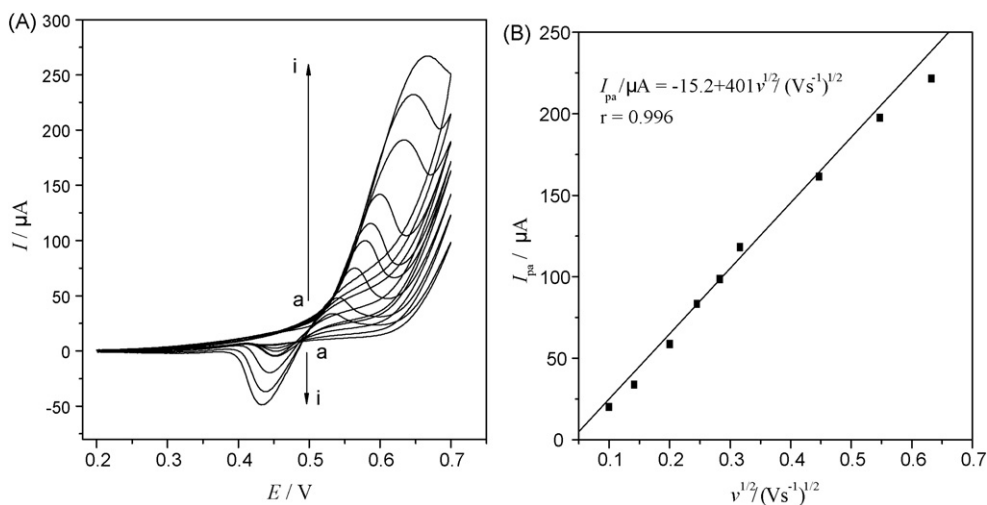

Fig. 7. (A) Cyclic voltammograms of Ni(II)–BA–MWCNT-PE in 0.1 M NaOH solution containing 2.0 mM hydrazine at various scan rates (from a to i): 0.010, 0.020, 0.040, 0.060, 0.080, 0.10, 0.20, 0.30, 0.40 V s^{-1}. (B) Plot of I_{pa} vs. $v^{1/2}$.
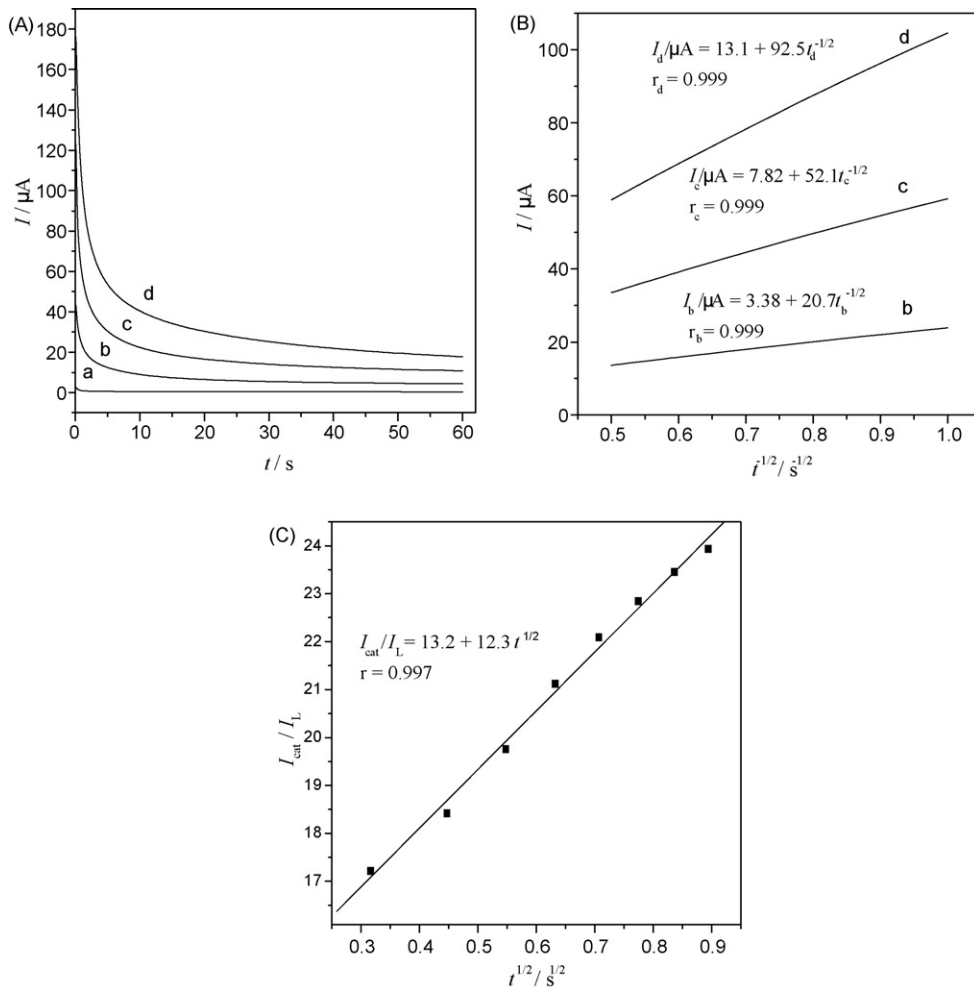
Fig. 8. (A) Chronoamperograms of Ni(II)–BA–MWCNT-PE in 0.1 M NaOH solution containing (a) 0 mM, (b) 1.0 mM, (c) 2.0 mM and (d) 3.0 mM hydrazine. (B) Plot of I vs. $t^{-1/2}$. (C) Plot of I_{cat}/I_L vs. $t^{1/2}$ for 1.0 mM hydrazine.

deviation (R.S.D.) of 1.8%. Five pieces of Ni(II)–BA–MWCNT-PE were prepared and the R.S.D. for the individual determination of 0.2 mM hydrazine was 3.2%. The long-term stability of the modified electrode was tested after stored under dry condition at room temperature for 30 days and no significant change in current responses was observed. Thus, the Ni(II)–BA–MWCNT-PE exhibited acceptable stability and reproducibility for hydrazine measurement.
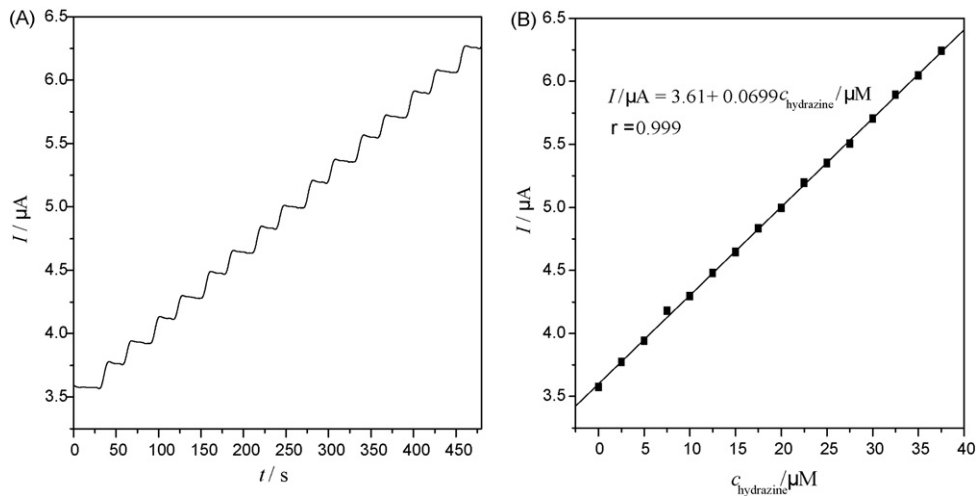

Fig. 9. (A) Amperometric response of Ni(II)–BA–MWCNT-PE in 0.1 M NaOH solution by successive addition of 2.5 μM hydrazine. Applied potential: +0.65 V. (B) Plot of I vs. $c_{hydrazine}$.

Table 1
Comparison of analytical characteristics of various modified electrodes for the electrocatalytic oxidation of hydrazine.

Electrode	pH	Linear range (μM)	Detection limit (μM)	Sensitivity (μM mM^{-1})	Reference
Chlorogenic acid–GCE	7.5	50–3000	–	5.43	[1]
NiHCF–GWE[a]	7.0	2.4–8200	1	1130	[9]
Pd–CILE[b]	7.0	5–800	0.82	12.2	[10]
FePc–SAM–AuE[c]	13.3	13–92	5	16.2	[11]
DHsalophen–GCE[d]	7.0	10–400	1.6	17.04	[12]
Quinizarine–GCE	2.0	0.2–10	–	–	[13]
Curcumin–MWCNT–GCE	8.0	2–44	1.4	22.9	[14]
Ni(II)–BA–MWCNT-PE	13	2.5–200	0.8	69.9	This work

[a] Nickel hexacyanoferrate modified amine functionalized graphite–wax composite electrode.
[b] Palladium nanoparticles modified carbon ionic liquid electrode.
[c] Iron phthalocyanine (FePc) complex-linked-mercaptopyridine–SAM–modified gold electrode.
[d] N,N′-bis(dihydroxybenzylidene)-1,2-diaminobenzene modified GCE.
Other symbols had their conversional meanings.

Table 2
Determination results of hydrazine in wet preservation solution of boiler.

Sample	Hydrazine found (mg/L)[a]		Relative error (%)
	Proposed method	Standard method	
1	180.2 ± 1.7	177.3 ± 2.5	1.6
2	176.9 ± 3.1	181.0 ± 1.9	2.3
3	178.5 ± 2.1	182.2 ± 2.6	2.0

[a] Average of five measurements ± R.S.D.

4. Conclusions

A new composite material modified electrode Ni(II)–BA–MWCNT-PE was prepared by electrodepositing Ni(II)–BA complex on the surface of MWCNT-PE in alkaline solution. The combination of unique properties of MWCNT and Ni(II)–BA complex resulted in the improvement of both the reversibility and current responses of Ni(II)–BA–MWCNT-PE due to their remarkable synergistic augmentation on the electrochemical responses. The Ni(II)–BA–MWCNT-PE also exhibited enhanced electrocatalytic activity toward the oxidation of hydrazine. Some kinetic parameters, such as the electron transfer coefficient α, rate constant k_s of the electrode reaction, the diffusion coefficient of hydrazine D and the catalytic rate constant k_{cat} of the catalytic reaction were calculated. A sensitive amperometric method was proposed for the determination of hydrazine with the advantages of fast response, high sensitivity and good reproducibility.

Acknowledgement

References

[1] S.M. Golabi, H.R. Zare, J. Electroanal. Chem. 465 (1999) 168.
[2] E.H. Vernot, J.D. MacEwen, R.H. Bruner, C.C. Haus, E.R. Kinkead, Fund. Appl. Toxicol. 5 (1985) 1050.
[3] J.S. Budkuley, Microchim. Acta 108 (1992) 103.
[4] J.W. Mo, B. Ogorevc, X. Zhang, B. Pihlar, Electroanalysis 12 (2000) 48.
[5] A. Safavi, A.A. Ensafi, Anal. Chim. Acta 300 (1995) 307.
[6] A.L. Ensafi, B. Rezaei, Talanta 47 (1998) 645.
[7] A. Safavi, M.A. Karimi, Talanta 58 (2002) 785.
[8] M.H. Pournaghi-Azar, R. Sabzi, J. Electroanal. Chem. 543 (2003) 115.
[9] S.J.R. Prabakar, S.S. Narayanan, J. Electroanal. Chem. 617 (2008) 111.
[10] N. Maleki, A. Safavi, E. Farjami, F. Tajabadi, Anal. Chim. Acta 611 (2008) 151.
[11] K.I. Ozoemena, T. Nyokong, Talanta 67 (2005) 162.
[12] M. Revenga-Parra, E. Lorenzo, F. Pariente, Sens. Actuators B 107 (2005) 678.
[13] M.M. Ardakani, P.E. Karami, P. Rahimi, H.R. Zare, H. Naeimi, Electrochim. Acta 52 (2007) 6118.
[14] L. Zheng, J.F. Song, Sens. Actuators B 135 (2009) 650.
[15] M. Revenga-Parra, T. Garcia, E. Lorenzo, F. Pariente, Sens. Actuators B 130 (2008) 730.
[16] M.Y. Elahi, H. Heli, S.Z. Bathaie, M.F. Mousavi, J. Solid State Electrochem. 11 (2007) 273.
[17] S. Majdi, A. Jabbari, H. Heli, A.A.M. Movahedi, Electrochim. Acta 52 (2007) 4622.
[18] D.E. Shieh, L.T. Liu, C.C. Lin, Cancer Res. 20 (2000) 2861.
[19] S. Ikemoto, K. Sugimura, N. Yoshida, R. Yasumoto, S. Wada, K. Yamamoto, T. Kishimoto, Urology 55 (2000) 951.
[20] J.A. Wu, A.S. Attele, L. Zhang, C.S. Yuan, Am. J. Chin. Med. 29 (2001) 69.
[21] H.J. Heo, D.O. Kim, S.J. Choi, D.H. Shin, J. Agric. Food Chem. 52 (2004) 4128.
[22] D. Hu, Y. Fang, N. Ma, Z. Sun, Z. Cao, J. Shaanxi Norm. Univ. (Nat. Sci. Edit.) 22 (1994) 31.
[23] M. Zhu, S. Rajamani, J. Kaylor, J. Biol. Chem. 279 (2004) 26846.
[24] M. Vestergaard, K. Kerman, E. Tamiya, Anal. Chim. Acta 538 (2005) 273.
[25] M. Trojanowicz, Trends Anal. Chem. 25 (2006) 480.
[26] L. Zheng, J.F. Song, Talanta 73 (2007) 943.
[27] Z. Wang, S. Li, Q. Lv, Sens. Actuators B 127 (2007) 420.
[28] L. Zhu, J. Zhai, R. Yang, C. Tian, L. Guo, Biosens. Bioelectron. 22 (2007) 2768.
[29] W. Zhang, T. Yang, D. Huang, K. Jiao, G. Li, J. Membr. Sci. 325 (2008) 245.
[30] Z. Li, J. Chen, D. Pan, W. Tao, L. Nie, S. Yao, Electrochim. Acta 51 (2006) 4255.
[31] G. Jin, F. Huang, W. Li, S. Yu, S. Zhang, J. Kong, Talanta 74 (2008) 815.
[32] A. Ciszewski, G. Milczarek, Anal. Chem. 71 (1999) 1055.
[33] M.I. Prodromidis, P.G. Veltsistas, M.I. Karayannis, Anal. Chem. 72 (2000) 3995.
[34] E. Laviron, J. Electroanal. Chem. 101 (1979) 19.
[35] A.J. Bard, L.R. Faulkner, Electrochemical Methods, Fundamentals and Applications, Wiley, New York, 2001, p. 163.
[36] State Bureau of Quality Technical Supervision, Water Quality—Determination of Hydrazine (GB/T 15507-1995), Standards Press of China, Beijing, 1995.

Determination of Prometryne in water and soil by HPLC–UV using cloud-point extraction

Jihai Zhou, Jiandong Chen, Yanhong Cheng, Daming Li, Feng Hu, Huixin Li*

College of Resources and Environmental Sciences, Nanjing Agricultural University, Nanjing, Jiangsu Province 210095, China

A B S T R A C T

A CPE-HPLC (UV) method has been developed for the determination of Prometryne. In this method, non-ionic surfactant Triton X-114 was first used to extract and pre-concentrate Prometryne from water and soil samples. The separation and determination of Prometryne were then carried out in an HPLC–UV system with isocratic elution using a detector set at 254 nm wavelength. The parameters and variables that affected the extraction were also investigated and the optimal conditions were found to be 0.5% of Triton X-114 (w/v), 3% of NaCl (w/v) and heat-assisted at 50 °C for 30 min. Using these conditions, the recovery rates of Prometryne ranged from 92.84% to 99.23% in water and 85.48% to 93.67% in soil, respectively, with all the relative standard deviations less than 3.05%. Limit of detection (LOD) and limit of quantification (LOQ) were $3.5 \mu g L^{-1}$ and $11.0 \mu g L^{-1}$ in water and $4.0 \mu g kg^{-1}$ and $13.0 \mu g kg^{-1}$ in soil, respectively. Thus, we developed a method that has proven to be an efficient, green, rapid and inexpensive approach for extraction and determination of Prometryne from soil samples.

1. Introduction

Prometryne [2,4-bis(isopropylamino)-6-(methylthio)-s-triazine], a selective herbicide of the s-triazine chemical family, has been extensively used as a pre- or post-emergence controller of annual grasses and broadleaf weeds in modern agriculture. Based on one classification scheme [1], the K_{oc} value is within 311–614, indicating that Prometryne is expected to have moderate to low mobility in soil and may be adsorbed to solids and sediment suspended in water. Prometryne is a ubiquitous environmental pollutant in water and soil. It is frequently detected in groundwater, surface water, and even breast milk [2,3]. It is not permitted to use in Europe, but still widely used in China. Therefore, we have an urgent need to assess the environmental risk of using Prometryne. The environmental risk from any given herbicide is determined by its toxicity to wildlife, its mobility and persistence in the environment, and the time, frequency and rate of application. In order to evaluate all of these parameters, a sensitive and selective analytical method is required.

In fact, some extraction methods have been developed to extract triazines from various samples, such as liquid–liquid extraction (LLE) [4], solid-phase extraction (SPE) [5–8], solid-phase microextraction (SPME) [9–11], supercritical fluid extraction (SFE) [12] and microwave-assisted extraction (MAE) [13–15] and so on. Unfortunately, some of these methods require a large sample volume or

a lot of organic solvents and are time-consuming or expensive. In particular, the traditional liquid–liquid extraction method exposes health risk to analysts due to large amounts of toxic and volatile organic solvents required. Therefore, a simple, rapid and less labor-intensive extraction method is needed for environment and food analysis. Recently, cloud-point extraction (CPE) is becoming particularly popular [16–21]. This method offers a convenient alternative to conventional extraction systems. Compared to the traditional liquid–liquid extraction, CPE requires a very small amount of relatively nonflammable and nonvolatile surfactants that are friendly to the environment. Another important merit is that there is no loss of analytes because it is unnecessary to evaporate solvent. Under conditions with appropriate temperature, concentration of surfactant and equilibration time, the micellar aqueous solutions prepared with non-ionic surfactants undergo phase separation above a certain temperature known as cloud-point temperature. During phase-separation process, these micellar vesicles will attract non-polar analytes due to hydrophobic interactions and aggregate into a surfactant-rich phase. The remaining is the aqueous phase containing a diluted surfactant with an approximate concentration to its critical micelle concentration (CMC) [22–25]. The hydrophobic analytes of the solution are extracted into the surfactant-rich phase. Compared to the initial solution volume, the surfactant-rich phase volume is negligible, thus a high enrichment factor can be obtained [26–31]. Because of the very small volume fraction of the surfactant-rich phase, the analytes can be highly concentrated. This leads to an enhanced sensitivity of chromatographic analysis and improved techniques for analysis and quantification of the analytes such as high-performance liquid chromatography (HPLC), gas

---

* Corresponding author. Tel.: +86 25 84395374.
  E-mail address: huixinli@njau.edu.cn (H. Li).

chromatography (GC), capillary electrophoresis (CE) without further sample clean-up or evaporation steps. This methodology offers the advantages of safety, low cost, concentrated solutes, easy disposal of surfactant, low toxicity compared with classical organic solvents, etc. [32]. The CPE methodology has recently been applied to the extraction of a wide range of analytes from biological and environmental media, including estrogens, vitamin A, vitamin E, kinds of proteins, as well as metal ions [33–38]. Taken together, this indicates that CPE has great analytical potential as an effective enrichment method. However, reports about application of this technique on how to extract Prometryne from water and other matrix, especially from soil were limited.

In this paper, we report the quantification of Prometryne in water and soil samples by CPE using Triton X-114 as the surfactant coupled with HPLC–UV and demonstrate the feasibility of CPE in the studies of extraction and analysis of Prometryne from environmental media.

2. Experimental

2.1. Chemicals and reagents

Prometryne was obtained from Anhui Huaxing Chemical Industry Co., Ltd. (He County, Anhui Province, China). Stock solution ($1 \, mg \, mL^{-1}$) was prepared by dissolving an appropriate amount of this compound in methanol. Working solutions were prepared daily by appropriate dilutions of the stock solution.

The non-ionic surfactant Triton X-100 and Triton X-114 were purchased from Sigma (USA) and used without further purification. Various concentrations (w/v) of aqueous surfactant solutions were prepared by dissolving appropriate amounts of surfactants in distilled water. Sodium chloride (Shantou Xilong Chemical Factory, Guangdong, China) was prepared before experiment. Methanol was obtained from Hanbon Sci. & Tech. Co., Ltd. (Jiangsu, China). All reagents were of HPLC or analytical reagent grade. All solutions were degassed with ultrasonication and filtered through a membrane ($0.45 \, \mu m$) before use.

2.2. Instrumentation

The HPLC system (Shimadzu, Tokyo, Japan) consists of a UV/VIS detector (model SPD-20A), two pumps (model LC-20AT), a workstation (model HW-2000 solution), and a system controller (model CBM-20A/20Alite). The analytical separation was accomplished using a VP-ODS C_{18} column with size of $250 \, mm \times 4.6 \, mm$ and particle $5 \, \mu m$ (Shimadzu, Tokyo, Japan), coupled with a column oven and a Shimadzu 5A 7725i injector. A personal computer equipped with an Agilent Chemstation program for LC systems was used to acquire and process chromatographic data. Area under peak was calculated as the analytical measure.

A thermostatic bath (HH-2, Guohua Medical Instrument Co., Ltd., China), set at the desired temperature within $\pm 1.0\,^{\circ}C$, was used to implement cloud-point extraction.

High-speed centrifuge (model Eppendorf 5418, Germany) was used to accelerate the phase separation process.

An ultrasonic (KQ-250B) from Kunshan Ultrasonic Instrument Plant (Jiangsu, China) was used as degassing of mobile and homogenization of samples.

2.3. Cloud-point extraction procedure

2.3.1. Extraction from aqueous samples

For the extraction and preconcentration of Prometryne, $50 \, \mu L$ of Prometryne standard solution ($20 \, mg \, L^{-1}$) were added to a 1.5 mL capped centrifugal tube. To this were added $500 \, \mu L$ of aqueous solution of Triton X-114 at concentration of 1% (w/v), $350 \, \mu L$ distilled

water and $100 \, \mu L$ 30% (w/v) sodium chloride solution. The contents were mixed well with a Vortex Genie Mixture (WH-2, Shanghai Huxi Instrumental Factory, China) for 1 min, and then incubated in the thermostatic bath at $50\,^{\circ}C$ for 30 min. The phase separation was then accelerated by centrifugation at 4000 rpm for 5 min. After the water phase was removed, a surfactant-rich phase stuck to the bottom of the tube was obtained. Prometryne and most of the surfactant were removed from the surfactant-rich phase by precipitation with $200 \, \mu L$ of methanol–water (90:10, v/v), vortex-mixed and centrifuged at 16,000 rpm for 5 min. The upper layer solution ($20 \, \mu L$) was injected into the HPLC system for analysis.

With the method above, water samples spiked with $0.4 \, mg \, L^{-1}$, $2.0 \, mg \, L^{-1}$, $10.0 \, mg \, L^{-1}$ of Prometryne, respectively, were used to test the applicability of CPE method to water media.

2.3.2. Extraction from soil samples

Soil samples spiked with $0.4 \, mg \, kg^{-1}$, $2.0 \, mg \, kg^{-1}$, $10.0 \, mg \, kg^{-1}$ of Prometryne, respectively, were used to test the applicability of CPE method to soil meida. Triton X-114 and Water (0.5:100, w/v) mixture was used for extraction of Prometryne from soil. A 2.00 ± 0.02 g sample was sonicated in the presence of 10 mL of the mixture at $20\,^{\circ}C$ for 30 min. A portion of the liquid phase was transferred into a centrifugal vial through a paper filler. The residual was re-extracted with another 10 mL of above mixture, and the supernatant was isolated and mixed with the fraction obtained from the first extraction. The surfactant-rich phase was separated as described in Section 2.3.1 by adding 6.0 g of NaCl.

2.4. HPLC conditions

The separation and determination of Prometryne were carried out by directly injecting the extracts in the LC–UV (DAD). The mobile phase of methanol–water (90:10, v/v) was used. The flow rate was set at $1.0 \, mL \, min^{-1}$. The column temperature was maintained at $30\,^{\circ}C$ and the injection volume was set to $20 \, \mu L$. Prometryne was recorded at the wavelength of 254 nm.

3. Results and discussion

3.1. Selection of surfactants

To ensure that the cloud-point extraction is processed at a desired temperature, it is imperative to have detailed information on clouding behaviors and cloud-point temperatures of surfactants. The cloud points were determined mainly by visual observation of the temperature at which the clear micellar solutions turn turbid upon heating and the milky surfactant solutions lose their turbidity upon cooling in a thermostatic bath. As a result, the measured cloud-point temperatures were reproducible within $0.5\,^{\circ}C$.

Fig. 1 shows the cloud-point curves of Triton X-100 and Triton X-114 themselves in water without any additives with surfactant concentration ranging from 0.25 to 10% (w/v). Below the curve, there exists only one liquid phase, i.e. micellar phases, commonly denoted as L_1 phase, whereas two coexisting liquid phases, surfactant-rich micellar phase (i.e. concentrated L_1 phase) and water phase (W), are found in the region above the curve, both of which represent typical clouding behaviors of non-ionic surfactants. Notably, these surfactants are commercial blends and mixtures and it is quite common to find temperature deviation of the cloud-point curves within $1\,^{\circ}C$ or so using surfactants manufactured in different batches.

Very often, the extracts, such as pesticides and biological products, may be sensitive to elevated temperature. Therefore, an alternative method is developed to render the cloud points lower enough, instead of heating up surfactant solutions, so as to facilitate the CPE processes at lower temperatures. Triton X-114 was
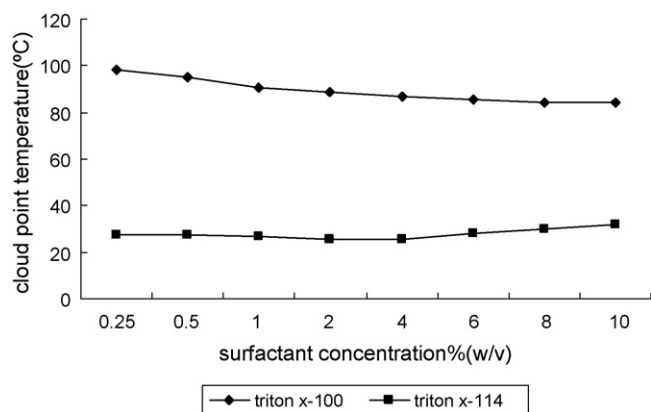
Fig. 1. Cloud-point temperature of non-ionic surfactants as a function of surfactant concentrations.

chosen as the CPE surfactant because of its appropriate cloud-point temperature of 23–32 °C.

3.2. HPLC chromatograms of the extracted Prometryne in soil sample

Fig. 2 shows typical HPLC chromatograms of extracted and pre-concentrated Prometryne, Fig. 2a is the chromatogram of blank soil, Fig. 2b is the chromatogram of standard Prometryne without cloud-point extraction and Fig. 2c is the chromatogram of Prometryne after its cloud-point extraction from soil spiked with it. Compared with the conventional extraction [16], CPE has higher extraction efficiency under the same experimental conditions. The precon-centration effect of cloud-point extraction is clearly demonstrated in Fig. 2b and c. Although Triton X-114 has low UV absorbance, as shown in Fig. 2, it does not interfere with the determination of Prometryne.

3.3. Optimization of the extraction process

Triton X-114 was chosen as the CPE surfactant for its low cloud-point temperature and low UV absorbance [17]. Several different parameters that can influence the extraction efficiency were inves-tigated in our experiments using the absorbance from the spiked samples of Prometryne at concentration of 2 μg mL^{-1} in water. Six replicates were performed to obtain a mean value.

3.3.1. Effect of the concentration of surfactant

The theoretical preconcentration factor depends on the con-centration of surfactant. For its low cloud-point temperature and high density, Triton X-114 was chosen as the extraction solvent, and phase separation was facilitated by centrifugation [18]. The effect of the concentration of surfactant was examined in our study and the result was shown in Fig. 3. Fig. 3 shows that when the concentra-tion of surfactant in solution varies in the range 0.25–3.0% (w/v), the highest extraction efficiency is at 0.5%. In this experiment, when the concentration of surfactant is below 0.5%, the surfactant is always soluble in the bulk solution and it is very difficult to separate it into two phases. Based on these results, 0.5% Triton X-114 was adopted as the optimal amount to achieve best analytical signals and highest extraction efficiency.

3.3.2. Effect of concentration of sodium chloride

The addition of salt to the solution can influence the extrac-tion efficiency. For most non-ionic surfactant, the presence of salts may facilitate phase separation since they increases the density of the aqueous phase [17]. Available electrolytes can also change
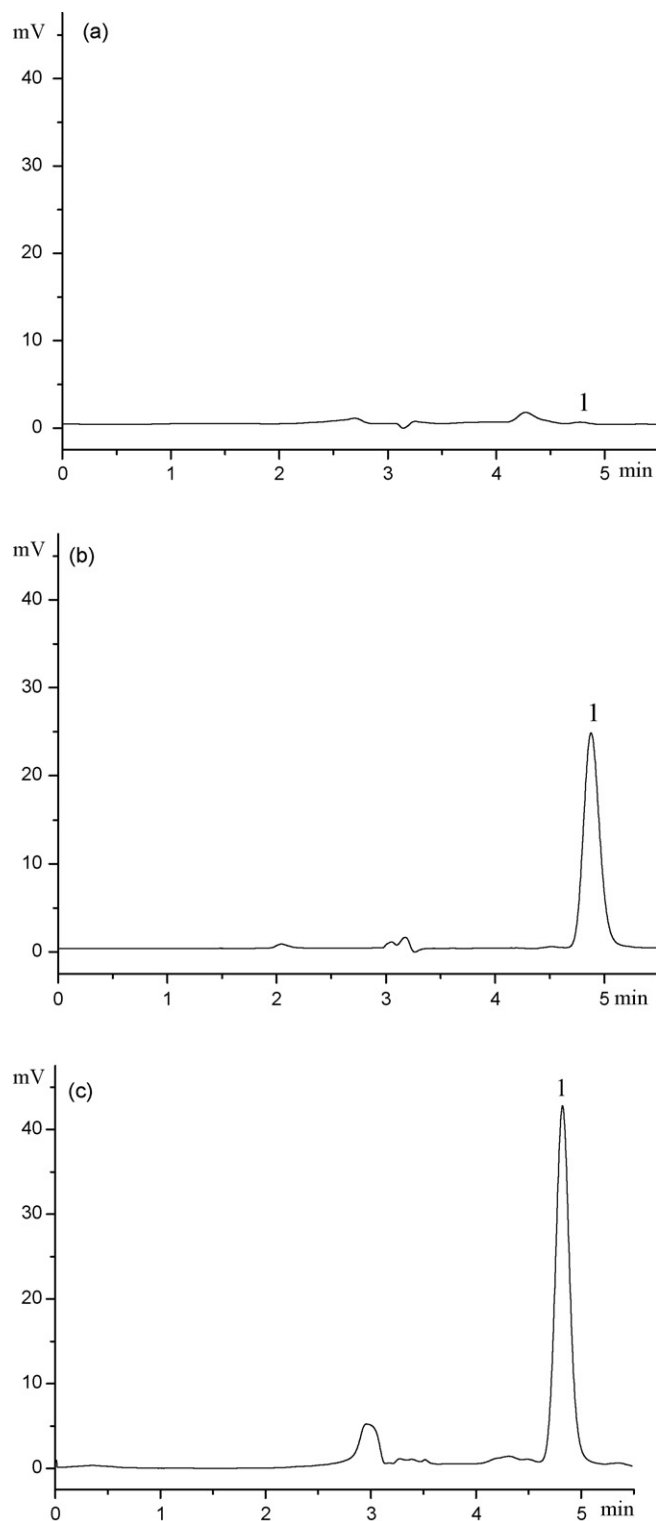

Fig. 2. HPLC–UV chromatograms: (a) blank soil, (b) standard, and (c) soil spiked with Prometryne (10 μg mL^{-1}). Peak no.: (1) Prometryne. HPLC conditions—mobile phase: methanol–water (9:1) (v/v); injection volume: 20 μL; flow rate: 1 mL min^{-1}; wavelength: 254 nm.

the cloud-point temperatures of non-ionic surfactant (Fig. 4). The relevant electrolytes are usually in high concentrations (exceeding 0.1 M) [19]. The salting-in and salting-out effects can be used to interpret the electrolyte effects on the cloud points of non-ionic surfactant [20]. To study the influence of the electrolyte, differ-ent concentrations of sodium chloride, ranging from 0.5% to 6%
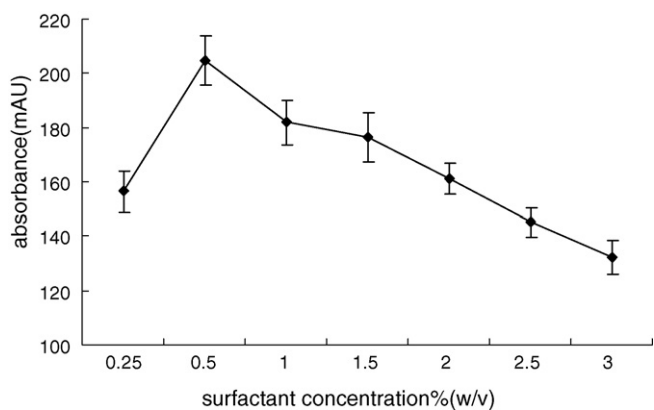
Fig. 3. Effect of Triton X-114 concentration on the recovery. Other extraction conditions—equilibrium temperature: 50 °C; equilibrium time: 30 min; concentration of sodium chloride solution: 3% (w/v).
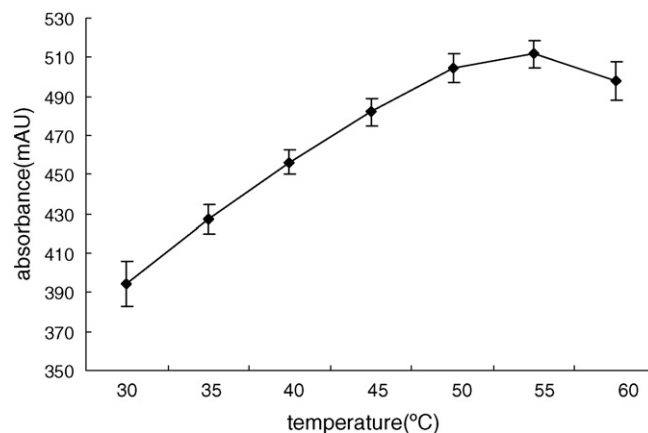

Fig. 4. Effect of electrolytic additives on the cloud-point temperature of 1% (w/v) surfactant solution.

(w/v) were added to the solution. The results are in concordance with other studies [38,39]. The final surfactant-rich phase volume was not noticeably influenced by the increased ionic strength [20]. When the concentration is higher than 4% (w/v), the surfactant-rich phase will be on the surface of the solution, which will make it more difficult to separate the extraction solvent into two phases, and the accuracy and reproducibility probably were not satisfactory. As shown in Fig. 5, the extraction effect is the best when the concentration is 3% (w/v).

Fig. 5. Effect of salt concentration on the recovery. Other extraction conditions—equilibrium temperature: 50 °C; equilibrium time: 30 min.

Fig. 6. Effect of the temperature on the extraction efficiency. Other extraction conditions—equilibrium time: 30 min; concentration of sodium chloride: 3% (w/v).
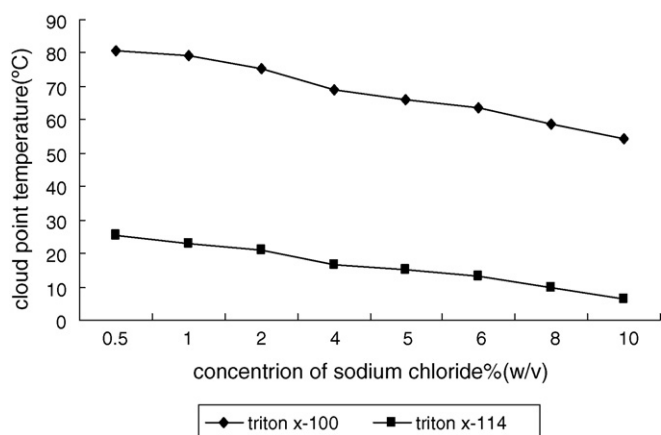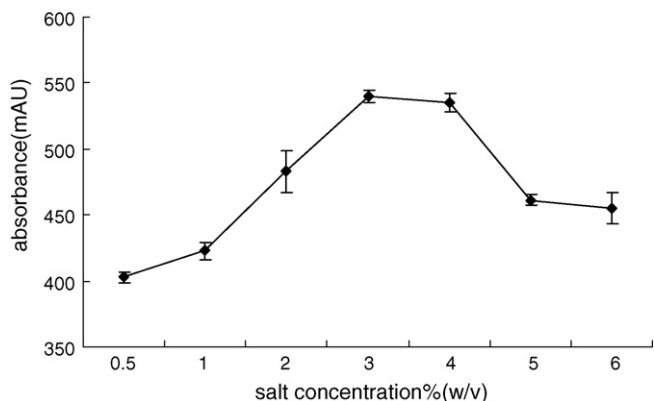
3.3.3. Effect of the equilibrium temperature

When the cloud-point extraction was processed at equilibrium temperature of the surfactant, the best extraction effect can be achieved [25]. Thus, it is necessary to examine the effect of temperature on cloud-point extraction. If the temperature is lower than the cloud-point, two phases cannot be formed. Higher temperature leads to the decomposition of Prometryne. In order to employ the lowest possible equilibrium temperature for the efficient separation of phases, the equilibrium temperature was examined. Theoretically, the optimal equilibrium temperature of the extraction occurs when the equilibrium temperature is 15–20 °C greater than the cloud-point temperature of surfactant [25]. So the influence of temperature on the extraction efficiency was studied in the range of 30–60 °C. When the temperature became higher (from 30 to 50 °C), the mean signal response increased from 394.70 mAU to 504.55 mAU. No significant increment in the signal was observed for higher temperatures from 50 °C to 60 °C. Fig. 6 shows the effects of equilibrium temperature on the extraction efficiency. Based on these results, 50 °C was selected as the working equilibrium temperature.

3.3.4. Effect of the equilibrium time

The influence of the extraction time on the ability of Triton X-114 to extract Prometryne from water was examined in the range between 5 min and 60 min (Fig. 7). Extraction time of less than 15 min produced low signal responses. As shown in Fig. 7,
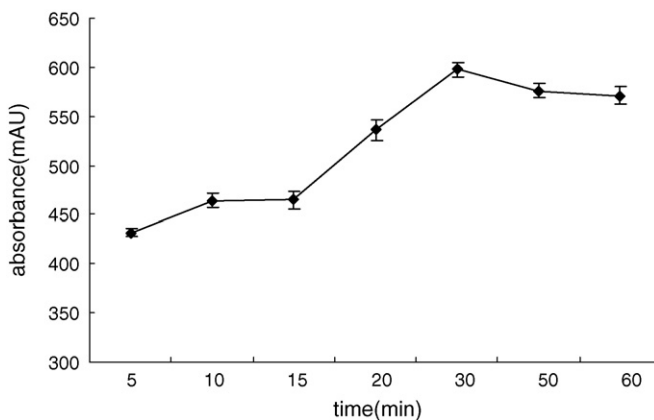

Fig. 7. Effect of the equilibration time on the extraction efficiency. Other extraction conditions—equilibrium temperature: 50 °C; concentration of sodium chloride: 3% (w/v).

Table 1
Recovery, repeatability, reproducibility and R.S.D. of water and soil spiked Prometryne.

Environmental matrix	Added (mg kg^{-1})	Day 1 ($n=6$)			Day 2 ($n=6$)			CV$_R$ (%)
		Found (mg kg^{-1})	R.S.D. (%)	Recovery (%)	Found (mg kg^{-1})	R.S.D. (%)	Recovery (%)	
Water	0.4	0.397	0.93	99.23	0.394	0.80	98.58	0.90
	2	1.941	1.90	97.06	1.940	2.35	97.00	2.04
	10	9.679	2.02	96.79	9.284	2.38	92.84	3.02
Soil	0.4	0.375	2.07	93.67	0.370	1.53	92.55	1.85
	2	1.748	1.96	87.40	1.710	1.48	85.48	2.03
	10	9.124	2.34	91.24	8.919	2.05	89.19	2.41

R.S.D. represents means of per concentration level in each day; CV$_R$ represents means of per concentration level in 12 times.

30 min extraction was enough to give the highest signal response; therefore, extraction with a duration of 30 min was recommended. In fact, the recovery values increased significantly from 5 min to 30 min. The slight decrease in the following 30 min, the weakening of signal response was achieved by the smaller phase volume ratio due to longer equilibrium time. This phenomenon was in quite accordance with other reports [28], and was only significant within the time range from 5 min to 30 min during this experiment. The procedure was then accelerated by centrifugation at 4000 rpm for 5 min, which was enough to get a complete phase separation.

On the other hand, the centrifugation parameters exhibited no significant alterations in the signals obtained from the recovery of Prometryne; therefore, centrifugation for 5 min at 4000 rpm was used to separate the surfactant-rich phase from aqueous solution.

3.4. Calibration and validation

The spiked standard samples at six different concentrations over the range 0.016–10 µg mL^{-1} were prepared and analyzed in three consecutive analytical runs, with two groups for each run. Standard curves were constructed using weighted linear least square regression analysis of the observed peak area ratios of Prometryne against concentration. The mean regression equation for the calibration curve was $y = 28093x - 959.09$ with a correlation coefficient above 0.9990. Limits of detection (LOD) for Prometryne in water and in soil samples were found to be 3.5 µg L^{-1} and 4.0 µg L^{-1} (S/N = 10), respectively; limits of quantification (LOQ) for Prometryne in water and in soil samples were 11.0 µg L^{-1} and 13.0 µg L^{-1} (S/N = 3), respectively. Quality control (QC) samples at three concentrations (0.4 µg mL^{-1}, 2 µg mL^{-1} and 10 µg mL^{-1}) were analyzed to assess the recovery, repeatability and reproducibility of the proposed method. Six replicates were analyzed in each of three consecutive analytical runs. The results are listed in Table 1, which indicate good analytical characteristics of this assay. The recovery, repeatability and reproducibility varied from 85.48% to 99.23%, from 0.80% to 2.38% (R.S.D.) and from 0.90% to 3.02% (CV$_R$), respectively.

4. Conclusions

In this study, a technique using CPE based on Triton X-114/NaCl was successfully developed. Compared with traditional LLE, the technique is higher in extraction efficiency in one-stop extraction and more environment friendly. Coupled with HPLC–UV detector, the method has been proved to be simple, rapid and reliable for Prometryne assay in water and soil samples, with a capability of determining Prometryne accurately down to 13 ng mL^{-1}.

References

[1] R.L. Swann, D.A. Laskowski, P.J. McCall, K.V. Kuy, H.J. Dishburger, Res. Rev 85 (1983) 17.
[2] T.A. Albanis, T.G. Danis, M.K. Kourgia, Sci. Total Environ. 156 (1994) 11.
[3] E. Papadopoulou-Mourkidou, D.G. Karpouzas, J. Patsias, A. Kotopoulou, A. Milothridou, K. Kintzikoglou, P. Vlachou, Sci. Total Environ. 321 (2004) 147.
[4] H. Sabik, R. Jednnot, J. Chromatogr. A 818 (1998) 197.
[5] I. Ferrer, D. Barcelo, E.M. Thurman, Anal. Chem. 71 (1999) 1009.
[6] H. Sabik, R. Jeannot, B. Rondeau, J. Chromatogr. A 885 (2000) 217.
[7] A. Asperger, J. Efer, T. Koal, W. Engewald, J. Chromatogr. A 960 (2006) 109.
[8] I. Ferrer, D. Barcelo, J. Chromatogr. A 737 (1996) 93.
[9] M.C. Sampedro, O. Martin, C. Lopez de Armantia, J. Chromatogr. A 893 (2000) 347.
[10] C. Basheer, H.K. Lee, J. Chromatogr. A 1047 (2004) 189.
[11] S.-D. Huang, H.-I. Huang, Y.-H. Sung, Talanta 64 (2004) 887.
[12] Z. Knez, A. Rizner-Hras, K. Kokot, D. Bauman, Fluid Phase Equilibria 152 (1998) 95.
[13] G.H. Xiong, B.Y. Tang, X.Q. He, M.Q. Zhao, Z.P. Zhang, Zh.X. Zhang, Talanta 48 (1999) 333.
[14] G. Shen, H.K. Lee, J. Chromatogr. A 985 (2003) 167.
[15] R. Hoogerbrugge, C. Molins, R.A. Banmann, Anal. Chim. Acta 348 (1977) 247.
[16] Q.H. Chen, S.X. Hou, J. Zheng, Y.Q. Bi, Y.B. Li, X.J. Yang, Z. Cai, X.R. Song, J. Chromatogr. B 858 (2007) 199.
[17] R. Carabias-Martinez, E. Rodriguez-Gonzalo, B. Moreno-Cordero, J.L. Perez-Pavon, C. Garcia-Pinto, E. Fernadez Laespada, J. Chromatogr. A 902 (2000) 251.
[18] F. Shemirani, M. Baghdadi, M. Ramezani, M.R. Jamali, Anal. Chim. Acta 534 (2005) 163.
[19] M.K. Purkait, S.S. Vijay, S. DasGupta, S. De, Dyes Pigments 63 (2004) 151.
[20] V. Pino, J.H. Ayala, A.M. Afonso, V. Gonzalez, J. Chromatogr. A 949 (2002) 291.
[21] A. Ohashi, T. Hashimoto, H. Imura, K. Ohashi, Talanta 73 (2007) 893.
[22] R.P. Frankewich, W.L. Hinze, Anal. Chem. 66 (1994) 944.
[23] H. Watanabe, H. Tanaka, Talanta 25 (1978) 585.
[24] N.C. van de Merbel, J.J. Hageman, U.A.Th. Brinkman, J. Chromatogr. A 634 (1993) 1.
[25] P.M. Holland, D.N. Rubingh (Eds.), Mixed Surfactant Systems, American Chemical Society, Washington, DC, 1992.
[26] F. Merino, S. Rubio, D. Perez-Bendito, J. Chromatogr. A 998 (2003) 143.
[27] C.P. Sanz, R. Halko, Z.S. Ferrera, J.J.S. Rodriguez, Anal. Chim. Acta 524 (2004) 265.
[28] B. Delgado, V. Pino, J.H. Ayala, V. Gonzialez, A.M. Afonso, Anal. Chim. Acta 518 (2004) 165.
[29] J.C. Shen, X.G. Shao, Anal. Chim. Acta 561 (2006) 83.
[30] K.-C. Hung, B.-H. Chen, L.E. Yu, Sep. Purif. Technol. 57 (2007) 1.
[31] E. Pramauro, A. Bianco Prevet, Pure Appl. Chem. 67 (1995) 551.
[32] Z.S. Ferrera, C.P. Sanz, C.M. Santana, J.J.S. Rodriguez, Trends Anal. Chem. 23 (7) (2004) 469–479.
[33] L. Wang, Y.Q. Cai, B. He, C.G. Yuan, D.Zh. Shen, J. Shao, G.B. Jiang, Talanta 70 (2006) 47.
[34] J.G. Chen, H.W. Chen, X.Zh. Jin, H.T. Chen, Talanta 77 (2009) 1381.
[35] M. Du, W. Wu, N. Ercal, Y. Ma, J. Chromatogr. B 803 (2004) 321.
[36] M.D. Rukhadze, S.K. Tsagareli, N.S. Sidamonidze, V.R. Meyer, Anal. Biochem. 287 (2000) 279.
[37] P.R. Aranda, R.A. Gil, S. Moyano, I. De Vito, L.D. Martinez, Talanta 77 (2008) 663.
[38] N. Pourreza, S. Rastegarzadeh, A. Larki, Talanta 77 (2008) 733.
[39] A.R. Zarei, Anal. Biochem. 369 (2007) 161.

Supercritical fluid extraction—Achiral liquid chromatography with circular dichroism detection for the determination of menthone enantiomers in natural peppermint oil samples

Mohammed Zougagh, Purificación Aranda, Gregorio Castañeda, Ángel Ríos *

Department of Analytical Chemistry and Food Technology, Faculty of Chemistry, University of Castilla-La Mancha, Av. Camilo José Cela s/n, E-13004 Ciudad Real, Spain

A R T I C L E   I N F O

A B S T R A C T

A simple and enantioselective method for the determination of menthone enantiomers in peppermint essential oil samples is proposed. The method involves the initial supercritical fluid extraction (SFE) to clean-up and extraction of analytes and their preconcentration on C_{18} adsorption cartridges followed by achiral liquid chromatographic separation and direct circular dichroism (CD) detection. The calibration curve of the anisotropy factor (*g*) versus the enantiomeric excess was linear, with a correlation coefficient (R^2) of 0.9970. The precision evaluated by UV peak area and CD peak area was suitable both in terms of intra- and inter-day precision (RSD < 5.1% in all cases). The usefulness of the proposed method was demonstrated by analyzing natural and spiked peppermint oil samples. This method has the advantages of being rapid and precise without using an expensive chiral column. It was demonstrated to be suitable for the simultaneous determination of both enantiomers and for assessing the chemical purity of menthone.

© 2009 Elsevier B.V. All rights reserved.

1. Introduction

Menthone is a chiral compound (Fig. 1) that is found in various volatile oils, such as pennyroyal, peppermint and geranium. It is used in perfume and flavor compositions [1] and there are reports that (−)-menthone has an analgesic effect, whereas (+)-menthone lacks analgesic [2] and flavor [3] properties. Owing to the wide range of applications of menthone in food and drug production, the determination of enantiomeric excess (e.e.) is important for quality control, pharmacological studies and the evaluation of biosynthesis (in plants). Generally, the enantiomeric excess of chiral compounds is determined by liquid chromatography (LC) on chiral stationary phases such as cellulose [4], amylose [5], protein [6], Pirkle-type [7] or cyclodextrin derivatives [8] using common UV detection. However, such columns are expensive and samples require pre-treatment before LC analysis in order to eliminate matrix materials (biofluids, foods). In gas chromatography (GC), the resolution of menthol, isomenthone and menthone enantiomers has already been achieved using a column with α-cyclodextrin as the chiral stationary phase, but a quantitative study has yet to be reported [9]. The alternative approach presented here involves the use of an achiral stationary phase coupled with a circular dichroism detector, which is specific for optically active compounds. The

principle is based on the difference of absorbance between left and right circularly polarized light for two enantiomers [10,11]. The CD detector records simultaneously both the dichroic signal ($\Delta\varepsilon$) and absorbance (ε), and also measures the ratio of these two signals in order to calculate the anisotropy factor (*g* factor = $\Delta\varepsilon/\varepsilon$). The *g* factor was found to be proportional to the enantiomeric excess but is independent of concentration [12]. Lorin et al. [13] and other authors [14–17] have already demonstrated that this detector, coupled with an achiral stationary phase, was suitable to determine 99.8–98% enantiomeric excess values (0.1–2% enantiomeric purity). Nevertheless, a method has yet to be applied to the analysis of real samples.

On the other hand, supercritical fluid extraction (SFE) is a rapid preparation technique for use prior to the chromatographic analysis of samples and this approach simplifies and facilitates automation of the preliminary operations in analytical processes [18]. The possibility of adjusting the solvent power of the supercritical fluid (usually CO_2) simply by changing the pressure and temperature makes SFE extremely selective and suitable for class-selective extraction. In addition, the clean-up and preconcentrating effects of the supercritical fluid extractant, which is gaseous under ambient conditions, result in increased sensitivity and allow the use of smaller amount of samples.

In the work described here, we combined the advantages of SFE for automatic sample treatment, RP-C18 for preconcentration to achieve appropriate selectivity and sensitivity, non-enantioselective LC for its separation capabilities and circular

* Corresponding author. Tel.: +34 926 295232; fax: +34 926 295318.
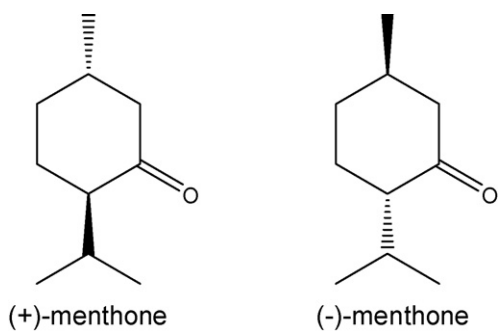*E-mail address:* angel.rios@uclm.es (Á. Ríos).

Fig. 1. Chemical structures of menthone enatiomers.

dichroism detection (CDD) for enantiomeric excess determination. This system has been designed and tested for this particular application and has the analytical potential to be expanded to include other methods involving samples with complex matrices.

2. Experimental

2.1. Reagents, standards and samples

Menthone isomers were supplied by Fluka with an enantiomeric purity greater than 99% for the (−)-enantiomer and above 98.5% for the (+)-enantiomer. Standard stock solutions were prepared in acetonitrile (LC grade) supplied by Sigma–Aldrich. These solutions were stored at 4 °C. Working standard solutions were prepared on a daily basis by dilution of stocks in acetonitrile:water (25:75).

SFC-grade carbon dioxide (Air Liquide Products, Paris, France) was used as the extraction fluid. Peppermint essential oil was obtained from a local herbalist's shop.

A solid phase extraction column (1.0 ml, 200 mg, BondElut-C18) from Varian (Harbor City, CA, USA) was used to preconcentrate supercritical extracts.

2.2. Instruments, apparatus and chromatographic conditions

Supercritical fluid extraction was performed with a Jasco system (Easton, MD, USA) consisting of a PU-1580 CO_2 delivery pump, a BP-1580-81 backpressure regulator and CO-2065 column oven as the extraction chamber.

The chromatographic system was a modular LC system consisting of an LC quaternary pump (Waters), an Agilent LC analytical column (model Sorbax SB-C18, 150 mm × 4.6 mm i.d., 5 μm particle size), a circular dichroism detector (JASCO CD-2095 PLUS) and a Rheodyne injection valve (model 1050i, 20 μl). Data were acquired and the equipment controlled using BORWIN software, which was run under Microsoft Windows XP on an IBM compatible personal computer. Elution was performed under isocratic conditions using a mobile phase containing a mixture of acetonitrile/water 60/40 (v/v) at a flow rate of 0.8 ml min^{-1}. The injection volume was 20 μl. Ellipticity, UV absorption and g factor signals were monitored at a wavelength of 280 nm.

2.3. Manifold, procedures and quantification strategy

The assembly used to combine SFE, preconcentration and LC–CD is shown in Fig. 2. In the extraction step, CO_2 was aspirated from a dip-tube cylinder at a constant flow rate of 2 ml min^{-1} (liquid) by means of a PELTIER pump and passed through the extraction vessel. A homogenized mixture of 2 g of sample and 0.5 g of diatomaceous earth was manually placed into a 10 ml stainless steel extraction vessel accommodated in the extraction chamber. Intimate contact with the extracting supercritical

fluid was allowed through the combination of static and dynamic extraction steps. Thus, once the target pressure (20 MPa) and temperature (70 °C) were reached, the sample was extracted in the static mode for 5 min. Dynamic extraction was then performed for 15 min, after which CO_2 was passed through the sample. The extracted menthone enantiomers were collected in the flask containing 25 ml of acetonitrile/water (25/75) inserted behind the programmable back-pressure regulator and maintained at 40 °C. Thus, the 25 ml of extracts were preconcentrated in RP-C18 cartridges, eluted with 2 ml of acetonitrile and therefore injected into the LC–CD system for the separation and quantification of menthone.

Firstly, the total concentration of menthone was determined with direct calibration with menthone standards. Secondly, the linearity of the calibration curves was estimated by plotting the g factor versus the enantiomeric excess [16] in the −100 to +100% e.e. ranges. Eutomer and distomer concentrations were adjusted in order to obtain the concentration of menthone found in the sample analyzed.

The g factor ($\Delta\varepsilon/\varepsilon$) is the ratio of dichroic signal ($\Delta\varepsilon$) and absorbance (ε) and the enantiomeric excess is related to the excess of one enantiomer compared to the other and is determined as follows [13]:

$$e.e.\, R(\%) = \left(\frac{[R] - [S]}{[R] + [S]} \right) \times 100$$

where $[R]$ and $[S]$ are the concentrations of the (S)- and (R)-enantiomers, respectively.

3. Results and discussion

As shown in Fig. 3a, the two enantiomers have identical spectra with the maximum absorption at 280 nm. In contrast, the CD spectra of the two menthone enantiomers have the same magnitude but have opposite sign.

The extraction procedure was designed and optimized to carry out the clean-up and preconcentration of the sample. Subsequently, the LC–CD method was developed for the separation and quantification of the menthone enantiomeric excess in peppermint essential oil samples. The mobile phase, which is composed of acetonitrile/water [60/40 (v/v)], was selected for its good chromatographic performance and because coelution did not occur between the menthone and contaminants present in extracts. UV- and CD-chromatograms when either the (+)- or (−)-enantiomer was injected onto the non-enantioselective column are shown in Fig. 3b and c. The g factor was calculated at the retention time of the analyte, as indicated previously.

3.1. Optimization of the extraction procedure

The extractability of menthone from test samples was studied by the SFE technique in order to maximize recovery. Menthone extracts in acetonitrile/water (25/75) were preconcentrated in RP-C18 cartridges eluted with acetonitrile and quantified using an LC–CD system. For this purpose, a mixture of 2 g of sample and 0.5 g of diatomaceous earth was homogenised and inserted in the extraction cell. Menthone was recovered at variable CO_2 flow rates at four different extraction temperatures (50, 60, 70 and 80 °C) with 5 min of static extraction followed by 10 min of dynamic extraction. Four isotherms were thus constructed at CO_2 flow rates in the range 1.0–2.0 ml min^{-1}. The effects of the supercritical-CO_2 flow rates and extraction temperature on menthone recovery are represented in Fig. 4. As can be seen, the best recoveries were achieved on using 2 ml min^{-1} at 70 °C. Increasing the dynamic extraction time resulted in a substantial effect on menthone recovery. For example, a dynamic extraction time
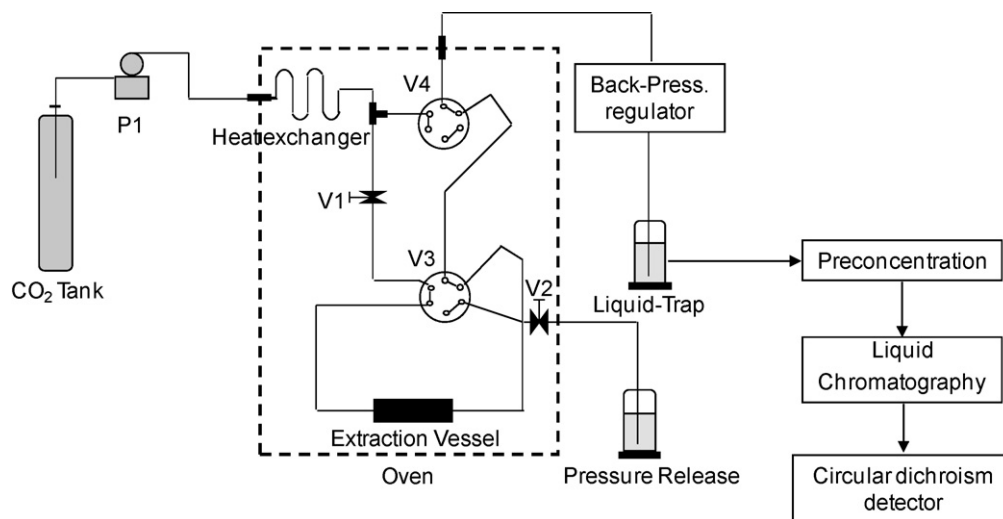
Fig. 2. Experimental set-up for the determination of (+)-menthone and (−)-menthone in peppermint essential oil samples. V_1 and V_2 are pressure selection valves; V_3 and V_4 are pressure injection valves; and P_1 is a high-pressure pump.

of 15 min increased the recovery from 85 to 95%. The addition of a modifier – such as acetonitrile, methanol or acetone – into the CO_2 stream did not lead to an improvement in the extraction. Once the optimum conditions for the extraction of menthone (*viz.* 2 ml min^{-1} at 70 °C, 5 min static extraction and 15 min dynamic extraction) were established, the menthone extracted from samples was collected in the flask containing 25 ml of acetonitrile/water (25/75), preconcentrated in RP-C18, eluted with 2 ml of acetonitrile and quantified using an LC–CD system at a wavelength of 280 nm.
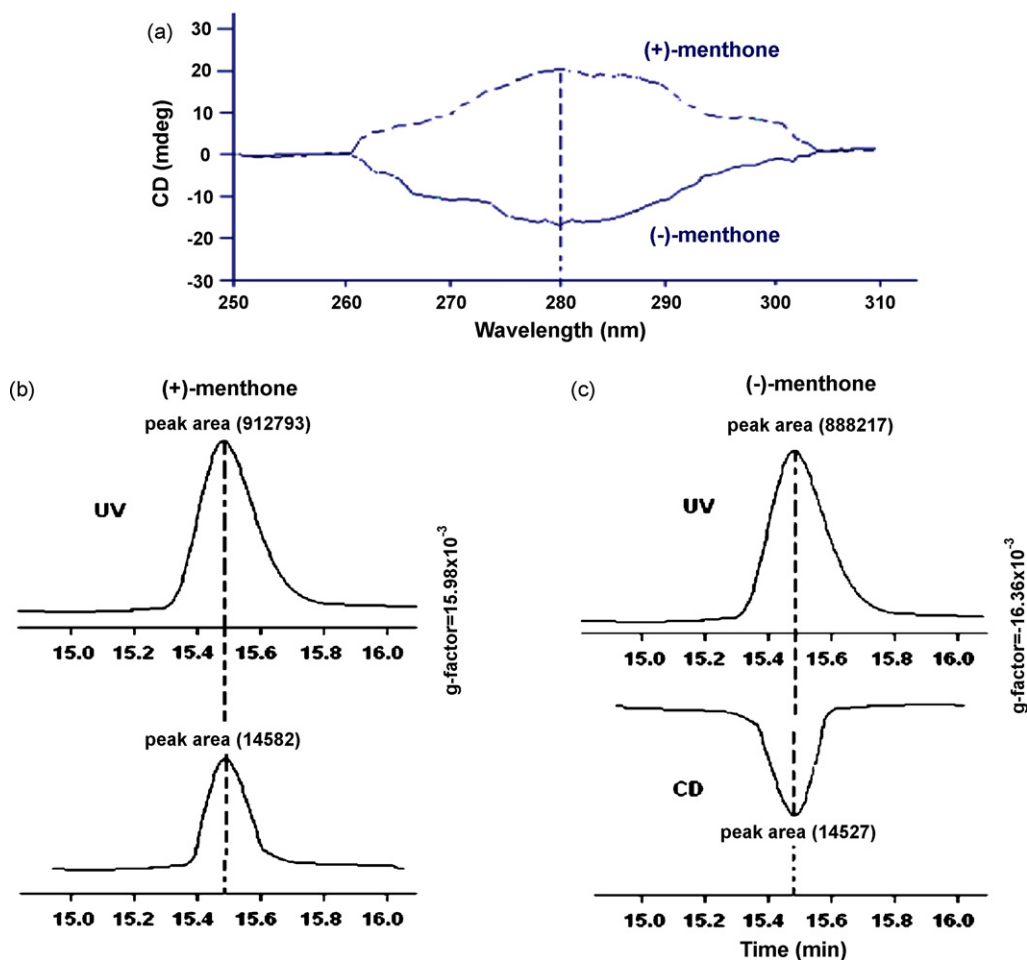

Fig. 3. (a) CD spectra of (+)-menthone and (−)-menthone. (b) and (c) UV and CD chromatograms after injection of each enantiomer. Column: Sorbax SB-C18, 150 mm × 4.6 mm i.d., 5 μm particle size; mobile phase: acetonitrile/water 60/40 (v/v); detector wavelength: 280 nm; flow rate: 0.8 ml min^{-1}; injection volume: 20 μl; temperature: 30 °C; enantiomer concentration: 100 μg ml^{-1}.
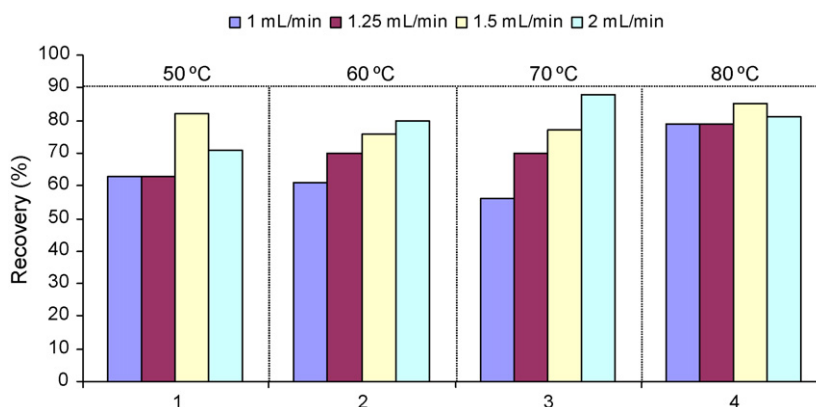
Fig. 4. Influence of the supercritical-CO_2 flow rates and extraction temperature on menthone recovery.

Table 1
Analytical characteristics of the method obtained for absorbance and dichroism signals (for details, see text).

Enantiomer	Absorbance		Dichroism	
	(−)-menthone	(+)-menthone	(−)-menthone	(+)-menthone
Linear range (μg ml^{-1})	100–1000	100–1000	100–1000	100–1000
$Y = aX + b$	$(9958 \pm 141)X - (64{,}250 \pm 92{,}992)$	$(9859 \pm 122)X - (109{,}507 \pm 80{,}928)$	$(177 \pm 2)XX - (4646 \pm 1624)$	$(171 \pm 2)XX - (1280 \pm 1631)$
R^2	0.9992	0.9994	0.9992	0.9992
$S_{y/x}$	1124,16	97,833	1963	1972
LOD (μg ml^{-1})	28	25	27	29
LOQ (μg ml^{-1})	93	82	92	96
RSD (%) (intra-day)	4.9	4.9	3,5	3,5
RSD (%) (inter-day)	5.0	5.1	3.9	4.1

a, slope; b, intercept; R, regression coefficient; $S_{y/x}$, standard deviation of residuals; LOD, limit of detection; LOQ, limit of quantification, RSD, relative standard deviation ($n = 11$).

3.2. Analytical features of the method and its application to the determination of menthone enantiomeric excess in selected peppermint essential oil samples

The combination of non-enantioselective LC with SFE seemed to be an excellent way to determine menthone enantiomeric excess in peppermint essential oil samples. This approach would provide the advantages of LC as well as the good sensitivity achieved after SFE treatment. Analytes were isolated from peppermint essential oil samples using supercritical fluid extraction followed by pre-concentration in RP-C18. Menthone enantiomers were retained in the C18 material, eluted with acetonitrile and therefore injected into the chromatographic system for determination of menthone enantiomeric excess in peppermint essential oil samples. A polar endcapped C18 column was used for the separation of menthone from other matrix materials present in the extract. A secondary mobile phase consisting of acetonitrile/water 60/40 (v/v) at a flow rate of 0.8 ml min^{-1} was selected for the separation of menthone from contaminants within 20 min with excellent resolution. In an effort to investigate the linearity of the CD detector, calibration curves were plotted as peak area versus concentration of each enantiomer. The tested concentrations were 100, 250, 500, 700, 900 and 1000 μg ml^{-1}.

The limit of detection (LOD) and quantification (LOQ), defined as the concentrations of analytes giving a signal equivalent to the blank

signal plus three and ten times its standard deviation respectively, were calculated [19].

The corresponding regression equation and other characteristic analytical parameters for the determination of these enantiomers are shown in Table 1. The precision of the method, expressed as RSD, for the determination of 500 μg ml^{-1} of each enantiomer, was in all cases <5.1% ($n = 11$).

On the other hand, as described previously in the 'manifold, procedures and quantification strategy' section, the linearity of the calibration curves was estimated by plotting the g factor versus the enantiomeric excess in the −100 to +100% e.e. range. Eutomer and distomer concentrations were adjusted in order to keep the total concentration of menthone constant at the concentration found in the sample. The linearity of the plot of g factor versus enantiomeric excess levels distributed over the range from −100 up to +100 is represented in Fig. 5 for a series of 16 e.e. levels: +100, +80, +75, +50, +40, +25, +20, 0, −10, −25, −30, −50, −60, −75,

Table 2
Determination of enantiomeric excess of (−)-menthone in synthetic samples.

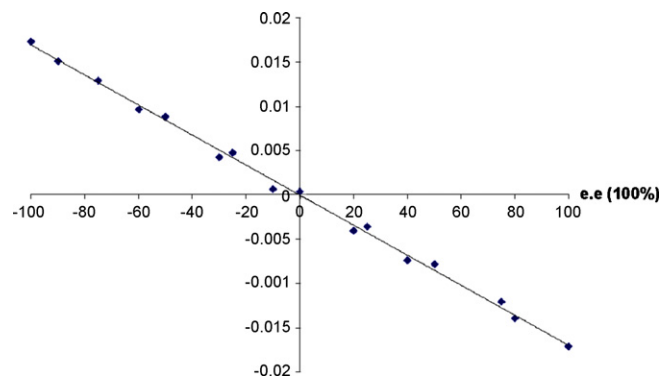| e.e.(%) added	e.e.(%) found	Error (%)
+80.00	+82.06 ± 2.34	+2.51
+40.00	+39 ± 2.08	−2.44
−60.00	−57.15 ± 2.13	−4.99
−90.00	−89.76 ± 2.35	−0.27
+75.00	70.98 ± 2.87	−5.60

Fig. 5. Linearity of the anisotropy factor (g-factor) vs. the enantiomeric excess of the (−)-menthone; total menthone concentration, 1000 μg ml^{-1}.

(A) SFE

UV [5 mAU

(B) SFE+C18

UV [5 mAU
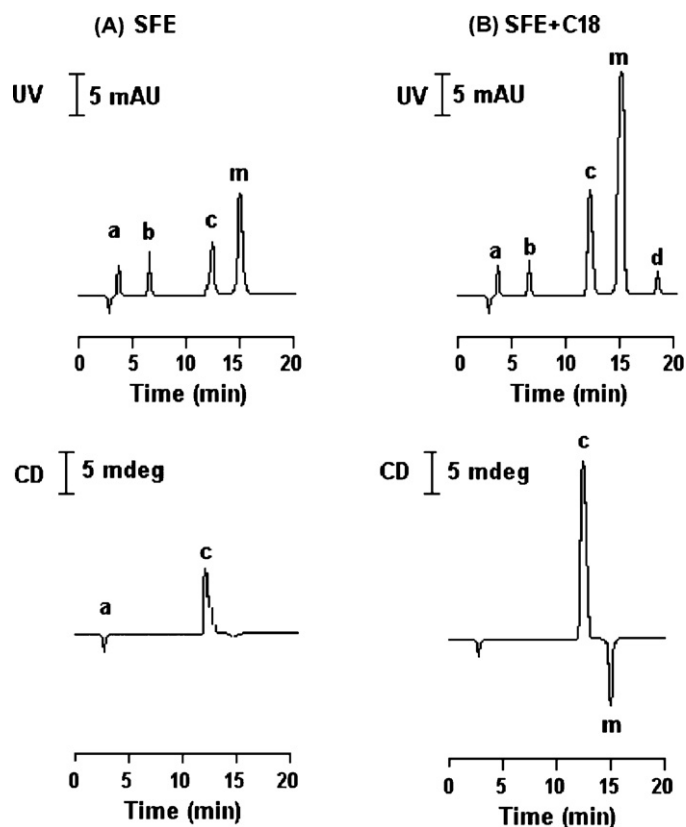

CD [5 mdeg

CD [5 mdeg

Fig. 6. Chromatogram for peppermint essential oil sample (sample S_1) before (A) and after (B) preconcentration step. Peak 'm' corresponds to menthone, whereas peaks a, b, c and d were not identified in this work.

Table 3
Determination of enantiomeric excess of (−)-menthone in natural and fortified peppermint essential oil samples.

Samples	Total conc. found/prepared[a] (g/l)	e.e. added (%)	e.e. found (%)	Recovery (%)
S_1	0.7	—	+87	—
S_{1F1}	0.7	+60	+62	103
S_{1F2}	0.7	+30	+32	107
S_{1F3}	0.7	0	+5	—
S_{1F4}	0.7	−80	−79	99
S_2	0.9	—	+45	—
S_{2F1}	0.9	+70	+73	104
S_{2F2}	0.9	+34	+34	100
S_{2F3}	0.9	+50	+52	104
S_{2F4}	0.9	−20	−18	90

[a] Concentration prepared for determination of e.e.

−90 and −100% from $1000\,\mu g\,ml^{-1}$ of menthone. The maximum anisotropy factor (g-factor) obtained for pure enantiomer was 0.017. The regression was found to be linear over the whole enantiomeric excess range.

In order to check the validity of the method, different synthetic samples ($1000\,\mu g\,ml^{-1}$ of menthone) were prepared using different enantiomeric excess levels of the (−)-menthone enantiomer. The results are reported in Table 2 and it can be seen that good agreement is obtained between added and found e.e. levels for this type of analytical system.

Two selected peppermint essential oil samples (S_1 and S_2) were chosen to demonstratie the real applicability of the proposed method. Fig. 6 shows a typical chromatogram obtained for sample S_1 extracted with SFE before (Fig. 6A) and after (Fig. 6B) the C18 preconcentration step. As can be seen in this figure, the dichroism signal did not appear in the supercritical extract (Fig. 6A), but was detected after preconcentartion with C18 (Fig. 6B). Menthone was detected and this compound is the prominent component in these samples. The samples were then spiked at different e.e. levels of (−)-menthone, while maintaining the total menthone concentration found in these samples. The results obtained for the determination of e.e. of (−)-menthone are shown in Table 3. As can be seen from the table, the spiked e.e. and the value determined are in good agreement and high recoveries were achieved (90–107%).

4. Conclusion

This study demonstrates that the development of a method, based on SFE-HPLC–CD detection, is of practical interest for the determination of menthone enantiomers in peppermint essential oil samples. A simple clean-up and effective preconcentration step with C_{18} adsorption cartridges eliminates matrix effects due to contaminants from supercritical extracts. The proposed methodology has the advantages of being rapid and precise and does not require the use of expensive chiral columns. For the first time, an HPLC method – with an achiral stationary phase and CD detection – has been applied to natural samples and can replace the classical HPLC approach (i.e. chiral stationary phase and UV detection).

References

[1] R. Klimek, Essential Oils, Light and Food Industry's Publishing, Warsaw, 1957, pp. 123–124.
[2] N. Galeotti, L.D.C. Mannelli, G. Mazzanti, A. Bartolini, C. Ghelardini, Neurosci. Lett. 322 (2002) 145.
[3] K. Hamasaki, K. Kato, T. Watanabe, Y. Yoshimurs, H. Nakazawa, A. Yamamoto, A. Matsunaga, J. Pharm. Biomed. Anal. 16 (1998) 1275.
[4] E. Lipka-Belloli, V. Glaçon, G. Mackenzie, D. Ewing, C. Len, C. Vaccher, J.-P. Bonte, J. Chromatogr. A 972 (2002) 211.
[5] H.Y. Aboul-Enein, I. Ali, G. Gübitz, C. Simons, P.J. Nicholls, Chirality 12 (2000) 727.
[6] A. Peter, A. Arki, E. Forro, F. Fülöp, D.W. Armstrong, Chirality 17 (2005) 193.
[7] C.J. Welch, M.H. Kress, M. Beconi, D.J. Mathre, Chirality 15 (2003) 143.
[8] S. Rudaz, J.-L. Veuthey, Chirality 11 (1999) 319.
[9] D. Sybilska, M. Asztemborska, J. Biochem. Biophys. Methods 54 (2002) 187.
[10] D.R. Bobbitt, S.W. Linder, Trends Anal. Chem. 20 (2001) 111.
[11] T. Taniguchi, N. Miura, S.-I. Nishimura, K. Monde, Mol. Nutr. Food Res. 48 (2004) 246.
[12] M.T. Reetz, K.M. Kuhling, H. Hinrichs, A. Deege, Chirality 12 (2000) 479.
[13] M. Lorin, R. el Delépée, J.P. Ribet, P. Morin, J. Chromatogr. A 1141 (2007) 244.
[14] C. Bertucci, V. Andrisano, V. Cavrini, E. Castiglioni, Chirality 12 (2000) 84.
[15] E. Bossu, V. Cotichini, G. Gostoli, A. Farina, J. Pharm. Biomed. Anal. 26 (2001) 837.
[16] M.R. Hadley, G.D. Jonas, Enantiomer 5 (2000) 357.
[17] K. Kudo, K. Iwaya, C. Yomota, S. Morris, M. Saito, Enantiomer 5 (2000) 369.
[18] M. Zougagh, M. Valcárcel, A. Ríos, Trends Anal. Chem. 23 (2004) 399.
[19] J.N. Miller, J.N.C. Miller, Statistics and Chemometrics for Analytical Chemistry, 3rd edition, Ellis Horwoord, 1993.